



HAL
open science

Proceedings of the 6th Plant biomechanics International conference

Bernard Thibaut

► **To cite this version:**

Bernard Thibaut. Proceedings of the 6th Plant biomechanics International conference. The 6th Plant biomechanics International conference, Nov 2009, Cayenne, French Guiana. 2009, Proceedings of the 6th Plant biomechanics International conference. hal-03590209

HAL Id: hal-03590209

<https://hal.science/hal-03590209>

Submitted on 26 Feb 2022

HAL is a multi-disciplinary open access archive for the deposit and dissemination of scientific research documents, whether they are published or not. The documents may come from teaching and research institutions in France or abroad, or from public or private research centers.

L'archive ouverte pluridisciplinaire **HAL**, est destinée au dépôt et à la diffusion de documents scientifiques de niveau recherche, publiés ou non, émanant des établissements d'enseignement et de recherche français ou étrangers, des laboratoires publics ou privés.



PROCEEDINGS OF THE
**SIXTH PLANT BIOMECHANICS
CONFERENCE**

*November 16th – 21st, 2009, Cayenne, French Guyana,
France*

*Published by
UMR EcoFoG, Campus Agronomique, BP 709,
F97310 Kourou, France*

Bernard Thibaut, Editor

December 21st 2009



Proceedings of the

Sixth Plant Biomechanics Conference

November 16th – 21st, 2009, Cayenne, French Guyana, France

Bernard Thibaut
Editor

Scientific Committee

Joseph Gril,	<i>CNRS - University Montpellier II, Montpellier, France;</i>
Meriem Fournier,	<i>AgroParis Tech, Nancy, France;</i>
Bruno Moulia,	<i>INRA - University Blaise Pascal, Clermont-Ferrand, France;</i>
Julian Vincent,	<i>Centre for Biomimetic and Natural Technologies, University of Bath, UK;</i>
George Jeronimidis,	<i>Centre for Biomimetics, Department of Engineering, University of Reading, UK;</i>
Hanns-Christof Spatz,	<i>Institute für Biologie III, University of Freiburg, Germany;</i>
Thomas Speck,	<i>Plant Biomechanics Group, Botanic garden, University of Freiburg, Germany;</i>
Frank Telewski,	<i>Michigan State University, East Lansing, MI, USA;</i>
Geoffrey Daniel,	<i>Swedish University of Agricultural Science Sweden;</i>
Lennart Salmén,	<i>STFI-Packforsk, Stockholm, Sweden;</i>
Hiroyuki Yamamoto,	<i>Laboratory of Bio-Material Physics, Nagoya University, Japan;</i>
Bernard Thibaut,	<i>CNRS – UMR EcoFoG, French Guyana, France</i>



Preface

This 6th Plant Biomechanics conference is hosted by French Guiana, a tiny part of the huge Amazonian forest, on the Guyana shield. French Guiana was a place where tree biomechanics research begins in the seventies in a close cooperation between French and Japanese scientists. Many participants to this conference made part of their work here in French Guiana and it is a pleasure to make the other discover this wonderful tropical rain forest.

As for the former conferences there will be papers dealing with all kind of plants and very different mechanical solutions at whole plant, organ or cell level. There is also a strong emphasis on useful material coming from plants and on bio-inspired solutions for engineering.

Some participants, old friends of the beginning, were actors of the five other PBM, but many young scientists and PhD come for the first time and this is good news for the future of our community. It is a pity that some of us cannot participate this time because of fund restrictions due to the economic crisis but they keep in contact and we will send them the proceedings of this conference.

I want to mention all the national or regional organizations that help us for the funding and the organization of PBM 2009, namely, AgroParisTech, CIRAD, CNES, CNRS, INRA, DRRT Guyane, IESG, IRISTA, IUFM, PUG, Région Guyane and UAG.

I want also to give a very special thank to Laetitia and Julien Ruelle. Without the energy of Laetitia this conference will not have been possible and without the expertise of Julien, these proceedings will not be under your eyes.

Thanks also to all the colleagues and PhD students who were there when needed for so many help in such an adventure.

And last, thanks to the members of the scientific committee for their reactivity and efficient reviewing of the text here after.

Have a good reading.

Bernard THIBAUT
Directeur de recherche au CNRS
Directeur de l'UMR Ecofog

Contents (titles are hyperlinks to papers)

1. Physics of growth	1
<i>Anisotropic and isotropic growth of the apical meristem</i> Yves Couder, Francis Corson, Olivier Hamant, Arezki Boudaoud and Jan Traas	2
<i>Leaf inclination and light interception in the sunflower (<i>Helianthus annuus</i> L.). Importance of the petiole's mechanical and structural properties</i> Luis F. Hernández	3
<i>High-resolution kinematics of gravitropic movement reveals an oscillatory dynamics. A key for efficient performance?</i> Renaud Bastien, Stéphane Douady and Bruno Moulia	11
<i>Mechanosensing quantitatively controls diameter growth and level of expression of PtaZFP2 mechanosensitive gene in poplar</i> Ludovic Martin, Catherine Coutand, Nathalie Leblanc-Fournier, Mélanie Decourteix, Catherine Lenne, Bruno Moulia and Jean-Louis Julien	19
<i>Contact Mechanics at the Insect-Plant Interface</i> Stanislav N. Gorb	27
<i>The influence of the wall contact angle on gas bubble behaviour in xylem conduits under tension and possible consequences for embolism</i> Wilfried Konrad and Anita Roth-Nebelsick	32
<i>Cytoskeletal control of cellular shape and directional growth in pollen tubes</i> Firas Bou Daher and Anja Geitmann	40
2. Modelisation	46
<i>Modelling collapse of xylem pine needles: effects of tracheid geometry and tracheids' arrangement</i> George Jeronimidis, Catherine Coutand, Nicole Brunel and Hervé Cochard	47
<i>Multi-scale modeling for moisture transport in wood</i> Dominique Derome, Wolfgang Zillig and Jan Carmeliet	53
<i>A scaling law reveals the control of tree vibration modes through tree architecture and branch allometry</i> Mathieu Rodriguez, Emmanuel de Langre and Bruno Moulia	59
<i>Free Coiling in Tendril-Bearing Plants</i> Annika Eberle, Kenny Quinn and Lori Bassman	67

<i>Evaluation of growth stress profiles in tree trunks: comparison of experimental results to a biomechanical model</i> Delphine Jullien, Tancrede Alméras, Miho Kojima, Hiroyuki Yamamoto and Pierre Cabrolier	75
<i>Comparing shapes for stress homogenization in nature and technique</i> Iwiza Tesari and Claus Mattheck	83
<i>Modelisation of the trunk daily diameter variation during wet season in a neotropical rain forest of French Guiana</i> Yamina Aimene, Clément Stahl, Damien Bonal and Bernard Thibaut	89
<i>Modelling surface growth for tree biomechanics</i> Thomas Guillon and Thierry Fourcaud	95
3. Plant and fluid mechanics	100
<i>Plant mechanical interactions with air and water</i> Emmanuel de Langre and Frédérick Gosselin	101
<i>Resistance of red mangrove (<i>Rhizophora mangle</i> L.) seedlings to extraction.</i> Sophie D. Boizard, and Stephen J. Mitchell	110
<i>Plant motion in heterogeneous landscapes: a coupled flow-tree simulation study</i> Yves Brunet, Sylvain Dupont, Pascal Roux and Damien Sellier	116
<i>Mechanical advantage of epidermal cells over stomatal guard cells, estimated from transient changes of leaf-level stomatal conductance for</i> Anu Sober and Julia Shilina	121
<i>Tapering of vascular elements from roots to distal shoots in <i>Pinus sylvestris</i>, <i>Picea abies</i> and <i>Betula pendula</i></i> Anna Lintunen and Tuomo Kalliokoski	122
<i>Modelling waving crops using Large-Eddy Simulation</i> Sylvain Dupont, Frédérick Gosselin, Charlotte Py, Emmanuel de Langre, Pascal Hémon and Yves Brunet	131
<i>Continual modeling of water uptake by plant roots</i> Alexander A. Stein, S.A. Logvenkov and E.N. Yudina	140
<i>Wave propagation in the conducting systems of plants</i> Natalya N.Kizilova	148
<i>The mirror effect on xylem and phloem radial conduction</i> Veronica Angyalossy, Guillermo Angeles and Carolina Madero-Vega	156

<i>Diversity of hydraulic and biomechanical wood properties in 22 tropical rainforest species of French Guiana</i> Juliette Boiffin, Sandra Patino, Meriem Fournier, Sandrine Isnard, and Tancrede Alméras	163
<i>The Effects of Modified Lignin Monomer Ratios on Hydraulic Conductivity and Resistance to Embolism in Hybrid Poplar (P. tremula x P. alba)</i> Jeffrey A. Pierce, Frank W. Ewers, Jameel Al-Haddad, and Frank W. Telewski	164
<i>Hydraulic conductance of developing shoots of aspen</i> Anu Sober and Julia Shilina	168
4. Biomechanics aspects of plant development	169
<i>Study of the ultrafast trap of an aquatic carnivorous plant</i> Philippe Marmottant, Olivier Vincent and Catherine Quilliet	170
<i>Effect of fracture behaviour of crystalline plant waxes on insect pad contamination</i> Elena V. Gorb, Feodor M. Borodich and Stanislav N. Gorb	176
<i>Biomechanics of fern spores discharge: the sporangium opening</i> Xavier Noblin, Jared Westbrook, Nicolas Rojas, Médéric Argentina and Jacques Dumais	179
<i>A Biomechanical Study on Bursting Plant Fruit and Its Optimality</i> Jiro Sakamoto, Yasuhiro Endo and Eichiro Kinoshita	187
<i>Plant leaves as attachment devices: an experimental approach</i> Friederike Gallenmüller, Georg Bauer, Kirk-René Kubinski, Dagmar Voigt Stanislav Gorb and Thomas Speck	194
<i>The Unfolding Mechanism of Seed Capsules in Stone Plants</i> Matthew J. Harrington, Friedrich Ditsch, Peter Fratzl, Christoph Neinhuis and Ingo Burgert	202
<i>Mechanics and structure of the attachment system of English Ivy (Hedera helix L.)</i> Björn Melzer, Tina Steinbrecher, Robin Seidel, Oliver Kraft, Ruth Schwaiger and Thomas Speck	205
<i>Adhesive properties of tentacles of the protocarnivorous plant Roridula gorgonias and the mechanism of adhesion prevention in the mutualistic miridbug Pameridea roridulae</i> Dagmar Voigt and Stanislav Gorb	211
<i>Biomechanics of isolated cherry tomato fruit cuticles during growing</i> Laura España, Eva Domínguez, Jesús Cuartero and Antonio Heredia	212

5. Micromechanics **217**

Making shapes - mechanical principles of plant cell growth
Anja Geitmann 218

Towards nanomechanical characterization of developing wood cell walls at different maturation steps
Karl Bytebier, Olivier Arnould, Richard Arinero,
Bruno Clair and Tancrède Alméras 228

Stress of cellulose network in tension wood is induced shortly after cellulose deposition
B. Clair, T. Alméras, G. Pilate, D. Jullien, J. Sugiyama and C. Riekkel 236

Silica distribution in wheat awns to improve dispersal
Rivka Elbaum 244

A new interpretation of plant cell growth mechanics: Loss of stability and cell wall stress-relaxation.
Philip M. Lintilhac and Chungfang Wei 251

Structural and mechanical design of tissue interfaces in monocotyledonous plants
Markus Rüggeberg, Thomas Speck and Ingo Burgert 259

Comparison of Cell Wall Mechanical Properties of some Arabidopsis thaliana Mutants
Robert Palin, Jeremy Pritchard and Colin Thomas 265

Impact of selective extractives removal on micro and macromechanical properties of woody hemp core (chènevotte)
Rahime Bag, Johnny Beaugrand, Patrice Dole and Bernard Kurek 273

Is interlocked grain an adaptive trait for tropical tree species in rainforest ?
Pierre Cabrolier, Jacques Beauchêne and Bernard Thibaut 279

Ultrasonic device for the imaging of green wood
Loïc Brancheriau, Philippe Gallet, Patrice Thauhay and Philippe Lasaygues 285

Occurrence of the gelatinous cell wall layer in tension wood of angiosperms
Julien Ruelle, Bruno Clair, Nick Rowe and Hiroyuki Yamamoto 289

6. Biomechanics of trees **296**

Origins of abnormal behaviors of gelatinous layer in tension wood fiber: A micromechanical approach
Hiroyuki Yamamoto, J. Ruelle, Y. Arakawa, M. Yoshida, B. Clair and J. Gril 297

<i>Experimental analysis of the formation of tension wood induced by gravity for three mature beech trees on a 25 years duration.</i> Adélin Barbacci, Thiéry Constant, Vincent Magnenet, Gérard Nepveu and Meriem Fournier	306
<i>The gravitropic control of woody stems orientation: biomechanical parameters involved and consequences for stem allometry</i> Tancrede Alméras and Mériem Fournier	314
<i>Root growth in mechanically stressed environment: In situ measurements of radial root forces measured by a photoelastic technique</i> Evelyne Kolb, P. Genet, L.E. Lecoq, C. Hartmann, L. Quartier and T. Darnige	322
<i>Is the branch of Viburnum odoratissimum var. awabuki reaction wood? Unusual eccentric growth and various distributions of growth strain</i> Yue Wang, Joseph Gril and Junji Sugiyama	328
<i>Early selection of stem straightness in pinus pinaster ait based on the straightening process</i> Rosario Sierra-de-Grado, Valentín Pando, Pablo Martínez-Zurimendi, Alejandro Peñalvo, Esther Báscones and Bruno Moulia	335
<i>On stress generation mechanisms in compression wood and tension wood of trees</i> Ingo Burgert and Peter Fratzl	343
<i>Gravitropism plays a key role in the diversity of tree ecological strategies at the advance regeneration stage. A case study in the French Guiana tropical rainforest.</i> Meriem Fournier, Gaelle Jaouen, Emmanuel Duchateau, Bruno Clair, Catherine Coutand and Tancrede Alméras	349
<i>An Investigation on the Growth Strains and Stresses of Populus deltoides in north of Iran</i> Habibollah Khademi Eslam and Arash Faraj Pour	350
7. Biomimetics	356
<i>From stems to sticks - what can we learn for biomimetics from natural fibre-reinforced structures?</i> Tom Masselter and Thomas Speck	357
<i>Fast self-repair mechanisms in plants: biological lattices as role models for the development of biomimetic self-healing, mechanically loaded polymers</i> Georg Bauer, Anke Nellesen, Andreas Sengespeick and Thomas Speck	367
<i>Exploring the innovation potential of biomimetics for novel 3D micro- and nanoelectromechanical systems (MEMS and NEMS)</i> Gebeshuber I.C., Stachelberger H. and Majlis B.Y.	374

<i>Shape Optimization – Biomimetic or Naturemimetic?</i> Claus Mattheck and Roland Kappel	382
<i>Abstraction of plant movements for deployable structures in architecture</i> J. Lienhard, S. Poppinga, S. Schleicher, T. Masselter, T. Speck and J. Knippers	389
<i>Plant stems as building material for living plant constructions</i> Ferdinand Ludwig, Gerd de Bruyn, Marc Thielen and Thomas Speck	398
<i>Impact resistance of hierarchically structured fruit walls and nut shells in view of biomimetic applications</i> Robin Seidel, Andreas Bührig-Polaczek, Claudia Fleck and Thomas Speck	406
<i>Biomimetics in architecture – inspiration from plants</i> Petra Gruber	412
8. Ecology and Evolution	420
<i>Geometry of folds, geometry of leaves</i> Etienne P. Couturier, Sylvain Courrech Dupont and Stéphane Douady	421
<i>Modelling secondary growth stresses in recent and fossil plants</i> Tom Masselter and Thomas Speck	431
<i>Chiral structure in petiole vascular bundles</i> Derek G. Gray and Joshua G. Lucate	439
<i>Ontogenetic variations in morphology and attachment strength of permanent attachment pads of species of Parthenocissus</i> Tina Steinbrecher, Oliver Kraft, Thomas Speck, Björn Melzer and Ruth Schwaiger	444
<i>Using vegetation to stabilize steep slopes in Southern China: root biomechanics as a factor in the choice of species</i> Murielle Ghestem, Alexia Stokes, Kunfang Cao, Wenzhang Ma and Jianlei Xie	450
<i>Multi-stemming and mechanics of trees and shrubs growing along avalanche paths</i> François-Xavier Mine, Alexia Stokes and Loic Brancheriau	456
<i>Drag of red mangrove (<i>Rhizophora mangle</i> L.) seedlings in water.</i> Sophie D. Boizard and Stephen J. Mitchell	463
<i>Evolution of the mechanical architecture during domestication in manioc (cassava)</i> Nick Rowe, Léa Ménard, Bruno Clair, Gilda Mühlen and Doyle McKey	469

<i>Wood chemical and mechanical responses to modified lignin composition in upright and inclined hybrid poplar</i> Jameel Al-Haddad, Shawn Mansfield and Frank W. Telewski	477
<i>Fire resistance of trees and bark heat insulation as concept generators for biomimetic insulation and fire-stopping materials</i> Georg Bauer, Thomas Speck, Andreas W. Liehr and Olga Speck	482
<i>On the characterization of mechanical properties of porous and heterogeneous bio- and bioinspired materials</i> Klaus G Nickel	487
<i>Posture control of Fagus silvatica L and Acer pseudoplatanus L. in natural stands after thinning</i> Paul Igor A. Hounzandji, Meriem Fournier, Thiéry Constant and Catherine Collet	488
9. Mechanics of biomaterials	489
<i>Nonlinear elastic and moisture dependent behavior of wood: a first attempt to an adequate thermomechanical modeling</i> Jan Carmeliet, Robert Guyer and Dominique Derome	490
<i>The viscoelastic properties of some Guianese woods</i> J. Paul McLean, Olivier Arnould, Jacques Beauchêne and Bruno Clair	498
<i>Influence of the extractives of selected extraneous woods on the equilibrium moisture content - chemical and physical properties</i> Peter Niemz, Tamás Hofmann, Levente Albert, Tamás Rétfalvi and Rudolf Popper	505
<i>Structural and Functional Differences Among Transgenic Hybrid Poplar Lines with Varying Lignin Contents</i> Barbara Lachenbruch, Steven L. Voelker, Frederick C. Meinzer and Steven H. Strauss	514
<i>Yew wood: Axial elasticity, structure-function relationships and possible biomechanical background</i> Daniel Keunecke and Peter Niemz	522
<i>Soil property effects on the natural durability, extractive content and colour of teak (Tectona grandis L.f) wood in Togo</i> Adzo Dzifa Kokutse, N. Amusant, N. Boutahar and G. Chaix	529
<i>Mechanical damping of wood as related to species classification: a preliminary survey</i> Iris Brémaud, Kazuya Minato and Bernard Thibaut	536

*About structural determinants of the diversity of vibration properties
of ten tropical hardwoods*

Jana Dlouhá, Tancreède Alméras, Bruno Clair and Joseph Gril

543

Author index

X

1. Physics of growth

Anisotropic and isotropic growth of the apical meristem

Yves Couder*, ***Francis Corson*****, ***Olivier Hamant******, ***Arezki Boudaoud*****, ***Jan Traas******

**Matière et systèmes complexes
Université Paris 7 Denis Diderot, CNRS UMR 7057,
Batiment Condorcet, 10, rue Alice Donon et Léonie Duquet, 75013 Paris*

***Laboratoire de Physique Statistique
Ecole Normale Supérieure, 24, rue Lhomond, 75231 Paris Cedex 05*

****Laboratoire de Reproduction et Développement des Plantes,
ENS Lyon, 46, allée d'Italie, 69364 Lyon Cedex 07,*

Abstract

The growth of vascular plants is characterized by its anisotropy, obvious at macroscopic scale in the growth of the stems and that of the roots. It is also observed at the cellular scale in the orientation of the cortical microtubules, that of the microfibril deposition in the cell walls and in the preferential directions of cell division. In a recent work⁽¹⁾ it was shown that the orientation of the cortical microtubules was sensitive to externally applied mechanical stresses. This suggests that in the unstressed situation the anisotropy can be self-induced, the internal mechanical stresses orienting the microtubules.

In this context it is interesting to observe the effect of the suppression of the microtubules. The effect of oryzalin, an inhibitor of microtubule polymerization, on the development of the apical meristem of *Arabidopsis thaliana* is revisited. While cell divisions are entirely suppressed, the growth of meristematic regions is sustained, and the cells become huge. We analyse two effects.

- Each of the existing organs now grows isotropically and tends to become spherical.
- Correlatively, the geometry of the cells becomes similar to that of the bubbles in a soap froth.

A theoretical model is presented, in which a cellular structure evolves through the plastic yielding of its walls under turgor pressure. If a cell division process is included, the appearance of the structure is that of a normal tissue. If not, a "cell froth" very similar to that observed experimentally is obtained. In both the experimental and numerical simulations the same evolution of the vertices is observed where all angles tend towards 120°. To meet this condition a curvature of the cell walls appear, the cells with a number of sides smaller than 6 becoming convex while those with a larger number of sides become concave. In soap froth this generates a shrinking of the former and an expansion of the latter. This coarsening process is absent in the living tissue, suggesting constraints on the mechanisms of growth regulation.

(1) O. Hamant, M. Heisler, H. Jönsson, P. Krupinski, M. Uyttewaal, P. Bokov, F. Corson, P. Sahlin, A. Boudaoud, E. Meyerowitz, Y. Couder & J. Traas, **Mechanics of morphogenesis at the shoot apical meristem of *Arabidopsis thaliana*: an interdisciplinary view**, *Science*, 322, 1650-1655, (2008)

Leaf inclination and light interception in the sunflower (*Helianthus annuus* L.). Importance of the petiole's mechanical and structural properties

Luis F. Hernández^{1,2}

¹ Lab. de Morfología Vegetal, Dept. de Agronomía, Universidad Nacional del Sur (UNSur), Bahía Blanca, 8000 and ² CIC PBA, La Plata, 1900. Argentina.

Abstract

The relationships between leaf biomass and morphology (lamina area and petiole and lamina inclination), petiole's mechanical and structural properties and the vertical light gradient inside the crop's canopy were studied in field grown sunflower (*Helianthus annuus* L.) plants, maintained at an optimum soil water and mineral status.

The objective of this work was to study the role of petiole's mechanical properties on foliar inclination, and the relationships between leaf and petiole angle variation patterns along the canopy and leaf and petiole biomass partitioning and morphology.

At flowering, incident photosynthetic active radiation (PAR) was measured at the top of the canopy and on individual leaves using a quantum sensor. The fraction of direct incident radiation that passes through the canopy reaching each individual leaf was then calculated.

Individual petiole and lamina inclination angles (ia_{Petiole} and ia_{Lamina} respectively) were measured from sequential digital images taken from rotated plants and a stationary camera. Petiole length and lamina area were measured after detaching the leaves from each plant.

Leaves were separated in petiole, lamina and main veins, and their dry biomass obtained. Petiole transverse cuts stained with acid fluoroglucinol were used to measure the relative area occupied by lignified and fibrous tissue.

The petiole's structural Young's modulus (E_{Petiole}) for different leaves was calculated from a three-point bending test performed in petiole segments about 4.0 to 8.0 cm long. Petiole flexural stiffness (EI_{Petiole}) was calculated using elementary beam theory for homogenous materials. Intercepted PAR in the canopy for individual leaves decreased basipetally. The ia_{Petiole} increased acropetally from -9.0° to $+60.0^\circ$ while the ia_{Lamina} increased basipetally from $+1.0^\circ$ to -60.0° in concordance with increments in the intercepted PAR. Petiole specific weight (g/cm^2) did not change with leaf position whilst lamina specific weight decreased acropetally. Main veins dry weight increased basipetally. E_{Petiole} and EI_{Petiole} increased acropetally. The relationship between intercepted PAR and the ratio biomass dry weight_{Petiole}/biomass dry weight_{Lamina} was positively correlated. The relative area occupied by supporting tissue was significantly higher in upper petioles than in lower ones.

These results suggest that, in order to optimize the interception of incident PAR, the sunflower plant invests more energy in differentiating supporting tissues in the petioles of the upper canopy resulting the higher canopy strata in a preferentially planophyllous/erectophyllous leaf architecture.

Introduction

It is known that plants can maximize canopy light interception by increasing both leaf area or the efficiency in the way each unit of leaf area intercepts light [1, 2].

It has been found that the interception efficiency of both direct and diffuse irradiance increases in leaves with horizontal laminae [planophyllous leaf architecture; 3, 4].

As leaves adapt to a light gradient inside the canopy, not only the inclination angles, but also the morphology, anatomy, size and mass of their petioles and laminae are modified. Leaf inclination angles generally decrease with increasing leaf age. This is generally attributed to increases in both lamina weight and area [5] that can alter the bending momentum exerted on the petiole, changing lamina and/or petiole inclination angles [6, 7].

Petiole mechanical properties, as a result of changes in its material properties, and/or by modifications in the cross-sectional shape and dimensions [8] may then change along the vertical light gradient, allowing modifications of the lamina inclination angle [7, 8]. There is evidence that petioles are stiffer at higher irradiance [7, 9] as the result of larger biomass investments in supporting tissue [8, 10].

In the sunflower crop, biomass production and yield are positively coupled with solar radiation intercepted by the canopy [11]. If an increase in yield is expected after culturing sunflower in narrow rows or high densities [12], then, fixing *a priori* canopy parameters that could be associated with a better solar radiation interception is necessary to redesign the plant's ideotype.

The aim of this work was to study in field grown sunflower plants the role of petiole mechanical properties on foliar inclination, and the relationships between leaf and petiole angle variation patterns along the canopy and leaf and petiole biomass partitioning and morphology.

Material and methods

Sunflower (*Helianthus annuus* L.) plants (hybrid cultivar Macón, Syngenta Seeds, Argentina), were grown at the experimental field of the Agronomy Department-UNSur, Bahía Blanca, Argentina (Latitude S, 38°45'; Longitude W, 62°11'). The soil was a Typic Ustipsamment [13,14]. At 4-leaf stage [14] plant density was adjusted to 5.6 plants/m² (Fig. 1A). The crop was managed according to recommended conventional agronomical practices. Weeds and insects were adequately controlled. Soil water content and mineral nutrition were maintained at optimum levels by drip irrigation and by fertilization (NPK: 30-30-30; 80 kg/ha) at sowing and at anthesis [14].

Before first anthesis [14] a batch of plants were preselected for uniform size and developmental stage. Using a quantum sensor (LI-COR, NE, USA) PAR was measured at noon in different leaves in six of these selected plants (n=6) ten days before and at anthesis. Being the maximum incident PAR for the topmost leaf 100%, then the fraction of incident PAR (fIPAR) for each leaf inside the canopy was calculated [15]. fIPAR readings for both developmental stages were averaged (Fig. 2A).

Following the second PAR measurement and at predawn the selected plants were removed one at a time with a shovel from the experimental planting site retaining almost 90% of the root plate [soil-root system close to the base of the stem; 16] and immediately transferred to a 15-L plastic bucket containing tap water. The submerged soil-root system allows to keep the whole plant in a vertical position while maintaining a short-time optimum leaf water status (Fig. 1B). A 5.0 Mpixel digital camera mounted on a tripod was located at 7 m from the sampled plant pointing at its centre and operated by an assistant. The plant was then rotated clockwise 360° around its own stem at 20° intervals and three high resolution pictures of the whole plant per rotating position (center, top and bottom) were taken. Time spent since each plant was removed until the last picture was taken did not exceed 100 s.

Thereafter, all leaves for each plant were labeled, removed, packed in wet tissue paper, put in a plastic bag and transported immediately to the laboratory for biomechanical and morphological measurements.

In the laboratory each leaf lamina was quickly scanned using a desktop scanner. Afterwards the area of each leaf (Fig. 2B) was measured on the scanned images using the software *ImageJ* [17].

Leaf samples were separated with a razor blade in petiole, whole lamina and laminar tissue with the main veins removed, oven-dried at 70°C for 48 h and dry biomass of all leaf parts obtained (Fig. 3D).

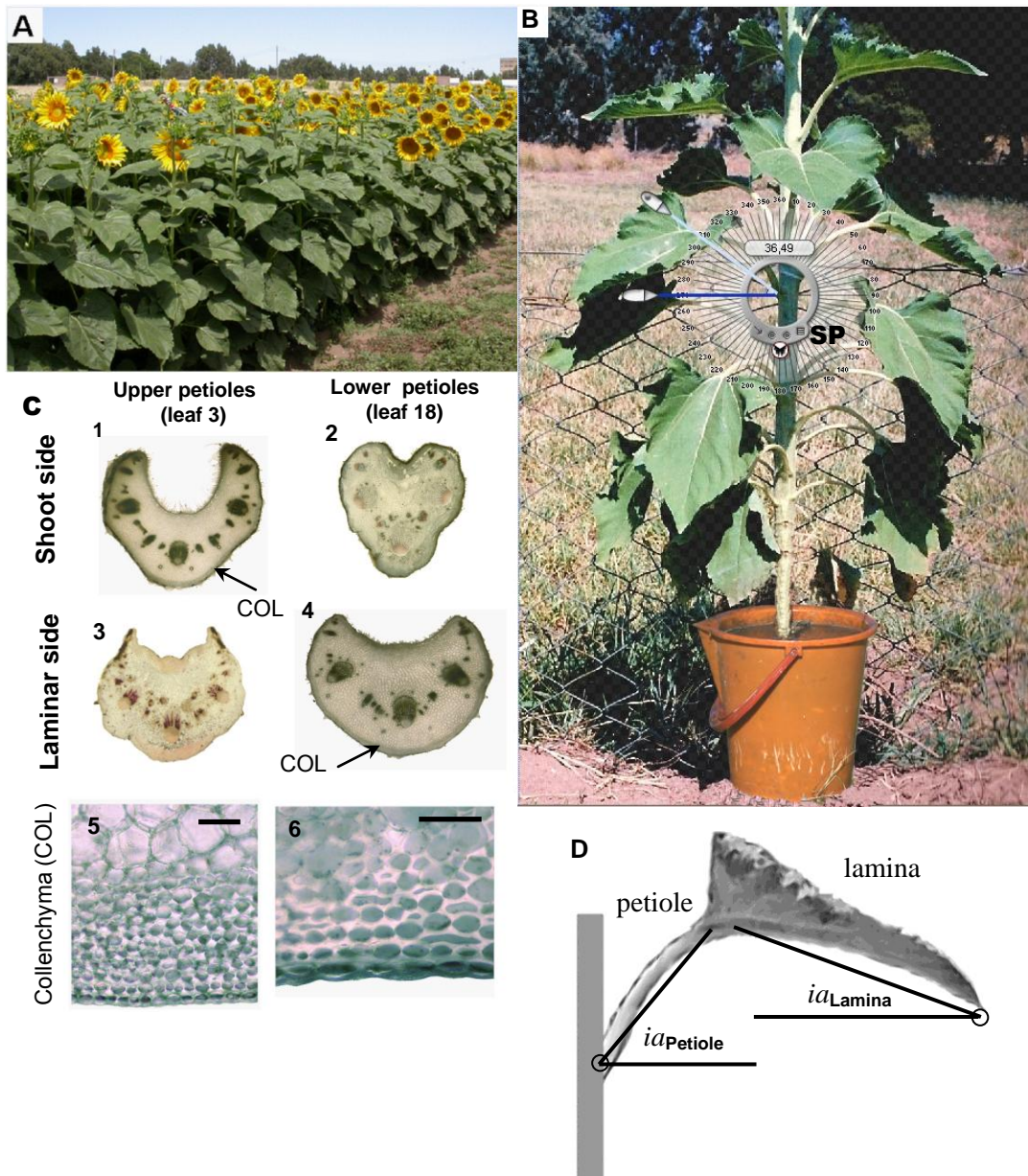


Fig. 1. A. Panoramic view of the crop at anthesis, when plant sampling leaf petiole and lamina angles measurement and biomechanical analysis were done. B. Plant removed from the planting site with the root system placed in a bucket and ready to start the photographic record. Inserted in the image is a schematic detail showing the criteria used to measure the inclination angles of the petiole under the environment of the software Screen Protractor (SP) C. Petiole transverse cuts for leaves 3 (upper) and 18 (lower) showing the anatomy and distribution of supporting tissues (COL: collenchyma). Note the increased number of collenchymatous layers in upper petioles (Fig. C5) than in lower ones (Fig. C6). Bars: C₁₋₄ = 5.0 mm; C₅₋₆ = 150 μ m. D. Estimation of petiole (ia_{Petiole}) and lamina (ia_{Lamina}) inclination angles from digital images of each plant's leaf. Petiole's inclination angle was defined as the angle between the points of petiole attachment to the shoot and lamina attachment to the petiole. Lamina inclination angle was measured at the fall line of the lamina.

Digital micrographs of transverse hand cuts of the petiole for leaves at two canopy levels (upper and lower) stained with acid phluoroglucinol [18] to visualize lignified tissue, were used to calculate the relative area occupied by different biostructural components, mainly parenchymatic, vascular and supporting tissue (Fig. 1C; Table 1).

Petiole specific biomass (dry biomass per unit volume and per transverse surface area) and dry matter concentration (dry biomass per unit volume) were calculated from petiole dry mass, length, and area of cross-sections. Lamina specific biomass (dry biomass per unit of lamina surface area) was also calculated.

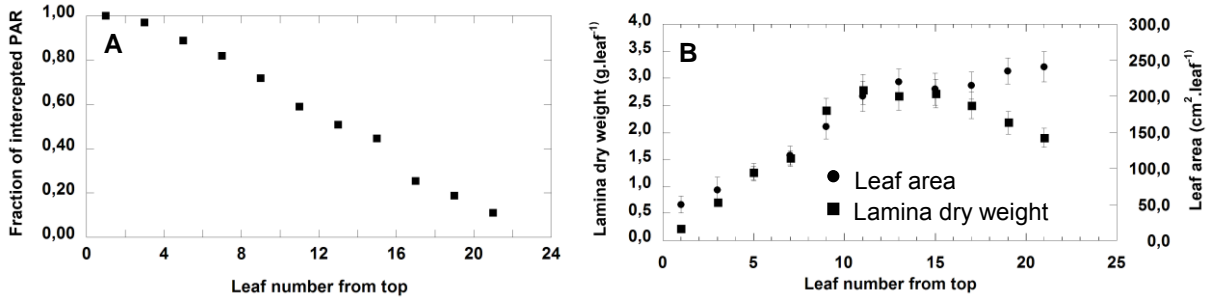


Fig. 2. A. Fraction of incident PAR ($\mu\text{mol}/\text{m}^2/\text{s}$) measured at each leaf level with a quantum sensor. B. Individual leaf mass and leaf area in the plants used in this work. Bars for each point (mean of $n=6$): $\pm 1\text{S.E.}$

The Young's elastic modulus of the petioles [E_{Petiole} ; 8] was calculated using a three-point bending method as described in [19]. Lacking at this stage of a reliable model to approximate the load of lamina on the petiole [7, 8], E and I were not measured and calculated for the lamina. Sections of the medium part of the petiole (4 cm from upper leaves to 8 cm from lower leaves) were placed horizontally over two supports that were 2 to 4 cm apart. Vertical applied forces (F , N) and resulting deflections (δ , m) were recorded using a testing machine as described in [20]. Young's modulus was calculated as follows [21]:

$$E_{\text{Petiole}} = (FL^3)/48 \delta I_{\text{Petiole}}$$

where L is the length between the supports (m) and I_{Petiole} the axial second moment of area (m^4) [21]. For all leaves I_{Petiole} was calculated from the petiole cross-sectional dimensions assuming it was a sector of a circular ring (see Fig. 1C) :

$$I_{\text{Petiole}} = (\pi/8) (R^4 - r^4) \text{ (See Fig. 3.3 in [8])}$$

For R , the radii of a laterally depressed cylindrical petioles (see Fig. 1C1-4) was estimated using a digital caliper as an average of three perpendicular measurements.

The flexural stiffness of the petiole was calculated as the product of E_{Petiole} and I_{Petiole} [MN m^2 ; 8, 22]. The petiole and lamina inclination angle (ia_{Petiole} and ia_{Lamina} respectively; Fig. 1D) for each leaf of each plant was obtained using the digital images of the rotated plants registered as described above (Fig. 1B) using the software *Screen Protractor* (Iconico Inc.; <http://www.iconico.com/protractor/>). The 3° to 4° parallax error generated in each picture between the upper and lower ends of each plant was corrected for each reading of lamina or petiole inclination angle straightening each set of three pictures per rotating position with the software *PTGui* (New House Internet Services B.V.; <http://www.ptgui.com/>). Linear regression analysis between different parameters were performed using the software *Kaleidagraph v.4.1* (Synergy Software).

Results and discussion

The upper leaves had shorter petioles (Table 1). These petioles also had a higher Young's elastic modulus (Fig. 3A; Table 1).

There was a continuous vertical light gradient along the plant canopy (Fig. 2A). The ai_{Petiole} increased acropetally (more PAR intercepted) from -9° to $+60^\circ$ while the ai_{Lamina} increased basipetally from $+1^\circ$ to -60° (Fig. 3B). The petioles specific biomass ($B_{\text{spPetiole}}$) did not change along the canopy

levels while the lamina specific biomass ($B_{spLamina}$) decreased acropetally (Fig. 3C). Main veins biomass increased basipetally (Fig. 3D). Magnitudes of $E_{Petiole}$ and $EI_{Petiole}$ increased acropetally (Fig. 3A,E). The relationship $B_{spcPetiole}/B_{spcLamina}$ was positively correlated with the fIPAR (Fig. 3F) being significantly higher from leaf 7 upwards (Fig. 3F).

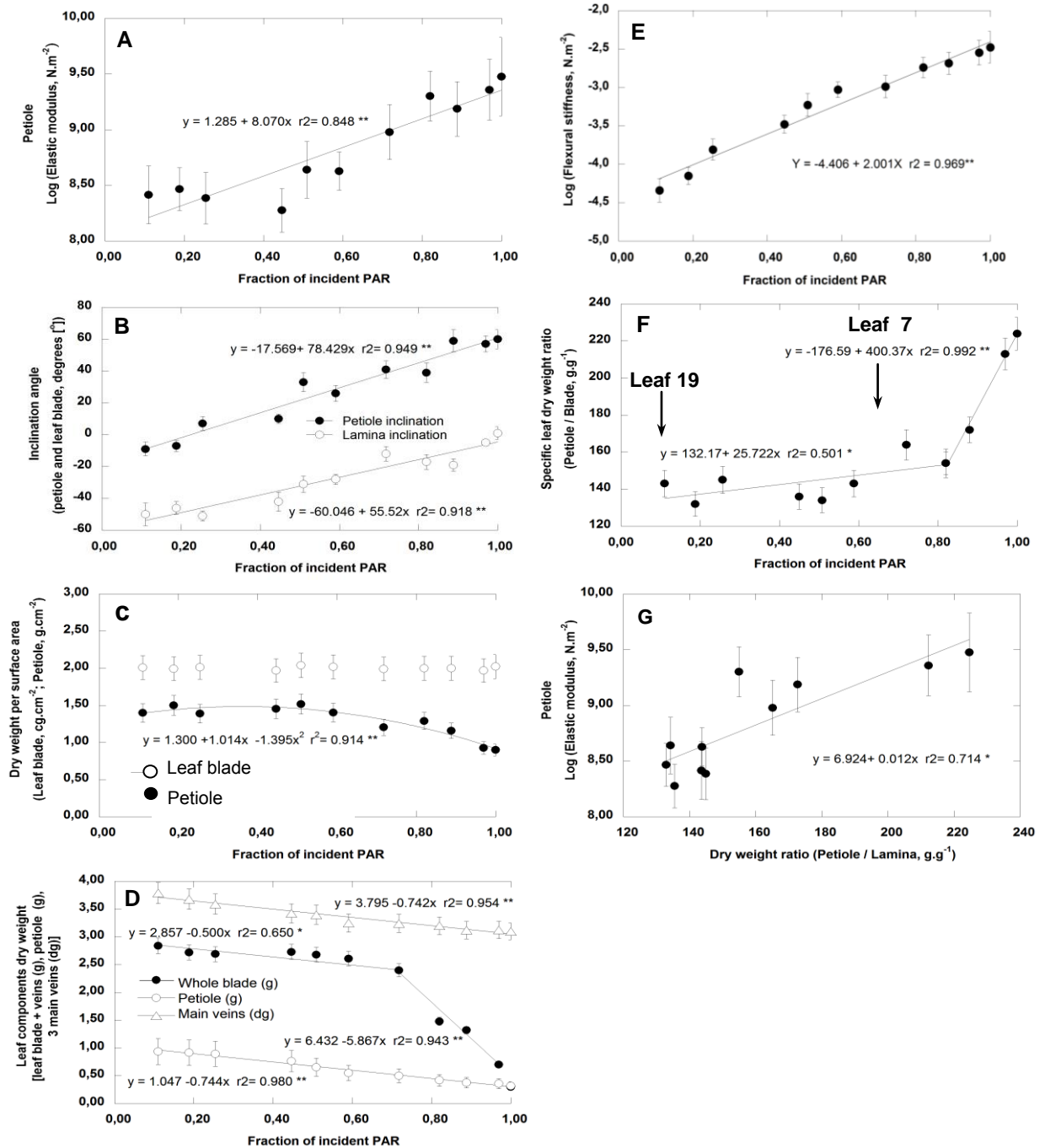


Fig. 3: A. Log of $E_{Petiole}$ vs. fIPAR; B. Lamina and petiole inclination ($^{\circ}$) vs. fIPAR; C: Lamina and petiole specific biomass vs. fIPAR; D: Biomass of different leaf components vs. fIPAR; E: Log of $EI_{Petiole}$ vs. fIPAR; F: relationship between the petiole/ lamina specific biomass vs. fIPAR; G: Log of $E_{Petiole}$ vs. the relationship petiole biomass/lamina biomass. Bars for each point (mean of $n=6$): $\pm 1S.E.$

A positive correlation was also found between lamina and petiole inclination angle and the fIPAR. However, the leaves in the upper canopy were more upwardly inclined, whilst those in the lower canopy were bent downwards (Fig. 3B). This suggests that the light interception efficiency did decrease with decreasing light availability towards the lower canopy strata, allowing to speculate that

a limited investment of biomass in mechanical support was taking place in lower petioles (Fig. 3G). In fact, a higher proportion of supporting tissue (collenchyma and sclerenchyma) in transverse sections of upper petioles was observed in comparison with the lower ones (Fig. 1C).

On the other hand it is known that the mechanical properties of petioles and other plant tissues can be also determined by their hydrostatic pressure [8] and there is consistent evidence that water stress in sunflower increases with increasing height in the canopy [23, 24, 25] driving to a lower water potentials in the intensively transpiring upper canopy leaves and hence reducing the elastic modulus of all involved tissues, lamina and petiole [8, 26]. Even though leaf water potential was not measured in this work, a comparison of number and diameter of the xylem vessels between the upper and lower petioles did not show relevant differences. Knowing that the lamina surface area increases downwards this observation suggests that tissue turgor in the lower leaves as well as the tissue elastic modulus could not be maintained at the same magnitude as in upper leaves. This could also explain the higher values of elastic modulus of petioles from the upper canopy leaves (Table 1, Fig. 1A).

Table 1. Main anatomical parameters of the petioles of leaves number 3 (upper canopy) and 18 (lower canopy) which can be associated with its mechanical properties and that were used to calculate its flexural stiffness (EI_{Petiole}). For the petioles located at the intermediate canopy, E was extrapolated assuming a linear relationship. For each column, values followed by different letters indicate significant differences at $P < 0.05$. (): Fibers, collenchyma and lignified tissue calculated from images of petiole's transverse cuts (See Fig 1C 1,4); P: petiole.*

	P length (mm)	P Log E (N/m ²)	Petiole transverse section (mm ²)		Transverse section with supporting tissue (*) (%)	
			Shoot side	Laminar side	Shoot side	Laminar side
Upper Petiole (leaf 3)	6.3±0.9 <i>a</i>	9.39±0.3 <i>a</i>	64.7±9.1 <i>a</i>	18.8±12.3 <i>a</i>	23.1±10.9 <i>a</i>	26.9±9.8 <i>a</i>
Lower Petiole (leaf 18)	19.8±1.3 <i>b</i>	8.26±0.4 <i>b</i>	96.8±11.2 <i>b</i>	66.5±10.7 <i>b</i>	14.1±13.5 <i>b</i>	15.5±11.7 <i>b</i>

Conclusion

It has been demonstrated that with increasing light availability, steeper inclination angles in the upper canopy in a broad leaf crop plants as the sunflower become more convenient from the point of view of the plant photosynthetic balance [11, 27]. Such canopy architecture allows more uniform distribution of light within the canopy, and thus enables greater exposure of the photosynthesizing foliar area to light [4, 28]. The results presented here suggest that in order to optimize the interception of PAR, sunflower plants invest part of the captured energy in synthesizing petiole structural supporting material. This investment has a multiplicative component from base to apex, so the petioles of the upper canopy show more supporting tissue (collenchyma and vascular fibers) than the lower ones. This results in the upper canopy having a preferentially planophyllous to erectophyllous architecture.

Acknowledgements

This work was funded by grants to L.F.H. of the Secretaría Gral. de Ciencia Tecnología (SeGCyT-UNS, Bahía Blanca) and the Comisión de Investigaciones Científicas (CIC, LaPlata) both of Argentina. The author thanks Ms. M.C. Franchini for laboratory assistance and Ms. M.C. Moreno (CIC) for revising the manuscript.

References

1. Huber, H. and J.F. Stuefer, (1997): *Shade-induced changes in the branching pattern of a stoloniferous herb: functional response or allometric effect?* Oecologia 110: 478-486.
2. Knapp, A.K. and D.L. Smith, (1997): *Leaf angle, light interception and water relations. Demonstrating how plants cope with multiple resource limitations in the field.* American Biology Teacher 59: 365-368.
3. Pearcy, R.W. and F. Valladares, (1999): *Resource acquisition by plants: the role of crown architecture.* In: Press M.C., J.D. Scholes and M.G. Baker (eds.), *Physiological Plant Ecology*, Blackwell, MPG, Cornwall, pp. 45-66.
4. Valladares, F. and R.W. Pearcy, (2000): *The role of crown architecture for light harvesting and carbon gain in extreme light environments assessed with a realistic 3-D model.* Anales de Jardinería y Botánica (Madrid) 58: 3-16.
5. Hamerlynck E.P. and A.K. Knapp, (1996): *Early season cuticular conductance and gas exchange in two oaks near the western edge of their range.* Trees 10: 403-409.
6. Huber, H., J. De Brower, H. De Caluwe, J. Wijschedé and N.P.R. Anten, (2008): *Shade induced changes in biomechanical petiole properties in the stoloniferous herb Trifolium repens.* Evolution Ecology 22: 399-416.
7. Niinemets, Ü. and S. Fleck, (2002): *Petiole mechanics, leaf inclination, morphology, and investment in support in relation to light availability in the canopy of Liriodendron tulipifera.* Oecologia 132: 21-33.
8. Niklas, K.J. 1992. *Plant Biomechanics.* Univ. Chicago Press, 607 pp.
9. Niinemets, Ü. (1998): *Adjustment of foliage structure and function to a canopy light gradient in two co-existing deciduous trees. Variability in leaf inclination angles in relation to petiole morphology.* Trees 12: 446-451.
10. Weijschedé, J., J. Martinkova, H. De Kroon and H. Huber, (2006): *Shade avoidance in Trifolium repens: costs and benefits of plasticity in petiole length and leaf size.* The New Phytologist 172: 655-666.
11. Connor, D.J. and A.J. Hall, (1997): *Sunflower physiology.* In: *Sunflower Technology and Production.* A.A. Schneiter (Ed.), ASA, CSSA, SSSA, Wisconsin, p.113-182.
12. Andrade, F.H., P. Calviño, A. Cirilo and P. Barbieri, (2002): *Responses to narrow rows depend on increased radiation interception.* Agronomy Journal 94: 975-980.
13. Soil Survey Staff, USDA, (1999): *Soil Taxonomy: A Basic System for Classifying Soils.* Soil Survey Staff, Agriculture, Homework, p. 436.
14. Schneiter, A.A. and J.F. Miller, (1981): *Description of sunflower growth stages.* Crop Science 21, 901-903.
15. Sadras, V.O., L. Echarte and F.H. Andrade, (2000): *Profiles of leaf senescence during reproductive growth of sunflower and maize.* Annals of Botany 85: 187-195.
16. Sposaro, M.M., C.A. Chimenti and A.J. Hall, (2008): *Root lodging in sunflower. Variations in anchorage strength across genotypes, soil types, crop population densities and crop developmental stages.* Field Crops Research 106:179-186.
17. Rasband, W.S. (2008): *ImageJ*, U. S. National Institutes of Health, Bethesda, Maryland, USA, <http://rsb.info.nih.gov/ij/>
18. Ruzin, S.E. (1999): *Plant Microtechnique and Microscopy.* Oxford University Press, Oxford, New York, p. 322.
19. Liu, Y., F. Schieving, J.F. Stuefer and N. P. R. Anten, (2007): *The effects of mechanical stress and spectral shading on the growth and allocation of ten genotypes of a stoloniferous plant.* Annals of Botany 99: 121-130.
20. Hernández, L. F. and P. M. Bellés, (2006): *A 3-D finite element analysis of the sunflower (Helianthus annuus L.) fruit. Biomechanical approach for the improvement of its hullability.* Journal of Food Engineering 78: 861-869.
21. Gere, J.M. and S.P. Timoshenko, (1997): *Mechanics of Materials*, 4th edition, PWS, Boston.
22. Vogel, S. (1992): *Twist-to-bend ratios and cross-sectional shapes of petioles and stems.* Journal of Experimental Botany 43: 1527-1532.
23. Black, C.R. (1979): *The relative magnitude of the partial resistances to transpirational water movement in sunflower (Helianthus annuus L.).* Journal of Experimental Botany 30: 245-253.
24. LoGullo, M.A., L. Castro Noval, S. Salleo and N. Nardini, (2004): *Hydraulic architecture of plants of Helianthus annuus L. cv. Margot: evidence for plant segmentation in herbs.* Journal of Experimental Botany 55: 1549-1556.
25. Rawson, H.M. (1979): *Vertical wilting and photosynthesis, transpiration, and water use efficiency of sunflower leaves.* Australian Journal of Plant Physiology 6: 109-120.

26. Smith, V.C. and A.R. Ennos, (2003): *The effects of air flow and stem flexure on the mechanical and hydraulic properties on the stems of sunflowers Helianthus annuus L.* Journal of Experimental Botany 54: 845-849.
27. Hernández, L.F. and G.A. Orioli, (1983): *Estudio comparativo de la estructura foliar, intercepción de luz y rendimiento en girasol.* Anales de Edafología y Agrobiología (Madrid) 42: 2137-2148.
28. Rey, H., J. Dauzat, K. Chenu, J.-F. Barczi, G.A. A. Dosio and J. Lecoeur, (2008): *Using a 3-D virtual sunflower to simulate light capture at organ, plant and plot levels: contribution of organ interception, impact of heliotropism and analysis of genotypic differences.* Annals of Botany 101: 1139 - 1151.

High-resolution kinematics of gravitropic movement reveals an oscillatory dynamics. A key for efficient performance?

Renaud Bastien^{1,2}, Stéphane Douady¹ and Bruno Mouliat²

¹ Laboratoire Matière et Systèmes Complexes, CNRS UMR 7057, Université Paris 7, 10 rue Alice Domon et Léonie Duquet 75205 Paris cedex 13, France ² UMR-PIAF Physiologie intégrée de l'arbre, INRA-Université Blaise Pascal, 234 avenue du Brézet, F-63039 Clermont-Ferrand Cedex 02, France

Abstract

The spatial display of stem and leaves is crucial for the functioning of plants and their mutual interactions. It involves complex movements: stem change curvature and orientation to grow vertically (gravitropism) and these movements are continuously regulated by the perception of the current shape (autotropism) [1]. If a lot is known about the Physiology, very few studies have dealt with the kinematics and dynamics of these movements, and the corresponding relevant physical and biological aspects (see [2] for a recent review). In this work we focused on the reaction of a wheat coleoptiles using a novel high spatio-temporal kinematical method called "Rod PIV" combining Particle Image Velocimetry [3] and contour and median line detection of the organ: When its orientation vs the gravity was modified by tilting, the organ bent through local variation of curvature due to differential growth, and displayed a complex spatio-temporal pattern including oscillatory and propagative aspects. Moreover elongative and differential growth displayed coupled propagative oscillation. The insights of these results in terms of the modelling of the biomechanical and regulatory processes of tropic bending are discussed as well as the possible adaptive significance of these coupled oscillators for the gravitropic performance.

Introduction

Most of the plants are growing straight and vertical in all or a part of their aerial system (orthotropism). Then they display their branches in the space around in order to maximise light capture. Verticality could thus provide a selective advantage in order to reach the sunlight [4].

This orthotropism is achieved through active growth movements involving i) phototropism, driven by the perception of direction of the light gradients, and ii) gravitropism, controlled through gravity perception [5] and demonstrated readily by orthotropic movements in the dark. These active tropic movements have also been shown to be required for continuous posture control [6]. Plants are thus constantly moving and growing, although at much lower rates than animals.

Plants display two different types of growth. The primary elongation growth sits in a zone localised near the apical meristem. The secondary growth is a property of many dicots; they grow in diameter in the non-elongating basal part of the stem. Both types of growth can produce equivalent tropic motion [7], but only movements related to primary growth will be studied here.

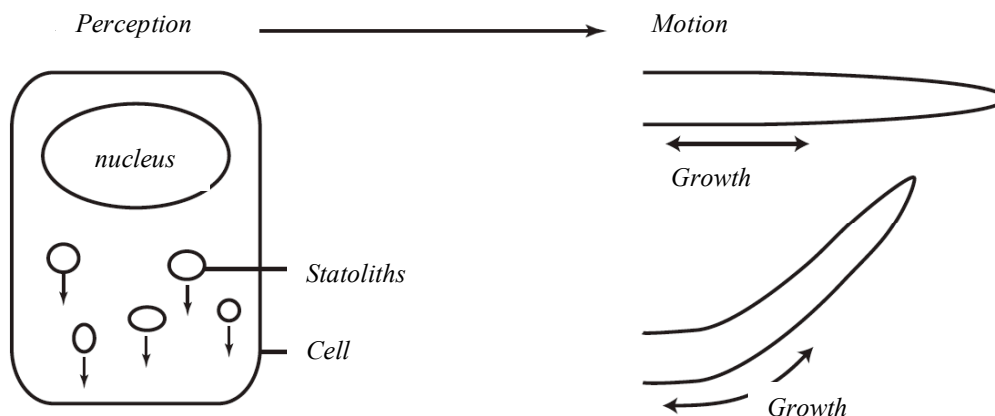


Fig 1. First cells perceive a signal. It comes from the sedimentation of the statoliths that apply a pressure on the lower wall. Many molecular mechanisms are involved in the transcription of the signal. Plants sense their local slope and respond through a transverse gradient in growth rate, called differential growth. Thereby plants can curve and reorient according to the stimuli.

Tropic movements in primary growth zone involve distributed curving powered by differential growth (see Figure 1). Many experiments have been done on such gravitropic movements since the pioneer works of Darwin, Pfeffer and Sachs (see review in [2]).

One of the classical experiments is to quantify the influence of the presentation angle on the gravitropic reaction [5, 8-10]. By looking at a tilted cylindrical organ, like coleoptiles or hypocotyls, this experiment focuses mainly on the variation in time of the apical angle. When comparing this angle with the presentation angle, a sine relation can be observed, but only for angle below 90° (see figure 2).

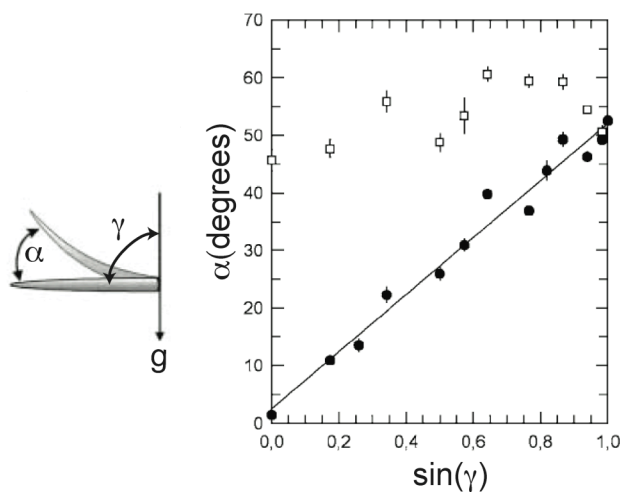


Fig. 2. From [8], Galland gives an example of sine law. *Avena coleoptiles* were placed in dark boxes and tilted from the vertical with an inclination angle γ . The orientation of the tip α were determined after 3 hours. For inclination angle below 90° the orientation of the tip is linearly related to the sine of the inclination angle (black dots). When the inclination angle is above 90°, the relation is modified (white squares).

In long time experiments, a deviation from the classical sine law occurs. As the organ is growing, and curving in an extended zone, this deviation cannot be understood by just looking at the tip angle. Indeed when the end of the stem is vertical, the basal curving still goes on. A continuous regulation of the orientation is therefore necessary to keep the apical part vertical when the basal part is curving (see figure 3). Moreover, the organ starts to straighten up its tip before it reaches the vertical avoiding overshooting. This has been called “auto tropism” because the plants need to get information on its self-shape to do so [1].

More recent works have been conducted to quantify the whole kinematics of plant growth movements. However several of them have neglected the measurement of the longitudinal growth (elemental elongation field), although growth is crucial to the mechanism (e.g. [11, 12]). Some other works have studied growth but not curvature. There are some recent studies on the whole kinematics of the two processes [13-15] but only in roots. However, the kinematics and mechanics of root gravitropism is different from that of aerial organs and in a way less complex in roots, the growth zone is really small and localised near the apex. And the root is supported by soil or nutrient solution buoyancy. There is thus no need for a postural control, and the shapes could be convoluted. In this

study we propose to analyse the whole kinematics of the straightening of wheat coleoptiles. To this aim we need to quantify at the same time the curvature and the elongation of the organ.



Fig 3. Straightening of a wheat coleoptile. From left to right and from top to bottom, the interval between each image is 2h. We see that the curvature is distributed over the whole length, and then once a part is vertical it remains even if the basal part continues to bend.

Material and methods

Plant material and treatments

Seeds of wheat (Recital cultivar) were soaked in water during 6 hours before being seeded. To be able to control the initial vertical of seedlings, the seeds were stuck on a tube filled with water at an angle of 30°, and the tubes placed in static holders with 1 rotational degree of freedom. The germination were set in a dark chamber at 25°C. After 3 days, when they were 10-20 mm long, they were transferred into a dark room at a 25°C, and placed in controlled initial inclination angle of 90° in the holders.

Time-lapse photography, were taken, every 10 to 15 minutes, with a camera Olympus SP-560UZ. In order to limit the photomorphogenetics effects during the photography, the flashlight of the camera was filtered to “safe” green light using a green LEE filter (139 Primary Green), (green light is far less perceived by plants than others wavelengths). Two series of experiments were performed in parallel, i) one with vertical coleoptiles, to get the growth field in the vertical position. ii) One with coleoptiles tilted 90° from the vertical. Each observation standed for 24 hours in order to let the organ to record the entire kinematics of gravitropic straightening movements.

Image analysis

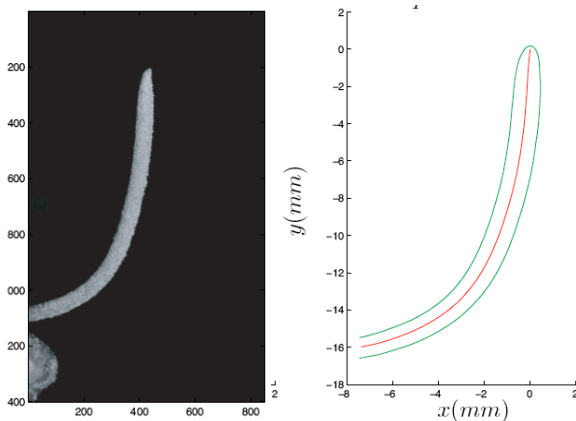


Fig. 4 The first part of the analysis process. We get the contour of the coleoptile, and then by voronoi skeletonisation we are able to find the median line.

Images were analysed with a specific Matlab program developed for this problem. As the coleoptile is a slender cylindrical organ, it can be described as a rod defined by its median line and by the radius of the rod as a function of the distance from the tip or curvilinear abscissa s . The elongation growth can then be recorded by monitoring the position of marker points $S(t)$ along the median line (see Figure 4) whereas the tropic movement can be described by changes in the local angle $a(s,t)$ and by local curvature $C(s,t)$ (i.e. the lineic rate of change in angle along the stem)

$$C(s,t) = \frac{\partial a(s,t)}{\partial s} \quad (1)$$

Where s is the curvilinear abscissa along the median line from the tip to the base and t is the time. To obtain the growth rate a fluorescent orange dye was set on the stem and used a set of markers to follow the displacement of each point. (Figure 5) In order to get the displacement $\delta(s,t)$ along the stem a modified version of the PIV (Particle Image Velocimetry) [3, 16] called Rod-PIV has been developed, in which the sub-window is moving only along the median line.

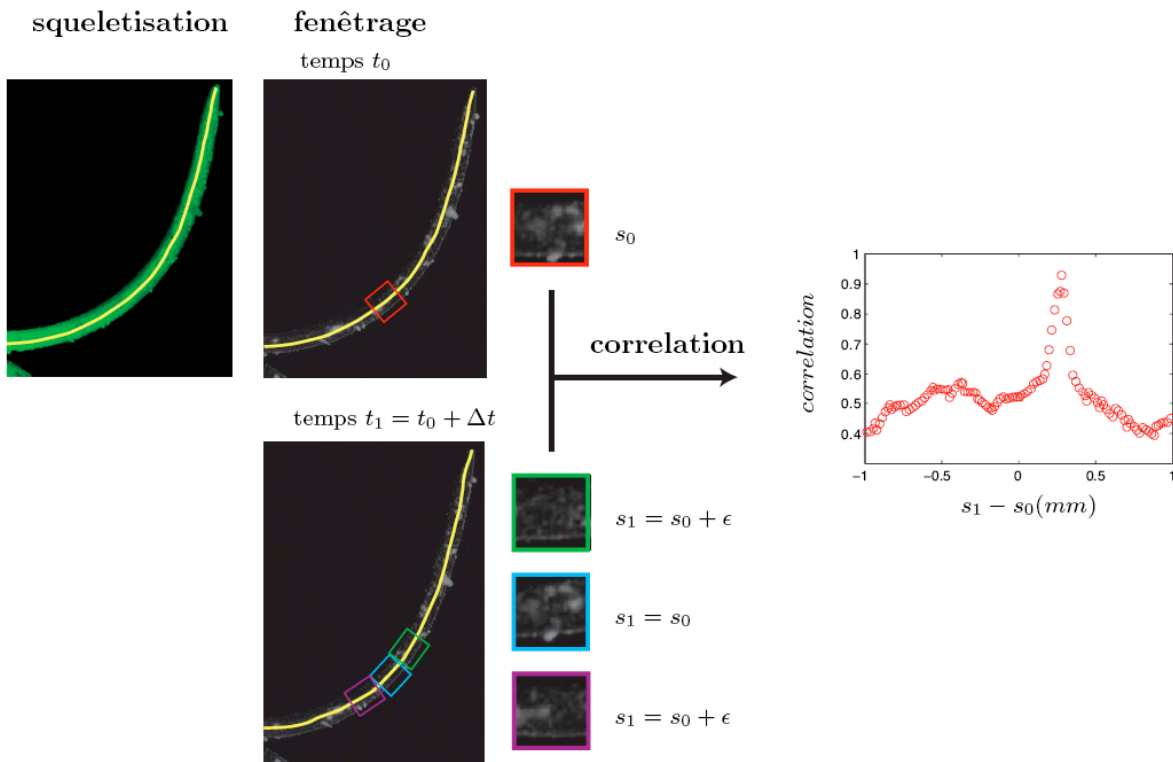


Fig. 5 Elongation along the median line. We separate Red and Green channel in the image. With the green channel we get the skeleton. Then we define sub-windows on the red channel. They are centred on the median line, as we have now directly the curvilinear abscissa s . We make the correlation of each sub-window $s = s_0$ at time t_0 with other sub-window as $t_1 = t_0 + \Delta t$, with the distance $|s_1 - s_0| < \epsilon$. Here we take $\epsilon < 1\text{mm}$. The correlation peak gives the displacement $\delta(s,t)$ on the line between two images.

By spatial derivation of the growth velocity we obtain the elemental elongation rate $E(s,t)$.

$$E(s,t) = \frac{1}{\Delta t} \frac{\partial \delta(s,t)}{\partial s} \quad (2)$$

E has been also called Relative Elemental Growth Rate or Strain rate in the literature; see [2, 17] for reviews.

As tissues elements are being stretched away by elongation, the derivative of curvature, according to position from the apex, is just a partial view of the change occurring to the organ segment (i.e. to a

group of cells). The material derivative (or derivative following growth induced points flow), has to be used, as introduced in plants studies by Silk [17])

$$\frac{D}{Dt} = \frac{\partial}{\partial t} + v(s,t) \cdot \nabla \quad (3)$$

Where v is the displacement velocity and ∇ is the gradient operator. The first term is the local variation in time on each position. The second accounts for the convection, the displacement of each point. Given the distribution of the elemental elongation rate, it is then possible to calculate the material derivative of the curvature using (3).

Results and discussion

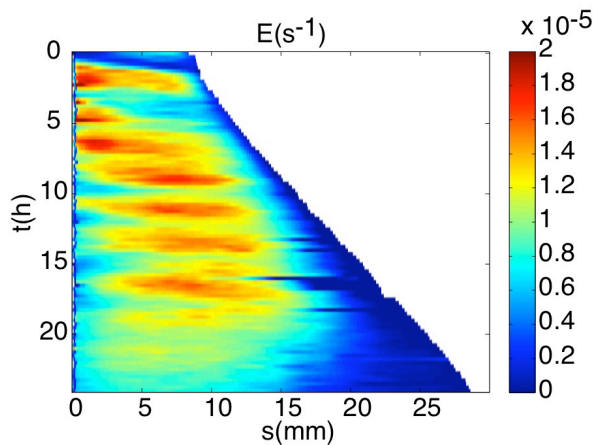


Fig 6. Measurement of the growth field according to the curvilinear abscissa in abscissa, from the apex to the base, and the time in ordinate. Oscillations appear, the period is around 2 hours.

In vertical coleoptile, the E field is not stationary (Figure 6). One can see phase of maximal elongation $E \sim 2.10^{-5} s^{-1}$ alternating in time with a phase of minimal $E \sim 1.10^{-5} s^{-1}$. These phases are regularly spaced in time. The period between two oscillations is approximately 2 hours. By following the position of the maximal elongation in the spatio temporal diagram figure 5, we see that the maximum is propagating from the apex to the base. There is a delay of 1 hour between the oscillation starting at the apex and reaching the base.

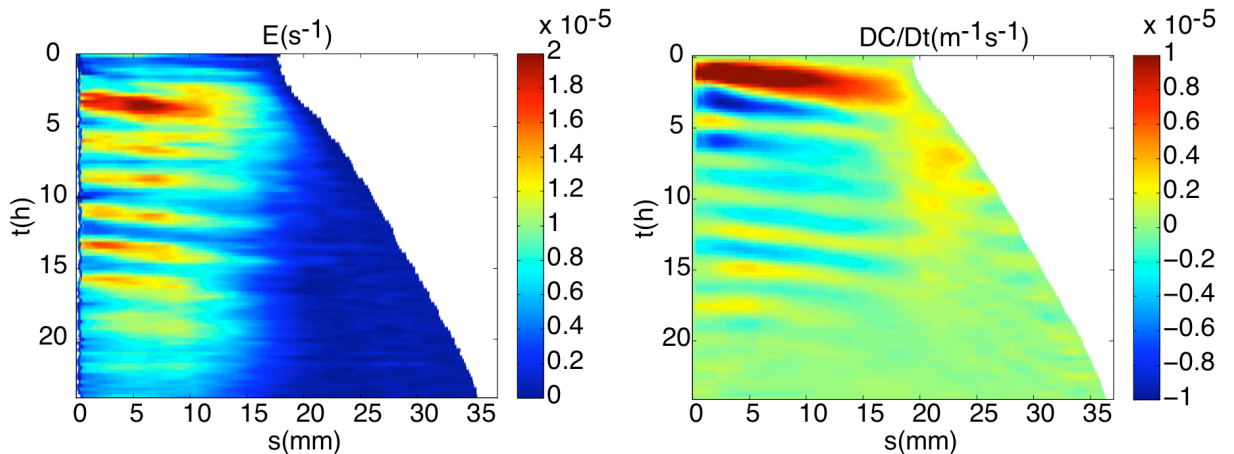


Fig 7. Left: Growth field of a tilted coleoptile. The results are comparable to previous on vertical coleoptiles. Right: Material derivative of the Curvature. After a first wave of curvature along the stem, oscillations clearly appear with the same period than the elongation pattern. The axes are the same than in the Figure 42. But the colormap accounts for the material derivative of the curvature in the right image.

The growth zone has a limited spatial extension in every coleoptile, independently of the flashlight frequency and of the temperature variations (data not shown).

In tilted coleoptiles (Figure 7), the spatio-temporal pattern of elemental elongation is unchanged. The oscillations have same frequency and amplitude. The propagation of the elongation is still present. The size of the growth zone remains the same. Therefore no redistribution or amplitude change in the elongation at the median line (i.e. the average elongation on the section) can be observed. The tropic movement is just due only to the lateral redistribution of the differential growth.

Near the base, curvature displays very little change, due to the low growth rate. Near the apex we observe oscillations of the material derivative of curvature, with a frequency similar to that of elemental elongation. Oscillations in the material derivative of curvature also displayed a spatial decay. However these oscillations were more damped. When the coleoptiles apex reached the vertical the amplitude of the motions went down.

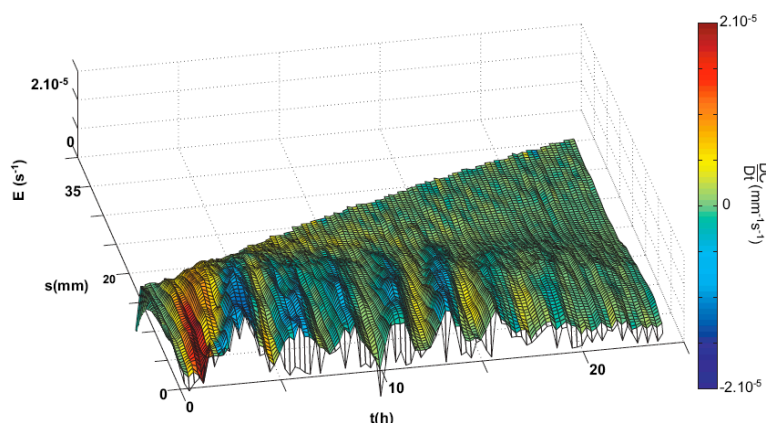


Fig 8. Surface of the growth field of a tilted coleoptile. The colour means the material derivative of curvature. The correlation between the two is really strong. When the growth is minimal the coleoptile bend otherwise it goes straight.

As a consequence the spatio-temporal field of the curvature variation is strongly correlated with the spatio-temporal field of elemental elongation (Figure 8). When the elongation is minimal, the coleoptiles curve. In the zone of maximal elongation, the coleoptile straightens up (decurve) or even bends in the opposite direction. Such coupling is not a geometric necessity and reveals a biomechanical coupling of the two processes. Despite very considerable changes in angle over time, the coleoptiles never overshoot the vertical.

Discussion

High-resolution kinematics analysis revealed that the tropic behaviour of coleoptiles is more dynamic than expected from the analysis tip angle and the sine law. The motion does not only consist on bringing the apex back to the vertical. Two different phases could be distinguished. First, the coleoptile bends on his whole length, during 3 hours, then it bends and straightens up alternatively in order to regulate its position and straighten most of its length. This last behaviour has been called auto tropism in literature [1, 18]. The straightening process could not be dependant of external stimuli, like gravity, but need to be induced internally although the inherent mechanism remains unknown. The sine law can only account for the first part of the straightening and neglect completely the auto tropic part.

It is interesting to notice that ultradian oscillatory growth pattern was observed for every coleoptile, whatever its inclination (tilted or not). This ultradian pattern was well reproducible from one plant to other and did not seem to depend on the orientation of the organ. Oscillatory growth patterns have only been described for circumnutating plants [19, 20]. In order to allow the plants to bend in different direction there is a differential growth across the section of the organ, with maxima and minima in the bending plane. In circumnutating organs the plants rotates by rotating their bending plane. So the position of the maxima and minima of elongation are moving around the cross-section of the stem. In that case the elongation on one side of the stem displays oscillations in growth between phases with maxima of elongation when the stem bends away, and minima when it bends toward the studied side. However upon gravitropic stimulation nutational movement were lost (see also [2]) the oscillations observed in this study were not due to rotations in the positions of minima and maxima around the

cross section but to oscillation in the amplitude of averaged elongation at the median line of the stem, with frequencies around 1h30. This is just a different phenomenon from nutational movements, which mechanism remains unknown. More precise local study would thus be required to understand the details of these oscillating growth [19].

The basipetal and cyclic propagation of the elongation peak from the apex to the base is also an original result. It can only be observed through kinematics analysis at high spatial resolution. Indeed the total elongation displays little or even no oscillation (depending on the time interval between two measurements) The characteristic velocity of the propagation is 20 mm / 1h30, i.e. approx 13 m.h⁻¹. This fits with the velocity of long-range longitudinal auxin transport [21, 22]. In coleoptile, auxin transport may thus be oscillatory rather than smooth.

From a functional point of view, it may be argued that that this decay improves the auto tropic process and the postural control. As the apex grows first, it can straighten up before the basal part of the coleoptile this is likely to avoid overshooting the vertical by stabilizing a straight vertical tip.

Except for the first oscillation that had bigger amplitude in graviresponding tilted coleoptiles, the oscillating growth pattern was not modified by a change in the orientation. The elongation growth was not redistributed neither concentrated in the zones of active curving. Gravitropism only acts on the modification of a property across the section of the stem. The global properties of the median line remain the same. Several hypotheses have been raised about the physiological control on the motor of the curvature (see [2]) but they have to comply with the previous results of the kinematics. Two of them could do so (being non exclusive one to the other): lateral redistribution of auxin (maintaining a mean concentration of auxin unchanged over each segment of the coleoptile, and a modification of the cell wall properties due to a gradient induce by the slope of plants.

Considering now the auto tropic part, a tight correlation between the spatio-temporal pattern of growth and curvature variation. The coleoptiles straighten up when the elongation is maximal and they bend when it is minimal. From simple geometrical model we see that the curvature variation of a material element is

$$\frac{DC}{Dt} = \frac{1}{e} ED \quad (4)$$

Where E is the growth rate, D is the growth differential between two opposites of the stem and e is the diameter of the stem. So if there is no differential, the curvature remains the same during the growth. At this point the link between the oscillations is still unknown. But it plays an important role in the regulation process As oscillations allow the plant to continuously regulate its position and avoid overshooting, with curving and straightening phases.

According to Baskin [18], ultradian growth oscillations do not seem to be found universally. But the main part of the literature focus on roots and the other studies are limited to the global elongation velocity at large time scales. As shown in this study, oscillations may be overlooked or underestimate but monitoring only tip displacement. Moreover if the oscillating period is shorter than the propagation from the apex to the base, it could damp the oscillations. As the results shown are often an average on many individuals [23], if the phase between them is not the same, the oscillations will vanish. But some studies have shown it is possible to find them in other case.

Conclusion

We have developed new algorithm and Matlab software, Rod-PIV, which allows following the elongation and the curvature in cylindrical organ even for large displacement of the tip. It proved to provide insights into the fundamental mechanism of gravitropism. The presence of oscillations and the correlation between the curvature variation and the elongation needs to be further investigated.

Acknowledgements

I would like to thanks Stéphane Ploquin and Nobert Frizot for their technical help.

References

1. R. D. Firn, J.D., *A study of the autotropic straightening reaction of a shoot previously curved during geotropism*. Plant, Cell and Environment, 1979. **2**(2): p. 149-154.
2. Moulia, B. and M. Fournier, *The power and control of gravitropic movements in plants: a biomechanical and systems biology view*. J. Exp. Bot., 2009. **60**(2): p. 461-486.
3. Supatto, W., et al., *In vivo modulation of morphogenetic movements in Drosophila embryos with femtosecond laser pulses*. Proceedings of the National Academy of Sciences of the United States of America, 2005. **102**(4): p. 1047-1052.
4. Fournier, M., et al., *Tree biomechanics and growth strategies in the context of forest functional ecology, in Ecology and biomechanics : a mechanical approach to the ecology of animals and plants* T.S. Eds Anthony Herrel, Nicholas P. Rowe, Editor. 2006, CRC Press. p. 1-33.
5. Iino, M., Y. Tarui, and C. Uematsu, *Gravitropism of maize and rice coleoptiles: Dependence on the stimulation angle*. Plant Cell and Environment, 1996. **19**(10): p. 1160-1168.
6. Moulia, B., C. Coutand, and C. Lenne, *Posture control and skeletal mechanical acclimation in terrestrial plants: Implications for mechanical modeling of plant architecture*. American Journal of Botany, 2006. **93**(10): p. 1477-1489.
7. Coutand, C., M. Fournier, and B. Moulia, *The Gravitropic Response of Poplar Trunks: Key Roles of Prestressed Wood Regulation and the Relative Kinetics of Cambial Growth versus Wood Maturation*. Plant Physiol., 2007. **144**(2): p. 1166-1180.
8. Galland, P., *Tropisms of Avena coleoptiles: sine law for gravitropism, exponential law for photogravitropic equilibrium*. Planta, 2002. **215**(5): p. 779-84.
9. Galland, P., et al., *Tropisms in Phycomyces: sine law for gravitropism, exponential law for photogravitropic equilibrium*. Planta, 2002. **214**(6): p. 931-938.
10. Perbal, G., et al., *The dose-response curve of the gravitropic reaction: a re-analysis*. Physiologia Plantarum, 2002. **114**(3): p. 336-342.
11. Meskauskas, A., S. Jurkoniene, and D. Moore, *Spatial organization of the gravitropic response in plants: applicability of the revised local curvature distribution model to Triticum aestivum coleoptiles*. New Phytol, 1999. **143**(2): p. 401-7.
12. Meskauskas, A., D. Moore, and L. Novak Frazer, *Mathematical modelling of morphogenesis in fungi: spatial organization of the gravitropic response in the mushroom stem of Coprinus cinereus*. New Phytol, 1998. **140**(1): p. 111-23.
13. Basu, P., et al., *A Novel Image-Analysis Technique for Kinematic Study of Growth and Curvature*. Plant Physiol., 2007. **145**(2): p. 305-316.
14. Chavarria-Krauser, A., et al., *Spatio-temporal quantification of differential growth processes in root growth zones based on a novel combination of image sequence processing and refined concepts describing curvature production*. New Phytologist, 2008. **177**(3): p. 811-821.
15. Walter, A., et al., *Spatio-temporal dynamics of expansion growth in roots: automatic quantification of diurnal course and temperature response by digital image sequence processing*. J. Exp. Bot., 2002. **53**(369): p. 689-698.
16. Cowen, J.K.S.a.E.A., *Quantitative imaging techniques and their applications to wavy flows*. 2004.
17. Silk, W.K., *Quantitative descriptions of development*. Annual Review of Plant Physiology, 1984. **35**: p. 479-518.
18. Tarui, Y. and M. Iino, *Gravitropism of oat and wheat coleoptiles: Dependence on the stimulation angle and involvement of autotropic straightening*. Plant and Cell Physiology, 1997. **38**(12): p. 1346-1353.
19. Baskin, T.I., *Ultradian Growth Oscillations in Organs: Physiological Signal or Noise?*, in *Rhythms in Plants*, S.S. Mancuso S., Editor. 2006, Springer.
20. Berg, A.R. and K. Peacock, *GROWTH-PATTERNS IN NUTATING AND NONNUTATING SUNFLOWER (HELIANTHUS-ANNUUS) HYPOCOTYLS*. American Journal of Botany, 1992. **79**(1): p. 77-85.
21. Shen-Miller, J., *Rhythmicity in the basipetal transport of indoleacetic acid through coleoptiles*. 1972. p. Pages: 108.
22. Shen-Miller, J., *Rhythmic Differences in the Basipetal Movement of Indoleacetic Acid between Separated Upper and Lower Halves of Geotropically Stimulated Corn Coleoptiles*. Plant Physiol., 1973. **52**(2): p. 166-170.
23. Liptay, A., et al., *OSCILLATIONS IN CORN SEEDLING GROWTH AS MEASURED BY OPTICAL-FLOW*. Journal of the American Society for Horticultural Science, 1995. **120**(3): p. 379-385.

Mechanosensing quantitatively controls diameter growth and level of expression of PtaZFP2 mechanosensitive gene in poplar

Ludovic Martin^{1*}, Catherine Coutand^{1*}, Nathalie Leblanc-Fournier^{1*}, Mélanie Decourteix¹, Catherine Lenne¹, Bruno Mouliat¹ and Jean-Louis Julien¹

¹MECA group, UMR 547 PIAF, INRA-Université Blaise Pascal, France

*the authors equally contributed to this work

Abstract

Plants growth and development are highly controlled by mechanical signals. The thigmomorphogenetical response to external mechanical loadings' generally consists in a decrease in elongation and a stimulation of diameter growth. A previous study has demonstrated that plants perceive the strains they are subjected to and not forces or stresses and proposed an integrative bio-mechanical model of mechanosensing ("sum-of-strains model"). It has been tested on tomato elongation but not on local responses such as diameter growth or gene expression. The first part of this study was dedicated to clone a mechanosensitive gene in poplar that could be used to measure one of the plant responses at the local level. To measure the other local response, plant diameter growth, we used LVDT. The second part studied the effect of a single transitory bending on poplar diameter growth and on the expression level of a mechanosensitive transcription factor gene, *PtaZFP2*. For this purpose, an original bending device was built to study stem responses according to a controlled range of sums of strains. The last part of this work assessed the model of mechanosensing on these local responses. A single bending modified plant diameter growth for several days and increased the relative abundance of *PtaZFP2* transcripts. Sums of longitudinal strains induced by bending computed on the stem bent zone were highly correlated to local plant responses. The "sum-of-strains" model of mechanosensing was thus applicable for local responses like diameter growth and gene expression. These novel results provide a set of basic data required for the establishment of an integrative model of thigmomorphogenesis linking gene expression with growth responses.

Introduction

Mechanical signals are actually rediscovered and emphasized as major cues that control plant morphogenesis [1,2,3] although their effects have been studied physiologically from the early 70's [4, 5] under the term of thigmomorphogenesis. The most encountered thigmomorphogenetical response in shoot axes is a reduction of elongation and an increase of radial growth indicating a mechanosensing process occurs in plants. Mechanosensing has been demonstrated in a lot of herbaceous [6] but also woody species [7, 8, 9, 3]. In the past 10 years, a quantitative analysis of plant mechanosensing has been initiated on tomato stem [10]. This work lead to a biophysical model of mechanoperception called the "sum of strains model"[11]. This model assumes that each individual volume of mechanosensing competent tissue (dV) perceives the strain it is subjected to which triggers an elemental signal ds:

$$dS = k \cdot \varepsilon \cdot dV \quad (1)$$

The elemental signals of all the volumes of mechanocompetent tissues add up into a thigmomorphogenetical signal S:

$$S = k \int \int \int_{\text{competentissues}} \varepsilon_{(x,y,z)} \cdot dx \cdot dy \cdot dz \quad (2)$$

This signal S triggers the observed growth response at the plant level. This model predicts a relationship between the sum of applied strains and the plant response, and has been validated on the prediction of the variability of the global response of primary growth to bending. Nevertheless, the hypotheses of the model remained to be tested. For doing so, local responses at the plant and cellular levels are required. A study on *Juglans regia* has identified a mechanosensitive gene expressed only in strained tissues; it is thus a good marker of mechanoperception at the cellular level [12]. After cloning the homolog of this gene in poplar [13], we thus analyze, in the present study, the diameter growth response and the level of expression of *PtaZFP2* mechanosensitive gene according to a range of applied sums of strains thanks to an original bending device.

Materials and methods

Plants

Young poplars (*Populus tremula* × *alba* cv 717-1B4) were obtained by *in vitro* micropropagation and grown on nutrient solution [14] after acclimation. Trees were grown in a growth chamber (L/D 16h/8h at 40 $\mu\text{mol}\cdot\text{m}^{-2}\cdot\text{s}^{-1}$ at 24°C/20°C with RH 60 ± 10%). Two months after micropropagation, the poplars were used in experiments; stems were about 35-cm high at this stage. The diameters of tested stems ranged from 4.3 to 6.3 mm with an average diameter of 5.18 ± 0.51 mm.

Bending experiments

For bending experiments, plants were transferred to another growth chamber with the same environmental conditions as for breeding. Plants were aligned in a vertical position along a metal bar to which they were attached with individual clamping rings. Foam was rolled around each stem in order to avoid stem wounds when the clamping ring was tightened. During entire experiment, roots bathed in a nutrient solution that was oxygenated by four aquarium pumps. Two vats (containing 100 L of nutrient solution) were available in the same growth chamber, with the possibility of experimenting on a set of eight plants (four plants on each vat) at the same time. During plant installation, plant leaves were removed in the basal part of the stem that was to be bent, in order to avoid uncontrolled mechanical stimuli on leaves during controlled bending (see below).

Bending device

An original experimental device was developed in order to impose a controlled level of strains to the stem; the basal part of the stem was pushed against a plastic tube in order to curve the stem up to a controlled and homogeneous curvature, and then returned to its initial position (Fig. 1). This bending device was used for growth experiments as well as for the study of *PtaZFP2* expression level. The diameter growth of each plant was monitored by a linear voltage displacement transducer (LVDT, DF/5.0 LIN 3M, Solartron Metrology Ltd.) before, during and after the transitory stem bending. The LVDT was placed at approximately 10 cm from the stem collar in the middle of an internode. Each LVDT was linked to an Omega bus (Omega, D5131, ± 5 Volts) linked to a computer where an in-house data acquisition program (LVDT.exe, B Adam, INRA umr PIAF) recorded average growth per minute. Each plant was equipped with a LVDT so that each of the two Omega buses gathered data from four plants (Fig. 1)

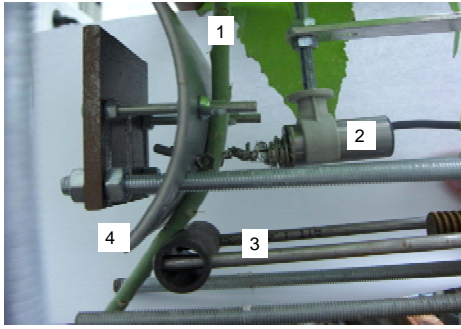


Fig. 1 The stem (1) was equipped with a LVDT (2) in order to monitor the diameter growth of the stem before, during and after bending was applied. A moving arm (3) pushed the stem against a plastic tube; the stem was thus bent around the tube (4). The stem was therefore submitted to a controlled curvature and thus to strains. The moving arm was then driven back and the stem is reset to its initial position.

Because of mechanical perturbation of plant growth induced by the installation (Fig. 2), plants in both types of experiments were let to recover during five days after installation, before the application of a controlled bending (in order to avoid interactions of the installation with the effects of the controlled bending).

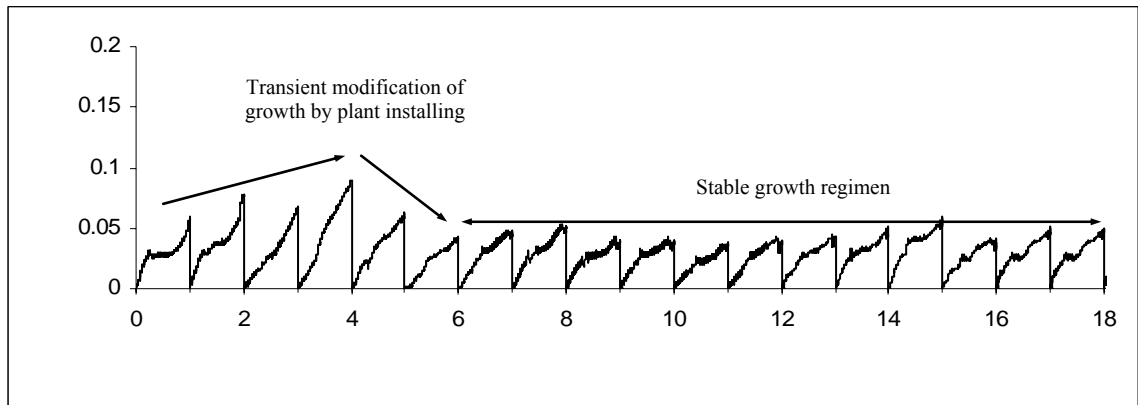


Fig. 2 Representative example of diameter growth of a control plant. The daily recorded diameter growth is plotted against time. Just after plant installation, the diameter growth rate exhibited an increase for three or four days, followed by a decrease, and finally reached a stable growth rate after five to six days. The daily growth appeared to be rhythmic with higher growth rates during the dark period and at the end of the light period.

Quantification of the applied strains

Within the framework of beam theory, under the assumption of small curvature and small strain, the cross section remains plane in the bent state and the maximal longitudinal strain is given by the product of the stem radius (r_{stem}) and the curvature of the neutral line (κ):

$$\varepsilon_{LL\max} = \kappa r_{stem} \quad (3)$$

The curvature of the central line can be computed as the inverse of the sum of the radius of the tube and the stem:

$$\text{With } \kappa = \frac{1}{r_{tube} + r_{stem}} \quad (4)$$

The sum of strains on the bent part was computed following Coutand and Moulia [11] as:

$$Sstrains = \frac{2}{3} r_{stem}^3 \kappa h \quad (5)$$

where r_{stem} is the radius of the stem in the middle of the bent part, κ is the imposed curvature and h is the length of the considered zone.

Given the sum of strains to impose, the length of the bent zone and the radius of the stems, we used Eq. 5 to choose the diameter of plastic tube to be used to create a range of applied sums of strains. The length of the response site was 1 mm for cambial growth and 30 mm for *PtaZFP2* expression. The imposed level of the sums of strains ranged from 0 to 20 mm³. Tubes of different diameters (40, 50, 75, 90, 140, 160, 200 mm) were used to control the level of applied strains.

Quantification of the growth response

The diameter growth response was quantified by the maximal average daily diameter rate reached by the plant after bending.

Effect of a single bending on *PtaZFP2* gene expression

For time course accumulation of *PtaZFP2* transcripts after bending, stems were bent as explained above for growth experiments and harvested several times after bending was applied. Thirty mm of the bent part of each stem was cut and immediately placed in liquid nitrogen. For expression analysis in different organs after stem bending, six types of organs were collected 1 h after stimulation. Total RNAs were extracted from about 150 mg of plant tissue using CTAB extraction buffer as described by Chang et al.[15], and then treated with RNase-free RQ1 DNase (Promega).

In RT-PCR experiments, first-strand cDNA was synthesized from 1 µg total RNA using oligodT and SuperScript III (Invitrogen). Each PCR reaction (30 µl) contained the following: cDNA (4 µl of 1:40 dilution of the first cDNA strands), PCR buffer (1X), MgCl₂ (1.66 mM), dNTP mix (200 µM of each), primers (0.3 µM of each), Platinum Taq DNA polymerase (0.5 unit, Invitrogen). After a heat step at 94°C for 5 min, PCR cycling were as follows: 29 cycles of denaturation (94°C, 15 s), annealing (61°C, 15 s) and elongation (72°C, 20 s), ending with a final elongation step at 72°C for 5 min. *PtaZFP2* transcripts were detected by amplifying 287 bp with primers Pe1S (5'-CGTGCGAGTCACAAGAAACC-3) and Pe1AS (5'-CACAGAACTCTCTTGCTGCT-3). The reference gene *EF-1α* (elongation factor-1α) transcripts were amplified with only 24 cycles using the primers EF1S (5'-GACAACACTAGGTACTACTGCACTGTC-3') and EF1AS (5'-TTGGTGGACCTCTCGATCATG-3').

For Northern blot analysis, a *PtaZFP2* gene-specific probe of 287 bp was generated by PCR with the primers Pe1S and Pe1AS, labeled with α³²-P-dCTP using a Ready-To-Go DNA Labeling Beads kit (Amersham). Total RNAs (15 µg) were separated by 1% agarose gel electrophoresis after denaturation with formaldehyde and blotted onto a nylon membrane Hybond-N+ (Amersham). The hybridization was carried out with a NorthernMax kit (Ambion). Membranes were exposed to a phosphoimager screen (Kodak) for 4 h and signals were quantified using Quantify One software (Bio-Rad).

Quantification of *PtaZFP2* gene expression

Plants were bent as explained above for growth experiments and harvested 30 minutes after bending was applied. Thirty mm of the bent part of each plant was cut and immediately placed in liquid nitrogen. Since the aim of the study was to determine if some quantitative relationship could be found between the applied level of strains and the expression level of *PtaZFP2*, the mRNA relative abundance of *PtaZFP2* was measured plant by plant by Real-Time Quantitative RT-PCR experiments following the PCR conditions described above, adding SYBR green I (1/1000, Sigma) as a fluorescent dye in the reaction. Amplifications were done using an iCycler IQ (Bio-Rad). Five plants were used as controls.

Relative quantitative abundance (Qr) of *PtaZFP2* transcripts was calculated by comparison to the expression of *EF-1α* using the delta-delta method mathematical model [16]:

$$Qr = \frac{2^{(C_{\text{control}} - C_{\text{reated}})_{PtaZFP2}}}{2^{(C_{\text{control}} - C_{\text{reated}})_{EF-1\alpha}}} \quad (8)$$

where C is the threshold of cycle number of PCR. Specificity of amplification was confirmed by determining the melt curves for the PCR products at the end of each run and by using a gel electrophoresis.

Results and discussion

Effect of a single bending on plant diameter growth

A representative example of the effect of a single controlled bending on stem diameter growth is shown on Fig. 3. Bending induced a long-lasting increase in the diameter growth rate. Diameter growth rate reached its maximal value the second (65% of the plants) or the third day (35% of the plants) after bending. The maximal diameter growth rate reached after bending was variable between stems, ranging from 0.09 to 0.22 mm.day⁻¹ with an average value of 0.16 ± 0.03 mm.day⁻¹. After this peak, the diameter growth rate regularly decreased and finally reverted to the values found before bending. The duration of the response was considered as the time between the application of bending and the time when diameter growth reverted back to the values observed before bending. Once the peak of diameter growth rate was reached, the time for the plant to recover a growth rate similar to the one before bending was estimated between 2 to 11 days with an average value of 4.8 ± 2.7 days. To our knowledge it is the first time the short term diameter growth after a single bending is described and quantified.

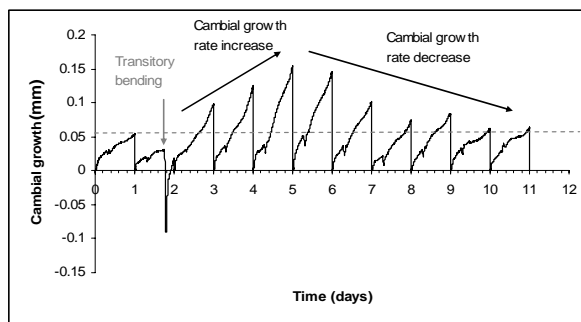


Fig. 3 Representative example of the effect of a single transitory bending on stem diameter growth. Before the application of a transitory bending, the diameter growth rate was stable. The application of a transitory bending (grey arrow) led to an increase in diameter growth. The daily diameter growth rate increased for three days and then decreased for several days before returning to its pre-bending value.

Relationship between diameter growth and thigmomorphogenetical stimulus

We assessed the relationship between the sum of longitudinal strains induced by bending and the plant responses using the model of mechanosensing (Eq. 2). A highly significant linear correlation ($R^2=0.74$) was found between the sum of applied strains on the portion of the stem where the LVDT recorded diameter growth and the growth response quantified as the maximal daily diameter rate reached after bending (Fig. 4). This demonstrated that the biophysical model of mechanosensing established on tomato (modification of elongation by bending of a zone distant from the primary growth zone) was also applicable in the case of diameter growth, a local response measured at the loaded zone. These results also suggested that in the case of diameter growth, the mechanosensitive control of the response is local.

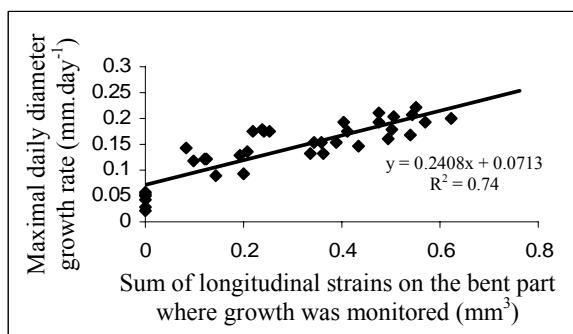


Fig. 4 Relationship between the sum of applied strains and the diameter growth response. A linear relationship was observed between the imposed sum of longitudinal strains computed on the width of the stem where the diameter growth was monitored and the maximal daily diameter growth rate reached after bending.

Our results are comparable with those of Soga et al. [17] on the effect of hypergravity on the gravimorphism of azuki bean epicotyls. Their data revealed a decrease of elongation and an increase of diameter growth induced by hypergravity. These responses are characteristic of the thigmomorphogenetical syndrome, even if presented as “gravity resistance” responses. As suggested by Telewski [18], gravimorphism and thigmomorphogenesis are both expressions of mechanosensing. Interestingly Soga et al. also found a correlation between the modification of growth and the intensity of hypergravity. They did not quantify the strains of tissues but as their plant material were probably very homogenous; tissue strain levels were probably proportional to the intensity of hypergravity. Expressing responses according to gravity or stress levels rather than tissue strain can be misleading since only tissue strains are sensed [11].

Effect of a single bending on *PtaZFP2* gene expression

The accumulation of *PtaZFP2* mRNAs after controlled bending in poplar stems was investigated by RT-PCR and northern-blot analyses. As shown in Figure 5A, no *PtaZFP2* transcripts were detected in the control plant stems. After bending, *PtaZFP2* transcripts accumulated within 5 min, reached a peak 10–30 min after the stem bending, and slowly decreased 1 h after bending. In contrast, levels of *PtaEF-1 α* mRNAs did not change after bending (nor 18S mRNA, data not shown)

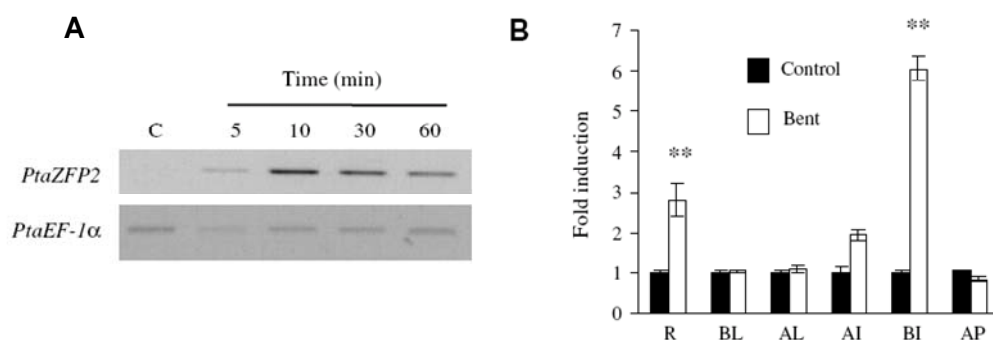


Fig 5: Time course accumulation and localization of *PtaZFP2* transcripts after stem bending.

(A) Total RNAs were extracted from the stems of control plants (C) and from bent stems at different times (5, 10, 30 and 60 min). *PtaZFP2* mRNAs abundance was analyzed by RT-PCR using specific primers. As a control, the expression of *EF-1 α* gene is also shown. (B) Northern blot analysis of *PtaZFP2* transcripts 1 h after basal internodes bending in several poplar organs. RNAs were extracted from roots (R), basal leaves (BL) localized 2 cm above the bent part of the stem, apical leaves (AL) below the apex, apical internodes (AI) localized 1 cm below the apex, basal internodes (BI) located 10 cm above the collar and apex (AP) of control and bent plants. After separation on formaldehyde gel, RNA were blotted and probed with ³²P-labeled *PtaZFP2* gene-specific probe. The expression of 18S RNA was used as control. The amount of *PtaZFP2* transcripts was obtained by quantifying each band and were corrected by 18S rRNA and expressed as a relative value of control plants. Double asterisks (**) represent Student's *t* test significant at $P < 0.01$.

As shown in Figure 5B, after local stem bending, *PtaZFP2* mRNAs were strongly accumulated in bent internodes and slightly in the roots. However, *PtaZFP2* transcripts were not detected in basal and apical leaves, apical internodes, and apex.

These results show that bending induced a rapid accumulation of *PtaZFP2* transcripts, which is only localized in the stressed part of the plants. *PtaZFP2* is thus a good marker of mechanoperception at the cellular level

PtaZFP2 transcripts level according to the sum of applied strains

The accumulation of *PtaZFP2* mRNAs after controlled bending was investigated by real-time quantitative RT-PCR analysis. *PtaZFP2* transcripts accumulation was highly correlated to the level of the applied sum of longitudinal strains (Fig. 6). The whole set of data was well fitted by a polynomial ($R^2=0.75$). For strain sums ranging from 0 to 12 mm^3 , the induction factor of *PtaZFP2* was linearly dependent on the sum of longitudinal strains. The model of mechanosensing was therefore also valid at the cellular level.

To our knowledge, the only studies that present a quantitative relationship between mechanical loading and the level of gene expression are those focused on the effects of hypergravity conditions [19]; Levels of expression of both *VaXTHS4* and alpha-tubulin are dependent on the level of hypergravity [20]. It appears that mechanosensing can quantitatively control the level of expression of some genes in plants. Mechanosensitive activation of genes following mechanical tissue strain has also been reported in animals (TWIST expression in drosophila [21]), but no quantitative action law for gene expression has yet been established.

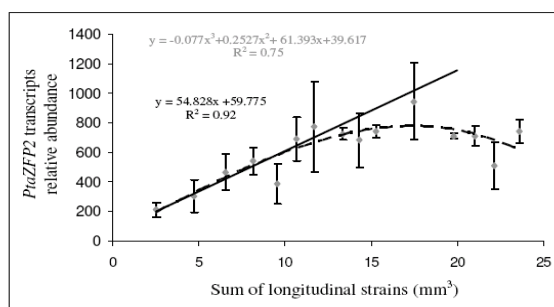


Fig. 6 Relationship between the level of expression of *PtaZFP2* and the sum of applied strain. Real-time quantitative RT-PCR analysis of the expression of *PtaZFP2* in 15 stems bent within a range of sum of applied strains from 3 to 24 mm^3 . Each point corresponds to one plant. All values were standardized to *PtaEF-1 α* transcripts levels. Errors bars correspond to \pm standard error. The expression level of *PtaZFP2* was correlated with the imposed sum of longitudinal strains. For sums of strains ranging from 3 to 12 mm^3 , the relationship between the sum of applied strains and the relative abundance of *PtaZFP2* transcripts was linear.

Conclusion

This interdisciplinary and collective work provides a quantitative study of mechanosensing in the case of bending of poplar stems. The results described the short-time effects of a single bending on poplar stem diameter growth. The study of the relationship established between the plant responses and the sum of applied strains opens areas in modelling plant growth in windy conditions and in studying the regulation of mechanosensing. Indeed it provides i) kinetics of plant response after a single bending ii) dose-response curves can be used to predict the plant diameter growth rate according to the axes variations of strains, and iii) validation of the integrative model of mechanoperception model. The characterisation of the kinetics of growth response after a single bending and the possibility to control the variability of plant responses due to variability of mechanical stimulus are the basic knowledge required to study the effect of multiple bendings'. It will be thus interesting in the future to study the effect of bending frequency and so plant acclimation under multiple bendings'. The model could also be used to study if some interspecific variability of mechanosensing exists by comparing the models parameters values of plants from different species submitted to the same range of strains. Both these aspects should open new avenues in the modelling of plant growth under wind.

Acknowledgements

We are grateful to Ginette Faure and Christelle Boisselet for plants production and preparation of nutrient solutions. We would like to thank Prof. Jeronimidis for the general discussion about this work.

References

1. Hamant O, Heisler MG, Jonsson H, Krupinski P, Uyttewaal M, Bokov P, Corson F, Sahlin P, Boudaoud A, Meyerowitz EM, Couder Y, Traas J (2008) Developmental Patterning by Mechanical Signals in Arabidopsis. *Science* 322: 1650-1655
2. Moulia B, Coutand C, Lenne C (2006) Posture control and skeletal mechanical acclimation in terrestrial plants: Implications for mechanical modeling of plant architecture. *Am J Bot* 93: 1477-1489
3. Coutand C, Dupraz C, Jaouen G, Ploquin S, Adam B (2008) Mechanical stimuli regulate the allocation of biomass in trees: Demonstration with young *Prunus avium* trees. *Ann Bot* 101: 1421-1432
4. Boyer N (1967) Modification de la croissance de la tige de bryone (*Bryonia dioica*) à la suite d'irritations tactiles. *CRAS*. 267: 2114-2117
5. Jaffe MJ (1973) Thigmomorphogenesis. The response of plant growth and development to mechanical stimulation. *Planta* 114: 143-157
6. Biddington NL (1986) The Effects of Mechanically-Induced Stress in Plants - a Review. *Plant Growth Regul* 4: 103-123
7. Jacobs MR (1954) The effect of wind sway on the form and development of *Pinus radiata* D. Don. *Aus J Bot* 2: 35-51
8. Larson PR (1965) Stem forms of young *Larix* as influenced by wind and pruning. *For Sci* 11: 412-424
9. Telewski FW, Pruyn ML (1998) Thigmomorphogenesis: a dose response to flexing in *Ulmus americana* seedlings. *Tree Physiol* 18: 65-68
10. Coutand C, Julien JL, Moulia B, Mauget JC, Guitard D (2000) Biomechanical study of the effect of a controlled bending on tomato stem elongation: global mechanical analysis. *J Exp Bot* 51: 1813-1824
11. Coutand C, Moulia B (2000) Biomechanical study of the effect of a controlled bending on tomato stem elongation: local strain sensing and spatial integration of the signal. *J Exp Bot* 51: 1825-1842
12. Leblanc-Fournier N, Coutand C, Crouzet J, Brunel N, Lenne C, Moulia B, Julien JL (2008) Jr-ZFP2, encoding a Cys2/His2-type transcription factor, is involved in the early stages of the mechanoperception pathway and specifically expressed in mechanically stimulated tissues in woody plants. *PCE* 31: 715-726
13. Martin L, Leblanc-Fournier N, Azri W, Lenne C, Henry C, Coutand C, Julien JL (2009) Characterization and expression analysis under bending and other abiotic factors of PtaZFP2, a poplar gene encoding a Cys2/His2 zinc finger protein *Tree Physiol* 29: 125-136
14. Morizet J, Mingeau M (1976) Effect of Environment on Water-Uptake, as Studied on Beheaded Exuding Tomato .1. Role of Nutrients. *Annales Agronomiques* 27: 183-205
15. Chang SJ, Puryear J, Cairney J (1993) A simple and efficient method for isolating RNA from pine trees. *Plant Mol Biol Rep* 11: 113-116
16. McMaugh SJ, Lyon BR (2003) Real-time quantitative RT-PCR assay of gene expression in plant roots during fungal pathogenesis. *Biotechniques* 34: 982-+
17. Soga K, Wakabayashi K, Kamisaka S, Hoson T (2006) Hypergravity induces reorientation of cortical microtubules and modifies growth anisotropy in azuki bean epicotyls. *Planta* 224: 1485-1494
18. Telewski FW (2006) A unified hypothesis of mechanoperception in plants. *Am J Bot* 93: 1466-1476
19. Soga K, Wakabayashi K, Kamisaka S, Hoson T (2007) Effects of hypergravity on expression of XTH genes in azuki bean epicotyls. *Physiol Plant* 131: 332-340
20. Saito Y, Soga K, Wakabayashi K, Hoson T (2003) Increase in expression level of alpha-tubulin gene in Arabidopsis seedlings under hypergravity conditions. *Biol Sci Space* 17: 177-178
21. Supatto W, Debarre D, Moulia B, Brouzes E, Martin JL, Farge E, Beaurepaire E (2005) In vivo modulation of morphogenetic movements in *Drosophila* embryos with femtosecond laser pulses. *PNAS* 102: 1047-1052

Contact Mechanics at the Insect-Plant Interface

Stanislav N. Gorb

Functional Morphology and Biomechanics, Zoological Institute University of Kiel, Germany

Abstract

Most of the one million insect species described so far are associated with plants. Such insects should be able to attach successfully to plant surfaces. Dealing with attachment, we have to consider a contact problem, in which two bodies are involved. Both these parts may have various geometries, mechanical and chemical properties. Moreover, insects produce and deliver a secretory fluid into a contact zone, whereas many plant substrates bear specialised surface coverage. This paper summarises our previous structural and experimental studies on insect attachment and the effect of plant substrates on it.

Insect attachment devices

Most recent data on insect attachment systems demonstrated their excellent adhesion and high reliability of contact (Gorb, 2001; 2005). Interestingly, these systems appeared several times independently in insect evolution (Gorb and Beutel, 2001). This fact may indicate that such surface structures must have an advantage for adhesion enhancement especially on real natural substrates, such as surfaces of plants. The physical background of the effect of adhesion enhancement was theoretically discussed in several recent publications (Smith et al., 1999; Arzt et al., 2003; Persson, 2003; Chung and Chaudhury, 2005).

Comparison of a wide variety of animal groups revealed that the size of single contacting points gets smaller and their density increases as the body mass of the animal group increases (Scherge and Gorb, 2001). This general trend was theoretically explained by applying the Johnson-Kendall-Roberts (JKR) theory, according to which specialised microstructured surfaces increase adhesion (Johnson et al, 1971; Arzt et al., 2003). There are other design principles, extracted from studies on biological systems. The effective elastic modulus of the fibre arrays is very small, which is of fundamental importance for adhesion on smooth and rough substrates (Persson, 2003). It is predicted that an additional advantage of patterned surfaces is the reliability of contact on various surface profiles and the increased tolerance of defects at individual contacts. In a real situation, failure of some microcontacts because of dust particles or mechanical damage of single hairs would minimally influence adhesion. In the case of a solitary contact, even slight damage of the contact due to the presence of contamination or surface irregularities will immediately lead to contact breakage, similar to the crack building and its propagation in bulk material.

Anti-adhesive plant surfaces

It is well known that insects attach well to microscopically rough surfaces and use their claws to interlock with surface irregularities (Betz, 2002; Dai et al., 2002). To attach to smooth and microrough substrates, insects apply adhesive pads (Gorb, 2001). Since plant surfaces range from rather smooth to those covered with trichomes or wax crystals, insect-plant interactions may often rely on insect attachment ability to the particular plant surface. In the course of the last five years, we carried out

numerous experiments, in order to understand insect-plant interactions at the level of the contacting surfaces. The studies were mainly performed with insects having hairy adhesive pads, the surfaces of which are densely covered with microscopic hairs.

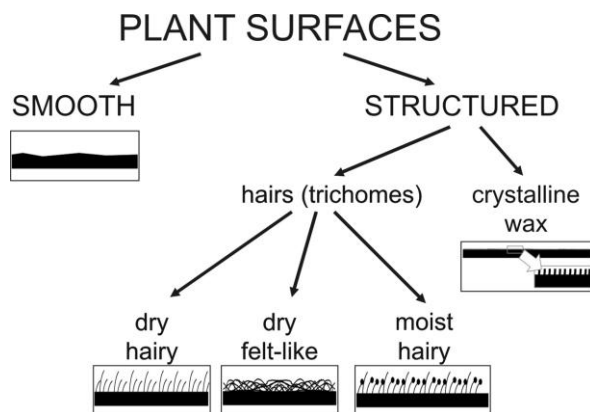


Figure 1. Diversity of the plant surface geometry.

Plant surfaces studied have a wide range of textures and microsculptures (Fig. 1). They may be smooth or structured, i.e. covered with various hairs (trichomes) or bear microscopic crystals of epicuticular waxes (Jeffree, 1986; Barthlott et al., 1998). To study the role of different structures of a plant surface in insect attachment, various plant surfaces were screened (Gorb and Gorb, 2002). Attachment ability of the chrysomelid beetle *Chrysolina fastuosa* was tested on 99 surfaces of 83 plant species, belonging to 45 families. Among these surfaces were smooth, dry hairy, felt-like, moist hairy and waxy ones. Insects attached successfully to smooth, dry hairy and felt-like substrates, but they could not attach properly to surfaces covered with wax crystals. To explain anti-adhesive properties of plant substrates, four hypotheses were proposed (Fig. 2). (A) *Roughness-hypothesis*: wax crystals and/or little trichomes cause microroughness, which considerably decreases the real contact area between the substrate and setal tips of insect adhesive pads. (B) *Contamination-hypothesis* or *cohesion-failure-hypothesis*: wax crystals are easily detachable structures that contaminate pads. Alternatively, liquids covering plant surface may detach from plants and contaminated insect pads (C) *Wax-dissolving-hypothesis*: Insect pad secretion may dissolve wax crystals. This would result in the appearance of a thick layer of fluid, making the substrate slippery. (D) *Fluid-absorption-hypothesis*: Structured wax coverage may absorb the fluid from the pad surface.

The influence of surface roughness on insect attachment has been tested experimentally in several studies (Gorb, 2001; Gorb and Gorb, 2006a; Voigt et al., 2007). Centrifugal experiments on the attachment ability of insects on artificial substrates with varying surface roughness showed that the fly *Musca domestica* and beetles *Gastrophysa viridula* (Fig. 3) and *Leptinotarsa decemlineata* generated much higher forces on either smooth or rough surfaces with an asperity size, exceeding 3.0 μm (Peressadko and Gorb, 2004; Voigt et al., 2008).

This effect may be explained by spatula-like terminal elements of setae that are able to generate sufficient contact with large surface irregularities. The worst attachment was observed on substrates with a roughness of 0.3 – 1.0 μm , corresponding to the size of plant wax crystals. Because of the small size of wax crystals, the area of real contact between these substrates and the tips of insect spatulae is very small. Since the attachment force depends on the area of real contact, insects are not able to attach successfully to surfaces with such a microroughness.

Since many wax crystals are easily erodable structures, they may contaminate adhesive pads, and this may reduce proper functioning of the pads. We proved the contamination-hypothesis experimentally for several insects and a series of plant species. Our data on the contamination of

Chrysolina fastuosa pads by wax crystals of 12 waxy plant surfaces (Gorb and Gorb, 2006b) showed that the plants differ essentially in their contaminating effects on insect pads. Differences were found in both the nature of the contamination, i.e. the structure of the contaminating material and the presence of recognisable crystals, and the degree of contamination (the portion of setal tip surface, covered with contaminating particles, and the portion of setae, covered with the wax). These differences were hypothesised to be caused by various micromorphologies of waxes in the plant species studied. Analysing the relationship between the contaminating ability and geometrical parameters of wax crystals, we found that the contamination is related to both the largest dimension and the largest aspect ratio of crystals.

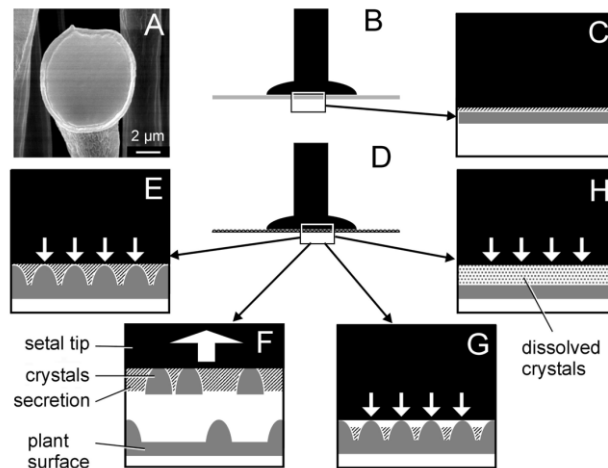


Figure 2. Hypotheses of anti-adhesive mechanisms of a waxy plant surface. A. Tenent seta of the adhesive pad of the *Chrysolina fastuosa* beetle. B, C. Setal contact with a smooth surface. D – H. Setal contact with a waxy surface. E. Roughness-hypothesis. F. Contamination-hypothesis. G. Fluid-absorption-hypothesis. H. Wax-dissolving-hypothesis [6].

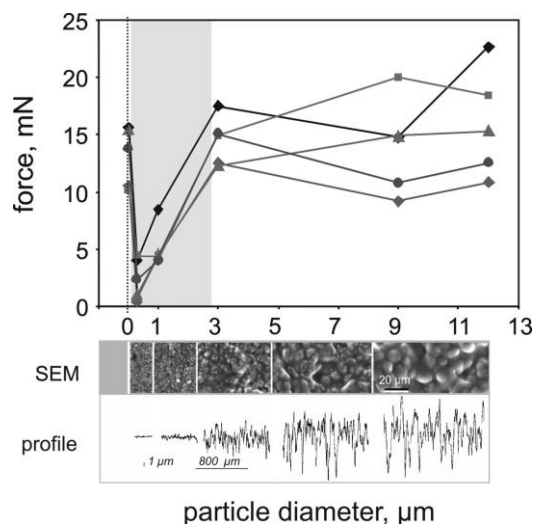


Figure 3. Attachment forces of the beetles *Gastrophysa viridula* on substrates with different roughness [15].

Pad contamination was also observed in our study on the waxy surface of the slippery zone in trapping organs (pitchers) of the carnivorous plant *Nepenthes alata* (Gorb et al., 2005). The wax coverage consists of two clearly distinguished superimposed layers, differing in their structure,

chemical composition and mechanical properties. Laboratory experiments with tethered beetles *Adalia bipunctata* showed that both wax layers essentially reduce the attachment force of insects, however, in different ways. Crystals of the upper wax layer contaminate the insects' adhesive pads, whereas the lower wax layer leads to the reduction of the real contact area of the insects' feet with the pitcher surface.

Conclusion

The attachment ability of insects to plant surfaces depends on the structure, roughness, and mechanical stability of the substrate. Wax bloom, specialised trichomes and fluid coverage found on some plant surfaces might be plant adaptations against insect attachment. Four hypotheses of anti-adhesion mechanism of plant surfaces are proposed, and two of them are experimentally supported.

Acknowledgement

This work was supported by the SPP 1420 priority program of German Science Foundation (DFG) "Biomimetic Materials Research: Functionality by Hierarchical Structuring of Materials" (project GO 995/9-1).

References

1. Arzt E., Gorb S. and Spolenak R. (2003): From micro to nano contacts in biological attachment devices. *Proc. Nat. Acad. Sci. USA*, 100, 10603–10606.
2. Barthlott W., Neinhuis C., Cutler D., Ditsch F., Meusel I., Theisen I. and Wilhelmi H. (1998): Classification and terminology of plant epicuticular waxes. *Botanical Journal of the Linnean Society*, 126, 237–260.
3. Betz O. (2002): Performance and adaptive value of tarsal morphology in rove beetles of the genus *Stenus* (Coleoptera, Staphylinidae). *Journal of Experimental Biology*, 205, 1097–1113.
4. Chung J.Y. and Chaudhury M.K. (2005): Roles of discontinuities in bio-inspired adhesive pads. *J. R. Soc. Interface*, 2, 55–61.
5. Dai Z., Gorb S.N. and Schwarz U. (2002): Roughness-dependent friction force of the tarsal claw system in the beetle *Pachnoda marginata* (Coleoptera, Scarabaeidae). *Journal of Experimental Biology*, 205, 2479–2488.
6. Gorb E.V. and Gorb S.N. (2002): Attachment ability of the beetle *Chrysolina fastuosa* on various plant surfaces. *Entomologia Experimentalis et Applicata*, 105, 13–28.
7. Gorb E.V., Haas K., Henrich A., Enders S., Barbakadze N., Gorb S.N. (2005): Composite structure of the crystalline epicuticular wax layer of the slippery zone in the pitchers of the carnivorous plant *Nepenthes alata* and its effect on insect attachment. *Journal of Experimental Biology*, 208, 4651–4662.
8. Gorb E.V. and Gorb S.N. (2006a): Combination of the surface profile and chemistry reduces the attachment of the beetle *Gastrophysa viridula* on the *Rumex obtusifolius* leaf surface. In: Salmén L. (ed.), *Proceedings of the 5th Plant Biomechanics Conference*, Stockholm, Sweden, Vol. 2, pp. 537–542.
9. Gorb E.V. and Gorb S.N. (2006b): Do plant waxes make insect attachment structures dirty? Experimental evidence for the contamination hypothesis. In: A. Herrel, N.P. Rowe & T. Speck (eds.), *Biomechanics and Ecology: A mechanical approach to the ecology of animals and plants*, Herrel A, Speck T, Rowe N. (eds.), CRC Press, Boca Raton, pp. 147–162
10. Gorb S.N. (2001): *Attachment Devices of Insect Cuticle*, Dordrecht, Boston, London, Kluwer Academic Publishers.
11. Gorb S.N. (2005): Uncovering insect stickiness: structure and properties of hairy attachment devices. *American Entomologist*, 51, 31–35.
12. Gorb S.N. and Beutel R.G. (2001): Evolution of locomotory attachment pads of hexapods. *Naturwissenschaften*, 88, 530–534.

13. Jeffree C.E. (1986): The cuticle, epicuticular waxes and trichomes of plants, with references to their structure, functions and evolution. In: Juniper BE, Southwood TRE. (eds), *Insects and the plant surface*, London, Edward Arnold, pp. 23–64.
14. Johnson K.L., Kendall K. and Roberts A.D. (1971): Surface energy and the contact of elastic solids. *Proc. Royal Soc. London A*, 324, 301–313.
15. Peressadko A and Gorb S.N. (2004): Surface profile and friction force generated by insects. *Proceedings of the 1st International Conference Bionik*, Boblan I, Bannasch R. (eds.), Hannover, Germany, pp. 257–263.
16. Persson B.N.J. (2003): On the mechanism of adhesion in biological systems. *J. Chem. Phys.*, 118, 7614–7621.
17. Scherge M. and Gorb S.N. (2001): *Biological Micro- and Nanotribology*, Berlin, Springer.
18. Smith B.L., Schäffer T.E., Viani M., Thompson J.B., Frederick N., Kindt J., Belcher A., Stucky G.D., Morse D.E. and Hansma P.K. (1999): Molecular mechanistic origin of the toughness of natural adhesives, fibers and composites. *Nature*, 399, 761–763.
19. Voigt D., Gorb E. and Gorb S.N. (2007): Plant surface - bug interactions: *Dicyphus errans* stalking along trichomes. *Arthropod-Plant Interactions*, 1, 221–243.
20. Voigt D., Schuppert, J.M., Dattinger S. and Gorb S.N. (2008): Sexual dimorphism in the attachment ability of the Colorado potato beetle *Leptinotarsa decemlineata* (Coleoptera: Chrysomelidae) to rough substrates. *Journal of Insect Physiology*, 54, 765–776.

The influence of the wall contact angle on gas bubble behaviour in xylem conduits under tension and possible consequences for embolism

Wilfried Konrad and Anita Roth-Nebelsick

Institute for Geosciences, University of Tübingen, Sigwartstrasse 10, D-72076 Tübingen, Germany

Abstract

Gas-filling of conduits decreases hydraulic conductance of the xylem vessels. Therefore, embolism formation and reversal is one of the crucial topics in plant water transport. The negative pressure (=tension) in xylem water during plant transpiration may cause embolism in two ways: (i) Homogeneous nucleation, the spontaneous formation of a water vapour bubble within the water column due to statistical fluctuations. (ii) Heterogeneous nucleation, the development of bubbles by air seeding, the drawing of gas present in already embolized conduits through pit membrane pores into functioning conduits. This contribution deals with the behaviour of gas bubbles caused by heterogeneous nucleation. These bubbles usually contain both water vapour and air and float either freely in the xylem water (which is under tension) or attach themselves to the vessel wall (which is characterised by its shape and contact angle). Based on the reversible free energy of this system, we derive conditions for two kinds of equilibria: (a) Mechanical equilibrium (and its stability or instability) between the forces which try to contract and expand bubbles containing air and water-vapour. (b) Equilibrium with respect to the exchange of air particles between the bubble and the surrounding xylem water by dissolution mechanisms.

The results — given as relations between xylem water pressure, bubble radius, bubble particle content and xylem wall morphology and contact angle — allow to predict whether appearing bubbles lead to embolism or not.

Introduction

Based on arguments from statistical physics and thermodynamics it has been shown ([4], [5]) that for the negative pressures to be expected in plant conduits spontaneous cavitation (= homogeneous nucleation) plays only a minor role in causing embolism because the tension values occurring in the xylem are not high enough to permit a significant formation rate of expanding bubbles.

Embolism is usually caused by air seeding (= heterogeneous nucleation), i.e. a group of “air” molecules finds its way into a tree water conduit through cracks and openings in the wood. If such a passage remains open, at least one segment of the embolised conduit is permanently lost for water transport. If it closes, however, after a limited number of “air molecules” has entered the conduit these form one or several embryonic air bubbles which may — but need not necessarily — cause the rupture of the water column (see Fig. 1).

As will be shown below, embryonic bubbles which do no harm as long as they are completely immersed into the xylem fluid may, however, cause embolism if they come into contact with the vessel wall.

The hazardousness of a given bubble is related to its ability to comply with the following equilibrium conditions:

- (i) Mechanical equilibrium: (a) the randomly moving gas particles in the bubble act as an outward directed force which tries to expand the bubble; (b) the surface tension of the gas/liquid interface tries to contract the bubble; (c) the pressure p_s of the xylem water contributes for $p_s < 0$ to the expanding force, for $p_s > 0$ to the contracting force. Equilibrium exists if these forces sum up to zero ([6], [7]).
- (ii) Diffusional equilibrium: the number of air molecules remains constant only if a balance with respect to the exchange of air molecules with the bubble's surroundings prevails between the air partial pressure within the bubble and the concentration of air molecules dissolved in the xylem water. Otherwise, air molecules from within the bubble either dissolve at the bubble's gas/liquid interface in the xylem water and diffuse towards regions of lower air molecule concentration, or else a diffusional current through the xylem water delivers air molecules to the bubble.

The exchange process between water vapour and water is faster than the exchange of air by a factor of about 10^6 . Hence, mechanical equilibrium is a necessary prerequisite for diffusional equilibrium.

The development of a bubble is essentially controlled by the mechanical forces. We assess them (and the equilibria they possibly adopt) by analysing the reversible free energy associated with the formation of an embryonic bubble of radius R (see [1], [4], [5], [6], [7]). In doing so we assume (i) $p_w \approx p_{sat}$ (p_{sat} : saturation pressure of water vapour): Because the exchange of water molecules between bubble and surrounding liquid is a very intensive one, the water vapour partial pressure in the bubble readjusts to the water vapour saturation pressure almost immediately. (ii) $n_a \approx \text{const.}$: This simplifying assumption is only valid on the very short time scale of bubble formation considered here. The assumption is based on the low solubility of air in water, implying that only a small fraction of the air molecules in the bubble's interior are lost to the surrounding liquid within the considered time scale.

Results and discussion

Floating bubble

The formation energy of a bubble filled with water vapour and n_a air molecules reads (see [1], [7])

$$W = 4\pi\gamma R^2 - \frac{4\pi}{3} (p_w - p_s) R^3 + 3\mathcal{R}T n_a \log\left(\frac{R_{max}}{R}\right) \quad (1)$$

where $R_{max} := -2\gamma/p_s$, \mathcal{R} is the gas constant and T the temperature. The bubble radii where equilibrium of forces prevails are found from the zeros of

$$\frac{\partial W}{\partial R} = [8\pi\gamma R] - \left\{ 4\pi (p_w - p_s) R^2 + \frac{3\mathcal{R}T n_a}{R} \right\} \quad (2)$$

and their stability is assessed by evaluating $\partial^2 W / \partial R^2$ at the equilibrium point(s). Notice that the term in brackets on the right hand side of equation (2) represents the surface tension and thus the contracting force acting on the bubble while the terms in braces represents expanding forces due to gas pressure and negative xylem water pressure. Bubble equilibrium radii (i.e. the solutions of $\partial W / \partial R = 0$) are located at

$$\begin{aligned} R_{stab} &= \frac{R_{vap}}{3} \left(1 - 2 \cos \left[\frac{1}{3} \arccos \left(1 - \frac{2n_a}{n_{crit}} \right) + \frac{\pi}{3} \right] \right) \\ R_{inst} &= \frac{R_{vap}}{3} \left(1 + 2 \cos \left[\frac{1}{3} \arccos \left(1 - \frac{2n_a}{n_{crit}} \right) \right] \right) \end{aligned} \quad (3)$$

where $n_{crit} := 128\pi\gamma^3 / [81\mathcal{R}T (p_w - p_s)^2]$ and $R_{vap} = 2\gamma / (p_w - p_s)$. For a pure water vapour bubble ($n_a = 0$) the equilibrium radii simplify to $R_{stab} = 0$ and $R_{inst} = R_{vap}$. Evaluating $\partial^2 W / \partial R^2$, we find that a bubble at radius R_{stab} is in stable, at radius R_{inst} , however, in unstable equilibrium. For $n_a > n_{crit}$ both R_{stab} and R_{inst} become undefined, meaning that the bubble expands without limits (see Figures 2(b) and 3).

The bubble behaviour is illustrated by Figure 2(b). A bubble which contains $n_{a,3} > n_{crit}$ air molecules fulfills for all $R > 0$ the condition $\partial W / \partial R < 0$. Equation (2) implies then that the bubble can

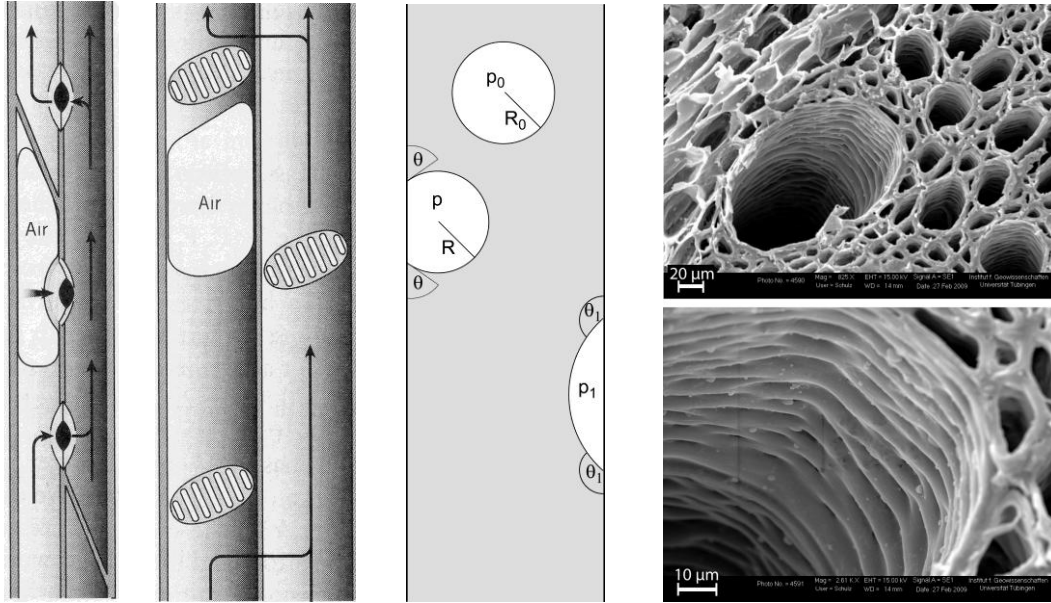


Fig. 1 Left/centre left: Conduit elements connected by torus-margopits (left) and membrane pits (centre left). In each case one embolised element has been hydraulically isolated and the water flow is redirected through its neighbours (Drawing taken from [8]). Centre right: Conduit with stable gas bubbles. Two of them are attached to the conduit walls forming the contact angles θ and θ_1 . Right: Cross section through the xylem of *Aristolochia macrophylla* showing an assemblage of conduits (upper right) and the ornamented inner wall of one conduit (lower right) (Photos: Tatiana Miranda, Institute for Geosciences, University of Tübingen).

only expand. If the bubble contains $n_{a,1} < n_{crit}$ air molecules its future depends also on its initial radius R : in the case $R > R_{inst}$ it expands, in the case $0 < R < R_{inst}$ the bubble expands or contracts towards R_{stab} .

Figure 3 illustrates the interdependence of initial radius and air content in a stability diagram in the (n_a, R) -plane:

- (i) The ability of an air-water vapour bubble to seed embolism increases with its air content (with the water pressure p_s being constant): A bubble of initial radius R_2 containing n_1 air molecules contracts towards the stable radius R_{stab} , a bubble of the same initial radius containing n_4 air molecules (with $n_4 > n_1$), however, bursts.
- (ii) If p_s decreases (i.e. becomes more negative) the stability region which represents all bubbles (of radius R and containing n_a air molecules) drifting to stable equilibrium shrinks. Hence, bubbles which were within the stability region at a given water pressure may become unstable because the borderline between stability and instability has wandered across their (fixed) location in the (n_a, R) -plane, due to the drop in p_s .
- (iii) Immediate collapse of an air-water vapour bubble is impossible. This is because — different to the water vapour molecules in the bubble — the air molecules cannot condensate to the liquid state (at least not under temperatures and pressures compatible with living plants). Hence, a stable air-water vapour bubble can only disappear by dissolution via diffusion of the air content into the surrounding water. Whether or not this will happen depends on the concentration C_{air} of air molecules already dissolved in the surrounding water.

Bubble attached to a flat portion of the vessel wall

In order to describe an air/water vapour bubble attached to the vessel wall we have to extend expression (1) to

$$W = \left[4\pi\gamma R^2 - \frac{4\pi}{3} (p_w - p_s) R^3 \right] \xi(\theta) + 3\mathcal{R}T n_a \log\left(\frac{R_{max}}{R}\right) \quad (4)$$

where θ denotes the contact angle at the line where solid, liquid and gaseous phase meet, and $\xi(\theta) := (2 + 3 \cos \theta - \cos^3 \theta) / 4$. Due to $\xi(0) = 1$, expression (4) reduces in the limit $\theta = 0$ to expression (1).

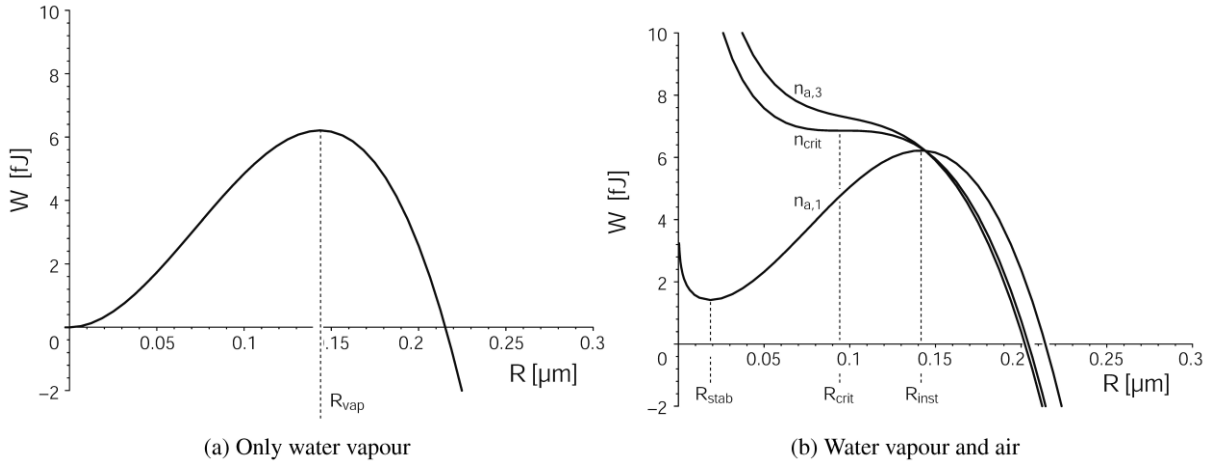


Fig. 2 Energy of bubble formation W plotted against bubble radius R . Water pressure in the conduit amounts to $p_s = -1\text{MPa}$. Equilibrium between expanding and contracting forces is realised only at bubble radii R representing extrema of $W(R)$. Maxima indicate unstable, minima stable equilibrium. (a) Bubble filled only with water vapour. (b) Bubble filled with water vapour and air. Curves are plotted for the following numbers of air molecules: $n_{a,1} = 7.5 \times 10^{-20}$ mol, $n_{crit} = 7.5 \times 10^{-19}$ mol and $n_{a,3} = 9 \times 10^{-19}$ mol.

Thus, in the case of complete wettability a freely floating bubble and one attached to the vessel wall behave in the same way.

Exploiting $\partial W/\partial R = 0$, we find that the (mechanical) equilibrium radii of an attached bubble have exactly the same form as those (see (3)) of its freely floating counterpart, provided we include into the critical (maximum) number n_{crit} the factor $\zeta(\theta)$ (i.e. $n_{crit} \rightarrow n_{crit} \zeta(\theta)$). The other features of the equilibrium radii (stability, the limits for $n_a \rightarrow 0$ and $n_a \rightarrow n_{crit}$ and the behaviour for $n_a > n_{crit}$) are as for a freely floating bubble.

Figure 3(c) illustrates that because of $0 \leq \zeta(\theta) \leq 1$ an attached bubble can not accomodate as many particles as a freely floating bubble (apart from the case $\theta = 0^\circ$ when $\zeta = 1$). This feature turns out to be potentially hazardous: Mechanically stable floating bubbles may realise during attachment that the number of air particles they house and the vessel wall's contact angle are incompatible. Thus, they can not settle to a new stable mechanical equilibrium and burst. The upper bubble on the curve related to $\theta = 0^\circ$ in part (c) of Figure 3 will suffer this fate if it tries to attach to a wall with contact angle $\theta = 90^\circ$. The lower bubble on the same curve is more lucky: it houses less particles than $n_{crit}(\theta = 90^\circ)$ allows and finds a new stable mechanical equilibrium. From the family of curves depicted in Figure 3(c) it is obvious that the radius of the attached bubble segment is always greater than the radius of the freely floating bubble, i.e. $R_{stab}(n_a, \theta) > R_{stab}(n_a, 0)$ for $\theta > 0$. (Recall that we assume that the floating bubble attaches to an at least approximately flat vessel wall. Hence, attached bubbles are shaped like segments of a sphere with radius R .)

Conditions for spontaneous attachment

In order to explore whether (and if so, under which conditions) a mechanically stable floating bubble attaches *spontaneously* to an (approximately flat) vessel wall we have to compare the energies associated with the formation of a floating and of an attached bubble. If the free energy of the final state is smaller than the free energy of the initial state, the process proceeds spontaneously. The energies related to the two bubble states have already been calculated in (1) and (4).

Since the formation energy of a floating and of an attached bubble coincide in the case $\theta = 0$ we may first calculate what happens to $W_{stab}(\theta)$ if θ is infinitesimally increased and integrate afterwards up to

$$dW_{stab} = \left[\frac{\partial W_{stab}}{\partial \theta} + \frac{\partial W_{stab}}{\partial R} \frac{dR}{d\theta} + \frac{\partial W_{stab}}{\partial \xi} \frac{d\xi}{d\theta} \right] d\theta \quad (5)$$

the desired value of θ . Because we compare mechanically stable bubbles (with n_a and p_s fixed) the rules of partial differentiation yield

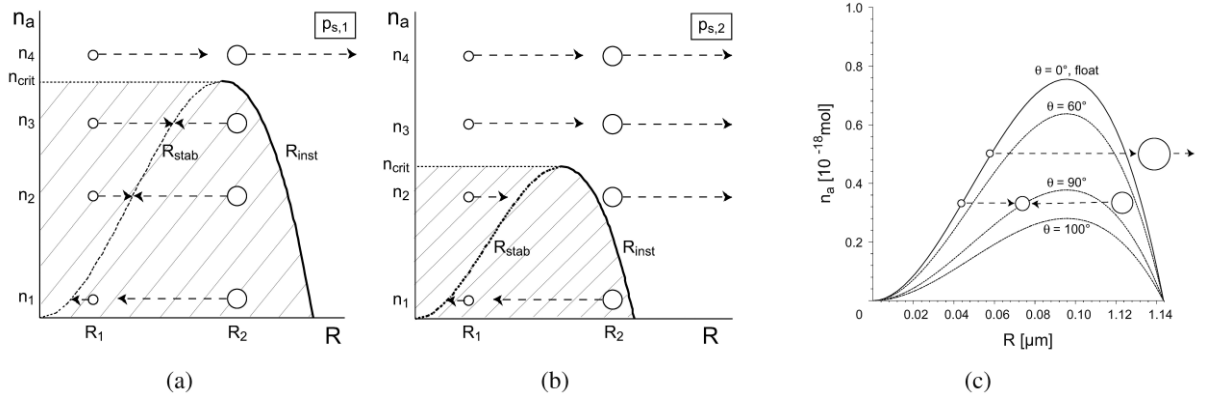


Fig. 3 Regions of stability and instability of bubbles of radius R , filled with water vapour and n_a air molecules. (a): Stability diagram for a given water pressure $p_{s,1}$. (b): Stability diagram for a water pressure $p_{s,2}$ with $p_{s,2} < p_{s,1}$ (i.e. $p_{s,2}$ is more negative than $p_{s,1}$). Only bubbles lying on the curves R_{stab} (broken line) and R_{inst} (solid line) are in stable resp. unstable equilibrium. Bubbles represented by other (n_a, R) -values either contract or expand (indicated by broken arrows). Bubbles belonging to the hatched region (left and below the solid curve R_{inst}) contract or expand towards the stable radius R_{stab} lying on the dotted curve. Bubbles characterised by (n_a, R) -values outside the stability region expand. If p_s decreases, the region of stability shrinks. Hence, bubbles which are in equilibrium under water pressure $p_{s,1}$ (like those inhabited by n_3 air molecules in part (a) of the figure) fall outside of the equilibrium region if p_s drops to $p_{s,2} < p_{s,1}$ (see part (b) of the figure). (c): Bubbles attached to a flat vessel wall with contact angles $\theta = 0^\circ, 60^\circ, 90^\circ, 100^\circ$. R_{stab} of a completely wetting vessel wall ($\theta = 0^\circ$) is identical to R_{stab} of a floating bubble.

The first two terms of the right hand side of this expression vanish because W depends not explicitly on θ (hence, $\partial W/\partial\theta = 0$), and mechanical equilibrium requires $\partial W/\partial R = 0$. Thus,

$$dW_{stab} = \left[\frac{\partial W_{stab}}{\partial \xi} \frac{d\xi}{d\theta} \right] d\theta = \left[4\pi\gamma R_{stab}^2(\theta) - \frac{4\pi}{3} (p_w - p_s) R_{stab}^3(\theta) \right] \left(-\frac{3}{4} \sin^3 \theta \right) d\theta < 0 \quad (6)$$

Manipulations based on the Young-Laplace-Equation imply that the expression in brackets is positive and $\sin^3\theta$ is positive within the interval $0 < \theta < 180^\circ$. Therefore, an increase of θ by the amount $d\theta > 0$, is related to a decrease of the formation energy $W_{stab}(\theta)$ by $dW_{stab}(\theta) < 0$. Thus, the formation energy of a floating bubble (characterised by $\theta = 0$) which attaches to a vessel wall (characterised by $\theta > 0$) changes by the necessarily negative amount

$$\Delta W_{stab} = \int_0^\theta dW_{stab} < 0 \quad (7)$$

The last relation allows the following conclusions:

- (i) The attachment process of a floating bubble proceeds spontaneously and without energy input.
- (ii) *Detachment* needs energy input, spontaneous bubble detachment is therefore improbable.
- (iii) The conclusion $\Delta W_{stab}(\theta) < 0$ applies for *any* $\theta > 0$.
- (iv) If the contact angle θ varies across the vessel wall, the bubble will show a tendency to move (and enlarge) its contact circle towards regions of higher θ . (The contact circle is the line where the air/water-interface touches the flat, solid vessel wall.)

Diffusional equilibrium and dissolution of bubbles

The following reasoning applies both to freely floating bubbles and to bubbles which are attached to the conduit wall. The “long term” behaviour of an mechanically equilibrated bubble rests upon two physical effects ([2]):

- (i) At the bubble’s air/water-interface, air particles dissolve into or escape from the water. Thus, the (partial) pressure p_a of the air inside the bubble and the concentration C_R of the dissolved air particles in the liquid in the near vicinity of the bubble are proportional to

each other as stated by Henry's Law $C_R = k_H p_a$ where the constant k_H depends on the gas and liquid species involved.

- (ii) If the concentration C_R of dissolved gas particles close to the bubble deviates from the value C_{air} farther away in the liquid, diffusional currents, directed from areas of higher to areas of lower concentration arise

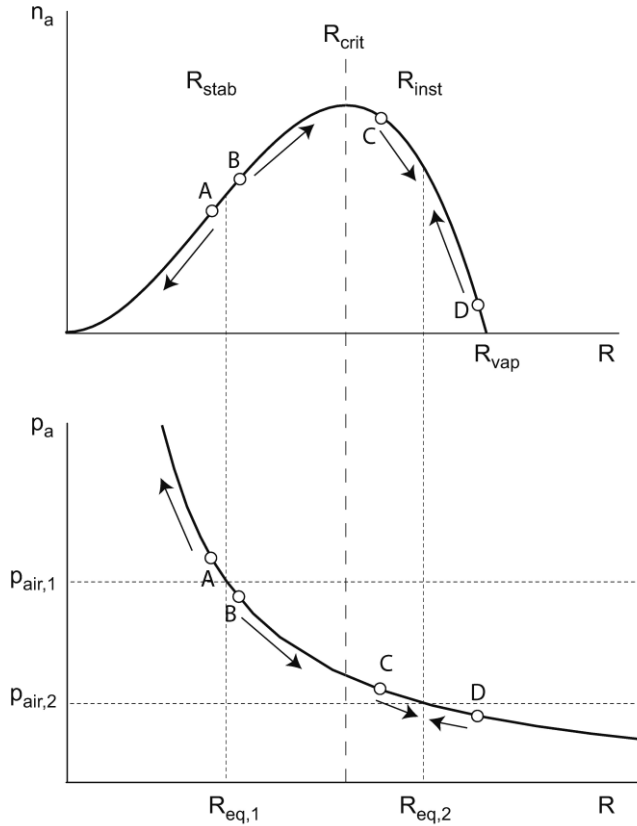


Fig. 4 Diagram explaining the behaviour of gas bubbles which are in equilibrium with respect to mechanical forces but not with respect to exchange of air particles between bubble and surrounding water (for explanation see text).

As the combined result of both processes we expect that air particles are transported either out of and away from the gas bubble or into the opposite direction until an diffusional equilibrium situation between the concentrations C_R and C_{air} is attained. To facilitate further notation we define in analogy to Henry's Law a (fictitious) pressure $p_{air} := C_{air}/k_H$ which allows to state diffusional equilibrium as $p_{air} = p_a$. The Young-Laplace-Equation

$$p = p_s + \frac{2\gamma}{R} \quad (8)$$

connects the gas pressure p within an mechanically(!) equilibrated bubble with the surface tension γ at the liquid/gas-interface, the bubble radius R and the pressure p_s of the liquid surrounding the bubble. Splitting the gas pressure into the partial pressures of water vapour and air according to $p = p_w + p_a$ we find from (8) for bubbles in mechanical equilibrium $p_a = p - p_w = p_s - p_w + 2\gamma/R$. Observing that this relation establishes a one-to-one correspondence between p_a and R we use $p_{air} = p_a$ to define an equilibrium radius

$$R_{eq} := \frac{2\gamma}{p_{air} + p_w - p_s} \quad (9)$$

Notice, that R_{eq} defines an equilibrium with respect to the exchange of air particles between the bubble and the surrounding water whereas the radii R_{stab} and R_{inst} (which were defined in (3)) represent equilibria with respect to the mechanical forces which try to expand or contract the bubble.

We can now understand the behaviour of gas bubbles which are in equilibrium with respect to mechanical forces but not with respect to exchange of air particles between bubble and surrounding

water (consult Figure 4): Exchange equilibrium exists if $p_a = p_{air}$ is realised. (In the lower part of Figure 4, this case is indicated by the intersections between the broken, horizontal lines and the $p_a(R)$ -curve at $(R_{eq,1}, p_{air,1})$ and $(R_{eq,2}, p_{air,2})$.) Depending on whether R_{eq} lies in the interval $0 < R_{stab} < R_{crit}$ or $R_{crit} < R_{inst} < R_{vap}$, the bubble goes through qualitatively different developments:

- (i) The bubble starts at position **A** or **B**, close to $(R_{eq,1}, p_{air,1})$ in the interval $0 < R_{stab} < R_{crit}$:
 - a) At position **A** the inequality $p_a > p_{air}$ is valid, causing air particles to leave the bubble. This loss entails a contraction of the bubble, as can be seen from the $n_a(R)$ diagram in the upper part of the figure. This contraction raises the bubble's partial air pressure p_a which accelerates the particle loss and so on, until the bubble has dissolved.
 - b) At position **B** we have $p_a < p_{air}$. Now air particles from the surrounding water enter the bubble which reacts by an expansion, according to the $n_a(R)$ -diagram. The bubble's partial air pressure p_a decreases whereupon still more air particles enter the bubble and so on. This process continues either until n_a exceeds n_{crit} , or until all air particles within the xylem water have assembled in the bubble.
- (ii) The bubble starts at positions **C** or **D**, close to $(R_{eq,2}, p_{air,2})$ in the interval $R_{crit} < R_{inst} < R_{vap}$. Applying the same reasoning as in case (i), the bubble is found to move towards the equilibrium position $(R_{eq,2}, p_{air,2})$.

Obviously, equilibria with respect to the exchange of air particles related to a bubble radius R_{eq} lying within the interval $0 < R_{eq} < R_{crit}$ are unstable, similar equilibria within $R_{crit} < R_{eq} < R_{vap}$ are, however, stable.

Hence, *stable* mechanical and exchange equilibria preclude each other: For $0 < R < R_{crit}$ the mechanical equilibrium is stable and the exchange equilibrium is unstable, for $R_{crit} < R < R_{vap}$ it is the other way round. The different time scales on which the processes connected with the two equilibria operate impose a clear hierarchy on their relevance: Since the exchange of air particles is a very slow process, compared to the action of the expanding and contracting forces, a mechanically unstable bubble with $R_{inst}(n_a)$ has negligible chances to settle down to a stable exchange equilibrium. It is much more probable that it either bursts or shrinks to the corresponding stable radius $R_{stab}(n_a)$ where an unstable exchange equilibrium awaits it. Depending on the relation between p_a and p_{air} this state will finally develop into a bubble burst due to congestion (i.e. $n_a > n_{crit}$) or to complete bubble dissolution.

A condition which guarantees that dissolution occurs can be read off from Figure 4: If the inequality $R_{eq} > R_{crit}$ holds all bubbles in stable mechanical equilibrium dissolve. This condition can be reformulated as a relation between the concentration C_{air} of gas particles dissolved in the surrounding liquid, the (negative) pressure p_s of this liquid, and the water vapour saturation pressure p_w , namely $C_{air} = k_H p_{air} < k_H (p_w - p_s)/2$. Solving this relation for p_s we find $p_s < -2 p_{air} + p_w$. Since groundwater in the soil is in contact with air of atmospheric pressure it is reasonable to assume $p_{air} \approx p_{atmosphere} \approx 10^5$ Pa. Neglecting the term p_w on the right hand side (at 25 °C we find $p_w \approx 3167$ Pa \ll 100 000 Pa $\approx p_{air}$) this equation reduces to

$$p_s \lesssim -2 \times 10^5 \text{ Pa} \quad (10)$$

Hence, if condition (10) is fulfilled embryonic bubbles appearing in the stability regions depicted in Figure 3 dissolve after a while in the surrounding water.

As stated above, the results related to bubble dissolution apply to floating and to attached bubbles. Fig. 3 shows that the bubble radius R increases if attachment occurs and results in mechanical stability. This increase in bubble radius entails a second potential hazard (cf. Figure 4): A floating bubble in situation **A** (with $p_{air} = p_{air,1}$) is on the route to dissolution because its radius is slightly smaller than the equilibrium radius $R_{eq,1}$. If its particle content and the wall's contact angle allow a new stable mechanical equilibrium after attachment it may well happen, that the bubble finds itself, due to the inevitable radius increase, after attachment at position **B** from where its radius and particle content increases until it bursts.

Conclusion

Spontaneous cavitation (“homogenous nucleation”): The spontaneous emergence of a water vapour filled bubble is *extremely* unlikely for the water tensions found in plants of $p_s \geq -1$ MPa. Should

homogenous nucleation occur nonetheless, the fate of the emerging bubble depends on its initial radius R : For $R < R_{vap} = 2\gamma/(p_w - p_s)$ the bubble disappears immediately, for $R > R_{vap}$ it bursts, causing cavitation of the befallen vessel segment.

Air seeding (“heterogenous nucleation”): Decisive for the fate of a bubble containing air and water vapour are two different processes each of which may or may not lead to an equilibrium. They occur on different time scales:

- (i) **Mechanical stability/instability (quick adjustment):** If initial bubble radius R and initial number of air particles n_a satisfy the inequalities $n_a < n_{crit}$ and $R < R_{inst}(n_a)$ simultaneously the bubble approaches mechanical stability at the radius $R = R_{stab}(n_a)$. Otherwise, the bubble bursts.
- (ii) **Diffusional stability/instability (slow adjustment):** A bubble which has established mechanical stability (i.e. $R = R_{stab}(n_a)$) either loses air molecules to the surrounding xylem water (and dissolves eventually completely) or it accumulates air from the xylem water. This accumulation lasts until the bubble bursts (when $n_a = n_{crit}$ is achieved) or until no more air molecules are available in the xylem water. If the xylem water is in contact with the atmosphere, mechanically stable bubbles dissolve completely, provided the xylem water pressure p_s satisfies $p_s \leq -2 \times 10^5$ Pa.

Bubble attachment to vessel wall: Basically, an attached bubble behaves like a freely floating bubble. The major difference is that its maximum particle capacity may fall short of or exceed n_{crit} of a freely floating bubble. Whether this happens or not depends on the contact angle and one (or more parameters) describing the vessel wall morphology.

This gives rise to two effects which make themselves felt when a floating bubble attaches to a flat wall with contact angle θ :

- (i) A bubble that is mechanically stable while it is floating, bursts during wall attachment if $n_a > n_{crit}(\theta)$.
- (ii) Depending on the value of the diffusional equilibrium bubble radius R_{eq} , a floating bubble which is mechanically stable, loses particles, and fulfills point (i), may remain stable upon attachment but will start to accumulate particles (instead of losing them). This accumulation lasts until the bubble bursts (when $n_a = n_{crit}(\theta)$ is achieved) or until no more air molecules are available in the xylem water.

Comparison of the reversible free energies associated with the formation of a floating and an attached bubble reveals:

- (i) Bubble attachment to a flat vessel wall happens spontaneously and without energy input for any $\theta > 0$.
- (ii) If the contact angle θ varies across a flat vessel wall, the bubble will show a tendency to move (and enlarge) its contact circle towards regions of higher θ .

References

1. DeBenedetti, P. G. (1996): *Metastable Liquids*, Princeton University Press, Princeton, New Jersey.
2. Konrad, W., Roth-Nebelsick, A. (2003): *The dynamics of gas bubbles in conduits of vascular plants and implications for embolism repair*. Journal of Theoretical Biology **224**, 43–61.
3. Nobel, P. S. (2005): *Physicochemical and environmental plant physiology*, 3rd ed. Elsevier Academic Press, Amsterdam.
4. Oertli, J. J. (1971): *The stability of water under tension in the xylem*. Zeitschrift für Pflanzenphysiologie **65**, 195–209.
5. Pickard, W.F. (1981): *The ascent of sap in plants*. Prog. Biophys. molec. Biol. **37**, 181–229.
6. Shen, F., Gao, R., Liu, W., Zhang, W. (2002): *Physical analysis of the process of cavitation in xylem sap*. Tree Physiology **22**, 655–659.
7. Shen, F., Wenji, L., Rongfu, G., Hu, H. (2003): *A careful analysis of gas bubble dynamics in xylem*. J. Theoretical Biology **225**, 229–233.
8. Taiz, L., Zeiger, E. (2006): *Plant Physiology*. Sinauer Associates, Sunderland, Massachusetts.

Cytoskeletal control of cellular shape and directional growth in pollen tubes

Firas Bou Daher, Anja Geitmann

Université de Montréal, département de sciences biologiques, Institut de recherche en biologie végétale, Canada.

Abstract

Pollen grains produce a cylindrical protuberance - the pollen tube - that has to invade the apoplast of the pistillar tissues to deliver the sperm cells to the ovule embedded deep within the ovary. To do so, the pollen tube expands exclusively at the apex resulting in tip growth. To ensure sperm transfer, the pollen tube has to maintain its cylindrical shape and to respond to external signals to be able to reach its target. We study the role of the cytoskeleton in the mechanical aspects of pollen tube tip growth such as control of cellular shape and directional growth. We show that the subapical actin fringe has a crucial role in controlling the cylindrical shape and the diameter of the pollen tube, and in sustaining its elongation. Our results also reveal that the actin cytoskeleton is involved in the tropic response of the pollen tube in a calcium concentration dependent manner.

Introduction

Pollen tubes are cellular protuberances formed by pollen grains, the male gametophytes in flowering plants. Their function is the delivery of the sperm cells from the pollen grain to the ovule. During its passage through the stylar tissues, the pollen tube has to resist external pressures and to produce an invasive force that allows it to elongate within the apoplast of the transmitting tissue. To find its target, the embryo sac, it has to respond to external signals, change direction when required, and exhibit tropic behavior (Cheung and Wu 2001). Similar to root hairs and fungal hyphae, pollen tubes are tip growing cells. The driving force for the growth process is generated by the turgor pressure and elongation is sustained by a continuous supply of new cell wall material deposited at the growing apex (Bove *et al.* 2008; Zonia and Munnik 2008).

While many studies have been done on the animal cell cytoskeleton and its role in cellular extension, motility, and architecture, little is known about the mechanical role of the cytoskeletal elements in the control of plant cellular architecture. Focus has hitherto been on the implication of microtubules in anisotropic cell wall expansion (Baskin 2005). The reason for this scarcity of information on cytoskeletal mechanics in plants is the fact that the relationship between turgor pressure and cell wall has been considered to be the dominant player determining plant cell growth in general and pollen tube tip growth in particular (Geitmann and Steer 2006). Therefore, while the role of the cytoskeleton in vesicle and organelle transport within the pollen tube cytoplasm is well defined (Lovy-Wheeler *et al.* 2007), its implication in the mechanics of the tip growth process is poorly understood.

The pollen tube cytoskeleton has two main components: microtubules and actin microfilaments (Geitmann and Emons 2000). Microtubules do not seem to be directly involved in pollen tube tip growth, since inhibition of their polymerization does not prevent

pollen tube elongation (Gossot and Geitmann 2007). Actin on the other hand is crucial as revealed by inhibitors that interfere with actin polymerization (Vidali and Hepler 2001). Actin filaments in the pollen tube are oriented longitudinally, parallel to the growth axis and they form a fringe of fine filaments in the subapex of the tube (Lovy-Wheeler *et al.* 2005). It has been shown that microfilaments play a role in the capacity of pollen tubes to invade a mechanical obstacle and to elongate in stiffened media (Gossot and Geitmann 2007).

The configuration of the actin cytoskeleton, the dynamics of its remodeling through polymerization, cross-linking, and bundling is controlled by the cytoplasmic Ca^{2+} and H^+ concentrations through activation and inactivation of actin binding proteins. Ca^{2+} also plays a role in exocytosis and vesicle-membrane fusion (Battey *et al.* 1999). A supply of Ca^{2+} in the growth medium is, therefore, indispensable for pollen germination and pollen tube growth (Pierson *et al.* 1994). Reflecting the polarized distribution of growth activity and actin configuration in this cell, the cytoplasmic Ca^{2+} concentration displays a steep, tip high gradient (Feijó *et al.* 1995). Its disruption causes the arrest of pollen tube growth (Pierson *et al.* 1994). The connection between actin cytoskeleton and calcium is a two-way control mechanism, however, since actin microfilaments were shown play an important role in the regulation of plasma membrane located Ca^{2+} channels and thus the Ca^{2+} influx into the cell (Wang *et al.* 2004).

Artificial displacement of the cytoplasmic calcium gradient to the side of the growing pollen tube apex induces the tube to change direction (Malhó and Trewavas 1996). Whether this is due to a remodeling of the apical actin cytoskeleton or to a direct effect on the location of exocytosis is unknown, however. We want to investigate the role of the actin cytoskeleton in controlling the shape of the growing cell and in the capacity of the pollen tube to change its growth direction and hence to respond to an external signal. For the latter, we devised an assay that allows us to apply a directional signal in quantitative manner and to measure the precise time course of events associated with the cellular response. In vitro grown pollen tubes are exposed to an electrical field and their response is monitored using brightfield and fluorescence microscopy.

Material and methods

Plant material

Camellia japonica pollen was collected from a plant growing in the Montreal Botanical Garden, dehydrated in gelatin capsules on anhydrous silica gel overnight and stored at -20°C . *Camellia* pollen growth medium contained 1.62 mM H_3BO_3 , 2.54 mM $\text{Ca}(\text{NO}_3)_2 \cdot 4\text{H}_2\text{O}$ (unless mentioned otherwise), 1 mM KNO_3 , 0.81 mM $\text{MgSO}_4 \cdot 7\text{H}_2\text{O}$, 8% sucrose (w/v).

Actin labelling

After one hour of growth, *Camellia* pollen tubes were fixed for 40 seconds in the microwave (PELCO cold spot[®] biowave 34700) under 150 Watts in 3% formaldehyde, 0.5% glutaraldehyde and 0.05% Triton X-100 solution in a buffer composed of 100 mM PIPES, 5 mM MgSO_4 and 0.5 mM CaCl_2 at pH 9. Pollen tubes were then washed 3 times for one minute each in the same buffer then incubated overnight at 4°C in a rhodmine-phalloidin (Molecular Probes) in a buffer composed of 100mM PIPES, 5 mM MgSO_4 , 0.5 mM CaCl_2 and 10 mM EGTA at pH 7. Next day, pollen was washed 5 times for one minute each in the same buffer. All washing steps were conducted in a microwave (model) at 150 Watts. Pollen was then mounted on glass slides in a drop of citifluor (Electron Microscopy Sciences), covered with a cover slip, sealed and immediately observed in the microscope.

Microscopic observations

Confocal images were taken on a Zeiss LSM 510 META confocal microscope equipped with a LSM 5 LIVE setup and pictures were processed with the LSM Image Examiner software.

Time lapse series for the galvanotropic experiments were taken with a Nikon TE2000 microscope equipped with a Roper fx cooled CCD camera and ImagePro software (Media Cybernetics, Carlsbad, CA).

Galvanotropic experiment

Camellia growth medium solidified with 1% agarose type VII (Sigma-Aldrich) was precooled to 40°C before addition of latrunculin B. The medium was spread into a thin layer and left for 5 minutes to solidify. Pollen was then applied in a line parallel to the electrical field. Pollen was left to germinate in an electrophoresis chamber designed in way that can be mounted on an inverted microscope. This chamber consisted of a petri dish with a 2x1 cm opening sealed with a coverslip.

Results and discussion

The actin fringe controls pollen tube diameter

It is intriguing how the pollen tube is able to strictly control its diameter and form a perfectly tubular shape. The actin cytoskeleton and in particular the subapical actin fringe are likely to be crucial in the control of the growth process as they deliver the secretory vesicles to precisely identified sites on the cellular surface. In order to identify the role of the actin fringe in maintaining the tubular shape of the pollen tube, we used pharmacological agents that have the capacity to affect the degree of crosslinking between actin filaments. Ethylene glycol bis[sulfosuccinimidylsuccinate] (sulfo-EGS) is known to be a strong actin cross-linker (Lovy-Wheeler *et al.* 2005; Gossot and Geitmann 2007). It has been used to block the advancement of the actin fringe in poppy and lily pollen tubes (Gossot, unpublished data). We tested different concentrations of sulfo-EGS on *Camellia* pollen tubes and monitored pollen tube velocity and tip shape. At 500mM sulfo-EGS, and after just few seconds of application of the drug, pollen tube velocity was decreased by half (from 0.2 to 0.1 $\mu\text{m}/\text{sec}$) followed by a swelling at the tip (Figure 1B). After few minutes, pollen tube recovered its original shape (Figure 1 D) but failed to recover its original velocity during the remaining observation time.

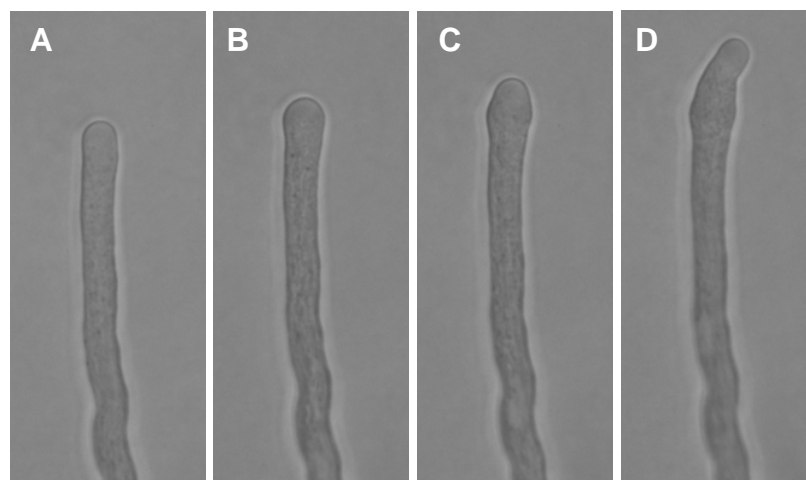


Figure 1: Time lapse series of *Camellia japonica* pollen tubes treated with sulfo-EGS. (A) Before the application of the drug, (B) 1 minute after the application, (C) 6 minutes after and (D) 15 minutes after.

To determine how this drug affects the actin cytoskeleton, we labeled sulfo-EGS treated tubes with rhodamine-phalloidin. At 10 minutes of treatment with sulfo-EGS, the pollen tube lost its specific actin conformation at the tip; the actin fringe was lost and the actin arrays had an unorganized distribution in the swelling tip (Figure 2 B). After 20 minutes actin arrays seemed to assemble at the very tip of the apical swelling (Figure 2 C) and subsequently these form a fringe-like structure, that allows the recovery of the pollen tube growth in its original diameter (in less than 30 minutes) (Figure 2 D).

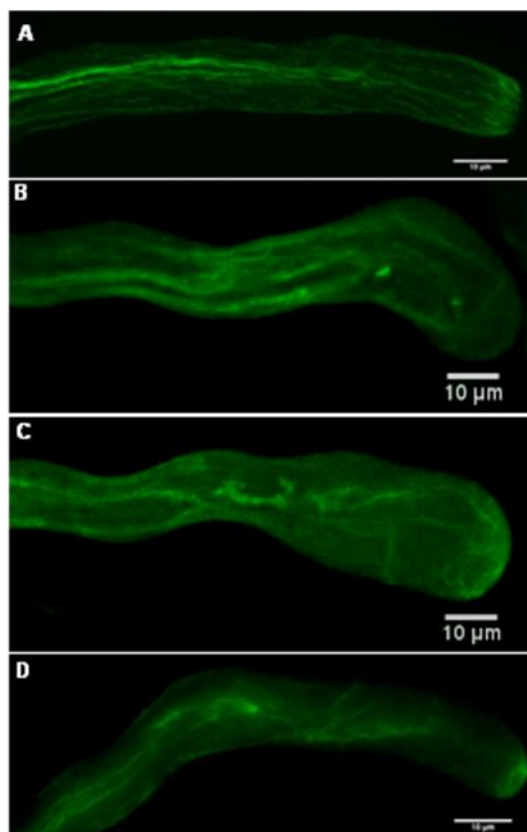


Figure 2: Actin cytoskeleton in *Camellia* pollen tubes labeled with rhodamine-phalloidin. Growing pollen tubes were treated with 500 mM sulfo-EGS (B-D) for 10 (B), 20 (C) and 30 minutes (D). The scale bars represent 10µm.

This indicates the importance of the role of this cytoskeletal structure in maintaining the integrity of the pollen tube tubular shape and the normal growth rate.

The actin cytoskeleton controls the pollen tube's capacity to perform directional growth

While *in planta* growing pollen tubes are likely to react to chemical and mechanical cues, we wanted to devise an experimental setup that allowed us to switch on a directional trigger at a particular point in time and at a well defined parameter setting. Chemical signals have the disadvantage of having to diffuse which takes time, and secondly, the local concentration of the signal is virtually impossible to determine since the diffusing chemical forms a gradient. Therefore, we resorted to establishing an electrical trigger, which had been shown before to induce tropic behavior in pollen tubes (Nakamura *et al.* 1991; Malhó *et al.* 1992).

To assess the role of the cytoskeletal elements in the pollen tube's ability to respond to an electrical field, we grew pollen in a solid medium and once they achieved a length of

approximately 400 μm , an electrical field perpendicular to the direction of pollen tube growth was applied. We compared tubes growing in the control medium with tubes growing in the presence of Latrunculin B (an inhibitor of F-actin polymerization). In addition, we tested the effect of an increase in calcium concentration in the surrounding medium on the pollen tube behavior.

To quantify pollen tube response, we measured the percentage of pollen tubes showing a response (i.e. change in growth direction), the angle between new and old direction of growth and time between application of electrical field and first visible response.

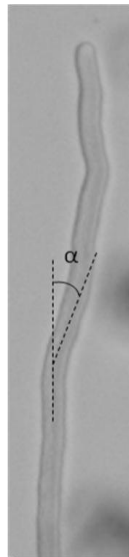


Figure 3: *Camellia japonica* pollen tube changing growth direction by an angle α after the application of an electrical field perpendicular to the growth direction.

From these data we can conclude in preliminary manner that actin has a role in mediating the tropic response of the pollen tube. In addition, it seems clear that calcium ions in the medium seem to be implicated as an increase in their concentration results in a faster tropic response.

Conclusion

Our experiments showed that the actin cytoskeleton in the growing pollen tube, and, more specifically, the actin fringe is strongly implicated in the elongation and maintenance of the cylindrical shape of the pollen tube. We also showed that the actin cytoskeleton plays an important role in the tropic response of the pollen tube in calcium concentration dependent manner.

References

- Baskin, T. I. (2005). Anisotropic expansion of the plant cell wall. *Annual Review of Cell and Developmental Biology* **21**(1): 203-222.
- Batley, N. H., N. C. James, A. J. Greenland and C. Brownlee (1999). Exocytosis and endocytosis. *Plant Cell* **11**(4): 643-659.

- Bove, J., B. Vaillancourt, J. Kroeger, P. K. Hepler, P. W. Wiseman and A. Geitmann (2008). Magnitude and direction of vesicle dynamics in growing pollen tubes using spatiotemporal image correlation spectroscopy and fluorescence recovery after photobleaching. *Plant Physiology* **147**(4): 1646-1658.
- Cheung, A. Y. and H.-m. Wu (2001). Plant biology: pollen tube guidance--right on target. *Science* **293**(5534): 1441-1442.
- Feijó, J. A., R. Malhó and G. Obermeyer (1995). Ion dynamics and its possible role during in-vitro pollen germination and tube growth. *Protoplasma* **187**(1-4): 155-167.
- Geitmann, A. and A. M. C. Emons (2000). The cytoskeleton in plant and fungal cell tip growth. *Journal of Microscopy* **198**(3): 218-245.
- Geitmann, A. and M. Steer (2006). The architecture and properties of the pollen tube cell wall. *The Pollen Tube*. M. R., Springer Berlin / Heidelberg: 177-200.
- Gossot, O. and A. Geitmann (2007). Pollen tube growth: coping with mechanical obstacles involves the cytoskeleton. *Planta* **226**(2): 405-416.
- Lovy-Wheeler, A., L. Cardenas, J. G. Kunkel and P. K. Hepler (2007). Differential organelle movement on the actin cytoskeleton in lily pollen tubes. *Cell Motility and the Cytoskeleton* **64**(3): 217-232.
- Lovy-Wheeler, A., K. L. Wilsen, T. I. Baskin and P. K. Hepler (2005). Enhanced fixation reveals the apical cortical fringe of actin filaments as a consistent feature of the pollen tube. *Planta* **221**(1): 95-104.
- Malhó, R., J. A. Feijó and M. S. S. Pais (1992). Effect of electrical fields and external ionic currents on pollen-tube orientation. *Sexual Plant Reproduction* **5**(1): 57-63.
- Malhó, R. and A. J. Trewavas (1996). Localized apical increases of cytosolic free calcium control pollen tube orientation. *The Plant Cell* **8**(11): 1935-1949.
- Nakamura, N., A. Fukushima, H. Iwayama and H. Suzuki (1991). Electrotropism of pollen tubes of *Camellia* and other plants. *Sexual Plant Reproduction* **4**(2): 138-143.
- Pierson, E. S., D. D. Miller, D. A. Callahan, A. M. Shipley, B. A. Rivers, M. Cresti and P. K. Hepler (1994). Pollen tube growth is coupled to the extracellular calcium ion flux and the intracellular calcium gradient: effect of BAPTA-type buffers and hypertonic media. *The Plant Cell* **6**(12): 1815-1828.
- Vidali, L. and P. K. Hepler (2001). Actin and pollen tube growth. *Protoplasma* **215**(1-4): 64-76.
- Wang, Y.-F., L.-M. Fan, W.-Z. Zhang, W. Zhang and W.-H. Wu (2004). Ca²⁺-permeable channels in the plasma membrane of *Arabidopsis* pollen are regulated by actin microfilaments. *Plant Physiology* **136**(4): 3892-3904.
- Zonia, L. and T. Munnik (2008). Vesicle trafficking dynamics and visualization of zones of exocytosis and endocytosis in tobacco pollen tubes. *Journal of Experimental Botany* **59**: 861-873.

2. Modelisation

Modelling collapse of xylem pine needles: effects of tracheid geometry and tracheids' arrangement

George Jeronimidis¹, Catherine Coutand², Nicole Brunel³ and Hervé Cochard²

¹ University of Reading, Composite materials Engineering and Centre for Biomimetics, Reading, UK; ²INRA, UMR 547 PIAF, Clermont-Ferrand, France; ³Université Blaise Pascal, UMR 547 PIAF, Aubière, France

Abstract

Xylem sap transport in vascular plants can be limited by cavitation (breakage of water column) or by the collapse of cell walls under negative pressures. Cavitation has received more attention than collapse of cell walls but recent work has demonstrated the existence of cell wall collapse in lignin-deficient Arabidopsis [1] but also in non-mutant structures like the xylem of pine needles [2]. In this paper we present a study of cell wall collapse in the needles of four pine species (*P. cembra*, *P. mugo*, *P. sylvestris* and *P. nigra*). Finite Element Modelling (FEA) has been used to predict the sequence of events leading to the collapse of cells subjected to increasing negative pressures, typically down to – 5 MPa. The folding of cell walls and the associated reduction of lumen cross-sectional area has been investigated and the relative importance of material properties and geometry on collapse have been assessed. The results of the FEA simulations have been compared globally with experimental results obtained from the four pine species investigated. The comparison has been made using the changes in the isoperimetric coefficient and in the lumen cross-sectional area at various negative pressures and corresponding stages of collapse.

The results suggest that the collapse of the cell walls within a given xylem tissue is a progressive phenomenon driven by the reduction of pressure and not a sudden instability event, akin to buckling. The "rate" of collapse with pressure differs between species, depending mainly on specific morphological and geometrical characteristics of the xylem cells (deviation from circularity, cell-wall thickness, diameter for given thickness), as well as on the level of heterogeneity of the tissue (cell size and cell "roundness" distributions, in particular). The study has revealed inter-specific variability of collapse vulnerability and demonstrated that collapse onset starts before the cavitation process, raising the possibility of cell wall collapse as protection mechanism from cavitation, as suggested by Cochard *et al.* [2].

Introduction

Xylem sap in vascular plants is transported under negative pressures in xylem lignified conduits [3]. This transport can be affected by two phenomena: collapse of the water column (cavitation) or collapse of the conduit walls. In 2001, Hacke *et al.* [4] proposed the risk of conduit collapse to be related to the dimensions of cell. They suggest that the probability of cell collapse is a function of the ratio of cell-wall thickness (t) to cell diameter (b). Specifically:

$$P_{collapse} = f \quad t^2/b^2 \quad (1)$$

Applying the above equation to experimental data from pine needles' xylem leads, as expected, to a negative correlation between $P_{collapse}$ and tracheids anatomy but the correlation is weak. Moreover, the $P_{collapse}$ values obtained using simple cell geometry as the predictor, were two to six times more negative than the measured ones. The "collapse" model used by Hacke *et al.* is based on a regular array of cells of rectangular cross-section, of constant dimensions and wall thickness. In their model the force due to the pressure acts on flat cell walls which bend inwards as a plate. Indeed, for such a system the maximum wall stress and the maximum deflection due to bending are given by [5]:

$$\sigma_{max} = \beta \frac{pb^2}{t^2} \quad (2)$$

$$\delta_{max} = \gamma \frac{pb^4}{Et^3} \quad (3)$$

where t = cell wall thickness, b = cell wall side length, E = Young's modulus and β and γ are coefficients which depend on boundary conditions and length/side ratio of the plate.

Hacke's model implies that collapse occurs when the maximum stress in the cell wall is reached (Equation 2). As mentioned earlier, the cell walls of observed collapsed cells can deform very significantly without any apparent break, suggesting that excessive deformation is more important than limit stress in relation to collapse.

The limitations of Hacke's model in explaining the results obtained on pine needles suggested that it was necessary to take into account both the specific cellular structure of any given xylem tissue and the heterogeneity of tracheids' geometries because collapse is likely to depend on individual cell geometry but also on a "structure effect" i.e. on the arrangement of cells. In this study it has also been found that, although the Young's modulus used in the FEA simulations does have an effect on the development of collapse, its influence is much smaller than that of the heterogeneity of shape and size of cells. One additional interesting result of the work presented here is that the maximum strains in the folded cell walls at the advanced stages of collapse can easily reach values of 25% or more (predictions from FEA supported by direct measurements). No obvious "failure" can be detected in the micrographs of collapsed xylem cell walls for the four species and it is also known that the collapse phenomenon is to a large extent reversible [2].

Materials and methods

Experimental data for xylem wall deformation in the needles of different *Pinus* species were obtained by Cochard *et al* [2]. In short, cut branches were dehydrated on a bench in order to obtain a range of xylem pressures between 0 and -5MPa, as determined by the pressure chamber technique. At regular intervals during dehydration, needles were removed and instantly frozen by immersion in liquid nitrogen. Xylem wall deformation was observed with a cryo-SEM on cryo-fractured cross-sections. Lumen area (A) and wall perimeter (P) were measured using ImageJ for the different xylem tracheids and the isoperimetric coefficient Q of individual cells is defined as:

$$Q = \frac{4\pi A}{P^2} \quad (4)$$

where A is the lumen area and P the cell perimeter. $Q = 1$ for a perfectly circular lumen.

The available experimental data give the average isoperimetric coefficient of sets of xylem cells according negative pressure. In order to compare experimental data with simulated data (see below) we also computed the average isoperimetric coefficient of a given needle xylem by the means of isoperimetric coefficients of individual cells.

The FEA modelling was carried out using two different software codes, MSC/NASTRAN/MARC and Strand7. The various assumptions and details of the models are:

Model Geometry: The cell geometry obtained from microscopy sections was converted into meshed FEA models. Only the xylem cells were modeled in detail. In pine needles, the xylem cells are surrounded by parenchyma tissue which, owing to its stiffness, has a restraining effect on the inward collapse of the xylem cells. To minimize the complexity of the model, the parenchyma tissue was not modelled as system of individual cells but, rather, as a homogeneous material having the elastic modulus of average parenchyma tissue.

Meshing and FEA Elements: For the purpose of this study, the models used were 2D plane strain models, meshed mainly with 4-noded quadrilaterals and a small number of triangles. The cell-wall thickness of the four species investigated is of the order of 1 μ m and, typically, four to six quadrilateral elements were used across the wall thickness. Higher order 8-noded quadrilaterals were used on one or two occasions for comparison but no significant differences between the two types of elements could be observed and the 4-noded elements have been used for most simulations.

FEA Analysis: Large displacements during collapse and folding of the cell walls under negative pressure can lead to contact between walls or within the same wall. MARC was used for some simulations because of the easier way in which it deals with contact problems. With both MARC and Strand 7 a non-linear analysis was used, with large displacements options. In our model, all xylem cells of the portion of tissue analysed are under the same negative pressure which varies between 0 and -5 MPa in steps of 0.1 MPa in the simulations.

Material Properties: There are no data for the mechanical properties of xylem tissue in pine needles. Because of the type of analysis used (2D plane strain), the relevant Young's modulus of the xylem cells is the modulus in the circumferential direction. The material used in the FEA cell wall models of the xylem is isotropic and a value of 100 MPa was chosen (Fig. 1), based on data available for the modulus in the radial and tangential directions of wet wood [6]. This value fitted the experimental results for *Pinus Nigra* quite well and was used also for the other species of pine. A Poisson's ratio of 0.35 was used in all cases. For the parenchyma tissue, a value of 5 MPa was used, typical of this type of tissue in plants [7].

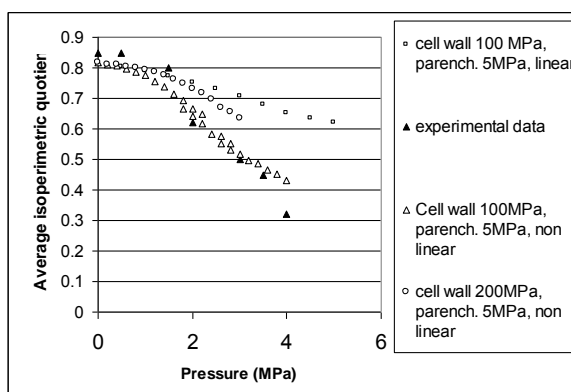


Fig. 1 Comparison of evolution of average isoperimetric coefficient as a function of pressure from simulations (FEA) and experimental data. The best agreement between FEA and experimental results was obtained with $E_{cell\ wall} = 100\ MPa$ and $E_{parenchyma} = 5\ MPa$

Results and discussion

Successive images from the FEA analysis of deformed xylem of *Pinus sylvestris* needle are shown on Fig. 2. The “degree” of collapse as a function of pressure, measured by the evolution of the isoperimetric coefficient, hides the high heterogeneity in individual cells behaviour. Fig. 3 shows the evolution of the isoperimetric coefficient of individual cells of *Pinus nigra* needle xylem presented in Fig 2. Some cells (e.g. cell 15) exhibited almost no collapse whereas some other cells, such as cell 1, exhibited high variation of the average isoperimetric coefficient with increasing pressure. It is worth noting that the non-collapsing cell 15 in Figure 2 is nearly circular and with thick walls. It should also be observed that the isoperimetric coefficient may be not the best convenient variable to describe the intensity of collapse. Indeed, some cells are highly deformed under pressure so that their cell walls come into contact (cell 9 in Figure 2, for example). In this case the isoperimetric coefficient increased instead of keeping decreasing with increasing pressure. In the following we thus measured the degree of collapse using the isoperimetric coefficient but also measuring on the images the evolution of cell lumen area.

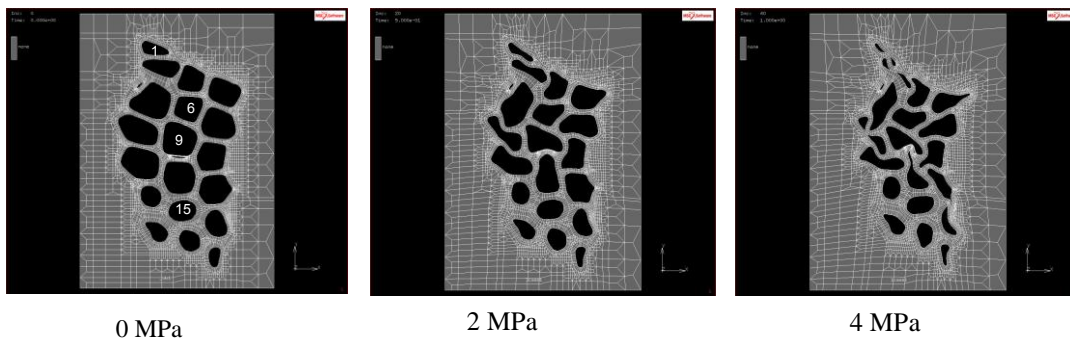


Fig. 2 Images of simulated collapse for *Pinus nigra* at three different pressures: 0, 2 and 4 MPa.

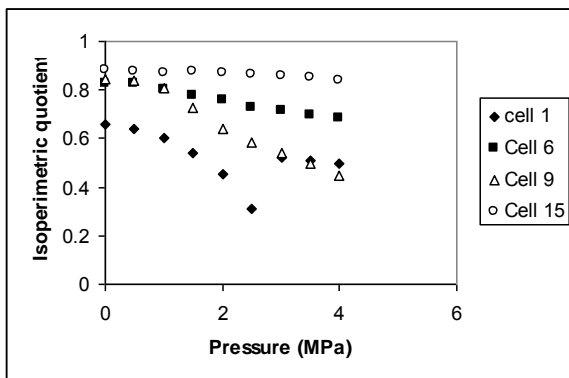


Fig. 3 Evolution of the isoperimetric coefficient of the individual cells which are numbered in the left image of Fig2.

It can be seen that the evolution of the isoperimetric coefficient varied greatly between cells: cell 15 remained almost undeformed, whereas cell 1, for example, exhibited a large decrease of the isoperimetric coefficient with pressure. It should be noted that the isoperimetric coefficient can lead to problems when cell walls came into contact with themselves (folding) or with other walls.

Fig. 4 shows the evolution of both average isoperimetric coefficient and average cell lumen area of a needle xylem of *Pinus cembra*. The simulations were done keeping the Young's modulus of the cell wall equal to 100 MPa and the parenchyma Young's modulus equal to 5MPa. To a first approximation, the simulated data are in the range of the experimental measurements. As can be seen in Figure 4, the average lumen area decrease with pressure gives better fit to the experimental data than the isoperimetric coefficient.

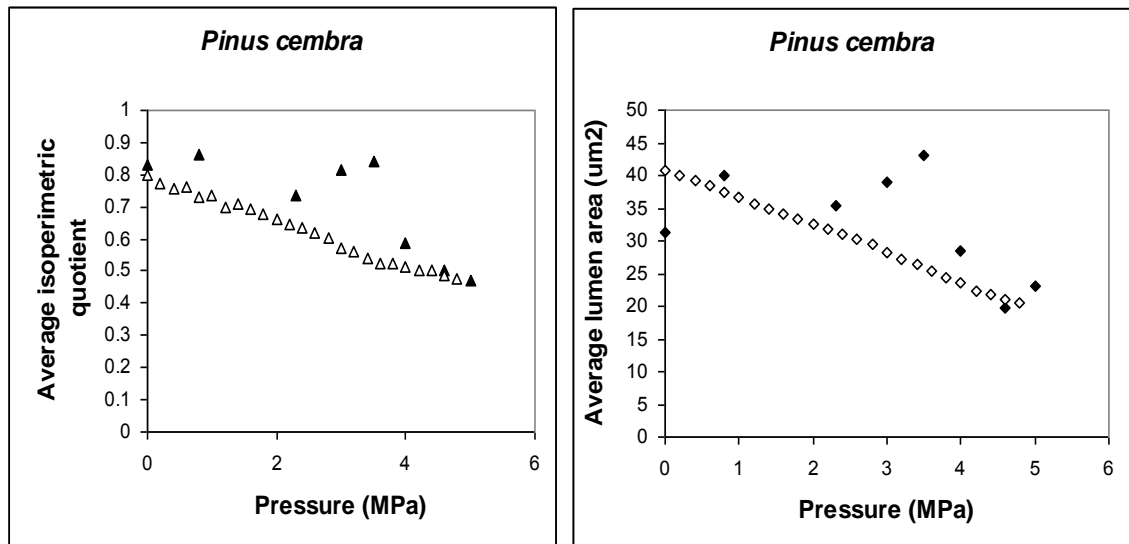


Fig 4 Simulated evolution of average isoperimetric coefficient and average lumen area of xylem of *Pinus cembra* as a function of pressure. The experimental results are shown by the solid symbols. The simulated data have been obtained with a Young's modulus of cell wall equal to 100 MPa and Young's modulus of parenchyma equal to 5 MPa.

In order to test the effect of the position of a cell on its mechanical behaviour and the effect of wall thickness, we reduced the cell-wall thickness of selected cells in the FEA analysis (by removing a layer of elements on the lumen side) and studied the evolution of their isoperimetric coefficient according pressure. The results obtained with cells of *Pinus cembra* are shown on Fig. 5. The cell walls thickness of cells 6, 7 and 11 was reduced by about 15 %. These cells were chosen because they are all surrounded by other xylem cells and because they had similar value of original cell wall thickness and size of lumen and were also similar in shape. These three cells behaved very differently in the FEA simulation: thinning of the cell wall had almost no effect on the mechanical behaviour of cells 6 and 11 but had significant effect on the behaviour of cell 7. It should be noted that cells 6 and 11 have only one common thinned wall with cell 7, whereas cell 7 has two common thinned walls, one with cell 6 and one with cell 11. This suggests that not only the geometry of cells influences the collapse but that there is also a strong structure and position effect of the considered cell within the xylem structure.

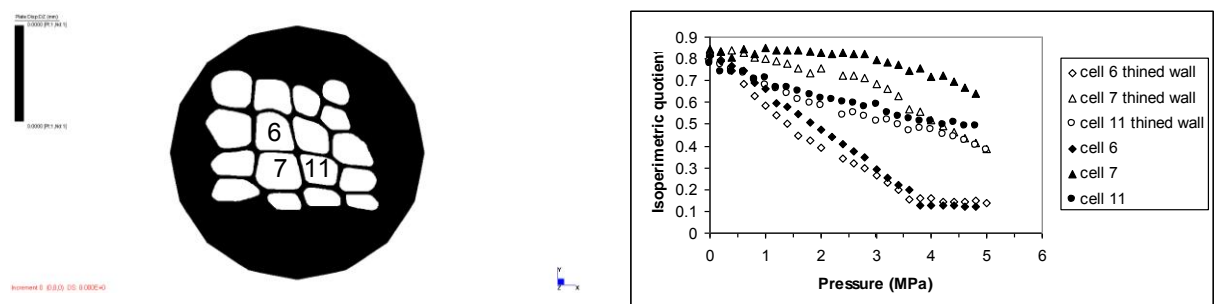


Fig 5
 Left: Digitised part of needle xylem of *Pinus cembra*. Cells walls of cells 6, 7 and 11 were thinned compared to the original, before running the simulation.
 Right: Comparison of evolution of the isoperimetric coefficient of “intact” and “thinned-wall” cells of *Pinus cembra* as a function of pressure. Cells 6, 7 and 11 had comparable size of lumen and cell wall thickness but they behave differently under increasing negative pressure: thinning the cell wall has almost no effect on the isoperimetric quotient of cells 6 and 11 but has a large effect on the collapse behaviour of cell 7.

It would be interesting to be able to predict the propensity to collapse of cells within an heterogeneous xylem structure using only a few geometrical parameters that could be measured. When checking the correlation between the parameters measuring the degree of collapse (e.g. isoperimetric coefficient or lumen area) with the square of the ratio of cell wall thickness and the diameter of the cell (t/b)², as in the study of Sperry and Hacke, only about 30% (data not shown) of the heterogeneity of the degree of collapse observed between the different cells at a given pressure can be explained. As shown on Fig. 5, the rest of the variability may be due to "structure or position" effects. It would be thus interesting to find a variable which could describe the "environment" of a cell within the xylem structure in order to get a better prediction of individual cells collapse as a function of pressure. In addition, the FEA models can be refined further, introducing for example elastic moduli which vary as a function of local strains in the cell walls during collapse. This work is currently under process.

Conclusion

In this work, we modelled the xylem collapse of pine needles. Xylem of different pine species were digitised and imported in a Finite Elements code capable of dealing with non-linear analysis, large displacements and large strains. Given the heterogeneity of the xylem system, the possibility of collapse being due to an instability, such as buckling of a cylinder under negative internal pressure, has not been pursued since the cells are not perfectly circular and their wall thickness is not uniform, two essential assumptions for a buckling analysis. The analysis of experimental results also strongly suggests that the collapse is more a progressive deformation than a real buckling process, except perhaps for *Pinus mugo*. The results of experimental measurements and FEA simulations on the collapse of xylem tissue under negative pressure suggest that the mechanics of the process are controlled to a significant extent by the heterogeneity of the xylem tissue: cells of different diameters, different shape and different wall thicknesses. As the pressure decreases, the most vulnerable cells (large diameter/cell wall thickness ration, pronounced non-circularity) deform first with the walls bending inwards. This leads to a redistribution of internal stresses acting on the cell walls of all the cells, especially those in direct contact with the first deformed cells, resulting from the changes of curvature of the cell walls during deformation. In some cases internal contact will occur and, at extreme deformation levels, cell walls can fold onto themselves. These internal contacts can have a stabilising effect on further cumulative development of collapse. Cells within a collapsed tissue that very round and thick-walled, will deform only marginally. The progression of collapse with increasing negative pressure, as measured by the reduction in lumen cross-sectional area, is progressive in all cases studied, the rate of accumulated collapse being dependent on species.

References

1. Taylor, N.G., Scheibe, W.R., Cutler, S. Sommerville, C.R. and Turner S.R. (1999): *The irregular xylem3 locus of Arabidopsis encodes a cellulose synthase required for secondary cell wall synthesis*, Plant Cell **11**:769-779.
2. Cochard, H., Froux, F., Mayr, S. and Coutand, C. (2004): *Xylem wall collapse in water-stressed pine needles*, Plant Physiology, **134**:401-408.
3. Pockman, W.T., Sperry, J.S. and Oleary, J.W. (1995): *Sustained and significant negative pressure in xylem*, Nature **378**:715-716.
4. Hacke, U.G., Sperry, J.S., Pockman, W.T., Davis S.D. and McCulloh, K.A. (2001): *Trends in wood density and structure are linked to prevention of xylem implosion by negative pressure*, Oecologia **126**:457-461.
5. Young W.C. (1966): *Roark's Formulas for Stress and Strain, McGraw Hill International Editions, 6th Edition, New York*.
6. Holmberg, S. and Petersson, H. (2000): *Modelling and simulation of machining processes related to initial wood defibration*, in Proceedings of International Symposium on Wood Machining, S.E. Stanzl-Tschegg and A. Reiterer editors, Christian Doppler laboratory for Fundamentals of Wood machining, Vienna, p 265-274.
7. Niklas, K.J. (1992) *Plant Biomechanics – An Engineering Approach to Plant Form and Function*, The University of Chicago Press, Chicago.

Multi-scale modeling for moisture transport in wood

Dominique Derome¹, Wolfgang Zillig² and Jan Carmeliet³

¹EMPA, Switzerland; ²Fraunhofer IBP, Germany; ³ETHZ and EMPA, Switzerland

Abstract

Moisture transport properties of wood are highly dependent on the direction (longitudinal, radial or tangential) due to its anisotropic material structure. The purpose of this paper is to present a methodology to determine location dependent orthotropic moisture transport properties for study of their influence on the global hygroscopic behavior of wood. In order to derive location dependent moisture transport properties, micro structural images are obtained by Scanning Electron Microscopy of a full growth ring. Based on the line configuration of the cellular structure, a triangular mesh is generated and finite element analyses are performed using a moving window methodology to obtain the position dependent material properties. In a second step, the location dependent moisture transport properties are used to analyze the water vapor transport at meso- and macroscale. The macroscopic moisture transport properties are then compared with measurements on wood. The method allows to determine location-dependent density and water vapor permeability. These location-dependent material properties can then be used to model the influence of growth ring structure on the total moisture transport in the wood ignoring the actual geometry of single cells in the growth ring.

Introduction

Moisture transport in wood is complex due to its anisotropic material structure, resulting from the cells anatomy, growth ring where early- and latewood alternate, and the presence of vessels, rays and pits. As a result, the moisture transport properties of wooden components are highly dependent on the direction (longitudinal, radial or tangential). Moreover, due to variations in cell geometry and growth ring structure, the moisture transport properties, such as moisture capacity and water vapor permeability depend on location. The purpose of this paper is to present a methodology to determine location dependent moisture transport properties for the study of their influence on the global hygroscopic behavior of wood.

In order to derive location dependent moisture transport properties, 2D micro structural images are obtained by Scanning Electron Microscopy of a full growth ring. The image is then thresholded to obtain a binary representation of the cell wall–cell lumen structure. The geometry of the cells is extracted and the cell borders are represented by lines. Based on the line configuration, a triangular mesh is generated. Finite element analyses are performed using a moving window methodology to obtain the position dependent material properties. A vapor pressure difference is imposed at two opposite sides, while the other sides remain vapor tight and the water vapor flux and water vapor diffusion coefficient are determined. These calculations are repeated for different relative humidities.

The method allows to determine location-dependent density and water vapor permeability. These location-dependent material properties can then be used to model the influence of growth ring structure on the total moisture transport in the wood ignoring the actual geometry of single cells in the growth ring.

The approach is applied here on the real cell structure measured with a visualisation method. Thus, the work presented is two-dimensional. However, as the cell dimensions in longitudinal direction are

long compared to the dimensions in radial and tangential directions, the influence of the third dimension is considered negligible for the determination of radial and tangential properties.

Material and methods

Determination of the geometry

In the work presented here, we assume that the water vapor transport properties depend on the underlying cellular structure. The cellular microstructure is thus determined using a Scanning Electron Micrograph (SEM) of a spruce specimen. Figure 1a shows the cross section of one growth ring. The cellular structure of earlywood and latewood can be clearly distinguished. However, the gray contrast between wall and lumen is too limited in order to derive a binary image by thresholding. Therefore, the lumen and the cell wall are manually marked black and white using an image editing software. Figure 1b gives the obtained binary image. This binary image representing a full growth ring is then further processed for numerical analysis.

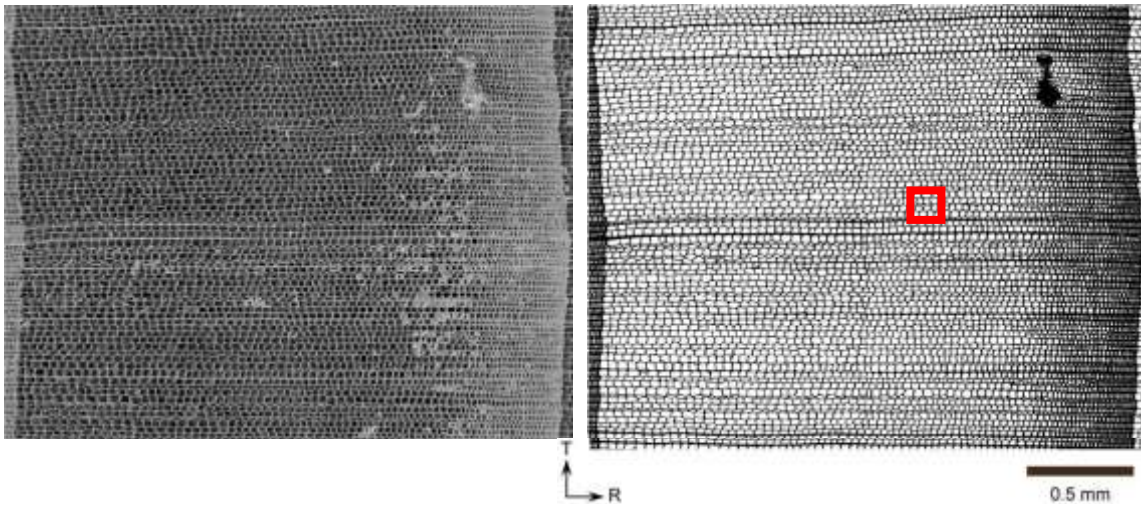


Fig. 1. a) at left, scanning electron micrograph (SEM) from one growth ring. (b) at right, binary representation of the cell walls and lumens. The bold square highlights the area shown in Figure 2.

Prediction of the upscaled water vapor permeability

The water vapor permeability of a growth ring can be determined solving a stationary water vapor transport problem. This can be simulated by imposing a water vapor pressure gradient as boundary conditions and no flow on the perpendicular sides of the calculational domain. The solution yields the stationary flow rate Q . The upscaled water vapor permeability, or the resistance factor, can then be determined as:

$$\delta(\phi) \stackrel{-}{=} \frac{Q}{A \Delta p_v} \quad \text{or} \quad \mu(\phi) \stackrel{-}{=} \frac{\delta_a A \Delta p_v}{Q} \quad (1)$$

with $\delta(\phi)$ is the water vapor permeability [s], Q the vapor flow [kg/s], A the cross section traversed by the flow [m²], Δp_v the vapor pressure differential [Pa], $\mu(\phi)$ the water vapor resistance factor [-] is defined as the ratio of the vapor permeability of the material to the vapor permeability of dry air [s], δ_a .

This process is repeated for different moisture contents (or relative humidities) to obtain the relationship between the water vapor resistance factor and relative humidity. Applying the boundary conditions on the perpendicular sides and repeating the simulations, the permeability in the perpendicular direction is obtained.

The stationary flow problem is solved using the finite element method. Therefore, the domain is divided into finite elements and material properties have to be assigned to the elements. To generate a mesh of elements representing the geometry of one growth ring, first the boundaries of the lumen are determined by graphical software [1]. This results in a set of polygons describing the boundaries between lumen and cell wall. These polygons are then used for the generation of the mesh using [2]. This process is graphically shown in Figure 2. The domain is represented by an unstructured mesh of triangular linear elements. The final mesh consists of 147063 elements and 74654 nodes for the domain shown in Figure 1b.

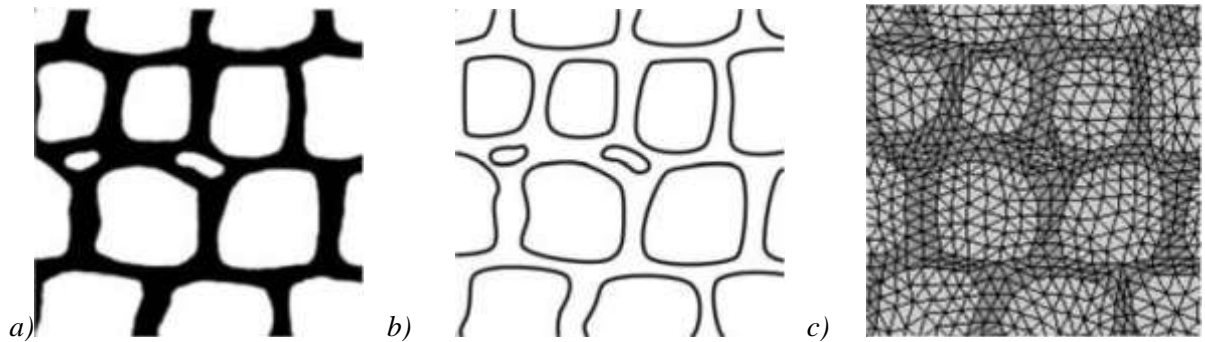


Fig. 2 Detail views of the meshing process. a) Binary representation of the wood microstructure. b) Extracted outlines for all cells. c) Finite element mesh created using the outlines.

Each lumen is defined as air with a water vapor resistance factor of 1. The remaining part is identified as cell wall with a water vapor resistance factor of $\mu_{w\perp}$. We assume that the water vapor permeability of the cell wall is equal in the radial and tangential directions.

The only remaining unknown is the water vapor resistance factor of the cell wall. The vapor permeability of the cell wall is determined by comparing the upscaled water vapor resistance factor for the complete growth ring to measured values determined with the cuptest method. One way to determine the water vapor resistance factor of the cell wall is to first determine the relationship between the upscaled water vapor resistance factor of the growth ring and the water vapor resistance factor of the cell wall. An almost linear relationship is obtained, as shown in Figure 3. This linear relationship is then used to determine the water vapor resistance factors of the cell wall for the three different relative humidities, corresponding to the RH where the water vapor resistance factors were measured. These results are listed in Table 1. We observe that the determined water vapor resistance factor of the wall $\mu_{w\perp}$ varies highly with relative humidity. It is possible to fit μ_w to the measurements in radial and tangential directions within 8% accuracy of the measurement, which is a reasonable agreement given that the growth ring measured may not represent the “average” growth ring structure and that rays are not included in the 2D mesh.

Table 1 Water vapor resistance factors for wood determined from the linear fit to the data shown in Figure 3. Experimental results are given in brackets.

RH (%)	30	62.5	71.5
μ_w	1453	329	125
μ_R	295 (237)	68 (72)	27 (29)
μ_T	314 (341)	72 (68)	28 (26)

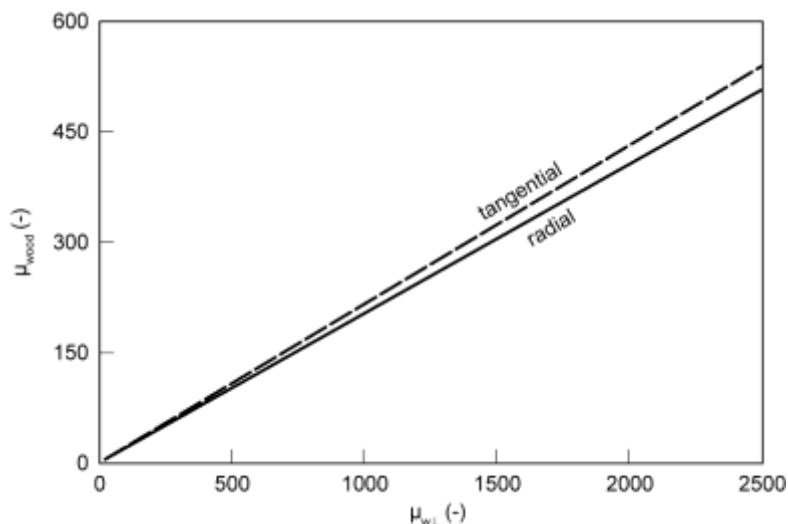


Fig. 3 Water vapor resistance factor of the total growth ring in radial and tangential directions in dependence on the cell wall water vapor resistance factor.

Results and discussion

The upscaling method also allows determining the spatial variation of the density and water vapor transport properties over the growth ring. This is done by subdividing the domain of $3100 \times 2400 \mu\text{m}$ is subdivided into smaller parts with a side length of $100 \mu\text{m}$ and calculating the properties of the different sub-domains.

First, the density variation over the growth ring is analyzed. Therefore the fraction of the cell wall area to the total area is determined and multiplied by the cell wall density which, is according to Kollmann [4], 1533 kg/m^3 . For the analysis, earlywood is defined from the left side of the calculational domain and has a width of $2500 \mu\text{m}$. Latewood fills the rest of the domain. Therefore the earlywood–latewood boarder is located at the relative ring position of 0.806. Figure 4 shows the calculated density over the domain. The average densities for earlywood, latewood and the complete growth ring are listed in Table 2.

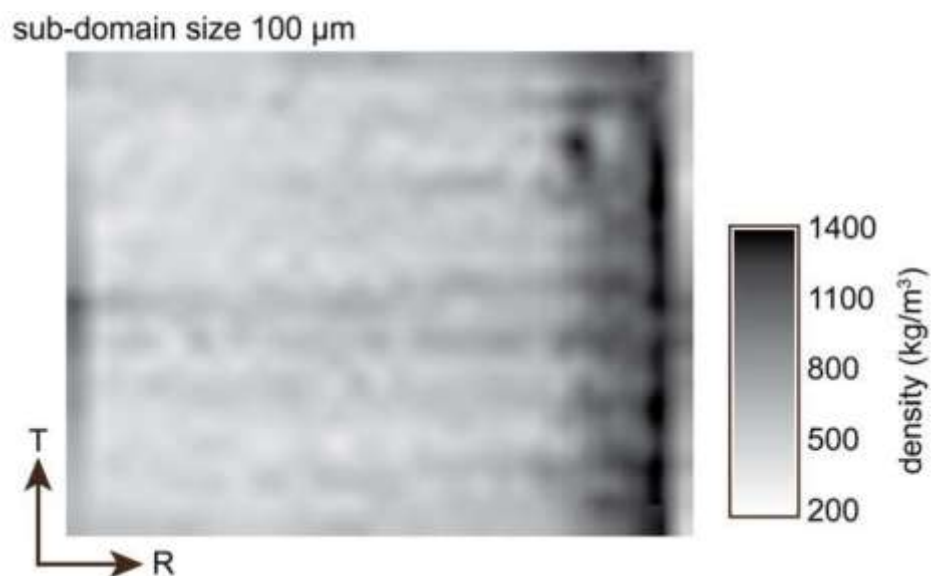


Fig. 4 Density distribution determined by the ratio of cell wall and lumen for sub-domain size of $100 \mu\text{m}$.

The average density of 654 kg/m³ is clearly higher than the average density determined by measuring classically mass and volume, which gives values between 360 kg/m³ and 460 kg/m³. This is explained by the fact that we did not consider the porosity of the cell wall which is approximately 30%. The density of the wall is then around 1073 kg/m³. Thus, most likely, the solid matrix density of 1533 kg/m³ as given by [4] is not suitable for determination of the density by image analysis. [4] had determined the solid matrix density by helium pycnometry and it is likely that helium can access a bigger pore volume than the pore space recognizable by image analysis. Also Decoux [3] states that this commonly used cell wall density is too high for determination of the density by image analysis. They suggest a cell wall density between 1000 and 1400 kg/m³. Recalculating the cell wall density so that the resulting density equals the measured average density results in a cell wall density of 945 kg/m³, which is somewhat below the range mentioned by [3].

Table 2 Average density and vapor resistance factor of earlywood, latewood and the complete growth ring. The corresponding standard deviation is given in brackets.

	earlywood	latewood	total wood
density (kg/m ³)	559 (108)	1047 (209)	654 (235)
water vapor resistance factor (-)	294 (105)	902 (336)	431 (314)

In a second step, the local water vapor resistance factors are determined solving the stationary flow problem for each sub-domain in radial direction. In Figure 5, the spatial distribution of the water vapor resistance factors in the radial direction is shown.

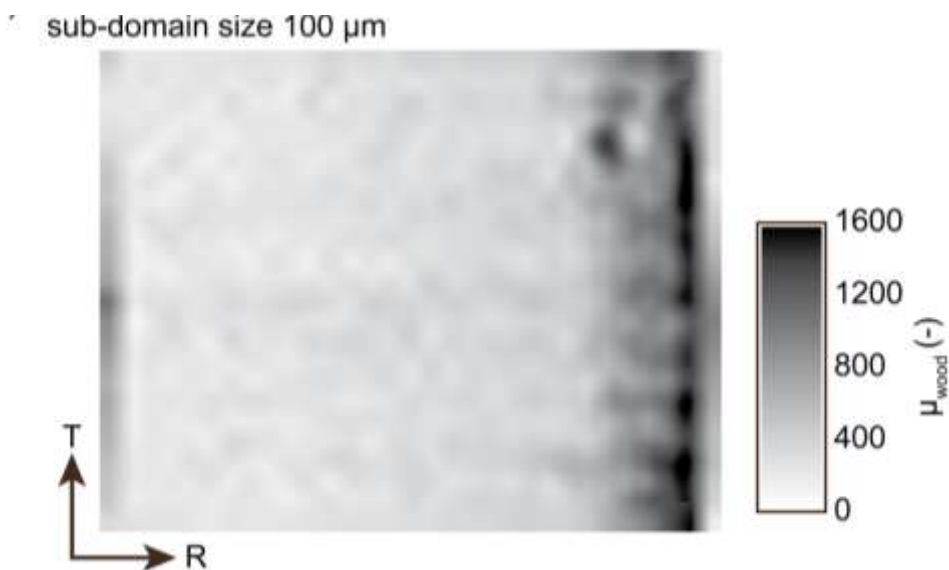


Fig. 5 Location dependent water vapor resistance factors in radial direction. The results are shown for a cell wall water vapor resistance factor μ_w of 815.

We observe that the μ -values highly differ between earlywood and latewood. The different patterns originated in the different sub-domain sizes correspond well to the patterns of the spatial density distribution. Table 2 gives the average μ values (the standard deviation is given in brackets) for earlywood and latewood in radial direction.

Figure 6 shows the local water vapor resistance factors plotted against the local densities. We observe that there is a trend showing higher water vapor resistance factors for higher density values. An almost linear relationship is observed.

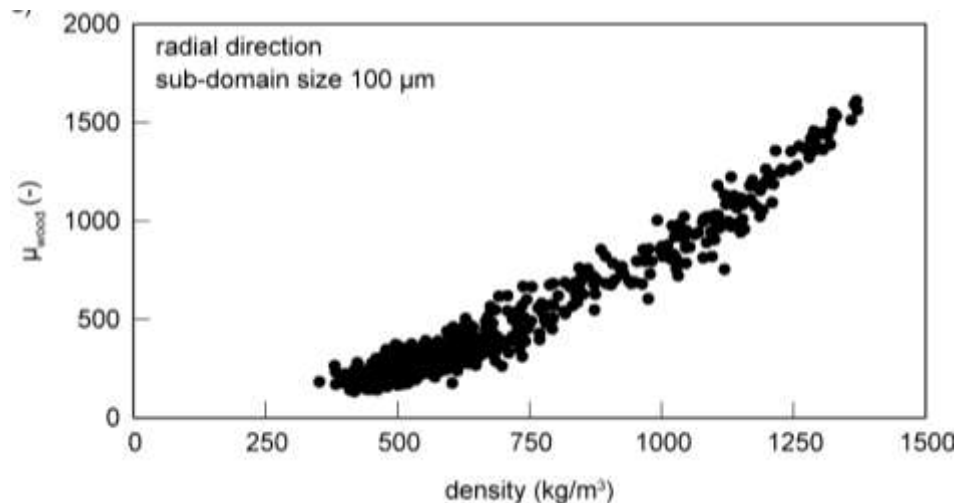


Fig. 6 The local water vapor resistance factor in relation to local density for radial direction for sub-domain size of 100 μ m.

Conclusion

We can conclude that the real cell geometry can be used to obtain good predictions of the vapor permeability. The work presented here was also performed for the determination of water vapour transport property in the tangential direction. As rays can contribute to moisture transport, in a next step, rays should be considered in the model using the wood microstructure obtained by nano-CT. The applicability of nano-CT on wood is shown by [5] and [6]. The same methods as applied here could be applied to a three-dimensional geometry. A further step will be to take into account the swelling of wood with increasing moisture content.

References

1. Adobe Illustrator CS3: <http://www.adobe.com>
2. Gid, v9.02: <http://gid.cimne.upc.edu>
3. Decoux, V., É. Varcin, and J. Leban, (2004): *Relationships between intra-ring wood density assessed by X-ray densitometry and optical anatomical measurements in conifers. Consequences for the cell wall apparent density determination.* Ann. For. Sci., 61, 251-262.
4. Kollmann, F. and W.A. Côté, (1968): *Principles of wood science and technology. Part 1: Solid wood.* Springer Verlag.
5. Trtik, P., J. Dual, D. Keunecke, D. Mannes, P. Niemz, A. Kaestner, A. Groso and M. Stampanoni, (2007) *3D imaging of Microstructure of Spruce Wood*, Journal of Structural Biology, 159 :46-55
6. Van den Bulcke, J., B. Masschaele, M. Dierick, J. Van Acker, M. Stevens and L. Van Hoorebeke (2008): *Three-dimensional imaging and analysis of infested coated wood with X-ray submicron CT.* International Biodeterioration & Biodegradation, 61, 278-286.
7. Zillig, W., J. Carmeliet and D. Derome, (2008): *Influence of the growth ring structure on the vapor transport in wood.* 8th Nordic Symposium on Building Physics, 16-18.06, Copenhagen, Denmark. Conference Proceedings, 983-990.
8. Zillig, W. (2009): *Moisture transport in wood using a multiscale approach*, PhD thesis, KULeuven, Belgium, May.

A scaling law reveals the control of tree vibration modes through tree architecture and branch allometry

Mathieu Rodriguez^{1,2} *Emmanuel de Langre*¹ and *Bruno Moulia*²

¹ *Department of Mechanics, LadHyX, Ecole Polytechnique-CNRS, 91128 Palaiseau, France;*

² *UMR547 PIAF, INRA, Univ Blaise Pascal, F-63100 Clermont Ferrand.*

Abstract

Wind is a major ecological factor for plants and a major economical factor for forestry. Mechanical analyses have revealed that the multimodal dynamic behavior of trees is central to wind – tree interactions. Moreover, the trunk and branches influence dynamic modes, both in frequency and location. Because of the complexity of tree architecture, finite element models (FEMs) have been used to analyze such dynamics. However, these models require detailed geometric and architectural data and are tree-specific. In this work, closed-form scaling laws for modal characteristics were derived from the dimensional analysis of idealized fractal trees that sketched the major architectural and allometrical regularities of real trees [16]. These scaling laws were compared to three-dimensional FEM modal analyses of two completely digitized trees with maximal architectural contrast. Despite their simplifying hypotheses, the models explained most of the spatiotemporal characteristics of modes that involved the trunk and branches, especially for sympodial trees. These scaling laws reduce the tree to (1) a fundamental frequency and (2) one architectural and three biometrical parameters. They also give quantitative insights into the possible biological control of wind excitability of trees through architecture and allometries. It is shown that the mechanical design of tree depends on branching symmetries and allometries, and is likely to be controlled through thigmomorphogenesis.

Introduction

Wind – tree interaction is a major concern for the management of forest and urban trees because windthrow and windbreak result in substantial economical costs and potential human risks [6, 9]. Moreover, mechanosensing by trees of wind-induced strains [2] and induced thigmomorphogenetic responses are fundamental issues in understanding how trees can control their susceptibility to wind hazard and acclimate to their wind climate. Over the last decades, time-dependent dynamic effects have been found to play a major part in wind deformations and windbreaks [10]. A central question to be investigated is then obviously the influence of branched architecture and tree geometry on the dynamics of trees and the potential biological control of tree resistance to wind through the morphological development of the tree.

The oscillatory elastic behavior of the structure is driven by the exchange between two forms of the internal mechanical energy: (1) kinetic energy and (2) elastic-strain potential energy [8]. This oscillatory elastic behavior can be analyzed as the superposition of distinct modes of deformation through modal analysis. Each mode, numbered j , is an eigen form of oscillatory exchange between kinetic energy and elastic-strain potential energy [8]. The mode j is defined by the modal deformation Φ_j (the displacement vector field defining the shape of the deformed tree), modal frequency f_j .

A few authors have used modal analysis on trees [4, 12, 17]. All have concluded that modes involving significant branch deformation could rank in between modes deforming mainly the trunk [4, 17]. [9] also showed that the measured frequency spectra of the responses under wind excitation of four trees were also significantly dependent on the branching system.

In view of such complex effects, it may seem that only detailed finite element models (FEM) of the three-dimensional (3D) architecture of trees can be used [12, 17]. Such simulation studies provide a limited perspective for generality. The geometry of trees, however, has in most cases some architectural symmetry related to the branching pattern (monopodial vs. sympodial growth) and spatial biometrical regularities — such as the allometry law for slenderness [11]. The geometry of a tree can thus be approximately summarized using a few parameters. Moreover, the setting of some of these parameters is controlled through thigmomorphogenetic processes [13]. But the issue of whether such regularities can be reflected in general scaling laws for modal characteristics has not been addressed yet. The hypothesis here is that simple scaling laws should occur. If they were to exist, these laws would make the studies of tree dynamics easier and give insights into the possible biological control of the overall tree dynamics excitability.

The aims of the present paper are thus (1) to explore the respective role of the architecture and allometry parameters on modal characteristics and (2) to assess whether more generic scaling laws, relating tree multimodal dynamics and architectural and geometrical parameters, can be defined and to discuss their biological significance. In the first section, the modal characteristics of an extensively digitized 3D model are analyzed. Then in the second section, idealized fractal tree models are defined to explore the influence of biometrical regularities and branching patterns on the modal characteristics of a tree. Scaling laws between the successive modes of a tree based on the global parameters characterizing architecture and slenderness are then derived in these idealized trees. Finally, in the third section, we show that walnut modal characteristics can be approximated using these scaling laws, so that the general multimodal behavior of trees can be reduced as a first approximation to (1) the first mode and to (2) general scaling laws for higher modes. The same procedure, applied on a pine tree with a very distinguished architecture, is presented in [16].

Modal analysis of a walnut

Material and methods

A 20-yr-old walnut tree (*Juglans regia* L.), Fig. 1, described in [18], is considered. It was 7.9m high, 18cm in diameter at breast height (dbh), and had a sympodial branching pattern and eight orders of branching. The geometry of the tree (positions, orientations, diameters of the stem segments, and the topology of branching points) is known in great detail through 3D magnetic digitizing [18]. Because our central concern was on the effects of branch architecture and allometry, the tree is analyzed here without considering leaves.

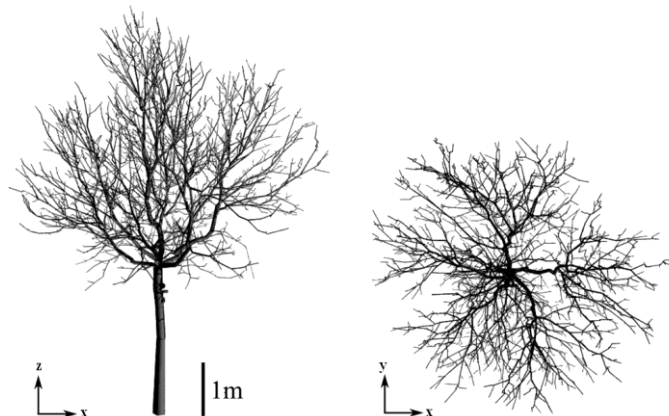


Fig. 1. Geometry of a walnut tree (from [18]).

In slender structures such as trees, the beam theory applies [14], and modal deformations involve mainly bending and torsion. The mechanical model used was thus based on representing each branch segment as a beam, assumed to be circular, with a variable diameter along the beam (taper) when

available. Connections between branch segments were set as rigid. The root anchorage was modeled as a perfect clamping condition at the tree basis. The green-wood material properties (density ρ , Young modulus E , and Poisson ratio ν) were assumed to be uniform over all branches. Their values were estimated using Eq. 1 in [5]. Thus $E=11.3\text{GPa}$, $\rho=805\text{kg}\cdot\text{m}^{-3}$, and $\nu=0.38$. A finite element representation of the tree was built using the CASTEM v.3M software. The stiffness and the mass matrices of the finite element formulation were then computed. By solving the equations for free motions using these matrices, modes were fully defined.

Results

The first 25 modes were found in the range between 1.4 and 2.6 Hz, Fig 2. A small but clear frequency gap ($\sim +0.4$ Hz) occurred between the first two modes and the following ones. Then modal frequencies continued to increase with mode number but at a smaller rate.

These modes can be classified according to their modal deformation Φ_j (Fig. 2B). The first group of modes, labeled I, displayed a bending deformation mainly in the trunk basis. This resulted in a lateral displacement of the upper part of the bole mostly through rigid-body rotational effect, as sketched in Fig. 2B. In other words, deformations occurred mostly in the trunk up to the crotch, and the branches swayed like rigid bodies. Group I included two modes, corresponded to the bending in the x and y direction, respectively, with identical frequencies of ~ 1.4 Hz. The second group, labeled II, corresponded to deformations mainly located on first-order branches, with mostly rigid-body displacements of the branches of higher orders. Because there were six main branches bending in the x and y directions, respectively, this second group included 12 distinct modes, each one with different contributions of the deformation of these branches (modes 3–14). The third group, labeled III, corresponded to modes 15–25 with deformations mainly localized on third order branches.

Modal frequencies were concentrated in a small frequency range. With frequencies of 1 Hz order of magnitude and ~ 10 modes per Hz, the frequency spacing of the modes was typically 0.1 Hz.

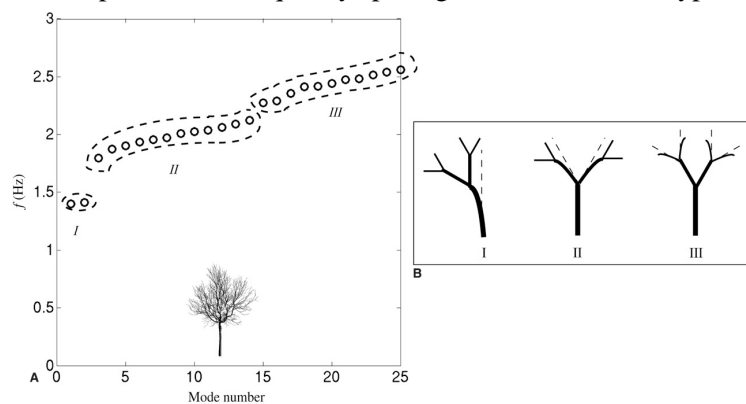


Fig. 2. (A) Mode frequencies of the walnut tree classified in terms of main localization of bending deformations: I, in the trunk; II, in 2nd branches; III, in 3rd branches. (B) Sketches of the mode deformations.

Theoretical considerations: Scaling laws in idealized trees

To explore the respective effects of tree architecture and allometry on modal characteristics, we defined idealized fractal trees. Two different fractal models were built. The first model tree is inspired from the Leeuwenberg architectural model and will be referred to as “the sympodial tree” in the following. At each branching point, the sympodial tree has symmetric lateral segments and no axial segment (Fig. 3A). The second model tree is a highly hierarchical tree inspired from the Rauh architectural model (e.g., pine) and will be referred to as monopodial. It has an axial segment and lateral segments at each branching point (Fig. 3B). Only the case of the sympodial fractal tree, with no axial branching, is derived here. More general cases are detailed in [16].

Tree branches were indexed using the numbers of lateral branching upstream in the direction of the tree base (Fig. 3). A branch segment of a sympodial tree is indexed N when it has $N - 1$ lateral upstream branch segments. Segments sizes were defined using three parameters (Fig. 3): (1) the slenderness coefficient β (Fig. 3C); (2) the lateral branching ratio λ , which define, respectively, the ratio between cross-sectional areas of segments after and before branching (Fig. 3D); and (3) the angle α of divergence of lateral branches from the axial direction of the parent segment (Fig. 3E).

The mean slenderness of the population of branch segments of both trees was thus described using an allometric law that relates the length L and the diameter D of each segment, in the form $D \sim L^\beta$, whereas the successive diameters at branching points were $D_{(N,P+1)} = \sqrt{\mu} D_{(N,P)}$.

The algorithm for generating a fractal tree, as in Fig. 3, is detailed in [16]. For the sympodial idealized tree model (Fig. 3), the relation between successive segments is

$$L_{N+1}/L_N = \lambda^{1/2\beta} \text{ and } D_{N+1}/D_N = \lambda^{1/2}, \text{ so that } L_N/L_1 = \lambda^{(N-1)/2\beta} \text{ and } D_N/D_1 = \lambda^{(N-1)/2}. \quad (1)$$

An axis length, l_N , is defined as the sum of the lengths of the segment L_N and all successive segments following a path of lateral branching, giving

$$l_N = \sum_{N'=N}^{\infty} L_{N'} = L_N \frac{1}{1 - \lambda^{1/2\beta}}. \quad (2)$$

Thus, the slenderness coefficient, β , also links an axis length to its diameter: $D_N = k_1 L_N^\beta = k_2 l_N^\beta$.

Finally, in the idealized fractal trees, self-similar subsets of the tree starting from any branch bifurcation may be identified, as illustrated in Fig. 4A. These subsets thus follow the same index as their basal segment (i.e., N). Because of the assumption of the reiterated self-similar branching law, a given subset is identical to the whole tree, except for its length scale, l_N , and its diameter scale d_N .

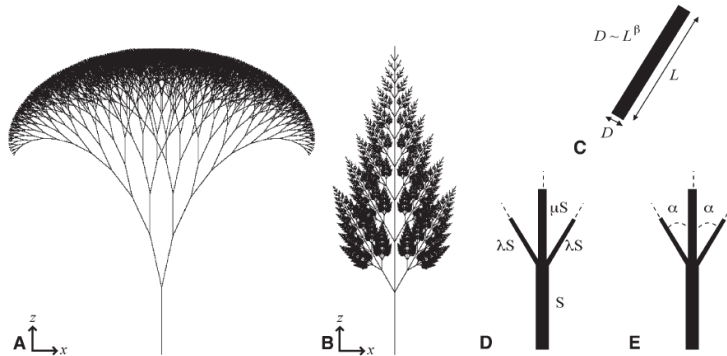


Fig. 3. Examples of model fractal trees and parameters defining model trees. (A) Sympodial case, $\alpha=12.5^\circ$, and (B) monopodial case, $\alpha=30^\circ$; (C) Branch slenderness coefficient, β ; (D) branching ratios, λ and μ ; and (E) angle of branching connections, α , illustrated here in the case of two lateral branches.

In a mechanical model of a system in which segments are represented as beams of circular sections, two length scales exist. The first one, l , fixes the scale of coordinates of these segments. A second one, d , which scales the diameters of these segments, is needed. Moreover, we can assume that material properties of the wood (density ρ , Young modulus E , and Poisson ratio ν) are constant within the tree. The relation between modal frequencies and these two scales may then be assessed by standard dimensional analysis. A modal frequency f depends on lengths, scaled by l , on masses per unit length, scaled by ρd^2 , and on the bending stiffness k , scaled by Ed^4 , and is written as

$$f = F(\rho d^2, Ed^4). \quad (3)$$

But, because a physical law is by nature independent of units, this relation must be expressed in terms of dimensionless parameters [15]. Considering the respective dimensions of these four variables ($f \sim \text{Time}^{-1}$, $\rho d^2 \sim \text{Mass Length}^{-1}$, $Ed^4 \sim \text{Mass Length}^3 \text{Time}^{-2}$), all four variables may thus be combined in a dimensionless parameter implying:

$$f l^2 \rho d^2 \sim Ed^4 \sim 1/2 = \text{constant}. \quad (4)$$

Or equivalently,

$$f \sim l^{-2} \left(d^2 \right)^{1/2} \left(E d^4 \right)^{1/2} \sim l^{-2} \cdot d \cdot \left(\frac{E}{\rho} \right)^{-1/2} . (5)$$

In a given tree, where an allometric law relates length and diameter of each segment, $d/l^\beta = \text{constant}$, i.e., $d \sim l^\beta$. Then, from Eq. 5, the frequencies of modes are expected to follow:

$$f \sim l^{\beta-2} \sim d^{\frac{\beta-2}{\beta}} . (6)$$

Due to the symmetries of the fractal structure, groups of modes can be deduced and classified according to their modal deformation. Some modes involve trunk deformation (group I in sympodial tree. Other modes involve mainly the bending deformation of the basal branch of all subsets of the same order (e.g., modes II for $N = 2$ subsets, modes III for $N = 3$ subsets in the sympodial tree), with negligible deformation of upstream segments.

For a sympodial, idealized tree, the modal deformations of three groups of symmetric modes (I, II, and III) can easily be deduced from one to the other. Because of the symmetry of the branching pattern, a mode of group II is associated with the deformation of a subset with a fixed part at its base. Therefore, the modal frequency of the group II of the whole tree can be considered as the frequency of a mode of group I of the subset if it is isolated. The dependence of f_{II} on l_{II} and d_{II} should therefore be identical to the dependence of f_I on l_I and d_I , hence yielding:

$$\frac{f_{II}}{f_I} = \frac{d_{II} l_{II}^{-2}}{d_I l_I^{-2}} = \left(\frac{d_{II}}{d_I} \right)^{\frac{\beta-2}{\beta}} . (7)$$

Using the relation between successive diameters in a fractal sympodial tree, Eq. 7 yields

$$\frac{f_{II}}{f_I} = \lambda^{\frac{\beta-2}{2\beta}} \quad \text{and} \quad \frac{f_N}{f_I} = \lambda^{\frac{N-1}{2\beta} \cdot \frac{\beta-2}{\beta}} . (8)$$

Therefore, all frequencies can be deduced from the first one, given the allometric parameter β , and the area reduction parameter at branching λ . A similar approach has been used to determine the evolution of modal mass and modal stiffness, see [16].

The scaling laws derived in the preceding section were applied to a particular occurrence of the idealized trees. The allometric and geometrical parameters defining its geometry are $\beta=3/2$, $\lambda=1/2$, $\alpha=20^\circ$.

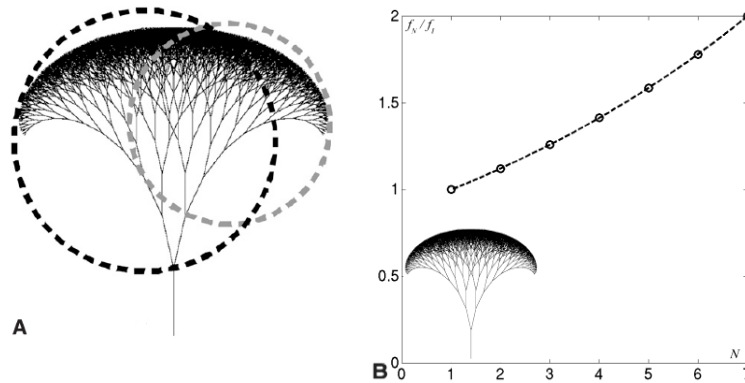


Fig. 4. (A) Identification of subsets in the sympodial model tree (encircled in black or gray). (B) Vibration modes of the sympodial tree. Modal frequencies, relative to the first one, as a function of the index of the corresponding subsets.

Thus the series of frequencies for the sympodial [N] idealized trees read as

$$\frac{f_N}{f_I} = 2^{\frac{N-1}{6}} . (9)$$

Frequencies of group of modes are seen to increase progressively, Fig. 4B. The organization of frequencies is clearly dependent on the architecture, through the parameters λ of area reduction at branching, and on the slenderness allometry, through the parameter β .

Test of the scaling laws on models of real trees

The scaling law for modal frequencies (Eq. 9) is then applied to “real” tree model (i.e., the symodial walnut, Fig. 1). The results are then compared with the modal characteristics computed using 3D finite element models (see section *Modal analysis of a walnut*; Fig. 2).

Orthogonal regressions were applied to estimate slenderness allometric coefficients, β , and branching ratios, λ , from the walnut geometry. Slenderness coefficient, β , was estimated from the linear orthogonal regression $\log(d)=\beta \log(l)+k$. Lateral branching ratios, λ , was estimated from linear orthogonal regression $(d_N)^2 = \lambda (d_{N-1})^2$. Regression results are reported in Table 1.

A highly significant, tight allometric relation was found between l and d (Fig. 5), capturing 87% of the total variance. The relation between d_{N+1} and d_N was a little bit more biased, but still a highly significant λ could be defined. A mean angle of branching, $\alpha=20^\circ$, was retained.

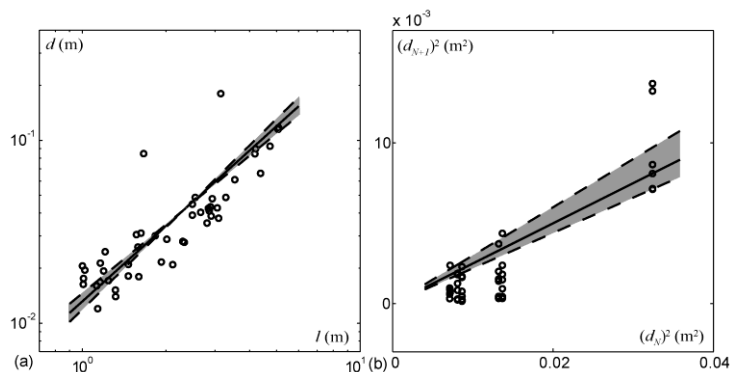


Fig. 5. Biometrical relations in the walnut tree. (a) Allometric relation between length and diameter of branches. (—) Orthogonal regression $D \sim L^\beta$, with $\beta=1.37$. (B) Branches cross-sectional areas before and after a lateral branching. (—) Orthogonal regression $(d_N)^2 = \lambda (d_{N-1})^2$, with $\lambda=0.25$. Gray areas in the graphs correspond to the 90% confidence level. (○) measured data from [18].

Using the parameters corresponding to the real tree (Table 1), we applied the scaling law derived in the *Theoretical considerations* section, then compared the results to the modal characteristics computed using the 3D finite element model. Figure 6 displays the frequencies of the three groups of modes (I, II, and III, see Fig. 2 and section *Modal analysis of a walnut*) estimated using the 3D FEM vs. the group number N . On the same graph, the dotted lines show the frequencies predicted using Eq. 9 with the 90% confidence range of parameters as in Table 1. Though the geometry of the real walnut is much more complex than that of the idealized fractal symodial tree, the prediction using the scaling laws quite closely brackets the range of modal characteristics of the FEM model.

Discussion

Branches are important to the tree dynamics — The detailed FEM modal analysis of an entirely digitized tree confirmed and extended previous reports: modes involving significant branch deformation could have frequencies very close to — and even rank in between — modes deforming mainly the trunk [4, 9, 12, 17]. Although these modes are complex, they can be classified using their frequencies and modal deformations. Branch deformation is thus an important aspect of trees dynamics whatever the architecture and size [3, 5, 12, 17, 20].

Scaling laws can be defined — As hypothesized, and despite the aforementioned complexity of the 3D architecture and modal structure of real trees, scaling laws based on the assumptions of (1) idealized allometric fractal trees and (2) symmetric modes of branches, are able to explain a large part of the temporal characteristics of the modes involving the successive orders of branches relative to the first mode deforming the trunk (Fig. 6). The distribution of modal characteristics was particularly well predicted. The spatial characteristics of modes deduced from scaling laws are discussed in [13].

Such scaling law has two major uses. From a methodological and practical point of view, the overall dynamics of a complex tree can be reduced to (1) the measurement or estimation of the most

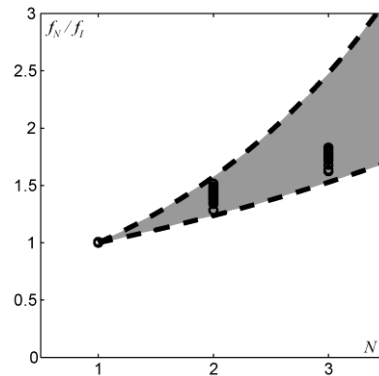


Fig. 6. Comparison of the prediction from the scaling law with the finite element results on the tree geometry.

basal mode, which is the easiest to characterize and has been studied or modeled in numerous studies [7]; (2) a standard description of the branching mode, i.e., sympodial vs monopodial mode [1]; and (3) three simple biometrical parameters that have been measured in many biomechanical and ecological studies [11]. This compact description of the overall dynamics of a complex tree is to be compared with the extensive work on detailed 3D digitizing [18] followed by complete modal analysis.

Effects of architecture and biometrical characteristics on modal content: Tuning and compartmentalization — Both area reduction ratios and the slenderness coefficient affect the relative frequency and the location of modes. For example, in the case of the sympodial tree, variations in λ and β both influence the value of the frequency of a given group of modes. It should be noted here that both λ and β have been reported to be under similar control of wind mechanoperception through thigmomorphogenetic secondary growth responses [21]. Thus, thigmomorphogenetic responses may be able to tune the multimodal frequencies range of the whole tree, whatever the genetic specific traits of its architecture.

Last but not least, a very unexpected salient conclusion that is captured by the scaling laws is that branching and secondary growth are tuned so that the reduction of cross sectional area at branching points induce a clear structural compartmentalization of the modal spatial distribution and a scaling similarity between successive modes. Whatever the architecture, modes have been found to be more and more local as their modal frequency increases.

Trees in a forest stand may have more significant shoot abrasion or crown asymmetry. At last, competition for resources and photomorphogenetic responses to shade may interact with the mechanoperceptive acclimation to wind [5]. But some elements affecting the biomechanical significance of multimodal scaling of trees to the response to wind load can already be directly discussed from our results.

Significance of multimodal dynamics and scaling laws to the responses of trees to wind — Wind excites trees through the drag force applied to the constitutive elements of the trees, branches, and possibly leaves or needles. From surface area considerations, most of the drag thus occurs at in the distal, possibly leafy, segments of the tree. All the modes in this study have a common characteristic: their larger displacements sits on the extremities of the tree. Therefore, they should reciprocally all be excited by a force applied at the extremities, such as the wind-drag force [8]. Moreover, because wind spectra usually have a large frequency band overlying most of the modal frequencies of the considered modes, several modes may be excited directly by highly fluctuating winds.

[9, 20] have argued that dynamics including branch deformation with close modal frequencies could be beneficial to the tree by enhancing aerodynamic dissipation through a mechanism called multiple resonance damping or multiple mass damping. A prerequisite for this mechanism to occur is a multimodal behavior of the tree, with high modal density in the frequency range and significant branch deformations, exactly what was found here for trees with contrasting architectures. This dense multimodal dynamics, a consequence of the branched structure, can then be interpreted as a strategy to prevent the trunk from bending excessively until the rupture.

Table 1. Slenderness coefficients β , lateral and axial branching ratios μ and λ , respectively, and branching angles α estimated from walnut geometry (orthogonal regression coefficients, confidence intervals at 90% level [CI], coefficients of determination [R^2], and root mean square of the residual errors [σ_{res}]).

Tree	β	λ	μ	α
Walnut	1.37	0.25	0	20°
CI	$1.25 < \beta < 1.49$	$0.22 < \lambda < 0.29$		
R^2	0.87	0.74		
σ_{res}	0.2	0.008		

References

1. Barthelemy, D., and Y. Caraglio. 2007. *Plant architecture: A dynamic, multilevel and comprehensive approach to plant form, structure and ontogeny*. Annals of Botany 99: 375 – 407.
2. Coutand, C., and B. Moulia. 2000. *A biomechanical study of the effect of a controlled bending on tomato stem elongation. II. local mechanical analysis and spatial integration of the mechanosensing*. Journal of Experimental Botany 51: 1825 – 1842.
3. De Langre, E. 2008. *Effects of wind on plants*. Annual Review of Fluid Mechanics 40: 141 – 168.
4. Fournier, M., P. Rogier, E. Costes, and M. Jaeger. 1993. *Modélisation mécanique des vibrations propres d'un arbre soumis aux vents, en fonction de sa morphologie*. Annales des Sciences Forestieres 50: 401 – 412.
5. Fournier, M., A. Stokes, C. Coutand, T. Fourcaud, and B. Moulia. 2005. *Tree biomechanics and growth strategies in the context of forest functional ecology*. In A. Herrel, T. Speck, and N. Rowe [eds.], *Ecology and biomechanics: A biomechanical approach of the ecology of animals and plants*, 1 – 33. CRC Taylor & Francis, Boca Raton, Florida, USA.
6. Gardiner, B. A., and C. P. Quine. 2000. *Management of forests to reduce the risk of abiotic damage – A review with particular reference to the effects of strong winds*. Forest Ecology and Management 135: 261 – 277.
7. Gardiner, B. A. 1992. *Mathematical modelling of the static and dynamic characteristics of plantation trees*. In J. Franke and A. Roeder [eds.], *Mathematical modelling of forest ecosystems*, 40 – 61. Sauerländer, Frankfurt/Main, Germany.
8. Gerard, M., and D. Rixen. 1994. *Mechanical vibrations: Theory and application to structural dynamics*. Wiley, Chichester, UK.
9. James, K. R., N. Haritos, and P. K. Ades. 2006. *Mechanical stability of trees under dynamic loads*. American Journal of Botany 93: 1522 – 1530.
10. Mayer, H. 1987. *Wind-induced tree sways*. Trees — Structure and Function 1: 195 – 206.
11. McMahon, T. A., and R. E. Kronauer. 1976. *Tree structures: Deducing the principle of mechanical design*. Journal of Theoretical Biology 59: 443 – 466.
12. Moore, J. R., and D. A. Maguire. 2008. *Simulating the dynamic behaviour of Douglas-fir trees under applied loads by the finite element method*. Tree Physiology 28: 75 – 83.
13. Moulia, B., C. Coutand, and C. Lenne. 2006. *Posture control and skeletal mechanical acclimation in terrestrial plants: implications for mechanical modeling of plant architecture*. American Journal of Botany 93: 1477 – 1489.
14. Niklas, K. J. 1992. *Plant biomechanics: An engineering approach to plant form and function*. University of Chicago Press, Chicago, Illinois, USA.
15. Niklas, K. J. 1994. *Plant allometry: The scaling of form and process*. University of Chicago Press, Chicago, Illinois, USA.
16. Rodriguez, M., E. de Langre, and B. Moulia. 2008. *A scaling law for the effects of architecture and allometry on tree vibration modes suggests a biological tuning to modal compartmentalization*. American Journal of Botany 95: 1523–1537.
17. Sellier, D., T. Fourcaud, and P. Lac. 2006. *A finite element model for investigating effects of aerial architecture on tree oscillations*. Tree Physiology 26: 799 – 806.
18. Sinoquet, H., P. Rivet, and C. Godin. 1997. *Assessment of the three dimensional architecture of walnut trees using digitising*. Silva Fennica 31: 265 – 273.
20. Spatz, H.-C., F. Brüchert, and J. Pfisterer. 2007. *Multiple resonance damping or how do trees escape dangerously large oscillations?* American Journal of Botany 94: 1603 – 1611.
21. Telewski, F. W. 2006. *An unified hypothesis of mechanoperception in plants*. American Journal of Botany 93: 1466 – 1476.

Free Coiling in Tendril-Bearing Plants

Annika Eberle, Kenny Quinn and Lori Bassman

Harvey Mudd College, USA

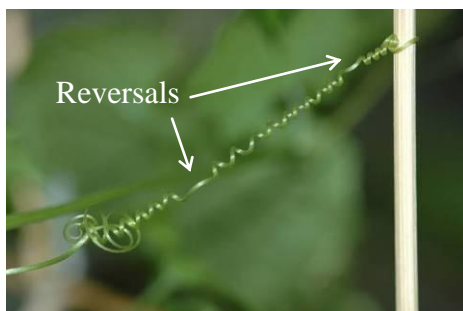
Abstract

Tendrils are structural supports that extend from a plant stem. Once the distal tip of a tendril touches an object, contact coiling follows rapidly to tether the tendril to the support. After the tip is secured, free coiling of the tendril occurs along the length to draw the stem closer to the support. While these growth processes are not well understood, it is believed that free coiling results from differential dorsal-ventral growth caused by asymmetric response to auxin distribution. Through computational modelling and experimental observation, this study has explored the structural changes that cause free coiling. Finite element analysis utilizing differential dorsal-ventral growth and experimentally-measured growth patterns has been employed to determine strain patterns that correspond to realistic coil geometries. Computational results show that even when a positive growth stimulus is applied to both dorsal and ventral sides of a tendril under tension, total strain on the dorsal side is positive while total strain on the ventral side is negative. Results also indicate that either i) the previously observed equilibrium distribution of auxin alone does not produce free coiling as seen in nature, or ii) the growth response is not linearly related to auxin concentration.

Background and motivation

Within seconds of touching an object, a tendril begins contact coiling to attach itself to the support. After the tip of the tendril is secured, the tendril draws the plant closer to the supporting object by free coiling along its length over a period of several hours [1]. While the physiologies of these two thigmotropic responses are well documented, the mechanosensory events initiated by thigmotropism are still not completely understood [2]. This paper discusses some of these mechanisms in more detail, specifically those involved in the process of free coiling after contact coiling is complete. Through the development of a finite element model of free coiling and experimental observation of live plant tendrils, the potential of various biological mechanisms in free coiling has been examined.

One interesting structural component of free coiling is the formation of one or more reversals along the length of the tendril (Figure 1). These reversals result from the need to maintain zero net twist when both ends of the tendril are anchored (on one end by the stem and on the other by the supporting object).



*Fig. 1 Coiled tendril of *Luffa cylindrica* with the appearance of multiple reversals along the length.*

Some of the first recorded observations of tendril-bearing plants were made by Charles Darwin in *The Movements and Habits of Climbing Plants* published in 1865. In this work, Darwin described the process of circumnutation that tendrils undergo when they are searching for a support [3]. In addition, Darwin performed some preliminary marking experiments to determine if the length of the tendril changed during coiling. He concluded that it was unlikely that the overall length of the tendril changed and thought it probable that coiling resulted from contraction of the ventral side of the tendril.

It was not until the 1960s that experimental research on tendrils began to provide more insight into tendril coiling. Several studies noted that auxin, a plant hormone previously thought to cause tendril coiling, was unlikely to result in contact coiling because of the long response time for auxin (several hours) compared to the short coiling initiation time (several seconds) [4,5]. Junker indicated that the dorsal to ventral ratio of auxin concentration remained asymmetric (56:44) across the tendril before and after stimulation, but he believed that this difference was too small to cause growth changes for contact coiling [4]. Instead, Junker suggested that acid growth, brought about by an action potential or an altered ionic environment, might be more likely to cause contact coiling.

In a different approach, Jaffe described how ethylene gradients caused by basipetal redistribution of auxin could result in curvature in tendrils [6]. In addition, Jaffe reiterated Darwin's suggestion of contraction of the ventral side of the tendril. Still, these works, like most published on tendrils during the 1960s, focused on contact coiling and not free coiling.

Several mathematical models were also developed to describe the coiling patterns of tendrils. Raugh modeled the helical structure of a tendril without reversals, incorporating structural variations such as vascular bundles, and proved that this model achieved volume invariance and bilateral symmetry [7]. This work was later modified by Keller [8] to incorporate a single reversal and recently by Raugh himself to include analysis in higher dimensions and to relate his work to tubes in manifold theory [9]. Goriely and Tabor showed that the appearance of a single reversal in tendrils can be understood through a dynamic analysis of thin elastic rods and concluded that the intrinsic curvature of the tendril causes coiling [10]. In order to explain the appearance of multiple reversals, Domokos and Healey developed a finite length model with boundary constraints and were able to predict the formation of multiple reversals in an intrinsically curved rod [11]. Their model is quite good at predicting the formation of multiple reversals but some of their geometric assumptions are not physically accurate. Still, none of these models take into account growth within the rod as might occur within an actual tendril.

As described above, there is no clear answer for which biological mechanism(s) or mechanical system(s) is responsible for coiling in tendril-bearing plants. Since contact coiling is caused by a vectorial stimulus (touch) and results in directional growth causing free coiling, other types of tropic responses may provide insight into the mechanisms that cause free coiling. For example, the physiology and development of root systems in plants resulting from gravitropism have been studied more thoroughly than tendril coiling. Laskowski et al. found that curvature in root systems increases auxin levels along the dorsal side of the root [12].

Although many articles have stated that auxin does not cause coiling in plant tendrils, these claims are often made because of the short time period associated with contact coiling. However, it is likely that there are two different mechanisms: one that initiates contact coiling and another that causes free coiling. A goal of this work has been to implement growth patterns that could correspond to different coiling stimuli in a finite element model and to compare the results to geometries of live plant tendrils. In order to verify accurate boundary conditions for the model, the magnitude of the tension force developed in a tendril was determined experimentally. To implement meaningful growth patterns, the growth along the length of a tendril and across the dorsal-ventral diameter was also studied with a marking experiment.

Material and methods

Cultivation of *Luffa cylindrica*

For tension force experiments, *Luffa cylindrica* seeds were planted in individual pots and grown in a growth chamber. The growth chamber was set to provide 14 hours of light, during which the temperature was 30°C, and 10 hours of darkness, during which the temperature was 24°C. Humidity

was held constant at 40%. The plants required 50 to 60 days between planting and the formation of mature tendrils.

Experimental determination of tension force

When coiling, the tendril develops a tension force with which it pulls the plant stem. The magnitude of this tension force was experimentally determined by a pendulum experiment (after [13]). A pendulum was constructed with a trapeze structure as the pendulum arm to provide a gripping structure for the distal tip (Figure 2).

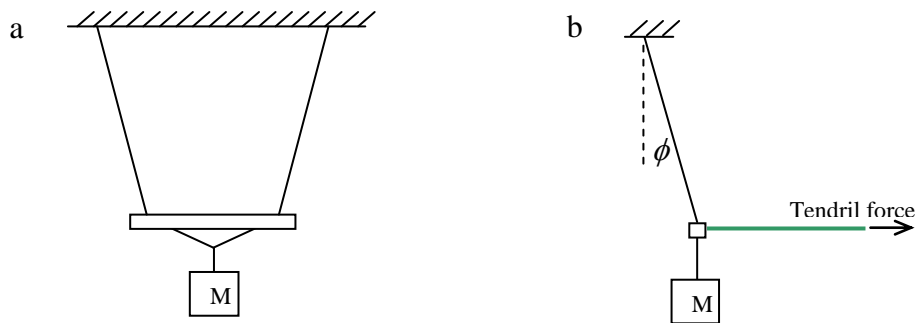


Fig. 2 Diagram of the trapeze structure of pendulum arm in (a) front view and (b) side view.

The plant stem was restrained against a clamp to prevent displacement, and the distal tip of the tendril was allowed to coil around the horizontal support of the pendulum arm. The subsequent free coiling of the tendril caused a rotation of the pendulum. Once equilibrium was reached, the angle of rotation ϕ was measured. Equations of static equilibrium relate the pendulum arm angle and mass to the tension force. Note that in this experiment the stem remains stationary and the tendril pulls the support closer. In nature the situation is typically reversed, with the support fixed and the stem flexible, but the force developed in the tendril should be similar in both cases.

Experimental observation of growth patterns

A method for performing marking experiments was developed to observe the relative growth of the dorsal and ventral sides of tendrils. Once an uncoiled tendril reached mature length, small dots of gel pen ink were applied to the tendril with the side of a sewing needle. Three different colors of ink were applied in a repeated sequence to each side of the tendril, for a total of six colors. Pictures of the markings were taken against a graph paper backdrop (Figure 3a).

Coiling of the tendril was then induced by rubbing the distal tip against a suitable support. Once free coiling was completed (approximately 48 hours later), the tendril was cut from the stem and support, and pictures of the coiled tendril were taken, again with a graph paper backdrop (Figure 3b).

By comparing the before and after pictures, an estimation of growth at different points along the length of the tendril was determined. Differences in distances due to positioning of the camera were corrected by comparing the size of one square of the graph paper in each picture. The distances between pairs of ink marks were estimated in the coiled tendril pictures and compared to the distances between those same points in the uncoiled pictures to determine the extent of growth at that location on the tendril.

While the distance between two points along the uncoiled tendril was easily determined using the ruler tool in Adobe Photoshop, the determination of the distance between points on the coiled tendril was more complex. The arc length of a helix, s , is given by $s = \theta\sqrt{(2\pi R)^2 + H^2}$, where R is the radius of the helix, H is the pitch of the helix, and θ is the rotation of the helix in radians. Because the tendril is tapered, measurements of the radius and pitch were made for every rotation along the length of the tendril. Note that the radius of the dorsal and ventral sides of the tendril differ by the diameter, d , of the tendril.

The number of rotations between points along the length of the tendril was determined for as many ink points as possible on each of the dorsal and ventral sides. This measurement was the main source

of error in determining the arc length between points; it was not possible to reliably determine t with better than $\pm 0.1\pi$ accuracy.

This experiment was performed at the Rose Hills Foundation Conservatory for Botanical Science (Huntington Botanical Gardens, San Marino, CA) on tendrils of *Adenia lobata*.

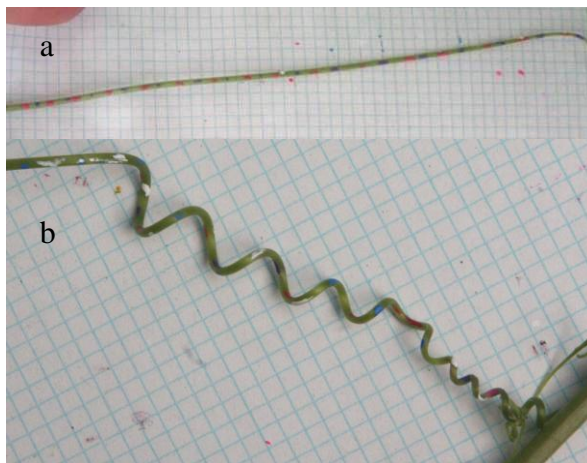


Fig. 3 Colored markings on a tendril when (a) uncoiled and (b) coiled (10x10 boxes is a 1 inch square grid).

Computational model

A finite element model of a tendril was constructed in ANSYS (version 11.0, ANSYS, Inc. Cannonsburg, PA, USA). The model utilizes specialized beam elements subject to thermal expansion to mimic the strains caused by growth. Just as the concentration of a growth hormone dictates a certain growth rate, the coefficient of thermal expansion (CTE) of a material dictates the strain (normalized growth) of a material subject to a change in temperature. By constructing a gradient in the CTE across a cross-section and then applying a temperature load T , differential dorsal and ventral elongations are achieved.

Previous modelling employed lengthwise (x -direction) tapering of the tendril and cross-sectional (y -direction) differential growth, but the results did not contain the correct change in the spatial frequency of coils along the length of the tendril [14]. In this model variable growth is achieved along the length of the tendril with a spatially-varying applied temperature (analogous to a spatially varying growth stimulus) along the length. Temperature profiles are specified as a function of x only, where x is the normalized length along the tendril and varies from 0 at the stem to 1 at the tip of the tendril. In addition, the CTE is different on the dorsal and ventral halves of the cross section, so that the imposed thermal strain $\epsilon(x,y) = \text{CTE}(y)\Delta T(x) = (L_f - L_o)/L_o$, where L_f is the final length and L_o is the original length. In the analogy with biological growth, this strain function incorporates an assumption of a linear growth response to hormone concentration.

The need to vary properties and geometry, as well as the large deformations involved in tendril coiling, require the use of a specialized beam element [14]. The “Beam188” element in ANSYS is a 3D linear finite-strain beam element with six degrees of freedom per node that allows the use of user-input cross sections and the implementation of a lengthwise taper. The user-defined cross sections in this model are circular and specify two sets of material properties: one for the dorsal side of the beam and one for the ventral side of the beam [14]. To improve convergence of the numerical solution, this model uses a nonlinear stabilization method that is based on the energy dissipation ratio. The results shown use an elastic modulus of 33 MPa [14], and a tendril length of 10 cm and radius with a linear taper from 0.30 mm to 0.15 mm (for *Luffa cylindrica*) or a length of 7 cm and radius with a linear taper from 0.52 mm to 0.40 mm (for *Adenia lobata*).

The simplest simulation of free coiling was demonstrated by fixing all degrees of freedom at the large (stem) end of the beam. Using *Luffa cylindrica* dimensions and the experimental measurements of tension, a force of similar magnitude was applied at small (tip) end of the tendril, along with a small rotation (0.05 radians) in order to break symmetry. All other degrees of freedom at the small end were fixed. The computational setup was also modified to utilize flexible boundary conditions at the large end to simulate the experimental setup used to determine tension in the tendril or to model the stiffness

of the stem. When a stem is used it is implemented as a cantilever with length of 3.5 cm, radius of 0.65mm (uniform along the length) and the same modulus as the tendril. It does not change length during the simulation.

Experimental results

Tension force

Six pendulum experiments, one of which is shown in Figure 4, resulted in an average pendulum angle of 14.0 ± 1.8 degrees after tendril coiling. The pendulum mass and trapeze support combined had a mass of 1.39 g, resulting in an average tendril tension force of 0.0034 ± 0.0002 N. Experiments with significantly lower or higher pendulum masses did not result in satisfactorily coiled tendrils.

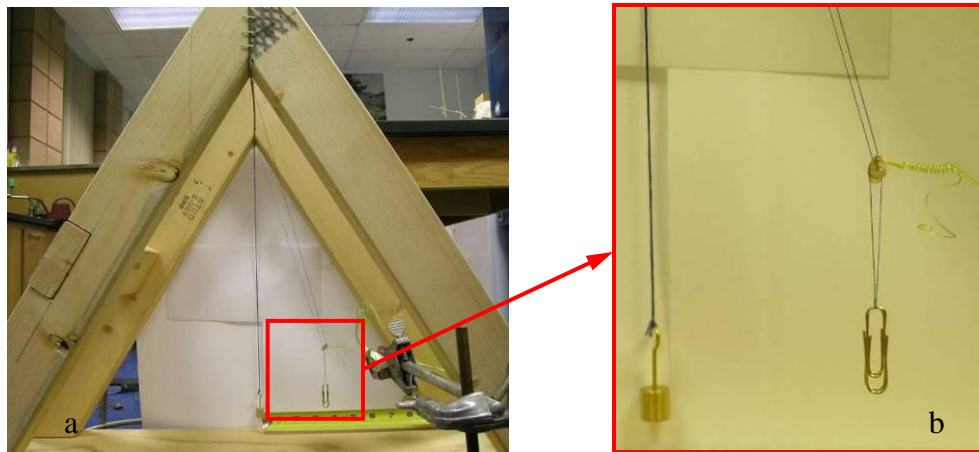


Fig.4 (a) Setup of tension force experiment and (b) close up of attached coiled tendril with reference vertical indicator.

Growth patterns

The growth rate experiments provided a preliminary evaluation of the lengthwise growth pattern of both the dorsal and ventral sides of a tendril. While over twenty tendrils were marked with ink patterns, fewer than ten coiled appropriately for observation. Analysis of two of the best coiled tendrils indicated that while the dorsal side of the tendril grows, the ventral side appears to shrink (Figure 5). This result confirms Darwin's original hypothesis about contraction along the ventral side of a tendril during coiling [3]. Results from Tendril 1 (Figure 5a) were used for computational modelling.

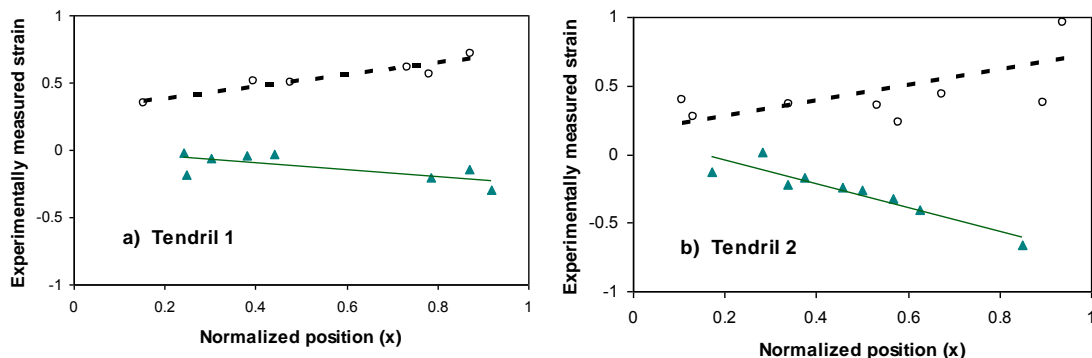


Fig. 5 Experimental strain results from two of the best tendrils. Note the trends of linearly increasing dorsal strain (white circles, curve fit illustrated by dashed line) and linearly decreasing ventral strain (solid triangles, curve fit illustrated by solid line). Curve fits for the dorsal strain were $\epsilon = 0.43x + 0.29$ and $\epsilon = 0.58x + 0.15$ for Tendrils 1 and 2, respectively. Curve fits for the ventral strain were $\epsilon = -0.25x + 0.01$ and $\epsilon = -0.87x + 0.14$ for Tendrils 1 and 2, respectively.

Computational results

Overall, the computational results could be made to closely match the geometries of actual tendrils, including the appearance of multiple reversals and the increase in spatial frequency of coils near the tips of the tendrils (Figure 6). The multiple reversals in Figure 6 were generated by increasing the length of the tendril (with *Adenia lobata* radii) to 15 cm. Multiple reversals were also generated when the applied tension was increased.

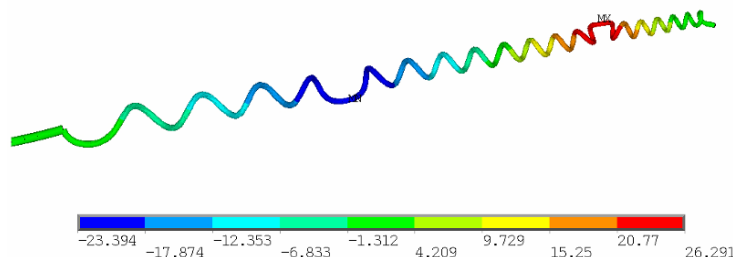


Fig. 6 Computational example showing multiple reversals. Colors indicate relative rotation.

Tension force setup

An example solution of the computational model of the tension experiment using *Luffa cylindrica* geometric parameters is shown in Figure 7. The force generated by the tendril in the model was 0.01 N (compared to 0.0034 N experimentally), however varying the length of the tendril in the computational model dramatically changes the pendulum angle, and hence the force developed, once the tendril is coiled.

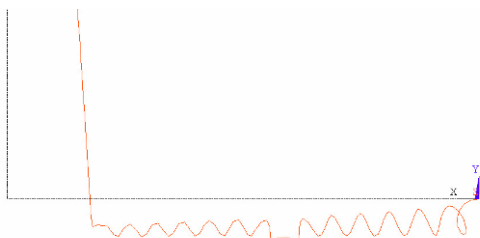


Fig. 7 Computational solution for pendulum tension experiment. The black lines indicate the initial positions of the uncoiled tendril and pendulum.

Flexible stem

The total strain observed in the computational results was a combination of thermal strain (analogous to growth strain) and mechanical strain due to the tension force in the tendril. Although in the model these contributions were separable, only the total strain was measurable in experiments. Because the main goal was to understand the differential growth required to cause realistic coiled geometries, the exact temperature function (which dictated how growth changed along the length) was not critical; in fact the qualitative results were insensitive to changes in slope, and quadratic functions as well as linear produced realistic geometries. With this in mind, the temperature function used was based on the strain measured on the dorsal side of Tendril 1 (Figure 5a). This function, $T(x) = 43x + 29$, in combination with a dorsal CTE of 10^{-2} , produced the total dorsal strain measured. This was kept constant for all results shown below. Only the dorsal to ventral CTE ratio was changed.

The qualitative results were very sensitive to the length of the stem because it changes the tension in the tendril. If the tension is not sufficiently high the tendril becomes a jumble of loops instead of an orderly helix. This is also seen in some actual growing tendrils. If the tension is too high the helix is extremely stretched, which leads to few revolutions of the helix and multiple reversals in the model. An actual tendril under such conditions would likely not remain connected to its support.

When a 56:44 dorsal to ventral CTE ratio (CTEs of 10^{-2} and 7.86×10^{-3} , respectively) was used in the computational model (following the 56:44 dorsal to ventral ratio of auxin concentration proposed by Junker [4]), the results did not resemble natural coiling (Figure 8). This finding was confirmed for a wide variety of temperature functions.

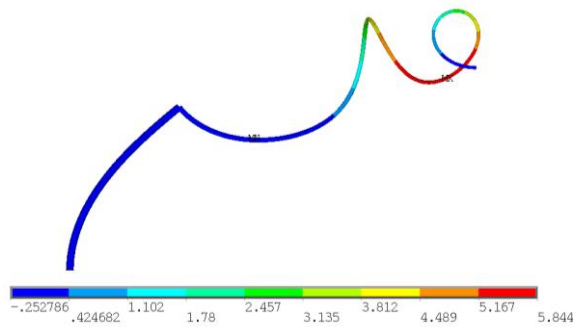


Fig. 8 Contour plot of results with 56:44 dorsal to ventral CTE ratio with $T = 43x+29$. Colors indicate relative rotation about the longitudinal (x) axis.

However, when the dorsal to ventral ratio was increased to 10:1 (CTEs of 10^{-2} and 10^{-3} , respectively) the geometry did resemble coils found in actual plant tendrils (Figure 9a). It is interesting to note that even though the applied thermal strains on the dorsal and ventral sides are positive, the total strain (thermal plus mechanical) is negative on the ventral side and positive on the dorsal side (Figure 9b). This is due to the radial contraction and commensurate increase in pitch of the helix produced by mechanical tension.

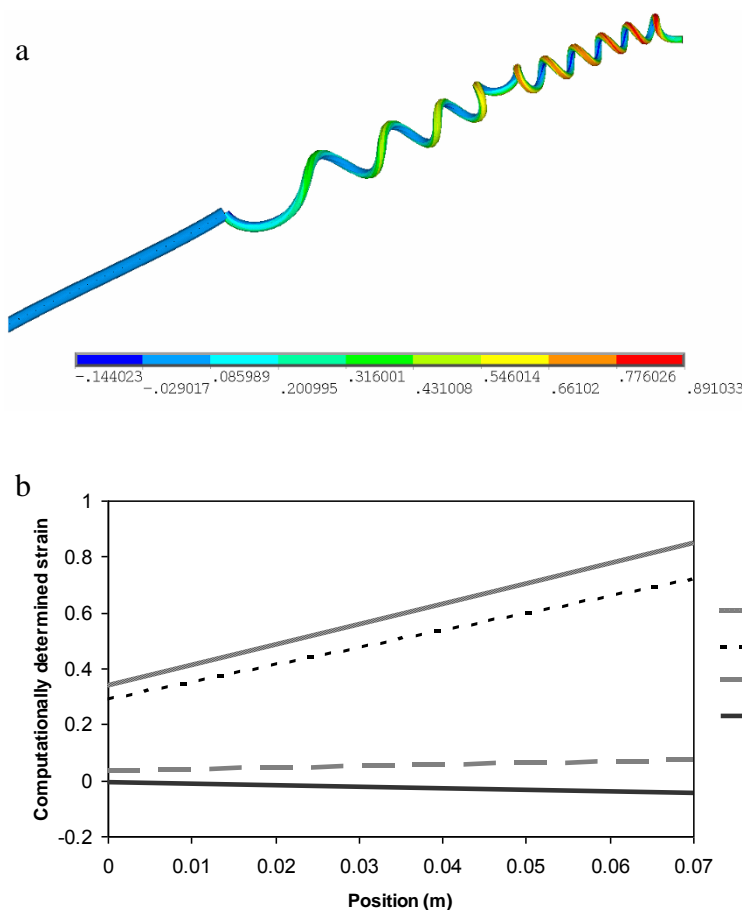


Fig. 9 a) Contour plot of total strain (thermal plus mechanical) with 10:1 dorsal to ventral CTE ratio with $T = 43x+29$. The only change to the model relative to that in Figure 8 is the dorsal to ventral CTE ratio. b) Trends of thermal strain and total strain on the dorsal and ventral sides of the tendril. Note that even though both the dorsal and ventral applied thermal strains are positive, the dorsal total strain is positive while the ventral total strain is negative.

Conclusion and future work

While the biological process that causes free coiling has yet to be discovered, biomechanical modelling provides insight into the solution. A computational model that can reproduce realistic tendril geometries, including multiple reversals, has been developed to explore variation in growth along the length of a tendril and relative growth on dorsal and ventral aspects of the tendril. The model produced solutions that closely match coil geometries encountered in nature when a dorsal to ventral

strain ratio of 10:1 was applied but not when a 56:44 ratio was used. If the 56:44 ratio is in fact an accurate representation of the dorsal to ventral auxin concentration ratio, then this model indicates that either i) the previously observed equilibrium distribution of auxin alone does not produce free coiling as seen in nature, or ii) the growth response is not linearly related to auxin concentration. The latter possibility may be explored with this model in future work by implementing a CTE that varies with temperature. This would be analogous to a growth response that is non-linearly related to the concentration of a growth hormone, as has been shown in many studies.

Future work will also include additional marking experiments in multiple species of tendril-bearing plants to accurately determine growth patterns and to verify that they are similar across species. Finally, future studies utilizing the proposed computation approach may allow for the determination of the parameters that cause multiple reversals as well as the locations of these reversals.

Acknowledgements

We thank Dr. Mary Williams for allowing us to use her growth chamber and for consulting with us about plant biology, the Biology Department staff at Harvey Mudd College for lab support, the Engineering Department at Harvey Mudd College for ANSYS license funding, Dr. Marta Laskowski at Oberlin College for describing the correlation between curvature and auxin, Rachel Vourlas and other staff at the Huntington Botanical Gardens for arranging access to their facility, and Dr. Michael Raugh for introducing us to the problem of tendril coiling.

References

1. Jaffe, M.J. and Galston, A.W., (1970): *Physiological studies of pea tendrils VII. Evaluation of a technique for the asymmetrical application of ethylene*. *Physiology of Plants*. 45: 449-454.
2. Monshausen, G., Swanson, S. and Gilroy, S., (2008): *Touch sensing and thigmotropism*, in *Plant tropisms*, Editors, Gilroy S. and Masson P.: Oxford, Blackwell Publishing. p. 91-122.
3. Darwin, C., (1888): *The movements and habits of climbing plants*, in *The works of Charles Darwin*, Vol. 18, Editors, Barret, P.H., Freeman R.B., New York University Press.
4. Junker S., (1977): *Thigmonastic coiling of tendrils of Passiflora quadrangularis is not caused by lateral redistribution of auxin*. *Physiology of Plants*. 41: 51-54.
5. Carrington C.M.S. and Esnard J., (1989): *Kinetics of thigmocurvature in two tendril-bearing climbers*. *Plant, Cell and Environment*. 12: 449-454.
6. Jaffe M.J., Galston A.W., (1966): *Physiological studies of pea tendrils I. Growth and coiling following mechanical stimulation*. *Plant Physiology*. 41: 1014-1025.
7. Raugh, M.R., (1979): *Some geometry problems suggested by the shapes of tendrils*. Stanford University Dissertation in Mathematics.
8. Keller, J.B., (1980): *Tendril shape and lichen growth*. *Lectures on Mathematics in the Life Sciences*. 13: 257-274.
9. Raugh, M.R., (2008): *Some Differential Geometry Motivated by Tendril Coiling*. In preparation.
10. Goriely A. and Tabor M., (1998): *Spontaneous Helix Hand Reversal and Tendril Perversion in Climbing Plants*. *Phys. Rev. Letters* 80: 1564-1567.
11. Domokos, G. and Healey, T.J., (2005): *Multiple helical perversions of finite, intrinsically curved rods*. *Int. J. of Bifurcation and Chaos*. 15: 871-890.
12. Laskowski, M., Grieneisen V., Hofhuis H., Hove C., Hogeweg P., Marée A. and Scheres B., (2008): *Root system architecture from coupling cell shape to auxin transport*. *PLoS Biology*. 6: 2721-2735.
13. Putz F.E. and Holbrook N.M., (1991): *Biomechanical studies of vines*, in *The biology of vines*, Editors, Putz F.E. and Mooney H.A.: Cambridge, Cambridge University Press. p. 73-98.
14. Thomson S., Bassman L. and Williams M., (2006): *Development of helix structures in tendril-bearing plants*, in *Proceedings of the 5th plant biomechanics conference*, 28 Aug.-1 Sept., Stockholm, Sweden.

Evaluation of growth stress profiles in tree trunks: comparison of experimental results to a biomechanical model

Delphine Jullien¹, Tancrede Alméras¹, Miho Kojima², Hiroyuki Yamamoto² and Pierre Cabrolier³

¹ LMGC, UMR 5508 CNRS - Université Montpellier 2, France ; ² Laboratory of Biomaterial Physics (Wood Biomechanics), Nagoya University ; ³ LERFOB, UMR INRA-AgroParisTech 1092, Nancy, France

Abstract

During tree growth, mechanical stresses accumulate in the stem because of the increasing tree weight and wood maturation. These “growth stresses” fulfil essential biomechanical functions: they allow the control of the tree orientation and improve its resistance against bending loads. But they generate technological problems during tree transformation, causing heart checks after cross-cutting, checks and deformations of boards after sawing, etc... Research in this area aims at understanding how these stresses appear during growth, in order to find solutions to reduce them.

Radial profiles of growth stress were studied by measuring the longitudinal strains due to the release of growth stress at different radial positions on diametrical boards. A biomechanical model based on the beam theory adapted to growing structures is presented. It allows calculating growth stress accumulation in a cross-section of any shape, with any distribution of material properties. Experimental profiles were compared to those simulated by the model assuming particular growth scenarios. They were consistent with the predictions of biomechanical models, showing a maximal tension at the periphery of the tree, and an increasing compression towards the tree centre. Asymmetric profiles were sometimes observed, and were consistent with simulations obtained when eccentric diameter growth and asymmetric maturation strains were taken into account. The correspondence between experimental results and simulations provides a first validation of the biomechanical model of growth stress accumulation in stems.

Introduction

Growth stresses are mechanical stresses accumulated in tree stems during growth. They are a source of technological problems occurring during tree exploitation and wood processing, sometimes causing log-end splits when felling the tree, checks or deformations in boards when processing logs. Research in this area aims at better understanding factors that affect the growth stress patterns, in order to find ways reducing them.

Growth stresses result from the superposition of two distinct sources of stress: “support stress” due to the increasing weight of the tree crown and the stem itself, and “maturation stress”, due to the physico-chemical modifications of wood occurring during its formation [2]. In a straight vertical tree, weight applies a compressive support stress distributed over the stem section. A tensile maturation stress appears in a newly formed wood layer in the grain direction, which applies a compressive stress on the core of the stem. Accumulation of these different sources of stress during tree growth results in specific stress patterns where a tensile stress is found at the tree periphery and a compressive stress is found at its centre. It can be simulated by a simple axisymmetric biomechanical model [5].

However a tree is never perfectly straight and vertical, so that its increasing weight also applies a bending moment on the stem, resulting in a non-axisymmetric field of support stress and changes in stem curvature that modify its orientation. When stem orientation is disturbed by its increasing self-weight or any external action, a higher level of maturation stress is produced on one side of the stem, generating a bending moment that counteracts the disturbance and maintains or restores stem orientation [1]. This reaction is often associated to eccentric diameter growth. Biomechanical models

[3,4] allow predicting the growth stress field resulting from such complex situations, in order to evaluate the effect of biomechanical parameters of the tree growth, such as the tilt angle of the stem, the eccentricity of diameter growth, and the magnitude of maturation strains on each side of the tree. In the present paper, the formulation of a biomechanical of growth stress accumulation is presented, and its outputs are compared to profiles of residual strains measured on real trees, in order to provide a first validation of the biomechanical models for non-axisymmetric cases.

Material and methods

Measurement of residual strains

4 poplar trees (*Populus* sp.) and 3 sugi trees (*Cryptomeria japonica*) were chosen for the study. The trees had diameter ranging from 6 to 23 cm, and were straight or slightly tilted. Trees were fell down and 1m-long logs were cut from the basal part and taken for the measurement of residual strain profiles. Diametrical boards, approximately 2cm-thick, were extracted from green logs. One side of the board was supposed to cross the pith in its center (Fig. 1b). In some cases, the pith location was slightly shifted towards the center of the board (Fig. 2b). Strain gauges were glued in the longitudinal direction at different radial positions on each board (Figs. 1a, 2a), onto the side the closest to the pith.

In case of eccentric logs, the pith is not in the middle of the board. We define two radii for the stem: one for the lower side of the inclined tree, the other one for the upper side of the inclined tree. For poplar trees, the upper side is larger than the lower side and presumably corresponds to an area of tension wood. Sugi trees were only slightly tilted, had low eccentricity, and did not contain apparent zones of compression wood. *Table 1* indicates the respective radii for each tree, and the number of gauges positioned onto the board.

The boards were cut on each side of the gauges (Fig. 1b), and the strains released by this operation were recorded at each radial positions. Thus an experimental radial profile of residual growth strains is obtained for each tree. A contraction of the wood during stress release corresponds to a tensile stress within the tree, and an expansion corresponds to a compressive stress. To remain consistent with the usual representation of growth stress profiles, the opposite of the residual strain is presented in the results (i.e. a positive value corresponds to a tensile stress, and a negative value to a compressive stress).

Table 1 Radii of boards and number of strain gauges, for 3 sugi and 4 poplar trees.

	Sugi			Poplar			
	<i>S1</i>	<i>S2</i>	<i>S3</i>	<i>P1</i>	<i>P2</i>	<i>P4</i>	<i>P5</i>
Lower side radius (cm)	12.25	10	4.15	1.9	2.3	3.35	3
Upper side radius (cm)	11	8.8	4.15	3.5	4.1	4.35	10.5
Number of gauges	18	19	9	7	7	8	11



Fig. 1a Poplar board with 9 strain gauges

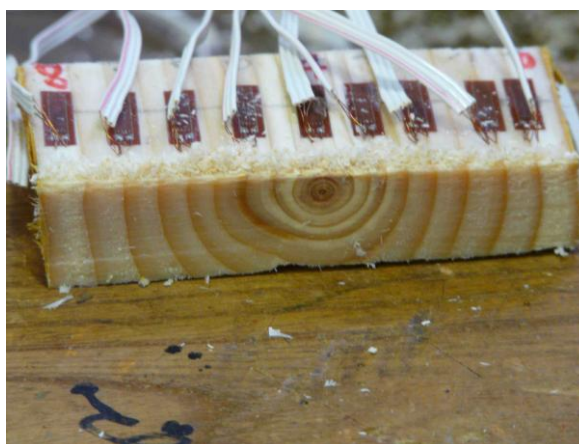


Fig. 1b same board after cutting to release residual strains

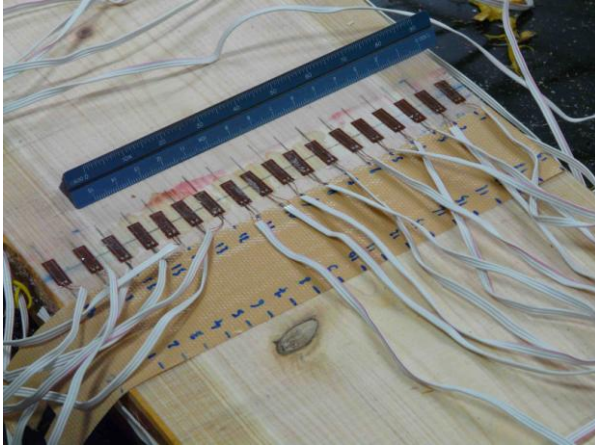


Fig. 2a Sugi board with 18 strain gauges



Fig. 2b The pith is located in the thickness of the board

Biomechanical model of growth stress accumulation

The biomechanical model developed by Alm eras [1,3] was used to simulate growth stress profiles. The model is based on beam theory applied to growing structures [4]. During the growth, the weight of the tree is increasing (growth in mass), and acts on a structure of increasing stiffness (growth in diameter), while maturation stress is induced in wood after its formation. Therefore, the effect of a given increment of mass of maturation stress depends on the diameter of the stem at the time it is added. Thus, the application of the beam theory to growing tree stems is not straightforward: the state of stress of a self-supporting stem differs from that of a beam that would be first made in an unstressed state, and then loaded. To compute the state of stress of a growing structure, an incremental formulation is necessary, so that changes in diameter and load are properly integrated over the tree life. During an elementary time step associated to an elementary load increment, the change in diameter of the beam can be neglected and its stiffness considered constant. Beam theory can be used to compute the stress increment at the level of a cross-section associated to the load increment. The longitudinal stress increment in response to a load increment is uniform within a homogeneous cross-section submitted to a purely axial load, and is heterogeneous otherwise. Accumulation of stress increments over the tree life always leads to a heterogeneous field of stress within a cross-section. Central parts of the tree contribute to bear the load increments from the beginning of the tree life, while peripheral parts only contribute since they have been formed.

The model allows calculating growth stress accumulation in a cross-section of any shape, with any distribution of material properties. It is restricted to a case where the tree and the section have bilateral symmetry (Fig. 3). The condition for static equilibrium at the level of a cross-section S implies that, during any time step, the variations of internal loads (due to changes in the mechanical state of the wood at the section level) equal the variations of external loads (due to the action of external forces on the section; here external forces refer to the action of tree weight on the section). Internal and external loads are described by the resulting force N perpendicular to the section, and the bending moments M . The total external load due to the tree weight depends on the local orientation of the section with respect to the gravity, ϕ , on the weight of the tree applied on the section, W , and on the horizontally projected distance between the section center and the center of mass of the tree, p_G (see Fig. 3):

$$\begin{aligned} N_E &= -W \cdot \cos\phi \\ M_E &= W \cdot p_G \end{aligned} \quad (1)$$

Variations in external loads during an elementary growth step (δN_E , δM_E) can thus be deduced from the increase in weight and the changes in stem configuration.

$$\begin{aligned} \delta N_E &= -(\delta W \cdot \cos\phi + W \cdot \delta(\cos\phi)) \\ \delta M_E &= \delta W \cdot p_G + W \cdot \delta p_G \end{aligned} \quad (2)$$

Variations in internal loads depend on the variations of the field of stress $\delta\sigma(x,y)$ within the section:

$$\begin{aligned} \delta N_I &= \iint_S \delta\sigma(x,y) \cdot dx \cdot dy \\ \delta M_I &= \iint_S y \cdot \delta\sigma(x,y) \cdot dx \cdot dy \end{aligned} \quad (3)$$

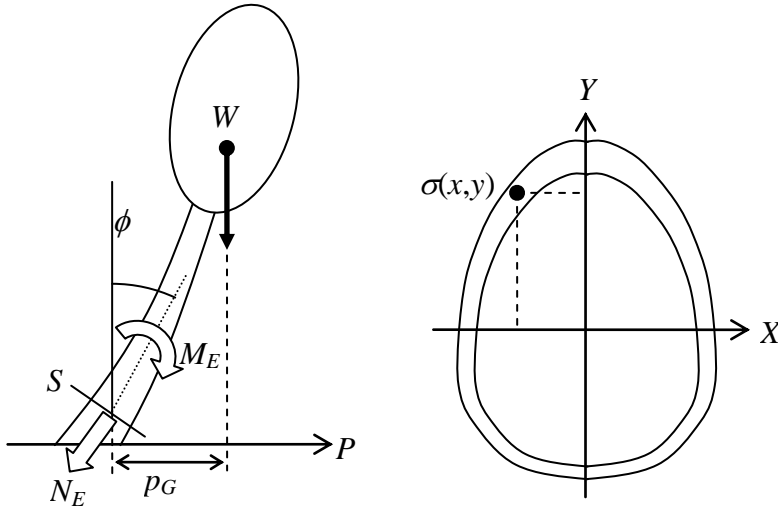


Fig. 3 Schematic representation of the geometry of a tree bending under its own weight.

We consider here two sources of variations of internal stress in wood: the elastic stress related to the deformation of the stem and the inelastic stress induced in peripheral wood during its maturation. The state of stress σ is related to the maturation strain α , the total strain ε , and the elastic modulus of wood E :

$$\sigma = E \cdot (\varepsilon - \alpha) \quad (4)$$

The variation of stress during an elementary time step can thus be expressed as:

$$\delta\sigma = \delta\sigma_{elas} - \delta\sigma_{matur} = E \cdot \delta\varepsilon - E \cdot \delta\alpha \quad (5)$$

Integration of the stress over the section allows expressing the variation in internal load as the sum of elastic and maturation loads:

$$\begin{pmatrix} \delta N_I \\ \delta M_I \end{pmatrix} = \begin{pmatrix} \delta N_I^{elas} \\ \delta M_I^{elas} \end{pmatrix} - \begin{pmatrix} \delta N_I^{matur} \\ \delta M_I^{matur} \end{pmatrix} \quad (6)$$

We will assume that the induction of maturation stress is completed immediately after a new wood layer is formed, *i.e.* that $\delta\alpha=0$ for internal wood layers, and $\delta\alpha=\alpha$ for the currently added wood layer δS . The maturation load can then be simply computed as:

$$\begin{aligned} \delta N_I^{matur} &= \iint_{\delta S} E(x, y) \cdot \alpha(x, y) \cdot dx \cdot dy \\ \delta M_I^{matur} &= \iint_{\delta S} y \cdot E(x, y) \cdot \alpha(x, y) \cdot dx \cdot dy \end{aligned} \quad (7)$$

The elastic load increment (δN_{elas} , δM_{elas}) is related to the field of strain increment $\delta\varepsilon(x, y)$ occurring in the section. For a slender solid such as a tree stem, this field is plane, so that the strain increment at any point of the section can be deduced from the strain increment $\delta\varepsilon_0$ at the reference point in the section and the gradient of strain increment in the section (which by definition is equal to the variation of curvature at the level of the section δC):

$$\delta\varepsilon(x, y) = \delta\varepsilon_0 + y \cdot \delta C \quad (8)$$

From equations (3), (5) and (8), one can deduce the relation between the elastic loads and the deformations occurring at the section's level:

$$\begin{pmatrix} \delta N_I^{elas} \\ \delta M_I^{elas} \end{pmatrix} = \begin{pmatrix} K_0 & K_1 \\ K_1 & K_2 \end{pmatrix} \begin{pmatrix} \delta\varepsilon_0 \\ \delta C \end{pmatrix} \quad (9)$$

Where K_0 is the axial stiffness, K_2 the bending stiffness and K_1 the coupling term, given by:

$$K_j = \iint_S y^j \cdot E(x, y) \cdot dx \cdot dy \quad (10)$$

The static equilibrium is achieved when internal loads balance external loads. Using equations (6) and (9), this condition is reduced to:

$$\begin{pmatrix} \delta\varepsilon_0 \\ \delta C \end{pmatrix} = \begin{pmatrix} K_0 & K_1 \\ K_1 & K_2 \end{pmatrix}^{-1} \left(\begin{pmatrix} \delta N_E \\ \delta M_E \end{pmatrix} + \begin{pmatrix} \delta N_I^{matur} \\ \delta M_I^{matur} \end{pmatrix} \right) \quad (11)$$

Right hand terms express the load increments due to the weight increase and wood maturation, so that this relation can be used to compute the deformation increment at the level of the section. The stress increment at each step can be deduced from these data and cumulated to obtain the total stress field within the section at final time.

The final step of the calculation consists in simulating the effect of felling the tree (*i.e.* suppressing the support stress due to the tree weight) and extracting the board from the log (*i.e.* suppressing the growth stress of the parts of the log removed when extracting the board). Finally the residual stress profile within the board is converted into a residual strain profile, and compared to experimental data.

Simulations and comparison to experimental results

The biomechanical model was run to find a growth scenario compatible with each set of experimental data. The stem radii measured on each side of the tree were used to specify eccentric growth. Eccentric stems suggest that trees were tilted from vertical. Their angle was assumed to range between 0 and 25° and adjusted to fit experimental data. The maturation strain was supposed to differ between the two sides of the stem in order to simulate asymmetric reaction in response to the tilt angle. The maturation strains on each side of the stem are supposed to change with time, and their evolution is defined by 3 parameters specifying the maturation strain at the beginning of the growth period, at the end, and at an intermediate time. These values were adjusted in order to minimize the difference between simulated and measured residual strain profiles. The effect of the weight was accounted for by allometric power functions specifying the evolution of tree weight as a function of its basal diameter. Because strains were used as input parameters (maturation strains) and output parameters (residual growth strains), the wood elastic modulus has only a second-order influence, so that we used an arbitrary value of 12 GPa for all trees.

Experimental profiles of residual strains

Figure 4 shows the results obtained for the 3 sugi trees and figure 5 for the 4 poplar trees. The diagrams on the left-hand side show the experimental profiles of residual strain (squares) and the simulated profiles obtained after fitting the evolution of maturation strains on both sides of the tree. Adjusted values of maturation strains are shown on the right-hand side of the diagrams.

The experimental profiles obtained are consistent with the general predictions of earlier biomechanical models [4,5], *i.e.* a tension at the periphery of the tree, and an increasing compression towards the tree centre. In most cases, the compression near the section centre corresponds to a strain of approximately -1000 microstrains (and up to -8000 microstrains for the case P5), which is consistent with the results of previous authors [2,5]. However, many of the measured experimental profiles showed discrepancies compared to the simplest model proposed by Kübler [5]: the profiles are most of the time not symmetric between the two sides (*e.g.* S3, P1, P2, P4, P5) and the profiles on each side do not fit the log-shape predicted by Kübler's model. The maximal compressive stress was not always found at the level of the pith (*e.g.* S3, P4, P5), consistently with the prediction of biomechanical models in case of eccentric growth. Moreover, in some cases, the profile is not monotonous, showing local minima (*e.g.* P1 at $R = +2.5$ cm, P2 at $R = +1.8$ cm, P4 at $R = +2$ cm, P5 at $R = +5.5$ cm).

Comparison between experimental profiles and simulations

The model parameters have been adjusted to fit experimental data. The optimisation yielded satisfactory results, although the correspondence between experimental points and simulations curves is imperfect in some instances. Note however that the optimisation problem showed multiple local optima, so that the proposed set of parameters and simulated profiles do not always reflect the best possible fit. They should not be interpreted as the unique solution of the problem, but rather as plausible scenarios of the biomechanical history of the tree. Nevertheless, the simulated profiles successfully reproduce most of the qualitative features of experimental data (asymmetric and non-monotonous profiles) with the correct order of magnitude.

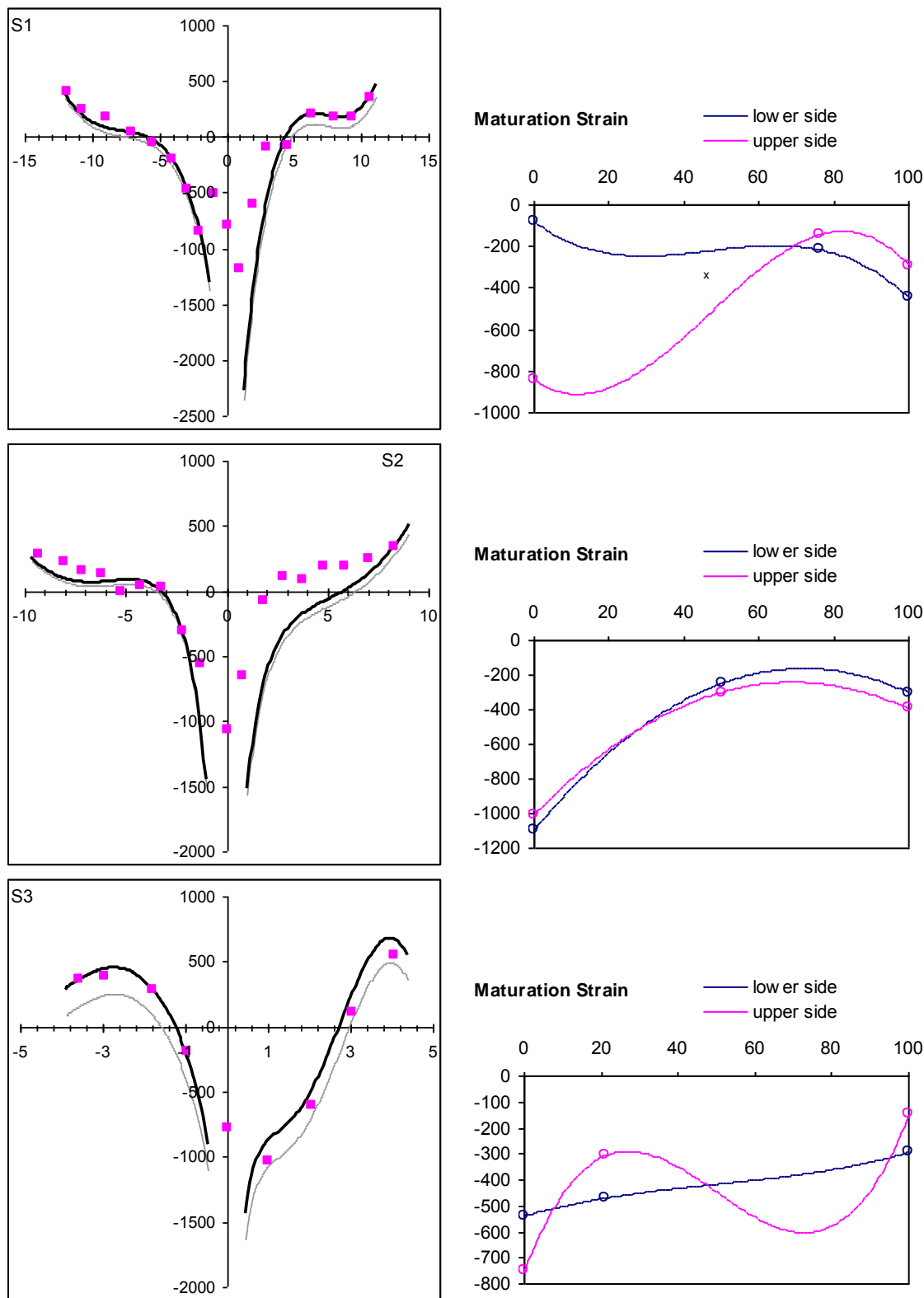


Fig. 4 Left-hand side: Residual longitudinal strain (in microstrain) function of the radial position (in cm) for 3 sugi trees. Grey line: computed profile of residual strain in the tree (before extracting the board), black line: computed profile of residual strain in the board, squares: experimental residual strains. Right-hand side: hypothetic evolution of maturation strain (in microstrain) during growth as a function of relative radius (% of final radius) on each side of the tree. The parameters were adjusted to minimize the difference between simulated and experimental residual strain profiles.

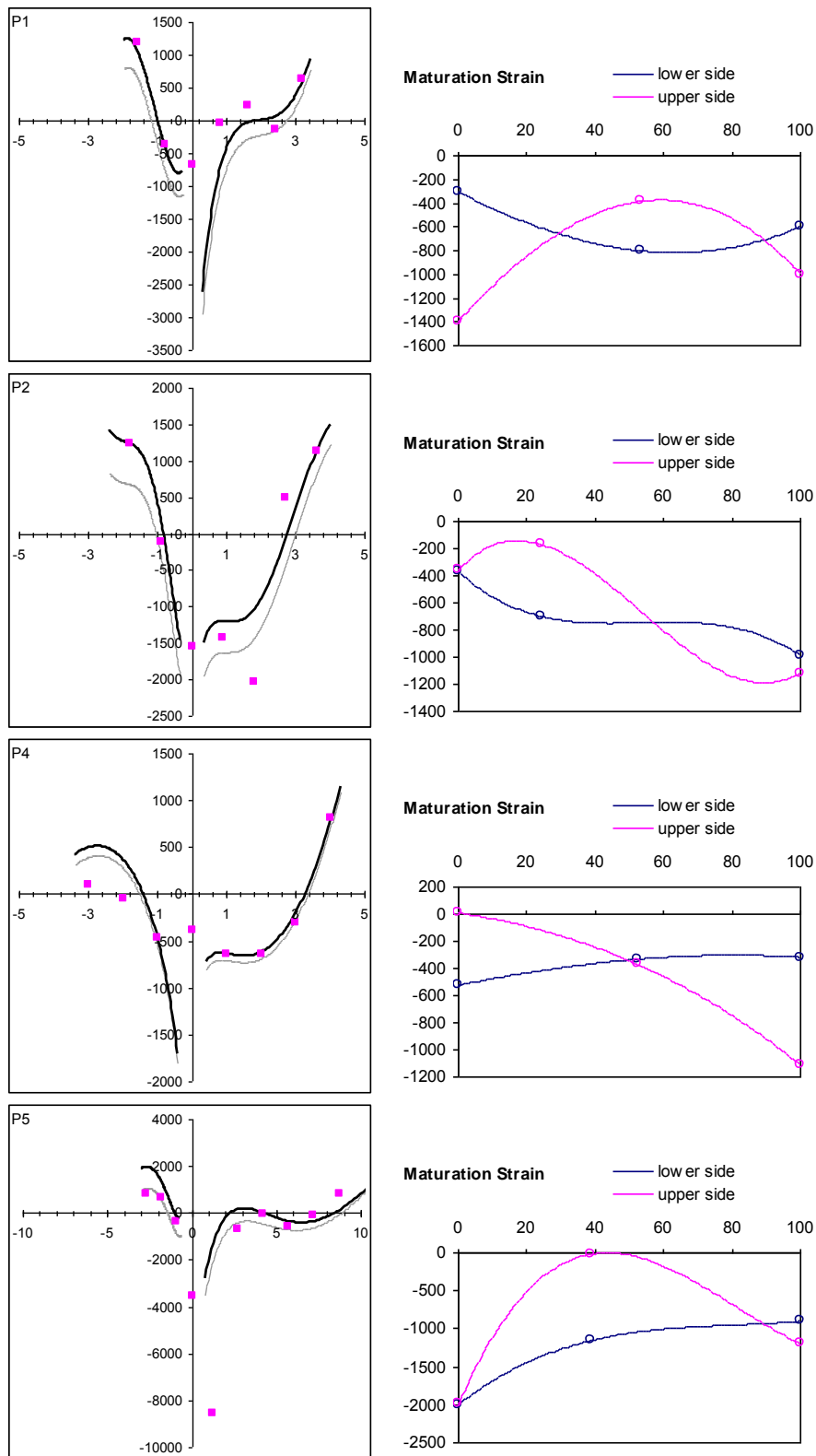


Fig. 5 Left-hand side: Residual longitudinal strain (in microstrain) function of the radial position (in cm) for 3 poplar trees. Grey line: computed profile of residual strain in the tree (before extracting the board), black line: computed profile of residual strain in the board, squares: experimental residual strains. Right-hand side: hypothetical evolution of maturation strain (in microstrain) during growth as a function of relative radius (% of final radius) on each side of the tree. The parameters were adjusted to minimize the difference between simulated and experimental residual strain profiles.

Adjusted scenarios of tree reaction

The adjusted evolution of maturation strains on each side of the tree is shown in figs. 4-5 (left-hand diagrams). The adjustment yielded realistic values of maturation strains, ranging from 0 to –2000 microstrains. Maturation strains are most of the time not symmetric between the upper and the lower side, showing that the trees were actively reacting against gravity. For the poplar trees, large values of tension (> 1000 μ strains in magnitude) were often found on one side, suggesting the unilateral production of tension wood. For sugi trees, most values of maturation strains are tensile and < 1000 μ strains in magnitude, suggesting that the reaction occurred by variations of maturation strain in normal wood, rather than by the production of compression wood, which is expected in the case of almost straight tree with a moderate reaction. For all trees (except S2) it was necessary to assume important changes in maturation strain along the radius on both sides, suggesting that the reaction was not constant during the growth of the tree, and sometimes reversed from a side to another. This suggests that the biomechanical history of the tree was complex, involving several phases of bending and up-righting.

Assessment of the experimental method for evaluating in-situ growth stress profiles

The experimental method we used to evaluate the profile of growth stress in the tree consists in measuring profiles of residual strain in diametrical boards. Comparison between the simulated profiles in the log (grey lines in figs. 4-5) and in the board (black lines in figs. 4-5) shows that the strain is generally lower in the log than in the board, *i.e.* that the board extended slightly during its extraction from the log. The difference is generally small, so that this method seems reliable to obtain an approximate evaluation of growth stress profiles.

Conclusion

Experimental profiles of growth strain have been compared to profiles computed with a biomechanical model accounting for non-asymmetric diameter growth and wood maturation. The scenarios of tree growth obtained to fit the experimental data seem to be quite realistic, providing a first validation of the mechanical model. The model also confirms that the method consisting in measuring the residual longitudinal strains on a diametrical board gives a good approximation of the residual longitudinal strains in the standing tree, as long as the strain profile is not highly unbalanced.

Acknowledgements

The authors want to thank the France-Japan (CNRS/JSPS) cooperative research for bio-diversity and biomechanics of tropical forest tree and the “Woodiversity” project supported by the French National Research Agency (ANR-05-BDIV-012-04), that financed part of the work.

References

1. Alméras T, M Fournier (2009) *Biomechanical design and long-term stability of trees: morphological and wood traits involved in the balance between weight increase and the gravitropic reaction*. Journal of Theoretical Biology 256: 370-381.
2. Archer RR (1986) *Growth stresses and strains in trees*. Berlin/Heidelberg/New York: Springer Verlag. 240 p.
3. Dlouhà J, T Alméras, B Clair, J Gril, P Horàvek. *Impact of viscoelasticity and juvenile wood occurrence on the tree reorientation process*. In: Salmen L, editor; 2006 28.8-1.9.06; Stockholm, Suède. STFI-Packforsk AB. pp. 503-508.
4. Fournier M, B Chanson, B Thibaut, D Guitard (1991) *Mécanique de l'arbre sur pied : modélisation d'une structure en croissance soumise à des changements permanents et évolutifs. 2. Analyse tridimensionnelle des contraintes de maturation, cas du feuillu standard*. Annales des sciences forestières 48: 527-546.
5. Kubler H (1987) *Growth stresses in trees and related wood properties*. Forest products abstracts 10: 62-119.

Comparing shapes for stress homogenization in nature and technique

Iwiza Tesari and Claus Mattheck

Forschungszentrum Karlsruhe GmbH

Abstract

Merciless selection pressure of evolution forces biological carrier structures, e.g. trees or bones, to use their material efficiently. For lifetime, they try to achieve as homogeneous a stress distribution as possible and, thus, prevent weak points as well as excessive material consumption. Design principles of natural constructions were studied at the Forschungszentrum Karlsruhe. From them, based on the Finite Element Method, computer methods were derived for the optimization of technical components. By computer-simulation of adaptive growth the methods remove excessive stresses by simulated local material deposition and, thus, homogenize the stresses on the component surface. In the computer, components grow like trees. Due to the stress reduction the service life of the optimized component is increased compared to the initial value.

A breakthrough towards simplicity was the development of the simple, purely graphical “Method of Tensile Triangles” (MTT) by Mattheck for the reduction of stress concentrations by notch shape optimization. The Method was inspired by the shape of buttress roots in trees. Like them it bridges a corner-like notch with tensile loaded triangles. The notch shape found with the MTT may be scaled up and down according to the individual design space limitations of the technical structure.

In this paper the Method of Tensile Triangles will be explained and the results of Finite Element Analyses on tension loaded stepped plates with circular and by MTT formed notches will be presented. The study shows the effect of this notch shapes on stress concentration factor due to variation of diameter ratio and design space. It also quantifies the amount of design space and mechanical stress which could be lowered by the use of biologic based MTT fillets compared to the “technical” circular rounding.

Introduction

Good mechanical constructions are reliable during their estimated lifetime, light-weighted and have a high load-capability. A main reason for failure are local stress concentrations which occur where the force flow is disturbed, e.g. at notches even if they are rounded and not sharp. The stress concentrations at notches on the surface of a component cause material fatigue during its lifetime. Therefore, a prevention of such stress-raising effects is of great importance in nature as well as in engineering design. Trees make an effort to grow into a homogeneous state of stress on their surface [1]. The outermost annual ring tries to adapt to external loading by locally increased or reduced growth according to high or low stresses [2]. Computer Aided Optimization CAO [3] transfers the principle of adaptive biological growth into technical application and simulates this effect by a Finite Element (FE) calculation. The component starts to grow in the highly loaded zones and, in analogy to trees, forms the locally thickest growth increment. By this, the stress peaks will be reduced. The procedure is done iteratively until a constant stress state on the surface is achieved.

Even if the grown wood has a fibrous structure and therefore mainly orthotropic material properties and on the other hand most technical materials are almost isotropic, there is little difference in optimal shapes. Because the wood fibre direction is largely in agreement with the force flow in the tree, the

smaller transverse effects are somewhat falsified due to using only the Youngs-modulus in grain direction [1].

Further studies show, that an optimized shape can also be found much easier than by use of laborious FE-calculations. Now, about 15 years after the CAO-method the ‘Method of Tensile Triangles’ has been developed. It is a new and easy graphic optimization method. The Tensile Triangles contour was found in many natural structures [4] and applied with good results in terms of stress reduction to different technical problems [5, 6]. The approach can be applied even by layperson without a deeper mechanical understanding and without computer verification by the user. Not least therefore the characterisation of MTT and comparison with the technological standard, like it is done in this paper, is essential.

Material and methods

Like buttress roots in trees the Method of Tensile Triangles bridges corner-like notches with a tensile loaded triangle (Fig. 1). The tree stem forms a sharp cornered notch with the ground surface. It bridges and defuses this corner by the root spur (buttress), which is usually most pronounced on the windward side. The sawn section through the root shows very large growth increments on the upper side. This one-sided root growth forms the tensile triangle.

Technical components usually aren’t able to grow, so stress concentrations have to be minimised early in the design process, which can easily be done by the Method of Tensile Triangles. Starting from the 45° angle at the bottom we stick a triangle into the sharp corner (Fig. 2). This procedure creates two notches of larger angles which are less dangerous because the more obtuse the angle of a corner-like notch is the lower is the stress concentration there. After repeating the procedure one or two times and smoothing the remaining kinks with radii one has a close-to-optimum notch contour or at least a highly improved notch shape with significant stress reduction.

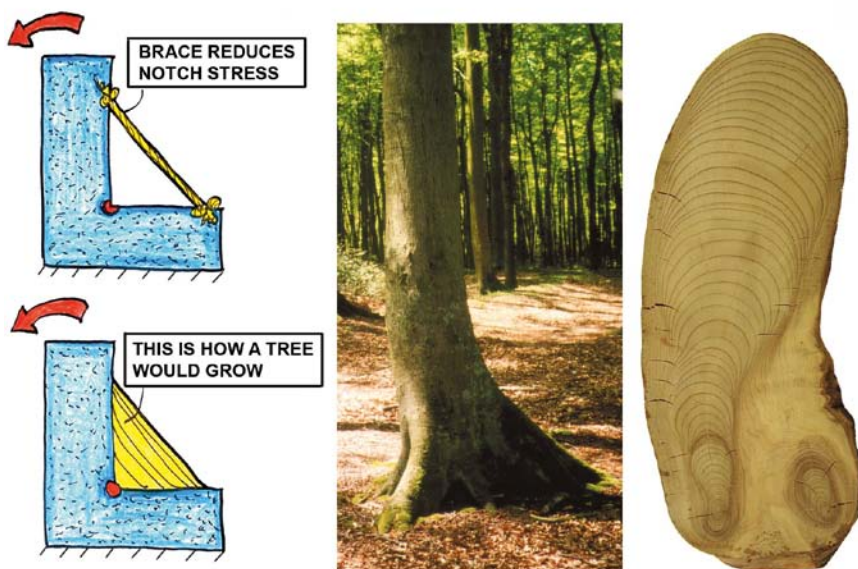


Fig. 1 Biological inspiration for the Method of Tensile Triangles: The buttress root bridges the kink at the base of a tree, like a rope [7]

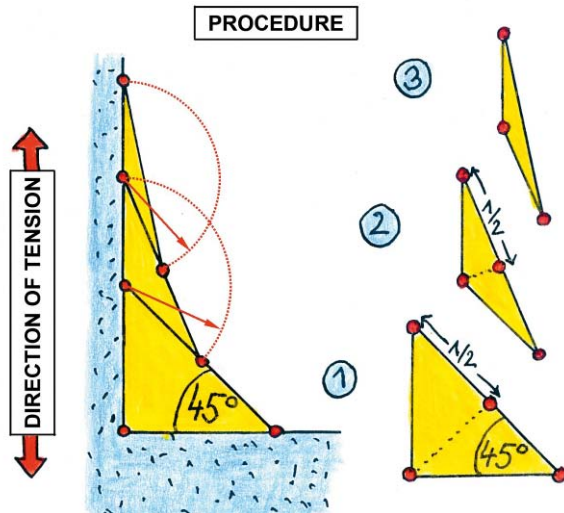


Fig. 2 Procedure of the Method of Tensile Triangles for a corner transition [7]. First the corner is bridged with some triangles. Finally, the remaining kinks have to be rounded by circles

In this study the stress distribution in stepped tension plates with varying dimensions and fillet shapes have been analysed by use of the Finite Element Method, which is a numerical analysis technique. It is mainly used to obtain solutions for differential equations that describe physical problems. In structural mechanics it is used for simulation of the behaviour of technical components. First a model of the construct has to be generated. Then the complex shape will be sub-divided into series of small regions (elements) which are connected by nodes, the so-called mesh. After defining bearing, loading, material and physical data e.g. deformation, strain and stress can be estimated.

With the FEM software ANSYS [8] models of the plates with radii and MTT fillets have been generated (2D, Plane82-Elements) and analysed (Fig. 3). The material behaviour was set isotropic and linear-elastic. Due to axial symmetry only the half of the structure has to be modelled. For evaluation the v. Mises stress was used which is an equivalent stress as shown in equation (1).

$$\sigma_{v.Mises} = \sqrt{\frac{1}{2}[(\sigma_I - \sigma_{II})^2 + (\sigma_{II} - \sigma_{III})^2 + (\sigma_{III} - \sigma_I)^2]} \quad (1)$$

Theoretically there is a stress singularity at the sharp kink, where the MTT fillet connects into the broad part of the plate. The calculated result there is mesh-dependent, which means that finer meshes with smaller elements cause higher values. In praxis this is meaningless and therefore remained out of consideration.

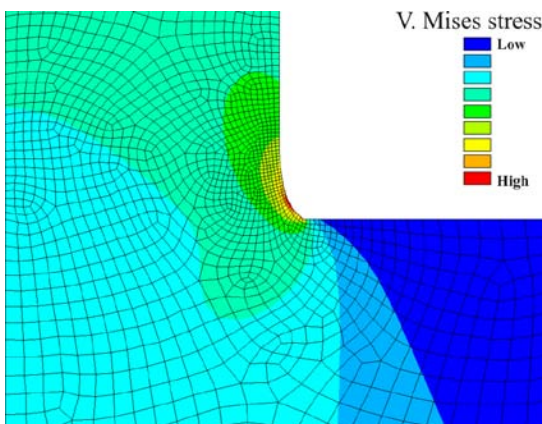


Fig. 3 Finite Element mesh and v. Mises stress distribution

The width-ratio D/d of the plates was varied between 1.04 and 3, the ratio of the fillet radius R/d ranged between 0.02 and 1. The plates have been clamped at the broad end and loaded by tension at the small end (Fig. 4).

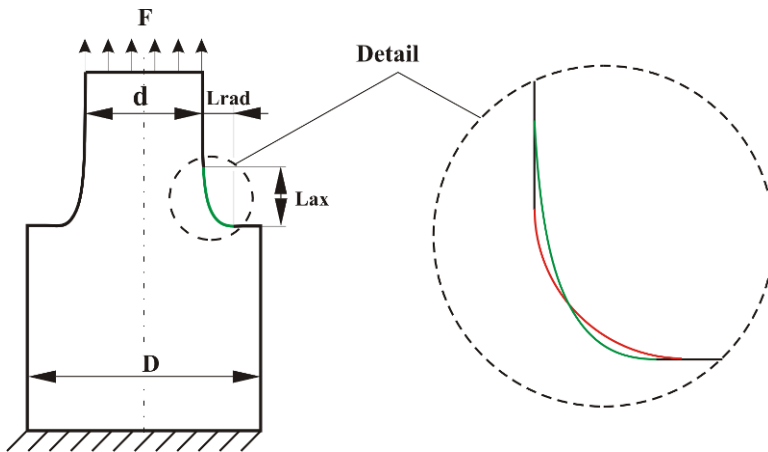


Fig. 4 Model of the stepped tension plates. The fillet shapes formed by radius (red) and MTT (green) are shown in Detail

Results and discussion

Figure 5 shows the V. Mises stress distribution in three tension plates with a width ratio of $D/d=2$. The red colour marks, where the highest stresses occur. This localisation of high stresses is known as stress concentration and measured by the stress concentration factor. It is defined as the ratio of the highest stress to a nominal or reference stress [9] and depends on the local curvature radius and the deflection angle. In general the concentration factor raises with lower curvature radii and higher deflection angle [10]. At the radius with $R/d=0.1$ it amounts to 2.49 (see Fig. 5 A). The stress concentration factor is reduced by the MTT shaped fillet with the same lateral size $Lrad/d=0.1$ (B) to the value of 1.76. Reducing the extent of the MTT fillet increases the stress concentration factor. A laterally much smaller MTT fillet (C) with $Lrad/d=0.0435$ reaches the same value as the radius with $R/d=0.1$.

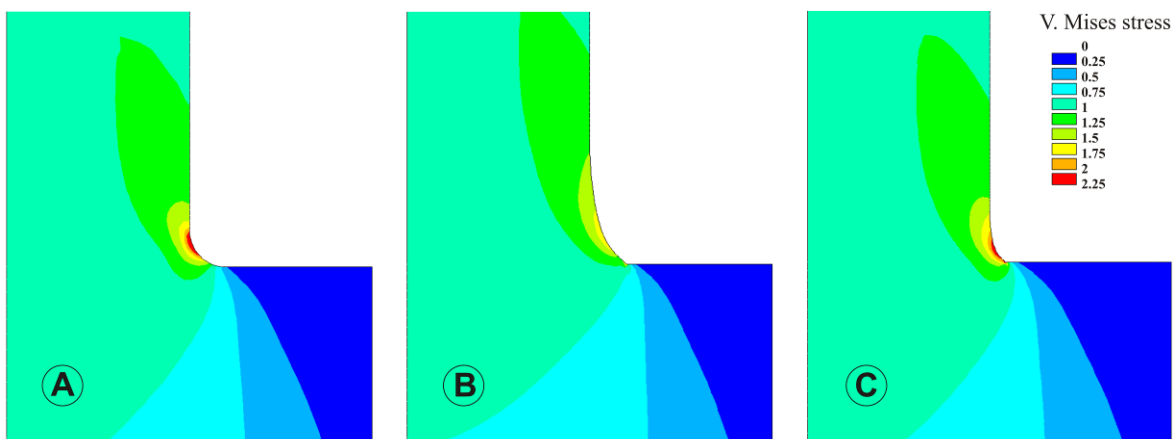


Fig. 5 V. Mises stress distribution in tension plates ($D/d=2$) with various fillet shapes and dimensions. (A) radius, $R/d=0.1$; (B) MTT, $Lrad/d=0.1$; (C) MTT, $Lrad/d=0.0435$

Table 1 list the size of radius and MTT shaped fillets with equal stress concentration factors, which decline with higher fillet sizes and rise with higher plate width ratios.

In Figure 6 is shown exemplarily for the plates with a width ratio of 3, how the stress concentration factor is lowered by larger fillets. Thereby at equal stress levels the MTT fillets always require less lateral design space than the radii. At small fillet sizes (compared to plate width) the longitudinal dimensions of the MTT fillet are higher than that of the radius. But with enlarging fillets the longitudinal dimensions of the MTT also become smaller than that of the radii.

Table 1 Dimensions of radius and MTT shaped fillets with equal stress concentration factors in stepped tension plates with various width ratios.

Dimensions				Stress concentration factor
Radius	MTT			
R/d	Lax/d	Lrad/d	D/d	
0.02	0.0351	0.0106	3	5.04
0.02	0.034	0.01025	2	4.61
0.02	0.0315	0.0095	1.4	3.84
0.02	0.0288	0.0087	1.2	3.23
0.02	0.0252	0.0076	1.1	2.67
0.02	0.0194	0.00584	1.04	2.01
0.05	0.0839	0.0253	3	3.45
0.05	0.0789	0.00238	2	3.21
0.05	0.0693	0.0209	1.4	2.77
0.05	0.0597	0.018	1.2	2.38
0.05	0.0477	0.0144	1.1	2.05
0.1	0.1565	0.0472	3	2.63
0.1	0.1442	0.0435	2	2.49
0.1	0.121	0.0365	1.4	2.2
0.1	0.0971	0.0293	1.2	1.95
0.2	0.2851	0.086	3	2.04
0.2	0.2569	0.0775	2	1.96
0.2	0.1939	0.0585	1.4	1.8
0.5	0.5802	0.0175	3	1.52
0.5	0.4807	0.0145	2	1.51
1	0.862	0.026	3	1.28

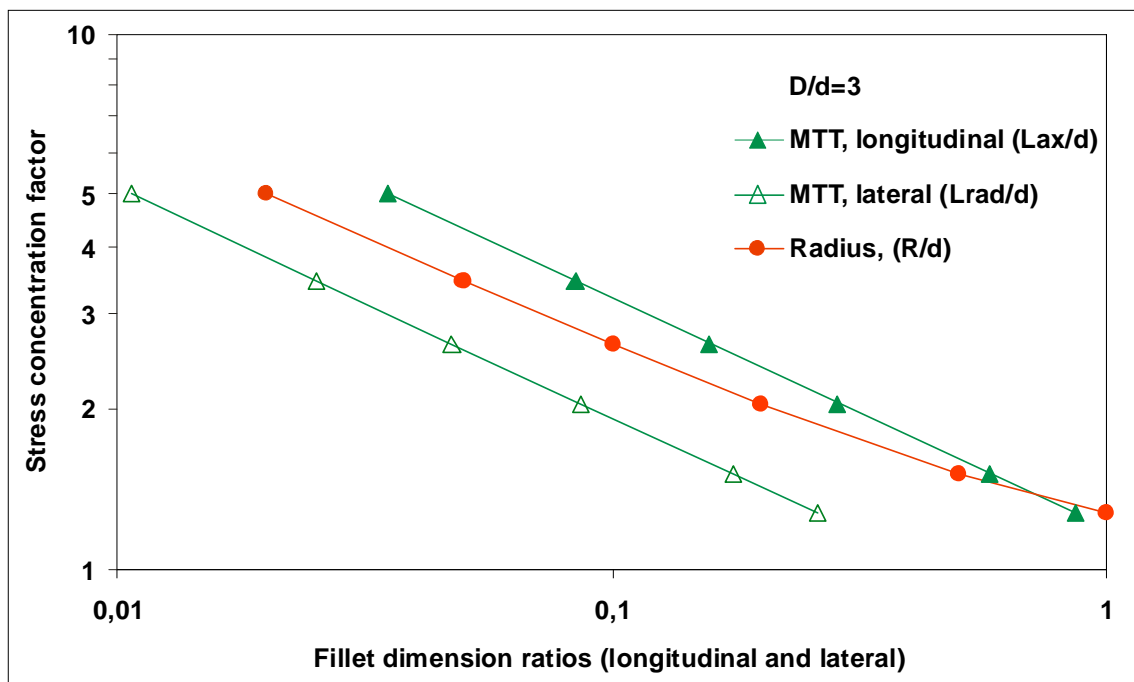


Fig. 6 Stress concentration factor subject to the size of radius and MTT fillets in stepped tension plates (logarithmic scale)

Conclusion

With the new graphical Method of Tensile Triangles, following the design rules of nature, reduction of stress concentrations and stress homogenisation on the surface of technical components can be realised easily. The results of the parameter study, presented in this paper, can be used for characterising the Method and estimating stress levels in similar technical components. Compared with a radius fillet with equal lateral extension a MTT shaped notch reduces the maximum stress. At equal stress concentration factors the MTT always has less lateral extension than the radius. If the fillet dimensions relating to the plate width become large, the MTT fillet also requires less longitudinal design space than the comparable radius.

References

1. Mattheck, C. (1998): *Design in Nature*. Springer Verlag Berlin.
2. Mattheck, C. (1990): *Why they grow, how they grow - the mechanics of trees*. Arboricultural J., Vol. 14, p 1-17.
3. Mattheck, C. and S. Burkhardt, (1990): *A new method of structural shape optimization based on biological growth*. International Journal of Fatigue, Vol. 12, p. 185-190.
4. Mattheck, C. (2009): *Universalformen der Natur*. labor&more, 1/2009, p. 18-20.
5. Sauer, A. (2008): *Untersuchungen zur Vereinfachung biomechanisch inspirierter Strukturoptimierung*. Verlag Forschungszentrum Karlsruhe GmbH.
6. Soerensen, J. (2008): *Untersuchungen zur Vereinfachung der Kerbformoptimierung*. Verlag Forschungszentrum Karlsruhe GmbH.
7. Mattheck, C., (2007): *Secret design rules of nature - Optimum shapes without computers*. Verlag Forschungszentrum Karlsruhe GmbH, (www.mattheck.de).
8. ANSYS, Inc., (2007): *ANSYS 11.0 Documentation*.
9. Petersen, R.E. (1973): *Stress concentration factors*. John Wiley & Sons.
10. Mattheck, C. (2004): *The face of failure – in nature and engineering*. Verlag Forschungszentrum Karlsruhe GmbH.

Modelisation of the trunk daily diameter variation during wet season in a neotropical rain forest of French Guiana

Y. Aimene¹, C. Stahl^{2,3}, D. Bonal² and B. Thibaut³

¹IUFM - Ecofog, Guyane; ²INRA - Ecofog, Guyane; ³CNRS - Ecofog, Guyane

Abstract

Tree trunk diameter usually changes during the day and the night and along full year with both a rainy and a dry season. Aside of cambial growth, tree trunk diameter changes is the combination of successive layers contribution: purely passive mechanical strains of the heartwood, change in hydrostatic pressure in the sapwood and in the living phloem, changes in the maturation stress during the year and swelling or shrinkage of dead outer bark due to change in relative humidity of surrounding air.

Trees were equipped with home-made dendrometers and their diameters were measured daily and monthly almost 2 years with both a rainy and a long dry season. Change in tree trunk diameter is due to different phenomena those operated in different successive layers. On some species, no daily variation in the trunk diameter is observed even if large daily water fluctuations are observed.

Mechanical model based on coaxial cylindrical layers is developed and implemented in Matlab in order to highlights these variations. The model shows apparent strains variations synchronic with daily water variation. The effects of heartwood thickness on the tree trunk daily apparent strains variation make in evidence small apparent strains for high values of relative heartwood thickness that can explain the no daily variation in some species.

Introduction

Trunk variation can be pronounced in neotropical rainforest and the stem shrinkage, principally during the dry season [1], [2], [3], and [4]. Aside of cambial growth, tree trunk diameter changes is the combination of successive layers contribution. The function of the successive parts of the trunk section is rather different. Firstly, the bark (outer and/or inner) appears to be the main deformable “**elastic**” tissue in trunk [5] and potentially explain the great variations between dry and rainy seasons [2]. Roth in 1981 [6] observed a dilatation growth, which was very specific of the species. This phenomenon could occupy up to 70% of the entire bark width, and this was in axial and tangential direction. Secondly, the sapwood have primordial role for involved water to photosynthetic apparatus. The water content of this tissue is quite constant during the year. Sapflow is variable among species and fluctuate among the seasons [7]. Daily trunk fluctuation were caused by development of the tensions in the water columns of transpiring trees [8], by only the fluctuation of the bark [9] or by potential hydraulic connection between bark and sapwood [5] and [10]. The bark content more water than sapwood and the seasonal fluctuation is potentially more pronounced [3]. The daily and seasonal fluctuations of the bark could also be explicated by the air humidity [9]. The bark is the thinnest and the wettest tissue. Its external position contributes to its climatic dependent variation [11]. The bark sensitivity of the climatic variations was already exposed and could explain also the trunk variation [9; 11; 13]. Compared with the sapwood, the heartwood appears to be relatively limited in terms of effective water storage. Heartwood formation results from numerous physiological and biological changes, including the death of any living cells and, with some exceptions, a decline in water content. Moreover, seasonal

variation in water content is generally much less pronounced in the heartwood than in the sapwood [11].

Information on the relative contributions of different stem tissues to daily and seasonal changes in diameter is scarce in tropical rainforest. Experiments were performed in-situ to measure these variations at Paracou in French Guiana. Trees were equipped with home-made dendrometers and their diameters were measured daily and monthly almost 2 years with both a rainy and along dry season. A diminution in tree trunk diameter was observed in dry season in spite of the radial growth due to the cambium activity and a large augmentation was observed in the onset of rainy season. In addition, daily variation in the trunk diameter was observed on some species, but not on some other species even if large daily water fluctuations are observed, in dry and wet season [7]. This is the case of the *Vantanea* sp for which circumference variation was very stable and not synchronic with the water status (Figure 2b, red curve).

A mechanical model is performed to explain the experimental observations. The transverse section of the tree trunk is modelled as multi-layered coaxial cylinders. The layers are the tissues including heartwood, sapwood, inner bark (living phloem) and outer bark (non conductive phloem and cork). We focus on daily variations in wet season such as the only daily variation is the sapwood hydrostatic pressure dues to the circulation of the xylem. The exterior air relative humidity is always high so the bark moisture content stands over the fibre saturation point and daily bark shrinkage is null or negligible.

Mechanical formulation: coaxial-cylindrical model:

Problem position

A transverse section of tree trunk is composed of different layers (Fig. 1a). In addition to dimensional variation of tree trunk due to growth by the cambium, under water tension in the sapwood and the inner bark, and the variation of the humidity of external atmosphere, tree trunk observe variation of its diameter. So, first tree trunk can be idealized as a cylindrical structure (Fig.1b) having a different material proprieties in each layer.

In mechanical point of view, the problem consists in computing the state of equilibrium of cylindrical structure composed of different layers of orthotropic material, and subjected to an internal stress and an external constraints at its borders.

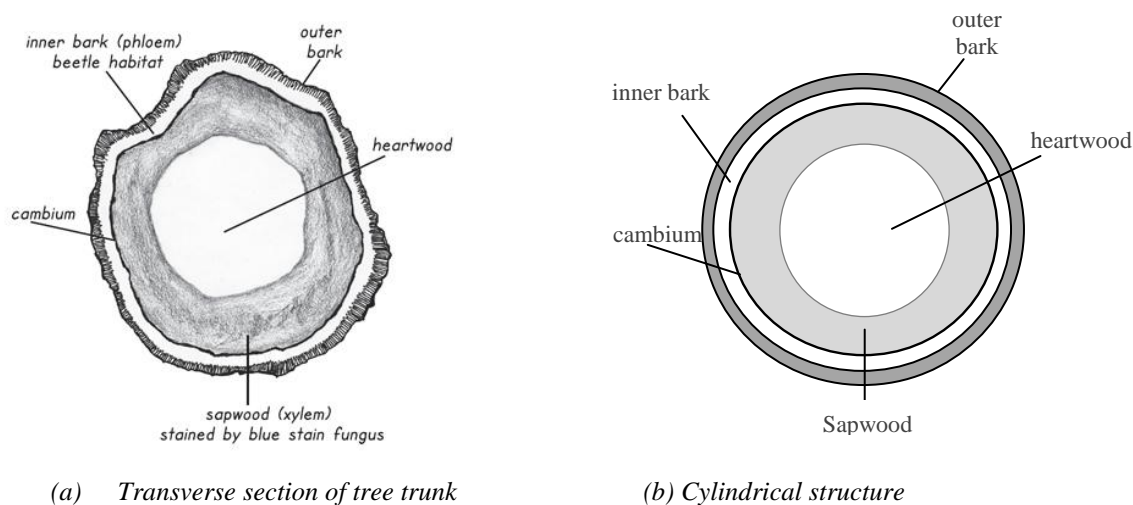


Fig. 1 (a) Tree trunk section (b) cylindrical model

Formulation of the mechanical problem

For a mechanical analysis of a dimensional variation of a tree trunk, the complete model must include all the equations of the mechanics, especially equilibrium, constitutive equations, and boundary conditions. Under the internal and external actions considered in this paper (hydrostatic pressure principally) and an hypothetic regular cylindrical structure, the displacement, strain and stress fields generated are only radial dependent, in addition, no shear stresses and no shear strains occurs in the tree trunk. All these considerations simplify the mechanical equations.

In the following, we first briefly remind the essential of the mechanical equations of an homogenous cylindrical layer and then, present solutions for a multi-layer structure. So, let's consider an adequate cylindrical system (R, T, L), where R, T and L are radial, tangential and longitudinal directions respectively. At a given radial position r, the induced displacement vector and associated strains and stresses are respectively represented by the following vectors.

$$\underline{u} = u_R, u_T, u_L, \quad \underline{\varepsilon} = \varepsilon_R, \varepsilon_T, \varepsilon_L \quad \text{and} \quad \underline{\sigma} = \sigma_R, \sigma_T, \sigma_L$$

Where strains components are given by:

$$\varepsilon_R = \frac{du_R}{dr} \quad \text{and} \quad \varepsilon_T = \frac{u_R}{r} \quad (1)$$

u_R and ε_R are radial displacement and strain and ε_T are tangential displacement and strain.

Wood is commonly modelled as an orthotropic linear elastic material [14]. In our case, the constitutive law is restricted to this relation:

$$\underline{\sigma} = \underline{\underline{C}} \cdot \underline{\varepsilon} + \underline{\beta} \quad \text{where} \quad \underline{\underline{C}} = \begin{bmatrix} C_{RR} & C_{RT} & C_{RL} \\ C_{TR} & C_{TT} & C_{TL} \\ C_{LR} & C_{LT} & C_{LL} \end{bmatrix} \quad (2)$$

$\underline{\underline{C}}$ is the behaviour tensor and $\underline{\beta}$ is the initially induced stresses vector, that is relate in our case to hydrostatic pressure in the sapwood and inner bark. It is given by: $\underline{\beta} = \beta_R, \beta_T, \beta_L$.

Equilibrium equations are restricted to the following equation:

$$\frac{d\sigma_R}{dr} + \frac{\sigma_R - \sigma_T}{r} = 0 \quad (3)$$

Equilibrium equation can be expressed in displacement term by combining behaviour law, equation (2), strains expressions given by equation (1) with equilibrium equation (3). It is given by:

$$r \frac{d^2 u_R}{dr^2} + \frac{du_R}{dr} - \gamma^2 \frac{u_R}{r} = \kappa \quad (4)$$

Where $\gamma^2 = \frac{C_{RR}}{C_{TT}}$ and $\kappa = \frac{\beta_T - \beta_R}{C_{RR}} + \frac{C_{TL} - C_{RL}}{C_{RR}} \varepsilon_L$

The general solution of equation (4) is [2]:

$$u_R \cdot r = Ar^\gamma + Br^{-\gamma} + r \frac{\kappa}{1 - \gamma^2} \quad (5)$$

A and B are integration constants. Their values are determined using the boundary conditions of the problem. The strain field can then directly derive from equation (1) and the associated stress field from the constitutive law given by equation (2).

Multi-layered model

The formulation is extended to a cylindrical layered structure composed in our case of 4 layers numbered 1 to 4 from the inside of the cylinder. When writing equation (5) for each layer, and when considering interface and boundary conditions, we obtained 9 equations with 9 unknown parameters (8 unknown integration constants and longitudinal strain ϵ_L). These equations form a linear system. A Matlab program based on this cylindrical formulation was realized to resolve the linear system and to compute all displacement, strain and stress fields through tree trunk transverse section. This model was initially formulated by Alméras and Gril [15; 16]

Results and discussion

Daily water status and apparent strains measured in-situ are illustrated in figures (2a and b curve red) for the *Vantanea* sp in wet season (see table 1). Large daily fluctuations are observed but the measured circumference was very stable and not synchronic with the water status. Figure (2b, blue curve) shows apparent strains daily variation given by the model in wet season. In opposition to the experimental observations, the apparent strains daily variations given by the model are synchronic with the water flow. This result is expectable as the model just takes in account different layers rigidity.

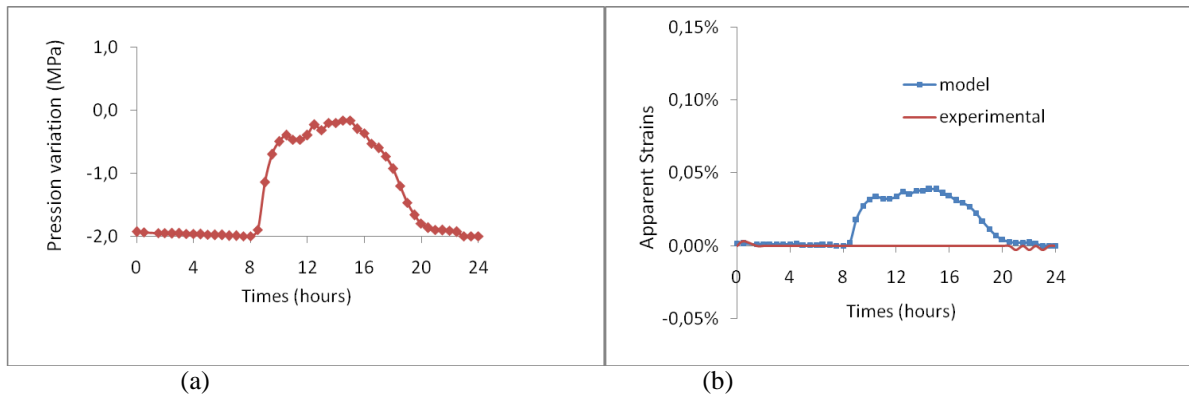


Fig. 2: (a) Daily variation of water status, (b) apparent strains for *Vantanea* sp. In wet season.

The effect of heartwood thickness on the apparent strains variation given by the model (Figure 3) shows a rapid diminution of the apparent strains with the heartwood thickness for relative thickness values above 20%. Most of the considered species relative had a heartwood thickness above 80% (see table 1). So, as compare to small trees with few heartwood as often described in the literature, the daily apparent stains variation given by the model is nearly 10 times less due to the effect of heartwood compensation of the sapwood swelling or shrinking. Then the measurements in strain values (diameter growth divided by tree diameter) should be 10 times more accurate than for small trees, which was not the case in this experiment.

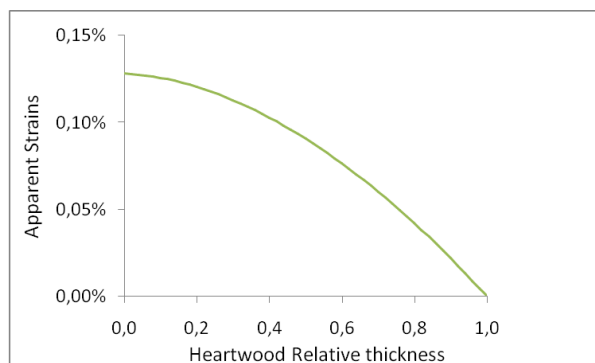


Fig. 3: Daily apparent strains variation with heartwood relative thickness.

Table 1 Relative thickness of different layers of species from Paracou – French Guiana

Species	Family	radius	Thickness (mm)			Relative thickness (%)		
			Bark	Sapwood	Heartwood	Bark	Sapwood	Heartwood
<i>Dicorynia guianensis</i>	Caesalpiniaceae	202.65	3.5	19.635	179.8	1.72	9.67	88.59
<i>Dicorynia guianensis</i>	Caesalpiniaceae	163.05	3	32.95	127.1	1.84	20.21	77.95
<i>Dicorynia guianensis</i>	Caesalpiniaceae	172.65	2.5	32.62	137.5	1.45	18.89	79.64
<i>Goupia olabra</i>	Celastraceae	394.25	6.75	61.15	326.35	1.71	15.51	82.78
<i>Licania heteromorpha</i>	Chrysobalanaceae	112.45	2	7.295	103.2	1.78	6.49	91.77
<i>Recordoxylon speciosum</i>	Caesalpiniaceae	223.85	3.5	7.085	213.25	1.56	3.17	95.26
<i>Slonea sp.</i>	Eaeocarpaceae	234.85	5.5	21.885	207.45	2.34	9.32	88.33
<i>Vantanea sp.</i>	Humiriaceae	201.05	5	39.27	156.8	2.49	19.53	77.99
<i>Oxandra asbecki</i>	Annonaceae	82.6	1	7.515	74.1	1.21	9.10	89.71
<i>Vouacapoua americana</i>	Caesalpiniaceae	139.8	1.25	6.165	132.4	0.89	4.41	94.71

Conclusion

Change in tree trunk diameter is due to different phenomena those operated in different successive layers. In addition, on some species, no daily variation in the trunk diameter is observed even if large daily water fluctuations are observed.

Mechanical model based on the analytical cylindrical model initially by Alméras and Gril is implemented in Matlab routine, and used to explain the experimental observations by the tree trunk transverse structure and the phenomena those operate at different layers. Contrarily to the experimental observation, the model shows fluctuations of the apparent strains synchronic with the water pressure in the sapwood. But the model also shows that apparent strains strongly decrease for high heartwood relative thickness. So the no daily apparent stains variation observed in some species can be explained by both the effect of heartwood compensation and the lack of precision of dendrometers.

It will be interesting to verify this model on trees with different heartwood thickness ratios, in the wet season. Then the model could be used to explain the role of external bark shrinkage durin dry season on the surprising diameter decrease of some species in that period.

References

1. Daubenmire, R., (1973): *Phenology and other characteristics of tropical semi-deciduous forest in north-western Costa Rica*. J. Ecol. 60, 147–171.
2. Prévost, M.F and H. Puig, (1981): *Accroissement diamétral des arbres en Guyane : observations sur quelques arbres de forêt primaire et de forêt secondaire*. Bulletin du Muséum National d'Histoire Naturelle 3(2): 147-171.
3. Borchert, R. (1994): *Water status and development of tropical trees during seasonal drought*. *Trees-Structure and Function* 8: 115-125.
4. Baker, T. R., K. Affum-Baffoe, D. F. R. P. Burslem, and M. D. Swaine. (2002): *Phenological differences in tree water use and the timing of tropical forest inventories: conclusions from patterns of dry season diameter change*. *Forest Ecology and Management* 171: 261-274.
5. Zweifel, R. H. Item, and R. Häslér, (2000): *Stem radius changes and their relation to stored water in stems of young Norway spruce trees*. *Trees - Structure and Function* 15(1): 50-57.
6. Roth I. (1981): *Structural patterns of tropical barks*. Berlin: Gebruder Borntraeger.
7. Bonal, D., T. S. Barigah, A. Granier, and J-M. Guehl. (2000): *Late-stage canopy tree species with extremely low delta C-13 and high stomatal sensitivity to seasonal soil drought in the tropical rainforest of French Guiana*. *Plant Cell and Environment* 23(5): 445-459.
8. Irvine, J and J. Grace, (1997): *Continuous measurements of water tensions in the xylem of trees based on the elastic properties of wood*. *Planta* 202: 455-461.

9. Gall, R. W., Landolt, P., Schleppei, V., Michellod, and J. B. Bucher. (2002): *Water content and bark thickness of Norway spruce (Picea abies) stems: phloem water capacitance and xylem sap flow*. 22: 613-623.
10. Scholz, F. G., J. Bucci, G. Goldstein, F. C. Meinzer, A. C. Franco, and F. Miralles-Wilhelm, (2008): *Temporal dynamics of stem expansion and contraction in savanna trees: withdrawal and recharge of stored water*. Tree Physiology 28: 469-480.
11. Holbrook, N. M. (1995): *Plant stems: physiology and functional morphology* San Diego: Academic Press.
12. Granier A., (1985) : *Une nouvelle méthode pour la mesure du flux de sève brute dans le tronc des arbres*. Annals of Forest Science. 42(2): 193-200.
13. Zweifel, R., Item, H. & Häslér, R. 2000. *Stem radius changes and their relation to stored water in stems of young Norway spruce trees*. Trees - Structure and Function 15(1):50-57.
14. Guitard, D., (1987) : *Mécanique du matériau bois et composites*. Cepadues Edition, Toulouse, France, 238p.
15. Alméras, T. and J. Gril, (2007): *Mechanical analysis of the strains generated by water tension in plant stems. Part I: stress transmission from water to the plant material at the cell level*, Tree Physiol. 27: 1505-1516.
16. Alméras, T. (2008): *Mechanical analysis of the strains generated by water tension in plant stems. Part II: Strain in wood and bark and apparent compliance*, Tree Physiol. 28: 1513-1523.

Modelling surface growth for tree biomechanics

Thomas Guillon¹ and Thierry Fourcaud²

¹ University of Montpellier II, UMR AMAP, Montpellier, F-34000, France; ² CIRAD, UMR AMAP, Montpellier, F-34000, France.

Abstract

The analysis of the shape evolution of growing trees requires modelling accurately the interaction between tree growth and its biomechanical response. In this work, we study the mechanics of surface growth to model the generation of wood at the cambium. During the growth process, mass and material points are added along a growing surface and then deform the whole tree. The main difficulty of this purpose is to define an evolving reference configuration according to the growth velocity over the surface. Balance equations of mass, linear and angular momentum which include the effect of mass accretion are provided giving the basis for further studies on surface growth mechanics.

Introduction

The analysis of the shape evolution of growing trees requires modelling accurately the interaction between tree growth and its biomechanical response, including passive deformations due to external loads and active movements of the plant, e.g. tropisms. However, this coupling between tree growth and tree biomechanics exceeds the traditional framework of structural mechanics due to the changing in size of the studied domain and the resulting non-conservation of mass.

In this context, Fourcaud *et al.* [1] consider a solution with a discrete time model at the stem and tree scale by separating growth effects and mechanical effects. In a more general view of mechanics including growth effects, many works were devoted to model volumetric growth [2] which occurs when mass is added to existing points of the body. For example, Senan *et al.* [3] propose a rod-based model to model volumetric growth of plants.

Another way to model plant growth without the assumption that growth occurs only on existing material points is to consider surface growth which is linked with the accretion of material on external (or internal) surface of a body. Skalak *et al.* [4,5] consider analytical expression of surface growth for rigid body and a review of this issue is proposed by Garikipati [6]. However, it seems very difficult to take into account the effect of stress and strain while the body keeps growing. The main problem is to define a mechanical response of a deformation with respect to material points that appear during the growth [7].

The aim of this work is to model surface growth for deformable bodies. To this purpose, we first define the reference configuration with curvilinear coordinates which are evolving according to the growth velocity. Then, we give the balance equation of mass and with the virtual power method, the balance equations of the linear and angular momentum. This work gives the basis to develop equations of surface growth in structural mechanics and their implementations to study tree biomechanics.

Kinematics of a body with surface growth

Here, we describe the kinematic of surface growth based on the works of Skalak *et al.* and Segev & Epstein [8]. We consider a growing surface G_0 at time $t=0$ and the grown body $B = G_0 \times [0, T]$ with curvilinear coordinates denoted by $(\theta_1, \theta_2, \tau)$. The variables (θ_1, θ_2) are the coordinates of a point on

the surface G_0 and the variable τ is the time at which material points appears due to the displacement of the growing surface $G(t)$. We note \mathbf{v}_G the velocity of the growing surface (bold characters represent vector or tensor quantity) and we define the growth velocity as $\mathbf{v}_g = \mathbf{v}_G - \mathbf{v}_M$ with \mathbf{v}_M the velocity of a material point in the neighbourhood of the surface $G(t)$.

We now consider the reference configuration B_t at time t with cartesian coordinates (X_1, X_2, X_3) and S , the spatial configuration (deformed configuration) with cartesian coordinates (x_1, x_2, x_3) . The evolution of the reference configuration is driven by the growth velocity whose direction may depend on the deformations of the body (see Fig. 1). Then, for any fixed (θ_1, θ_2) and $0 \leq \tau \leq t$, we define :

$$\mathbf{X} = \Theta_t(\theta_1, \theta_2, \tau) = \int_0^\tau \mathbf{v}_g(\theta_1, \theta_2, \tau') d\tau'$$

By denoting $\mathbf{x} = \phi_t(\mathbf{X})$ the deformation map, we have a complete description of the mechanics and the growth of the body B . The spatial configuration of the growing body at time t is then given by $\phi_t(B) = \phi_t(B_t) = \phi_t \circ \Theta_t(B)$.

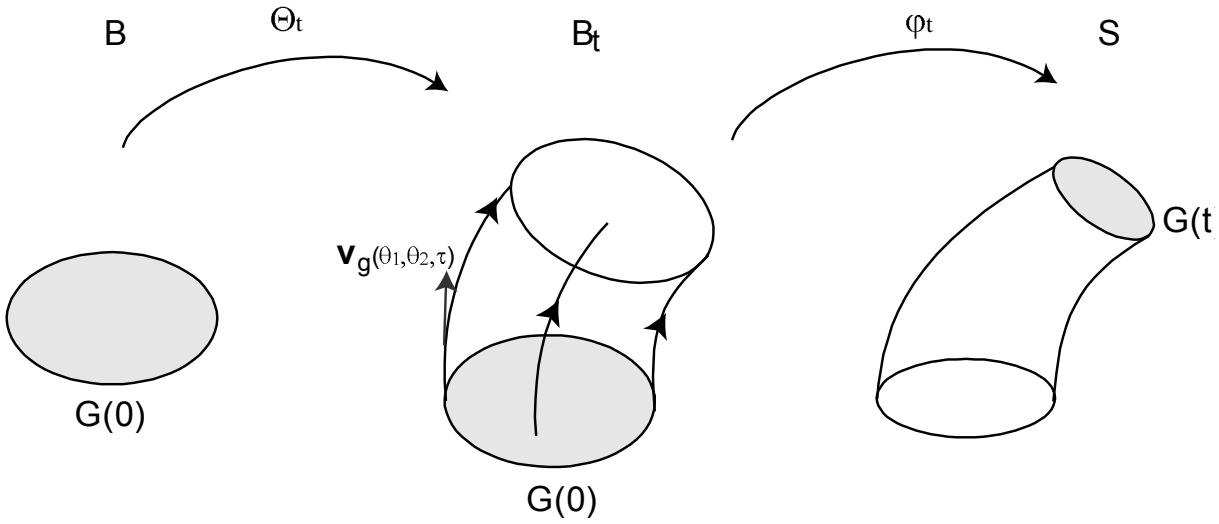


Fig. 1 Evolution of the reference configuration

Balance of mass

We consider the body in the spatial configuration, and we assume that at each point $\mathbf{x} \in G(t)$ we have a surface growth mass rate $\mu(\mathbf{x}, t)$. This rate is related to the growth velocity by $\mu = \rho_g \mathbf{v}_g \cdot \mathbf{n}$, with ρ_g the mass per unit volume of the newly created matter and \mathbf{n} the normal exterior to the surface $G(t)$. We denote the whole body in the spatial configuration by $\Omega(t)$ and its border by $\partial\Omega(t) = \Sigma(t) \cup G(t)$. The mass balance is thus:

$$\frac{d}{dt} \int_{\Omega(t)} \rho d\Omega = \int_{G(t)} \mu d\Sigma$$

The development of the left side of the equation leads to:

$$\begin{aligned} \frac{d}{dt} \int_{\Omega(t)} \rho d\Omega &= \int_{\Omega(t)} \frac{\partial \rho}{\partial t} d\Omega + \int_{\Sigma(t)} \rho \mathbf{v} \cdot \mathbf{n} d\Sigma + \int_{G(t)} \rho \mathbf{v}_G \cdot \mathbf{n} d\Sigma \\ &= \int_{\Omega(t)} \frac{\partial \rho}{\partial t} d\Omega + \int_{\partial\Omega(t)} \rho \mathbf{v} \cdot \mathbf{n} d\Sigma + \int_{G(t)} \rho (\mathbf{v}_G - \mathbf{v}) \cdot \mathbf{n} d\Sigma \end{aligned}$$

$$\frac{d}{dt} \int_{\Omega(t)} \rho d\Omega = \int_{\Omega(t)} \frac{d\rho}{dt} + \rho \operatorname{div}(\mathbf{v}) d\Omega + \int_{G(t)} \rho (\mathbf{v}_G - \mathbf{v}) \cdot \mathbf{n} d\Sigma$$

And hence, the local equation of balance of mass is:

$$\begin{aligned} \frac{d\rho}{dt} + \rho \operatorname{div}(\mathbf{v}) &= 0 \\ \rho (\mathbf{v}_G - \mathbf{v}) \cdot \mathbf{n} &= \mu \text{ on } G(t) \end{aligned}$$

This is the same equation as in classical mechanics with an additional boundary condition on the growing surface.

Balances of linear and angular momentum

We apply the virtual power principle [9,10] to obtain a weak formulation of the balance equations of linear and angular momentum. The body $\Omega(t)$ is subject to external forces and the description is detailed on Fig 2.

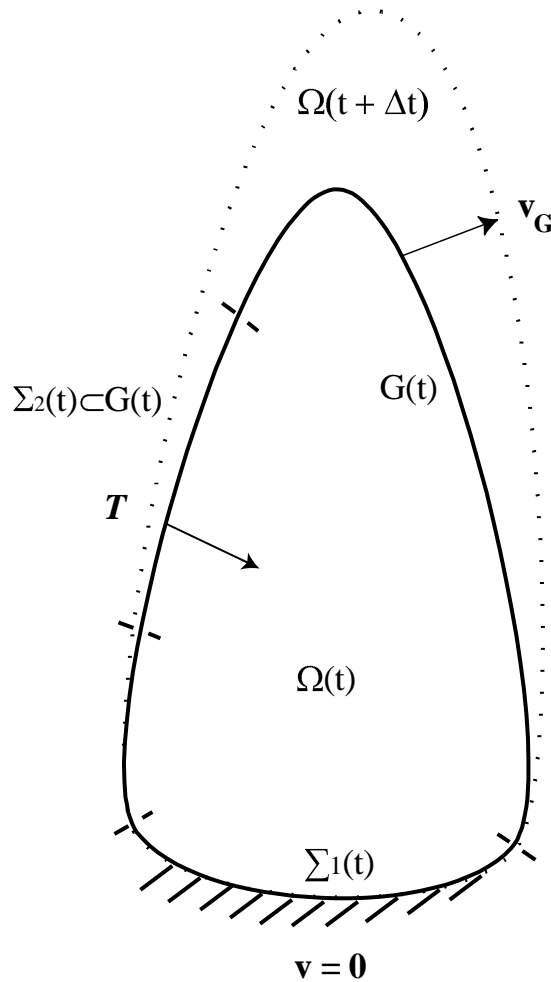


Fig. 2 The body $\Omega(t)$ with a prescribed displacement on the surface $\Sigma_1(t)$, a prescribed traction on the surface $\Sigma_2(t)$ and a growing surface $G(t)$.

Let \mathbf{V}^* be the space of virtual velocity field on $\Omega(t)$ with the prescribed value $\mathbf{v}^* = \mathbf{0}$ on $\Sigma_1(t)$. Then, the virtual power principle gives :

$$\mathbf{P}_a(\mathbf{v}^*) = \mathbf{P}_i(\mathbf{v}^*) + \mathbf{P}_e(\mathbf{v}^*)$$

With P_a the virtual power of acceleration, P_i the virtual power of internal forces and P_e the virtual power of external forces. The virtual power of the acceleration is given by the material derivative of the virtual power of momentum:

$$P_a(\mathbf{v}^*) = \frac{d}{dt} P_K(\mathbf{v}^*) = \frac{d}{dt} \int_{\Omega(t)} \rho \mathbf{v} \cdot \mathbf{v}^* d\Omega$$

By developing the last term and using the balance of mass, we obtain:

$$P_a(\mathbf{v}^*) = \int_{\Omega(t)} \rho \boldsymbol{\gamma} \cdot \mathbf{v}^* d\Omega + \int_{G(t)} \mu \mathbf{v} \cdot \mathbf{v}^* d\Sigma$$

Thus, there is an additional inertial term with the supply of mass due to the growth process. The others virtual power terms remain the same as in first grade theory of continuum mechanics:

$$P_i(\mathbf{v}^*) = - \int_{\Omega(t)} \boldsymbol{\sigma} : \mathbf{D}^* d\Omega$$

with $\boldsymbol{\sigma}$, the Cauchy stress tensor (symmetric second order tensor) and

$$\mathbf{D}^* = \frac{1}{2} (\nabla \mathbf{v}^* + {}^t \nabla \mathbf{v}^*)$$

The virtual power of external forces is:

$$P_e(\mathbf{v}^*) = \int_{\Omega(t)} \rho \mathbf{b} \cdot \mathbf{v}^* d\Omega + \int_{\Sigma_2(t)} \mathbf{T} \cdot \mathbf{v}^* d\Sigma$$

Finally, the weak formulation of the balance of momentum is:

$$\int_{\Omega(t)} \rho \boldsymbol{\gamma} \cdot \mathbf{v}^* d\Omega + \int_{G(t)} \mu \mathbf{v} \cdot \mathbf{v}^* d\Sigma = - \int_{\Omega(t)} \boldsymbol{\sigma} : \mathbf{D}^* d\Omega + \int_{\Omega(t)} \rho \mathbf{b} \cdot \mathbf{v}^* d\Omega + \int_{\Sigma_2(t)} \mathbf{T} \cdot \mathbf{v}^* d\Sigma$$

The strong formulation is thus given by :

$$\begin{aligned} \operatorname{div}(\boldsymbol{\sigma}) + \rho \mathbf{b} &= \rho \boldsymbol{\gamma} \text{ on } \Omega(t) \\ \boldsymbol{\sigma} &= \boldsymbol{\sigma}^T \\ \mathbf{v} &= 0 \text{ on } \Sigma_1(t) \\ \boldsymbol{\sigma} \cdot \mathbf{n} &= \mathbf{T} \text{ on } \Sigma_2(t) - G(t) \\ \mu \mathbf{N} + \boldsymbol{\sigma} \cdot \mathbf{n} &= 0 \text{ on } G(t) - \Sigma_2(t) \\ \mu \mathbf{N} + \boldsymbol{\sigma} \cdot \mathbf{n} &= \mathbf{T} \text{ on } G(t) \cap \Sigma_2(t) \end{aligned}$$

We have now described the dynamics of the growing body in the spatial configuration. These equations could be express in the reference configuration using the relation defined in the kinematic description of surface growth. Then, we have to use curvilinear coordinates [11] to take into account the evolution of the reference configuration due to the growth process.

Conclusion

In this work we have extended the analytical description of surface growth from Skalak *et al.* to take into account the deformations of the body during the growth process. On the one hand, we have defined an evolving reference configuration with curvilinear coordinates. On the other hand, balance equations of mass, linear and angular momentum are provided in the spatial configuration. These results are the basis of a mechanical theory of surface growth for tree biomechanics, and further works are needed to solve and implement the above equations.

Acknowledgements

The authors would like to thank Guillaume DELTOUR and Benoit MICHEL (University of Montpellier II) for their comments. We thank also the CIRAD and Agropolis Fondation for their support and funding.

References

- [1] Fourcaud, T.; Blaise, F.; Lac, P.; Castéra, P. & de Reffye, P., 2003. Numerical modelling of shape regulation and growth stresses in trees. Part II: implementation in the AMAPpara software and simulation of tree growth. *Trees* 17, 31-39.
- [2] Epstein, M. & Maugin, G., 2000. Thermomechanics of volumetric growth in uniform bodies. *International Journal of Plasticity* 16, 951-978.
- [3] Senan, N. A. F.; O'Reilly, O. M. & Treserras, T. N., 2008. Modelling the growth and branching of plants: A simple rod-based model. *Journal of the Mechanics and Physics of Solids* 56, 3021-3036.
- [4] Skalak, R., Dasgupta G. & Moss M., 1982. Analytical Description of Growth. *Journal of theoretical Biology*, 94, 555-577.
- [5] Skalak, R.; Farrow, D. A. & Hoger, A., 1997. Kinematics of surface growth. *Journal of Mathematical Biology* 35, 869-907.
- [6] Garikipati, K., 2009. The Kinematics of Biological Growth. *Applied Mechanics Reviews* 62.
- [7] Ambrosi, D. & Mollica, F., 2002. On the mechanics of a growing tumor. *International Journal of Engineering Science* 40, 1297-1316.
- [8] Segev, R. & Epstein, M., 1996. On theories of growing bodies. In : Battra, R. C., Beatty, M. F. (Eds), *Contemporary research in the mechanics and mathematics of materials*. I.M.N.E, Barcelona, pp. 119-130.
- [9] Germain, P., 1973. La méthode des puissances virtuelles en mécanique des milieux continus. première partie : Théorie du second gradient. *Journal de Mécanique*, 12, 235-274.
- [10] Maugin, G. A., 1980. The method of virtual power in continuum mechanics : Application to coupled fields. *Acta Mechanica*, 35, 1-70.
- [11] Marsden J. E. & Hughes J. R. *Mathematical Foundations of Elasticity*. Prentice Hall, 1983, reprinted by Dover, 1994.

3. Plant and fluid mechanics

Plant mechanical interactions with air and water

Emmanuel de Langre, Frédéric Gosselin

Ecole polytechnique, France

Abstract

External flow is an essential element of the environment of plants. From a mechanical point of view it is certainly the main abiotic stress, gravity aside. In this paper I review some mechanisms, with a focus on the need to use proper dimensionless numbers. This is particular, when comparing the situations of plants in air and in water, or plants of various mechanical properties. The two main interactions that are reviewed are (a) dynamics flow interaction with plant canopies, (b) static flow interaction with plant organs. Here the point of view is that of the mechanisms of the interactions.

Introduction

The physics of fluid-structure interaction in plants is somewhat specific [22]. This is related to the complex geometry of plant systems and to their complex elastic behaviour, due to a large flexibility. Moreover, plants in air and in water differ very significantly in terms of architecture and flexibility, as they have to counterbalance gravity forces quite differently. There are still some mechanism of interactions between plants and external flow that can be compared in air and water. The first one is related to the interaction of flow with a canopy, which is a general situation that can be applied to forests, crops and river beds or sea beds. The second one is that of large deformation of plants or parts of plants, leading to a large reduction in drag. This is a feature of the utmost importance to allow plants to withstand extreme wind or currents. Although there two cases do not cover the immense variety of flow-plant interaction, they give some indications of how these can be analysed. The reader is referred to [19,22,34] for further details on the results shortly presented below.

Flow interaction with plant canopies: honamis and monamis.

We focus here on the strong coupling between the dynamics of a fluid flow such as the wind or water current and that of a plant canopy. By plant canopy, we mean a large collection of individual plants such as a dense forest, a crop field, or an aquatic plant cover. The perspective we take on the plants is focused on the canopy as a whole; we perceive the canopy as a poroelastic continuum [4]. Understanding the mechanisms of interactions between flow and a plant canopy is crucial in predicting and avoiding wind-induced damage to trees [1,18,20,33] and crops [3]. Such an understanding is also essential to properly model the heat, mass and momentum exchanges between plants and the atmosphere or between aquatic plants and the water stream they thrive in. Other motivations for pursuing research in this field relate to artistic rendering of realistic vegetation movements [8] and to predicting the mechanical stimulus of wind on plants which influences the growth of plants [10,12].

The structure of the wind over a vegetation canopy is dominated by a Kelvin–Helmholtz (KH) instability due to the difference of air velocity above and inside the canopy [6,15,16], Figure 1. A similar phenomenon is observable in aquatic flows over fully-submerged vegetation [8]. The KH instability, which is due to the presence of an inflection point in the velocity profile, engenders coherent eddies of canopy scale which dominate the turbulent motion of the canopy flow. When the vegetation canopy is flexible, these coherent eddies are responsible for wavelike motions at the canopy top.

These wavelike motions are called honami [9] on crop fields and monami on aquatic plants, Figure 2. Py et al. [14] showed with on-site experiments using an image correlation technique that honami occurs at the free-vibration frequency of the plants. They also proposed an analytical model which couples a mixing-layer flow with a vegetation canopy free to oscillate. The movements of the canopy are coupled with the perturbation flow arising from the instability of the mean mixing-layer flow above the canopy. The two-dimensional conservation of momentum equations are coupled to the canopy oscillator equation through a drag term. This linear model predicts a lock-in mechanism similar in form, but different mechanically to what is observed in vortex-induced vibration [11]. As the mean mixing-layer flow velocity is increased from zero, its KH instability frequency increases and as it approaches the natural frequency of the plants, it deviates and locks onto it. In this lock-in range, the growth rate of the instability is significantly increased. By comparing their experimental observations and the theoretical predictions of their model, Py et al. [17] concluded that “it is thus the lock-in mechanism suggested by the analysis of the coupled model that explains why the coherent wave-motion of the crops occurs at their eigenfrequency independently of [the wind velocity]”.

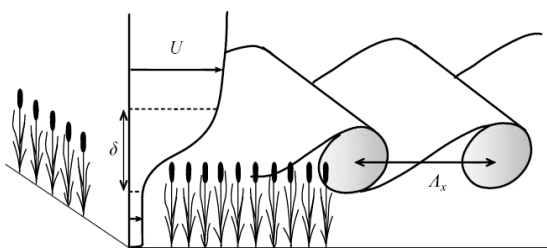


Fig. 1 Flow over a plant canopy: large coherent vortices result from the instability of the flow profile.

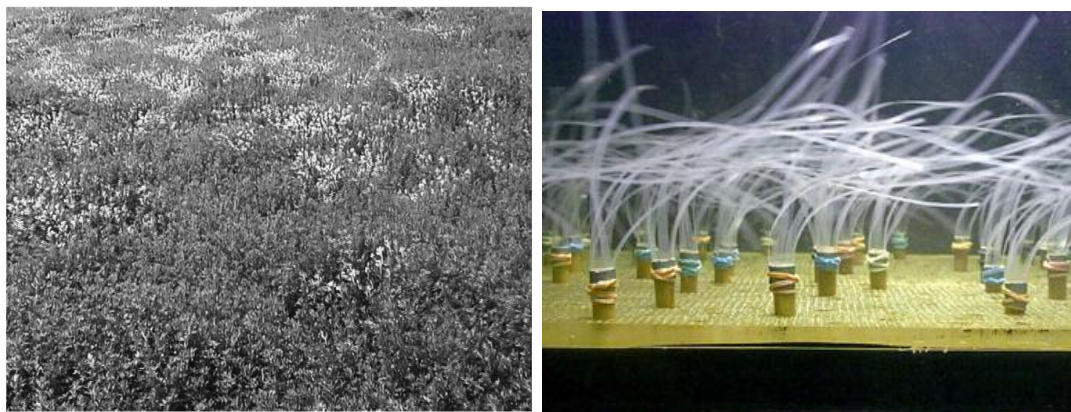


Fig. 2 Left: wind-induced waves on an alfalfa field [14]. Right : current induced oscillations on simulated aquatic vegetation [8]

In order to understand the difference between the case of wind flow or water flow, dimensionless numbers need to be used. The first one is the mass number which reads

$$M = \frac{\rho_{Fluid}}{\rho_{Solid}}$$

It is significantly different in air and in water. The second number scales the ratio of flow velocity with plant velocity [22]. It is therefore a reduced velocity where f is the frequency of motion and L is a length scale of the plant.

$$U_R = \frac{U}{fL}$$

where f is the frequency of motion and L is a length scale of the plant. These two numbers can be used in a comparative analysis of the lock-in mechanism between honamis and monamis [19], based on the method developed in [17]. Figures 3 and 4 give the main results. In Figure 3, which corresponds to wind flow over a crop canopy, it is seen that the range of lock-in, in terms of reduced velocity, is quite narrow. Honamis are expected to exist only in a limited range of wind velocities. In the case of water flow, Figure 4, lock-in is seen to exist over a very large range of flow velocities. Hence much more significant coupling can be expected in water than in air. This is consistent with the role of the mass number on other coupling effects such as added mass.

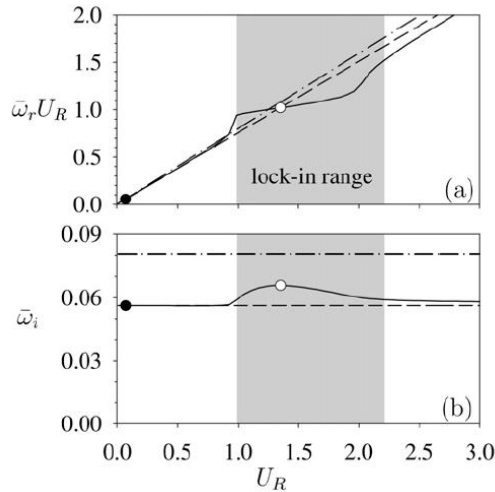


Fig. 3 Lock-in of wind and plant motion [19] using a model coupling a flow-instability with a poroelastic canopy. The low density of the external flow limits the existence of lock-in to a small range of flow velocity.

Here U_R is a dimensionless flow velocity and

ω_r, ω_i are respectively the frequency and the growth intensity of the instability. The lock-in range is shown in grey

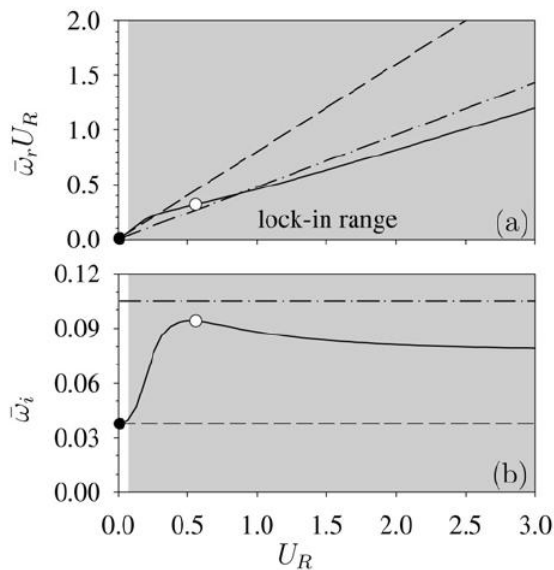


Fig. 4 Same figure as Figure 3 but in the case of water flow. Here lock-in persists over a very large range of flow velocity

Flow interaction with individual plants: reconfiguration

In most traditional engineering applications, structures are designed to be stiff such that the loads they must bear do not deform them substantially. In nature, it is quite the contrary [28]. Especially when it comes to fluid loading, natural structures tend to be compliant and flexible where man-made structures are rigid and unyielding. Plants, which seek to maximise their surface area to capture the most sunlight as well as to facilitate their exchanges with the surrounding fluid, make use of their flexibility by

changing their shape when they are subjected to a fluid loading, whether water flow or wind [24]. By bending and twisting under fluid loading, on the one hand plants reduce their projected area perpendicular to the flow, and on the other hand they also become more streamlined [28]. This a general feature of drag reduction by flexibility, see [21,25,26,27]. Through these two mechanisms of reconfiguration, the drag load plants must support does not grow with the square of the velocity of the flow they are subjected to—as it would on a rigid bluff body—but rather more slowly. How much slower is described with the Vogel exponent ν such that

$$F \propto U^{2+\nu}$$

where F is the drag load and U the flow velocity. For example, the leaf of the tulip tree studied by Vogel [28] rolls up in a cone with increasing wind speed, hence decreasing its cross-sectional area and making itself more streamlined. Whereas if the leaf were rigid, its drag would increase with the square of the velocity of the flow ($\nu = 0$), Vogel [28] found that due to its reconfiguration, the drag increases more or less linearly with flow speed ($\nu = -1$). Experimental measurements on the reconfiguration of plants are abundant in the literature. See for example the collection of Vogel exponents and data on the reconfiguration efficiency of different terrestrial and aquatic plant species by Harder et al. [24] or the wind tunnel measurements on different hardwood tree species by Vollsinger et al. [27]. However, little theoretical interpretation is available. The issue of drag on flexible systems has obvious implications in biology, agriculture and forestry for understanding the adaptation of plants to their habitats as well as for predicting and preventing phenomena of lodging.

Two simple geometries of plates deforming in pure bending were tested: rectangles and disks cut along many radii. Firstly, thin rectangular plates of length L , width W , and flexural rigidity B were glued at their centre onto the support as depicted in the schematics of Figure 5 (a). As the air flow velocity was increased inside the wind tunnel, the rectangular plate folded more and more as pictured in the photograph mosaic of Figure 6. The maximum velocity reached in the experiment was limited by the maximum static and fluctuating loads allowable for the load cell. Flutter localised at the ends of the rectangular plate appeared when the plate was highly deformed thus causing fluctuating loads. In Figure 6 it is possible to see that the most deformed shape is blurry because of flutter. The second geometry tested was a thin disk of radius R cut along many radii constrained by an inner rigid disk of radius R_i and screwed at its centre onto the support as shown in Figure 5 (b). When exposed to increasing flow velocity, the cut-out sectors held at the centre of the disk bend downstream as shown in the photographs taken at incrementing flow velocity in Figure 6. This pattern of deformation is reminiscent of the petals of the daffodils bending downstream in the wind flow as studied by Etnier & Vogel [23].

Typical results of the measured drag of rectangular plates are shown in Figure 7. In Figure 7 (a) is represented the drag of three specimens of similar size versus flow velocity. At small flow velocity, the drag of all three specimens is similar, but differs more and more as the flow velocity is increased. For a rigid plate the drag follows well the quadratic fit while for a flexible plate the drag increases more slowly, and for a more flexible plate the drag increases more slowly still. At high flow velocities, the influence of flexibility on the drag is tremendous. The drag on the most flexible plate is an order of magnitude smaller than that on the rigid plate. The trends observable in Figure 7 (a) are representative of results obtained for rectangular and disk-shaped specimens. In Figure 7 (b) the evolution of drag with flow velocity is shown for three plates of similar width W and rigidity B but differing length L . At small flow velocities, where the plates are not significantly deformed, the longest plate (diamonds) and hence the one with the largest surface area has the largest drag; the second longest has the second largest drag; and the shortest plate has the least amount of drag. At high flow velocities, the shortest plate has the largest drag and the longest plate has the smallest one.

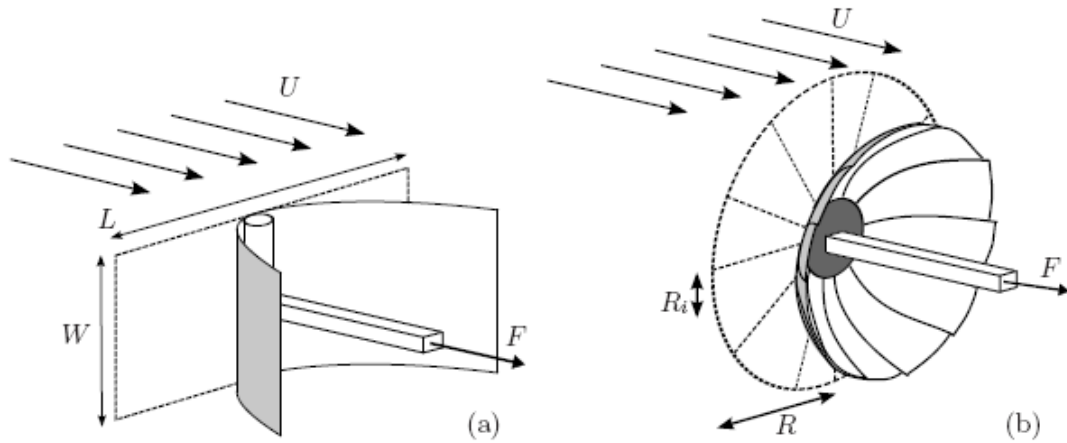


Fig. 5 : Experiments of drag reduction of flexible systems. Left: flexible plates. Right, Flexible disk

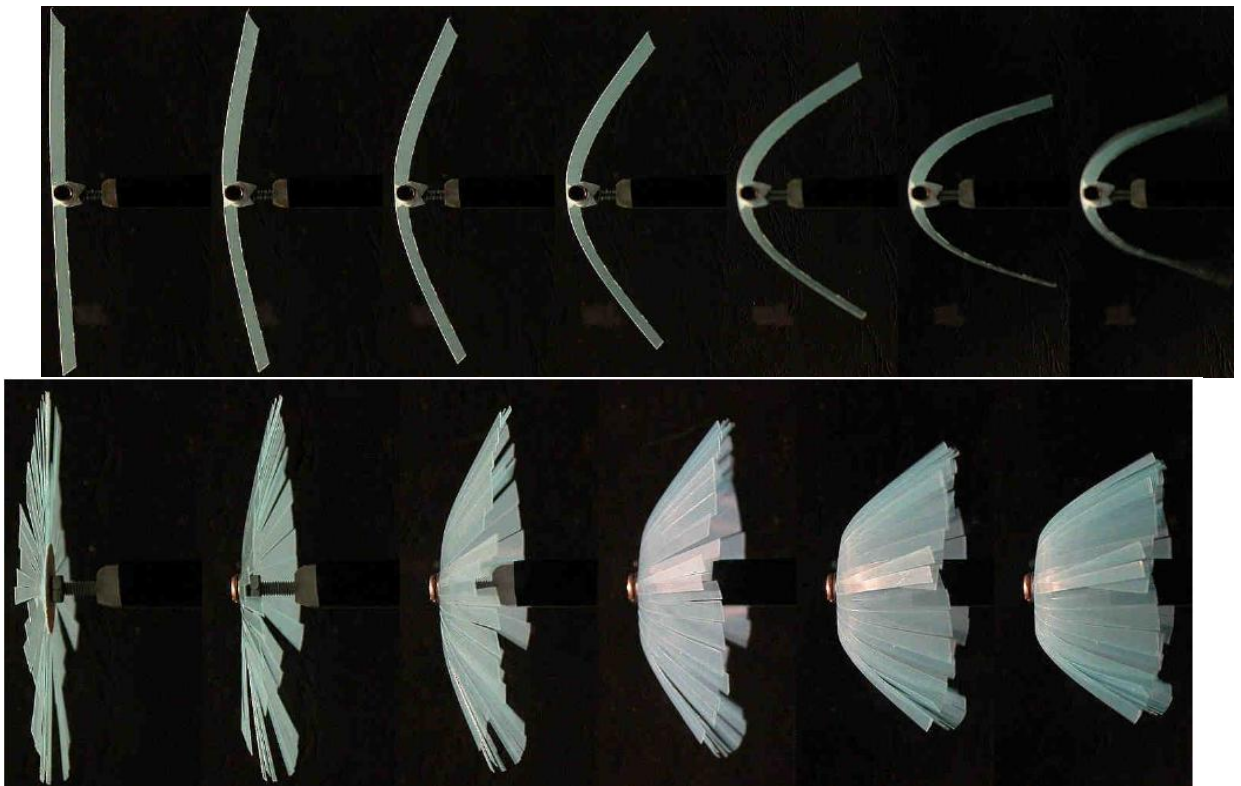


Fig. 6 : Deformation of specimen as the flow velocity is increased from left to right. Top : rectangular plate, Bottom Disk.

These results can be analysed in terms of dimensionless number. First, the drag reduction can be expressed as a ratio between the drag of the flexible system and the drag of the same system if it were rigid. This defines the reconfiguration number

$$R = \frac{\text{Drag}}{\text{Drag rigid}} = \frac{F}{\rho U^2 S C_D / 2},$$

where F is the drag, U is the flow velocity ρ is the flow density, S is the original cross-flow area and C_D is the drag coefficient of the rigid system. The flexibility of the system to flow is expressed through the Cauchy number [22].

$$C_Y = \frac{\text{Fluid force}}{\text{Stiffness}} = \frac{\rho U^2}{E}$$

Note that the Cauchy number must be defined more precisely for slender systems such as those considered here, see the discussion in [19] and [22].

Figure 8 shows the evolution of the reconfiguration number as a function of the Cauchy number for all tests, with plates and with disks. These dimensionless numbers allow gathering all data from various geometries and various stiffness. On the same graph is shown the prediction using a simple fluid-structure interaction model based on the following ingredients [34] : the deformation of the plate is described using non-linear elasticity theory (elastica model) and the fluid loading is approximated by the dynamic pressure defined with the normal velocity $p = \rho U^2 \cos^2 \theta$ where θ is the angle of the plate to the impinging flow. Clearly, the evolution of drag reduction with the flow is well reproduced.

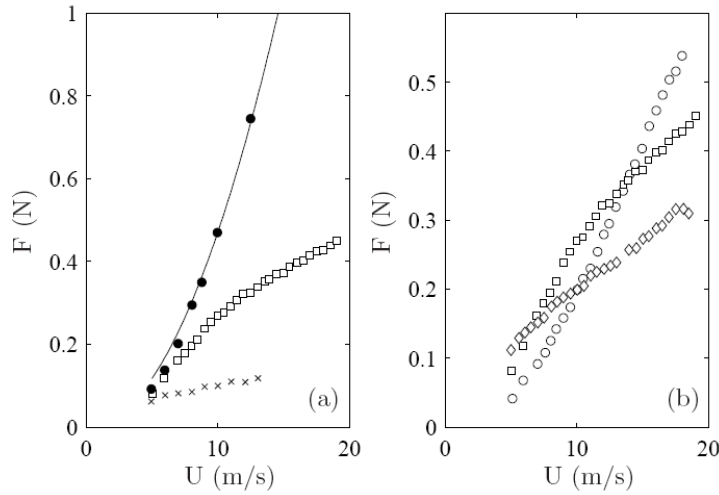


Fig. 7 : Evolution of drag with flow velocity. Left : plates of identical geometries but different flexibilities. Right: plates of identical flexibilities but different width. The widest plate has the lowest drag at higher flow-velocity.

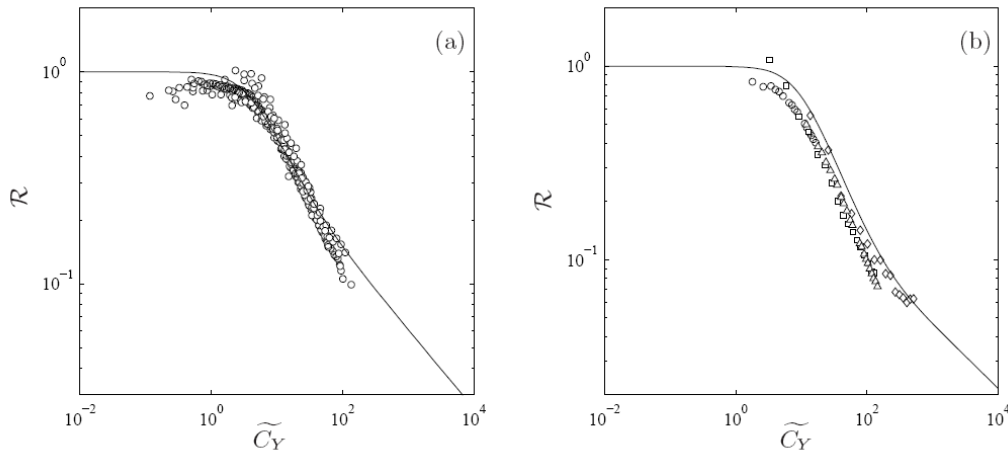


Fig. 8 : Drag reduction effect on a rectangular plate, left, and on disk, right. The reconfiguration number is seen to decrease with the Cauchy number. Symbols correspond to experiments with various sizes and flexibilities. The continuous line results from a fluid-structure interaction model [34].

In water, a similar approach may be defined. Here, we model the data of Harder on drag on seaweed [24]. In that case the mechanism of drag reduction differs: neither area reduction nor streamlining are involved, but rather packing of the branched system [32]. As the flow increases, drag on elements induced tension and thereby bending of the upstream parts of the plant. This results in packing of the system, and consequently a lower flow velocity inside the bundle. Let U_E be the effective velocity in the bundle: the corresponding pressure gradients varies as U_E^2 / H where H is the cross-flow distance between elements. As the pressure gradient outside the bundle varies as U^2 and is independent of H , one may state that

$$U_E^2 / H \propto U^2.$$

Note that this equation only related the form of variations with U, U_E, H and is not an equality. Similarly, the distance H varies with the drag F because of the flexibility of the bundle results in packing. If it is assumed that flexibility is mainly due to bending effects, the essential variable that scales the deformation energy of the system is the moment $M = FH$. In the limit where the system is densely packed, the deformation energy of the system reaches a limit and becomes independent of the moment M , so that in terms of variation we have $H \propto 1/F$. Considering that the drag is related to the effective velocity yields $F \propto U_E^2$. By combining these equations the drag is found to vary linearly with the external flow :

$$F \propto U.$$

A more elaborate model, [35], based on these simple approximations, lead to a drag force that progressively switches from a U^2 dependence to a U dependence. This is illustrated Figure 8 in comparison with the experimental data from [24].

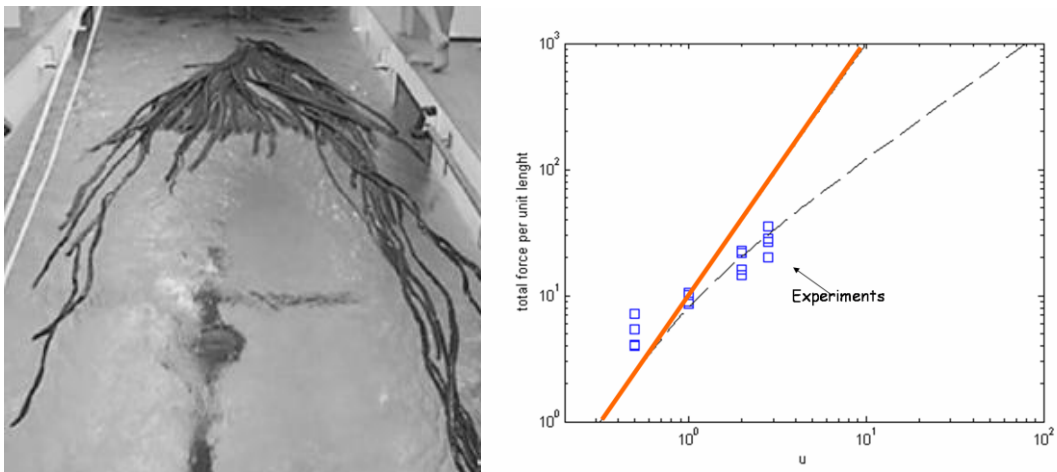


Fig. 8 : Drag reduction effect on a seaweed in bundle. Left, experiments on *Antartica durvillae* [24]. Right: drag as a function of flow velocity. Squares are experimental points. The continuous line is the drag of a rigid body. The broken line corresponds to the model described in the text.

Conclusion

By analysing these two cases we have shown that even in simplified geometries the interaction of flow with a flexible plant system is quite complex. The use of adapted dimensionless numbers are a necessary step to organize and compare experimental data, and to develop simple mechanistic models.

Acknowledgements

We are pleased to acknowledge the help of Pascal Hémon in the experiments, and fruitful discussions with Bruno Moulia, Sylvain Dupont, Yves Brunet, and all participants of the French research program on wind and plants, ANR Chene-roseau, project “Blanc-2-134798”.

References

1. Baker, C. J. 1995 *The development of a theoretical model for the windthrow of plants*. J. Theor. Bio. **175**, 355–372.
2. Blevins, R. D. 1990 *Flow-Induced Vibration*. Van Nostrand Reinhold.
3. Berry P, Sterling M, Spink J, Baker C, Sylvester-Bradley R, et al. 2004. *Understanding and reducing lodging in cereals*. Adv. Agron. 84:217–71
4. Doaré, O., Moulia, B. & de Langre, E. 2004 *Effect of plant interaction on wind-induced crop motion*. Trans. ASME: J. Biomech. Engng **126**, 146–151.
5. Farquhar, T., Zhou, J. & Haslach, H. 2003 *A possible mechanism for sensing crop canopy ventilation*. In Sensors and Sensing in Biology and Engineering (ed. F. Barth, J. Humprey & T. Secomb), Ch. 15. Springer.
6. Finnigan, J. J. 2000 *Turbulence in plant canopies*. Annu. Rev. Fluid Mech. **32**, 519–571.
7. Flesch, T. K. & Grant, R. H. 1992 *Corn motion in the wind during senescence: II. Effect of the dynamic plant characteristics*. Agronomy J. **84** (4), 748–751.
8. Ghisalberti, M. & Nepf, H. M. 2002 *Mixing layers and coherent structures in vegetated aquatic flows*. J. Geophys. Res. **107** (C2), 1–11.
9. Inoue, E. 1955 *Studies of the phenomena of waving plants (“honami”) caused by wind. Part 1: Mechanism and characteristics of waving plants phenomena*. J. Agric. Met. (Japan) **11**, 71–82.
10. Jaffe, M. 1973 *Thigmomorphogenesis: the response of plant growth and development to mechanical dioica*. Planta **114**, 143–157
11. de Langre, E. 2006 *Frequency lock-in is caused by coupled-mode flutter*. J. Fluids Struct. **22**, 783–791.
12. Moulia, B. & Combes, D. 2004 *Thigmomorphogenetic acclimation of plants to moderate winds greatly affects height structure in field-grown alfalfa (medicago sativa l.), an indeterminate herb*. Comp. Biochem. Physiol. A: Molec. Integrative Physiol. **137** (3-S1), 77.
13. Py, C., de Langre, E. & Moulia, B. 2004 *The mixing layer instability of wind over a flexible crop canopy*. C. R. Méc. **332**, 613–618.
14. Py, C., de Langre, E., Moulia, B. & Hémon, P. 2005 *Measurement of wind-induced motion of crop canopies from digital video images*. Agric. Forest Met. **130**, 223–236.
15. Raupach, M. R., Finnigan, J. J. & Brunet, Y. 1996 *Coherent eddies and turbulence in vegetation canopies: the mixing layer analogy*. Boundary-Layer Met. **78**, 351–382.
16. Raupach, M. R. & Thom, A. S. 1981 *Turbulence in and above plant canopies*. Annu. Revi. Fluid Mech. **13**, 97–129.
17. Py, C., de Langre, E. & Moulia, B. 2006 *A frequency lock-in mechanism in the interaction between wind and crop canopies*. Journal of Fluid Mechanics **568**, 425–449.
18. Sellier, D., Brunet, Y. & Fourcaud, T. 2008 *A numerical model of tree aerodynamic response to a turbulent airflow*. Forestry **81** (3), 279–297.

19. Gosselin, F. & de Langre, E. 2009 *Destabilising effects of plant flexibility in air and aquatic vegetation canopy flows*. European Journal of Mechanical B/Fluids 28, 271–282.
20. Dupont, S. & Brunet, Y. 2006 *Simulation of turbulent flow in an urban forested park damaged by a windstorm*. Boundary-Layer Meteorology 120 (1), 133–161.
21. Alben, S., Shelley, M. & Zhang, J. 2004 *How flexibility induces streamlining in a two-dimensional flow*. Physics of Fluids 16, 16941713.
22. de Langre, E. 2008 *Effects of wind on plants*. Annual Review of Fluid Mechanics 40, 141–168.
23. Etnier, S. A. & Vogel, S. 2000 *Reorientation of daffodil (narcissus: Amaryllidaceae) flowers in wind: drag reduction and torsional flexibility*. American Journal of Botany 87 (1), 29–32.
24. Harder, D., Speck, O., Hurd, C. & Speck, T. 2004 *Reconfiguration as a prerequisite for survival in highly unstable flow-dominated habitats*. Journal of Plant Growth Regulation 23, 98–107.
25. Jenkins, C. H. M. 2005 *Compliant Structures in Nature and Engineering*. Southampton, UK:WIT Press.
26. Rudnicki, M., Mitchell, S. J. & Novak, M. D. 2004 *Wind tunnel measurements of crown streamlining and drag relationships for three conifer species*. Canadian Journal of Forest Research 34, 666–676.
27. Schouveiler, L. & Boudaoud, A. 2006 *The rolling up of sheets in a steady flow*. Journal of Fluid Mechanics 563, 71–80.
28. Vogel, S. 1989 *Drag and reconfiguration of broad leaves in high winds*. Journal of Experimental Botany 40, 941948.
29. Vollsinger, S., Mitchell, S. J., Byrne, K. E., Novak, M. D. & Rudnicki, M. 2005 *Wind Drag reduction of flexible plates by reconfiguration tunnel measurements of crown streamlining and drag relationships for several hardwood species*. Canadian Journal of Forest Research 35, 1238–1249.
30. . Diener J, Rodriguez M, Baboud L, Title: *Wind projection basis for real-time animation of trees* Computer Graphics Forum Volume: 28 Issue: 2 Pages: 533-540
31. Moulia B, Fournier M T *The power and control of gravitropic movements in plants: a biomechanical and systems biology view* Journal Of Experimental Botany Volume: 60 Issue: 2 Pages: 461-486
32. Koehl MAR, Silk WK, Liang H, *How kelp produce blade shapes suited to different flow regimes: A new wrinkle* Integrative And Comparative Biology Volume: 48 Issue: 6 Pages: 834-851
33. Rodriguez M, de Langre E, Moulia B *A scaling law for the effects of architecture and allometry on tree vibration modes suggests a biological tuning to modal compartmentalization* American Journal Of Botany Volume: 95 Issue: 12 Pages: 1523-1537
34. F. Gosselin, E. de Langre and B. Machado-Almeida. *Drag reduction of flexible plates by reconfiguration*. Submitted to Journal of Fluid Mechanics. (2009).
35. Gosselin F. Mécanismes d'interaction fluide-structure dans des systèmes végétaux ; PhD Ecole polytechnique 2009.

Resistance of red mangrove (*Rhizophora mangle* L.) seedlings to extraction.

Sophie D. Boizard, and Stephen J. Mitchell

University of British Columbia, Canada

Abstract

Red mangrove (*Rhizophora mangle* L.) is the dominant tree species in the intertidal zone of ecosystems on the Atlantic shores of the Caribbean and tropical western Atlantic. The propagules of this species are initially buoyant, then become negatively buoyant before rooting in a variety of substrates. While established mangrove communities assist in stabilizing coastlines, seedlings are susceptible to wave, current and wind energy and this limits the habitats that they can successfully colonize. This experiment is part of a larger study of mangrove disturbance and regeneration dynamics. In this experiment, we measured seedling form and mechanical resistance at five sites with different substrate and canopy conditions at Turneffe Atoll, Belize. The 78 seedlings tested ranged in height from 27 to 47 cm, had between one to ten pairs of leaves but had not yet formed aerial roots. Seedlings growing under mangrove canopies were more slender than open grown seedlings. We applied a horizontal force to failure in the landward direction. Seventy-five percent of the seedlings failed at the root system and the remainder failed near the base of the stem. Seedlings growing outside of mangrove overstory on coral rubble were 3.5 times more resistant to failure than those growing within the mangrove overstory on sand.

Introduction

Mangroves are a specialized group of woody plants that form intertidal fringing communities along the coastlines of continents, islands and atolls throughout the tropics. They grow in one of the most mechanically challenging environments of all plants, being subject to a gradient of wind and wave energy from quiet lagoon environments to shorelines with full exposure to tropical storms [1]. These communities provide a number of critical ecosystem services including shoreline protection from waves, storms and tsunamis, fisheries, carbon fixation and tourism. They are under considerable pressure from development, and the projected consequences of global warming, sea level rise and increased storm severity, will place these ecosystems under further stress [2]. While established mangrove communities appear mechanically robust and dissipate routine wind and wave energy [e.g. 3], they are periodically damaged by extreme winds, wind driven waves, and storm surge during severe storms. For example, Hurricane Mitch in 1999 destroyed over 90 percent of the mangroves on islands in Honduras through defoliation, uprooting, burial, and erosion [4].

The red mangrove (*Rhizophora mangle* L.) grows in tropical and subtropical regions of the Atlantic and Pacific Oceans and is the dominant mangrove species in the Caribbean. It is a typical mangrove species, well adapted to growing in the intertidal zone with high salt tolerance, aerial roots, and viviparous reproduction [1]. Recolonization by red mangrove seedlings requires the arrival of propagules from dispersal sites. These seedlings must take root before being buoyed away by tidal or wave action[5]. One might think that this would limit recruitment to zones with very low energy, but mangroves do establish across a gradient of substrates and wave energy [6]. During the early stages of colonization, seedlings are single-stemmed and individually isolated. Sometime after establishment, seedlings begin forming aerial roots and secondary branching, and where seedling densities are high

enough, this leads to communities of plants with complex, intercrossing networks of branches and aerial roots.

This study is part of a larger program of research on red mangrove disturbance and regeneration dynamics. The main objective of this study was to characterize the nature and mode of seedling resistance to horizontal loads as a function of seedling size, substrate and overstory canopy condition. We examined i) seedling size-resistance relationships, ii) whether anchorage differs between different substrates and within or outside of overstory canopies; and iii) whether the mode of failure varies with seedling size, substrate or canopy condition.

Material and methods

This study was conducted on Turneffe Atoll, 50km east of mainland Belize, outside the Mesoamerican Barrier Reef. The atoll is *ca* 48 km long and 16 km wide and is composed of low elevation islands or cays. Our study sites were on reef-crest cayes along the eastern, storm-exposed side of the atoll. These low profile cayes are composed of sands and rubble and are fringed by red mangrove forests that are still expanding following the de-vegetation caused by Hurricane Hattie in 1961[7]. The tides in this area are classified as mixed semidiurnal with an average range of less than 30 cm [8]. The occurrence of heavy rains and strong to catastrophic winds increases between July and November as a result of seasonal tropical storms and hurricanes typical of the Caribbean Region. The main coastal current flows from south-east to northward. However, the Gulf of Honduras is influenced by a anti-clockwise counter-current resulting in predominantly southerly water movements over the coastal shelf [7].

Populations of seedlings of *R. mangle* were sampled at five locations in close proximity of Calabash Caye (17°16'57.76"N, 87°48'41.96"W) on the east side of the atoll. The bathymetry and substrate size distribution within the study area indicates that energy due to tides and waves attenuates with distance from the reef [e.g. 9]. The five sampling sites differed in the type of substrate (coral sand, unconsolidated coral rubble and peat) and the degree of overstory red mangrove canopy under which they grew (canopy or open). Sand and rubble substrates are found both outside and within mangrove forests. However, since the peat is formed by leaf and fine root deposition, it is not found outside areas of established mangrove canopy. The rubble locations are closer to the reef crest than the sand locations.

Each sampling location was approximately 30 m x 40 m wide. Sample seedlings, substrate attributes, and canopy cover were obtained throughout each sampling location. Mangrove canopy cover was estimated with a convex spherical densiometer. Within each sampling location, six sediment cores were taken with an aluminium cylinder coring device (7.5 cm diameter X 40 cm depth). Particle size distribution analysis (PSDA) was performed using sieves. Cores extracted from plots within canopies were processed prior to sieving to separate the peat and root fraction from coral sediment.

Seedlings growing in isolation from each other, and with no damage, branching or aerial roots were selected to represent a range of stem height classes. Prior to pulling, seedling height was measured from the substrate surface to the base of the terminal bud. Diameters were measured as follows: basal diameter just above the substrate surface, at the hypocotyl apex, midway along the first stem internode above the hypocotyl. We also measured the number of internodes, and the number of leaves. Slenderness was calculated as the stem height divided by the basal stem diameter (slenderness 1) and the stem height divided by the first internode diameter (slenderness 2). Only one seedling had secondary branching. No seedlings had aerial roots. Fresh weight was measured in the field immediately after pulling with a precision spring-scale. A spring-scale (1 kg) was attached to the seedling with a binder clip lined with rubber tubing to prevent damage to the seedling stem. This attachment point was at five-sixth of the stem height, typically this was just below the first pair of leaves. Two pieces of flat webbing were woven around the stem for 10-20 cm. This webbing was tied

into a loop at the top, at 5/6 of the stem height, to which a spring scale was attached (*Fig. 1*). This method, which mimicked a Yale Grip™, allowed us to maintain a firm grip, avoiding slippage along the stem during pulling. Seedlings were manually pulled except for the largest ones which were pulled using a hand powered winch. Seedlings were pulled horizontally to failure at a constant rate (approx. 1-2 cm/sec) in the direction of the prevailing incoming waves and winds (e.g. pulled toward the west). The force at failure and failure mode (root failure or stem failure) were recorded.

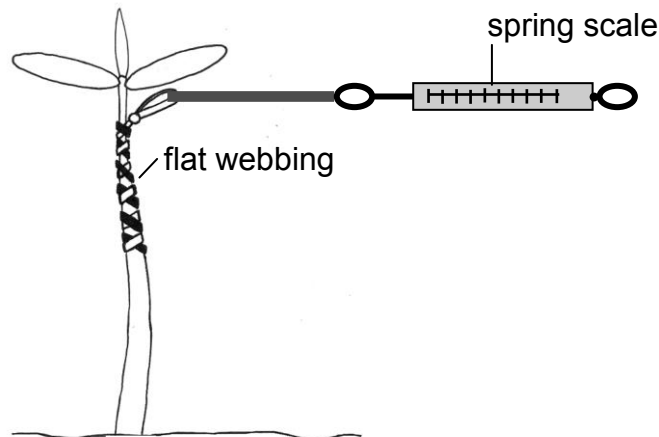


Fig. 1 Schematics of spring scale attachment to seedling showing flat webbing woven around seedling stem.

Statistical analyses were carried out on a sample of 78 seedlings, which included only seedling size classes present at all 5 sites (stem height ranging from 27.5 to 47.5 cm). One-way ANOVA was used to test for difference in failure resistance among locations. Pearson's correlation coefficients were calculated to investigate linear relationships between failure resistance and each morphological variables. Contingency table and logit log-linear analyses were used to compare mode of failure among substrates and between canopy cover. All statistical analyses were performed using SPSS V.11 (SPSS Inc. Chicago, Illinois). The level of significance for all statistical tests was evaluated using a value of $\alpha=0.05$.

Results and discussion

The five sampling locations are referred to as Rubble-Open (e.g. rubble substrate, no-canopy), Sand-Open, Rubble-Canopy, Sand-Canopy, Peat-Canopy. Differences in stem heights among locations were minimal, however other morphometric parameters differed between locations (*Fig. 2*).

Larger seedlings required more force to be uprooted than smaller ones. The force required to uproot seedlings was positively correlated with height, diameter (basal and of first internode) and mass (*Table 1*). The force for stem break was positively correlated with the diameter of the stem at the first internode and with mass.

The percentage of seedlings that uprooted vs broke in the stem varied between locations. Uprooting was the dominant mode of failure for seedlings growing in open locations (*Fig. 3*). Force at failure differed significantly among locations ($p<0.004$) when seedlings with both failure modes are pooled (*Fig. 4*).

As expected, resistance to failure increased with increases in plant size, particularly with plant weight. A strong association between failure resistance and plant weight has been observed in many studies with terrestrial trees [e.g. 10], but there is as yet no biomechanical explanation for this relationship. The five locations examined differed in light regime and substrate properties, and presumably in the competition and mechanical stresses experienced by the seedlings. The difference in

mean failure resistance between sites is substantial and it appears that the presence of canopy is more important than substrate type in failure resistance.

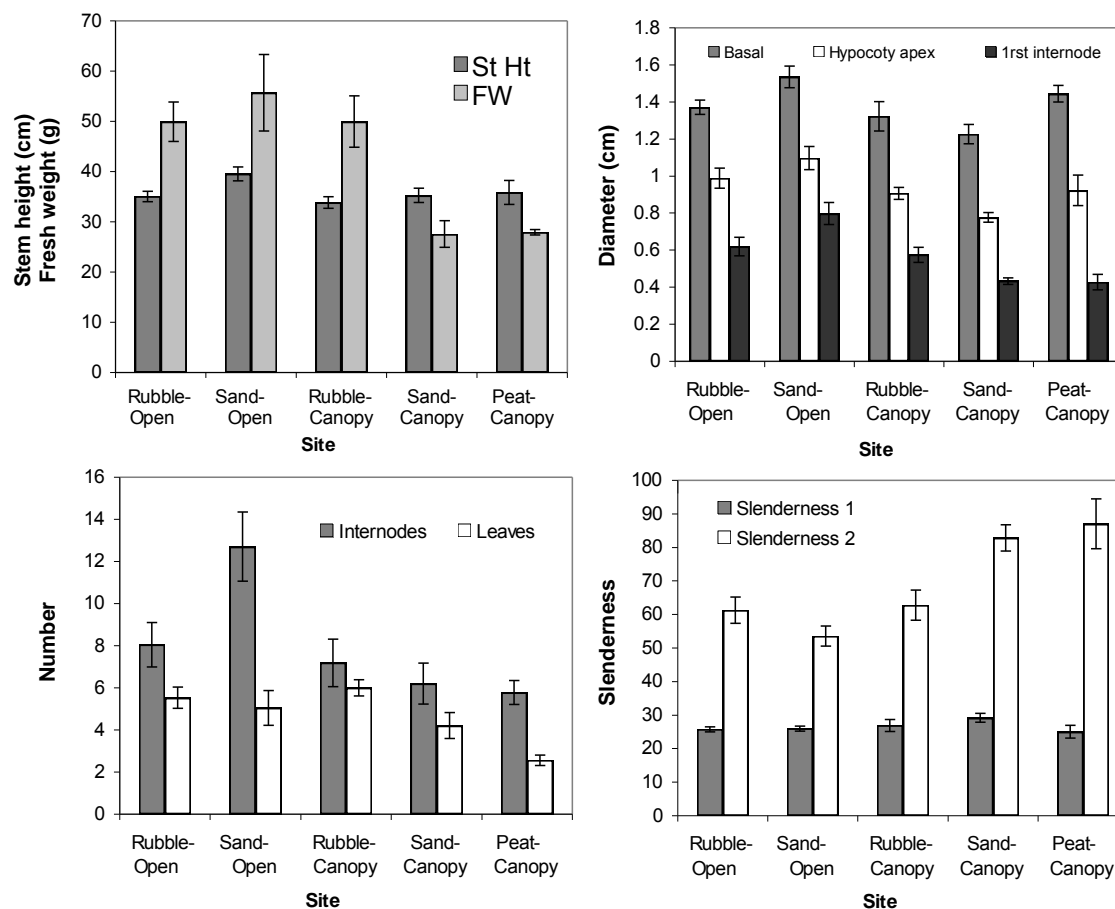


Fig. 2 *Rhizophora mangle* morphometrics a) stem height and fresh weight, b) stem diameters, c) total number of internodes, d) slenderness (1-height/basal diameter, 2-height/1st internode diameter). Sample sizes were 19 rubble-open, 20 sand-open, 15 rubble-canopy, 15 sand-canopy, and 9 peat-canopy.

Table 1. Pearson's correlation coefficients (*r*) between the force at failure and morphological variables for significant relationships.

Force at failure	Morphological variables	<i>r</i>
Stem Failure n=18	Height	ns
	Basal diameter	ns
	First internode diameter	0.50
	Fresh weight	0.50
Root Failure n=60	Height	0.29
	Basal diameter	0.44
	First internode diameter	0.56
	Fresh weight	0.66

We restricted our sample to seedlings over comparable height range, and the range and mean of seedling basal diameters were also similar. However, the seedlings growing under the canopy had smaller diameters at the first internode (above the pod) and were in consequence more slender than open grown seedlings. Overhead shade has been found to result in increased slenderness and reduced bending resistance in conifer seedlings [11]. It is also possible that the remaining seedlings in the open

study locations represented a subset of all of the seedlings that initially colonized the site. Seedlings that were less resistant to failure have already been broken or uprooted by routine wave activity in these more exposed locations.

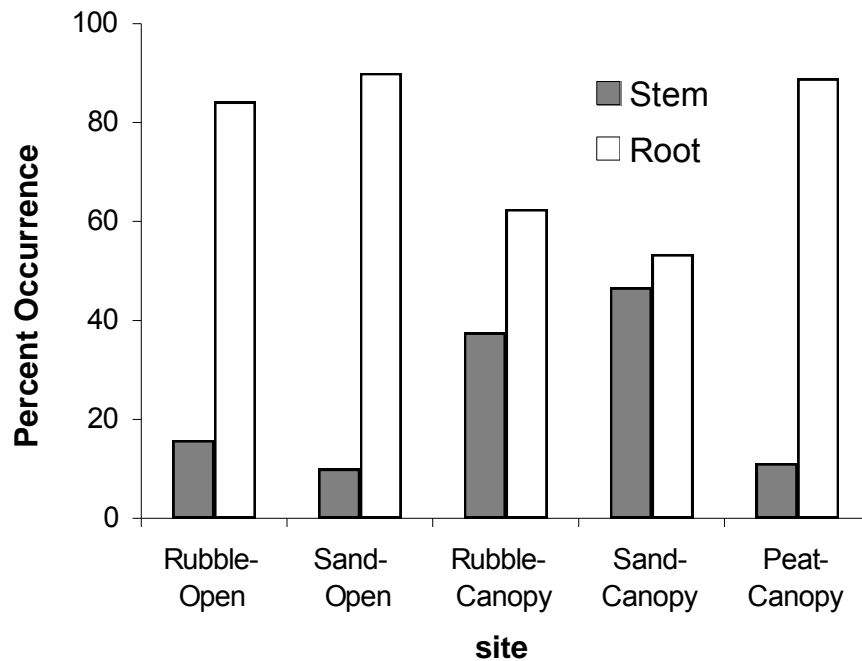


Fig. 3 Percent occurrence of stem break and uprooting at each of the five locations.

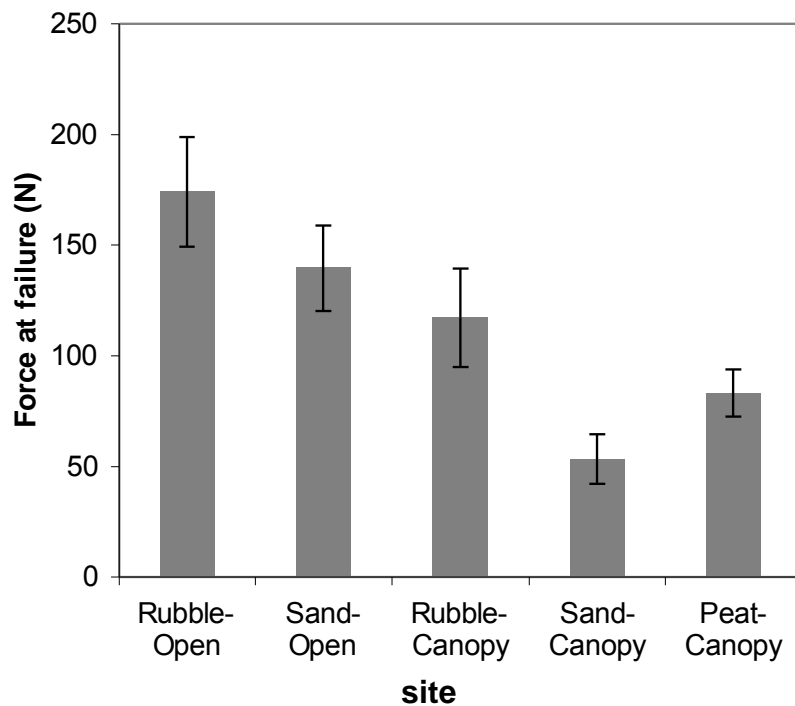


Fig. 4. Mean force to failure of *Rhizophora mangle* seedlings at each of the five locations.

Conclusion

In this study we have gained insights into the size dependence of mechanical resistance in mangrove seedlings and the variability that exists between sites with different substrates and canopy cover. In our companion paper we measure seedling deflection and drag forces as a function of current velocity. The forces required to uproot or break seedlings are substantial relative to the size of the seedlings, for the seedlings that have successfully colonized these sites to-date. It is probable that for seedlings of this size, without aerial roots or secondary branching, that substrate scour and abrasion by moving debris are more important sources of mortality than direct loading of winds and waves during storms.

Acknowledgements

This research was funded in part by the Natural Sciences and Engineering Research Council of Canada. The assistance of the staff at the Marine Research Station of the University of Belize is greatly appreciated.

References

1. Tomlinson, P. B. (1986): *The botany of mangroves*. Cambridge University Press, Cambridge, England.
2. UNEP-WCMC (2006): *In the front line: shoreline protection and other ecosystem services from mangroves and coral reefs*. Publisher, UNEP-WCMC, Cambridge, England.
3. Mazda, Y., M. Magi, Y. Ikeda, T. Kurokawa and T. Asano (2006): Wave reduction in a mangrove forest dominated by *Sonneratia* sp. *Wetlands Ecology and Management* 14.
4. Cahoon, D. R., P. Hensel, J. Rybczyk, K. L. McKee, C. E. Proffitt and B. C. Perez (2003): Mass tree mortality leads to mangrove peat collapse at Bay Islands, Honduras after Hurricane Mitch. *Journal of Ecology* 91, 1093-1105.
5. Sousa, W. P., P. G. Kennedy, B. J. Mitchell, Ord, B. ez L and M. n (2007): Supply-side ecology in mangroves: do propagule dispersal and seedling establishment explain forest structure? *Ecological Monographs* 77, 53-76.
6. Lugo, A. (1980): Mangrove ecosystems: Successional or steady-state. *Biotropica* 12, 65-72.
7. Stoddart, D. R. (1963): Effects of Hurricane Hattie on the British Honduras Reefs and Cays, October 30-31, 1961. *Atoll Research Bulletin* 95, 142.
8. Piou, C., I. Feller, U. Berger and F. Chi (2006): Zonation patterns of Belizean offshore mangrove forests 41 years after a catastrophic hurricane. *Biotropica* 38, 365–374.
9. Hartstein, N. and W. Dickinson (2006): Wave energy and clast transport in eastern Tasman Bay, New Zealand. *Earth Surface Processes and Landforms* 31, 703-714.
10. Nicoll, B. C., B. A. Gardiner, B. Rayner and A. J. Peace (2006): Anchorage of coniferous trees in relation to species, soil type, and rooting depth. *Canadian Journal of Forestry Research* 36, 1871-1883.
11. Mitchell, S. J. (2003): Effects of mechanical stimulus, shade, and nitrogen fertilization on morphology and bending resistance in Douglas-fir seedlings. *Canadian Journal of Forest Research-Revue Canadienne De Recherche Forestiere* 33, 1602-1609.

Plant motion in heterogeneous landscapes: a coupled flow-tree simulation study

Yves Brunet¹, Sylvain Dupont¹, Pascal Roux¹, Damien Sellier²

¹INRA, UR1263 EPHYSE, France; ²SCION, New Zealand

Abstract

Landscape heterogeneities such as forest edges, clearings or gaps, as well as the presence of topography, induce spatial variations in turbulence properties that may have considerable impact on the aerodynamic sollicitations exerted on plants. The heterogeneity in the damages caused by windstorms in forested landscapes can be partly attributed to such spatial variations in windload. We investigate here the impact of landscape heterogeneity on tree motion using a coupled flow-tree modelling approach. The simulation of flow fields is provided at fine spatial and temporal resolution by a large-eddy simulation (LES) model and the simulation of tree movements induced by instantaneous wind forces is provided by a mechanistic, dynamic model of tree behaviour. One-way coupling of the models is ensured by forcing the mechanical tree model with instantaneous velocity fields computed by the LES model, so that the tree response to a fluctuating wind field can be predicted at any location in a virtual landscape. Using this coupled model we illustrate the influence of canopy architecture on the streamwise variations in tree motion in two cases: a forest edge flow and a flow over a forested hill. The ultimate aim of the approach is to provide guidance for sustainable forest management practices.

Introduction

Landscape heterogeneities such as forest edges, clearings or gaps, as well as the presence of topography, substantially alter mean velocity and turbulence fields. They induce spatial variations in turbulence properties that may have considerable impact on the aerodynamic sollicitations exerted on the trees. The observed heterogeneity in the damages caused by windstorms in forested landscapes can be partly attributed to such spatial variations in windload. In the perspective of designing sustainable forest management practices, it is therefore of importance to better understand the coupling between wind flow and tree motion.

Because of the complexity of the processes responsible for windthrow in heterogeneous landscapes, modelling both plant and flow dynamics should provide adequate tools for allowing tree vulnerability to windload to be quantified at any position in heterogeneous environments. Over the past few years it has been shown that Large-Eddy Simulation (LES) of flow dynamics can reproduce the main features of canopy flow in horizontally homogeneous canopies [1], across canopy edges [2] [3] [4] and over forested hills [5]. In parallel, mechanistic models have been developed to simulate plant dynamics [6] [7]. More recently a new model has been developed to simulate the dynamics of a tree forced by a field of fluctuating velocities [8]. This model has been validated using field measurements of turbulent velocities and tree movements.

Here we couple a LES flow model with this latter model for tree dynamics, in order to simulate tree motion at any given position in a heterogeneous forested landscape. We use the coupled model in two distinct situations: a forest edge flow and a flow over a forested hill. In both cases we illustrate the influence of stand density and canopy architecture on the streamwise variations in tree motion and mechanical stresses.

Material and methods

LES provides instantaneous dynamical fields and is consequently able to simulate the wind gusts responsible for plant motions. The LES model used in this study (ARPS) was initially developed to simulate convective and cold-season storms as well as weather systems at larger scales. It is a three-dimensional (3D), non-hydrostatic, compressible model where Navier-Stokes equations are written in terrain-following coordinates. The model solves the conservation equations for the three wind velocity components, pressure and potential temperature. At such high spatial resolution as is required here, these equations are filtered so that all turbulent structures larger than the filter scale are explicitly solved by the model (which is the case of most turbulent eddies generated by wind shear), while smaller turbulent structures (subgrid-scale turbulent motions) are modelled through a 1.5-order turbulence closure scheme. A detailed description of the standard version of the model and its validation cases is available in the ARPS User's Manual. The model was modified so as to simulate turbulent flows over plant canopies at very fine scales (Dupont et al., 2008a). The canopy is implemented in the model by adding a pressure and viscous drag-force term in the momentum equation and by adding a sink term in the equations for subgrid-scale turbulent kinetic energy and its dissipation. The latter term accounts for the acceleration of the dissipation of turbulent eddies in the inertial subrange. The grid is orthogonal in the horizontal direction and stretched in the vertical direction. This modified model has been validated in various cases: homogeneous canopy flow [1], edge flow [2] and flow over a forested hill [5].

A dynamic model has also been developed to analyse the mechanical response of trees submitted to a turbulent airflow [8]. It is based on a standard motion equation written in matrix form:

$$M \ddot{q} + D \dot{q} + K q = F + G$$

where M , D and K are the inertia, damping and stiffness matrices of the structure, respectively; F is the column vector of the aerodynamic drag and G the column vector of gravitational forces; \ddot{q} , \dot{q} and q are the column vectors of acceleration, velocity and displacement, respectively. The terms $M\ddot{q}$ and $D\dot{q}$ represent the inertia forces and dissipative forces, respectively. This equation is solved at all places on a given 3D tree structure, using the finite-element method, after the structure has been divided into a finite number of 3D beam elements with associated elastic properties. The term allowing coupling with the flow is the drag term F , that is a function of the drag coefficient, the plant area exposed to the wind (frontal area density), the wind velocity and the displacement velocity of the tree elements. Instantaneous values can be ascribed to the wind velocity, so that the dynamic model can be forced by wind values recorded at high frequency. The model was validated against experimental data collected during 30 min in a pine forest canopy [8]. In the original version of the model the equation system was solved using the Abaqus software. In the present study the open-access Cast3m software has been used. At the current stage only small displacements have been considered, so that non-linear processes cannot be properly accounted for.

Forcing the tree model by measured turbulent time series is adequate for validation purposes. However this approach becomes limiting for characterizing the tree behaviour in various environments or for performing sensitivity studies to tree architecture for example. Indeed, velocity fields strongly depend on canopy structure and landscape heterogeneities. In other words, the forcing functions have to be adapted to each case. LES provides a powerful solution to this problem: for a given tree architecture and plantation pattern, it can indeed generate time series of instantaneous 3D wind velocity that can be used to generate adequate forcing drag terms. The procedure is then as follows: (1) choose a particular tree architecture (tree 1 of [8] was used here); (2) assume a plantation density, that can be variable in space, throughout the LES domain; (3) run the LES model over a certain time period, after the leaf area density has been calculated at each grid point; (4) run the dynamic model at given locations of interest, using the velocity field calculated locally as a forcing function to the drag term on all tree elements. Two types of heterogeneities have been treated here using this procedure: a forest edge flow and a flow over a forested hill.

Results and discussion

For the edge and hill flow studies the density of the pine forest was chosen so as to correspond to the forest canopy described in [8], where the leaf area index (LAI) was 1.83. Two cases were considered, *i.e.* with and without an understorey. The understorey was obtained by adding leaf area uniformly between the soil surface and the crown basis, so that the added frontal area density was equal to that of the crown.

In both cases of the edge flow study, 30-min time series were computed at various locations downstream of the edge, for variables such as tree deflection at various heights, axial stress, shearing stress, torsional stress, flexural stress, Von Mises stress, etc. As trees may adapt their structure to local mean conditions, tree vulnerability may be estimated to a first approximation from the ratio between extreme and mean values of these variables [3]. As an example, Fig. 1 represents maximum tree displacement and Von Mises stress observed over the simulated period at height $z = 17$ m (middle of the crown layer), normalised by their mean value. Both variables exhibit similar patterns. With no understorey they show a slight increase down to about $x/h = 8$, and they tend to stabilize further downstream to an equilibrium value. In the presence of a thick understorey they both show a marked peak at $x/h = 6$ where they take about twice their value with no understorey. They then quickly decrease down to $x/h = 8$, where they take an equilibrium value. These results can be interpreted by looking at the spatial variations in the velocity statistics (not shown here): in the first case the absence of understorey allows the flow to adapt slowly and smoothly to the canopy, due to the presence of a sub-canopy wind jet starting at the edge, in the sparsest layers of the canopy, whereas in the second case the tree behaviour results from the combination of the strong intermittency observed in the upper canopy in the region $1 < x/h < 6$ and the development of a region of strong turbulence after $x/h \approx 4$. It is interesting to note that this peak at $x/h = 6$ cannot be seen on related variables such as the gust factor [8], often used as a surrogate for tree vulnerability. This underlines the interest of our coupled flow-tree approach.

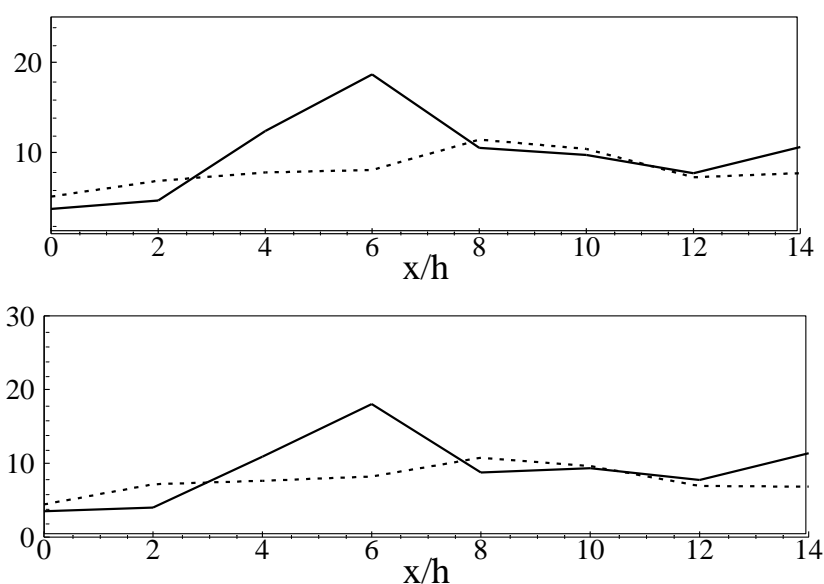


Fig. 1 Top: streamwise variation in the streamwise tree displacement ratio (maximum/mean), downstream from the forest edge. Bottom: streamwise variation in the Von Mises stress ratio (maximum/mean), downstream from the forest edge. Case of a pine forest canopy of LAI = 1.83, with (solid line) or without (broken line) an understorey. The edge is located at $x/h = 0$.

In the hill flow study we focus on the forested hill considered by Dupont et al. [5] after the work of Finnigan and Brunet [9]. The simulated hill is 30 m in height H and 84 m in length L (half hill width at mid-hill height). The forest canopy has the same characteristics as those considered in the edge flow study. Two cases, with and without an understorey, were also considered.

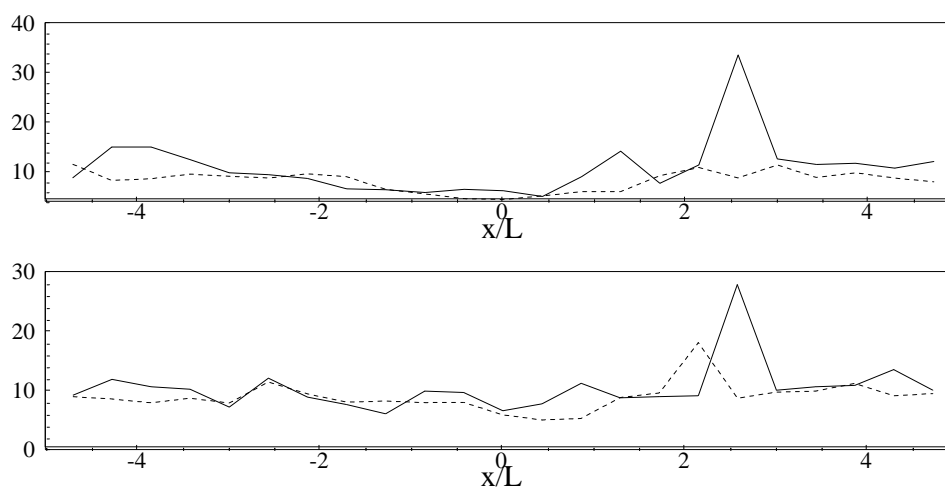


Fig. 2 Top: streamwise variation in the streamwise tree displacement ratio (maximum/mean), along the hill. Bottom: streamwise variation in the Von Mises strain ratio (maximum/mean), along the hill. Case of a pine forest canopy with (solid line) or without (broken line) an understorey. The hill top is located at $x/L = 0$.

Fig. 2 shows the same variables as Fig. 1, for this hill flow. In both understorey cases the tree deflection and Von Mises stress ratios tend to decrease slightly from positions upstream of the foot of the hill up to the top of it. The absolute magnitude of the displacement and stress slightly increases but, as the flow velocity increases within the canopy on its way up to the hill top, their mean values increase too, at a slightly larger rate. In the understorey case both variables exhibit a marked peak at about $x/L = 2.5$, i.e. near the downwind foot of the hill. This region is located somewhat upstream than the region identified by Dupont et al. (2008) as being particularly intermittent and strongly dominated by sweep motions. With no understorey a slight maximum is visible on the Von Mises stress ratio, but a little less downstream ($x/L \approx 2$) than in the previous case.

Conclusion

A one-way coupled model between turbulent flow and plant motion has been presented. It consists in using a LES model in various landscape and canopy configurations to produce time series of instantaneous velocity components, and later use these velocities to force a dynamic tree model. Two cases have been explored, an edge flow and a flow over a forested hill. In the absence of any understorey (which is typically the case of a maritime pine forest) the streamwise variations in tree displacement and internal stress are fairly smooth. However, when the leaf area is distributed over the whole depth of the canopy, regions of larger tree vulnerability to windload were identified, at a few canopy heights downstream of the edge in the first case, and at 2-3 hill length scales in the second one. This preliminary study shows the potential of this approach since these particular regions could not be a priori identified on the sole basis of the mean wind and turbulence fields. A more systematic study will be carried out in the future, in order to cover a wider range of canopy and landscape configurations.

Acknowledgements

Financial support from the ANR programme “Chêne-Roseau”, involving Inra, Inria and Ecole Polytechnique, is gratefully acknowledged.

References

1. Dupont, S., Brunet, Y., (2008): *Influence of foliar density profile on canopy flow: a large-eddy simulation study*. Agric. For. Meteorol. 148: 976-990.
2. Dupont, S., Brunet, Y., (2008): *Edge flow and canopy structure: a large-eddy simulation study*. Boundary-Layer Meteorol. 126: 51-71.
3. Dupont, S., Brunet, Y., (2008): *Impact of forest edge shape on tree stability: a large-eddy simulation study*. Forestry. 81: 299-315.
4. Dupont, S., Brunet, Y., (2009): *Coherent structures in canopy edge flow: a large-eddy simulation study*. J. Fluid Mech. 630: 93-128.
5. Dupont, S., Brunet, Y., Finnigan, J.J., (2008): *Large-eddy simulation of turbulent flow over a forested hill: validation and coherent structure identification*. Q. J. Roy. Meteorol. Soc. 134: 1911-1929.
6. Kerzenmacher, T., Gardiner, B.A., (1998): *A mathematical model to describe the dynamic response of a spruce tree to the wind*. Trees. 12: 385-394.
7. Moore, J.R., Maguire, D.A., (2005): *Natural sway frequencies and damping ratios of trees: influence of crown structure*. Trees. 19: 363-373.
8. Sellier, D., Brunet, Y., Fourcaud, T., (2008): *A numerical model of tree aerodynamic response to a turbulent airflow*. Forestry. 81: 279-297.
9. Finnigan, J.J., Brunet, Y., (1995): *Turbulent airflow in forests on flat and hilly terrain*. In : Wind and Trees. Coutts, M.P., Grace, J. (Eds.), Cambridge University Press, Cambridge, 3-40.

***Mechanical advantage of epidermal cells over stomatal guard cells,
estimated from transient changes of leaf-level stomatal conductance
for***

Anu Sober, Julia Shilina

University of Tartu, Institute of Ecology and Earth Sciences, Tartu, Estonia

Abstract

Previous analyses of stomatal mechanics have demonstrated, that the turgor - generated force of the epidermal cells dominates that of the guard cells in determining stomatal aperture (DeMichele, Sharpe, 1973, 1974, Sharpe and Wu, 1978, 1979). It was interpreted based upon geometric relationships calculated from anatomical dimensions of guard and epidermal cells (Wu et al. 1984). Domination of epidermal cells was seen as transient increase in stomatal conductance in our experiments with rapid desiccation of leaves and occurred in wide range of deciduous tree species. These transients in stomatal conductance were different in different species, as it was expected from different cell dimensions, measured for these species (Aasamaa, Sober, 2001). In general, transient stomatal opening during leaf desiccation was more pronounced in shade tolerant tree species (with bigger values of leaf hydraulic resistance) than in pioneer species with smaller hydraulic resistance of leaves. However, these transients in stomatal conductance also widely varied in one species (dependently on leaf position in canopy light gradient and initial transpiration rate). We used a simple mathematical model to analyse transient changes of g_s in desiccation experiments. The mechanical advantage of epidermal cells over guard cells.

Tapering of vascular elements from roots to distal shoots in Pinus sylvestris, Picea abies and Betula pendula

Anna Lintunen¹ and Tuomo Kalliokoski^{1,2}

¹ Department of Forest Ecology, University of Helsinki, Finland;

² Finnish Forest Research Institute

Abstract

We studied the effect of the tree architecture on the tapering of the xylem conduits along the water transport pathway from roots (diameter > 2 mm) to distal shoots or leaf petioles in *Pinus sylvestris* L., *Picea abies* (L.) H. Karst., and *Betula pendula* Roth. We determined the difference in the mean conduit size between the different organs i.e. lateral roots, main root, stem, branches, and leaf petioles. We also applied the general scaling model of plant vascular anatomy (WBE model) to our data in order to examine its assumption of the conduit size dependence on the branch generation (BG). The average conduit diameter decreased at whole tree level when moving from roots to stem and branches in all the studied species, and further to leaf petioles in *B. pendula*. This pattern was illustrated by the significant relationship between BG and the mean conduit diameter in all species. However, aboveground, stem and branches had different patterns; conduit tapering was steeper in branches than in stems. Conduit diameter at the beginning of each branch was independent of its position in the crown and, therefore, the WBE-like pattern was possible to observe only when the first segment of the each branch was assigned BG=1 i.e. the effect of stem furcations below the branch on BG was removed. After this modification, observed pattern in *P. sylvestris* and *B. pendula* corresponded the predictions of the WBE model quite well, whereas in *P. abies*, conduits tapered more slowly than predicted by the WBE model. In the aboveground woody compartments, mean conduit diameter decreased clearly in all species with increasing Gravelius order (GO). Belowground, similar pattern was observed clearly in *B. pendula* and slightly in *P. sylvestris*, while conduit diameter was rather stable in *P. abies*. In leaf petioles, mean conduit diameter was not affected by GO.

Introduction

Xylem conduits have been observed to taper along the water pathway from the roots to stem base, and finally to the leaves, e.g. [1, 2, 3]. Sanio in 1872 [4] found that tracheid diameters in *Pinus sylvestris* increased from the apex downwards until a maximum was reached and declined thereafter until to the stem base, but there was also differences in conduit characteristics between branches, stems and roots. Zimmermann [5, 6] deduced the reason for conduit tapering to be in controlling the water distribution. By having the lowest conductivities in the minor branches at the end of the flow path, plant can control the distribution of water regardless of the transport distance, which would lead to similar values of total root-shoot conductance despite of different path lengths.

West, Brown and Enquist [7, 8], recently stated in their model of universal scaling of vascular networks (hereafter referred as WBE model) that the plant vascular architecture conforms to the energy minimization principle leading to the tapering of conduits from the stem base to the photosynthesizing organs. WBE-model employs several assumptions about tree architecture e.g. crown is constituted with self-similar branching pattern, leaves are situated at a terminal branching generation (BG), and conduits furcate in each step to next BG, and thus conduit tapering appears to be continuous on a tree level. Branch generation follows the developmental sequence starting from proximal segment at stem base as generation 1, its children as generation 2 etc. At whole tree level, the

first two assumptions correspond Leeuwenberg's model in the tree architecture classification of Hallé [9].

The obtained empirical results seem to both support and question the general hypothesis of conduit tapering along the BG. In stems of both angio- and gymnosperms more or less WBE-like tapering have been observed, e.g. [4, 10, 11, 12]. However, only in a few studies also side branches [13, 14] and root systems [15] have been accounted for. Nygren and Pallardy [15] tested the WBE-predictions with *Populus deltoides* and found WBE-like tapering at tree level. Yet tapering was not continuous along the BGs, but occurred rather as leaps from one morphological level to the next. This kind of pattern was observed also in studies concerning *B. pendula* [13, 14]. In fact, Mencuccini et al. [4] concluded that their model produced more precise congruence with data, when they let the tapering ratio change along the pathway. Their model suggested also steeper tapering in the roots compared to stems. Moreover, tapering of conduits may vary within individual trees during ontogeny [12], and between different species growing in different environments [11].

Since the architecture of our study species does not follow Leeuwenberg's model, and also self-similarity assumption is violated [16], question could be raised if, or how well, the tapering of conduits follows the pattern predicted by WBE model. Therefore, our general objective was to study how tree architecture affects the conduit diameter along the whole water pathway from roots to distal shoots in *Pinus sylvestris* L., *Picea abies* (L.) H. Karst., and *Betula pendula* Roth. The specific study question was to determine the effect of organ and branching pattern on conduit diameter.

Material and methods

Study material: Our study species were *Pinus sylvestris*, *Picea abies* and *Betula pendula*. The mixed study stands were located in Southern Finland around the Hyytiälä Forestry Field Station (61° 50'N, 24° 18'E, 160 m a.s.l.). The stands represented varying stand productivities according to Finnish forest type system [17]. Three individuals per species from dominant trees were sampled with mean age of 35 years, *Table 1*.

Table 1. Characteristics of the studied, naturally born boreal tree species growing in mixed forests.

Study tree number	Tree species	Forest type	Stand characteristics, per species/total			Study tree information		
			No of trees per ha	Mean height, m	Mean D _{1.3} ,cm	Tree age, years	Tree H, m	D ₀ , cm
1	<i>P. sylvestris</i>	VT	390/1900	8.7/8.2	10.4/8.8	37	11.23	17.1
2	<i>P. sylvestris</i>	VT	390/1900	8.7/8.2	10.4/8.8	33	10.33	14.9
3	<i>P. abies</i>	VT	920/1900	7.9/8.2	8.7/8.8	43	7.91	15.5
4	<i>P. abies</i>	VT	920/1900	7.9/8.2	8.7/8.8	40	10.88	16.6
5	<i>B. pendula</i>	VT	480/1900	8.8/8.2	7.9/8.8	31	11.52	13.5
6	<i>B. pendula</i>	MT	480/5690	12.9/8.2	11.5/8	26	11.58	12.2
7	<i>P. sylvestris</i>	OMT	3150*/4380	14.4/8.8	14.4/8.4	39	15.54	19.3
8	<i>P. abies</i>	OMT	270/4380	5.8/8.8	6.0/8.4	34	14.10	15.5
9	<i>B. pendula</i>	OMT	530/4380	14.0/8.8	12.6/8.4	31	18.46	20.0

* Planted

Architectural measurements : The study trees were felled gently after which both their above- and belowground architecture was measured. The crown 3D-architecture was determined by digitizing five sample branches shoot by shoot. Sample branches were systematically chosen to represent all sections of the crown from the lowest branch to the top. Digitizing was done with Polhemus Fastrak, equipped with a digitizing pen and Longranger-transmitter (Polhemus Inc., Colchester, VT, USA). All

roots attached to the root collar were exposed to the first branching event, and 1-3 sample roots per tree were selected. Main branch and all lateral branches of sample roots were excavated down to the preset minimum diameter of 2 mm. Excavation was carried out by a pneumatic Soil-Pick tool (MBW SP125; M-B-W, Ltd., Bolton, UK). Details of the root field data are described by Kalliokoski et al. [18]. We characterized the tree architecture using tree organs, Gravelius ordering (GO) [19] and branching generation (BG), Fig 1.

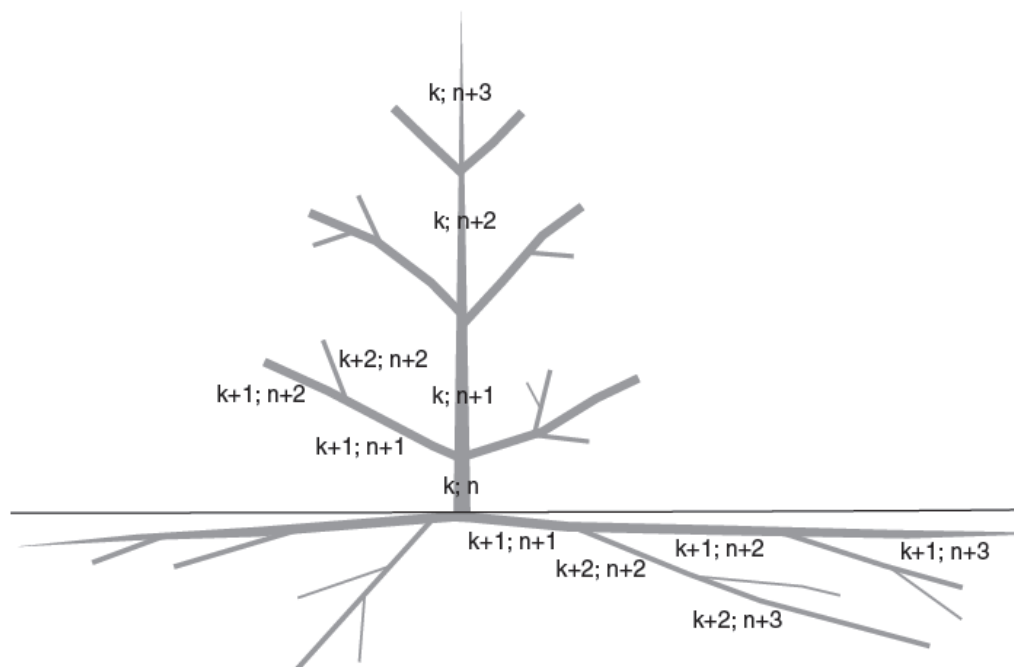


Fig. 1 Schematic figure of the structural hierarchy patterns used in this paper. Gravelius order (GO) assigns the same order number (k) to segments belonging to the same axis and one order number higher to lateral segments ($k+1$, $k+2$). Stem is the main axis assigned the order 1 (k); lateral branches attached to stems are assigned the order 2 ($k+1$) etc. (Barthélémy and Caraglio 2007). Similarly in belowground parts, main axis of the root is assigned the order 2 ($k+1$), and lateral branches get one order higher ($k+2$) etc. Branching generation (BG) of a segment, in turn, follows the developmental sequence starting with proximal segment at stem base as generation 1 (n), its children as generation 2 ($n+1$) etc. BGs are negative values belowground.

Sampling: Vascular samples were taken so that the whole water pathway was covered i.e. from the 2-mm lower limit in roots to the final segment in branches (leaf petioles in *B. pendula*, distal shoots in conifers). Six stem discs were collected: the first disc just above the root collar and one below each sample branch. Analogously, from the sample roots, 5-6 discs were collected along the main axis. From lateral branches three discs were sampled from each existing GO both in the above- and belowground compartments. Total number of sample discs was 547 and 313 in above- and belowground, respectively.

The tissue samples were stored in a freezer, petioles in liquid nitrogen. Transverse sections of defrosted aboveground samples were taken with sledge microtome with a thickness of 100-150 μm . The root samples were sectioned with a cryomicrotome fitted with disposable microtome blades at thickness of 16 μm . The petioles were embedded into the paraffin, and cut with rotary microtome at thickness of 8 μm [20]. All the sections from stem, branches and petioles were stained with the mixture of safranin and Alcian blue (ratio 1:2).

Digital images were taken with digital cameras mounted on a microscope. The petiole samples were imaged as a whole, whereas from other samples a subsample was taken from pith to bark; in roots a path of successive images with even distances, and in stem discs and branches same growth rings were followed through the different heights. Early and late wood of conifers was separated. In stem discs, three images were taken following a south line from early to late wood: from the second outer most growth ring, from one ring in the middle of the disc, and from the second innermost growth ring. In branches, even distances were used in selection of the measured growth rings. If the reaction

wood was observed in the sample, the effect of it was avoided by taking images from the side of it [21].

Image and data analysis: The images were analyzed with Image-Pro Plus imaging software (Media Cybernetics Inc., Bethesda, Maryland, USA). From the images of the crown samples, the area of the conduit lumen was measured. Conduit diameter was calculated assuming conduits to be circular. In roots and petioles, lumen diameter was directly measured as a mean of several directions. The number of measured conduits per image was 101-613 in leaf petioles, 8-71 in branches, 25-273 in stem and 4-145 in roots. Total number of measured conduits in the study was 114 699.

According to the WBE-model conduit radius (v) tapers (1):

$$\frac{v_{k+1}}{v_k} = n^{-\frac{b}{2}} \quad (1)$$

where n is the number of links formed in a branching point, k is the link order, and b is a parameter. Since we did not take samples at all branching generations and n varied between 2 and 6, equation (1) was modified:

$$v_{k+q} = v_k \sum_2^6 f n^{-\frac{qb}{2}} \quad (2)$$

where f is the observed relative frequency of each n class and q is the number of BG between two subsequent diameter measurements [15]. Non-linear regression was used to iterate the value of parameter b from measurements of each tree species. Value 1/6 [8] was used as an initial guess for the iterations. The observed conduit radius at the 2 mm limit in roots was used as initial v_k . Values for initial v_k was 21 μm , 16.5 μm , and 40 μm for *P. sylvestris*, *P. abies*, and *B. pendula*, respectively.

Statistical analyzes were carried out with SAS Statistical Software v. 9.1 (SAS Institute, Cary, North Carolina, USA). Differences between organs and gravelius orders were tested by analysis of variance. Tukey-Kramer paired comparisons method was used for multiple comparisons. In statistical testing, variables were transformed logarithmically in order to normalize variables and remove heteroscedasticity of residuals if needed.

Results and discussion

The average conduit diameter decreased at whole tree level when moving along the water pathway from roots to stem and branches in all the studied species, and further to leaf petioles in *B. pendula*, Fig 2. In *P. sylvestris* and *B. pendula* also lateral and main roots distinguished from each other, conduits being larger in main roots, Fig 2. This result corresponds the well-known general phenomenon that conduit dimensions differ between different tree organs [1, 2, 3, 6, 22, 23].

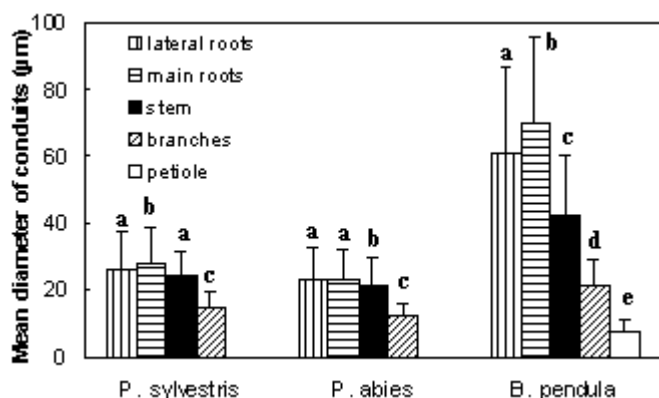


Fig. 2 Average conduit diameter in different organs of *Pinus sylvestris*, *Picea abies* and *Betula pendula*. In stems and branches, only spring wood was measured. Error bars indicate standard deviation. Distinct letters indicate to significant differences ($P < 0.05$) between organs within each species based on Tukey's test made with log-transformed values.

The more detailed characterization of tree architecture revealed that in the aboveground woody compartments, mean conduit diameter decreased clearly in all species with increasing GO, Fig 3. Belowground, similar pattern was observed clearly in *B. pendula* and slightly in *P. sylvestris*, while conduit diameter was rather stable in *P. abies*, Fig 3. The pattern of decreasing conduit diameter

between hierarchical branch levels has been observed earlier in the crown of *B. pendula* by Atala and Lusk [13] as well as by Sellin et al. [14], and in the crown of *P. deltoides* by Nygren and Pallardy [15]. In the studies of Atala and Lusk as well as Nygren and Pallardy, branch hierarchy was described with morphological level instead of organs and GO. In small trees, the difference between morphological level and GO is rather small, the only difference being the grouping of those "terminal"/"leafy" branches that are located at the end of each "primary"/"main" branch as an extension of the main axis (compare the Fig. 2 in Nygren and Pallardy [15]). Nygren and Pallardy [15] reported also decrease in conduit diameter when moving from lateral roots to main roots i.e. opposite trend than in our dataset.

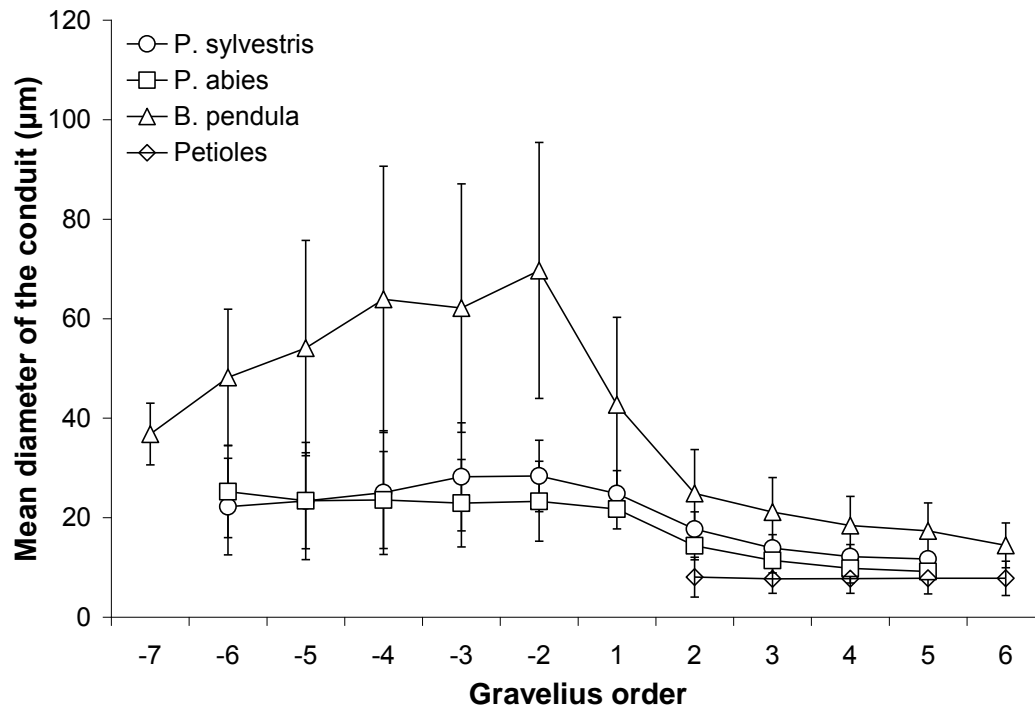


Fig. 3 The effect of Gravelius order on mean conduit diameter in *Pinus sylvestris*, *Picea abies* and *Betula pendula*. The markers denote to mean conduit diameter and the error bars denote to standard deviations. GOs are positive aboveground and negative belowground. Vessel diameter in the petioles of *B. pendula* is presented separately.

We did not find difference in the diameter of petiole vessels related to GO or BG, although measured petioles were found at GO levels from 1 to 6. Invariant vessel radius in petioles was found also in *P. deltoides* [15]. Petioles are mechanically supported by turgor pressure and collenchyma and thus vessels are free from any mechanical task [24] other than that caused by water pressure. The constant vessel size in terminal units is in accordance with the assumptions of the WBE model [25], although the terminal units can be in birch at any existing BG contradictory to that assumed in WBE [7, 8].

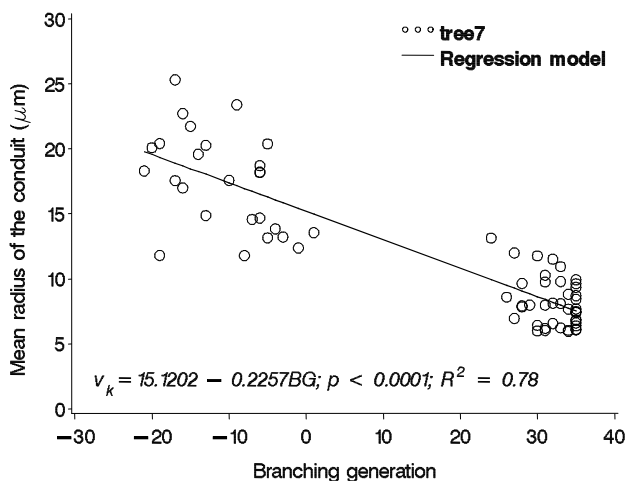
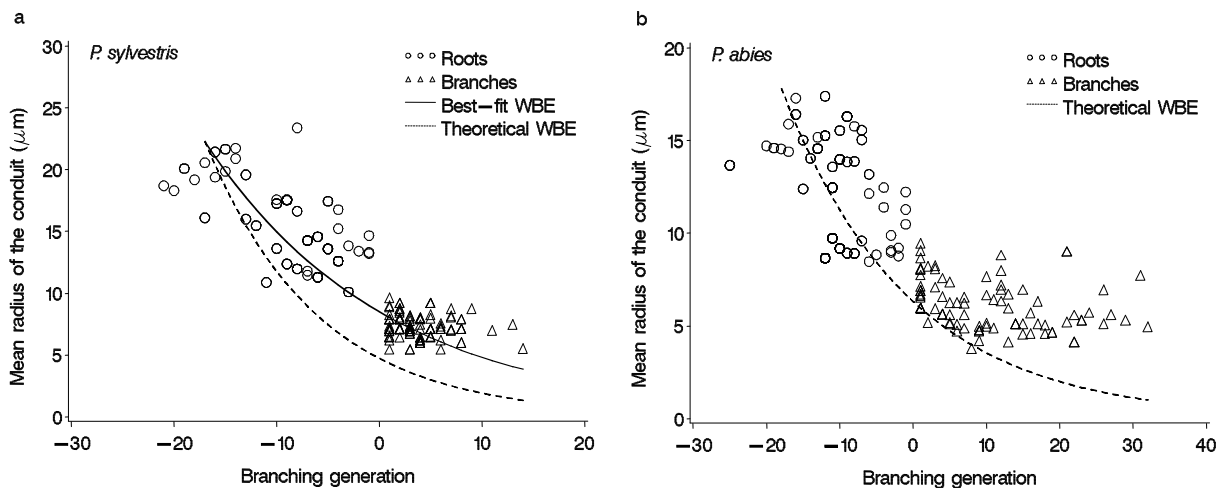


Fig. 4 Conduit size dependence of the branching generation (BG) at whole tree level in a *Pinus sylvestris* tree. v_k =conduit radius. Belowground $BG < 0$ and aboveground $BG > 0$.

Mean conduit diameter decreased along the increasing BG from roots towards the crown top in all species, Fig 4. However, tapering of the conduits was different in different compartments and thus continuous tapering along the BG predicted by the WBE model [8] applied only for roots in our data. Nevertheless, at whole tree level, tapering can be seen as the conduit diameter changes when moving from organs and orders to another [13, 15]. A distinct deviation from the WBE model predictions was that conduit tapering was much slower in stem than predicted by the model; values of parameter b were essentially zero in stems of all species. Therefore, we calculated values of b parameter for dataset consisted only of the roots and branches. In addition, conduit diameter at the beginning of each branch was independent of its position in the crown, and therefore WBE-like curve was possible to observe only when the first segment of each branch was assigned with $BG=1$ i.e. the effect of stem on BG was removed. After this modification, observed tapering patterns corresponded the predictions of the WBE model more closely. Yet, in all species, conduits tapered more slowly than predicted by the WBE model, Fig. 5.



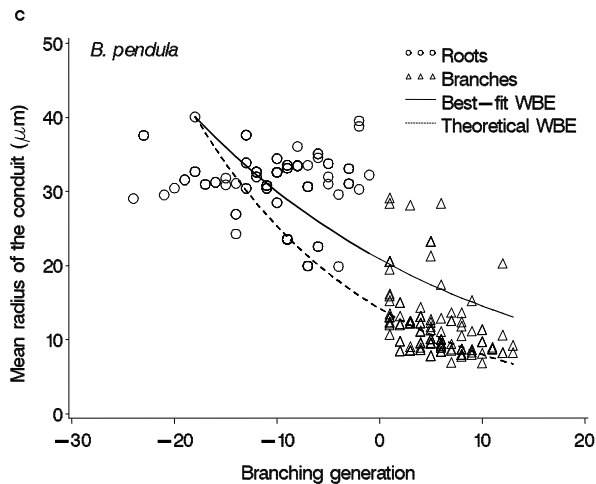


Fig. 5 The effect of branching generation (BG) on mean conduit diameter in roots and branches of a) *Pinus sylvestris*, b) *Picea abies*, and c) *Betula pendula*. In branches, the first segment was assigned as BG=1 in order to remove the effect of stem. Solid curves represent WBE estimations with best-fit b -parameter values and mean n values; 0.1032 and 3 for *P. sylvestris*, and 0.1047 and 2 for *B. pendula* respectively. Dashed line represents values obtained with same n values and theoretical b value 1/6. For *P. abies*, non-linear regression produced unrealistic low b -value and, thus, the curve is not drawn. The conduit radius used as a starting point for recursion was set according to the measurements as 21 μm at the BG -19 for pine, and 40 μm at the BG -18 for birch.

As the architecture of our study species does not fulfill the assumptions of WBE, it is not unexpected to have results that differ from its predictions. The fitted values of parameter b ; 0.1032, 0.0205 and 0.1047 for *P. sylvestris*, *P. abies*, and *B. pendula* respectively, did not correspond to the value 1/6 predicted by the WBE model [8]. The exception was branches of *B. pendula*, in which b had the value of 0.1413. Mäkelä and Valentine [26] have shown that the hydrodynamic significance of this factor is debatable, because the value 1/6 of b does not result in invariant resistance to water flow as claimed by West et al. [8]. Yet, when only roots and branches were accounted for, curves derived with b value 1/6 conformed to data quite well. Thus, although the actual interpretation of 1/6 power tapering is debatable, it seems to grasp something essential of conduit tapering between plant organs. The results of this study are in line with some earlier results that while the WBE model has gained considerable support in tests considering general patterns in plants, testing it on real trees presents a challenge [27]. Observed deviation of the WBE model in this study may be explained as a result of different crown structures from that assumed in it: branches were not of equal radii in branching points and terminal units had not the same BG. Also the extension of the measurements to side branches in addition to the main pathway clearly showed that assumption of the constant tapering at whole tree level may be oversimplification of the complex structure.

In a previous paper [4], steeper anatomical scaling has been predicted in roots compared to stems, because of the lower construction costs of thinner walled root conduits. Roots have lower mechanical requirements and lower risk of implosion following from less negative water potentials. Our results support this hypothesis in conifers. However, in *B. pendula*, tapering of the conduits was steeper in the branches than in roots. In the crown, tracheids and to some extent also vessels of diffuse-porous trees participate into mechanical task, which is probably one of the explanations of why the tapering in the stem strongly deviated from that predicted by the WBE model for optimal water transportation. Perhaps the vascular network in plants is a compromise between optimization of production with minimum costs and survival under limiting water conditions, since efficient water transportation and survival under high negative pressures are best achieved in different water transport systems [13].

Conduits increase in the stem from pith outwards, from juvenile to mature wood [28]. When conduits from the second growth ring from stem surface were analyzed separately in the trunk and plotted against relative height from the stem base, the decrease in the vessel size in *B. pendula* from stem base to the top was clear, but in conifers, no trend occurred, Fig 6. In roots, no clear pattern from pith outwards was observed; conduit size increased, was quite stable, or even decreased. This could be the result of different mechanical demands of the proximal and distal parts of the roots [29].

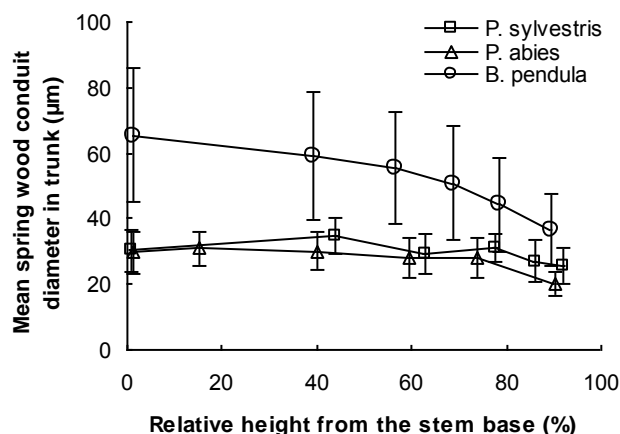


Fig. 6 The effect of relative height on mean conduit diameter in stem in a growth ring of the same year (second outer most ring) in *Pinus sylvestris*, *Picea abies* and *Betula pendula*. The mean conduit diameters of the measured three trees per species are presented together with standard deviations. The relative height on x-axis is calculated as mean of the sample heights from measured trees.

Conclusion

It is a well known phenomenon in the studied tree species that dimensions of the xylem conduits change in main stem from stem base to leaves. Nevertheless, the pattern of conduit tapering within a whole pathway from roots to shoots through branches of varying hierarchies was not determined earlier. We have presented here the conduit tapering inside different compartments of three boreal tree species, two conifers and one broadleaved species. At a whole tree level, we did not find tapering according to the WBE model. However, considering only roots and branches, and removing the effect of the branch position within crown, tapering followed predictions of the WBE model more closely. It is an interesting question for further studies, if the found pattern of decreasing conduit diameter between GOs is a general pattern in trees of similar architecture with the studied trees.

Acknowledgements

We thank our supervisors Pekka Nygren, Risto Sievänen and Pekka Kaitaniemi. We also thank all the trainees that assisted us in the field and laboratory. We appreciate the help we got from Metla, especially from Tuula Jyske. Thank you also for Teemu Hölttä for constructive comments on the manuscript. The study was funded by the Academy of Finland (Projects 210875 and 208661) and by the Finnish Graduate School in Forest Science.

References

1. Baas, P. (ed), (1982): *New perspectives in wood anatomy*. Nijhoff, Junk, The Hague: 252 pp.
2. Bailey, I.W. (1958): *The structure of tracheids in relation to the movement of liquids, suspensions, and undissolved gases*. In: Thinman, K.V. (ed) *The physiology of forest trees*. Ronald, New York: pp 71-82.
3. Fegel, A.C. (1941): *Comparative anatomy and varying physical properties of trunk, branch and root wood in certain northeastern trees*. Bulletin of the N.Y. State College of Forestry at Syracuse University. Technical Publication No. 55, vol. 14: 5-20.
4. Mencuccini, M., Hölttä, T., Petit, G. and F. Magnani, (2007): *Sanio's laws revisited. Size-dependent changes in the xylem architecture of trees*. Ecology letters. 10: 1084-1093.
5. Zimmermann, M.H. (1978): *Hydraulic architecture of some diffuse-porous trees*. Canadian Journal of Botany. 56: 2286-2295.
6. Zimmermann, M.H. (1983): *Xylem structure and the ascent of sap*. Springer-Verlag, Berlin: 143 pp.
7. West, G.B., Brown, J.H. and B.J. Enquist, (1997): *A general model for the origin of allometric scaling laws in biology*. Science. 276: 122-126.

8. West, G.B., Brown, J.H. and B. J. Enquist, (1999): *A general model for the structure and allometry of plant vascular systems*. Nature. 400: 664-667.
9. Hallé, F., Oldeman, R.A.A. and P.B. Tomlinson, (1978): *Tropical trees and forests: an architectural analysis*. Springer-Verlag, Berlin: 441 pp.
10. Anfodillo, T., Carraro, V., Carrer, M., Fior, C. and S. Rossi, (2006): *Convergent tapering of xylem conduits in different woody species*. New Phytologist. 169: 279-290.
11. Coomes D.A., Jenkins, K.L. and L.E.S. Cole, (2007): *Scaling of tree vascular transport systems along gradients of nutrient supply and altitude*. Biology Letters: 86-89.
12. Weitz, J.S., Ogle, K. and H.S. Horn, (2006): *Ontogenetically stable hydraulic design in woody plants*. Functional Ecology. 20: 191-199.
13. Atala, C. and C.H. Lusk, (2008): *Xylem anatomy of Betula pendula Roth saplings: relationship to physical vascular models*. Guyana Botany. 65: 18-27.
14. Sellin, A., Rohejärvi, A. and M. Rahi, (2008): *Distribution of vessel size, vessel density and xylem conducting efficiency within a crown of silver birch (Betula pendula)*, Trees. 22: 205-216.
15. Nygren, P. and S. Pallardy, (2008): *Applying a universal scaling model to vascular allometry in a single-stemmed, monopodially branching deciduous tree (Attim's model)*. Tree Physiology. 28: 1-10.
16. Kalliokoski, T., Sievänen, R. and P. Nygren, (2009): *Tree roots as self-similar branching structures; axis differentiation and segment tapering in coarse roots of three boreal forest tree species*. Revised version under review in journal: Trees-Structure and Function.
17. Cajander, A.K. (1909): *Ueber Waldtypen*. Acta Forestalia Fennica. 1: 1-176.
18. Kalliokoski, T., Nygren, P. and R. Sievänen, (2008): *Coarse root architecture of three boreal tree species growing in mixed stands*. Silva Fennica. 42 (2): 189-210.
19. MacDonald, N. (1983) *Trees and networks in biological models*. John Wiley & Sons, Chichester.
20. Anderson, G. and J. Bancroft, (2002): *Tissue processing and microtomy including froze*, in Theory and practice of histological techniques, editors, J. D. Bancroft, M. Gamble: Churchill Livingstone, London, p. 85-107.
21. Timell, T. (1986): *Compression wood in gymnosperms, volumes 1-3*. Springer, Heidelberg: 2150 pp.
22. Oliveras, I.M., Martínez-Vilalta, J., Jimenez-Ortiz, T., José-Lledó, M., Escarré, A. and J. Pinöl, (2003): *Hydraulic properties of Pinus halepensis, Pinus pinea and Tetraclinis articulata in a dune ecosystem of Eastern Spain*. Plant Ecology, 169: 131-141.
23. Bhat, K.M. (1981): *Wood anatomy and selected properties of stems, branches and roots of Finnish birch species*. University of Helsinki, Department of logging and utilization of forest products. Doctoral dissertation: 22 pp.
24. McCulloh, K.A., Sperry, J.S. and F.R. Adler (2003): *Water transport in plants obeys Murray's law*. Nature. 421: 939-942.
25. Enquist, B.J. (2002): *Universal scaling in tree and vascular plant allometry: toward a general quantitative theory linking plant form and function from cells to ecosystems*. Tree Physiology. 22: 1045-1064.
26. Mäkelä, A. and H. T. Valentine, (2006). *The quarter-power scaling model does not imply size-invariant hydraulic resistance in plants*. Journal of Theoretical Biology, 243:283-285.
27. Niklas, K.J. (2006): *Scaling the paths of resistance*. New Phytologist. 169: 219-222.
28. Saranpää, P., Pesonen, E., Sarén, M., Andersson, S., Siiriä, S., Serimaa, R. and T. Paakkari, (2000): *Variation of the properties of tracheids in Norway spruce (Picea abies (L.) Karst.)*, in Cell and molecular biology of wood formation, editors, R. Savidge, J. Barnett and R. Napier: BIOS Scientific Publishers Limited, Oxford, p. 337-345.
29. Christensen-Dalsgaard, K.K., Ennos, A.R. and M. Fournier, (2008): *Are radial changes in vascular anatomy mechanically induced or an ageing process? Evidence from observations buttressed tree root systems*. Trees-Structure and Function. 22: 543-550.

Modelling waving crops using Large-Eddy Simulation

*Sylvain Dupont¹, Frédérick Gosselin², Charlotte Py³, Emmanuel de Langre²,
Pascal Hémon² and Yves Brunet¹*

*¹ INRA, UR1263 EPHYSE, France; ² LadHyX, CNRS-Ecole Polytechnique, France;
³MSC, UMR 7057 CNRS-Université Paris-Diderot, France*

Abstract

In order to investigate the possibility of modelling plant motion at the landscape scale, an equation for crop plant motion, forced by the instantaneous wind flow, is introduced in a large-eddy simulation (LES) airflow model that was previously validated over homogeneous and heterogeneous canopies. The canopy is simply represented as a poroelastic continuum medium, which is similar in its discrete form to an infinite row of identical rigid stems. Only one linear mode of plant vibration is considered. The two-way coupling between the plant motion and the wind flow occurs through the drag force term. This coupling model is validated on a crop canopy of alfalfa whose motions have been previously analysed in great details from video recordings. It is shown that the model is able to reproduce the well-known phenomenon of *honami*. Moreover, the wavelength of the main coherent waving patches, extracted using a bi-orthogonal decomposition (BOD) of the crop velocity fields, is in agreement with that deduced from video recordings. The spatial and temporal main characteristics of these waving patches exhibit the same dependence on the magnitude of the mean wind velocity as in the in-situ measurements. Also they differ from the coherent eddy structures of the canopy-top wind flow. Finally, it is observed that the impact of crop motion on the wind flow is negligible for current wind speed values.

Introduction

Turbulent wind flows over vegetation canopies are dominated by intermittent, energetic downward-moving gusts, known as large coherent eddy structures, which evolve in unorganised random background turbulence. It has been demonstrated that these coherent structures are generated by processes similar to those occurring in a plane-mixing layer flow [1]. Under the passage of those structures, plants sway like damped harmonic oscillators subjected to intermittent impulsive loading [2][3]. A striking visualisation of the interaction between wind flow coherent structures and plant motions on windy days is known as *honami*, which refers to wavelike crop motions [4][2]. While turbulent wind flow over canopies has been widely studied (see [5] for a review), coherent motions of plant canopies and their strong interactions with the wind flow have received so far little attention. Possibly the most detailed study on wind-plant interaction was performed by [6] and [7] from a video recording experiment of alfalfa and wheat crop motions, which allowed them to characterise the spatio-temporal motion of crops subjected to wind. Their experiment was completed with a linear stability analysis done with an analytical model coupling a mixing-layer flow with an oscillating vegetation canopy through a drag force [7]. With their linear stability analysis, they observed a lock-in mechanism similar in form to what is observed in vortex-induced vibrations. Hence, for a specific range of flow velocities, flow and vegetation canopy may move in phase. This lock-in mechanism was further studied by [8] for a water stream over aquatic plants from a revisited version of [7]'s model

The main motivations for better understanding wind-induced plant motion in a fully-coupled way are, as reported in the recent review of [9], (i) environmental applications such as agricultural

management for limiting forest and crop damage due to windthrow and lodging under high wind conditions, (ii) agronomical applications for improving plant growth and biomass production due to the thigmomorphogenesis effect [10], and (iii) biological or image production applications.

The wind-induced plant motion is all the more complex as agricultural landscapes often exhibit large spatial variability caused by the presence of different crops, clearings, roads, forest patches of various height, etc. Such heterogeneities influence turbulent structures of the lower atmosphere and so canopy motions. Because of the complexity of the various processes responsible for plant motions in heterogeneous landscapes, modelling both plant and flow dynamics appears necessary to quantify plant motion following their position in an heterogeneous environment.

Developing and validating such computational tool for better understanding wind-plant interaction is the subject of the present study. For that purpose, an equation of plant motion has been introduced into an atmospheric Large-Eddy Simulation (LES) model. Provided that the grid is fine enough, the LES technique allows one to have access to instantaneous dynamic fields and consequently is capable of reproducing wind gusts in a plant canopy since eddy motions larger than twice the grid mesh are explicitly solved, whereas only subgrid-scale eddy motions are modelled. In this modified LES model, the canopy is represented as a poroelastic continuum. This representation is similar in its discrete form to an infinite row of identical mechanical oscillators where only one linear mode of plant vibration is considered. The two-way coupling between plant motion and wind flow occurs through the drag force term. This modified LES model is validated against video recording of alfalfa crop motion performed previously by [6].

Material and methods

The Advanced Regional Prediction System (ARPS) used in this study was developed at the Center for Analysis and Prediction of Storms (CAPS) at the University of Oklahoma to simulate convective and cold-season storms as well as weather systems at larger scales. A detailed description of the standard version of the model and its validation cases are available in the ARPS User's Manual [11].

Recently, [12] modified the model so as to simulate turbulent flows at very fine scales ($0.1h$, where h is the mean canopy height) within canopies of fixed plants with the LES approach. To this purpose, a drag force approach was implemented by adding a pressure and viscous drag force term in the momentum equation and by adding a sink term in the equation for subgrid-scale turbulent kinetic energy in order to represent the acceleration of the dissipation of turbulent eddies in the inertial subrange. The mean turbulent fields and the development of coherent structures, as simulated by this modified version of ARPS, were successfully validated against field and wind-tunnel measurements, over homogeneous canopies [12], a simple forest-clearing-forest pattern [13][14][15] and a forested hill [16]. Here, the model is further extended so as to simulate plant motion and its strong interaction with the wind flow.

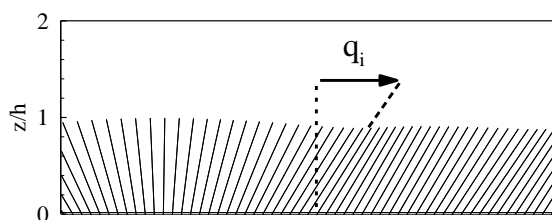


Fig. 1 Schematic representation of crop plants as rigid stems under wind where q_i is the canopy-top plant displacement in the i direction.

Plants of crop canopy can be seen as identical mechanical oscillating stems with two degrees of freedom, as verified by [17] and confirmed by vibration tests performed by [6] on alfalfa and wheat crops. Following the modal analysis, the deformation of plant stems can be decomposed into a set of different vibration modes such as its displacement q_i in the i direction is the sum of the contributions of each vibration modes: $q_i(t) = \sum_n \lambda_i^n(t) \varphi_i^n$, where φ_i^n represents the mode shape n of the stem and λ_i^n its associated displacement. As the architecture of crop plants considered in this study is “simple”, only one mode of vibration, i.e. the linear mode shape $\varphi_i = z/h$, is considered (see Fig. 1). This crop plant

representation is consistent with previous studies [7][18][19]. Plant displacements associated to higher modes should be unlikely significant. With this approach, plant stems are only characterized by their height h , mass m , non-dimensional damping coefficient ζ , and natural vibration frequency f_0 .

At crop scale, the canopy can be seen as a succession of infinite rows of identical bi-dimensional mechanical oscillating rigid stems, where each stem displacement is resolved from a simple mass-spring-damper equation. In order to use the same horizontal resolution between wind flow and plant motion, the canopy is not seen as a succession of individual stems but as a poroelastic continuum medium whose motion is described by the grid volume-averaged displacement $\tilde{q}_i | x, y, t |$ at canopy top. The continuous form of a mass-spring-damper equation writes as follows:

$$M \frac{\partial^2 \tilde{q}_i}{\partial t^2} + C \frac{\partial \tilde{q}_i}{\partial t} + R \tilde{q}_i = \bar{\rho} \int_0^h C_D \left| \tilde{u}_i - |1 - \delta_{i3}| \frac{x_3}{h} \frac{\partial \tilde{q}_i}{\partial t} \right| \left(\tilde{u}_i - |1 - \delta_{i3}| \frac{x_3}{h} \frac{\partial \tilde{q}_i}{\partial t} \right) \varphi_i dz \quad (1)$$

where $i \in \{1, 2\}$; t is time; x_i ($x_1 = x$, $x_2 = y$, $x_3 = z$) refer to the streamwise, lateral, and vertical directions, respectively; u_i ($u_1 = u$, $u_2 = v$, $u_3 = w$) is the instantaneous velocity component along x_i ; $M = m/3$; $C = c/h^2$; and $R = r/h^2 - mg/(2h)$, where g is the acceleration due to gravity. The damping coefficient c is computed from $c = 4\pi m h^2 f_0 \zeta / 3$, and the stiffness coefficient r is deduced from the relationship $f_0 = R / (4\pi^2 M)$, which leads to $r = 4\pi^2 m h^2 f_0^2 / 3 + m g h / 2$. The terms on the left-hand side of equation (1) represent, respectively, the inertia, damping, stiffness and gravity terms. The term on the right hand side represent the wind-induced load term. This latter term is proportional to the relative velocity between the wind u_i and the plant deflection velocity $(x_3/h) \partial \tilde{q}_i / \partial t$. In this term, $C_D = C_D^{plant} A_f^{plant}$, where C_D^{plant} and A_f^{plant} are the mean plant drag coefficient and frontal area density. For simplicity, the vertical profile of C_D is assumed constant with wind velocity and plant deflection, which is quite reasonable as only small wind speeds are considered within the canopy in this study.

Interactions between neighboring plants are neglected as they were found negligible by [7] for alfalfa crop canopy. Nevertheless, with this continuous form of crop motion equation, elastic contacts between plants could be in future easily considered as shown by [18] through an additional term depending on the second spatial derivative of plant displacement, transforming equation (1) to a wave like equation.

The two-way coupling between plant motion and wind flow occurs through the drag force term. Using the Einstein summation convention, the momentum equation, written for a Boussinesq fluid, is:

$$\begin{aligned} \frac{\partial \tilde{u}_i}{\partial t} + \tilde{u}_j \frac{\partial \tilde{u}_i}{\partial x_j} = & - \frac{1}{\bar{\rho}} \frac{\partial}{\partial x_i} \left(\tilde{p}'' - \alpha_{div} \frac{\partial \tilde{p}''}{\partial x_j} \right) - g \left(\frac{\tilde{\theta}''}{\bar{\theta}} - \frac{c_p}{c_v} \frac{\tilde{p}''}{\bar{p}} \right) \delta_{i3} \\ & - \frac{\partial \tau_{ij}}{\partial x_j} - \frac{C_D}{l^2} \left| \tilde{u}_i - |1 - \delta_{i3}| \frac{x_3}{h} \frac{\partial \tilde{q}_i}{\partial t} \right| \left(\tilde{u}_i - |1 - \delta_{i3}| \frac{x_3}{h} \frac{\partial \tilde{q}_i}{\partial t} \right) \end{aligned} \quad (2)$$

where the overtilde indicates the filtered variables or grid volume-averaged variables, l is the average plant spacing, δ_{ij} is the Kronecker delta, α_{div} a damping coefficient meant to attenuate acoustic waves, p the air pressure, ρ the air density, θ the potential temperature, τ_{ij} the subgrid stress tensor, c_p and c_v are the specific heat of air at constant pressure and volume, respectively. The terms on the right-hand side of equation (2) represent, respectively, the pressure-gradient force term, the buoyancy term, the turbulent transport term, and the drag force term induced by the vegetation.

In order to validate the present LES model on a homogeneous continuous alfalfa crop canopy against measurements of [6] and [7], four three-dimensional simulations were performed with different values of canopy-top wind speed U_h : 1.0, 2.0, 2.9 and 3.8 ms^{-1} . These wind speed values represent usual values observed over crop canopies. Extreme values of wind speed were not considered in this study. These four simulations are referred hereafter as case 1 to case 4. Properties of alfalfa plant were chosen similar as those deduced by [7] from an average of measured properties of six individual plants ($h = 0.69$ m, $m = 0.014$ kg, $f_0 = 1.05$ Hz, $l = 0.05$ m, $\zeta = 0.55$). The vertical distribution of the frontal area density of the alfalfa plant A_f^{plant} was assumed identical to the average vertical mass distribution of the six plants measured by [7]. The magnitude of A_f^{plant} was chosen so as to respect a leaf-area index (LAI) of about 3, which is typical of alfalfa crop [20]. The drag coefficient C_D^{plant} was taken as 0.2.

All simulations were performed with the same computational domain. This latter one extends over $30 \times 15 \times 8 \text{ m}^3$, corresponding to $200 \times 100 \times 65$ grid points in the x , y and z directions, respectively, and with a horizontal resolution of 0.15 m. The vertical grid resolution is 0.08 m below 3.5 m, above the grid is stretched using a hyperbolic tangent function. The lateral boundary conditions are periodic, the bottom boundaries are treated as rigid and surface momentum flux is parameterised by using bulk aerodynamic drag laws. A 2.5 m deep Rayleigh damping layer is used at the upper boundary in order to absorb upward propagating wave disturbances and to eliminate wave reflection at the top of the domain. Additionally, the flow is driven by a depth-constant geostrophic wind corresponding to a base-state wind at the upper boundary. The velocity fields are initialised using a meteorological pre-processor with a constant vertical profile of potential temperature and a dry atmosphere.

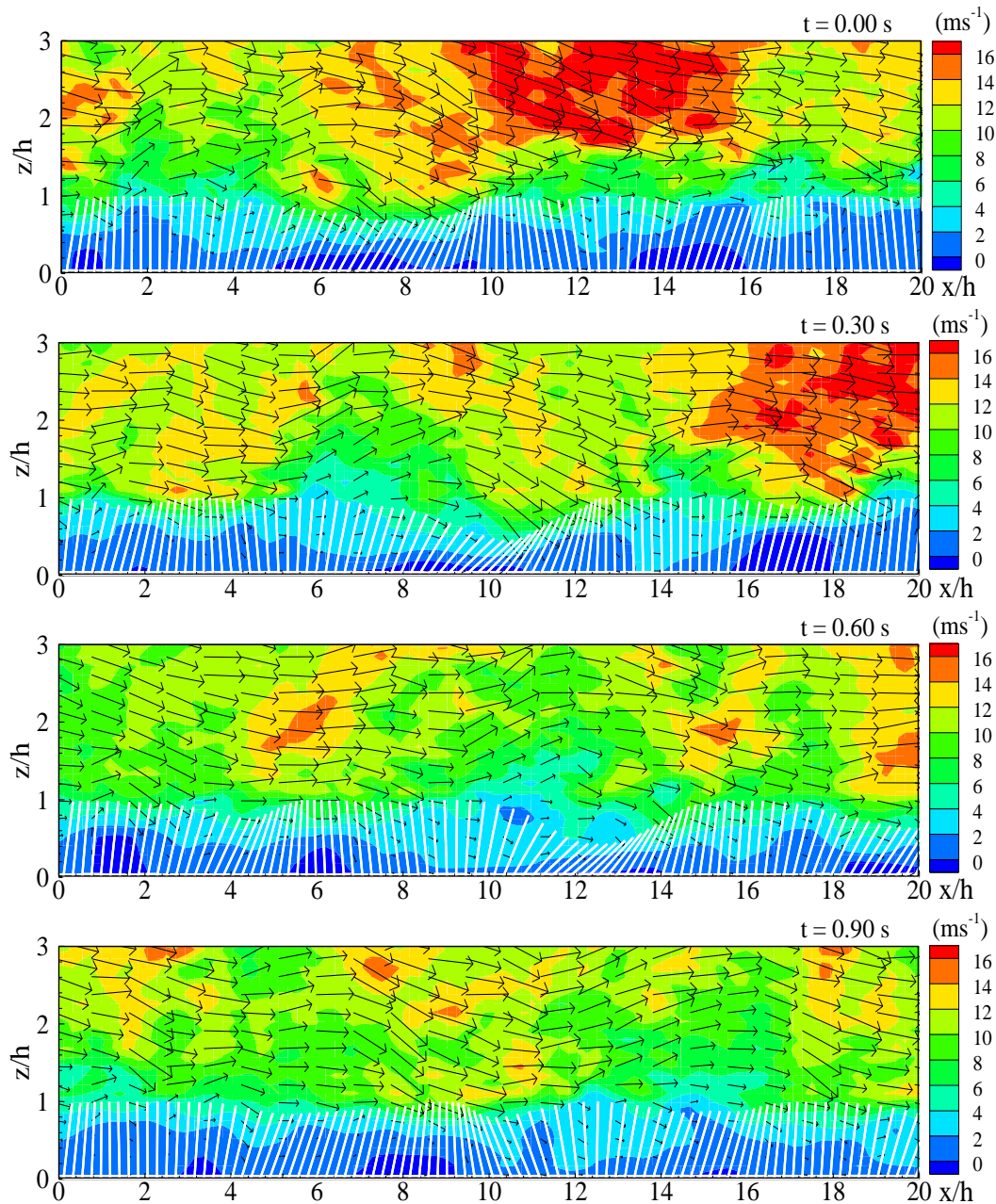


Fig. 2 Streamwise cross section of instantaneous wind-plant interaction at 0.30 second intervals during a period of 0.90 seconds (case 4). The background color represents the magnitude of the streamwise wind velocity, arrows wind vectors, and white stems sketch plant displacement under wind. For a better visualization, angular plant displacement was multiplied by a factor of 5.

Results and discussion

It is interesting at first to have a qualitative look at instantaneous wind-plant interaction simulated by our LES model. To that purpose, *Fig. 2* shows a time sequence of wind-plant interaction in a vertical streamwise slice over a 0.90 second period for the high wind speed case (case 4). The background color indicates the intensity of the streamwise wind velocity component, the arrows the wind direction, and the white stems sketch canopy plants where plant displacements have been accentuated in order to have a better view of the waving structures. At $t = 0$ s, a wind gust penetrates within the canopy around $x = 8h$ inducing a forward deflection of a group of plants. Then, after the gust passage, plants spring back ($t = 0.30$ s), and vibrate around their axis ($t = 0.60$ and 0.90 s), before being damped and hit by another gust. *Fig. 3* shows an instantaneous three dimensional view of the simulated alfalfa crop motion. The dark patches appearing on the crop surface correspond to regions where plants are highly deflected downwind with the passage of strong wind gusts as observed in *Fig. 2*. We observed from crop motion animation that these patches move essentially in the wind direction. Wind gusts inducing plant swaying are characterized by large positive values of u and large negative values of w (figure not shown). This is the signature of sweep motions, i.e. downward turbulent structures, which constitutes a part of the sweep-ejection cycle of canopy flow coherent structures. They are induced by the development or impingement of wind flow coherent structures at canopy top. These wavelike crop motions are known as *honami* waves; they also look like cat's-paws observed on water surfaces. Furthermore, unlike wind velocity, we observed that plant deflection (amplitude and velocity) exhibits a dominant periodicity of about 1 second (figure not shown), which corresponds to the natural vibration frequency of alfalfa plant, $f_0 = 1.05$ Hz.

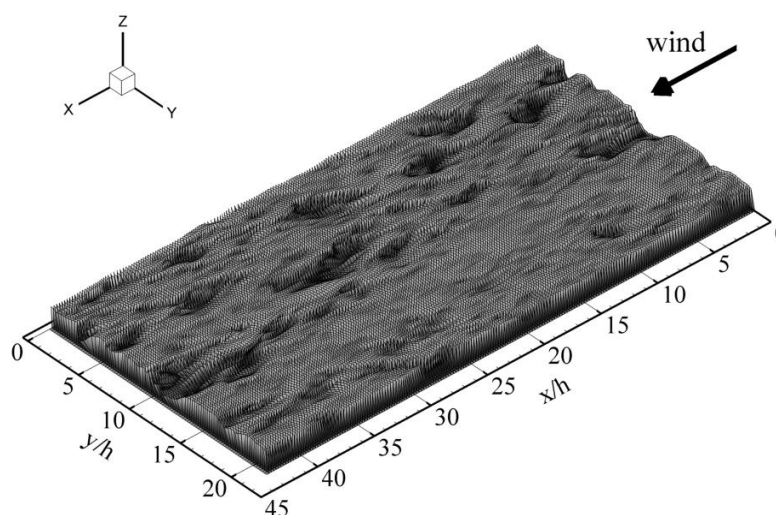


Fig. 3 Snapshot of the simulated alfalfa crop motion for case 4. For a better visualization, angular plant displacement was multiplied by a factor of 5.

The amplitude of plant deflection is about 0.1 m for a canopy top wind speed of about 10 ms^{-1} . This value is in agreement with the 0.1 m deflection observed by [7] for alfalfa stems under a vertically average windload of 3 ms^{-1} , which corresponds, from the average wind profile, to a canopy-top wind speed of about 9 ms^{-1} . The velocity of plant deflection is slightly more than one order lower than that of the wind flow. *Fig. 4* compares for various canopy-top wind speed U_h the standard deviation of plant velocity σ_ζ (where ζ is the scalar plant velocity at canopy top) simulated by our model with those deduced from measurements of [7]. The magnitudes of the simulated σ_ζ are in agreement with measurement values. Like the measurements, σ_ζ increases with U_h due to the enhancement of the wind turbulence induced by the larger canopy-top wind shear.

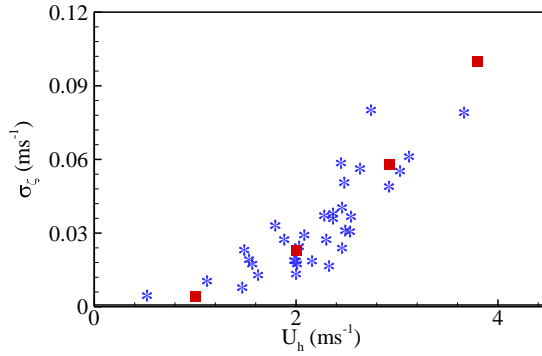


Fig. 4 Comparison between observed (stars) and simulated (squares) average standard deviation of alfalfa plant velocity against the canopy-top wind speed. The experimental dataset is from [7].

The main spatio-temporal features of plant waving structures identified in Fig. 3 were extracted for the four simulated cases, similarly as [6], from a bi-orthogonal decomposition (BOD) of the crop velocity fields, which were recorded during a 30-second period with a 10 Hz frequency. The Reader could refer to [21] for a complete review of the BOD approach and to [6] for its application on plant motion. The normalised wavelength λ_p/h and frequency f_p/f_0 of the main spatial organised crop structures deduced from the BOD technique, are plotted in Fig. 5 against the reduced velocity $U_r = U_h/(f_0 h)$. Compared to values obtained from video-recorded alfalfa crop motion by [7], simulated values of λ_p/h and f_p/f_0 are in relative good agreement although λ_p/h is slightly overestimated by the model. The ratio λ_p/h appears to increase with U_r while f_p/f_0 is independent on U_r . The reason for the slight overestimation of λ_p/h by our model is not clear but it could be related to the homogeneity of alfalfa plant properties considered in our simulation compared to the variability of plant properties in the real crop. These coherent motions are characterized by a frequency close to the natural vibration frequency of the plants and by a wavelength that increases with canopy-top wind speed.

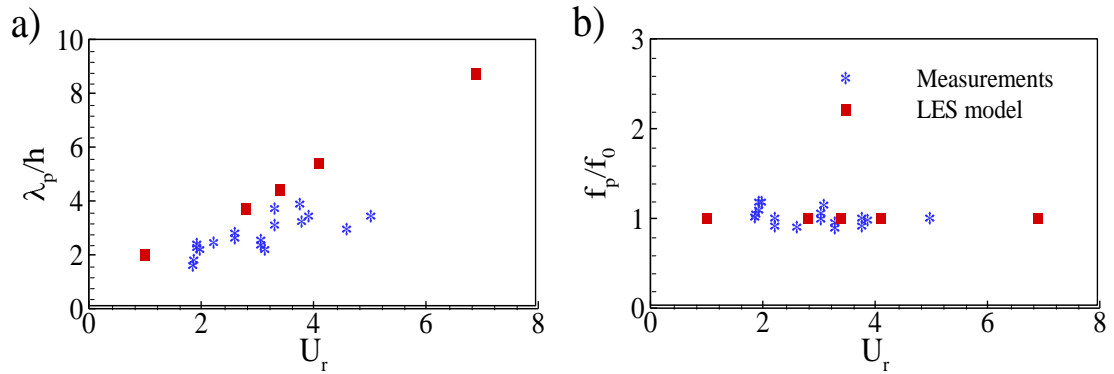


Fig. 5 Comparison between experimental measurements (stars) and LES (squares) of the normalised wavelength (a) and frequency (b) of coherent waving patches (extracted from bi-orthogonal decomposition (BOD) of alfalfa plant velocity field) versus the reduced velocity. The experimental dataset is from [7].

The wavelength λ_w of wind flow coherent structures was deduced for the four simulated cases from the peak wavenumber of the resolved-scaled spectrum of the vertical wind velocity at canopy top. In the four cases, the spectra exhibit the same peak λ_w around $3.8h$ (figure not shown). As a consequence, even though wavelengths of organised crop motion λ_p and turbulent structures λ_w are of the same order, they behave differently with increasing wind speed U_h . The wavelength of crop motion increases with U_h while its frequency is independent of U_h . Conversely, turbulent coherent structure wavelength is independent on U_h , as predicted by the plane-mixing layer analogy [1], while their frequency increases with U_h . Consequently, organised crop motion are not a direct signature of coherent eddy structures of the flow although the latter may initiate the former.

In order to estimate the importance of plant motion on wind flow, an additional simulation has been performed similarly as case 4 one, but with fixed plants. Plant motion has been found negligible on the

wind flow. As a consequence of this independence of the turbulent wind flow on plant motion, the increase of crop motion wavelength with wind speed obtained from our LES model results from passive motion of crop plants under the wind: a larger group of plant deflects downwind the passage of a coherent eddy as this latter one goes faster (higher wind speed) while the frequency of plant vibration remains unchanged. This result appears in contradiction with the lock-in mechanism predicted by the linear stability analysis performed by [7]. In a forthcoming paper [22], we observed that an improved version of the linear stability analysis of [7] and [8], including a realistic wind profile and an eddy viscosity deduced from LES, still turns out to predict a lock-in phenomenon in the velocity range where coherent canopy motions are observed. This discrepancy between linear stability analysis and LES may be attributed to the presence of a non-linear saturation mechanism in LES, independent on canopy motion, which is not considered in the linear stability analysis.

Conclusion

A three-dimensional two-way coupling model between wind flow and crop plant motion has been presented for the first time. This model consists of an atmospheric large-eddy simulation (LES) coupled with a simple mechanical oscillator equation for crop plant motion. The canopy is represented as a poroelastic continuum medium, which is similar in its discrete form to an infinite row of identical rigid stems. Only one linear mode of plant vibration is considered. We think that this simplified representation of crop plants is reasonable and should not impact significantly the realism of model results as only small plant displacements were considered in the present study.

This model has been validated successfully against video-recording measurement performed previously by [6][7]. The magnitude of plant displacement and velocity were simulated accurately by our model for various wind speed values. The bi-orthogonal decomposition (BOD) of plant velocity field has revealed the presence of coherent waving motion with spatial and time characteristics in agreement with those obtained by [7]. These structures correspond to *honami* motion usually observed over wheat crop in windy days. They have a time frequency close to the natural vibration frequency of the crop plants and a spatial wavelength of few canopy height that increases with the canopy-top wind speed. Although these organised structures of crop movements are initiated by wind-flow coherent eddy structures, their spatial and temporal characteristics differ. Indeed, spatial wavelength of canopy-top coherent eddy structures were observed independent on wind speed as predicted by the plane-mixing layer analogy of the canopy wind flow [1], while their frequency increases with wind speed. Hence, organised crop motions are not a mere footprint of coherent eddy structures. As a consequence, extracting wind flow information from crop motion is not straightforward.

Furthermore, for the range of wind speed considered in this study, up to 4 ms^{-1} , corresponding to usual values observed over crop fields, we observed that alfalfa plant motion has a negligible impact on wind flow and no lock-in mechanism was observed between wind flow and plant motion. The next steps of this study should consist in (i) studying with the LES the transient growth of the Kelvin-Helmholtz instability and its saturation over a canopy and (ii) developing a weakly non-linear stability analysis in order to confirm the importance of non-linear terms in minimizing the lock-in mechanism.

Finally, the LES model was only applied in the present study on crop canopy where plant structure is quite “simple” compared to tree one. In future, this model could be extended to forest canopy by representing tree as flexible stem with various modes of vibration and with interaction between neighboring trees. Such model should be able to simulate vegetated canopy motion at an heterogeneous landscape scale, and, therefore, should be able to quantify plant vulnerability to windload or wind stimulus on plant and its consequence on plant growth (thigmomorphogenesis) following plant position in the landscape.

Acknowledgements

We would like to thank the Center for Analysis and Prediction of Storms (CAPS) at the University of Oklahoma for providing the ARPS code. This work was performed using HPC resources from

GENCI-IDRIS (Grant 2009-i2009011833) as well as Ephyse cluster. Thanks are expressed to Ephyse computing team (P. Moreau, T. Rabemanantsoa, G. Pracros and Dr. M. R. Irvine) for their help with the cluster administration. We would like to thank Professor P. Huerre for insightful discussions on mixing layers. Financial support from the ANR program “CHENE-ROSEAU”, involving INRA, INRIA, and Ecole Polytechnique, as well as support from the FQRNT is gratefully acknowledged.

References

1. Raupach, M. R. and Finnigan, J. J. and Brunet, Y. (1996): *Coherent eddies and turbulence in vegetation canopies: The mixing-layer analogy*. Boundary-Layer Meteorology. 78: 351-382.
2. Finnigan, J. J. and Mulhearn, P. J. (1978): *Modelling waving crops in a wind tunnel*. Boundary-Layer Meteorology. 14: 253-277.
3. Gardiner, B. A. (1995): *The interactions of wind and tree movement in forest canopies*, Coutts, M. P and Grace J., Cambridge University Press. p. 485.
4. Inoue, R. (1955): *Studies of the phenomena of waving plant ("honami") caused by wind. Part 1: Mechanism and characteristics of waving plant phenomena*. Journal of Agricultural and Meteorology (Japan). 11: 71-82.
5. Finnigan, J. (2000): *Turbulence in plant canopies*. Annual Review of Fluid Mechanics. 32: 519-571.
6. Py, C. and de Langre, E. and Moulia, B. and Hemon, P. (2005): *Measurement of wind-induced motion of crop canopies from digital video images*. Agricultural and Forest Meteorology. 130: 223-236.
7. Py, C. and de Langre, E. and Moulia, B. (2006): *A frequency lock-in mechanism in the interaction between wind and crop canopies*. Journal of Fluid Mechanics. 568: 425-449.
8. Gosselin, F. and de Langre, E. (2009): *Destabilising effects of plant flexibility in air and aquatic vegetation canopy flows*. European Journal of Mechanical B/Fluids. 28: 271-282.
9. de Langre, E. (2008): *Effects of wind on plant*. Annual Review of Fluid Mechanics. 40: 141-168.
10. Moulia, B. and Combes, D. (2004): *Thigmomorphogenesis acclimation of plant to moderate winds greatly affects height structure in field-grown alfalfa (medicago sativa l.), an indeterminate herb*. Comparative Biochemistry and Physiology - Part A: Molecular & Integrative Physiology. 137 (3-S1): 77.
11. Xue, M. and Droegemeier, K. K. and Wong, V. and Shapiro, A. and Brewster K. (1995): *ARPS version 4.0 user's guide.*, , University of Oklahoma, Norman, OK: Center for Analysis and Prediction of Storms. p. 380.
12. Dupont, S. and Brunet, Y. (2008): *Influence of foliar density profile on canopy flow: a large-eddy simulation study*. Agricultural and Forest Meteorology. 148: 976-990.
13. Dupont, S. and Brunet, Y. (2008): *Edge flow and canopy structure: a large-eddy simulation study*. Boundary-Layer Meteorology. 126: 51-71.
14. Dupont, S. and Brunet, Y. (2008): *Impact of forest edge shape on tree stability: a Large-Eddy Simulation study*. Forestry. 81: 299-315.
15. Dupont, S. and Brunet, Y. (2009): *Coherent structures in canopy edge flow: a large-eddy simulation study*. Journal of Fluid Mechanic. 630: 93-128.
16. Dupont, S. and Brunet, Y. and Finnigan, J. J. (2008): *Large-eddy simulation of turbulent flow over a forested hill: validation and coherent structure identification*. Quarterly Journal of the Royal Meteorological Society. 134: 1911-1929.
17. Finnigan, J. J. and Mulhearn, P. J. (1978): *A simple mathematical model of airflow in waving plant canopies*. Boundary-Layer Meteorology. 14: 415-431.
18. Doare, O. and Moulia, B. and De Langre, E. (2004): *Effect of plant interaction on wind-induced crop motion*. Journal of Biomechanical Engineering-Transactions of the Asme. 126: 146-151.
19. Flesch, T. K. and Wilson, J. D. (1999): *Wind and remnant tree sway in forest cutblocks. II. Relating measured tree sway to wind statistics*. Agricultural And Forest Meteorology. 93: 243-258.
20. Russell, G. and Marshall, B. and Jarvis, P.G. (1990): *Plant canopies: their growth, form and function.*, , Cambridge University Press. p. 192.

21. Hemon, P. and Santi, F. (2003): *Applications of biorthogonal decompositions in fluid-structure interactions*. Journal Of Fluids And Structures. 17: 1123-1143.
22. Dupont, S. and Gosselin, F. and Py, C. and de Langre, E. and Hémon, P. and Brunet, Y. (2009): *Modelling waving crops using Large-Eddy Simulation: comparison with experiments and a linear stability analysis*. Journal of Fluid Mechanics. in revision: .

Continual modeling of water uptake by plant roots

A.A. Stein, S.A. Logvenkov, and E.N. Yudina

Institute of Mechanics, Moscow University, Russia

Abstract

The water and solute uptake by plant roots is investigated on the basis of multiphase continuum mechanics. The transport from the environment to the xylem is considered as the flow of a two-phase fluid through a solid framework. Two fluid phases, both containing a generalized solute, are identified with the intra- and extracellular fluids that fill the symplast and apoplast. The interphase mass exchange is regulated by membrane-type relations that take into account the active solute transport, the interface permeability to solute and water, and the osmotic water transfer. Calculations demonstrate good agreement with experimental data if the presence of active transport only in the outer (cortical) part of the root, a non-uniform radial distribution of the membrane permeability to the solute (higher in the outer part), and the presence of a localized inner barrier impermeable to the extracellular phase (Casparian bands) are assumed.

Introduction

We cannot assert that the mechanisms responsible for water and solute uptake by plant roots are in full measure known. It is agreed that the active solute transport and the osmotic displacement of water play an important part in this process but the sufficiency of these mechanisms, as well as the spatial organization of their operation, are a subject of discussion.

In order to explain various effects observed in experiments on xylem sap exudation from excised roots, the radial flow through the non-specialized root tissues that separate the xylem from the environment has been described using lumped parameter models in which coaxial root layers are treated as compartments separated from one another, the environment, and the xylem by membranes with different characteristics (see [1] and references thereafter) that include the rates of active transmembrane solute transport. This approach is fairly empirical and does not take into account the essential features of the functioning of the root as a distributed mechanical system [2].

Actually, the root tissues between the environment and the xylem are a complex mechanical system formed by cellular walls with two ways for water and solutes: extracellular (apoplastic) and intracellular (symplastic). The latter includes the inner spaces of the cells connected by plasmodesmata. There is mass exchange between the intra- and extracellular spaces.

In the radial direction the root mainly consist of a layer of cortex parenchyma cells and a layer of stele cells separated from the cortex by an endodermis layer. In the inner stele region, the conducting elements of the xylem through which water and salts dissolved in it are transported into the above plant organs are located. An important characteristic of the endodermal cells is the presence of so-called Casparian bands formed by thickenings of the cell walls. It is commonly agreed that the Casparian bands are a barrier impermeable to the radial solute and water displacement via the cell walls and the intercellular space, so that the displacement is here only possible via the intracellular way. However, the physiological role of this barrier is nowadays a subject of discussions: some authors assume that it may be partly permeable, and in different degrees for water and solutes.

We here present a continual model that takes into account the realistic anatomical structure of the root and the main physical mechanisms that affect mass transfer. We first formulated the basic concept of this model in [3]. We compare the results of calculations based on the model with experimental data

available and, considering the impermeable or permeable Casparian bands, demonstrate the mechanical role of this barrier.

Material and methods

The approach we develop is based on the representation of the water and solute transport from the environment to the xylem as the flow of a two-phase fluid through a solid matrix. Two fluid phases are identified with the intra- and extracellular fluids that fill the symplast and apoplast. Thus, within the framework of the macroscopic model, each of these fluids, spatially separated at the microscopic level, fills the entire tissue space. We will assume that in each phase a generalized chemical component with the mass concentration c_i ($i = 1, 2$) is dissolved. Here and in what follows we use the subscripts 1 and 2 for the extra- and intracellular fluids, respectively. We here ignore the fact of the presence of various solute species that differ in molar mass, permeability and active behavior. The solute considered is, so to say, an average solute with average characteristics, and its molar concentration is the sum of the molar concentrations of all its components.

Assuming that the root is axially symmetric, we will consider the domain which occupies the region $r_0 \leq r \leq r_1$, where r is the radial coordinate and r_0 and r_1 are the coordinates of the boundaries with an inner reservoir identified with the xylem vessels and the environment, respectively (Fig. 1).

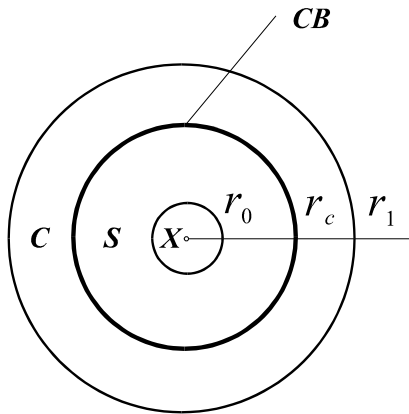


Fig. 1 Calculation domain.

r_0 , r_1 - radial coordinates of the domain boundaries with the xylem and the environment, respectively; r_c - radial coordinates of the Casparian bands; **X** - xylem, **S** - stele, **C** - cortex, **CB** - Casparian bands.

The interphase water exchange is here considered to be controlled by only hydraulic and osmotic mechanisms. Therefore we can write down the phase mass conservation laws in the form:

$$\rho_1 \frac{1}{r} \frac{\partial v_1 r}{\partial r} = J, \quad \rho_2 \frac{1}{r} \frac{\partial v_2 r}{\partial r} = -J \quad (1)$$

where ρ_i are the apparent densities of the phases (neglecting the water compressibility, $\rho_i = \rho_0 \alpha_i$, where α_i is the volume phase concentration and ρ_0 is the water density), v_i are the velocities of the corresponding phases ($i = 1, 2$), and the water exchange rate J is regulated by the relation

$$J = L_p \left[p_2 - p_1 + \sigma RT (c_1 - c_2) \right] \quad (2)$$

where p_i are the pressures of the phases, T is the absolute temperature, $R = \rho_0 R_0 / \mu$ (R_0 is the absolute gas constant and μ is the effective molar mass of the solute), L_p is the hydraulic membrane permeability recalculated for the volume flow, and σ is the membrane reflection coefficient. The densities ρ_1 and ρ_2 do not add up to unity since the solid phase (cell wall material) is present. The concentrations are assumed to be small.

We will write the dynamic equations of the fluid phase flow through the solid framework in the quasi-static form neglecting inertial effects. The extracellular phase is treated as only viscous, whereas for the intracellular fluid, taking into account that in its way it crosses membranes, a form that implies the presence of a distributed osmotic force is assumed. Thus, the dynamic equations for the phases take the following, solved for the phase velocities, form:

$$v_1 = -\beta_1 \frac{\partial p_1}{\partial r}, \quad v_2 = \beta_2 \left(-\frac{\partial p_2}{\partial r} + \zeta RT \frac{\partial c_2}{\partial r} \right) \quad (3)$$

The coefficients β_1 and β_2 are the phase permeabilities and the dimensionless coefficient ζ depends on the characteristics of the distributed membranes and the intracellular space between them. This coefficient is positive and less than unity. Strictly speaking, the symplastic way includes narrow apoplast interlayers between the membranes of adjacent cells (in addition to the plasmodesmata), whereas on the apoplastic way there are no membranes.

We will describe the motion of the solute in each phase by the equations

$$\rho_1 \left(\frac{\partial c_1}{\partial t} + \frac{1}{r} \frac{\partial c_1 v_1 r}{\partial r} \right) = -k + \lambda c_2 - c_1 + (1 - \sigma) \bar{c} J + \rho_1 D_1 \frac{1}{r} \frac{\partial}{\partial r} \left(r \frac{\partial c_1}{\partial r} \right) \quad (4)$$

$$\rho_2 \left(\frac{\partial c_2}{\partial t} + \frac{1}{r} \frac{\partial (1 - \zeta) c_2 v_2 r}{\partial r} \right) = k - \lambda c_2 - c_1 - (1 - \sigma) \bar{c} J + \rho_2 D_2 \frac{1}{r} \frac{\partial}{\partial r} \left(r \frac{\partial c_2}{\partial r} \right) \quad (5)$$

Here, k is the active interphase solute flux, λ is the permeability of the phase-separating cell membranes to the solute (recalculated to volume flow), and D_i are the diffusion coefficients in the apoplast ($i=1$) and in the symplast ($i=2$). The second term in the brackets on the left side of equation (5) is related with the imperfection of the membranes crossed by the solute on the symplastic way and the presence of the intracellular space. It disappears if $\zeta=1$. The third terms on the right sides of equations (4) and (5) represent convective solute mass exchange between the phases. These terms contain the mean transmembrane concentration \bar{c} which can on certain assumptions be in a standard way expressed in terms of c_1 and c_2 [4]. We note that in equations (2) and (3) we could, instead of the concentrations, use directly the osmotic pressures but it would then be necessary to recalculate the concentrations to the osmotic pressures in (4) and (5).

In [2, 5] we developed the model of a cellular unit which consists of the intracellular space of an individual cells and two cell walls adjacent to it. Within the framework of that model, expressions for the coefficients characterizing the symplastic transport β_2 , ζ , and D_2 can be obtained in terms of cellular-level model parameters.

In accordance with the known fact that the plant cell membranes have a very large reflection coefficient, we will assume σ to be equal to unity. Since in the symplast the distributed reflection coefficient ζ is smeared over the entire cell length, we will assume it different from unity but close to it.

Equations (1) – (5) form a closed system for six variables v_1 , v_2 , p_1 , p_2 , c_1 , and c_2 . The boundary conditions vary depending on the specific problem we consider.

In all the problems solved in the present study we fix the pressures in the apoplast p_1 on the both boundaries. We thus assume that the extracellular space directly contacts the environment and the xylem space, whereas the intracellular space does not. These conditions correspond to experiments with excised roots. If we consider the root in the whole plant, the apoplast pressure on the inner surface must be linked with the xylem sap parameters.

We will assume that the concentration in the outer solute around the root is also given. In so doing, we neglect the boundary diffusion layer near the root surface and assume the surface concentration to be equal to that in the ambient medium. This assumption is also realizable under laboratory conditions and must generally be replaced by certain relations specifying the regularities of solute exchange with the environment. The concentration c_1 is thus fixed on the outer boundary.

For the intracellular fluid and solute characteristics we generally must assign the conditions that describe the osmotic water transfer and the active and diffusion solute transport across the membranes separating the intracellular space from the environment ($r = r_1$)

$$\rho_2 v_2 = L_{pe} \left[p_2 - p_e + RT (c_e - c_2) \right], \quad \rho_2 \left(1 - \zeta c_2 v_2 - D_2 \frac{\partial c_2}{\partial r} \right) = -k_e + \lambda_e c_2 - c_e \quad (6)$$

and from the xylem ($r = r_0$)

$$\rho_2 v_2 = L_{px} \left[p_x - p_2 + RT (c_2 - c_x) \right], \quad \rho_2 \left(1 - \zeta c_2 v_2 - D_2 \frac{\partial c_2}{\partial r} \right) = k_x + \lambda_x c_x - c_2 \quad (7)$$

In relations (6) and (7) the reflection coefficients of the domain-bounding membranes that separate the intracellular space from the environment and the xylem are assumed to be equal to unity. Here, by the subscripts *e* and *x* we denote the quantities characterizing the outer space and the xylem, as well as the coefficients corresponding to the domain-bounding membranes.

Since the apoplast-symplast contact area is much greater than the area of the symplast contact with the environment (even taking the root hairs into account) or the xylem, one could expect that the role of mass exchange between the symplast and these compartments is unimportant as compared with the exchange on the symplast-apoplast interface. Our calculations confirm this. Therefore, we will here neglect the right sides of relations (6) and (7). The set of boundary equations thus takes the form:

$$r = r_1: \quad p_1 = p_e, \quad c_1 = c_e, \quad \rho_2 v_2 = 0, \quad \rho_2 \left(1 - \zeta c_2 v_2 - D_2 \frac{\partial c_2}{\partial r} \right) = 0 \quad (8)$$

$$r = r_0: \quad p_1 = p_x, \quad \rho_2 v_2 = 0, \quad \rho_2 \left(1 - \zeta c_2 v_2 - D_2 \frac{\partial c_2}{\partial r} \right) = 0 \quad (9)$$

The system of boundary conditions (8) – (9) is incomplete. Additional conditions are required to regulate the solute behavior on the boundary with the xylem. Experiments are possible when the solute concentration (or osmotic pressure) on the inner boundary (at $r = r_0$) is maintained. In this case, we just have to fix the corresponding constant:

$$c_1 = c_x \quad (10)$$

However, in experiments with free exudate outflow from the root cut this condition is inapplicable. This is also very far from what can be assumed on this boundary for the whole plant. If we assume that the solution inflows with the same concentration over the entire boundary of the xylem vessel, then, for natural conditions for the concentration at its ends, the concentration inside the vessel will be constant (independent of the radial and axial coordinates). Taking into account the continuity conditions for the concentration, the flow velocity and the solute flux on the interface with the xylem vessels, we obtain the boundary condition analogous to the condition of convective solute entrainment on the interface with the xylem, which is common in compartmental models [1]

$$\frac{\partial c_1}{\partial r} = 0 \quad (11)$$

If we assign condition (11), the output concentration c_1 remains to be found. In the calculations here presented we will use either condition (10) or (11), depending on the specific problem considered.

If we treat the Casparian bands as a barrier impermeable to both the fluid and the solute, then we must formulate the following additional boundary conditions on the inner and outer sides of the surface with the radius $r = r_c$ (Fig. 1; by the superscripts "+" and "-" we denote the values on different sides):

$$v_1^+ = v_1^- = 0, \quad \frac{\partial c_1^+}{\partial r} = \frac{\partial c_1^-}{\partial r} = 0 \quad (12)$$

which should be completed by the continuity conditions at $r = r_c$ for the symplast parameters v_2 , p_2 , c_2 , and $\partial c_2 / \partial r$.

The form of the relations formulated makes it sometimes possible to eliminate chemical components that cannot be transported through the cell membranes. For example, let high-molecular components present in the intracellular fluid create a uniform osmotic pressure π_h in the corresponding phase. We can then identify the generalized solute with only the low-molecular components and just redefine the pressure p_2 replacing it by the difference $p_2 - \sigma \pi_h$, since in this case the presence of the high-molecular components affects only relation (2) which regulates the interphase water exchange and this component thus manifests itself only in a uniform increase in the intracellular pressure. It can be shown that such elimination is also possible in an arbitrary case of

high-molecular components transportable only inside the symplast if both the reflection coefficients σ and ζ are equal to unity [5]. Therefore, we will imply the presence in the generalized solute of only low-molecular species.

In this study we restrict our consideration to stationary problems (in (4) and (5) the derivatives with respect to time vanish), which removes the problem of formulating the initial conditions.

In order to estimate the possible mechanical role of the Casparian bands, we will here seek solutions both discontinuous for the apoplast with conditions (12) and continuous over the entire interval $[r_0, r_1]$. The two regimes determined by the boundary conditions (10) or (11) will be analyzed.

For the coefficients present in the model the orders of magnitude can be estimated from both local and global (tissue) measurements. Such estimation requires, especially in the case of tissue-level data, a detailed analysis, including the solution of corresponding problems within the framework of our model itself. We will here reproduce only rough estimates that can be made immediately.

The hydraulic permeability is often estimated experimentally from the pressure-flux curves for high pressure differences when the active and osmotic processes can be neglected [6, 7]. The flux is usually specified as the volume flux per unit root cut area. The hydraulic permeability so found, which obviously is a certain integral characteristic of the system as a whole, is of the order of $10^{-13} - 10^{-12}$ m/(Pa s). Attributing the entire permeability to the symplast, taking into account that $(\rho_1 + \rho_2) / \rho_0 \approx \rho_2 / \rho_0 \ll 1$, recalculating the flow J_v to the velocity and using the geometrical parameters of the root given in [7], we can very roughly find that $\beta_2 \ll 10^{-19} - 10^{-18}$ m²/(Pa s). However, we do not know how the permeability is distributed between the symplast and apoplast. Our numerical experiments have shown that better agreement with the experimental data [6] can be achieved for $\beta_1 > \beta_2$. The formally defined effective pore diameter of the symplastic way determined by the cell size is much greater than that of the apoplastic way. Most probably, the latter inequality means that in the symplast the resistance is mainly created by the membranes across which water passes.

The characteristics of membrane permeability to water and solute L_p and λ calculated per unit volume, present in relations (2), (4), and (5), differ from the similar parameters L_p' and P_s' measured in experiments at the cellular level [8-10] ($L_p' \ll 5 \cdot 10^{-14} - 9 \cdot 10^{-13}$ m/(Pa s), $P_s' \ll 3 \cdot 10^{-11} - 7 \cdot 10^{-9}$ m/s), which are calculated per unit membrane surface area. The following formulas hold: $L_p \sim \nu L_p' \rho_0 / l$, $\lambda \sim \nu P_s' \rho_0 / l$, where l is the characteristic cell size (diameter) and ν is a geometrical coefficient equal to unity for a cubic cell if the diameter is identified with the cube edge length. Taking this coefficient to be of the order of unity and the cell diameter of the order of 30 μ m, we obtain from the data presented in the papers cited $L_p \sim 2 \cdot 10^{-6} - 3 \cdot 10^{-5}$ s/m² and $\lambda \sim 10^{-3} - 2 \cdot 10^{-1}$ kg/(m³ s). It is of interest that in order of magnitude the above estimate for β_2 based on the hydraulic whole-root experiments is more or less consistent with the estimate that can be obtained from the data on membrane permeability if the hydraulic permeability of the symplast way is attributed to the permeability of the membranes.

For the diffusion coefficient in the apoplast we assume values of the order (or somewhat smaller) of the low-molecular diffusion coefficient in free water. Assuming that in the symplast the main resistance to solute flow is concentrated in the cell-separating membranes, very narrow as compared with the cell length, and smearing this resistance over the entire cell length, we can estimate the diffusion coefficient in apoplast as $D_2 \sim P_s l \sim 10^{-17} - 10^{-19}$ m²/s.

The intensity of active transport k must be recalculated from the molar fluxes I_s , determined experimentally and divided by unit cell surface area, in accordance with the formula $k \sim \nu I_s \mu / l$. Summing the data given in [11, 12] for K⁺ ($I_s \ll 3 \cdot 10^{-8} - 3.6 \cdot 10^{-7}$ mol/(m² s)), we obtain the estimate $k \ll 3 \cdot 10^{-5} - 3.6 \cdot 10^{-4}$ kg/(m³ s) which cannot be considered as the upper one due to the presence of other actively transported species.

The above consideration yields only rough and initial estimates for the model parameters since, firstly, the constants were obtained from indirect data (for example, we cannot be sure that diffusion in the apoplast is similar to that in a free fluid) and, secondly, these constants may significantly vary for different species: our estimates based on scarce data available evidence in favor of this assertion.

In calculations all the coefficients of the system were assumed to be constant, except for k and λ that characterize the intensity of solute mass exchange between the intra- and extracellular spaces. For these quantities we took values different in the cortex and in the stele. We will denote the k and λ values by the superscripts “+” in the cortex ($r > r_c$) and “-” in the stele ($r < r_c$). It is natural to assume that there are no active transport in the inner region, that is, $k^- = 0$. Calculation with $\lambda^- = \lambda^+$ lead to inappropriate results; therefore, the difference in λ is also important.

The calculations were carried out numerically using the stabilization method based on the solution of the nonstationary equations.

Results and discussion

We calculated the flow over a wide range of parameters of the same orders as discussed above. Here we reproduce the results for a set of values that ensure satisfactory agreement with the experimental data presented in [6] (Table 1).

Table 1 Parameter values used in the calculation.

Parameter	Value	Parameter	Value
ρ_1/ρ_0	0.07	λ^+	$1.4 \cdot 10^{-2}$ kg/(m ³ s)
ρ_2/ρ_0	0.63	λ^-	$2 \cdot 10^{-3}$ kg/(m ³ s)
L_p	$3.3 \cdot 10^{-6}$ s/m ²	D_1	$3 \cdot 10^{-10}$ m ² /s
RT	$3.3 \cdot 10^7$ Pa	D_2	$5 \cdot 10^{-15}$ m ² /s
σ	1	ζ	0.9
β_1	$8 \cdot 10^{-18}$ m ² /(Pa s)	r_0	0.07 mm
β_2	$1.1 \cdot 10^{-18}$ m ² /(Pa s)	r_1	0.28 mm
k^+	$6.25 \cdot 10^{-5}$ kg/(m ³ s)	r_c	0.1 mm
k^-	0	π_e	$1.5 \cdot 10^5$ Pa

In the calculations the Casparian bands were first assumed to be totally impermeable to water and solute. From Fig. 1 it can be seen that the integral characteristics of the excised root are satisfactorily reproduced by our model with the above parameter values. The root operates as a pump and can provide an inward flow even in the absence of pressure gradient ($\Delta p = 0$). The system can also ensure a certain solute concentration in the xylem different from that in the environment, for sufficiently slow flows higher.

Our numerical experiments showed that a necessary condition of agreement with the experiment is a significantly lower permeability to the solute of the symplast-apoplast separating membranes in the inner part of the root as compared with the outer one, close to the lower estimate for λ given above.

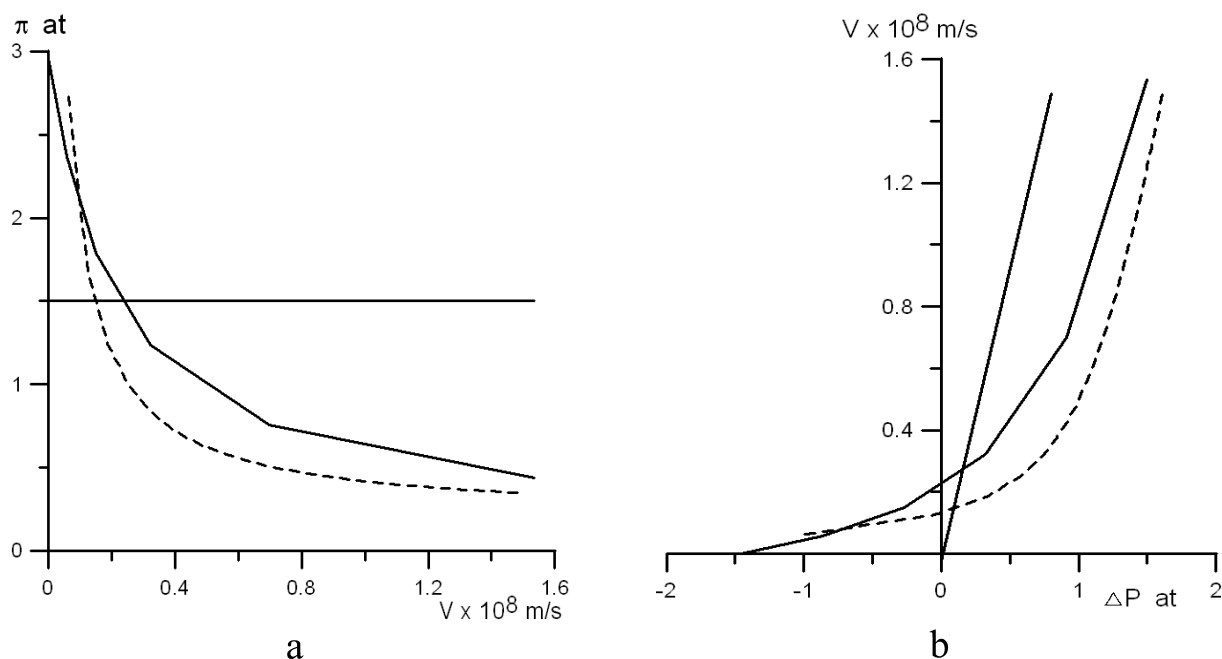


Fig. 2 (a) Dependence of the xylem sap osmotic pressure on the fluid velocity across the root cut. The broken curve corresponds to the experimental data and the continuous curve to the model-based calculations. The horizontal line shows the osmotic pressure in the environment.

(b) Dependence of the fluid velocity across the root cut on the hydrostatic pressure difference between the environment and the xylem. The broken curve corresponds to the experimental data and the continuous curve to the model-based calculations. The practically straight line represents the calculation result in the absence of an apoplastic barrier.

We also carried out calculations assuming that the Casparian bands are totally permeable to water and solute. In this case, for the same parameter values given in *Table 1*, the Δp dependence of v is almost straight line that practically passes through the point $\Delta p = 0$ on the abscissa axis (*Fig. 1b*). Thus, the system cannot ensure the presence of a positive root pressure, which is related with the fact that the large diffusion coefficient in the apoplast now provides an almost uniform distribution of the solute concentration in the apoplast and, as a result, the practical coincidence of the inner and outer osmotic pressures. This form of the dependence of the velocity on the pressure drop was obtained in the absence of a permeable barrier over a wide range of the calculation parameters varying within the above-estimated limits.

Solutions obtained under the free outflow condition (11) were considered so far. If the output solute concentration is maintained, which corresponds to boundary condition (10), even in the absence of an apoplastic barrier the system operates as an osmotic pump (for example, if the output-input difference in osmotic pressure is equal to $\Delta\pi = 1$ at, then the flow velocity $v = 0.4 \cdot 10^{-8}$ m/s). However, these conditions are inconsistent with the physiological situation and the presence of an impermeable barrier on the apoplastic way turns out to be mechanically necessary.

Conclusion

It is shown that the known experimental data can be satisfactorily described if we assume the presence of active solute pumping only in the outer (cortical) part of the root, a non-uniform radial distribution of the membrane permeability to solute (higher in the outer part), and the presence of a localized barrier impermeable to the extracellular phase and the solute contained in it (Casparian bands). In the absence of this barrier the system, though can work as an “osmotic pump” if an input-output osmotic pressure difference is maintained, is not able to pump water efficiently under the

conditions of free outflow with convective entrainment of the solute. From the continual model developed various compartmental models can be obtained using averaging procedures.

It is of importance that our model is, so to say, open. It can easily be generalized to include different additional possible mechanisms. Since the model developed adequately reproduces the main characteristics of the root as a physical system, it may be a useful and universal tool in analyzing various aspects of transport in the root. However, in its minimal form here presented, it is sufficient for describing at least certain integral characteristics of water and solute transport from the environment to the xylem. In future it can be built in the model of root-xylem-leaf flow in the whole plant, with output boundary conditions that mate the flow characteristics with those in the xylem.

Acknowledgements

The work was supported financially by the Russian Foundation for Basic Research (project No. 08-01-00492) and the State Program of Support for Leading Science Schools (project No. NSh-1792.2008.1).

References

1. Murphy, R., (2000): *Some compartmental models of the root: Steady-state behavior*. Journal of Theoretical Biology. 207: 557–576.
2. Logvenkov, S.A. and A.A. Stein, (2000): *Mechanics of plant growth: Interaction between growth and transport processes*. Modern Problems of Biomechanics. 10: 291-358 [in Russian].
3. Stein A.A., S.A. Logvenkov, and A.T. Chalyuk (2003): *Mathematical modelling of the plant root as a water-pumping cellular system*, in Mathematical Modelling and Computing in Biology and Medicine, Editors, V. Capasso, Soc. Ed. Esculapio: Bologna: p. 206–212.
4. Kedem O. and A. Katchalsky (1958): *Thermodynamics analysis of the permeability of biological membranes to non-electrolytes*. Biochimica et Biophysica Acta. 27: 229-246.
5. Logvenkov, S.A. and A.A. Stein, (2008): *Compartmental model of water uptake by plant roots with account for cellular-level processes*. Russian Journal of Biomechanics, 12 (4): 23-36.
6. Fiscus E.L., (1977): *Determination of hydraulic and osmotic properties of soybean root system*. Plant Physiology. 59: 1013-1020.
7. Reiger M. and P. Litvin (1999): *Root system hydraulic conductivity in species with contrasting root anatomy*. Journal of Experimental Botany. 50 (331): 201-209.
8. Steudle E., R. Oren, and E.-D. Schulze (1987): *Measurement of hydraulic conductivity, solute permeability, and of reflection coefficients of excised roots using the root pressure probe*. Plant Physiology. 84: 1220-1232.
9. M.G. Pitman (1976): *Ion uptake by plant roots*, in Encyclopedia of Plant Physiology: Vol.2 (Pt B), Editors, U. Luttge and M.G. Pitman, Springer, Berlin: p.95-128.
10. Raven J.A. (1976): *Transport in algal cells*, in Encyclopedia of Plant Physiology: Vol.2 (Pt A), Editors, U. Luttge and M.G. Pitman, Springer, Berlin: p.129-188.
11. Anderson W.P. (1976): *Transport through roots*, in Encyclopedia of Plant Physiology: Vol.2 (Pt B), Editors, U. Luttge and M.G. Pitman, Springer, Berlin: p.129-156.
12. Steudle E., M. Murrman, and C. Peterson (1993): *Transport of water and solutes across maize roots modified by puncturing the endodermis. Further evidence for the composite transport model of the root*. Plant Physiology. 103: 335-349.

Wave propagation in the conducting systems of plants

Natalya N. Kizilova

Kharkov National University, Ukraine

Abstract

Plant sensitivity to the external physical and chemical factors is determined by chemical, electrical and hydraulic signalling. A brief review of the wave phenomena in the conducting systems of plants is given. Wave-mediated mechanisms of the long distance root-to-shoot signalling are discussed. The pressure and concentration waves, oscillations of the surface electric potentials and acoustic waves observed in experiments play an important role in the organ-to-organ communication while the corresponding mathematical formalism and biomechanical explanation of the measured parameters are absent. In this paper the steady transpiration flux and wave propagation along the conducting elements are considered as a model of the plant sensitivity to the osmotic pressure in the soil solution. Nonlinear concentration distribution along the tube and the parabolic velocity profiles are computed. The range $U=20-60$ m/s is obtained for the wave velocity, which correspond to the measurement data.

Introduction. Mechanisms of the long-distance signalling: an overview.

Wave phenomena in long-distance liquid motion and signalling in high plants are widely discussed in the recent literature. Pressure and concentration waves propagating along the xylem, electromagnetic waves in the phloem, acoustic waves propagating in the plant tissues have been discussed as possible mechanisms of the long distance communication. Plants are continuously exposed to different perturbations including variation of light and temperature, mechanical load by wind, water, snow or fruits, gravity and electromagnetic waves, air and soil pollution, drought, deficiency of nutrients, attacks by insects, etc. Like animals, plants can sense and respond to external physical and chemical stimuli. Gravitropic, thigmomorphic and thigmotropic reactions in plants, their ability to percept the turgor pressure, growth strains, xylem water potential, wave propagation, warmth and cold and a variety of chemical signals are confirmed in numerous experiments.

The gravitropic reactions of plants result in differential cell elongation on opposite sides of the displaced organ (in primary growth) and in formation of reaction wood, tension wood in porous angiosperms and compression wood in nonporous angiosperms and gymnosperms (in secondary growth). Besides two approved mechanisms of gravisensing (the starch–statolith hypothesis and the hydrostatic model) a theory of the gravity-induced waves controlling plant shapes by the wave velocity, vertical to horizontal velocity ratios, and the stepwise change in velocity from horizontal to vertical values has been proposed [1-3].

Long distance root-to-shoot signalling regulating the shoot branching, the root-derived hormonal signals regulating leaf growth and development ensure everyday communication between distant plant organs [4]. Plant roots can sense variations in soil water [5,6] and soil oxygen contents [7], soil bulk density [8], and changes in the nutrient composition of soil (both enrichment and depletion) [9]. The soil water deficit induces a sequential reduction of tissue water content, stomatal conductance and leaf growth. Jones [10] has suggested that this might involve transfer of root-sourced chemical signals *via* the xylem from the roots to shoots, which is termed non-hydraulic or chemical signalling. Chemical messengers can be transferred acropetally at the rate of the transpiration stream [11]. Abscisic acid, pH, cytokinins, malate and some other factors are discussed as possible chemical messengers of the soil water contents [12]. Fast xylem transport of the fluorescent dye applied on cut petiole of the upper leaf has been detected in tobacco plants [13], which indicates that some signalling chemicals can be quickly delivered from shoots to leaves or from the damaged into the undamaged leaves with xylem

flow. Evidence of the fast chemical root-to-shoot signalling of partial soil drying has been shown in many studies [14,15], but in some plants the hydraulic mechanism precedes the chemical signalling [16], as it was confirmed for bell pepper and some woody plants [17]. It was shown the soil drying-induced reduction in leaf conductance could be progressively reversed by the pressurization of the root system [18] and the leaf conductance could return to its pre-pressurization level within minutes after the pressurization.

Long distance signalling on attacks of the microbial pathogens and herbivorous insects includes jasmonic and salicylic acid, ethylene and the peptide messenger systemin [19]. The root-to-shoot transmission of signals provides the long-distance signalling for leaf senescence [20]. Putative candidates of the chemical signalling in plant development, flowering and tuberization are discussed in [21]. The presence of the pesticides can be rapidly detected by the soybeans [22], which makes them high sensitive environmental biosensors.

Plant cells can detect variations in the osmotic pressure and respond with compensatory molecular adaptations reestablishing homeostasis of osmotically disturbed parameters of cell structure and function [23]. When cells are no longer able to compensate for osmotic stress and the amount of damage is too great, they trigger a self-destruction program called programmed cell death (apoptosis) [24]. The mitogen-activated protein kinase cascade was found an important intracellular signal-transduction pathways activated in response to the variations in the osmotic pressure [23]. In tobacco cells, osmotic stress induced the rapid activation of two protein kinases [25]. For the first one the reaction was detected 5 to 10 min after the cells were exposed to osmotic stresses, and its activity persisted for 30 min while another was activated within 1 min after osmotic stress and its activity was maintained for 2 hr.

When a part of the plant is mechanically damaged other leaves accumulate various proteinase inhibitors which are toxic to insects [26]. The reaction is fast (minutes to hours); a rapid increase in concentration of the inhibitors can be detected in the potato leaves remote from the wound in 20 min after the damage [11]. In other plants the inhibition of photosynthetic rate and stomata conductance were observed in the undamaged distant leaves within 1 hour [13] and jasmonic and abscisic acids were found to be involved as chemical signals. Mass transfer with the sap flow is insufficient for the rapid signalling and some combinations of the physical, chemical and local tissue mechanisms are proposed [11, 13, 27-29]. Among the physical factors the electrical [30] and hydraulic [11] (stimulated by water release at the wound site) signalling are discussed.

Plants can generate various types of intracellular and intercellular electrical signals mostly in the form of action and variation potentials in response to the environmental changes. A hypothesis of the electrical transmission of the signals involving membrane activity of living cells was suggested by Bose (1928). The action potential appears usually as a single pulse or as several repeated pulses that propagate along the conducting bundles of stem inducing functional responses in distant organs. There is no unanimous view on whether the action potential propagates over the root and the leaf directly or as a transformed signal or whether it acts via a series of mediators [31]. In soybeans the speed of the propagation of action potentials is up to 2 m/s, which is 5 to 10 times faster than the speed of action potential propagation in *Dionaea* flytrap (0.2 m/s) [32], and the duration time of single action potentials is typically 20 ms [22]. Spontaneous action potentials have been shown to correlate with turgor-controlled growth movements [28].

Hydraulic signalling represents the root-to-shoot or leaf-to-leaf transmission of information *via* changes in the xylem sap tension. A hypothesis of the positive pressure hydraulic transfer through the xylem was proposed by Haberlandt (1914). The stomatal conductance is correlated with soil water potential, which can be determined by the hydraulic signalling via the interconnected water system soil-root-stem-leaf. Since root is in direct contact with soil and variations in the soil water status could have had a hydrostatic impact of the xylem system of the entire plant, it gives the dependence between the stomatal conductance g , the hydraulic conductance h of the plant and the soil water potential ψ_s : $g = (\psi_s - \psi_l)g/h$, where ψ_l is the leaf water potential [27]. Rapid variations in the xylem pressure could produce changes in the hydraulic conductivity of the whole plant by alterations of the conductivity of the microchannels in the membranes of the intervessel bordered pits [33].

Some plants like *Mimosa* exhibit fast mechanical reaction of the leaves to touching, warming or shaking and both electrical and hydraulic hypothesis have been considered as possible mechanisms of

the phenomenon. When the plant is disturbed by a knocking almost all the mimosa leaves at once fold inward and close up simultaneously. In the case the knocking-generated acoustical wave can be a direct mechanical messenger providing rapid long-distance signalling [11]. A strong evidence of wound-induced hydraulic signals in *Mimosa* has also been shown [11]. When a leaf is damaged by a flame, the distant basal leaves swell up almost at once after the damage, which could be produced by a water flow from the damaged leaf towards the distant regions of the plant. The presence of the hydraulic mechanism rather than electrical one was confirmed by the observation that swelling of the distant leaves was not accompanied by the closure of the pairs of leaflets. The observing hydraulic signal can be separated into a fast pressure wave and a slower mass flow of the sap from the wound site [11]. The hydraulically-induced basipetal mass flow transfers the signalling molecules from the wound at rates of $v=10-15$ mm/s and a possibility of the fast waves with $v=300$ mm/s is also discussed.

The mechanisms of the wound and non-wound (touching) signalling in plants are different. The non-wound signalling is usually slow (1 mm/s) and can propagate to the neighbouring leaves and through alive tissues, while the wound-induced signalling is faster (≥ 10 mm/s) and can even propagate through the dead (frozen or scorched) tissues involving the plant into the systemic reaction [11]. Mass transfer with transpiration flow is insufficient for explanation of the wound-induced signalling, because the wound signals can travel both acro- and basipetally and are faster than the transpiration stream which is acropetal. Apparently, basipetal and acropetal hydraulic signalling dominates in the plants with significant xylem tension existing prior to the damage and is produced by rapid rupture of the water threads in the xylem conduits [11].

Hydrodynamic phenomena have also been discussed as a mechanism of restoration of the xylem conductivity after its embolization [33]. Cavitation of the gas bubbles and acoustic emission are detected in plants at low temperatures [34] and dehydration [35, 36]. Propagation of the waves generated by the oscillated pressure applied to the stem or the roots as well as the acoustic emission parameters are useful for determination the quality of the wood and physiological state of the plant organs [34, 35, 37].

Continuous monitoring of the water potential ψ in plants at different experimental conditions reveals short- and long-wave oscillations. Auto-oscillatory mode of ground-water absorption by roots [38] and short-period ($t \sim 15-80$ min) oscillations of water exchange [39] have been observed in experiments with pot plants. Rapid variations of osmotic pressure of the root solution produce quick alterations of the stem diameter. The alterations have been observed at rather small variations of the concentration ($C \sim 0.01$ M) and pass ahead of the bioelectric reaction that is noticeable at $C \sim 0.3-0.5$ M only. The alterations of the stem diameter propagates along the stem in a wave-like way with velocity $v \sim 10^{-1}-1$ m/s, that considerably exceeds the rate of the transpiration flow $v \sim 10^{-4}$ m/s. Possible explanation of the quick reaction of the plants is connected with wave propagation in the tissues [39, 40]. Similar slow waves with $v \sim 96$ cm/s that can carry information (molecules of phytohormones and other regulatory substances) along the plant have been observed in experiments [1, 2]. The relation between the rates of movement of the slow waves in longitudinal and transverse directions is the same as for acoustic waves. In this paper possible role of the concentration waves in the long-distance signalling of the osmotic pressure of the root solution [41, 42] and the pressure waves providing the wound-induced hydraulic signals [11] is studied on the mathematical model.

Mathematical model

Conducting elements of plants can be considered as long thin vertical tubes (xylem vessels) and long chains of elongated cells separated by porous plates (phloem vessels). The radius a and the length L of the tube are constant values and $a/L \ll 1$ (fig.2). The coordinates $x=0$ and $x=L$ correspond to the inlet and outlet of the phloem vessel and the outlet and inlet of the xylem vessel accordingly. The propelling force of the sap motion through the xylem is provided by water pumping by the roots and water evaporation by the leaves. Water pumping due to the osmotic effect at the inlet of the phloem vessels ($x=0$) increases the hydrostatic pressure p at $x=0$ that causes the descending motion of the phloem sap to the roots, growing leaves, flowers and fruits (the Münch hypothesis). The

1d axisymmetric flow of a viscous compressible liquid with an osmotically active dissolved component through the long thin tube ($a \ll L$) with impermeable rigid wall is considered. The model corresponds to the sap motion along the part of stem or shoots between the side branches. The governing equations are the following [41, 42]:

$$\frac{\partial \rho}{\partial t} + \frac{\partial \rho V_x}{\partial x} = 0 \quad (1)$$

$$\frac{\partial V_x}{\partial t} + V_x \frac{\partial V_x}{\partial x} = -\frac{1}{\rho} \frac{\partial p}{\partial x} + \nu \left(\frac{\partial^2 V_x}{\partial r^2} + \frac{1}{r} \frac{\partial V_x}{\partial r} + \frac{\partial^2 V_x}{\partial x^2} \right) \quad (2)$$

$$\frac{\partial C}{\partial t} + \frac{\partial}{\partial x} (V_x C) = \frac{\partial}{\partial x} \left(D \frac{\partial C}{\partial x} \right) \quad (3)$$

where V_x is the axial velocity, ρ, ν are density and kinematic viscosity of the sap, C, D are concentration and diffusion coefficient of the dissolved component. According to the Münch hypothesis, the hydrodynamic pressure p inside the vessel is maintained by the live cells at an osmotic equilibrium with respect to the surrounding water-containing tissues where the hydrodynamic pressure p_0 is held constant so that

$$p = \pi + p_0 \quad (4)$$

Here π is the osmotic pressure that can be calculated from the van't Hoff equation for a dilute solution:

$$\pi = \frac{RT}{M_c} C \quad (5)$$

where M_c is the molar mass of the dissolved component, R is the gas constant, T is the absolute temperature. The boundary conditions for the problem (1)-(5) are given by

$$r = 0 : \quad \frac{\partial V_x}{\partial r} = 0, \quad r = a : \quad V_x = 0 \quad (6)$$

$$x = 0 : \quad C = C_1(t), \quad x = L : \quad C = C_2(t) \quad (7)$$

$$t = 0 : \quad C = C_0(x) \quad (8)$$

Steady flow in the tube

When $D, C_{1,2}$ are constant the nondimensional parameters $c = C/C^\circ$, $v = V_x/V^\circ$, $X = x/L$, $z = r/a$, $T = t/T^\circ$ can be introduced and the equations (2)-(3) can be rewritten as

$$\frac{1}{St} \frac{\partial c}{\partial T} + \frac{\partial}{\partial X} (vc) = \frac{1}{Pe} \frac{\partial^2 c}{\partial X^2} \quad (9)$$

$$\frac{1}{St} \frac{\partial v}{\partial T} + v \frac{\partial v}{\partial X} = -\frac{1}{\alpha} \frac{\partial c}{\partial X} + \frac{1}{Re} \left(\frac{\partial^2 v}{\partial z^2} + \frac{1}{z} \frac{\partial v}{\partial z} + \left(\frac{a}{L} \right)^2 \frac{\partial^2 v}{\partial X^2} \right) \quad (10)$$

where $St = V^\circ T^\circ / L$, $Pe = V^\circ L / D$, $Re = V^\circ a / \nu$, $\alpha = \rho M_c (V^\circ)^2 / (RT C^\circ)$. Typical values for the parameters are $a = 10^{-5} - 10^{-4}$ m, $L = 10^{-2} - 10^{-1}$ m, $D = 10^{-10} - 10^{-9}$ m²/s, $V^\circ = 10^{-4} - 10^{-3}$ m/s, $\nu = (0.9 - 3) \cdot 10^{-6}$ m²/s [41, 43]. One can obtain here the estimations of the

Reynolds and Peclet numbers $Re = 10^{-3} - 10^{-1}$, $Pe = 10^4 - 10^5$. When $Re \ll 1$ the derivatives of v with respect to X can be neglected as compared to the derivatives of v with respect to z and the nonlinear term in (10) can be omitted. Solution of (1)-(9) can be considered as a series expansion

$$c = c_0 + c_1\varepsilon + c_2\varepsilon^2 + \dots, \quad v = v_0 + v_1\varepsilon + v_2\varepsilon^2 + \dots \quad (11)$$

where $\varepsilon = 1/Pe$ is the small parameter.

Substituting (11) in (9)-(10), assuming $\partial v/\partial T = 0$ and comparing the values of the same order on ε give the equations for c_0, v_0 instead of (9)-(10) (subscripts are omitted for simplicity):

$$\frac{1}{\alpha} \frac{\partial c}{\partial X} = \frac{1}{Re} \left(\frac{\partial^2 v}{\partial z^2} + \frac{1}{z} \frac{\partial v}{\partial z} \right) \quad (12)$$

$$\frac{1}{St} \frac{\partial c}{\partial T} + \frac{\partial}{\partial X}(vc) = 0 \quad (13)$$

The system (12)-(13) describes Poiseuille-like flow with concentration gradient as a driving force instead of the pressure drop. In that way the solution of the system is:

$$v(Z, X) = \frac{Re}{4\alpha} (1 - Z^2) \frac{\partial c}{\partial X}, \quad c = \sqrt{s_1^2 - (s_1^2 - s_2^2)X} \quad (14)$$

where $s_{1,2} = C_{1,2}/C^0$. The model (1)-(5),(7)-(9) has been studied in [41] for investigation the stationary flow of the phloem sap at some simplifying conditions. Now we can substitute (14) into the equations for c_1, c_2, \dots and calculate the high-order terms in (9)-(10). Some results of numerical calculations of distributions $c(X), v(X)$ are presented in *Fig.1-2*.

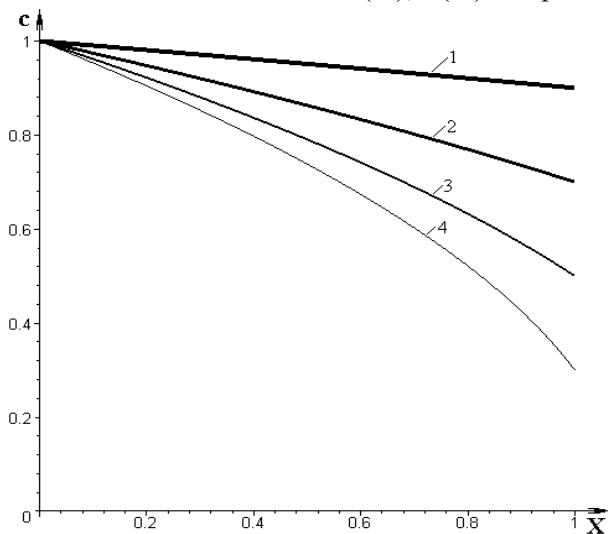


Fig.1. Dependences $c(X)$ for $C_2/C_1 = 0.9, 0.7, 0.5, 0.3$ (curves 1-4 respectively).

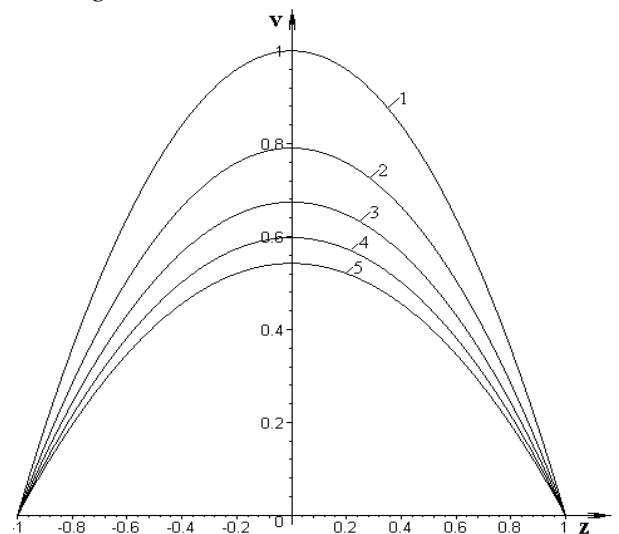


Fig.2. Dependences $v(X)$ for $X = 1, 0.8, 0.6, 0.4, 0.2$ (curves 1-5 respectively).

Wave propagation in the tube

We consider here the wave propagation through the tube as possible biophysical mechanism of long-distance signaling in high plants. The linearized equations (1)-(2) when they are considered as a system for $V_x, p, \rho(p)$ describe propagation of small excitations in the form $f = f' e^{i\omega(t-x/w)}$, where $f = \{V_x, p\}$, f' are small amplitudes, $w = (d\rho/dp)^{-1}$ is the wave velocity. Numerical

estimations give the values $w \sim 10^3$ m/s. That sort of waves can carry information between the leaves and the roots of the plant at rapid variations of the pressure conditions at the ends of the tube, for instance in experiments with plants in pressure bomb chamber [37]. The relatively slow concentration waves can be investigated by assuming $c = s_c + c'$, $v = v_c + v'$ in (9)-(10), where $s_c = s_1 = s_2$ and $v_c = 0$ are unperturbed values, c' , v' are small perturbations that can be introduced as

$$c' = c^* e^{i\omega(T-X/u)}, \quad v' = v^* e^{i\omega(T-X/u)} \quad (15)$$

where u is the wave velocity. Substituting (15) in (12)-(13) we obtain the uniform algebraic system of equations for the small amplitudes c^* , v^* in the form:

$$A \begin{pmatrix} c^* \\ v^* \end{pmatrix} = \begin{pmatrix} 0 \\ 0 \end{pmatrix}, \quad A = \begin{pmatrix} 1 & -\frac{s_c}{u} \\ \frac{St}{\alpha u} & 1 \end{pmatrix} \quad (16)$$

The solvability condition for (16) is $\det(A) = 0$ that gives the next expression for the wave velocity (in dimension form):

$$U = \sqrt{\frac{RTC_1}{M_c \rho}} \quad (17)$$

In the phloem vessels the sucrose solution moves through the tubes and for that case $M_c = 0.3423$ kg/mol, $\rho = 1300$ kg/m³, $C_1 = 200 - 300$ kg/m³ [41]. Assuming the temperature variations $T = 283 - 303$ K we can obtain from (17) the range of the wave velocities $U = 20 - 60$ m/s. The wave is rather small one as compared to the longitudinal wave in compressible liquid. When the plant stem has the total length $L_\Sigma = 0.1 - 1$ m, the slow wave passes the distance L_Σ in $t \sim 1.7 - 50$ ms.

Results and discussions

At dynamical equilibrium conditions the concentration gradient between the inlet and outlet of the conducting vessel that is maintained by active synthesis (absorption) of the dissolved component in different vegetative organs of the plant defines the propelling force of the liquid motion through the vessel. The governing equations give the parabolic velocity profiles and nonlinear concentration distribution along the vessel for the stationary flow.

Slow concentration waves can be caused by variation of the concentration of the dissolved component at the inlet of the tube. At variation of the parameters of the model within the physiological limits for high plants the wave velocity $U = 20 - 60$ m/s is obtained. For the stem length $L_\Sigma = 0.1 - 1$ m the time delay between application of the stimuli and reaction of the distant vegetative organs is $t \sim 1.7 - 50$ ms, which is comparable to the experimental data [39, 40]. In that way the slow waves can mediate long-distance high-speed transferring information between the organs that can not be carried by convective flow of the liquid which moves at $V \sim 10^{-5} - 10^{-4}$ m/s and reaches its maxima $V = 0.02 - 0.04$ m/s in lianas. The small variations $C(t)$ as well as the small concentration gradients ∇C can be sensed by leaf cells far from the source of the osmotic stress.

Propagation of the concentration jump δC_1 along the vessel as well as non-stationary conditions $C_1(t), C_2(t)$ at the ends of the vessel can be investigated on the basis of the developed model. The results can be generalized to the model of the conducting system as a bundle of thin tubes with porous walls [44] with different geometrical parameters [45].

Acknowledgements

The work is partially supported by the DFFD- RFFI research grant F28.1/011.

References

- [1] Wagner, O.E. (1996): *Anisotropy of wave velocities in plants: gravitropism*. Physiological Chemistry and Physics and Medical NMR. 28:173-186.
- [2] Wagner, O.E. (1999): *A plant's response to gravity as a wave phenomenon*. Journal of Gravitational Physiology. 6:17-18.
- [3] Wagner, O.E. (2007): *Plants respond to gravity with gravity related waves*. Journal of Gravitational Physiology. 14:119-120.
- [4] Mouchel, C.F. and O. Leyser (2007): *Novel phytohormones involved in long-range signalling*. Current Opinion in Plant Biology. 10:473-476.
- [5] Davies, W.J., S.Wilkinson and B. Loveys. (2002): *Stomatal control by chemical signalling and exploitation of this mechanism to increase water use efficiency in agriculture*. New Phytologist. 153:449-460.
- [6] Wilkinson, S. and W.J. Davies. (2002): *ABA-based chemical signalling: the co-ordination of responses to stress in plants*. Plant Cell Environment. 25:195-210.
- [7] Drew, M.C., J. Webb and L.R. Saker. (1990): *Regulation of K⁺ uptake and transport to the xylem in barley roots; K⁺ distribution determined by electron probe X-ray microanalysis of frozen-hydrated cells*. Journal of Experimental Botany. 41:815-825.
- [8] Masle, J. and G.D. Farquhar. (1988): *Effects of soil strength on the relation of water-use efficiency and growth to carbon isotope discrimination in wheat seedlings*. Plant Physiology. 86:32-38.
- [9] Schachtman, D.P. and R. Shin. (2007): *Nutrient sensing and signaling: NPXS*. Annual Review on Plant Biology. 58:47-69.
- [10] Jones, H.G. (1980): *Interaction and integration of adaptive responses to water stress: the implication of an unpredictable environment*. in: Adaptation of plants to water and high temperature stress. Turner, N.C. and P.J. Kramer, Ed. Wiley, New York, 353-365.
- [11] Malone, M. (1994): *Wound-induced hydraulic signals and stimulus transmission in Mimosa pudica L.* New Phytologist. 128:49-56.
- [12] Schachtman, D.P. and J.Q.D. Goodger. (2008): *Chemical root to shoot signalling under drought*. Trends in Plant Science. 13:281-287.
- [13] Hlaváčková, V. and J. Nauš. (2007): *Chemical signal as a rapid long-distance information messenger after local wounding of a plant?* Plant Signaling & Behavior. 2:103-105.
- [14] Croker, J.L., T.W. Williard and R. Auge. (1998): *Stomatal sensitivity of six temperate, deciduous tree species to non-hydraulic root-to-shoot signalling of partial soil drying*. Journal of Experimental Botany. 49:761-774.
- [15] Stikic R., Popovic S., Srdic M., et al (2003): *Partial root drying (PRD): a new technique for growing plants that saves water and improves the quality of fruit*. Bulgarian Journal of Plant Physiology. Special Issue. p.164-171.
- [16] Christmann, A., E.W. Weiler, E. Steudle and E. Grill. (2007): *A hydraulic signal in root-to-shoot signalling of water shortage*. Plant Journal. 52:167-174.
- [17] Jia, W. and J. Zhang. (2008): *Stomatal movements and long-distance signaling*. Plant Signaling & Behavior. 3:772-777.
- [18] Fuchs, E.E. and N.J. Livingston. (1996): *Hydraulic control of stomatal conductance in Douglas fir and alder seedlings*. Plant Cell Environment. 19:1091-1098.
- [19] Pieterse, C.M.J., A. Schaller, B. Mauch-Mani and U. Conrath. (2006): *Signaling in Plant Resistance Responses: Divergence and Cross-Talk of Defense Path*. in: Multigenic and Induced Systemic Resistance in Plants. Springer, N.-Y. P.166-196.

- [20] Gowing, D.J.G., H.G. Jones and W.J. Davies. (1993): *Xylem-transported abscisic acid: the relative importance of its mass and its concentration in the control of stomatal aperture*. Plant Cell Environment. 16:453-459.
- [21] Suárez-López, P. (2005): *Long-range signalling in plant reproductive development*. International Journal of Developmental Biology. 49:761-771.
- [22] Mwesigwa, J., D.J. Collins and A.G. Volkov. (2000): *Electrochemical signalling in green plants: effects of 2,4-dinitrophenol on variation and action potentials in soybean*. Bioelectrochemistry. 51:201–205.
- [23] Kültz D. and M. Burg. (1998): *Evolution of osmotic stress signaling via map kinase cascades*. The Journal of Experimental Biology. 201:3015–3021.
- [24] Schwartz, L.M. and B.A. Osborne. (1993): *Programmed cell death, apoptosis and killer genes*. Immunology Today. 14:582–590.
- [25] Mikolajczyk, M., O.S. Awotunde, G. Muszynska, et al. (2000): *Osmotic stress induces rapid activation of a salicylic acid-induced protein kinase and a homolog of protein kinase ASK1 in tobacco cells*. Plant Cell. 12:165–178.
- [26] Ryan, C.A. (1974): *Assay and biochemical properties of the proteinase inhibitor-inducing factor, a wound hormone*. Plant Physiology. 54:328-332.
- [27] Comstock, J.P. (2002): *Hydraulic and chemical signalling in the control of stomatal conductance and transpiration*. Journal of Experimental Botany. 53:195-200.
- [28] Wagner, E., et al. (2005): *Hydro-electrochemical integration of the higher plant - basis for electrogenic flower induction*. in: Baluska R, Mancuso S., Volkmann D. (eds.) Communication in Plants. Neuronal Aspects of Plant Life. Springer. P.369-389.
- [29] Tardieu, F. and W.J. Davies. (1993): *Integration of hydraulic and chemical signalling in the control of stomatal*. Plant Cell Environment. 16:341-349.
- [30] Stankovic, B., D.L. Witters, T. Zawadzki and E. Davies. (1998): *Action potentials and variation potentials in sunflower: An analysis of their relationships and distinguishing characteristics*. Physiologia Plantarum. 103:51-58.
- [31] Pyatygin, S.S., V.A. Opritov and V.A. Vodeneev. (2008): *Signaling role of action potential in higher plants*. Russian Journal of Plant Physiology. 55:285–291.
- [32] Burdon-Sanderson, J. (1973): *Note on the electrical phenomena which accompany stimulation of the leaf of Dionaea muscipula*. Proceedings of the Royal Society London. 21:495–496.
- [33] Zwieniecki, M.A., P.J. Melcher and N.M. Holbrook. (2001): *Hydrogel Control of Xylem Hydraulic Resistance in Plants*. Science. 291:1059–1062.
- [34] Kikuta, S.B. and H. Richter. (2003): *Ultrasound acoustic emissions from freezing xylem*. Plant, Cell & Environment. 26:383-388.
- [35] Kikuta, S.B., et al. (1997): *Ultrasound acoustic emissions from dehydrating leaves of deciduous and evergreen trees*. Plant, Cell and Environment. 20:1381-1390.
- [36] Nardini, A., M.T. Tyree M.T. and S. Salleo. (2001): *Xylem cavitation in the leaf of prunus laurocerasus and its impact on leaf hydraulics*. Plant Physiology. 125:1700–1709.
- [37] Wei, C., M.T. Tyree and J.P. Bannink. (2000): *The transmission of gas pressure to xylem fluid pressure when plants are inside a pressure bomb*. Journal of Experimental Botany. 51:309-316.
- [38] Lazareva, N.P., T.A. Borisova and V.N. Zolkevitch. (1986): *On auto-oscillating character of pumping action of Zea Mays L. root system*. Doklady Akademy of Science of the USSR. p.761-764.
- [39] Karmanov, V.G. et al. (1974) *Water exchange dynamics of high plants and its informational role*. Physiology and Biochemistry of High Plants. 6:69-75.
- [40] Karmanov, V.G. and S.N. Meleshchenko. (1982): *Mechanism of auto-oscillations of water metabolism in plants*. Biophysics. 27:144-149.
- [41] Henton, S.M., A.J. Greaves, G.J. Piller and P.E. Minchin. (2002): *Revisiting the Munch pressure-flow hypothesis for long-distance transport of carbohydrates: modelling the dynamics of solute transport inside a semipermeable tube*. Journal of Experimental Botany. 53:1411-1419.
- [42] Kizilova, N.N. and L.O. Poszniak. (2005): *Biophysical mechanisms of long-distance transport of liquids and signaling in high plants*. Biophysical Bulletin. 15:99-103.
- [43] Thornley, J.H. and I.R. Johnson. (1990): *Plant and crop modeling: A mathematical approach to plant and crop physiology*. Oxford Univ.Press.
- [44] Kizilova, N.N. (2005) *Hydraulic Properties of Branching Pipelines with Permeable Walls*. International Journal of Fluid Mechanics Research. 32:98-109.
- [45] Kizilova, N.N. (2004): *Computational approach to optimal transport network construction in biomechanics*. Lecture Notes in Computer Science. 3044:476-485.

The mirror effect on xylem and phloem radial conduction

Veronica Angyalossy¹, Guillermo Angeles², Carolina Madero-Vega²

¹Universidade de São Paulo, Brazil; ²Instituto de Ecología, A.C. Xalapa, Veracruz, Mexico

Abstract

The axial conduction of the vascular system is supplied by specialized conducting cells of stems and roots. Such cells are present in the xylem as well as in phloem rays, and are denominated, respectively, as perforated ray cells (PRC) and sieve ray cells (SRC).

There are reports of their presence in the secondary xylem of more than 40 families of trees and lianas in the literature, whereas for the presence of SRC in the secondary phloem, there are only few previous reports. This could be due, in part, to the difficulty in studying this tissue with a functional-structural approach. We have observed that the presence of PRC is associated with the presence of SRC, and that this close association is linked to “the mirror effect” of the vascular cambium. That is, that the same radial initials forming the PRC in the xylem, give rise to the SRC in the phloem. Because of this mirror effect, those radial conducting cells of xylem and phloem present the same form of connection with the axial system, i.e., they form a bridge connecting two axial conducts at each side of a ray, via the perforation plate or the sieve plate, depending if they are in the xylem (in the first case) or in the phloem (in the latter). The perforated ray cells (PRC) are strongly related with the absence of parenchyma around the vessels in arboreous species, and connect the smallest vessel elements in trees and the smallest with the largest vessel elements in lianas. Micro casting of the vascular system of some tree and liana species, showing the network formed between PRC, SRC, and the axial vascular system of woody plants, give additional clues about the way in which the secondary phloem can play an important role in the refilling of embolized vessels in the secondary xylem.

Key words: Perforated ray cells; ray sieve cells, xylem, phloem, radial water transport.

Introduction

The axial conduction of the vascular system is supplemented by specialized conducting cells of the shoot and root radial systems, which originate from the radial initial cells of the cambium. In the secondary xylem, these cells, termed perforated ray cells (PRC), were described for the first time, in a very detailed manner, by Chalk & Chattaway [8] in the stem of 64 species comprising different, non-related families. After 40 years, presence of these cells started to be observed in different tree species by several authors, predominantly in tropical species [1, 6, 8, 11, 13, 15, 17, 20, 21, 22, 23, 24, 25, 27, 30, 31, 34, 35, 36].

Observations made by the above mentioned authors confirmed what was described by Chalk & Chattaway [9] and by the IAWA Committee [16], i.e., that the perforation plates of PRC could be of the same type, or different, as those of the vessel elements they make contact with; and that they occur in the upright and square cells of the uniseriate portion of multiseriate rays and, less frequently, can occur in the multiseriate portion of multiseriate rays (lianas, Cactaceae) where rays are very wide.

With respect to the phloem, such cells are denominated sieve ray cells (SRC), and their presence is less well documented than that of PRC, being the work of Chavan *et al.* [10] one of the first to document them in the phloem rays, where they were observed in isolated form, along with their companion cells, in species of three woody families. Later, Lev-Yaudin & Aloni [19] discussed their presence in rays in development; Rajput & Rao [29] observed them isolated or in groups in five woody species; finally, Pace *et al.* [28] observed them in some Bignoniaceae lianas.

Even though a lot of evidence accumulates on the presence of radial conducting cells in the xylem and phloem, our objective is to provide here more information on the connections between these radial cells and their neighbors, as well as to suggest a role for them in forming an integral vascular network.

Material and methods

For this study, we examined the wood of four arboreal species and the stem of two liana's species. Three species belong to *Siparuna* Aubl. (Monimiaceae), from the Brazilian Amazon Forest: *S. amazonica* Mart. ex A. DC.; *S. decipiens* (Tul.) A. DC.; *S. guianensis* Aubl.. One Cerrado species *Styrax camporum* Pohl, Styracaceae, São Paulo, Brazil. Two lianas species of the Bignoniaceae tribe, Bignoniaceae: *Stizophyllum riparium* (Kunth) Sandwith and *Tynanthus cognatus* (Cham.) Miers from Reserva Florestal São Paulo, Brazil, and from the tropical rainforest of Los Tuxtlas, Veracruz, Mexico.

For the wood samples, the histological sections were prepared according to standard techniques (18), stained with safranin and mounted in synthetic resin. The secondary xylem and phloem of liana stems were examined in detail. Therefore, in order to guarantee the integrity of these tissues, stem segments were fixed in FAA 70% [5]. After this procedure, the stems were sectioned after embedding them with polyethyleneglycol 1500 (10-25µm thickness), following Rupp [32]. Smaller portions of approximately 9 mm², with phloem, cambium, and xylem were embedded in Historesin® (Leica Microsystems), to obtain anatomical sections with less than 10 µm, that were stained in 0.05% toluidine blue in glacial acetic buffer at pH 4.7 [26].

Microcasting of the vascular system. Stems were left to dry in an oven at 80 °C for several days. Then, they were trimmed carefully with a razor blade, to expose open the vessels and sieve tube members. For the *Stizophyllum* lianas (Bignoniaceae) the regions of indented phloem (wedges of phloem) were treated separately from the regions of pure xylem (inter wedges). A mixture of Rhodorsil RTV 141 silicone was made following the package instructions, combining solutions A and B 10:1, respectively (by weight). Samples were immersed in this mixture in a tall, transparent plastic bag, and placed under vacuum for 20-25 minutes. After releasing the vacuum slowly, the samples were taken out, wiped with paper towels, and left in the freezer for 24 hours, at -30 °C, to allow the silicon to penetrate the tissues. Then, samples were placed in the oven at 60 °C for 24 hours, to allow the reticulation process to occur [4]. The tissues were exposed by removing the excess of hard silicon from around the samples, leaving intact only the transverse surfaces. This is a convenient way to avoid the silicon molds to disperse, after releasing them. After exposing the tissue, the sample is immersed in sulphuric acid 70% , diluted with frappé ice. The samples were left to digest in the acid solution, in an ice bath, for 24-36 hours, depending on the sample volume. When the samples were completely black and soft, they are immersed in a saturated solution of sodium bicarbonate in water, to neutralize the acid. When the solution stopped bubbling, the samples were washed in clean water, placed in an ultrasonic bath, to release the debris of tissue. Finally, the samples were placed in a solution of 50% sodium hypochlorite overnight, to complete the digestion process. Once the molds were released completely, they were oven-dry at 70 °C for 24 hours. After drying the molds in the air, they were mounted on SEM Stubbs, sputter-coated with Au-Pd, and observed under the SEM at an accelerating voltage of 25 Kv.

Results and discussion

The study of liana stems showed the “mirror effect” of the cambium, since the radial conducting cells were present at both sides of the cambium. The abundant literature on the subject mentions the presence of PRC in ca. 40 plant families, and Sonsin [34] confirmed that the occurrence of this character has neither a taxonomic nor a phylogenetic value. Its importance resides on functional aspects, as the role that they could play in assisting and adding to the axial transport, which is evidenced in the way the radial conducting elements are connected to the axial vessel elements.

In the case of the tree species analyzed, the perforated ray cells (PRC) are connected to the minor diameter vessels, as shown in *Fig. 1*. They are generally found isolated or in groups of two-three cells,

which are found in the uniseriate portion, beside to upright and/or square cells in multiseriate rays, as mentioned in the literature [9]. Furthermore, one other feature which is intimately related to the presence of PRC, is the presence of scarce to diffuse apotracheal parenchyma (*Fig. 1*). That is, there is a direct relationship between the absence of parenchyma abutting the vessels, and the presence of PRC, indicating that PRC must have a role as accessory tissue, *sensu* Braun [7].

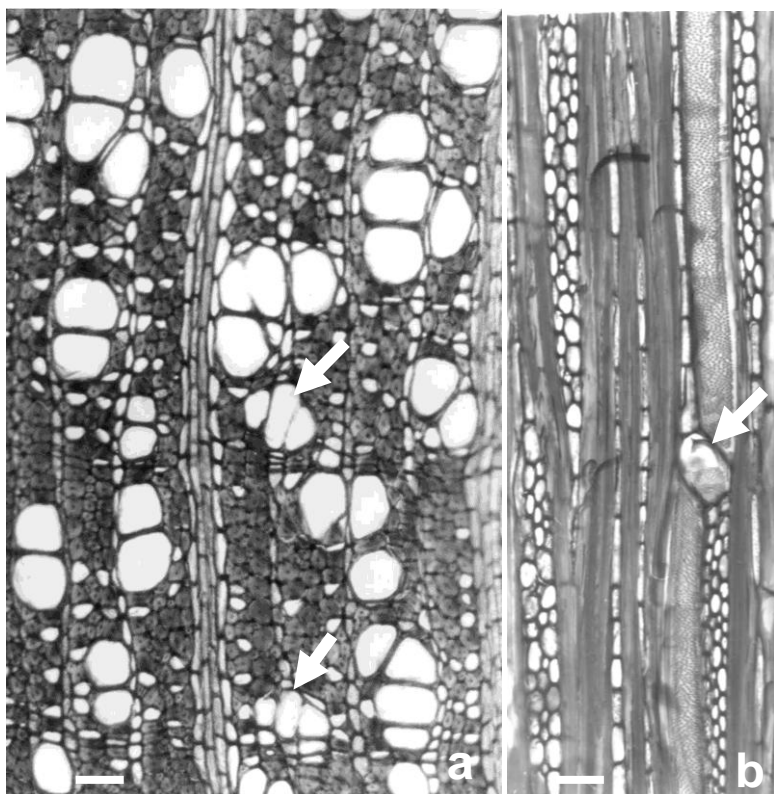


Fig. 1. Siparuna guianensis Tree. Wood.
a. Transversal Section (TA). b. Tangential section (TG).
Perforated ray cell (arrow) communicating two

On the other hand, in the two lianas species (*Tynanthus cognatus* and *Stizophyllum riparium*), the PRC are common in the xylem and confirm the observation of [12] for the species of the tribe Bignonieae. We observed that PRC are isolated or grouped, and are haphazardly distributed in the rays, since most of them are multiseriate; they could be in the lateral portion of rays (*Fig. 2a*), as well as in their central portion (*Fig. 2b*), in contact with square or upright cells. In these species very wide vessels are common and are associated to very thin vessels. An interesting finding was that PRC's have a strategic position within the radial cells, establishing a connection between wide and narrow vessels (*Fig. 2*). These cells have simple perforation plates at the contact areas between the two vessel elements touching them, and also have bordered pits on their lateral walls (*Fig. 4*).

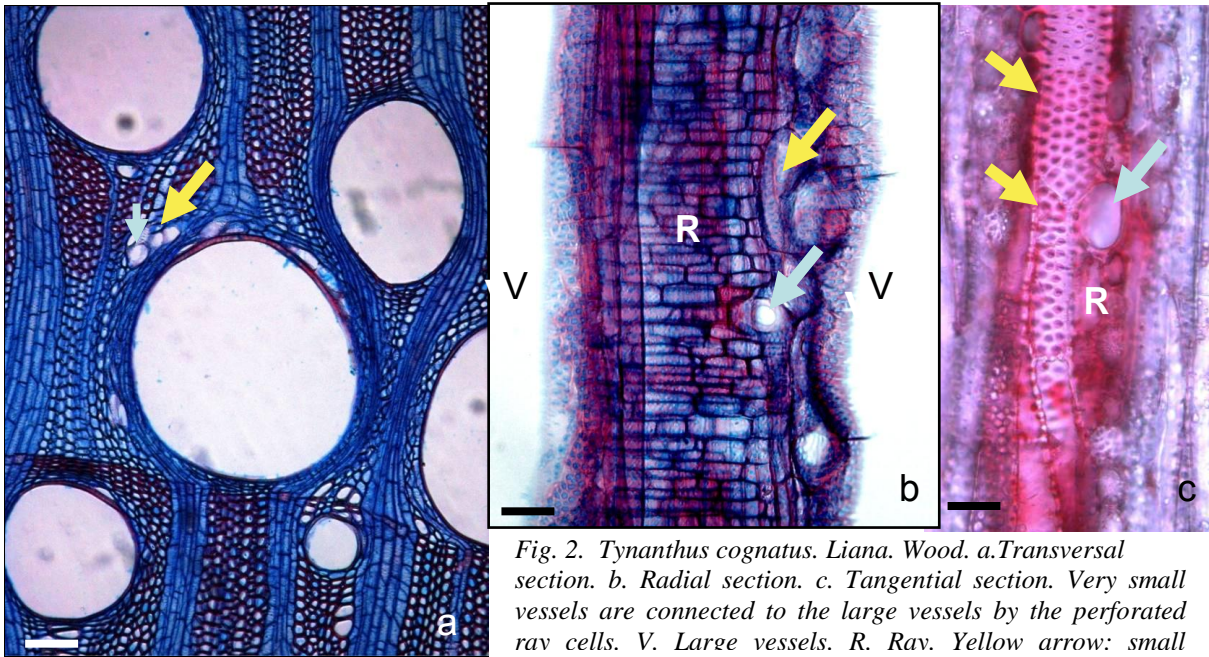


Fig. 2. *Tynanthus cognatus*. Liana. Wood. a. Transversal section. b. Radial section. c. Tangential section. Very small vessels are connected to the large vessels by the perforated ray cells. V. Large vessels. R. Rav. Yellow arrow: small

The sieve ray cells (SRC) observed in the tree and liana species are smaller than the sieve tube elements, they show a sieve plate similar or different to that of the axial conducting element in the phloem. In the tree species *Styrax camporum* (Angyalossy and Machado *in prep.*), the SRC are found by the uniseriate portion of multiseriate rays, in contact with the upright and/or square cells (Fig. 4), in a similar way to that of PRC, as shown in Fig. 1b.

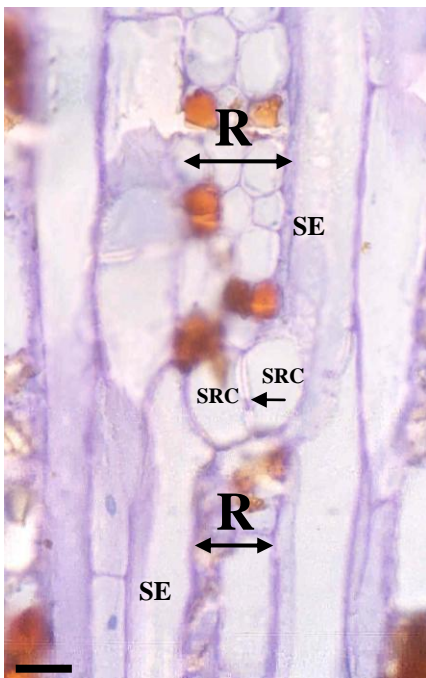


Fig.3. *Styrax camporum*. Tree. Phloem. Tangential section. Two sieve ray cells (SRC) connecting two sieve tube elements (SE). Note the compound sieve plate (arrow) communicating these two SRC. Ray (R): note that the SRC are present at the uniseriate portion of the multiseriate ray. Scale: 30 μ m

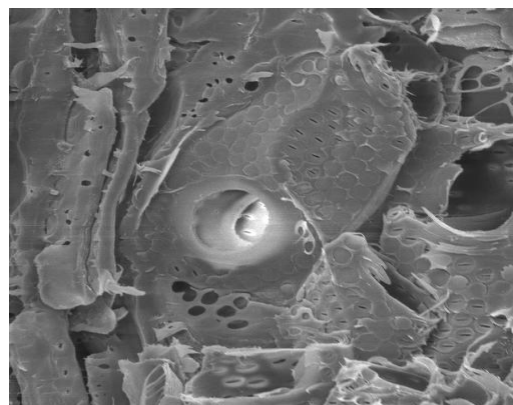


Fig. 4. *Tynanthus cognatus*. Liana. Detail of a perforated ray cell, with simple perforation plate and bordered pits. 700x.

In the liana species, the position of the SRC varies, and they can be found on the lateral portion of the ray, or inside of it, in contact with square and/or upright cells. The lianas of the Bignoniaceae family have very huge sieve tube elements, as seen in Fig. 5, which was also mentioned by Pace et al [28]. In the microcasting of the conducting cell of the liana shown in (Fig. 6), its large volume and compound sieve plate made of several sieve areas can be clearly observed.

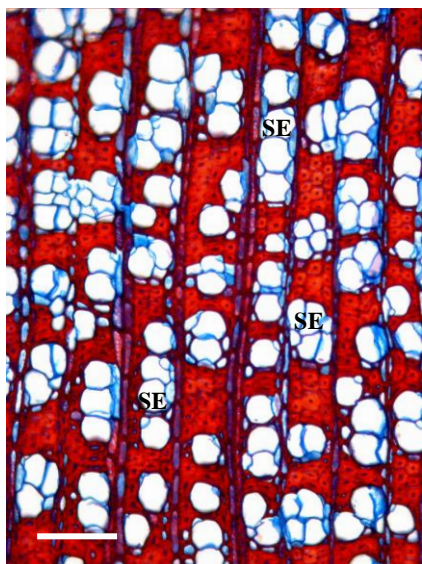


Fig. 5. *Stizophyllum riparium*. Liana. Variant Phloem. Transversal section. Sieve tubes elements (SE), with companion cells immerse on fibers matrix. Scale: 100 μ m

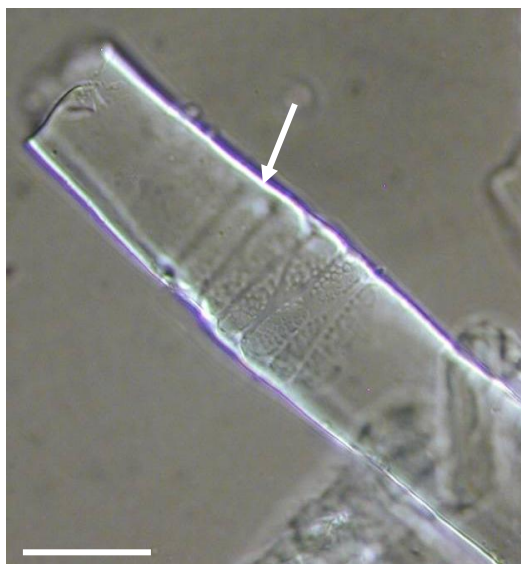


Fig. 6. *Stizophyllum riparium*. Liana. Variant Phloem. Microcasting of a sieve tube element with a compound sieve plate. Arrow indicates a sieve area of the sieve plate. Scale: 50 μ m

Redundancy in the vascular system is a key issue in hydraulic safety for the plant [14, 33]. This redundancy has been described as it only existed in the axial system. However, there is a complex network of radial conducting elements in the radial system that contributes significantly with this redundancy. The presence of radial conducting elements in the ray parenchyma of the secondary xylem of trees, lianas and shrubs is well established, but there are only few reports that these elements have a counterpart in the secondary phloem. We hypothesized that, because of the mirror effect of the vascular cambium differentiation, they have to occur radial sieve elements in the secondary phloem, of the reported species that present them on the xylem. Interestingly, we found that the radial cambial initial gives rise to the phloem and xylem radial conducting elements at the same position and on the vicinity of the same kind of ray cells, as a consequence of the mirror effect.

In spite of the mirror effect of the cambium, there is a marked difference in the frequency of radial conducting cells, those at the secondary xylem being more frequent than those at the secondary phloem. That difference could have two explanations: 1) the minor amount of tissue normally produced towards the phloem, as compared with the xylem, and 2) it could be a response to a condition of water stress in the axial system, as a measure to reinforce the axial hydraulic transport. The latter explanation is supported by experiments done by Aloni and Peterson [2] in which they induced the interruption of the axial phloem transport in *Dahlia pinnata*, causing the activation of the lateral phloem connections of the stems for the translocation of the assimilations [3]. Under natural conditions these phloem anastomoses are inactive.

Conclusion

As a consequence of the mirror effect of the activity of the radial initials of the cambium, we conclude: 1) the species reported as having perforated ray cells they have to possess also sieve ray cells as a network of radial conduction; 2) xylem and phloem radial conducting elements arise at the same position and on the vicinity of the same kind of ray cells; 3) the “mirror effect” is apparent only in the shape and position of the radial conducting elements, but not in the amount of tissue produced at both sides of the vascular cambium. PCR predominate of SCR.

Acknowledgements

The authors acknowledge financial supports by the National Council of Research and Development (CNPq) and the National Council of Science and Technology from Brazil and Mexico, respectively, for funding this research through grants No. 481034 and 90406. Fernando Ortega, from Instituto de Ecología, A.C. (Mexico) assisted us in taking some of the photographs, while Antonio C. F. Barbosa and Marcelo Pace provided some slides to illustrate our work.

References

1. Agarwal, M., S. Gupta, L. Chauhan and V. Painuly, (2002): *Perforated ray cells in Pistacia terebinthus: A new record for Anacardiaceae*. Indian Forester 128 (5): 562-566.
2. Aloni, R and C. A. Peterson, (1990): *The functional significance of phloem anastomoses in stems of Dahlia pinnata Cav.* Planta 182:, 583-590.
3. Aloni, R and J. R. Barnett, (1996): *The development of phloem anastomoses between vascular bundles and their role in xylem regeneration after wounding in Cucurbita and Dahlia.* Planta 198, 595-603.
4. André, J. P., (2002). *Organisation vasculaire des angiospermes : une vision nouvelle*. INRA editions. Paris.
5. Braun, H. J., (1984): *The significance of accessory tissues of the hydrosystem for osmotic water shifting as the secondary principle of water ascent, with some thoughts concerning the evolution of the trees.* IAWA Bulletin n.s. 5: 275 – 294.
6. Berlyn, G. P. and J. P. Miksche, (1976): *Botanical microtechnique and cytochemistry*. Iowa State University Press, Ames, USA.
7. Botosso, P.C and A.V. Gomes, (1982): *Radial vessels and series of perforated ray cells in annonaceae.* IAWA Bulletin 3(1): 39-44.
8. Ceccantini G.C.T and V. Angyalossy-Alfonso, (2000). *Perforated ray cells in Bathysa meridionalis (Rubiaceae).* IAWA Journal 21: 77–82.
9. Chalk, L. and M.M. Chattaway (1933): *Perforated ray cells.* Proc. Roy. Soc. 113:82-108.
10. Chavan, R. R.; J. J. Shah, J.J. and K. R. Patel (1983): *Isolated Sieve Tube(s)/elements in the bark of some angiosperms.* IAWA Bull. n.s. 4(4): 255-263.
11. Dayal, R., Vijendra Rao and B. Sharma, (1984): *Perforated ray cells in woods on indian Myrsinaceae and Loganiaceae,* IAWA Bulletin 5(3): 225-228.
12. Dobbins, D. R., (1971): *Studies on the anomalous cambial activity in Doxantha unguis-cati (Bignoniaceae). II. a case of differential production of secondary tissues.* American Journal of Botany 58: 697-705.
13. Dos Santos, G. M. A., (1995): *Wood anatomy, chloroplast DNA, and flavonoids of the tribe Bignonieae (Bignoniaceae).* Ph.D. Dissertation. University of Reading, Reading, United Kingdom.
14. Eom, Y.G., and Y.J. Chung, (1996): *Perforated ray cells in Korean hardwoods of Berberidaceae and Euphorbiaceae,* Journal of Korean Forestry Society 88 (3): 74-378.
15. Ewers, F. W., J. M. Ewers, A. L. Jacobsen and J. López-Portillo, (2007): *Vessel redundancy: Modeling safety in numbers.* IAWA Journal 28: 373:388.
16. Gupta, S. and M. Agarwal, (2005): *Wood microstructure of Indian Staphyleaceae with particular reference to unusual type of perforated ray cell.* Indian Forester 131: 1049-1055.

- IAWA Committee, (1989). *IAWA list of microscopic features for hardwood identification*. IAWA Bulletin n.s. 10(3): 219-332.
16. Joffily, A., D. Freire Dominigues and R. Cardoso Vieira, (2007): *Perforated ray cells in the root and stem of Maytenus (Celastraceae)*, IAWA Journal 28: 311-314.
17. Johansen, A., (1940): *Plant microtechnique*. McGraw-Hill Book Co, New York.
18. Lev-Yadun, S. and R. Aloni. (1991): *Polycentric vascular rays in Suaeda monoica and the control of ray initiation and spacing*. Trees - Structure and Function 5(1): 22-29.
19. Machado, S.R. and V. Angyalossy-Alfonso, (1995): *Occurrence of perforated ray cells in wood of Styra camporum Pohl. (Styracaceae)*, Revta bras. Bot., 18: 221-225.
20. Machado, S. R, B. L. Morretes and V. Angyalossy-Alfonso, (1997): *Comparative wood anatomy of root and stem in Styra camporum (Styracaceae)*. IAWA Journal 18: 13-25.
21. McLean, J.D. and P.E. Richardson, (1973): *Vascular ray cells in woody stems*, Phytomorphology 23: 59–64.
22. Merev, N., Z. Gerçek, B. Serdar, F. Ersen Bak and T. Birtürk, (2005): *Wood anatomy of some Turkish plants with special reference to perforated ray cells*. Turkish Journal of botany 29: 269-281.
23. Nagai, S., J. Ohtani, K. Fukazawa and J. Wu, (1994): *SEM observations on perforated ray cells*, IAWA Journal 15 (3): 293-300.
24. Nazma, B.S. and R. Vijendra Rao, (1981): *Occurrence of perforated ray cells in the wood of Dryp roxburghii (Wall.) Hurusava*, IAWA Bull n.s. 2: 201–202.
25. O'Brien, T. P., N. Feder and M. E. McCully, (1964): *Polychromatic staining of plant cell walls by toluidine blue O*, Protoplasma 59: 368-373.
26. Otegui, M. (1994): *Occurrence of perforated ray cells and splitting in Rapanea laetevirens and R. lorentziana (Myrsinaceae)*, IAWA Journal 15(3): 257-263.
27. Pace, M. R., L. G. Lohmann and V. Angyalossy, (2009): *Evolução da variação cambial e do floema em Bignoniaceae (Bignoniaceae)*, Dissertação de Mestrado, Universidade de São Paulo, São Paulo, Brasil.
28. Rajput, K. S. and K. S. Rao, (1997): *Occurrence of sieve elements in phloem rays*, IAWA Journal 18 (2): 197-201.
29. Rudall, P.J. (1982): *An unusual type of perforation plate in Canthium barbatum (Rubiaceae)*. IAWA Bull. 3(2): 127–129.
30. Rudall P.J. (1985): *Perforated ray cell in Hyptis hagei – a new record for Labiatae*. IAWA Bull. n.s. 6: 161–162.
31. Rupp, P. (1964): *Polyglikol als Einbettungsmedium zum Scneiden botanischer Präparate*. Mikrokosmos. 53: 123-128.
32. Schenk, H. J., S. Espino, C. M. Goedhart, M. Nordenstahl, H. I. M. Cabrera and C. S. Jones, (2008): *Hydraulic integration and shrub growth form linked across continental aridity gradients*. PNAS 105 (32): 11248-11253.
33. Sonsin, J.C., S.R. Machado and C.R. Marcati. (2008): *Perforated ray cells in the wood of roots and branches of Cerrado species from Brazil*. IAWA Journal 29: 291–299.
34. Terrazas, T. (2000): *Occurrence on perforated ray cells in genera of Pachycereae*. IAWA Journal 21(4): 457-462.
35. Van Vliet, G.I.C.M. (1976): *Radial vessels in rays*. IAWA Bulletin 3:35-37.

Diversity of hydraulic and biomechanical wood properties in 22 tropical rainforest species of French Guiana.

Juliette Boiffin¹, Sandra Patino², Meriem Fournier³, Sandrine Isnard⁴, Tancrède Alméras⁵

¹*INRA, Ecologie des Forêts de Guyane « ECOFOG », UMR CIRAD 93 CNRS 8172
AgroParisTech-ENGREF INRA 745 UAG 43, BP 316, 97300 Kourou*

²*INRA, Ecologie des Forêts de Guyane « ECOFOG », UMR CIRAD 93 CNRS 8172
AgroParisTech-ENGREF INRA 745 UAG 43, BP 316, 97300 Kourou*

³*AgroParisTech-ENGREF, Laboratoire d'Etude de la Ressource Forêt Bois « LERFOB »
UMR INRA AgroParisTech-ENGREF 1092, 14 rue Girardet F-54000 Nancy*

⁴*CNRS, UMR AMAP TA A51 / PS2, 34398 Montpellier cedex 5*

⁵*CNRS, Laboratoire de Mécanique et Génie Civil, Université de Montpellier 2/CNRS UMR
5508. cc 048 – Place Eugène Bataillon, F-34095 Montpellier*

Abstract

We aimed at analysing some functional trade-off or associations between wood traits among the diversity of tree species in a tropical rain-forest and how they are related to the ecological functioning of species, along a gradient from pioneer to shade tolerant species. 22 species have been studied at the early sapling stage in the natural site of Paracou in French Guiana . Wood basic density, hydraulic traits (specific conductivity and vulnerability to embolism) and mechanical traits (modulus of elasticity and maximal strain at fracture limit) have been measured. Species sampling cover a wide range of mechanical and hydraulic performances. Wood basic density varies from 0.4 to 1. There is a narrow, and not strongly associated to the species ecology, relation between the modulus of elasticity and the wood density. As known by wood technologists, such a relation is strongly determined by physical causes, as wood density mainly represent the material porosity. Mechanical safety measured by the maximal strain at fracture limit, which is quite independent to the modulus of elasticity, is also positively correlated with wood density. As expected since specific conductivity is linked to the fourth power of lumen diameter, specific conductivity is negatively but less strongly correlated to basic density. All the species are hydraulically vulnerable that is not surprising in a wet environment as the tropical rainforest, but the pioneer species are less vulnerable. Thus, the less hydraulically vulnerable woods are also the more conducting and the less mechanically stiff and deformable. At this level of sampling (the range of tree species that coexist in a wet tropical rainforest), there is no absolute physical necessity of trade-off between hydraulic safety and performance, neither between hydraulic performance and mechanical stiffness. Therefore, results obtained at wider scale, i.e. by comparing species on a wide range of environmental conditions from wet to dry forests, cannot be extrapolated : some trade-off or associations depend strongly on the sampled environment variations, while others as association between density and Young's modulus are more stable . According to their needs in their environment, pioneer species in the Paracou site combine a low wood density, a high hydraulic performance and a lower hydraulic vulnerability of wood. The relations are mainly influenced by some extreme behaviour and actually, traits varies quite independently with a great variability. Such results concerning wood are discussed in relation with the stem performance that integrate wood and geometrical or size effects.

The Effects of Modified Lignin Monomer Ratios on Hydraulic Conductivity and Resistance to Embolism in Hybrid Poplar (*P. tremula* x *P. alba*)

Jeffrey A. Pierce^{1,2}, Frank W. Ewers³, Jameel Al-Haddad², and Frank W. Telewski^{1,2}

¹W.J. Beal Botanical Garden, Department of Plant Biology, Michigan State University, East Lansing, MI, U.S.A., pierce28@msu.edu, telewski@cpa.msu.edu

² Department of Plant Biology, Michigan State University, East Lansing, MI, U.S.A., jameel@msu.edu

³ Biological Sciences, California State Polytechnic University, Pomona, CA, U.S.A.,

fwewers@csupomona.edu

Abstract

The mechanical properties of lignin have long been studied. However, there has been little research into how lignification of the cell wall affects hydraulic properties in water conducting cells. Most experiments that have looked into this have focused on comparing hydraulic properties across species and wood density could be used as a proxy for lignin content. Observed differences in these experiments could be attributed to differences in vascular anatomy and not solely differences in lignin composition. The ability to genetically manipulate the ratios of lignin monomers present in tissues allows us to examine the role of lignin content and lignin monomers in hydraulic movement of vascular tissues without modifying the overall anatomy of the vascular system. In this experiment, we used a line of poplar (*Populus tremula* x *P. alba*) clones genetically modified to over-express the Ferulate 5-Hydroxylase (F5H) enzyme. Over-expression of the F5H enzyme resulted in an increased syringyl:guaiacyl ratio within the plants' cell walls. The F5H clones and wild type poplars were subjected to water stress over a 4 week period, and hydraulic conductivity and vulnerability to embolism were measured. Gas exchange was monitored throughout the experiment to assess stress levels in the plants. Initial measurements have shown an increased initial hydraulic conductivity in the F5H clones over the wild type before water stress was induced. However, as water stress increased the F5H clones showed an increase in vulnerability to embolism and a decreased hydraulic conductivity compared to the clones. This may suggest an increased brittleness and vulnerability to cavitation in the modified cell walls. No differences in gas exchange values have been observed between the F5H and wild type clones.

Introduction

Lignin's role in growth and development has mainly been attributed to providing structural support, mechanical strength, and protection from pests (Jung and Ni 1998). However, Boyce *et al.* 2004, suggested that lignification of cell walls may also play a role in a plants hydraulic properties. There have been a number of experiments that have examined the trade offs between mechanical strength and hydraulic conductivity in plants. However, most of these experiments have found only a weak relationship between mechanics and hydraulics (Kern *et al.* 2004; Wagner *et al.* 1998; Woodrum *et al.* 2003; Rosner *et al.* 2008). None of these experiments have looked at a the role of wall cytochemistry in their analyses. It has been postulated in the literature that the evolutionary development of syringyl lignin was a functional response of the cells shifting specialization from water movement to mechanical strength (Yoshinaga *et al.* 1992). This would suggest that an increase in syringyl lignin in the vessel elements would actually decrease hydraulic conductivity since syringyl is a main component of fiber cells and the primary monomer in vessels elements is guaiacyl in wild type plants. The genetic modification of plants to produce lower lignin contents or a higher syringyl to guaiacyl, S:G, ratio have been

developed as an alternative (Baucher *et al.* 2003). The modification of the lignin biosynthetic pathway provides an easier way to process cellulose pulp for paper and biofuel crop manufacturers. Yet, concerns over how this manipulation may affect the functional ecology and fitness of these plants have arisen. Many experiments on modifying the lignin biosynthetic pathway have focused on how manipulation affects biomechanical and carbon fixation properties. Coleman *et al.* 2008, recently examined how a decrease in overall lignin content affects hydraulic conductivity and gas exchange properties in hybrid poplar. The results showed an overall decrease in gas exchange properties and hydraulic conductivity. This experiment is one of the first to look at how manipulation of lignin monomer ratios in hybrid poplar changes the plant's ability to transport water effectively. The experiment was approached with three overarching objectives. First, to quantify the effects of modified lignin monomer ratios on the overall hydraulic conductivity and resistance to embolism. Second, to examine the role of lignin monomers in providing mechanical strength and water transport and whether there is evidence for trade offs between mechanics and hydraulics. Finally, to further elucidate the possible role of lignin monomer evolution in the adaptation of separate conducting and supporting tissues of Angiosperms.

We hypothesized that modifying the S:G lignin monomer ratio will significantly affect the water relations in hybrid poplar. More specifically, the F5H clones, with increased S:G lignin monomer ratios, will show increased hydraulic conductivity and resistance to embolism. This was informed by preliminary tests done by the Telewski lab during biomechanical testing (unpublished; Al-Haddad).

Material and methods

For this experiment hybrid poplars (*P. tremula* x *P. alba*) modified to over-express the *Arabidopsis* gene encoding Ferulate 5-Hydroxylase enzyme driven by the cinnamate-4-hydroxylase promoter were used (Franke *et al.* 2000; Humphreys *et al.* 1999). The over-expression of F5H increases the syringyl:guaiacyl ratio within the cell walls. The plant material was obtained from Dr. David Ellis (CellFor Inc., Vancouver, BC).

The experiment involved a two way test between the wild type clones and clones over-expressing F5H. There were 30 clones per treatment for a total of 60 trees in all (30 clones x 2 treatments). The clones were propagated by root stock and allowed to grow for 4 months. This method has been used in our lab before and tests have shown the lignin content and monomer ratios to stay constant through this method. The clones were set up in a randomized 6 x 10 block in a greenhouse at Michigan State University.

At the beginning of the experiment, all trees were watered to field capacity. Initial measurements were taken and samples (n=6) were harvested on the first day (t=0) to quantify values for well watered trees. Water was then withheld from the trees to examine the effects of water stress on the trees. Preliminary tests on the clones' response to water stress have shown a minimum of 30 days until the clones reached permanent wilting point, PWP. This can be largely affected by both temperature and humidity during the stress period and so the time until PWP may change throughout the experiment. For this experiment, the clones underwent water stress for approximately 24 days. Throughout this time, measurements on gas exchange, pressure potential, and chlorophyll fluorescence were taken every 2-3 days. Samples were also collected every 12 days for measurements of hydraulic conductivity and vulnerability to embolism (n=6 per clone per measurement; n=12 per clone in total). After 24 days, 6 plants from each clone were randomly selected to be watered and 6 plants remained under water stress. This was used to examine the clones' ability to refill cavitated vessels and the effects of cavitation fatigue. Clones selected for re-watering were watered to field capacity every day for six days. All remaining trees, both stressed and re-watered, were then harvested after the six days (t=30).

Hydraulic conductivity was measured using a Sperry apparatus (Sperry *et al.* 1988). Samples were harvested underwater to ensure no air infiltration into the xylem during cutting. The samples were cut down to 14cm segments underwater. Stem samples were tested for initial hydraulic conductivity and then flushed with pressurized water to clear any embolism. After flushing the stems were measured again to calculate the maximum hydraulic conductivity. Vulnerability curves were constructed to examine the clones' resistance to embolism. The samples were attached to a centrifuge and then placed under varying levels of negative pressure. The samples were measured for hydraulic conductivity again to calculate the percent loss of conductivity, PLC at each negative pressure. The methods for both hydraulic conductivity and vulnerability curves were the same as those used in previous experiments (Alder *et al.* 1996; Jacobsen *et al.* 2005; Sperry *et al.* 1988).

In order to monitor the degree of stress within the trees, as well as, measure how the water stress affects the trees a number of physiological parameters were measured. The stomatal conductance and transpiration of the clones were measured using a Li-Corr 1600 steady state porometer. Leaves from each clone were harvested and used to measure pressure potentials using a Scholander pressure chamber. Finally, the chlorophyll fluorescence of each clone was monitored using a Li-Corr 6400. The Li-Corr 6400, also measures transpiration, E , assimilation, A , and internal carbon, C_i , but these values may be influenced by the saturating light pulse delivered during measurement of chlorophyll fluorescence. Further testing is under way to see if the Li-Corr 6400 can be effectively utilized to take these additional measurements simultaneously with fluorescence measurements.

The gas exchange and chlorophyll fluorescence measurements were taken every 2 days. Pressure potential measurements require the destructive harvesting of leaves. Reducing leaf area can affect the degree of water stress a plant experiences. To avoid over harvest of leaves pressure potentials were measured every 4 days.

Results and discussion

Experiments on the well-watered plants have shown an increase in hydraulic conductivity in the F5H clones compared to the wild type. It is unclear at this time if this is due to the increase in syringyl within the vessel elements or due to changes in the overall vessel cell wall anatomy. Jacobsen *et al.* 2005 examined the role of xylem fiber cells in providing resistance to embolism in vessels. They found that modulus of elasticity (MOE) and modulus of rupture (MOR) had a strong correlation with xylem pressure at 50% loss of conductivity, P50. These results suggest that fiber strength may play a key role in protecting vessel elements from cavitation. Increasing the S:G ratio and thereby increasing the mechanical strength of the stem, may be effectively increasing the protection the fibers contribute to resistance to cavitation. It is unclear if the observed increase is due to changes in the fibers or vessel elements. Analyses done by our lab have shown that over-expression of F5H causes an increase in the overall S:G monomer ratio but relative proportions of S:G ratios according to cell type and function are still maintained. That is, vessel elements will still maintain a higher guaiacyl to syringyl ratio. The conservation of this gradient suggests a possible importance of balancing mechanical strength and hydraulic conductivity between vessels and fibers (Koehler and Telewski 2006).

While an increase in S:G ratio will increase hydraulic conductivity and resistance to embolism in well watered plants, the F5H clones have actually shown decreased hydraulic conductivity and resistance to embolism compared to the wild type while under water stress. Our initial tests on the hydraulic conductivity and resistance to embolism in the F5H clones and wild type during water stress has shown that the wild type has a higher hydraulic conductivity and resistance to embolism. These results are opposite to the tests on well watered treatments. We have speculated that the increase in strength and rigidity in the vessel elements may make the vessels more brittle and therefore more susceptible to microfractures and implosion due to high negative pressures associated with water stress. This may increase the incidence of air seeding and/or cavitation fatigue experienced by clones expressing increased S:G ratios. Examination of the anatomical structure of the clones experiencing water stress may clarify this further.

Acknowledgments

The authors wish to thank Jason Kilgore, David Rayman and Peter Carrington for their assistance in conducting this research. This research was supported by the National Research Initiative of the USDA CSREES grant number 2005-35103-15269.

References

- Alder NN, WT Pockman, JS Sperry and S Nuismer. 1997. Use of centrifugal force in the study of xylem cavitation. *Journal of Experimental Botany* 48: 665-674.
- Baucher M, *et al.* 2003. Lignin: Genetic Engineering and Impact on Pulping. *Critical Reviews in Biochemistry and Molecular Biology* 38: 305-350.
- Boyce CK, *et al.* 2004. Evolution of Xylem Lignification and Hydrogel Transport Regulation. *Proc. Natl. Acad. Sci. USA* 101: 17555-17558.
- Coleman HD, *et al.* 2008. Perturbed Lignification Impacts Tree Growth in Hybrid Poplar – A Function of Sink Strength, Vascular Integrity, and Photosynthetic Assimilation. *Plant Physiology* 148: 1229-1237.
- Franke R, McMichael CM, Meyer K, Shirley AM, Cusumano JC, Chapple C (2000) Modified lignin in tobacco and poplar plants over-expressing the *Arabidopsis* gene encoding ferulate-5-hydroxylase. *Plant J* 22, 223-234
- Humphreys JM, Hemm MR, and Chapple C. 1999. New routes for lignin biosynthesis defined by biochemical characterization of recombinant ferulate 5-hydroxylase, a multifunctional cytochrome P450-dependent monooxygenase. *PNAS* 96 (18): 10045-10050.
- Jacobsen AL, *et al.* 2005. Do Xylem Fibers Affect Vessel Cavitation Resistance? *Plant Physiology* 139: 546-556.
- Jung HJ, and W Ni. 1998. Lignification of Plant Cell Walls: Impact of Genetic Manipulation. *Proc. Natl. Acad. Sci. USA* 95: 12742-12743.
- Kern KA, *et al.* 2005. Mechanical Perturbation Affects Conductivity, Mechanical Properties and aboveground Biomass of Hybrid Poplars. *Tree Physiology* 25: 1243-1251.
- Koehler L and Telewski FW. 2006. Biomechanics and Transgenic wood. *American Journal of Botany* 93(10): 1433-1438.
- Rosner S, A Klein, U Muller, and B Karlsson. 2008. Tradeoffs between Hydraulic and Mechanical Stress Responses of Mature Norway Spruce Trunk Wood. *Tree Physiology* 28: 1179-1188.
- Sperry JS, Donnelly JR, Tyree MT. 1988. A method for measuring hydraulic conductivity and embolism in xylem. *Plant, Cell & Environment* 11(1): 35-40.
- Wagner KR, FW Ewers, and SD Davis. 1998. Tradeoffs between Hydraulic Efficiency and Mechanical Strength in the Stems of Four Co-occurring Species of Chaparral Shrubs. *Oecologia* 117: 53-62
- Woodrum CL, FW Ewers, and FW Telewski. 2003. Hydraulic, Biomechanical, and Anatomical Interactions of Xylem from Five Species of Acer (Aceraceae). *American Journal of Botany* 90(5): 693-699.
- Yoshinaga A, Fujita M, Saiki H (1992) Relationships between cell evolution and lignin structural varieties in oak xylem evaluated by microscopic spectrophotometry with separated cell walls. *Mokuzai Gakkaishi* 38, 629-637

Hydraulic conductance of developing shoots of aspen

Anu Sober, Julia Shilina

University of Tartu, Institute of Ecology and Earth Sciences, Tartu, Estonia

Abstract

To create a driving force for water upward movement, the water potential of upper part of shoot must be more negative than water potential at the shoot base. Usually water potential of upper leaves is also more negative compared to that of lower leaves. However, our measurements showed reverse gradient of water potential between upper and lower leaves on terminal branches of 3 year old trembling aspen and hybrid aspen trees (in average -0,6 for upper and -2 MPa for lower leaves). To explain the reverse gradient in leaf water potential we proposed, that the difference in water potential between brshoot xylem and leaf must be much less in upper, developing leaves than in lower mature leaves. Also hydraulic resistance of leaves must be significant compared to hydraulic resistance in tree roots and trunk, The degree how low water potential drops in leaves depends on leaf hydraulic conductance and transpiration rate. Leaf hydraulic conductance and stomatal conductance were estimated and significant differences between developing and mature leaves were found. Hydraulic conductance was higher and stomatal conductance was lower in upper developing leaves compared to lower mature leaves. Differences in pathways of water movement in developing and mature leaves

4. Biomechanics aspects of plant development

Study of the ultrafast trap of an aquatic carnivorous plant

Philippe Marmottant, Olivier Vincent and Catherine Quilliet

*Laboratoire de Spectrométrie Physique
CNRS / Université de Grenoble
140 av de la Physique, 38042 Grenoble, France*

Abstract

A process difficult to perform within the channels of a miniaturized lab, called Lab on a chip, is the sudden transfer of a small sample of fluid in a closed container. This operation is naturally found in the vegetal kingdom when considering the aquatic carnivorous plants *Utricularia* (common name bladderwort). These plants are gifted with suction traps [1]: a contact opens a door, the trap sucks in liquid, and then the door closes hermetically, all this sequence within the impressive time of a few milliseconds, barely visible with the naked eye. We present an on-going experimental study of the biomechanics of the trap. The motion of the trap door is recorded by a high-speed camera. We could record the natural activation of the trap (using different fresh water crustaceans), and then provoked activation of the trap with a fine needle. With this artificial triggering, we could focus on the succession of the two distinct phases of the suction : first the door opens, and second the door closes hermetically after suction. The motion is therefore different from the close-only traps of the Venus flytrap [2]. We also record the associated fluid motion. We find that the door is curved inwards at opening, and that an intense flow of liquid (1 m/s) is generated during a very short time (0.4 ms). These observations are interpreted with a biomechanical approach involving elasticity and flow. The door opening is described as a buckling of the door under the a preexisting pressure, because of a softening of the door following the touch of sensitive trigger hairs. The door closure results from the equilibration of pressures, and from the fact that the relaxed shape of the door is the closed position. An original behavior was also recorded: after a few hours the trap activates spontaneously. If the precise biological function of this phenomenon is unclear, it expresses the fact that the sensibility of the plant increases considerably at time of 5 hours, and is trigger by very small fluctuations. We conclude by the presentation of a simple analytical model that will prove useful for the design of a biomimetic reproduction of the trap, and its implementation in a microfluidic circuit as a miniaturized pipette.

Introduction

Carnivorous plants

It exist more than 600 species of know carnivorous plants, resulting from a spectacular adaptation to difficult environmental conditions (lack of nutriments or poor lightning [3]). These plants present different kind of traps to catch animals. It is possible to classify these traps into two groups:

- Passive traps, where the plant is immobile, such as the one from the *Nepenthes* (fig. 1a)
- Active traps, such as the one from the *Dionea* (fig 1b).

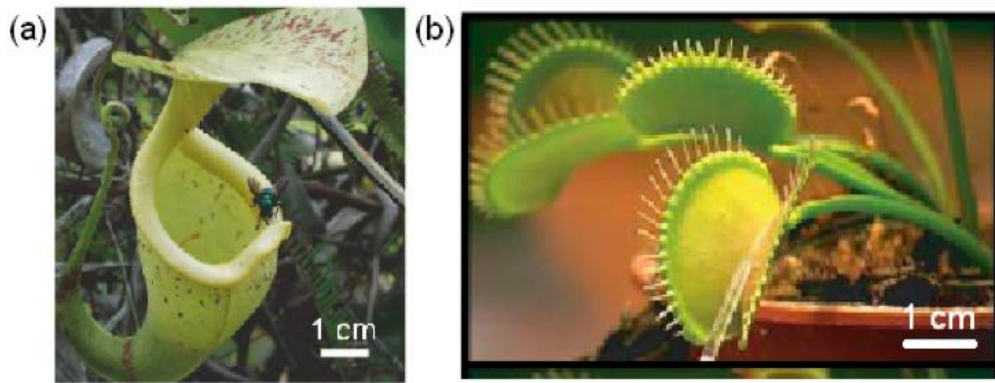


Fig. 1 Two kinds of carnivorous plants (a) *Nepenthes* with a passive trap (taken from [4]), (b) *Dionea* with an active trap (taken from [2]).

A complementary approach between physicists and biologists has recently helped to elucidate the mechanisms of certain traps, such as the use of an elastic instability to maximize the speed of capture with the *Dionea* [2] or the presence of a visco-elastic fluid in the receptacle of the [4].

Bladderwort (*Utricularia*)

The bladderworts are a type of aquatic carnivorous plant that regroups 180 species, including the one we study, *Utricularia inflata*. Numerous biologists have contributed to their description, and to the explanation of their mechanism. First studied in the 19th century, their carnivorous character has been discovered in 1876 [5]. A first detailed study is due to Lloyd [6], who described the plant constitution and proposed an electromechanical analogy to describe its behaviour. This model was later abandoned by the author himself, because of its extreme complexity.

The plant consists in a long stem, from which ramifications are attached, and where the traps are situated. The traps, sometimes called utricles have a size of the order of 1mm.

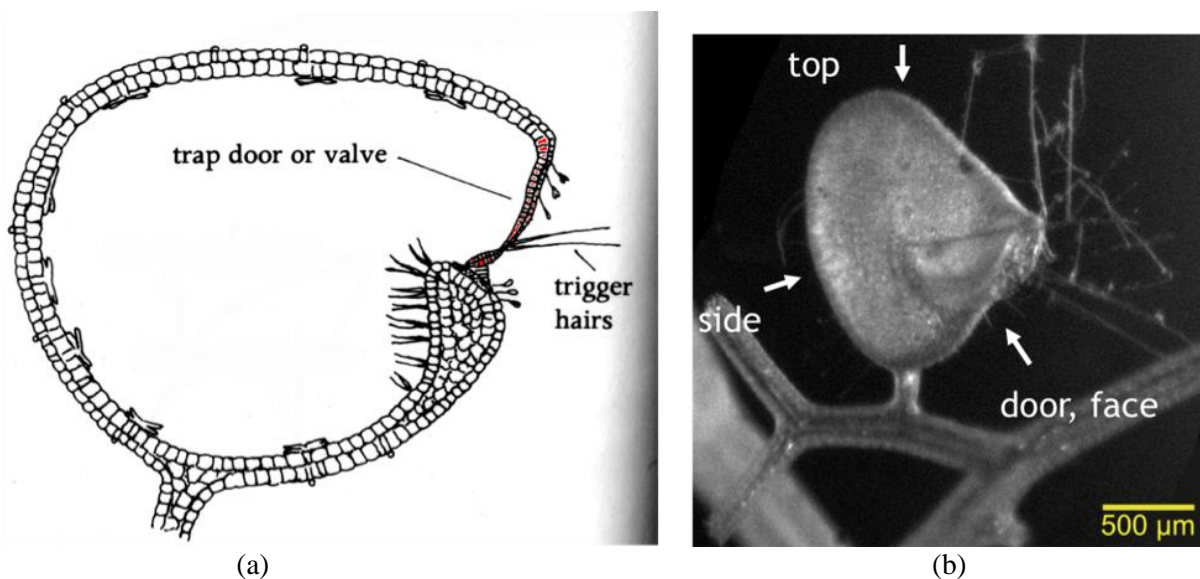


Fig. 2. Description of the trap of the *Utricularia* (a) Cutview of the trap, taken from Juniper 1989, (b) The three main view of the trap.

It is possible to distinguish two main parts:

- the wall, made of only two layers of cells. Its thickness is sensibly constant all over the surface (we measured 60 micrometers), and increases near the door to form a quasi-circular (ring) rigid structure, whose bottom part is called the threshold.
- the door is attached to the upper part of this ring. The bottom part is in compression against a threshold called the velum whose role is to avoid any leaks when the door is closed. The door is also composed of only two cell layers, thinner than in the wall. The precise structure is complex. Several trigger hairs are located on the door wall, and are responsible for the triggering of the door. The thickness of the door is around 15 micrometers.

Summary of the literature on the trap mechanism

We now sum up a few results that generally admitted concerning the trap mechanism of the bladderwort.

Trap setting. The plant is able to pump water from the inside to the outside of the trap, probably through the action of glands situated in the wall (bifide and quadrifide glands, see [7]). The utricle is waterproof, and this deflates the trap, with a depression of the water inside as low as 0.17 bars. The time need to set the trap varies from 30 minutes to 4 hours. The plants resist the pressure thanks to its reaction on the velum [8].

Trap activation. When a prey approaches the trap, it can trigger the trap by touching one of the sensitive hairs situated at the bottom of the door, which provokes its aperture and the suction of the water, the prey included. The door then closes back, which impedes the prey from escaping and renders the utricle waterproof again. The capture time is evaluated to be 30 milliseconds approximately [6,9]. The door opening and closing mechanism remains poorly understood, and two main hypothesis are generally put forward:

1. Mechanical hypothesis: the trigger hairs act as levers, and un-block the door, which provokes the entrance of water, until the pressures are established again [10]. We showed that this hypothesis remains un-probable in view of our observations.
2. Active hypothesis: touching the hair triggers a stimulus that propagates in neighbouring cells, and provokes a softening of the door, that is therefore not able to resist the applied pressure anymore [11]. Measurements have shown a change of electrical potential [12], which would corroborate this hypothesis.

The originality and complexity of the trap arise from the fact that, contrary to the other carnivorous plants that have only a closing phase, the bladderwort are able to open and close in a fraction of a second.

The comprehension of the trap triggering is limited by several aspects: the observation of ultra-fast phenomena, and a modelisation of the physical phenomena at play.

Material and methods

Plants were cultivated indoors, in deionized water, in order to reproduce their natural inhabitat.. Traps were placed in a Petri dish and were observed under an inverted microscope (up to 10x, with an IX70, Olympus), or under a stereomicroscope (up to 8x, Discovery V8, Carl Zeiss).

The dynamics of the trap were studied with two kinds of imaging techniques:

- time-lapse, with a 'slow' camera operated at 1 frame every 100s (0.01 Hz)
- high-speed, with a camera that could operate up to 8000 frames per seconds (8000 Hz, Phantom Miro 4, Vision Research).

Image analysis was performed with ImageJ (freeware) and Matlab (Mathworks, Inc.).

A more detailed study can be read in the master thesis by Olivier Vincent (in French, [13]).

Results and discussion

We present results obtained from the analysis of image sequences, for the two phases of the trap.

3.1 Trap setting

Seen from the top, it is convenient to evaluate the volume diminution of the trap measured by its thickness e , at the waist of the trap profile (figure 3). The shape evolves with time, with an exponential decrease of the thickness (figure 4), with a characteristic time of 52 minutes.

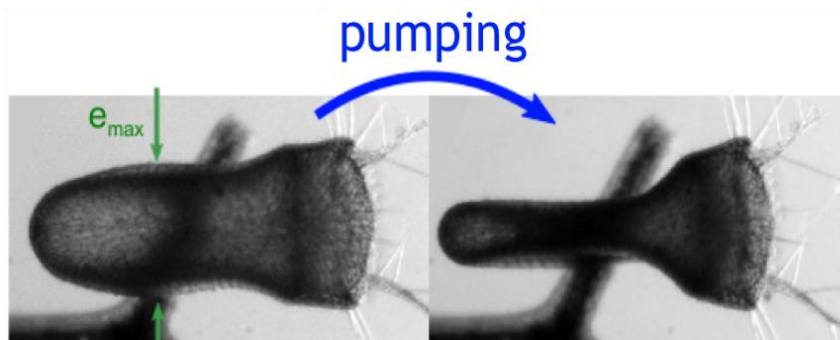


Fig. 3. Evolution of the trap profile, monitored by the thickness e .

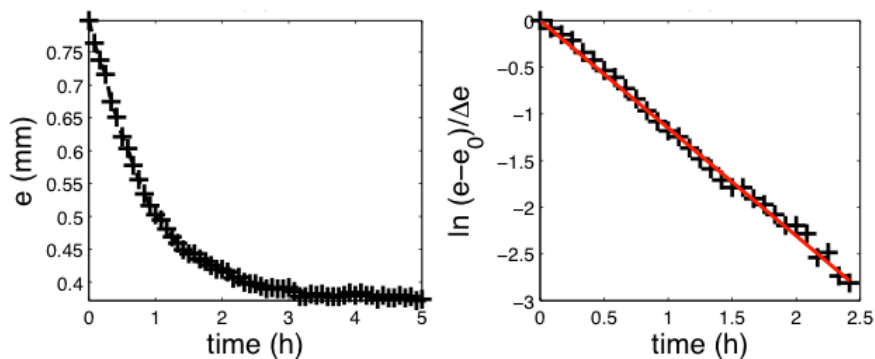


Fig. 4 exponential decrease of the thickness, represented in linear units (left) and in logarithmic units (right).

3.2 Trap suction

The door is activated manually with the tip of a needle, by touching one of the sensitive hairs. We could show that a very small bending of the trigger hair is enough to trigger the response. The duration of the suction is extremely short: around 2 ms, see figure 5.

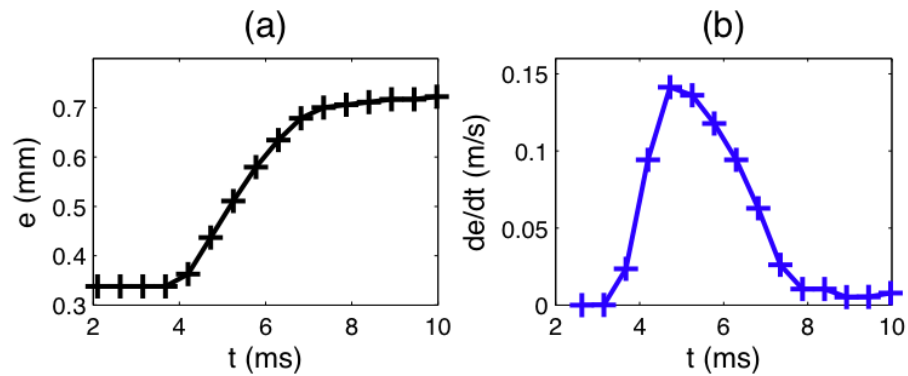


Fig. 5. Fast inflation of the plant after trap activation.

The aspiration is monitored using tracer particles (hollow glass beads), placed near the door. The maximum fluid velocity measured is extremely high: 1.5 m/s at the largest.

We distinguish two zones:

- an aspiration zone, where the particles, followed during their motion are completely trapped (red particles on figure 6),
- the outer zone, where particles are moved by the suction, but do not enter (black particles on figure 6).

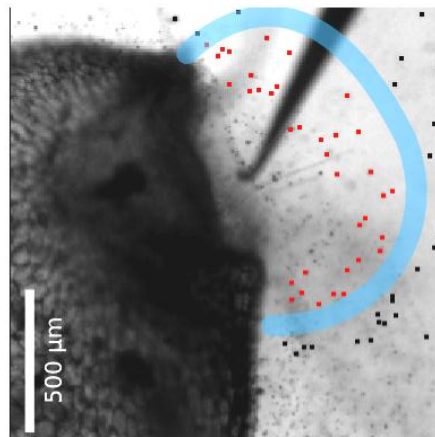


Fig. 6. Aspiration zone.

Moreover, the examination of the sequence of images reveals that the door closes completely after a short time (estimated as 20 ms).

Conclusion

A low-speed and high-speed video study revealed the huge dissymmetry of time scales at play during the trap setting and activation. The trap setting can be interpreted as a storage of elastic energy, and is similar to the bending of an arc.

The release of the energy is violent and occurs with a few milliseconds, suggesting large amplitude bifurcation of the behaviour, triggered by touching the hair. We could confirm that the species *Utricularia inflata*, has an active mechanism, since a slight touch, not enough to create a lever effect, was at the origin of the trap triggering.

The door opens and closes in a very short time interval of around 20 ms: we are currently undertaking detailed experiments of the phases of the door opening. In our presentation we will play high-speed recordings, that help see the succession of the door opening and closing.

The spontaneous activation of the trap was also recorded. In our presentation, we will show that even in the absence of manual trigger, small fluctuations (from instance from tiny swimming paramecium present in the medium, or maybe just thermal fluctuations) were enough to trigger the trap, on average after 5 hours.

As a perspective, this work is also at the source of a biomimetical inspiration to design a miniature suction apparatus, helpful to isolate very small quantities of liquid. This biomimetical design would find its place within the realm of Lab-on-chip devices, that need to treat very small amounts of liquid.

Acknowledgements

We would like to acknowledge fruitful discussions with Yoël Forterre.

References

1. Skotheim, J.M. and L. Mahadevan (2005): *Physical limits and design principles for plant and fungal movements*. Science, 308 (5726): 1308–1310.
2. Forterre, Y, and J. M. Skotheim, Jan M., Dumais, and L. Mahadevan. (2005): *How the venus flytrap snaps*. Nature, 433(7024): 421–425.
3. Juniper, B.E., R. J. Robins, and D. M. Joel (1989): *The carnivorous plants*. Academic Press.
4. Gaume, L. and Y. Forterre (2007): *A viscoelastic deadly fluid in carnivorous pitcher plants*. PLoS One 2: 1185.
5. Treat, M (1876) *Is the valve of utricularia sensitive ?* Harper's New Monthly Magazine, 52: 382–387.
6. Lloyd, F.E. (1942) *The carnivorous plants*. Chronica Botanica Company.
7. Sasago, A., and T. Sibaoka (1985) *Water extrusion in the trap bladders of utricularia vulgaris i. a possible pathway of water across the bladder wall*. Bot. Mat. Tokyo, 98: 55–66.
8. Lloyd, F.E. (1929) *The mechanism of the water tight door of the utricularia trap*. Plant Physiol., 4(1) :87–102.
9. Sydenham, P.H. and G. P. Findlay (1973) *The rapid movement of the bladder of utricularia sp*. Aust. J. biol. Sci., 26: 1115–1126.
10. Heide-Jorgensen, H.S. (1981) *Parasitisme og carnivoi. Kompedium*, Institut for Planteanatomi og Cytologi, Kobenhavns Universitet.
11. Stuhlman, O Jr and E. B. Darder (1950) *The action potentials obtained from venus's-flytrap*. Science, 111: 491–492.
12. Sydenham, P.H and G.P Findlay (1975) *Transport of solutes and water by resetting bladders of utricularia*. Functional Plant Biol., 2(3): 335–351.
13. Vincent, O. (2009) *Une approche physique du fonctionnement du piège d'une plante carnivore aquatique: l'Utriculaire*, Master thesis, University of Grenoble I.

Effect of fracture behaviour of crystalline plant waxes on insect pad contamination

*Elena V. Gorb*¹, *Feodor M. Borodich*² and *Stanislav N. Gorb*³

¹Max Planck Institute for Metals Research, Stuttgart, Germany; ²Cardiff University, UK;

³University of Kiel, Germany

Abstract

Attachment ability of insects depends on various factors. Thus, depending on the texture of the substrate, insects use different mechanisms of attachment. For example, they can apply their claws to interlock with surface irregularities on rough (at the mesoscale) surfaces. On smooth and microrough substrates, insects rely on specialised attachment organs called adhesive pads [1].

In the case of attachment to plant surfaces, roughness and other surface features affect the adhesion of insects. It is well known that most of aerial surfaces of land plants are covered by epicuticular waxes. Microscopically small crystals often emerge from the wax film, covering the plant cuticle, and cause the pruinosity or powdery appearance of the surface in many plant species (*Fig. 1*) [1-4]. Length of the wax crystals ranges from few hundred nanometres to several micrometers. Such pruinose waxy surfaces are found on stems, leaves, flowers, seeds and fruits in many plants [4].

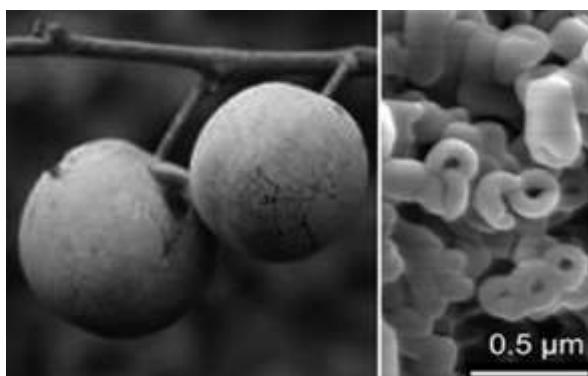


Fig. 1 Prunus domestica fruits (left) covered by tubular wax crystals (right, SEM-micrograph).

The plant crystalline waxes perform different functions (see reviews [5] and [6]). In particular, they can protect plants by reducing insect attachment to plant surfaces covered by wax crystals. This phenomenon is very important, because most of insect species are associated with plants, and hence, they should be able to attach successfully to plant surfaces [7].

Dealing with insect attachment to plant substrates, one has to consider a problem of interaction between insect adhesive organs and the plant surface. Contacting surfaces of many insect adhesive devices and pruinose waxy plant surfaces possess various patterns of micro- or nanostructures. The reduction of insect adhesion on the plant surfaces, covered with the crystalline epicuticular wax, may be explained by (1) the decrease of the real contact area between the substrate and insect adhesive pads caused by plant surface microroughness (roughness-hypothesis); (2) the absorption of the pad fluid from the pad surface by the structured wax coverage (fluid-absorption-hypothesis); (3) the dissolving of the wax by the pad secretion, resulting in hydroplaning and substrate slipperiness (wax-dissolving-hypothesis); and (4) the contamination of pads by wax crystals (contamination-hypothesis) [8].

The contamination-hypothesis has been proven experimentally for several insects and a series of plant species [9,10]. In this study, the possible mechanisms of the plant wax crystals fracture during adhesive contact formation between insect adhesive organs and plant surface were examined, in order to explain the contamination of insect pads by wax crystals. The crystals with high and low slenderness (aspect) ratios were investigated. The models are presented for crystals of a tubular shape, but the general approach is valid also for crystals of other shapes.

It is shown that mechanisms of the wax crystal fracture may be rather different, depending on the slenderness ratio of the crystals. If the values of the slenderness ratio are higher than the critical values, one has to apply the formulae of either elastic or elastic-plastic buckling. For five plants species under consideration (*Aquilegia vulgaris*, *Berberis vulgaris*, *Chelidonium majus*, *Prunus domestica*, and *Aristolochia fimbriata*), the critical value of the slenderness ratio for elastic buckling is 26.5, while for elastic-plastic buckling it is 18.7. If the values of the slenderness ratio are lower than the critical values, one has to consider bending of the crystals, because rather short crystals may be bent under the weight of insects as elastic-plastic beams. The bending moment in the crystal at the fixed end is proportional to the crystal length. These conclusions are not only in agreement with our previous observations [10] that the contamination ability of insects is related to both the largest dimension and the largest aspect ratio of crystals, but they give also more quantitative insight into these observations. The calculations show that from all considered plant wax crystals having tubular shapes, only crystals of *A. fimbriata* (Fig. 2) could buckle elastically. In this plant species, wax crystals on specialised weir trichomes in flowers contribute to trapping and retention of insects and consequently, to cross-pollination [11]. Failure behaviour of wax crystals of *A. fimbriata* is important, in order to capture extremely small brachyceran flies, associated with this plant.

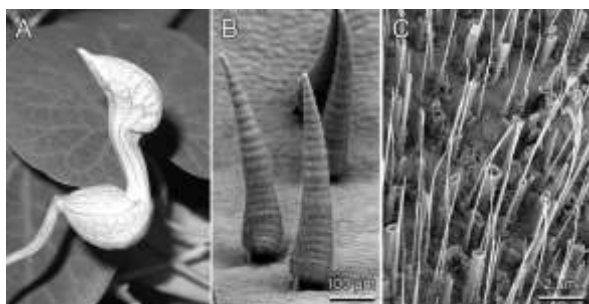


Fig. 2. *Aristolochia fimbriata* flower. A. Flower. B. SEM-micrograph of trichomes on the inner surface of the flower trap. C. Wax crystals covering the trichome surface (SEM-micrograph). from [11]

However, since the calculated values of the slenderness ratio for most tubular plant crystals are lower than the critical value and, therefore, formulae of the elastic-plastic buckling can not be applied, these crystals should be examined for their resistance to elastic-plastic bending. The examination of possible fracture mechanisms of plant waxes showed that it is very unlikely that plant crystals could buckle, while it is likely that an insect may break crystals by elastic-plastic bending and contaminate attachment pads.

The full length paper on this topic is submitted to the Journal of Theoretical Biology (2009).

References

1. Gorb, S. (2001): *Attachment devices of insect cuticle*, Kluwer Academic Publishers: Dordrecht, Boston, London.
2. Barthlott, W. and Ehler, N. (1977): *Raster-Elektronenmikroskopie der Epidermis-Oberflächen von Spermatophyten*. Trop. Subtrop. Pflanzenwelt. 19: 367-467.
3. Barthlott, W. and Wollenweber, E. (1981): *Zur Feinstruktur, Chemie und taxonomischen Signifikanz epikutikularer Wachse und ähnliche Sekrete*. Trop. Subtrop. Pflanzenwelt. 32: 7-67.

4. Barthlott, W., Neinhuis, C., Cutler, D., Ditsch, F., Meusel, I., Theisen, I. and Wilhelmi, H. (1998): *Classification and terminology of plant epicuticular waxes*. Bot. J. Linn. Soc. 126: 237-260.
5. Barthlott, W. (1990): *Scanning electron microscopy of the epidermal surfaces in plants*, in Scanning electron microscopy in taxonomy and functional morphology, Claugher, D. (Ed.), Clarendon Press: Oxford. p. 69-94.
6. Bargel, H., Koch, K., Cerman, Z. and Neinhuis, C. (2006): *Structure-function relationship of the plant cuticle and cuticular waxes – a smart material?* Func. Plant Biol. 33: 893-910.
7. Gorb, E.V. and Gorb, S.N. (2009): *Contact mechanics at the insect-plant interface: How do insects stick and how do plants prevent this?*, in Scaling in solid mechanics, Borodich, F.M. (Ed.), Springer: Dordrecht. p. 243-252.
8. Gorb, E. and Gorb, S. (2002): *Attachment ability of the beetle Chrysolina fastuosa on various plant surfaces*. Entomol. Exp. Appl. 105: 13-28.
9. Gorb, E., Haas, K., Henrich, A., Enders, S., Barbakadze, N. and Gorb, S. (2005): *Composite structure of the crystalline epicuticular wax layer of the slippery zone in the pitchers of the carnivorous plant Nepenthes alata and its effect on insect attachment*. J. Exp. Biol. 208: 4651-4662.
10. Gorb, E.V. and Gorb, S. N. (2006): *Do plant waxes make insect attachment structures dirty? Experimental evidence for the contamination hypothesis*, in Ecology and biomechanics – A mechanical approach to the ecology of animals and plants, Herrel, A., Speck, T. and Rowe, N. P. (Eds.), CRC Press: Boca Raton, p. 147-162.
11. Oelschlaegel, B., Gorb, S. N., Wanke, S. and Neinhuis, C. (in press): *Structure and biomechanics of trapping flower trichomes and their role in pollination biology in Mediterranean Aristolochia (Aristolochiaceae)*. New Phytol.

Biomechanics of fern spores discharge: the sporangium opening

Xavier Noblin¹, Jared Westbrook^{2,3}, Nicolas Rojas⁴, Médéric Argentina⁴ and Jacques Dumais²

¹ Laboratoire de Physique de la Matière Condensée, UNSA, Parc Valrose, 06108 Nice Cedex 2, France; ² Organismic and Evolutionary Biology, Harvard University, Cambridge, MA, 02138 USA; ³ Department of Botany, University of Florida, Gainesville, FL, 32611 USA; ⁴ Laboratoire Jean-Alexandre Dieudonné, UNSA, Parc Valrose, 06108 Nice Cedex 2, France.

Abstract

We study the mechanism of spore discharge in ferns. It consists in the fast release of a spring-like structure, the sporangium, a capsule which contains the spores, after its opening due to dehydration. Thirteen cells constitute the annulus, the elastic structure that surrounds the capsule containing the spores. The water inside these cells evaporates through a thin membrane. The resulting decrease in volume, along with cohesive induced forces, lead to a change in the curvature of the annulus. We study here in detail the opening dynamics for natural, isolated sporangia dipped into osmotic solutions. We compare our results with a model and the corresponding numerical simulations. This allows us to extract the different physical parameters characteristic of the annulus. We also look at the cavitation threshold and deduce from our results on the opening dynamics the negative pressure reached in the cells which was up to 10 MPa. This work will allow a better understanding of the fast closing dynamics of fern sporangia which eject the spores.

Introduction

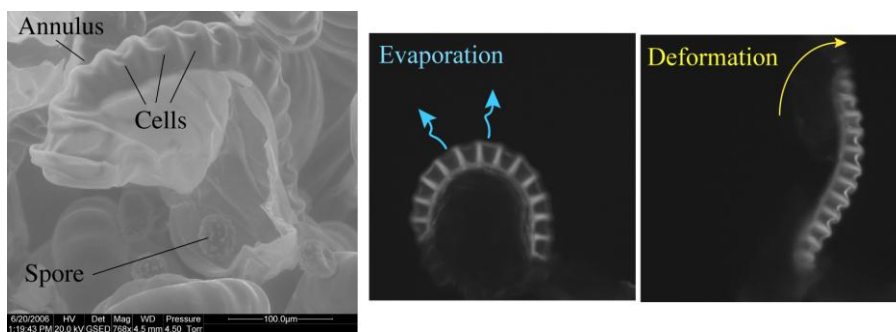
The catapult-like motion of sporangia ejecting fern spores is among the fastest in plant kingdom. It relies uncommonly on the use of water under large negative pressure more than a hundred times the atmospheric pressure, which generates initial spores speed higher than 10 m/s. Common ferns reproduce by means of spores that develop in a spherical shape capsule: the sporangium. These spores, 40 microns in size, are quickly ejected by the release of a spring-like structure: the annulus that surrounds a part of the circumference of the sporangium (see Fig. 1). By an astonishing mechanism, the water contained in the cells of the annulus evaporates under dry condition leading to a large deformation of the annulus. Due to the cohesion of water, high tension states are reached. When the water in the cell can no longer sustain such negative pressures, a cavitation bubble nucleates, the tension is quickly released. As in a catapult, the elastic energy thus stored is converted into kinetic energy for the spores and for the annulus as it springs back. The annulus closes then very rapidly to its initial curvature.

Fern reproduction has been studied for centuries and it has been known for a long time that sporangia act as a catapult (see [1], [2]). Almost a century ago, it has been shown that high negative pressures were reached in the annulus cells ([3]-[4]). Later the only theoretical study of the mechanism was performed by King [2], which was able to predict ejection speed for the spores based on an energy balance. Ritman and Milburn have confirmed that cavitation event triggers the spring release by using ultrasound method to detect cavitation bubbles [5].

To better understand the physical properties of the annulus, we focus here on the mechanical mechanism responsible for the opening of fern sporangia under dehydration. Depending on the external imposed water potential, we have looked at the dynamics of opening and the elastic energy storage in the annulus. We have also study the cavitation threshold and the negative pressure built in the cells.

We have studied experimentally isolated sporangia dipped into osmotic solution of given water potential Ψ_e . We have measured the evolution of their curvature as function of time and we have focused on the characteristics time of the process and the limiting curvature reached as function of Ψ_e . We have considered a particular species: *polypodium aureum* which presents sporangia with only 13 cells, leading to easier observation and analysis. By comparing to our theoretical model, we have extracted the numerical values of the important parameters and compared them to expected values for this system. Our model also allows us to determine the negative pressure built in the cells which can reach more than 10 Mpa. We discuss the works of Renner [3] and Ursprung [4] in the light of our results. We emphasize the difference between the external osmotic potential needed to cavitate and the actual negative pressure at which cavitation is observed because of the existence of an internal osmotic potential in cells of fern annuli that our study reveal. We present in the next section the materials and methods, then our results on the experiments and on the model, along with a discussion before the conclusion.

Fig. 1. Left: A fern sporangium and annulus in open state after spore discharge, ESEM image under controlled humidity. Right: Autofluorescence image showing deformation of the annulus under evaporation during the opening process. During the fast release, spores on the internal side of the annulus are ejected by its fast closure.



Material and methods

Sample preparation

We studied a particular species of a common fern *polypodium aureum*. Sori of mature plants were removed from leaves, and sporangia were separated and stored in pure water, one by one. The sporangia pedicels were rapidly glued to a glass pipet in ambient air and put back in water. When experiment is to be done, their spores release is provoked by placing the sporangia in ambient air. As in nature, water evaporation from the annulus cells induces strong annulus deformation which gets curved outward. When the tension in the cells overcomes a certain threshold, bubbles appear in cells. This releases the tension in the cells and the whole annulus springs back in some milliseconds, throwing away spores which were stuck together on the internal annulus wall.

Once the spores have been released, the sporangium is put back in water, until used for other experiments. The sporangium then comes back to a complete closed shape, as bubbles dissolve in pure water after a few minutes.

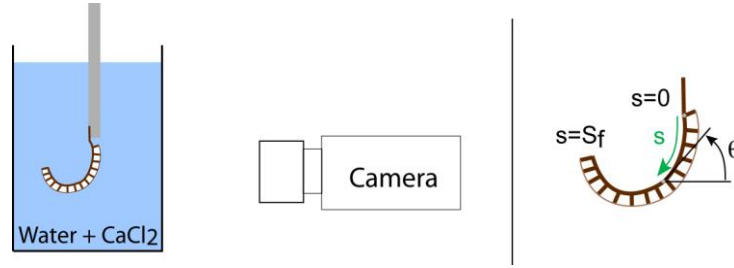
Opening experiments

During the opening experiments, we used such sporangia free of spores; we took them out of pure water to dip them into calcium chloride solutions at different concentration. At time $t=0$ we start to

film the sporangium, using a numerical camera (PCO) connected to a microscope objective (10X) through an optical tube. The sporangium is filmed from the side to observe the deformation of the annulus (see Fig. 1). Time lapse imaging is used, with movies lasting in general 25 minutes, and with a few seconds between each frame.

The annulus deformation speed and amplitude are modified by changing the difference in water potential between inside and outside of the cells. The water potential inside the cells Ψ_i have two components: the hydrostatic pressure P_i and the osmotic term θ_i . Outside of the natural cells, the water potential Ψ_e is controlled by humidity: $\Psi_e = RT \ln RH / V_w$. To have a better control on humidity, instead of putting the sporangia in humid air, we have used osmotic solutions in the range 0 - 2M of calcium chloride (CaCl₂) which corresponds roughly to a humidity range between 100 % and 80 %. In that case, the external water potential is mainly controlled by the osmotic potential: $\Psi_e = -\theta_e$, where θ_e is the osmotic pressure (we will use this positive quantity later on). Instead of having water evaporating from the cells into the atmosphere as in the natural case, we observe water flow out of the cells toward the solution.

Fig. 2. Left: Experimental setup. Right: Curvilinear abscissa.



By using image analysis, we determined the deformation of the annulus, that is the curvilinear abscissa s θ as shown in Fig. 2. The intersection between lateral cell walls and annulus is determined, leading to a set of N+1 points with N the number of cells.

We determine from this analysis the mean curvature of the whole annulus. The local curvature is given by: $K(s) = d\theta / ds$. And the mean curvature as function of s is: $\bar{K} = \int_0^{S_f} d\theta / ds ds / \int_0^{S_f} ds = \theta(s) - \theta_0 / S_f$. We performed different experiment for increasing osmotic pressure of the solution, which correspond to different concentration of CaCl₂, from 0 Mol/l to 2 Mol/l.

Force measurements

We have performed force measurement to determine the bending rigidity of the annulus. The experiment consists in measuring the force required to bend the annulus using a glass micropipet. To simplify the analysis, we have measured the average curvature K of a deformed annulus for different forces F, in a limited range of curvature variation. The annulus shape is assumed to be a half circle, the change in curvature is about 10 %. Following the calculation detailed in appendix, for small deformations around the initial curvature $K_0 = 1 / R_0$, the relation force-curvature is linear and given by (see [6] for detail):

$$K = \frac{1}{R_0} - \frac{2R_0}{\pi EI} F \quad (1)$$

We found for the annulus stiffness: $EI \approx 0.97 \cdot 10^{-10} N.m^2$. Using the relationship: $B = 2EI / lb^2$, using the value for b deduced from the fit: $b = 66 \mu m$, and $l = 80 \mu m$, we

found $B \approx 570 \text{ N.m}^{-1}$. This is close to the value deduced from the fit for B ($B \approx 444 \text{ N.m}^{-1}$, see later). Significant errors are made in those measurements in addition to the effect of turgor pressure since the cells are dipped into pure water, leading to an increase of the rigidity.

Results and discussion

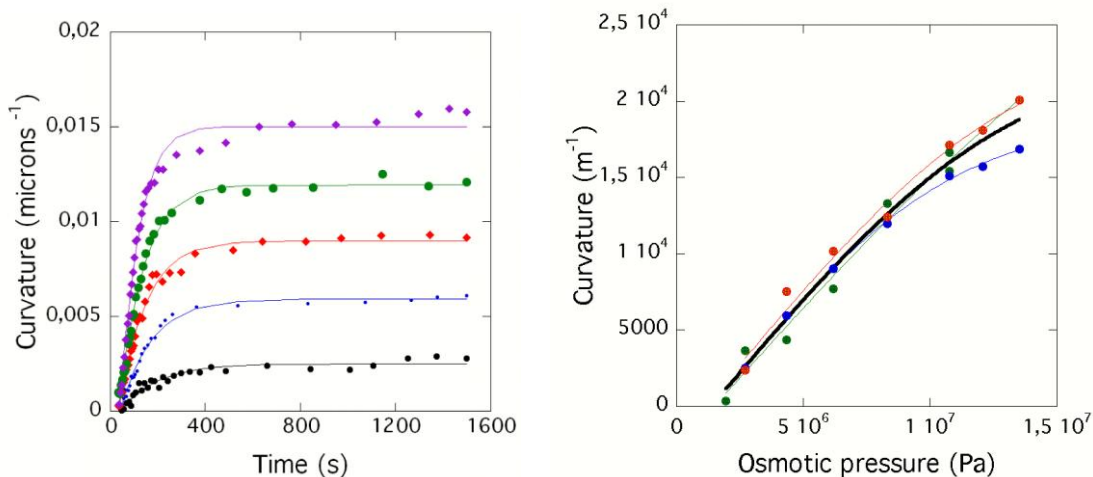
Curvature versus time

We have performed experiments to study the dynamics of opening of sporangia in osmotic solutions, as described in the materials and method section. We present in Fig. 3 different curves for the mean curvature for increasing concentrations. The general trend is the same for all the experiments: the mean curvature increases rapidly at the beginning, then the opening slows down, and the curvature saturates for long time to a value $K_\infty \theta_e$. As expected, the higher is the concentration, the higher is the deformation reached by the annulus, and the faster is the opening. For high concentrations, a cavitation event stop the opening process, in that case we have used the data before the closing phase. The characteristic time for the opening range between 20 s and 200 s in our experiments. In a natural environment (80 %RH), it takes then a few tens of seconds for the annulus to open. The opening is observed only above a threshold value for the external osmotic pressure, this is a clear evidence of an initial osmotic potential in the cells.

As we will see in the model, we could extract from our experimental data the value of the different parameters involved in the opening process. The stiffness B , the initial osmotic pressure in cells θ_0 and the membrane permeability L .

Fig. 3 (left) Mean curvature (μm^{-1}) versus time for osmotic pressures: 27.15, 43.39, 61.80, 83.24, 107.61 bar

Fig. 4 (right) Limit curvature vs. osmotic pressure of the solution. The three colors represent three experimental data series with different sporangia. The plain curve (black) represents a fit by Eq. (13).



Limit curvature versus solute concentration

We have traced the asymptotic deformation reached by the annulus as function of osmotic pressure (in Pa) in Fig. 4. We can check that it increases with increasing osmotic pressure. The plain curve in black is a fit from Eq. (10). We can note that a threshold osmotic pressure must be overcome to observe an actual opening of the sporangium: $\theta_E > \theta_0$. Its value is determined from the fit to be $\theta_0 \approx 13.9 \pm 3.6 \text{ bar}$. This must be due to the presence of solutes in the cells, which get more and more

concentrated as water leaks. This internal potential in the cells induces different consequences for the mechanism.

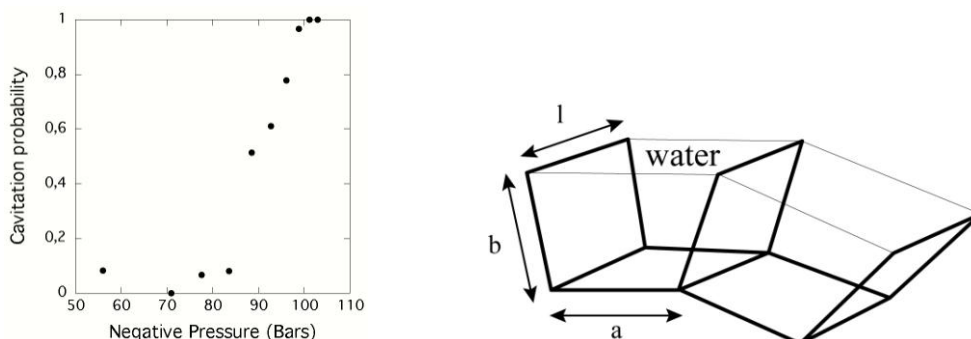
Firstly it gives a certain resistance to opening, for instance in order to avoid an early opening of non-matures sporangia. Secondly it modifies the way the pressure decreases in cells, in particular, for high potential; it reduces the dependency of the negative pressure over the external potential (or relative humidity). This ensures a sufficient deformation when critical negative pressure for cavitation is reached.

Cavitation threshold

When the cells are submitted to highly negative pressure, i.e. when the annulus gets very deformed, one or several cavitation events may occur and trigger the fast release of the annular spring. What we call events consists more generally in the growth of a vaporized water bubble in a cell. As the bubble grows, the tension is released, and the water can no more sustain the annulus spring far from its rest position, inducing its fast motion and spore dispersal. The exact microscopic mechanism for the nucleation of the bubble remains difficult to determine with our observation method and the poor spatial resolution associated with high speed imaging. A pre-existing bubble may grow, being inside the wall or coming from an air seeding phenomenon through the wall [7]. Spontaneous nucleation on the wall/liquid interface may also explain the appearance of the bubble [8].

We have analyzed in several experiments the probability of appearance of a cavitation event in at least one of the cells for different osmotic pressures. We have performed experiments during 850 s and calculated the ratio of cavitation events over the total number of trials for each osmotic pressure. We found a characteristic S-shape curve presented on Fig. 5.

Fig. 5 (left) Cavitation probability as function of the negative pressure estimated from our model. Fig. 6 (right) Cell characteristic dimension.



We find a threshold for 50 % cavitation around 8.9 MPa. Thus clearly here we see the difference between the external osmotic pressure (15 MPa) and the negative pressure at cavitation threshold (8.9 MPa).

Model

We note the concentration of solute inside the cell: $C_i(t)$, with an initial value : C_0 . The volume of the cell is: $V(t)$, with initial value: V_0 . We have the relation:

$$C_i(t) V(t) = C_0 V_0 \quad (2)$$

The water potential Ψ_e , in the solution, has only an osmotic component since the pressure outside the cells is the atmospheric pressure P_0 . In the low concentration regime, we have the

relation $\Psi_e = -RT\alpha_e C_e$ [9], C_e being the solute concentration. In our case, the general - nonlinear - relation has to be used, taken from [10] for CaCl_2 :

$$\Psi_e = -\theta_e C_e \quad (3)$$

The pressure inside the cells is P_i , the water potential noted: Ψ_i . We have: $\Psi_i = -\theta_i C_i + P_i - P_0$. We will make here the low concentration assumption, since the concentration inside the cell remains small. In the assumption:

$$\Psi_i = -RT\alpha_i C_i + P_i - P_0 \quad (4)$$

The water flux out of cell is noted: J_v in $\text{m}^3/(\text{m}^2.\text{s})$. We have:

$$J_v = L_{eff} (\psi_i - \psi_e) \quad (5)$$

L_{eff} is the effective permeability, in $\text{m.s}^{-1}\text{bar}^{-1}$, A is the area of the membrane. We will take L_{eff} to be only the permeability of the membrane L .

The water is assumed incompressible, the volume change is then: $V(t) - V_0 = -\int_0^t J_v(t')A(t')dt'$

and: $\frac{dV}{dt} = -J_v A = LA (\psi_e - \psi_i) = LA (-\theta_e C_e - \theta_i C_i + P_i - P_0)$

Finally:

$$\frac{dV}{dt} = LA t \left(RT\alpha_i \left(\frac{C_0 V_0}{V} \right) - \theta_e C_e - P_i - P_0 \right) \quad (6)$$

Water leakage induces a change in volume and cell walls deformation through a decrease of the pressure in the cell. We write the balance between bending moment from the annular spring and the moment from negative pressure on sidewalls, the other contributions are neglected.

For a simple trapezoidal geometry (see Fig. 6), the force due to pressure integrated over the height b of the cell lead to a torque of moment at its base $\frac{1}{2}dP_i lb^2$ which is balanced by the elastic response

of the annulus $EIdK : \frac{1}{2}dP_i lb^2 = -EIdK$

We have assumed that the material deforms linearly under stress. In case of large deformations, the cell walls can touch, leading to a non linear relation between K and P .

We deduce:

$$P_i(t) - P_0 = -\frac{2EI}{lb^2} (K(t) - K_0) \quad (7)$$

For such our idealized geometry, we can relate the change in volume to the change in curvature: $alb^2 dK = -dV$. Then, $dV/dt = -alb^2 dK/dt$, and $K(t) - K_0 = (V_0 - V(t)) / alb^2$. Finally:

$V(t) = alb^2 (K(t) - K_0) + V_0$. For $K = 0$, we have $V = alb$, we can then write:

$$V(t) = alb (1 - bK(t)) \quad (8)$$

Inserting Eq. (7), (8) in eq. (6), and introducing: $k = K - K_0$, $A = alb$ assumed constant, $B = 2EI/lb^2$ and $\theta_0 = \alpha RTC_0$, we find :

$$\frac{dk}{dt} = \frac{L}{b^2} \left(\theta_e - \frac{\theta_0 (1 - bK_0)}{1 - bK_0 - bk} - Bk \right) \quad (9)$$

This equation describes the relaxation of the curvature towards opening. Writing $dk/dt = 0$, this leads to an equation for the equilibrium value of the curvature. From the two possible solutions, we keep the one that leads to $k_\infty = 0$ when $\theta_e = \theta_0$. Thus we have:

$$k_\infty = \frac{b\theta_e + B(1 - bK_0) - \sqrt{b\theta_e + B(1 - bK_0)^2 + 4Bb(1 - bK_0)(\theta_e - \theta_0)}}{2Bb} \quad (10)$$

We have used a simple least square method to fit the Eq. (10) with our experimental results for k_∞ as function of the external osmotic potential. The value for k_∞ is determined by averaging the asymptotic value. The fit gives us θ_0 , b and B (first method)

We have also used a least square regression method to find the best combination of parameters that fits our data for the curvature versus time during opening: b, B, θ_0 and L. We varied the different parameters and solved numerically Eq. (9) using a shooting method to explore the parameters space. This method allows in addition to measure the permeability L.

We have studied three sporangia, giving 3 series: (s1, s2, s3). We found from the first and second method the results in tables 1 and 2 respectively:

Table 1 Parameters deduced from the fit of Eq. (10)

Parameter	value	unit
b	65.7 \square 8	μm
B	444 \square 72	N.m^{-1}
θ_0	13.9 \square 3.6	bar

Table 2 Parameters deduced from the

ⁿ Parameter	value	unit
^m b	52.7 \square 13,3	μm
^e B	307 \square 85	N.m^{-1}
^r θ_0	23.6 \square 5,1	bar
ⁱ L	6.9 \square 3.6 10^{-3}	$\mu\text{m}/(\text{bar.s})$

^c
al resolution of Eq. (9).

Due to the complex optimization process (a very large parameter space), the parameters deduced from the second method are not completely coherent with the values deduced from the first method. The reason is that for each curve of curvature versus time, four parameters are determined independently. An improve method have to be used to fit at the same time the data for the different concentrations in the same optimization procedure.

We comment on the results from the first method and the result for L from the second method.

We found $b = 65,7 \mu\text{m}$, which is a little larger than the actual distance measured on images (50 μm) for the height of walls separating cells. This light discrepancy can be explained because the precise cell geometry is not trapezoidal and this leads to an effective value for b slightly higher than actual maximum height.

We found $B = 444 \text{ N.m}^{-1}$, as mentioned this can be compared to our force measurements of the flexural rigidity EI times the geometrical parameters deduced from the fit for b, and measured for l

which leads to $B_f = 570 \text{ N.m}^{-1}$. The discrepancy can be explained by the large error in these measurements, and the fact that force experiments were done on turgid annuli (in water) that are stiffer than annuli in osmotic solution

We found $\theta_0 = 13.9 \text{ bar}$. That represents a quite high osmotic pressure. This has different interests. The first is that the opening occurs only when humidity is below a threshold, preventing early opening. A second is that if it would be null, the decrease in water potential to equilibrate an outside dry air would be taken only by the negative pressure leading to very high values that cannot be sustained by the water in the cells, leading to an early cavitation event.

We found $L = 0.0069 \mu\text{m}/(\text{bar.s})$. Most plant tissues present permeabilities in the range $0,01 - 0,2 \mu\text{m}/(\text{bar.s})$ [9]. Our value is then comparatively low, but very close to observed values in plant systems, in addition the use of an improved method for the fit may increase slightly this value. This relative low value prevents a too early water leakage from the cell when the sporangium is not mature yet to discharge its spores.

From our model, we can determine the pressure during the opening process by $P_i(t) = P_0 - B K(t) - K_0$. At equilibrium, $K = K_\infty$ and we have the relation:

$$P_i = P_0 - B K_\infty - K_0 = P_0 - \theta_e + \frac{\theta_0}{1 - bK_\infty}$$

leads to less negative pressure than the external osmotic potential imposed. Hence care has to be taken when discussing experiments from Ursprung, Renner... where the value at cavitation threshold in bar (up to 350 bar) is the equilibrium value of the external osmotic pressure, and it is not necessarily equal to the negative pressure. As detailed by Milburn in the study of cavitation in ascomycetes, the osmotic and negative pressure term (cavitation pressure) are of the same order. Here when the external potential is below -200 bars, the negative pressure does not continue to decrease a lot and saturates around 11 MPa. This ensures a not too early cavitation so that when it happens, the annulus deformation is almost complete. In fact, cavitation occurs when the sporangium is almost fully open. Geometrical and physical parameters are then optimized to match the tension the walls can sustain. In case of air-seeding, this corresponds to pore in the cell wall of size of order 15 nm which is a reasonable value for such plant cell wall structure [7].

Conclusion

We have described and modelled quantitatively the opening of fern sporangia using a controlled experiment in osmotic solution. We measured the cavitation threshold, and analyzed the data in terms of the actual negative hydrostatic pressure built in the cells. Our model explains the opening dynamics and equilibrium state with parameter in good agreement with expected values from the sporangia properties. An improved method for the optimization procedure will be developed in a future study [6].

References

1. Ingold C.T., Spore discharge in land plants, p.119 (1939)
2. King, A.L. PNAS, 30, p. 155 (1944)
3. Renner O., JAHR WISS BOT, 56, p. 647 (1915)
4. Ursprung A., BER DEUT BOT GES, 33, p. 153 (1915)
5. Ritman K.T., Milburn J.A., The acoustic detection of cavitation in fern sporangia, Journal of Experimental Botany, 41, 230, pp. 1157-1160 (1990)
6. Noblin et al. (in preparation)
7. Tyree M.T., Zimmermann M.H., Xylem Structure and the Ascent of Sap, Springer, 2nd ed. (2003)
8. DeBenedetti, P.G., Metastable Liquids: Concepts and Principles, Princeton University Press (1997)
9. Nobel, P.S., Physicochemical and environmental Plant Physiology, 3rd ed., Elsevier (2005)
10. Milburn J.A., Water Flow in Plants, Longman, London (1979)

A Biomechanical Study on Bursting Plant Fruit and Its Optimality

*Jiro Sakamoto*¹, *Yasuhiro Endo*¹ and *Eichiro Kinoshita*¹

¹ *Kanazawa University, Japan*

Abstract

Bursting of plant fruit is very interesting phenomenon in viewpoint of plant biomechanics, because it is mechanical phenomenon directly related to reproduce of the plant. If a kind of plant has fruit, which can burst powerfully and scatter seed widely, it has the advantage to expand breeding grounds of the plant in natural selection. Many types of plant fruit probably have been optimized mechanically and structurally in evolutionary process. We have studied on mechanics of bursting fruit dealing with *impatiens* as a research subject. Strain energy is stored in *impatiens* fruit due to swelling just before bursting. Mechanical stress of the fruit occurs in self-equivalent condition at that time. Then, stored strain energy of the fruit is released in very short time while bursting. Quickly and large motion of the fruit pericarp in a certain direction is advantageous to throw the seed far away. The bursting motion and deformation of fruit depend strongly on their mechanical stress just before burst. We analyzed the pre-burst stress generated in a pericarp of *impatiens* by using finite-element method based on its deformation history taken by high-speed video camera, in previous study. We treated one pericarp in the study, but *impatience* fruit is composed of five pericarps. In this study, finite-element model of the total fruit composed of five pericarps was created, and then swelling and bursting simulation of the fruit was performed. That is, we gave assuming temperature distribution on fruit surface of the FE model to generate thermal stress simulating swelling stress. Burst motion simulation of the fruit was performed by releasing a pericarp boundary after swelling. We considered an optimization problem to maximize peak velocity of the pericarp tip with varying swelling stress distribution as design variables under stress constrain. Optimal burst motion of the fruit was obtained by solving the problem, and compared with the real fruit motion. Optimality of the stress distribution was discussed.

Introduction

The plant seeds are moved by a variety ways, for example, carrying on the window, water, insect or animal. Dispersion of plant seed by bursting fruit is a typical moving way that is self-active and independent on other creature [1][2][3]. Fruit, which can burst powerfully and spread the seeds widely, are advantageous to extend breeding grounds of the plant in natural selection process [4]. So, fruit burst mechanism of survived plants in natural selection seems to be optimized mechanically and structurally. The bursting motion of fruit is important to throw the seeds far away and widely, and the motion strongly depends on mechanical stress just before burst. The pre-burst stress is considered as residual stress in viewpoint of mechanical engineering. The residual stress is which should be avoided in productive industry, e.g. welding or casting, because it often cause unexpected high stress. On the other hand, in living body, the residual stress is adapted to achieve favorable stress condition. For example, it is well known that stress concentration is cancelled by residual stress in outer wall of artery [5]. So, it is meaningful to study residual stress in living body for considering their fine biomechanical function. The residual stress of bursting fruit is also probably optimized to make fast bursting motion, which is advantageous to throw the seeds far away and widely. In order to clarify the bursting mechanism, it is necessary to evaluate residual stress distribution in the fruit.

We have studied the residual stress, in other word, the pre-burst stress generated in the fruit of *Impatiens*. *Impatiens* is a typical plant, which has fruits bursting and dispersing seeds. The pre-burst stress in a pericarp of *Impatiens* fruit was obtained by the reverse deformation procedure using finite-element method based on pre and post burst shape of the pericarp, in previous study [6]. The stress distribution was adequate to describe actual pericarp deformation with large bending on the stalk side half, and it was effective to lead the pericarp motion to fling the seeds far away. Although the simulation model of previous study was very faithful to actual shape of the pericarp, the fruit constructed of five pericarps was not considered. It has not been cleared that obtained pre-burst stress distribution was optimum to throw off the seeds. In this study, we constructed a finite-element model of *Impatiens* fruit, which has five pericarps. Computer simulation of burst of the fruit was performed by giving the pre-burst stress to pericarps. Furthermore, an optimization problem was formulated to maximize throw speed of the seed as varying the pre-burst stress distribution. The problem was solved by using response surface method, and optimality of the stress distribution was discussed.

Material and methods

We focused on burst fruit of *Impatiens* in this study. Fruit of *Impatiens* has five sheets of pericarp as shown in *Fig.1*. The pericarps are connected each other and their boundary is stiffer than the body of pericarps. According to visual observation, bursting process of the pericarps is considered as follows. Pericarps start to absorb water and swell at the bursting season. *Fig.2* shows micrographs of cells in transverse section of the *Impatiens* pericarp at the bursting season. It is observed that outside cell is larger than inside cell due to swell in the figure. Pericarps restrain their deformation each other, so swelling generate mechanical stress in pericarps. Tensile stress occurs inside and compressive stress occurs outside, because swelling of inside cell is larger. Such stress distribution was ensured by analysis in previous study. Once a pericarp boundary is ruptured by the stress, the pericarps deform quickly and throw the seeds outside.

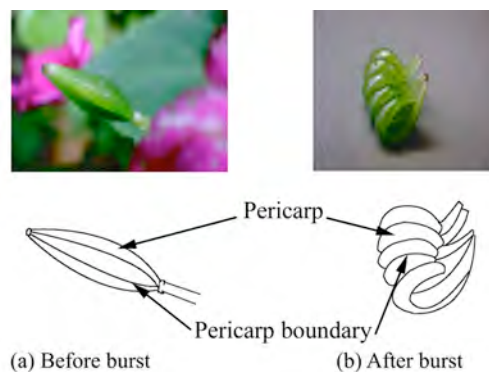


Fig.1 Shape of *Impatiens* fruit before and after burst.

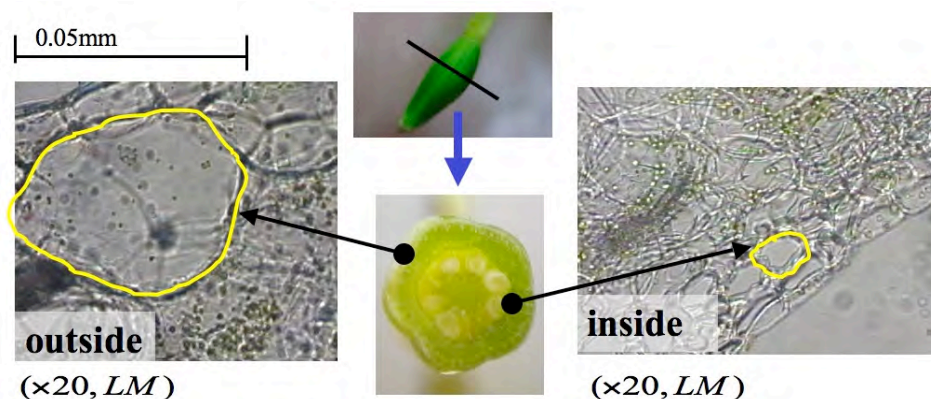
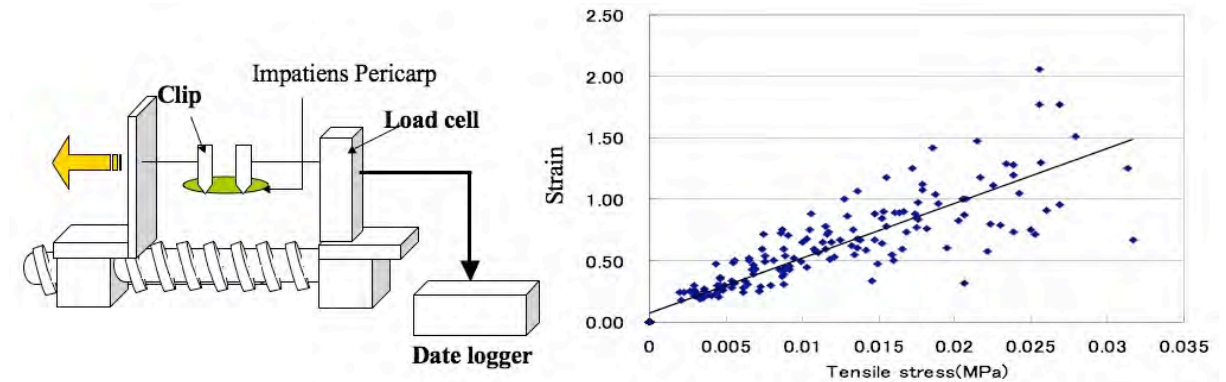


Fig.2 Micrographs of cells in transverse section of the *Impatiens* pericarp at the bursting season.

To obtain basic mechanical property of *Impatiens* fruit, tensile loading experiment of the pericarp was performed by using microscope and micro-motion stage. Experimental apparatus and stress-strain relation are shown in *Fig.3*. The pericarp was held by micro vascular clips at both ends. The clips were attached to micro-motion stage by wire strings. Tensile load was measured by load cell attached to micro-motion stage. Displacement of the pericarp was measured at sampling points plotted on the specimen by using microscope images, and strain was calculated. Experiment data of several specimens were plotted in the graph of stress-strain relation. Young's modulus of the pericarp was evaluated about 17KPa by assuming linear stress-strain relationship.



(a) Experimental apparatus

(b) Stress-Strain relationship

Fig.3 Tensile loading experiment of a pericarp of Impatiens at the bursting season.

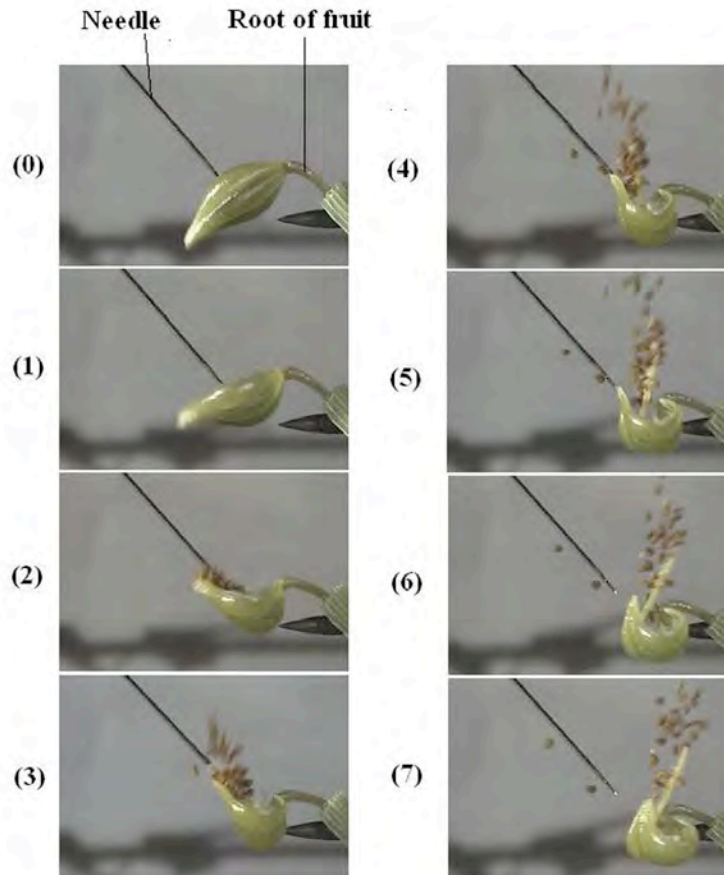


Fig. 4 Sequential images during fruit burst taken by high-speed video camcorder. Time interval is about 0.3msec.

The burst motion of the fruit of *Impatiens* was recorded by a high-speed video camcorder (nac Image Technology, MEMRECAM fx-k3) with 300 frames per second. An example of burst motion images of a fruit is shown in Fig.4. In the experiment, a pericarp was picked with stalk just before bursting, and the stalk of the pericarp was fixed on a steel rod using adhesive tape. The pericarp sheet junction was stimulated by a needle to induce pericarp burst. According to the images, after the pericarp sheet junction was ruptured, the pericarp opened circumferentially and then the pericarp sheets simultaneously curled inwardly in parallel. The remarkable motion of pericarp sheets was observed when seeds were catapulted. The bases of the pericarp sheet, where the stalk is located, bend, and this results in a large motion at their tip where the seeds are found. Figuratively speaking, the motion looks like a straight-arm rotation on its root joint. It seems advantageous to throw the seeds far away. The burst motion happens in a very short period. The elapsed time from rupture of the pericarp sheet junction to the end of the first curl of pericarp sheets is less than 9 msec.

The finite-element model of *Impatiens* fruit was shown in Fig.5. A pericarp model was created by reference to actual fruit and CT based model in previous study [6]. Shape of the pericarp model was simplified from previous CT based model in order to construct total fruit model by five pericarps without increase of computational time. Five models of pericarp were created by copying the pericarp model, and they were arranged circumferentially and connected each other. Each pericarp has common nodes in their inside boundary, except for the rupture boundary. Nodes on the rupture boundary are fixed before burst. Then, we simulate burst motion of the fruit and seeds by using finite-element analysis considering large deformation. In this analysis, Young's modulus and Poisson's ratio were given as 17KPa and 0.3 respectively in according to the tensile loading experiment of a pericarp shown in Fig.3. Although the pericarp has nonlinear anisotropic material property, we assumed linear elastic and isotropic material property because it was difficult to obtain in the experiment precisely. Pre-burst stress was generated by swelling of fruit. Thermal expansion was given to the fruit instead of swelling in the simulation. The temperature was set to each node to make pre-burst stress in the model. After thermal expansion of each pericarp was given, then the fixed rupture boundary was released in a moment. Bursting motion of pericarps started by releasing the boundary. Nodes at stalk side of the pericarp were always fixed. Contact condition without friction was considered between each pericarp.

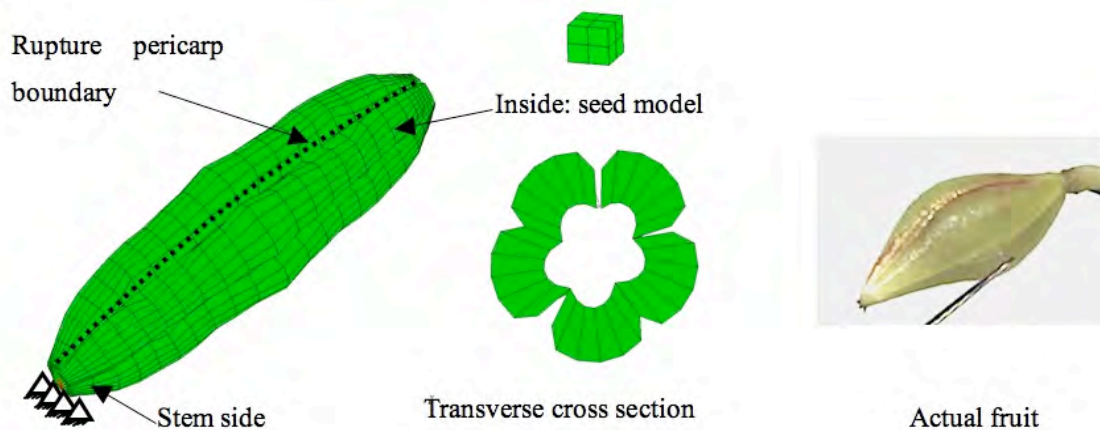


Fig.5 FE model of *Impatiens* fruit (after swelling)

Due to assuming that the pre-burst stress was optimized to catapult seeds farther, optimization problem of the stress distribution maximize seeds velocity was considered. Peak velocity of pericarp tip was defined objective function F , because catapulting seed velocity depends on speed of the pericarp. We divide a pericarp into 5 regions as shown in Fig.6 and set temperature to each region. We defined dimensionless value, which is obtained by dividing temperatures of each region by maximum temperature, as x_1, x_2, x_3, x_4 . Swelling was low in tip region, so temperature of the region was set to zero. An optimization problem can be formulated in the following form:

$$\text{Maximum } F = v(x_1, x_2, x_3, x_4) \quad (1)$$

$$\text{Subject to } \sigma_{Max} < \sigma_a, \quad 0 \leq x_i \leq 1 \quad (2)$$

Where F represents objective function. F is function of velocity with respect to the independent variables. σ_a is strength of pericarp tissue.

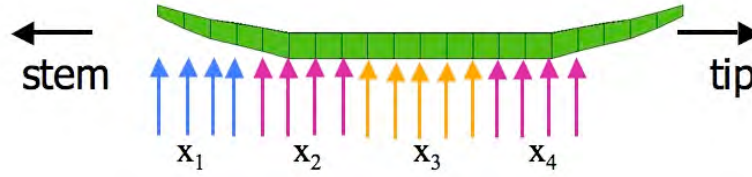


Fig.6 Design variable definition region on a pericarp (side view)

Response surface method with radial basis function (RBF) was applied to the optimum problem. RBF network is two layers feed forward network, which can approximate arbitrary non-linear function. Function of hidden layer is Gaussian function. RBF network superpose basis function, and then it create reaction surface. It is formulated as following form:

$$f(\mathbf{x}) = \sum_{j=1}^m w_j h_j(\mathbf{x}), \quad h_j(\mathbf{x}) = \exp\left(-\frac{\|\mathbf{x} - \mathbf{x}_j\|^2}{r_j^2}\right) \quad (3)$$

Where, \mathbf{x} is design variable vector, \mathbf{x}_j is sample date, w_j is weighting coefficient and r_i is radial function of basis function [7]. Temperatures of sampling points were set as three levels as 0, 10, 20 [°C]. That is, $x_i=0, 0.5, 1$. Peak velocity of pericarp tip F was calculated at the sampling points, and we get response surface of F by using RBF. Total number of sampling points is $3^4=81$ as three levels of four variables. Net number of sampling points is less than 81 because any convergence solution was not obtained at some sampling points.

Results and discussion

Fig.7 shows response surface plotted by using x_3 and x_4 include an optimal point. The response surface is multimodal functions, which has a lot of local optimal points. The best objective value of the response surface is 4.8 [m/sec] at $\{x_1, x_2, x_3, x_4\}=\{0, 0.5, 1, 0.5\}$. We simulate bursting of fruit for the optimal case. Fig.8 shows the simulation of bursting motion of the fruit and its distribution of principal stress major. Principal stress has three components, which is maximum, intermediate, minimum stress in three-dimensional problem. In usual case, maximum principal stress is tensile stress expressed as positive value, and minimum principal stress is compressive stress expressed as negative value. Principal stress major means the principal stress in which absolute value is largest in the three components. It is obvious that compressive stress occurs outside of the fruit, and tensile stress occurs inside of the fruit as shown in Fig.8. Large stress occurs in the central part corresponding to x_3 region. Before bursting ($t=0$), pericarps compress each other particularly in the central part, so that outside boundaries of the pericarps are closed. On the other hand, expansion of x_2 and x_4 region is not so large, so their outside boundaries are not closed. Just after opening the top boundary ($t=0.8$ ms), the split open widely in the central part. Then the pericarps open circumferentially and curl in axial direction simultaneously ($t=1.2, 1.6$ and 2 ms). Such bursting motion of the pericarps is similar to actual one as shown in Fig.4. It is suggested that the bursting fruit motion is optimized to catapult seeds fast by controlling distribution of pre-burst stress caused of swelling. It is considered that circumferential deformation is important to achieve optimum motion to throw the seed faster. If the circumferential deformation of the pericarps is not enough, longitudinal curl of the pericarps is constrained each other. As $\{x_1, x_2, x_3, x_4\}=\{1, 1, 1, 1\}$, strain energy stored in the fruit is absolutely maximum and larger pre-burst stress must occurs in each pericarp. Although larger stress occurs in the case, adequate circumferential deformation does not happen. Incline stress distribution from tip side to center shown in Fig.8 seems good for providing adequate circumferential deformation. That is one of reason why

$\{x_1, x_2, x_3, x_4\} = \{0, 0.5, 1, 0.5\}$ is optimal solution. Fig.9 shows side view of fruit deformation after burst in the optimal case $\{x_1, x_2, x_3, x_4\} = \{0, 0.5, 1, 0.5\}$ and quasi optimal case $\{x_1, x_2, x_3, x_4\} = \{1, 0, 0, 1\}$. The objective value of quasi optimal is 3.4 [m/sec], that is 70% of the optimal. Although circumferential deformation occurs in the quasi optimal case, bending deformation is small at middle part of fruit in comparison with optimal case. It is suggested that pre-burst stress in the middle region of fruit is effective to enhance catapulting seed fast.

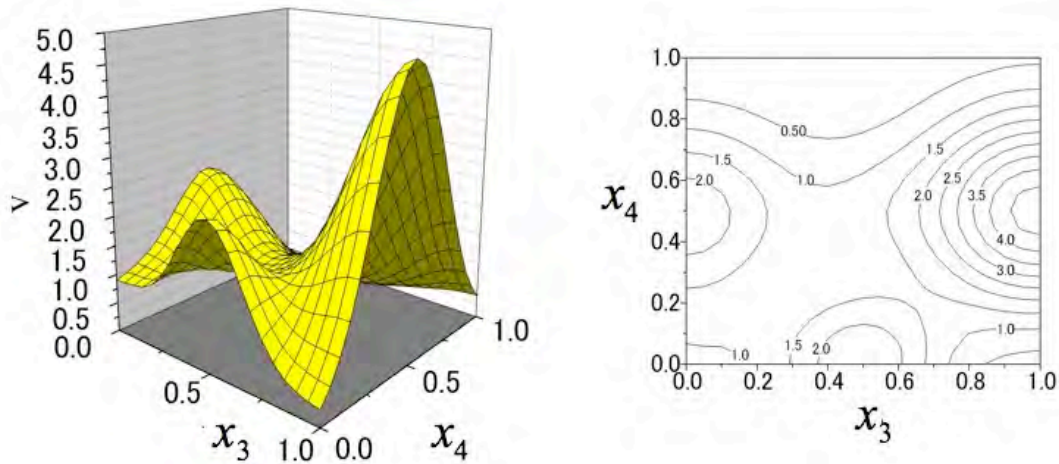


Fig.7 Response surface obtained by RBF network at $x_1=0, x_2=0.5$.

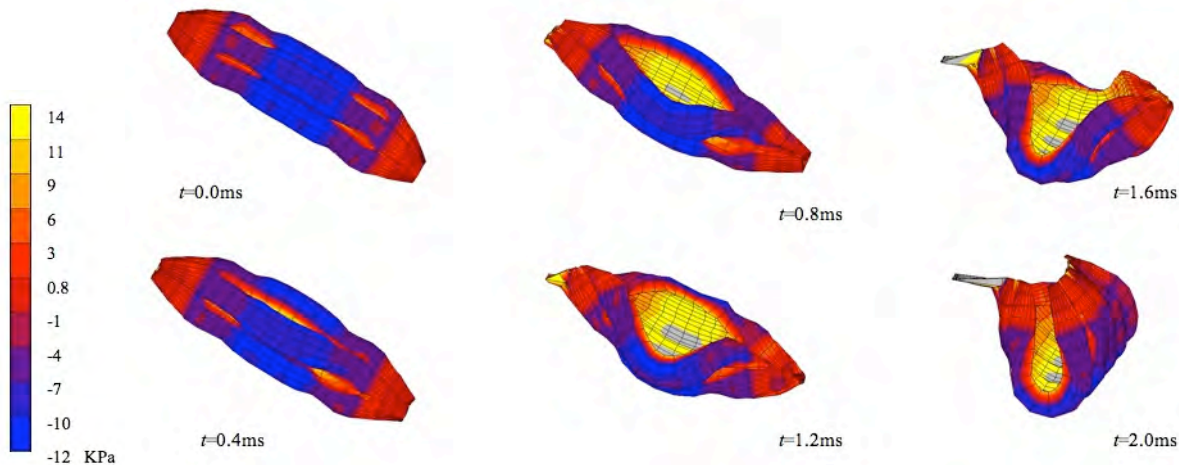


Fig.8 Simulation of fruit bursting motion (optimal case)

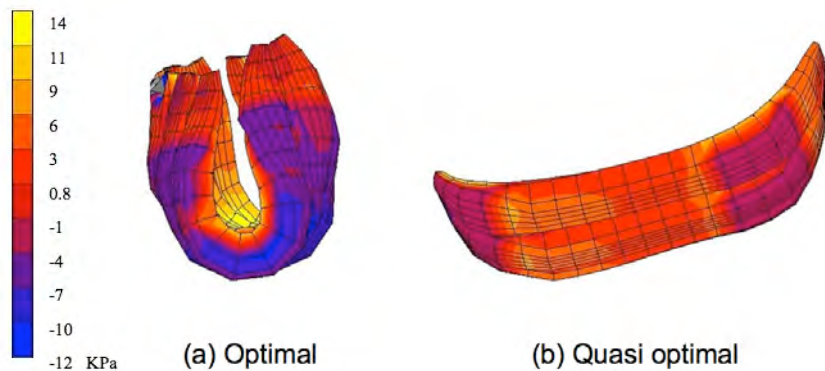


Fig.9 Deformation of fruit after burst in the optimal and quasi optimal case.

Extreme deformation is observed in tip of stalk side in the optimal case. Cause of the extreme deformation is related to fixed condition. Perfect fixation was given at the stalk side in the simulation, but actual stalk is not rigid. Deformable boundary condition should be given to stalk side of the fruit. The extreme deformation of stalk side seems not to be influenced to total behavior of the fruit because it is just local deformation.

There are some limitations in this analysis. First of all, it was assumed same swelling condition in each pericarp. Magnitude of swelling must be different in each pericarp. Top boundary of the pericarp is ruptured usually, and the pericarps with ruptured boundary are looked swelling larger, in fact. It is necessary to set different design variables for different pericarp to get more optimal solution. It is not so easy because number of sampling points to make response surface increase exponentially as increase of number of design variables. Dynamic non-linear analysis with contact problem has to be carried out to get a sampling point. As same reason, it is difficult to consider more precise swelling distribution. Efficient setting of design variables is required to over the limitation. Secondary, isotropic expansion was assumed in the analysis. Shape of cell in the pericarp is slender but not spherical. So, anisotropic expansion should be considered in future study.

Conclusion

Optimality of pre-burst stress of *Impatiens* fruit to scatter seed was studied. Mechanical property of *Impatiens* pericarp tissue was obtained by tensile loading experiment. Burst motion of *Impatiens* fruit was taken by high-speed video camera. Finite-element model of the *Impatiens* fruit constructed of five pericarps was created, and dynamic simulation of the burst motion was performed by giving thermal expansion that is equivalent to swelling. Simulation of the burst motion shows good correspondence with actual one. We formulated optimization problem to clarify optimal stress distribution of fruit for catapulting seed, and the problem was solved by response surface method using the RBF network. Burst motion of the optimal solution was similar to actual one. It suggests that *Impatiens* fruit optimize its pre-burst stress distribution to maximize velocity of catapult seed.

Acknowledgements

I would like to thank Dr. Satoshi Kitayama for the support of optimization method. This research was partially supported by the Ministry of Education, Science, Sports and Culture (Japan), Grant-in-Aid for Scientific Research (A), 18206014, 2006.

References

1. Simons, P. (1992): *The Action Plant: Movement and Nervous Behavior in Plants*, Blackwell Publishing, Cambridge.
2. Vogel, S. (2005): Living in a physical world III. Getting up to speed, *Journal of Biosciences*, 30 (3): 303–312.
3. Hara, N. (1994): *Plant Morphology*, Asakura Publishing Co., Ltd, Japan (in Japanese).
4. Schulgasser, K. and Witztum, A. (1995): The Mechanics of Seed Expulsion in Acanthaceae, *Journal of Theoretical Biology*, 176 (4): 531-542.
5. Fung, Y. C. (1990): *Biomechanics Motion, Flow, Stress and Growth*, Springer-Verlag, New York.
6. Endo, Y., Sakamoto, J., Kashiwano, Y., Yokota, H., Nakamura S. and Oda, J. (2006): A Biomechanical Study on Burst Mechanism of *Impatiens* Pericarps, Proc. 5th Plant Biomechanics Conference, L. Salmen (Ed.), STFI-PACKFORSK, Stockholm, Sweden, 2, 555-560.
7. Kitayama, S., Arakawa, M. and Yamazaki, K. (2007): Global optimization by generalized random tunneling algorithm (5th report, approximate optimization using RBF network), *Transactions of the Japan Society of Mechanical Engineers, Part C*, 73(5), 1299-1306.

Plant leaves as attachment devices: an experimental approach

*Friederike Gallenmüller¹, Georg Bauer¹, Kirk-René Kubinski¹, Dagmar Voigt²
Stanislav Gorb^{2,3} and Thomas Speck¹*

¹ *Plant Biomechanics Group, Botanic Garden, University of Freiburg, Germany;*

² *Evolutionary Biomaterials Group, Max Planck Institute Stuttgart, Germany;*

³ *Functional Morphology and Biomechanics, University of Kiel, Germany*

Abstract

Branch- or leaf-angle-climbers are climbing plants interlocking with their supporting structures via wide-angled branches or leaves. Their leaves often display particular friction properties. Here we present two methods developed for quantitative analysis of such friction properties and initial results obtained for the herbaceous species *Galium aparine* (a leaf-angle-climber) and for the woody species *Croton nuntians* (a branch-angle-climber).

Introduction

Branch- or leaf-angle-climbers are climbing plants which attach to their neighboring plants by wide-angled stiff branches or leaf petioles interlocking with the branches of the neighboring plants. Compared to the firmer attachment provided by twining stems or tendrils the attachment with wide-angled branches or leaves is less secure [1, 2, 3].

In field studies we observed that the leaves of several of such leaf- and branch-angle-climbers display particular friction properties. We hypothesize, that such leaves fortify the anchorage in the surrounding vegetation by increasing the frictional contact with neighbouring plants and represent an adaptation in the special growth form developed in branch- and leaf-angle-climbers [1]. In this study we have begun to analyse the structure and friction properties of the leaves of different temperate and tropical leaf- and branch-angle-climbers in comparison to twiners and tendril climbers.

In order to quantify the friction properties of leaves we have developed experimental setups for studies either at laboratory or field conditions. Here we present these methods and initial results obtained in the herbaceous species *Galium aparine* L. (Rubiaceae), a typical leaf-angle-climber attaching to neighbouring plants by whorls of wide-angled leaves, and in *Croton nuntians* Croizat (Euphorbiaceae), a tropical branch-angle-climber of the lowland rainforest in French Guyana developing imposing woody stems with up to 14 cm in diameter. Furthermore we discuss the relationship between microstructure on leaf surfaces and the friction properties of the leaves in the studied species [4].

Material and methods

Laboratory experiment

Friction force was measured by moving *Galium aparine*-leaves over different artificial surfaces (VELCRO® Vel-Loop and Spurr resin mouldings of abrasive paper (types P100 and P60)). Plants were

collected in July on the border of a woodland path. Intact fresh leaves were attached to a load cell force transducer (100 g capacity, Biopac Systems Ltd.) combined with a step motor drive which moved plant samples over the test surfaces at a constant speed of $3.1 \text{ mm}\cdot\text{s}^{-1}$ (Fig. 1). The distance between the force transducer and the test surface was 1.5 mm for the mouldings of abrasive paper and 3.3 mm for Velcro loops. Leaves were tested within 20 seconds after cutting them from the plant.

Abaxial and adaxial leaf surfaces were tested. Force-time-curves were recorded and processed using Biopac AcqKnowledge® Version 3.7.0 software (Biopac systems Inc.). For each test run the mean value of the ten maximum force peaks was calculated (cf. Fig. 4).

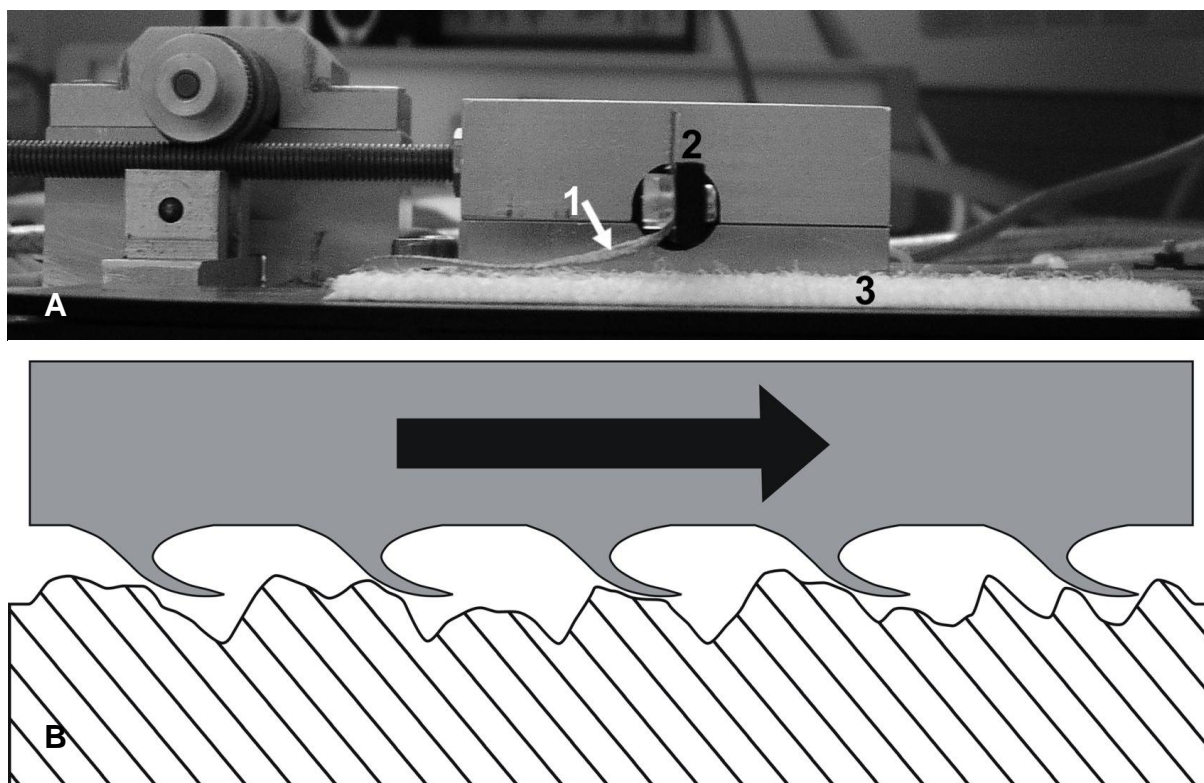


Fig. 1 Experimental set-up of a friction experiment with leaves of *Galium aparine*. A) Leaves (1) were attached to a load cell force transducer (2) and moved over a test surface (3). B) Schematic drawing of the experimental situation during friction measurements, where the abaxial leaf surface (grey) is moved over the test surface (hatched) in the direction (arrow) of the orientation of the abaxial leaf hooks. From [4].

Field experiments

In the field experiments we have positioned leaves on a test surface and measured the friction force necessary to produce sliding. The apparatus developed for these friction experiments under field conditions consists of two panels between which leaves can be clamped (Fig. 2). The leaf surface is accessible through a rectangular opening in the upper panel. Brass blocks fitting in the opening without touching the panel are used for the application of a normal force F_N pressing the test surface (glued to the brass block) against the leaf surface. F_N can be varied using brass blocks of different weight (2.5, 8.5, 17.0, 25.5 and 42.1 g).

For the application of a tangential force F_T required to move the brass block two methods were tested: 1) force application via a tension spring balance, and 2) force application via pipetting water in a recipient. Both the spring balance and the water recipient are connected to the brass block via a small pulley. The friction of the pulley proved to be minimal and is assumed to be zero in all calculations of tangential force F_T . F_T is increased up to the moment the brass block starts sliding and determined at this point as friction force F_F . Horizontal alignment of the apparatus is verified using a water-level. Load application via a spring balance proved to be inadequate because 1) jerking movements occur, 2)

precise reading of the force values is difficult (in particular if the experiment is carried out by one single person) and 3) steps of force increment are too high. Load application by pipetting water in the recipient proved to be the much more convenient and reliable method because the force increment is steadier, more precise and practicable in smaller steps, and was therefore used in all following experiments.

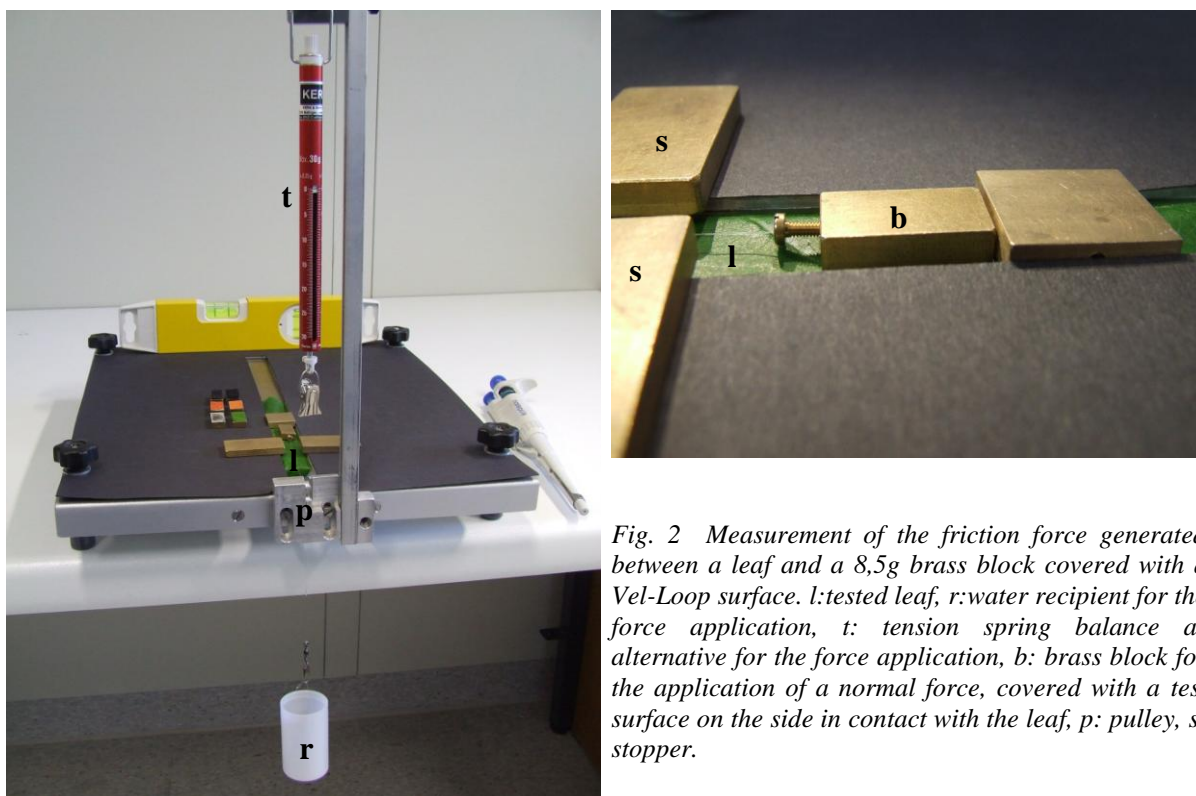


Fig. 2 Measurement of the friction force generated between a leaf and a 8,5g brass block covered with a Vel-Loop surface. l: tested leaf, r: water recipient for the force application, t: tension spring balance as alternative for the force application, b: brass block for the application of a normal force, covered with a test surface on the side in contact with the leaf, p: pulley, s: stopper.

Friction between abaxial and adaxial leaf surfaces of *Croton nuntians* was tested in the two directions parallel to the mid rib. Furthermore the friction between leaf surfaces and different technical surfaces and the friction between leaf surfaces was tested. Here we present initial results of friction tests between abaxial leaf surface (clamped into the apparatus) and adaxial leaf surface (glued to the brass block) of *Croton nuntians*.

Coefficient of friction μ was calculated using the equation

$$F_F = \mu F_N \quad (1)$$

where F_F is the friction force (measured as force necessary to produce sliding), F_N is the normal force pressing the two parallel surfaces together, calculated as $F_N = mg$ (m = mass, g = acceleration due to gravity) [5].

Results and discussion

Structure and friction properties of *Galium aparine* leaves (tested under lab conditions)

The friction properties of the leaves of *Galium aparine* are due to the existence of hooks on the abaxial and adaxial leaf surface.

The structure and properties of the leaf hooks differ conspicuously between hooks on the abaxial and adaxial leaf surface (Fig 3). On the abaxial leaf surface hooks are curved towards the leaf basis, are situated exclusively on the midrib and on the margins of the leaf, continuously lignified and are hollow (Fig 3) [4]. On the adaxial leaf surface hooks are curved towards the leaf tip, distributed evenly

over the whole leaf surface, lignified predominantly at the apex and are smaller in diameter than the hooks of the abaxial leaf surface (Fig 4) [4, cf. 6, 7].

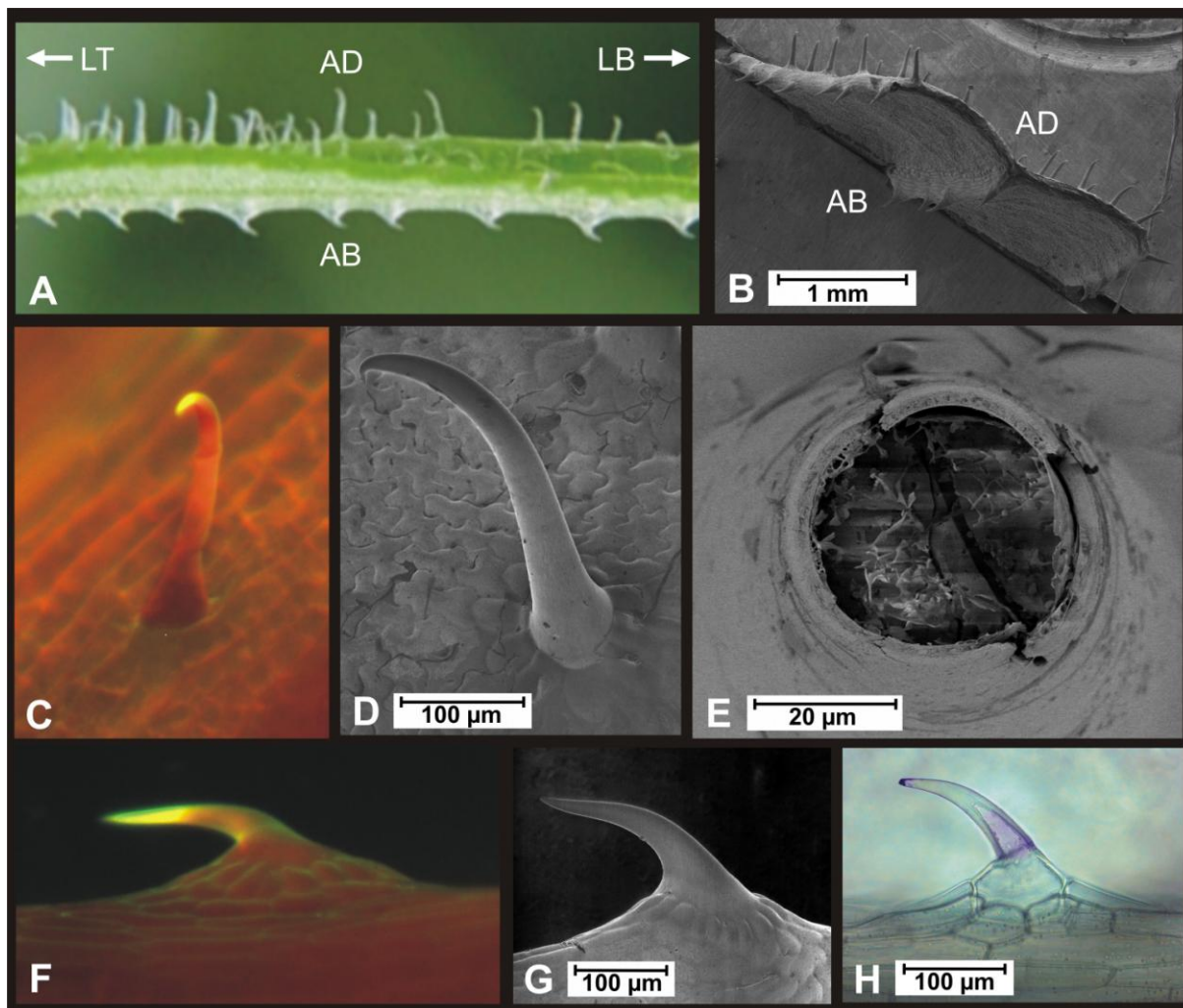


Fig. 3 Leaf hooks of *Galium aparine*. A) Lateral view of a leaf: hooks on the abaxial surface (AB) of the leaves are curved towards the leaf basis (LB), hooks on the adaxial surface (AD) are curved towards the leaf tip (LT), B) distribution of hooks: Adaxial hooks (AD) are distributed evenly over the surface area, abaxial hooks (AB) occur exclusively on the midrib and the leaf margins (Cryo-SEM micrograph), C) adaxial hook, stained with acridine orange, revealing the lignification of the tip in fluorescence microscopy, D) adaxial hook, SEM, E) freeze fracture at the base of an adaxial hook, F) fluorescence of an entirely lignified abaxial hook, stained with acridine orange, G) abaxial hook, Cryo-SEM micrograph and H) abaxial hook, stained with toluidine blue. From [4].

In accordance with these differences in orientation, distribution, structure and mechanical properties of the hooks, friction properties of the *G. aparine* leaves 1) depend on the direction of the applied force and 2) differ substantially between abaxial and adaxial leaf surfaces (Fig 4) [4]. When leaves are moved over a test surface in the direction opposite to the orientation of the hooks the generated frictional forces are minimal or not measurable at all. On the contrary, when leaves are moved in the direction of the orientation of the hooks (cf. Fig 2), considerable frictional forces are generated (Fig 4). When tested in the direction of the orientation of the hooks friction of the abaxial leaf surface is significantly higher than friction of the adaxial leaf surface (Fig 4).

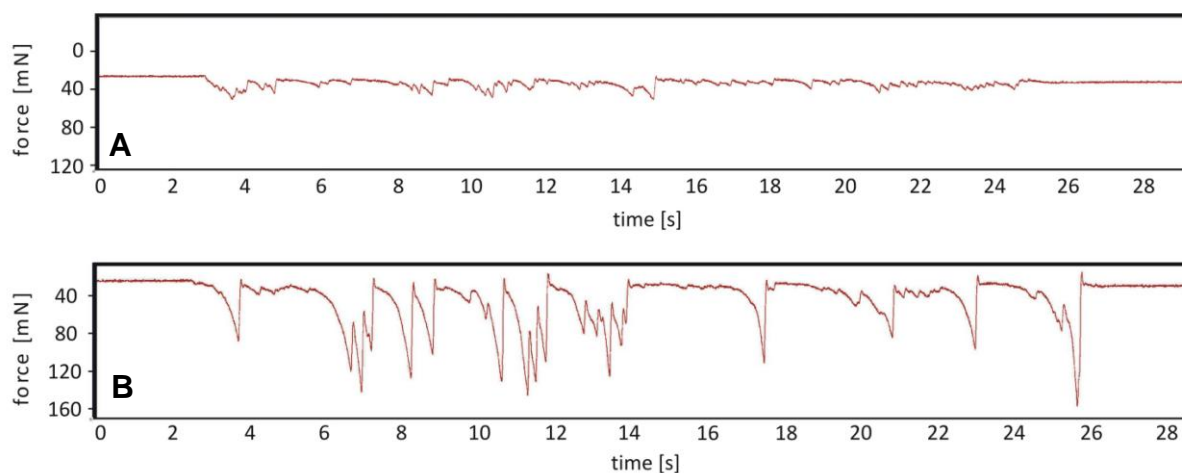


Fig. 4 Force-time curves obtained in the friction experiments with leaves of *Galium aparine*, moved over a Vel-Loop surface. A) adaxial leaf surface, mean value of the 10 maximum peaks = 17.3 ± 2.4 mN, B) abaxial leaf surface, mean value of the 10 maximum peaks = 101.0 ± 14.1 mN. Both surfaces were moved in the direction of the orientation of the leaf hooks. The forces generated by moving the leaves in the direction opposite to the orientation of the leaf hooks are minimal or too small to be measured (data not shown).

Friction properties of *Croton nuntians*-leaves (tested under field conditions)

Leaves of *Croton nuntians* are covered with trichomes that can be qualified as stellate-lepidote [8] (Fig 5) on the abaxial and on the adaxial surface. Due to these trichomes the leaves interlock with other rough surfaces. Leaves of *Croton nuntians* clinging to each other or to leaves of other plants with both their abaxial and adaxial surface are observed in the field. Often only the lobes of the compound leaves interlock with neighbouring plants structures (Fig 6).

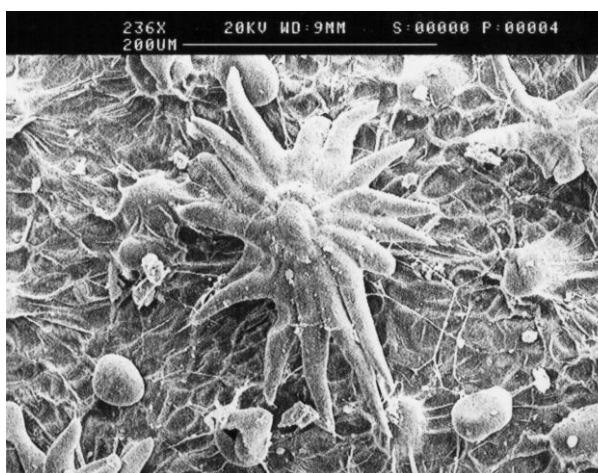


Fig. 5 Stellate-lepidote trichomes on the abaxial surface of a *Croton nuntians*-leaf, SEM micrograph.



Fig. 6 Leaves of *Croton nuntians*, A) clinging to a leaf of a neighbouring plant with a part of the abaxial surface and a part of the adaxial surface (arrows,) B) *Croton nuntians* leaves clinging to each other.

Tests of the friction between abaxial and adaxial surfaces of *Croton nuntians* leaves revealed that the variation between different leaves is very small (Fig 7). When data of the frictional force F_F obtained with different leaves are grouped and plotted against the normal force F_N the linearity following equation (1) becomes apparent (Fig 8). Based on these results we conclude that the measuring precision of the apparatus is adequate to analyse the friction properties of leaves under field conditions. In the tested system (abaxial leaf surface / adaxial leaf surface) the coefficient of static friction $\mu = 1.06$, which can be considered as relatively high (Fig 8). For comparison μ (ski/ice) = 0.005 [9], and μ (tire/dry road surface) = 1.0 [10].

Initial results suggest that in *Croton nuntians* no differences are found in the friction properties when friction in different force directions or between abaxial and adaxial leaf surfaces is compared (data not shown). This is in accordance with the observation, that abaxial and adaxial leaf trichomes are morphologically similar.

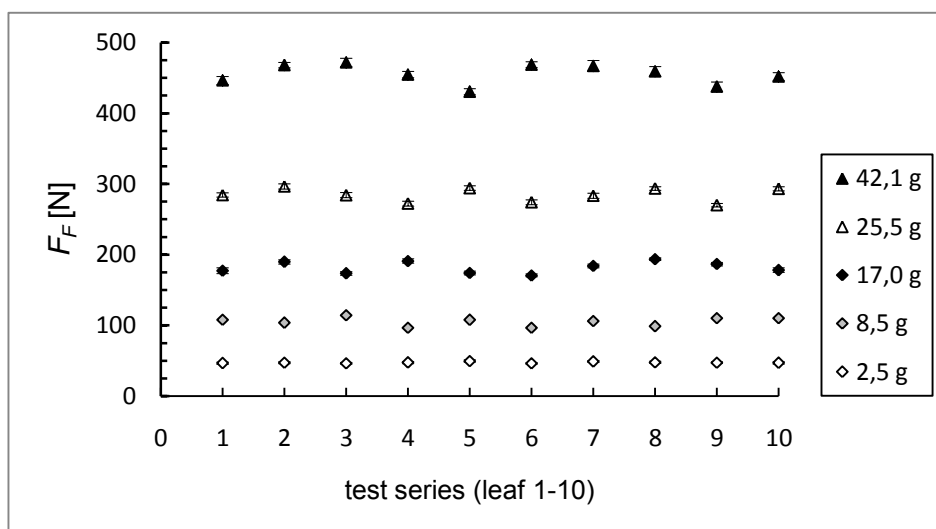


Fig. 7 Maximum friction forces generated in the field experiments by abaxial leaf surfaces of *Croton nuntians* on adaxial leaf surfaces of *Croton nuntians*. Each data point represents the mean value of 10 measurements performed with one leaf. Data are presented as mean values and standard deviations. For several test series the standard deviation is too small to be visible in the diagram.

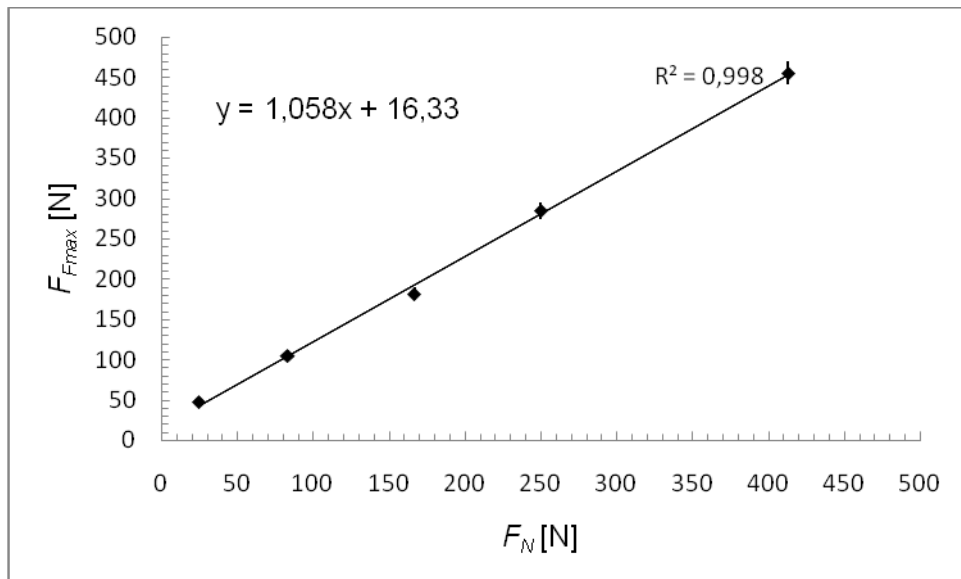


Fig.8 Maximum friction forces generated in the field experiments by abaxial surfaces of leaves of *Croton nuntians* on adaxial leaf surfaces of *Croton nuntians* pooled for different leaf specimen, presented as mean values ($n = 100$) and standard deviations and plotted against the normal force F_N . For several mean values the standard deviation is too small to be visible in the diagram. The slope of the linear regression line represents the coefficient of friction μ .

Conclusion

Galium aparine is an herbaceous plant and a typical leaf-angle-climber. When growing individuals reach a certain size and loose mechanical stability, attachment to supporting structures is provided mainly by the leaves. Due to the dependence of the attachment properties on the force direction and the differences between abaxial and adaxial leaf surface, the leaves of *G. aparine* interlock only with their abaxial surfaces on the leaves of neighboring plants. On the contrary, the adaxial surfaces of the leaves slip of the leaves of neighboring plants. This entails that the leaves of *G. aparine* are always positioned upon the leaves of the neighboring plants and do not get attached underneath them. Therefore, the leaves of *G. aparine* can function as attachment organs, and simultaneously orientate themselves properly for their photosynthetic function: they are “always on the bright side” [4].

In *Croton nuntians*, the situation is different. Its woody stems can reach considerable dimensions with lengths over 30 m and diameters up to 14 cm. As characteristic branch-angle climbers older individuals interlock with the surrounding vegetation via wide angled woody branches. The leaves are not the only “attachment organs” in this species but help securing the attachment provided by the branches. This is probably of particular importance when growing branches get into a first contact with the surrounding vegetation. In this species abaxial and adaxial leaf surfaces do not differ significantly in structure and friction properties.

The growth form of leaf- and branch-angle climbers has evolved in different Angiosperm families. Thus another example with leaves interlocking with other surfaces is found in the family of Cyperaceae. Leaves of *Scleria secans* L. (Urb.) are covered with hooks and display cutting edges (interpreted as defence against herbivores) and surfaces which attach strongly to nearly every surface they get in contact with even without a normal force pressing them against it (Kubinski et al. in prep).

With our initial results an overall picture starts to form, showing that leaves interlocking with different contact surfaces are characteristic of branch- and leaf-angle climbers. However, in different

taxa different structures have evolved, resulting in different functionalities of the leaves as attachment devices.

Acknowledgements

We thank Siegfried Fink for the preparation of stained microtome cuts and pictures in fluorescence microscopy of *Galium aparine*-leaves. Parts of the field experiments were supported within the Woodiversity Program financed by the ANR (Agence National de Recherche) and the IFN (Institut Français de la Biodiversité).

References

1. Rowe N., Isnard S., Gallenmüller F. and Speck T. (2005): Diversity of mechanical architectures in climbing plants: an ecological perspective. In: A. Herrel, N.P. Rowe & T. Speck (eds.), *Biomechanics and Ecology*, Dekker.
2. Gallenmüller F., Müller U., Rowe N. and Speck T. (2001): The growth form of *Croton pullei* (Euphorbiaceae) – functional morphology and biomechanics of a neotropical liana. *Plant Biology*, 3, 50 - 61.
3. Gallenmüller F., Rowe N. & Speck T. (2004): Development and Growth Form of the Neotropical Liana *Croton nuntians*: The Effect of Light and Mode of Attachment on the Biomechanics of the Stem. *Journal of Plant Growth Regulation*, 23, 83-97.
4. Bauer, G., Gorb, S., Voigt, D., Speck, T. and Gallenmüller, F. (2009): Always on the bright side- the climbing mechanism of *Galium aparine*. Submitted.
5. Euler, L. (1750) Sur le frottement des corps solides. *Memoires de l'academie des sciences de Berlin* 4, 122-132.
6. Gorb, E. V. and Gorb, S. (2002): Contact separation force of the fruit burrs in four plant species adapted to dispersal by mechanical interlocking. *Plant Physiol.Biochem.* 40:373-381.
7. Gorb, E. V., Popov, V. L. and Gorb, S. N. (2002): Natural hook-and-loop fasteners: anatomy, mechanical properties, and attachment force of the jointed hooks of the *Galium aparine* fruit. in: *Design and Nature*. C. A. Brebbia, L. J. Sucharov, and P. Pascolo. Southampton,Boston:WIT Press. 151-160.
8. Webster, G.L., Del-Arco-Aguilar, M.J. and Smith, B.A. (1996): Systematic distribution of foliar trichome types in *Croton* (Euphorbiaceae). *Botanical journal of the Linnean Society*, 121, 41-57.
9. De Konin, J.J., De Groot, G. and Van Ingen Schenau, G.J. (1992): Ice friction during speed skating. *Journal of Biomechanics*, 25, 6, 565-571.
10. Müller, S., Uchanski, M. and Hedrick, K. (2003): Estimation of the maximum tire-road friction coefficient. *Journal of Dynamic Systems*, 125, 4, 607-618.

The Unfolding Mechanism of Seed Capsules in Stone Plants

Matthew J. Harrington¹, Friedrich Ditsch², Peter Fratzl¹, Christoph Neinhuis² and Ingo Burgert¹

¹Max Planck Institute of Colloids and Interfaces, Potsdam, Germany;

²Technische Universität Dresden, Institute for Botany, Germany

Abstract

Plants are able to adapt the geometry of their organs and tissue properties to cope with external and internal stresses and to actuate organ movement [1-4]. Actuated movements due to moisture changes in cell walls are often controlled by stiff cellulose fibrils embedded in a swellable matrix [4]. Notably, many of these actuated movements function in the absence of an active metabolism, making them not only a fascinating natural phenomenon, but also an attractive model system for biomimetic technology transfer. A prime example of this actuation behavior is observed in the mature (non-living) seed capsules of Aizoaceae, which undergo complex hydration-dependent movements in which protective valves reversibly fold open when wetted and close when dried [5]. This movement permits a special mode of seed dispersal known as ombrohydrochory in which the plant utilizes the kinetic energy from raindrops to eject seeds long distances and which has been suggested to be a major factor in the rapid evolution and success of this plant group in arid and semi-arid climates [5,6]. Here, we explore the macroscale to nanoscale hierarchical organization of the seed capsule, as well as the molecular level mechanisms that control their sophisticated hydration-dependent unfolding. This was achieved through the use of several *in situ* characterization techniques including environmental SEM and Raman spectroscopy.

While the seed capsules of the Aizoaceae can be quite complex, the capsules of the species *Delosperma nakurense* (Engl.) Herre have a relatively simple design and were thus chosen as our model system. There are five protective valves that fit tightly together covering the five loculi where the seeds are stored, preventing the premature release of seeds in the dry state (Fig. 1). When capsules are moistened, the valves fold outwards and backwards over an angle of $>90^\circ$ in a matter of minutes, exposing the loculi. In the moistened state, one can see a prominent tissue running along the center of the extended valve known as the hygroscopic keel (Fig. 1), which has been previously suggested to mediate water-dependent movements in the seed capsule [7]. By dissecting the keel away from the rest of the tissue it was possible to observe the reversible water dependent expansion of this tissue.

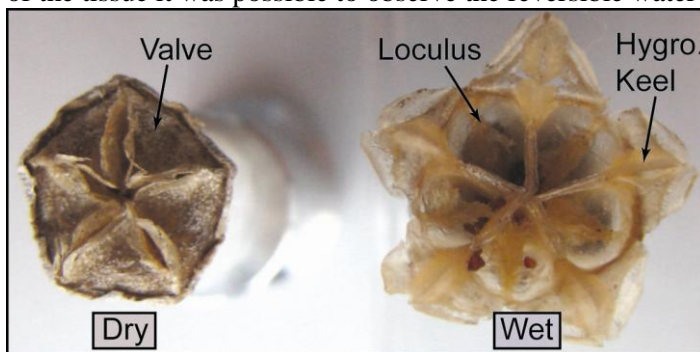


Fig. 1 Mature seed capsules of *D. nakurense* in the dried and hydrated states. Hydrating seed capsules actuates the opening of the five protective valves and exposes the seed loculi.

Light microscopy and environmental scanning electron microscopy (E-SEM) were employed to further investigate the suspected role of the hygroscopic keel at the level of the cellular architecture. E-SEM permits high resolution imaging at the submicron scale under hydrated conditions and allows one to regulate local humidity of the sample by controlling the pressure and temperature within the chamber. Using these microscopy techniques on extracted keel tissue, it was observed that the shape of cells within the hygroscopic keel is greatly influenced by the level of hydration. When viewed from above, cells changed from an expanded hexagonal shape in the hydrated state to a flat, collapsed shape in the dehydrated state (Fig. 2). Nearby cells that are not part of the keel do not undergo this same transition. Based on the geometrical and hierarchical organization of the cells within the keel, it seems likely that the water-dependent shape change of the cells is driving the macroscopic unfolding of the valves, but the molecular-level mechanism of cell expansion is still unclear. To further investigate this question, we utilize cellular staining techniques and Raman spectroscopy confocal imaging of thin sections of hygroscopic keel tissue in order to determine the identity and organization of the cellular constituents.

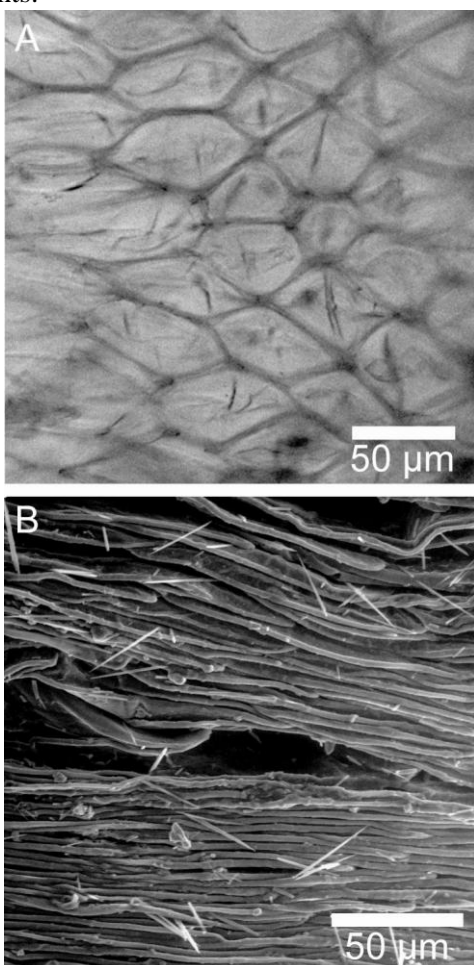


Fig. 2 (A) Light microscopy image of the cells of the hygroscopic keel in the hydrated state viewed from above. In the hydrated state, cells appear as expanded hexagonal or diamond shapes. (B) E-SEM image of the hygroscopic keel in the dried state viewed from above. When dried, the cells collapse and flatten causing the entire keel structure to contract.

Acknowledgements

The authors thank Michaela Eder, Markus Rüggeberg, and Nicole Schreiber for providing helpful discussion and insights.

References

1. Dawson, C., Vincent, J.F.V., and A..M. Rocca, (1997) *How pine cones open*. Nature 390: 668.

2. Skotheim, J.M. and L. Mahadevan, (2005) *Physical limits and design principles for plant and fungal movements*. Science 308: 1308-1310.
3. Elbaum, R., Zaltzman, L., Burgert, I., and P. Fratzl, (2007): *The role of wheat awns in the seed dispersal unit*. Science. 316: 884-886.
4. Fratzl, P., Elbaum, R., and I. Burgert, (2008): *Cellulose Fibrils direct plant organ movements*. Faraday Discussions. 139: 279-282.
5. P. Parolin, (2006): *Ombrohydrochory: Rain-operated seed dispersal in plants - With special regard to jet-action dispersal in Aizoaceae*. Flora. 201: 511-518.
6. Klak, C., Reeves, G., and T. Hedderson, (2004): *Unmatched tempo of evolution in Southern African semi-desert ice plants*. Nature. 427: 63-65.
7. S. Lockyer, (1932): *Seed dispersal from hygroscopic Mesembryanthemum fruits*. Annals of Botany. 46: 323-342.

Mechanics and structure of the attachment system of English Ivy (Hedera helix L.)

*Björn Melzer¹, Tina Steinbrecher², Robin Seidel¹, Oliver Kraft^{2,3}, Ruth
Schwaiger^{2,3} and Thomas Speck¹*

*¹Plant Biomechanics Group Freiburg, Botanical Garden, University of Freiburg,
Germany; ²Institute for Materials Research II, Forschungszentrum Karlsruhe, Germany;
³Institute for Reliability of Systems and Components, University Karlsruhe (TH), Germany*

Abstract

English Ivy (*Hedera helix* L.) is a prominent root climber the attachment mechanisms of which are not yet fully understood. This article gives an overview on the methods used in a systematic approach to analyse the functional morphology and the biomechanics of the attachment structures of English Ivy and presents some initial results. Mechanical as well as chemical components make up a four phase attachment mechanism which enables English Ivy to climb on various structured substrates and also on some smooth ones.

Introduction

As a common representative of the European flora, English Ivy (*Hedera helix* L.) has been studied thoroughly in respect to various aspects such as ecology [cf.1], pharmaceutical properties [cf.2] and physiology [cf.3].

An interesting attribute of *Hedera helix* is its climbing ability, which has not yet been studied in detail. During the juvenile life phase the ivy shoots develop adventitious climbing roots. They start growing at nodes on the shaded side of the shoot [4], forming root clusters sometimes stretching across the entire internode. These climbing roots enable the plants to climb up to 30 m on various substrates such as tree barks, rocks and house fineries [1]. The climbing roots are covered with root hairs, which probably play an important role in the attachment process. The different size scales of the involved attachment structures are shown in *Fig. 1*. Already Malpighi [5] described the excretion of a glue-like substance from the climbing roots which was recently subject of a first analysis [6].

The present paper discusses some of the methods used in a systematic approach to analyse

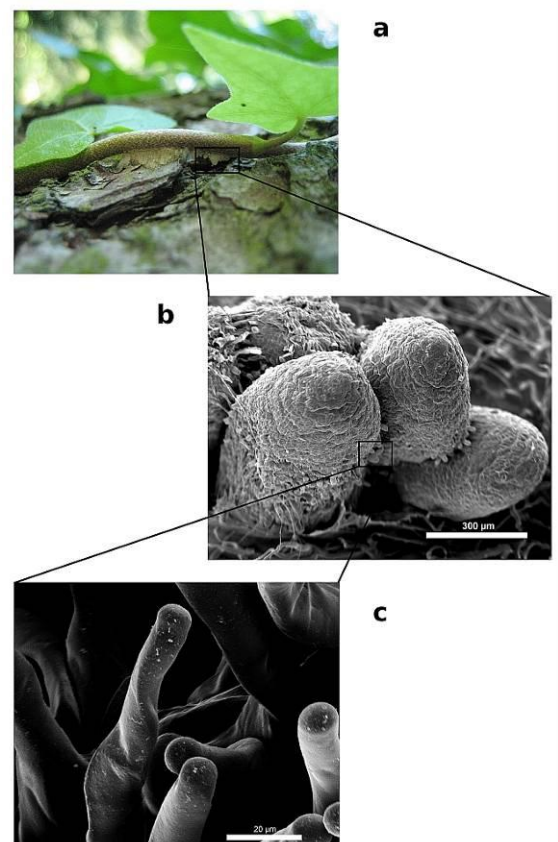


Fig. 1 Different levels involved in the attachment process. A, Attached shoot of English Ivy, B, climbing roots with root hairs, C, root hairs

quantitatively the biomechanical and the morphological properties of the attachment of English Ivy mechanisms and gives a short overview on some of the results.

Material and methods

Plant Material

In this study English Ivy plants grown outdoors as well as indoors were investigated. The outdoor grown specimen of *Hedera helix* used in this study represent established plants climbing on various substrates such as house fineries from two different locations and various tree barks. Some plants at the house finery sites were presented with test substrates (PVC, aluminium, steel, ceramic, glass, sponge rubber, cork, spruce wood, beech wood) in form of 5cm x 10 cm plates attached to the finery with double sided tape. Plants grown indoors were presented with commercial cork wallpaper as a basic climbing substrate, on which 5 cm x 10 cm plates of different test substrates (construction paper, Mylar foil, PVC, Plexiglas, glass) were mounted. The substrates were chosen to test whether structural (sRq via WLI), physical (stiffness) or chemical (inorganic/organic) characteristics (*Table 1*) have an influence on the ability of English Ivy to attach to a climbing substrate.

To characterise the attachment of nodal root clusters of English Ivy under outdoor conditions, established climbing plants were chosen. The tests started at the most apical attached node and continued node by node until either of the following situations were encountered:

1. Another Ivy stem crossed the probed stem
2. More than two consecutive nodes were not attached
3. Other plants got in the way of the testing device
4. Technical problems with the testing device occurred

For testing the attachment of single roots a micro-tensile testing device was constructed. For these tests attached stems with the climbing substrate will be collected. The tests will be performed with samples of plants growing outdoors in the Botanical Garden Freiburg attached to various tree barks and samples of plants growing indoors attached to different artificial substrates. Pieces of stem with single attached roots will be prepared (*Fig.2*).

Mechanical Tests

Outdoor tests were performed with a custom made, portable force-displacement gauge, the ‘Ivy plucker’ which is described in detail in [7]. The Ivy plucker was positioned at the growing site of the study object and set up so that the forcipies could be fastened at the Ivy stem at the middle of the probed attaching root cluster and a force perpendicular to the climbing substrate could be introduced. After positioning and connecting the gauge, the stem was cut above and below of the root cluster and the displacement forces were recorded.

The indoor tests with single attachment roots will be conducted with a modified custom made micro-tensile testing gauge [8]. The substrate and the stem piece are glued each to an aluminium pad. The pads are mounted in the micro-tensile testing gauge and the displacement forces are measured (*Fig.2*). With this device different relative angles between stem and substrate can be achieved and the influence of the angle on the attachment force can be tested.

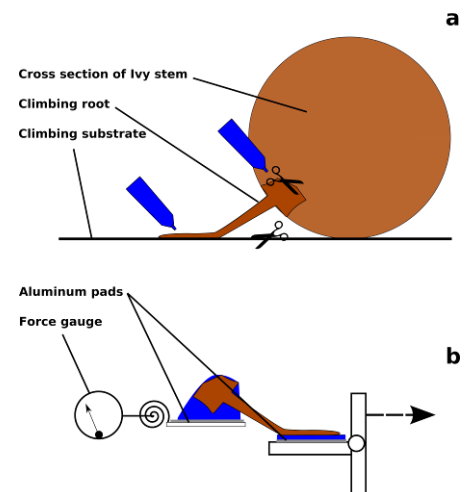


Fig 2 A, Schematic cross section of an Ivy stem with one attached climbing root. Scissors indicate cutting sites during the preparation, blue glue tubes indicate application areas of glue to fasten the sample onto aluminium pads. B, The mounted sample in the micro-tensile testing gauge

SEM and ESEM-Analyses

Samples for the SEM-analyses were taken from outdoor plants as well as from indoor grown specimens of English Ivy. The samples were cut, transported and prepared in a moist environment and put into methanol [9] as soon as possible to avoid artefacts. After the process of critical point drying the samples were mounted on aluminium stubs, gold coated and analysed with a LEO 435 VP. For ESEM-analyses fresh samples were taken from outdoor plants, transported and prepared in a moist environment and studied with a Phillips FEI ESEM XL 30 FEG at a base pressure of 133 Pa.

Light-Microscope-Analyses

Samples of indoor grown specimens of English Ivy attached to cork were taken, prepared and fixed in a solution of formaldehyde, ethanol and acetic acid. The samples were then embedded in paraffin, cut via microtome into 10µm thick slices and mounted on microscope slides. After removing the paraffin the samples were PAS stained, which is sensitive to polysaccharides. The samples were studied with an automated Olympus BX61, images were taken with an Olympus DP71.

Results and discussion

Climbing substrates

As shown in *Table 1* English Ivy is able to attach itself onto various structured surfaces. This seems to point to a mechanical interaction between the Ivy's climbing roots/root hairs and the surfaces rather than exclusively to a chemical adhesion.

A very strong attachment also occurs on Mylar foil (*Fig.3*), a smooth plastic material. This attachment is either possible due to the relative low Young's modulus (ca. 3GPa) of the Mylar foil compared to the other tested smooth surfaces and/or a very strong chemical adhesion between the climbing roots and the usually quite inert Mylar.

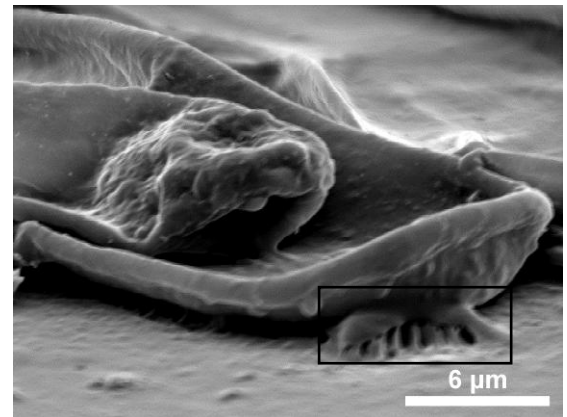


Fig. 3 Dried root hairs of English Ivy on Mylar foil. The box accents strands of glue between the undermost of the hairs and the substrate

Table 1 Attachment of English Ivy (Hedera helix L.) on various climbing substrates.

Material	Attachment		Material	Attachment	
	Yes	No		Yes	No
Aluminium (0.366 µm, stiff, inorganic-metallic)		X	Mylar foil (0.245µm, resilient, inorganic-polymer)	X	
Beech wood (9.465 µm, resilient, organic)	X		Plexiglas (0.531µm, stiff, inorganic-polymer)		X
Ceramic (0.079 µm, stiff, inorganic)		X	PVC (0.246µm, stiff, inorganic-polymer)		X
Construction paper (6.404 µm, resilient, organic)	X		Sponge rubber (4.948µm, resilient, inorganic-polymer)	X	
Cork (13.459µm, resilient, organic)	X		Spruce wood (4.425µm, resilient, organic)	X	
Glass (0.014 µm, stiff, inorganic)		X	Steel (0.389µm, stiff, inorganic-metallic)		X

Biomechanical Data

The outdoor displacement tests showed different modes of attachment failure:

- Failure of the substrate (*Fig. 4a*). Most often the house finery the Ivy was climbing on, cannot withstand the stresses applied during the tests. Pieces of it brake and remained at the root. Some tree barks such as the bark of firs brake in layers and parts of the bark remain at the climbing roots.
- Failure of the connection between substrate and root. The connection is broken (*Fig. 4b*), leaving the substrate and the climbing root undamaged. This mode of failure occurs most often in Ivies attached to house fineries.
- Failure of the root (*Fig. 4c*). The climbing root rips apart, leaving attached remains on the substrate. This failure mode is seen most often in Ivies climbing on tree barks.
- Failure of the Ivy stem (*Fig. 4d*). The Ivy stem is longitudinal ripped apart, leaving the attached underside of the stem on the substrate. This failure mode occurs most often in Ivies attached to tree barks.
- Combinations of the above modes of failure. Mixed failure occurred in most tests.

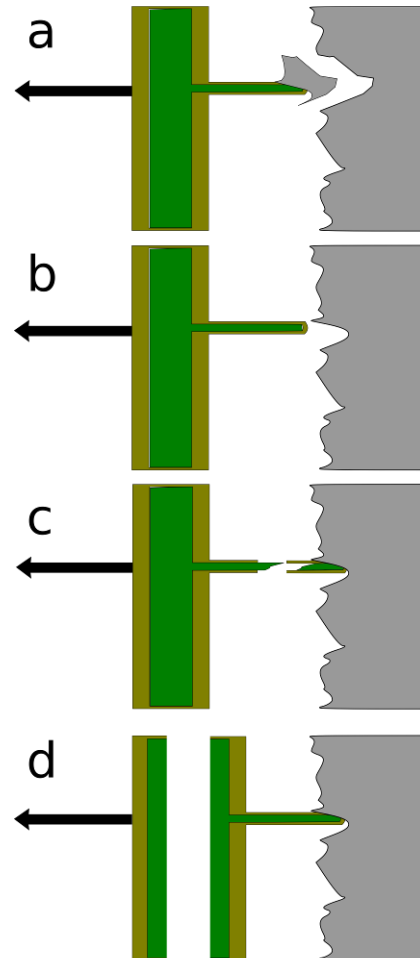


Fig 4 Modes of failure

In tensile tests of root-clusters the force-displacement curves showed in their initial phase typically a steep increase of the force until the maximal force is reached and the attachment of the root cluster starts to fail (*Fig. 5*). In most of the cases the curves showed not a continuous decrease until failure but a step-like drop of the force. This suggests a subsequent failure of single roots or small regions of the root cluster before the entire attachment structure finally fails (*Fig. 5*).

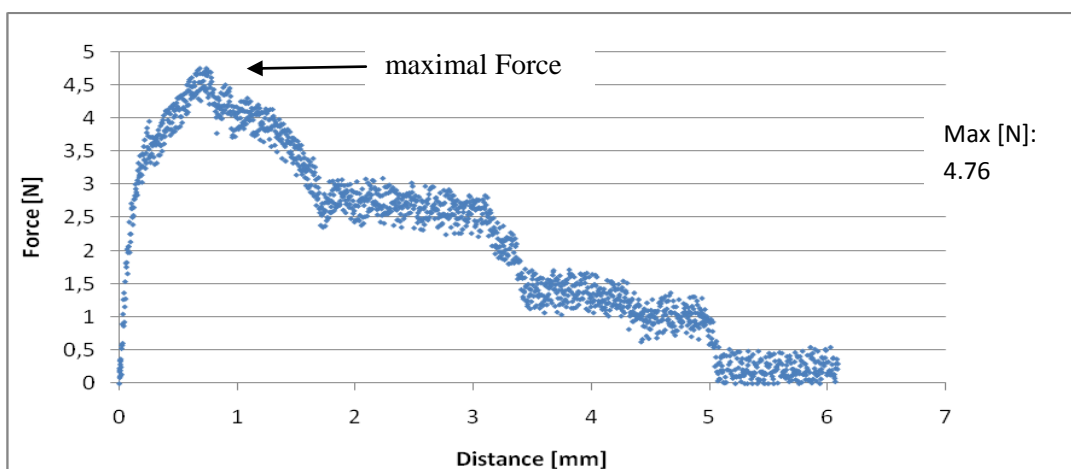


Fig. 5 Typical force-displacement diagram of a mixed failure mode

The indoor force-displacement tests of single climbing roots are expected to give insight to the contribution of the single climbing root to the combined attachment system of root clusters. Also the use of different testing angles will give data to analyse the effectiveness of the partial attachment system against component stresses.

Morphology

The roots excrete a glue-like substance which consists at least partly of polysaccharides (Fig.6). Source of the excrete are most likely roundish excrescences on the surface area of the climbing roots root hairs (Fig.7).

Fresh turgescient root hairs have a cylindrical shape with rounded tips (Fig.7).

When the root hairs dry they change into either a shoehorn-like shape (Fig.3), which is the only form found on Mylar foil as a climbing substrate, or a spiral shape (Fig. 8), which is predominately found on structured climbing substrates. The climbing roots, too, dry out after some time and shrink in girth and length.

Based on these observations, we suggest a four phase process for the English Ivy attachment:

- At the contact of the root hairs with the climbing substrate a first attachment is established. The contact area is increased due to the started flattening of the root hair. This may act as a starting signal for the following phases.

- The second phase consists of the chemical adhesion between the root hairs and the climbing substrate. The excretion of the glue substance is likely to be triggered due to the initial contact in the first phase.

- In the third phase the passive shape change of the root hairs, due to the drying process, provides additional hold. On smooth surfaces the shoehorn-like shape braces the rims of the hair with strands of glue against the substrate. On structured substrates the fresh root hair grows into gaps in the surface. When it dries out the spiral shape anchors the shrinking hair at protrusions within the gap.

- The fourth phase is the shrinking of the climbing root itself, also driven by the passive loss of water. Due to the attachment provided by the earlier phases, this shrinking process pulls the stem of the Ivy closer to the substrate and thereby further secures the attachment.

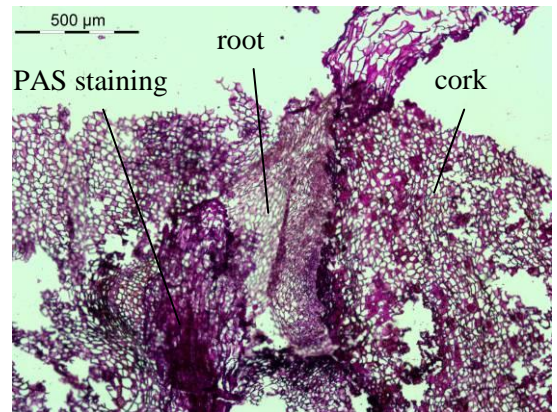


Fig. 6 PAS stained thin section of a climbing root growing in a cork gap

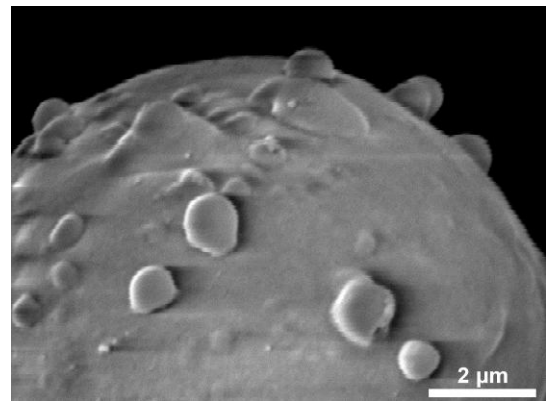


Fig. 7 Tip of a fresh root hair with roundish excrescences (SEM)

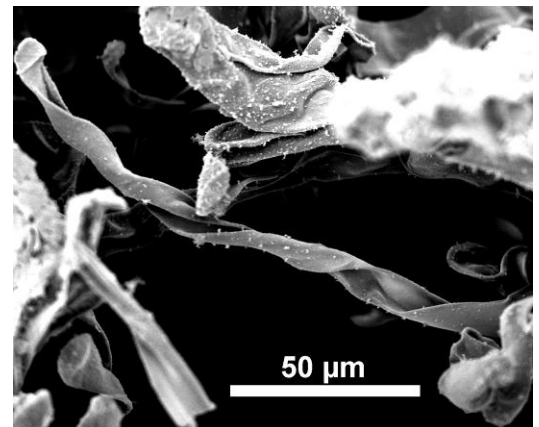


Fig. 8 Spiral shape of a dried root hair (SEM)

Conclusion

The attachment strength of English Ivy root clusters was investigated. After an initial force increase, Force-displacement curves of tensile tests show a stepwise decrease of force until final failure occurs. Four different failure modes were observed dependent on the climbing substrate. Mechanical experiments with single roots will clarify the contribution of single climbing roots and the influence of the angle of the root.

The morphological studies revealed biomechanical active components of the attachment system. This led to a suggested four phase model for the attachment process: (1) initial contact (2) chemical adhesion (3) shape change of the root hairs and (4) shrinking of the climbing roots.

Acknowledgements

We thank the Landesstiftung Baden-Württemberg for the funding of the project within the scope of the programme “Neue Materialien aus der Bionik” and Dr. Günter Beuchle of the Forschungszentrum Karlsruhe for the technical support with the ESEM.

References

1. Metcalfe, D. J. (2005): *Hedera helix L.* Journal Of Ecology , 44, 632-648
2. Majester-Savornin, B., Elias, R., Diazlanza, A. M., Balansard, G., Gasquet, M. and Delmas, F. (1991): *Saponins Of The Ivy Plant, Hedera-Helix, And Their Leishmanicidal Activity* Planta medica. 57: 260-262
3. Rogler, C. E. and Hackett, W. P. (1975): *Phase-Change in Hedera-Helix - Stabilization of Mature Form with Abscisic-Acid and Growth Retardants* Physiologia Plantarum. 34: 148-152
4. Negbi, M., Zamski, E. and Zeevi, O. (1982): *Photomorphogenetic And Thigmomorphogenetic Control Of The Attachment Of The Ivy (Hedera-Helix L) To Its Support* Zeitschrift Für Pflanzenphysiologie. 108: 9-15
5. Malpighi, M. (1679): *De capreolis et consimilibus vinculis* in Opera Omnia, Pars altera: London p. 61.
6. Zhang, M. J.; Liu, M. Z.; Prest, H. & Fischer, S.(2008): *Nanoparticles secreted from ivy rootlets for surface climbing* Nano Letters. 8: 1277-1280
7. Steinbrecher, T., Danninger, E., Harder, D, Speck, T., Kraft, O.,Schwaiger, R. (2009): *A new approach to quantify the excellent attachment strength of climbing plants in preparation*
8. Burgert, I., Fruhmann, K., Keckes, J., Fratzl, P. and Stanzl-Tschegg, S. E. (2003) *Microtensile testing of wood fibers combined with video extensometry for efficient strain detection* Holzforschung. 57: 661-664
9. Neinhuis, C. & Edelmann, H. G.(1996): *Methanol as a rapid fixative for the investigation of plant surfaces by SEM* Journal Of Microscopy-Oxford. 184: 14-16

Adhesive properties of tentacles of the protocarnivorous plant *Roridula gorgonias* and the mechanism of adhesion prevention in the mutualistic mirid bug *Pameridea roridulae*

Dagmar Voigt¹ and Stanislav Gorb^{1,2}

¹ Evolutionary Biomaterials Group, Department of Thin Films and Biological Systems, Max-Planck Institute for Metals Research, Heisenbergstraße 03, 70569 Stuttgart, Germany.

² Department of Functional Morphology and Biomechanics, Zoological Institute of the University of Kiel, Am Botanischen Garten 1–9, 24098 Kiel, Germany.

Abstract

The three-dimensional trap of the plant *Roridula gorgonias* Planch. (Roridulaceae) consists of several functional units of various levels. Its glandular trichomes release adhesive, visco-elastic, resinous secretion that traps variety of insects including those having a considerable body mass. In spite of such an elaborate trapping system of the plant, specialized mutualistic mirid bugs *Pameridea roridulae* Reut. (Heteroptera, Miridae) live on this sticky plant surface and feed on glued insects without being trapped by plant.

In this study we have analyzed (1) the role of different trichome types of *R. gorgonias* in insect trapping mechanism, and (2) the mechanism responsible for the non-sticky properties of the bug cuticle. We have visualized intact plant surfaces and insect cuticle using Cryo-SEM and measured adhesive properties of plant secretion in contact with different surfaces. Additionally, in a separate experiment we have estimated the stiffness of three different trichome types of the plant trap. A combination of structural and experimental results let us suggest that various trichome types with their different dimensions, stiffness and adhesive properties fulfil different functions in a complex trapping mechanism.

SEM study of cryo-fractures of the fresh cuticle of flies, representing typical prey of *R. gorgonias*, and *P. roridulae* bugs, has revealed a thin, fragmentary layer of epicuticular grease in flies. This result led us suggest that the plant adhesive may form proper contact with solid islands of the fly cuticle free of epicuticular grease. On the contrary, a thick and cohesively weak epicuticular greasy film in bugs acts as a sloughing off layer preventing contact formation between sticky plant secretion and solid insect cuticle.

Biomechanics of isolated cherry tomato fruit cuticles during growing

Laura España¹, Eva Domínguez², Jesús Cuartero² and Antonio Heredia¹

¹ Departamento de Biología Molecular y Bioquímica, Universidad de Málaga, E-29071 Málaga, Spain; ² Estación Experimental 'La Mayora' (CSIC) Algarrobo-Costa, E-29750 Málaga, Spain

Abstract

Aerial parts of higher plants are covered by a continuous extra-cellular layer, the cuticle or cuticular membrane (CM). The CM is a complex composite biopolymer basically composed of a cutin matrix, waxes, and hydrolysable polysaccharides. CM samples were stressed by uniaxial tension loads to determine their tensile modulus, breaking stress and maximum elongation. These biomechanical parameters of cuticle isolated from cherry tomato fruits have already been studied in mature green and red ripe CM. The present work focuses on the biomechanical parameters of cuticle isolated from cherry tomato fruits during growing. In general terms, the tendency observed in the tensile modulus was to increase during the tomato fruit development and the maximum value corresponded to red ripe stage.

Introduction

Aerial parts of higher plants are covered by a continuous extra-cellular layer, the cuticle or cuticular membrane. The main function ascribed to the cuticle is to minimize water loss [1]. Besides, it limits the loss of substances from plant internal tissues and also protects the plant against physical, chemical, and biological impacts, providing also mechanical support to maintain organ integrity [2]. Cuticles of higher plants are chemically heterogeneous in nature, basically consisting of a wax fraction, soluble in common organic solvents, and an insoluble cuticular matrix, that forms the framework of the cuticle. This cuticular matrix is mainly formed by the biopolymer cutin, a high-molecular weight polyester composed of various inter-esterified C16 and C18 polyhydroxyalkanoic acids [3]. In addition, some polysaccharide material is also present in variable amounts, mainly in the inner side of the cuticular matrix, as well as flavonoids in some species.

The structure-function relationship of the cuticle, together with the influence of its composition and organisation on the biomechanical properties is still poorly understood. The biomechanical properties of the isolated cuticle from leaves of several plant species and from tomato fruits were studied in some detail by [4], revealing a large variation between species and, important for tomato fruit, indicating that the cuticle provides structural support to fruits without hard internal tissues. In addition, the viscoelastic nature of plant cuticles and its physiological importance has been described [5,6,7,8] together with the effect of hydration and temperature on the mechanical properties of the isolated tomato fruit cuticles [7,8,9]. Recently our group documented the relative contribution of specific components of plant cuticle such as cutin and polysaccharides to its biomechanical properties. Polysaccharides incorporated into the cutin matrix were responsible for the elastic modulus, stiffness and the linear elastic behavior of the cuticle, while the viscoelastic behavior, characterized by low elastic modulus and high strain values, could be assigned to the cutin matrix [10]. It was also showed that the cutin elastic

modulus, independently of the temperature and hydration degree, was always significantly higher in red ripe cuticles than in the mature green ones, assuming that phenolics, mostly flavonoids, in the cuticle network could be the main candidates to explain the increase of rigidity from the mature green to the red ripe stage [10].

Material and methods

Solanum lycopersicum L. cv. Cascada plants were grown in a polyethylene greenhouse during spring at the Estación Experimental La Mayora, CSIC, in the south-east of Spain. Flowers were labelled at anthesis, hand-pollinated and fruits harvested every 10 days after anthesis (daa) from 15 daa until red ripe (55daa).

Cuticles were enzymatically isolated from tomato fruits at different stages of development following the protocol of [11] as modified by [12] using an aqueous solution of a mixture of fungal cellulase (0.2% w/v, Sigma) and pectinase (2.0% w/v, Sigma), and 1 mM NaN₃ to prevent microbial growth, in sodium citrate buffer (50 mM, pH 3.7). Vacuum was used to facilitate enzyme penetration, and fruit samples were incubated with continuous agitation at 35°C for at least 14 d. The cuticle was then separated from the epidermis, rinsed in distilled water and stored under dry conditions.

Small pericarp pieces from three fruits per developmental stage were fixed in a formaldehyde, acetic acid and ethanol solution (1:1:18); later on dehydrated in an ethanol dilution series (70-95%) and embedded in a commercial resin (Leica Historesin Embedding Kit, Heidelberg, Germany). Samples were cross-sectioned into slices 4 µm thick using a Leica microtome (RM2125, Germany). Sudan IV was employed to differentially stain the cuticle. Cuticle thickness was estimated from a minimum of 30 to 50 measurements from the cross-sectioned samples using an image capture analysis program (Visilog-Noesis 6.3, France). It was assessed from the central region between pegs since this area remains almost constant and is not affected by cuticle invaginations. Cuticular area was calculated using the same program and a minimum of 20 measures per stage.

The mechanical properties of the cuticle were measured following the previous work of [8] using an extensometer equipped with a linear displacement transducer (Mitutoyo, Kawasaki, Japan) that was customized to work with cuticle samples. Rectangular uniform segments (3 mm x 9 mm) of isolated cuticles were sectioned using a metal block and fixed between the ends of two hollow stainless- steel needles, by a small amount of fast-drying super glue. The system was enclosed in an environment controlled chamber that allowed the control of temperature and relative humidity (RH). Each cuticle sample was held inside the extensometer chamber for at least 30 min to equilibrate the temperature and humidity before beginning the extension test.

The cross-sectional area of the samples was measured by optical microscopy and image analysis software (Visilog-Noesis v 6.3) and the length of the exposed surface of the sample between the two supports was measured before mechanical extension tests. The mechanical tests were performed as a transient creep test to determine the changes in length of a cuticle segment by maintaining samples in uniaxial tension, under a constant load for 1200 s, with the longitudinal extension of each sample being recorded by a computer system every 3 s. Each sample was tested repeatedly using an ascending sequence of sustained tensile forces (from 0.098 N to breaking-point by 0.098 N load increments) without recovery time [8]. To determine stresses, the tensile force exerted along the sample was divided by the representative cross-sectional area of the sample. To obtain the corresponding stress-strain curve and elastic modulus (E), the applied stress was plotted against the total change in length (%) after 20 min. Breaking stress and maximum strain at the breaking stress were also determined for each sample. All the strain-time and the corresponding stress-strain curves were calculated for a set of 5–7 samples of the corresponding cuticles equilibrated at 25°C and 40% RH.

Results and discussion

Tomato fruit suffers dramatic increases in size during its development, especially in the first stages of growth during the immature – mature green period. This expansion is withstood by pericarp cell walls plus the cuticle. Thus, in these stages a fruit needs to withstand the internal pressure but at the same time expand their tissues. In a previous work [13] we described that cuticle accumulation in cherry tomatoes (expressed as micrograms per square centimetre) reached its maximum very early in fruit development (*Table 1*), around 15 days after anthesis (daa). Nevertheless, cuticle synthesis continued in order to maintain its amount as fruit increased size during development.

In the present work we describe the biomechanical behaviour of cherry tomato cuticles at different stages of growth. *Table 2* shows the biomechanical parameters thus obtained. The comparison of mature green (MG) and red ripe (RR) cuticles showed a significant increase in the elastic modulus implying a much higher stiffness of the cuticle material once it reaches the mature stage. A statistically significant increase in the elastic modulus between MG and RR has recently been shown for cuticles derived from tomatoes that accumulate flavonoids at the onset of ripening [14]. Thus, a role in modulating cuticle stiffness was demonstrated for flavonoids accumulated in tomato cuticle during ripening. Interestingly, at 45daa, when the cuticle is already accumulating flavonoids (breaker-orange stage), the elastic modulus was higher than in MG but still much lower than for the RR, suggesting an intermediate stage in flavonoid accumulation.

Table 1 Micrograms per square centimetre of Cascada cuticle at five stages of fruit development. Cuticle thickness (in microns), determined by microscopic observation, is also included. Data are presented as mean \pm standard error. Data from [13].

Stage	Amount of cuticle	Thickness
15 daa	1307.4 \pm 62.5	4.4 \pm 0.1
25 daa	1455.8 \pm 70.7	6.7 \pm 0.1
35 daa (MG)	1446.2 \pm 49.7	7.2 \pm 0.1
45 daa	1443.0 \pm 79.7	6.5 \pm 0.1
55 daa (RR)	1332.4 \pm 67.1	6.2 \pm 0.1

Table 2 Cuticle biomechanical parameters studied in five developmental stages of fruit development. Elastic modulus and maximum stress are measured in MPa, maximum strain is expressed as a percentage. Data are presented as mean \pm standard error.

Stage	Young modulus	Breaking stress	Maximum strain
15 daa	487.8 \pm 23.9	40.9 \pm 7.7	17.9 \pm 4.5
25 daa	235.0 \pm 7.6	25.7 \pm 5.4	20.0 \pm 5.3
35 daa (MG)	289.1 \pm 16.5	33.8 \pm 2.3	30.9 \pm 1.9
45 daa	536.2 \pm 8.6	50.6 \pm 0.1	18.1 \pm 1.0
55 daa (RR)	995.8 \pm 64.6	62.7 \pm 10.9	14.0 \pm 4.2

Following this hypothesis, a low elastic modulus would be expected at developmental stages before the MG since fruits are at full growth and expansion. Nevertheless, this seemed to be only partially true. At 25 daa a low elastic modulus, similar to the MG, is observed but at 15 daa the elastic modulus was 2-fold higher. At this stage the modulus value is similar to that of tomatoes at 45 daa. Thus, a high elastic modulus at a very early stage of development followed by a decay and further increase during ripening is observed in cherry tomatoes. Two possible explanations for this behaviour early in development could be postulated. First, a putative rapid accumulation of some phenolic material other than flavonoids at 15 daa that would later in development decrease its concentration as the fruit expands and synthesises more cuticle. This phenolic material would have a similar biomechanical role as that already described for flavonoids. Another explanation would be related to the rapid accumulation of cuticle material

that happens in the period between 10 and 15 daa [13]. Maybe this fast deposition leads to the formation of a very dense material that unfolds during the following stages. The increase in cuticle thickness during this period (*Table 1*) while maintaining the amount of cuticle per square centimetre points towards this possibility. Yet, further research is needed to clarify this point.

A similar behaviour during development was observed for another biomechanical parameter, the breaking stress. At 15 daa the cuticle needed a higher stress to produce a break than in the following 2 stages and only after the fruit had reached the onset of ripening the stress increased to values higher to those of 15 daa. On the other hand, the maximum stress, the ability of the cuticle to deform, followed a more logical behaviour according to the role of flavonoids above discussed [14]. The percentage of deformation increased during development and then decreased during ripening. However, the significant increase between 15 and 35 daa again points to the presence of some molecular compounds and/or molecular arrangement of cuticle components that constrains cuticle deformation making it stiffer. Thus, an in-depth study of the nature and molecular arrangement of the cuticle at 15daa it will be needed.

Conclusion

The biomechanical properties of the cuticle changed during fruit growth and ripening despite the amount of cuticle expressed as micrograms per square centimetre was similar among the different stages of development. The stiffness of the material, together with the stress needed to break the cuticle, increased significantly during growth until they reached a maximum at red ripe.

Acknowledgements

The authors would like to thank Ana Rico for technical assistance. This work has been partially supported by grant AGL2006-12494 from Plan Nacional de I+D, Ministerio de Educación y Ciencia, Spain.

References

1. Riederer, M. and L. Schreiber, (2001): *Protecting against water loss: analysis of the barrier properties of plant cuticles*. Journal of Experimental Botany. 52: 2023-2032.
2. Niklas, K..J. (1992): *Plant Biomechanics. An Engineering Approach to Plant Form and Function*. Editors. The University of Chicago Press: Chicago.
3. Heredia, A. (2003): *Biophysical and biochemical characteristics of cutin, a plant barrier biopolymer*. Biochimica et Biophysica Acta. 1620: 1-7.
4. Wiedemann, P. and C. Neinhuis, (1998): *Biomechanics of isolated plant cuticles*. Botanica Acta. 111: 28-34.
5. Marga, F., Pesacreta, T.C. and K.H. Hasenstein, (2001) *Biochemical analysis of elastic and rigid cuticles of Cirsium horridulum*. Planta. 213: 841-848.
6. Petracek, P.D. and M.J. Bukovac, (1995): *Rheological properties of enzymatically isolated tomato fruit cuticle*. Plant Physiology. 109: 675-679.
7. Round, A.N., Yan, B., Dang, S., Estephan, R., Stark, R.E. and J.D. Batteas, (2000): *The influence of water on the nanomechanical behavior of the plant biopolyester cutin as studied by AFM and solid-state NMR*. Biophysical Journal. 79: 2761-2767.
8. Matas, A.J., López-Casado, G., Cuartero, J. and A. Heredia, (2005): *Relative humidity and temperature modify the mechanical properties of isolated tomato fruit cuticles*. American Journal of Botany. 92: 462-468.

9. Edelman, H.G., Neinhuis, C. and H. Barga, (2005): *Influence of hydration and temperature on the rheological properties of plant cuticles and their impact on plant organ integrity*. Journal of Plant Growth Regulation. 24: 116-126.
10. López-Casado, G., Matas, A.J., Domínguez, E., Cuartero, J. and A. Heredia, (2007): *Biomechanics of isolated tomato (Solanum lycopersicum L.) fruit cuticles: the role of cutin matrix*. Journal of Experimental Botany. 58: 3875-3883.
11. Orgell, W.H. (1955): *The isolation of plant cuticle with pectic enzymes*. Plant Physiology. 30: 78-80.
12. Yamada, Y., Wittwer, S.H. and M.J. Bukovac, (1964): *Penetration of organic compounds through isolated cuticles with special reference to urea*. Plant Physiology. 39: R11-& Suppl. S.
13. Domínguez, E., López-Casado, G., Cuartero, J. and A. Heredia, (2008) *Development of fruit cuticle in cherry tomato (Solanum lycopersicum)*. Functional Plant Biology. 35(5): 403-411.
14. Domínguez, E., España, L., López-Casado, G., Cuartero, J. and A. Heredia, (2009) *Biomechanics of isolated tomato fruit cuticles during ripening: the role of flavonoids*. Functional Plant Biology. in press.

5. Micromechanics

Making shapes - mechanical principles of plant cell growth

Anja Geitmann

*Institut de recherche en biologie végétale, Département de sciences biologiques
Université de Montréal, Canada*

Abstract

Cellular growth is one of the fundamental underpinnings of morphogenesis. In plant cells, expansive growth is ultimately determined by the mechanics of the primary cell wall. Given that the driving force for cellular expansion, the turgor pressure, is isotropic, the generation of complex cell geometries relies on local differences and anisotropic distribution of cell wall mechanical properties at subcellular scale. Global changes in cell shape such as preferential elongation in one direction is greatly determined by the orientation of cellulose microfibrils. However, while the mechanics of the microfibrils is essential, overall cell wall extensibility is largely determined by the links between them and by the matrix surrounding them. Local growth events on the other hand are generated by the spatially confined reduction in cell wall stiffness involving changes to the mechanical properties of the matrix components. The geometry and mechanics of these spatially confined growth events is discussed and a categorization of cellular expansion patterns is presented.

Introduction

Plant development is the result of three essential processes: cell expansive growth, cell division, and cellular differentiation. Cellular expansion is involved both in increase in size and in the generation of changes to cell shape. Increase of cell volume during the differentiation of a meristematic cell into its destination cell type is typically between 10 and 1000-fold [1], but can reach up to 30 000-fold, for example in the case of xylem vessels [2]. While the increase in cellular surface (L^2 with L being the length of the cell) is smaller than the increase in cytoplasmic volume (L^3), the amount of additional cell wall that has to be generated is still impressive.

Implicit in cell expansive growth is a mechanical process that balances turgor generated tensile stress in the cell wall with the opposing force resisting stretching to allow expansion [3,4]. The balanced counterforce of primary wall stress to turgor pressure has prompted the comparison of plant cells with "hydraulic machines" [5]. Turgor pressure, however, is isotropic. Therefore, the only shape a cell with uniformly distributed and isotropic cell wall mechanical properties would be able to achieve is a sphere with ever increasing diameter. Differentiated plant cells come in a multitude of shapes ranging from simple cylindrical cells (e.g. palisade mesophyll) to star-shaped complex structures (e.g. astro-sclereids) [6,7]. The generation of complex geometries requires the mechanical properties of the cell wall to be non-uniformly distributed or to exhibit anisotropy. The fact that even complex shapes are determined by the cell wall can easily be demonstrated by enzymatic digestion of the latter resulting in a perfectly spherical protoplast. In the following, different types of cell shapes are categorized and the manner in which the cell wall controls their generation is discussed.

Cellulose mediated anisotropy of cellular expansion

For the cell to globally elongate in a particular direction, cell wall deformability in this direction must be lower. Once a geometry different from a sphere has been established, this mechanical anisotropy may have to be even bigger to sustain directional expansion since both surface geometry and local mechanical properties contribute to the spatial distribution of stresses on the cellular surface (Fig. 1) [8]. The orientation of cellulose microfibrils in the cell wall is generally recognized as a crucial parameter determining anisotropy in cell wall deformability under tensile stress [9,10]. Other cell wall components such as arabinogalactan proteins seem to mechanically influence cell wall anisotropy, but the mechanical principles of their molecular action is not understood [11]. Microfibrils are formed from crystalline cellulose polymers [12] and they are embedded in a matrix composed of hemicellulose and other polysaccharides. The comparison with a fiber reinforced composite material has been helpful for modeling this material behavior [13,14] and it seems logical that the microfibrils confer rigidity and strength to the cell material particularly in the direction of their principal orientation. Hence, in cells exhibiting elongation growth, microfibrils are typically oriented perpendicular to the long axis on the inner surface of the cell wall thus restricting deformation to the larger stresses in the circumferential direction [9,15-19].

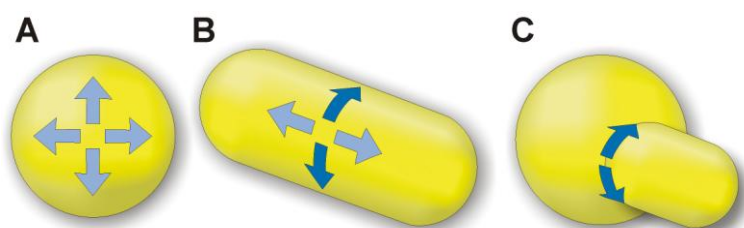


Fig. 1. Geometry dependence of surface stress patterns in thin-shelled pressure vessels. **A.** A spherical shell experiences isotropic stress patterns. **B.** In a cylindrical body the stress in circumferential direction is twice as large as the longitudinal stress. **C.** The largest stress in a body with local outgrowth is located at concave bend between the main body and the outgrowth. Arrows in dark blue represent relatively larger stress than arrows in light blue.

Modeling the plant cell wall by defining a two-term strain energy function, one term each for the matrix and the microfibril phases, Chaplain established that in addition to microfibril extensibility the matrix shear modulus is an important variable [20]. This aspect is occasionally neglected when discussing the effect of cellulose microfibrils on cell wall deformability. During elongation growth, the primary wall deforms predominately in the long axis, separating the space between the essentially transverse microfibrils and passively reorienting slightly tilted microfibrils toward the longitudinal axis. The latter process has been termed multi-net growth and is proposed to be responsible for the changing orientation of microfibrils through the thickness of the cell wall [17-19]. The multi-net concept has been challenged by Marga et al. [21] who did not find significant reorientation of microfibrils upon application of strain up to 30% during in vitro creep experiments. However, simple geometrical calculations based on the influence of the initial microfibril angle and the applied strain on the final microfibril orientation demonstrated that the expected reorientation would have been too small to be recognized in this experimental setup [22]. Hence, these experiments are not necessarily inconsistent with the classical multi-net growth hypothesis. In anisotropic elongation growth it is apparent that stretching and/or breaking of the hemicellulose connections between the microfibrils, and hence the mechanical properties of these linkages, must be an important limiting factor regulating extensibility. However, even in the case of tensile stress parallel to the direction of microfibril orientation, the cellulose fibers can only provide mechanical resistance if they are connected to each other - either directly, via hemicellulose tethers or by generating friction between each other, or indirectly, by generating shear within the polymer matrix. The reason for this is that unless the microfibrils form complete hoops or spirals around the cell, tensile stress would simply cause them to

slide against each other (Fig. 2). Since the typical length for microfibrils seems to be below 10 μm [23], it is unlikely that individual microfibrils form complete hoops around the cellular perimeter. Hence, the mechanical properties of the connecting matrix tethers, their abundance relative to the density of microfibrils, the deformability of the gel composed of the other matrix components, as well as the length of the microfibrils should be important parameters determining mechanical behavior of the cell wall not only perpendicular, but also parallel to microfibril orientation (Fig. 2). It has been proposed that matrix molecules do not actually act so much as a tether but rather as a spacer between the microfibril rods [24]. However, both functions are not mutually exclusive and the mechanical role of matrix molecules might depend on the particular situation and the angle of the microfibrils versus the direction of cell wall expansion [22]. The list of biophysical parameters determining extensibility will certainly have to be revised in the future, once the hierarchical organization and the interconnections between individual types of molecules are better understood (for a review of different conceptual models see [25]).

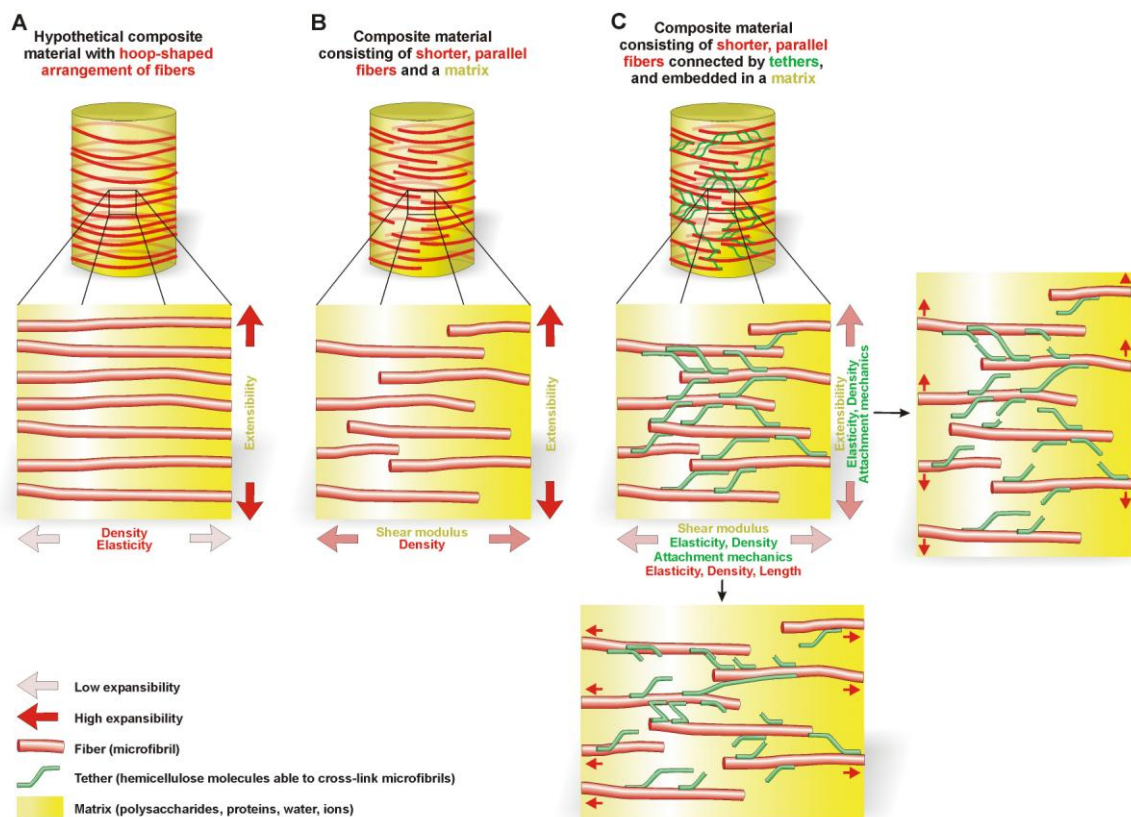


Fig. 2. Mechanics of a composite material with parallel arrangement of the fiber component.

A. Hypothetical composite material in which the fiber elements form hoops around the cellular circumference. Wall extensibility in the direction parallel to the fibers would be largely determined by the mechanical properties of the fibers and their relative density. **B.** Composite material consisting of fibers of limited length embedded and bonded to the matrix. Wall extensibility in direction parallel to the fibers is largely limited by the shear modulus of the matrix and the density of the fibers. **D.** Composite material in which the fibers (microfibrils) are connected by tethers (e.g. hemicellulose polymers) in addition to being embedded and bonded to the matrix. The mechanics of the tethers and their attachments largely influences both wall extensibility parallel to and perpendicular to the fiber orientation. The shade of red of the arrows indicates the overall wall extensibility of the material in the indicated direction (red - high extensibility). The terms between the arrows indicate the biophysical and structural parameters limiting extensibility in the indicated direction. The parameters represent the mechanical properties of fibers/microfibrils (red), tethers/hemicellulose links (green), and other matrix components (yellow).

Microtubule-microfibril interaction

For developmental biologists the question arises how cells control the orientation of their microfibrils. The importance of the role of the microtubule cytoskeleton is undisputed in this context [15,26,27], but our understanding of the mechanism of the interaction and mutual control between microtubules and microfibrils is still rather poor. In many plant cells microtubule arrays are arranged parallel to the main microfibril orientation which led to the concept that movement of cellulose synthase enzyme complexes in the plasma membrane is constrained by interactions with the cortical microtubules [28]. However, this concept turned out to be inconsistent with observations of continued synthesis of organized cellulose microfibrils following the disruption of cortical microtubules by pharmacological agents [15,29] or mutation [30,31]. In *mor1* mutants microtubules are shortened and disorganized in a temperature-sensitive manner leading to a loss in growth anisotropy. However, cellulose microfibrils continue to be deposited transverse to the long axis of the plant organ even after prolonged disruption of cortical microtubule arrays and the onset of radial expansion. This is true for both mutation and drug induced interference with microtubules. Even more dramatically, change in growth anisotropy of root cells occurred in *rsw4* and *rsw7* mutants despite the unaltered, horizontal orientation and abundance of *both* microtubules and microfibrils [32].

Several conceptual models have been proposed that could explain the role of microtubules in controlling cellular expansion other than by determining microfibril orientation. Microtubules might be required to concentrate and organize cellulose synthase complexes to ensure efficient cellulose assembly into higher order clusters of fibers [33]. Alternatively, microtubules might ensure the coordination between cellulose deposition and the delivery of proteins and other molecules to optimize cell wall structure [34]. Microtubule control of the mechanical cell wall properties might also be based on their influence on cellulose synthase turnover thus through the determination of microfibril length [35]. Shorter microfibrils might lead to an altered mechanical behavior of the cell wall thus allowing more expansion in the direction parallel to cellulose orientation. The number of microtubule mutants known to affect growth anisotropy is staggering [36] and hopefully the mechanics of the interaction between cytoskeleton and microtubules will be elucidated in the near future. Determining the actual length of microfibrils and their degree of clustering in the cells of these mutants will most certainly be necessary to validate any of the above models or allow the generation of better ones. There have been attempts to explain the orientation of microfibrils in cylindrical cells without the necessity of a guidance mechanism. These are essentially based on geometrical considerations, the hypothetical limitation of space into which microfibrils can be deposited, and the dynamics of cellulose synthases dispatching into the membrane [37-40]. These models have certainly provided food for thought and will help to develop experimental approaches that will be able to provide answers.

Spatially confined growth events

Cellulose-mediated anisotropy in the deformability of the cell wall is generally associated and most intensively studied with overall anisotropic cellular expansion. Approximately spherical or polyhedral cells derived from the apical meristem elongate by anisotropic deformation of large portions of their surface. Typically, cells that have differentiated through this mechanism do not have any sharp concave bends in their surface. Numerous cell types, however, do have such concave bends or exhibit other types of complex geometries. Dramatic examples include star-shaped trichoblasts, astro-sclereids, stellate aerenchyma cells, lobed leaf epidermis cells, and the cylindrical protrusions typical for pollen tubes and root hairs. How then are these more complex geometries generated? The common feature of many of these cell types is a relatively large cell body producing one or several roughly cylindrical or finger-like extensions that may be branched. These extensions are generated by spatially confined growth events that must rely on locally increased rates of cell wall deformation and deposition. To distinguish spatially confined growth events from global cell growth, I have proposed earlier [41] to name the former heterotropic and the latter homotropic (*Fig. 3*). The mechanics and geometry of heterotropic growth events varies largely between cell types and not in all cases have

surface expansion rates been assessed quantitatively. Spatial gradients in the biochemistry and distribution of the matrix polymers such as pectin play an essential role in the generation of these shapes [42].

In the stellate aerenchyma, the star-shaped cells are initiated by the detachment of adjacent cells parenchymatic at three or four way junctions. The resulting intercellular spaces increase in size to eventually become an anastomosing network. While developmental information is scarce and cell wall deformation patterns for this cell type have not been published to my knowledge, it is likely that the site of cell wall expansion is initially located at the concave bend and subsequently in the cylindrical walls of the branches (*Fig. 3*). On the contrary, lobe formation in the jigsaw puzzle shaped leaf epidermis cells seems to be generated by a cellulose-based reinforcement of non-growing regions and tip-growth like outgrowths of the lobes [43]. How "tip-focused" this growth really is remains to be seen. A high rate of cell wall expansion at the very pole of the lobes would generate friction with the adjacent concave bend of the neighboring cell and it is thus more likely that the side walls of the lobes represent the sites of highest expansion (*Fig. 3*).

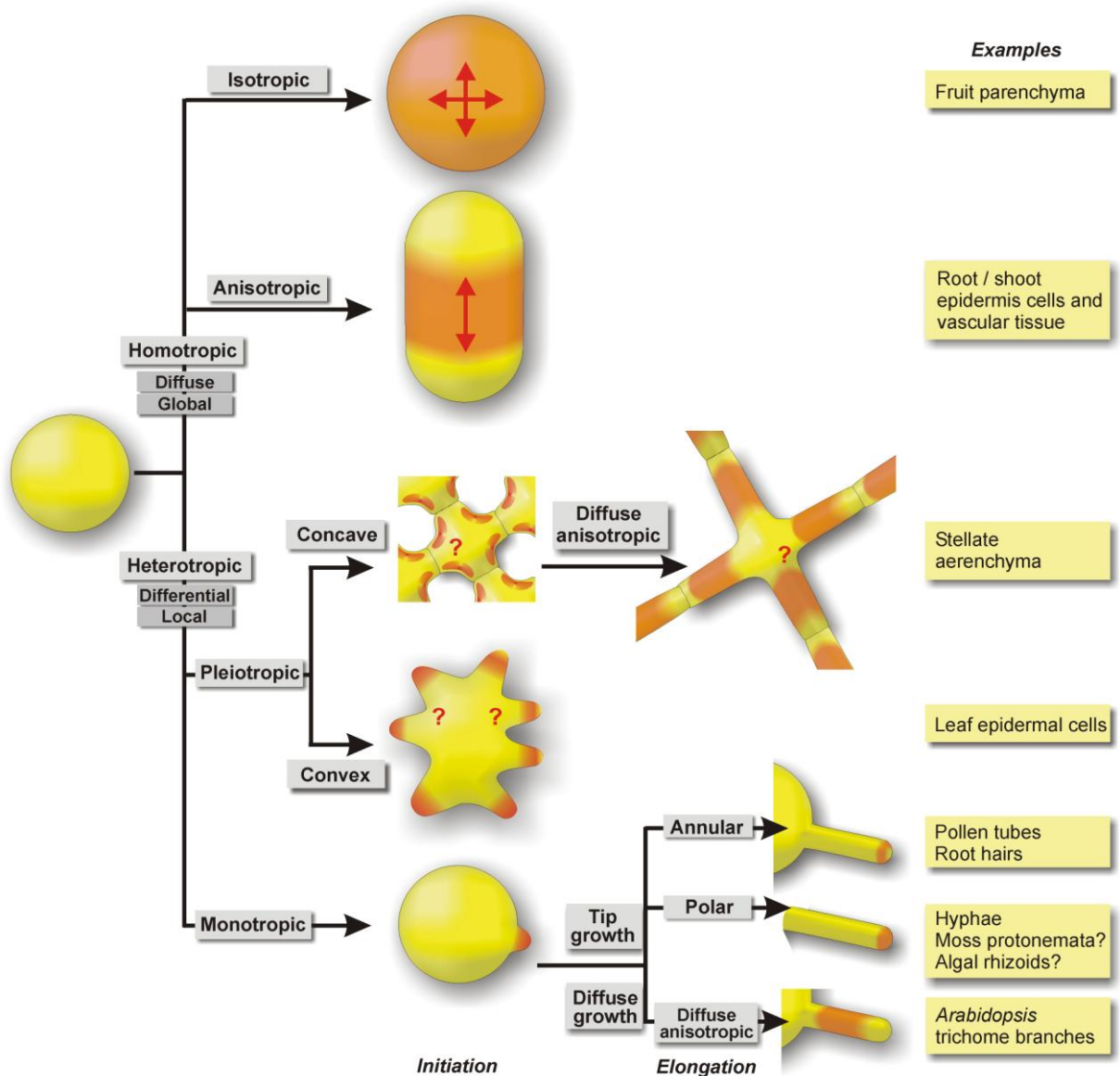


Fig. 3. Overview of cell wall expansion patterns resulting in various cellular geometries. Different types of cell wall expansion patterns can be combined in a single cell. They can occur simultaneously or at different times during differentiation. Areas on the cell surface undergoing expansion are marked in red. Question marks indicate lack of quantitative data on surface expansion patterns. For some categories alternative terms are provided. Typical cell types for each expansion pattern are listed on the right.

Branch formation in *Arabidopsis* trichomes is initiated by a highly spatially confined growth event on the surface of an existing trichome and branches elongate by large-surface expansion of the cylindrical side walls [7,44](Fig. 3). In contrast, cell wall expansion in pollen tubes and root hairs is confined to the apical tip of the cylindrical extension during the entire growth period, the cylindrical walls of these cells do not expand [45-47]. To distinguish cells with a single site of increased growth activity from those with multiple sites, such as the lobed epidermal cells, I have proposed the terms monotropic for the former and pleiotropic for the latter (Fig. 3).

This tip-focused pattern of surface expansion in pollen tubes is in part explained by the non-uniform distribution of different configurations of pectins [42] and the reinforcement of the cylindrical shank by callose [48] and cellulose. Recent evidence revealed, however, that tip growth in pollen tubes does not occur at the extreme tip or pole of the cell, but rather at an annular region around it [49]. The differences between "tip" growth and other growth patterns might therefore be quantitative rather than qualitative, with a growing region that is more spatially confined but not principally different from that in other cell types. This illustrates that despite being hailed for a long time as a very distinct growth mechanism, tip-growing cells might actually only represent the extreme end of a gradual spectrum defining the geometry of plant cell growth.

The question is what defines the more or less spatially confined surface areas that are subject to expansion in heterotropic growth events and what prevents adjacent areas from being deformed? Intriguingly, these stable, adjacent areas often have to resist higher tensile stress than the growing regions due to cellular geometry resulting in differential distribution of stress patterns on the cellular surface [47] (Fig. 1). Clearly, spatially confined sites of cellular expansion require the establishment of local differences in cell wall mechanical properties [8] and theoretical models of the geometry and structure provide information on the exact degree of difference in mechanical properties that is necessary to generate a particular heterotropic shape.

The simple radial symmetry of cylindrical, tip-growing protrusions such as those formed by pollen tubes, root hairs, and fungal hyphae, has made these cell types the subject of numerous theoretical models and, more recently, of cytomechanical studies. Ranging from relatively simple geometrical considerations [50,51] most treat the expanding cell using an elastic membrane model [52-56]. Micro-indentation has revealed that the growing apical region in pollen has indeed lower cellular elastic stiffness than the distal region of the same cell, which is at least in part due to the differences in cell wall mechanical properties [42,48,57,58]. The degree of apical stiffness also correlates with the dynamics of the growth rate, a relationship that is likely to be causal [59].

The question arises how the cell generates and controls such spatially confined areas of higher cell wall deformability. Root trichoblasts about to form root hairs show localized cell wall regions of lowered pH [60], high xyloglucan endotransglycosylase activity [61] and increased expansin concentration [62,63]. Pollen grains about to germinate exhibit an increased accumulation of methyl-esterified pectin at the aperture [48]. Clearly, the biochemistry of the cell wall can change over distances as small as few micrometers. The mechanism that is likely to be responsible for the establishment of a local "hot spot" of mechanically different cell wall are localized activation of proton pumps and/or targeted secretion. Other than the secretion of proteins affecting the degree of cross-linking between cell wall polymers, secretion induced cell wall softening may also be due to a lack of alignment and loose coiling of newly delivered cell wall polymers or a lack of gel formation due to their methyl-esterification or absence of calcium ions [42,64,65]. The targeting of vesicles containing cell wall precursor material or agents influencing cell wall properties is controlled by the cytoskeleton [7]. Contrary to the predominant role of microtubules in cellulose deposition, heterotropic growth is often accompanied by characteristic configurations of the actin cytoskeleton or a combination of the actin- and microtubule arrays at the future site of a polar outgrowth. This has been observed in pollen tubes, root hairs, algal zygotes and fungal hyphae [6,62,66-73]. This prominence of actin is consistent with the fact that in these cell types, contrary to animal cells, the actin microfilaments play an important and sometimes dominant role in cytoplasmic organelle transport. In pollen tubes both microtubule and actin arrays are involved in organelle transport, but the former is not critical for vesicle delivery [74]. Trichome branch initiation in *Arabidopsis* is dependent on actin- and microtubule-mediated Golgi transport to the cell cortex [75]. Drug or mutation induced interference with microtubule functioning affects the initiation of a new branch whereas the actin cytoskeleton seems to be responsible for maintaining the polarity [69,76,77]. Root hair initiation is preceded by a

reorientation of the microtubule cytoskeleton [78], but the disruption of the latter does not inhibit the process [79]. Drugs causing actin depolymerization or fragmentation on the other hand successfully interfere with root hair initiation [79-81] and germination in algal zygotes [82]. *der1* plants, which possess a point mutation in the gene encoding actin2, have enlarged or misplaced root hair initiation sites [83,84].

While interference with the cytoskeleton and hence the delivery of cell wall material is sufficient to hamper or alter growth [69], it is important to note that the simple piling on of cell wall polymers through secretion cannot by itself produce the formation of a protuberance even when it is highly localized. This is evident from tip growing cells in which growth is arrested while secretion is still ongoing [85,86]. A force causing tensile stress in the cell wall is still a prerequisite to explain expansion. Models that base cellular expansion solely on material addition [87,88] therefore only reflect one aspect of cellular reality, just as do those that focus exclusively on cell wall deformation. Our increasingly precise knowledge about vesicle delivery [89,90] and surface expansion [52] during heterotropic growth events should therefore make their way into the theoretical models that attempt to have the ability to reflect cellular biology and predict its behavior.

Conclusion

Cells are physical entities and as such they have to obey the laws of physics. The spatio-temporal patterns of plant cell growth can only be understood if the mechanical principles underlying cell wall mechanics are fully elucidated. Despite our increasing knowledge of the molecular players influencing cell wall mechanics our understanding of the interactions between these components is still sketchy. Advancement in theoretical modeling approaches and quantitative micro-mechanical studies will help in testing conceptual models and explaining the intriguing cellular shapes we can observe in plants.

Acknowledgements

The Geitmann lab receives funding from the Natural Sciences and Engineering Research Council of Canada (NSERC), the *Fonds Québécois de la Recherche sur la Nature et les Technologies (FQRNT)*, and the Human Frontier Science Program (HFSP). Firas Bou Daher is acknowledged for his linguistic assistance in questions of nomenclature. Parts of this manuscript and the figures are reprinted from [41].

References

1. Veytsmann, B. and Cosgrove, D.J. (1998): *A model of cell wall expansion based on thermodynamics of polymer networks*. *Biophys. J.* 75: 2240-2250
2. Cosgrove, D.J. (2005): *Growth of the plant cell wall*. *Nature Reviews - Molecular Cell Biology* 6: 850-861
3. Cleland, R. (1971): *Cell wall extension*. *Annual Review of Plant Physiology* 22: 197-226
4. Taiz, L. (1984): *Plant cell expansion: Regulation of cell wall mechanical properties*. *Annual Review of Plant Physiology* 35: 585-657
5. Peters, W., Hagemann, W., and Tomos, D. (2000): *What makes plants different? Principles of extracellular matrix function in soft plant tissues*. *Comparative Biochemistry and Physiology A* 125: 151-167
6. Mathur, J. (2006): *Local interactions shape plant cells*. *Curr. Opin. Cell Biol.* 18: 40-46
7. Smith, L.G. and Oppenheimer, D.G. (2005): *Spatial control of cell expansion by the plant cytoskeleton*. *Annu. Rev. Cell Dev. Biol.* 21: 271-295
8. Green, P.B. (1969): *Cell morphogenesis*. *Annual Review of Plant Physiology* 20: 365-394
9. Baskin, T. (2005): *Anisotropic expansion of the plant cell wall*. *Annu. Rev. Cell Dev. Biol.* 21: 203-222
10. Green, P.B. (1980): *Organogenesis - a biophysical view*. *Annual Review of Plant Physiology* 31: 51-82
11. Ding, L. and Zhou, J.K. (1997): *A role for arabinogalactan-proteins in root epidermal cell expansion*. *Planta* 203: 289-294

12. Somerville, C. (2006): *Cellulose synthesis in higher plants*. Annual Review in Cell and Developmental Biology 22: 53-78
13. Hettiaratchi, D. and O'Callaghan, J. (1978): *Structural mechanics of plant cells*. J. Theor. Biol. 45: 235-257
14. Davies, G.C. and Bruce, D.M. (1997): *A stress analysis model for composite coaxial cylinders*. J. Mat. Sci. 32: 5425-5437
15. Baskin, T. (2001): *On the alignment of cellulose microfibrils by cortical microtubules: A review and a model*. Protoplasma 215: 150-171
16. Castle, E. (1942): *Spiral growth and the reversal of spiraling in Phycomyces, and their bearing on primary wall structure*. Am. J. Bot. 29: 664-672
17. Green, P.B. (1960): *Multinet growth in the cell wall of Nitella*. Journal of Biophysical and Biochemical Cytology 7: 289-297
18. Preston, R.D. (1974): *The physical biology of plant cell walls*, London, Chapman and Hall
19. Roelofsen, P. (1951): *Cell wall structure in the growth zone of Phycomyces sporangiophores. II. Double refraction and electron microscopy. The origin of spiral growth in Phycomyces sporangiophores*. Biochimica et Biophysica Acta 6: 357-373
20. Chaplain, M.A.J. (1993): *The strain energy function of an ideal plant cell wall*. J. Theor. Biol. 163: 77-97
21. Marga, F., M, G., Cosgrove, D.J., and Baskin, T. (2005): *Cell wall extension results in the coordinate separation of parallel microfibrils: evidence from scanning electron microscopy and atomic force microscopy*. Plant J. 43: 181-190
22. Burgert, I. and Fratzl, P. (2006): *Mechanics of the expanding cell wall*. In The Expanding Cell (Verbelen, J.P. and Vissenberg, K., Editors, Springer-Verlag, Berlin Heidelberg
23. Somerville, C., Bauer, S., Brininstool, G., Facette, M., Hamann, T., Milne, J., Osborne, E., Paredez, A., Persson, S., Raab, T., Voorwerk, S., and Youngs, H. (2004): *Towards a systems approach to understanding plant cell walls*. Science 306: 2206-2211
24. Thompson, D.S. (2005): *How do cell walls regulate plant growth?* J. Exp. Bot. 56: 2275-2285
25. Cosgrove, D.J. (2000): *Expansive growth of plant cell walls*. Plant Physiol Biochem 28: 109-124
26. Wasteneys, G. and Yang, Z. (2004): *New views on the plant cytoskeleton*. Plant Physiol. 136: 3884-3891
27. Lloyd, C.W. and Chan, J. (2008): *The parallel lives of microtubules and cellulose microfibrils*. Curr. Opin. Plant Biol. 11: 641-646
28. Giddings, T.H. and Staehelin, L.A. (1991): *Microtubule-mediated control of microfibril deposition; a reexamination of the hypothesis*. In The Cytoskeletal Basis of Plant Growth and Form (Lloyd, C.W., Editor. eds.) pp. 85-100, Academic Press, London
29. Sugimoto, K., Himmelpach, R., Williamson, R.E., and Wasteneys, G.O. (2003): *Mutation or drug-dependent microtubule disruption causes radial swelling without altering parallel cellulose microfibril deposition in Arabidopsis root cells*. Plant Cell 15: 1414-1429
30. Whittington, A.T., Vugrek, O., Wei, K.J., Hasenbein, N.G., Sugimoto, K., Rashbrooke, M.C., and Wasteneys, G.O. (2001): *MOR1 is essential for organizing cortical microtubules in plants*. Nature 411: 610-613
31. Sugimoto, K., Williamson, R.E., and Wasteneys, G.O. (2000): *New techniques enable comparative analysis of microtubule orientation, wall texture, and growth rate in intact roots of Arabidopsis*. Plant Physiol. 124: 1493-1506
32. Wiedemeier, A.M.D., Judy-March, J.E., Hocart, C.H., Wasteneys, G.O., Williamson, R.E., and Baskin, T.I. (2002): *Mutant alleles of Arabidopsis RADIALLY SWOLLEN 4 and 7 reduce growth anisotropy without altering the transverse orientation of cortical microtubules of cellulose microfibrils*. Development 129: 4821-4830
33. Paredez, A., Wright, A., and Ehrhardt, D.W. (2006): *Microtubule cortical array organization and plant cell morphogenesis*. Curr. Opin. Plant Biol. 9: 571-578
34. Robert, S., Bichet, A., Grandjean, O., Kierzkowski, D., Satiat-Jeunemaitre, B., Pelletier, S., T., H.M., Höfte, H., and Vernhettes, S. (2005): *An Arabidopsis endo-1,4-beta-D-glucanase involved in cellulose synthesis undergoes regulated intracellular cycling*. Plant Cell 17: 3378-3389
35. Wasteneys, G. (2004): *Progress in understanding the role of microtubules in plant cells*. Curr. Opin. Plant Biol. 7: 651-660
36. Sedbrook, J. and Kaloriti, D. (2008): *Microtubules, MAPs and plant directional cell expansion*. Trends Plant Sci. 13: 303-310
37. Emons, A.M.C. and Mulder, B.M. (1998): *The making of the architecture of the plant cell wall: How cells exploit geometry*. Plant Biol. 95: 7215-7219
38. Emons, A.M.C. and Mulder, B.M. (2000): *How the deposition of cellulose microfibrils builds cell wall architecture*. Trends Plant Sci. 5: 35- 40
39. Mulder, B.M. and Emons, A.M.C. (2001): *A dynamical model for plant cell wall architecture formation*. J. Math. Biol. 42: 261-289

40. Mulder, B.M., Schel, J.H.N., and Emons, A.M.C. (2004): *How the geometrical model for plant cell wall formation enables the production of a random texture*. Cellulose 11: 395-401
41. Geitmann, A. and Ortega, J.K.E. (2009): *Mechanics and modeling of plant cell growth*. Trends Plant Sci 14: in press.
42. Parre, E. and Geitmann, A. (2005): *Pectin and the role of the physical properties of the cell wall in pollen tube growth of Solanum chacoense*. Planta 220: 582-592
43. Panteris, E. and Galatis, B. (2005): *The morphogenesis of lobed plant cells in the mesophyll and epidermis: organization and distinct roles of cortical microtubules and actin filaments*. New Phytologist 167: 721-732
44. Schwab, B., Mathur, J., Saedler, R., Schwarz, H., Frey, B., Scheidegger, C., and Hülskamp, M. (2003): *Regulation of cell expansion by the DISTORTED genes in Arabidopsis thaliana: actin controls the spatial organization of microtubules*. Molecular and General Genomics 269: 350-360
45. Shaw, S.L., Dumais, J., and Long, S.R. (2000): *Cell surface expansion in polarly growing root hairs of Medicago truncatula*. Plant Physiol. 124: 959-969
46. Bibikova, T.N. and Gilroy, S. (2003): *Root hair development*. Journal of Plant Growth Regulation 21: 383-415
47. Geitmann, A. and Steer, M.W. (2006): *The architecture and properties of the pollen tube cell wall*. In The pollen tube: a cellular and molecular perspective, Plant Cell Monographs (Malhó, R., Editor. eds.). pp. 177-200, Springer Verlag, Berlin Heidelberg
48. Parre, E. and Geitmann, A. (2005): *More than a leak sealant - the physical properties of callose in pollen tubes*. Plant Physiol. 137: 274-286
49. Geitmann, A. and Dumais, J. (2009): *Not-so-tip-growth*. Plant Signaling & Behavior 4: 136-138
50. Da Riva Ricci, D. and Kendrick, B. (1972): *Computer modelling of hyphal tip growth in fungi*. Can. J. Bot. 50: 2455-2462
51. Denet, B. (1996): *Numerical simulation of cellular tip growth*. Phys. Rev. 53: 986-992
52. Dumais, J., Long, S.R., and Shaw, S.L. (2004): *The mechanics of surface expansion anisotropy in Medicago truncatula root hairs*. Plant Physiol. 136: 3266-3275
53. Dumais, J., Shaw, S.L., Steele, C.R., Long, S.R., and Ray, P.M. (2006): *An anisotropic-viscoplastic model of plant cell morphogenesis by tip growth*. Int. J. Dev. Biol. 50: 209-222
54. Goriely, A. and Tabor, M. (2003): *Biomechanical models of hyphal growth in actinomycetes*. J. Theor. Biol. 222: 211-218
55. Goriely, A. and Tabor, M. (2003): *Self-similar tip growth in filamentary organisms*. Phys. Rev. Lett. 90: 1-4
56. Goriely, A. and Tabor, M. (2008): *Mathematical modeling of hyphal tip growth*. Fungal Biology Reviews 22: 77-83
57. Geitmann, A. and Parre, E. (2004): *The local cytomechanical properties of growing pollen tubes correspond to the axial distribution of structural cellular elements*. Sex. Plant Reprod. 17: 9-16
58. Bolduc, J.F., Lewis, L., Aubin, C.E., and Geitmann, A. (2006): *Finite-element analysis of geometrical factors in micro-indentation of pollen tubes*. Biomechanics and Modeling in Mechanobiology 5: 227-236
59. Chebli, Y. and Geitmann, A. (2007): *Mechanical principles governing pollen tube growth*. Functional Plant Science and Biotechnology 1: 232-245
60. Bibikova, T.N., Jacob, T., Dahse, I., and Gilroy, S. (1998): *Localized changes in apoplastic and cytoplasmic pH are associated with root hair development in Arabidopsis thaliana*. Development 125: 2925-2934
61. Vissenberg, K., Fry, S.C., and Verbelen, J.P. (2001): *Root hair initiation is coupled to a highly localized increase of xyloglucan endotransglycosylase action in Arabidopsis roots*. Plant Physiol. 127: 1125-1135
62. Baluška, F., Salaj, J., Mathur, J., Braun, M., Jasper, F., Šamaj, J., Chua, N.H., Barlow, P.W., and Volkmann, D. (2000): *Root hair formation: F-actin-dependant tip growth is initiated by local assembly of profilin-supported F-actin meshworks accumulated within expansin-enriched bulges*. Dev. Biol. 227: 618-632
63. Cho, H.-T. and Cosgrove, D.J. (2002): *Regulation of root hair initiation and expansin gene expression in Arabidopsis*. Plant Cell 14: 3237-3253
64. Hasegawa, Y., Nakamura, S., Kakizoe, S., Sato, M., and Nakamura, N. (1998): *Immunocytochemical and chemical analyses of Golgi vesicles isolated from the germinated pollen of Camellia japonica*. Journal of Plant Research 111: 421-429
65. Levy, S. and Staehelin, L.A. (1992): *Synthesis, assembly and function of plant cell wall macromolecules*. Curr. Opin. Cell Biol. 4: 856-862
66. Gibbon, B.C., Kovar, D.R., and Staiger, C.J. (1999): *Latrunculin B has different effects on pollen germination and tube growth*. Plant Cell 11: 2349-2363
67. Ketelaar, T., De Ruijter, N.C., and Emons, A.M. (2003): *Unstable F-actin specifies the area and microtubule direction of cell expansion in Arabidopsis root hairs*. Plant Cell 15: 285-292

68. Čiamporová, M., Dekánková, K., Hanáčková, Z., Peters, P., Ovečka, M., and Baluška, F. (2003): *Structural aspects of bulge formation during root hair initiation*. Plant and Soil 255: 1-7
69. Mathur, J. (2004): *Cell shape development in plants*. Trends Plant Sci. 9: 583-590
70. Alessa, L. and Kropf, D.J. (1999): *F-actin marks the rhizoid pole in living *Pelvetia compressa* zygotes*. Development 126: 201-209
71. Hable, W.E., Miller, N.R., and Kropf, D.J. (2003): *Polarity establishment requires dynamic actin in fucoid zygotes*. Protoplasma 221: 193–204
72. Torralba, S. and Heath, I.B. (2001): *Cytoskeletal and Ca²⁺ regulation of hyphal tip growth and initiation*. Curr. Top. Dev. Biol. 51: 135-187
73. Harris, S.D. (2008): *Branching of fungal hyphae: regulation, mechanisms and comparison with other branching systems*. Mycologia 100: 823–832
74. Cai, G. and Cresti, M. (2009): *Organelle motility in the pollen tube: a tale of 20 years*. J. Exp. Bot. 60: 495-508
75. Lu, L., Lee, Y.R., Pan, R., Maloof, J.N., and Liu, B. (2005): *An internal motor kinesin is associated with the Golgi apparatus and plays a role in trichome morphogenesis in Arabidopsis*. Mol. Biol. Cell 16: 811-823
76. Ishida, T., Kurata, T., Okada, K., and Wada, T. (2008): *A genetic regulatory network in the development of trichomes and root hairs*. Annual Review of Plant Biology 59: 365-386
77. Szymanski, D.B., Marks, M.D., and Wick, S.M. (1999): *Organized F-actin is essential for normal trichome morphogenesis in Arabidopsis*. Plant Cell 11: 2331–2347
78. Emons, A.M.C. and Derksen, J. (1986): *Microfibrils, microtubules, and microfilaments of the trichoblast of *Equisetum hyemale**. Acta Botanica Neerlandica 35: 311-320
79. Bibikova, T.N., Blancaflor, E.B., and Gilroy, S. (1999): *Microtubules regulate tip growth and orientation in root hairs of Arabidopsis thaliana*. Plant J. 17: 657-665
80. Braun, M., Baluska, F., Von Witsch, M., and Menzel, D. (1999): *Redistribution of actin, profilin and phosphatidylinositol-4,5-bisphosphate in growing and maturing root hairs*. Planta 209: 435- 443
81. Müller, D.D., De Ruijter, N., Bisseling, T., and Emons, A.M.C. (1999): *The role of actin in root hair morphogenesis: Studies with lipochito-oligosaccharide as a growth stimulator and cytochalasin as an actin perturbing drug*. Plant J. 17: 141-154
82. Bisgrove, S.R. and Kropf, D.L. (2001): *Cell wall deposition during morphogenesis in fucoid algae*. Planta 212: 648-658
83. Ringli, C., Baumberger, N., Diet, A., Frey, B., and Keller, B. (2002): *ACTIN2 is essential for bulge site selection and tip growth during root hair development of Arabidopsis*. Plant Physiol. 129: 1464-1472
84. Nishimura, T., Yokota, E., Wada, T., Shimmen, T., and Okada, K. (2003): *An Arabidopsis ACT2 dominant-negative mutation, which disturbs F-actin polymerization, reveals its distinctive function in root development*. Plant Cell Physiol. 44: 1131-1140
85. Lancelle, S.A., Cresti, M., and Hepler, P.K. (1997): *Growth inhibition and recovery in freeze-substituted *Lilium longiflorum* pollen tubes: structural effects of caffeine*. Protoplasma 196: 21-33
86. Zerkour, R., Kroeger, J.H., and Geitmann, A. *Micro-indentation reveals spatially confined dynamic changes in mechanical cell wall properties during cellular morphogenesis in pollen tubes*.
87. Gierz, G. and Bartnicki-Garcia, S. (2001): *A three-dimensional model of fungal morphogenesis based on the vesicle supply center concept*. J. Theor. Biol. 208: 151-164
88. Tindemans, S.H., Kern, N., and Mulder, B.M. (2006): *The diffusive vesicle supply center model for tip growth in fungal hyphae*. J. Theor. Biol. 238: 937-948
89. Bove, J., Vaillancourt, B., Kroeger, J., Hepler, P.K., Wiseman, P.W., and Geitmann, A. (2008): *Magnitude and direction of vesicle dynamics in growing pollen tubes using spatiotemporal image correlation spectroscopy (STICS)*. Plant Physiol. 147: 1646-1658
90. Zonia, L. and Munnik, T. (2008): *Vesicle trafficking dynamics and visualization of zones of exocytosis and endocytosis in tobacco pollen tubes*. J. Exp. Bot. 59: 861-873

Towards nanomechanical characterization of developing wood cell walls at different maturation steps

Karl Bytebier¹, Olivier Arnould^{1}, Richard Arinero²,
Bruno Clair¹ and Tancrede Alméras¹*

¹ *Laboratoire de Mécanique et Génie Civil, Université Montpellier 2/CNRS UMR5508
cc 048 – Place Eugène Bataillon, 34095 Montpellier, France;*

² *Institut d'Electronique du Sud, Université Montpellier 2/CNRS UMR5214
cc 082 – Place Eugène Bataillon, 34095 Montpellier, France*

Abstract

Improved knowledge on the way cell wall stiffness changes during the maturation process is of great importance to feed and help theoretical modelling on growth stress generation in trees. This paper outlines one of the most promising techniques to measure viscoelastic properties within the different layers of the developing cell wall based on the so-called Resonant Contact mode using an Atomic Force Microscope. This mode and the required calibrations are briefly described here and an application on chestnut mature tension wood is shown. It demonstrates the ability of the technique for drawing qualitative viscoelastic maps within a cell wall layer. Limitations and necessary development of this method to do quantitative measurements are briefly discussed.

Introduction

The elastic properties of wood originate mainly in those of its secondary cell wall layers. Secondary walls are formed during cell differentiation by addition of constitutive material (*i.e.*, cellulose, hemicellulose and lignin) extruded from the plasma membrane and progressively incorporated into the wall. The mechanical properties of the wall depend on the amount of constitutive polymers, their spatial organisation, and also on the way they are bound to each other during cell development. To date, very little is known about how the mechanical properties of a wall layer progressively change during the early stages of its formation. Improved knowledge of the timing of wall stiffening may be useful to understand its assembly process. More specifically, it is necessary for understanding and modelling the apparition of maturation stress in wood [1-5], because wall stiffness determines the amount of stress generated by an impeded dimensional change of its constituents. In this context, our goal is to measure mechanical properties within the different cell wall layers and their evolution during wall formation, in order to understand, for example: i) if the stiffening of the secondary layers occurs immediately after their deposition; ii) if there is a time lag between wall formation and stiffening; or iii) if the whole wall stiffens simultaneously at the end of its formation. In an other words, is there a gradient in mechanical properties within the cell wall during its formation? How does this gradient change during the time course of the maturation process? This can be assessed by mapping the viscoelastic properties of cell walls taken along a differentiation sequence, from the cambium to the mature wood.

Mechanical property measurements at the cell wall level can be estimated using numerical computations of the properties of its constituents or are more usually carried out experimentally on chemical compounds extracted from cell walls and on mechanically or chemically isolated fibres [6]. Other measurements consisted in “classical” tensile tests on the scale of the tree rings with specific strain fields’ measurements. These techniques require a reverse identification of the local stress fields from the overall loading to yield the mechanical properties of the material. In the present case, it is necessary to have access to the *in situ* mechanical properties within cell walls with as few

* corresponding author : arnould@lmgc.univ-montp2.fr

modifications as possible. Moreover, because of the weak nature of developing cells it is almost impossible to work on extracted fibres. Thus, one of the most promising techniques for this work is nanoindentation [7]. It has already been applied to estimate average elastic modulus of some wall layers of mature cells [8-10] or to compare elastic properties of S₂ layers during the lignification process with those of mature cells [11]. However, this technique requires the layer thickness to be greater than the indent size [12], *i.e.*, typically greater than some micrometres. As the width of the cell wall layers varies from ~0.1 µm (primary wall) to less than 10 µm (mature S₂ or G layer), interpretation of measurements obtained by nanoindentation in the presence of a properties gradient or within a thin layer is not straightforward due to boundary effects [13]. Mechanical measurements done by Atomic Force Microscopy (AFM), using force-distance curves, force modulation microscopy, etc., require similar approaches as in nanoindentation but with a spatial resolution of the order of some tens of nanometre or less [14]. It should then be well adapted for measuring property variations within a developing cell wall layer. In our case, we used a specific mode of an AFM, sometimes called Resonant Contact-AFM (RC-AFM) that has already been applied on wood [15]. It has been more recently improved with a mathematical processing that allows us to perform a quite fast mapping of mean viscoelastic properties [16]. The present article is restricted to the case of mature cells of chestnut tension wood and mainly focused on demonstrating the ability of this technique to obtain local semi-quantitative measurement and qualitative mapping of the viscoelastic properties at the ultrastructural level.

Material and methods

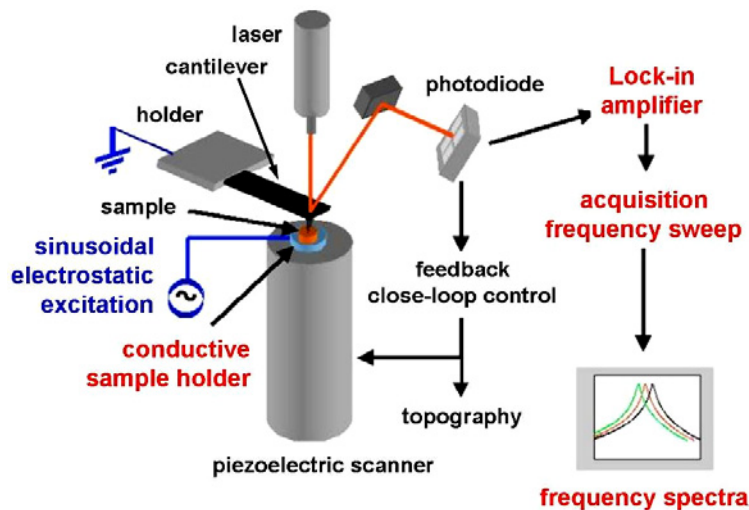


Fig. 1 Schematic view of the basic principle of an AFM and its modification for doing Resonant Contact measurements with the use of a sinusoidal electrostatic excitation of the cantilever and a “lock-in” amplifier.

The basic principle of an AFM relies on measuring the interaction(s) of a physical probe, *i.e.*, a tip, with a sample surface (Fig. 1). This interaction induces the bending of a very soft cantilever (*i.e.*, stiffness usually between 0.01 and 100N/m) at the end of which the tip is. The angular deflection of this cantilever is measured through the reflection of a laser on its back onto a position-sensitive photodetector. Relative in-plane (x , y) and out of plane (z) displacement of the sample *vs.* the probe is achieved through piezoelectric material actuators with a resolution better than 0.1 nm. There is a large variety of utilisation of AFM and way to measure the sample surface viscoelastic properties [14]. In the so-called contact mode, the tip remains in contact with the sample and the cantilever deflection is proportional to the applied contact force. As the tip scans the surface, a feedback loop keeps the contact force constant by adjusting the z -displacement of the actuator that is recorded and corresponds mainly to the surface topography. In that mode, since the tip touches the sample, it is sensitive to the sample viscoelastic properties. In this work, a specific operating contact mode, sometime called RC-AFM, was used [14].

It consists in applying a small periodic force to the cantilever by means of an electrostatic potential between the tip and the sample holder (*Fig. 1*). When the excitation frequency is close to the natural frequency of the cantilever, in contact with the sample surface through its tip, a resonance occurs. Basically, the measurement is based on performing a frequency sweep in a given point on the surface and recording the cantilever vibrations through the photodetector. According to several authors [14, 17], the resonance frequency, f_0 , and the quality factor, Q , of the obtained frequency spectrum can be related respectively to the real, k' , and imaginary, k'' , parts of the normal contact stiffness *at the resonance frequency*. It is then necessary to use the appropriated contact model [14] to derive the elastic contact modulus M of the tested volume of material from k' . The tangent of the loss angle, $\tan \delta = k''/k'$, which characterizes the viscous dissipation of the material in the tested volume (if all other dissipations like tip sliding are negligible) is, in our case, close to Q^{-1} for value of the quality factor higher than unity [16] and is not dependant on the contact model. The last step, as in all nanoindentation measurements, is to identify the material viscoelastic parameter(s). This is not so obvious in the case of an anisotropic fibrous material such as the wood cell wall layers [12, 18]. This aspect will not be presented in this paper. Finally, without any significant modification in the AFM device, this method theoretically offers nanometre spatial resolution, as the mean and vibrating applied forces can be tuned as low as possible, and reduced lateral force effect due to the cantilever tilt angle. Moreover, by scanning the surface at a constant mean force and excitation frequency, close to the resonance of the different materials composing the area of interest, it is possible to do a reasonably fast mapping of the resonance frequency and quality factor whilst acquiring the sample topography without doing a frequency sweep at each point. This imaging technique is based on the cantilever vibration parameters (*i.e.*, the real and imaginary parts) that are directly linked to the parameters of the resonant spectrum of Lorentzian shape [16].

In our case, a commercial AFM (Veeco Enviroscope) is used and its photodetector signal analysed by a lock-in amplifier (EG & G model 5302) to extract the real and the imaginary part of the cantilever vibration generated by the electrostatic excitation through an external generator (FLUKE PM5138A). In order to achieve the frequency sweep and resonance spectra acquisitions, an automated measurement was realized using Labview software and GPIB National Instruments interface. Our experiments show that the use of a theoretical model of cantilever vibration is not so obvious. This is why we decided here to use a series of “reference” materials like more or less stiff polymers (Polyurethane PU, Polyester PE, PMMA) and stiffer and less viscous materials like glass. Frequency spectra are carried out on them and compared to the theoretical contact stiffness. This stiffness is computed using a contact model (*i.e.*, Hertz) and macroscopic elastic modulus obtained at different frequencies (DMA, ultrasonic wave propagation, etc.). The strongest assumption here is that these reference samples are assumed to be homogeneous even at the submicrometre scale and that properties at this scale are equal to those at the macroscopic level.

In order to obtain as quantitative as possible viscoelastic properties, it is moreover necessary to calibrate the cantilever stiffness (or spring constant) and the shape (*i.e.*, mean radius of curvature) of its tip apex. As the optimal cantilever stiffness is between some N/m to some tens of N/m and after comparing some classical calibration techniques [19], we decided to do it by using calibrated reference cantilevers (CLFC-NOBO Veeco Probes). This calibration protocol relies on measuring the deflection of the cantilever when applied on a known spring constant [20]. For the tip apex shape, we compared different calibration gratings and SEM images. The main problem arising during the experiment is that, as the tip is always in contact with the surface during imaging, more or less wear occurs and can lead to a drastic change in the tip apex shape. It is then necessary to have a fast way to characterise the shape between two measurements. We have finally chosen a calibration grating (NT-MDT TGT-01) that consists in an array of very sharp spikes with a radius lower than about 8 nm. It allows for some kind of (fast) reverse imaging of the actual apex shape with enough accuracy in the present case. The (average) technical specifications of the cantilever used for the experiments (Nanoworld Arrow FMR) are: thickness 3 μm , length 240 μm , width 35 μm , stiffness 2.8 N/m, free natural frequency 75 kHz. The average tip radius is estimated to be around 55 nm during the measurements. The mean applied force is estimated to be around 180 nN and the sinusoidal electrostatic excitation is applied with amplitude of 10 V.

In order to investigate the RC-AFM imaging technique in the case of wood, chestnut (*Castanea sativa*) mature wood containing normal as well as tension wood was used. Tension wood is

characterized, in the case of chestnut, by the presence of a so-called G layer with a microfibril angle close to zero and a thin S₂ layer. All mechanical measurement based on indentation requires samples with a surface as flat as possible compared to the contact radius in order to be able to estimate accurately the contact area. Moreover, in the case of AFM, the tip is very brittle and surface roughness (or holes) must be as low as possible to reduce breakage risks. Wood samples were then embedded in a resin in order to fill the lumen and to decrease the surface roughness by reducing deformation during the cutting process. Sticks (1 cm in longitudinal direction, 1 × 1 mm² in transverse section) were obtained by splitting to guarantee a good axial direction. They were then cut manually with a razor blade to produce a clear transverse surface and to obtain cubes of about 1 mm³ in size. Samples were dehydrated with an ethanol series (50%, 75%, 90% and 100%) under vacuum and embedded in increasing ratio of LR White medium resin. The whole resin block with the sample was then machined to reduce its cross section. A rotary microtome (Leica RM2235) was then used first with a glass knife to remove the first 100 μm of material containing the border effects that occurs during initial sample preparation [21]. Then a diamond knife (Diatom Histo) was used to cut a series of very thin section (about 500 nm in thickness) at the lowest cutting speed to minimize compression during the cutting process. The resulting topography of the remaining wood block sample surface is obtained during the mechanical measurement in RC-AFM mode and shown in Fig. 2. Some steps in the topography due to difference in the stiffness of the different layers are observed. However, the typical Root-Mean-Square (RMS) roughness in the thicker, G and S₂, layers is usually around 10 nm. Note that the transverse sections are not used for the mechanical measurements as they are too thin and lead to artefacts.

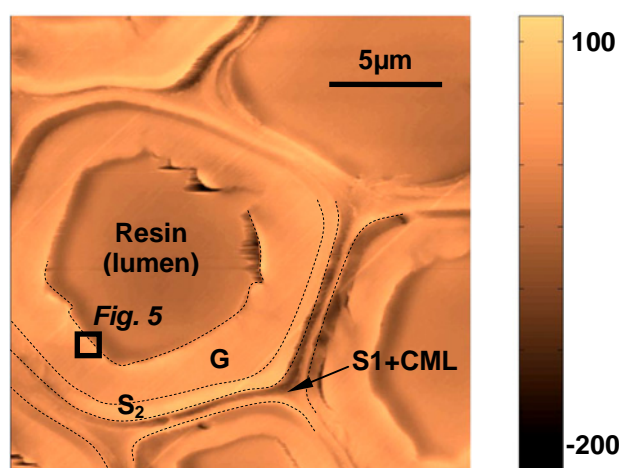


Fig. 2 AFM topography (256 × 256 points) in contact mode of the chestnut tension wood cross section. Identification of the different cell wall layers and of the embedding LR White resin in the cell lumina. The box corresponds to the area of interest in Fig. 5. The scale bar corresponds to the height in nm.

Results and discussion

The RC-AFM experiments are done in two steps. The first step is to engage the tip in contact with the sample and to carry out frequency spectra at different points. In Fig. 3, the amplitude of the output signal of the photodetector is plotted as a function of the electrostatic excitation frequency. The resonance frequency f_0 and the quality factor Q of the frequency spectrum in each layer are then deduced. The indentation modulus in the longitudinal direction M_L is then computed using the different calibrations done (as depicted in the previous chapter). The results are given in Table 1. They correspond to the mean values obtained from at least 3 spectra done in 3 different positions within the same layer. The uncertainty in this table only represents the variation in the value computed from one point to another. It doesn't take into account all the uncertainty coming from the different calibration steps and measurements accuracy that can be much higher and must be estimated soon. These results are consistent with those obtain previously on oak [15] and other S₂ cell wall layer [8-10]. Moreover, using an elastic anisotropic indentation model [18] and a multi-scale cell wall model [3] with the estimated elastic properties of the cell wall constituents given in [6] and a given composition of the S₂ or G layer (*i.e.*, 30% crystalline cellulose and 70% amorphous cellulose and matrix material), leads to

an indentation modulus around 16 GPa for an MFA of 0°. The results obtained by RC-AFM seem quite good given all the assumption made on the composition of the layer, the properties of its constituent and the fact that the MFA of the S₂ layer is not known. The fact that they are lower may be explained by the fibrous nature of the material that could lead to different contact behaviour even when anisotropy is taken into account. Moreover, this fibrous structure leads to nanometre topography during the cutting process [22] (Fig. 5a). This nano-roughness can lead to an underestimation of the real contact area using a classical contact model that assumes a perfectly flat surface, and yields an estimated indentation modulus lower than the real one. Moreover, the indentation model used is developed for pyramidal (deep) indentation and not for a sphere-plane contact. Finally, measurements in progress show that the accuracy and sensitivity of the RC-AFM to the elastic modulus can be improved by using a stiffer cantilever.

The last step of the measurement is to do mapping at a given excitation frequency f_{im} . To be able to compute the resonance frequency and quality factor from the real and imaginary parts of the cantilever vibration, f_{im} must be chosen as close as possible to the resonance frequency on each layer. In the present case, as we want to demonstrate the ability of this technique to sense differences in mechanical properties mainly in the S₂ and G layers, the imaging frequency is chosen close to that obtained on these layers (Fig. 3). As a result, the mechanical properties of the embedding resin and, to a less extent, that of the CML will be poorly estimated.

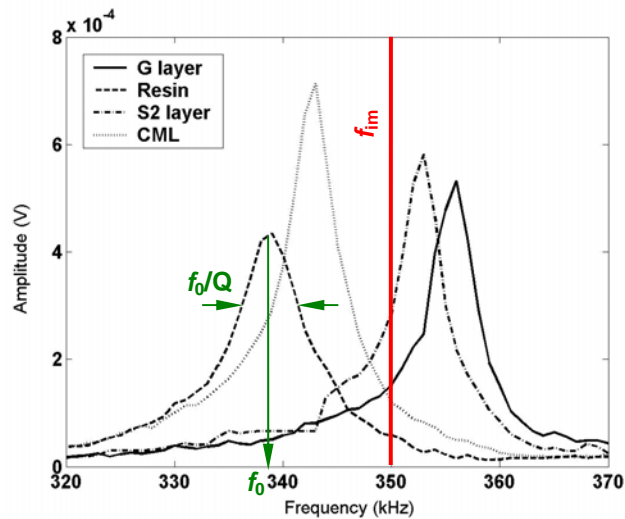


Fig. 3 Amplitude frequency spectrum for the different layers. Definition of the resonance frequency f_0 and quality factor Q in the case of the embedding resin. Choice of the imaging frequency f_{im} for Figs. 4 and 5.

Table 1 Indentation modulus M_L and reverse of the quality factor Q^{-1} ($\sim \tan \delta$ at the resonance frequency) in the longitudinal direction for the different layers of the cell wall computed from the spectra of Fig. 3. Specified uncertainties only correspond to the variations between 3 measurement locations.

	M_L (GPa)	Q^{-1}
Resin	6±1.5	0.013±0.002
CML	6.5±0.5	0.009±0.003
S ₂	12±0.5	0.006±0.003
G	14±1.5	0.009±0.003

The resulting indentation modulus and reverse of the quality factor maps are given in Fig. 4 for an imaging frequency of 350 kHz. In Fig. 4a, the S₂ and G layers clearly appear to be the stiffest ones whereas the S₁ and CML layers are the softest as in Table 1. Layers appear far more clearly than in the topography image of Fig. 2. Variations in the indentation modulus of the S₂ layer are observed. These variations could be due to natural gradient properties within the layer (e.g., tangential vs. radial wall), or to a slightly oblique cross section combined with the MFA that induce a different type of loading with respect to the microfibrils axis: the highest frequencies would then mean a loading closer to the microfibril axis than the lowest values. In the latter case, contribution of the matrix in the measured

frequency is higher. Furthermore, G layers sometime appear to be composed of two slightly different stiffness parts (see the two arrows in Fig. 4). We don't know if it's a real property variation in the layer or if it's due to the embedding protocol as resin penetration within the cell wall may change the measured viscoelastic properties. The evaluation of this resin penetration is in progress by using Raman spectroscopy [23] and first results tend to confirm such a situation in the inner layer. However, it can be inferred that resin presence in the gel of the G layer should increase the elastic modulus. Lastly, it can be seen that topography (*e.g.*, scratches due to the cutting and step height to a less extent, see Fig. 2) has an effect on the measurement such as roughness. Whatever the real origin of all these observations, it demonstrates the ability of the RC-AFM to highlight elastic properties variations within a single cell wall layer.

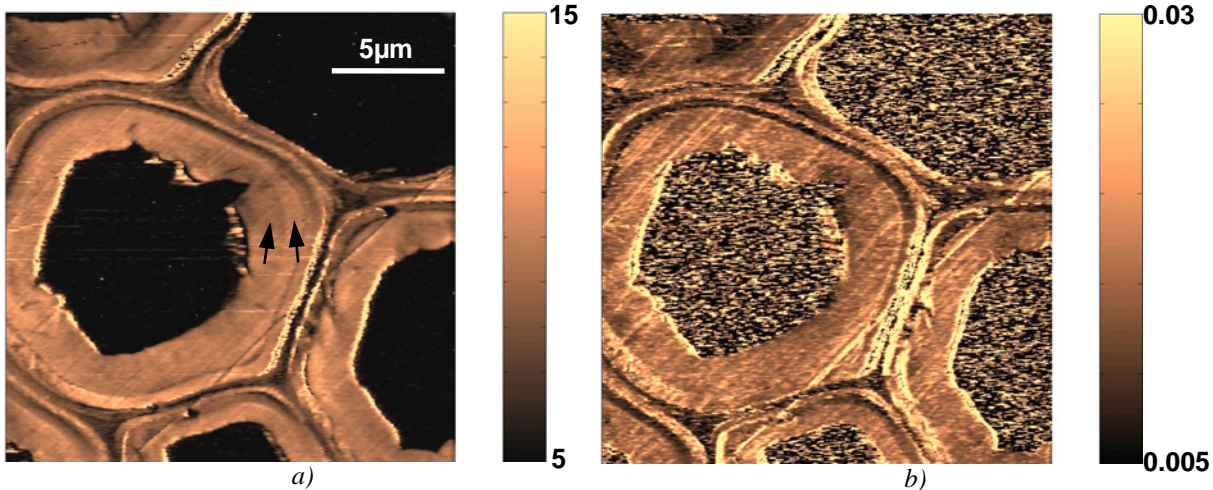


Fig. 4 Qualitative mapping at 350 kHz in the same area as in Fig. 2: a) indentation modulus M_L – scale bar in GPa; b) reverse of the quality factor Q^{-1} ($\sim \tan \delta$ at the resonance frequency).

For the viscous parameter, $\tan \delta$ in Fig. 4b, results are not so clear as the CML seems to be surprisingly less viscous than the S_2 layer whereas the S_1 is more. This contradicts the values of Q^{-1} obtained in Table 1 and it seems to be mostly due to the choice in the imaging frequency that is too far from the resonance of the CML (*e.g.*, see the noise in the resin part). It is interesting to note that, on average, the G layer is more viscous than the S_2 as in Table 1. The assumption we made above on the origin of the elastic variations in the S_2 layer due to a slightly oblique cross section is not really confirmed here. If the indentation modulus increased because the microfibril axis is closer to the contact normal, the mechanical contribution of the matrix is lower and then the dissipation too. Again, the effect of the fibrous nature of the layers, and the resulting cutting nano-roughness, on the contact properties are questioned. Note that topography has a stronger effect in that case. Lastly, one can wonder what is the physical meaning (in the frame of tree biomechanics or usual use of wood as a material) of a viscous parameter obtained at a so high frequency. More work has to be done on this aspect of the measurements.

Fig. 5 shows closer views of the G layer topography, indentation modulus and dissipation in the same experimental conditions as in Fig. 4. Similar conclusions can be drawn and the ability of the RC-AFM mode to highlight the layer structure at this scale as observed on Fig. 5b when compared to Fig. 5a. In the latter case, a slight topography linked with the cutting scratches can be seen whereas, in the former, structures with typical size around 50 to 100 nm appear. They could be ascribed to microfibrils bundles whose size is typically around 20 nm in softwoods [22] and hardwoods [24]. The fact they appear larger here can be mainly due to the classical tip dilation effect: the apparent maximum size of the microfibrils bundles is roughly equal to its real size plus the tip radius. This leads to an apparent size around 75 nm. The effect of the nano-roughness is clearly highlighted here: the indentation modulus is higher when on the top of a roughness ridge (lower contact area than expected) and lower in the groove between two ridges (higher contact area). The difference in the elastic moduli between the microfibrils bundles and the matrix could have an effect here particularly in the ridge. But

considering the quite large tip radius size and the space available between two bundles [22], it's not likely that the tip is in contact with the matrix in the present measurements.

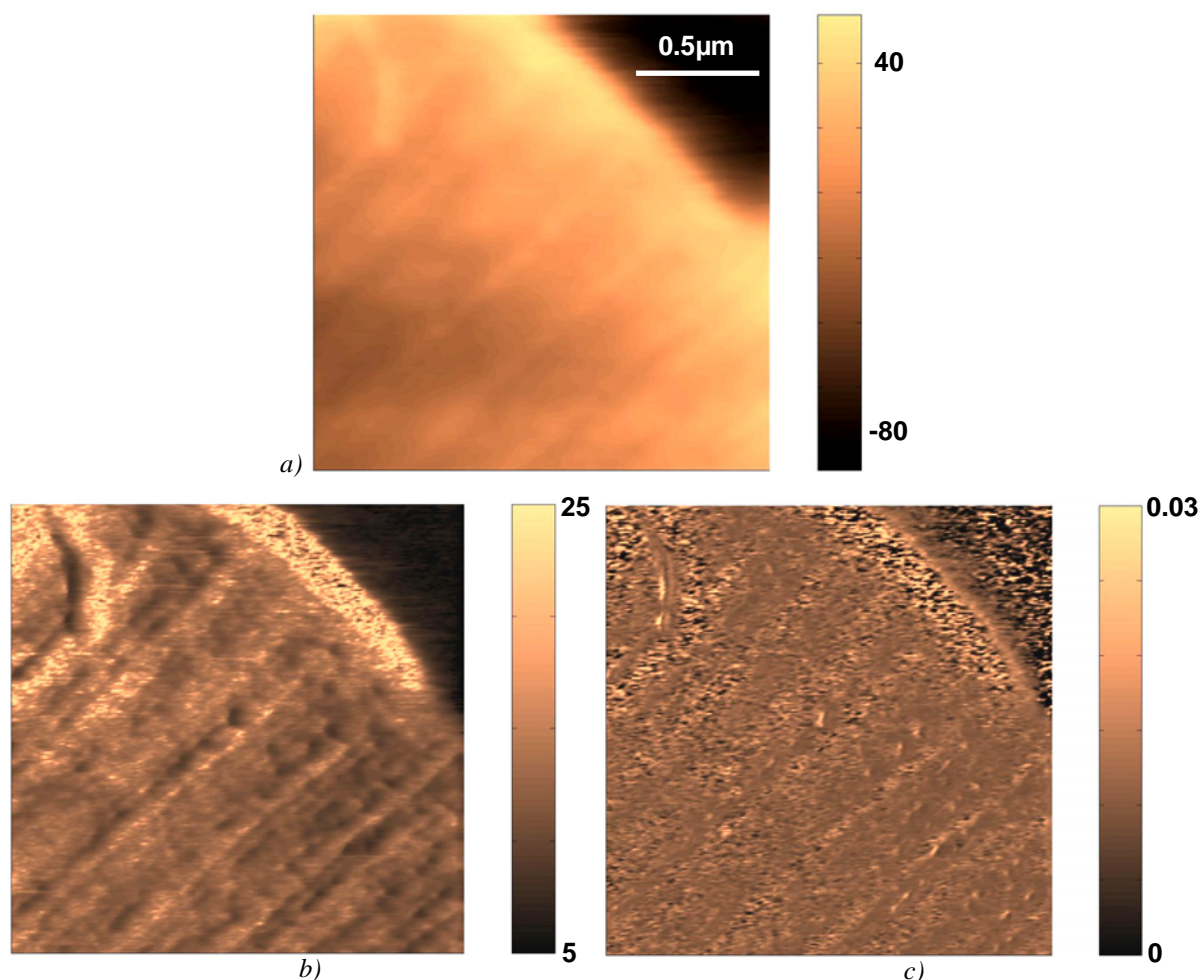


Fig. 5 Measurements done on a smaller scale as depicted by the box in Fig. 2. a) AFM topography (256×256 points) in contact mode. Qualitative mapping at 350 kHz of b) indentation modulus M_L – scale bar in GPa; c) reverse of the quality factor Q^{-1} ($\sim \tan \delta$ at the resonance frequency).

Conclusion

This study shows that RC-AFM allows for semi-quantitative estimation of stiffness in a given point and qualitative estimation of its variations at a submicrometre scale. Studies are in progress on improving its calibration and the experimental conditions to make it more quantitative for the estimation of viscoelastic properties. Concerning the estimates of viscous properties of the material, some questions remain on their significance during these kinds of measurements. This technique should be able to provide data on the stiffness gradient within the cell wall and its evolution during the maturation process. In the case of developing cells, the sample preparation is not so obvious as for mature cells. Resin penetration can be stronger in that case and have a higher effect on the measurement as the cell wall is softer. First samples of developing cells taken along a differentiation sequence, from the cambium to the mature wood, are currently prepared using the above embedding technique. Further development with less invasive protocol must then be conducted.

Acknowledgements

Financial support by the CNRS (French National Centre for Scientific Research) is gratefully acknowledged.

References

1. Thibaut, B., Gril, J. and Fournier, M. (2001): *Mechanics of wood and trees: some new highlights for an old story*. Comptes Rendus de l'Académie des Sciences Paris, Série II b. 329: 701-716.
2. Yamamoto, H., Kojima, Y., Okuyama, T., Abasolo, W.P. and Gril, J. (2002): *Origin of the biomechanical properties of wood related to the fine structure of the multi-layered cell wall*. Transactions of the ASME. 124: 432-440.
3. Alméras, T., Gril, J. and Yamamoto, H. (2005): *Modeling anisotropic maturation strains in wood in relation to fibre boundary conditions, microstructure and maturation kinetics*. Holzforschung. 59: 347-353.
4. Coutand, C., Fournier, M. and Moulia, B. (2007): *The gravitropic response of poplar trunks: Key roles of prestressed wood Regulation and the relative kinetics of cambial growth versus wood maturation*. Plant Physiology. 144: 1166-1180.
5. Goswami, L., Dunlop, J.W.C., Jungnickl, K., Eder, M., Gierlinger, N., Coutand, C., Jeronimidis, G., Fratzl, P. and Burgert, I. (2008): *Stress generation in the tension wood of poplar is based on the lateral swelling power of the G-layer*. Plant Journal. 56: 531-538.
6. Salmén, L. (2004): *Micromechanical understanding of the cell-wall structure*. Comptes Rendus Biologies. 327: 873-880.
7. Moon, R.J., Frihart, C.R. and Wegner, T. (2006): *Nanotechnology applications in the forest products industry*. Forest Products Journal. 56: 1-10.
8. Wimmer, R., Lucas, B.N., Tsui, T.Y. and Oliver, W.C. (1997): *Longitudinal hardness and Young's modulus of spruce tracheid secondary walls using nanoindentation technique*. Wood Science and Technology. 31: 131-141.
9. Gindl, W., Gupta, H.S., Schöberl, T., Lichtenegger, H.C. and Fratzl, P. (2004): *Mechanical properties of spruce wood cell walls by nanoindentation*. Applied Physics A: Materials Science & Processing. 79(8):2069-2073.
10. Tze, W.T.Y., Wang, S., Rials, T.G., Pharr, G.M. and Kelley, S.S. (2007): *Nanoindentation of wood cell walls: Continuous stiffness and hardness measurements*. Composites: Part A. 38: 945-953.
11. Gindl, W., Gupta, H.S. and Grünwald, C. (2002): *Lignification of spruce tracheid secondary cell walls related to longitudinal hardness and modulus of elasticity using nano-indentation*. Canadian Journal of Botany. 80: 1029-1033.
12. Gindl, W. and Schöberl, T. (2004): *The significance of the elastic modulus of wood cell walls obtained from nanoindentation measurements*. Composites: Part A. 35: 1345-1349.
13. Jakes, J.E., Frihart, C.R., Beecher, J.F., Moon, R.J., Resto, P.J., Melgarejo, Z.H., Suarez, O.M., Baumgart, H., Elmustafa, A.A and Stone, D.S. (2009): *Nanoindentation near the edges*. Journal of Materials Research. 24(3): 1016-1031.
14. Nysten, B. (2007): *Nanomechanics with the Atomic Force Microscope: Polymer surfaces, interfaces and nanomaterials*. Associate Professor Thesis, Université Catholique de Louvain, Belgium, 228p.
15. Clair, B., Arinero, R., Lévêque, G., Ramonda, M. and Thibaut, B. (2003): *Imaging the mechanical properties of wood cell wall layers by atomic force modulation microscopy*. IAWA Journal. 24: 223-230.
16. Arinero, R., Lévêque, G., Girard, P. and Ferrandis, J.Y. (2007): *Image processing for resonance frequency mapping in atomic force microscopy*. Review of Scientific Instruments. 78: 6p.
17. Arinero, R. and Lévêque, G. (2003): *Vibration of the cantilever in Force Modulation Microscopy analysis by a finite element model*. Review of Scientific Instruments. 74: 104-111.
18. Delafargue, A. and Ulm, F.J. (2004): *Explicit approximations of the indentation modulus of elastically orthotropic solids for conical indenters*. International Journal of Solids and Structures. 41: 7351-7360.
19. Ohler, B. (2007): *Practical advice on the determination of cantilever spring constants*. Veeco Application Note #94. <http://www.veeco.com/library>.
20. Torii, A., Sasaki, M., Hane, K. and Okuma, S. (1996): *A method for determining the spring constant of cantilevers for atomic force microscopy*. Measurement Science and Technology. 7: 179-184.
21. Clair, B., Gril, J., Baba, K., Thibaut, B. and Sugiyama, J. (2005): *Precautions for the structural analysis of the gelatinous layer in tension wood*. IAWA Journal. 26(2): 189-195.
22. Falhén, J. and Salmén, L. (2005): *Ultrastructural changes in a holocellulose pulp revealed by enzymes, thermoporosimetry and atomic force microscopy*. Holzforschung. 59: 589-597.
23. Gierlinger, N., Hansmann, C., Röder, T., Sixta, H., Gindl, W. and Wimmer, R. (2005): *Comparison of UV and confocal Raman microscopy to measure the melamine-formaldehyde resin content within cell walls of impregnated spruce wood*. Holzforschung. 59: 210-213.
24. Ruelle, J., Yoshida, M., Clair, B. and Thibaut, B. (2007): *Peculiar tension wood structure in Laetia procera (Poepp.) Eichl. (Flacourtiaceae)*. Trees. 21: 345-355.

Stress of cellulose network in tension wood is induced shortly after cellulose deposition

B. Clair¹, T. Alméras¹, G. Pilate², D. Jullien¹, J. Sugiyama³, C. Riekel⁴

¹CNRS, University of Montpellier, France; ²INRA Orléans, France;
³Kyoto university, Japan, ⁴ESRF Grenoble, France

Abstract

An efficient posture control system based on the development of mechanical stress during the maturation of wood cell walls allows trees to achieve successful height growth and adaptive reorientations. In some hardwood species, a tensile stress is generated by a specialized wall layer, the G-layer, made of a polysaccharide hydrogel reinforced by cellulose microfibrils aligned with the cell axis.

The mechanism generating this tension has long been a matter of debate. It seems doubtful that stress is induced in crystalline microfibrils after their deposition, because of their high stiffness and chemical stability. Alternative hypotheses involve cellulose re-crystallisation or interaction between the G-layer and other layers.

In vivo investigation on the state of stress of these components was necessary to elucidate this mechanism. Here we provide experimental evidence that tension appears in crystalline microfibrils of cellulose shortly after their deposition.

Using microbeam synchrotron X-ray diffraction, we measured how the lattice spacing of cellulose changes from the cambium to the mature wood of poplar trees, and found it to increase before formation of G-layer. These observations contrast with current conceptions of maturation stress generation, exclusively based on the action of the G-layer.

Introduction

Wood cells are produced in the cambium at the periphery of the stem. The formation of the secondary wall occurs at the end of cell elongation by the deposition of successive layers made of cellulose microfibrils bounded by amorphous material. Each layer has potentially a specific chemical composition and is characterised by a particular orientation of the microfibrils relative to the cell axis [1]. Microfibrils are made of crystalline cellulose, and are by large the stiffest constituent of the cell wall. The microfibril angle (MFA) in each layer is determinant for cell wall architecture and wood mechanical properties.

During the formation of wood cells, a mechanical stress of large magnitude, called “maturation stress” or growth stress [2,3] appears in the walls. This stress fulfils essential biomechanical functions for the tree. It provides the tree with a motor system [4], necessary to maintain the stem at a constant angle during growth [5] or to achieve adaptive reorientations. In angiosperms a large tensile maturation stress is generated by a specialized tissue called tension wood. In poplar, as in most temperate tree species, tension wood fibers are characterized by the presence of a specific layer, called the G-layer [6,7], where the matrix is almost devoid of lignin [8] and the microfibrils are oriented parallel to the fiber axis [9]. This type of cells is also widespread in plant organs whose function involves the bending or contraction of axes, such as tendrils, twinning vines [10] or roots [11].

The mechanism at the origin of this tensile stress has been the subject of a lot of controversy and is still not fully understood. However, several recent publications have greatly improved our knowledge about the ultra-structure, chemical composition, molecular activity and the mechanical state and behaviour of tension wood. Different models have been proposed and discussed to explain the origin

of maturation stress [12-23]. The specific organisation of the G-layer suggests that a tensile force induced in the microfibrils during the maturation process. Different hypotheses have been proposed to explain this mechanism, e.g. the contraction of amorphous zones within the cellulose microfibrils [23], action of xyloglucans [24] during the formation of microfibril aggregates [19,24] or the effect of changes in moisture content stimulated by pectine-like substances [16]. A recent work [18] argued for an alternative model, initially proposed by Münch [25], assuming that the maturation stress originates in the swelling of the G-layer and is transmitted to the adjacent secondary layers in which the larger microfibril angle allows an efficient conversion of lateral stress into axial tensile stress. Although several observations allow to reject this model, this hypothesis attracted attention on a possible role of cell-wall layers other than the G-layer. As a matter of fact, many types of wood fibers lacking a G-layer are known to produce axial tensile stress, e.g. normal wood of angiosperms and conifers [2], or the tension wood of many tropical species [26-28], so that mechanisms strictly based on an action of the G-layer cannot provide a general explanation for the origin of tensile maturation stress in wood.

In order to progress on this issue, direct observations are needed about the mechanical state of the different cell wall layers, and their evolution during the formation of the tension wood fibers. X-Ray diffraction can be used to investigate the orientation of microfibrils [29-34] and the lattice spacing of crystalline cellulose. The axial lattice spacing d_{004} is the distance between successive monomers along a cellulose microfibril, and reflects its state of mechanical stress [32,35]. If cellulose microfibrils indeed support a tensile stress, they should be found in an extended configuration. Under this assumption, the progressive development of maturation stress during the cell wall formation should be accompanied by an increase in cellulose lattice spacing. Here, we report on a first experiment where a microbeam was used to analyze the structural changes of cellulose in the cell wall layers of tension wood and normal wood fibers along the sequence of xylem cell differentiation extending from the cambium to mature wood (Fig. 1).

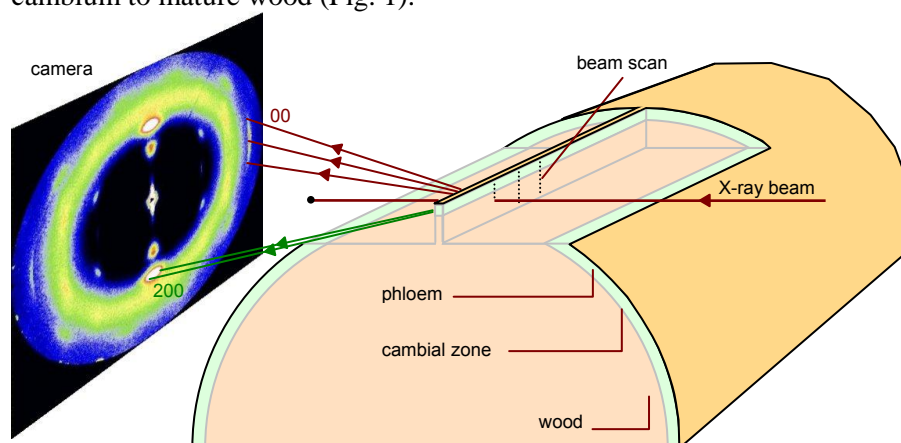


Fig. 1: Schematic of the experimental setup, showing the X-Ray beam impacting perpendicular to the longitudinal-radial plane of wood, and the contribution of the (004) crystal plane to the diffraction pattern recorded by the camera

Material and Methods

Plant material and sample preparation: Experiments were performed on young tilted poplar trees (*Populus deltoides* x *P. trichocarpa* cv. I45-51). Sample preparation was designed to prevent the release of mechanical stress within the segment, in order to keep the sample as close as possible from its *in planta* mechanical state [35]. On each tree, a 40-cm long stem segment (approximately 3 cm in diameter) was taken from the curved basal part of the stem. The segment was then prepared so as to leave a thin strip (400 μm thick) of peripheral wood on its mid-part of one side (Fig. 1), including the bark and the cambial area, and extended 2 mm within wood. The samples were kept wet during the whole preparation.

X-ray setup and experimental method: The experiment was carried out at the ID13 beamline of the ESRF using a 5 μm beam [36]. The wavelength of the monochromatic X-Ray beam was $\lambda=0.961176$ \AA . The sample holder was designed to maintain the stem segment perpendicular to the beam, while allowing precisely monitored vertical and lateral displacements. On each wood strip 3 radial profiles (distant 1 mm from each other along the fiber direction) were recorded in the transition

zone between bark and mature wood (Fig. 1). Each profile contains 150 shots at successive radial positions separated by 10 μm , extending from outer bark to mature wood. Samples were kept wet during the measurements using a micro-drop system fixed to the wood segment.

Data processing Diffraction patterns were processed using the Fit2D software (<http://www.esrf.eu>) and home made software procedures programmed with Microsoft Excel/Visual Basic. Despite the very small amount of wood material crossed by the X-Ray beam (low thickness and small beam size) the data yielded a high quality signal with very low noise, allowing a detailed analysis of the 004 reflections.

The 004 reflection was used to obtain information about cellulose lattice spacing. The diffraction patterns were integrated on a defined azimuthal sector and the intensity was plotted as a function of the radial position on the image. The radial position of maximal intensity (r_{max}) was determined using local polynomial fitting. Any radial position r on the pattern corresponds to a value of the Bragg angle: $\theta_{004} = \frac{1}{2}\text{atan}(r/L)$, where L is the distance between the sample and the camera. The Bragg angle of the cellulose 004 reflection is approximately equal to 10.73° at the experimental wavelength, but variations in cellulose lattice spacing d_{004} induce slight changes according to the equation of diffraction: $d_{004} = \lambda/(2\sin\theta_{004})$. The mean lattice spacing was therefore computed as $d_{004} = \lambda/(2\sin[(\text{atan}(r_{\text{max}}/L))/2])$.

A given microfibril contributes to the 004 reflection at an azimuthal position that depends on the microfibril orientation. Therefore, the lattice spacing of cellulose can be computed separately for different classes of MFA, by analyzing the signal in specific azimuthal sectors. The above-mentioned calculations were carried out for 2 distinct azimuthal integration sectors ($\pm 0^\circ$ - 12° and $\pm 12^\circ$ - 24°) yielding two distinct sets of lattice spacings. The first is representative of the fraction of cellulose with MFA $< 16^\circ$, and the second of the fraction with MFA $> 16^\circ$. This value has been chosen because it corresponds to the median value of MFA in normal wood.

Microscopic observations: One- μm thick transverse sections of the studied wood strips were stained with methylene blue/AzurII mix and observed under a light microscope. Microscopic sections allowed comparison between X-ray diffraction signal and anatomical structure. In particular, anatomical observations show that formation of G-layer appears 650 μm away from cambium in tension wood sample and confirm the absence of G-layer in the cell wall of normal wood.

Results

Changes in amount of cellulose along a development sequence

Typical diffraction patterns observed from one tension wood and one normal wood strip are shown in Figs. 2.

The intensity of the 004 reflection depends on the amount of diffracting microfibrils crossed by the beam. Therefore local variations in density (for example related to the presence of vessels) create slight fluctuations of the intensity profiles (but this does not affect the position of the peak, i.e. the lattice spacing of cellulose). The contributions to the intensity profiles of low MFA ($< 16^\circ$) and large MFA ($> 16^\circ$) are shown separately in Figs. 2. Intensity is shown on a log scale so that variations at low intensity can be seen despite the high intensity reached in mature wood. Comparison between these profiles indicates the relative abundance of cellulose oriented with low and large angle at each position.

After the first peak in the periphloem fibers, the cambial zone is characterized by a very low signal due the absence of secondary walls. The intensity increases along 400 μm after the cambium, parallel to the thickening of the cell wall. During this phase, similar intensity profiles are observed for low MFA and large MFA, for both normal wood and tension wood. After this phase, the signal of normal wood and tension wood clearly differ. In normal wood, low and large angles have similar low-intensity patterns, consistent with the fact that the cell walls have reached their final thickness. In tension wood, the signal emerging from low angle microfibrils deviates from the large MFA signal

and becomes 3 to 5 time higher. This steep increase in intensity for low MFA starts approximately 420 μm after cambium, much before any G-layer has become visible.

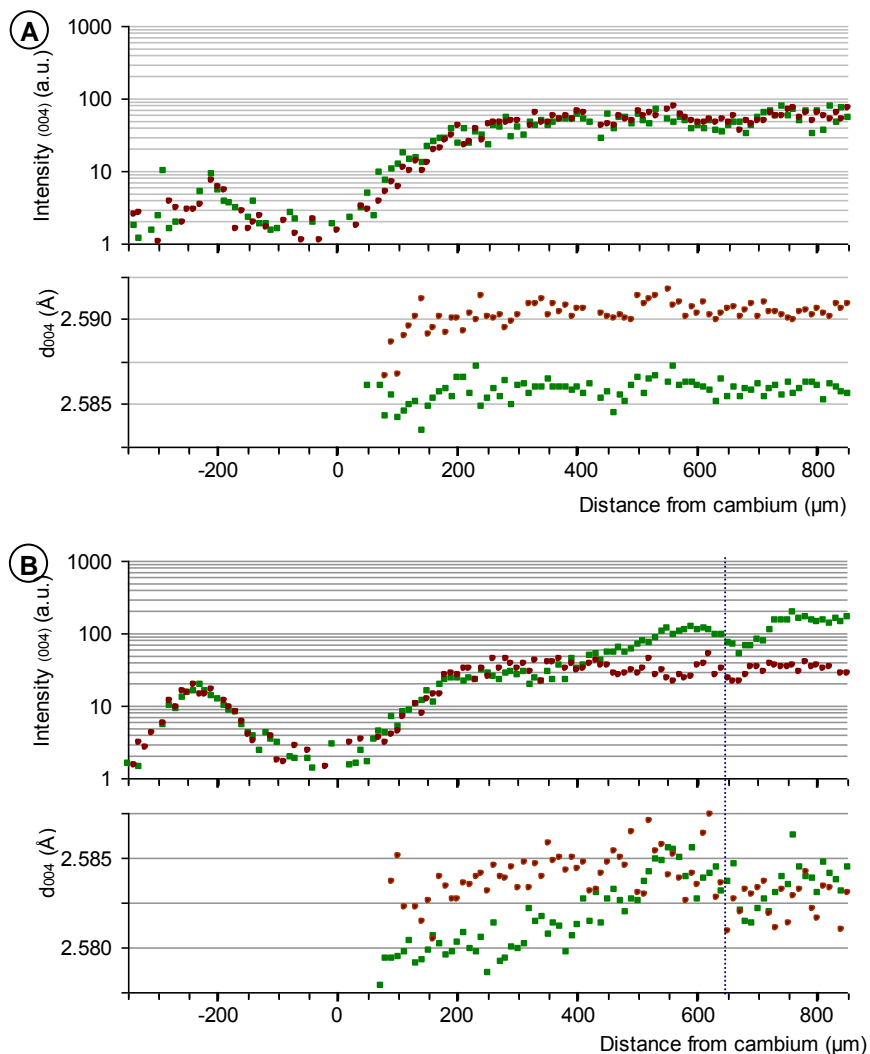


Fig. 2: Profiles of the 004 reflection intensity and d_{004} lattice spacing along a sequence of development of normal wood (A) and tension wood (B). Intensity (in log scale) and lattice spacing are given with distinction between contribution of microfibrils oriented with large angle ($>16^\circ$, red circles) and low angle ($<16^\circ$, green squares). Dotted line at $650 \mu\text{m}$ indicate the appearance of G-layer.

Changes in axial lattice spacing of cellulose along a development sequence

The evolution of the (004) planes mean lattice spacing is shown separately for the low MFA ($<16^\circ$) and large MFA ($>16^\circ$) classes (Figs. 2). The graph displays only the points with a signal high enough to accurately determine the lattice spacing.

In normal wood, d_{004} remains constant along the profile for both low and large angle microfibrils. In tension wood, the d_{004} profile for large angles is also roughly constant, although more scattered because of the comparatively lower intensity of the signal for this category of angles. For low microfibril angle in tension wood, one can clearly see a progressive increase in lattice spacing in the first 550 μm after cambium. This increase occurs before the G-layer being visible. It is particularly steep in the area where the innermost part of the S2 layer, dominated by low MFA, diverges on the intensity signal.

A tentative of measurement of the lattice spacing after release of tensile stresses by isolating fibre from both sides has been done, however, the displacement of the thin wood strip due to sectioning made impossible the use of data for lattice spacing measurements.

The axial strain of cellulose was computed as the relative change in d_{004} observed in this area. For low angle microfibrils in tension wood, it ranged between +0.1 to +0.3 % with a mean of +0.18 % on tension wood profiles. No or very few delay was observable between the deposition of cellulose (detected by intensity) and the increase in mean lattice spacing.

Discussion

X-Ray micro-diffraction allowed exploring changes in cellulose ultrastructure along sequences of cell walls development in normal and tension wood. Variations in intensity were consistent with the progressive thickening of the cell walls.

Our procedure was designed to measure the evolution of cellulose axial lattice spacing along a sequence of cell wall development. We assume that the d_{004} of cellulose at mechanical equilibrium is a constant, so that its variations are reflecting mechanical strain and stress in the cellulose crystal, as was previously demonstrated [35]. The major result we obtained is a clear difference between the patterns of changes in d_{004} between normal wood and tension wood. We evidenced that the cellulose lattice spacing increases in the inner part of the S2 layer only in tension wood. Moreover, we could demonstrate that this increase was correlated to the deposition of microfibrils with very low MFA, that occurred before G-layer formation. This may indicate that, inside the inner part of the S2 layer of tension wood, cellulose is put under tension just after its deposition. Furthermore, the magnitude of the strain deduced from our experiments (between 0.1% and 0.3%) is very close to the macroscopic released strain of maturation stress usually reported for poplar tension wood [6].

Acknowledgements

The authors gratefully acknowledge Richard Davies (ID13-ESRF) for technical support, Françoise Laurans and Alain Moreau (UAGPF, INRA Orléans), for excellent assistance to prepare the histological sections.

References

1. Mellerowicz EJ, B Sundberg (2008) *Wood cell walls: biosynthesis, developmental dynamics and their implications for wood properties*. Current Opinion in Plant Biology 11: 293-300.
2. Archer RR (1986) *Growth stresses and strains in trees*. Berlin/Heidelberg/New York: Springer Verlag. 240 p.
3. Fournier M, B Chanson, B Thibaut, D Guitard (1991) *Mechanics of standing trees : modelling a growing structure submitted to continuous and fluctuating loads. 2. Tridimensional analysis of maturation stresses. Case of standard hardwood* Annales des sciences forestières 48: 527-546 (in French).
4. Moulia B, C Coutand, C Lenne (2006) *Posture control and skeletal mechanical acclimation in terrestrial plants: implications for mechanical modeling of plant architecture*. American journal of botany 93: 1477-1489.
5. Alméras T, M Fournier (2009) *Biomechanical design and long-term stability of trees: Morphological and wood traits involved in the balance between weight increase and the gravitropic reaction*. Journal of Theoretical Biology 256 370-381.
6. Fang C-H, B Clair, J Gril, S-Q Liu (2008) *Growth stresses are highly controlled by the amount of G-layer in poplar tension wood*. IAWA Journal 29: 237-246.
7. Jourez B, A Riboux, A Leclercq (2001) *Anatomical characteristics of tension wood and opposite wood in young inclined stems of poplar (Populus euramericana CV "Ghoy")*. IAWA Journal 22: 133-157.
8. Pilate G, B Chabbert, B Cathala, A Yoshinaga, J-C Leplé, et al. (2004) *Lignification and tension wood*. Comptes rendus biologiques 327: 889-901.
9. Fujita M, H Saiki, H Harada (1974) *Electron microscopy of microtubules and cellulose microfibrils in secondary wall formation of poplar tension wood fibers*. Mokuzai Gakkaishi 20: 147-156.
10. Bowling AJ, KC Vaughn (2009) *Gelatinous fibers are widespread in coiling tendrils and twining vines*. American journal of botany 96: 719-727.
11. Fisher JB (2008) *Anatomy of axis contraction in seedlings from a fire prone habitat*. American journal of botany 95: 1337-1348.

12. Alméras T, J Gril, H Yamamoto (2005) *Modelling anisotropic maturation strains in wood in relation to fibre boundary conditions, microstructure and maturation kinetics*. *Holzforschung* 59: 347-353.
13. Alméras T, M Yoshida, T Okuyama (2006) *The generation of longitudinal maturation stress in wood is not dependent on diurnal changes in diameter of trunk*. *Journal of wood science* 52: 452-455.
14. Bamber RK (1987) *The origin of growth stresses : a rebuttal*. *IAWA Bulletin n.s* 8: 80-84.
15. Bamber RK (2001) *A general theory for the origin of growth stresses in reaction wood : how trees stay upright*. *IAWA Journal* 22: 205-212.
16. Bowling AJ, KC Vaughn (2008) *Immunocytochemical characterization of tension wood: Gelatinous fibers contain more than just cellulose*. *American journal of botany* 95: 655-663.
17. Boyd JD (1972) *Tree growth stresses - Part V : Evidence of an origin in differentiation and lignification*. *Wood science and technology* 6: 251-262.
18. Goswami L, JWC Dunlop, K Jungnikl, M Eder, N Gierlinger, et al. (2008) *Stress generation in the tension wood of poplar is based on the lateral swelling power of the G-layer*. *Plant Journal* 56: 531-538.
19. Mellerowicz EJ, P Immerzeel, T Hayashi (2008) *Xyloglucan: the molecular muscle of trees*. *Annals of botany* 102: 659-665.
20. Okuyama T, H Yamamoto, M Yoshida, Y Hattori, RR Archer (1994) *Growth stresses in tension wood: role of microfibrils and lignification*. *Annales des sciences forestières* 51: 291-300.
21. Okuyama T, M Yoshida, H Yamamoto (1995) *An estimation of the turgor pressure change as one of the factors of growth stress generation in cell walls. Diurnal change of tangential strain of inner bark*. *Mokuzai Gakkaichi* 41: 1070-1078.
22. Yamamoto H (1998) *Generation mechanism of growth stresses in wood cell walls : roles of lignin deposition and cellulose microfibril during cell wall maturation*. *Wood science and technology* 32: 171-182.
23. Yamamoto H (2004) *Role of the gelatinous layer on the origin of the physical properties of the tension wood*. *Journal of wood science* 50: 197-208.
24. Nishikubo N, T Awano, A Banasiak, V Bourquin, F Ibatullin, et al. (2007) *Xyloglucan endo-transglycosylase (XET) functions in gelatinous layers of tension wood fibers in Poplar--A glimpse into the mechanism of the balancing act of trees*. *Plant and cell physiology* 48: 843-855.
25. Münch E (1938) *Statik und Dynamik des Schraubigen Baus der Zwellwand, besonders der Druck- and Zugholzes*. *Flora* 32: 357-424 (in German).
26. Clair B, J Ruelle, J Beauchêne, M-F Prévost, M Fournier (2006) *Tension wood and opposite wood in 21 tropical rain forest species. 1. Occurrence and efficiency of the G-layer*. *IAWA Journal* 27: 329-338.
27. Ruelle J, H Yamamoto, B Thibaut (2007) *Growth stresses and cellulose structural parameters in tension and normal wood from three tropical rainforest angiosperm species*. *BioResources* 2: 235-251.
28. Onaka F (1949) *Studies on compression and tension wood* *Wood research* 1: 1-88 (translation from Japanese).
29. Cave ID (1966) *Theory of X-ray measurement of microfibril angle in wood*. *Forest products journal* 16: 37-42.
30. Cave ID (1997) *Theory of X-ray measurement of microfibril angle in wood Part 1. The condition for reflection X-ray diffraction by materials with fibre type symmetry*. *Wood science and technology* 31: 143-152.
31. Cave ID (1997) *Theory of X-ray measurement of microfibril angle in wood Part 2. The diffraction diagram X-ray diffraction by materials with fibre type symmetry*. *Wood science and technology* 31: 225-234.
32. Peura M, K Kölln, I Grotkopp, P Saranpää, M Müller, et al. (2007) *The effect of axial strain on crystalline cellulose in Norway spruce*. *Wood science and technology* 41: 565-583.
33. Peura M, M Müller, U Vainio, M-P Saren, P Saranpää, et al. (2008) *X-ray microdiffraction reveals the orientation of cellulose microfibrils and the size of cellulose crystallites in single Norway spruce tracheids*. *Trees - Structure and function* 22: 49-61.
34. Peura M, M-P Saren, J Laukkanen, K Nygard, S Andersson, et al. (2008) *The elemental composition, the microfibril angle distribution and the shape of the cell cross-section in Norway spruce xylem*. *Trees - Structure and function* 22: 499-510.

35. Clair B, T Alméras, H Yamamoto, T Okuyama, J Sugiyama (2006) *Mechanical behavior of cellulose microfibrils in tension wood, in relation with maturation stress generation*. Biophysical journal 91: 1128-1137.
36. Riekel C (2000) *New avenues in X-ray microbeam experiments*. Reports on Progress in Physics 63: 233-262.

Silica distribution in wheat awns to improve dispersal

Rivka Elbaum

The Hebrew University of Jerusalem, Israel

Abstract

Seed dispersal is a central stage in the life cycle of higher plants. It is important for the growth and collection of agricultural products, and in understanding the spread of invasive weeds. Plants develop specific structures that help their seeds move from the mother plant to a germination site, such as hairs, wings, thorns and edible parts, among others. Many grasses have awns, which are long, narrow appendages to the dispersal unit. The awns passively affect the course taken by the seeds as they fall from the mother plant, and in addition they may actively push the seeds along and into the soil via a hygroscopic mechanism. Wheat awns bend at their base when dry and straighten when damp, and so a long lever arm is created. This movement causes locomotion of the dispersal unit when the surface of the awns, acting as a ratchet, interacts with surfaces.

Using electron microscopy, I identified a continuous silica layer deposited at the epidermis, and covering hairs and papillae. The silicified surface appears to induce low friction when the awns slide in the direction of the seeds, and high friction when they slide in the opposite direction. Together with a sophisticated hygroscopic mechanism, the awns' structure is optimized for assisting the seed in moving short distances through plant litter, along and into the soil, increasing its chances of reaching a safe germination site.

Introduction

Seeds are the plants' emissaries to the next generation. As such, they set the starting point for renewal of annual populations and survival of perennial ones. For successful propagation, they need to find a position in the soil in which they can germinate and thrive [1], [2]. This requires some mobilization mechanisms, often involving animals, wind, or water, combined with specific forms of the dispersal unit [3], [4], [5]. Soil structures also affect seed distribution and successful germination [6] [7]. Seeds may stay on the mother plant until it wilts, or until they are picked. More often the seed-dispersal unit develops a special tissue at its base that allows the seed to separate from the mother plant [8]. This tissue is called abscission tissue when the whole dispersal unit is shed, and dehiscence tissue if the fruit, still connected to the plant, opens and the seeds themselves are shed. After disconnecting, the dispersal unit desiccates and dies, but even in this state it can direct the seed to a germination position through specific morphologies that interact with the environment [9], [10], [11]. These can be wings and feathers or simply a small size for flying, hooks and thorns for clinging to fur, mucilage for attaching to surfaces, an oily compartment (elaiosome) for attracting ants, or autonomous dispersal mechanisms. Some seeds have a simple round shape and thus disperse via the soil's random movements. Others have elaborate appendages, which often operate via changes in the hydration of the cell wall.

In drying plant tissues, stress develops when one part of the tissue shrinks in a specific direction more than a neighboring part. The organs move so as to relieve this stress. The direction of the movement reflects the orientation of the cellulose fibrils that make up the cell wall: as the cell wall dries, the matrix between the fibrils shrinks but the fibrils themselves do not. Therefore, the cell wall contracts in a direction perpendicular to fibril orientation. This phenomenon has been described in a

wide variety of dry-dispersal mechanisms [12], [13], [8], [14]. The actuating tissue divides into active and resistant parts. The active part contains fibrils at an angle to the cell axis, and therefore while drying, the cell length decreases. The cell wall in the resistant part consists of fibrils lying along the cells axis. This part resists the movement and stabilizes the moving structure [15].

Self-dispersal (autochory) using hygroscopic mechanisms

To study the mechanism of pod dehiscence in relation to the evolution of the legume family, nearly 100 legume pods were investigated [16]. In this classic work, the cellulose fibril orientation was estimated using polarized light microscopy. It was found that to achieve dehiscence, the valves must contain layered sclerenchymatous tissue with cellulose fibrils in orthogonal directions. The fully dehiscent pods were found to represent the most primitive members of the family and with evolution, dehiscence was partially or fully lost.

The dehiscence tissue controls the explosive ejection of seeds in the subfamily Acanthaceae [15]. In this case the fruit opens very rapidly due to the sudden release of tension stored in the septum. Using polarized light microscopy, the septum was found to contain active parts with cellulose fibrils tilted 30° to 40° relative to the septum axis, and parts that resist the bending with fibrils running parallel to the septum.

A slow-moving hygroscopic dispersal mechanism exists in pine cones, in which the scales open as the cone dries up. Polarized light microscopy of macerated cells showed that the sclerenchymatous cell wall in the lower part of the scales is built of cellulose fibrils running at an angle of $74 \pm 5^\circ$ to the scale axis. These cells contract when they dry. Fiber cells appear at the center of the scale. They consist of fibrils tilted 30° to the cell axis. Under humid conditions, the fiber cells' extension coefficient is only about a third that of the sclerenchyma cells, and their stiffness is about five times that of the sclerenchyma. This suggests that the pine cone scale is built of an active part that responds to humidity changes, and an adjacent part that resists this movement [14]. These examples show that groups of plants with remote evolutionary histories use a similar strategy when building a hygroscopic device, and that these structures are common in self-dispersal mechanisms.

Hygroscopic movement in wheat awns

I studied the micro- and nanostructure of the active and resistant parts in awns of wheat. Wheat awns are long, stiff filaments attached to the dispersal unit (*Fig 1*). When green, they function as a photosynthetic unit, supplying 10 to 40% of the seed's nutrients [17]. The base of each awn bends as it dries and conversely, straightens in a humid environment. The active part in the actuating region was found to contain cellulose fibrils arranged in rotated plywood-like layers. This highly anisotropic microscopic arrangement was thought to make it hypersensitive to ambient changes in humidity. In contrast, the resistant part was found to contain fibrils aligned along the awn, which are packed densely and bind water molecules more strongly than the active part. Thus, the awns respond to moderate changes in humidity, and have an adaptive advantage under diverse humidity conditions [18]. The fibril orientation governs the tissue's rigidity. In wheat awns, the fibrils' organization in the active part is optimized for high stiffness, which allows them to push the seed-dispersal unit against tough surfaces without changing their form [19].

The movement of wheat awns enables dispersal-unit crawling, possibly to optimize germination [20]. In order to slide along a surface, friction forces must be created. In this work, I show that the awns are encapsulated in a silica crust and suggest that this allows the dispersal unit to slide in the seed direction.

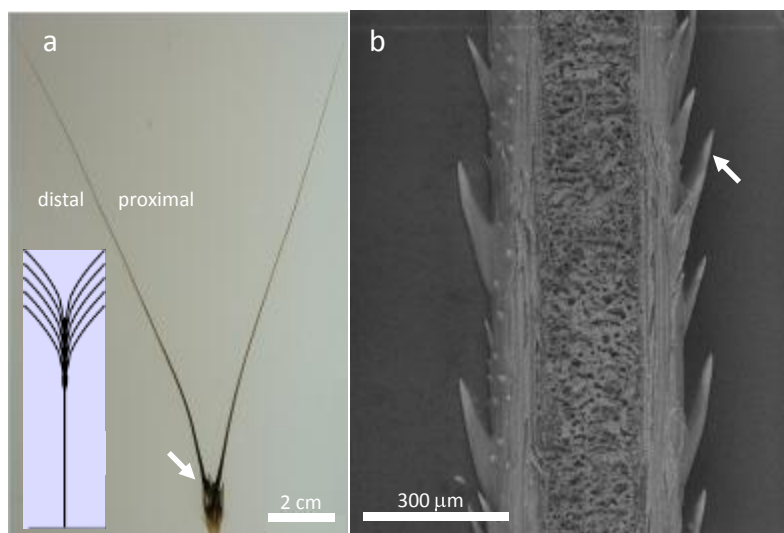


Fig. 1 (a) Wild wheat dispersal unit. The distal and proximal sides of the awn are indicated. The arrow points to the seed case, which contains two seeds. Inset: a schematic diagram showing a wheat inflorescence with awned seeds. (b) Scanning electron micrograph of longitudinally sectioned wild wheat awn. White arrow indicates a silicified hair. Note the dense mechanical tissue at the periphery of the awn, and the chlorenchyma porous tissue at the center.

Materials and methods

Plant material

Wild emmer wheat plants, *Triticum turgidum* ssp. *dicoccoides*, accession TTD 12, from Ammiad, Eastern Galilee, Israel, were grown in the net greenhouse of the Max Planck Institute for Molecular Plant Physiology in Golm, Germany, starting on Feb 21 2006, for about 4 months. Dry inflorescences and seed-dispersal units were collected and kept under ambient conditions until analysis. Additional awns from a large wild wheat collection [21] were analyzed using electron microscopy.

Electron microscopy

Samples of mature and dry awns were prepared via three methods. To examine the surface of the awns, pieces of about 2 mm in length were cut from the base. Samples were mounted as is on an aluminium stub using double-sided carbon tape. To study the awn in cross section, thin sections of 50 μm were obtained as described in Elbaum et al. [20]. Lastly, samples were embedded in a plastic material to create a smooth cross section, thereby eliminating the SEM contrast that originates from sample topography. Pieces of about 1 cm were placed in a 70% ethanol solution overnight. The samples were dried by washing them twice for 10 min each in 90% then 96% ethanol, twice for 20 min each in 100% ethanol, and twice for 10 min each in 100% propylene oxide. The samples were immersed overnight in 50% propylene oxide in Epon (SPI-Pon™ 812 Epoxy Embedding Kit, SPI-CHEM, hard mixture). The vials were then opened for 2 h to allow the propylene oxide to evaporate, and the samples were moved to pure Epon solution for overnight incubation. The Epon solution was replaced twice, after 1 h incubation each time, and then the samples were placed in fresh Epon for final curing at 60°C for 3 days. The blocks were sectioned transversely and the cross sections of the awns were cut on a microtome (Reichert-Leica Ultracut E) using a glass knife.

Images were scanned in a Philips XL-30 environmental scanning electron microscope (ESEM). We used two detectors in low-vacuum mode: the back-scattered electron (BSE) detector, in which the signal intensity increases with the atomic number of the elements composing the scanned area, and the energy-dispersive spectrometer (EDS) that identifies the elements according to the X-ray photons they emit under excitation of the electron beam. Image processing was performed with ImageJ (NIH).

X-ray micro computed tomography (micro-CT)

Pieces of about 2 cm were cut from the bases of mature and dry awns. The samples were measured in a micro-CT system (Skyscan-1072) operated at 100 kV and 100 μ A. Data reconstruction was performed using a filtered back-projection algorithm for cone beam tomography including corrections for beam hardening (NRecon, Skyscan). Three-dimensional (3D) representations were rendered using ImageJ (NIH) and the plugin “Volume Viewer”.

Results and discussion

In our previous work, we showed that wheat awns bend as a reaction to drying, and straighten back up at high humidity [20]. We suggested that this movement is initiated by the daily humidity cycle, and enables the crawling of wheat seeds along and into the soil. The bending can generate movement only if a friction force is created between the soil and the awn. In this work, I show that the awns are covered with a continuous layer of silica, and discuss its roles in seed dispersal.

In Figures 1 and 2, one can see the unidirectional silica hairs that point away from the seed case. The distribution of the hairs is not even around the awn: they are present at higher density along a ridge facing the distal direction of the dispersal unit. This ridge is probably responsible for most of the contact of the dispersal unit with surfaces. The hairs and papillae, known to contain silica [22], can withstand significant friction forces. In addition, we can discern a row of stomata on either side of the ridge, as previously described [23].

The distribution of silica in cross section was characterized by SEM using a BSE detector, and an EDS. A tight correlation was found between regions of high brightness in the BSE micrographs and regions with high silicon concentrations (*Fig 3*). I therefore associated the high-brightness regions detected by BSE with highly silicified regions, and concluded that the major mineral in the sample is silica. Silica was found to form a crust on top of the epidermal cells, and to integrate into their cell walls (*Fig 4*). In the ridge region, more of the epidermal cell wall is silicified.

The high-atomic-weight components, which are visible through BSE detection, attenuate X-ray radiation most efficiently. As most of these materials contain silicon, we can obtain a 3D distribution of silica using micro-CT. Figure 5 shows a 3D reconstruction of the epidermal silicification. The silicified hairs and papillae are connected through an almost continuous layer of the mineral, which is disturbed in the stomatal regions. This may have a physiological explanation, because deposition of silica in the stomata might exclude them from opening during photosynthesis and closing at other times.

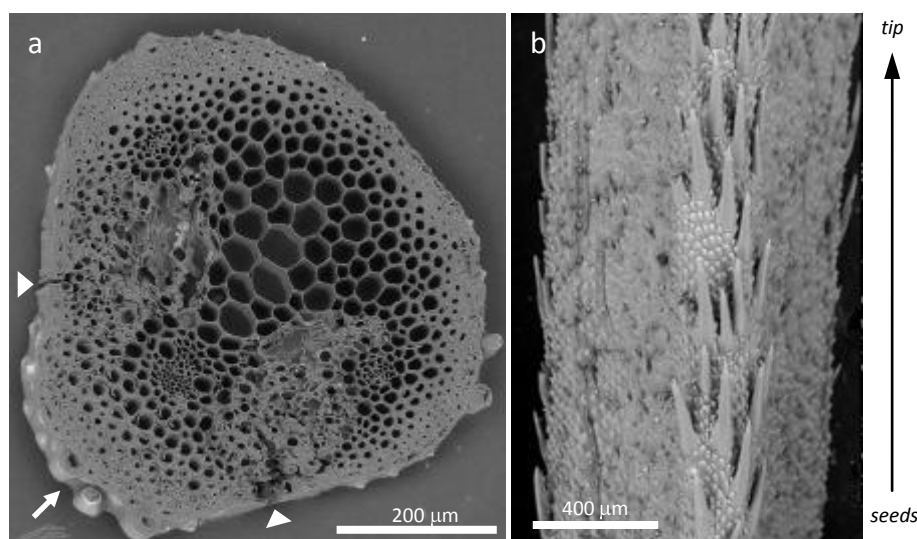


Fig. 2 Scanning electron micrograph of a wild wheat awn. (a) A cross section of an awn. One can recognize a narrower region (arrow), which forms a ridge on the awn surface. Stomata can be identified on both sides of the ridge (arrowheads). (b) The surface of the awn is imaged from the ridge direction. Silica hairs and papillae can be recognized. The hairs are more abundant on the ridge, while the papillae cover uniformly the awn.

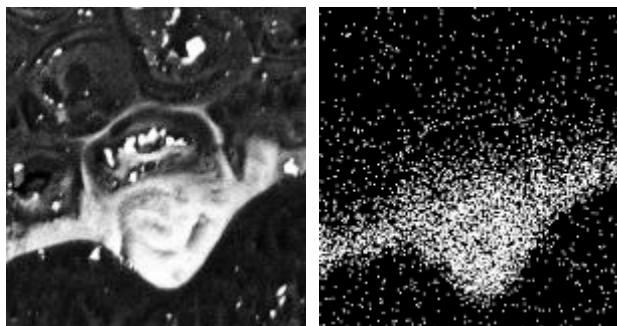


Fig. 3 Scanning electron micrographs of a transverse section of a wheat awn embedded in Epon, showing the correlation between high-brightness regions in back-scattering mode (left), and the silicon X-ray emission line, as detected by the energy dispersive spectrophotometer (right). The width of the images is 40 μm .

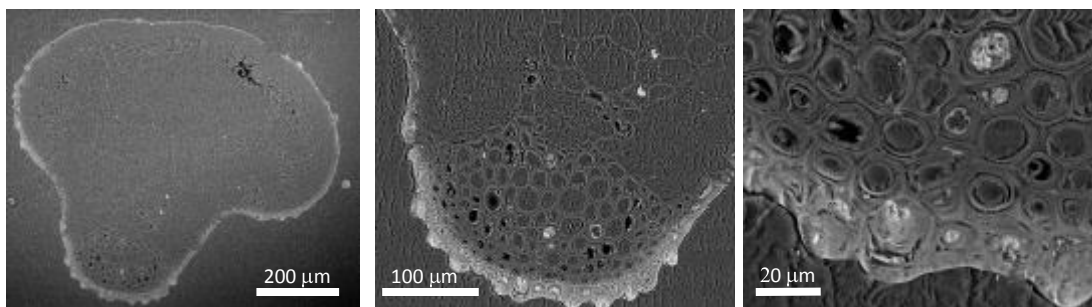


Fig. 4 Scanning electron micrographs of a cross section of a wheat awn. The left image shows the complete cross section, the middle image shows the ridge region of the same cross section, and the right image magnifies a region at the epidermis. The brightness levels reflect the atomic number of the elements and in this case, the bright regions correspond to regions that are rich in silica. Note the accumulation of silica above the epidermis, in the papillae and hairs. Silica is also incorporated in the epidermal cell wall.

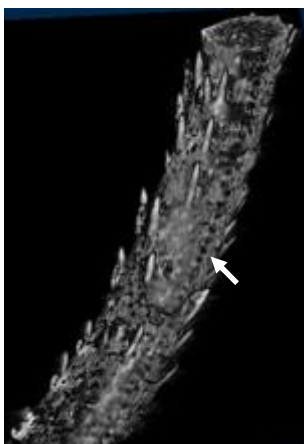


Fig. 5 A 3D rendering of a wild wheat awn reconstructed from micro-computed tomography data. The mineralized silica hairs can be easily observed as they absorb the X-ray radiation, in contrast to the row of black stomata that contain small amounts of the mineral (arrow).

Conclusion

In this work, I show that a crust of silica covers the wild wheat awns. Silica is carried with the water evaporation stream [24]. In green awns, the mineralized crust may reduce evaporation from the cuticle and add to their ability to photosynthesize under drought. The stomata are not silicified. As a major evaporation locus, we would expect to find silica in the stomatal region; on the other hand, solid silica would disturb the free movement of the guard cells and prevent their function. Therefore, we conclude that silica is actively directed away from the stomata. These findings indicate that silica is

deposited under cellular control, and that the silica crust plays a physiological role in the awn's structure.

The silica layer is thicker on the ridge, which is distinguished by a higher density of silica hairs. The ridge faces the distal direction of the awns, and is therefore more likely to interact by friction with surfaces than other regions on the awn surface. The thicker silica layer protects it from damage that may occur during physical interaction with surfaces. The silica solidifies as an amorphous mineral that forms a smooth durable surface, and the stiff hairs, acting as a ratchet, prevent backsliding of the seeds. This design thus restricts the awns' movement through plant litter and along and into the soil to the seed direction.

Acknowledgements

The author thanks Peter Fratzl for many fruitful discussions, Moshe Feldman and Zvi Peleg for their generous provision of unique data on wild wheat and plant material, Eugenia Klein for her invaluable assistance in the electron microscopy work, Christine Pilz-Allen for her kind help in obtaining the micro-CT scans and reconstructions, and Liron Zaltzman and Lital Nakar for their devoted work. This work was supported by the Helen and Milton A. Kimmelman Center for Biomolecular Structure and Assembly. The author thanks the Charles Clore Program and the Koshland Center for Basic Research for fellowships.

References

1. Fowler, N.L. (1988): *What is a safe site?: Neighbor, litter, germination date, and patch effects*. *Ecology*. 69: 947-961.
2. Howe, H.F and J.S. Mallwood (1982): *Ecology of seed dispersal*. *Annual Reviews in Ecology and Systematics*. 13: 201-228.
3. Van der Pijl, L. (1982): *Principles of dispersal in higher plants*. 3rd ed. Springer-Verlag.
4. Sorensen, A.E. (1986): *Seed dispersal by adhesion*. *Annual Reviews in Ecology and Systematics*. 17: 443-463.
5. Rabinowitz, D. and J.K. Rapp (1981): *Dispersal abilities of seven sparse and common grasses from a Missouri prairie*. *American Journal of Botany*. 68: 616-624.
6. Peart, M.H. and H.T. Clifford (1987): *The influence of diaspore morphology and soil-surface properties on the distribution of grasses*. *Journal of Ecology*. 75: 569-576.
7. Chambers, J.C. (2000): *Seed movements and seedling fates in disturbed sagebrush steppe ecosystems: implications for restoration*. *Ecological Applications*. 10: 1400-1413.
8. Fahn, A. and E. Werker (1972): *Anatomical mechanisms of seed dispersal*, in *Seed biology*, Kozlowsky, T.T. Academic Press: New York. p. 151-221.
9. Harper, J.L., P.H. Lovell and K.G. Moore (1970): *The shapes and sizes of seeds*. *Annual Reviews in Ecology and Systematics*. 1: 327-356.
10. Peart, M.H. (1979). *Experiments on the biological significance of the morphology of seed-dispersal units in grasses*. *Journal of Ecology*. 67: 843-863.
11. Carey, P.D. and A.R. Watkinson (1993): *The dispersal and fates of seeds of the winter annual grass *Vulpia ciliata**. *Journal of Ecology*. 81: 759-767.
12. Uphof, J.C.T. (1924): *Hygrochastic movements in floral bracts of *Ammobium*, *Acroclinium*, *Rhodanthe*, and *Helichrysum**. *American Journal of Botany*. 11: 159-163.
13. Zohary, M. and A. Fahn (1941): *Anatomical-carpological observations in some hygrochastic plants of the oriental flora*. *Palestine Journal of Botany*. 2: 125-135.
14. Dawson, C., J.F.V. Vincent and A. Rocca (1997): *How pine cones open*. *Nature*. 390: 668.

15. Witztum, A. and K. Schulgasser (1995): *The mechanics of seed expulsion in acanthaceae*. Journal of Theoretical Biology. 176: 531-542.
16. Fahn, A. and M. Zohary (1955): *On the pericarpial structure of the legumen, its evolution and relation to dehiscence*. Phytomorphology. 5: 99-111.
17. Tambussi, E.A., J. Bort, J.J. Guiamet, S. Nogués and J.L. Araus (2007): *The photosynthetic role of ears in C3 cereals: metabolism, water use efficiency and contribution to grain yield*. Critical Reviews in Plant Sciences. 26: 1-16.
18. Elbaum, R., S. Gorb and P. Fratzl (2008): *Structures in the cell wall that enable hygroscopic movement of wheat awns*. Journal of Structural Biology. 164: 101-107.
19. Fratzl, P., R. Elbaum and I. Burgert (2008): *Cellulose fibrils direct plant organ movements*. Faraday Discussions. 139: 275-282.
20. Elbaum, R., L. Zaltzman, I. Burgert and P. Fratzl (2007): *The role of wheat awns in the seed dispersal unit*. Science. 316: 884-886.
21. Peleg, Z., T. Fahima, S. Abbo, T. Krugman, E. Nevo, D. Yakir and Y. Saranga (2005): *Genetic diversity for drought resistance in wild emmer wheat and its ecogeographical associations*. Plant, Cell & Environment. 28: 176-191.
22. Ball, T., J.S. Gardner and J.D. Brotherson (1996): *Identifying phytoliths produced by the inflorescence bracts of three species of wheat (Triticum monococcum L., T. dicoccon Schrank., and T. aestivum L.) using computer-assisted image and statistical analyses*. Journal of Archaeological Science. 23: 619-632.
23. Grundbacher, F. (1963): *The physiological function of the cereal awn*. The Botanical Review. 29: 366-381.
24. Epstein, E. (1994): *The anomaly of silicon in plant biology*. Proceedings of the National Academy of Sciences of the United States of America. 91: 11-17.

***A new interpretation of plant cell growth mechanics:
Loss of stability and cell wall stress-relaxation.***

Philip M. Lintilhac¹ and Chungfang Wei^{1,2}

¹University of Vermont; ²Guangxi National University, China

Abstract

We propose replacing Preston and Probine's creep/viscoelasticity-based model for cell wall stress-relaxation with a newer and more predictive model based on the Eulerian concept of Loss of Stability. This model, derived from physical first principles, permits the prediction of working turgor pressures for any growing plant cell for which the geometry, wall thickness, and wall modulus can be determined. Our model eliminates experimental inconsistencies inherent in the viscoelastic/creep model and makes it possible to define a critical pressure (P_{cr}) for cell wall stress-relaxation as turgor pressure rises gradually, implying that turgor pressures in all growing plant cells must necessarily be hovering at or near their critical pressures.

Introduction

Our work separates the biophysical from the biochemical aspects of growth by outlining a theory of plant cell-wall stress-relaxation which can stand on its own. The physical approach is embodied in the notion of *stress-relaxation* which describes the physical process by which load induced mechanical stresses relax after loading, whether by catastrophic failure or by some more controlled process. Our starting premise is that since stress-relaxation is a physical process, it can be approached entirely on a physical and mathematical basis, without any reference to cellular biochemistry or metabolism. *Wall loosening* on the other hand refers to the biochemical process by which cross-linking elements within the wall are either broken or otherwise modified, and along with wall synthesis must be understood in biochemical and ultrastructural terms.

Preston's model [1] describes a turgid cell whose wall stretches irreversibly when placed under tensile stress exceeding some material parameter which can be called the *yield threshold* Y . The relationship between yield threshold and cell volume growth (dV/dt) has been formalized in the well-known Lockhart Equation [2] which proposes that the volume growth rate of a cell is proportional, by some empirically determined amplification coefficient m , to the difference between the cell turgor pressure P and the yield threshold pressure Y_p .

$$dV/dt = m(P - Y_p) \quad \text{Eq 1}$$

As long as the turgor pressure P is higher than the yield threshold pressure Y_p the right hand side of the equation remains positive and growth will occur -- the greater the divergence the faster the growth.

The first implication of this expression is that there is a real turgor threshold for growth which reflects the yield threshold of the wall material, and that turgor must rise above this threshold for growth to occur. Y_p therefore represents the lower limit of turgor in growing cells and the actual turgor pressure of a growing cell must rise above Y_p by an unspecified amount in order to result in non-zero growth. Consequently the Lockhart expression cannot predict the working turgor pressure of the growing cell accurately.

Preston attempted to integrate what he knew about wall ultrastructure with the Lockhart equation, thereby creating a model which could serve as a basis for the interpretation cell wall behavior. The biophysical model that Preston settled on was based on the observation that segments of cell-wall material, when subject to tensile loading under experimental conditions, appear to exhibit a continued period of extension after the initial imposition of the load. This kind of delayed stress-relaxation has been termed *viscoelasticity*, or *viscoplasticity* [3,4]. Viscoelastic creep represents a special case of elastic behavior which becomes apparent under specific conditions and refers to an extended period of stress-relaxation (and deformation) that persists after a sudden and finite change in

strain. It is only seen under conditions where the initial deformation is applied rapidly so that the equilibration of stresses within the material does not have time to keep up with the sudden change in strain. This dependency on rapid loading makes it a rather unlikely candidate as an explanation for stress-relaxation in normal living cells where sudden increases in cell turgor are unlikely to occur. Nevertheless, viscoelastic behavior has been seen in isolated plant cell-wall materials under experimental conditions and exhibits a characteristic log-linear relationship between time and deformation [5,6].

We have shown that although viscoelastic/viscoplastic extension can occur under experimental conditions, during normal growth plant cell wall stress-relaxation most likely follows an entirely different dynamic, termed *Loss Of Stability* (LOS), [7,8,9]. LOS theory follows directly from the extension of pre-existing mathematical theory without reference to empirically derived concepts of cell wall biochemistry or to presumed viscoelastic or viscoplastic stress-relaxation. In its purest form it is an all-or-nothing process in that the conditions for stress-relaxation through LOS in a turgid cell are either met, or they are not met; and perhaps more importantly, when applied to water-filled pressure vessels it reveals an internal control cycle that is inherent in the physics of the system, rigorously defining a maximum turgor pressure for any growing cell

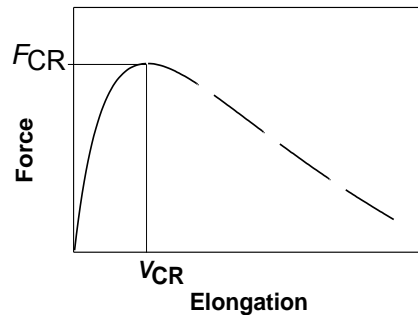
Our most recent application of LOS theory defines the conditions which lead to loss of stability in cylindrical cells [9]. This constitutes what we believe to be a viable model for stress-relaxation in cylindrical plant cells, which is also able in principle to predict the working turgor pressure of any growing cylindrical cell. Specifically, we have developed a *Critical Pressure* solution to the problem of instability in a cylindrical pressure vessel:

$$P_{critical} = \frac{Et_0}{eR_0(1+\nu)} \quad \text{Eq 2}$$

Where $P_{critical}$ = the internal pressure value at which wall instability occurs, E = wall modulus, t_0 = initial thickness, e = base of the natural log, R_0 = initial radius, and ν = Poisson's ratio of the wall material. Note that this equation predicts the upper limit for increasing turgor pressure in a growing plant cell directly from the geometry and mechanical properties of the cell wall and without the need for empirically determined constants.

LOS of Elastic Materials in Tension LOS theory, as we have applied it to the problem of plant cell growth, derives directly from the work of the renowned mathematician and physicist Leonhard Euler, who in 1778 formalized the concept of instability in a vertical column under axial compression, (the "Euler Column") in which the load/deformation curve rises smoothly to a peak where, at zero slope, the structure transits from a stable state to an unstable state, followed by failure according to a variety of modes depending on the material.

The mathematics of Loss of Stability was then extended by the Russian engineer Aleksei Rzhanitsyn first to a column in tension, and then to a spherical pressure vessel [10] all of which were shown to exhibit the characteristic behavior first described by Euler. In the case of a column in tension Rzhanitsyn established that as the force acting on the column increases, the stress in the column also rises to a point at which it becomes unstable, although the subsequent modes of failure are



very different from those which might occur in compression. The force required to trigger instability behavior, which he termed the Critical Force, F_{cr} is determined solely by the geometry of the column and its material properties. F_{cr} can therefore be unequivocally predicted from measurable values. As Euler had noted before him, the distinguishing feature of this kind of behavior is the characteristic shape of the force/deformation curve.

Rzhanitsyn then applied the notion of tensile instability to a spherical pressure vessel. He showed that a spherical vessel, pressurized gradually to create tensile stress in the vessel wall, will similarly undergo a loss of stability at a critical pressure P_{cr} which can be predicted from the material properties and thickness of the wall and the geometry of the vessel, just as the critical force F_{cr} which predicts instability in a column can be determined solely from the geometry and properties of the column. Fig 2.

Fig 1 Typical curve for loss of stability in tension, where F_{cr} is the critical force at the moment of instability, and V_{cr} is the change in dimension at instability. The points on the rising portion of the curve are stable states in which the material retains some elasticity. Note that at F_{cr} the force-elongation curve is at zero slope, indicating that there is no elasticity in the system. Points on the falling portion of the curve represent unstable states.

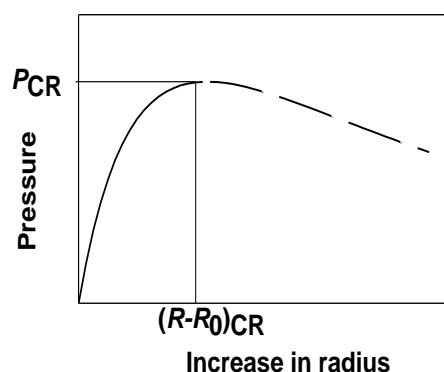


Fig 2. Loss of stability in a spherical pressure vessel. P_{cr} is the critical pressure (at zero slope) where the wall of the vessel becomes unstable. $(R-R_0)_{cr}$ is the change in radius of the vessel wall at criticality.

This work has been well reviewed by Panovko and Gubanov [11] who also note that when the pressure vessel wall is inhomogeneous, with thin spots, (or local regions of lower modulus) then loss of stability will occur first in those regions where P_{cr} has its lowest value [11]. Furthermore, in a water-filled pressure vessel, because of the almost complete incompressibility of water any instability-driven yielding, no matter how localized, will result in a small increase in volume and an immediate drop in pressure, thereby potentially rescuing the vessel from catastrophic failure.

The applicability of this thinking to the problem of plant cell growth is obvious. Any growing plant cell can be thought of as a water-filled pressure vessel whose wall although complex and anisotropic, is necessarily constrained by the same physical laws that govern instability behavior in any pressure vessel. When the internal pressure (turgor) rises to the point where some local region becomes unstable then instability-driven yielding must result, followed by a small volume increase and a drop in pressure. When multiple local instabilities begin to flicker across the wall, (always finding locations where P_{cr} is at its lowest value), then growth will result in a seemingly continuous extension of the wall surface. In any multicellular growing tissue (imagine a rapidly extending hypocotyl) the individual cell turgor pressures will all be “hovering” at, or just below, the local value of P_{cr} .

Instability-driven yielding is thus very different from viscoelastic yielding. Viscoelastic behavior is much less predictable, and depends heavily on the stress mechanical history of the sample. To quote Fung and Pin Tong [12]:

“Viscoelasticity is characterized by a constitutive law that the current state of stress depends not only on the current strains, but also on the full history of their development...”

By way of comparison LOS behavior happens only if the mathematical conditions specific to the geometry and material properties of that cell are met. The previous history of the sample is irrelevant as long as molecular rearrangement can keep up with the strain rate. This means that in a gradually pressurized cell the wall will lose stability only when the turgor pressure rises to the value of P_{cr} , regardless of the prior history of the sample. Conversely, as long as the system retains some elasticity (as long as the slope of the force/deformation curve remains positive) true loss of stability cannot happen. In this article we provide further direct evidence of LOS behavior in plant cell wall materials and discuss its relevance to the problem of plant cell growth.

Material and methods

Plant material and growth conditions Cultures of *C. corallina* were grown in a medium of 5% soil mixture in distilled water. Fast growing intact plants each consisting of 5-6 internodal cells were used for measurements (very young cells less than 3mm in length were considered unusable). The most mature internode (i.e. the most basal one), labeled cell #1 in this study, grew at a rate of about 5% increase in length per day. The youngest internodes (cell #5) grew at about 20% increase in length per day.

Measurement of cell turgor pressure The turgor pressures of internodal cells were measured directly using the cell pressure probe method [13]. Probing was carried out sequentially from the youngest to the oldest internodes while the whole intact plant was kept in water. Six intact plants were used for these turgor measurements.

Measurement of wall stress-strain relationships After probing, the cells were opened with a razor blade and the cytoplasm was removed with a hair loop. The walls were then cut into longitudinal ribbons for elastic modulus measurements. Cell wall thickness was measured by means of image duplicating interference microscopy. For the calculation of the optical path difference we assumed the refractive index of the wall materials to be 1.55 [1]. The lengths and widths of the ribbons were measured with an optical micrometer. The elastic moduli E of individual fully hydrated wall ribbons were then determined by a cyclic loading/unloading method described in detail elsewhere [9]. The ramp-loading experiments described here (Fig 3,4) were conducted under load-controlled conditions using a microprocessor-controlled miniature forcing frame (Vitrodyne V-200, formerly made by LiVeCo Biomechanical Instruments, Burlington, VT, USA).

Results and discussion

Experimentally the distinction between viscoelastic behavior and LOS behavior can be demonstrated dramatically in plant cell wall materials. When we excise a portion of *Chara* cell-wall material, secure it in a mechanical testing apparatus and stretch it suddenly, we will in fact see a continued extension of the wall segment, an extension whose rate decays over time in a log/linear manner, suggesting that the stress-relaxation process as falls into the viscoelastic/viscoplastic regime. However, if we take an identical portion of cell-wall material, clamp it in an identical manner, but load it gradually, under rate conditions that more nearly approximate those which might occur in a living cell, we find that the extension of the wall fragment follows an entirely different modality and exhibits none of the log-linear decay signature that characterizes viscoelastic extension.

In Fig 3, curve **a** illustrates the response of a cell wall strip under pH neutral conditions where the ramp-time (5 minutes) is sufficiently gradual to eliminate any continued viscoelastic extension after the load is held constant.

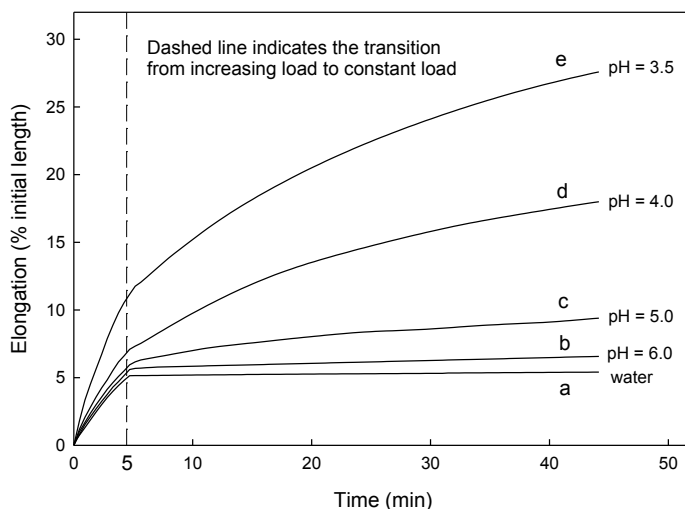


Fig 3 At pH 7.0 a cell wall strip subject to gradually increasing tensile load for 5 minutes will maintain its final length when the load stops increasing. However, as the pH drops the original 5 minute ramp-

time is too short to permit deformation to keep up with the increasing stress and some continued extension will be seen even when the load is held constant.

Another illustration of classical LOS leading to failure is seen in Fig 4, which illustrates Eulerian loss of stability behavior in a cell wall strip subject to tensile load increasing gradually over a period of 60 minutes. As the load continues to ramp up in a linear manner, the force/deformation curve follows the characteristic LOS profile, ending in failure as the sample becomes unstable at zero slope.

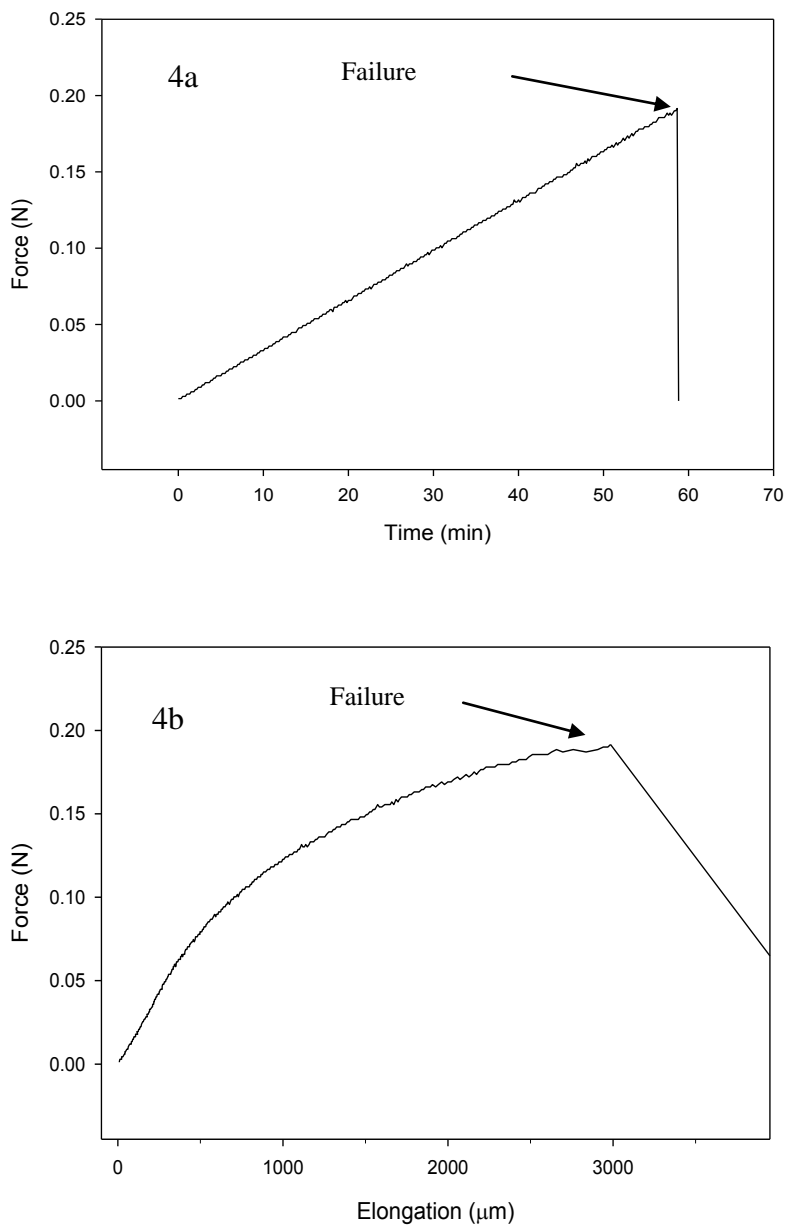


Figure 4. Two views of the behavior of a longitudinal wall ribbon when the intensity of the applied tensile force is increased gradually. Curve A shows the loading regime (Force vs. Time). A continuous

linear rise in applied load is applied to a cell wall strip excised from a growing *Chara* cell. Curve B shows the same event re-plotted as force vs. elongation of the sample. The peak of the curve (zero slope) establishes the occurrence of *Loss of Stability*, which is the point when the force reaches the critical value leading to instability and failure of the strip.

When taken in the context of previous experimental work which has clearly demonstrated viscoelastic extension in plant cell wall materials this means that *cell-wall materials are capable of two entirely different modes of stress-relaxation behavior depending on the loading conditions to which they are subjected.*

One substantial fact that emerges from our study is the ability of LOS theory to predict the working turgor pressure of living cells. We took fast-growing plants of *Chara corallina* and subjected them to systematic analysis after measuring the turgor pressures of their individual cells directly with a cell pressure probe. The analysis was designed to establish values for the variables in the cylindrical LOS equation (Eq 2 above) which could then be substituted back into the equation to provide a calculated prediction of the working turgor pressure. In each case a plant at least six internodes in total length was chosen. The oldest and most basal cell was labeled cell 1. Dissection of each individual cell enabled us to measure wall thickness t , cell radius R , and wall modulus E . Values for t_0 and R_0 were estimated by a procedure discussed in Wei and Lintilhac 2006 [8]. Poisson's Ratio ν was introduced as a range of values from 0.0 to 0.5. The entire analysis was repeated for 6 similar plants. Pressure measurements are presented in MegaPascals as a mean \pm standard deviation, $n=6$.

The predicted working turgor pressures which represent calculated values for P_{cr} according to Equation 2, are always higher than the values measured by probe. This is due to the fact that values for modulus E are determined using thickness measurements that only reflect the approximate overall thickness of a measured segment; whereas the real working turgor pressure reflects the limits imposed by the thinnest or lowest modulus region of the wall (see Panovko & Gubanova p. 88, as noted above) which may be too small to resolve by microscopic interferometry. This systematic error thus appears to result from an inability to resolve local regions of low P_{cr} . Despite these difficulties it is clear that the calculated values are reasonably close to the pressures measured by cell pressure probe, and support our hypothesis.

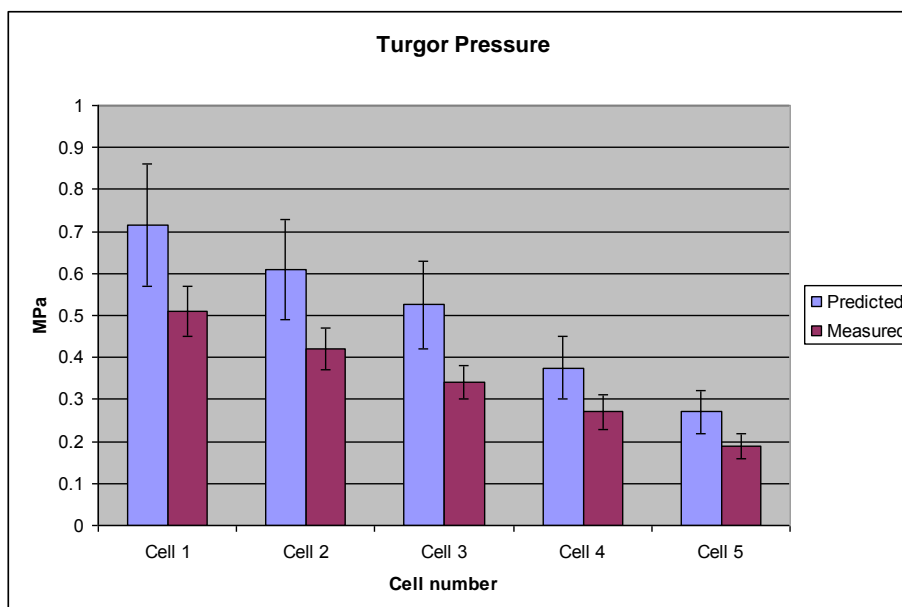


Fig 4. Measured vs. predicted values for turgor pressure in living *Chara* cells, For each of 6 comparable *Chara* plants Cells 1 -5 were probed, dissected and measured. For each individual cell turgor pressure was measured by cell pressure probe. Cell wall thickness t , cell radius R , and wall modulus E were then obtained by direct measurement. Values for t_0 and R_0 were estimated by a procedure discussed in Wei and Lintilhac 2006. Poisson's Ratio ν was introduced as a range of values

from 0.0 to 0.5 and reflected as a mean predicted pressure \pm Poisson's ratio variance. Pressure measurements are presented in MegaPascals (MPa) as mean \pm standard deviation, n=6.

As a predictive tool the Lockhart Equation (Eq 1) is beset by a number of problems. First among these is the well known difficulty in establishing the value of the yield threshold Y . This is because viscoelastic behavior depends upon the entire stress/strain history of the specimen [12] and therefore looks different in the hands of different experimenters who load their materials at different rates, and return different values for Y depending on their own methods. Another issue is the lack of any representation of the geometry of the cell or of cell wall dimension. This is particularly problematic in the case of plant cells where the working turgor pressure necessary to sustain growth is so clearly linked to wall geometry. One only has to reflect on the fact that high pressure cells tend to have thicker walls than low pressure cells to realize that dimension and geometry must figure into the determination of working turgor pressure.

LOS theory provides a purely physical context from which to try to understand the complexities of plant cell growth. Specifically it tells us that there is a direct physical relationship between cell geometry, the mechanical properties of the wall, and the Critical Pressure (P_{cr}) which limits the working turgor pressure. Furthermore, it implies that because of the pressure drop that occurs instantly after an LOS event there is an inherent negative feedback on continued cell wall expansion, and that in any multicellular growing tissue the individual cell turgor pressures will all be "hovering" at, or just below, the local value of P_{cr} . The difference between the traditional "Lockhart" view and the LOS view of turgor-driven growth is highlighted by the observation that in the Lockhart equation (Eq 1) Y_p represents the lower limit of turgor pressure during growth, whereas in the LOS model P_{cr} represents the upper limit.

Conclusion

LOS theory may form the basis of a new paradigm for understanding the physics of cell wall extension during plant cell growth, but the details of how it manifests in real living cells, where the texture of the wall is variable and where local values of P_{cr} vary from one location to another, are a matter for further inquiry. It may require the re-interpretation of a cell wall surface as a pixellated field, where a hypothetical census of local regions would show that the distribution of pixels of different P_{cr} value affects the response of the cell wall as a whole to increasing pressure; with regions of relatively high P_{cr} continuing to exhibit some elastic behavior while regions of low P_{cr} transit into instability.

References

- 1 Preston, R. (1974) *Physical Biology of Plant Cell Walls* Chapman and Hall, London
- 2 Lockhart, J. (1965a) An analysis of irreversible plant cell elongation *J. Theor. Biol.* 8, 264-275
- 3 Dorrington, K. (1980) The theory of viscoelasticity in biomaterials. In *The Mechanical Properties of Biological Materials* SEB Symposia XXXIV pp 289-314 Cambridge University Press
- 4 Dumais, J. et al (2006) An anisotropic-viscoplastic model of plant cell morphogenesis by tip growth. *Int. Jnl. Dev. Biol* 50, 209-222
- 5 Metraux J. and Taiz L. (1978) Transverse viscoelastic extension in *Nitella* I. Relationship to growth rate. *Plant Physiol* 61, 135-138
- 6 Taiz L. (1984) Plant cell expansion: regulation of cell wall mechanical properties. *Ann Rev Plant Physiol* 35, 585-657
- 7 Wei, C and P. M. Lintilhac. 2003. Loss of Stability - A New Model for Stress-relaxation in Plant Cell Walls. *Journal of Theoretical Biology* 224: 305-312.
- 8 Wei, C., L. S. Lintilhac, P. M. Lintilhac, 2006. Loss of Stability, pH, and the anisotropic extensibility of *Chara* Cell Walls. *Planta*. 223: 1058-1067.
- 9 Wei, C. and Philip Lintilhac, 2007 Loss of Stability: A New Look at the Physics of Cell Wall Behavior during Plant Cell Growth. *Plant Physiology*, 145:763-772
- 10 Rzhantsyn A. (1955) Stability of the equilibrium of elastic systems. *Gostekhizdat*, Moscow.
- 11 Panovko Y. and Gubanova I. (1965) *Stability and oscillations of elastic systems* Consultants Bureau, New York
- 12 Fung Y. and Pin Tong (2001) *Classical and Computational Solid Mechanics* p 857, World Scientific, Hong Kong
- 13 Steudle E. (1993) pressure probe technique. In Smith & Griffiths, eds, *Water Deficits*. BIOS Scientific.

Structural and mechanical design of tissue interfaces in monocotyledonous plants

Markus Rüggeberg¹, Thomas Speck² and Ingo Burgert¹

¹ *Max-Planck-Institute of Colloids and Interfaces, Department of Biomaterials, Potsdam, Germany;*

² *Plant Biomechanics Group Freiburg, Botanic Garden, University of Freiburg, Germany*

Abstract

In monocotyledonous plants, stiffening elements are dispersed in soft parenchymatous tissue. Therefore, they exhibit a very heterogeneous stress distribution under mechanical loading. This puts some constraints on the structural and mechanical design of the interface. Additionally, this biological structure is very similar to the structure of technical composites. We present an overview on recent structural and (micro-)mechanical analyses of a stem of the palm *Washingtonia robusta* and give an outlook to the Giant Reed *Arundo donax*. The data help to understand why in the group of palms and woody grasses plants with an excellent mechanical stem performance are found.

Introduction

Hardwoods and softwoods exhibit a rather uniform distribution of stiffening tissues in the trunk, whereas monocotyledonous plants possess numerous vascular bundles with stiff fibre caps which are embedded in soft parenchymatous tissue. In many monocotyledonous plant species, the fibre caps of the vascular bundles are the main stiffening elements of the palm trunk. The fact that stiff tissues such as fibre caps are embedded in relatively soft parenchymatous tissue puts some interesting constraints on the mechanical design of the interface between both tissue types. Due to mechanical loading, high stresses are generated in the stiff fibres, whereas the stresses in the soft parenchyma cells stay rather low. Such inhomogeneous structures are prone to fail under external loads, because stress discontinuities are likely to occur at the interfaces.

For palms, the influence of the distribution of vascular bundles on the mechanical properties with respect to different radial positions and heights within the palm trunk was investigated by Rich and co-workers in a series of papers [1-3] on functional anatomy and mechanical architecture of arborescent palms. A close correlation between mechanical stiffness and volume fraction of vascular bundles was found. The stiffness increased from centre to periphery and from the top to the base of the stem. The palm stem can therefore be considered as structurally optimised for flexural stiffness at its macroscopic and integral scale [4].

The culms of the Giant Reed *Arundo donax* can be seen as optimised to flexural stiffness as well. The culms are hollow with several nodes stabilizing it against local buckling. Besides the vascular bundles with enclosing fibre sheaths a sclerenchymatous ring is located at the periphery of the culm wall and stiffens the culm. The Giant Reed has proven to be a suitable organism to study various biomechanical aspects [5-8].

Despite these investigations on palms and on the Giant Reed on the macroscopic level, possible strategies to accomplish the differences in stiffness by micro- and nanostructural adaptations have been only marginally considered yet. At these levels of hierarchy, the mechanical constraints and underlying principles of the embedding of stiff vascular bundles in soft parenchymatous tissue are of particular interest. Analysing the micro- and nanostructural changes across individual vascular bundles

leads, on the one hand, to a deeper understanding of the biomechanics of the palm, on the other hand, the knowledge gained may serve as a source of bio-inspiration for the design of advanced technical fibre-reinforced composites.

By correlating stiffness profiles with changes in cell and cell wall parameters, possible adaptation strategies are unravelled according to the mechanical constraints arising in the trunk when dealing with high bending loads. Results are presented for the palm *Washingtonia robusta* and an outlook is given for the Giant Reed *Arundo donax*.

Material and methods

Samples were taken from the trunk of one individual of the palm *Washingtonia robusta* H.Wendl (Mexican Fanpalm, Fig. 1a) and from two culms of the giant reed *Arundo donax*. The palm stem was 10 m long and was cut down at the age of 33 years. Samples were taken at the height of 5 m. The culms of *Arundo donax* (Fig 2) were about 4 m high and samples were taken from the fourth and fifth internode above soil level which corresponds to a height of about 40 cm above soil level. For sample conservation and preparation, blocks of about 1 cm³ were embedded in the water-soluble artificial wax Polyethylenglycol 2000 (PEG 2000). The method has been described in detail in [9]. Upon washing in water, the wax was completely dissolved. The sections were kept wet during the entire investigation and testing to resemble fresh state.

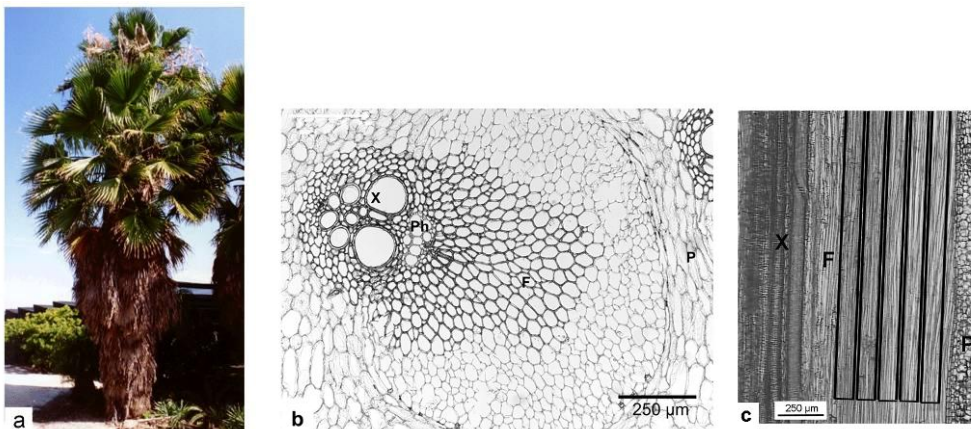


Fig.1 a) *Washingtonia robusta*. b) Cross section of an vascular bundle. c) Radial-longitudinal section of a fibre cap with rectangles marking the fibre strips to be cut with the microlaser for later mechanical testing. F, fibre cap; P, parenchyma; Ph, phloem; X, xylem. Taken from [9, 10].

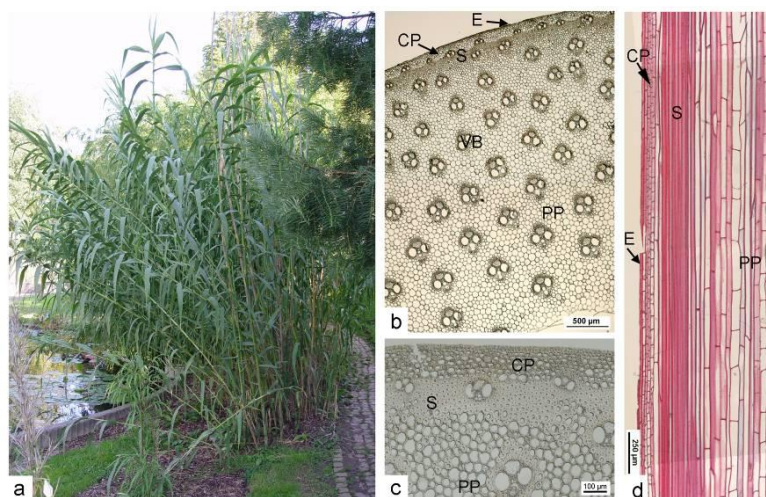


Fig. 2 *Arundo donax*. (b) Cross section of the entire culm wall. (c) Cross section of the periphery of the culm wall. (d) Radial-longitudinal section of the periphery of the culm wall. E, epidermal layer; CP, cortical parenchyma; PP, pith parenchyma; S, sclerenchyma; VB, vascular bundle; FR, fibre ring of VB..

For micro-mechanical testing, a tensile testing stage with video extensometry for strain detection was used as described in Burgert et al. [11]. For cutting of consecutive tissue strips of ~3 mm length, ~100 µm width and ~80 µm thickness (see Fig. 1c), the technique of microlaser dissection (P.A.L.M. Microlaser Technologies GmbH, Germany) was used to provide high quality and exact geometries for all samples. The stresses applied to a sample during one experiment were calculated on the basis of the cross-sectional area of the entire fibre strip and cross-sectional area of only cell walls of all cells in the respective cross-section. The cell wall area fractions at consecutive radial positions within the stem were determined on images of cross-sections using the software ImageJ. For calculation of mean values, areas were chosen containing at least thirty cells (Figure 1a)

Microfibril orientation with single cell resolution was obtained with synchrotron wide angle X-ray diffraction (WAXD) on radial-longitudinal sections at the µ-Spot beamline at BESSY II (Berlin, Germany) as described in [9].

Lignification was qualitatively investigated by staining of cross sections with phloroglucinol/hydrochloric acid [12].

A universal microspectrophotometer (UMSP 80, Zeiss, Germany) was used to resolve the topochemical distribution of lignin and other cell wall phenolics with high spatial resolution. Sample blocks were embedded in Spurr according to [13] for preparing 1 µm thick cross sections for the measurements. The wavelength of the maximum absorbance was used for two-dimensional scans across the fibre caps with a step width of 0.25 µm. Details can be found in [9].

Results and discussion

The investigations on the fibre caps of the palm *Washingtonia robusta* showed a gradual decrease in tissue and cell wall stiffness of more than one order of magnitude (see Fig. 3). In the periphery of the fibre caps, values in stiffness of 20-50 MPa were measured which are comparable to those obtained for non-lignified parenchymatous tissue of potato tubers [14].

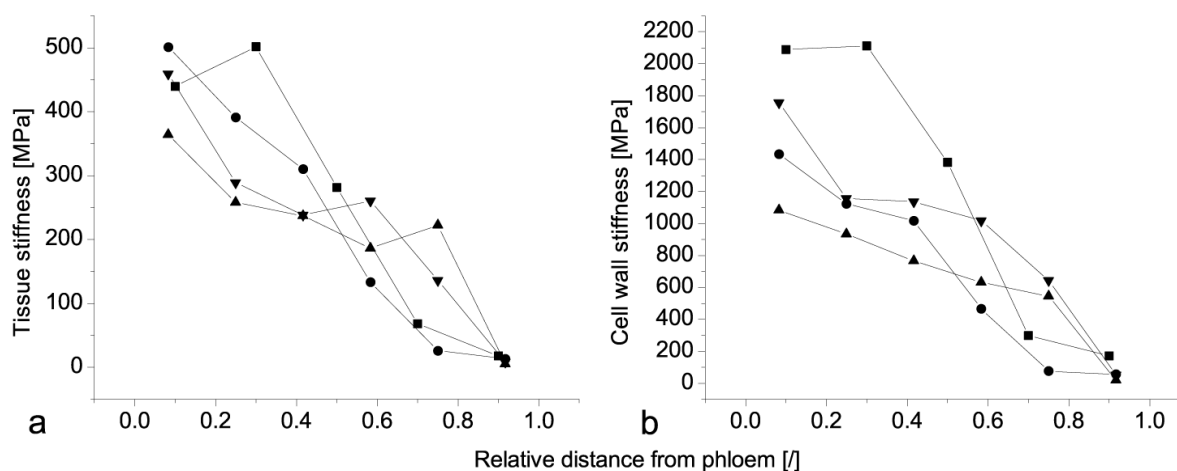


Fig. 3a) Tissue stiffness of fibre strips of four different fibre caps versus their radial position. b) Cell wall stiffness versus radial position, taken from [9].

The cell wall area fraction was taken as relative indication of tissue density which influences tissue stiffness. Values of cell wall area fraction decreased only slightly within the fibre caps with the exception of the very periphery of the cap, which exhibited much smaller values. This means that stiffness is varied mainly by alterations at the cell wall level, which is also obvious when comparing the course of tissue and cell wall stiffness across the cap.

X-ray diffraction measurements with single cell resolution revealed values for microfibril angle in the range of 12-40°. The high microfibril angle corresponded with the rather low stiffness compared to softwoods and hardwoods. The orientation is also consistent with the high extensibility of the tissue strips in the microtensile tests. Thus, on the ultrastructural level, the palms seem to be adapted to cope with large deformations under wind loads. No trend in microfibril orientation was visible across the fibre cap [9]. Therefore, in the palm species investigated the alteration in cell wall stiffness could not be correlated with the microfibril orientation which indicates that, the microfibril orientation is not used to alter mechanical properties within the fibre caps to create the gradient in stiffness.

However, cell wall stiffness could be correlated with the amount of lignification. A gradual decrease in lignification became visible across the fibre cap with the peripheral fibre cells being hardly lignified (Fig. 4). These variations at the biochemical level have most probably an effect on the shear modulus of the matrix, which in turn influences the longitudinal cell wall stiffness. These findings point to an additional concept of how plants control and change the stiffness of their tissues besides the well known strategy of changing the orientation of cellulose microfibrils in the secondary cell wall layers.

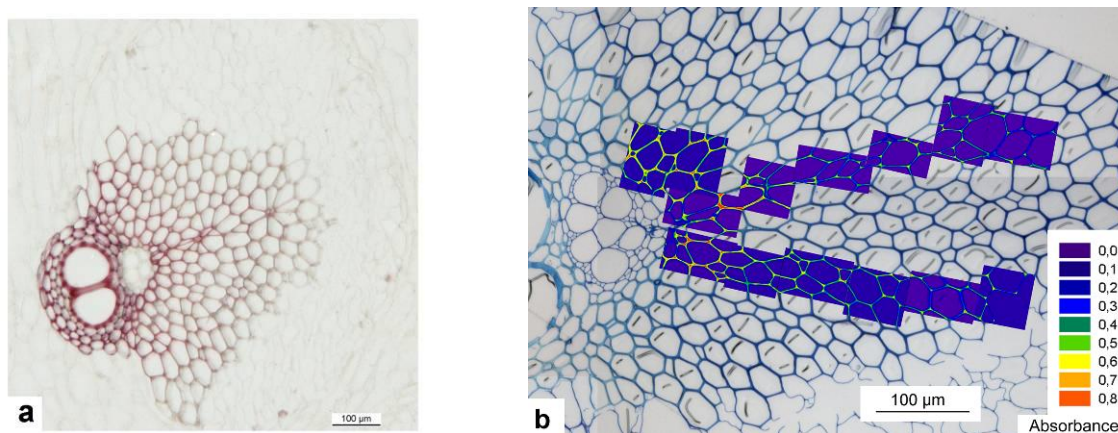


Fig. 4 Cross-sections of a vascular bundle a) stained with phloroglucinol/hydrochloric acid. b). Composite image of a toluidine blue stained cross section and 2D UV-absorbance scans taken of an unstained cross section at 262 nm. b) taken from [9].

The Giant Reed belongs to the grasses and possesses hollow culms of a few centimetres diameter growing to heights of 4-6 m. Hence, very high aspect ratios are reached which favours Euler buckling. The culms of the Giant Reed die after two years, whereas palms with their massive trunks can reach life times of more than a hundred years. Therefore it is likely to find a different strategy in coping with the stress discontinuities at the interfaces of sclerenchymatous and parenchymatous tissues.

The anatomy of *Arundo donax* points to an optimisation towards flexural stiffness on the integral and macroscopic level, yet in a different way than seen for the palm. As the culms of *A. donax* are hollow, several nodes stabilize the culm against buckling. The vascular bundles are evenly distributed throughout the culm wall (see Fig. 1b) and the culms are additionally stiffened by a sclerenchymatous ring at the periphery of the culm wall.

Spatz et al. [5] measured an elastic modulus of 10 GPa for the very periphery of the culm wall of *Arundo donax*, which is one order of magnitude higher than the values measured for *Washingtonia robusta*. For the inner part of the culm a modulus of 9 GPa was measured. However, Spatz and coworkers concluded that the differences between the sclerenchymatous fibres and the parenchymatous tissues are most likely bigger as numerous vascular bundles are embedded in the parenchymatous tissue. In contrast to *Washingtonia robusta*, a clear gradient in cell size and cell wall thickness can be seen in cross-sections, which results in a gradient in tissue density influencing tissue stiffness. Staining with phloroglucinol/hydrochloric acid revealed a lignification of the entire culm wall with a more intense staining in the sclerenchymatous ring and in the fibre sheaths of the vascular bundles (Fig. 5).

The high elastic modulus might be a contribution to lowering the risk of buckling in the case of the high aspect ratios as a result of the culm geometry. Such a high elastic modulus should be a result of a low microfibril angle. Assuming a gradual transition in stiffness between the sclerenchymatous ring and the (lignified) parenchymatous tissue, the mentioned aspects would point towards a different setting of the gradient compared to *Washingtonia robusta* and can therefore reveal additional concepts for certain geometrical and mechanical constraints.

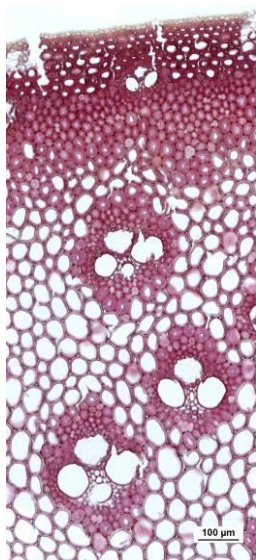


Fig. 5 Cross section of *Arundo donax*, stained with phloroglucinol/hydrochloric acid...

Conclusion

The embedding of stiff sclerenchymatous tissue in soft parenchymatous tissue is of particular interest from a biomechanics as well as biomimetics perspective. In palms, a combination of a high microfibril angle and a gradient in lignification seem to be responsible for the measured gradual decrease in stiffness across the fibre cap. This stiffness gradient is believed to be a key factor for the mechanical optimisation of palms under the given biological constraints. In *Arundo donax*, a gradient in cell wall area fraction within the sclerenchymatous ring in the periphery of the culm wall was found, which points towards a gradual transition in tissue stiffness. The insights into the design of

interfaces in the different plant species may serve as inspiration for a biomimetic transfer of the underlying principles to technical fibre-reinforced composites.

Acknowledgements

We thank the gardeners of the Botanical Garden of the University of Freiburg for cutting down the *Washingtonia robusta* palm and the Botanical Garden of Dresden for the petiole of a *Washingtonia robusta* palm.

We further like to thank Gerald Koch and Tanja Potsch from the Federal Research Institute for Rural Areas, Forestry and Fisheries (Hamburg, Germany) for the possibility of using the universal microspectrophotometer for the UV-measurements and for the embedding of the samples for these measurements.

We are grateful for the help of Stephan Siegel, Gundolf Weseloh and Chenghao Li at BESSY and the help of Oskar Paris in evaluating and discussing the X-ray data.

Markus Rüggeberg was funded within the scholarship programme “Biomimetics” (Stipendenschwerpunkt “Bionik”) of the German Federal Environmental Foundation (Deutsche Bundesstiftung Umwelt) which is gratefully acknowledged.

References

1. Rich, P.M., *Developmental Anatomy of the Stem of Welfia-Georgii, Iriartea-Gigantea, and Other Arborescent Palms - Implications for Mechanical Support*. American Journal Of Botany, 1987. **74**(6): p. 792-802.
2. Rich, P.M., *Mechanical Structure of the Stem of Arborescent Palms*. Botanical Gazette, 1987. **148**(1): p. 42-50.
3. Rich, P.M., et al., *Height and Stem Diameter Relationships for Dicotyledonous Trees and Arborescent Palms of Costa Rican Tropical Wet Forest*. Bulletin of the Torrey Botanical Club, 1986. **113**(3): p. 241-246.
4. Speck, T., N.P. Rowe, and H.C. Spatz, *Pflanzliche Achsen, hochkomplexe Verbundmaterialien mit erstaunlichen mechanischen Eigenschaften*, in *BIONA-report 10 - Akademie der Wissenschaften und Literatur Mainz*, W. Nachtigall and A. Wissler, Editors. 1996, Fischer-Verlag: Stuttgart. p. 101-131.
5. Spatz, H.C., et al., *Biomechanics of the giant reed Arundo donax*. Philosophical Transactions Of The Royal Society Of London Series B-Biological Sciences, 1997. **352**(1349): p. 1-10.
6. Spatz, H.C., et al., *Mechanical anisotropy and inhomogeneity in the tissues comprising the hollow stem of the giant reed Arundo donax*. Biomimetics, 1995. **3**(3): p. 141-155.
7. Speck, O. and H.C. Spatz, *Mechanical properties of the rhizome of Arundo donax L*. Plant Biology, 2003. **5**(6): p. 661-669.
8. Speck, O. and H.C. Spatz, *Damped oscillations of the giant reed Arundo donax (Poaceae)*. American Journal Of Botany, 2004. **91**(6): p. 789-796.
9. Rüggeberg, M., et al., *Stiffness gradients in vascular bundles of the palm Washingtonia robusta*. Proceedings of the Royal Society B-Biological Sciences, 2008. **275**(1648): p. 2221-2229.
10. Rüggeberg, M., T. Speck, and I. Burgert, *Structure-function relationships of different vascular bundle types in the stem of the Mexican fanpalm (Washingtonia robusta)*. 2009.
11. Burgert, I., et al., *Microtensile testing of wood fibers combined with video extensometry for efficient strain detection*. Holzforschung, 2003. **57**(6): p. 661-664.
12. Nakano, J. and G. Meshitsuka, *The Detection of Lignin*, in *Methods in Lignin Chemistry*, S.Y. Lin and C.W. Dence, Editors. 1992, Springer-Verlag: Berlin, Heidelberg, New York. p. 22-32.
13. Koch, G. and G. Kleist, *Application of scanning UV microspectrophotometry to localise lignins and phenolic extractives in plant cell walls*. Holzforschung, 2001. **55**(6): p. 563-567.
14. Niklas, K.J., *Dependency Of The Tensile Modulus On Transverse Dimensions, Water Potential, And Cell Number Of Pith Parenchyma*. American Journal of Botany, 1988. **75**(9): p. 1286-1292.

Comparison of Cell Wall Mechanical Properties of some *Arabidopsis thaliana* Mutants

Robert Palin¹, Jeremy Pritchard², Colin Thomas¹

¹School of Chemical Engineering, University of Birmingham

²School of Biosciences, University of Birmingham

Abstract

Mechanical properties of the plant cell wall are important in many industrial applications including bio-fuels, food quality and biotechnology. The plant cell wall consists of a network of cellulose microfibrils cross-linked with hemi-cellulose and interpenetrated by pectin. It is known that changes in the composition and architecture of the cell wall lead to detectable differences in the mechanical properties, but the relationship is not yet fully understood. In this work, three cell wall mutations of *Arabidopsis thaliana*, *IDA*, *Mur1* and *qua-2* (Snakeskin-SKS), were compared to the *Columbia* wild type (WT). Shoot and root growth were characterised to evaluate the effects of the mutations on plant growth. Cells were also grown in suspension culture and their viability determined by neutral red staining before the force required to break the cell (the rupture force) and deformation at rupture were obtained by compression testing. Compression testing showed significant differences in these mechanical properties between mutant and WT cells. These data, however, appear to conflict with those from whole plant growth. This may be because the rupture force and deformation at rupture are not intrinsic material properties of the cell wall or because cell wall characteristics of cells grown in suspension culture may differ from those in whole organisms.

Introduction

The plant cell wall is integral to the development of many modern industries, including bio-reactors, bio-fuels and food quality. Although much is known about cell wall composition, there remain gaps in the understanding about the link between wall composition, architecture and mechanical properties. The cell wall provides mechanical strength, mediates cell-to-cell adhesion and dictates cell dimensions (Martin *et al*, 2001). The composition of the cell wall has been well studied and consists mainly of polysaccharide chains (Nevins *et al*, 1967). Some aspects of the arrangement of these molecules within the cell wall are currently unknown, but many theoretical models have been proposed. The most popular is a layered model, with the elasticity, plasticity and strength functions in a primary cell wall composed of cellulose microfibrils cross-linked with hemi-cellulose fibers. Pectin penetrates this structure and also constitutes the middle lamella, which is thought to control cell-to-cell adhesion. The

pectin however, is not thought to have a role in determining the strength of the wall (Willats *et al.* (2001).

Changes in the composition of the cell wall components should yield differences in wall properties and functioning of the various wall layers. Plants with varying cell wall composition were obtained by using mutants of the Columbia (Col0) wild type (WT), with altered genes involved in cell wall biosynthesis. The different mutations used were IDA (Stenvik *et al.*, 2006) and *qua-2* (aka SKS) (Mouille *et al.*, 2007) which affect the middle lamella, and *Mur1* (Bonin *et al.*, 1997) which affects the hemi-cellulose in the primary cell wall and the pectin backbone in the middle lamella.

The effects of these mutations were determined by phenotyping growth at the whole organism level (Cosgrove, 2000) and single cell compression testing by micro-manipulation (Thomas *et al.* 2000). Single, viable, near-spherical cells were produced by suspension culture (Encina *et al.*, 2001). Compression testing has previously been used to calculate some intrinsic properties of cultured tomato cells (Wang *et al.*, 2004) but research was limited due to the lack of genetic understanding of this system. *Arabidopsis thaliana*, being the model organism for plants, represents a good candidate for compression testing since its genome is small and fully sequenced and many relevant genes have been identified.

Materials and Methods

All chemical purchased from Sigma Aldrich (UK) unless otherwise specified.

Whole plant phenotyping of cell wall mutants

For stems, seeds were sown in a soil vermiculite mix and subjected to a 16:8 hours light to dark cycle, with constant temperature and adequate water. Growth was scored over 35 days on various above ground characteristics. For roots, seeds were surface sterilised and placed at one end of a square petri dish containing a 0.5% Long Ashton agar supplemented with sucrose (10g/l). The plates were stood vertically and growth was scored every 24 hours until the first root reached the bottom of the plate. The longitudinal length of the roots cell moving back along the root from the root tip was measured using binocular light microscope with a $\times 40$ objective lens. To accurately measure the cells close to the root tip, it was squashed on a glass slide. The first 250 μ m could not be accurately measured due to cell density of the apical meristem. Cells in the root tip were measured over the first 3000 μ m, covering the majority of the zone of elongation.

Generation of suspension cultures

Sterile seeds were germinated on a basal MS (Murashige and Skoog) 4.4g/l, 30g/l sucrose and 0.2g/l myoinositol at pH 5.7. Roots were excised after 2 weeks and transferred to callus induction media (CIM) containing plant growth factors. Cytokinin and auxin in equal concentrations for cause the cell to divide without differentiation, 0.5mg/L Benzylaminopurine (BAP), 1mg/L naptaline acetic acid (NAA), 1mg/L indole-3-acetic acid (IAA), 1mg/L 2,4-Dichlorophenoxyacetic acid (2,4-D), 0.2g/l myoinositol, 4.4g/l MS media, 30g/l sucrose and adjusted to pH 5.7. The resulting callus was transferred after approximately 1 month into a liquid CIM and rotated at 120 rpm to prevent aggregation and promote single cell generation.

Microcompression

After 1 and 2 weeks in suspension culture, samples of single cells were compressed with the high strain rate tester (HSRT). A glass probe attached to a force transducer (400A, Aurora Scientific Inc, Canada) was positioned above the cell. Using the peizo-electric motor (peizostack) (PI, Germany) compression speeds of $3000\mu\text{m s}^{-1}$ were used to compress the cell, generating voltage/time traces for each compression. The voltage signals from the transducer were amplified using a $\times 10$ amplifier. From the voltage/time trace a force/displacement curve was calculated. The viability of the cell was shown by neutral red (NR) staining. NR is transported into the vacuoles of plant cells and will accumulate in those with membranes are intact thus highlighting viable cells suitable for compression. NR was added an hour prior to compression to a final concentration of $1 \times 10^{-6}\text{M}$.

Results and Discussion

Stem growth showed significant differences ($p > 0.05$) on several characteristics. The most prominent was the differences seen in stem high on days 30 and 35 (Fig. 1). IDA grew to comparable levels to *Col0* at both time points. *Mur1* showed a non-significant reduction ($p < 0.05$) at both time points, but SKS showed a significant difference at both time points to the WT.

Significant differences to *Col0* were seen in both root length (Fig. 2A) and growth rate (Fig. 2B) of SKS and *Mur1* mutations but not IDA, which remained similar to *Col0*. Root growth is determined by two factors, the extension of the roots in the elongation zone and the number of cell being produced in the meristem.

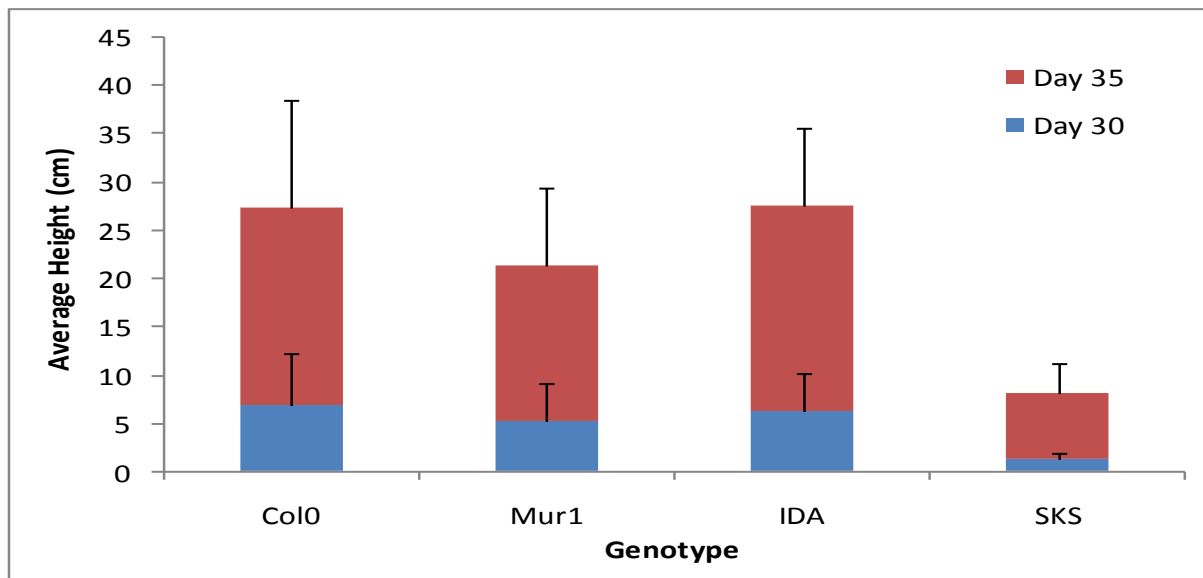


Figure 1. Average stem heights of the wild type and three mutants genotypes at 30 and 35 days. A significant increase in plant stem height is seen in all four samples between day 30 and 35. Error bars represent the SD. Three technical repetitions with 20 biological reps in each.

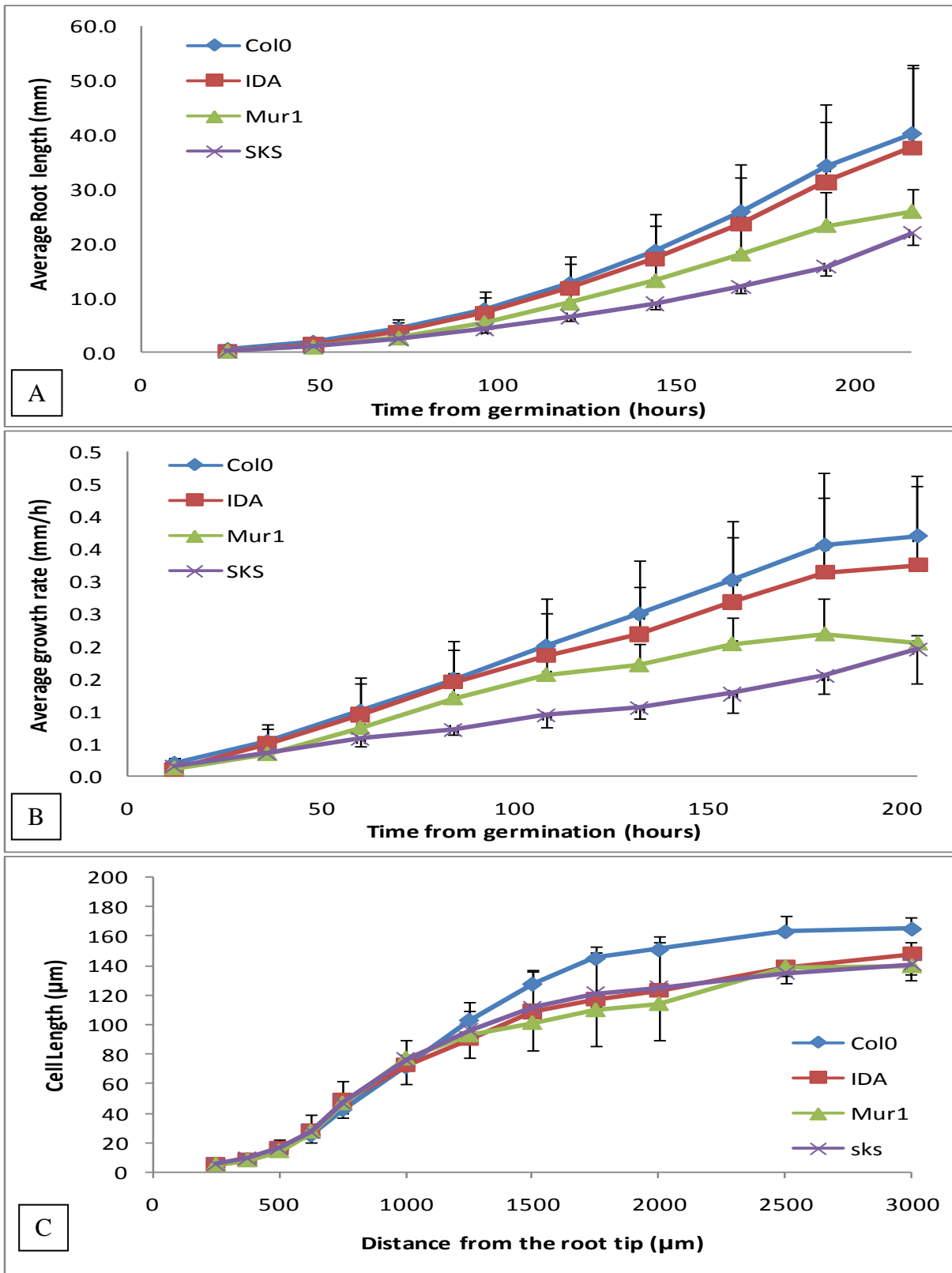


Figure 2. Average root length (A), average growth rate (B) and average longitudinal length of roots cells, moving backwards from the root tip (C) of *Col0*, *Mur1*, *IDA* and *SKS* genotypes. Error bars represent SD. 5 technical repetitions with 24 biological reps in each

When cell extension was analysed all mutant genotypes showed a significant difference in the proximal region of the elongation zone. (Fig. 2C) IDA was slightly lower than the *Col0* but remained higher than the other mutations but not significantly. No significant differences were seen in the distal region of the elongation zone until approximately 1000 μ m. It is hypothesized that cell production (assumed to be proportional to cell division) in the meristem is reduced in IDA compared to Col as the mature cell length was reduced but growth rate was unchanged.

Cell culturing techniques were successful in producing viable single cells suitable for compression testing by micromanipulation. Viable single cells (Fig. 3A) were easily identifiable from ghosts or plasmolysed cells. The latter lacked a visible vacuole after NR staining suggesting the lack membrane integrity. Such cells were not compressed (Fig. 3B).

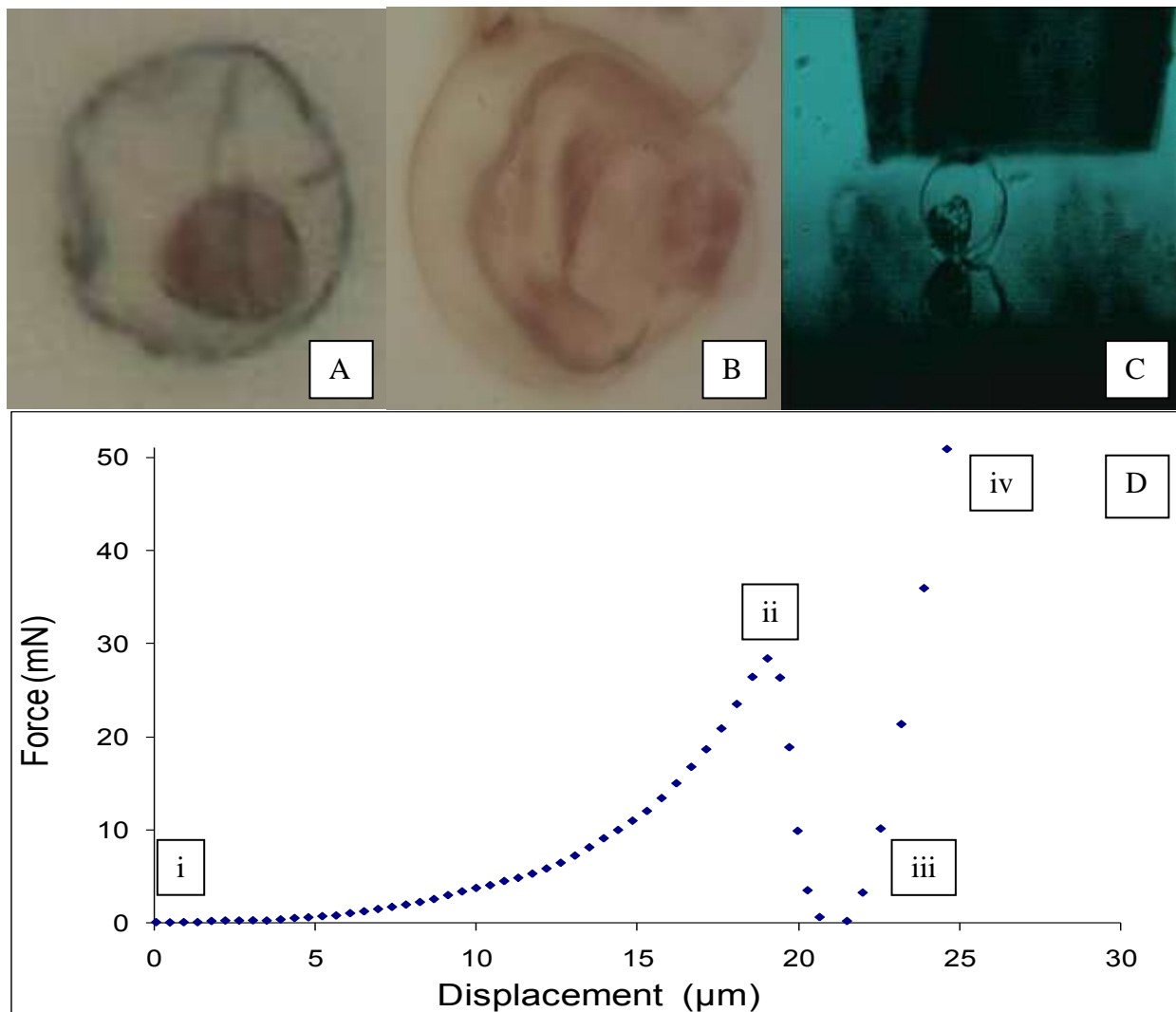


Figure 3. A viable single cell with an intact vacuole stained with NR, approximately 25 μ m in diameter (A). A plasmolysed non-viable cell with no membrane integrity, the plasma membrane has been pulled from the wall and the vacuole has been ruptured, approximately 30 μ m in diameter (B). The differences between A and B are clear enabling the identification of cells to be compressed. A still taken from the high speed video of a compression, a single NR stained cell (approximately 30 μ m in diameter) positioned under the glass probe prior to the movement of the probe (C). A force/displacement graph calculated for the compression of a single cell approximately 25 μ m in diameter. The point at which the probe touched the cell (i) the point of rupture (ii) the initial point at which the probe touched the chamber base (iii) and the diameter of the cell (iv) can be seen (D).

Viable single cells from suspension culture were compressed (Fig. 3C) and force/displacement graphs calculated (Fig. 3D). From each of these graphs, the point of rupture, displacement at rupture and diameter of the cell can be determined (Table 1). Cell diameters of *Col0*, IDA and SKS showed a decrease between weeks 1 and 2 with the opposite for the *Mur1*; these differences were not significant. Between the genotypes SKS and *Mur1* were similar to *Col0*, with IDA slightly smaller. *Col0* rupture forces increased between weeks 1 and 2, *Mur1* and IDA remained constant and SKS reduced slightly. Compared to the *Col0*, SKS was similar, IDA lower and *Mur1* higher. The percentage displacement at rupture showed decreases from week 1 to week 2 for *Col0*, *Mur1* and SKS but an increase for the IDA.

With the rupture force of SKS similar to *Col0*, this suggests that the reduction in pectin in SKS does not affect the wall strength. *Mur1* differences may be attributed to a decrease in tension in the cell wall causing an increase in cell wall deposition making it stronger, with the opposite being the case for the IDA.

Cells in suspension culture are not restricted in their maximum size by their proximity to other cells like those in the whole plant. Similarly, the cells are not influenced by where they are in the plant, which forces specific dimensions. Size and shape, therefore, are determined solely by 3-dimensional expansion driven by turgor pressure with no spatial or positional component. This may explain the similarities in the average cell diameter.

This change in growth conditions may also be attributed to the differences seen when comparing the single cells to those in the root or stem. However, it cannot account for those seen between the cultured cells, these must be real differences. The root and shoot growth data would have suggested that *Col0* and IDA would be stronger than *Mur1* and IDA, but the results from the compression do not support this. However, these parameters are not intrinsic material properties of the cell wall and can only be used as a preliminary marker for properties that might correlate with growth.

Genotype	Week	Cell Diameter (μm)	Rupture Force (mN)	Displacement at rupture (%)
<i>Col0</i>	1	26.8 \pm 5.3	1.1 \pm 0.6	59.6 \pm 16.8
	2	24.6 \pm 3.5	1.6 \pm 0.9	55.0 \pm 12.1
<i>Mur1</i>	1	25.4 \pm 6.8	1.4 \pm 0.9	65.3 \pm 13.3
	2	28.4 \pm 7.0	1.4 \pm 0.8	58.0 \pm 14.6
IDA	1	23.0 \pm 2.4	0.8 \pm 0.4	52.2 \pm 11.6
	2	22.7 \pm 0.7	0.8 \pm 0.2	56.2 \pm 10.5
SKS	1	26.8 \pm 2.7	2.0 \pm 1.4	59.0 \pm 12.0
	2	24.2 \pm 6.3	1.8 \pm 1.0	44.4 \pm 14.7

Table 1. Average cell diameter, rupture forces and percentage displacement at rupture for 1 and 2 week old suspension cultures of the WT and the three mutant genotypes analysed.

Conclusions

It is clear that the effects of changes in cell wall composition can be measured using several techniques. Data obtained from organ level measurements support each other. Root and shoot analysis show that two of the mutations, *Mur1* and SKS, experience significant growth reductions while the third, IDA, showed reduced growth at certain times but were mostly similar to *Col0*.

Suspension culture of *Arabidopsis thaliana* yields single viable cells that are suitable for micro-compression. It is clear from force/displacement data that differences exist between the genotypes. Some of the results, however, are not concordant with predictions drawn from plant growth data. It is possible that *A. thaliana* cells grown in suspension culture are not representative of those in the whole plant. Cultured cells may have different properties to those *in planta*, affecting the way they perform under compression testing. Unfortunately, due to the nature of plant cells it is impossible to extract representative single cells from the plant without damage; hence the reliance on cultured cells. To address these differences, an investigation into the effect of the culturing process on the cell wall must be undertaken. This will also enable a comparative study of the components present in each cell type of all genotypes.

Further to this, mathematical modeling should be applied to the compression data in an attempt to yield intrinsic values for the physical properties of the wall, for example the low strain elastic modulus. This would give a greater insight into the nature of cell wall mechanics at the molecular level and would enable individual influences for each of these mutations on the wall to be given a comparable value.

Acknowledgements

We would like to thank BBSRC for funding and Alan Marchant for his supply *qua-2* seeds.

References

- Martin C., Bhatt K. and Baumann K. (2001). Shaping in plant cells. *Current Opinion in Plant Biology* 4:540–549
- Nevins D.J., English P.D., and Albersheim P. (1967). The Specific Nature of Plant Cell Wall Polysaccharides. *Plant Physiol.* 42: 900-906.
- Carpita N., Tierney M. and Campbell M. (2001). Molecular biology of the plant cell wall: searching for the genes that define structure, architecture and dynamics. *Plant Molecular Biology* 47: 1–5.
- Willats W.G.T., McCartney L., Mackie W. and Knox J.P (2001). Pectin: cell biology and prospects for functional analysis. *Plant Molecular Biology* 47: 9–27.
- Stenvik G. *Et.al.* (2006). Overexpression of inflorescence deficient in abscission activates cell separation in vestigial abscission zones in *Arabidopsis*. *The Plant Cell*, 18: 1467–1476

Bonin C.P., Potter I., Vanzin G.F. and Reiter W.D. (1997). The *MURI* gene of *Arabidopsis thaliana* encodes an isoform of GDP-D-mannose-4,6-dehydratase, catalyzing the first step in the *de novo* synthesis of GDP-L-fucose. *Plant Biology* 94, 2085–2090.

Mouille, G. *Et al*, (2007). Homogalacturonan synthesis in *Arabidopsis thaliana* requires a Golgi-localized protein with a putative methyltransferase domain. *The Plant Journal*, 50: 605–614.

Cosgrove D. J. Expansive growth of plant cell walls (2000). *Plant Physiol. Biochem.*, 38: 109–124.

Thomas C.R., Zhang Z. and Cowen C. (2000). Micromanipulation measurements of biological materials *Biotechnology Letters* 22: 531–537.

Encina C.L., ConstantinM. and Botella J. (2001). An Easy and Reliable Method for Establishment and Maintenance of Leaf and Root Cell Cultures of *Arabidopsis thaliana*. *Plant Molecular Biology Reporter*, 19: 245–248.

Wang C. X., Wang L. and Thomas C.R. (2004). Modelling the Mechanical Properties of Single Suspension-Cultured Tomato Cells. *Annals of Botany* 93: 443-453.

Impact of selective extractives removal on micro and macromechanical properties of woody hemp core (chènevotte)

Rahime Bag, Johnny Beaugrand, Patrice Dole and Bernard Kurek

*INRA– UMR 614 Fractionnement des Agroressources et Environnement
2 Esplanade Roland Garros BP224 - 51686 REIMS*

Abstract

This work is a study of the mechanisms by which cell wall extractable molecules intervene on its cohesion during defibrization, particularly at *in situ* polymers viscoelastic properties. We aim at pointing out the impact of quantitative/qualitative modulation of extractive class compounds on the chain mobility of hemicelluloses and lignin, the two major cell wall matrix amorphous polymers, and on the breaking mechanisms of the sticks at the macroscopic level.

Introduction

Hemp (*Cannabis sativa* L.) is a wood like material used for the pulping process for paper making or for composites making (Rowell, Young et al. 1997). In hemp, the woody core (chenevotte) accounts for 70% of the hemp stem. Typically, the wood core contains 33–37% of cellulose, 16–20% hemicelluloses, 17–22% lignin. These high percentages of amorphous polymers are interesting for studying the interaction between the cell wall polymers.

Moreover, woody hemp core is also composed of small amounts of extractives, ash and silica at 1–5% (Bouloc 2006). According to works done before in the laboratory on poplar, extractives seem to have an important role in the cell wall cohesion (Meyer-Pinson, Ruel et al. 2004). Among the various factors which affect the mobility via the direct environment of the macromolecules, the effect of extractible was scarcely studied. Matsunaga (2000) has studied the effect of extractives in the cell wall. He observes that some extractives were acting as a plasticizer. Obataya and Norimoto (1999) also proved the change in mechanical relaxation of wood used for musical instrument (*Aroundo donax* L.) by removing water soluble extractives. Some authors suggest that mechanical properties of wood are dependent on extractives but no dedicated studies have been done on their nature and role in the cell wall.

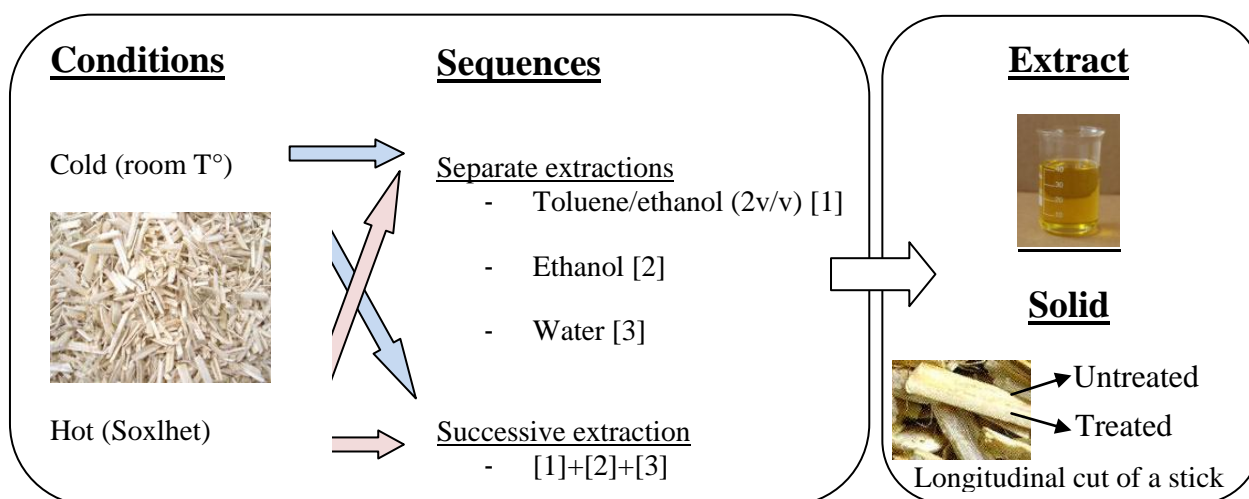
The objective of the work is to determine the mechanisms by which such cell wall extractable molecules intervene on its cohesion during defibrization, in particular hygrometric and temperature condition. With this study, we aim at pointing out the impact of quantitative/qualitative modulation of extractives on the chain mobility of hemicelluloses and lignin, the two major cell wall matrix amorphous polymers and on the breaking mechanisms of the sticks at the macroscopic level.

Material and methods

The samples studied were the cultivar Fedora 17 issued from the stem of hemp cultivated and refined according to the procedures of La chanvrière de l'aube (LCDA) in Bar sur Aube (France).

Extractions:

The removal of extractives was made by using three solvents (toluene/ethanol, ethanol and water) separately or successively (in the previous order) and at two temperature conditions (see scheme).



Biochemical analysis of the woody hemp core and their extracted products:

Carbohydrate analysis of chenevotte was performed using a high performance anion-exchange chromatography (HPAEC) after sulphuric acid hydrolysis.

Aromatic compounds content which are generally associated to lignin was measured spectrophotometrically (acetyl bromide method).

The Carbon and Nitrogen content of the samples was determined with an elemental analyzer (NA 1500, Carlo Erba).

The amount of soluble protein was determined colorimetrically (Bradford method).

The ash content in samples was determined by incinerating samples in a muffle furnace at 525±25 °C for three and an half hour according to (**Tappi T 211. om-07**).

The main minerals frequently associated with plant metabolism were identified and measured with an atomic emission spectrometer ICP (Varian Liberty series II).

DMA: the Dynamic mechanical analysis in tension mode and in immersion

DMA is the specific method used to characterize *in situ* lignin relaxation because the peaks observed in the range of 80-110°C are assimilated to their glassy transition (**Salmen, Wennerblom et al. 1996; Sun and Frazier 2007**) for the same conditions.

DEA: the Dielectric Analysis in controlled humidity

DEA is a specific method used to characterize *in situ* hemicelluloses chain mobility. The peaks observed are generally associated to the different relaxations of hemicelluloses (**William L. James 1975**) depending on frequency and relative humidity (**Lenth and Kamke 2001; Sugimoto and Norimoto 2005**).

Breaking mechanisms

4-point-bending test is the method used to characterize the fracture of woody hemp core sticks. From each curve obtained the breaking energy, modulus and strain were calculated. Experiments were done at water saturated condition and at different temperature to determine the optimized condition for the breaking study of extracted samples(**Bardet, Beauchêne et al. 2003**).

Results and discussion

Biochemical analysis:

In cold extractions, for each solvent used to remove entities, extractives in solvents vary in quantity but present similar quality. Less extractive are removed with Toluene and ethanol solvents, mainly

composed of carbon and lignins, whereas polar solvents specially remove protein, nitrogen and ash compounds.

In hot conditions, the extraction percentage with solvents becomes higher, even if lignin and protein contents are not influenced by thermal effect. Moreover, hot water enhances the monosaccharides extraction (twice more) and reduces the ash content (twice less) compared to cold condition.

Table 1 biochemical composition of extractives in different conditions.

	% of raw material ^a		In % of extractives ^b				
	Extraction	N	C	Protein	Total mono saccharide	Lignin	Ash
Cold Tet (1)	0.6	0.5	69.9	0.1	4.6	61.1	1.0
Cold Et (2)	0.6	0.8	61.7	0.2	9.2	65.8	10.1
Cold Water (3)	2.5	2.3	45.1	1.8	7.4	26.0	57.7
Cold Succ (1)+(2)+(3)	3.0	1.3	41.4	1.3	15.4	30.1	37.2
Hot Tet (1)	2.4	0.5	62.2	nd	5.1	64.0	2.2
Hot Et (2)	2.2	1.3	51.6	0.2	11.1	69.0	7.8
Hot Water (3)	2.6	1.5	30.1	1.3	15.3	27.4	36.2
Hot Succ (1)+(2)+(3)	5.0	0.9	49.3	0.9	7.7	52.8	27.6

^a in percentage of the initial dry woody hemp core mass sample

^b in percentage of the total mass of extractives removed from woody hemp core samples

Viscoelastic properties:

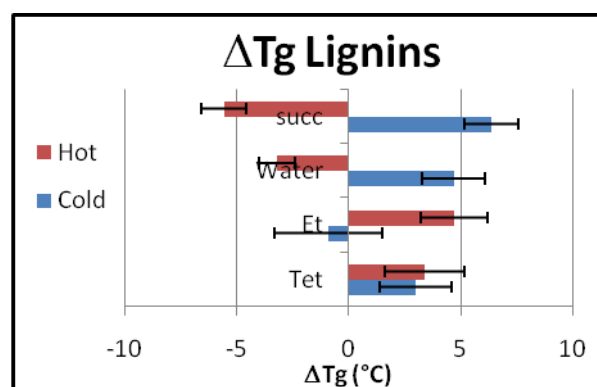


Fig. 1 Influence of solvent on ΔT_g lignin.

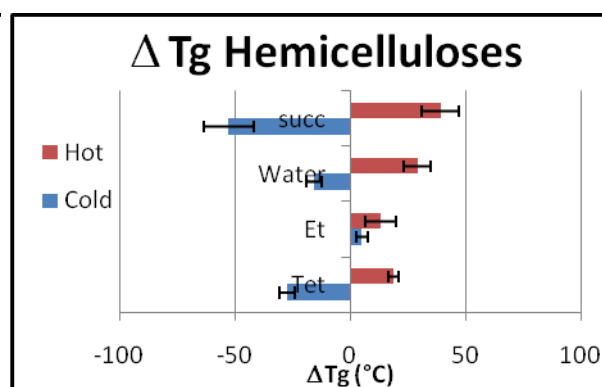


Fig. 2 Influence of solvent on ΔT_g hemicelluloses.

ΔT_g is expressed as the difference calculated from the untreated reference and the treated sample.

For both polymer relaxations, each solvent has a specific effect on the shift of glass transitions. Hemicelluloses are much more affected by the extractions (shift up to 40 °C) whereas lignin have smaller changes (the measures were done in ethylene glycol immersion therefore the effect of extraction can be smoothed). In nearly every case, hemicelluloses with hot extractions have an opposite behavior to cold extractions. Whereas for lignin, only extractions integrating hot water lead to a decrease of Tg values.

Correlations between ΔT_g /extractions:

Looking the evolution of ΔT_g with the extraction rate, the entities removal clearly affects the mobility of the two amorphous polymers. The bigger is the extraction level, the higher is the difference in glass transition temperature either in the two evolution senses (positive or negative sign of ΔT_g).

Absolute value of ΔT_g is highly correlated with extraction percentage, their calculated index for lignin and hemicelluloses are 0.75 and 0.58 respectively.

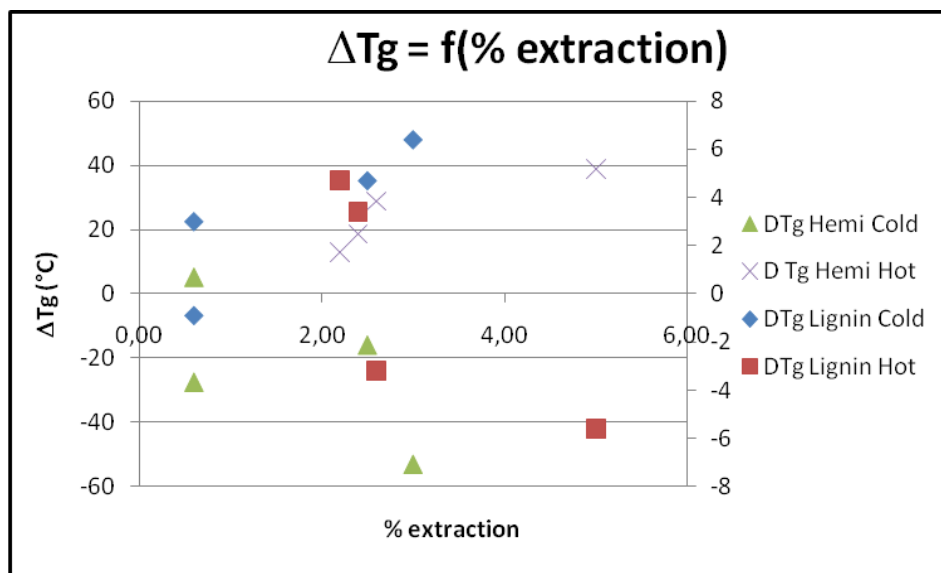


Fig. 3 Influence of extraction percentage on ΔT_g lignins and hemicelluloses.

Four-point-bending test :

Fracture behavior versus temperature of characterization:

These experiments describe the load-displacement curves and the influence of temperature on mechanical criteria. Strain and modulus vary on the same way (diagram 4 and 5), both of them decrease. We can note a drastic change of the mechanical properties which can be explained by the glassy transition of one continuous polymeric constituent of wood: lignin (Bardet, Beauchêne et al. 2003). This value seems to be around 55°C.

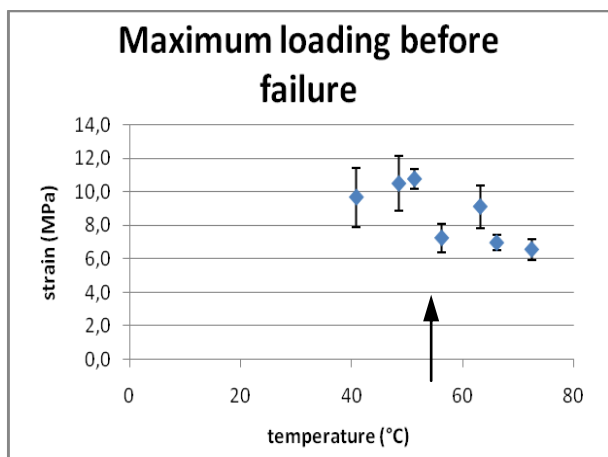


Fig.4 Strain vs temperature.

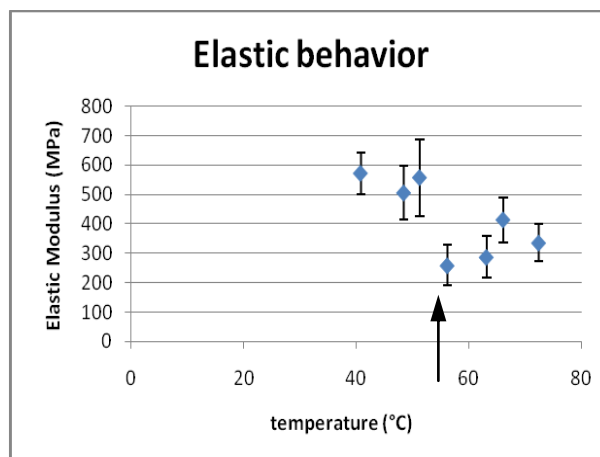


Fig. 5 Elastic modulus vs temperature.

These preliminary experiments were necessary to find the best measuring condition close to T_g lignins and to be able to observe little changes in mechanical properties after extraction.

Indeed, when measuring the T_g with DMA, the nature and frequency of solicitation is different. In water saturated condition for a raw material, T_g lignin is ~ 70°C (1Hz on loss modulus). The measured activation energy is around 170 kJ/mol. If we do the same calculation with the 3-point bending test, taking into the frequency change, we found theoretically a T_g value near 57°C which is in accordance with the one we found above experimentally.

Difference in mechanical properties between treated and non-treated specimens

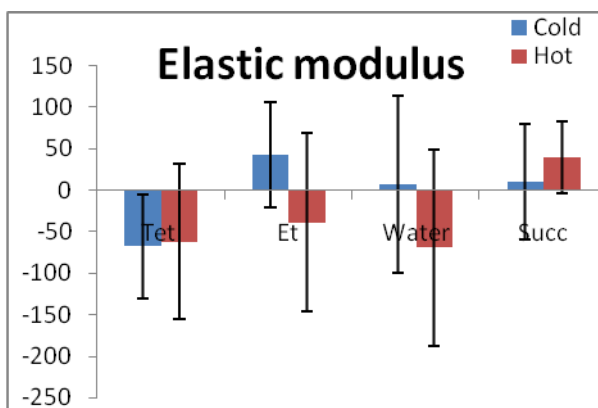


Fig.6 Influence of extraction solvent and temperature on ΔE .

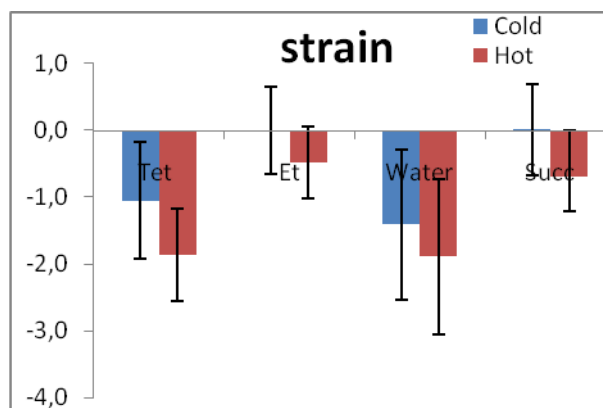


Fig.7 . Influence of extraction solvent and temperature on $\Delta strain$.

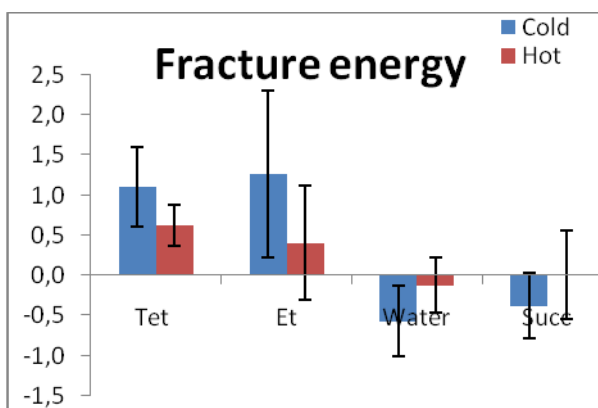


Fig 8 Influence of extraction solvent and temperature on $\Delta fracture energy$.

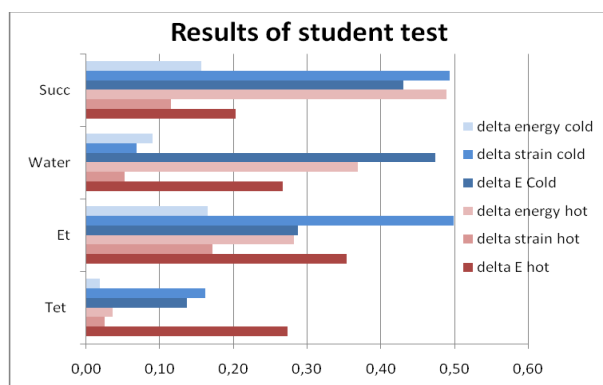


Fig 9 Probability coefficients from student test for each mechanical properties.

These first results (Fig 6 to 8) show that all properties measured in different experimental condition tested have important variation for a same condition, leading to no clear significant different observation, unless for some series. To better see the difference in average values, student tests have been processed (Fig 9). If we consider the probability to have a distinct mean value for the two series with a reasonable limit confidence value of 0.1, only water and Tet extraction conditions have significantly different mechanical behavior for some properties: Cold water changes strain and breaking energy into lower values, whereas hot water changes only strain to a lower value. Cold Tet changes breaking energy into a higher value and hot Tet changes breaking energy to higher and strain to lower values.

Conclusion

Extractions clearly lead to a consequence on the different properties of woody hemp core in micro and macro scale. We have seen more or less intense different viscoelastic behavior highly correlated with extractives solvation. And we have also notified changes in mechanical behaviors which were in some case smoothed by the characterization condition happening in water at 55°C.

Studying samples as pairs of specimen is of course a way of reducing natural variability but it also have its limit while looking for specific parameters as the elastic modulus. This last characterization of breaking type must be optimized by coupling with microscopic observation of the failure surface. Some kind of properties which cannot be quantified by measurement can be observed visually. Failure propagation is still under investigation to explain difference behavior of cell wall extractive removal.

Acknowledgements

We would like to thank INRA and the Region “Champagne-Ardennes” for their financial support.

References

1. Bardet, Beauchêne, et al. (2003). Influence of basic density and temperature on mechanical properties perpendicular to grain of ten wood tropical species. *Annals of Forest Science* 60(1): 49-59.
2. Bouloc, P., Ed. (2006). *Industriel Hemp Production and Uses*.
3. Lenth, C. and F. Kamke (2001). Moisture Dependent Softening Behavior of Wood. *Wood and Fiber Science* 33(3): 492-507.
4. Matsunaga, M., E. Obataya, et al. (2000). Working mechanism of adsorbed water on the vibrational properties of wood impregnated with extractives of pernambuco (*Guilandina echinata* Spreng.). *Journal of Wood Science* 46(2): 122-129.
5. Meyer-Pinson, V., K. Ruel, et al. (2004). Oxalic acid: a microbial metabolite of interest for the pulping industry. *Comptes Rendus Biologies* 327(9-10): 917-925.
6. Obataya, E. and M. Norimoto (1999). Mechanical relaxation processes due to sugars in cane (*Arundo donax* L.). *Journal of Wood Science* 45(5): 378-383.
7. Rowell, R. M., R. A. Young, et al., Eds. (1997). *Processing of Agro-Based Resources into Pulp and Paper*. Chapter in composites from Agro-based resources.
8. Salmen, Wennerblom, et al. (1996). Softening properties of earlywood and latewood of spruce. *Nordic Pulp and Paper research journal* 4: 279-280.
9. Sugimoto, H. and M. Norimoto (2005). Dielectric relaxation due to the heterogeneous structure of wood charcoal. *Journal of Wood Science* 51(6): 554-558.
10. Sun, N. and C. E. Frazier (2007). Time/temperature equivalence in the dry wood creep response. *Holzforschung* 61(6): 702-706.
11. Tappi T 211. om-07 Ash in Wood, Pulp, Paper and Paperboard: Combustion at 525 Degrees C.
12. William L. James (1975). Dielectric properties of wood and hardboard: variation with temperature, frequency, moisture content, and grain orientation. *USDA Forest Service Research Paper FPL 245*.

Is interlocked grain an adaptive trait for tropical tree species in rainforest ?

Pierre Cabrol¹, Jacques Beauchêne¹, Bernard Thibaut²

1^() CIRAD, UMR “Écologie des Forêts de Guyane”, 97310 Kourou, French Guiana*

2 CNRS, UMR “Écologie des Forêts de Guyane”, 97310 Kourou, French Guiana

Abstract

Many trees in tropical rain forest exhibit interlocked grain. This phenomenon was observed, using a splitting method, on 10 trees from different genera in French Guiana. There were rather strong variations between and within trees. Different indexes were used and compared to describe this interlocked grain. Previous results have shown that the rupture energy necessary to create a radial-longitudinal surface by wood splitting grows more than 2 or 3 times with interlocked grain occurrence. Moreover, radial splitting of large tropical trees with high density wood is more prone to appear due to the decrease of the ratio between rupture energy and Young’s modulus when wood density increases. Finally the long lasting high level of maturation stress in tropical trees growing in primary forest means a very high level of stored elastic energy in the trunk that could be dangerous for the living tree. Interlocked grain can be a good solution to prevent the risk of radial splitting for these adult trees.

Introduction

Interlocked grain (IG) is a particular structure of wood present in a great number of tropical species. It is formed when the grain inclination changes from S or Z helix to the opposite slope during growth (Fig1.A). Due to differences in absorption and reflection of light, bands appear on the radial plane of IG wood, often called ribbon wood [5]. These bands are not always aligned with the longitudinal direction, due to a combination of interlocked and wavy grain (Fig1.B).

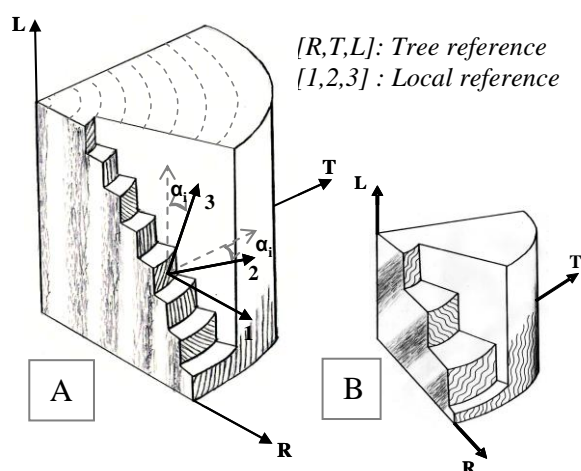


Fig1. A - B

*A: Principle of interlocked grain (IG).
The grain direction changes during the tree growth and make an angle α_i with the longitudinal direction with oscillate on the radius. Bands appear on the radial plane, often called ribbon wood.*

*B: Principle of IG coupled with wavy grain.
During the growth the global direction of the grain make an angle with the longitudinal direction of the tree, and a wavelength of few millimetres to many centimetres in length.*

According to Kribs (1950) cited by Hernandez and Almeida [6], 75% of 258 tropical trees analyzed had IG. Several theories have been considered for the genesis of spiral or IG. Détienne [4] observed on

** Present address: LERFOB “Laboratoire d’Etude des Ressources Forêt-Bois »
AgroParisTec/ENGREF/INRA, 54000 Nancy, France*

Faro (*Daniellia spp.*), which has a storied cambium, a small IG with a period of some millimeters and an amplitude lower than 10°. He showed that every oscillation fitted with one vegetative year, implying that the period is a function of growth speed in the case of Faro. He tried to explain the change of grain direction by some constant radial rearrangement between the cambial cells of one storey, in relation to the adjoining storeys. But he didn't explain the origin of the phenomenon. According to Kojs & al. [7], who has worked on the history of cellular events in the storied cambium of *Lonchocarpus sericeus* (Poir.) DC, the parenchyma arrangement is constant, but the cells' orientation varies quickly with IG. He observed a tangential intrusion on the top of cells during the periclinal division, which takes part in the change of direction. Schulgasser and Witztum [10] showed with a mechanical approach that the spiral angle of the grain could be formed during the process of cell division and maturation in the cambial region. They tried to explain this phenomenon by the evolution of microfibril angle (MFA) between juvenile and adult wood, along with the senescence phases in the case of older trees. The microfibrils apply a shear on the cells, inducing a tendency to twist. He suggested that trees with straight grain block this effect and avoid twisting, while spiral trees do not. In a previous work, Brémaud & al. [2] have measured MFA in relation with grain angle on an IG species (*Pterocarpus soyauxii* Taub.). We observe a tendency of MFA to decrease with increasing grain angle, but the variations are not clearly synchronous (grain angle variation of 40° against MFA variation of 8°). Anyway, the issue of the IG formation seems to remain open.

In this study, we have observed the diversity of IG in ten French Guiana species and address the following question: how does wood IG benefit to the tree?

Material and methods

Ten trees from 10 different species were collected from the tropical rain forest of French Guyana (Table 1). Several methods exist to describe the IG in a tree. The two most used are anatomical successive cuts in the TL plane [4, 7]; and the radial splitting [13, 6, 12, 5]. For reasons of availability, we chose to use the method of radial splitting, with image analysis in the software ImageJ. After splitting, Webb [13] or Hernandez and Almeida [6] measured two parameters to describe and characterize the IG: the maximum angular deviation (MAD) in degrees, estimated as the maximum left spiral angle plus the maximum right spiral angle, and the interlocked grain index (IGI) in millimeters, calculated by dividing the area between the projection of the median radial line EF and the tracing resulting of the split, by the length of the line EF (Fig2).

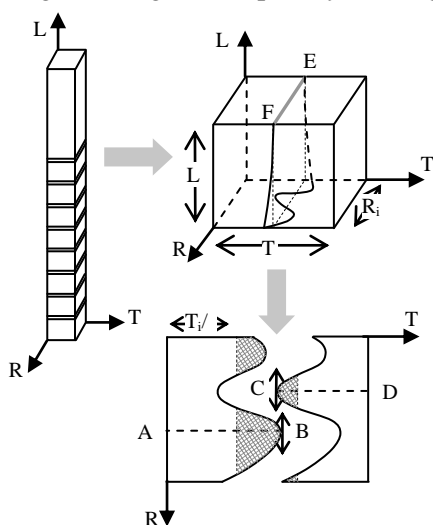


Fig 2. Protocol on cubes splitting and measurements done. The maximum angular deviation (MAD) in degrees, and the interlocked grain index (IGI) in millimeters.

Between 5 and 9 cubes have been machining on the longitudinal direction for each species.

$$\text{MAD} = \text{Atan} \left(\frac{AB - T_i/2}{L_i} \right) + \text{Atan} \left(\frac{CD - T_i/2}{L_i} \right)$$

$$\text{IGI} = \frac{\text{Atched area}}{R_i}$$

The measurements of the radial Young's modulus (E_R) and rupture energy were made on 10 French Guiana species of various densities as described in Bardet & al [1], the method to measure the rupture energy is describe in Beauchêne [3].

Results and discussion

A strong relationship was found between the two IG parameters (MAD and IGI) with a R^2 of 0.81 for the whole sample. This is in agreement with the observations by Hernandez and Almeida [6] and Webb [13]. It is important to note the strong variability of IG between trees and species. Table 1 summarizes the IG types. Some species, such as *Dipteryx odorata* or *Tabebuia* sp. have a small IG with a period of a few millimeters and amplitude of 2 or 3°. At the opposite *Parkia nitida* or *Erisma uncinatum* have a large IG with a period of about 50mm and small amplitude of 2 or 3°.

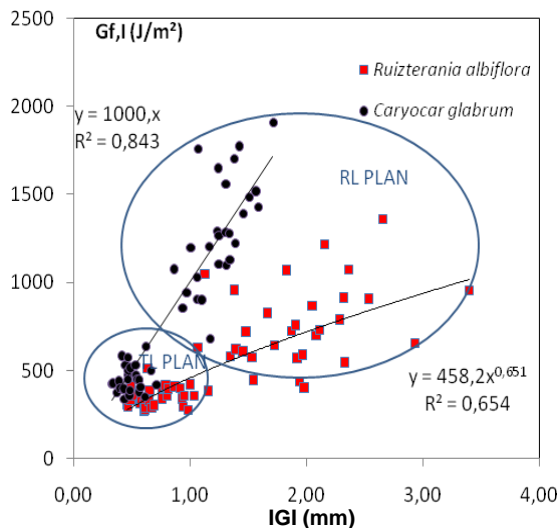


Fig3. Evolution of rupture energy in TL and RL planes against IGI for 2 species with large interlocked grain

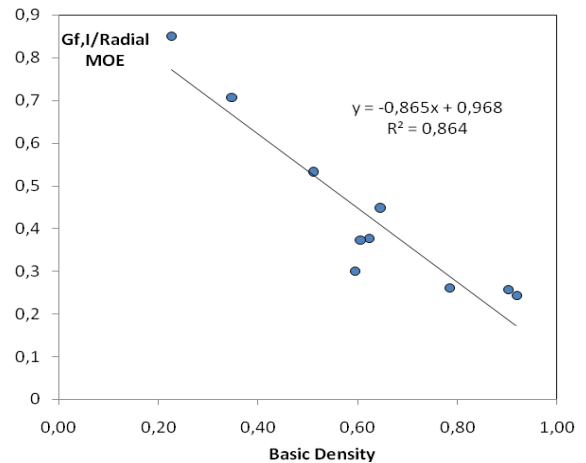


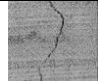

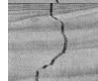


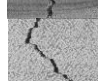
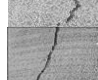



Fig4. Evolution of the ratio: rupture energy radial MOE equivalent against Basic Density for ten French Guiana species

The rupture energy Gf,I necessary to create a radial-longitudinal surface by wood splitting increases when the rupture changes to the tangential-longitudinal plane due to IG occurrence. As we show in Fig3, the effect of the IG plays a great role in the level of rupture energy, for 2 species with relative similar visual IG *Qualea rosea* and *Caryocar glabrum*, the values of Gf,I is around 2 times greater in the RL plan that in the TL plan for *Ruiztenaria* and around 3 times greater for *Caryocar*. The influence of the IGI on the rupture energy is very different for the two species, suggesting a more complex influence of the micro rupture in the middle lamella between the two species.

The rupture energy Gf,I necessary to create a radial-longitudinal surface by wood splitting increases with the density of the wood species [3], but much less than E_R as shown in Fig4, the slope of the ratio $Energy/E_R$ decreases significantly as wood density increases, which means that the denser the wood, the higher the radial splitting risk.

Therefore, the trees of high wood density (basic density above 0.6) are more sensitive to radial splitting. As the mean basic density of sapwood for 555 French Guiana species by Saramento & al [11] is 0.63; this could be a good reason to explain the frequency of IG in tropical families.

Table 1. Summary of the ten species studied, the splitting cubes and showdown between the mean MAD and IGI indices, (COV % is the coefficient of variation, and ROV the range of variation)

Pilot name (Botanical Name)	Number of cubes	MAD (°)		IGI (mm)		Picture	Remarks
		(ROV)	(COV)	(ROV)	(COV)		
Tatajuba (<i>Bagassa guianensis</i>)	8	15,2 (3,7)	(7%)	2,8 (0,6)	(7%)		IG constant on the longitudinal axis + IG similar between different trees
Cupiuba (<i>Goupia glabra</i>)	9	15,8 (11,1)	(24%)	2,5 (2,4)	(35%)		Interlocked and wavy grain important but irregular + important variations on the longitudinal axis
Timborana (<i>Pseudopitadenia suaveolens</i>)	8	15,9 (7,6)	(17%)	2,9 (1,3)	(15%)		Specific growth of the cambium + variation on L
Faveira (<i>Parkia nitida</i>)	8	7,2 (1,0)	(4%)				Small MAD and long period (about 50mm)
Cumaru (<i>Dipteryx odorata</i>)	5	11,9 (7,4)	(24%)				Interlocked and wavy grain + small period and MAD + very little fissile
Mandioqueira (<i>Ruizterania albiflora</i>)	7	16,3 (9,5)	(22%)	2,8 (1,3)	(20%)		Important interlocked and wavy grain
Satine (<i>Brosimum rubescens</i>)	7	12,9 (5,4)	(15%)				Variation between trees often important
Ipe (<i>Tabebuia sp.</i>)	9	6,1 (5,9)	(30%)	0,9 (1,4)	(48%)		small period and MAD + Link between interlocked and growth rings
Jaboty (<i>Erisma uncinatum</i>)	9	4,3 (6,1)	(55%)				Little MAD and long period
Araracanga (<i>Aspidosperma sp..</i>)	7	11,1 (6,9)	(21%)	1,8 (0,8)	(18%)		Important variability along the radius + important variation on L but no wavy grain

Conclusion

There is a very important variability of IG (form, wave and angle) between the species observed. Thus, it is difficult to correlate directly the geometrical characteristics and the amplitude of the IG to the real advantage for the radial cohesion of the wood. Nevertheless, the presence of the IG causes a systematic increase of the rupture energy necessary to create a radial-longitudinal surface.

The long-lasting high level of maturation stress in tropical trees growing in primary forest results in a very high level of stored elastic energy in the trunk that could be dangerous for the living tree [9]. Interlocked grain can be a good solution to prevent the risk of radial splitting for these adult trees.

So, given the fact that a lot of tropical trees species present interlocked grain, it may be reasonably assumed that it presents a significant environmental benefit. Rudinski and Vite (1959), quoted by Webb [13], developed the theory that the interlocked grain improves the distribution of water from the roots to the crown. Détienne [4] also supported this hypothesis.

The most significant disadvantage is in the domain of woodworking. Webb [13] noted some significant problems, such as torsion, or lifting, when machining veneer or furniture. But it is also a feature sought after for its aesthetic appearance. On the radial plane, bands appear due to differences in absorption and reflection of light. They are often call “ribbon wood”. Some interlocked species are used in woodworking, and considered as “noble woods”, like the Satiné / Bloodwood (*Brosimum rubescens*), or African Mahogany (*Khaya spp.*) for African species.

Acknowledgements

We thank all members of the Laboratory of Wood Sciences of CIRAD who participated in field and laboratory collection and treatment of specimens.

References

1. Bardet S., Beauchêne J., Thibaut B. (2003), Influence of basic density and temperature on mechanical properties perpendicular to grain on ten tropical species », *Annals of Forest Science*. 60 (2003) p. 49-59
2. Beauchêne J. (1996) Evolution du comportement mécanique du bois vert avec la température : application à l'étude du déroulage de quelques bois guyanais *Doctorat de l'ENGREF en sciences du bois*, Kourou.
3. Brémaud I., Cabrolier P., Gril J., Clair B., Gérard J., Minato K, and Thibaut B. (accepted 2009), Identification of anisotropic vibrational properties of Padauk wood with varying grain angle, *Wood Science and Technology* (accepted under minor revisions).
4. Détienne P. (1979). Contrefil à rythme annuel dans les Faro, *Daniellia* sp. *Bois et Forêts des Tropiques*, n°183
5. Hejnowicz, Z. and Romberger J. A. (1979). The common basis of wood grain figures is the systematically changing orientation of cambial fusiform cells. *Wood Science and Technology* 13: 89-96.
6. Hernandez, R.E. and G. Almeida. (2003). Effects of wood density and interlocked grain on the shear strength of three Amazonian tropical hardwoods. *Wood and Fiber Sci.* 35(2): 154-166.
7. Kojas P. Wloch W. Rusin A. (2004) Rearrangement of cells in storeyed cambium of *Lonchocarpus sericeus* (Poir.) DC connected with formation of interlocked grain in the xylem. *Trees* 18:136-144
8. Ogata Y. and Fujita M. (2005). New anatomical method of grain angles measurement using confocal microscopy and image cross-correlation. *Trees* 19: 73-80

9. Ruelle J., Beauchene J., Thibaut A. & Thibaut B. 2007 Comparison of physical and mechanical properties of tension and opposite wood from ten tropical rainforest trees from different species, *Annals of Forest Sciences*, 64 (5): 503-510
Schulgasser K. and Witztum A. (2006). The mechanism of spiral grain formation in trees. *Wood Science and Technology*. 41(2): 133-156.
10. Saramento C., Patino S., Paine C.E. T, Beauchêne J., Thibaut A., Baraloto C. (2009); Wood density in tropical trees, Within-individual variation in tropical tree wood density (*Submitted*).
11. Thinley C., Palmer G., Vanclay J.K., and Henson M. (2005). Spiral and interlocked grain in *Eucalyptus dunnii*. *Holz als Roh- und Werkstoff* 63: 372-379.
12. Webb C.D. (1969). Variation of interlocked grain in Sweetgum. *Forest Products Journal* Vol. 19, No. 8.

Ultrasonic device for the imaging of green wood

Loïc Brancheriau¹, Philippe Gallet¹, Patrice Thaunay¹, Philippe Lasaygues²

¹ Agricultural Research Centre for International Development CIRAD, France; ² Laboratories of Mechanics and Acoustics LMA, France

Abstract

Wood is a biological and natural growth-medium. This medium is orthotropic and its production varies in response to environmental conditions, and obviously, according to tree age. As such, variations in material properties are much more complex than anisotropy. For standing trees, numbers of auscultation tools are available and marketed. The objective of the BioGMID project is to create an efficient and optimized procedure for characterization and cross-sectional imaging of standing trees based on ultrasonic and X-ray imaging. An ultrasound measurement suitably combined with an X-ray measurement should allow a qualitative and quantitative high-resolution analysis of the structure. This article reports the development of a specific ultrasonic imaging device which can be used in tropical forest plantations. Fast characterization of plantation trees could be a useful tool for clonal selection and genetic improvement.

Introduction

Non-destructive techniques based on X-rays or acoustic waves were developed and adapted to wood material from the 1960s [2]. The main acoustical tomographic devices such as “Picus Sonic” [6, 7] and “Fakhopp 2D” [3] and Arbotom [4, 5], are based on speed-of-sound measurement throughout the cross-section. A limitation of these tools is that only the transmitted waves are exploited and the dominant parameter measured is only the velocity of the longitudinal waves, which is an important parameter, but not sufficiently sensitive to identify different layers and properties. An improved measure would be based on both diffraction and transmission measurements of ultrasounds. The use of diffraction allows qualitative imaging like *echography*. The transmission wave analysis allows the local assessment of specific modulus and internal damping (quantitative imaging).

The research project BioGMID (Biological Growth Medium Integrity Diagnoses using bi-modality tomographies) relates to the development of a methodological tool based on X-ray and ultrasound computed tomographies. Firstly, a qualitative approach may be applied to characterize the integrity of multi-scaled materials, and secondly, a quantitative approach may be applied to assess physical properties (density, atomic effective number, elastic stiffness constants). This project provides an enhanced knowledge of wave/medium interaction phenomena. This article is focused on the ultrasonic aspect of the project, particularly the development of a specific ultrasonic device for the imaging of standing trees.

Methodology of conception

Our objective is to develop a specific ultrasonic imaging device which can be used in tropical forest plantations. We believe that non-destructive characterization of plantation trees, in terms of mechanical behavior and also in early detection of internal deterioration, could be a useful tool for clonal selection and genetic improvement.

The main requirements for the tomographic device were:

- Weight between 10 and 20kg.
- Assembly done in few minutes.
- Use of battery power supply.
- Trunk diameter between 15 and 50 cm.
- Two ultrasonic sensors should be moved around the tree separately.
- Optimal scanning time was between five and 10 minutes (depending on the image resolution).

The conception and production of the device were made at CIRAD during one year. The production process is not yet achieved. The mechanical parts were designed using computer-aided design software, so that a virtual device was first built to verify its functionalities compared with the requirements. The electronic parts were also designed at CIRAD including the square impulse generator, the analogic to digital converter, the specific data storage and the control card with its specific driver for the automatic scanning process.

Results

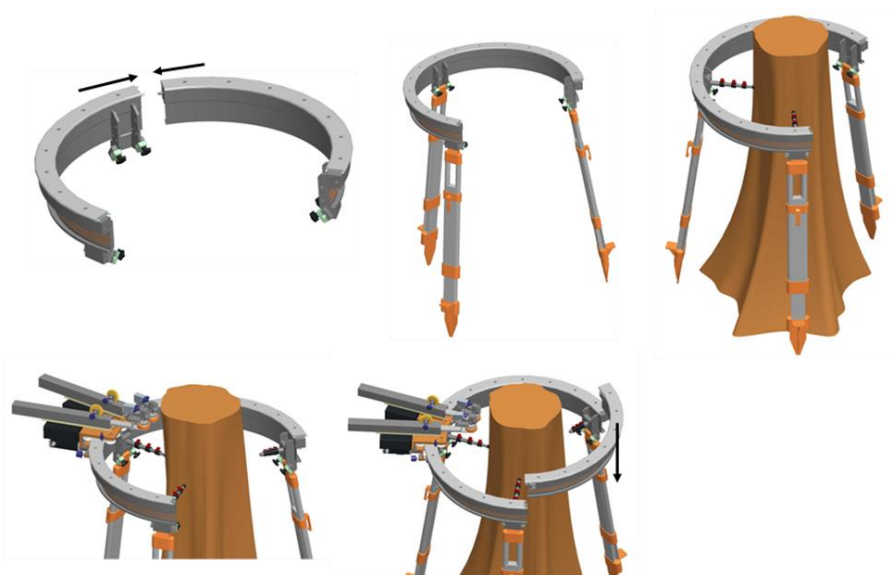


Fig. 1 Schematic view of the device assembly.

The device consists of an aluminum ring supported by a tripod (Fig 1). The height of the ring can be adjusted from 1 m to 1.6 m but the typical height is 1.3 m. The two parts of the ring are first assembled, and then the tripod is fixed. The apparatus is then placed against the trunk using two narrowing elements. Each probe is mounted on a trolley and these trolleys are slipped within the ring. Finally, the last part of the ring is fixed and the third narrowing element is applied.

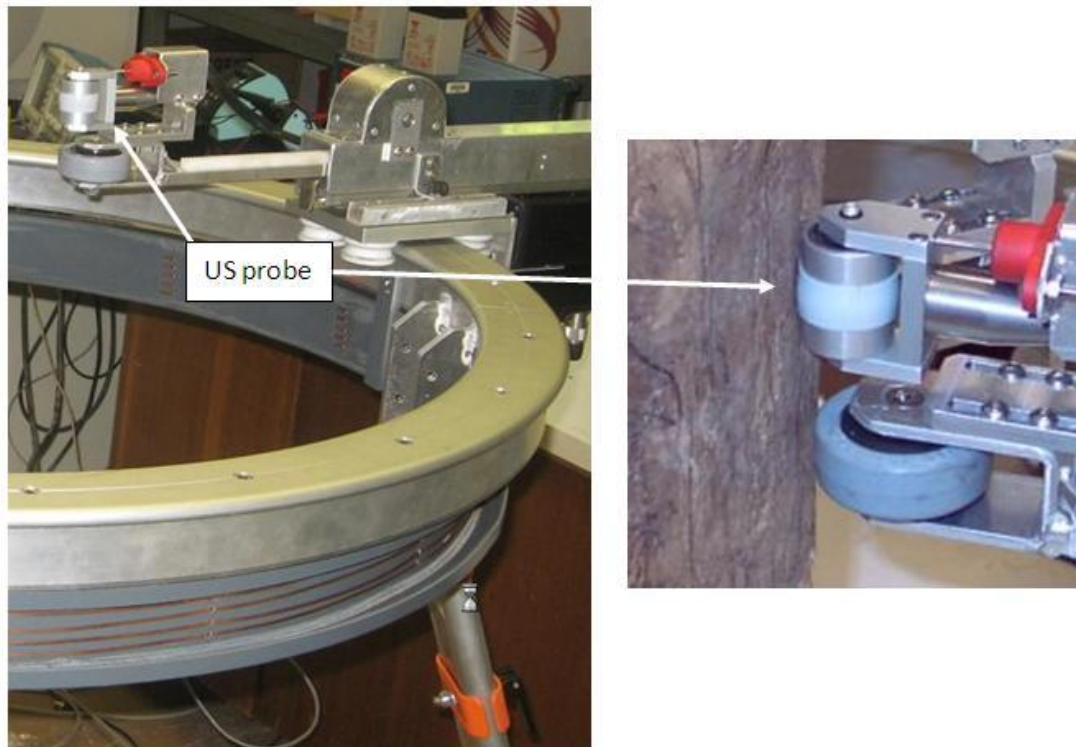


Fig. 2 Development of the ultrasonic device in CIRAD laboratory.

The ultrasonic probes have a frequency bandwidth centered on 300kHz. The associated wavelength is around 5 mm in the case of transverse scanning. The probe consists of a wheel in which the emitter is placed. The coupling medium is made by an elastomer surrounding the wheel (Fig 2). The emission is a square impulse of a 500V magnitude. The acquisition is performed by a converter of 16 bits resolution and a sampling frequency of 5 MHz. The duration of acquisition is set to 1800 μ s (667 μ s is the theoretical duration for a diameter of 50 cm).

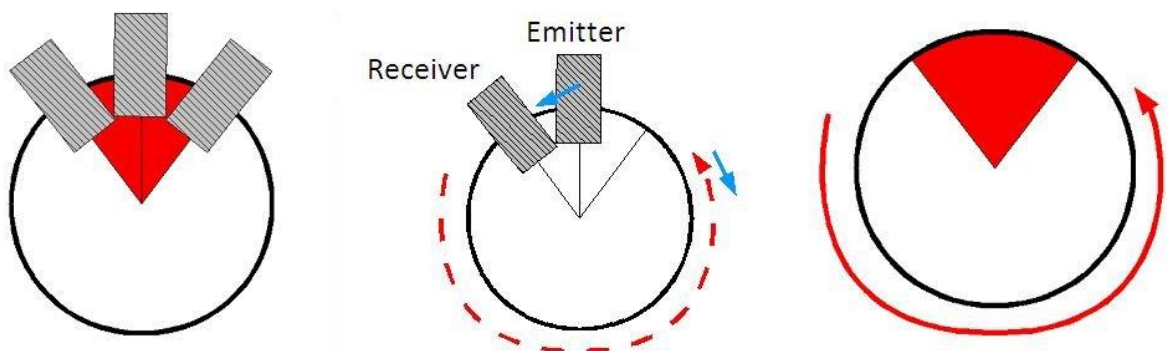


Fig. 3 Principle of the scanning process for quantitative imaging.

The tomographic image can be obtained in quantitative analysis (two probes) or in echographic analysis (one probe). The echographic analysis technique was previously discussed [1]. Concerning quantitative imaging, the scanning process is shown in the Fig 3. Because of the dimension of each trolley, an angular sector of 120° cannot be scanned in one projection (red sector, Fig 3). A typical angular step of 5° leads to a number of acquisition of about 48 for 1 projection. For a complete scan, the total number of acquisition is thus 3456. For a projection, the emitter is motionless while the receiver moves around the ring. The next projection is initiated by a 1 angular step motion of the emitter followed by another motion of the receiver all around the ring (an acquisition is done at each angular step).

Perspectives

The ultrasonic tomographic device will be fully functional in October 2009. At this time, laboratory tests will start first on an “academic” object to determine the real bias in the image computation. Subsequently, green logs will be assessed. These logs are already stored in a water tank at CIRAD and were selected based on the irregularity of their bark. The irregularity of the bark induces a problem of coupling between the probe’s elastomer strip and the wood. It is indeed planned to test the logs with and without the bark; and a new design of the probe shape could also be considered.

Partnerships

The partners of the wood aspect of the BioGMID project have significant experience of imaging and tomography of biological media.

LMA (Laboratoire de Mécanique et d’Acoustique), the French leader on ultrasonic tomography, has developed experimental and theoretical/numerical solutions, and signal processing tools, for non-destructive evaluation and control of biological, natural or manufactured materials.

CNDRI (INSA Lyon, Laboratory of Contrôle Non Destructif par Rayonnements Ionisants) is specialist in non-destructive testing using ionising radiation and has developed efficient experimental devices of X-ray tomography, and has developed image analysis and simulation tools.

CIRAD (Centre de coopération internationale en recherche agronomique pour le développement, Production and Processing of Tropical Woods unit) is the French agricultural research centre working for international development in tropical areas, involved in developing the use of wood, for construction, housing and civil engineering purposes, and has developed acoustic vibration analysis devices to evaluate timber properties and their variability (<http://www.xylo-metry.org/>).

Acknowledgements

This research is supported by a grant from the French National Research Agency (BLAN07-1_183692, “BioGMID”) to Philippe Lasaygues (LMA).

References

1. Brancheriau L., Lasaygues P., Debieu E., Lefebvre JP. (2008) *Ultrasonic tomography of green wood using a non-parametric imaging algorithm with reflected waves*, Annals of Forest Science, Vol. 65, N°7, pp. 712-718.
2. Bucur, V. (2003) *Nondestructive Characterization and Imaging of Wood*, Springer-Verlag, Berlin, 324 p.
3. Divos, F. (2000) *Stress wave based tomography for tree evaluation*. Proc. Of 12th Int. Symposium on NDT of Wood, Sopron 13-15 Sept. 2000: 469.
4. Rinn, F. (2003) *Technische Grundlagen der Impuls-Tomographie*. Baumzeitung 8:29–31.
5. Rinn, F. (2004) *Holzanatomische Grundlagen der Schall-Tomographie an Bäumen*. Neue Landschaft 7:44–47.
6. Rust, S. (2000) *A new tomographic device for the non – destructive testing of trees*, 12th International Symposium on Nondestructive Testing of Wood, University of Western Hungary, Sopron, 233-237.
7. Rust, S., Göcke L. (2000) *PICUS Sonic Tomograph – a new device for nondestructive timber testing*. International Symposium on Plant Health in Urban Horticulture, Braunschweig, Germany, 300.

Occurrence of the gelatinous cell wall layer in tension wood of angiosperms

Julien Ruelle¹, Bruno Clair², Nick Rowe³ and Hiroyuki Yamamoto⁴

¹ UMR EcoFoG, French Guyana; ² LMGC, University of Montpellier II, France;

³ UMR AMAP, France; ⁴ BMP University of Nagoya, JAPAN

Abstract

In many angiosperms, tension wood is characterised by the occurrence of fibres with a particular morphology and chemical composition due to development of the so-called gelatinous layer (G-layer). However, the G-layer is not always present in certain species that nevertheless produce mechanical characteristics of tension wood. Several studies have shown that the supplementary G-layer is not always formed in tension wood fibres. We have observed, for example, that some species can show tension wood that (i) not show any anatomical differences compared with wood from the opposite side of the axis, or (ii) show a novel secondary wall structure comprised of alternating thick and thin layers and a type of opposite wood with typical secondary wall structure. Given the relatively large number of observations on tension wood mechanics and anatomy, we carried out an overview of G-layer presence/absence in angiosperms. We reviewed most of the available studies on tension wood in angiosperms and attempted to provide a synthesis of this information within the context of angiosperm phylogeny.

Introduction

Most trees are able to progressively bend their trunk and branches by an active mechanical mechanism driven by cambial activity [1]. This reorientation is associated with the formation of a particular type of wood known as reaction wood and is widely implicated in maintaining an upright orientation of the main stem and maintaining branches at a given angle. In gymnosperms, reaction wood (compression wood) is formed on the lower side of the tilted axis, while in most angiosperms tension wood is formed on the upper side. Both types of reaction wood show major differences from normal wood in terms of biomechanical properties and at different scales of organisation. Such differences include: (i) at the macroscopic level - division and differentiation of the cambial initials leading to eccentric growth, and (ii) at the microscopic level - production of fibres that can markedly differ in structural organisation compared with normal fibres.

Among angiosperms, diversity in the form of tension wood fibres has long been recognized [2, 3]. The most typical form of temperate angiosperm tension wood is characterized by the development of a so-called gelatinous layer (G-layer), which is essentially made up of highly crystalline cellulose [4, 5] having a very low microfibril angle [6]. However, studies have also shown that some angiosperm species show mechanical evidence of tension wood but do not develop G-fibres [2, 7-9]. The main purpose of this study was to: (1) compile and plot tension wood characters on a recent phylogenetic tree of all angiosperms, (2) explore some of the overall patterns and trends of tension wood evolution in angiosperms, and (3) attempt to interpret where and how tension wood appeared among angiosperms.

Material and methods

We surveyed most of the available literature [1-20] for accounts on the mechanical and anatomical traits characterising tension wood in angiosperms. This included a total of 20 references, which provided us with data on a total of 489 angiosperm species from 112 families. We also sourced recent mechanical studies that combined both anatomical and mechanical observations of diverse angiosperms, including some of our own recent work on tropical trees in French Guyana. We used a phylogenetic tree from the Angiosperm Phylogeny Website database (<http://www.mobot.org/MOBOT/research/APweb/>).

Results and discussion

Observation of various anatomical features of tension wood

Tension wood of many temperate species shows a typical G-layer; which is generally considered to be the only type of anatomically distinguishable tension wood. However, tension wood can also show at least three anatomical variations [2, 3, 7, 21] (Fig. 2):

- tension wood fibres with a G-layer,
- tension wood fibres with poly laminate secondary wall structure,
- tension wood not differing from normal wood fibres.

A first general observation based on combined anatomical observations and mechanical measurements [2, 15] is that presence of a peculiar structure such as G-layer or poly laminate organisation are not prerequisite for the production of high tensile stressed wood. It is clear that various cell wall structures can occur in tension wood; so the question still remains as to what kind of advantage is achieved by the synthesis of a modified secondary wall organization in tension wood?

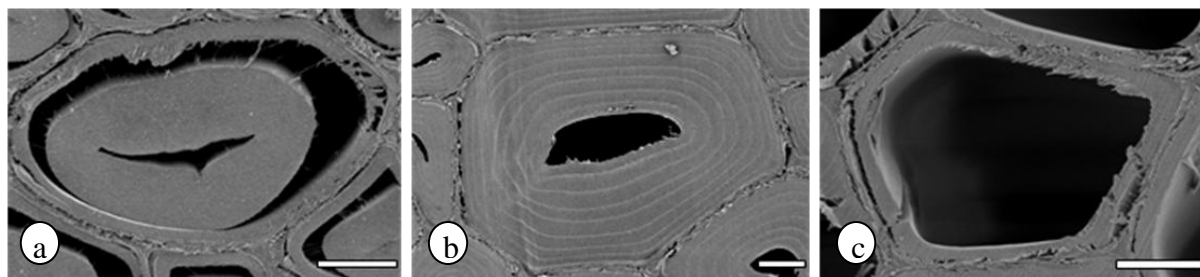


Fig. 2 Cross sections of tension wood (a) *Eperua falcata* showing a well-developed G-layer (b) *Laetia procera* showing a poly laminate organisation, and (c) *Simarouba amara* showing no difference with normal wood fibres Bars, 5 μ m (from [15])

Appearance of the G-layer in angiosperms

Data concerning tension wood characteristics from angiosperm families are listed in Table 1. The main advantage of the approach was the wide number of families represented with reliable anatomical observations. The main disadvantage of the approach was the very low number of representative species per family or per genus. The G-layer was observed in 276 out of a total of 489 species, representing about 57 %. Fifty six of a total of 112 families do not show any peculiar structure in the tension wood.

Among the 68 families for which more than one species was studied, 44 of these showed G-layer in at least one of their species. Among the 44 families, 21 represent families in which *all* observed species produce a G-layer, while 9 of these have a G-layer present in less than 50 % of the species observed. The results suggest that the majority of families that show the presence of a G-layer tend to have a majority of species with a G-layer. However, further sampling and clade-by-clade resolution within each family are clearly required to substantiate this proposal.

Among the 71 genera for which more than one species was studied, we observed that only 7 (10%) included some species with, and some species without a G-layer. This suggests that G-layer presence/absence is possibly more conserved at the generic level, although this also needs far more sampling is required to substantiate this indication.

There is no simple, overall trend in G-layer presence in angiosperms from the available data. The study indicates that the presence/absence of the G-layer is highly heterogeneous across all angiosperm families with a suggestion that, when present at the family and generic levels, it tends to be conserved or present in most species.

We were particularly interested in the appearance and early evolution of tension wood and the G-layer in angiosperms and we present a brief overview of the findings here. The G-layer is not common among species studied from families within the magnoliids or “magnoliid” complex of “basal” angiosperms: Illiciaceae, Chloranthaceae, Winteraceae or Magnoliaceae (Fig. 3). Among these, the Laurales appears to be the earliest branch of angiosperms in which G-layer morphology is consistently observed. Our own observations of *Amborella* (Rowe et al. Pers. com.), which is currently thought to be the species occupying the most basal branch of the angiosperm phylogeny, does not show G-layer morphology.

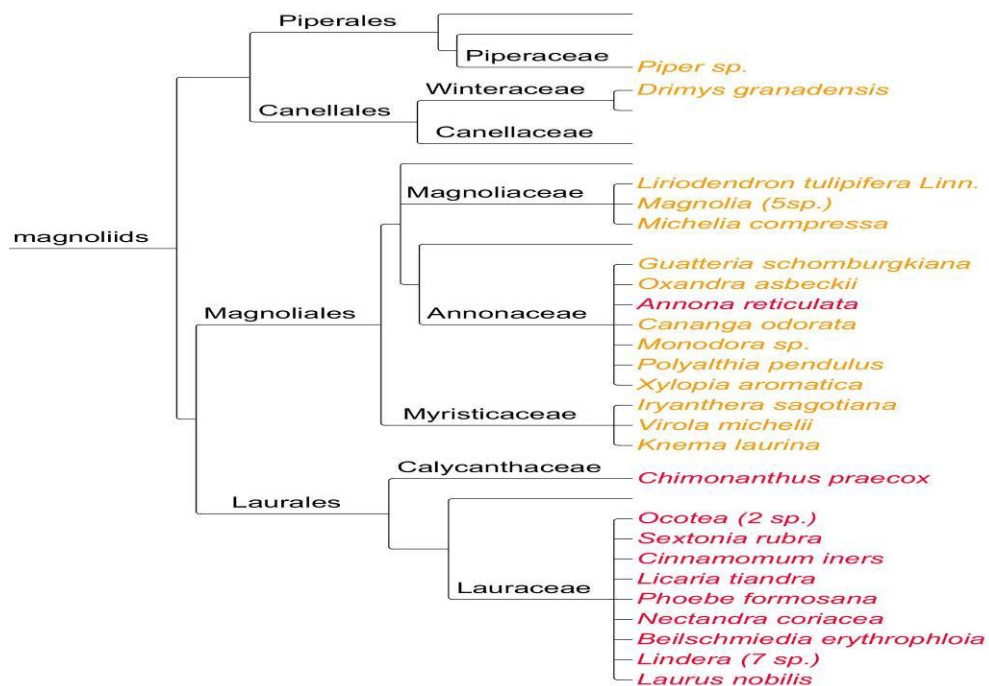


Fig. 3 Observation on the occurrence or lack of G-layer in the magnoliid clade. Species in red synthesize a G-layer in their tension wood while for species in orange it is absent.

Our survey of tension wood in angiosperms emphasizes several key points that contribute towards furthering ways of studying the phenomenon than answering the questions that initially prompted our study. First, some angiosperms can produce mechanical tension wood without G-layer morphology, either by using other derived cell organisations or with fibre tissue that shows no visual difference from normal wood fibres [2, 15, 16]. This has a significant influence on how the phenomenon of tension wood should be studied on living as well as fossil plant species. Second, the evolution of tension wood morphology and the G-layer appears to be complex and does *not* involve the simple appearance of the characteristic and its subsequent persistence in all woody angiosperms. Third, any further resolution of the appearance of mechanical tension wood in angiosperms must therefore incorporate both mechanical tests, and anatomical characterisation to precisely characterize the presence or absence of tension wood and its underlying developmental causes.

Even taking into account the extreme under representation of the sampling presented here for so many families, genera and species, angiosperms do show a remarkable heterogeneity in terms of G-layer presence/absence. Future research should therefore also focus more on specific clades and detail how and why mechanical tension wood and G-level morphology vary so much across species. Further studies should also concentrate on how environmental and/or mechanically mediated constraints and changes in growth form - herbaceous, woody, lianescence, epiphytism and aquatic life histories - may be linked to how plants have modified tension wood characteristics and how this then affects subsequent evolution of these traits.

Table 1 List of families studied, with number of genera and species from references, ratio of studied genera and species / total number of genera and species in each family (according to Angiosperms Phylogeny Website) and number and ratio of species synthesizing G-layer in their tension wood. Results for species where only one species was studied are indicated in dark red.

Families	Number of genera and species studied per family		% of genera and species studied of total genera/ species of family		Number of species with G-layer	% of species with G-layer occurring in number of species studied in family
	Genus	Species	Genus	Species		
Illiciaceae	2	2	66.7%	2.2%	0	0%
Chloranthaceae	1	1	25.0%	1.3%	0	0%
Winteraceae	1	1	14.3%	1.1%	0	0%
Calycanthaceae	1	1	20.0%	9.1%	1	100%
Lauraceae	9	16	18.0%	0.6%	16	100%
Annonaceae	7	7	5.4%	0.3%	1	14%
Magnoliaceae	3	7	100.0%	3.1%	0	0%
Myristicaceae	3	3	15.0%	0.6%	0	0%
Piperaceae	1	1	20.0%	0.0%	0	0%
Berberidaceae	3	3	21.4%	0.4%	0	0%
Eupteleaceae	1	1	100.0%	50.0%	1	100%
Lardizabalaceae	2	3	22.2%	8.3%	0	0%
Menispermaceae	1	1	1.4%	0.2%	0	0%
Ranunculaceae	1	1	1.6%	0.0%	0	0%
Platanaceae	1	1	100.0%	10.0%	1	100%
Sabiaceae	1	2	33.3%	2.0%	1	50%
Trochodendraceae	1	1	50.0%	50.0%	1	100%
Buxaceae	1	2	20.0%	2.9%	0	0%
Loranthaceae	1	1	1.5%	0.1%	0	0%
Olaceae	1	1	7.1%	1.0%	0	0%
Santalaceae	2	2	4.5%	0.2%	1	50%
Altingiaceae	1	1	100.0%	7.7%	1	100%
Daphniphyllaceae	1	2	100.0%	20.0%	0	0%
Grossulariaceae	1	1	100.0%	0.7%	0	0%
Hamamelidaceae	4	5	14.8%	6.1%	5	100%
Iteaceae	1	1	100.0%	5.6%	0	0%
Saxifragaceae	1	1	3.0%	0.2%	0	0%
Cercidiphyllaceae	1	1	100.0%	50.0%	1	100%
Vitaceae	2	2	14.3%	0.2%	0	0%
Nyctaginaceae	1	1	3.3%	0.3%	0	0%
Polygonaceae	1	1	2.3%	0.1%	0	0%
Tamaricaceae	1	1	20.0%	1.1%	0	0%
Cornaceae	2	6	100.0%	7.1%	6	100%
Hydrangeaceae	2	4	11.8%	2.1%	0	0%

Actinidiaceae	1	2	33.3%	0.6%	0	0%
Clethraceae	1	1	50.0%	1.3%	0	0%
Ebenaceae	1	6	25.0%	1.1%	6	100%
Ericaceae	7	12	5.6%	0.3%	0	0%
Lecythidaceae	2	2	8.0%	0.6%	0	0%
Maesaceae	1	2	100.0%	1.3%	0	0%
Myrsinaceae	2	4	4.9%	0.3%	0	0%
Pentaphylacaceae	2	3	16.7%	0.9%	3	100%
Sapotaceae	4	5	7.5%	0.5%	4	80%
Styracaceae	2	5	18.2%	3.1%	5	100%
Symplocaceae	1	2	50.0%	0.6%	2	100%
Theaceae	3	5	42.9%	2.6%	4	80%
Garryaceae	1	1	50.0%	5.9%	0	0%
Aquifoliaceae	1	6	100.0%	1.5%	0	0%
Helwingiaceae	1	1	100.0%	33.3%	1	100%
Apocynaceae	7	9	1.7%	0.2%	2	22%
Gentianaceae	1	1	1.1%	0.1%	0	0%
Rubiaceae	9	9	1.4%	0.1%	0	0%
Bignoniaceae	1	2	0.9%	0.3%	0	0%
Lamiaceae	5	6	2.1%	0.1%	1	17%
Oleaceae	6	8	25.0%	1.3%	7	88%
Paulowniaceae	1	1	100.0%	16.7%	0	0%
Scrophulariaceae	1	1	1.5%	0.1%	0	0%
Araliaceae	7	9	16.3%	0.6%	5	56%
Pittosporaceae	1	2	11.1%	1.0%	0	0%
Adoxaceae	2	5	40.0%	2.5%	0	0%
Caprifoliaceae	1	1	20.0%	0.5%	0	0%
Diervillaceae	1	1	50.0%	6.3%	0	0%
Solanaceae	2	2	2.0%	0.1%	0	0%
Boraginaceae	2	7	1.4%	0.3%	1	14%
Asteraceae	1	1	0.1%	0.0%	0	0%
Boraginaceae	2	7	1.4%	0.3%	1	14%
Stachyuraceae	1	1	100.0%	20.0%	0	0%
Staphyleaceae	1	2	50.0%	4.4%	0	0%
Combretaceae	2	10	14.3%	2.0%	10	100%
Lythraceae	2	3	6.5%	0.5%	3	100%
Melastomataceae	5	5	2.7%	0.1%	4	80%
Myrtaceae	2	6	1.5%	0.1%	4	67%
Anisophylleaceae	1	1	25.0%	2.9%	0	0%
Coriariaceae	1	1	100.0%	20.0%	0	0%
Polygalaceae	1	1	4.8%	0.1%	1	100%
Fabaceae	27	32	3.7%	0.2%	32	100%
Bonnetiaceae	1	1	33.3%	2.9%	0	0%
Chrysobalanaceae	1	1	5.9%	0.2%	0	0%
Clusiaceae	6	8	42.9%	1.3%	2	25%
Euphorbiaceae	7	10	3.2%	0.2%	10	100%
Goupiaceae	1	1	100.0%	50.0%	0	0%
Hypericaceae	1	1	11.1%	0.2%	0	0%
Linaceae	1	1	8.3%	0.3%	1	100%
Phyllanthaceae	2	2	3.4%	0.1%	2	100%
Rhizophoraceae	3	3	18.8%	2.0%	1	33%
Salicaceae	9	19	16.4%	1.9%	16	84%

Elaeocarpaceae	2	3	16.7%	0.5%	1	33%
Oxalidaceae	1	1	16.7%	0.1%	0	0%
Cannabaceae	3	4	27.3%	2.4%	4	100%
Elaeagnaceae	1	3	33.3%	6.7%	0	0%
Moraceae	4	7	10.5%	0.6%	7	100%
Rhamnaceae	6	8	11.5%	0.9%	8	100%
Rosaceae	15	28	16.7%	1.1%	16	57%
Ulmaceae	4	7	66.7%	20.0%	7	100%
Urticaceae	1	1	1.9%	0.0%	1	100%
Zygophyllaceae	1	1	4.5%	0.4%	0	0%
Dipterocarpaceae	1	1	5.9%	0.1%	0	0%
Malvaceae	12	20	4.9%	0.5%	1	5%
Thymelaeaceae	3	3	6.0%	0.3%	0	0%
Anacardiaceae	2	4	2.9%	0.7%	4	100%
Burseraceae	2	2	11.1%	0.4%	2	100%
Meliaceae	4	4	7.7%	0.6%	2	50%
Rutaceae	10	12	6.2%	0.7%	8	67%
Sapindaceae	6	15	4.4%	0.9%	14	93%
Simaroubaceae	3	3	15.8%	3.2%	3	100%
Celastraceae	3	5	3.3%	0.4%	0	0%
Betulaceae	5	15	83.3%	10.3%	15	100%
Casuarinaceae	1	1	25.0%	1.1%	1	100%
Fagaceae	6	16	85.7%	2.4%	16	100%
Juglandaceae	4	6	40.0%	12.0%	5	83%
Myricaceae	1	1	33.3%	1.8%	1	100%
Caricaceae	1	1	25.0%	2.9%	0	0%

Acknowledgements

The authors would like to thank Ivan Scotti (INRA, UMR EcoFoG) for his contribution to this paper.

References

1. Sinnott, E.W., *Reaction Wood and the Regulation of Tree Form*. American Journal of Botany, 1952. **39**(1): p. 69-78.
2. Clair, B., et al., *Tension wood and opposite wood in 21 tropical rain forest species I. Occurrence and efficiency of the G-layer*. IAWA Journal, 2006. **27**(3): p. 329-338.
3. Onaka, F., *Studies on compression and tension wood*. Wood research, Bulletin of the Wood research Institute, Kyoto University, Japan, 1949. **24**(3): p. 1-88.
4. Cote, W.A., A.C. Day, and T.E. Timell, *A Contribution to Ultrastructure of Tension Wood Fibers*. Wood Science and Technology, 1969. **3**(4): p. 257-271.
5. Norberg, P.H. and H. Meier, *Physical and chemical properties of the gelatinous layer in tension wood fibres of Aspen (Populus tremula L.)*. Holzforschung, 1966. **20**(6): p. 174-178.
6. Fujita, M., H. Saiki, and H. Harada, *Electron Microscopy of Microtubules and Cellulose Microfibrils in Secondary Wall Formation of Poplar Tension Wood Fibers*. Mokuzai Gakkaishi, 1974. **20**(4): p. 147-156.
7. Fisher, J.B. and J.W. Stevenson, *Occurrence of reaction wood in branches of Dicotyledons and its role in tree architecture*. Botanical Gazette, 1981. **142**(1): p. 82-95.
8. Yoshida, M., et al., *Tensile growth stress and lignin distribution in the cell walls of yellow poplar, Liriodendron tulipifera Linn*. Trees-Structure and Function, 2002. **16**(7): p. 457-464.
9. Yoshizawa, N., et al., *Anatomy and lignin distribution of reaction wood in two Magnolia species*. Wood Science and Technology, 2000. **34**(3): p. 183-196.
10. Abe, K. and H. Yamamoto, *The influences of boiling and drying treatments on the behaviors of tension wood with gelatinous layers in Zelkova serrata*. Journal of Wood Science, 2007. **53**(1): p. 5-10.
11. Ferrand, J.-C., *Etude des contraintes de croissance Première partie : méthode de mesure sur carottes de sondage*. Annals of Forest Science, 1982. **39**: p. 109-142.
12. Chang, S.S., et al., *Mesoporosity as a new parameter for understanding tension stress generation in trees*. Journal of Experimental Botany, 2009: p. doi: 10.1093/jxb/erp133.
13. Clair, B. and B. Thibaut, *Shrinkage of the gelatinous layer of poplar and beech tension wood*. IAWA Journal, 2001. **22**(2): p. 121-131.
14. Clair, B., J. Ruelle, and B. Thibaut, *Relationship between growth stress, mechanical-physical properties and proportion of fibre with gelatinous layer in chestnut (Castanea sativa Mill.)*. Holzforschung, 2003. **57**(2): p. 189-195.
15. Ruelle, J., H. Yamamoto, and B. Thibaut, *Growth stresses and cellulose structural parameters in tension and normal wood from three tropical rainforest angiosperms species*. BioResources, 2007. **2**(2): p. 235-251.
16. Ruelle, J., et al., *Peculiar tension wood structure in Laetia procera (Poepp.) Eichl. (Flacourtiaceae)*. Trees, structure and function, 2007. **21**(3): p. 345-355.
17. Satiatjeunemaitre, B., *Cell-Wall Morphogenesis and Structure in Tropical Tension Wood*. IAWA Bulletin, 1986. **7**(2): p. 155-164.
18. Washusen, R., J. Ilic, and G. Waugh, *The relationship between longitudinal growth strain, tree form and tension wood at the stem periphery of ten- to eleven-year-old Eucalyptus globulus Labill*. Holzforschung, 2003. **57**(3): p. 308-316.
19. Yoshida, M., H. Ohta, and T. Okuyama, *Tensile growth stress and lignin distribution in the cell walls of black locust (Robinia pseudoacacia)*. Journal of Wood Science, 2002. **48**(2): p. 99-105.
20. Yoshida, M., T. Okuda, and T. Okuyama, *Tension wood and growth stress induced by artificial inclination in Liriodendron tulipifera Linn. and Prunus spachiana Kitamura f. ascendens Kitamura*. Annals of Forest Science, 2000. **57**(8): p. 739-746.
21. Ruelle, J., et al., *Peculiar tension wood structure in Laetia procera (Poepp.) Eichl. (Flacourtiaceae)*. Trees, structure and function, 2007: p. online.

6. Biomechanics of trees

Origins of abnormal behaviors of gelatinous layer in tension wood fiber - A micromechanical approach

H. Yamamoto¹, J. Ruelle², Y. Arakawa¹, M. Yoshida¹, B. Clair² and J. Gril²

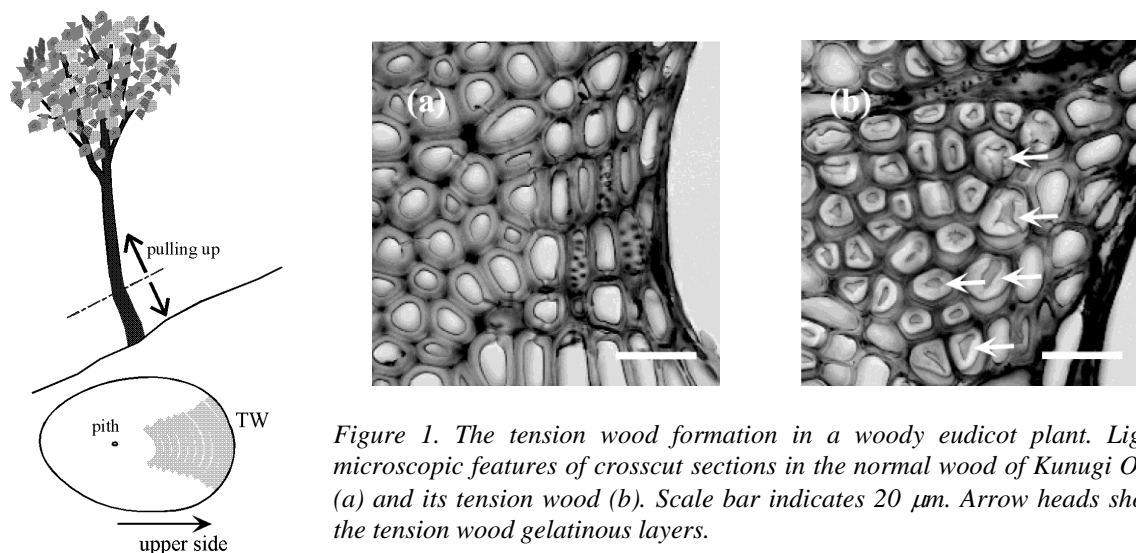
¹ Nagoya University, Japan; ² Université Montpellier 2, France

Abstract

The mechanism responsible for unusual mechanical properties of tension wood gelatinous fiber (G-fiber) was investigated. We discussed origins of high tensile growth stress, high drying shrinkage, and rapid increase of Young's modulus due to drying, in association with microscopic structure of gelatinous layer (G-layer). Anatomical, crystallographic, and micromechanical approaches were employed. As the result, it is cleared that G-layer structure as hydro-gel has a key to understand various physical properties in the tension wood G-fiber.

Introduction

Tension wood xylem often produces an unusual wood fiber known as gelatinous fiber (G-fiber) along the upper sides of leaning stems or branches in woody eudicot species. The G-fibers form a gelatinous layer (G-layer) as the innermost layer of the multilayered cell wall, characterized by the absence of lignin and a high concentration of rigid cellulose microfibrils aligned along the fiber axis (see Fig.1) [1](Onaka 1949).



G-fibers generate high tensile growth stress during the maturation process [2-12], which enables hardwood species to perform negative-gravitropic behavior in inclined shoots [13-15]. However, in timber production, tension wood is often the source of various problems, such as processing defects caused by its abnormal growth stress [16,17]. Other particularities are a high longitudinal Young's modulus and a high longitudinal drying shrinkage [4,6,8,18], the combined effect of which cause

serious complications during the drying process, such as distortion and longitudinal cleavage of the sawn lumber.

Some studies have suggested that the distinctive properties of G-fibers could be attributed to the intrinsic behavior of the G-layer [2,3,11,4,6,19,8,9], while others have emphasized the role of the lignified layer (L-layer), which often peels off the G-layer along the same direction during microtoming [20,21,22]. Recently, Clair et al. [23] noted that detachment of the G-layer, often observed in the microtomed surface of a fresh block, disappeared at a distance greater than 100 μm from the block surface, which was embedded in resin after being oven-dried. This finding supports the view that the intrinsic property of the G-layer is the source of the characteristic behavior of G-fibers. However, the generation mechanism of the G-layer properties is still unknown. In the present study, we focused on generation of the abnormal tensile growth stress, and moisture-dependent changes in the longitudinal Young's modulus and longitudinal shrinkage in tension wood of two Kunugi oak (*Quercus acutissima*) trees, revealing the property difference between the G-layer and L-layer.

Material and methods

Sampled trees

The studied specimens were two Kunugi oaks (*Quercus acutissima*), a 75-year-old tree (Kunugi A) and a 40-year-old tree (Kunugi B), grown in Nagoya, Japan. The girths at chest height were 103 cm (Kunugi A) and 73 cm (Kunugi B); both trees had inclined stems.

Measurement of the released strain of the surface growth stress (ϵ_L)

At the chest height, 10 or 11 points were set around the circumference of each stem. Released strain of the surface growth stress (ϵ_L) was measured at each point, using the strain-gauge method. Measurement was done in December 2002.

Measurements of longitudinal Young's modulus (E_L)

Thin blocks were prepared from each measuring point of the released strain, and were cut for the tensile and shrinkage tests at the macroscopic level, with specimen size 70 (Longitudinal, L) \times 10 (Tangential, T) \times 4 (Radial, R) and 50 (L) \times 13 (T) \times 5 (R) mm^3 , respectively.

Tensile tests at the macroscopic level were performed in green and oven-dried conditions at the temperature controlled room (20 °C). For each specimen, two strain gauges were bonded at the center of the flat-sawn surfaces and connected to the strain-meter. Tensile test was performed by using a commercial equipment. The outputs from both strain-gauges were collected and averaged. And, the macroscopic longitudinal Young's modulus (E_L) was determined from the stress–strain curve.

Measurements of longitudinal drying shrinkage (α_L)

A hand-made comparator with a high precision dial gauge (0.001 mm in accuracy) was employed for the measurement of the dimension of the specimen [4,24]. Thus, macroscopic oven-dried shrinkage (α_L) was calculated as

$$\alpha_L = (l_{\text{wet}} - l_{\text{dry}})/l_{\text{wet}} \times 100 \quad (\%) \quad (1)$$

where l_{wet} and l_{dry} are the longitudinal dimensions of the macroscopic specimen at the green condition and under the oven-dried condition, respectively.

X-ray diffraction properties of cell wall cellulose

Specimen:

From both the heavy tension and opposite wood (normal wood) sides in Kunugi A, a sample block was taken, and two types of specimen were prepared, flat-sawn sections [15 (L) \times 10 (T) \times 0.2 (R)

mm] and coarse sawdust powder. For the flat-sawn sections, eight specimens were prepared from extra-porous zones in the wood blocks. For the sawdust powders, sufficient amounts of powder were prepared, and they were fully stirred to become uniform. Those samples were seasoned inside a small air-conditioned desiccator with water until equilibrium so as to remove liquid water that remarkably increases a halo peak in the X-ray diffraction diagram. The powder sample was packed into the plate-like specimen holder before seasoning. The moisture condition of the samples in this stage was regarded as the fiber saturation point (FSP), and we used them for diffraction analysis at the FSP with the reflection technique using a X-ray diffractometer. Samples were then air-dried until equilibrium and X-ray measurements retaken, followed by oven-drying for 24 h at 105 °C after seasoning inside a desiccator with a powder of P₂O₅ and further measurements retaken [25].

Measurements of width of a single crystallite (WSC) and lattice distance from [200] plane (d_{200}):

CuK α was used as a line-focused incident X-ray with a power of 35 kV, 35 mA, and passed through a Ni filter. For flat-sawn sections, diffraction intensity was recorded in the 2θ angular range from 5° to 40° to determine the half width of the [200] diffraction peak (β) that was transformed into width of a single fibrous crystallite (WSC) in a direction perpendicular to the [200] plane. In addition, the diffraction intensities from the powder samples were recorded in the 2θ angular range from 20° to 25° to determine the peak angle from the [200] lattice plane ($2\theta_{200}$) under the various moisture condition. In this measurement, three powder samples were prepared for each of tension wood and normal wood, while one sample for isolated G-layer powder that was prepared from a heavy tension wood block using the technique described by Norberg and Meier [20].

The WSC value was estimated from flat-sawn sections based on the study of Hengstenberg et al. [26] using the modified Scherrer's equation:

$$WSC = K \cdot \lambda / (\beta \cdot \cos \theta_{200}) \quad (\text{nm}) \quad (2)$$

where K is a constant (The present study assumed $K = 1$), λ is the wavelength of CuK α ($= 0.154$ nm), β is the half-width of the [200] diffraction peak, and θ_{200} is the peak position from the [200] plane.

The value of d_{200} was determined from powder samples based on Bragg's equation:

$$d_{200} = \lambda / (2 \sin \theta_{200}) \quad (\text{nm}) \quad (3)$$

Histo-mechanical approach for modeling

After the Young's modulus and drying shrinkage measurements, a small block was sampled from each specimen. A transverse section was cut from each block on a sliding microtome and microscopic images at high and low magnification were recorded within the outermost annual rings of the mounted section under a light microscope connected to an image processor. Macroscopic xylem consists of vessel elements including the vasicentric parenchymae (V), ray parenchymae (R), and wood fiber (F). From the low magnification images, the areal composition of each domain in cross section was computed. The areal ratio of the G-fiber in the domain of wood fiber (ϕ) was also measured. From high magnification images, the ratios of the G-layer (g), L-layer (l), and total cell wall (w) areas in the domain of wood fiber were determined. Moreover, the areal ratios of the G-layer (γ) and L-layer (λ) in wood-fiber cell wall were also calculated. The relationships between the anatomical parameters were as follows: $V + R + F = 1$, $g + l = w$, and $\gamma + \lambda = 1$.

The simple law of mixture gives the following formulae to estimate growth strain (ε_L^F), Young's modulus (E_L^F), and drying shrinkage (α_L^F) of the wood-fiber domain along the fiber axis in each specimen [6]:

$$\varepsilon_L^F \cong \varepsilon_L, \quad E_L^F \cong E_L / F, \quad \text{and} \quad \alpha_L^F \cong \alpha_L \quad (4)$$

assuming that the vessel and ray tissues are not involved in determining the axial growth strain, elasticity and shrinkage of the xylem.

The wood-fiber domain is composed of two types of slender, thick-walled fibers—gelatinous (G-fiber) and normal fibers (N-fiber)—arranged in rows in a direction parallel to the wood-fiber axis. In

previous works by Clair et al. [8] and Yamamoto et al. [6], the simple law of mixture was applied to relate the longitudinal properties in a macroscopic wood with fiber properties. We then used the following equations:

$$\begin{aligned}\varepsilon_L^F (\cong \varepsilon_L) &= \frac{\phi \cdot E_L^g \cdot \varepsilon_L^g + (1-\phi) \cdot E_L^n \cdot \varepsilon_L^n}{\phi \cdot E_L^g + (1-\phi) E_L^n}, & E_L^F &= \phi \cdot E_L^g + (1-\phi) E_L^n, \\ \alpha_L^F (\cong \alpha_L) &= \frac{\phi \cdot E_L^g \cdot \alpha_L^g + (1-\phi) \cdot E_L^n \cdot \alpha_L^n}{\phi \cdot E_L^g + (1-\phi) E_L^n},\end{aligned}\quad (5)$$

where ε_L^g and ε_L^n are the growth strains of the G- and N-fiber, respectively, and E_L^g and E_L^n are their respective Young's modulus, and α_L^g and α_L^n are drying shrinkages in respective fibers.

The cell wall of the wood fiber consists of G- and L-layers, which are also arranged in rows parallel to the wood-fiber axis. The simple law of mixture now gives the following equations:

$$\begin{aligned}\varepsilon_L^W (\cong \varepsilon_L) &= \frac{\gamma \cdot E^G \cdot \varepsilon^G + (1-\gamma) \cdot E^S \cdot \varepsilon^S}{\gamma \cdot E^G + (1-\gamma) \cdot E^S}, & E_L^W &= \gamma \cdot E^G + (1-\gamma) E^S, \\ \alpha_L^W (\cong \alpha_L) &= \frac{\gamma \cdot E^G \cdot \alpha^G + (1-\gamma) \cdot E^S \cdot \alpha^S}{\gamma \cdot E^G + (1-\gamma) \cdot E^S},\end{aligned}\quad (6)$$

where ε_L^W is the growth strains, and $E_L^W (= E_L^F/w)$ is the substantial Young's modulus, and $\alpha_L^W (\cong \alpha_L^F)$ is the drying shrinkage of the cell wall in the direction parallel to the fiber axis. ε^G and ε^S are the growth strains of the G- and L-layer, respectively, and E^G and E^S are the Young's modulus of the G-layer along the direction of the fiber and that of the L-layer, respectively, and α^G and α^S are their respective shrinkages.

The values of E_L^g and E_L^n in the green and the oven-dried specimen were optimized by applying the least square method using the second formula of (5) to the observed relationship between E_L^F and ϕ . After that, the values of ε_L^g , ε_L^n were determined from the observed relationship between ε_L^F and ϕ . When determining the values of ε_L^g and ε_L^n using the first formula of (5), we adopted the determined values of E_L^g and E_L^n in the green specimen to the calculation. Moreover, the values of α_L^g , α_L^n , and $r (=E_L^g/ E_L^n)$ in the third equation of (5) were also determined from the observed relationship between α_L^F and ϕ . In the same manner as those cases, E^G , E^S , ε_L^g , ε_L^n , α^G , α^S , and $s (=E^G/ E^S)$ were determined from the observed relations between E_L^W , ε_L^W , α_L^W and γ through the least square method using equations (6).

Results

Young's moduli of the fibers and layers

Estimated values of E_L^g , E_L^n , E^G , and E^S are displayed in Table 1. The values of E_L^g and E_L^n were quite different between two trees. This is because the most of wood fiber has a quite thicker cell wall in Kunugi B than in Kunugi A. After eliminating the effect of cell-wall thickness, those differences became smaller as shown in Table 1.

As a result of drying from green to oven-dried condition, the Young's modulus in L-layer (E^S) increased by 22.1% in Kunugi A and 29.7% in Kunugi B. Those values are in close agreement with values reported previously for Spruce [27] and Japanese cedar [28]. On the other hand, the Young's modulus of G-layer increased considerably with the drying process at a ratio of 204.6% in Kunugi A and 80.4% in Kunugi B.

Growth strain in fibers and layers

The estimated values of growth strains in fibers ($= \varepsilon_L^g$ and ε_L^n) and wall layers are displayed in Table 2. It is clearly concluded that contractive growth strain becomes quite higher in the G-layer than

in the normal lignified layer, which causes generation of a very large tensile growth stress in the G-fiber.

Drying shrinkage of fibers and layers from green to oven-dried condition

The estimated values of α_L^g , α_L^n , α^G , and α^S were determined as displayed in Table 3. As a result of drying from green to oven-dried condition, each layer contracted in the direction parallel to the fiber axis. On the other hand, the G-layer contracted several times higher than the L-layer in each tree, which causes generation of a very large drying shrinkage in the G-fiber. It is considered that the combined effect of increase in Young's modulus and drying shrinkage along the fiber direction causes serious complications during the drying process, such as distortion, longitudinal cleavage of the sawn lumber, and so forth.

Table 1. Young's moduli of fiber and layer.

	Kunugi A		Kunugi B	
	green	Oven-dried	Green	Oven-dried
Fiber Young's modulus (GPa)				
E_L^s	14.79 (+/- 0.60)	17.70 (+/- 1.61)	22.79 (+/- 1.01)	29.52 (+/- 1.61)
E_L^g	15.98 (+/- 0.84)	39.61 (+/- 2.26)	25.02 (+/- 1.40)	41.64 (+/- 2.23)
Layer Young's modulus (GPa)				
E^S	19.49 (+/- 1.04)	23.79 (+/- 2.50)	24.86 (+/- 1.51)	32.24 (+/- 1.96)
E^G	27.88 (+/- 9.94)	84.92 (+/- 7.40)	38.10 (+/- 4.02)	68.73 (+/- 5.22)

Parentheses stand for +/- 95 % confidence interval of the mean value.

Table 2. Growth strains in fiber and layer.

	Kunugi A	Kunugi B
Fiber growth strain (%)		
ϵ_L^s	-0.0167 (+/- 0.0051)	-0.0334 (+/- 0.0056)
ϵ_L^g	-0.3222 (+/- 0.0182)	-0.2499 (+/- 0.0322)
Layer growth strain (%)		
ϵ^S	-0.0192 (+/- 0.0041)	-0.0334 (+/- 0.0091)
ϵ^G	-0.4625 (+/- 0.0389)	-0.3206 (+/- 0.0552)

Parentheses stand for +/- 95 % confidence interval of the mean value.

Table 3. Drying shrinkage in fiber and layer.

	Kunugi A	Kunugi B
Fiber shrinkage (%)		
α_L^s	0.294 (+/- 0.083)	0.058 (+/- 0.056)
α_L^g	1.000 (+/- 0.085)	0.914 (+/- 0.081)
Layer shrinkage (%)		
α^S	0.293 (+/- 0.083)	0.058 (+/- 0.058)
α^G	1.108 (+/- 0.100)	1.122 (+/- 0.108)

Parentheses stand for +/- 95 % confidence interval of the mean value.

X-ray diffraction properties in TW cellulose

Figure 1 shows X-ray diffractograms of various powder samples under air-dried conditions. The diffractogram of the isolated G-layer (c) was almost identical to that of Avicel powder (a), which suggests that the G-layer contains large amounts of native cellulose crystallites. The diffractogram of normal wood (b) showed a typical pattern of ligno-cellulosic material in which the peak separation between [110] and [110] was unclear. The diffraction of tension wood powder (d) gave a similar pattern as the G-layer (c), which shows that tension wood contains a large number of G-layers.

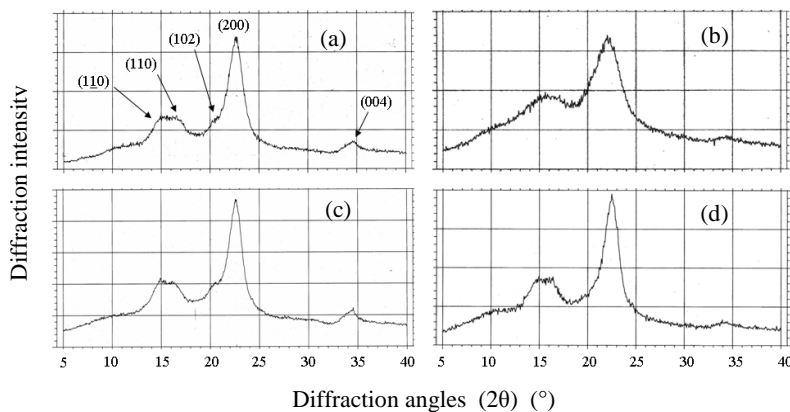


Fig.1. X-ray diffraction patterns from (a) native cellulose powder (Avicell), (b) Kunugi normal wood powder, (c) isolated G-layer powder from Kunugi tension wood, and (d) Kunugi tension wood powder. The measurements were done in the air-dried condition.

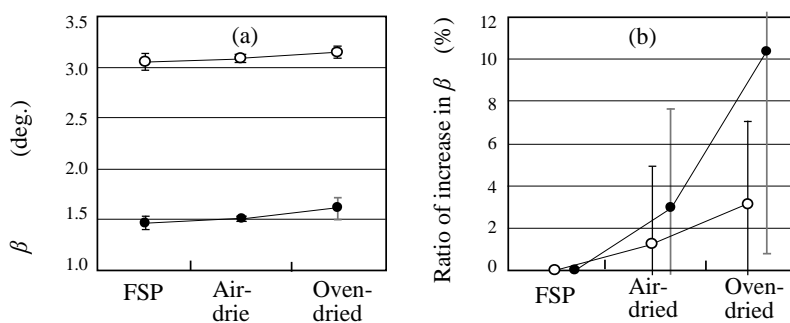


Fig. 2 (a) Half width of [200] peak (β) under various moisture conditions. (b) Changes in the ratio of increase of β , calculated on the basis of β at the FSP. The error bar denotes \pm SD of eight samples. Solid circle: tension wood sections; open circle: normal wood sections.

Figure 2(a) shows the half width of the [200] diffraction peak (β) in normal and tension wood sections under various moisture conditions. Figure 2(b) shows the ratios of increase in β calculated on the basis of β at the FSP. The value of β tended to increase with drying, which was noticeably higher in the tension wood than in the normal wood. Figure 3(a) shows values of WSC, calculated from equation (2), in normal and tension wood sections under various moisture conditions. Figure 3(b) shows the ratios of increase in WSC calculated on the basis of WSC at the FSP. Figures 3 indicate that the WSCs in the normal and tension wood sections decreased with drying, with the ratio of decrease being higher in the tension wood (9.06%) than in the normal wood (3.05%).

Figure 4(a) shows the lattice distance in the [200] plane (d_{200}) in normal and tension wood powders under various moisture conditions; Fig. 4(b) shows the ratios of increase in d_{200} on the basis of d_{200} at the FSP. The values of d_{200} increased as the drying proceeded, and the ratios of increase from FSP to oven-dry were more or less identical in both wood (1.88 % in the tension wood, and 1.77 % in the normal wood).

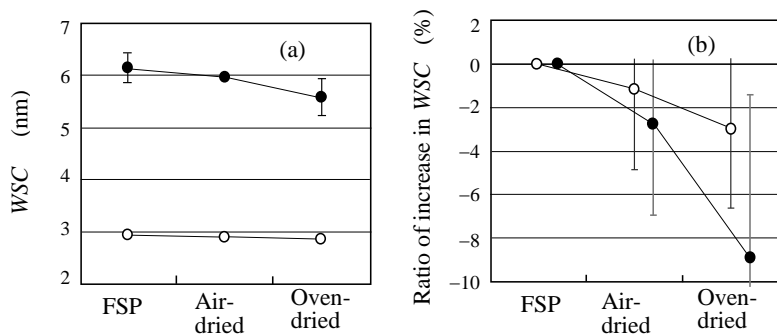


Fig. 3 (a) Width of a single crystallite in the direction perpendicular to the [200] plane (WSC) under various moisture conditions. (b) Changes in the ratio of increase in WSC, calculated on the basis of WSC at the FSP. The error bar denotes \pm SD of eight samples. Solid circles: tension wood sections; open circles: normal wood sections.

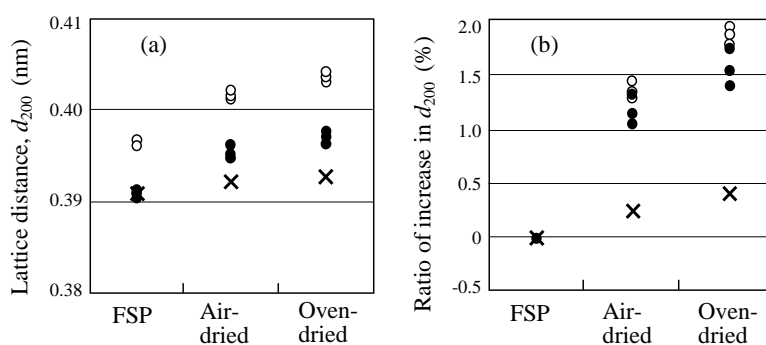


Fig. 4. (a) Lattice distance (d_{200}) of powder samples under various moisture conditions. (b) Ratio of increase in d_{200} , calculated on the basis of d_{200} at the FSP. Solid circles: tension wood powders; open circles: normal wood powders; cross: powder of isolated G-layer.

Discussion

In the present study, we showed that contractive growth strain was larger in the G-layer than in the L-layer, and the ratio of increase in the longitudinal Young's modulus with drying was higher in the G-layer than in the L-layer, a pattern repeated with longitudinal drying shrinkage. Thus, we concluded that the generation of abnormally large tensile stress in the G-layer causes the large tensile growth stress in the tension wood region, and that the increased Young's modulus with drying in the G-layer compared to the L-layer causes the large increase in the Young's modulus of tension wood after drying. We also concluded that an abnormally large shrinkage with drying in the G-layer compared to the L-layer causes the large shrinkage in the drying tension wood.

As reported by Clair et al. [29], transverse sectioning often causes an artefactual swelling in the crosscut shapes of the G-layer, resulting in an overestimation of the values of g and γ . This could lead to an underestimation of the differences in the physical properties between the G-layer and the L-layer. However, we consider that the obtained conclusion is not disturbed by such an artifact because difference of the properties between the G- and the L-layers would be even greater if we took the possible overestimation of g and γ into consideration.

We also discovered that the lattice distance in the [200] plane (d_{200}) increased with drying, while the width of a single crystallite (WSC) in the direction perpendicular to the [200] plane became smaller after drying, which is especially noticeably in the tension wood. The latter result comes from the increase in the half width of the [200] diffraction peak (β) with drying. Lately, Clair et al. [30] showed that the tension wood cell wall has a gel-like structure characterized by a pore surface more than 30 times higher by analyzing nitrogen adsorption-desorption isotherms of supercritically dried tension and normal wood. Although the present results seem to be unrelated, the origin of these complex phenomena can be explained in the following manner via the gel-like structure of the tension wood cell wall proposed by Clair et al. [30].

The G-layer matrix consists of a substantial amount of noncrystalline polysaccharides (NCPs), which in the green state, behaves as a water-swollen gel. During water desorption after lumbering, the swollen gel of the NCPs collapses under surface tension. As a result, the matrix is transformed into a condensed structure by strong hydrogen bonding between NCP molecules, which is a form of xerogelation, leading to an abnormal increase in the Young's modulus and high shrinkage in the drying G-layer. It is considered the NCPs consist of small amount of hemicellulose besides non-crystalline cellulose, e.g., galactan, xyloglucan, and so forth [20,31]. According to Nishikubo et al. [31], most of non-cellulosic polysaccharide consists of xyloglucan, therefore, it is considered that xyloglucan might have something important role to control the mechanical behaviors of G-layer.

Lately, Fang et al. [32] reported that relative thickness of G-layer became significantly smaller than that of the lignified layer after drying; moreover, lumen size in G-fiber increased while that in the N-

fiber decreased after drying. Their discovery suggests a possibility that a tensile stress is generated in the dried G-layer not only in the longitudinal but also circumferential directions. In other word, it is considered that some cellulose microfibrils in the dried G-layer are subject to transverse tensile and longitudinal buckling stresses from the shrinking NCP matrix. The combined effect causes disarray in the cellulose lattice arrangements, especially at the surface layer of each crystallite, which may cause increase of β and thus apparent decrease of WSC after drying. This may explain why d_{200} increases while WSC decreases in the dried G-layer. The possibility of longitudinal buckling in cellulose crystallites was also noted by Clair et al. [9]. Considering that anisotropic structure of cellulose crystallite, transverse stiffness is relatively lower in the direction perpendicular to the [200] lattice plane than in the direction along b-axis in unit cell, possibly causing each crystallite more easily to deform or delaminate in the direction perpendicular to the [200] lattice plane than in the direction along b-axis under external negative pressure.

In the L-layer matrix, NCP molecules are reinforced by large amounts of lignin whose rigidity is higher than that of the NCPs under the wet condition [33,34]. As with the NCP matrix in the G-layer, the NCP domain in the green, lignified cell wall collapses with moisture desorption; however, its condensation and resulting xero-gelation is mechanically prevented by the lignin, which acts as a rigid skeleton in the matrix [35,36]. Thus, the ratio of increase in the longitudinal Young's modulus with drying is lower in the L-layer than in the G-layer; longitudinal drying shrinkage also displayed a similar pattern of behavior. The increases in β values (and decrease in WSC) were thus lower in the L-layer than in the G-layer.

At this time, the mechanism of generation of contractive force in the maturing G-layer is still unknown, however, the structure and behavior of water swollen gel may give some key to solve it.

References

1. Onaka, F. (1949): *Study on reaction wood*. Wood Research (Bull Wood Res Inst Kyoto Univ). 1: 1-99.
2. Okuyama, T., H. Yamamoto, M. Iguchi and M. Yoshida (1990): *Generation process of growth stresses in cell walls. II. Growth stress in tension wood*. Mokuzai Gakkaishi. 36: 797-803.
3. Okuyama, T., H. Yamamoto, M. Yoshida, Y. Hattori and R.R. Archer (1994): *Growth stresses in tension wood. Role of microfibrils and lignification*. Annals Sciences Forestierre. 51: 291-300.
4. Yamamoto, H., T. Okuyama, K. Sugiyama and M. Yoshida (1992): *Generation process of growth stresses in cell walls. IV. Action of the cellulose microfibrils upon the generation of the tensile stresses*. Mokuzai Gakkaishi. 38: 107-113.
5. Yamamoto, H., T. Okuyama and M. Yoshida (1993): *Generation process of growth stresses in cell walls. V. Model of tensile stress generation in gelatinous fibers*. Mokuzai Gakkaishi. 39: 118-125.
6. Yamamoto, H., K. Abe, Y. Arakawa, T. Okuyama and J. Gril (2005): *Role of the gelatinous layer (G-layer) on the origin of the physical properties of the tension wood of Acer sieboldianum*. Journal of Wood Science. 51: 222-233.
7. Yoshida, M., H. Ohta and T. Okuyama (2002): *Tensile growth stress and lignin distribution in the cell walls of black locust (Robinia pseudoacacia)*. Journal of Wood Science. 48: 99-105.
8. Clair, B., J. Ruelle and B. Thibaut (2003): *Relationship between growth stress, mechanical- physical properties and proportion of fibre with gelatinous layer in chestnut (Castanea sativa Mill.)*. Holzforschung 57: 189-195.
9. Clair, B., T. Almeras, H. Yamamoto, T. Okuyama and J. Sugiyama (2006): *Mechanical Behavior of cellulose microfibrils in tension wood, in relation with maturation stress generation*. Biophysics Journal. 91: 1128-1135.
10. Yamamoto, H. (1998): *Generation mechanism of growth stresses in wood cell walls: Roles of lignin deposition and cellulose microfibril during cell wall maturation*. Wood Science and Technology. 32: 171-182.
11. Yamamoto, H. (2004): *Role of the gelatinous layer on the origin of the physical properties of the tension wood*. Journal of Wood Science. 50: 197-208.
12. Fang, C.H., B. Clair, J. Gril and S.Q. Liu (2008): *Growth stresses are highly controlled by the amount of G-layer in poplar tension wood*. IAWA Journal. 29: 237-246.

13. Wilson, B. and R.R. Archer (1979) *Tree design – Some biological solutions to mechanical problems*. Bioscience 29: 293-298.
14. Yoshida, M., T. Okuda, and T. Okuyama (2000): *Tension wood and growth stress induced by artificial inclination in Liriodendron tulipifera Linn. And Prunus spachiana Kitamura f. ascendens Kitamura*. Annals of Forest Science. 57: 739-746.
15. Yamamoto, H., M. Yoshida and T. Okuyama (2002): *Growth stress controls negative gravitropism in woody plant stems*. Planta 216: 280-292.
16. Kubler, H. (1987) *Growth stresses in trees and related wood properties*. Forest Products Abstract. 10: 62-118.
17. Okuyama, T., J. Doldan, H. Yamamoto and T. Ona (2004): *Heart splitting at crosscutting of Eucalyptus grandis logs*. Journal of Wood Science. 50: 1-6.
18. Abe, K. and H. Yamamoto (2007): *The influence of boiling and drying treatments on the behaviors of tension wood with gelatinous layers in Zelkova serrata*. Journal of Wood Science. 53: 5-10.
19. Clair, B. and B. Thibaut (2001): *Shrinkage of the gelatinous layer of poplar and beech tension wood*. IAWA Journal. 22: 121-131.
20. Norberg, H. and H. Meier (1966): *Physical and chemical properties of the gelatinous layer in tension wood fibres of aspen (Populus tremula L.)*. Holzforschung 6: 174-178.
21. Panshin, A.J. and C. de Zeeuw (1971): *Textbook of wood technology*, 3rd edn. McGraw-Hill Book Company, New York.
22. Boyd, J.D. (1977): *Relationship between fiber morphology and shrinkage of wood*. Wood Science and Technology. 11: 3-22.
23. Clair, B., B. Thibaut and J. Sugiyama (2005a): *On the detachment of the gelatinous layer in tension wood fiber*. Journal of Wood Science. 51: 218-221.
24. Abe, K. and H. Yamamoto (2006): *Behavior of the cellulose microfibril in shrinking woods*. Journal of Wood Science. 52: 15-19.
25. Abe, K. and H. Yamamoto (2005): *Mechanical interaction between cellulose microfibril and matrix substance in wood cell wall determined by X-ray diffraction*. Journal of Wood Science. 51: 334-338.
26. Hengstenberg, J. and H. Mark (1928): *Rontgenuntersuchungen uber den Bau der C-Ketten in Kohlenwasserstoffen*. Zeitschrift fur Kristallographie. 67: 583.
27. Kollmann, F. and H. Krech (1960): *Dynamic measurement of Damping Capacity and elastic properties of wood*. Holz als Roh- und Werkstoff. 18: 41-54.
28. Kojima, Y. and H. Yamamoto (2004): *Properties of the cell wall constituents in relation to the longitudinal elasticity of wood – Part 2. Origin of the moisture dependency of the longitudinal elasticity of wood*. Wood Science and Technology. 37: 427-434.
29. Clair, B., Gril J, K. Baba, T. Thibaut and J. Sugiyama (2005b): *Precautions for the structural analysis of the gelatinous layer in tension wood*. IAWA Journal 26: 189-196.
30. Clair, B., J. Gril, F. Di Renzo, H. Yamamoto and F. Quignard (2008): *Characterization of a gel in the cell wall to elucidate the paradoxical shrinkage of tension wood*. Biomacromol 9, 494-498.
31. Nishikubo, N., T. Awano, A. Banasiak, V. Bouquin, F. Ibatullin, R. Funada, H. Brumer, T.T. Teeri, T. Hayashi, B. Sundberg and E.J. Mellerowicz (2007): *Xyloglucan end-transglycosylase (XET) functions in gelatinous layer of tension wood fiber in Poplar – A glimpse into the mechanism of the balancing act of trees*. Plant and Cell Physiology. 48: 843-855.
32. Fang, C.H., B. Clair, J. Gril and T. Almeras (2007): *Transverse shrinkage in G-fibers as the function of cell wall layering and growth strain*. Wood Science and Technology. 41: 659-671
33. Cousins, W.J. (1976): *Elastic modulus of lignin as related to moisture content*. Wood Science and Technology. 10: 9-17.
34. Cousins, W.J. (1978): *Young's modulus of hemicellulose as related to moisture content*. Wood Science and Technology. 12: 161-167.
35. Salmén, L. and A.M. Olsson (1998): *Interaction between hemicellulose, lignin and cellulose: Structure-property relationships*. Journal of Pulp and Paper Science. 24: 99-103.
36. Akerholm, M. and L. Salmén (2003): *The oriented structure of lignin and its viscoelastic properties studied by static and dynamic FT-IR spectroscopy*. Holzforschung 57: 459-465.

Experimental analysis of the formation of tension wood induced by gravity for three mature beech trees on a 25 years duration.

*Adelin Barbacci*¹, *Thiéry Constant*¹, *Vincent Magnenet*², *Gérard Nepveu*¹ and *Meriem Fournier*³

¹ INRA UMR 1092, Laboratoire d'Etude des Ressources Forêt-Bois (LERFoB), Centre INRA de Nancy, F-54280 Champenoux, France.

² LAEGO-ENSG, Nancy-Université, Rue du Doyen Marcel Roubault, B.P. 40, 54501 Vandoeuvre-lès-Nancy, France

³ AgroParisTech, UMR 1092, Laboratoire d'Etude des Ressources Forêt-Bois (LERFoB), ENGREF 14 rue Girardet, F-54000 Nancy, France.

Abstract

The growth of three mature beech trees has been reconstructed in retrospect on 25 years (e.g. from 2005 to 1980) thanks to a mechanical model fed by experimental data. Thus, two hypotheses concerning the link between the growth of the tree and the localisation of the differential of maturation strain, associated with the presence of tension wood, have been tested. In the first case, the differential of maturation strain and the tension wood were created on the upper side of leaning parts of the stem and, in the second case, the same elements were created to counteract the effect on the bending moment generated by the crown and due to the growth of the tree. The comparison between, the measured areas of tension wood and the assumed ones, has not allowed to give a preferential order between both mechanisms. However, the second assumption could be considered as attractive from the mechano-perception point of view but difficult to distinguish from the gravity perception especially in the case of mature trees, considered here.

Introduction

The tree morphology must be very plastic for adapting the plant to available resources. Thus, the morphology and the architecture of a tree are dependent of time and environment and they are led by different tropisms. Maturation stresses in the last age-ring act an important role in the tropisms allowing axes reorientation all along the life of the tree [1, 7, 12]. During the first development stages, the existence of a growth maturation differential is without effect on the future wood quality except in few cases. Nevertheless, for mature trees, the accumulation in time of important growth stresses could decrease the technological and the financial economical value of a tree [13]. In beech trees (*Fagus sylvatica* L.), high growth stresses level is most of time associated with reaction wood and known as one of the main factors decreasing the wood quality.

In a forestry context where high forests are less and less the standards, the limits of empirical models are often reached [6, 9]. A more functional approach concerning the formation of high growth maturation stresses is needed but through this work a simple mechanical approach, at tree scale, is tested..

Conceptually, the annual growth of a tree could be divided into two parts. In the first one, the elongation of the apical parts and the cambial growth, leading to a biomass increment, could participate in the global disequilibrium of the whole tree. Thus, in the second part, a differential of wood maturation in the last age-ring could be created [2, 11, 12] in order to oppose the effect of this differential to the disequilibrium. This conceptual sketch has already been investigated by several

mechanical models [3, 10, 12] . The purpose of this work consists in an experimental validation of this scheme for three mature beech trees by testing two possible assumptions governing the tension wood formation along the trunk and linked to different perceptions of the gravity effect : i) local leaning ii) local bending moment The virtual angular locations of the tension wood areas were compared with the measured ones [4] thanks to a software based on the mechanical model and fed by experimental data in a retrospective way starting from the last known configuration.

Material and methods

Our mechanical model has been established to describe the displacement of the trunk under the loading of the crown [5]. In this model, the action of the crown on the trunk has been described by a force corresponding to the weight of the crown, and the moment relative to this force expressed at the end of the trunk.

If we call $s(t)$, the generatrix of the trunk in time, r the radius of the crosscut disc, m^{crown} the mass of the crown, G^{crown} its barycenter, m^{trunk} the mass of the trunk, E the modulus of elasticity and GSI the growth stresses indicators we can write:

The perturbation contribution (1)

The reaction contribution (2)

And (3)

The measurement of the parameters involved in the equations (1) and (2) as well as the expression of f and g have been presented at the last plant Biomechanics conference [5].

Thanks to a software based on this model, a virtual experiment has been performed in retrospect (from the last position of the tree to the virtual position of the tree 25 years before) using the measured configuration of the tree on the year 2005 and some time-dependent measurements available for three mature beech trees e.g. horizontal crown projections, ring widths. Thus, from the last configuration of the tree, the position of the barycentre of the crown and its biomass increment between these two years were estimated and assumed areas of tension wood (TW), determined by two scenarios, are virtually generated. Then the biomass of the last age-ring in the trunk has been removed to obtain the tree in a configuration corresponding to the year before. This loop has been repeated twenty four times. Thus, in the following the emphasis is put on the reconstruction of the time dependency of the parameters. The crucial case of the barycentre of the crown is presented in detail.

1. Reconstruction of the history of growth

The time dependency of the radius has been determined directly from measurements of tree rings size. These sizes have been measured on four directions for one crosscut discs corresponding to one meter long log. In our model, the shape of the crosscut surfaces has been supposed circular and the size of a ring set equal to the average of the four measured values. As we have supposed the length of each log constant over our time range, the volume of each log has been easily calculated. As we have assumed the green density constant in time, the mass of each log has been calculated as the product of the latter and the volume.

To estimate the weight of the crown we have assumed that that weight was proportional to the surface S of the crown projection on the ground so:

(4)

2. Specific case of the barycentre of the crown

To determine the time dependency of the barycentre of the crown the easiest parameter usable was the surface of the projected crown. The vertical position of the barycentre has no influence in the value of the bending moment which is only function of its position in the horizontal plane. Assuming the geometrical centre of the projected crown as the centre of the weight of the crown would be very useful. This assumption has ever been performed in several works [3, 14]. In the next lines a mathematical demonstration is developed confirming its validity.

a. Mathematical formulation

The aimed result is that for a given crown projection whatever is the mass distribution, the distance between the geometrical centre of the crown projection area and the barycentre was not sensitive to a small variation of the mass distribution.

The geometrical centre of the projected crown is defined as:

$$OG_g = \frac{1}{S} \int_S O M \, dS \quad (5)$$

M is a point belonging to the projected surface S and have the coordinates (x,y) . dS is a surface element around M . We called $\rho = \rho(x,y)$ the mass per area unit and G_m the centre of the mass defined as:

$$OG_m = \frac{1}{m} \int_S \rho O M \, dS \quad (6)$$

with $m = \int_S \rho \, dS$. We are interested by the vector $G_g G_m$ which represents the “difference” between the center of the mass and the geometrical one. With (5) and (6) we write

$$G_g G_m = OG_m - OG_g = \frac{1}{m} \int_S \rho O M \, dS - \frac{1}{S} \int_S O M \, dS \quad (7)$$

From a mathematical point of view, the application associating the vector $G_g G_m(\rho)$ to the function $\rho(x,y)$ is an functional integral. If we take into account the term proposed by Olver [16], the space variables x,y are the independent variables whereas ρ is the dependent one. To study the influence of a variation $\delta\rho$ on $G_g G_m$ we introduce the variation:

$$\rho \rightarrow \rho + \delta\rho$$

and the Lagrangian L of the functional:

$$L = \int_S \rho O M \, dS - \frac{1}{S} \int_S O M \, dS \quad (8)$$

The variation of this functional inferred by the variation $\delta\rho$ may be calculated by the general variation formulae (see e.g. [16]):

$$\delta L = \int_S \left(\frac{\partial L}{\partial \rho} \delta\rho \right) dS \quad (9)$$

in which the so-called Euler operator E accounts for all the derivatives of L with respect to ρ :

$$E = \frac{\partial}{\partial \rho} - \sum \left(\frac{\partial}{\partial x} \frac{\partial}{\partial \rho_x} + \frac{\partial}{\partial y} \frac{\partial}{\partial \rho_y} \right) \quad (10)$$

Since the functional given in (8) does not depend on the derivatives in space of ρ , that is $\partial\rho/\partial x$ and $\partial\rho/\partial y$, the Euler operator (10) identifies here to the derivative with respect to ρ . Consequently, Eq. (9) rewrites in the present case:

$$\delta L = \int_S \delta\rho O M \, dS \quad (11)$$

We call χ_i , the parameters involved in the expression of ρ . A variation $\delta\chi_i$ of these parameters allows to write:



$$\text{Diagram (12)} \quad (12)$$

In order to numerically compute the integral of the equation (6), the surface of the projected crown S has been rasterized in N sub-surfaces S_j . So, we can write:



$$\text{Diagram (13)} \quad (13)$$

with M_j the barycenter of S_j . We know that the mass of the crown is a decreasing function of the distance to the main axis of the tree. To model a flexible weight distribution, ranging from a rather uniform to a punctual distribution of the mass, an exponential function has been chosen:

$f(r) = A e^{-\beta r}$ with r the norm of the vector \mathbf{OM} . An additional constraint has been added to impose a low mass ε when the point M belonged to the outline of the projected area ∂S . If we consider the point $N(x_N, y_N)$ as $N \in \partial S$ such as $N \in \mathbf{OM} \perp \partial S$, ρ is written:



$$\text{Diagram (14)} \quad (14)$$

The surface on the crown has been meshed with GMSH [15]. The value of $\mathcal{G}_g \mathbf{G}_m$ has been computed with (7) and the expression of $\frac{\partial \rho}{\partial \beta}(M)$ and $\frac{\partial \rho}{\partial \varepsilon}(M)$ calculated with (14).

b. Test of sensitivity

The parameters χ_i (e.g. ε , β) have been chosen in order to represent a great range of crown biomass variation since the interval represent every distribution from the quite punctual one ($\varepsilon \ll \beta$) to a constant one ($\varepsilon = \beta$). The values of the variations of $\delta \chi_i$ have been chosen small e.g. 3%, 5% and 10% of the value of the parameter χ_i (Table 1). The results of the test of sensitivity are presented on the figure 1.

Table 1: Numerical values of the parameter for the sensitivity test

Parameter χ_i	β	ε
If constant	100	0.01
Range of variation	[1;100]	[0.01;10]

The value of the parameter β has no incidence on the variation of the length $G_g \mathbf{G}_m$ when ε was set constant and $\delta \varepsilon = 0$. Moreover, this variation could be considered as exclusively function of $\delta \beta$. ε was more important for the variation of $G_g \mathbf{G}_m$: the more ε was great and the more its variation implied an important variation of $G_g \mathbf{G}_m$. However this variation has the order of size of the centimeter. Even if our assumptions concerning the distribution are coarse this results pinpoint the importance of change of mass events at the periphery of the crown.

c. Experimental validation

To give an idea of the variation of weight between two years, we have used a model [17] giving the total aboveground biomass by using as inputs data coming from each tree. This variation was found as equal to approximately 10%. If we assumed that the weight of the main axis of the tree is proportional to this volume then the annual growth could be reflected by the 10% variation of β . If we assumed a variation of the parameter ε we can conclude that the difference between both centers (e.g. the distance $G_g \mathbf{G}_m$) is around five centimetres. This length is small compared with the precision of measurement so we have concluded that by considering the distance $G_g \mathbf{G}_m$ as not affected by a variation of growth between two consecutive years can be a valid assumption for calculation.

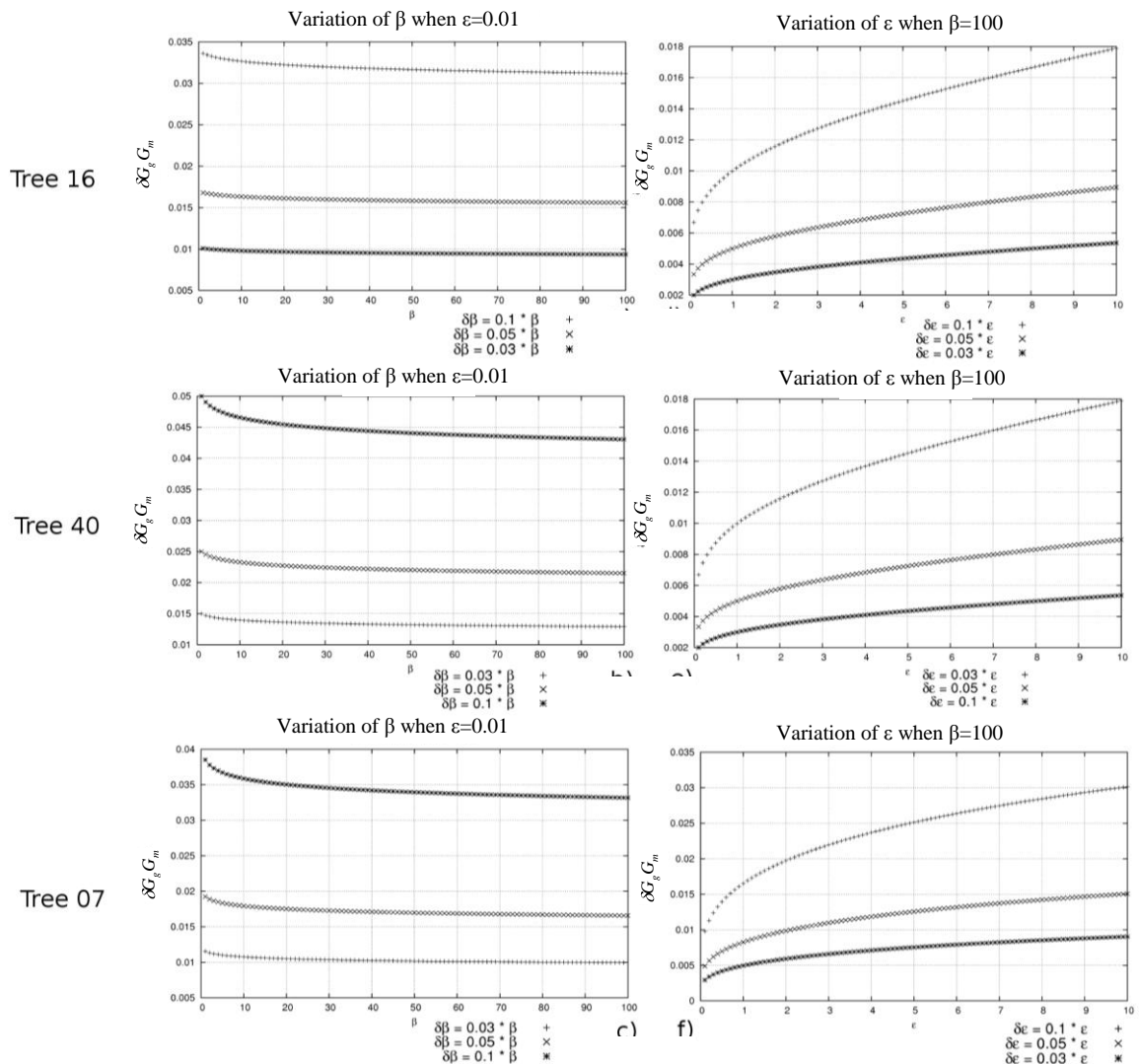


Fig 1 Results of the sensitivity test for the three trees. Left column: variations of β . Right column: variations of ϵ .

The table 2 presents for the three trees, the position of the barycentre and the position of the geometrical centre of the crown of the trees. They could be considered as in the same position. So, as the growth do not perturbed the distance between the both centres and as they are in the same position at the last time, they could be considered as identical points all along the growth of the tree.

Thus in our work we have considered the barycentre situated at the geometrical centre of the projected crown area.

Table 2 Numerical value of the parameters needed to experimentally justify the sensitivity test

Tree	16	07	40
Variation of the volume of the crown (between 2002 and 1997) (m ³)	0.04	0.01	0.08
Variation of the volume of the crown (between 2002 and 1997) (%)	8	9	10
Centre of weight 2002 (OG _m)	(0.64;-0.15)	(0.53;-0.68)	(0.9;-0.17)
Centre of the geometry 2002 (OG _g)	(0.64;-0.18)	(0.52;-0.60)	(0.72;-0.48)

Results and discussion

The successive configurations of the tree have been computed on 25 years. To perform that, an assumption, concerning the position where the differential of maturation strain was created, was needed. Two scenarios have been tested. In the first one, the classical hypothesis which considered that the differential is created on the upper face of inclined logs has been tested. An other hypothesis, assuming that the differential of tension wood is created in order to counteract the effect on the bending moment created by the action of the crown on the trunk has been tested. In both scenarios, virtual azimuth has been associated to each log at each time step. This assumed tension wood area have been compared with the area measured on the surface of each crosscut discs [4]. In the case of scenario 1, if the hypothesis is true then the area of tension wood is formed in the same direction than the local upper face of each. In the case of the scenario 2, if the hypothesis is true then, the area of tension wood is formed orthogonally to the direction of the bending moment. To show the difference between both assumptions, Figure 2 presents the relative proportion of calculated areas exhibiting an angular difference of orientation grouped by angular sector of sixty degrees.

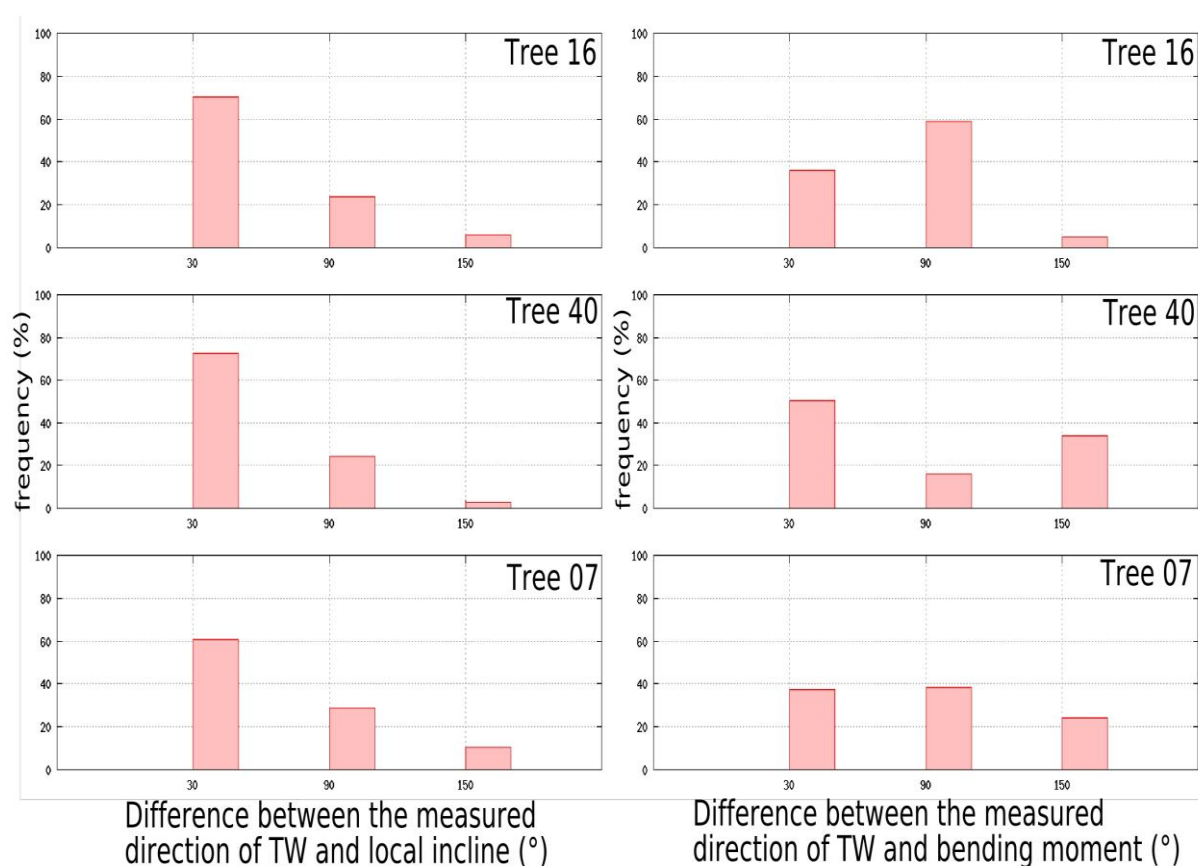


Fig 2 Frequency of the angular difference between the measured areas of tension wood and the assumed ones for the 3 trees. Left column: scenario “incline”. Right column scenario “bending moment”.

In the case of scenario 1, the majority of point was located in the direction which confirmed the hypothesis assuming that the TW associated to the highest value of maturation strain is created in the upper face of each log. Concerning the scenario 2, the tendency was less obvious but, except for the tree 40, the majority of point has been created such as the differential of maturation strain countered the effect of bending moment created by the growth of the crown.

The statistical representativeness of the pool is quite null and void (only 3 trees) so, it is not possible to give a ruling on the better validity of one hypothesis. Moreover, a coupling between the incline and the bending moment exists and, on mature trees, not easily separable. However, from a qualitative point of view, observations relate that in straight and vertical trees, TW can occur in the

last age ring (for example when the tree has compensated the disequilibrium due to the growth in one season). So, this assumption is not always satisfying. The second hypothesis tends to confirm the theory suggested by Coutand et al. [8] and observed on tomato stems demonstrating that the signal received by the tree is the integration of the longitudinal strain. Indeed, as



the azimuth of the highest strain is the same than the bending moment one. More investigation are needed to discriminate both hypothesis. In the case of mature trees in forest stand, some metrological development, allowing the measurement of the spatial distribution of the geometry, are necessary. Tools based on the exploitation of a point cloud given by a terrestrial LIDAR are developed nowadays by LERFoB for these reasons.

Acknowledgements

The authors acknowledge financial support by the french forestry office (ONF) for (contract Model for Contract n°12B06146, INRA DS-ECONAT ECOGER Project P000295) and the regional council of Lorraine support for the emergent project (n°532-2005). The authors wish also to thank the technicians involved in the field work: Emmanuel Cornu, Etienne Farre, Pierre Gelhaye, Maryline Harroué, Claude Houssement, Alain Mercanti.

References

1. Alméras, T., J. Gril, and E. Costes, (2002) *Bending of apricot tree branches under the weight of axillary growth: test of a mechanical model with experimental data*. *Trees-Structure & Function*. **16**(1): p. 5-15.
2. Almeras, T., A. Thibaut, and J. Gril, (2005) *Effect of circumferential heterogeneity of wood maturation strain, modulus of elasticity and radial growth on the regulation of stem orientation in trees*. *Trees-Structure and Function*. **19**(4): p. 457-467.
3. Ancelin, P., T. Fourcaud, and P. Lac, (2004) *Modelling the biomechanical behaviour of growing trees at the forest stand scale. Part I. Development of an Incremental Transfert Matrix Method and application to simplified tree structures*. *Ann For Sci*. **61**: p. 263-275.
4. Barbacci, A., T. Constant, E. Farré, M. Harroué, and G. Nepveu, (2008) *Shiny beech wood is confirmed as an indicator of tension wood*. *IAWA*. **29**(1): p. 35-46.
5. Barbacci, A., T. Constant, and G. Nepveu. *Restoring shape history of a beech tree using growth stresses analysis: acquisition of necessary data*. in *Fifth plant biomechanics conference*. 2006. Stockholm, Sweden: STFI-PACKFORSK.
6. Becker, G., T. Beimgraben, and R. Mutz. *Stresses in beech: occurrence and consequences for wood quality; prediction on the base of stand and tree parameters*. in *Fourth workshop IUFRO*. 2002.
7. Castera, P. and V. Morlier, (1991) *Growth patterns and bending mechanics of branches*. *Trees-Structure & Function*. **5**(5): p. 232-238.
8. Coutand, C., J.L. Julien, B. Moulia, J.C. Mauget, and D. Guitard, (2000) *Biomechanical study of the effect of a controlled bending on tomato stem elongation: global mechanical analysis*. *Journal of Experimental Botany*. **51**(352): p. 1813-1824.
9. Ferrand, J.C., (1982) *Etude des contraintes de croissance. Deuxième partie: variabilité en forêt des contraintes de croissance du hêtre (Fagus sylvatica L.)*. *Annales des Sciences Forestières*. **39**(3): p. 187-217.
10. Fourcaud, T., F. Blaise, P. Lac, P. Castéra, and P. de Reffye, (2003) *Numerical modelling of shape regulation and growth stresses in trees. II. Implementation in the AMAPpara software and simulation of tree growth*. *Trees-Structure & Function*. **17**(1): p. 31-39.

11. Fourcaud, T. and P. Lac, (2003) *Numerical modelling of shape regulation and growth stresses in trees. I. An incremental static finite element formulation*. *Trees-Structure & Function*. **17**(1): p. 23-30.
12. Fournier, M., H. Bailleres, and B. Chanson, (1994) *Tree biomechanics: growth, cumulative prestresses and re-orientations*. *Biomimetics*. **2**: p. 229-251.
13. Fournier, M., B. Chanson, B. Thibaut, and D. Guitard, (1991) *Mécanique de l'arbre sur pied: modélisation d'une structure en croissance soumise a des chargements permanents et évolutifs. 2. Analyse tridimensionnelle des contraintes de maturation, cas du feuillu standard*. *Annales des Sciences Forestières*. **48**(5): p. 527-546.
14. Fournier, M., P. Langbour, and D. Guitard, (1990) *Mécanique de l'arbre sur pied : les relevés dendrométriques classiques pour quantifier les efforts gravitationnels supportés par un tronc - leurs limites*. *Ann For Sci*. **21**: p. 565-577.
15. Geuzaine, C. and J.F. Remacle, *Gmsh: a three-dimensional finite element mesh generator with built-in pre-processing facilities*. 2007.
16. Olver, P., *Application of Lie groups to differential equations*. 1989: Springer Verlag.
17. Vallet, P., J.F. Dhote, G. Le Moguedec, M. Ravart, and G. Pignard, (2006) *Development of total aboveground volume equations for seven important forest tree species in France*. *Forest Ecology and Management*. **229**(1-3): p. 98-110.

The gravitropic control of woody stems orientation: biomechanical parameters involved and consequences for stem allometry

Tancrede Alméras¹, Mériem Fournier²

¹ CNRS-University of Montpellier, France; ²Agro-Paris-Tech, Nancy, France

Abstract

Tree stems are slender structures and are never perfectly vertical and symmetric. As a consequence, the increase in tree mass that occurs during growth always causes bending movements disturbing stem orientation. In the absence of a compensatory mechanism, the accumulation of these downward bending movements over time would necessarily result in an ever-increasing curvature of the stems, preventing vertical growth and ultimately leading to a weeping habit. To control the orientation of growing aerial organs in the field of gravity, some gravitropic correction is needed. In trees, this correction is achieved by the asymmetric production of mechanical stress during the maturation of the newly formed wood, often associated to the presence of reaction wood. The change in orientation of a growing stem depends on the balance between the disturbance related to the increase in mass, and the correction, related to the increase in diameter and the associated gravitropic reaction. A biomechanical model was developed to compute the rates of disturbance and correction theoretically associated to a growth increment. They were analytically expressed as a function of parameters defining stem morphology, cross-section anatomy and wood properties. The efficiency of the gravitropic correction depends on the asymmetry of wood maturation strain, eccentric growth, and gradients in wood stiffness. For a tree to keep its stem at a constant orientation during growth, the correction must compensate the disturbance at any time. Analyzing the size effects in the formulae, we show that this necessity might constrain stem allometric growth to be such that $H \sim D^{1/2}$. This allometric constraint was quantified using literature data and compared to the condition for elastic stability ($H \sim D^{2/3}$). When a tilted stem grows, the gravitropic constraint quickly becomes more constraining than elastic stability, and this constraint is larger when the tilt angle is larger. We conclude that traits determining the gravitropic performance set constraints on the growth of tilted stems, and may be the main constraint limiting the horizontal extension of branches.

Introduction

Plant stems are slender mechanical structures. Their erect habit is mainly constrained by bending movements in response to wind and gravity. Quantitative mechanical analyses of these bending movements and forces usually focus on instantaneous mechanical disturbance, using stiffness, breakage or buckling analyses [8,9,10,12,13]. However, gravitropism (the ability of plant to sense and respond to the gravity), plays a key role in explaining how plant stems can maintain an erect habit, by generating internal forces that counteract the above-mentioned disturbance. The control of aerial organ orientation with respect to gravity is necessary to allow the self-standing habit of terrestrial plants, especially in extremely slender, long-lived gigantic structures such as trees [11]. The motor of such internal bending forces in lignified axes is wood maturation: at the end of the differentiation of new wood layers, mechanical stresses named ‘growth stresses’ or ‘maturation stresses’ appear in wood. Asymmetric maturation stresses are usually observed around the stem circumference, often associated to the unilateral presence of reaction wood. This causes the axis to bend during growth, and is the

basic mechanism of the gravitropic reaction in trees [14]. Without this control process, the increasing mass of growing trees would make the stem bend more and more, and gravity would be a terrific ecological constraint: with the currently observed mechanical designs (slenderness ratio, mass distributions and wood stiffness), trees would adopt a weeping habit because of the interaction between growth and gravity [4,5]. Thus, long-term mechanical safety is not only a question of stiffness, breakage or buckling, but also involves a balance between the slow and long-term mechanical disturbance due to self weight, and the gravitropic correction process related to reaction wood production.

A simple model has been previously published [4] providing a tool to quantify the gravitropic process and its dependence to stem size and wood properties. It is however restricted to a circular cross-section and concentric growth. When applying this model to an ecophysiological analysis of gravitropic movements of young poplars [3], we noticed that this version is too limited to properly describe some real world situations. The aim of the present work was to develop a more general biomechanical model relating the bending movements (*i.e.* changes in curvature) of woody stems to a finite number of measurable traits describing the stem dimensions, growth allocation and wood properties. It combines a model of the disturbance induced by gravity and a model of the correcting gravitropic process. By analyzing this model, we infer theoretical predictions about the mechanical design of trees and the conditions for long-term biomechanical stability, and compare them to the conditions for elastic stability based on buckling analysis [6,8].

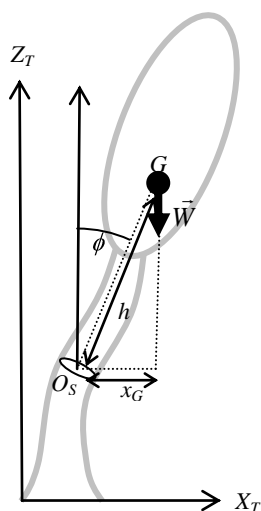
Material and methods

The bending movements of tree stems during growth are modelled using beam theory. The tree is assumed perfectly anchored at its base and having bilateral symmetry, so that it is sufficiently described in a vertical plane (*fig. 1*). The analysis concentrates at the level of a section, and focuses on predicting the local changes in curvature dC (*i.e.* the local rate of rotation) that happens during the growth of an elementary increment in section diameter dD . The section is supposed circular and its neutral line is assumed to be located at its centre, but the wood increment is potentially eccentric and with heterogeneous material properties (*fig. 2*). The total change in curvature results from the superposition of two additive contributions: the effect dC^{weight} of the increase in tree weight associated to growth, and the effect dC^{matur} of the maturation of the new wood increment:

$$dC^{total} / dD = (dC^{weight} + dC^{matur}) / dD \quad (1)$$

The changes in curvature dC can be deduced from the changes in bending moment dB , the homogenized modulus of elasticity of the section E and the diameter of the section D :

$$dC = dB / \left(\frac{\pi}{64} ED^4 \right) \quad (2)$$



*Fig. 1 Schematic representation of the effect of self weight in a tree with bilateral symmetry. O_S is the center of a given cross-section, W is the weight of the part of the tree located distally to the section, G is the location of the center of mass of the distal part, defined by its tilt angle ϕ and its distance h with respect to O_S . The lever arm, *i.e.* the projected distance between the section and the center of mass is $x_G = h \cdot \sin \phi$.*

The bending moment induced by the tree weight at the level of a cross-section can be expressed as $B^{weight} = W \cdot h \cdot \sin\phi$, where W is the weight of the tree located distal to the section, h is the distance between the section and the centre of mass of the distal part of the tree, and ϕ is the angle of the line joining the section centre to the centre of mass of the distal part of the tree (fig. 1). We assume that the taper and load distribution along the tree stem can be described by allometric power functions, which fit generally well experimental data [8]. For a stem having total length H , basal diameter D , and total mass M , at a given position along the stem defined by its curvilinear abscissa s from the stem base, the diameter is given by $D(s) = D \cdot (1 - s/H)^n$ and the mass of the distal part is given by $M_>(s) = M \cdot (1 - s/H)^m$. Parameters n and m characterise the shape of the diameter changes and mass distribution along the stem. Consistently with [8], we define the load ratio of the stem L as the ratio between the total mass of the tree and the stem volume. The tree weight W and the distance to the centre of mass h can be expressed as functions of these parameters and the gravity constant g , finally yielding the following expression for B^{weight} :

$$B^{weight} = \frac{\pi}{4} g \frac{L \sin\phi}{(m+1)(2n+1)} H^2 D^2 \quad (3)$$

To compute the change in bending moment dB^{weight} associated to dD , we need to specify how these parameters change during growth. We will ignore the change in global orientation of the stem ϕ and assume that morphological parameters n , m and L are constant during growth. The change in height is assumed related to the change in diameter by a power function, so that $dH/H = b \cdot dD/D$. Differentiating equation (3) with respect to D , and using equation (2), the rate of change of curvature due to the weight increment associated to diameter growth can be expressed as:

$$\frac{dB^{weight}}{dD} = 32g \frac{L \sin\phi(1+b)}{E(m+1)(2n+1)} \frac{H^2}{D^3} \quad (4)$$

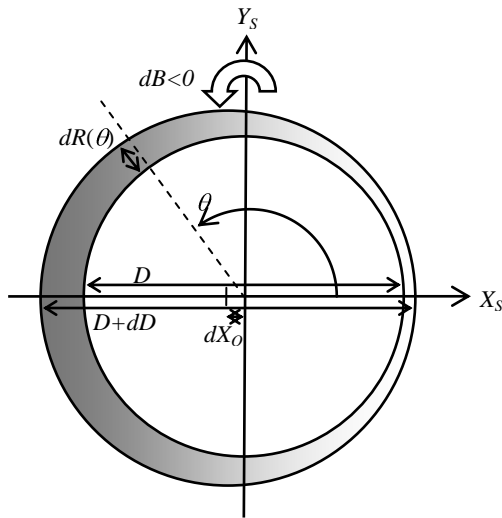


Fig. 2 Model of heterogeneous eccentric section of diameter D submitted to a diameter increment dD . Eccentric growth implies a change dx_o in the position of the section's center, and heterogeneous wood thickness $dR(\theta)$ around the circumference. The stem is assumed to be leaning in the positive X_s direction so that the left side on the figure is the upper side of the tilted stem, and the right side on the figure is the lower side of the tilted stem. Variations in greyness indicate heterogeneity of the material properties within the new growth ring (see text). The reaction (here illustrated for a hardwood species) is expected to generate a negative change in bending moment $dB < 0$, generating a change in curvature $dC < 0$ (i.e. up-righting movement).

The bending moment induced by the maturation of the wood increment can be computed from its geometry and the distribution of material properties. The distributions of modulus of elasticity E within the increment, the maturation strain α and the ring thickness dR are defined as cosine functions of the polar coordinate in the ring, θ :

$$\alpha(\theta) = \bar{\alpha} + \Delta\alpha/2 \cdot \cos\theta \quad (5),$$

$$E(\theta) = \bar{E} \cdot \left[+k_E \cdot \cos\theta \right] \quad (6),$$

$$dR(\theta) = dR \cdot \left[+k_o \cos\theta \right] \quad (7),$$

where $\bar{\alpha} = \left[\alpha(0) + \alpha(\pi) \right] / 2$ is the mean maturation strain, $\Delta\alpha = \alpha(0) - \alpha(\pi)$ is the difference in maturation strain between the lower and the upper side of the section, $\bar{E} = \left[E(0) + E(\pi) \right] / 2$ is the mean

modulus of elasticity, $k_E = \frac{E(0) - E(\pi)}{E(0) + E(\pi)}$ characterizes the heterogeneity of the elastic modulus, dR is half of the diameter increment and $k_o = \frac{R(0) - dR(\pi)}{R(0) + dR(\pi)}$ characterizes the degree of eccentricity. The increment in bending moment due to the maturation of the ring is integrated as:

$$dB^{matur} = -dR \cdot \int_0^{2\pi} R \cdot \cos(\theta) \cdot \alpha(\theta) \cdot E(\theta) \cdot (1 + k_o \cdot \cos(\theta)) \cdot R \cdot d\theta \quad (8)$$

Finally yielding the following expression:

$$dB^{matur} = -\pi / 2 \cdot \bar{E} \cdot R^2 \cdot dR \cdot (\Delta\alpha \cdot (1 + 3/4 \cdot k_E \cdot k_o) + 2\bar{\alpha} \cdot (E + k_o)) \quad (9)$$

Using equation (2), the change in curvature due to wood maturation is computed as:

$$\frac{dC^{matur}}{dD} = -4 \frac{\Delta\alpha \cdot f \cdot \bar{E} / E}{D^2} \quad (10),$$

where $f = 1 + 3/4 \cdot k_E \cdot k_o + (E + k_o) \cdot 2\bar{\alpha} / \Delta\alpha$ is a form factor that mainly depends on the ring eccentricity and heterogeneity of its elastic modulus. Factor f is 1 for a concentric ring with homogeneous elastic modulus, as assumed in earlier models [4], and is >1 if the part of the ring containing reaction wood has a larger thickness and larger modulus of elasticity than the opposite side.

Results and discussion

Changes in curvature due to the weight and maturation are at the first order proportional to the amount of growth dD . Equations (4) and (10) show how the coefficient of proportionality depends on biomechanical traits related to the tree morphology and the distribution of wood properties. Equation (10) shows that the effect of wood maturation is submitted to a size effect (D^2 in the denominator). The numerator defines the “efficiency” of the gravitropic reaction ($e_r = \Delta\alpha \cdot f \cdot \bar{E} / E$), *i.e.* the intrinsic ability of the mechanical design to induce curvature changes, independently of the size or growth rate. It is noteworthy that this efficiency depends on gradients in wood properties rather than on the mean value of these properties. The effect of the circumferential gradient in maturation strain $\Delta\alpha$, which was the only one taken into account in earlier models [4], has been demonstrated to be the most important effect [2]. Circumferential gradients in wood thickness and stiffness, accounted by the form factor f , have a complementary role that is often non-negligible [2]. Another complementary factor was identified in the present analysis: the radial gradient in stiffness, accounted by factor \bar{E}/E . Quantitative analysis shows that this factor can be non-negligible, *e.g.* in stems of small diameter where the pith represents an important part of the section diameter (for a more detailed analysis, see [1]).

The gravitropic control of the stem shape and orientation results from the balance between two actions: the disturbance dC^{weight} due to gravity and the correction dC^{matur} due to the gravitropic reaction. In order to quantify the overall ability of a stem to control its orientation, we define an integrated trait of “gravitropic performance”, P_g , as the ratio between the correction and the disturbance:

$$P_g = \frac{-dC^{matur}}{dC^{weight}} = \frac{1}{8g} \cdot \bar{E} \cdot \Delta\alpha \cdot f \cdot \frac{1}{L} \cdot \frac{1}{\sin\phi} \cdot \frac{(n+1)}{(1+b)} \cdot \frac{D}{H^2} \quad (11)$$

The gravitropic performance indicates the dynamics of bending induced by growth: if it is >1 growth creates an upward curving process, if it is <1 growth creates a downward bending, and if it is $=1$ the stem is at biomechanical equilibrium, *i.e.* the curvature does not change when the stem grows. P_g is larger if the wood produced is stiff (large \bar{E}), with large asymmetry of maturation strains ($\Delta\alpha$), a good form factor (large f , achieved by a larger ring width and wood stiffness on the side with reaction wood), and if the stem has a low load ratio (L), a low tilt angle (ϕ), a low center of mass (large m), a large tapering coefficient (n), a small ratio of relative height growth to relative diameter growth (b), a large diameter (D) and a small height (H).

For a tilted stem to keep a constant angle during growth, it must keep $P_g=1$. Usually, this can be achieved just by adjusting the level of gravitropic reaction in the newly formed wood, *i.e.* the values of $\Delta\alpha$, f and \bar{E} . If the tilt angle ϕ is large, it may also be necessary to adjust morphological parameters (L ,

m, n, b). Biomechanical parameters can exhibit adaptive or ontogenetic variations, but are contained within relatively narrow ranges of value linked to the developmental constraints of their species, so that their maximal value can be regarded as constant during growth. On the contrary, stem dimensions (D and H) increase dramatically during growth. Therefore, for a stem to remain at a constant angle while it grows, the term D/H^2 should remain constant, *i.e.* the stem should satisfy an allometry such that H is proportional to $D^{1/2}$ (*i.e.* $b=1/2$). Moreover, even if the stem obeys this allometric rule, one can deduce from equation (11) that the maximal angle at which it can sustainably lie depends on the biomechanical parameters, and is given by $P_g=1$:

$$\sin \phi_{\max} = \frac{\bar{E} \cdot \Delta\alpha \cdot f \cdot \overline{C_{n+1}} \cdot \overline{C_{n+1}}}{12g \cdot L} \cdot \frac{D}{H^2} \quad (12)$$

If the tilt angle becomes larger than ϕ_{\max} because of a mechanical accident or an insufficient reaction, then the stem forms an unstable biomechanical configuration ($P_g < 1$). Indeed, to induce an up-righting movement, the stem must produce new wood, but the weight increment associated with this wood would induce an additional downward bending larger than the attempted correction. Moreover, this downward bending would increase the tilt angle ϕ , which would further reduce P_g , condemning the stem to bend more and more. A stem could probably recover from such a situation, for example by an appropriate timing and location of the reaction along the stem, but this would severely constrain height growth. The maximal height that a stem can achieve while keeping a constant tilt angle can be deduced by reversing equation (12):

$$H_{\max}^{\text{gravitropism}} = \left(\frac{\bar{E} \cdot \Delta\alpha \cdot f \cdot \overline{C_{n+1}} \cdot \overline{C_{n+1}}}{12g \cdot L \cdot \sin \phi} \right)^{1/2} \cdot D^{1/2} \quad (13)$$

The allometric rule $H \sim D^{1/2}$ and the maximal height can be compared to those associated to other biophysical constraints. Greenhill [6] showed that to keep a constant safety factor against the risk of elastic buckling, the allometric growth of a vertical stem should be such that $H \sim D^{2/3}$. The relationship between the maximal height before buckling, the stem basal diameter and the value of biomechanical parameters (adapted from [8]) is:

$$H_{\max}^{\text{buckling}} = \left(\frac{E \cdot \overline{C_{n+1}} \cdot c^2 \cdot \overline{C_{n-4n+2}}}{64 \cdot g \cdot L} \right)^{1/3} \cdot D^{2/3} \quad (14)$$

where c is a function of n and m detailed in [8].

The critical buckling height computed from measured biomechanical parameters [8] is plotted on *fig. 3* as a function of stem basal diameter, and compared to the maximal height computed from equation (13), for various tilt angles ϕ .

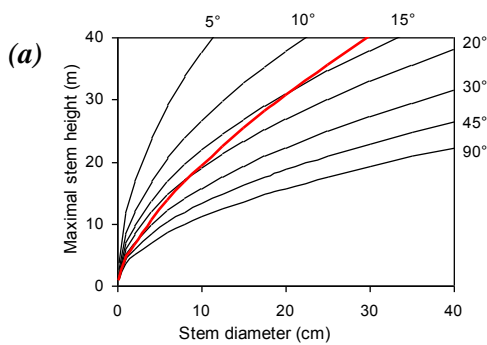
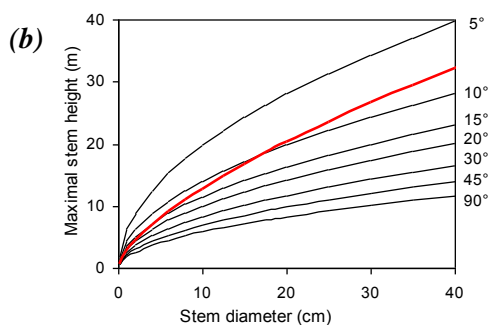


Fig. 3. Relation between basal diameter and maximal height, for a vertical stem submitted to the risk of elastic buckling (thick red line), and for growing stems leaning at various angles (thin black lines). Data are based on mean gravitropic parameters ($\Delta\alpha=0.17\%$, $f=1.54$) measured on 11 tropical angiosperm tree species [2] and mechanical and morphological parameters measured on 15 tropical angiosperm tree species [8]:

(a) Using overall mean parameters: $E=1.23 \cdot 10^{10} \text{ N.m}^{-2}$, $m=1.62$, $n=0.66$, $c=4.72$, $L=1340 \text{ kg.m}^{-3}$

(b) Mean stem of a severely constrained species (*Sextonia rubra*): $E=8.50 \cdot 10^9 \text{ N.m}^{-2}$, $m=0.63$, $n=0.3$, $c=2.61$, $L=1438 \text{ kg.m}^{-3}$.



These numerical applications show that the maximal height of a stem may be constrained either by its gravitropic performance or by its elastic stability, depending on its diameter and tilt angle. A stem growing at a constant angle is limited by elastic stability until it reaches a critical diameter, after which gravitropism becomes more limiting. The two constraints theoretically represent mutually exclusive situations: elastic buckling is relevant for a vertical stem, whereas gravitropic control is relevant only for a tilted stem. A real stem is never perfectly vertical, so that bending movements always occur and some gravitropic control is needed. If the stem is close enough to vertical (ϕ is small so that P_g is large), this control can be easily achieved and only elastic stability limits stem allometric growth. For a larger tilt angle however, the requirements for gravitropic control quickly become more constraining than elastic stability as the stem grows.

The extent to which allometric growth is limited by either of these biomechanical constraints strongly depends on the value of the biomechanical parameters. Figure 3 provides a comparison between a “mean” stem (average of biomechanical parameter over 15 tropical angiosperm tree species, *fig. 3-a*), and a particular species that is severely constrained by gravitropism (*Sextonia rubra*, *fig. 3-b*). For instance, for a stem diameter of 20 cm, height growth of the mean stem is limited by elastic stability if the tilt angle is $<15^\circ$, but limited by gravitropism if the angle is $>15^\circ$. The maximal height is 30 m if the angle is 15° , and is lower if the tilt angle is larger (*e.g.* 13 m if the angle is 90° , *i.e.* for a plagiotropic branch). For the same diameter, height growth *S. rubra* is limited by gravitropism at an angle of 10° (which is a common situation for main stems in forest edges). Its maximal height would be 20 m for that angle. The maximal length of a plagiotropic branch would be as low as 7 m. These numerical examples clearly show that biomechanical parameters might determine severe constraints on the dimensions and orientation of stems.

Conclusion

We have developed an analytical model of the stem curvature variations due to long-term biomechanical actions during growth. The model uses a differential formulation of the beam theory, adapted to growing structures, to calculate the bending moments and curvatures induced by the increase in tree weight (due to growth) and the asymmetric maturation stress (usually associated with reaction wood formation). Explicit formulas for ecological or ecophysiological studies are proposed that assume realistic simplifications but take into consideration anisotropic radial growth (eccentricity) and gradients of wood stiffness within the cross-section. The model allows the role played by the different components (size described by diameter and height, allometric relations between mass, height and diameter, wood quality and its variations within the cross-section) to be studied. The

maturation strain asymmetry is clearly the main motor of the reaction, so that the strong assumptions of simple models used in previous studies [3,4] are justified a posteriori. Other aspects of growth asymmetry (in ring thickness and wood stiffness), contribute significantly to improve the curving process.

A synthetic trait expressing the “gravitropic performance”, P_g , has been defined as the ratio of maturation to gravitational curvatures. The larger this indicator, the more effectively can the tree control its angle. P_g is given explicitly as a function of stem morphological parameters and wood biomechanical parameters. At the critical steady limit $P_g=1$, the tree maintains its angle when it grows. This limit can be associated with a critical lean, expressing the angle above which a stem of given dimensions can no longer remain stable or move closer to vertical, *i.e.* the limit below which the stem can sustainably control its posture [11]. By examining the effects of size on this limit, an allometric relation between height and diameter has been proposed, which ensures that at each stage of height growth, diameter growth will be able to maintain the stem below the critical lean. Comparisons between this long-term stability allometry ($H \sim D^{1/2}$) and the elastic stability ($H \sim D^{2/3}$) show that the requirements for gravitropic control can be more constraining than elastic stability for tilted trunks or branches.

This theoretical work gives new insights into the functional significance of tree design and wood quality, adding new concepts and operational analytical formulas to the biomechanical ecological toolbox, which up to now has been focused on safety against buckling, wind throw or wind break. In reality, tree stems are never perfectly vertical, and this situation is biomechanically unstable and the effect of additional weight must be corrected. Thus the maximum size at which the stem can sustain this tilted situation depends on the gravitropic performance. We believe that this constraint may be of major biological significance: it limits the ability of stems to move away from verticality, even when lean is a great advantage for maximizing light capture, as is the case for branches, and also for main stems in response to competition with neighbors or heterogeneity of the environment, for instance on slopes [7] or forest edges.

Acknowledgements

This research was carried out as part of the "Woodiversity" project supported by the French National Research Agency (ANR-05-BDIV-012-04). The authors would like to thank Professor Daniel Guitard, now retired, who was at the origin of such discussions in our wood science community 20 years ago.

References

1. Alméras T, M Fournier (2009) Biomechanical design and long-term stability of trees: morphological and wood traits involved in the balance between weight increase and the gravitropic reaction. *Journal of Theoretical Biology* 256: 370-381.
2. Alméras T, A Thibaut, J Gril (2005) Effect of circumferential heterogeneity of wood maturation strain, modulus of elasticity and radial growth on the regulation of stem orientation in trees. *Trees* 19: 457-467.
3. Coutand C, M Fournier, B Moulia (2007) The gravitropic response of poplar trunks: key roles of prestressed regulation and the kinetics of cambial growth versus wood maturation. *Plant Physiology* 114: 1166-1180.
4. Fournier M, H Baillères, B Chanson. *Tree Biomechanics: Growth, Cumulative Prestresses, and Reorientations*; 1994; Plenum Press New York London. Plenum Press, NY.
5. Fournier M, A Stokes, C Coutand, T Fourcaud, B Moulia (2006) Tree biomechanics and growth strategies in the context of forest functional ecology. In: Herrel A, Speck T, Rowe NP, editors. *Ecology and biomechanics*: Taylor & Francis CRC Press. pp. 1-33.
6. Greenhill AG (1881) Determination of the greatest height consistent with stability that a vertical pole or mast can be made, and the greatest height to which a tree of given proportions can grow. *Proceedings of the Cambridge Philosophical Society* 4: 65-73.

7. Ishii R, M Higashi (1997) Tree coexistence on a slope: an adaptive significance of trunk inclination. *Proceedings of the Royal Society of London* 264: 133-140.
8. Jaouen G, T Alméras, C Coutand, M Fournier (2007) How to determine sapling buckling risk with only a few measurements. *American Journal of Botany* 94: 1583-1593.
9. King DA, SJ Davies, S Tan, NSM Noor (2006) The role of wood density and stem support costs in the growth and mortality of tropical trees. *Journal of Ecology* 94: 670-680.
10. McMahon TA, RE Kronauer (1976) Tree structures: deducing the principle of mechanical design. *Journal of Theoretical Biology* 59: 443-466.
11. Moulia B, C Coutand, C Lenne (2006) Posture control and skeletal mechanical acclimation in terrestrial plants: implications for mechanical modeling of plant architecture. *American Journal of Botany* 3: 1477-1489.
12. Niklas KJ (1994) The allometry of safety-factors for plant height. *American Journal of Botany* 81: 345-351.
13. Rowe NP, T Speck (1996) Biomechanical characteristics of the ontogeny and growth habit of the tropical liana *Condylocarpon guianense* (Apocynaceae). *International Journal of Plant Sciences* 157: 406-417.
14. Wilson BF, RR Archer (1977) Reaction wood: induction and mechanical action. *Annual Review of Plant Physiology* 28: 23-43.

Root growth in mechanically stressed environment: In situ measurements of radial root forces measured by a photoelastic technique

E. Kolb¹, P. Genet², L.E. Lecoq^{1,2}, C. Hartmann³, L. Quartier¹, T. Darnige¹

¹ PMMH, ESPCI, 10 rue Vauquelin, 75231 Paris Cédex 05, France;

²BIOEMCO, ENS, 46 rue d'Ulm, 75230 Paris Cédex 05, France ;

*³IWMI - IRD Office/o National Agriculture and Forestry Research Institute (NAFRI)
PO Box 7170 - Nongviengkham - Xaythany District -Vientiane - Lao P.D.R.*

Abstract

The mechanical and topological properties of a soil like the global porosity and the distribution of void sizes greatly affect the development of a plant root, which in turn affects the shoot development. The aim of the present study is to simultaneously quantify in situ forces and root's morphological characteristics in the case of a discontinuous soil. In the first step of this experimental study the discontinuous soil is modelled by only two fixed grains with a controlled minimum gap between them. The root is a radicle at its first stage of development (no secondary root) and is constrained to grow through this pore along a main vertical direction. The originality of our technique is that the grains are photoelastic discs, i.e. optically birefringent when submitted to a deviatoric mechanical stress. During its development, the root exerts a radial pressure on these two grains, thus creating an evolving pattern of optical fringes in these neighbouring photoelastic grains. This is a way to observe the temporal coupling between root diameter increase and radial force evolution for different root/gap ratios. These first results validate the experimental device which can therefore be used with more complex geometries (using several grains) to study the strategies of root development in mechanically stressed environment.

Introduction

When roots develop into soil pores, they have simultaneously i) to adapt to the tortuosity of the pores and ii) to reorganize the solid components in order to enlarge the pores to fit with their constantly increasing root diameter. Thus, in a soil, there is a constant coupling between root development and soil reorganization. Plants are well known for their penetrating capacities [1], however most cultivated plants have low penetrating capacities. When roots grow into physical inhospitable soil, they send inhibitory signals to leaves, even as the first leaf is emerging and when the seedling is still dependent on seed reserves [2]. Due to this inhibitory signal, above ground biomass and agricultural production are likely to be greatly reduced despite the availability of water or mineral elements [3].

Contrasting this, the constantly increasing size and weight of tractors in all the regions of the world has had a profound effect on soil compaction that has been estimated to contribute to a 13 % decrease in soil productivity. To mimic a compacted soil and to study root and plant development, several mediums have been used: compressed and uncompressed sand cores [5] agar and agarose [6], a mixture of paraffin and vaseline [7], etc. Special devices isolating single roots, made it possible to

measure the growth force of impeded roots as a function of time or depth [8] [9] [10] and values ranging 0.6 to 1 N have been recorded. When impeded, root axes elongate slowly and swell radially with the diameters of root tips of plants grown in soil with a compacted layer consistently being larger than those from uncompacted soil [11]. The latter suggested that the soil ahead of a root that expands radially has a greater concentration of stress on it and is more likely to crack as previously mentioned by Abdalla et al. [12] in [5] and as recently observed for worms in mud sediment [13]. Thickening of the root would not only relieve stress in front of the root apex but also decrease buckling [14]. The increase in root diameter in response to impedance is caused by cortical cells enlarging radially rather than axially [5] or from enhanced radial cell expansion and decreased root elongation [14].

All the aforementioned studies have neglected to study the situation where radial root development is impeded without any restriction on axial development. This is the standard situation for i) most of young roots and, more importantly for ii) roots growing in compacted soils which indeed grow preferentially within macropores, cracks, biopores, *etc.* and therefore sustain the plant development [4] [14][15][16][17]. Our objectives were to setup an original device for measuring the radial root forces and associated morphological changes when grown in a model soil with only radial constraints; this paper presents preliminary results and focus on force development.

Material and methods

Biological material

We choose Chickpea (*Cicer arietinum* L.) as a test plant for validating our device: first Chickpea is a major source of human and animal food and the world's third most important pulse crop after beans (*Phaseolus vulgaris* L.) and peas (*Pisum sativum* L.) [18]. Second, Chickpea seeds are suitable for studying root growth because of their large single pivot under unstressed conditions (the radicle's diameter is approximately 1 mm), therefore the gap between the grains where the root can develop could easily be controlled (from 0.5 to 1.5 mm).

Experimental setup

Chick pea seeds are soaked during 2 to 3 days for germination till the radicle reaches a length of around 5 mm. Then each individual seed is fitted into a cylindrical hole dug in a wet foam block that is fixed above the 2 dimensional cell of observation (see Fig 1). The root emerges from below the foam block and is inserted vertically inside the 2D cell with its apex just above the gap between grains.

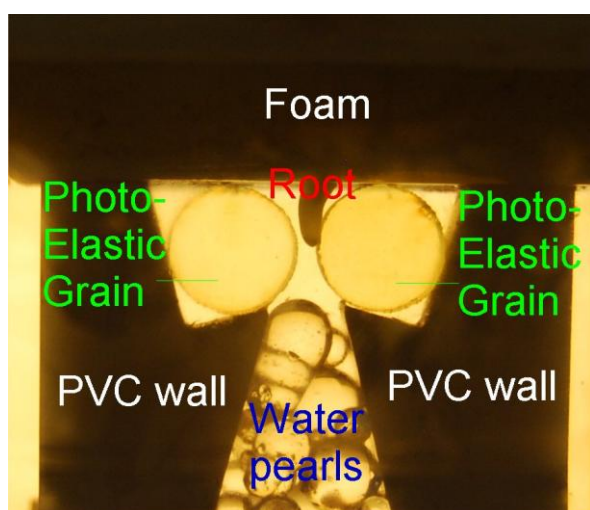


Fig.1 Photo of the 2 dimensional cell with the 2 photoelastic grains fixed on each side on specially designed PVC walls. The gap between the photoelastic grains determines the pore space where the root is allowed to grow. The seed is placed inside the wetted foam above the cell. The root emerges from below the foam and is visible on the picture in the gap between the grains.

The 2D cell is made of two PVC lateral walls in between 2 squares of 4 cm side transparent altuglass walls, allowing observation of root development. The gap between grains is precisely controlled. During the course of an experiment a peristaltic pump maintains the floral foams wet. The bottom of the cell is fixed inside a transparent rectangular container and immersed in polyacrylate gel beads commonly called “water pearls”. This design ensures a 100% relative humidity inside the cell. Up to 6 different cells can be placed at once in the container. This allows replicate measurements with the same environmental conditions.

Due to the cell design, the root is expected to grow vertically and cross the gap. During its development, the root exerts a radial pressure on the two lateral grains in a cell. Because these grains are photoelastic, the force exerted by the root can be measured. These cylindrical grains have a diameter of $D = 2R = 9$ mm and a thickness $t = 7$ mm. They are made of PSM-4 (Vishay Corp.), a polyurethane material of low Young modulus ($E = 4$ MPa). The cells container are illuminated from behind by a sodium-vapour lamp that provides a yellow monochromatic light of wavelength $\lambda = 589.3$ nm. Then the container is placed between two inversed circular polarizers for visualisation of the optical black fringes inside the photoelastic grains, which allows further force measurements. Finally a CCD camera equipped with a macro-lens placed in front of the set-up is automatically taking pictures of each cell with a controlled time lapse (from 15 minutes up to one hour) between each record. Each picture has a resolution of 3872×2592 pixels². Once a picture has been recorded, the translation stage (Fig 2) is moved automatically at a low velocity to place the next cell in front of the camera and stop the motion while the next picture is captured. The cycle is repeated for each cell during a total time of experiment of several days. Thus we simultaneously monitor the evolution of the root morphology and of the photoelastic fringes in grains for different cells as a function of time.

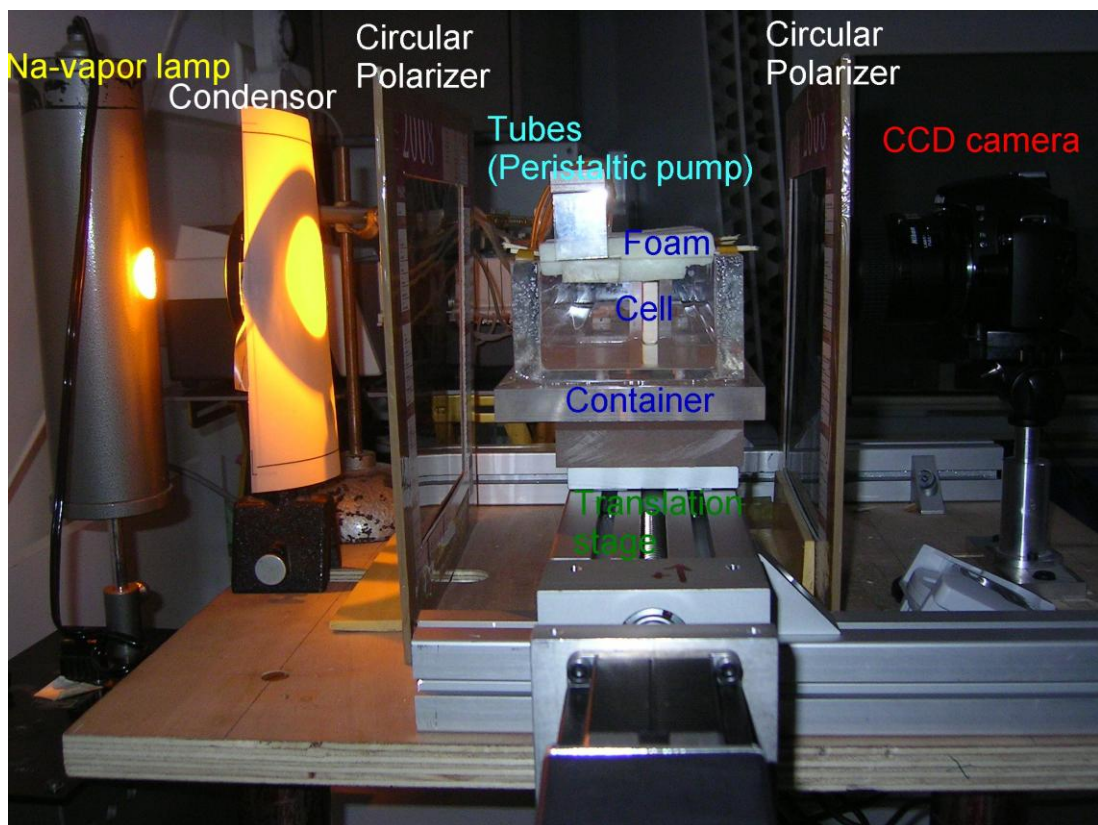


Fig 2. Lateral view of the experimental set-up: A container with different cells is placed on a translation stage between inverse circular polarizers and illuminated from behind by a monochromatic light (sodium-vapor lamp). Each cell is designed for the growth of one root of cheek-pea. A peristaltic pump provides water supply to the floral foam above each cell. A CCD camera is placed in front of the set-up to record images at different times.

Photoelasticity

The values of the radial force are inferred indirectly from the locations of black fringes. Next we present the details of the photoelastic calculations. We recall that the photoelasticity is the property of some materials to become birefringent under mechanical load, ie. the refraction index is no more a scalar constant but has a tensorial form. A plane polarized light of wavelength λ passing through a 2D sheet of photoelastic material of thickness t will be decomposed along the two local principal stress directions 1 and 2 and each of these components will experience different refractive indices, n_1 and n_2 according to the principal values σ_1 and σ_2 of the local stress tensor at the position (x,y) of the sheet where the light ray arrives. Both quantities are related through a linear relation (the stress optic law of equation (1)) by introducing the photoelastic constant C :

$$n_1 - n_2 = C(\sigma_1 - \sigma_2) \quad (1)$$

The difference in the refractive indices leads to an optical path difference δ and therefore to a relative phase retardation ϕ (equation (2)) between the two component waves.

$$\phi = \frac{2\pi}{\lambda} \delta = \frac{2\pi}{\lambda} (n_1 - n_2) t \quad (2)$$

This phase retardation gives interference patterns for the emerging light according to the values of ϕ . By combining equations (1) and (2), one obtains the value of the light intensity $I(x,y)$ as a function of the local deviatoric stress.

$$I(x, y) = I_0 \sin^2(\phi/2) = I_0 \sin^2\left(\frac{\pi Ct}{\lambda}(\sigma_1 - \sigma_2)\right) \quad (3)$$

Especially the black fringe (destructive interference) of order m will be obtained for the positions (x,y) where the principal stress difference $(\sigma_1 - \sigma_2)$ verifies:

$$\sigma_1 - \sigma_2 = \frac{m\lambda}{Ct} \quad (4)$$

The goal of photoelasticimetry is to extract informations on the stresses (or forces) from the positions of (black) fringes.

In the experiment, the photoelastic material is a circular disc of radius R and thickness t as used in [19]. We needed a preliminary experimental calibration to determine the photoelastic constant C in a simple loading test of a diametrical compression along the y axis of the photoelastic disc. We thus related the observed positions of the black fringes to the measured applied force F (by use of a scale). For more complicated geometries of loading (normal and tangential forces applied at more than 2 contact points), it is still possible to extract informations on forces from optical fringes by using numerical solutions of elastic theory and/or solve the inverse problem as was done by [20].

For simplification in this article, we limit our analysis to the cases where the root was inducing a diametrical compression of the photoelastic grain.

Results and discussion

The device presented before allows the development of root growth. The photoelastic sensitivity of the grains has been proven to be in the right range for measuring forces exerted by the root as can be seen from the temporal evolution of fringe pattern in *Fig 3*. These observations validate the concept of our experiments. Moreover we obtained the first quantitative measurements of root forces and growth by using these photoelastic grains.

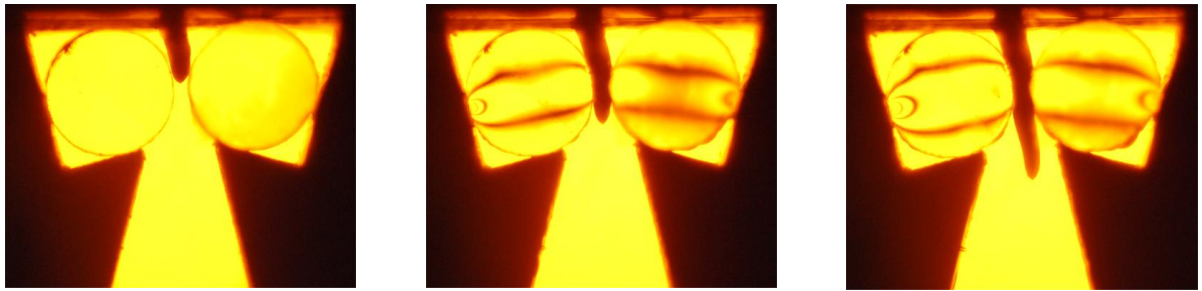


Fig 3. Root growth inside the setup. We observe the evolution of the length and diameter of the root while growing inside the gap between the two photoelastic discs placed between circular polarizers. The evolution of the black fringe pattern is a way to measure the force exerted by the root during its growth. The different pictures are obtained from left to right, at 45 min after the experiment launching, 5.5 hours after, 10.25 hours after. The minimum gap between grains is 1 mm.

Next we present a typical measurement of force and length / diameter versus time of growth corresponding to the example shown in Fig 3. The force has been obtained directly from the positions of black fringes along a diameter of the photoelastic disc perpendicular to the axis of compression exerted by the root. From the right panel of Fig 4, we observe values of forces which are consistent with preceding measurements on axial forces, i.e. the force is of the order of 1 N. For a typical area of contact of 1 mm², it will give pressure of the order of 1 MPa. Note that the turgor pressure inside the root cells can not be presently measured in our device but it should be of the same order of magnitude as the estimated radial pressure. At the same time and independently, the diameter and the length of the root have been measured by using image analysis software. We observe their evolution in Fig 4 during the first ten hours of growth in the setup. The root length has been measured from a point corresponding to the top of the cell. The diameter of the root is also taken at the same point above the gap and its initial diameter is only slightly larger than the gap. Actually we see that the root length (left panel of Fig 4) evolves quasi-linearly with time in this example with a growth rate of 0.65 mm/hour. We also observe that the top diameter (central panel of Fig 4) does not evolve much before 4 hours in the setup, but begins to increase for times larger than 4 hours reaching a global increase of around 10% after 10 hours. The increase in the top diameter around a time of 4 hours begins when the root apex is crossing the minimum gap between grains. This increase of diameter leads to an increase of the lateral force (Fig 4 right) exerted by the root on its neighbouring grains and allows the further longitudinal growth of the root.

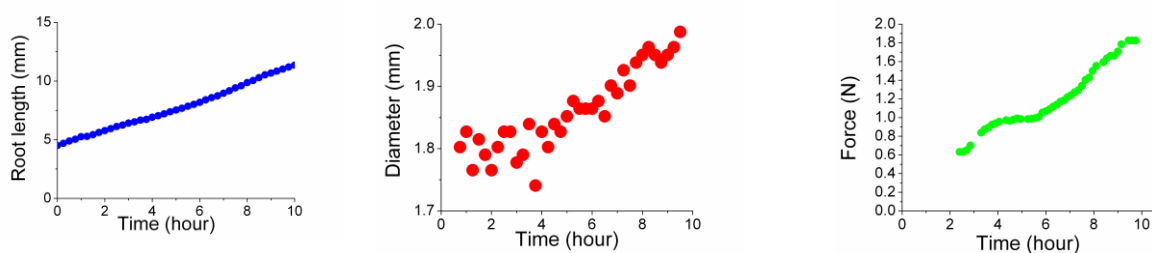


Fig 4. Root length (observed in the camera frame), top diameter and measured force exerted by the root on the right photoelastic disc during the 10 first hours in the setup.

Conclusion

By means of a photoelastic technique, we simultaneously observed the root growth as well as the radial force exerted by the root when it is forced to pass a gap of controlled width. These first results validate the experimental device for systematic studies with different root/gap ratios, in order to

elucidate the different mechanisms of penetration of a root in a tortuous soil with different pore sizes. These technique of photoelasticity can also be used with more complex geometries (using several grains which are not blocked) to study the strategies of root development in mechanically stressed environment and the coupling between grains reorganisations and root growth.

Acknowledgements

We acknowledge Prof. Tom Mullin from Manchester Center for Non Linear Dynamics (U.K.) for very kindly providing us with photoelastic grains. We also acknowledge Prof. Bob Behringer from Duke University (U.S.A.) for initiating us so nicely with photoelastic measurements.

References

1. Lesturgez, G., Poss, R., Hartmann, C., Bourdon, E., Noble, A., Ratana-Anupap, S., (2004). *Roots of Stylosanthes hamata create macropores in the compact layer of a sandy soil*. Plant and Soil 260, 101-109.
2. Passioura, J.B., (2002). *Soil conditions and plant growth*. Plant Cell and Environment 25, 311-318.
3. Cairns, J.E., Audebert, A., Townend, J., Price, A.H., Mullins, C.E., (2004). *Effect of soil mechanical impedance on root growth of two rice varieties under field drought stress*. Plant and Soil 267, 309-318.
4. Vannoordwijk, M., Brouwer, G., Harmanny, K., (1993). *Concepts and Methods for Studying Interactions of Roots and Soil Structure*. Geoderma 56, 351-375.
5. Croser, C., Bengough, A.G., Pritchard, J., (2000). *The effect of mechanical impedance on root growth in pea (Pisum sativum). II. Cell expansion and wall rheology during recovery*. Physiologia Plantarum 109, 150-159.
6. Clark, L.J., Whalley, W.R., Leigh, R.A., Dexter, A.R., Barraclough, P.B., (1998). *Evaluation of agar and agarose gels for studying mechanical impedance in rice roots*. Plant and Soil 207, 37-43.
7. Kubo, K., Jitsuyama, Y., Iwama, K., Watanabe, N., Yanagisawa, A., Elouafi, I., Nachit, M.M., (2005). *The reduced height genes do not affect the root penetration ability in wheat*. Euphytica 141, 105-111.
8. Clark, L.J., Whalley, W.R., Dexter, A.R., Barraclough, P.B., Leigh, R.A., (1996). *Complete mechanical impedance increases the turgor of cells in the apex of pea roots*. Plant Cell and Environment 19, 1099-1102.
9. Iijima, M., Higuchi, T., Barlow, P.W., Bengough, A.G., (2003). *Root cap removal increases root penetration resistance in maize (Zea mays L.)*. J. Exp. Bot. 54, 2105-2109.
10. Souty N. (1987). *Aspect mécanique de la croissance des racines. I- -Mesure de la force de pénétration*. Agronomie 7(8), 623-630.
11. Materechera, S.A., Alston, A.M., Kirby, J.M., Dexter, A.R., (1992). *Influence of Root Diameter on the Penetration of Seminal Roots into a Compacted Subsoil*. Plant and Soil 144, 297-303.
12. Abdalla A.M., Hettiaratchi D.R., Reece A.R. (1969). *The mechanics of root growth in granular media*. J. Agr. Eng. Res., 1-14(3), 236-248.
13. Dorgan, K.M., Jumars, P.A., Johnson, B., Boudreau, B.P., Landis, E., (2005). *Burrow extension by crack propagation*. Nature 433, 475-475.
14. Bengough, A.G., Bransby, M.F., Hans, J., McKenna, S.J., Roberts, T.J., Valentine, T.A., (2006). *Root responses to soil physical conditions; growth dynamics from field to cell*. Journal of Experimental Botany 57, 437-447.
15. Stewart, J.B., Moran, C.J., Wood, J.T., (1999). *Macropore sheath: quantification of plant root and soil macropore association*. Plant and Soil 211, 59-67.
16. Pierret, A., Moran, C.J., Pankhurst, C.E., (1999). *Differentiation of soil properties related to the spatial association of wheat roots and soil macropores*. Plant and Soil 211, 51-58.
17. Stirzaker, R.J., Passioura, J.B., Wilms, Y., (1996). *Soil structure and plant growth: Impact of bulk density and biopores*. Plant and Soil 185, 151-162.
18. Saxena M.C., (1990): *Problems and potential of Chickpea production in the Nineties*, Pages 13-27 in: Chickpea in the Nineties. Proc. Int. Workshop Chickpea Improvement, 2nd International Crop Research Institute for the Semi-Arid Tropics, Andhra Pradesh, India.
19. Zuriguel, I., Mullin, T., and Rotter, J. M. (2007) , *Effect of Particle Shape on the Stress Dip Under a Sandpile*, Phys. Rev. Lett. **98**, 028001 .
20. Majmudar, T.S.; Behringer, R.P., (2005). *Contact force measurements and stress-induced anisotropy in granular materials*, Nature 435, 1079-1082.

Is the branch of *Viburnum odoratissimum* var. *awabuki* reaction wood?

Unusual eccentric growth and various distributions of growth strain

Yue Wang,¹ Joseph Gril² and Junji Sugiyama¹

¹Laboratory of Biomass Morphogenesis and Information, Research Institute for Sustainable Humanosphere, Kyoto University, Uji, Kyoto 611-0011, Japan; ²Laboratoire de Mécanique et Génie Civil, Université Montpellier 2, CNRS, Montpellier, France

Abstract

For *Viburnum odoratissimum* var. *awabuki*, a pronounced growth was observed on the lower side of the branches, which is a special case in angiosperms. To study the biomechanics of *V. odoratissimum* branch, we measured the growth strain (GS) in the standing tree using a cumulative method and a direct method. GSs showed various distribution patterns: for some branches, the values on both sides corresponded to a tensile growth stress typical of normal wood, sometimes a high tensile GS was found in the upper side similar to tension wood, and for other branches, the values on the lower side corresponded to a compressive growth stress. In most measuring positions, a larger GS was found on the upper side of the branches opposite to the eccentric growth direction, which is unusual in angiosperms. To investigate the effect of eccentric growth on the mechanical properties of the branch wood, we measured basic density (BD), microfibril angle (MFA), elastic modulus (E_L), and creep deformation of the samples cut from the upper and lower sides of the branch. BD of the lower-side wood was relatively larger, but the influence of BD on the creep deformation was slight. Although MFAs differed between both sides, E_L of the lower-side wood was commonly larger than that of the upper-side wood, suggesting that MFA does not play an important role in the mechanical properties of the branch wood. Moreover, the creep compliance curves show that the upper-side wood had low elasticity and high fluidity, whereas the lower-side wood had large elasticity and low fluidity. These results mean that the stable growth of the branches in *V. odoratissimum* should have a unique mechanism different from that in reaction wood to adapt to environmental changes.

Keywords: growth stress, microfibril angle, creep compliance, reaction wood

Introduction

In trees, the pith may be located eccentrically in the trunk or the branch because the stem deviates from the vertical position or because of an uneven distribution of loading on a branch. Generally, most woody angiosperms show a pronounced growth promotion on the upper side of the leaning stems and branches, whereas growth eccentricity occurs on the lower side in gymnosperms. This phenomenon of eccentric growth is usually associated with the formation of reaction wood (Tsoumis 1991). However, growth eccentricity on the lower side in angiosperms has occasionally been reported. For example, Onaka (1949) and Yoshizawa (1993) observed that *Buxus microphylla* exhibits pronounced growth on the lower side of the inclined stems. Its xylem has some anatomical features similar to those of compression wood. Kucera and Philipson (1977, 1978) have reported that growth eccentricity of *Pseudowintera colorata* occurs on the lower side of the inclined branches. The lower-side tracheids have a large microfibril angle, but *P. colorata* develops neither tension wood nor compression wood.

We recently found that the inclined branches of *Viburnum odoratissimum* var. *awabuki* also have pronounced growth on the lower side. Compared with *B. microphylla* and *P. colorata*, *V. odoratissimum* has no anatomical feature similar to that in reaction wood, and the anatomical features

of the xylem do not obviously differ between the upper and lower sides of the branches (Wang et al. 2009). However, the information about the growth stress and the wood properties of the inclined branch for *V. odoratissimum*, is few. Therefore, in this study, to understand the effects of unusual eccentric growth on the branch biomechanics, we measured the released surface growth strain (GS) in the trunk and the inclined branches of three *V. odoratissimum* trees, and examined some wood properties of the branch wood.

Materials and methods

Plant material

Three 12-year-old trees (I, II, and III) of *V. odoratissimum* growing in Uji campus (130°82' E, 34°81' N~130°80' E, 34°81' N), Kyoto University, Japan were studied. The trees were about 6m high with several branches in various orientations.

Growth strain measurement

Measurements were made twice in September 2007 and December 2008. There were two measuring positions (no.1 and 2) in the trunk and each branch. Position no.1 was about 30 cm from the base of the branch to avoid the influence of growth stress around the joint. The distance between no.1 and no.2 was at least 5 times greater than the diameter of the branch. After removing the bark at the measuring position, electrical resistance strain gauges (FLA-5-11-5LT, Tokyo Sokki Kenkyujo Co., Ltd, Japan) were glued with cyanoacrylate adhesive to the xylem in the longitudinal direction on the trunk and the upper and lower sides of the branches. Measurements were made with a portable digital strain meter (TDS500, Tokyo Sokki Kenkyujo Co., Ltd, Japan) with an 80-channel scanner.

At the first time, we used a cumulative method to measure GSs of the trunk and all branches of tree I (Wang et al. 2009). After calibrating the strain gauges to zero, first, the twigs at the branch tips that induced bending of the branch were cut down, and the spring-back strains resulting from the removal of twigs ($\epsilon_s = \delta\epsilon_s$) were measured in the standing tree; then, GSs (ϵ_r) of the upper and lower sides of the branches were measured after they were released by cutting grooves 3-5 mm deep with a handsaw on both sides of the strain gauges (Yoshida et al. 2002). The value of ϵ_r ($\epsilon_r = \delta\epsilon_s + \delta\epsilon_r$) is equal to the sum of the strain increment at the steps of load removal and stress release.

At the second time, GSs in several branches of two trees (II and III) were measured with a direct method. That is, no twigs and branches were cut down from the trees; GS (ϵ_r) of the branch was directly measured by cutting grooves in the standing trees. The value of ϵ_r ($\epsilon_r = \delta\epsilon_r$) including the influence of self-loading is equal to the strain increment at stress release. Theoretically, values of ϵ_r obtained from both methods approach the real growth stress of the standing tree (Yamamoto et al. 1989).

Creep experiment

After GS measurement, the branches of trees II and III were cut down, and samples ($25 \times 2 \times 1 \text{ mm}^3$, L, T, R) were cut from the upper and lower sides of the branches between the measuring positions. These samples were kept in water as green wood. The creep deformation of each green wood was tested on the cantilever condition for 5.7 h. The load was 0.45 N, well within the proportional limits, and the span was 20 mm. After the test, the sample was heated at 80 °C to release internal stress, and slowly cooled. After 24 h, the creep deformation of heated sample was tested. The microfibril angles (MFAs) of the air-dried samples were measured using an X-ray diffraction (XRD) method. Finally, the basic density of the sample was expressed on the basis of the oven-dried weight and the swollen volume.

Results and discussions

Growth eccentricity and growth strain of the trunk and branches

Table 1 shows growth eccentricity, MFA, spring-back strain, and GS of tree I. Except for branch no. I-A, which exhibited no growth eccentricity, the other branches showed pronounced growth promotion

on the lower side and the pattern of growth eccentricity did not change along their length. The MFAs of the base position for the branches were about 11-14° based on polarizing-light microscopic (POM) observation. There was little difference in the MFAs of the upper and lower sides of the branches for tree I.

Table 1. MFAs, spring-back strains, and growth strains in the trunk and branches of tree I

Trunk and branch no.	R ₁ (mm)		R ₂ (mm)		MFA by POM (°) *		Spring back strain (μ m/m) (ε _s = δ ε _s)		Released growth strain (μ m/m) (ε _r = δ ε _s + δ ε _r)	
	upper radius	lower radius	Upper	Lower	Upper	Lower	Upper	Lower		
Trunk 1	100	100	13.8	12.1	32	11	-535	-549		
	55	30	-	-	16	13	-394	-414		
Branch	A1	10	11	12.8	13.5	-313	382	32	-172	
	A2	10	10	-	-	-170	247	-21	-244	
	B1	17	22	12.1	13.5	-382	1378	-205	16	
	B2	15	18	-	-	-1169	1302	-706	433	
	C1	14	50	13.6	13.0	-48	-255	-191	-326	
	C2	10	20	-	-	-415	532	-494	23	
	D1	22	55	12.9	11.5	-389	175	-669	-53	
	D2	24	45	-	-	-958	932	-553	-57	
	E1	25	55	12.4	14.8	-892	567	-545	-212	
	E2	25	51	-	-	-911	1171	-520	-152	

The spring-back strains of the branches were caused by excising the twigs. The spring-back strain was contractile in the upper side and extensive in the lower side of most branches. This is the expected response to the suppression of the gravity load, that in the standing tree tends to bend the branch downward and compress it along its length. A different behavior was the base of branch no.I-C-1, which not only produced a contraction on both side, but also a higher contraction on the lower side.

On the other hand, the released GS ranged from -706 to 433 με. For the trunk, the strain value was moderate and similar in both sides, indicating stable vertical growth of the whole tree. For the branches, the values of GS differed between the upper and lower sides at all positions, and various patterns were observed. The values were in most cases negative (contraction), corresponding to a low tensile growth stress typical of normal wood. In branch no. I-A and I-C-1, the upper side produced little GS (positive or negative) while the lower side contracted. In branch no. I-B and I-C-2, there were positive growth strains (corresponding to a compressive growth stress) on the lower side. Branches no. I-D and I-E produced a contraction in both sides, corresponding to a tensile growth stress, with a higher value on the upper side. Furthermore, we found that the larger growth strain occurred in the upper side opposite to eccentric growth and counteracted the gravity effect, which is unusual in angiosperms.

To clarify the biomechanical advantage of eccentric growth, we examined the relationship between the downward bending trend, quantified by the spring-back bending (ε_{s lower} - ε_{s upper}) and the eccentricity (ratio of R₂ to R₁) of the branch. As shown in Figure 1, there was a negative relationship (R² = 0.78) between both factors (except for the thinnest branch no. I-A), This suggests that eccentric growth, which appears to be a common feature of this species, resulted in a disadvantage for upright movement or stabilization of the branch orientation so that it had to be somewhat reduced when the

bending load became higher.

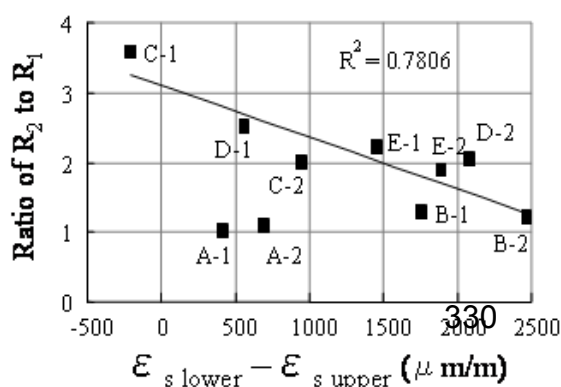


Figure 1. Relationship between the downward bending trend and eccentricity for tree I (excepting the thinnest branch no. I-A)

To inspect the results of GSs in *V. odoratissimum* branches at the first measurement, we measured the GSs of the branches of two more trees using a direct method. Table 2 shows growth eccentricity and GSs in the branches of trees II and III. Growth eccentricity displayed on the lower side for all branches. Excepting for tree III-1A, where an abnormal compressive stress occurred on the upper side, the distribution of GS showed two patterns similar to those in tree I. One is tensile stress on the upper side and compressive stress on the lower side (the main pattern in trees II and III); the other is high tensile stress on the upper side and slight tensile stress on the lower side, such as tension wood (the main pattern in tree I). Moreover, although the elastic modulus in longitudinal direction (E_L) (see Table 3) of the lower side was slightly larger than that of the upper side, we can calculate that the growth stress in the upper side was greater than that in the lower side. This confirms that in contrast to reaction wood, there was not a larger growth stress in the eccentric growth side of branch.

Table 2. Growth strains in the branches of trees II and III

Branch no.	R ₁ (mm) upper radius	R ₂ (mm) lower radius	Released GS ($\epsilon_r = \delta \epsilon_r$, $\mu\text{m/m}$)	
			Upper	Lower
Tree II				
A1	11	31	-445	181
A2	15	16	-304	345
B1	12	21	-236	474
B2	12	16	-329	100
C1	11	30	-41	220
C2	18	24	-848	35
Tree III				
A1	12	36	1395	-91
A2	18	24	-357	-141
B1	8	15	-471	373
B2	9	12	-466	323
C1	14	28	-602	200
C2	12	19	-648	329
D1	12	18	-287	279
D2	12	14	-430	392

According to the above results, we found that the eccentric growth in the lower side of the branch was a normal growth pattern for *V. odoratissimum* tree. The distribution of GS in the branch depended on the individual tree, but larger growth stress was displayed in the upper side to fulfill the biomechanical requirements. This suggests that the mechanism of eccentric growth of the branch is different from that of reaction wood. Thus, the branches of *V. odoratissimum* formed neither tension wood nor compression wood.

Mechanical properties of the branches of V. odoratissimum

To clarify the wood properties of the branch, we cut the samples from the upper and lower sides of the branches, and examined the basic density, E_L , and creep deformation of the samples. Furthermore, to understand the influence of microstructure, we measured MFA using XRD. Table 3 shows the basic density, MFA, and E_L of the branches of tree II and III. For most positions, the basic density of the upper-side wood was less than that of the lower-side wood. MFA showed a different trend in trees II

and III. MFAs of the upper side were larger than those of the lower side for tree II, whereas MFAs of the upper side were smaller than those of the lower side for tree III. These results suggest that E_L of the lower-side wood should be relatively larger in tree II and that of the upper-side wood should be relatively larger in tree III. However, E_L of most positions for both trees displayed the same trend: E_L of the lower-side wood was larger than that of the upper-side wood. This means that MFA was not closely related with the mechanical properties of the branch wood, and that the difference of MFA in trees II and III may be due to branch architecture. The relationship between MFA and E_L in *V. odoratissimum* trees suggests that the stable growth mechanism of branches differs from that of reaction wood.

Table 3. Basic density, MFA, and E_L in the branches of trees II and III

Branch no.	Basic density (g/mm ³)		MFA by XRD (°)		E_L (GPa)*	
	Upper	Lower	Upper	Lower	Upper	Lower
Tree II						
A	0.51	0.57	21.5	17.8	3.23	5.02
B	0.48	0.51	19.6	17.9	-	-
C	0.52	0.59	23.4	22.3	4.65	5.59
Tree III						
A	0.52	0.58	19.2	20.3	3.87	5.73
B	0.47	0.51	16.5	17.9	-	-
C	0.48	0.53	15.5	18.8	5.54	6.27
D	0.51	0.48	17.7	20.4	-	-

*: The block samples [60(L) × 3(T) × 3(R)mm] were used.

Figure 2 shows the creep curves of green wood cut from the upper and lower sides of the branches. The creep compliance (J_t) of the upper-side sample was larger than that of the lower-side sample, suggesting that the upper-side sample had low relatively rigidity and high relatively fluidity. After heating, the J_t of heated sample also had the same trend as green wood. Figure 3 shows the relationship between the relative creep compliance ($J_{20000\text{sec}}/J_{10\text{sec}} - 1$) of the samples and GS. The upper side of branch wood that produced tensile stress exhibited higher fluidity.

Effect of density on the viscoelastic property of the sample is shown in Figure 4 because of the large basic density of the lower-side wood. We found that there was a slight relationship between both factors, suggesting that the density is not an important factor influencing the viscoelastic property of the branch wood.

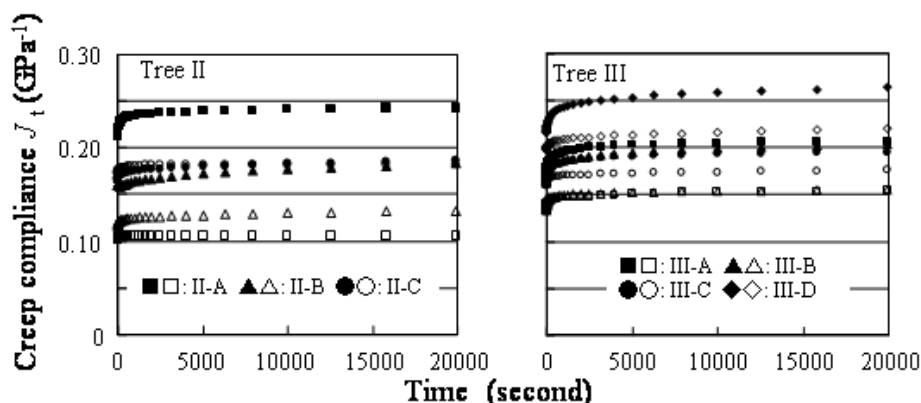


Figure 2. The creep compliance curves of green wood cut from the upper and lower sides (mark: the lower side)

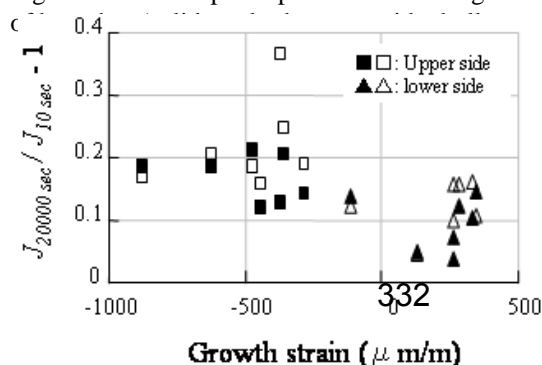


Figure 3. Relationship between the growth strain and relative creep compliance for green wood (solid mark) and heated wood (hollow mark). The GSs of trees II and III are average value of two measuring positions of each branch.

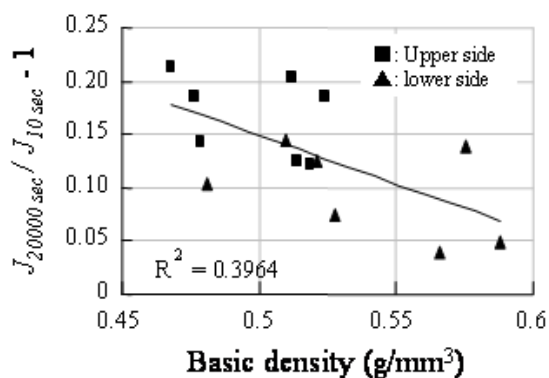


Figure 4. Relationship between the basic density and relative creep compliance for green wood

After considering GS and the mechanical properties of the branch, we found that the branch of *V. odoratissimum* has some features similar to reaction wood. From the viewpoint of GS, the branch showed a distribution of GS similar to tension wood because of a large tensile growth stress on the upper side. However, eccentric growth did not occur in the upper side, and there was no anatomical feature of tension wood exhibited on both sides of the branch. From the viewpoint of the viscoelastic property, the larger elasticity of the lower-side wood is similar to that of compression wood. However, MFAs of both sides were moderate for hardwood and did not influence the mechanical properties of the branch. Therefore, the factors that decide viscoelastic property of branch are limited in chemical components and matrix structure of cell wall.

At this stage, we analyzed the chemical components of the branches for tree I. We found that lignin content of the lower-side wood was about 2% more than that of upper-side wood. Distribution of lignin of the branch was similar to that of compression wood. On the other hand, the results of syringyl/guaiacyl molar (S/G) ratio showed that the S/G ratio of the upper-side wood was larger than that of lower-side wood. Moreover, softening temperature of upper-side wood was lower based on dynamic mechanical analysis (DMA). These results are the same as tension wood (Pilate et al. 2004, Placet et al. 2007). Now, we cannot decide which factor support compressive stress and improve E_L of the branch, however these results of chemical component suggest that the eccentric growth of *V. odoratissimum* combined some advantages of tension wood and compression wood.

Conclusion

For *V. odoratissimum*, eccentric growth is found in the lower side of the branches. Generally, GSs of the branches displayed different distribution patterns: one is the values on both sides corresponded to a tensile growth stress typical of normal wood, sometimes a high tensile GS was found in the upper side similar to GS of tension wood; the other is the values on the lower side corresponded to a compressive growth stress. For both patterns, a larger growth stress was observed on the upper side of the branches. Thus, the relationship between growth stress and eccentric growth is unusual in angiosperms. Furthermore, the mechanical properties of branch were not greatly influenced by MFA and BD. The upper-side wood had low elastic modulus and high fluidity, whereas the lower-side wood had large elastic modulus and low fluidity. Although there was no anatomical features of reaction wood occurred in both sides, the chemical component of the branches exhibited some features combining the characteristics of reaction wood.

Acknowledgments

This study was supported by a Grant-in-Aid for foreign research fellows (No.20.08105) provided by the Japan Society for the Promotion of Science. The authors thank Dr. Bruno Clair of Montpellier 2 University, France for microfibril angle measurement, Dr. Tomoyuki Fujii of Forestry and Forest Products Research Institute, Japan and Dr. Keiichi Baba and Dr. Takuro Mori of Kyoto University for their valuable comments, and the members of the Laboratory of Biomass Morphogenesis, Kyoto University for assistance with measurements.

References

- Kucera, L.J. and W. R. Philipson. 1977. Growth eccentricity and reaction anatomy in branchwood of *Drimys winteri* and five native New Zealand trees. *New Zealand J. Bot.* 15:517-524.
- Kucera, L.J. and W. R. Philipson. 1978. Growth eccentricity and reaction anatomy in branchwood of *Pseudowintera colorata*. *Amer. J. Bot.* 65:601-607.
- Onaka, F. 1949. Studies on compression- and tension-wood. *Wood Res.*1:1-88. In Japanese.
- Placet, V., J. Passard and P. Perre. 2007. Viscoelastic properties of green wood across the grain measured by harmonic tests in the range 0-95°C: Hard wood vs. soft wood and normal wood vs. reaction wood. *Holzforschung* 61:548-557.
- Pilate, G., B. Chabbert, B. Cathala, A. yoshinaga, J.C. Leple, F. Laurans, C. Lapiere and K. Ruel. 2004. Lignification and tension wood. *Plant Biol. Pathol.* 327:889-901.
- Tsoumis, G.T.1991. Science and technology of wood: structure, properties, utilization. Van Nostrand Reinhold, New York, pp88-91.
- Wang, Y., J. Gril and J. Sugiyama. 2009. Variation in xylem formation of *Viburnum odoratissimum* var.*awabuki*: growth strain and related anatomical features of branches exhibiting unusual eccentric growth. *Tree Physiol.* 29:707-713.
- Yamamoto, H., T. Okuyama and M. Iguchi. 1989. Measurement of growth stresses on the surface of a leaning stem. *Mokuzai Gakkashi* 35:595-601.
- Yoshida, M. and T. Okuyama. 2002. Techniques for measuring growth stress on the xylem surface using strain and dial gauges. *Holzforschung* 56:461-467.
- Yoshizawa, N., M. Satoh, S. Yokata and T. Idei. 1993. Formation and structure of reaction wood in *Buxus microphylla* var. *insularis* Nakai. *Wood Sci. Technol.* 27:1-10

Early selection of stem straightness in pinus pinaster ait based on the straightening process

Rosario Sierra-de-Grado¹, Valentín Pando¹, Pablo Martínez-Zurimendi¹, Alejandro Peñalvo¹, Esther Bäscones¹, Bruno Moulia².

¹ University of Valladolid, Spain; ²INRA, France

Abstract

Stem straightness is a major trait for *Pinus pinaster* Ait. breeding programs. Despite the stability of performance in provenance trials, the efficiency of breeding programs based on scoring stem forms remains low. An alternative approach for early selection is to analyse the biomechanical processes involved in the control of the stem form, instead of evaluating the form itself. The rationale is that genetic differences in the biomechanical ability to straighten in young plants will be active in controlling stem form lifelong. In this study, the components contributing most to the genetic differences between provenances in the straightening process were analyzed. To do so, a kinetic analysis and a biomechanical model that defines the non-linear interactions between the variables involved in the straightening process driven by secondary growth and reaction wood formation (Fournier's model) were used. This framework was tested on three *P. pinaster* provenances, selected for their differences in adult straightness and growth. One year-old plants were tilted 45° and individual stem position and size were recorded weekly during 5 months. The radial extension of reaction wood and the anatomical features of wood cells were measured on serial cross-sections. From this, the integral effect of reaction wood on stem leaning was computed using Fournier's model. Both primary and secondary-growth driven responses were involved in the straightening process of the plants, but the latter was more significant in the differences between provenances. Plants from the straight provenance showed higher ability in the straightening process due mainly to i) a more efficient compression wood (higher maturation strains) and ii) more pronounced secondary-growth driven autotropic decurving than the sinuous provenances. These two process-based traits are thus good candidates for early selection of stem straightness, as illustrated by their comparison with the more standard use of a quantitative flexuosity index of stem form. This new approach is nowadays being tested on a greater number of genotypes, as well the viability of the method with greater plants and in other species.

Introduction

Pinus pinaster Ait. is a major timber species in many countries, but it has a strong tendency for stem flexuosity that reduces its value. Tree stem flexuosity shows large natural variability, but in provenance trials, stem straightness is usually stable, suggesting genetic control [1,2]. However, the success of early selection for stem straightness in *P. pinaster* breeding programs has proved variable [3,4,5]. Variable selection efficiency is due in part to the limitations of current methods of quantifying stem form that ignore the factors and processes causing stem defects [6]. Stem straightness of juvenile and adult plants is not necessarily correlated, because many external factors can affect stem form; however, a process of stem straightening (i.e., recovery of vertical orientation) occurs whenever the stem is tilted or bent [7].

The few kinematic studies of stem straightening conducted on young *P. pinaster* plants [8, 9, 10] have revealed three components: (1) negative gravitropic curvature in the apical segment within hours caused by differential primary elongation; (2) slower gravitropic curvature of the basal segment undergoing

secondary growth and reaction wood formation [11]; and (3) counter-curvature (autotropic) that counteracts the gravitropic curvatures and straightens the stem before it passes the vertical.

The biomechanics of reaction-wood-mediated stem curvature have been analyzed in detail, because it is the only process actively influencing stem straightness and internal growth stresses [11]. Secondary cell walls of wood cells undergo longitudinal shrinkage or swelling (maturation strains) during their final differentiation. In pines, two types of wood are produced during stem straightening. So-called normal wood (NW), which undergoes longitudinal shrinkage during cell wall differentiation, and reaction wood (RW) (referred to as compression wood), with more rounded cells and thicker and more lignified cell walls, that displays longitudinal swelling during cell wall differentiation [12]. When a sector of compression wood is produced on one side of a cross section during cambial growth, the asymmetry of maturation strains and of the resulting growth stresses between compression wood and the NW on the opposite side drives active tropic bending of the stem toward the opposite side. The mechanics of this compressionwood- driven bending have been modeled [11]. A parsimonious summary model of the active tropic curvature has been proposed by Fournier et al. (1994) [9] and is considered robust and fairly generic to juvenile and adult trees of several species [11, 13]. Because the model specifies quantitatively the nonlinear interactions between the variables influencing the efficiency of straightening, it might be a useful tool for analyzing the contributions of the components to variability in stem form.

We analyzed differences in the stem straightening process after controlled tilting of 2-year-old plants of three *P. pinaster* provenances characterized by large genetic differences in adult stem straightness [1, 2]. We tested whether the gravitropic and autotropic reactions involving RW formation in young trees are related to differences in stem straightness in adult trees. We attempted to identify the component processes that contribute most to the genetic differences in straightness with Fournier's model. A comparison with a quantitative global flexuosity index [6] was conducted to assess the benefits of our more mechanistic and dynamic approach for early selection of stem straightness.

Material and methods

Plant material and controlled tilting experiment

Three Spanish provenances of *P. pinaster* were chosen for their differences in stem straightness and growth. Trees from the Sierra de Gredos provenance reach great heights and have straight stems; trees from the Bajo Tiétar provenance are tall but have sinuous stems. And trees from the Sierra de Oña provenance have poor growth and crooked stems. Hereafter, Gredos, Tiétar and Oña, respectively. Ten plants from each population were sown in square pots. In their second year, they were tilted to an angle of 45° from the vertical, pointing southward.

Kinetic recording of stem form changes

The structures holding the tilted pots included a rigid frame holding a digital camera in fixed position. Photographs were taken periodically of each plant from exactly the same location, to cover the N–S plane (plane of maximum stem deformation). The frame incorporated two graduated bars as reference scales. Photographs of each plant were taken 24 h after tilting and then weekly from early May until mid September. A simplified analysis of the kinematics of the field of curvature along the stem was performed. The stems was divided in portions as shown in Fig. 1a.

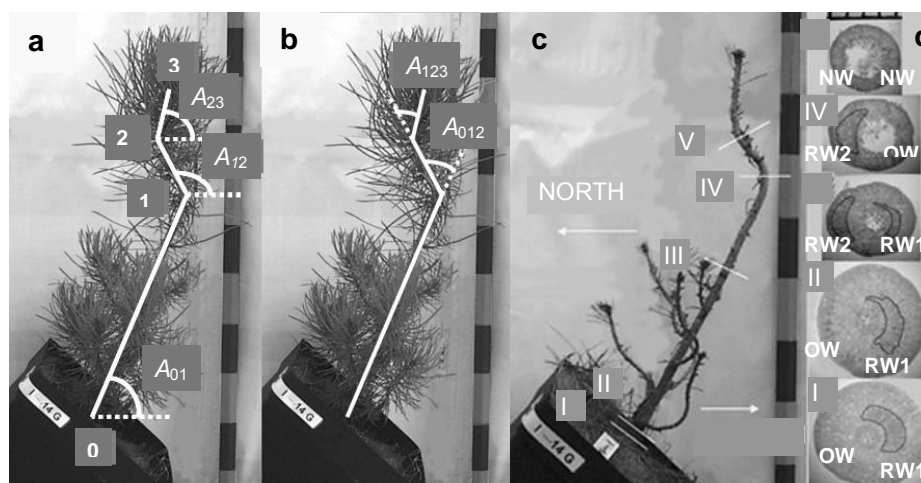


Fig. 1. Parts of the stem, angles and sections analyzed: a: Parts in the stem: 01: from the base (0) to the end of the first growing season (1); 12: from 1 to the point of inflexion of the stem during the experiment (2); 23: from 2 to the apex (3). A01, A12 and A23: inclination angles of segments 01, 12, 23 with respect to the horizontal. b: A012 and A123: angles between the different segments of the stem. c: Positions of the cross-sections for anatomical inspection on a defoliated plant at the end of the experiment. Scale on pictures of the stem (a,b,c): each division in the graduated bar on the right side of the pictures is 5 cm. d: (I to V) Studied cross sections; reaction wood areas are drawn on each section, RW1: reaction wood type 1 (South side), RW2: reaction wood type 2 (North side). NW: Normal wood, OW: opposite wood (scale on pictures: each division in the graduated bar on the top of the pictures is 1mm).

Based on the picture, changes in stem position were measured as angles of deviation from the horizontal (A01, A12 and A23) of Parts 01, 12 and 23, respectively. Because the values of A12 and A23 depend on changes in the values of previous basal angles (i.e., A12 depends on A01 and A23 depends on A12), angles A012 and A123 were measured (Figure 1b). These angles provide an indication of the curvature at Points 1 and 2. Longitudinal growth of the stems was determined as the sum of the lengths of Parts 01, 12 and 23. All measurements were made on the pictures with Photoshop 5.5 and 6.0 (Adobe Systems), correcting for scale.

Quantitative anatomical analysis

At the end of the experiment, six plants per provenance were defoliated, marked on the south and west side, respectively, and then harvested. Cross sections were taken at the base of the stem (Section I), just over the cotyledons (Section II), at the middle (Section III) and end (Section IV) of Part 12 of the stem, and in the middle of Part 23 (Section V) (Figures 1c and 1d). The sections were mounted on slides and the presence of compression wood determined based on the anatomy of the tracheid [12].

In each section, the presence of RW or NW was assessed (Figure 1d). For each sector of RW, the inner and outer radii (relative to the pith, on the N–S diameter of the section) were measured with Photoshop 5.5 and 6.0. Percentage of RW was measured in Sections II, III and IV. Sections I and V were also included in the cell anatomical analysis.

Fournier's model

With Fournier's model [9], we computed the integral effect of RW on stem leaning from measurements of the radial extension of RW in serial anatomical cross sections along the stem. The increment in longitudinal curvature at one location along the stem due to the occurrence of RW during growth, dR , of its cross section at time t can be modeled from mechanical principles. Assuming a sinusoidal distribution of maturation strains along the inner circumference of the cambium and neglecting eccentric growth and the differences in the modulus of elasticity between RW and NW, Fournier et al. [9] found that the local curvature caused by RW formation and asymmetric maturation strains in a new layer of cells deposited by the cambium during secondary growth is (1) proportional to the thickness of the layer, dR (and thus to the growth rate in girth dR/dt), (2) proportional to the difference in maturation strains between opposite sides of the stem ($2\alpha_j$) and (3) inversely proportional to the square of the radius of the stem $R(t)$ that resists the bending as:

$$\partial C = -4 \cdot \alpha_j \cdot \frac{dR}{R} \quad (1)$$

where ∂C is the change in local curvature of the stem, α is half the difference in maturation strain between the upper side of the trunk and that of its OW, R is the radius of the stem at time t and at position j along the stem and the minus sign denotes the downward sector of RW inducing upward curving. If the stem is straight and not producing a sector of RW, then $\alpha_j = 0$.

Because measurement of RW is destructive, we observed only total RW formed by the end of the experiment. Therefore, an integrated version of Equation 1 was used [13]. Our approach was to first compute the changes in curvature from the records on RW sectors for each individual plant (Figure 1d), based on a common value for α taken from measurements of one young individual of *P. pinaster* from the French Landes provenance ($\alpha_L = 0.0015$; Loup et al. 1991), and then test whether these results correlated with the total curvature and straightening of individual plants (validation of the model). If so, the slope of the regression between the measured values and the value (β_i) estimated by the model for the provenance i (where $i = \text{Gredos, Tiétar or Oña}$) will give an estimate of the value of α_i for that provenance, relative to α_L of the French Landes provenance. It was also necessary to integrate changes in curvature along the stem to estimate the final angle of the stem resulting from RW formation. For more details about calculations see [14].

The angle $\Phi_{01}(tf)$ estimated from the integration of Fournier's model was compared with total straightening of Part 01 as experimentally measured. Then, for the i th provenance, a significant linear relationship can be fitted between the values $\Delta A01$ and $\Phi_{01}(tf)$:

$$\Delta A01(tf) = \beta_i \Phi_{01}(tf) + \varepsilon_i$$

where β_i is a constant estimating the (unknown) mean α_i , relative to α_L .

$$\beta = \frac{\alpha_i}{\alpha_L} + b_i \quad (2)$$

If systematic biases b can be neglected, then $\beta_i = 1$, implying that α_i is equal to α_L . Thus, β_i can be interpreted as a dimensionless or relative α_i .

Flexuosity index

To evaluate the final straightness of each plant, a flexuosity index (FI) was computed that compares the length of the line from the stem base to the stem top to the sum of the lengths of the three parts of the stem (Figure 1).

$$FI = \left(1 - \frac{L_{03}}{L_{01} + L_{12} + L_{23}} \right) \cdot 100 \quad (3)$$

Statistical analysis

Data for growth and angles were subjected to a repeated measures analysis of variance (ANOVA) with covariables $A01(t = 0)$ (initial angle at tilting) for angles and $L01(t = 0)$ (initial length) for growth. Percentage of RW was analyzed by a repeated measures ANOVA with provenances as between-subjects factors and section as within-subjects factor. Individual contrasts were performed to allow all possible comparisons.

Results and discussion

Growth

Length in Oña provenance was significantly less than in Gredos and Tiétar at the beginning of the experiment. Slightly significant differences in total length increment in the whole experiment were found.

Diameter in Oña plants grew less than the others at the base, but not in section IV (Table 1).

Table 1. Individual contrasts between provenances: L0: Initial length; $\Delta L127$: increase in length between the beginning of the experiment and the end of the experiment (0 to 127 days); D0: Initial diameter; $\Delta D127$: diameter growth since the beginning to the end of the experiment. Means with the same letter are not significantly different at the 5% level.

	L0 (cm)	$\Delta L127$ (cm)	Section II		Section IV	
			D0 (mm)	$\Delta D127$ (mm)	D0 (mm)	$\Delta D127$ (mm)
Gredos	22,77 a	6.18 a	5.16 a	1.39 a	2.82 a	2.00 a
Oña	15,02 b	4.80 ab	4.25 b	1.10 b	2.13 b	1.60 a
Tiétar	22,92 a	4.14 b	5.07 a	1.44 a	2.00 b	1.77 a

Kinetics

The changes undergone by all the plants after tilting followed a similar pattern, although there were differences between provenances in the magnitude and velocity of the changes.

Basal part of the stem (angle A01): After the 45° tilting of the pot, the stem bent down immediately. For one week after tilting, part 1 of the stems increased leaning (sagging phase), until reaching horizontal (A01=0) or even slightly negative angles (A01 ~ -5°). Then a phase of fast upward bending to nearly 50° at day 34 was observed. Then an almost stable position was reached, around 60° (Tiétar and Oña) or 70° (Gredos) (Fig. 2). During the phases of sagging and fast upward bending, differences between provenances were not detected, but plants from Gredos provenance continued upward bending longer than the others, reaching at the end an average angle A01 10° significantly larger.

Part of the stem developed during the experiment (angles A12 and A23): When the plants were tilted, the apex reacted rapidly, bending upward and straightening. Twenty-four hours later, the change of orientation of the apical part of the stem was perfectly noticeable (Fig. 2), with part 12 forming a pronounced crook. A12 then increased quickly, reaching a maximum value at day 34 that clearly passed the vertical. It then decreased slightly until the end of experiment. Between one and five weeks after tilting, the apex again changed its direction of growth and produced a second crook in the stem (allowing to define segment 23 and angle A23). Surprisingly, angle A23 remained stable in all cases until the end of August (day 76), and then showed a slight decrease. There was a difference in mean angle A23 of 10° approximately between Oña and the other two provenances.

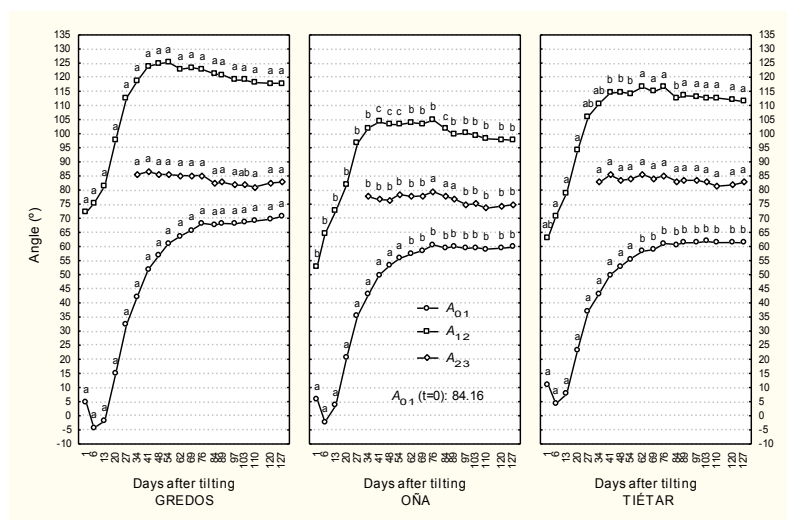


Fig. 2. Changes over time in the angle of the basal, second and upper part of the stem (angles A01, A12 and A34 respectively) in tilted plants from three provenance regions. Each point is the LS mean over 10 trees from the same provenance. Contrast between provenances at the same date for each angle: Means with the same letter are not significantly different at the 5% level.

Relative angles (A012 and A123): Angle A012 (Figures 1 and 3) increased during 13 days after tilting as the hook progressively developed. However, from day 13 on, it sharply decreased until the end of the

experiment, showing that a counter-curving process was going on. Twenty-four hours after tilting, the angle A012 in Gredos plants was 67.4°, significantly higher than the values reached in Tiétar (52°) and in Oña plants (47°). The A012 maximum values reached 13 days after tilting were by provenance 83.3°, 71.3° and 68.9° respectively, again higher in Gredos by approx 10°. From day 54 until the end of the experiment the rate of decrease in Oña and Tiétar was slow, remaining significantly higher in Gredos. In sum A012 in Gredos increased more rapidly (faster curving) but then decreased faster and for a longer period (faster and longer de-curving). The variation in A123 was smaller than in A012. Once part 34 was established, A123 remained almost constant over time (within a range of 7°).

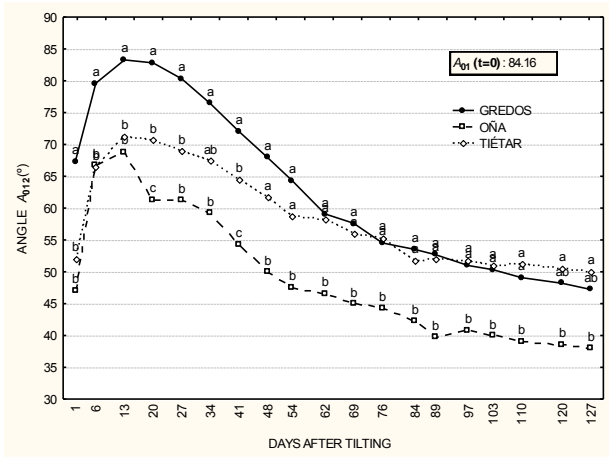


Fig. 3. Changes over time in A012, angle between the first (basal) and second part of the stem, in tilted plants from three provenance regions. Each point is the LS mean over 10 trees from the same provenance. Contrast between provenances at the same date: Means with the same letter are not significantly different at the 5% level.

Effect of the reaction wood on the leaning of the stem

There were no differences between provenances in % of RW type 1 (South side), in any sections. However, Gredos provenance produced a significantly larger percentage of RW type 2 (North side) in sections III and IV than the other two populations.

To assess the general validity of the biomechanical model, $\Phi 01(tf)$ was first compared to the measured angle A01 at the end of the experiment: A01(tf). The correlation between the calculated angle $\Phi 01(tf)$ and the measured angle A01(tf) is high. The model explains 66% of the variability, and is highly significant ($p=0.0009$).

The β estimates were similar for Oña and Tiétar. Moreover the β value in these provenances was not different from 1. These two provenances thus displayed mean α very similar to that of the Landes provenance used for estimation of $\Phi(tf)$ in eq. (8). On the contrary, pines from Gredos displayed an β 50% higher (Table 2). In other words, Gredos had higher α , i.e. higher differences in maturation strains between RW and OW, and thus a more efficient RW.

Table 2. Estimates and 95% confidence intervals for the parameters β of the model (2).

Provenance	Parameter β Estimates		
	Parameter	-95% Cnf. Lmt.	+95% nf. Lmt.
Gredos	1.50	1.34	1.67
Oña	1.13	0.96	1.29
Tiétar	1.02	0.85	1.19

To identify the components of the straightening process that contribute most to the differences in straightness between provenances, we have to focus specially in that in which Gredos plants differed significantly from the other provenances, as Gredos is the only one producing straight-stemmed plants in our study.

From a kinematical point of view, Gredos was significantly different in its i) faster secondary gravitropic up-bending (Gredos reached 10° significantly higher A01 (+17%) than the other provenances

at the end of the experiment), and ii) faster curving and secondary autotropic de-curving processes at point 1 (A012 in Gredos reached a maximal value significantly higher (+19%), and then A012 decreased more and for a longer period).

Biomechanical analysis revealed that these differences were due to two main traits, related to RW: First, Gredos has a 50% higher α (Table 2), so that the mean difference in maturation strains between RW and NW was much higher than in the sinuous provenances. Second, Gredos also developed twice to four times more type 2 RW at sect IV, with slightly thicker cell walls. These differences are synergetic in producing a more efficient and long lasting autotropic decurving, as illustrated for example by a 39% decrease in trunk flexuosity as compared to Tiétar. Consequently, at the end of the experiment Gredos plants achieved more vertical trunks (10° higher A01) with a flexuosity similar to the other provenances.

These results suggest a greater importance of the secondary rather than primary reactions influencing stem straightness. In fact, Oña plants had a significantly smaller apical reaction (A12 at the beginning) while Tiétar population had an apical reaction similar to Gredos; but the secondary responses are closer between Tiétar and Oña plants, both being much weaker than in Gredos. Moreover, these results emphasize the importance of secondary autotropism for straighter trunks, a process that has been disregarded in breeding programs.

Also of importance is that given the same initial stimulus, secondary straightening reactions can be greater in some populations without an increment in the final percentage of area of RW. This is crucial for breeding programs interested in selection for wood quality.

Although longer term research is needed, we can argue that the plants with higher response at the beginning will be straighter in the future and with less RW than the others.

Stem straightness

Direct assessment of global stem straightness was then analyzed by plotting the flexuosity index FI (as defined in eq.3) over time. In all three provenances the flexuosity index increased after tilting until day 13 and then decreased (Fig. 4). Gredos plants demonstrated the maximum values of FI during almost the whole experiment. In other words, Gredos had the least straightness of the three provenances. However, while Gredos provenance displayed the most deformation, it also showed the highest recovery, the differences in the flexuosity index between the maximum value and the value at the end of the experiment being 13.6, 11.3 and 8.3 for Gredos, Oña and Tiétar respectively.

If a classical breeding program based on indices of stem straightness were conducted on these juvenile pines, Gredos provenance would not be selected as it showed the worst form during most of the study. As stem straightness has already been evaluated at the provenance level in adult trees [1,2] we know that Gredos would be the correct selection. The present experiment can thus be interpreted as retrospective. Our alternative process-based, biomechanical approach explains the better stem straightness in adult trees from Gredos by their greater ability to straighten. The selection should be based on this ability, and not on the present stem form of the plants.

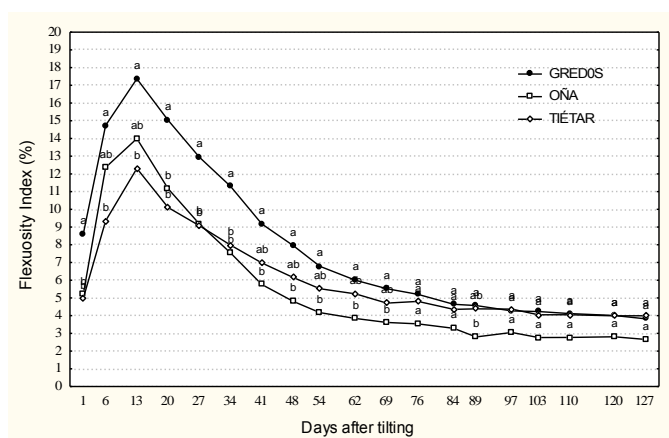


Fig. 4. Flexuosity index for the three provenances over time. Each point is the LS mean over 10 trees from the same provenance. Contrast between provenances on the same date: Means with the same letter are not significantly different at the 5% level.

Conclusion

The efficiency of reaction wood can underlie the differences in stem straightness between provenances in *Pinus pinaster*. The parameter α and the intensity of autotropic counter-curvature were the major traits distinguishing the straight provenance from the sinuous ones in this juvenile test. They are thus good indirect candidate traits for early selection of stem straightness.

The validation with a greater number of genotypes and the comparison with previously evaluated provenances will be a useful way to identify the more relevant processes and components of the models for future stem straightness.

Acknowledgements

This work was supported by the Spanish CICYT, projects AGF 97-0809

References

1. Alía, R., L.Gil and J.A. Pardos (1995). *Performace of 43 Pinus pinaster provenances on 5 locations in central Spain*. *Silvae Genet.* 44 (2/3):75-81.
2. Sierra-de-Grado, R., R. Díez-Barra and R. Alía (1999). *Evaluación de la rectitud del fuste en 6 procedencias de Pinus pinaster Ait.* *Investigación Agraria. Serie Recursos Forestales.* 8 (2):263-278.
3. Magini, E. (1969). The heritability of stem form in *Pinus pinaster*. *FAO-FTB* 3/8.
4. Coterill, P.P., C.A. Dean and G. Van Wyk (1987). *Additive and dominance genetic effects in Pinus pinaster, P. radiata and P. elliotii and some implications for breeding strategy*. *Silvae Genet.* 36 (5-6): 221-232.
5. Zas, R. 2006. *Iterative kriging for removing spatial autocorrelation in analysis of forest genetic trials*. *Tree Genetics and Genomes.* 2(4): 177-185.
6. Sierra-de-Grado, R., B. Moulia, M. Fournier, R. Alía and R. Díez-Barra (1997). Genetic control of stem form in *Pinus pinaster* Ait. seedlings exposed to lateral light. *Trees-Struct. Funct.* 11:455-461.
7. Moulia, B., C. Coutand and C. Lenne (2006). *Posture control and skeletal mechanical acclimation in terrestrial plants: implications for mechanical modelling of plant architecture*. *Am. J. Bot.* 93 (10) 1317-1329.
8. Loup, C., M. Fournier, B. Chanson and B. Moulia (1991). *Redressements, contraintes de croissance et bois de réaction dans le bois d'un jeune Pinus pinaster Ait. artificiellement incliné*. In *Proceedings of the third Seminar "Architecture, Structure, Mécanique de l'Arbre"*. Ed. B. Thibaut. Montpellier LMGC Université Montpellier II, Montpellier.
9. Fournier, M., H. Bailleures and B. Chanson (1994). *Tree Biomechanics: Growth, cumulative prestresses and reorientations*. *Biomimetics.* 2 (3): 229-252.
10. Archer R. R. and B. F. Wilson (1973). *Mechanics of the compression wood response. II On the location, action and distribution of compression wood formation*. *Plant physiol.* 51:777-782.
11. Fournier, M., A. Stokes, C. Coutand, T. Fourcaud and B. Moulia (2006). *Tree biomechanics and growth strategies in the context of forest functional ecology*. In *Ecology and Biomechanics: a biomechanical approach of the ecology of animals and plants*. Eds. A. Herrel, T. Speck and N. Rowe. CRC Taylor and Fancis, Boca Raton FL, USA, pp 1-33.
12. Timell, T.E. (1986). *Compression wood in gymnosperms*. Springer Verlag, Berlin, 2150 p.
13. Coutand, C., M. Fournier and B. Moulia (2007). *Gravitropic response of poplar trunk: key roles of the regulation of wood prestressing and of relative kinetics of cambial growth versus wood maturation*. *Plant physiol.* (44): 1166-1180.
14. Sierra-de-Grado, R., V. Pando, P. Martínez-Zurimendi, E. Bascónes, A. Peñalvo and B. Moulia (2008). *Biomechanical differences in the stem straightening process among Pinus pinaster provencances. A new approach for early selection of stem straightness*. *Tree physiol.* 28,835-846.

On stress generation mechanisms in compression wood and tension wood of trees

Ingo Burgert & Peter Fratzl

*Max Planck Institute of Colloids and Interfaces, Department of Biomaterials,
Potsdam, Germany*

Abstract

Trees form reaction wood tissues to bend leaning stems and branches upwards. The underlying principles of compressive stress generation by compression wood in softwoods and tensile stress generation by tension wood in hardwoods are still debated. In two recent articles [1,2] we have proposed new concepts for the stress generation in compression wood tracheids and tension wood fibres. This article comprises the most relevant findings of the two approaches and discusses possible constraints that may explain the change of strategy in reaction wood formation from softwoods to hardwoods.

Introduction

In straight trunks, trees pre-stress their tissues in the peripheral parts in tension in the longitudinal direction [3-5]. These internal stresses are generated during the differentiation process of the cells. It is believed that the stresses are a result of the interaction of cellulose fibrils and matrix polymers during cell wall formation. Particularly, the temporally delayed insertion of lignin has been proposed to be of crucial relevance for the generation of the internal stresses [6-8]. These longitudinal tensile stresses help to protect the compression side under wind loads because during bending of the trunk the rather low compressive strength of wood is not (or later) exceeded [9]. Moreover, trees utilize the generation of internal stresses to direct growing organs towards a predetermined position, eg. to bend leaning stems and branches upwards. For this purpose softwoods and hardwoods form different reaction wood tissues with specific stress generation capacities. In softwoods, compression wood is built for compressive stress generation on the under side of the organs. In hardwoods tension wood with a tensile stress generation that exceeds the internal tensile stresses in normal wood is built on the upper side of leaning stems and branches [10].

Both reaction wood types show specific structural features of their characteristic cell types. Compression wood tracheids of softwoods differ from the normal wood cells in possessing a round shape (Fig. 1a,c), a much higher microfibril angle in the S₂-layer, and a different chemical composition regarding lignin content and types of hemicelluloses [11,12]. Tension wood fibres of many hardwood species are characterized by an additional cell wall layer in comparison to regular fibres. This gelatinous layer (G-layer) which may replace some of the secondary cell wall layers is added on the lumen side on the formed secondary cell wall layers (Fig. 2a). The G-layer consists of almost pure cellulose oriented parallel to the cell axis [2, 13-15]. However, also certain amounts of hemicelluloses, pectins and lignin have been reported [16-19].

The underlying mechanisms of stress generation in compression wood and tension wood are still rather uncertain. Little work has been performed on the mechanisms of compressive stress generation in softwoods [8] whereas the tension wood formation and function has been recently quite extensively studied [15, 20-21]. Although the G-layer is usually interpreted as being the operative part of the tension wood fibre [11, 15, 22], in several species tension wood functions without the G-layer [23,24] and tensile stresses can be generated in its absence [25,26]. Recent findings proposed a crucial role of xyloglucan at the interface between the G-layer and the secondary cell wall in tensile stress generation [16, 21]. Assuming that the axially oriented cellulose fibrils in the G-layer can not contract along their

axial length, a longitudinal shortening of the tension wood fibres seems counterintuitive. However, Clair and coworkers [15] could show by synchrotron X-ray studies that the cellulose microfibrils of the G-layer contract upon release of the growth stresses. A further possible explanation first suggested by Münch [27] was recently examined and is based on a mechanism in which the G-layer forces the surrounding secondary cell wall to contract longitudinally [2].

In this article we report on recent own work on the underlying mechanisms of stress generation in compression wood and tension wood. Based on the different conclusions reached, possible reasons for the strategy change from reaction wood formation in softwoods to hardwoods are discussed.

Material and methods

In the Material and methods chapter only a brief overview on the sample preparation and treatment steps is given. For a more detailed description the reader is referred to the original publications [1, 2].

Compression wood in spruce

Single tracheids were isolated mechanically from never-dried wood samples of normal wood and compression wood of spruce (*Picea abies*) [28]. These never-dried cells were stored in a saturated sodium iodide solution to additionally swell the cell walls beyond the fibre saturation point. The longitudinal lengths of the tracheids were measured before and after treatment. As the salt penetrates into the wood cell wall it increases the amount of water which can be adsorbed.

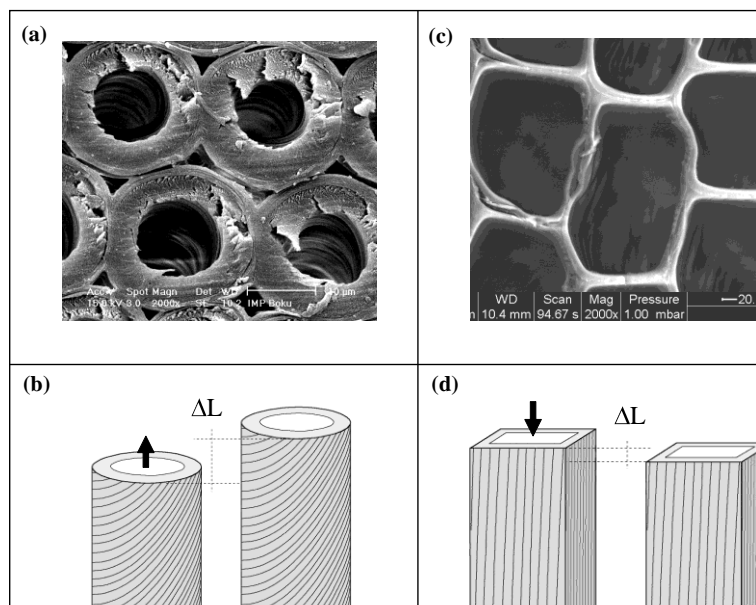
Tension wood in poplar

The material came from an artificially tilted three year old poplar tree (*Populus nigra x Populus deltoides*). Never-dried longitudinal-tangential (LT) slices from the area where the G-layer was prominently visible were used to compare native tension wood tissues and enzyme-treated tension wood tissues. For the enzymatic treatment a cellulase which acts on cellulose and xylan was used to remove the G-layer. Longitudinal and transverse dimensions of the longitudinal-tangential (LT)-slices were measured before and after the enzyme treatment. For the mechanical tests, untreated and enzyme-treated tissue slices of tension wood were strained until failure. Wide-angle X-ray scattering (WAXS) experiments were performed to determine the cellulose microfibril angle (MFA).

Results and discussion

The further swelling of wet compression wood and normal wood tracheids by a saturated sodium iodide solution results in different responses by both cell types. Normal wood tracheids show a slight reduction in length of ~0.3% (Fig. 1c,d), whereas compression wood tracheids possess a pronounced enlargement in length of ~2.5% (Fig. 1a,b). Upon the same swelling treatment an opposite deformation pattern can be observed which is probably related to the different cell wall architectures.

Fig. 1 Cross-sections of (a,) compression wood and (c) normal wood tracheids and their longitudinal deformation upon sodium iodide treatments (b,d). Arrows indicate the stress generation (after[1]).



These deformation patterns coincide with the stress generation capacities as normal wood tracheids generate longitudinal tensile stresses in their cell walls whereas compression wood cells are pre-stressed in compression along the longitudinal direction. This can be explained by treating the cell wall as a two-phase material in which stiff cellulose fibrils are embedded in a soft matrix which swells upon the sodium iodide treatment. It has been calculated that the microfibril angle determines the direction of stress generation as long as no torsion of the cell is allowed. Swelling of a cell wall with a microfibril angle below 45°, leads to a shortening of the cell in the longitudinal direction, above 45° the cell is elongating. Compressive stresses are always generated, if a slight torsion of the cell is allowed which might be facilitated in compression wood tracheids by the round the shape, the helical cavities and the lignin distribution across the cell wall.

In terms of tension wood the enzymatically treated tissue slices change their longitudinal and transverse dimensions due to the removal of the G-layers (Fig. 2c). In the longitudinal direction the tension wood slices increase in length by ~1.6 % whereas the transverse direction is shortened by ~1 %. These dimensional changes upon G-layer removal indicate that a tension wood fibre is actively shortened by the G-layer. The stress-strain curves of the untreated and enzymatically treated tension wood tissues reveal that the presence of the G-layer leads to a fundamentally different mechanical behaviour (Fig. 2d). The tension wood tissues in which the G-layer was removed show a behaviour which is rather typical for normal plant tissue with a high cellulose microfibril angle in the dominating cell wall layer [29-31]. This is in good agreement with the determined microfibril angle of ~36° in the surrounding secondary cell wall layer. The natural tension wood tissues with G-layers show an initial stiffness which is higher by a factor of ~4 in comparison to the enzymatically treated tissues. After yield, the stress-strain curve is characterized by a jagged appearance. This deformation pattern indicates a friction of the G-layer and considering the dimensional changes after enzyme treatment it seems reasonable to assume that the G-layer exerts a transverse pressure onto the cell wall.

In a geometrical model it was shown that depending on the microfibril angle in the surrounding secondary cell wall, a transverse pressure of the G-layer would result in a longitudinal shortening of the fibre. The optimal microfibril angle in the secondary cell wall for the generation of longitudinal tensile stresses was found to be close to the observed microfibril angle of ~36°. Hence, hardwoods seem to be able to generate high tensile stresses by the combination of an axially stiff and laterally swellable G-layer with an adapted cellulose microfibril angle in the surrounding secondary cell wall.

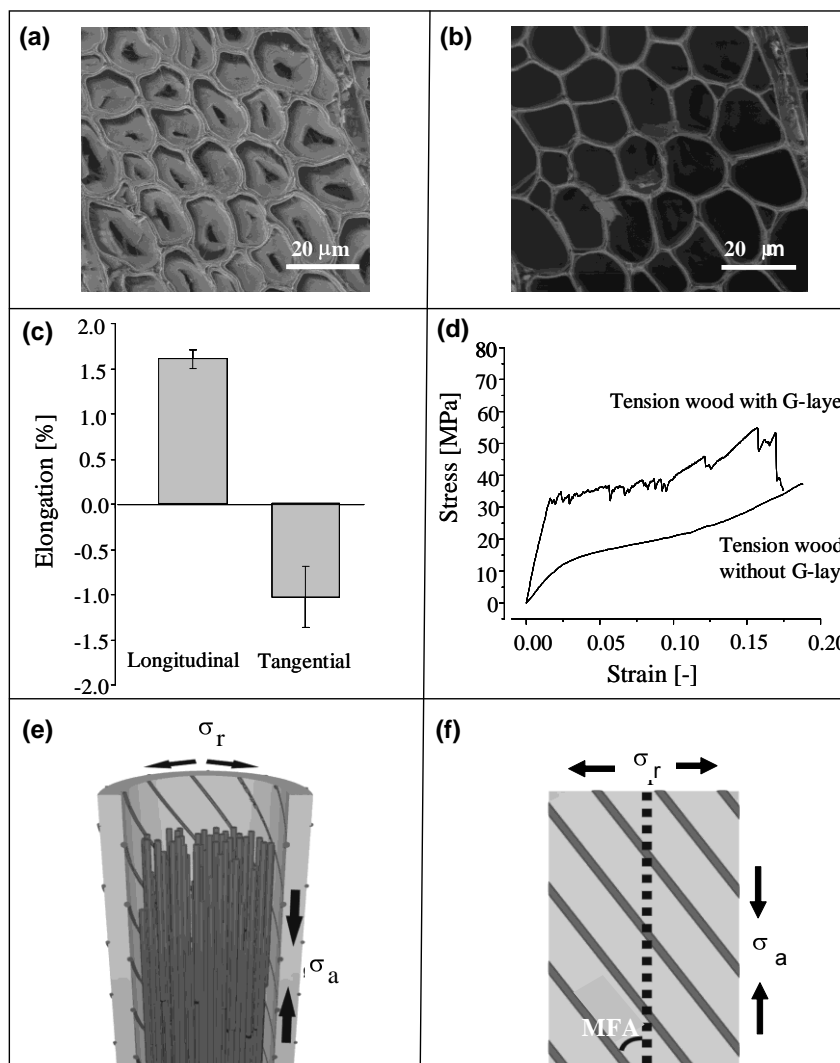


Fig. 2 Cross-sections of (a,) natural tension wood and (b) enzymatically treated tension wood without G-Layer. (c) Longitudinal and transverse change in tissue dimensions upon G-layer removal. (d) Stress-strain curves of natural tension wood tissues and enzymatically treated tension wood tissues. (e,f) Model in which transverse stresses exerted by the swollen G-layer on the secondary cell wall are converted into longitudinal tensile stresses depending on the microfibril angle (MFA) in the secondary cell wall (after[2]).

Besides the underlying mechanisms of stress generation in tension wood and compression wood, it is of interest to know why softwoods and hardwoods follow such different strategies for reaction wood formation. Experimental measurements and modelling clearly show that softwoods are able to generate tensile stresses in their normal wood. In consequence, the compression wood formation requires a change in the direction of stresses between neighbouring tissues. It might be speculated that this change in the direction of stresses could bear some risk for the living tree. The transition from the tensile to the compressive stressed tissues must go along an unstressed zero phase which is not “protected” by growth stresses. The change in the direction of stresses also makes the fine-tuning of the spatial orientation of plant organs more complicated than just an “add-on” of tensile stresses. This can be seen when comparing the precision of the organ response to artificial tilting of softwood and hardwood stems. While softwoods overshoot and “meander” to relocate the top back to the vertical position, hardwoods are more precise in their response [32]. Therefore it seems that a reaction wood type generating a higher tensile stress in reaction wood than in normal wood is preferable over a change in the direction of stresses. Moreover, the compressive stress generation in compression wood may not be sufficient to push leaning stems and branches upwards and softwoods may additionally need the supportive contribution by the opposite wood tissues.

However, softwoods may have not been able to form a reaction wood tissue which exceeds the tensile stresses in normal wood. This might have been achieved by the hardwoods by the evolution of the G-layer, although high tensile stresses can also be observed in hardwoods that form no G-layer [24-26]. On the other hand, it does not seem as if the formation of tension wood makes hardwoods by

far more elaborated in controlling the growth direction than the softwoods. Therefore it might also be likely that tension wood formation is a necessity of the higher cell diversification in hardwoods; in particular the formation of large vessel elements which might not tolerate adjacent cells that generate longitudinal compressive stresses.

Conclusion

Two theories have been presented on stress generation mechanisms both in compression wood and tension wood. It has been shown for softwoods that the change in the direction of stresses between normal wood and compression wood, e.g. generation of either tensile or compressive stresses, can be controlled by the tree through the smart arrangement of cellulose fibrils in the cell walls. In terms of tension wood fibres containing a G-layer, it has been proposed that a transverse swelling of the G-layer might cause the cell to contract longitudinally and that the magnitude of this depends on the cellulose fibril orientation in the secondary cell walls of the tension wood fibre. Further the strategy change in reaction wood formation from softwoods and hardwoods has been discussed.

Acknowledgements

The authors thank Luna Goswami, Burgi Gierlinger, Michaela Eder, John Dunlop, Karin Jungnikl, Catherine Coutand and George Jeronimidis for their contributions to the projects presented [1,2].

References

1. Burgert, I., Eder, M., Gierlinger, N. and Fratzl, P. (2007): *Tensile and compressive stresses in tracheids are induced by swelling based on geometrical constraints of the wood cell*. *Planta* 226: 981-987.
2. Goswami, L., Dunlop, J.W.C., Jungnikl, K., Eder, M., Gierlinger, N., Coutand, C., Jeronimidis, G., Fratzl, P. and Burgert, I. (2008): *Stress generation in tension wood of poplar is based on the lateral swelling power of the G-layer*. *The Plant Journal* 56: 531-538.
3. Boyd, J.D. (1950a): *Tree growth stresses I: Growth stress evaluation*. *Austr J Sci Res Series B - Biol Sci* 3: 270-293.
4. Okuyama, T. and Sasaki, Y. (1978): *The residual stresses in wood logs due to growth stress (IV)*. *Mokuzai Gakkaishi* 24: 77-84.
5. Kubler, H. (1987): *Growth stresses in trees and related wood properties*. *For Prod Abstracts* 10: 31-119
6. Boyd, J.D. (1950b): *Tree growth stresses III: The origin of growth stresses*. *Austr J Sci Res Series B- Biol Sci* 3: 294-309
7. Bamber, R.K. (1979): *The origin of growth stresses*. *Forepride Digest* 8: 75-79 and 92.
8. Yamamoto, H. (1998): *Generation mechanism of growth stress in wood cell walls: roles of lignin deposition and cellulose microfibril during cell wall maturation*. *Wood Sci Technol* 32: 171-182
9. Mattheck, C. and Kubler, H. (1996): *Wood - the internal optimization of trees*. Springer, Heidelberg
10. Wardrop, A.B. (1965): *The formation and function of reaction wood*. In: *Cellular ultrastructure of woody plants* (Côté, W.A. ed). New York: Syracuse Univ. Press, pp. 371-390.
11. Côté, W.A. and Day, A.C. (1965): *Anatomy and ultrastructure of reaction wood*. In: Côté WA (ed.) *Cellular ultrastructure of woody plants*. Syracuse Univ Press, NY, pp 391-418
12. Timell, T.E. (1982): *Recent progress in the chemistry and topochemistry of compression wood*. *Wood Sci Technol* 16: 83-122
13. Daniel, G., Filonova, L., Kallas, A.M. and Teeri, T.T. (2006): *Morphological and chemical characterization of the G-layer in tension wood fibres of Populus tremula and Betula verrucosa: Labelling with cellulose-binding module CBM1HjCel7A and fluorescence and FE-SEM microscopy*. *Holzforschung* 60: 618-624.
14. Müller, M., Burghammer, M. and Sugiyama, J. (2006): *Direct investigation of the structural properties of tension wood cellulose microfibrils using microbeam X-ray fibre diffraction*. *Holzforschung* 60: 474-479.

15. Clair, B., Alméras, T., Yamamoto, H., Okuyama, T. and Sugiyama, J. (2006): *Mechanical behaviour of cellulose microfibrils in tension wood, in relation with maturation stress generation*. Biophys. J. 91: 1128-1135.
16. Nishikubo, N., Awano, T., Banasiak, A., Bourquin, V., Ibatullin, F., Funada, R., Brumer, H., Teeri, T.T., Hayashi, T., Sundberg, B. and Mellerowicz, E.J. (2007): *Xyloglucan endo- transglycosylase (XET) functions in gelatinous layers of tension wood fibres in poplar – a glimpse into the mechanism of the balancing act of trees*. Plant Cell Physiol. 48: 843-855.
17. Joseleau, J.P., Imai, T., Kuroda, K. and Ruel, K. (2004): *Detection in situ and characterization of lignin in the G-layer of tension wood fibres of Populus deltoids*. Planta 219: 338-345.
18. Lehringer, C., Gierlinger N. and Koch, G. (2008): *Topochemical investigation on tension wood fibres of Acer spp., Fagus sylvatica L. and Quercus robur L.* Holzforschung 62: 255-263.
19. Bowling, A.J. and Vaughn, K.C. (2008): *Immunocytochemical characterization of tension wood: Gelatinous fibers contain more than just cellulose*. Amer. J. Bot. 95: 655-663.
20. Yamamoto, H. (2004): *Role of the gelatinous layer on the origin of the physical properties of the tension wood*. J. Wood Sci. 50 : 197-208.
21. Mellerowicz, E.J., Immerzeel, P. and Hayashi, T. (2008): *Xyloglucan: The molecular muscle of trees*. Annals of Botany 102: 659-665.
22. Clair, B., Ruelle, J. and Thibaut, B. (2003): *Relationship between growth stresses, mechano-physical properties and proportion of fibre with gelatinous layer in chestnut (Castanea sativa Mill.)*. Holzforschung 57: 189-195.
23. Fisher, J.B. and Stevenson, J.W. (1981): *Occurrence of reaction wood in branches of dicotyledons and its role in tree architecture*. Botanical Gazette 142: 82–95.
24. Clair, B., Ruelle, J., Beauchene, J., Prevost, M.F. and Fournier, M. (2006): *Tension wood and opposite wood in 21 tropical rain forest species I. Occurrence and efficiency of the G-layer*. IAWA Journal 27: 329–338.
25. Qiu, D., Wilson, I.W., Gan, S., Washusen, R., Moran, G.F. and Southerton, S.G. (2008): *Gene expression in Eucalyptus branch wood with marked variation in cellulose microfibril orientation and lacking G-layers*. New Phytologist 179: 94-103.
26. Okuyama, T., Yamamoto, H., Yoshida, M., Hattori, Y. and Archer, R.R. (1994): *Growth stresses in tension wood: role of microfibrils and lignification*. Ann. Sci. For. 51: 291-300.
27. Münch, E. (1938): *Statik und Dynamik des schraubigen Baus der Zellwand, besonders des Druck- und Zugholzes*. Flora 32: 357-424.
28. Burgert, I., Gierlinger, N. and Zimmermann, T. (2005): *Properties of chemically and mechanically isolated fibres of spruce (Picea abies [L.] Karst.)*. Part 1: Structural and chemical characterisation. Holzforschung 59: 240-246.
29. Bodig, J. and Jayne, B.A. (1993): *Mechanics of wood and wood composites*. Krieger Publishing, Malabar, Florida, USA.
30. Köhler, L. and Spatz, H.-C. (2002): *Micromechanics of plant tissues beyond the linear-elastic range*. Planta 215: 33-40.
31. Burgert, I. (2006): *Exploring the micromechanical design of plant cell walls*. Amer. J. Bot. 93: 1391-1401.
32. Coutand, C., Fournier, M. and Moulia, B. (2007): *The gravitropic response of poplar trunks: key roles of prestressed wood regulation and the relative kinetics of cambial growth versus wood maturation*. Plant Physiology 144: 1166-1180.

Gravitropism plays a key role in the diversity of tree ecological strategies at the advance regeneration stage. A case study in the French Guiana tropical rainforest.

Meriem Fournier¹, Gaëlle Jaouen², Emmanuel Duchateau³, Bruno Clair⁴, Catherine Coutand⁵, Tancrède Alméras⁶

¹*AgroParisTech-ENGREF, Laboratoire d'Etude de la Ressource Forêt Bois « LERFOB »
UMR INRA AgroParisTech-ENGREF 1092, 14 rue Girardet F-54000 Nancy*

²*Ecole Doctorale RP2E, Ecologie des Forêts de Guyane « ECOFOG », UMR CIRAD 93
CNRS 8172 AgroParisTech-ENGREF INRA 745 UAG 43, BP 316, 97300 Kourou*

³*INRA, Laboratoire d'Etude de la Ressource Forêt Bois « LERFOB », UMR INRA
AgroParisTech-ENGREF 1092, Centre de Nancy. F-54280 Champenoux*

⁴*CNRS, Laboratoire de Mécanique et Génie Civil, Université de Montpellier 2/CNRS UMR
5508. cc 048 – Place Eugène Bataillon, F-34095 Montpellier*

⁵*INRA, UMR547 Physiologie intégrée de l'arbre fruitier et forestier PIAF INRA-Univ.
Clermont II. 234 avenue du Brézet. INRA Site de Crouël. F-63100 Clermont-Ferrand*

⁶*CNRS, Laboratoire de Mécanique et Génie Civil, Université de Montpellier 2/CNRS UMR
5508. cc 048 – Place Eugène Bataillon, F-34095 Montpellier*

Abstract

Gravitropism is a major process in vertical growth as it allows the positioning of plant in the gravity field and thus, for trees, it takes part in the light foraging strategies. Without any gravitropism, trees would adopt a weeping habit or fall on the ground due to the increasing with growth supported weight, especially at the advance regeneration stage (sapling stage) in the understorey, where tree are very slender and poorly stiff. Most of the gravitropic studies are made by physiologists in order to understand the process and thus are associated to complex laboratory methods (genetic engineering, anatomical studies, accurate 2D ou 3D measurements of form changes with time). In order to study the ecological relevance and the specific diversity of gravitropic performances in natural forests, we developed a framework that uses different kinds of datas. Synchronical analysis has been done i) at the population level in large sample of trees and ii) at the tree level from destructive measurement of the dissymmetry maturation strains known to be the main motor of the posture control reaction of trees. In both cases, biomechanical models allows to estimate some aspects of the dynamic gravitropic process. Diachronical analysis has been done in natural conditions on permanent plots, or in a more traditional way, by observing in greenhouse experiments the righting movements of plants artificially tilted. In the first case, the problem is the high variability of natural disturbances and the slowness of growth and movements in the dark understorey. The second choice allows a measurement of a capacity (i.e. the ability of the species to react in quite extreme conditions of verticality disturbance but good for growth light and nutrient conditions) that is more easy to analyse, but is maybe not so relevant for estimating the ecological strategy (some species could have developed a high efficiency of gravitropic reaction in natural conditions by avoiding the mechanical disturbance or adapting the reaction to slow growth and changing environments in natural conditions). All approaches use the same basic biomechanical modelling, i) to analyse simultaneously the reaction and the disturbance (due to the weight increase) during growth, or ii) to combine different parameters (geometry, growth, weight, maturation strains) involved in shape changes and posture control. They give a classification of the species according to their gravitropic performances. Results on 15 species are discussed, with relation to shade-tolerance or avoidance.

An Investigation on the Growth Strains and Stresses of

Populus deltoides in north of Iran

Habibollah Khademi Eslam¹, Arash Faraj Pour²

¹ *Laboratory of Wood Science and Technology, Science & Research Branch, Islamic Azad University (IAU), Tehran, Iran*

² *Laboratory of Wood Science and Technology, Science & Research Branch, Islamic Azad University (IAU), Astara, Iran*

Abstract

In order to make an estimation on the amount of the longitudinal and tangential growth strains, 22 trees were selected from two different regional locations in north of Iran. The single-hole strain gauge method was used to measure the percentage of LRSM (longitudinal released strain maturation) and HTR (hygrothermal recovery) of transverse strains. Results showed that a good relationship exists between some environmental conditions and the amount of LRSM. Also, according to the data obtained from lab experiments, the amount of HTR increases by applying heat treatments and shows a good relationship with the increase of temperature at heat treatments. It was found that the increase in release of transverse strains in most of the samples obeyed a similar fashion and it was discovered that the best and optimum heat treatment in order to reach less deformation of wood texture could be in temperatures of around 45°C for *Populus deltoides*.

Material and methods

Populus deltoides obtained from two locations near Mazandaran province, in north of Iran was used in this study, a total number of 22 *Populus* trees were used: 10 *Populus* in site I and 12 trees in site II. The “single hole method” was used on all trees for evaluating the longitudinal residual strain at tree periphery. It consists in removing the bark, nailing two pins aligned along the fibers on the standing stem and measuring their distance change induced by the drilling of a hole between them. The displacement can be quantitatively related to the strains locked in the trunk by using correction factors taking into account the degree of material anisotropy. The measurement of stress level is possible on the standing tree and on logs by the single hole drilling method, which measures the increment of strain at the circumference of the tree when a hole (20mm diameter) is bored into the xylem with approximately 20mm depth. Generally, 4 measurements at 90° angle interval were made at breast level all around the trunk.

Table 1: Summary of sample quantities from each location

Location	Trees (Qty)	Description	Number of disks	DBH (cm)	approx. Age (yrs)
site I	10	6 logs selected & 2 disks extracted from each	12	15-30	12
site II	12	2 disks from 6 trees collected	12	20-45	18
Totally	22	---	24	---	---

Note: Thickness of all disks was between 3 and 6 cm.

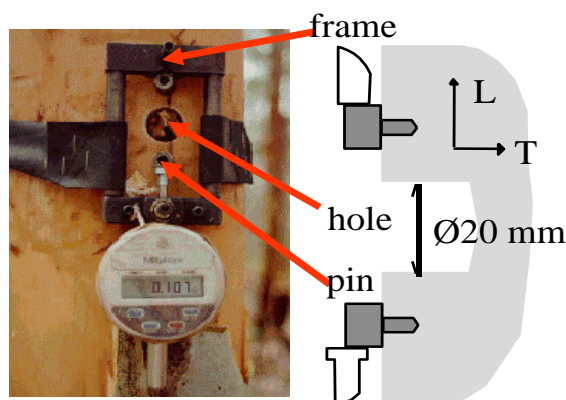


Fig. 1 The single-hole method for measurement of longitudinal residual strain at stem periphery

The transverse strains were measured using the “V-cut” method [2], based on the measurement of the relative displacement of two pins nailed on the green disk next to the periphery. Elastic residual strains are released by the sawing off of an angular sector from the periphery to the heart between the two pins. Then, the steaming of this opened disk induces a further “hygrothermal” strain release. Both V-cutting and steaming normally make the two pins to get closer to each other. The difference between the initial and the new distance divided by the remaining circumference of the sample is called the “transverse strain” because it usually combines the effect of tangential and radial locked-in strains. This was measured using 20 or 30 mm thick wood disks sawn from each green trunk, next to the level of the longitudinal measurements described above. The hygrothermal strains were measured at increasing bath temperature, from 20 to 80 °C.

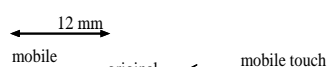


Fig. 2 Schematic illustration of strain gauge used for measuring transverse strains

Results and discussion

A. Longitudinal residual displacement

Growth stresses develop as a consequence of internal strain in the wood tissue during the xylem development. Internal growth stresses occur in the stem of living trees and develop in all trees as a consequence of growth and wood formation [1]. Some site factors like the inclination of the trees, the slope of the ground etc. are very important to the amount of growth stress. Local strains were measured at the periphery of standing trees.

The average of longitudinal released strain of maturation (LRSM) values of field trials on all specimens is presented in Table 2. The maximum LRSM of site I samples ranged from 17 to 63 μm with an average of 35.25 μm . The maximum LRSM of site II samples ranged from 30 to 83 μm with an average of 51.13 μm . It is clear that mean values of LRSM obtained from site I were lower than the ones from site II. Meanwhile, the larger standard deviation of the site I data indicates that the values are far from the mean in contrast with site II data which could be, however, due to the effect of variable and higher ground-slopes at site I on generating more longitudinal growth strains.

Table 2 Summary outcome of the average of LRSM obtained from Site I and Site II

Results of the average of LRSM obtained from Site I and Site II			
Locations	Functions	LRSM	LRSM Max
Site I	MEAN	35.25	55.10
	STDEV	5.40	11.72
Site II	MEAN	51.13	65.42
	STDEV	3.63	4.94

LRSM average radar graph for all measuring points of site I samples are displayed in Figure 3. From Figure 3 it is obvious that values of LRSM at the inclined part of the stem which was under tensile growth strain were higher than the other three circumferential points. With regard to this matter that site I contains slope of the ground of approximately 10 - 15 degrees, it is apparent that the average radar diagram shows an asymmetrical geometric shape which could be related to the slope of the ground that could exert a bending force and consequently generating more reaction wood in trunks and thus more LRSM values in leaning parts. These positive values reveal a longitudinal shrinkage at the periphery of the tree and thus correspond to negative longitudinal strains.

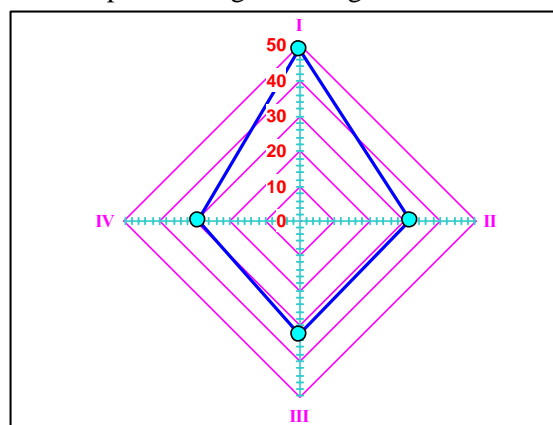


Fig. 3 Average of LRSM (Site I)

LRSM average radar graph of all points of site II is shown in Figure 4. From this figure it is obvious that values of LRSM at all circumferential points are nearly around each other and this shows that differences between obtained data were not significant as a semi-symmetric geometric shape could be observed. Due to less slope of the ground at site I (approx. 10 degrees), the main factor that could affect and apply external forces, is related to the prevailing North wind that could result in

higher value at position I of trunk circumference.

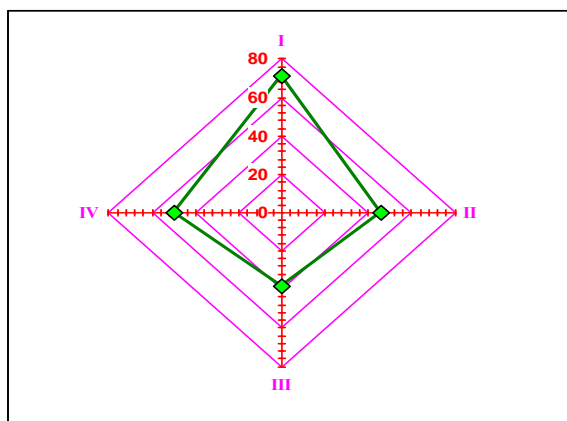


Fig. 4_Average of LRSM (Site II)

Figure 5 presents a comparison between LRSM of site I and site II which shows that the range of data of site II comprises a wider distribution than site I. As can be observed in these figures, there is a comparison between LRSM values of site I and site II in accordance with cardinal points which shows a higher amount of LRSM in North direction for two sites. Therefore, the effect of environmental conditions such as a prevailing North-wind and a South-slope at high elevations revealed that both of the aforesaid factors were responsible for generating longitudinal growth strains in samples of site I and II, respectively. Also, as it is clear from Table 3 and its relevant graph which is shown in Fig. 6, this could be demonstrated that the values of site I and site II are more concentrated around the four and five categories.

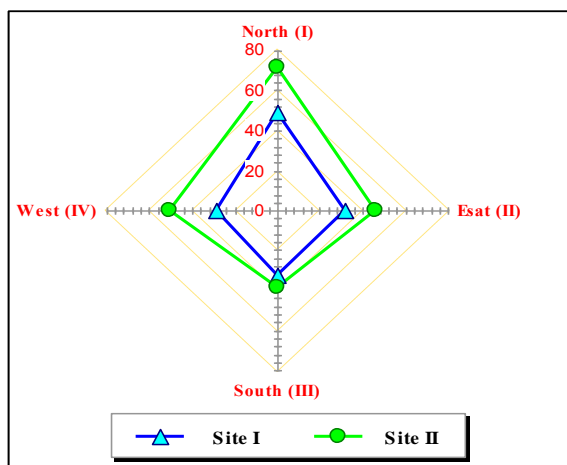


Fig. 5 Comparison between LRSM of Site I and Site II

Table 3 Frequency of LRSM values of Site I and Site II

LRSM CLASSES	Site I	Site II
0	0	0
20	5	0
40	23	10
60	10	30
80	1	10
>80	0	3

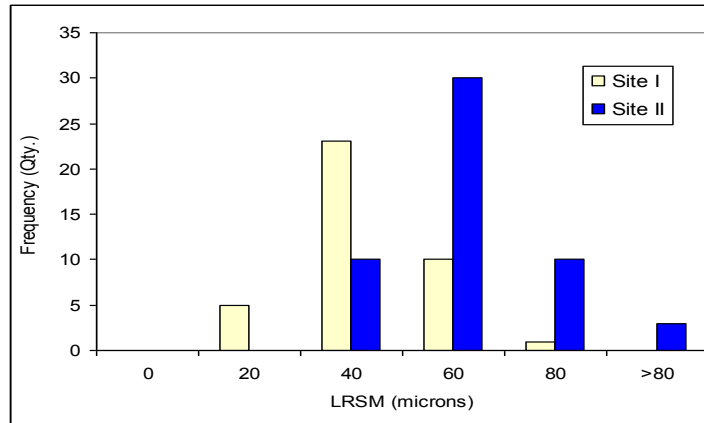


Fig. 6 Comparison between the frequencies of LRSM values of Site I and Site II

The influence of tension wood on the variations, depending on the circumference, has been specifically shown up for the GSI: in general, a marked angular dissymmetry. However, in certain cases, a flat angular profile was observed. The most marked GSI is most often recorded on the upper part of the stem in the case of a tree with an overall slant or visually noticeable curvature. The peak deformation position may be explained by a sharp dissymmetry of the presence of a large branch. This is when the tree stands at a slight angle and has a well balanced crown. High GSI values are associated with the presence of tension wood.

LRSM radar graphs for all measuring points of site samples are displayed by four categories in Figure 5. It is obvious that values of LRSM at the inclined part of the stem which was under tensile growth strain were higher than the other circumferential points. With regard to this matter that site I had a slope of the ground of approximately 10 degrees, it was apparent that the average radar diagram shows an asymmetrical geometric shape which could be related to the slope of the ground that could exert a bending force and consequently generating more reaction wood in trunks and thus higher LRSM values in leaning parts.

B. Transverse strains

Fig. 7 shows transverse strain values of site I and II, for each sample that could be attributed to hygrothermal recoveries (HTR) at four different temperatures [3]. It is clear there is a direct relation between increase of temperature and release of tangential strains especially at higher temperatures (80°C). When applying more heat treatments at higher temperatures the effect of temperature on release of tangential strains is more apparent [5, 6].

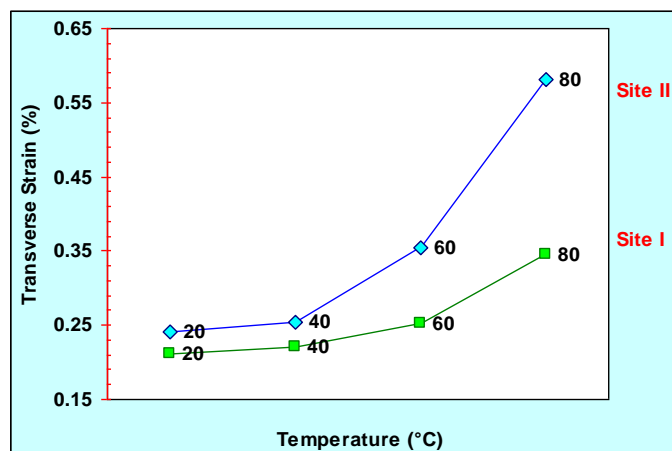


Fig. 7 Comparison between HTR values of Site I and Site II

Values obtained from site II samples show higher in amount than the ones of site I which could be attributed to higher diameter of site II samples and also more severe environmental conditions such as

prevailing wind and the slope of the ground. In addition, it is apparent that the main increase of transverse HTR, started from third stage of heat treatment which was found at temperatures of around 60°C.

Conclusions

The results of this study show that good relationship exists between the environmental conditions and growth strains. As a matter of fact, the influence of site factors such as wind, slope of the site, minor trembling of the ground etc. could affect the growth strains. According to the data obtained from HTR experiments, the amount of hygrothermal recovery of transverse strains has a positive relationship with the increase of temperature at heat treatments. Actually, there is no doubt that application of heat treatment plays an important role on expedition of relaxation and release of growth strains. Results of laboratory experiments showed that samples of site I have lower tangential strain values than site II which could be due to smaller diameter of the site I samples and also the moderate environmental conditions at site I. According to the comparison between the samples of two different locations, the increase of age in trees could be followed by increase on stem diameter and accordingly there would be an increase on the amounts of growth strains and stresses and more deformation on wood texture at production or even at service. Hence, this could be logic to promote the utilization of trees at relatively lower ages to prevent the application of high stressed timbers but with consideration of a good protection in forest nature.

References

1. Archer, R.R. (1986): *Growth stresses and strains in trees*. Springer Verlag, 240p.
2. Jullien, D. (1995): *Analyse expérimentale et numérique des contraintes résiduelles dans un matériau élastique orthotrope élaboré par couches successives. Cas d'un disque de bois vert*. Thèse de doctorat, Université Montpellier II, 214p.
3. Jullien, D. and J. Gril. (1996): *Mesure des déformations bloquées dans un disque de bois vert. Méthode de la fermeture*, *Annales des Sciences Forestières*, 53, 955-966.
4. Baillères, H. (1994): *Précontraintes de croissance et propriétés mécano-physiques de clones d'eucalyptus (Pointe Noire, Congo): hétérogénéités, corrélations et interprétations histologiques*. Thèse de doctorat, Université Bordeaux I.
5. Jullien, D. and J. Gril, (1996): *Numerical analysis of residual stresses remaining in a green wood crosscut after V-cutting and heating*. *Third biennial joint conference on Engineering Systems Design and Analysis*, July 1-4, Montpellier, ed ASME, PD-Vol 77, pp 205-212.
6. Gril, J., Jullien, D., Fournier, M. and B. Thibaut. (1996): *Modeling non axisymmetric growth stresses and related problems*. *Second Workshop*.

7. Biomimetics

From stems to sticks - what can we learn for biomimetics from natural fibre-reinforced structures?

Tom Masselter and Thomas Speck

Plant Biomechanics Group, Botanic Garden, University of Freiburg, Germany

Abstract

The economic importance of fibre-reinforced composites is increasing as they can meet a number of demands: low weight, excellent mechanical performance in stiffness, strength and energy damping, benign fracture behaviour and low production costs. This holds true for unramified, ‘linear’ fibre-reinforced composites as well as for branched ones. In the last few years the research in the Plant Biomechanics Group Freiburg concentrated upon developing ‘linear’ fibre-reinforced structures resulting in the realisation of the ‘technical plant stem’, a biomimetic product inspired by a variety of structural and functional properties found in different plants. The stems of the giant reed (*Arundo donax*, Poaceae) and the Dutch rush (*Equisetum hyemale*, Equisetaceae) have been the most important biological concept generators. The studies have led to a biomimetic, lightweight, fibre-reinforced composite structure with optimised mechanical properties that was developed and produced together with the Institute for Textile Technology and Process Engineering Denkendorf. Another challenging problem is the development of branched biomimetic fibre-reinforced structures by using stem-branch attachments of natural role models. There is a strong demand for a solution of how to manufacture nodal elements and/or ramifications with an optimised force flow, a demand evident in many areas of fibre-reinforced composite technology. Examples are hubs of wind-power plants, branch points in framework constructions in the building industry and in aerospace, ramified vein prostheses in medical technology or the connecting nodes of bicycle frames. Investigations were carried out in order to assess the potential of hierarchically structured plant ramifications as concept generators for innovative, biomimetic branched fibre-reinforced composites. Ramified plant species with pronounced fibre matrix structure served as biological role models, amongst others monocotyledons of the genera *Dracaena* and *Freycinetia*, and columnar cacti. These plants possess a special hierarchical stem organisation, which markedly differs from that of other woody plants by consisting of isolated fibres and/or wood strands running in a partially lignified ground tissue matrix. The plants exhibit Y- and T-shaped ramifications, which in their angles resemble those of the branched technical structures. Preliminary investigations confirm that the ramifications possess mechanical characteristics that are of interest for a transfer into technical applications, including a benign breaking behaviour, a good oscillation damping caused by high energy absorption and a high potential for lightweight construction. The results demonstrate the great potential for a successful technical transfer and are leading to the development of concepts for demonstrators in lab scale that already incorporate “solutions inspired by nature”.

Introduction

The increasing demand for lightweight materials with good damping and other beneficial mechanical properties is leading to the production of an ever increasing number and diversity of fibre-reinforced composites. This development is also being driven by the combination of decreasing fossil fuel resources, long-term increase of costs for raw material (e.g. steel, carbon) and high standards for

excellent performance, which can be found for many structures that are subjected to extreme tension, torsion and bending forces and moments. In many instances, these loads are dynamic and thus especially critical for the structural integrity of the component (*Fig. 1*).

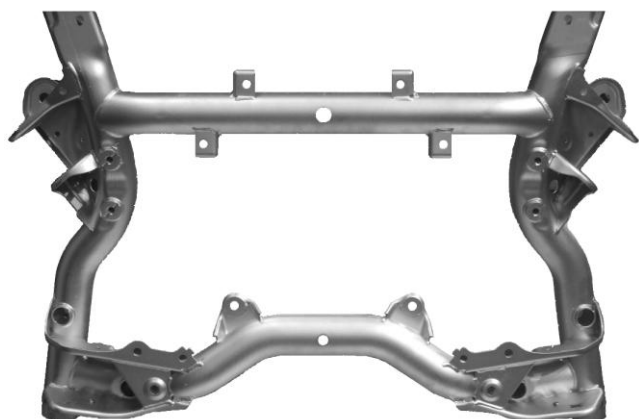


Fig. 1 Cross-member from the company Ilseburger Grobblech.

This is especially the case for mechanical parts in moving objects like cars or planes. Some of these parts cannot be easily made of fibre-reinforced composites because the production of complexly shaped structures is still difficult, particularly so when these are branched. Here, the limits of classic engineering optimisation techniques have been reached. The approach of biomimetic optimisation is very promising as 1) it combines different substructures into a superordinate structure in order to optimise mechanical characteristics, a principle that is common in nature, and 2) the laminated configuration of technical products, as e.g. a carbon-fibre-reinforced epoxy resin and some plant stems, as e.g. the layered structure of a bamboo stalk are highly comparable (*Fig. 2*) [1]. Thus, the potential of nature as a role model for designing fibre-reinforced components is very high and consequently, here the biomimetic approach is very promising. The general potential of biomimetic approaches will be described for the concrete specific example of unbranched and branched technical fibre-reinforced composites that are studied in the Plant Biomechanics Group Freiburg in cooperation with several other research institutes.

The 'technical plant stem' is a case study for the development of a 'linear' biomimetically optimised fibre-reinforced structure by the 'Bottom-Up Process' as defined by the Plant Biomechanics Group Freiburg [2, 3]. The methodological approach for developing 'branched' composite structures can be described as a 'Top-Down Process'.

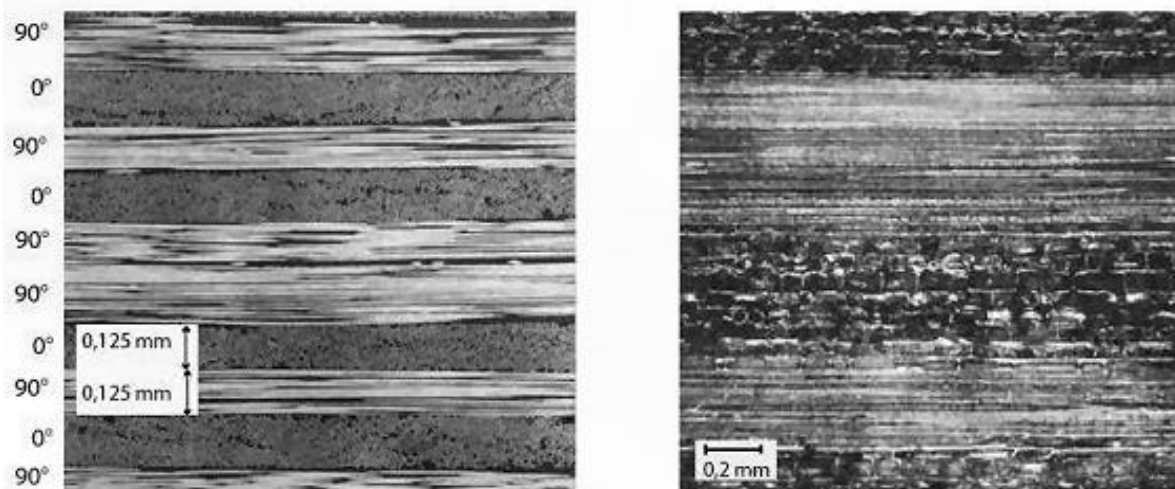


Fig. 2 Section of carbon-fibre-reinforced EP-resin-laminate (left) and bamboo stem wall (right), from [1].

Material and methods

Material

Plant material from *Equisetum hyemale* (Dutch rush, Fig. 3A) and *Arundo donax* (giant reed, Fig. 3B) was gathered in the Botanic Garden Freiburg and natural habitats near Montpellier.

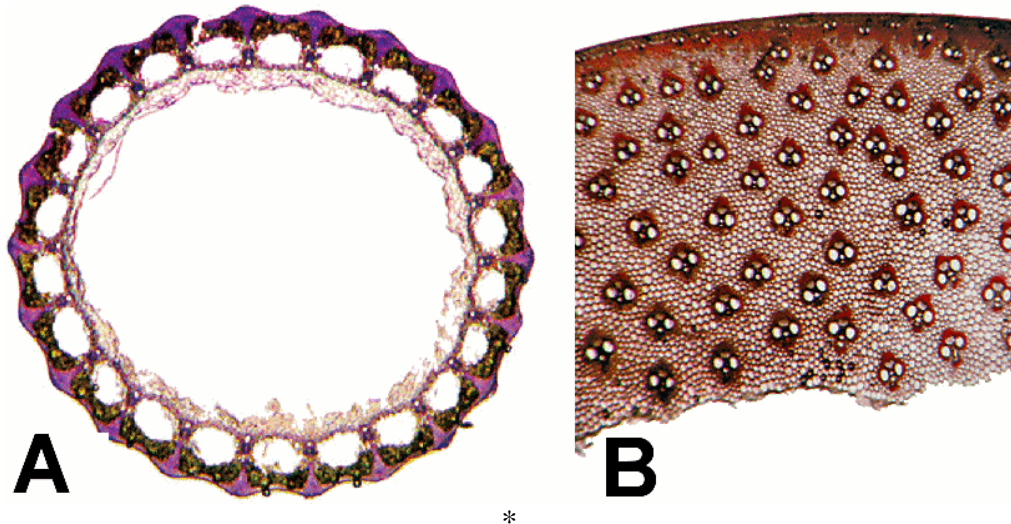


Fig. 3 Two of the five biological concept generators for the 'technical plant stem'. Cross-section of the stem (diam. 6 mm) of the horsetail *Equisetum hyemale* (Dutch rush) and of the stem wall (width 4.3 mm) of the giant reed (*Arundo donax*), from [5].

These species were the two most important of the five botanical concept generators investigated for the 'technical plant stem' (Fig. 4) [4-6]. Monocotyledons and cacti used as role models for the studies on branched structures originated from diverse commercial greenhouses as well as from the Botanical Gardens in Dresden and Freiburg.

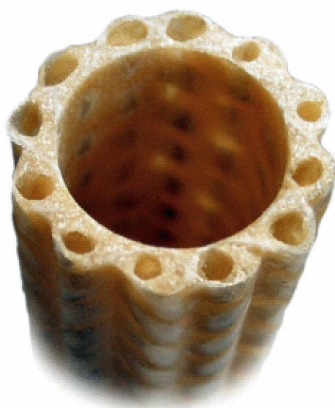


Fig. 4 The 'technical plant stem' as an example for a 'linear' biomimetically optimised fibre-reinforced composite, from [5].

Methods: 'linear' fibre-reinforced composites

The botanical concept generators for the 'technical plant stem' were first investigated within basic research projects, which represent the starting point of the 'Bottom-Up Process' for carrying out a biomimetic research and development project (biology push) [2, 3]. In a first step, the functional morphology as well as the biomechanics of the plant stems was analysed. The stems were structurally analysed by means of light and electron microscopy and subjected to cyclic loading experiments, vibration tests and various static mechanical tests both within the elastic range and until failure [7-12]. The excellent mechanical properties proved the potential for a transfer into technical applications by

using the plant structures as role models for developing a biomimetic product. The next and most crucial step in the ‘Bottom-Up Process’ was the abstraction, i.e. the conceptual detachment of the principles inferred from their natural role models and introduction into a technical product. The technical implementation was done on the lab scale in the labs of the Plant Biomechanics Group Freiburg and on pilot plant scale with the Institute for Textile Technology and Process Engineering Denkendorf, a research institute specialized in producing technical textiles and fibre-reinforced composites with high complexity (for a detailed overview see [4-6]).

Methods: ‘branched’ fibre-reinforced composites

An R&D project based on a ‘Top-Down Process’ in biomimetics is initiated by a concrete technical problem (1, Fig. 5) posed by an engineer of a company (technology pull). While such a question – ‘How can the performance and the production of branched fibrous composite structures be optimised?’ - is the undeniable origin of the project, the solution is not limited to the needs of one particular application, but rather can be used in a large number of products and may even generate new technical applications. After the technical problem has been described and clearly defined, the second step is seeking adequate concept generators in nature (2). The concept generators with the highest potential of solving the technical problem are retained at the end of this step. When the screening procedure is completed, appropriate principles based on structures and functions of one or more concept generators are identified (3). In order to do this, biomechanical tests as well as various optical methods (see below) are used to analyse quantitatively the form-structure-function relationships of the model plants. The next step is the abstraction, a part of the project with great importance for the success of the whole project (4). In the abstraction, the principles found in nature are detached from the biological role models and translated to technical materials and structures. After this knowledge-transfer from the biologists to the engineers has been accomplished, the possibilities for a technical implementation are assessed and technical feasibility tests are carried out (5). Modelling of the natural structures and of technological implementations as well as manufacturing demonstrators on the lab scale and pilot plant scale is performed prior to prototyping. In the last step of a successful R&D project the biomimetically optimised structures are introduced onto the market, accompanied by flanking measures from the industrial partner (6).

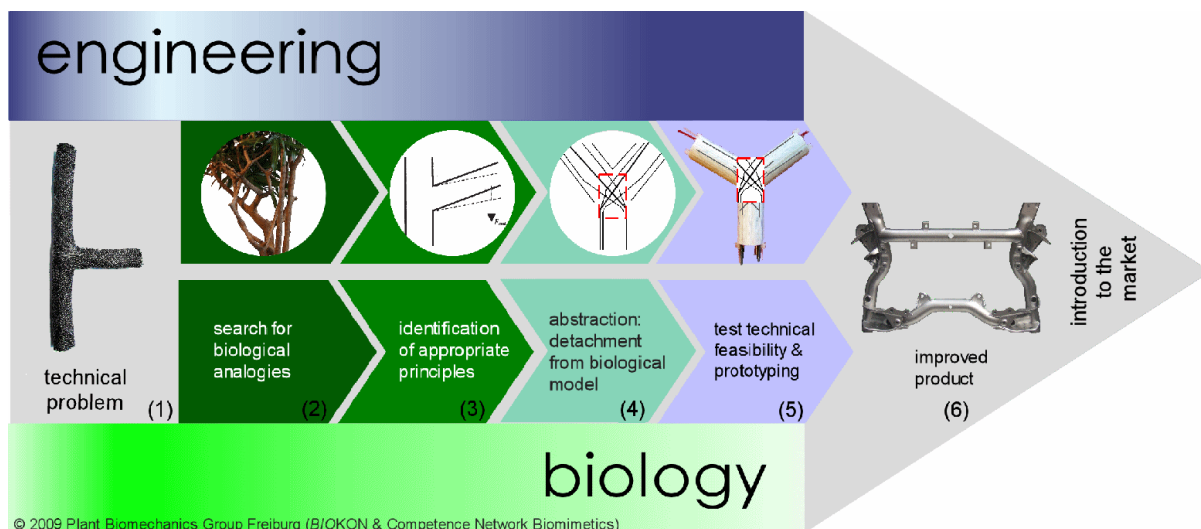


Fig. 5 Top-Down Process for developing biomimetically optimised branched fibre-reinforced structures .

For analysing the anatomy of the branch-stem attachment regions of *Dracaena* and *Freycinetia*, two of the role models for branched biomimetic fibre-reinforced composites, serial thin and semi-thin sections were made (Fig. 6A) [13]. Additionally, scanning electron microscopy and microtomography were employed for analysing the external and internal organisation of the branching regions in

monocotyledons and cacti. The biomechanical tests include breaking experiments in which a force is applied to a lateral twig until this twig breaks (Fig. 7A), using similar methods as described in [14]. This setup allows determining the force necessary to break the twig and the fracture toughness as well as the stress and strain at fracture.

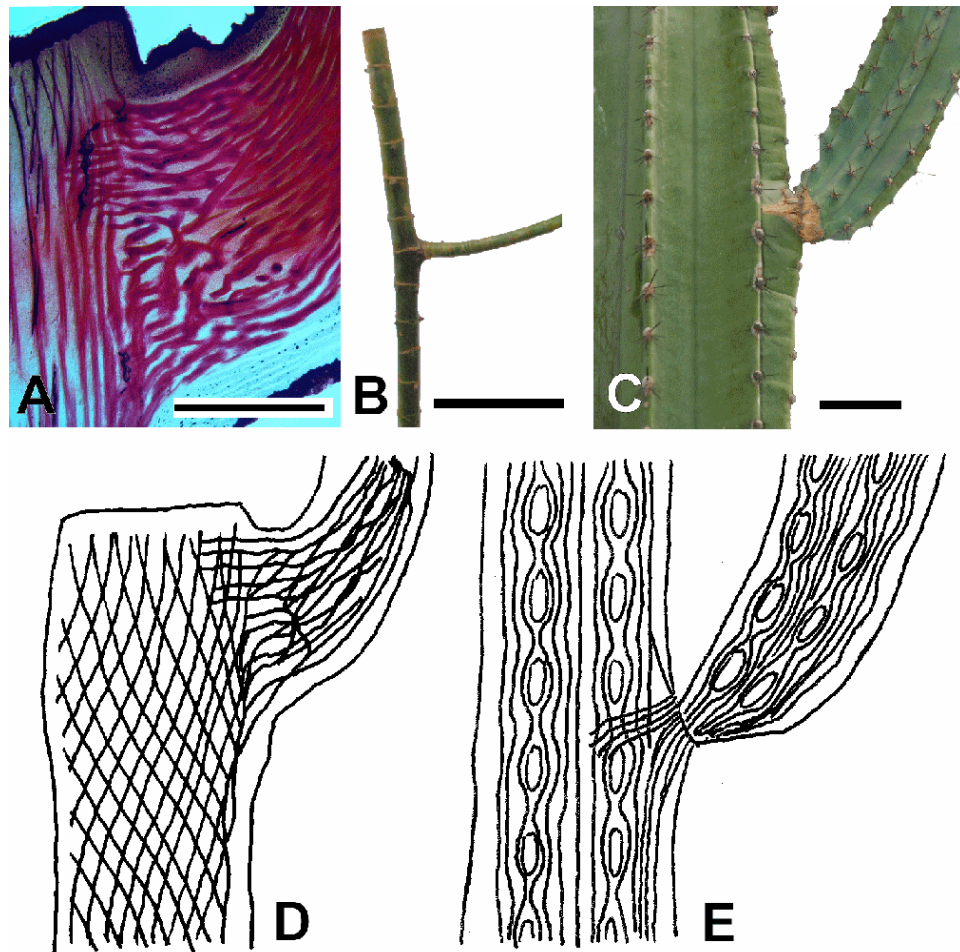


Fig. 6 Biological concept generators. Longitudinal sections of the stem-branch attachment regions of *Dracaena marginata* (A) and drawings of *Freycinetia insignis* (B), as well as an external view of the stem-branch attachment of *Cereus* sp. (C). Schematic drawing of the arrangement of fibrous bundles or wood strands, respectively, in the stem-branch attachment region of *Dracaena* (D) and *Cereus* (E). Scale bars: (A): 5 mm; (B)(C): 50 mm.

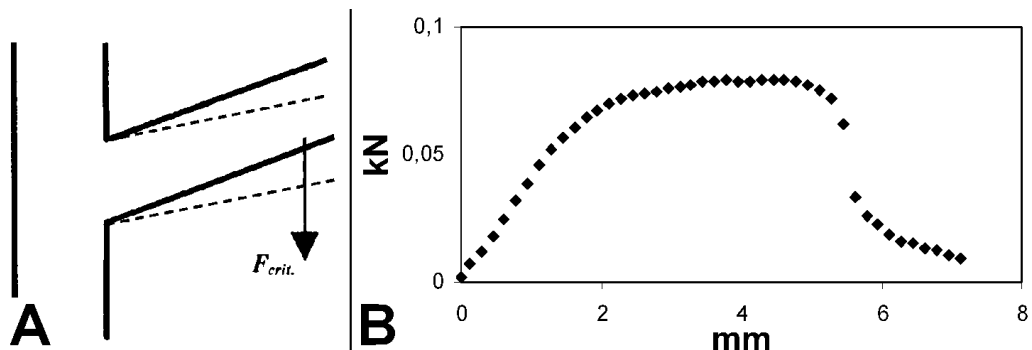


Fig. 7 Breaking experiments. Schematic drawing of the geometry of the stem-branch attachments (A). The solid line represents a lateral twig before bending, the dashed line represents a lateral twig shortly before fracture, F_{crit} is the critical force necessary to break the twig. Exemplary force-displacement curve (B) measured for *Dracaena reflexa* by the fracture mechanics test setup shown in (A).

Straight, unbranched fibre-reinforced composites

The axes of *Equisetum hyemale* and *Arundo donax* (Fig. 3), two of the biological concept generators of the ‘technical plant stem’, show a compromise between high stability and low weight. Furthermore, the giant reed has excellent vibration damping properties (Fig. 8) [4, 12]. The outstanding mechanical properties are attained by several structural design principles in *Equisetum hyemale* and *Arundo donax*.

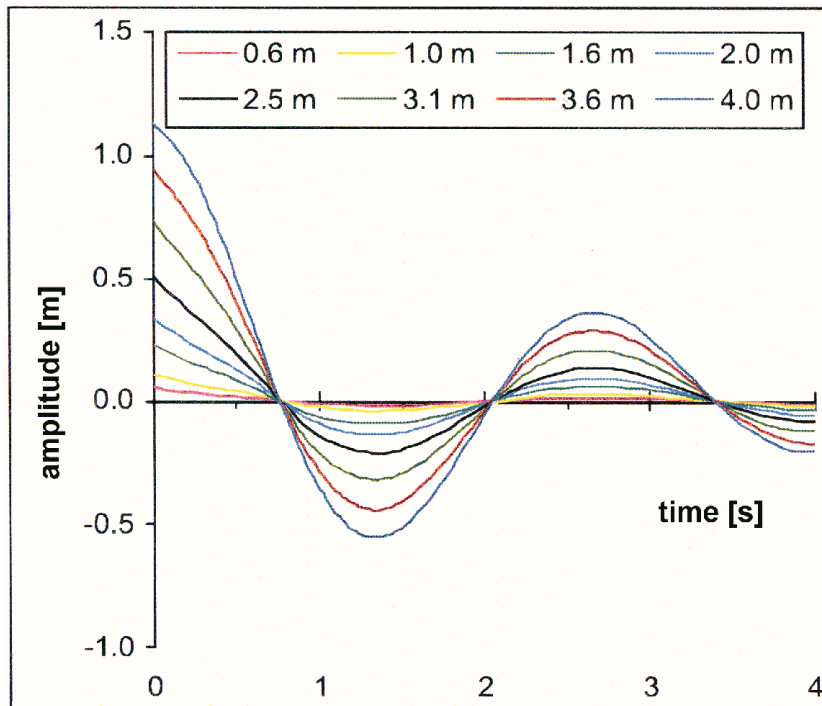


Fig. 8 The culm of the giant reed shows harmonic bending vibration with exponential damping (the eight curves represent synchronous measurements at different levels above soil in a single stem), from [4].

In *Equisetum hyemale*, a double ring structure with ‘T-strut-shaped’ interconnections between the inner ring (two layered endodermis with lignified Casparian strips) and the outer ring (collenchymatous hypodermal sterome) is at the base of the highly stable lightweight construction (Fig. 3A). This is achieved in *Arundo donax* by another sophisticated, weight-optimised structure: the axes are composed of strengthening elements such as the sclerenchymatous caps of the vascular bundles which are embedded in a more flexible matrix of parenchymatous tissue, which is lignified to various degrees (Fig. 3B). As mentioned above, the similarity of the fibre-matrix arrangement in bamboo or in *Arundo donax* and in a technical fibre-reinforced composite is striking (Fig. 2). The hierarchical structuring of the culms, i.e. the existence of structural variations and gradients on different hierarchical levels, is responsible for the excellent mechanical properties of *Arundo donax*: 1) the angles of the fibre bundles may vary along the plant according to the main mechanical loads as e.g. in the transition between the horizontal rhizome and the upright culms, 2) most of the load-carrying material is placed in areas of the highest stress, i.e. towards the outside of the culm wall (Fig. 3B), 3) a gradual decrease of stiffness towards the hollow pith can be observed: this gradient is expressed through 3.1) a decrease of the amount of load-carrying material, 3.2) a decrease of the lignifications of the parenchymatous ground tissue, 3.3) an increase in size of the parenchyma cells. Additionally, a high-damping of oscillating wind forces is made possible by this structure and further improved by 4) a gradual transition in stiffness between fibre bundles (high stiffness) and the surrounding parenchyma matrix (low stiffness), a structure that creates many interfaces with (slightly) different mechanical properties that may improve damping by friction on a nano- or molecular scale. (see [5] for details).

The structural basis of the interesting mechanical functions was abstracted and translated into a technical product, thereby creating an innovative, new technical fibre-reinforced composite material, the ‘technical plant stem’.

The production process combines a thermo-set pultrusion set with a computer controlled braiding machine (Fig. 9). This machinery setup allows winding helically intertwining fibre strands (with different angles) around a core system. It is possible to vary the density, the arrangement and the angles of the fibres or fibre bundles in order to optimally design technical structures for a given load situation.



Fig. 9 Braid pultrusion setup, © Institute for Textile Technology and Process Engineering Denkendorf.

Potential areas of implementation of the ‘technical plant stem’ are manifold, including optimised components for aerospace, automotive engineering, architecture, tool building, prostheses and sporting goods. A special application is the use of optimised biomimetic struts for the damping elements of a biomimetic shock-absorbing transportation pallet (Fig. 10A) [15]. The damping elements are integrated in the structures that connect the upper and lower cover plate of the pallet (Fig. 10B,C) The pallet can be used for safely transporting shock-sensitive goods like high-end computer hardware.

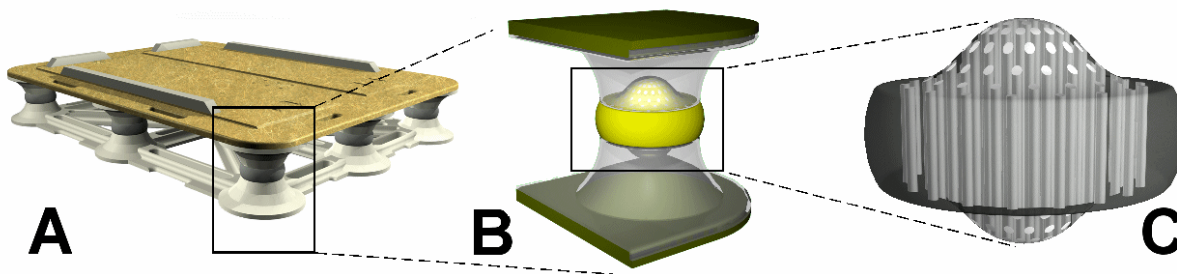


Fig. 10 Bio-inspired, optimised shock-absorbing transportation pallet. (A) Complete view of a model of the transportation pallet. (B) Foot of the transportation pallet with damping element between the two holders. (C) Damping element consisting of fibre-reinforced struts (light grey) and silicon matrix (dark grey).

Branched fibre-reinforced composites

The biological role models like the genera *Dracaena* (Fig. 6A) and *Freycinetia* (Fig. 6B) as well as columnar cacti like *Cereus* (Fig. 6C) show Y- and T-shaped branchings that in their angles resemble those of branched technical components. In both monocotyledons and columnar cacti, isolated fibres and/or wood strands run in a partially lignified ground tissue matrix, so that they form *per se* natural fibre-reinforced composites (Figs. 2, 6D,E). However, the morphology and hierarchical structuring of the stem-branch attachments are quite different: while the axes of monocots and cacti are optimised at various hierarchical levels, the angles, the course and the arrangement of the fibre or wood bundles in the matrix highly differ in the two groups of plants. The hierarchical bauplan of the plants can be subdivided in at least 5 levels: 1) the form of the branching, 2) the arrangement of the fibre-bundles, 3) the course of the individual fibre-bundles, 4) the anatomy of the fibre-bundles and the ultra structure of the fibres as well as 5) the gradients between fibres and matrix (Fig. 11).

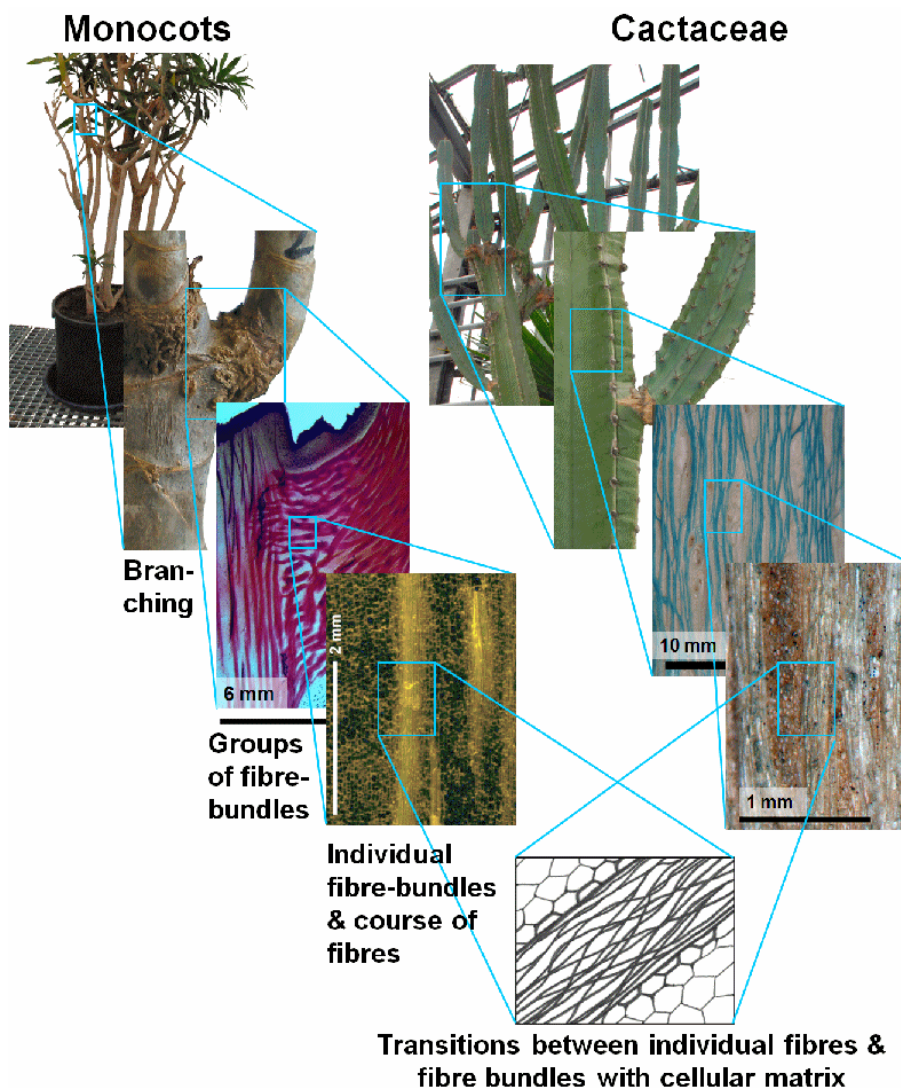


Fig. 11 Hierarchical organisation of natural concept generators © Plant Biomechanics Group Freiburg and Botanical Institute TU Dresden.

In *Dracaena*, the evolutionary optimisation to complex loads has led to a network of somewhat helically, but mostly paraxially arranged fibrous bundles in large parts of both stem and branch and to a complex interwoven pattern in the regions where the branch is connected to the stem (Fig. 6D). In a simplistic view, one could consider the stem and branch to be 1) non-hollow tubes that are interconnected by 2) a complex pattern of fibres with a 3) larger diameter at the interconnecting

region. The wood bands in stems and branches of columnar cacti are also more or less paraxially arranged showing net-like interconnection but form a very different pattern at the stem-branch interconnection (Fig. 6E). The stems and branches of columnar cacti can be considered as 1) woody tubes filled by a parenchymatous pith with an interconnection displaying a 2) complex but differently arranged pattern of wood bands and 3) a smaller diameter at the interconnection.

First results for the fracture mechanics in the monocotyledons and cacti indicate that there exist different modes of fracture with distinct force-displacement curves. For example, in one of the modes of fracture of *D. reflexa* the form of the fracture is sickle-shaped. This mode of fracture can be correlated with a force-displacement curve that shows a benign breaking behaviour (Fig. 7B), i.e. with a long plastic range.

For the transfer of the branched biological role models into technical products and the manufacture of circular preforms, the braiding technique is predestinated. Nowadays the overbraiding technique or the 3D-rotary braiding technique is used to manufacture braids of elementary shapes, which can be used as reinforcement of lightweight structures [16-18]. The producibility of braided branchings, which shall be used for the technical translation, has been proved possible in principle in recent years [16, 18]. A potential braiding unit and a first prototype of a braided T-shaped preform are shown in Fig. 12A and 12B, respectively.

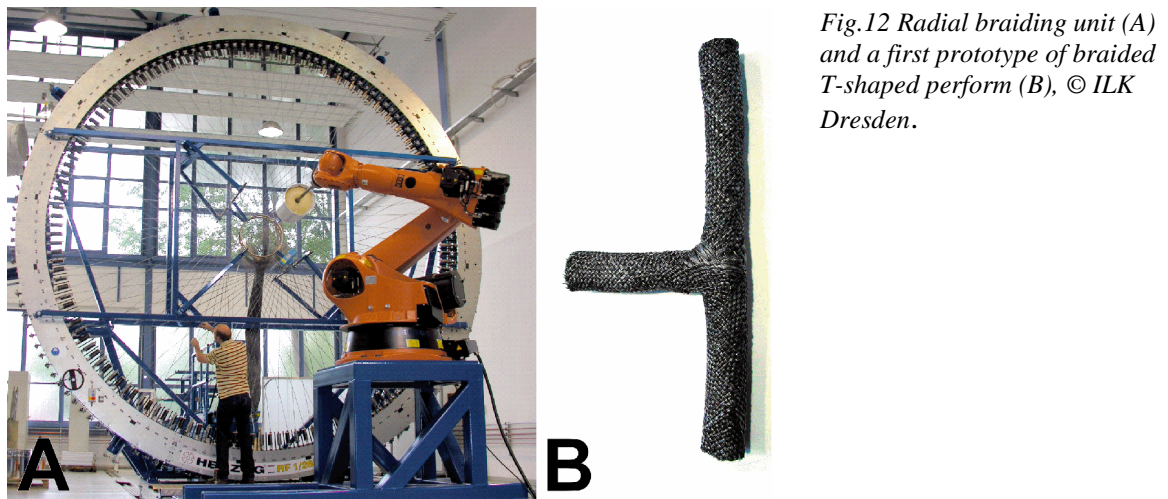


Fig.12 Radial braiding unit (A) and a first prototype of braided T-shaped preform (B), © ILK Dresden.

The potential fields of implementation are similar to those of the ‘technical plant stem’ but have the added advantage of connective joints that can connect tubular shaped fibre-reinforced composites. The joints shall be able to bear high loads and moments following the example of the biological role models. Our goal is to design these joints in a way that the continuation of the fibres from the tubular structures through the joint and to the next tubular structure is guaranteed. By adjusting the amount, the diameter and the arrangement pattern of the fibres in the joint, following the example of the biological role models, the mechanical load capacity in the joint can be adjusted to be higher than the load capacity in the tubes if this is of technical interest. It is intended to implement these adjustments on several hierarchical levels. This technique will help to reduce cracks that form through excessive notch stresses in the joints and thus will help to increase the life-span and safety of components for automotive engineering, aerospace and many other areas of lightweight engineering.

Acknowledgements

We would like to acknowledge Markus Milwich from the Institute for Textile Technology and Process Engineering Denkersdorf and Maik Gude from the Institute of Lightweight Structures and Polymer Technology of the TU Dresden for the kind permission to reproduce Figures 9 and 12 respectively. We would also like to thank the publisher Hanser Fachbuchverlag for the kind permission to reproduce Figure 2. We are grateful to Christoph Neinhuis and Hannes Schwager from

the Botanical Institute of the TU Dresden for the permission to use one picture of a cactus shown in figure 11. The part of this paper dealing with branched fibre-reinforced composites is funded within the DFG Priority Programme SPP 1420. We thank our project partners, Christoph Neinhuis, Hannes Schwager, Maik Gude, Werner Hufenbach, Markus Milwich and Olga Speck for many helpful discussions.

References

1. Ehrenstein, G.W. (2006): *Faserverbund-Kunststoffe: Werkstoffe, Verarbeitung, Eigenschaften*. Hanser Fachbuchverlag, Muenchen.
2. Speck, T., Harder, D. and O. Speck (2007): *Gradient materials and self-repair: learning technology from biology*. VDI-Report: 1-13.
3. Speck, T. and O. Speck (2008): *Process sequences in biomimetic research* in Design and Nature IV, ed.: Brebbia, C.A., WIT Press: Southampton, Boston. p. 3-11.
4. Speck, O., Milwich, M., Harder, D. and T. Speck (2005): *Vom biologischen Vorbild zum technischen Produkt: der "technische Pflanzenhalm"*. Museo 22: 96-103.
5. Milwich, M., Speck, T., Speck, O., Stegmaier, T. and H. Planck (2006): *Biomimetics and technical textiles: solving engineering problems with the help of nature's wisdom*. American Journal of Botany 93:1455-1465.
6. Milwich, M., Planck, H., Speck, T. and O. Speck (2007): *Der technische Pflanzenhalm: ein bionisches Schmaltextil*. Melliand Textilberichte – Band- und Flechtindustrie 44: 34–38.
7. Spatz, H.-C., Beismann, H., Emanns, A. and T. Speck (1995): *Mechanical anisotropy and inhomogeneity in the tissues comprising the hollow stem of the giant reed Arundo Donax*. Biomimetics 3: 141-155.
8. Spatz, H.-C., Beismann, H., Brüchert, F., Emanns, A. and T. Speck (1997): *Biomechanics of the giant reed Arundo donax*. Philosophical Transactions of the Royal Society of London B 352: 1-10.
9. Spatz, H.-C., Köhler, L. and T. Speck (1998): *Biomechanics and functional anatomy of hollow-stemmed sphenopsids. 1. Equisetum giganteum (Equisetaceae)*. American Journal of Botany 85: 305-314.
10. Speck, T., Speck, O., Emanns, A. and H.-C. Spatz (1998): *Biomechanics and functional anatomy of hollow stemmed sphenopsids: 3. Equisetum hyemale*. Botanica Acta 111: 366-376.
11. Speck, O. and H.-C. Spatz (2003): *Mechanical properties of the rhizome of Arundo donax L.* Plant Biology 5: 661-669.
12. Speck, O. and H.-C. Spatz (2004): *Damped oscillations of the giant reed Arundo donax*. American Journal of Botany 91: 789 - 796.
13. Masselter et al. (in prep.): *Biomechanics and functional morphology in stem-branch connections of Dracaena reflexa and Freycinetia insignis*
14. Beismann, H., Wilhelmi, H., Baillères, H., Spatz, H.-C., Bogenrieder, A. and T. Speck (2000): *Brittleness of twig bases in the genus Salix: fracture mechanics and ecological relevance*. Journal of Experimental Botany 51: 617-633.
15. Masselter, T., Milwich, M., Monnerat H., Scharf, U., Hartel, M. and T. Speck (2008): *Bio-inspired solutions for technical problems: biomimetic cable entries and shock-absorbing pallets* in Design and Nature IV, ed.: Brebbia, C.A., WIT Press: Southampton, Boston. p. 51-58.
16. Drechsler, K. (2001): *Composites im Flugzeug- und Automobilbau*, in Conference proceedings of Denkendorfer Kolloquien, Technische Textilien, Denkendorf.
17. Hufenbach, W., Blazejewski, W., Kroll, L., Böhm, R., Gude, M. and A. Czulak (2005): *Manufacture and multi-axial test of composite tube specimen with braided glass fibre reinforcement*. Journal of Material Processing Technology 162/163: 65-70.
18. Cherif, C., Diestel, O. and T. Gries (2007): *Textile Halbzeuge und Halbzeugfertigung*, in Textile Verbundbauweisen und Fertigungstechnologien für Leichtbaustrukturen des Fahrzeug- und Maschinenbaus, ed.: Hufenbach, W., Progress-media Verlag, Dresden.

Fast self-repair mechanisms in plants: biological latices as role models for the development of biomimetic self-healing, mechanically loaded polymers

Georg Bauer¹, Anke Nellesen², Andreas Sengespeick² and Thomas Speck¹

¹ *Plant Biomechanics Group Freiburg, Botanic Garden, University of Freiburg, Germany,*

² *Fraunhofer Institute UMSICHT, Oberhausen, Germany*

Abstract

In nature many self-healing processes can be found, e.g. involving the coagulation of latices. The transfer of these mechanisms into technical applications may yield biomimetic polymeric components with intrinsic and autonomous self-healing capacities. Chemical, physical and mechanical analyses of the latices of *Hevea brasiliensis* and *Ficus benjamina* were conducted to characterize the changes taking place during coagulation. In the case of *H. brasiliensis* latex, particle size analyses, particle surface charge measurements and IR-spectroscopic measurements support the theory that coagulation is initiated by the protein hevein which links rubber particles to larger polymer units. Thus larger particles can be found in the latex as soon as the process of coagulation is initiated. The same analysis was done for the latex of *F. benjamina*. However, in this case the particle size analysis shows no larger particles after coagulation. Tensile tests of the bark of *F. benjamina* revealed the self-healing properties of the coagulation process in planta.

Introduction

Polymers are often used in applications subjected to heavy mechanical loads. In individual cases components may fail spontaneously even below their maximum critical load. This fatigue fracture is caused by micro-cracks which can exist in every component. Under cyclical loading these cracks grow to overcritical lengths, resulting in the failure of the component. Stopping or even healing these micro-cracks might inhibit or at least decelerate crack expansion. Especially intrinsic and autonomous self-healing strategies as found in nature might serve as concept generators for biomimetic self-healing elastomers. Within the past decade research yielded several technical materials with self-healing effects which are at least partly inspired from biological self-healing mechanisms [1,2]. These effects can be achieved by compartmentalised systems, where micro capsules [3] or hollow fibres/ micro tubes [4,5] filled with a healing agent are embedded into a polymer matrix. By damage-induced breaking of these micro capsules or hollow fibres/micro tubes, the healing agent enters the lesion and heals the damage. However, no such self-healing system was realised for (elastic) polymers used in the project presented here, yet. Apart from the compartmentalised systems, vascular self-healing systems were investigated [6,7]. As the production process of these systems is relatively complex, a network that could be worked into a self-healing system more easily would be advantageous. Another biomimetic approach uses turgescient cellular plant structures that seal and repair fissures caused by internal growth processes or external lesions. These plant systems have been used successfully as concept generator for the development of self-repairing foams for pneumatic technical structures [8,9].

Several plant species like *Hevea brasiliensis* seal fissures by coagulation of latices, which occur as healing agents in branched micro-pipe systems. These micro-pipe systems are mainly found in the bark and are under a pressure of up to 8 bar. As described by [10], *H. brasiliensis* seals lesions after injury by cross-linking rubber particles with the protein hevein (*Fig 1*).

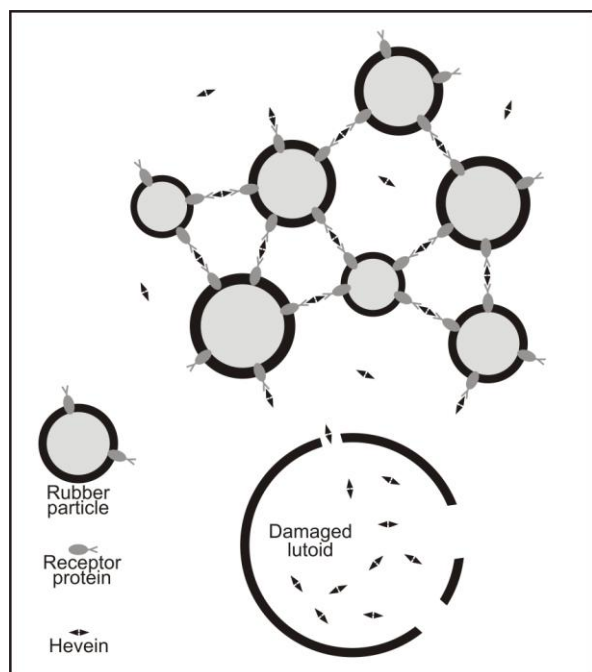


Fig. 1 Coagulation of *H. brasiliensis* latex. The protein hevein is stored in vacuolar structures called lutoids. Rubber particles and lutoids are present in the latex. After injury the lutoids burst due to the pressure drop caused by the pressure difference between latex-bearing micro-pipes and air pressure. Thus they release the hevein, which cross-links the rubber particles via receptor proteins enveloping the rubber particles (modified from [1]).

Ficus benjamina, known as the Weeping Fig or Benjamin's Fig, is another latex bearing plant. The latices of *H. brasiliensis* and *F. benjamina* were compared by quantitatively analysing structural and functional parameters, as particle size distribution, zeta potential, IR-spectra and rheology. Furthermore biomechanical analyses were conducted.

Material and methods

Latex of *H. brasiliensis* was acquired by purchase (JaLaTEX, a liquid ammonia latex) and the latex of *F. benjamina* was extracted by tapping fresh plant material. Biomechanical analyses were conducted using freshly prepared bark samples of about 1.5 years old *F. benjamina* plants.

The particle size distribution of both latices was measured by a Malvern Mastersizer 2000 by laser diffraction where particles in the sample passing a laser beam scatter light at an angle that is directly related to their size. Particles are assumed as spherical and the diameter is read out. Particle sizes of both fresh latex samples and latex samples spread out on an object slide for 20 min in the case of JaLaTEX and 32 min in the case of *F. benjamina* latex were analysed.

The zeta potential of the particles in both latex dispersions was measured by a Malvern Zetasizer Nano-ZS. In this method the zeta potential, the surface charge of a particle, is measured by applying an electrical field across the dispersion. The electrical field influences the mobility of particles, which can be converted to the zeta potential. Fresh latex samples were used and analysed in both an alkaline (ammonia solution) and a neutral (H_2O) milieu.

Analyses of changes in chemical bonds during coagulation were conducted by TG-IR (thermogravimetry with infrared interconnection; Brukeroptics Vertex 70) with attenuated total reflection (ATR). Analyses were started immediately after spreading out the fresh latex samples on the measuring instrument. During the infrared spectroscopy a measuring beam penetrates the latex sample. Due to interactions with the covalent bonds presented by the sample's molecules the beam is attenuated and reflected. Measuring these effects permits conclusions on the chemical composition of the sample within the depth of penetration of the measuring beam. The limited measuring depth made it necessary to measure both the upper side and the bottom side of coagulated latex samples as changes in the IR-spectra during coagulation might also result from sedimentation of substances within the depth of penetration of the measuring beam.

Rheological analyses of JaLaTEX were conducted in a rotary viscosimeter (Bohlin Rheometer Gemini). The torque required to rotate a disk in a fluid, which is a function of the viscosity of that fluid, is measured. A 'cone and plate' system was used with a cone of an angle of 1° and a diameter of 20 mm.

Biomechanical analyses involved tensile tests of both uninjured and injured bark of *F. benjamina*, using an Inspekt retrofit, Hegewald & Peschke. The last-mentioned tests were conducted by injuring plants and preparing bark samples right after injuring and after a latency time of 35 min. Only tests were evaluated where samples were not ripped apart at the experimental setup clamps.

Results and discussion

Both fresh JaLaTeX and the fresh latex of *F. benjamina* show a bimodal particle size distribution (Fig 2). Particle sizes in JaLaTeX peak at 0.25 μm and 1 μm whereas particles in *F. benjamina* latex peak at 0.8 μm and 3.3 μm and thus are larger than those in JaLaTeX. The JaLaTeX particle size distribution changes when tested 20 min after spreading out on an object slide, where the curve of particle size is spread towards larger sizes and a third peak of even larger particles (about 7 μm) becomes apparent. These results support the above mentioned theory of coagulation of *H. brasiliensis* latex as in JaLaTeX larger particles than those observed in fresh JaLaTeX form after coagulation. Since ultrasonics, which separates agglomerates, was applied right before measuring, these larger particles must have developed by formation of chemical bonds. However this increase in particle size is not observed for the latex of *F. benjamina*, where even after 32 min no further peaks appeared and the shape of the particle size curve remained nearly unaltered.

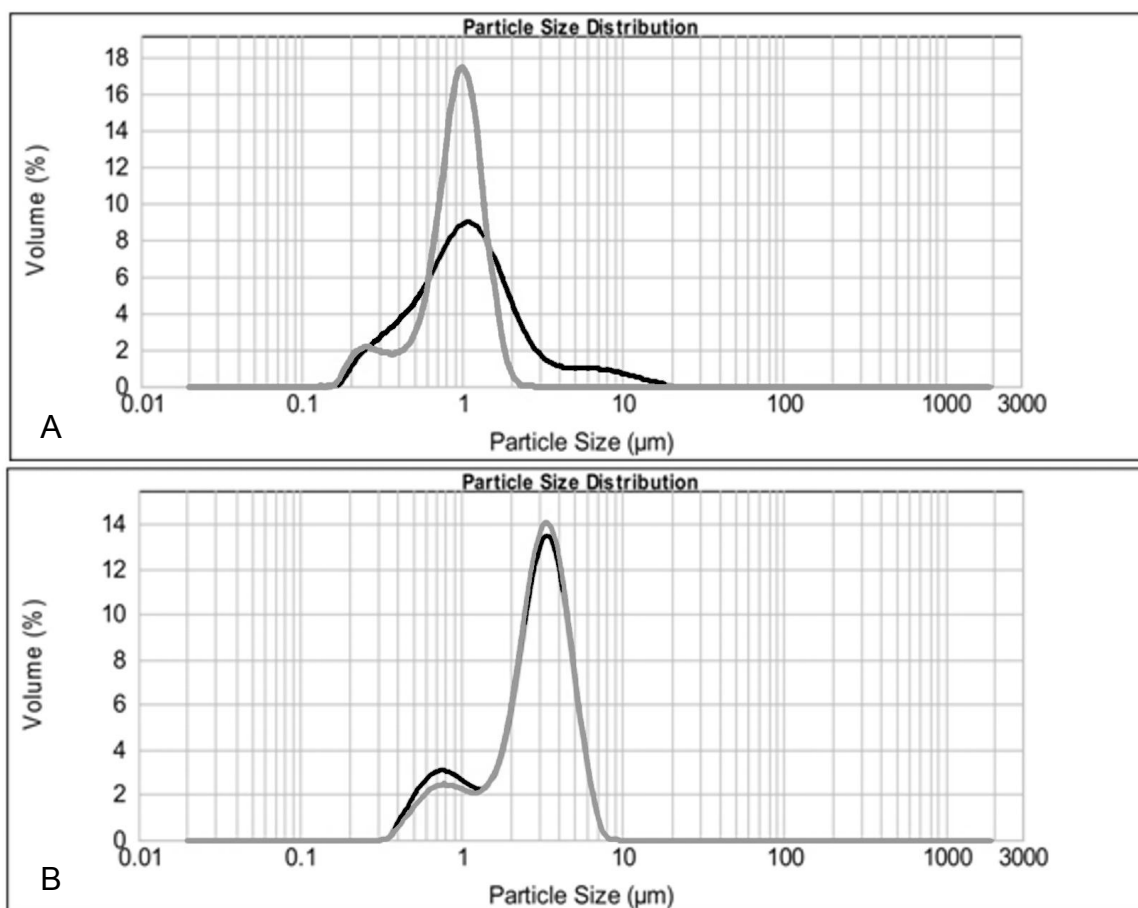


Fig. 2 Particle size distributions of JaLaTeX (A) and *F. benjamina* latex (B) in fresh latex (grey) and several minutes after spreading out the latex on an object slide (black: 20 min for JaLaTeX and 32 min for *F. benjamina* respectively).

The surface of particles in *F. benjamina* latex is negatively charged in an alkaline milieu and thus particles are stabilised under these conditions. In a neutral milieu the surface is only faintly negatively charged, which supports the aggregation of latex particles. A negatively charged particle surface was also found in JaLaTeX due to the storage in a stabilising ammonia solution.

IR-spectroscopic measurements of both latices revealed greatest changes in the spectra about 6 to 10 min after initiating the coagulation process (Fig 3). Observations of the latex during coagulation showed that in this period of time the transparency of the latex changes as well. When comparing the spectra before and after this period it becomes apparent that besides the decrease of water (absorption between ca. 3000 cm^{-1} and 3700 cm^{-1}) caused by evaporation, both amide bonds (absorption at e.g. 1540 cm^{-1}) and CH_3 - and CH_2 -bonds (absorption at e.g. 2870 cm^{-1}) increase within the measuring depth. Comparisons of the upper side and the bottom side of coagulated latex showed that the increase in the above mentioned bonds does not arise from sedimentation of proteins but rather indicates the formation of new protein bonds. It is still to be clarified what the increase of CH_3 - and CH_2 -bonds can be ascribed to.

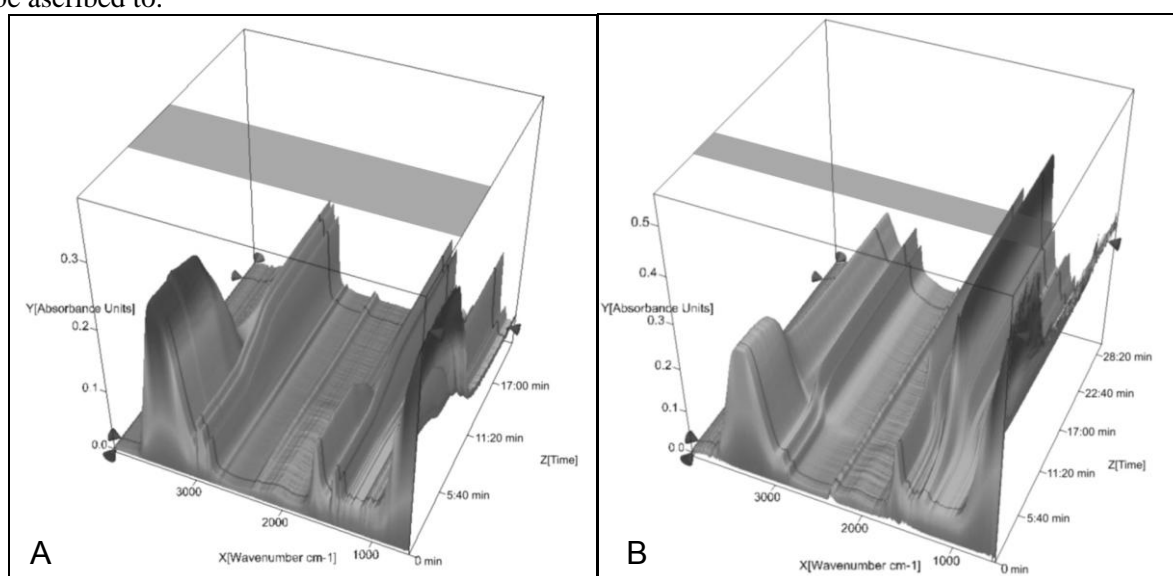


Fig. 3 IR-spectroscopic picture of the coagulation process of JaLaTeX(A) and *F. benjamina* latex (B). Greatest changes in the spectra occur after 6 to 10 min (shaded grey)

Rheological analyses of JaLaTeX revealed an abrupt increase in viscosity (Fig 4). The time of this increase is related to the shear stress applied. In the case of a shear stress of 120 Pa only a slight increase up to $3 \cdot 10^{-7}\text{ MPa}\cdot\text{s}$ can be observed until about 200 s. After that the viscosity increases steeply up to $0.6\text{ MPa}\cdot\text{s}$ after 230 s. This result indicates that an abrupt change in viscosity may also appear after several minutes under natural conditions, but this remains to be tested.

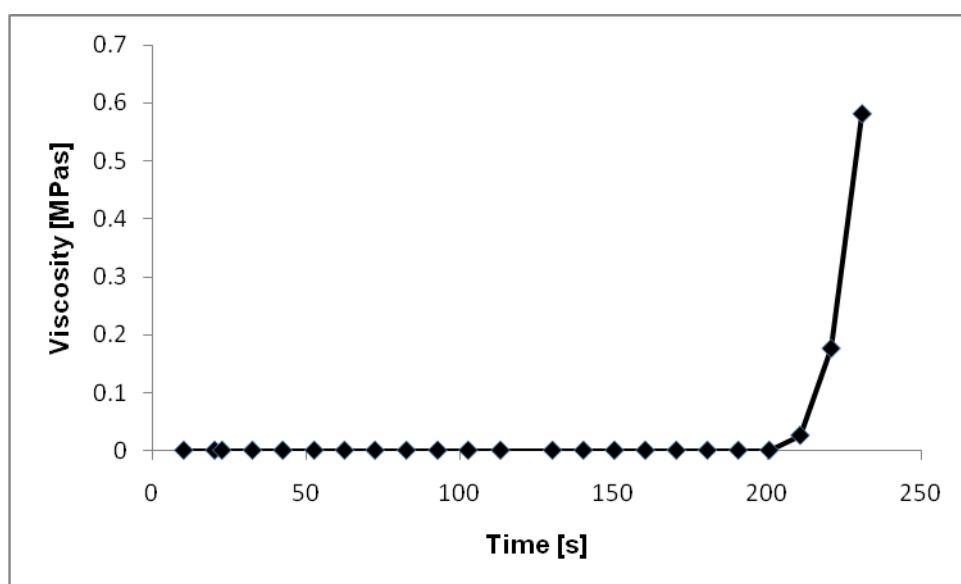


Fig. 4 Viscosity of JaLaTeX. Applied shear stress was 120 Pa.

The curve shapes of the tensile strength tests (*Fig 5*) elucidate two phases of sample behaviour before failure of the specimen. After a linear-elastic phase where the sample elongates by an elongation of cells, a linear-plastic phase succeeds where an elongation is reached probably by sliding of fibres, characterized by a smaller slope of the curve. After reaching the tensile strength the samples failed in all tensile strengths tests by rupture of the whole specimen. The tensile strength of the bark varies with the heal-up time after injuring. The tensile strength of bark immediately after injuring is smaller than that of uninjured bark. 35 min after injuring the tensile strength is partly restored, however, does not reach the values of uninjured bark. Thus a self-healing mechanism can be attributed to the coagulation of latex in *F. benjamina* bark as other self-healing mechanisms start later than 35 min after injuring.

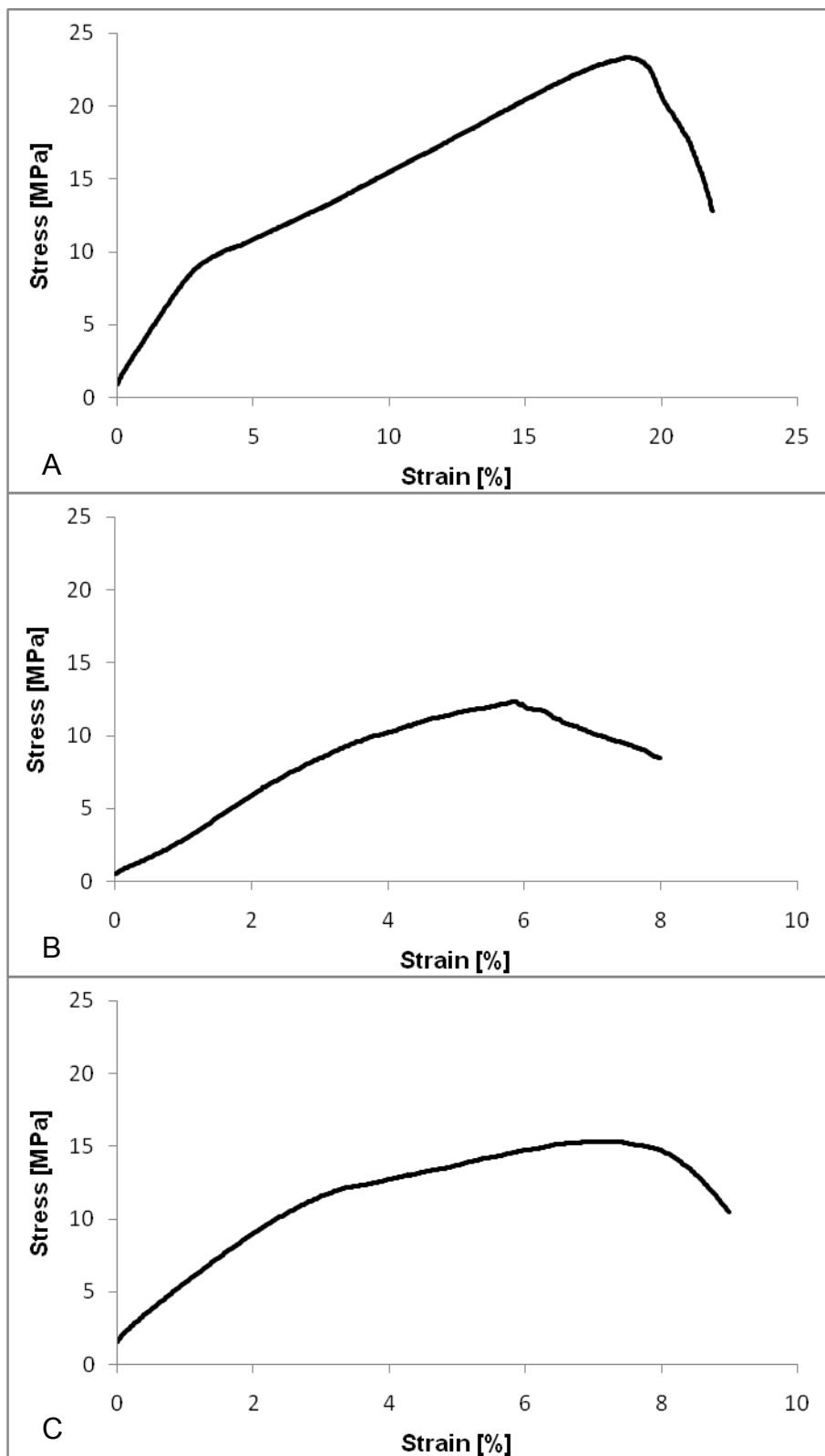


Fig. 2 Tensile tests of the bark of *F. benjamina*. (A) Stress-strain curve of uninjured bark. (B) Stress-strain curve of bark immediately after injuring. (C) Stress-strain curve of bark 35 minutes after injuring.

Conclusion

Particle size analyses, particle surface charge measurements and IR-spectroscopic measurements support the coagulation theory described in literature for the latex of *Hevea brasiliensis*. A similar process is also supported by our measurements for the latex of *Ficus benjamina*. However, in the latex of this species no increase in particle size could be observed during coagulation. These findings, in combination with the results of biomechanic analyses of the bark of *F. benjamina*, corroborate the existence of a fast self-healing process by coagulation of latex.

Acknowledgements

We thank the staff of the Fraunhofer Institute UMSICHT involved in assistance with the chemical and physical analyses of the latices. We gratefully acknowledge the funding of the BMBF within the scope of the programme BIONA.

References

1. Yuan Y.C., Yin T., Rong M.Z., Zhang M.Q. (2008): *Self healing in polymers and polymer composites. Concepts, realization and outlook: A review*. eXPRESS Polymer Letters 2: 238-250
2. Trask R.S., Williams H.R., Bond I.P. (2007): *Self-healing polymer composites: mimicking nature to enhance performance*. Bioinsp. Biomim. 2: 1–9
3. White S.R., Sottos N.R., Geubelle P.H., Moore J.S., Kessler M.R., Sriram S.R., Brown E.N., Viswanathan S. (2001): *Autonomic healing of polymer composites*. Nature, 409: 794-797
4. Pang J.W.C., Bond I.P. (2005): *'Bleeding composites'-damage detection and self-repair using a biomimetic approach*. Composites A, 36: 183-188
5. Dry C. (1996): *Procedures developed for self-repair of polymer matrix composite materials*. Composite Structures, 35: 263-269
6. Kim S., Lorente S., Bejan A. (2006): *Vascularized materials: Tree-shaped flow architectures matched canopy to canopy*. J. Appl. Phys., 100: 063525
7. Toohey K.S., Hansen C.J., Lewis J.A., White S.R., Sottos N.R. (2009): *Delivery of Two-Part Self-Healing Chemistry via Microvascular Networks*. Adv. Funct. Mater., 19: 1399-1405
8. Speck, T., Luchsinger, R., Busch, S., Rüggeberg, M. & Speck, O. (2006): *Self-healing processes in nature and engineering: self-repairing biomimetic membranes for pneumatic structures*. In: Brebbia, C.A. (ed.), Design and Nature III, 105 – 114. WIT Press, Southampton
9. Speck, O., Luchsinger, R., Busch, S., Rüggeberg, M. & Speck, T. (2006): *Self-repairing membranes for pneumatic structures: transferring nature's solutions into technical applications*. In: L. Salmen (ed.), Proceedings of the 5th International Plant Biomechanics Conference Vol. I, Stockholm, STFI Packforsk AB, Stockholm, 115 – 120
10. d'Auzac J., Prevot J.-C., Jacob J.-L. (1995): *What's new about lutoids? A vacuolar system model from Hevea latex*. Plant physiology and biochemistry. 33: 765-777

Exploring the innovation potential of biomimetics for novel 3D micro- and nanoelectromechanical systems (MEMS and NEMS)

Gebeshuber I.C. ^{1,2,3}, Stachelberger H. ² and Majlis B.Y. ¹

¹ Universiti Kebangsaan Malaysia, Malaysia; ² University of Technology Vienna, Austria;
³ Austrian Center of Competence for Tribology, Austria

Abstract

Science currently goes through a major change, with biology gaining increasing importance. A new Leitwissenschaft that can be called “Biological Physics“ is evolving. Biomimetics, i.e., technology transfer from biology to engineering, is especially promising in MEMS development because of the material constraints in both fields. Biomimetic concepts such as integration instead of additive construction, optimization of the whole instead of maximization of a single component feature, multi-functionality instead of mono-functionality and development via trial-and-error processes can also be applied by engineers not at all involved in biology.

A novel way to describe the complexity of biological and engineering approaches depending on the number of different base materials is proposed: Either many materials are used (*material* dominates) or few materials (*form* dominates) or just one material (*structure* dominates). The complexity of the approach (in biology as well as in engineering) increases with decreasing number of base materials. Biomimetics is a field that has the potential to drive major technical advances and that continuously contributes to “Biological Physics”.

The Biomimicry Innovation Method is applied to identify high-potential biological systems, processes and materials that can inspire emerging MEMS technologies as well as optimizing existing ones. Best practices identified comprise algae, horses, Malaysian tropical rainforest understory plants, iridescent fruits, peacock feathers, bird skin, green algae, humans (immune system), adhesive pads in the gecko and in herbivorous insects as well as the mechanical defense strategies of their food.

Introduction

In biomimetics, materials, processes and systems in Nature are analyzed, the underlying principles are extracted and subsequently applied to science and technology [1][2][3]. Biomimetics is a growing field that has the potential to drive major technical advances [4]. It might substantially support successful mastering of current challenges in the development of novel 3D micro- and nanoelectromechanical systems (MEMS and NEMS), e.g., concerning friction, adhesion and wear in such systems (tribological aspects) [5]. The biomimetic approach can result in innovative new technological constructions, processes and developments [3]. Biomimetics can aid MEMS developers to manage the specific requirements in systems or product design, which are even more relevant than for conventional products, especially to create products and processes that are sustainable and perform well (e.g. to overcome stiction), to integrate new functions, to reduce production costs, to save energy, to cut material costs, to redefine and eliminate “waste”, to heighten existing product categories, to define new product categories and industries, to drive revenue and to build unique brands [6][7][8][9].

Recurrent principles in biological materials and systems are hierarchy [10][11] and multi-functionality. Vincent and co-workers analyzed 500 biological phenomena, covering over 270 functions, at different levels of hierarchy [10]. Depending on the extent to which each level of the hierarchy is dependent on its lower levels, adaptation or optimization of the biomaterial is

independently possible at each level of hierarchy. Size differences between hierarchy levels tend to be about a factor of ten [11]. A major advantage of hierarchical structuring is that the material can be made multifunctional and that a specific material property, such as fracture toughness, can be improved by optimization at different size levels. A direct consequence is the increase in adaptability of natural materials. Functions can be modified or enriched by structuring on an additional level of hierarchy. Adaptability increases, therefore, as a function of the number of levels of hierarchy. This is probably why such a wide range of material and structural properties (see Figure 1 for biological SiO₂ structures in glass-making microorganisms, [7]) can be provided in Nature by such a small range of base materials [12][13].

Biological materials show excellent characteristics that are difficult to grasp in terms of commonly used material properties such as resilience (a component of ecosystem stability: the ability of an ecosystem to recover after disturbance) [14][15][16], self-repair [17], adaptability [16], benevolent behavior [18] and redirected crack propagation [19][20].

Structure and function as well as structure and material are closely related in natural systems. Gordon [21] states “Structures are made from materials and we shall talk about structures and materials; but in fact there is no clear-cut dividing line between a material and a structure.” Historically interested readers might also want to read Haeckel’s book “Art forms in nature” [22] and D’Arcy Thompson’s book “On Growth and Form” [23], especially chapters V on biomineralized structures and VIII on form and mechanical efficiency. Investigations on the cause of the excellent properties of natural materials lead to investigations of intrinsic material properties.

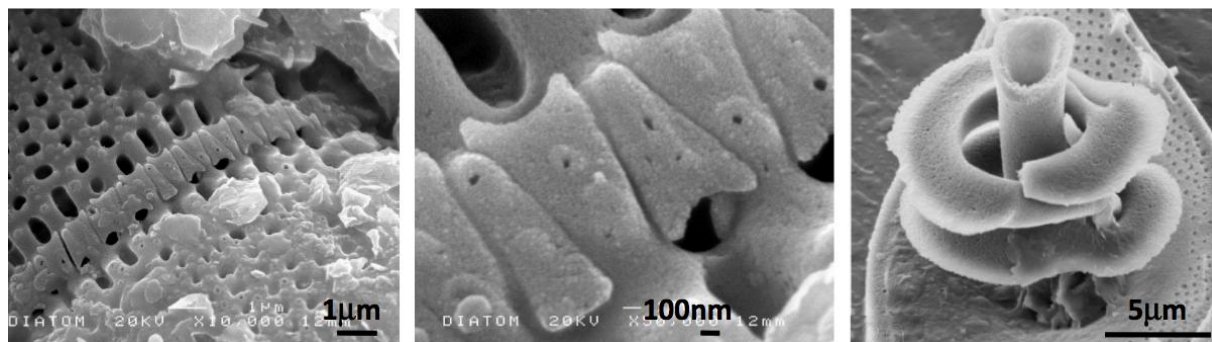


Fig. 1 Structure dominated micromechanical components (SiO₂ shells of algae). Left: Zipper-like structure in *Aulacoseira*. Middle: Zoom into the same image. © Duncan Waddell, XTAL Enterprises, Australia. Right: Spring-like structure in *Rutilaria grevilleana*. © R.M. Crawford, AWI Bremerhaven, Germany. Images used with permission. From [7].

Science currently goes through a large change: in biology more and more causation and natural laws are being uncovered [24]. Biology has changed from being very descriptive to a science that can be acknowledged and understood (in terms of concepts) by researchers coming from “hard sciences” such as chemistry, physics, engineering. The “hard sciences” rely on experimental, empirical, quantifiable data or the scientific method, and focus on accuracy and objectivity [25]. The amount of causal laws in this new biology (indicated by the ratio of causal versus descriptive knowledge, Figure 2) is steadily growing and a new field that can be called “Biological Physics” is emerging [24]. The languages of the various fields of science increasingly get compatible, and the amount of collaborations and joint research projects between researchers coming from the “hard sciences” and biologists have increased tremendously over the last years.

Recurrent concepts in biomimetics are integration instead of additive construction, optimization of the whole instead of maximization of a single component feature, multi-functionality instead of mono-functionality and development via trial-and-error processes. Such concepts can easily be transferred to technology, and can be applied by engineers with no knowledge of biology at all [3][9][24].

The complexity of biological and engineering approaches depend on the number of different base materials used (Figure 3): Either many materials are used (*material* dominates) or few materials (*form* dominates) or just one material (*structure* dominates) [7].

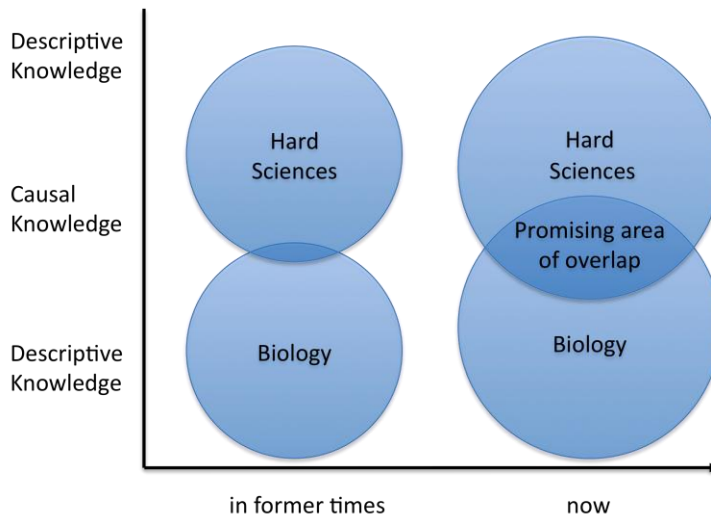


Fig. 2 The increasing amount of causal laws in biology generates promising areas of overlap with hard sciences such as physics, chemistry and engineering.

The importance of structures and the complexity of the approach (in biology as well as in engineering) increase inversely with the number of different materials that are or can be used. This can be seen in technology from the meter to the nanometer length scale. The Eiffel tower, e.g., which is mainly made from steel, has many levels of structural hierarchy with important structures on every length scale [7].

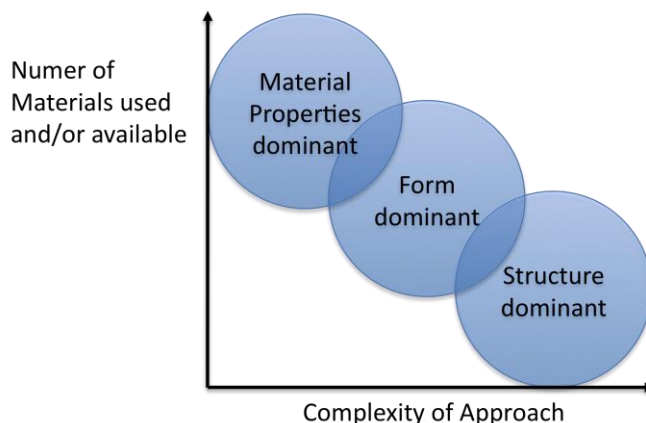


Fig. 3 The complexity of biological and engineering approaches depends on the number of different base materials used and/or available.

Material and methods

In MEMS and NEMS technology – comparable to biology - a limited number of base materials such as Si, SiO₂, Silicon nitride, GaAs, Silicon carbide, diamond, InP, SiGe, ferroelectric materials and polymers is used, providing a wide range of functional and structural properties. Therefore, biomimetics seems to prove especially promising for MEMS development [7].

Nachtigall promoted analogy search and states that the nature of qualitative analogy research is impartial, open-minded comparison. He presents numerous examples of insect micromorphology and relates functional mechanisms to technological examples in a visual comparison [26].

Here, the Biomimicry Innovation Method (BIM) [27] is applied to identify high-potential biological systems, processes and materials that can inspire emerging MEMS technologies as well as optimizing existing ones. BIM is an innovation method that seeks sustainable solutions by emulating Nature's time-tested patterns and strategies. The goal is to create products, processes, and policies - new ways of living - that are well adapted to life on earth over the long haul. BIM involves specifically trained biologists as well as engineers, natural scientists, architects and/or designers from universities or companies. BIM is for example used in the rainforest (high species variety resulting in high innovation potential) to learn from and emulate natural models.

Table 1 Application of the Biomimicry Innovation Method regarding structure dominated components

Function	Biologized question: How does nature ...	Nature's best practice	Generated process/ product ideas
Hinges and interlocking devices	... mechanically connect hard single cells?	Diatoms in chains [28][29][30][31][32][33]	micromechanical optimization of 3D-MEMS structure
Click-stop mechanism	... unfold structures and then fix them?	<i>Corethron pennatum</i> , <i>C. criophilum</i> [29][34][35]	obtain 3D structures from 2D structures
Springs	... reversibly store mechanical energy?	<i>Rutilaria grevilleana</i> , <i>R. philipinnarum</i> [36]	Energy storage in MEMS
Parts connected in a chain with adjustable length	... provide stability to chains in turbulent environments?	<i>Ellerbeckia arenaria</i> [32]	MEMS with moveable parts
Movable rigid parts	... optimize moveable parts?	<i>Melosira sp.</i> , <i>Ellerbeckia arenaria</i> [32]	3D MEMS with moveable parts
Pumps	... move fluids?	<i>Rutilaria grevilleana</i> , <i>Rutilaria philipinnarum</i> [36]	micropumps for lab-on-a-chip
Unfoldable structures	... make 3D structures from rigid parts?	<i>Corethron pennatum</i> , <i>C. criophilum</i> [29][34][35]	obtain 3D structures from 2D structures
Energy dissipation	... dissipate mechanical energy?	<i>Solium exsculptum</i> [5][37]	3D-MEMS
Fracture control, Crack redirection	... mechanically protect viable parts?	<i>Equus ferus caballus</i> [19][20]	quality assurance of MEMS
Lubrication	... prevent wear?	Unknown diatom species [33]	preventing stiction
Stability (reinforcement)	... mechanically protect viable parts?	<i>Solium exsculptum</i> [5][37]	quality assurance of MEMS
Surface texturing	... structure surfaces?	diatoms [28], especially <i>Solium exsculptum</i> [5][37]	MEMS
Photoprotective coating	... protect photo-sensitive plants?	<i>Begonia pavonina</i> , <i>Diplazium tomentosum</i> , <i>Phyllagathis rotundifolia</i> [38], <i>Selaginella willdenowii</i> , <i>S. uncinata</i> [39]	MEMS
Photonic components	... make colours without pigments?	diatoms [28], feathers [40], butterflies and moths [41][42], iridescent plants [38][39][43][44][45] [46][47][48][49], bird and mammal skin [50][51] [52], iridescent marine algae [53][54], blue spruce [55]	photonic micro- and nanodevices, MEMS
Pressure resistant containers	... deal with high pressures?	<i>Euglena gracilis pellicle</i> [56]	lab-on-a-chip
Fixation	... mechanically fix structures?	<i>Corethron pennatum</i> , <i>C. criophilum</i> [29][34][35]	3D-MEMS, lab-on-a-chip
Selective, switchable adhesion	... reversibly and switchable adhere to structures?	<i>Homo sapiens sapiens</i> immune system [5][31][57][58][59]	reusable lab-on-a-chip devices [60]
Dry adhesives	... reversibly attach to surfaces?	gecko foot [61][62], insect attachment pads [63][64], plant wax surfaces [65][66]	connect MEMS parts, nanoadhesives [67][68]
Self-healing adhesives	... prevents breaking of adhesive bonds?	self-healing diatom adhesives [69][70][71]	self-healing MEMS parts connections, nanoadhesives [72]

The steps in BIM are as follows: Identify function, biologize the question, find Nature's best practices and generate product ideas.

Identify function: The biologists distil challenges posed by engineers/natural scientists/architects and/or designers to their functional essence.

Biologize the question: In the next step, these functions are translated into biological questions such as “How does Nature mechanically connect hard single cells?” or “How does Nature generate 3D structures from rigid parts?” The basic question is “What would Nature do here?” The experience of one of the authors (ICG) on the boundary between biology and engineering, literature search, talks with experts from biology and the AskNature.org database provided by the Biomimicry Institute are utilized in course of the BIM to exploit the large biodiversity in rainforests and in the water bodies of the world and to find biological inspiration for functions relevant for MEMS such as click-stop mechanisms, micropumps, energy dissipation and lubrication (Table 1).

Find Nature's best practices: Screens of the relevant literature in scientific databases as well as entering a highly inspiring environment with the biologized questions in mind (task-oriented visit) are used to obtain a compendium of how plants, animals and ecosystems solve the specific challenge. The inspiring environments should preferably be habitats with high species diversity, e.g., the rain forest or a coral reef. Thereby a compendium of how plants, animals and ecosystems solve the specific challenge is obtained.

Generate process/product ideas: From these best practices (90% of which are usually new to clients) ideas for cost-effective, innovative, life-friendly and sustainable products and processes are generated.

Results and discussion

The best practices identified are biological micro- and nanostructures in organisms as diverse as algae, horses, Malaysian tropical rainforest understory plants, peacocks, birds, green algae, humans (immune system), adhesive pads in the gecko and in herbivorous insects as well as the mechanical defense strategies (wax crystals) of their food. The summary of the results is given in Table 1.

The organisms that occur most often in the table are diatoms. Diatoms are unicellular microalgae with a cell wall consisting of a siliceous skeleton enveloped by a thin organic case [28]. The cell walls of each diatom form a pillbox-like shell consisting of two parts that fit within each other. These microorganisms vary greatly in shape, ranging from box-shaped to cylindrical; they can be symmetrical as well as asymmetrical and exhibit an amazing diversity of nanostructured frameworks. These biogenic hydrated silica structures have elaborate shapes, interlocking devices, and, in some cases, hinged structures.

The silica shells of the diatoms experience various forces from the environment and also from the cell itself when it grows and divides, and the form of these micromechanical parts has been evolutionarily optimized during the last 150 million years or more (Figure 1). The diatom species *Rutilaria grevilleana* and *Rutilaria philipinnarum* have structures that might be interpreted as springs [7][36]. However, more detailed investigation is needed to confirm this. *Ellerbeckia arenaria* [73] is a diatom that lives in waterfalls. *E. arenaria* cells form string like colonies, which can be several millimeters long and can reversibly be elongated by one third of their original length [32][37][7]. The diatoms *Melosira sp.* [32], *Solium exsculptum* [5][4] and *Ellerbeckia arenaria* are interesting best practices for optimization of moveable parts in Nature. The diatom species *Solium exsculptum* lived 45 million years ago. Scanning Electron Microscopy images of this Eocene fossil from a deposit at Mors, Denmark reveal that the connections between sibling cells are still in good condition [5].

Rutilaria philipinnarum is a fossil colonial diatom thought to have lived in inshore marine waters (Crawford, personal communication 2008). In this species, the single diatoms connect by linking spines and by a complex siliceous structure termed the periplekton. These linking structures on the one hand keep the cells together, but on the other hand also keep distance between the cells. The shape of the spines allows expansion of the chain to a certain maximum distance and compression to a minimum distance, in which case there is still some fluid between the cells. The links allow movement of single cells in the chain against or from each other in a rather one-dimensional way [29].

Structural photonic components in biology exhibit a huge variety [28][40]-[42][38][39][43]-[55].

Conclusion

Application of the Biomimicry Innovation Method concerning 3D micro- and nanomechanical systems might prove highly useful concerning MEMS development. The inspiring organisms, structures and function already identified lay a sound foundation to proceed to the next step: MEMS developers interested in including the bioinspired approaches presented in this work have already been approached and bioinspired 3D MEMS will be designed and modeled and prototypes will be constructed. Further analysis of the rich flora in South East Asia might provide further useful input concerning novel approaches regarding MEMS. Increasing awareness about the innovation potential of the rainforest might cause a paradigm shift in the way locals view the pristine forests.

Acknowledgements

The authors thank P. Gruber for carefully reading the manuscript and valuable input, and R.M. Crawford and D. Waddell for images and discussion. Part of this work has been funded by the Austrian *Kplus*-Program via the Austrian Center of Competence for Tribology, AC²T research GmbH, Wiener Neustadt. The Austrian Society for the Advancement of Plant Sciences has funded part of this work via the BioScreen Pilot Project.

This book chapter is an extended and updated version of a 4-page article [7].

References

1. Bhushan, B. (2009): *Biomimetics: lessons from nature-an overview*. Philosophical Transactions of the Royal Society A. 367: 1445-1486.
2. Bar-Cohen, Y. (2005): *Biomimetics: biologically inspired technologies*, CRC Press.
3. Gebeshuber, I.C. and M. Drack, (2008): *An attempt to reveal synergies between biology and engineering mechanics*. Journal of Mechanical Engineering Science. 222, 1281-1287.
4. Gebeshuber I.C., Majlis B.Y. and Stachelberger H. (2009): *Tribology in Biology: Biomimetic studies across dimensions and across fields*. International Journal of Mechanical and Material Engineering, submitted
5. Gebeshuber, I.C., (2007): *Biotribology inspires new technologies*. Nano Today. 2(5): 30-37.
6. Gebeshuber, I.C., A. Pauschitz and F. Franek. (2006): *Biotribological model systems for emerging nano-scale technologies*, in: Proc. 2006 IEEE Conference on Emerging Technologies - Nanoelectronics, Editors, p. 396-400.
7. Gebeshuber, I.C., Stachelberger H., Ganji B.A., Fu D.C., Yunas J. and Majlis B.Y. (2009): *Exploring the innovational potential of biomimetics for novel 3D MEMS*. Advanced Materials Research. 74, 265-268.
8. Gebeshuber, I.C., H. Stachelberger and M. Drack. (2005): *Diatom tribology*, in: Life Cycle Tribology, Editors, Tribology and Interface Engineering Series, 48, Series Editor B.J. Briscoe, Elsevier, p. 365-370.
9. Gebeshuber, I.C., B.Y. Majlis, L. Neutsch, F. Aumayr and F. Gabor. (2009): *Nanomedicine and biomimetics: life sciences meet engineering & physics*, Proceedings of the 3rd Vienna International Conference on Micro- and Nanotechnology Viennano09, Editors, p. 17-23.
10. Fratzl, P. and R. Weinkamer, (2007): *Nature's hierarchical materials*. Progress in Materials Science. 52 (8), 1263-1334.
11. Vincent, J.F.V., (2005): *Deconstructing the design of a biological material*. Journal of Theoretical Biology. 236, 73-78.
12. Jeronimidis, G. and A.G. Atkins, (1995): *Mechanics of biological materials and structures—Nature's lessons for the engineer*. Proceedings of the Institution of Mechanical Engineers Part C: Journal of Mechanical Engineering Science. 209, 221-235.
13. Vincent, J.F.V., (2009): *Biomimetics – A review*. Proceedings of the Institution of Mechanical Engineers Part H: Journal of Engineering in Medicine, submitted
14. Holling, C.S., (1973): *Resilience and stability of ecological systems*. Annual Review of Ecological Systems. 4, 1-23.
15. *Resilience and the behavior of large-scale systems* (2002). Scope Report 60, Editors, Island Press.
16. Walker, B., C.S. Holling, S.R. Carpenter and A. Kinzig (2004): *Resilience, adaptability and transformability in social-ecological systems*. Ecology and Society. 9(2), 5.

17. *Proceedings of the first workshop on self-healing systems* (2002). Charleston, South Carolina.
18. Trivers, R.L. (1971): *The evolution of reciprocal altruism*. The Quarterly Review of Biology. 46(1), 35-57.
19. Kasapi, M.A. and J.M. Gosline, (1997): *Design complexity and fracture control in the equine hoof wall*. Journal of Experimental Biology. 200, 1639-1659.
20. Kasapi, M.A. and J.M. Gosline, (1999): *Micromechanics of the equine hoof wall: optimizing crack control and material stiffness through modulation of the properties of keratin*. Journal of Experimental Biology. 202, 377-391.
21. Gordon, J.E. (1981): *Structures, or why things don't fall down*, Da Capo Press New York. p. 29.
22. Haeckel E. (1899): *Art forms in nature*. Biobliographisches Institut, Leipzig and Vienna.
23. Thompson D'A. (1917): *On growth and form*. Cambridge University Press, Cambridge, England.
24. Gebeshuber, I.C., P. Gruber and M. Drack, (2009): *A gaze into the crystal ball - biomimetics in the year 2059*. Proceedings of the Institution of Mechanical Engineers Part C: Journal of Mechanical Engineering Science, submitted
25. Lemons, J., (1996): *Scientific uncertainty and its implications for environmental problem solving*, Blackwell Publishing.
26. Nachtigall, W., (2003): *Das große Buch der Bionik*. Deutsche Verlagsanstalt, Germany, p. 214f.
27. *Biomimicry innovation method* (2008). Biomimicry Guild, Helena, MT, USA.
28. Round, F.E., R.M. Crawford and D.G. Mann (1990): *The diatoms: biology and morphology of the genera*. Cambridge University Press, Cambridge, UK.
29. Gebeshuber, I.C. and R.M. Crawford, (2006): *Micromechanics in biogenic hydrated silica: hinges and interlocking devices in diatoms*. Journal of Engineering Tribology. 220(J8), 787-796.
30. Crawford, R.M. and I.C. Gebeshuber, (2006): *Harmony of beauty and expediency*. Science First Hand. 5(10), 30-36.
31. Gebeshuber, I.C., M. Drack and M. Scherge, (2008): *Tribology in biology*. Tribology - Materials, Surfaces & Interfaces. 2(4), 200-212.
32. Gebeshuber, I.C., H. Stachelberger and M. Drack, (2005): *Diatom bionanotribology - Biological surfaces in relative motion: their design, friction, adhesion, lubrication and wear*. Journal of Nanoscience and Nanotechnology. 5 (1), 79-87.
33. Gebeshuber, I.C., J.H. Kindt, J.B. Thompson, Y. Del Amo, H. Stachelberger, M. Brzezinski, G.D. Stucky, D.E. Morse and P.K. Hansma, (2003): *Atomic force microscopy study of living diatoms in ambient conditions*. Journal of Microscopy. 212 (Pt3), 292-299.
34. Crawford, R.M. and F. Hinz, (1995): *The spines of the centric diatom Corethron criophilum: light microscopy of vegetative cell division*. European Journal of Phycology. 30: 95–105.
35. Crawford, R.M., F. Hinz and C. Honeywill, (1998): *Three species of the diatom genus Corethron Castracane: structure, distribution and taxonomy*. Diatom Research. 13: 1–28.
36. Srajer, J., B.Y. Majlis and I.C. Gebeshuber, (2009): *Microfluidic simulation of a colonial diatom chain reveals oscillatory movement*. Acta Botanica Croatia, in press
37. Gebeshuber, I.C., M. Aumayr, O. Hekele, R. Sommer, C.G. Goesselsberger, C. Gruenberger, P. Gruber, E. Borowan, A. Rosic and F. Aumayr. (2009): *Bacilli, green algae, diatoms and red blood cells – how nanobiotechnological research inspires architecture*, in: Bio-Inspired Nanoscience, edited by Yong Zhou, Nova Science Publishers 2009, in press
38. Gould, K.S. and D.W. Lee (1996): *Physical and ultrastructural basis of blue leaf iridescence in four Malaysian understory plants*. American Journal of Botany. 83(1), 45-50.
39. Hebant C. and D.W. Lee, (1984): *Ultrastructural basis and developmental control of blue iridescence in Selaginella leaves*. American Journal of Botany. 71(2), 216-219.
40. Zi J., X. Yu, Y. Li, X. Hu, C. Xu, X. Wang, X. Liu and R. Fu, (2003): *Coloration strategies in peacock feathers*. Proceedings of the National Academy of Sciences USA. 100(22): 12576-12578.
41. Prum, R.O., T. Quinn and R.H. Torres, (2006): *Anatomically diverse butterfly scales all produce structural colours by coherent scattering*. The Journal of Experimental Biology. 209, 748-765
42. Stavenga, D.G., S. Stowe, K. Siebke, J. Zeil and K. Arikawa, (2004): *Butterfly wing colours: scale beads make white pierid wings brighter*. Proceedings of the Royal Society London B. 271, 1577-1584.
43. Lee, D.W. and J.B. Lowry, (1975): *Physical basis and ecological significance of iridescence in blue plants*. Nature. 254, 50-51.
44. Lee, D.W. (2007): *Nature's palette: the science of plant color*. University of Chicago Press, Chicago, USA.
45. Richards, P.W., (1952): *The tropical rainforest*, Cambridge University Press.
46. Fox, D.L. and J.R. Wells (1971): *Schemochromic blue leaf-surfaces of Selaginella*. American Fern Journal. 61, 137-139
47. Lee, D.W., (1977): *On iridescent plants*. Gardens Bulletin Singapore. 30, 21-29.

48. Lee, D.W. (1991): *Ultrastructural basis and function of iridescent blue colour of fruits in Elaeocarpus*. Nature. 349, 260-262.
49. Lee, D.W., G.T. Taylor and A.K. Irvine, (2000): *Structural fruit coloration in Delarbrea michieana (Araliaceae)*. International Journal of Plant Sciences. 161(2), 297-300.
50. Fox, D. S. (1976): *Animal structural colors and biochromes*. University of California Press, Berkeley, USA.
51. Prum, R.O. and R. Torres, (2003): *Structural colouration of avian skin: convergent evolution of coherently scattering dermal collagen arrays*. The Journal of Experimental Biology. 206, 2409-2429
52. Prum, R.O. and R.H. Torres, (2004): *Structural colouration of mammalian skin: convergent evolution of coherently scattering dermal collagen arrays*. The Journal of Experimental Biology. 207, 2157-2172.
53. Gerwick, W.H. and N.J. Lang, (1977): *Structural chemical and ecological studies on iridescence in Iridaea (Rhodophyta)*. Journal of Phycology. 13(2), 121-127
54. Pederson, M., G.M. Roomans and A. Hofsten, (1980): *Blue iridescence and bromine in the cuticle of the red alga Chondrus crispus Stackh.* Botanica Marina. 23, 193-196
55. Pfündel, E.E., G. Agati and Z.G. Cerovic (2006): *Optical properties of plant surfaces*, in Biology of the plant cuticle. Editors, Blackwell Publishing, Oxford, 23, p. 216-249.
56. Gruenberger, C., R. Ritter, F. Aumayr, H. Stachelberger and I.C. Gebeshuber, (2007): *Algal biophysics: Euglena gracilis investigated by atomic force microscopy*. Materials Science Forum. 555: 411-416.
57. Tees, D.F. and D.J. Goetz, (2003): *Leukocyte adhesion: an exquisite balance of hydrodynamic and molecular forces*. News in Physiological Sciences. 18, 186-190.
58. Orsello, C.E., D.A. Lauffenburger and D.A. Hammer, (2001): *Molecular properties in cell adhesion: a physical and engineering perspective*. Trends in Biotechnology. 19(8), 310-316.
59. Kawasaki E. and A. Player (2005): *Nanotechnology, nanomedicine, and the development of new, effective therapies for cancer*. Nanomedicine: Nanotechnology, Biology and Medicine. 1(2), 101-109.
60. Sakhalkar, HS, M.K. Dalal, A.K. Salem, R. Ansari, J. Fu, M.F. Kiani, D.T. Kurjiaka, J. Hanes, K.M. Shakesheff and D.J. Goetz, (2003): *Leukocyte-inspired biodegradable particles that selectively and avidly adhere to inflamed endothelium in vitro and in vivo*. Proceedings of the National Academy of Sciences USA. 100: 15895-15900.
61. Autumn, K., Y.A. Liang, S.T. Hsieh, W. Zesch, W.P. Chan, T.W. Kenny, R. Fearing and R.J. Full (2000): *Adhesive force of a single gecko-foot hair*. Nature. 405, 681-685.
62. Dubrow, R., (2003): *Structures, systems and methods for joining articles and materials and uses therefore*. US Patent 7056409
63. Scherge, M. and S. Gorb, (2001): *Biological micro- and nanotribology – Nature’s solutions*. Springer Verlag, Berlin Heidelberg.
64. Gorb, E.V. and S.N. Gorb, (2002): *Attachment ability of the beetle Chrysolina fastuosa on various plant surfaces*. Entomologia Experimentalis et Applicata. 105 (1), 13-28.
65. Gorb, E., K. Haas, A. Henrich, S. Enders, N. Barbakadze and S. Gorb, (2005): *Composite structure of the crystalline epicuticular wax layer of the slippery zone in the pitchers of the carnivorous plant Nepenthes alata and its effect on insect attachment*. Journal of Experimental Biology. 208, 4651-4662.
66. Koch, K. A. Dommissse, W. Barthlott and S.N. Gorb, (2007): *The use of plant waxes as templates for micro- and nanopatterning of surfaces*. Acta Biomaterialia. 3 (6), 905-909.
67. Northen, M.T. and K.L. Turner (2005): *A batch fabricated biomimetic dry adhesive*. Nanotechnology. 16 (8): 1159-1166.
68. Shah, G.J. and Sitti M. (2004): *Modeling and design of biomimetic adhesives inspired by gecko foot-hairs*, In: IEEE International Conference on Robotics and Biomimetics (ROBIO), p. 873-878.
69. Gebeshuber, I.C., J.B. Thompson, Y. Del Amo, H. Stachelberger and J.H. Kindt, (2002): *In vivo nanoscale atomic force microscopy investigation of diatom adhesion properties*. Materials Science and Technology. 18, 763-766.
70. Higgins, M.J., P. Molino, P. Mulvaney and R. Wetherbee, (2003): *The structure and nanomechanical properties of the adhesive mucilage that mediates diatom-substratum adhesion and motility*. Journal of Phycology. 39: 1181-1193.
71. Higgins, M.J., J.E. Sader, P. Mulvaney and R. Wetherbee, (2003): *Probing the surface of living diatoms with atomic force microscopy: the nanostructure and nanomechanical properties of the mucilage layer*. Journal of Phycology. 39, 722-734.
72. Hansma, P.K., P.J. Turner and R.S. Ruoff, (2007): *Optimized adhesives for strong, lightweight, damage-resistant, nanocomposite materials: new insights from natural materials*. Nanotechnology. 18, 044026(3p).
73. Schmid, A-M.M. and R.M. Crawford, (2001): *Ellerbeckia arenaria (Bacillariophyceae): formation of auxospores and initial cells*. European Journal of Phycology. 36: 307-320.

Shape Optimization – Biomimetic or Naturemimetic?

Claus Mattheck, Roland Kappel

Forschungszentrum Karlsruhe GmbH, Germany

Abstract

Evolution in biology is a competition of the species for survival. To survive, plants and animals are forced to most efficiently apply energy and material. To improve the mechanical load capacity of supporting structures, material and shape are optimized. One of the main approaches to optimizing the shape is the Axiom of Uniform Stress, which has a great explanatory value in biological design.

This concept provides for a homogeneous stress distribution along the surface of self-optimizing structures. With a minimal use of material, they become as strong as necessary to reliably perform their function. Plants and animals realize this by load-adapted growth, which means that higher growth increments occur at higher loaded areas. In the end, the given mechanical load dominates the current design.

The principles of this highly effective but individual biological design have been explored and transferred to mechanical engineering. In a first step, this was done for technical components by a computer simulation of load-adapted growth. Further developments led to a tremendous simplification in the design process. The state of the art is the Method of Tensile Triangles - a simple graphic method to implement the Axiom of Uniform Stress along surface contours.

By applying the Method of Tensile Triangles, engineering components can be designed according to biological design rules and existent biological structures can be reconstructed. Amazingly, also some abiotic natural phenomena, without the feature of biological growth and, of course, which are not subject to evolutionary processes, exhibit analogue forms. The present paper will focus on the design of selected abiotic natural phenomena and compare it to biological design. The design of erosion products in the geomechanical formation and of juvenile stalactites and icicles will be highlighted. It appears to be subject to the same design rules of nature as biological structures.

Introduction

Since more than 15 years the design of biological load carriers is explored at Forschungszentrum Karlsruhe. Biological structures are highly optimized to their mechanical load. Exquisite toughness and durability are not only an effect of material properties and bearing load. Also their shape plays an important role for their stability [1]. In the course of evolution not only the shape of individual structures is optimized but also the mechanisms to achieve an ultimate design [2].

A basic design rule of nature is the “Axiom of Uniform Stress” avoiding weak spots due to overstressed areas as well as waste of material due to minor stressed areas. Along the surface of biological structures this design rule is realized due to local growth increments governed by load.

The software program CAO (Computer Aided Optimization) was written to simulate the mechanism of load adapted growth by computer calculations. They enable redesign of biological structures as well as the design of engineering components according to the design rules of nature [3].

The experience of many components designed with the CAO software identified similar contours for many results. Therefore an enormous simplification by fitting the contour with the Method of Tensile Triangles was possible [4]. But applying the Method of Tensile Triangles it becomes obvious that the contour seems to be abundant in nature, even for abiotic structures.

Material and methods

To explore the extension of validity for the Axiom of uniform stress an observant screening of nature and a deeper mechanical understanding is necessary. A good agreement with the contour of the Tensile Triangles is a good indicator for a uniform stress state along the fitted contour.

In the following the simple but effective tools “Shear-Square“ and the “Method of Tensile Triangles” are introduced.

The square formation of shear stresses that is common in mechanical literature can be also used to visualize the force flow. The descriptive approach of a small rotatable square “nailed” on the slip line of the shear show that it would turn under longitudinal shear stress (Fig 1a). As imaginary shear-squares do not rotate inside the component, counteracting transverse shear stresses of equal magnitude avoid the rotation (Fig. 1b). Tensile and compressive stresses displaced by 45° are equivalent to these shear stresses (Fig. 1c). This simple but effective tool does not substitute any stress calculations but it gives a good view of the local force flow [5].

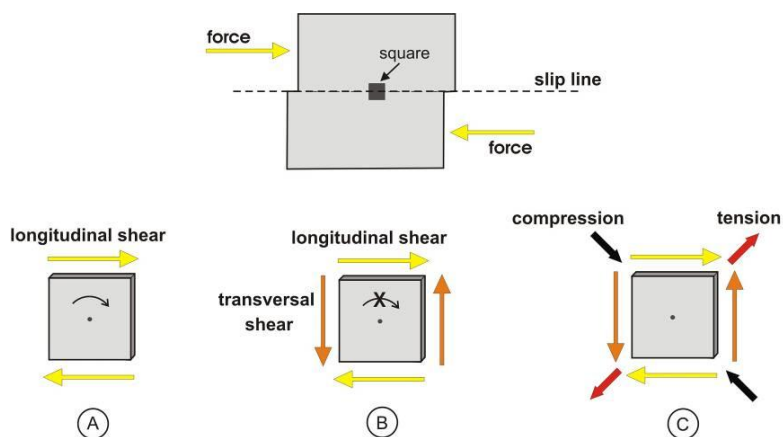


Figure 1: Non-rotating Shear-Square and equivalent tension and compression stresses [6].

The Method of Tensile Triangles provides the reduction of notch stresses along a sharp kinked contour [3]. Notch stresses also could be explained by use of the Shear-Square [4]. Looking at the rectangular edge in Fig. 2a under tension loading, we can identify the direction of tension stresses resulting of the longitudinal shear along the potential slip line. To avoid stress peaks the shoulders may be bridged by a supporting rope (Fig. 2b). The substitution of the rope with a “tension triangle” results in a new contour with two less dangerous notches of larger angles (Fig. 2c).

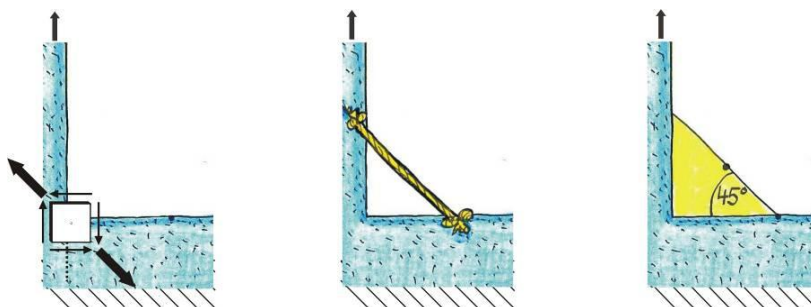


Figure 2: 45°-angle for bridging a rectangular notch [7].

For an uniaxial stress state the more dangerous notch of them can also be bridged by an isosceles tensile triangle starting at the centre of the hypotenuse of the previous. The repetition of this procedure is the Method of Tensile Triangles (Fig 3). In a last step, the segments are to be rounded to obtain an optimized notch design. The new contour line follows the local force flow and also separates required from needless material.

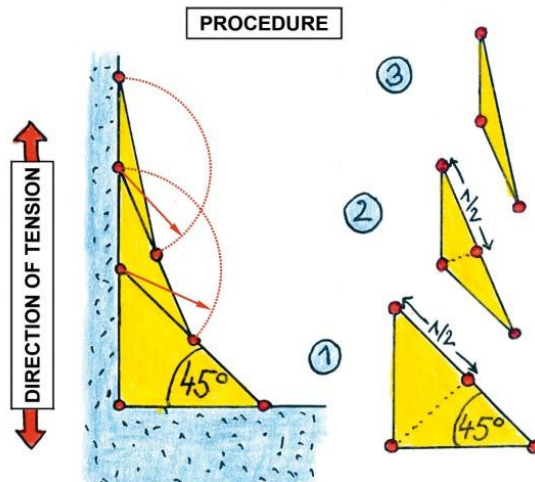


Fig. 3: Procedure to create the contour of the Tensile Triangles [8]

The Method of Tensile Triangles is also applicable to forks or brackets. The contour is attached on each lever while the extension of the first triangle is proportional to the given load. The ratio of the first triangles is equal to the ratio of the load magnitude.

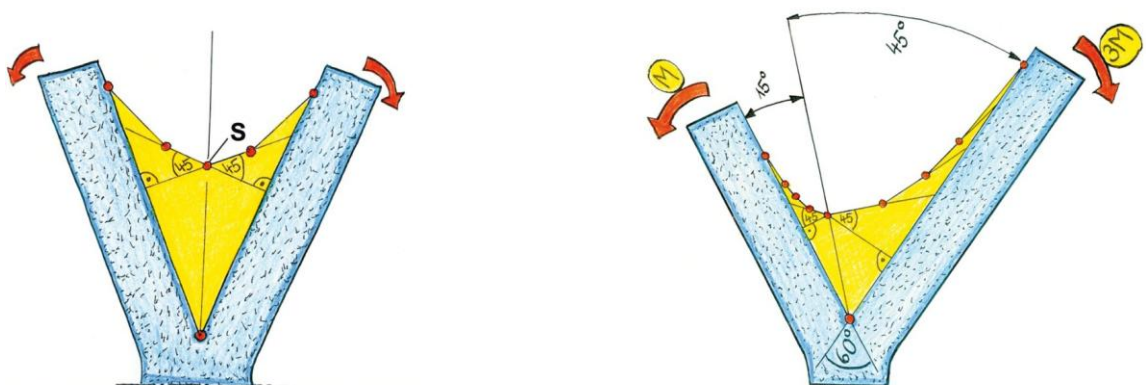


Figure 4: Application of the Method of Tensile Triangles for forks. Fork with load of equal magnitude (left). Fork with load of different magnitude (right). [8]

The application of the Method of Tensile Triangles to the shape of plants and animals gives a good analogy to natural design [8]. Figure 5 shows the redesign by fitting the surface contour of some aerial parts. At the right picture the transition at the foot of a tree's trunk to the broader root plate at the windward side is fitted. The longitudinal cut through the tree fork in the middle of Figure 5 shows a good congruence with the fork in Figure 4 on the left side. The contour tells us the direction of the load as well as its ratio between the two lever arms. On the right side the leaf of a red oak exhibit between two veins the same contour along the outline of its lamina like the tree fork. More examples of biological load carriers fitted with the Method of Tensile Triangles are given in [8].

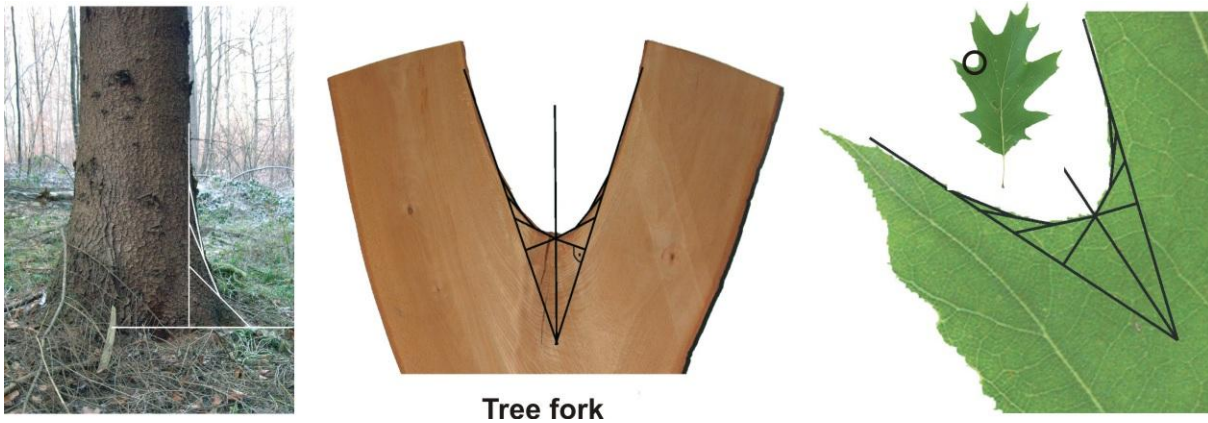


Fig. 5: Fitting surface contours of plants with the Method of Tensile Triangles. Left: buttress root of a tree; middle: tree fork; right: leaf [8].

Results and discussion

In previous work [2] it was shown that the Axiom of uniform stress is a major design rule for biological load carriers. They achieve their optimized design due to load adapted biological growth. The enormous simplification using the Method of Tensile Triangles to identify stress optimized contours extended the possibilities to monitor our environment.

It seems to be obvious that this contour is not limited to biological structures. Also a number of abiotic structures are designed in the same way. Non living structures are not subject to processes of biological evolution take same shape as biological structures extracted by evolution.



Fig. 6 Earth pyramid fitted with the Method of Tensile Triangles. (Ritten, Italy)

A earth pyramid (also hoodoo, tent rock, fairy chimney,) is a tall thin spire that protrudes from the bottom of an erosive drainage basin. Earth pyramids are formed by the erosion of the conglomerate of an old alluvial fan and are topped by a piece of harder, less easily eroded stone. This stone does not only protect the column from the elements, it also compresses the soil below and therefore increases the shear strength. The contour line fitted with the Method of Tensile Triangles in Figure 6 shows the current separation line between eroded and non eroded Material. This line follows the local material properties which are additional governed by weight of the covering stone.

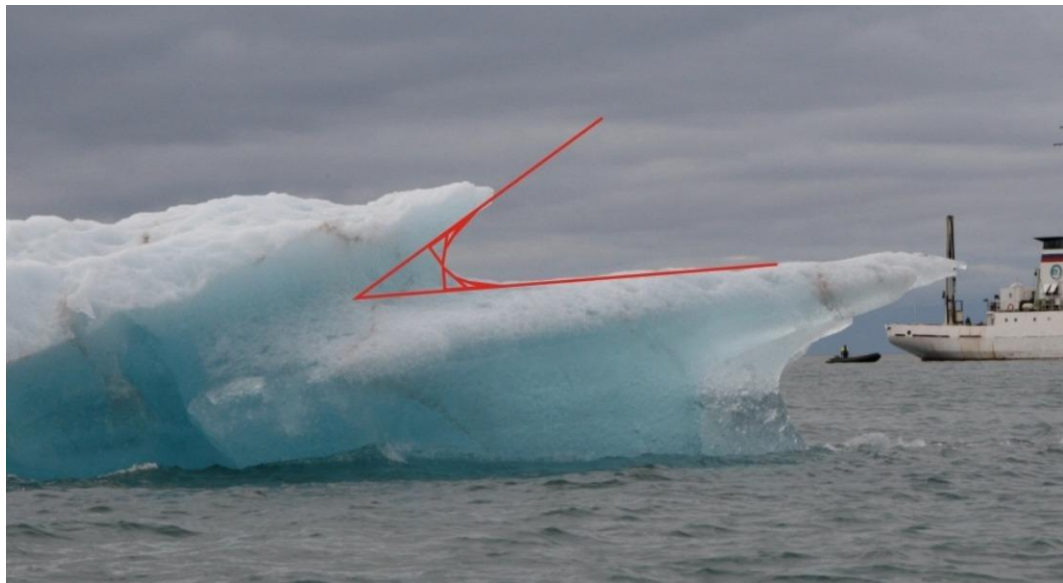


Fig. 7 Ice floe fitted with the Method of Tensile Triangles (Photo: Winfried Keller). (Spitzbergen, Norway)

The contour of the ice floe in Figure 7 fitted with the Method of Tensile Triangles results from the wash of the waves at the water line. The contour washed out at the edge of the ice flow seems to be symmetric to the water line and is nearly identical to the contours of the tree fork and the lamina of the red oak leaf shown in figure 5. The local material loss of the ice floe results in a change of the balance conditions. The ice floe will rise up locally in the area of the erosion and start to rotate. The wave action continues its work in the same way below as you can see in figure 7.

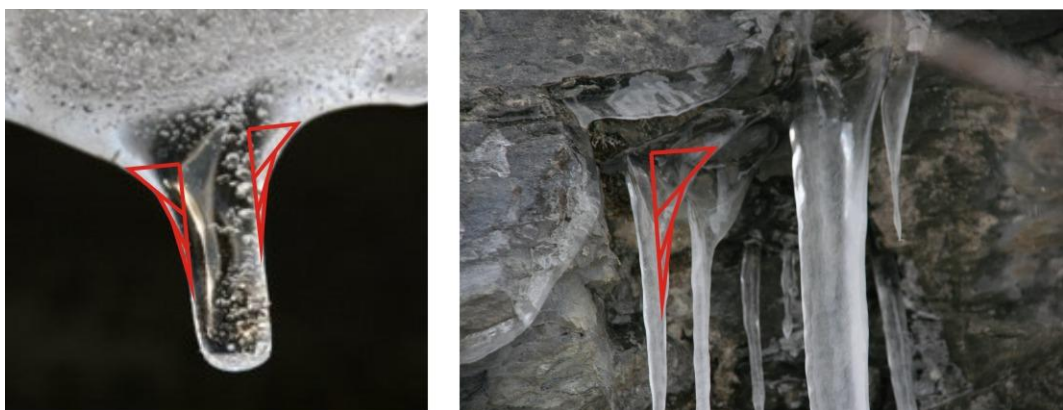


Fig. 8 Icicles fitted with the Method of Tensile Triangles. Refreezing Icicle at the bottom edge of a melting snowfield (left). Icicles grown at a craning rock (right). (Lauterbrunnen, Switzerland)

Icicles are spikes of ice formed when dripping, falling or sputtering water freezes. In Figure 8 the base of icicles is fitted with the Method of Tensile Triangles. The icicles result from melting water of the snow which runs off into an area where the ambient temperature is below the freezing point, causing the water to refreeze. Over time continued water runoff will cause the icicle to grow. At the

base of the growing icicle the water starts to freeze. This transition zone of many icicles shows an impressive congruence with the contour of the Method of Tensile Triangles.

The icicle on the left side is located at the bottom edge of a snow field. Both sides of the icicle is supplied by melting water and can be fitted with the Method of Tensile Triangles. The icicle on the right side is growing down beneath a craning rock. The main water support comes from the snow on the rock and is routed from the right side to the icicle, where the contour fitted with the Method of Tensile Triangles is highly developed.



Fig. 9 Stalactites fitted with the Method of Tensile Triangles. Juvenile stalactite in the form of a soda straw (left). Transition between two matured stalactites with broken off tips (right). (Bärenhöhle, Germany).

Stalactites are formed by the deposition of calcium carbonate and other minerals, which is precipitated from mineralized water solutions. In subterranean cavities water drops are formed at the ceiling by dripping water coming down a small crack, hold against gravity by the surface tension of the water. The water drop grows until the weight of the water gets too large for the surface tension and finally drips downwards. Due to gas release of carbon dioxide from the water drop into the cave air a small amount of limestone crystallizes at the ceiling. It forms rings around the drop, growing to a soda straw. Those soda straws look very similar to the icicle in figure 8 on the right side and the contour at their base could be described with the Method of Tensile Triangles as well (figure 9 left). If they become plugged, water begins flowing over the outside, depositing more calcite and creating the more familiar cone-shaped stalactite. Figure 9 on the right side shows the fit with the Method of Tensile Triangles of the transition between two stalactites growing together.

Conclusion

Plants and animals are exceedingly adapted to their natural habitat. Due to selection of evolution optimization is an advantage for survival in the competition between the species. Therefore material and shape of biological supporting structures are optimized to the given service load. A lifelong adaptation is managed by biological growth [2]. The contour of load adapted grown biological load carriers easily can be fitted with the Method of Tensile Triangles [8]. But the same contour occurs at abiotic structures which are not subject to processes of biological evolution like earth pyramids, ice floes, icicles and stalactites as shown in the given examples.

Common for the analyzed examples is an available material flow to achieve this contour, which seems to be a balance of mechanical, physical and / or chemical effects. Materialized independent from live the question of a superior general mechanically optimizing principle valid as well in the world of biotic and abiotic natural load bearing structures can be assumed. The extent of validity for this contour is not foreseeable at the moment, but to explore the superior principle behind this contour an extension from biomimetic to naturemimetic is required.

References

1. Mattheck, C. (2004): The face of failure – in nature and engineering. Verlag Forschungszentrum Karlsruhe, (www.mattheck.de).
2. Mattheck, C. (1998): Design in nature - learning from trees. Springer Verlag, Heidelberg
3. Mattheck, C. and S. Burkhardt, (1990): A new method of structural shape optimization based on biological growth. International Journal of Fatigue, Vol. 12, p. 185-190.
4. Mattheck, C., Kappel, R., Sauer, (2007): A., Shape optimization the easy way: The “Method of Tensile Triangles”. Int. Journal of Design & Nature. Vol. 2, No. 4, 1-9.
5. Mattheck, C., Bethge, K., (2007): Ein Denkwerkzeug – Die Methode der Schubvierecke. Konstruktionspraxis 3, 32-34.
6. Mattheck, C., Kappel, R., Kraft O., (2008): Meaning of the 45°-angle in mechanical design according to nature. WIT-Press, Design and Nature IV, p.139 – 146.
7. Kappel, R. (2007): Zugseile in der Natur. FZKA 7313, Verlag Forschungszentrum Karlsruhe GmbH.
8. Mattheck, C., (2007): Secret design rules of nature - Optimum shapes without computers. Verlag Forschungszentrum Karlsruhe GmbH, (www.mattheck.de).

***Abstraction of plant movements for deployable
structures in architecture***

J. Lienhard^{1,3}, *S. Poppinga*^{2,3}, *S. Schleicher*^{1,3}, *T. Masselter*^{2,3},

T. Speck^{2,3}, *J. Knippers*^{1,3}

*1 Institute of Building Structures and Structural Design (ITKE),
University of Stuttgart, Germany;*

2 Plant Biomechanics Group Freiburg, Botanic Garden, University of Freiburg, Germany;

3 'Competence Network Biomimetics' Baden-Württemberg, Germany

Abstract

New construction materials such as fibre-reinforced polymers can combine high tensile strength with low bending stiffness, allowing large elastic deformations. These mechanical properties enable us to think about a completely new interpretation of convertible structures which work on reversible elastic deformation. This potential has not yet found its use in building and construction. In a current research project a group of engineers and biologists are aiming at closing this gap by developing a new type of convertible structures. The kinetics¹ of these pliable structures will be based on the flexible deformation principles found in plant movements. Here, growth or change of turgor pressure are the most common causes for the movement or deformation of fibres, tissues, or whole plant organs. Bending can be caused by an unequal contraction and elongation of the tissues and their embedded fibres which is generated by asymmetrical growth or uneven distribution of turgor pressure. Most of these deformations are within a visco-elastic range and reversible. Based on these principles plants have evolved a multitude of kinetics which serve the opening and closing of flowers, leaf orientations, anchoring, trapping, pollination etc. Some of these elastic kinetic systems may be used as concept generators for technical applications. The object of this paper is to describe a biomimetic working progress; from selection and investigation of plant movements to the abstraction methods which were developed to translate plant movements into elastic kinetics for deployable structures in architecture.

Introduction

Plant movements are particularly adequate for translation into kinetic architectural structures. Unlike animal locomotion which is usually laid out for a variety of complex movements, the actuation systems of plants are evolutionary optimized to perform a single type of movement. There are numerous examples of organ locomotions, such as active trapping mechanisms in some carnivorous plants, described by Juniper et al [1]. The kinetics of these systems use little actuation energy, are usually reversible and work with the absence of local hinges. Plant movements can be differentiated in terms of active kinetics such as cell growth [2], faster movements induced by a local change in turgor

¹ Kinetics: (from Greek *kinesis*: motion) relationship between the motion of bodies and its causes

pressure [3] or cohesion forces [4]. Other movements are based on passive kinetics actuated by outer influences such as change in humidity causing passive cell wall swelling and shrinking [5] or passive kinetics, e.g. actuation by the weight of an attracted pollinator [6].

In architecture, adaptability as a structural response to a change of ambient conditions (e.g. intensity/direction of solar radiation) can be realized with deployable systems. These systems are usually based on the combination of stiff compression members and soft tension members connected with hinges and rollers. The mechanical properties of fibre reinforced polymers are highly dependent on the fibre orientation; enabling the design of profiles with high tensile strength and low bending stiffness, allowing large elastic deformations. This renders the possibility of developing deployable structures which work on the basis of reversible deformation, here referred to as elastic or pliable structures. One of the main advantages is the diversity of structurally stable positions which the structure can attain between fully opened and closed. The structures are thus adaptable to different marginal conditions which could optimize efficiency in shading systems.

The work presented in this paper concentrates on the abstraction and modification of natural deformation principles. This article describes the biomimetic workflow with particular emphasis on the abstraction methods which were developed to translate plant movements into elastic kinetics for deployable structures in architecture. These methods are shown with the example of the passive kinetics performed in the pollination mechanism of *Strelizia reginae*.

Abstraction method

In the last decade the use of nature as an inspirational source to solve technical problems has become increasingly recognized. Through the evolutionary pressure of natural selection on organisms to survive under particular boundary conditions, highly optimized systems have been developed. The top ‘down approach’ [7] can be used to solve technical problems by formulating a concise question which nature may have already had to develop an answer for.

Question: *Elastic kinetics, adaptability.* The overriding question in the work presented here is the optimization of small and medium sized deployable systems in architecture towards more adaptability and energy efficiency as well as less weight and maintenance. The first step in finding nature inspired solutions is a screening, biological concept generators with a high potential for a translation into technical applications are collected. The most developed and complex answers are often found organisms that developed structures under high selective pressure, e.g. pollination mechanisms [8].

Screening criteria: *reversible elastic or visco-elastic deformation in plants.* Plant movements are based on many different ecological reasons some of which only occur in highly specialized plant groups, e.g. trapping mechanisms in carnivorous plants. In contrary to animals that show diverse and multifunctional locomotion abilities, e.g. leg movement for running, swimming, or climbing, plants perform single types of movements (nasties, autonomous, hygroscopic and cohesive movements) [9]. For the purpose of this research, these evolutionary optimized actuation systems in plants are excellent concept generators for a transfer into elastic structures in architecture. As the plant kingdom holds

ready a multitude of kinetic systems that come into consideration, the screening must be confined to plants whose moving organs show clear structure-function-principles as opposed to growth movement. This is the case when movements follow predetermined directions due to the organ's anatomy.

Selection criteria: *large bending radii, small actuation energy, avoidance of local hinges.* The successful implementation of an elastic kinetic system in an architectural structure is dependent on the scalability of the biological concept generator. High stresses are caused for example if the bending radius is relatively small in comparison to the thickness of the structure. The selection criteria are therefore aimed at finding examples with potentially efficient cost, energy and material solutions. An example which fulfils the selection criteria above is the Bird-Of-Paradise (*Strelizia reginae* Banks ex Aiton, *Strelitziaceae*) [6]. Due to evolutionary pressure, this plant has evolved an astonishing pollination mechanism.

Phenomenon: *presentation of the natural system.* The elastic kinetic system of *Strelizia reginae* is found in the flower, it is a consequence of an adaption for bird pollination. Here, two adnate and locally hardened petals form a perch (*p*) Fig. 1. They are loosely connected with an elongated stylus and five stamina (here referred to as strands) enclosed in the petal lamina. As a bird lands on this construct to feed on nectar, the perch bends down. This bending down induces a simultaneous sideways bending of the lamina (*d*). The previously enclosed stamina (*s*) thereby become exposed and are enabled to attach their pollen to the bird's feet.

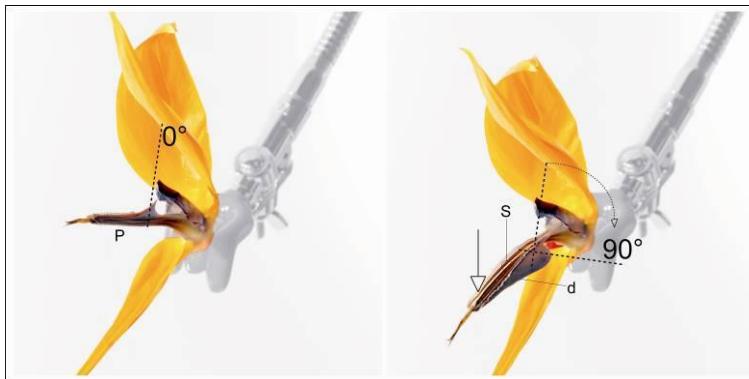


Fig. 1 Phenomenon: The bending down of the *Strelizia*'s perch under the weight of the pollinator causes simultaneous sideways rotation of the lamina by 90°.

Left: Closed position, lamina at 0°

Right: Open position, lamina at 90°

Analysis of the functional morphology: *dissection of the biological example to expose the decisive members.* The perch is stiffened by 5 elongated and hardened strands. At the petal adnation point, strand *a* is made of two loosely attached strands. The lamina *d* is flexibly attached to the strand *c*. The stylus and five stamina are loosely embedded and thus not submitted to tension forces during bending of the system, Fig. 2.

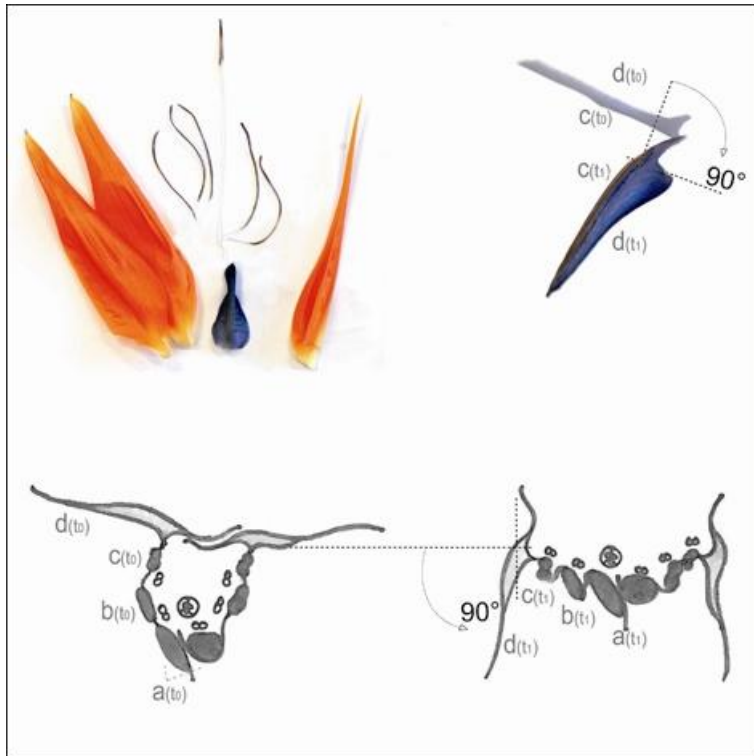


Fig. 2 Analysis of the functional morphology

Top left: off cut of non decisive members

Top right: exposed kinetic system

Bottom left: section through perch closed (t_0), showing the lamina d , the top strands c , the middle strands b and the double strand at the bottom a .

Bottom right: section through perch open (t_1)

First level abstraction: *rebuilding the kinetic system in a physical model.* The verification of the first level abstraction can be done with a physical model; this is a very quick method to gain an understanding of the system and to prove the functionality of the extracted system, Fig. 3. The physical model consists of a vertical paper lamina d mounted on a glass fibre rod c that is fixed at one end and free at the other. The lamina bends sideways to an angle of ca. 90° , when a vertical force is applied to the free end of the rod.

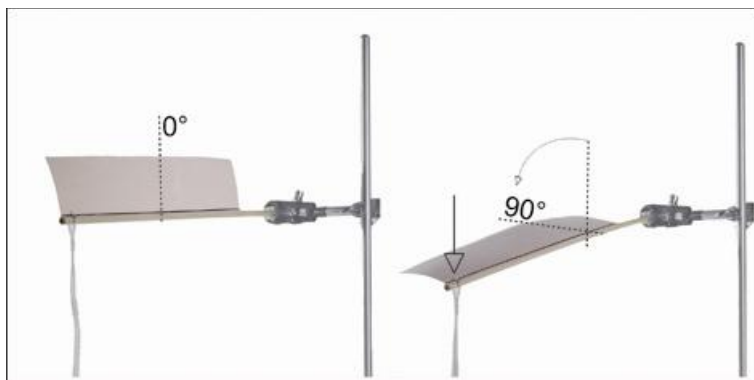


Fig. 3 second level abstraction: Physical model

Left: Closed, lamina d at 0°

Right: Open, lamina d at 90°

Second level abstraction: *structural system, stiffness distribution, actuation system.* The structural system is shown in orthographic projection with the internationally used symbol conventions for supports and hinges as e.g. described by Hugi [10]. The whole system of the perch with the 5 strands is shown in its configuration, Fig. 4. Here the strand c with the attached lamina d is performing the actuated motion; sideways bending of the lamina d during down bending of the strand c . The extracted system with only strand c and lamina d (bottom right in Fig. 4) needs an additional support in order to prevent the system from yielding to horizontal forces. These horizontal forces are shortcut in the complete perch system with the 5 adjacent strands meeting at the tip. The strands vary in stiffness; while the relatively stiff strands a and b seem to be designed to carry the pollinators weight, strand c

is a lot more flexible, enabling it to easily change the bending radius and hence induce sideways bending into the lamina.

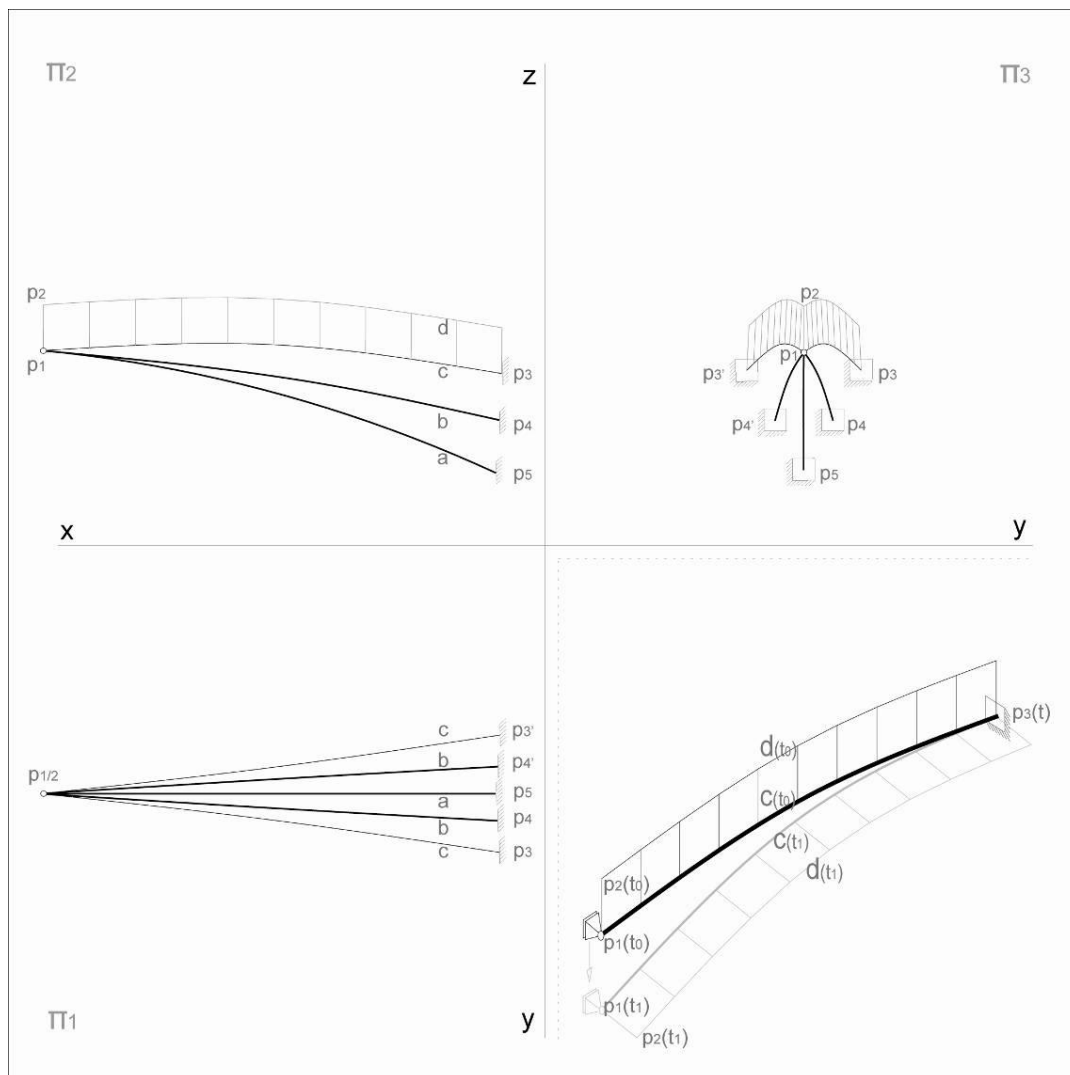


Fig. 4 Second level abstraction: Structural system of the whole perch and abstracted kinetic system.

Top left: Projection plane π_2 : side view of whole perch system

Top right: Projection plane π_3 : front view of whole perch system

Bottom left: Projection plane π_1 : top view of whole perch system

Bottom right: 3d illustration of the extracted kinetic structure

Fourth level abstraction: *Simulation of the kinetics in finite elements.* In order to gain a more profound knowledge of the structural behaviour of the system a finite element model is developed, Fig. 5. The *Strelizia* kinetics are modelled with a 2m long beam representing the strand *c* and a 0.25m high 5mm thick shell element representing the lamina *d*. The material properties of both members are standard glass fibre reinforced plastic (GFRP) values; Young-modulus E 30000 MPa, Young-modulus E_{90° 1500 MPa, Shear-modulus 780 MPa.

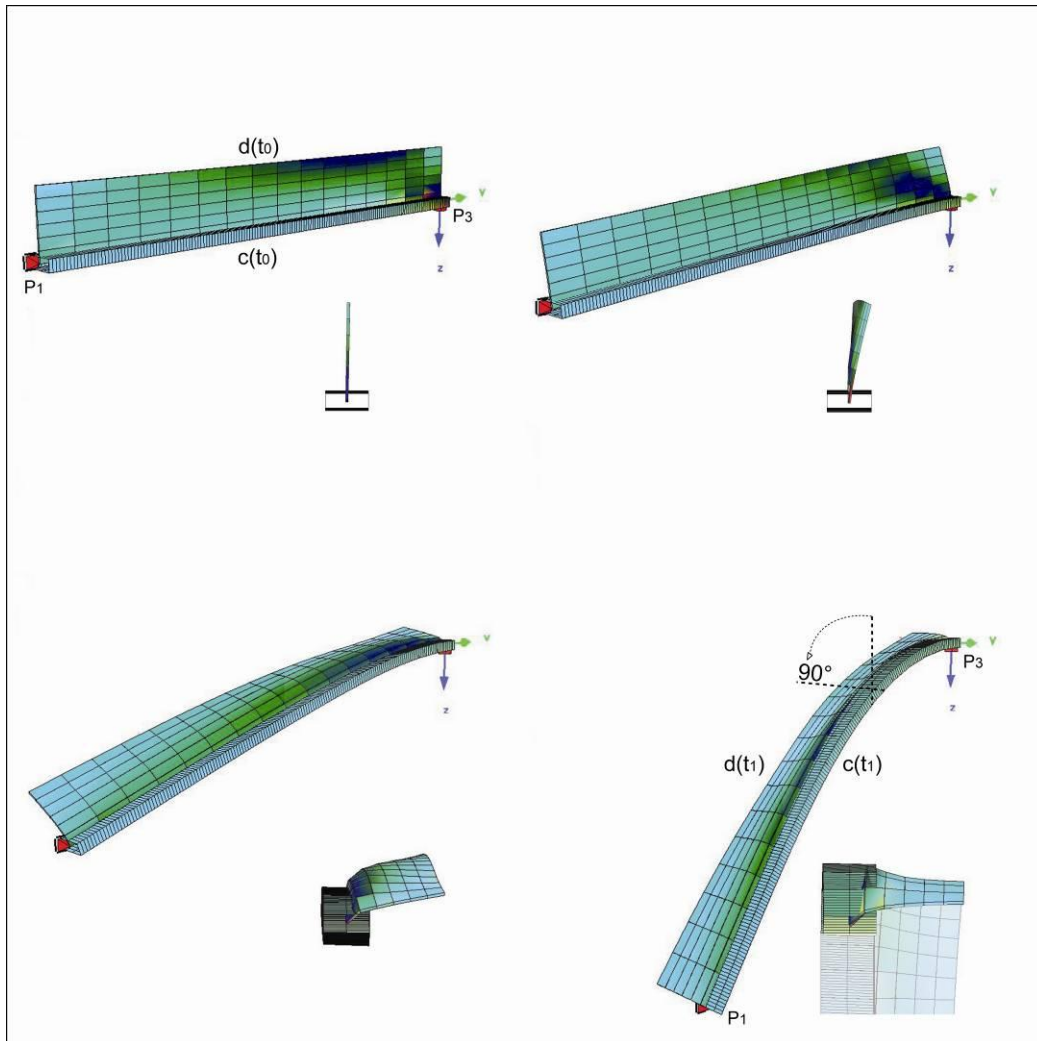


Fig. 5 Fourth level abstraction: Simulation of the kinetic structure in finite elements.

Top left: step 1: 5mm (vertical displacement of $p1$)
 Top right: step 2: 120mm
 Bottom left: step 3: 500mm
 Bottom right: step 4: 1300mm

Function and technical application

The completion of the Third abstraction level allows a detailed investigation of the system. An analysis of the principal membrane forces at four vertical displacement steps show the rearrangement of the tension (left) and compression (right) stresses through buckling and sideways bending of the shell elements d , Fig. 6. Step one shows a standard stress distribution of a cantilever beam with the highest tension forces at the upper edge of the lamina. In step two the shell starts buckling near the fixed support where compression stress is the highest. Buckling causes the outer edge of the shell elements to bend sideways. The newly formed edge re-stabilizes the shell; the main tension lines are moving inwards to run along the buckling edge in the surface and are now starting to pull the deformed shell further sideways. In step three the buckling edge expands further away from the fixed support and simultaneously starts forming an arch which is moving down towards the beam. In step four the whole shell has bent sideways by approximately 90° . The buckling edge is now forming a

shallow arch spanning between P1 and P3. The main tension lines are very close to the beam, compression in the shell reoccurs due to double curved of the outer edge. In summary, the sideways bending of the *Strelizia* lamina actuated by bending of the attached strand is a failure mode initiated by buckling. Once buckling has started, the tension forces on the surface (lamina) form an arch between P1 and P3 which enhances the sideways bending up to 90° relative to its original position. Here a new double curved surface (see r_d and r_c in Fig. 6) is formed which provides higher stiffness also for the attached strand.

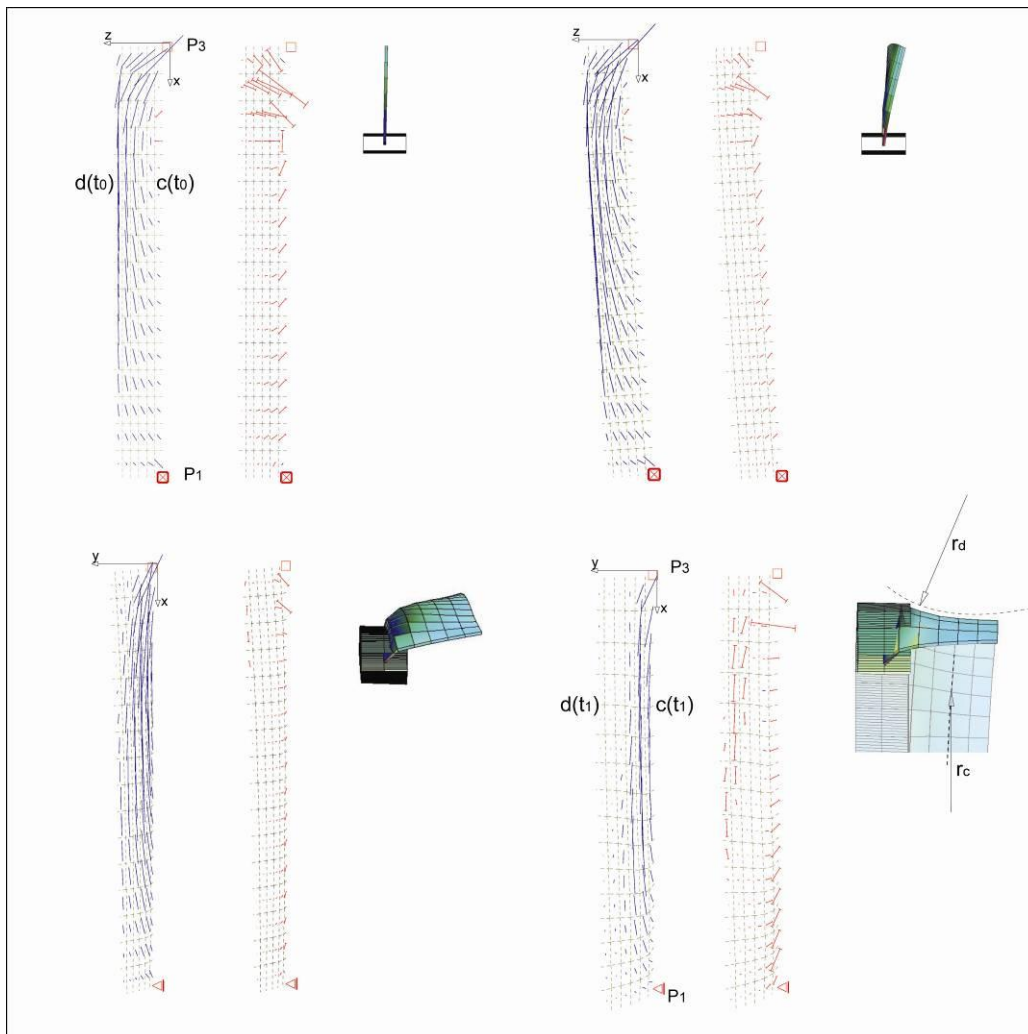


Fig. 6 Distribution of principal membrane tension forces in the shell elements.

Top left: step 1: 5mm (displacement of p1)

Top right: step 2: 120mm

Bottom left: step 3: 500mm

Bottom right: step 4: 1300mm

Reverse Bionics: *geometrical proportions, stiffness ratio, material properties, fibre orientation etc.* In order to optimize the abstracted model and demonstrators at lab scale, a focused analysis of the functional morphology and biomechanics becomes necessary. This process is referred to as reverse bionics [11]. On the biological level further studies need to clarify open points: How does *Strelizia* avoid material fatigue in the places of small bending radii? Which is the fibre orientation in these

areas? What differences in mechanical properties (e.g. stiffness) occur in parts of the system (e.g. in the strands *a*, *b* and *c*)?

The research progress is currently at the stage of screening and selection. A prospect for the *Strelizia* kinematic as a technical application is given in Fig. 7. Here structures of high flexibility are built in order to be able to induce large deformations without overstressing the structural members or using an uneconomic amount of actuating force.

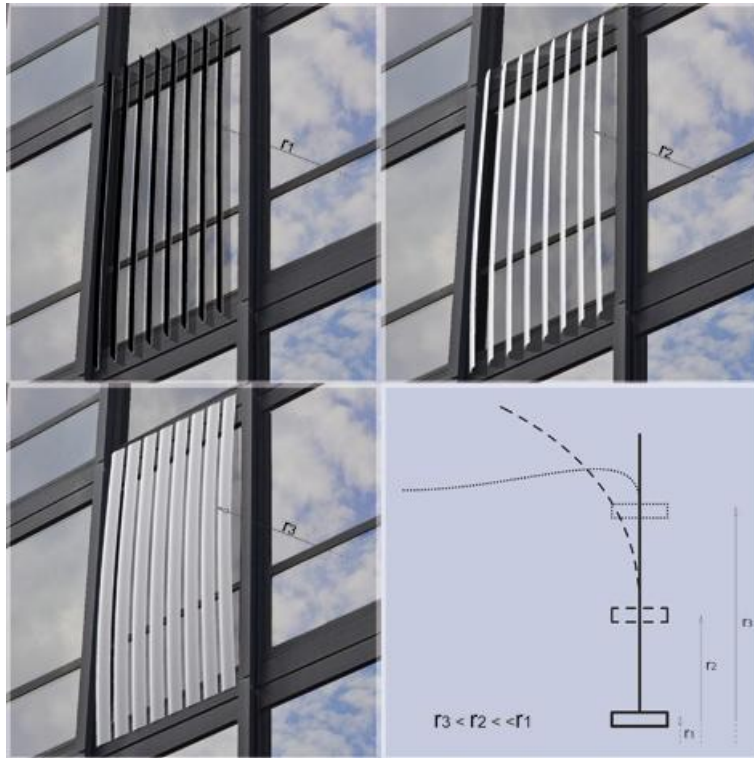


Fig. 7 Vision of a facade shading system based on the kinetic system of *Strelizia reginae*.

Bending of the strand can be induced by displacement of a support, or through change of temperature in a laminate with different temperature expansion coefficients.

Top left: open position

Top right: intermediate position

Bottom left: closed position

Bottom right: section through one lamella in the three shown positions

For some pliable structures the high elasticity may lead to serviceability problems. According to most national building codes the deformation of a structure is restricted to 1/200 of its span. For smaller convertible sun shading systems we may find more expectance for larger deformation, yet we will not be able to go the same way as *nature* does; yielding to external loads to elude high forces. In some cases the architectural applications will work with variable stiffness; structures which can temporarily go into a flexible state at the moment of deformation and go back into a stiff state to withstand external loads such as snow and wind. The development of such systems is part of the authors research and will be published separately.

Conclusion

The analysis of the anatomy, functional morphology and biomechanics of plants is a promising approach for concept generation and optimization in the field of architecture, building and construction. The mostly sessile structures of plants are optimized for similar boundary conditions as the architectural structures we inhabit. This study shows that even kinetic structures can be derived from some highly specialized plants. The movement of these plants which is usually based on (visco-) elastic deformation serves as innovative, biomimetic approach for deployable surface structures in architecture.

Acknowledgements

The Authors would like to thank the following institutions for their financial and professional support: The work presented in this paper is supported within the funding directive BIONA by the German Federal Ministry of Education and Research. The authors are supervised and consulted by the Competence Network Biomimetics

References

- [1] Juniper, B. E.; Richard, J.; Robins, D. M. Joel (1989): *The Carnivorous Plants*, Academic P., U.S
- [2] Cosgrove, D. J. (2005): *Growth of the plant cell wall*. Nat. Rev. 6
- [3] Forterre, Y., Skotheim, J. M., Dumais, J. & Mahadevan, L. (2005): *How the Venus flytrap snaps*, in Nature 433, 421–425.
- [4] Haupt, W. (1977): *Bewegungsphysiologie der Pflanzen*, in Thieme Verlag Stuttgart, Germany: p. 406
- [5] Fengel, D. & Wegener, G. (1984): *Woodchemistry, ultrastructure, reactions*, in De Gruyter Berlin, Germany
- [6] Endress, P. K. (1994): *Diversity and evolutionary biology of tropical flowers*. Cambridge University Press, Cambridge Tropical Biology Series
- [7] Milwich, M.; Speck, T.; Speck, O.; Stegmaier, T.; Planck, H. (2006): *Biomimetics and technical textiles: solving engineering problems with the help of nature's wisdom*, in American Journal of Botany 93(10): p. 1455-1465
- [8] Reith M., Baumann G., Claßen-Bockhoff R. & Speck T. (2007): *New insights in the functional morphology of the lever mechanism of Salvia pratensis*. Annals of Botany 100: 393-400
- [9] Sitte, P., Ziegler, H., Ehrendorfer, F., Bresinsky, A. (1991): *Strasburger. Lehrbuch der Botanik*. Gustav Fischer Verlag (33. Auflage): p. 456-469
- [10] Hugi, Hans R. (1992): *Einführung in die Statik der Tragkonstruktionen*, in Autographie zur Vorlesung an der ETH Zürich. Zürich: Verl. der Fachvereine [u.a.].
- [11] Csete, M. E., Doyle, J. C. (2002): *Reverse Engineering of Biological Complexity*. Science 295: p. 1664-1669

Additional References

- Matini, M.R (2007): *Biegsame Konstruktionen in der Architektur auf der Basis bionischer Prinzipien*, Institut für Tragkonstruktionen und Konstruktives Entwerfen (ITKE); University of Stuttgart
- Burgert, I., Fratzl, P. (2009): *Actuation systems in plants as prototypes for bioinspired devices*. Phil. Trans. R. Soc. A 367: p. 1541-1557
- Rowe, N., Speck, T. (2005): *Plant growth forms - an ecological and evolutionary perspective*. New Phytologist 166: p. 61-72
- Speck, T., Masselter, T., Prüm, B., Speck, O., Luchsinger, R., Fink, S. (2004): *Plants as concept generators for biomimetic light-weight structures with variable stiffness and self-repair mechanisms*. J. Bionic Eng. 1 (4): p. 199-205

Plant stems as building material for living plant constructions

Ferdinand Ludwig¹, Gerd de Bruyn¹, Marc Thielen², Thomas Speck²

¹Research Group Baubotanik, Institute for Theory of Modern Architecture, University of Stuttgart, Germany; ²Plant Biomechanics Group Freiburg, Botanic Garden, University of Freiburg, Germany

Abstract

The main aim of this project is to employ living woody plants and use their growth processes for architectural and constructive demands. For this purpose it is necessary to describe and ‘produce’ living plant stems as technical material with special characteristics. The plants have to fulfil several physiological and especially morphological and biomechanical prerequisites. In order to achieve stems with a form and structure applicable for architectural and constructive demands, seedlings of *Platanus acerifolia* were grown under different, artificially adjusted environmental conditions in special growth chambers. As key-factors influencing form, structural and mechanical parameters of the stems the photosynthetic active radiation (PAR) and the relative rate of red (R) and far red (FR) radiation were altered by using light filters, causing reactions of the plants known as ‘shade avoidance’ and ‘phytochrome effect’. Our results show correlations between light conditions and morphological, anatomical and biomechanical characters of the examined plant stems.

Introduction

The German term ‘Baubotanik’ refers to a type of architecture where natural growth processes are used to create living plant constructions. In ‘Baubotanik’-projects the stems of woody plants are interconnected to create an artificial ‘tree-construction’ or building. So far only simple and small structures have been built, using basic techniques and common plant materials (Figure 1 left). The aim of our research is to develop complex, artificial, yet living architectural structures in the dimension of fully grown trees (Figure. 1 top right). Thereby the aesthetic and constructive potentials of trees can be integrated in architectural projects and the ecological capacity of tall trees, normally delayed for generations, will be immediately available [1]. To build structures like these young small plants (including the roots and containers with growth substrate) are arranged in space and shaped into a three-dimensional framework-like structure (Figure.1 step 1 and 2). Then the plants are interconnected with each other in a way that they will merge to one physiological unit. Over the course of time the plants at the base develop a sufficiently large root system in the ground and the roots above ground can be removed step by step (Figure. 1 step 3). Due to secondary growth processes the in the beginning delicate structure develops a high mechanical load capacity.

The plants used to form the initial structure have to meet specific demands. It is advantageous if they are very slender, long and un-branched and their stems must be able to be bent to a narrow radius. Therefore it seems to be useful if the stems show a high degree of slenderness¹, a low Young’s modulus of elasticity and a high tensile strength. The aim of the current research project is to investigate how the above mentioned morphological characteristics can be controlled using different environmental factors and how biomechanical and anatomical properties are influenced by these factors. In our experiments we have tried to carry the parameters ‘total length’ and ‘degree of slenderness’ to the extremes of phenotypic plasticity.

¹ Defined here as the relation between the total length of the axis and the diameter 5cm above the basis

In particular, the photosynthetic active radiation (PAR) and the spectral characteristics of the radiation were chosen as key factors². Especially the relation between the relative fluence rate of red (R) and far red (FR) radiation is of great importance because plants react to this relation by photoreceptors of the phytochrome family (phytochrome effect). Commonly a low R/FR-relation is interpreted as an indicator for potentially competing neighbour plants and leads to a considerable enhancement of growth in length (= shade avoidance reaction, see e. g. [2][3][4])

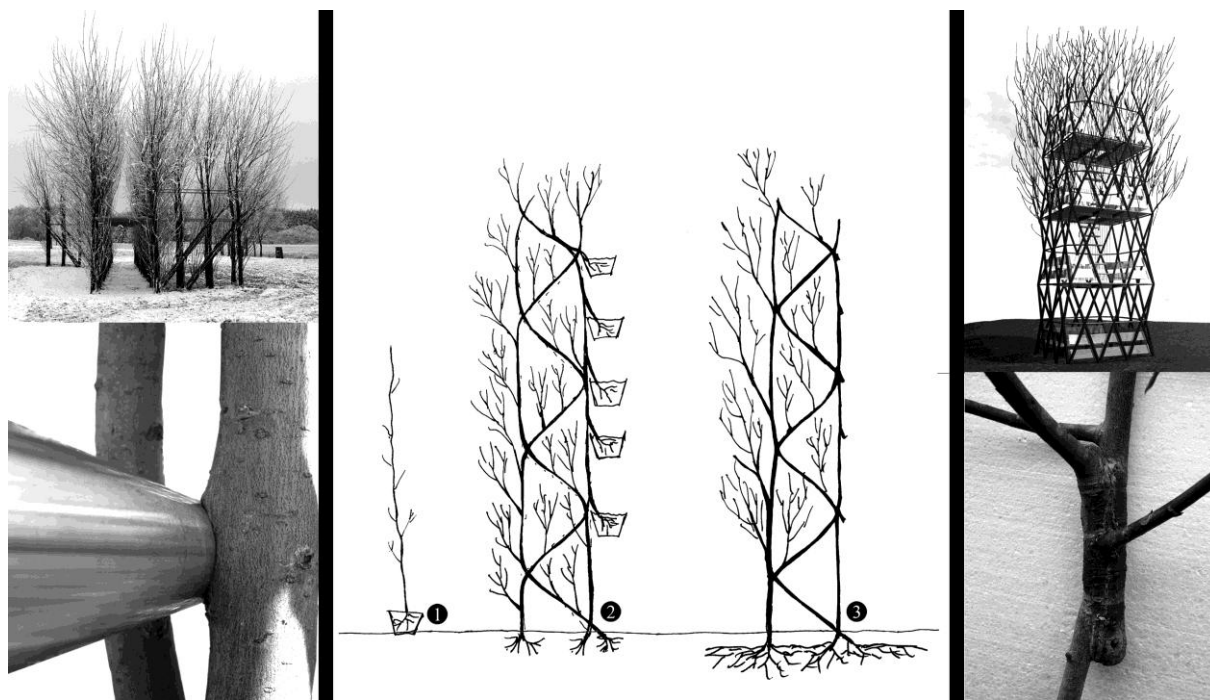


Figure 1 left: A catwalk made of living trees (realised in 2005, photo 2008 and a typical detail of this building. Middle: Schematic drawing explaining the method to construct tall and complex living structures by using young and slender plants (see text for a detailed explanation). Right: Visualisation of a prototypical structure based on this method and typical detail of such a structure.

Material and methods

All experiments were carried out with *Platanus x hispanica* (London Plane Tree), a hybrid that seems to be quite suitable for ‘Baubotanik’-projects (see e. g. [5]). One year old seedlings which were cut back to two or three buds were grown for one season under controlled conditions in a special greenhouse that consisted of nine separated growth chambers (Figure 2). By covering the outer walls with shading cloth or light filtering film, the light condition in the different chambers were altered³. Utilizing mechanical ventilation and a simple temperature control system (evaporative cooling with misting nozzles) the climatic conditions in all chambers could be set comparably⁴ (Figure 2).

In chamber 1 the outer walls were covered with a light filtering film (lee-filters, UK, ultimate violet #707) that filters out much of the red radiation while most of the radiation in the far red range can pass through (see spectral chart in Table 1). Thereby a low R/FR-relation is achieved. Unavoidably this reduces the intensity of the photosynthetic active radiation, too. To create growing conditions with a comparable PAR-radiation but without changing the spectral characteristics of the sunlight, the outer

² Additionally nutrient supply was altered, but these aspects aren’t discussed here.

³ Mechanical stimulation, e. g. caused by swaying in the wind, is an important factor affecting morphology, too. In our experiments all plants were staked to reduce mechanical stimulation as far as possible. To achieve comparable stems suitable for the mechanical investigations, all side branches were pruned regularly.

⁴ In this paper only the chambers 1, 4, 5, 7, 8 and 9 are described and discussed

walls of chamber 4 were covered with adequate shading cloths. Chamber 9 was used as a control without any further modifications of the lighting conditions (see Table 1 for details).



Figure 2: Experimental greenhouse with nine growth chambers (left: front view, right: side view). The chambers are about 4,5m high and have a floor space of about 0,9m x 1,2m. In each chamber there are six plants. The dividing walls are made of light tide white boards. The outer walls are made of greenhouse film (folitec UV5.)

In chamber 7 the stems of the plants were wrapped with a combination of two light filtering films that allow predominately far red light to pass (see spectral charts in table 1). Thus the stems were exposed to radiation with a very low R/FR-relation whilst the leaves were exposed to unaltered sunlight⁵. This experimental design is based on findings of Ballare and Scopel [6] and Ballare et al. [7]: When comparing plants grown in un-altered sunlight they discovered that the growth in length is correlated with the R/FR-relation of the horizontal radiation and that this horizontal radiation is mostly absorbed by the young growing stems and less by the horizontally oriented leaves. Hence creating a low R/FR-relation by wrapping the stems with light filters should increase growth in length.

Wrapping the stems in the described manner (see caption of Figure 3) not only changes the light quantity and quality at the stem but also causes some side effects, e.g. mechanical irritations or modifications of the micro-climate at the stem. To be able to further appreciate the influence of the light quality independently from these side effects, comparable experiments with transparent and light tight (black) PVC-film were carried out in chambers 5 and 8.

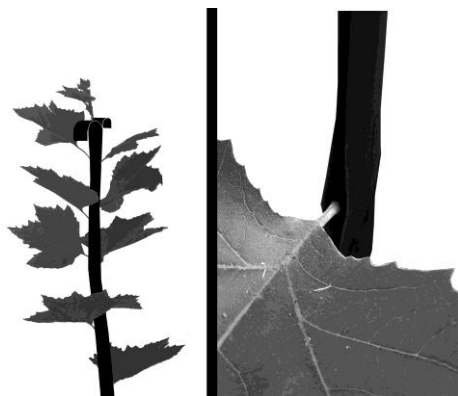


Figure3: Plant stems wrapped with light tight or light filtering film (left: general principle; right: detail). The stems are enclosed by two strips of film that are attached on each other with small straps of Velcro. At the nodes small vents for the petioles were left open. Near the apex, where the internodes are elongating, these vents were formed slot-like to enable a movement of the leaf. The uppermost 2 to 5 cm of the shoot were not wrapped because the young stem and the growing leaves are too delicate in this section. During the growing season the correct fit of the strips was controlled and adapted to the growth progress two times a week. Notice that some unfiltered light may reach the stem in the region of the vents.

During the growing season the diameter of all shoots were measured every three weeks and the degree of slenderness was calculated. In the winter following the growing season the stems were pruned at the base and cut in six to ten sections of adequate length⁶. For most of these sections the structural Young's modulus of elasticity⁷, the narrowest possible bending radius and the amount and arrangement of phloem, xylem and pith were investigated.

The bending experiments to investigate structural Young's modulus were carried out with an experimental setup for 4-point bending with a hanging swing for symmetrical mass application. Up to seven weights were applied manually and the maximum deflection for each weight was measured

⁵ Notice that all chambers are covered with greenhouse film which filters out UV radiation

⁶ For measuring the Young's modulus of elasticity the relation between the length of the section and the diameter has to have more than 20:1.

⁷ For the definition of structural Young's modulus see e.g. Rowe, N. P. and Speck, T. (1998) 'Biomechanics of plant growth forms: the trouble with fossil plants', *Review of Paleobotany and Palynology*, 102, 43-62.

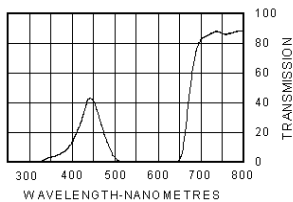
using a dissection microscope. Structural Young’s moduli were calculated from the slope of the linear regression of the applied bending force versus maximal deflection [8] [9] [10]. The axial second moment of area, required for these calculations, was calculated by direct measurements of two diameters at three representative points, assuming an elliptical cross section.

Table 1: The different experimental designs in the nine growth chambers

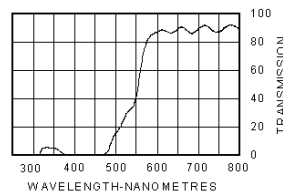
	Number of growth chamber								
	1	2	3	4	5	6	7	8	9
window covering	filter # 707 ¹		filters #707 ¹ + #179 ²	shading cloth		filter #707 ¹			
stem wrapping		filters #707 ¹ + #179 ²			trans-parent PVC		filters #707 ¹ + #179 ²	black PVC (light-tight)	
fertilizer		+				+			
PAR ³ (%)	12	100	3	9	100	12	100	100	100

Annotations

1.) Transmission (%) lee-filter #707



2.) Transmission (%) lee-filter #179



3.) Photosynthetic active radiation relative to control chamber. The intensity of the photosynthetic active radiation was measured with a quantum meter (Apogee Instruments, modell QMSS-ELEC, cosines corrected sensor)

Afterwards these stem sections were bent until breaking in a special bending apparatus causing Euler buckling. The bending apparatus is equipped with a computer interface and is capable of measuring and recording height h , length l and the force F continuously (see Figure 4). In the apparatus the stem sections are fixed between two hinges with a slender pre-bending. By moving the hinges towards each other with a constant speed, the stems bend more and more. Based on the assumption that the stems are bending spline-like the curvature K respectively the bending radius r can be calculated by using a spline-function ($K=12 \cdot h/l^2$; $r=1/K$) (Spatz et al. 1993). In most cases the point of breakage could be identified as a significant and more or less abrupt decrease of the bending moment M ($M=F \cdot h$) in a diagram, were the bending moment is plotted versus the curvature. Additionally all bending procedures were captured on video and in cases of doubt the coherence between the diagram and visually noticeable failure was checked.

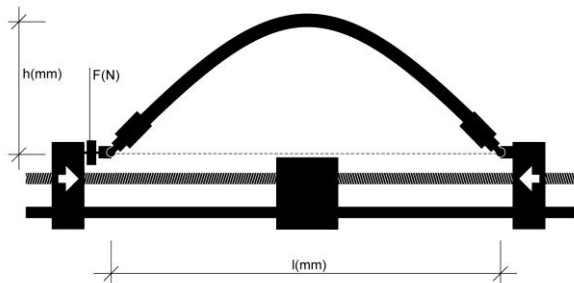


Figure4: Schematic drawing of the bending apparatus for bending up to failure caused by Euler buckling

For the anatomical analysis the stems were cross cut with a saw directly next to the breaking point. After flattening with a razor blade the cut surfaces were stained with phloroglucin-HCl and scanned with a common flat bed scanner (2400dpi). Using the software Labview, the tissues cortex, xylem and pith were manually circumscribed, and the cross section areas of the different tissues and their fractions of the second moment of area were calculated.

Results and discussion

At the end of the growing season the measured morphological characteristics of the stems clearly differed between samples from each chamber. The plants in the control chamber ended up with an average length of $234\text{cm} \pm 31\text{cm}$. The plants whose stems were wrapped with filtering or light tight film (chambers 7 and 8) grew somewhat longer (total length was $254\text{cm} \pm 40\text{cm}$ in both cases) whilst the plants wrapped with transparent film stayed a bit smaller than the controls. With average shoot lengths of $84\text{cm} \pm 8\text{cm}$ the plants in chamber 4 (shading cloth) showed the least growth in length. In contrast, the plants in chamber 1 (light filtering film lee #707) reached more than double the shoot length of these plants ($184\text{cm} \pm 15\text{cm}$). (Ludwig et al., in prep)

The calculated degree of slenderness of the control plants varied achieving values of around 144. The plants in chamber 4 (shading cloth) were a bit more slender whilst the plants wrapped with transparent film (chamber 5) ended up being a little bit less slender. With an average degree of slenderness of 230 the plants in chamber 1 were by far the most slender ones, while the plants wrapped with light tight or filtering film showed slenderness values in a range of around 200.

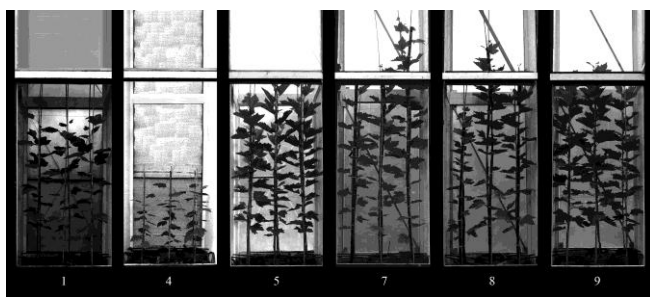


Figure 5: A view inside of the growth chambers at the end of the growing season shows the differences in the development.

The distinct differences between the light grown controls and the shaded plants underline the great importance of the intensity of the photosynthetic active radiation for plant growth. But the differences between chamber 1 and 4 are clearly influenced by a low R/DR-relation. Although the measured PAR in chamber 4 was 3% lower than in chamber 1 (see Table 1) the differences in length and slenderness are so explicit that distinct differences could be expected also at equal PAR intensities⁸.

The decreased length and slenderness of the transparently wrapped stems (chamber 5) can be explained by the fact that wrapping causes a noticeable mechanical irritation of the stems and petioles (thigmomorphogenesis, see e.g. [12]) and constrains the gas exchange of the stem. Although these factors also affect the plants wrapped with light tight or light filtering films, these plants are longer and more slender than the control plants. Only effects caused by the colour of the films are feasible to explain this result. The dark films filter or block the sunlight but alter the temperature, too. High temperatures, especially high temperature peaks on sunny days inside the dark wrappings are quite probable and could affect morphology but were not measured. But as the stems showed typical symptoms of etiolation, we regard light effects as the dominating trigger. Somewhat surprising is the fact that nearly no difference between light tight and light filtering wrapping were found. In both cases total light intensity at the stem was reduced drastically, but only in one case far red light was excluded. Hence our experiments can't answer the question if the observed morphological changes are caused by the reduction of the light intensity at the stem or by a low R/RF-relation at the stem. But at least the results show that a reduction of the light intensity at the stem can cause similar effects than a low R/FR-relation.

In our experiments all plants whose leaves were exposed to full and un-altered sunlight (chambers 5, 7, 8 und 9) regularly showed sylleptic branches which were pruned weekly, but plants growing in filtered or reduced light (chambers 1 and 4) do not branch. This fits with descriptions of shade avoidance reactions that typically are described as a suppression of branching combined with an

⁸ Concerning the measurement of PAR spectral composition of the light is not included in detail in this analysis

enhancement of growth in length, see e. g. [4]). Although exhibiting the typical increase in length and slenderness the darkly wrapped plants (chambers 7 and 8) branched like the control plants. This suggests the hypothesis that branching and growth in length are two aspect of shade avoidance that are controlled separately, the first by the leaves and the second by the stem.

Concerning tissue allocation especially the development of different tissue types along the stem, from the base to the apex, is noticeable. At the basal end all stems developed a very small cross section area of the pith (between 2 and 4 mm²). In chamber 4 (shading cloth) this area stays more or less constant along the whole length of the stems (see Figure 6 top right). In contrast the control plants show a drastic increase in the pith diameter with increasing distance from the base. Only in the uppermost stem parts the pith diameter decreases a little bit again (peak values around 20mm², see Figure 6 top left). The plants in chamber 1 (light filters) showed a similar trend, but here the cross section area of the pith only reached values of around 8mm². Wrapping the stems did not seem to affect the anatomy significantly and the patterns of tissue allocation in chambers 5, 7 and 8 are comparable to those of the control plants.

The radial width of the cortex seems to be more or less the same for all plants. Thus the cross sectional areas of cortex and xylem can be derived from the total cross sectional area and the cross sectional area of the pith. Because the diameters of the stems decrease with the distance from the base the fractions of pith and cortex of the cross section area increase continuously with height and the fraction of the xylem decreases (see cross sections with normalized diameters in Figure 6). These trends are also reflected by the contribution of the different tissues to the axial second moment of area. At the base of the light grown plants xylem often accounts for more than 80% of the axial second moment of the area. These values decrease, sometimes to less than 30% in the upper parts of the same plants. Because of its central location the pith normally doesn't contribute significantly to the axial second moment of area. Only in the most apical stem region the pith can reach a contribution of more than 20%. This trend is less distinct for the plants growing in filtered light (chamber 1) and quite marginal for the shaded plants (chamber 4) (Ludwig et al., in prep.).

Concerning the structural Young's modulus there were no obvious differences between the plants with wrapped stems and the control plants. All light grown plants showed a high Young's modulus between 5500 and 15000 MN/m² near the base and much lower values near the apex (mostly between 2500 and 6000 MN/m²). In chamber 1 (light filters) the basal samples had Young's moduli between 5000 and 8500MN/m². Near the apex these values were a little bit lower with values between 4000 and 6500 MN/m². In chamber 4 the Young's modulus varied considerably with peak values of around 11500 MN/m² near the base and between 3000 and 7000 MN/m² near the apex.

Segments from different heights of the stems and from different chambers showed quite varying fracture patterns. The basal stem parts of the light grown plants seem to be quite ductile and where breaking very slowly, often announced by many tiny pre-fracture events leading to the final break. The fracture surface looks more or less brush-like (Figure 6 middle left). Despite the large diameters of the stems in this stem region, the samples often could be bent to radii narrower than 5cm, sometimes resulting in no breakage at a bending radius of 1,5cm or even smaller. In contrast, the uppermost stem segments of the same plants showed a totally different breaking behaviour. These stem sections broke suddenly and abruptly with an audible crack (Figure 6, middle). These samples normally failed at a bending radius between 6 to 5 cm, despite having a much smaller diameter than the basal stem parts. In chamber 4, the normally quite thin stems typically showed a gradual buckling accompanied by a flattening of the cross section (Figure 6, middle right). With this type of failure it is difficult to identify the point of breakage exactly. The samples typically failed at bending radii somewhere between 2,5 and 1cm. The recognizable pattern in chamber 1 (light filters) was similar to those of the light grown plants but less distinct. Sometimes buckling like in chamber 4 could be observed.

Concerning anatomical and biomechanical properties the total light intensity seems to be the most important parameter. Of course, the ontogenetic stage of stem segments plays an important role as well. High light intensity enhances primary growth and thus is accompanied by a large pith diameter. The older the segment of the stem the more xylem accumulates by secondary cambial growth and the

cross section becomes more and more dominated by the xylem. Our investigations confirm findings that structural Young's moduli are increasing significantly with the contribution of xylem to the axial second moment of area (Ludwig et al., in prep; data not shown; c. p. [10]).

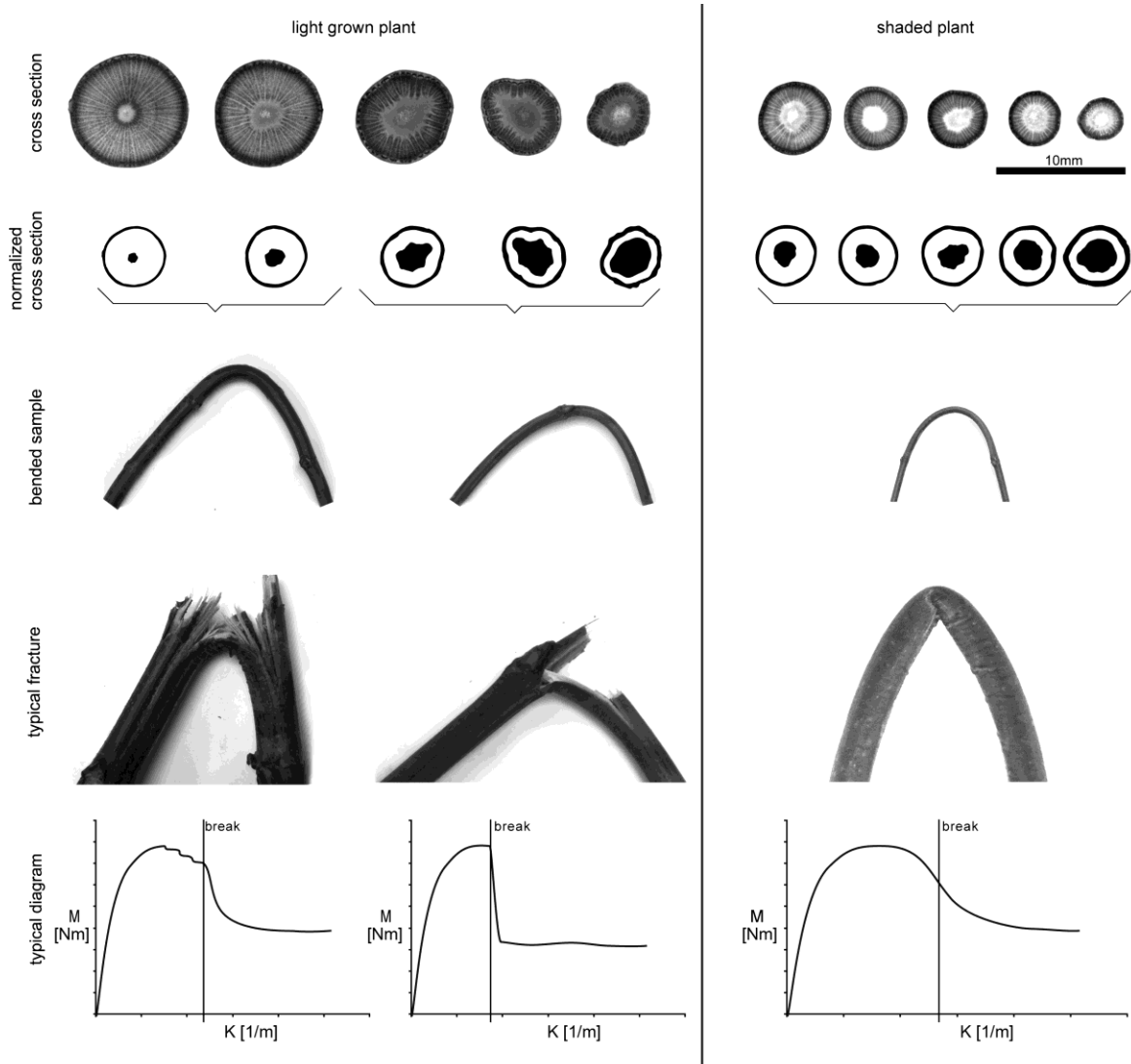


Figure 6: Top: Typical cross sections of a light grown and a shaded stem (cross cuts and cross cuts with normalized diameters); Middle: bending behaviour and fracture patterns of these stem segments; Bottom: Typical diagrams (bending moment M versus curvature K) for these samples.

Fracture behaviour and flexibility seem to be influenced significantly by the contribution of the pith to the cross section area. Whilst the basal parts of the light grown plants break like wooden solid cylinders the comparable segments of the shaded plants are buckling like hollow pipes. The fracture behaviour of the upper parts of the light grown plants (sudden cracks) suggests the hypothesis that the large pith is surrounded by a quite brittle xylem – once the bast fibres failed the whole segment breaks.

Conclusion

Concerning ‘Baubotanik’ needs, especially the darkly wrapped plants exhibit interesting properties because they combine a high degree of slenderness with a high total length⁹. The characteristics of the plants grown in filtered light are quite interesting as well, whilst shaded plants are definitely too short for usage. All stem segments exhibited a surprisingly narrow possible bending radius that is most

⁹ It has to be mentioned that wrapping is time-consuming and definitely not very practicable for mass-production.

likely sufficient for most ‘Baubotanik’-projects. However, this does not mean that all plants and stem segments showed an advantageous bending and breaking behaviour. The basal parts of the light grown plants showed advantageous breaking characteristics because failure is announced by many small pre-fracture events. Though, due to higher Young’s moduli and large diameters, high forces are necessary for bending these stem segments. This can lead to practical problems and obstructions during construction. On the other hand, the thin and young upper parts of these plants can be bent quite easily, although here the breaking behaviour is problematic for the use in ‘Baubotanik’. They break suddenly and unexpectedly and therefore are quite displeasing to handle.

The experiments demonstrate different possibilities to alter the morphology of *Platanus acerifolia* seedlings and highlight the fact that morphological changes always come along with anatomical and biomechanical changes. These changes are sometimes conflicting with the ‘Baubotanik’ demands and thus one has to seek the most useful compromise between morphological and mechanical characteristics.

Acknowledgements

This work is funded by Deutsche Bundesstiftung Umwelt (DBU) and enabled by the broad support from University of Stuttgart and Kulturbetrieb Wagenhallen. Thanks to all members of the Institute of Theory of Modern Architecture in Stuttgart and the Plant Biomechanics Group in Freiburg for their support.

References

- [1] Ludwig, F. (2007): *Bau(m)bionik - Baubotanik, Tragstrukturen aus lebenden Holzpflanzen*. in Bionik und Nachhaltigkeit - Lernen von der Natur, Brickwede, E. h. F., Erb, R., Lefèvre, J. and Schwanke, M., Erich Schmidt Verlag: Berlin, p. 245-253.
- [2] Casal, J. J. and Smith, H. (1989): *The function, action and adaptive significance of phytochrome in light-grown plants*, Plant, Cell & Environment, 12(9): 855-862.
- [3] Gilbert, J. R., Seavers, G. P., Jarvis, P. G. and Smith, H. (1995): *Photomorphogenesis and canopy dynamics. Phytochrome-mediated proximity perception accounts for the growth dynamics of canopies of Populus trichocarpa x deltoides 'Beaupré'*, Plant, Cell & Environment, 18(5): 475-497.
- [4] Taiz, L. and Zeiger, E. (1998): *Physiologie der Pflanzen*, Spektrum Akademischer Verlag: Heidelberg.
- [5] Reams, R. (2005): *Arborsculpture. Solutions for a small planet*, Arborsmith Studios: Williams Oregon.
- [6] Ballaré, C. L. and Scopel, A. L. (1990): *Far-red radiation reflected from adjacent leaves: An early signal of competition in plant canopies*, Science, 247: 329-332
- [7] Ballaré, C. L., Scopel, A. L. and Sanchez, R. A. (1989): *Photomodulation of Axis Extension in Sparse Canopies*, Plant Physiology, 89(4): 1324-1330
- [8] Speck, T. (1991): *Changes of the bending mechanics of lianas and self supporting taxa during ontogeny*, Proceedings of the Second International Symposium SFB 230 (6): 89-96
- [9] Rowe, N.P., Isnard, S., Gallenmüller, F. and Speck, T. (2006): *Diversity of mechanical architectures in climbing plants: an ecological perspective*. in Ecology and biomechanics: A mechanical approach to the ecology of animals and plants, Herrel A., Speck T. and Rowe N.P., Dekker Publishers/Taylor & Francis Group: Boca Raton, p. 35-59.
- [10] Hlawatsch, S., Arno, B. and Speck, T. (1988/89): *Funktionsanatomie und Biomechanik der Grau-Erle (Alnus incana): Vergleich von Pflanzen aus unterschiedlichen Höhenlagen im südlichen Schwarzwald*, Naturf. Ges. Freiburg i. Br.: Freiburg, p. 249-276.
- [11] Spatz, H.-C., Speck, T. and Vogelhehner, D. (1993): *Contributions to the biomechanics of plants. III. Experimental and theoretical studies of local buckling*, Bot. Acta., 106: 193-276.
- [12] Leyser, O. and Day, S. (2002): *Mechanisms in Plant Development*, Blackwell Publishers: Oxford

Impact resistance of hierarchically structured fruit walls and nut shells in view of biomimetic applications

Robin Seidel¹, Andreas Bührig-Polaczek², Claudia Fleck³ and Thomas Speck¹

¹ Plant Biomechanics Group, Botanical Garden, University of Freiburg, Germany;

² Foundry-Institute of the RWTH Aachen, Germany;

³ Materials Engineering, Berlin Institute of Technology, Germany

Abstract

As humans have to protect themselves from the large amounts of energy freed instantaneously, e.g. during a car crash, so some fruits have to cope with the impact on the ground when being shed. Understanding the principles of how combining structure and material in biological constructions yields a fully functional protection layer will allow constructing new lightweight bio-inspired materials of high impact and puncture resistance.

As biological role models serve the *Macadamia* nut with its tough pericarp, *Citrus grandis*, possessing a large spongy mesocarp and *Cocos nucifera*, having a combination of fibrous mesocarp and tough endocarp. All fruits are relatively heavy, lack any aerodynamic adaptation and share the same challenge of having to withstand impact from heights of more than 10 metres.

Conducting high speed camera controlled free fall experiments of *Citrus grandis* from six metres height and comparing the potential energy of the fruits before and after impact (n=13) shows that a high proportion of the energy, possibly up to 90%, is dissipated by the fruit wall and pulp. Compressing the fruit wall in a quasi static test to approximately 50% of its original height yields 50% to 70% energy loss during one hysteretic cycle. The immature fruit wall of *Cocos nucifera* shows a benign failure behaviour with a bell shaped stress-strain-curve having its maximum stress around 15% strain and failure only at up to 40% strain when loaded in tension nearly parallel to the main fibre orientation.

Until today these protective structures have only been used as an inspiration for packaging when seen from a biomimetic perspective. But combining these extraordinary properties of high energy dissipation, benign failure and almost full recovery from large deformations will lead to completely new bio-inspired light weight technical materials.

Introduction

The fruit wall, called pericarp, consists of three layers in all angiosperms: the exocarp as the outermost layer, followed by the mesocarp and the innermost layer named endocarp. In case of nuts the complete pericarp dries out and forms a highly lignified, mechanically very stable shell. In case of drupes only the endocarp lignifies and thereby forms a tough protective layer with the seed surrounded by its thin skin-like seed shell tightly attached on the inside.

Regarding the mechanical properties of nut shells the work of Jennings & MacMillan [1] and Wang & Mai [2,3] on *Macadamia* nuts (*Macadamia* sp.) revealed that the structure of the nut shell is highly optimised for toughness. The results obtained by compression tests on C-ring samples yielded values in the same range as ceramics and glass. Due to the relative low density of the pericarp the *Macadamia* nut shell even outperforms these two technical materials if the specific mechanical values divided by density are considered. Research conducted on other nuts also include *Balanites Aegyptiaca* [4], *Pistacia vera* [5] and roasted shells of cashew nuts, *Anacardium occidentale* [6]. The common aim of these research papers was to determine the mechanical properties in relation to the water content to obtain some information on how to best process the nuts in the food industry. Mostly compression

tests were used and the orientation varied. An interesting aspect in relation to impact is that some authors report a velocity dependence with higher loading velocities (500mm/min) resulting in increased deformation of the nut shell before breakage. In case of *Cocos nucifera* the main interest of research so far has been the mechanical properties of single dry coir fibres as they are used in carpets, ropes [7], and cushions and seat covers in the automotive industries [8]. The Young's moduli of single dried fibres are in the range of 3-6GPa and the strains in the range of 15-47% when tested in tension [8,9]. The importance of the entire hydrated mesocarp as a potential material to withstand impact has so far not been addressed. The mechanical properties of *Citrus* species have not yet been studied in detail.

Summarising it may be said that the investigations on fruit walls so far have mostly had their focus on mechanical issues important to the food and fibre industries and little has been done on the form-structure-function relationship which has been hardly studied at all in *Citrus grandis*, and only to some extent in *Cocos nucifera* and *Macadamia* though all of these fruit walls reveal quite extraordinary mechanical properties. Further no related studies on impact and energy dissipation during impact, which will be mostly achieved by the deformation of the mesocarp structure in drupes and *Citrus*, are available. Hence this represents a very valuable field for basic research as well as providing a promising starting point for the development of bio-inspired materials.

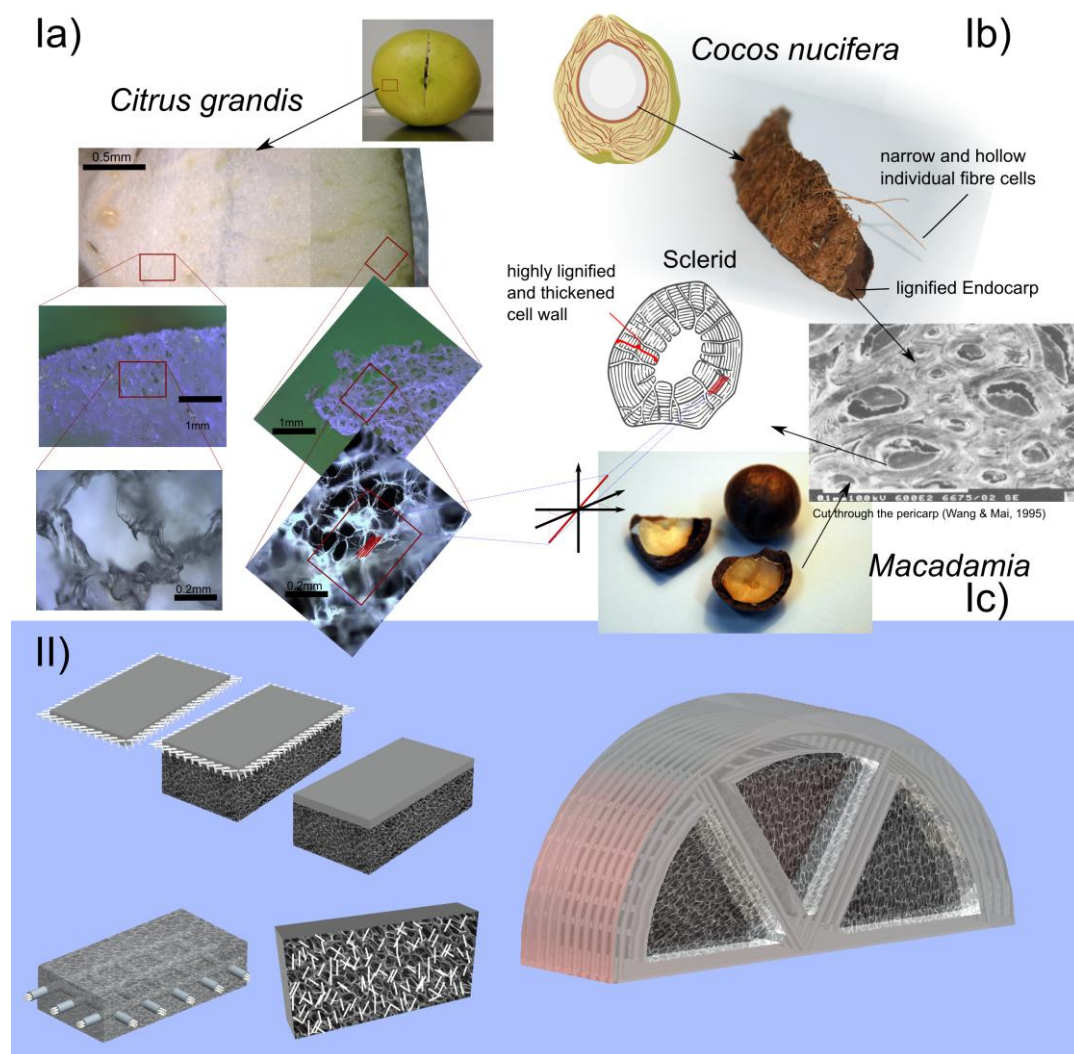


Fig. 1 Biological role models and technical implementation. The hierarchical organisation of fruit walls resulting in either (Ia) a highly damping spongy gradient structure (*Citrus grandis*) or (Ib) a combination of fibrous damping structure and tough shell (*Cocos nucifera*) or (Ic) an entirely tough shell (*Macadamia spec*) are used as biological role models and will be transferred into hierarchically organized technical materials (II) consisting of a solid layer in combination with a spongy fibre reinforced structure ensuring high toughness and high energy dissipation.

Material and methods

Morphology: The pericarp of *Citrus grandis* was cut into semi-thin sections of about 2mm thickness each at different positions on the fruit. The sections were immediately analysed using advanced light microscopy to prevent any artefacts due to dehydration of the tissue.

Dynamic testing: Whole *Citrus grandis* fruits were dropped from heights of 5, 8 and 15 metres onto a grassy ground to mimic the natural condition. The weights of the fruits were in a range of 1.35 to 1.6kg. The fruits were examined afterwards for macroscopical damage. To analyse the potential of the whole *Citrus grandis* fruit to absorb energy during impact free fall experiments were conducted. Single fruits were dropped from six metres onto a PMMA plate, which was allowed to rotate on one side and freely positioned on a force sensor on the opposite side (Fig. 2, left). The fruits' impact behaviour was filmed using two high speed cameras capturing at 250 and 1000 frames per seconds, respectively. The latter camera's path of vision was being guided through a mirror to film the impact from the bottom. This allowed to measure the area in contact and the force during impact (Fig 2, middle). The force was calculated by dividing the moment at the force sensor by the lever arm of the fruit's impact position.

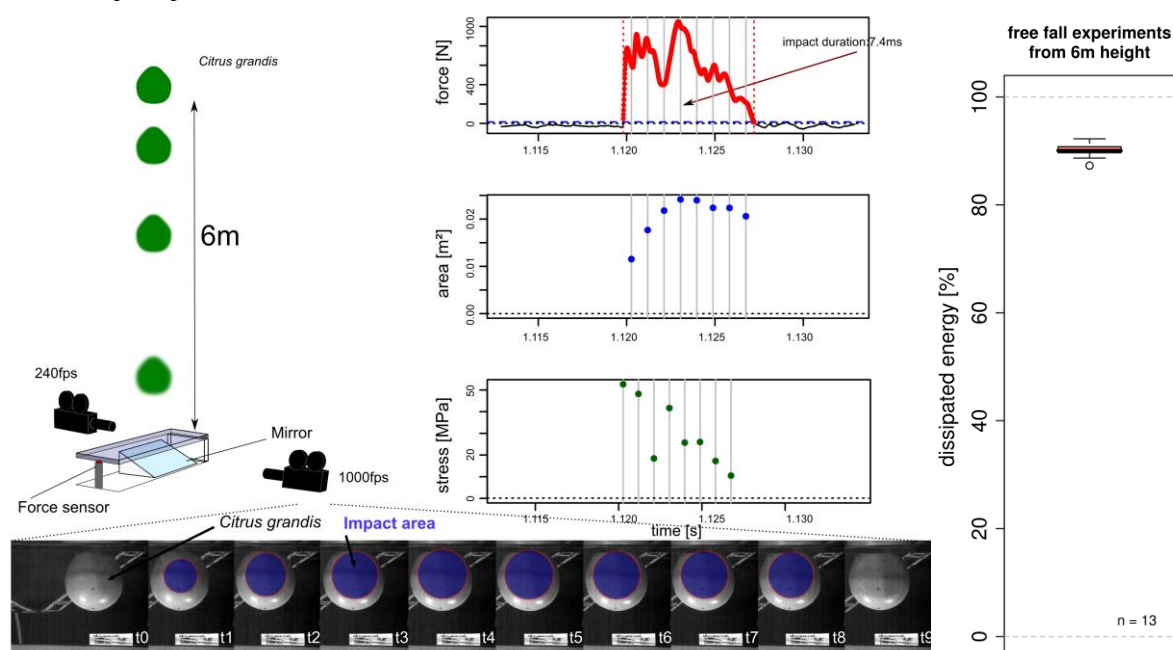


Fig. 2 Free fall setup. Left) Schematic drawing of the free fall experiment. Two high speed cameras were used to record the deformation of *Citrus grandis* during impact from the bottom via the mirror and directly from the side. From the images of the former the area of the fruit wall in contact with the PMMA plate could be measured at 8 timepoints. Combining this information with the forces measured by the force sensor at the same time intervals allowed to calculate the stress in the fruit wall. Right) Dissipated energy calculated from the difference in potential energy before and after impact.

Static testing: To characterise the loading behaviour of the mesocarp of young coconut in an ontogenetic stage shortly before abscission a quasi static tensile test was conducted. Cuboid samples were cut using razorblades with the long axis in parallel to the main fibre direction, which is parallel to the surface of the fruit. The samples were tested using an Instron testing machine along their main axis at a speed of 1.91mm/min. Samples of the spongy part of the pericarp of *Citrus grandis* were prepared and tested in the same manner. To examine the viscoelastic properties of the *Citrus grandis* quasi static testing of the entire pericarp under compression was conducted. Cubes of the complete pericarp were cut using razorblades and tested in compression along the radial axis of the fruit. The maximum compression was set to 50% of the initial height and the speed of the Instron to 5mm/min. Loading was done in 10 steps of additional 5% compression each. After each loading step the position was held for 60 seconds. The same pattern with 5% decompression was used during unloading.

Results and discussion

The fruit wall of *Citrus grandis* is divided into three macroscopically distinguishable parts, the exocarp with the epidermis and multiple compact layers of cells, the mesocarp present as a large spongy middle section and the endocarp consisting of a small dense layer adjacent to the pulp. The light microscopical examination at higher resolutions is shown in figure 1 (left). The epidermis and the collenchymatous tissue beneath contain closely stacked cells.

Immediately underneath the exocarp the cell density quickly diminishes and cells begin to form cavities composing a three dimensional porous spongy tissue. The pore size gradually increases from the outside of the fruit wall towards the inside. The cell walls composing the porous structure show a fibrous composition, though at 200 fold magnification a major orientation of the fibrous structures within the cell walls is not yet distinguishable. Just at the interface with the pulp there is an abrupt change in tissue morphology, changing from a porous structure to a layer of densely aligned cells building a compact tissue for the pulp suspension. The inhomogeneous structure revealed in the morphological analysis is also mirrored in the biomechanical behaviour of the fruit wall. During compression the tissue with the largest pore size compresses the most.

As *Citrus grandis* may fall from heights of about 15 meters, the complete fruit's impact behaviour was tested by free fall. After the first free fall of each fruit no macroscopic damage was perceived. In qualitative mechanical inspection it appeared that the tissue parts in contact with the ground during impact had decreased in stiffness. The second free fall from 15 meters caused the fruit to split open with a straight 7cm crack. The analysis of the structural damage indicates that beside of the crack the exocarp - epidermis and the adjacent tightly packed collenchymatic tissue - and the endocarp - the fruit suspension layer - remain undamaged whereas the porous mesocarp partly collapses. This may be its defined role, dissipating as much energy as possible via large partly plastic deformation during impact. Conducting high speed camera controlled free fall experiments of *Citrus grandis* from six metres and comparing the potential energy of the fruit before and after impact (n=13) shows that 90% of the energy is dissipated (Fig. 2, right). Further there is no decrease in energy dissipation from one to the next free fall dropping the same specimen up to seven times. These large values of energy dissipation correspond well with the values obtained during quasi static testing of the fruit wall of *Citrus grandis* under compression. Compressing the fruit wall to approximately 50% of its original height yields values between 50% to almost 70% energy loss during one hysteretic cycle (Fig 3, B). Quite extraordinary is the elastic potential of the structure as it recovers gradually to 75-95% of its initial height after having been compressed by 50%. In addition to the elastic recovery the fruit wall shows viscoelastic properties (Fig. 3, B). During the loading phase the force generated by the pericarp quickly drops by about 25-30% when the position is kept constant. The reverse effect is visible during the unloading procedure when the pericarp quickly generates higher forces once the position is held constant. The time dependence of the material properties of the porous mesocarp can be explained by a generalized Maxwell model, which consists of a parallel assembly of one elastic spring and a finite number of Maxwell elements composed of a combination of one spring and a dashpot in series. During loading the elastic spring and the Maxwell elements undergo compression until the distance is kept constant. From this point on the springs of the Maxwell elements start to relax completely in a time dependent manner. During unloading the elastic spring still remains under compression whereas the Maxwell elements are being put in tension. Once the motion is stopped again the springs of the Maxwell elements start again to relax completely, which cause the force to rise again. The viscoelastic effects appear to be more dominant in the parts of the tissue with larger pore size.

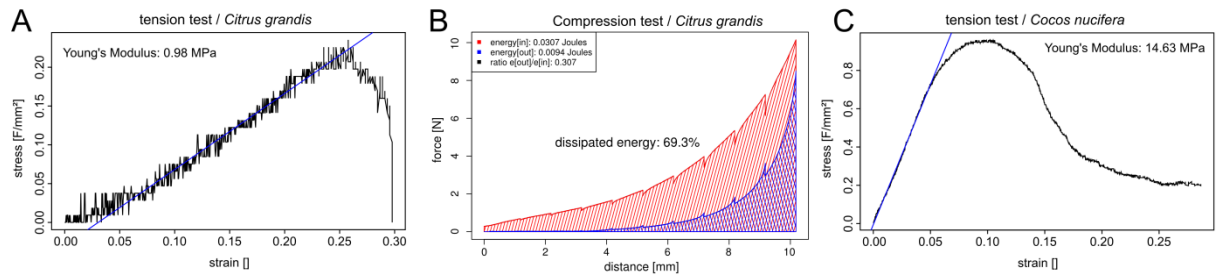


Fig. 3 A) Tensile test of the mesocarp of *Citrus grandis*. B) Viscoelastic compression test of the pericarp of *Citrus grandis*. Position was held constant for 60sec after each compression increment of 5% and each decrement of 5% during unloading. During loading the force drops quickly by about 10% once the position is kept constant; during unloading the force increases about 10% once the position is kept constant. C) Tensile test of the immature fibrous mesocarp of *Cocos nucifera* along the main fibre direction. After the yield point the curve becomes bell shaped with a long tail at low force.

The Young's modulus of *Citrus grandis* is surprisingly low with values ranging from 0.14MPa to 0.45MPa with a mean of 0.20MPa when tested in compression along the radial axis of the fruit and 0.39 to 0.98MPa when tested in tension normal to the radial axis of the fruit (Fig. 3, A). The pericarp of *Citrus grandis* is capable of withstanding strains from 30% to almost 60% when tested in tension.

The Young's modulus of the immature *Cocos nucifera* mesocarp obtained from specimen loaded in tension nearly parallel to the fibre orientation lies in the range of 10.4MPa to 14.6MPa (Fig. 3, C); these values are much lower than the reported 3-6GPa [8,9], which may be due to reduced lignifications of the fibres at this stage as their maturation process has only just started. In contrast to the fruit wall of *Citrus grandis* the samples of *Cocos nucifera* show benign failure behaviour with a bell shaped stress-strain-curve having its maximum stress at 10% to 20% strain and failure at 29% to 40% strain. There is a drastic difference between the composite mesocarp of the coconut tested here and single dried fibres [9], which do not exhibit this bell shape curve, but rather have some hardening effect after an initial elastic region followed by an abrupt rupture of the single fibre.

The fruit walls of *Citrus grandis* and *Cocos nucifera* both exhibit properties which are of high interest for the development of biomimetic impact resistant structures: *Citrus grandis* shows very high deformations of up to 60% strain until failure and large energy dissipation during loading and unloading, combined with impact resistance when being dropped from significant heights. Further the spongy structure is capable to recover its shape after loading. The fruit wall of *Cocos nucifera* having a fibrous matrix in contrast to the spongy mesocarp of *Citrus* also allows for large deformations of up to 40% strain but reveals a benign failure behaviour due to the successive rupture of single fibre strands. As impact not only causes compression of the tissue along the main axis of loading but also tension normal to this axis, having a fibrous matrix aligned in parallel to the surface seems to be a very 'clever' way to enhance the mechanical strength of the tissue to withstand impact. From a structural point of view the fruits achieve their special mechanical properties by hierarchical structuring. The lowest level of hierarchy in biological materials always present is the molecular level, though not of main interest within this study. In case of *Citrus grandis* the behaviour of the whole structure is dependent on the structure and the material properties of the single cell walls as well as on the porous spongy structure formed by multiple cell walls on the higher structural level. In case of *Cocos nucifera* the material properties can be adapted by changing arrangement and stiffness of single fibres and of the fibre-strand- matrix-combination at the next hierarchical level.

As discussed by Wang *et al.* (1995) the *Macadamia* nut shell is highly optimised for toughness. Properties very similar to the *Macadamia* can be predicted for the tough endocarp of the coconut as well, as it has a very similar structure using the same type of highly lignified cells.

Conclusion

Until today fruit walls have only been used as an inspiration for packaging when seen from a biomimetic perspective. But combining these extraordinary protective properties of high energy dissipation, benign failure behaviour and almost full recovery from large deformations will lead to new bio-inspired light weight technical materials by combining the high energy absorption outer layer with a very tough puncture resistant inner layer. *Cocos nucifera* seems to be the best natural role

model for man-made impact resistant structures. Though as impressively shown by *Citrus grandis* there are multiple ways to achieve high energy dissipation. In their hierarchical structures, biological materials make use of cellular foams, spongy structures, laminates, fibres and various combinations of these structures on different mechanical levels. The investment casting process foreseen will allow modelling of open-pore sponge structures, as well as the integration of fibres. The transfer of the naturally-occurring, organic materials to the technical materials of the metallic cast alloy and the fibre materials (metal, glass, ceramics, polymer) will be one of the major challenges in the technical transfer.

Potential applications for biomimetic impact resistant composite materials envisioned are for example the transportation of dangerous goods, e.g. explosives or hydrofluoric acid, space station protection against meteoroid impact, helmets and other protection wear, as well as impact protection of vehicles.

Acknowledgements

We would like to thank the German Research Foundation for the funding of this project as part of the Priority Program 1420 “Biomimetic Materials Research: Functionality by Hierarchical Structuring of Materials”.

References

- [1]. Jennings, J.S. and Macmillan, N.H. (1980): *A tough nut to crack*, Annals of Botany. 46: 313-321.
- [2]. Wang, C. and Mai, Y. (1995), *Deformation and fracture of Macadamia nuts Part 2: Microstructure and fracture mechanics analysis of nutshell*, International Journal of Fracture: 69, 67-85.
- [3]. Wang, C. And Mai, Y. (1995): *Deformation and fracture of Macadamia nuts Part 1: Deformation analysis of nut-in-shell*, International Journal of Fracture: 69, 67-85.
- [4]. Mamman, E., Umar, B. and Aviara, N. (2005): *Effect of Moisture Content and Loading Orientation on the Mechanical Properties of Balanites Aegyptiaca Nuts*, Agricultural Engineering International: The CIGR Ejournal 7, Manuscript FP 04 015.
- [5]. Ozden, K. and Alayunt, F. (2006): *The Determination of Some Physical Properties of Pistachio vera L.*, Pakistan Journal of Biological Sciences: 9(14), 2612-2617.
- [6]. Oloso, A. O. and Clarke, B. (1993): *Some aspects of strength properties of Cashew nuts*, Journal of agricultural engineering research: 55, 27-43.
- [7]. Varma, D.S., Varma, M. And Varma, I.K. (1984): *Coir fibers: Part I: Effect of Physical and Chemical Treatments on Properties*, Textile Research Journal. 54: 827-832.
- [8]. Goulart Silva, G., De Souza, D.A., Machado, J.C. and Hourston, D.J. (2000): *Mechanical and thermal characterization of native brazilian coir fiber*, Journal of Applied Polymer Science. 76: 1197-1206.
- [9]. Kulkarni, A.G., Satyanarayana, K.G., Sukumaran, K. And Rohatgi, P.K. (1981): *Mechanical behaviour of coir fibres under tensile load*. Journal of Material Science. 16: 905-914.

Biomimetics in architecture – inspiration from plants

Petra Gruber¹

¹ *Transarch, office for biomimetics and transdisciplinary architecture
Zentagasse 38/1, 1050 Vienna, Austria, peg@transarch.org, +43 699 19678151*

Abstract

Engineers, designers and architects often look to nature for inspiration, aiming at innovation and the improvement of architectural quality. In several design studies, supervised by the author at the Vienna University of Technology in recent years, biomimetics by induction (innovation process starting from a natural phenomenon to an architectural interpretation of an abstracted principle) was successfully applied in architectural design. The design program “Biomimetics design exercise” delivered insights into the transformation process as well as the applicability of natural phenomena in architecture. In this paper the focus lies on the realm of plants. Some functional requirements and environmental conditions of plants are very similar to those of houses, and thus can deliver usable principles for architectural problems. A discussion of historic plant-inspired architectural projects frames the presentation of a number of current students designs.

Introduction

The biomimetic approach lends itself for application in architecture, where novel solutions are important for various reasons. First of all, architects are always expected to deliver creative solutions differing from the ones before. But innovation in building is also needed to tackle problems that growth of cultural environment poses to society – urbanisation, climate change, loss of biodiversity, exploitation of natural resources to name a few. Built environment is estimated to have a share of 50% of the worlds energy and resource use [i], and thus is an important field for efforts in ecological and sustainable design. The author has successfully applied biomimetics as innovation method in the architectural context in many studies and design programs at the Vienna University of Technology and other architecture schools. In previous work [ii] an overview of biomimetics in architecture was given.

At all times architecture was strongly interrelated with the plant world.

Until today **plants deliver material for building**, and the efficiency of natural materials in terms of structural behaviour versus material use is unchallenged. In many regions of the world self-building of houses with natural materials is still common, and subtle technologies for the processing of these materials have been found. Exploitation of the environment has already resulted in a worldwide lack of natural building materials. Industrialised production and processing of plant material for building purposes and biofuels worsen the situation. Building, no matter if individual or industrialised, contributes considerably to the rapid loss of global natural environment and biodiversity.

As a result today we face the situation that increased use of natural materials, which is basically beneficial for the environment may lead on a larger scale to increased environmental damage.

The **use of material defines architectural construction and form**. In the history of architecture we find countless examples for the interrelation between material, construction and form of buildings, even if the connection between these aspects is never as strong and present at all structural scales as in living organisms. On the macroscopic scale, material and its inherent properties define the building. This interconnection becomes clearly visible with the transfer of formal characteristics to new building materials. The use of floral motives in Egyptian stone columns refers to the use of palm trees and reed bundles, that may have been used as structural elements [iii]. The formal characteristics of the classic

Greek temples (that are still used even today when “classic” impression has to be communicated) were developed in a transfer from wooden buildings to stone masonry.

As other natural phenomena also do, **plants deliver archetypes**, ready for imitation and interpretation. Portoghesi states “...*the column becomes the metaphor and abstract replica of the tree but also of the body*”. He presents the spiral columns of the Roman basilica St. Peter, pergola as representation of the vine, and refers to branches as ideal models for cantilevers etc. Antoni Gaudi found his own unequalled and expressive way of translating natural models into refined architectural form.

Especially in the Art Nouveau movement floral patterns were transformed into architectural elements, in functional parts like railings or as mere decoration. “*In architecture as well as in living beings, decoration as an element of self-representation serves to identify parts, reveal their hierarchy and even their stages of development.*” Portoghesi also states the **importance of appearance** in both nature and architecture as basis for all interaction between living organisms and organic and inorganic environment, that is among other factors determining form.

Citing the famous D’Arcy Thompson [iv] about **analogy**: “Nature seemed to work as if form was the result of function times economy. When these principles were applied to engineering structures like bridges, they were found to work in the same way and produce similar or analogous forms.” There is a commonly acknowledged analogy between the requirements that plants and buildings have to fulfil.

The notion of a **specific similarity between the problems and qualities of plants and houses** was also stated by George Jeronimidis in discussions about the overlaps between nature and architecture., initiating many of the thoughts mentioned in the following.

The most important aspect that relates the plant realm to architecture is that as a general rule **plants and architecture do not move**. Higher plants and houses usually stay where they grew up respectively where they were built. For the comparison presented in this paper the focus lies on the biological species and kinds of architecture that share this aspect, neglecting all existing exceptions that do move like for examples algae and caravans.

Immovability implies exposure to environmental conditions on the specific site, the necessity to adapt to the potentially changing availability of resources, stress, energy and other organisms. So what are the strategies, that have evolved in the plant world to cope with this situation, and what do we find in architecture?

Plants have developed very **efficient structures**: differentiation of cells has resulted in lightweight construction systems that are well adapted to different load conditions, but dynamic wind loads, the weight of fruit or the weight of snow for example can still lead to structural failure. Before breaking, plant parts use **flexibility** to give way to the stressing factor. According to Vogel [v] branches of trees and leaves move and twist in the wind to reduce drag. Some palm trees are even flexible enough to survive the destructive force of tsunamis. Constructive aspects are therefore interesting to investigate and transfer to architecture and construction. Nachtigall [vi] has described many analogies between constructions in nature and buildings in his book *Baubionik*. The most famous analogy to follow is the grassblade as tower, an example widely discussed already by Lebedew [vii], Vogel and Nachtigall. Even if a direct comparison of the mechanical behaviour would be wrong, there are still lessons to learn concerning adaptation and differentiation of structures with a high slenderness ratio. **Macroscopic structuring** of plant parts, folding structures and mechanisms are an inspiring field for architects and designers. The architect Biruta Kresling has devoted her research efforts to folding structures in nature, and based on her work the author has participated in the development of designs for a lunar base [viii]. Design exercises in biomimetics guided by the author at the Vienna University of Technology have explored the architects interest to translate aspects found in nature. A comparative view on biomimetic design studies was carried out earlier [ix].

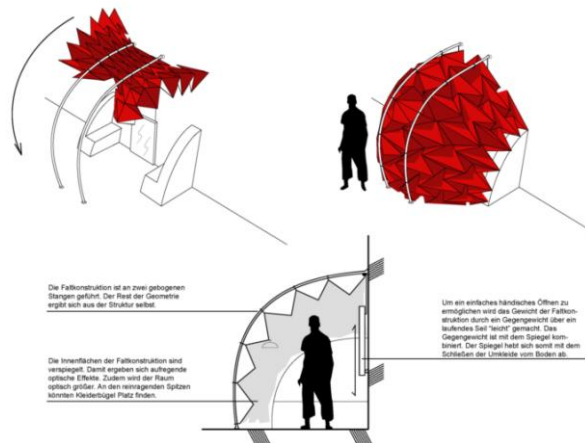


Fig. 1 Design of a changing room inspired by folding structures, Tobias Eglauer.

Mechanisms found in the plant world were also used as inspiration for spatial solutions. The technology of pneumatic buildings seems to be suitable to translations from the plant realm.

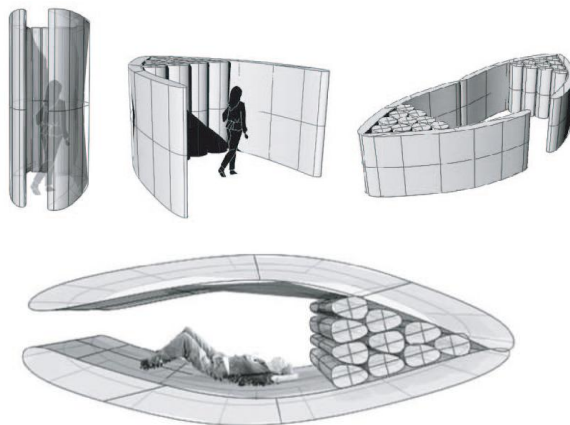


Fig. 2 Pneumatic spatial element, inspired by the mechanisms found in the Venus flytrap, Ariana Morina.

The group around Thomas Speck investigates on a microscopic scale as well, delivering insights about **gradient design** and **self-healing** as the most important principles being transferred to novel architectural solutions, for example the development of a self-healing membrane for pneumatic structures.

Analogies in construction were used in the history of architecture, but linked to the natural model more by analogue problems than by purposeful biomimetic transfer. Portoghesi presents among other examples the development of Islamic cupolas, as being obviously inspired by cacti figs and other fruits.

The famous 67.31m high eight-sided wooden pagoda of Foguang Si at Yingxian in China of 1056 is known for a double ring structure, similar to principles found in horsetail. The same plant has together with others served as model for the “technical plant stem”, a genuine biomimetic product representing a fibrous compound material made by braid pultrusion technology [x]. Based on this information, a student's project tried to integrate the growth process of horsetail to develop things further.

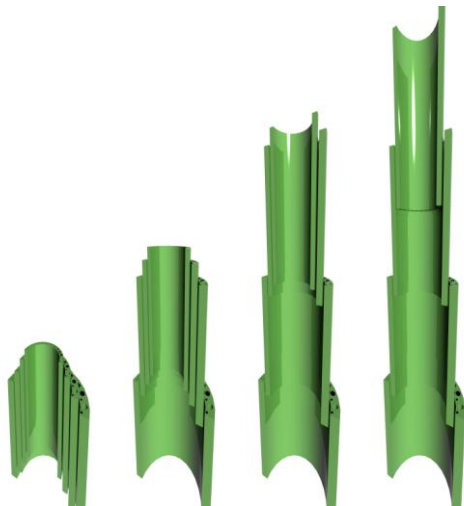


Fig. 3 Growth of building part inspired by the growth process in *Equisetum*, Katharina Gal.

Efforts in lightweight design and strict separation of compressive and tensile forces has resulted in the development of the so-called form active constructions, membrane and net structures. Frei Otto and his Institut für Leichte Flächentragwerke investigated natural constructions and developed membrane structures to a novel building typology [xi].

Interesting features of plants on the **scale of material** could deliver new building materials. The introduction of hierarchical structuring to otherwise homogenous materials could bring enhanced properties. For many reasons, some of them related to the processing, composite materials are only slowly introduced in architecture. Fibrous structures in plants do serve specific functions, and some of the tasks relate to the environmental conditions. Pinecones for example do open and close according to aerial humidity. This effect was exploited in the design study of a facade system with passive regulation of opening and closure.

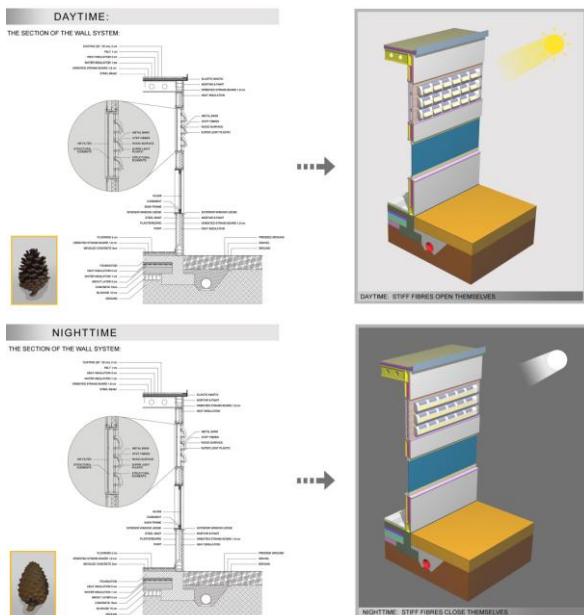


Fig. 4 Passive opening and closure of a facade, inspired by pinecones, Isilak Sencer.

On a **nanometre scale**, surface properties of plants are transferred in functional technical surfaces. The most famous biomimetic development is the Lotus effect®, that is introduced in building industry in many forms - wall paint, glass surface and coatings to name a few [xii].

Growth patterns are influenced by load conditions, and lead to **adapted geometry**, where form follows stress. Claus Matthecks computational optimisation methods exploit the principle of even stress distribution [xiii] in trees. In architecture, the tendency to have specific solutions rather than mass production has until now prevented optimisation methods like this to succeed. Growth algorithms and evolutionary processes are introduced in architectural design methods with great

success [xiv], but the transfer to other than proto-architectural projects is still difficult due to lack of new building technologies that resemble more to growth than mere addition of elements.

The diverse solutions for **anchoring in the ground** are specific for the plant world, but are not yet exploited for architectural translation. The “foundations” of plants do also fulfil the function of supply, and thereby adapt to both structural requirements and distribution of resources in the ground. For sufficient **resource supply** specialised structures have to cover a large enough area or volume of the environment. Plants have to rely on the local availability of solar energy, water, nutrients and air to survive, and have managed to develop strategies to overcome hard times or cycles of change. The embedding into ecosystems is advantageous and can be compared to architecture integrated into supply and disposal networks. Buildings rely on supply networks, infrastructure delivering matter and energy for operation – water, gas, oil, electricity etc. Together with integration in these systems dependency increases, making current urban structures most vulnerable in terms of supply infrastructure. Tendencies towards autonomous building units have been investigated since at least the 1960s. Paolo Soleris suggestions for the so-called arcologies are an impressive example of futuristic high density settlements [xv]. Current developments towards passive house and plus energy house concepts show consciousness and necessity to make buildings more autonomous, and at the same time regional supply systems are increasingly introduced.

Another functional aspect linking architecture to the plant realm is the **occupation and use of space**. If we oppose individual organisms to buildings and species to architectural typologies, we may investigate the use of space on a ontogenetic or individual level as well as on the phylogenetic, or typological level. Strategies to exploit space as efficiently as possible are needed in order to optimise the relation between elements and structure or supply efforts, to increase chances to survive. Spatial competition in plants exists on many hierarchical levels: for example densely packed cells on a leaf surface **compete for solar energy**, the distribution of branches and leaves on a tree shows optimisation for maximal exposure to the sun, the trees compete with other species again for light. Packing of seeds is another inspiring topic, that is being investigated by architects as well.

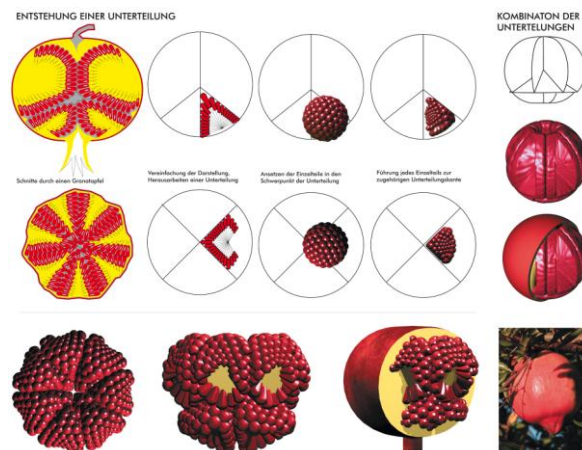


Fig. 5 The packing of the seeds in pomegranate fruit was investigated, without direct transfer to an architectural application, Laurenz Andritz.

In building it is important to have sufficient light in interior spaces, wherever the climate allows for openings. In Western countries sophisticated rules define the density of built environment, especially in urban areas. The buildings surface to volume ratio has to allow sufficient windows for the users to feel comfortable. Spatial competition between buildings does exist at the border to interesting areas, for example at waterfronts or parks. The density of packing of living space is also a matter of culture. Packing of living space has been experimented with since industrialisation and urbanisation. Examples for the biomimetic transfer of plant geometries to floor plans intend to produce high quality space rather than minimal housing. The use of hexagonal geometries for floor plans was investigated in many architectural projects throughout the 60ies and 70ies, and was meant to deliver an efficient and organic ordering system, neglecting the fact that the human orientation system is based on right angles. The current developments of tectonic landscape-like architectures dissolve the classic

separation of building elements, and the notion of space and openings has evolved from the two-dimensional plan to four-dimensional creation of “event spaces” with time as ordering element.

Both, plants and architecture, **change the environment**. The sheer existence of plants and houses has a wide range of consequences on the surroundings, providing a change in many respects.

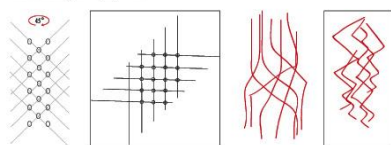
Both architecture and plants **deliver space** for other organisms. The creation of habitats by or in plants may not be their top priority, but symbiotic arrangements and the formation of ecosystems are crucial for the survival. Coevolution may be responsible for the “design” of certain constructions and forms of parts built especially for contact to insects, for seed delivery or pollination. The “space between” plants or plant parts is where activity can happen, and where functions like protection, shelter, meeting, feeding etc. takes place. Hollow trees, for example the *Pinus longaeva* in the US and the baobab in Africa, were used as homes. For humans, trees offer shelter from the sun and the rain.

In architecture the space between buildings is very often not designed but a leftover void with no spatial quality to enable activity. Architecture delivering high quality space not only inside but for the outside as well was achieved in many traditional building systems, but seems to have been lost in the current way of building. Many urban areas are developed for cars more than for people, and the outdoor quality of urban space is no longer attractive for humans. Interdependency of buildings in terms of mutual beneficial spatial arrangement is not considered a standard design task. More often, buildings seem to be entirely ignorant of the surrounding environment. The reintroduction of activity space for people in built environment and the outside space delivered by buildings should be a major concern for architects and decision makers.

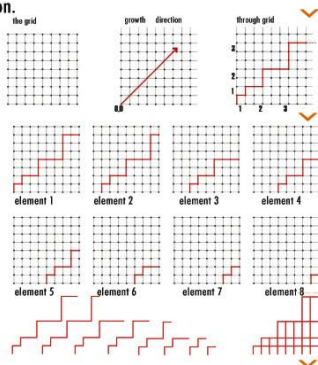
Shelter from adverse outside conditions is a basic function of architecture, and examples for shelter and protection relate directly to the requirement in the plant world to cope with a given environment. Protection measures are needed to withstand intense sun, UV radiation, humidity, dehydration, toxic or damaging substances, enemies, etc. The so-called old man cactus, for example, is protected from intense sunlight by its white long hairs. The natural pattern of these hairs and the function is interpreted in a proposal for a sunshade system that can be added to a conventional building facade [xvi].

//abstraction phenomena.

The pattern meets repetition,
thus creating an algorithm.



///composition.



////3d transformation.

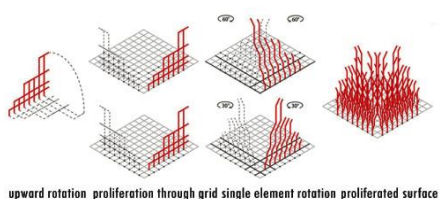


Fig. 6 Abstraction of hair pattern found in the Old mans cactus. Konstantin Trpenoski

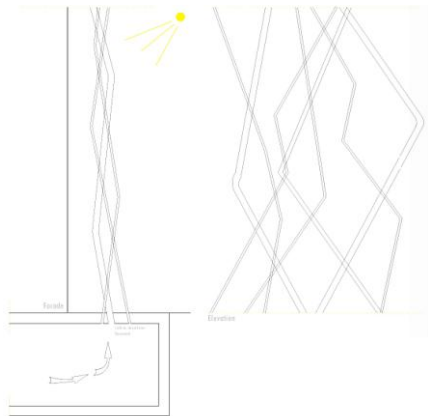


Fig. 7 Cactus facade as additional architectural sunshade layer.

The function of water storage and protection from sun was the main idea of a students project applying the lithops water storage cells to architectural skins. The technical solution is not elaborated, but the idea of a facade system controlling solar energy input, transparency and humidity for the internal space is well worth pursuing.

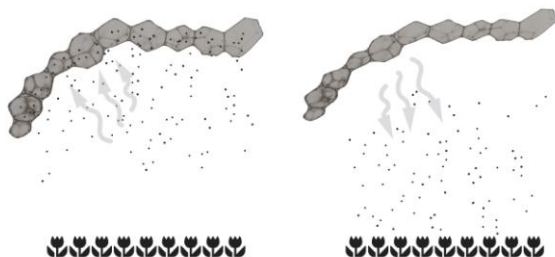


Fig. 8 Facade system inspired by water storage cells of Lithops. Water evaporates through a semi permeable membrane. Cornelia Steiner.



Fig. 9 The same system applied to a conventional glass facade could help control transparency as well as internal climate.

In the world of plants, the problem of immovability is only overcome by propagation. Strategies to spread seeds are diverse and well investigated. Building typologies seem to spread regionally as well, but the mechanisms of information transfer in a cultural environment work entirely different. After cultural landscape has spread all over the planet, we have to **reintroduce nature** into our artificial environments again, to increase quality of life for inhabitants, who have not yet adapted to the new environment. Most plants – in spite of their intense competition - are peaceful and simple to accommodate cohabitants for humans, and therefore ideal to combine with architecture. The integration of phenomena from nature shall enrich the sensory perception by visual, acoustic, tactile and olfactory stimuli, which have been lost in the urban environment. Some current architecture projects literally build for plants in providing not only the space but structural support. The Expo 2000

project of MVRDV in Hannover stacked different landscapes on each other in a multi-storey building. The green walls of Patric Blanc in Paris are another example for the increasing efforts to integrate natural elements in an urban environment. The newly defined field of Baubotanik even integrates living plants in buildings [xvii].

Conclusion

There are many overlapping fields between architecture and the plant realm. As there is a common analogy between the requirements that plants and buildings have to fulfil some of the solutions that have evolved are applicable to architecture, using a biomimetic approach for information transfer. This implies going beyond the phenomenological approach and using quantitative analysis methods from natural and engineering sciences. The selected studies, that were carried out under the supervision of the author, illustrate the findings and present an architectural approach, that hopefully inspires scientists to share their expertise and collaborate in interdisciplinary projects in the future.

References

- i. Edwards, B., International House, London (Ed.) (2001): AD Architectural Design 71, *Green Architecture*. John Wiley&Sons Limited, Bognor Regis, West Sussex.
- ii. Gruber, P. (2008): *Biomimetics in architecture [Architekturbionik] Architecture of life and buildings*. Doctoral thesis, Vienna University of Technology.
- iii. Portoghesi, P. (2000): *Nature and architecture*, Skira editore, Milan.
- iv. Thompson, D'Arcy W. (1992): *On Growth and Form*, The Complete Revised Edition. Dover Publications Inc., New York.
- v. Vogel, S. (1998): *Cats' Paws and Catapults, Mechanical Worlds of Nature and People*. W.W.Norton & Company, New York, London.
- vi. Nachtigall W. (2005): *Bau-Bionik, Natur, Analogien, Technik*. Springer, Berlin, New York, Heidelberg.
- vii. Lebedew, J.S. (1983): *Architektur und Bionik*. Verlag MIR, VEB Verlag für Bauwesen, Moskau, Berlin.
- viii. Gruber, P., Imhof, B., Häuplik, S., Özdemir, K., Waclaviceka, R., Jeronimidis, G., Perino M. A. (2006): *Lunar Exploration Architecture, Deployable Structures for a Lunar Base, Study for Alcatel Alenia Spazio*, Vienna, 2006
- ix. Gruber, P. (2008): *Transfer of nature to architecture - analysis of case studies*. In: Biological approaches to engineering, Inst. Sound Vibr. Res., Proc. BAEC proceedings, p. 58-61.
- x. Milwich, M., Speck, T., Speck, O., Stegmaier, T. & Planck, H. (2006): *Biomimetics and technical textiles: solving engineering problems with the help of nature's wisdom*. Am. J. Bot. 93. p.1455–1465.
- xi. Otto F. et al. (1985): *Natürliche Konstruktionen, Formen und Strukturen in Natur und Technik und Prozesse ihrer Entstehung*. Deutsche Verlags-Anstalt GmbH, Stuttgart.
- xii. Gebeshuber, I.C., Aumayr, M., Hekele, O., Sommer, R., Goesselsberger, C.G., Gruenberger, C., Gruber, P., Borowan, E., Rosic, A. & Aumayr, F.: *Bacilli, green algae, diatoms and red blood cells – how nanobiotechnological research inspires architecture*. In: Bio-Inspired Nanomaterials and Nanotechnology, Yong Zhou (Ed.), Nova Science Publishers, 2009, in press
- xiii. Mattheck, C. (1997): *Design in der Natur, Der Baum als Lehrmeister*, Rombach GmbH Druck- und Verlagshaus, Freiburg.
- xiv. Hensel, M., Menges, A., Weinstock, M. (Eds.) (2004): AD Architectural Design Vol 74 No 3, *Emergence Morphogenetic Design Strategies*, International House, London, John Wiley&Sons Ltd., Chichester, West Sussex.
- xv. Soleri, P. (1969): *Arcology: The City in the Image of Man*, Cambridge, Mass.
- xvi. Gruber, P. (2009): *Ideas for Space – Bioinspired Architectural Design*, in: „Bionik: Patente aus der Natur“; Kesel A., Zehren D. (Eds.) Bionik-Innovations-Centrum Bremen 2009
- xvii. <http://www.baubotanik.de/> [06/2009]

8. Ecology and Evolution

Geometry of folds, geometry of leaves

Etienne P. Couturier, Sylvain Courrech Dupont et Stéphane Douady

Laboratoire MSC, UMR CNRS - Université Paris 7 Denis Diderot

Abstract

Human is one of the rare animal which can identify plants thanks to their leaf shape. Insects recognise plants thanks to their flower because they are all identical among one species. In contrary Leaves can be very different even on the same branch of one plant. The evolutionary interest of leaves is a great surface to catch light of the sun to perform photosynthesis [1], and not the detail of their shape. In temperate climate, where dry and cold season alternate with more humid and warm season, a particular strategy govern leaf development. They grow folded in the bud during winter, so they minimize their exposure and loss of water and maximise their surface ready for opening in spring¹. Their fold geometry in the bud will decide their later shape. Leaf shape is then an indirect evolutionary consequence of bud filling. In this article, we show how different types of folding create different type of leaf shape.

Introduction

An important idea of plant development is reiteration. For many species, a branch is like a smaller tree growing on a tree [3]. At another scale, development of leaf is also a reiteration mechanism. Primordia arise as a little bump on the meristem. Then lobes are like second order primordia protruding from the first growing primordia. At gene's level, the same gene are expressed in both case: the gene KNOX is expressed both in the primordia and in the lobes, the gene CUC is expressed at the separation between the primordia and the meristem, and at the separation between the lobes [4-5].

The initiation of the growth of branches, and the growth of lobes is rather well-known. What coordinates the growth of different branches are environmental conditions. What coordinates the growth of lobes is unknown. In a previous article, we have proposed a new hypothesis to explain how different lobes coordinate their growth: lobes grow until they fill the space at their disposal in the bud [6]. We have explained how the shape of leaves is influenced by this effect and by another one: Leaves grow folded in the bud [7-8]. The simplest way of being folded is the case of maple leaves. Maple leaves have generally nine main folds, 5 peak folds, on the main veins, and 4 valleys, or “antifolds”. They all originate from the same point at the petiole. The volume that the folded leaf fills is half an ellipsoid (Fig. 1a). The folded leaf margin is situated on a plane at the middle of the bud (Fig. 1a). The result is the same as if you fold paper and cut it along a line. When you unfold, each time you had a fold, you have now either a sinus or a lobe (Fig. 1b-c). We have called these leaves “kirigami”, which means “cut-folds” in Japanese. We have found that these leaves margins can be refolded on a line even when they are mature (Fig. 1 e-f) [6]. In this text we show how different kind of folds and volumes to fill can change shape of leaves, even on closely related plants.

¹ In tropical climate, lobed leaves are much rare than in temperate ones [2]. Some folded leaves are present nevertheless (*Gunera manicata*, *Tetrapanax papyrifer*). The evolutionary interest may be to protect young lamina against insects.

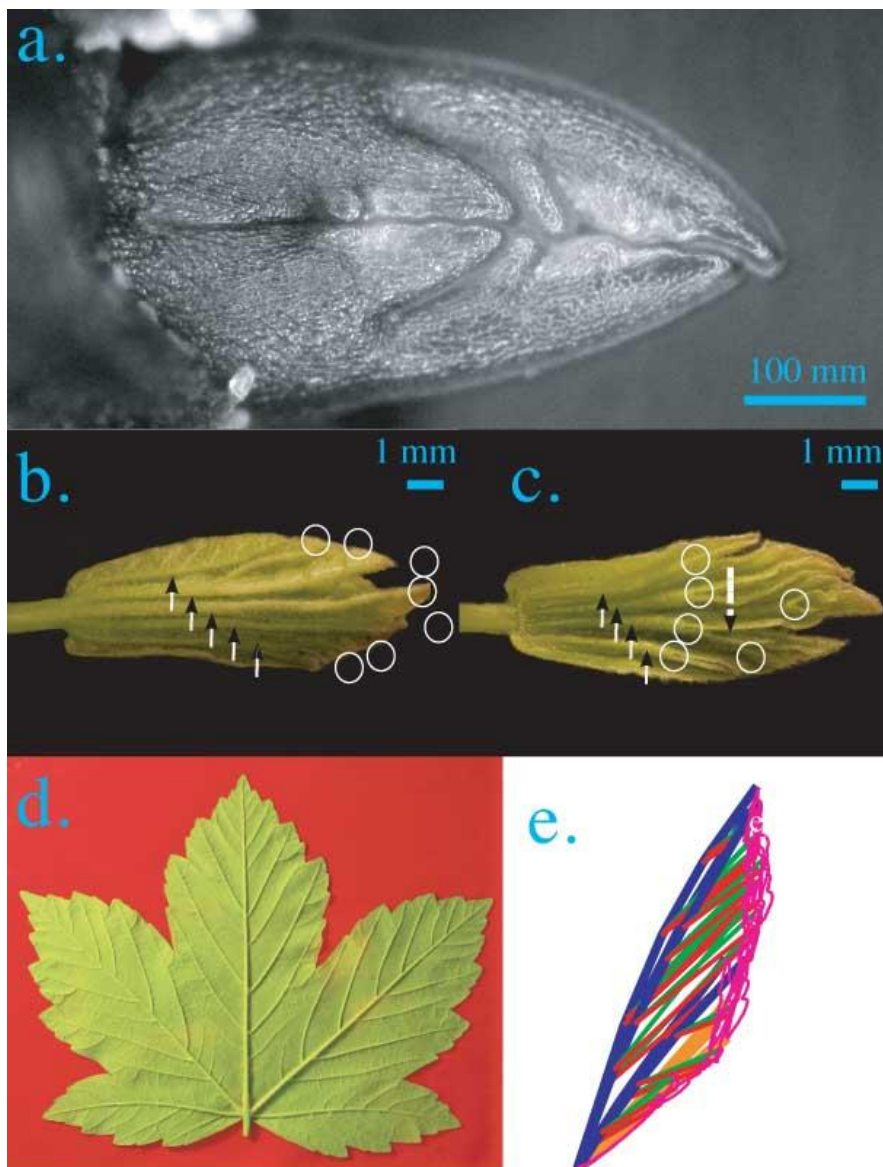


Figure 1. a. Two opposite *Acer pseudoplatanus* leaves whose edges are on a plane at the middle. b. Abaxial side of an *Acer campestre*. Arrows indicate abaxial folds which are along the veins. Circles indicate the fold ends, which correspond to lobes. c. Adaxial side of the same leaf. Arrows indicate adaxial folds, which are in the tissue. Circles indicate the fold ends, which correspond to sinus. d-e. Numerical folding of an *Acer pseudoplatanus* Leaf.. Secondary fold detail: unfolded (d) and folded in a plane (e). Blue and green segments are anticlinal folds while the synclinal fold is red. The “leaf” contour is pink.

Material and methods

Numerical folding

We have developed programs to fold leaves numerically. For that we measured the angle between the bases of main veins, and refold the main lobes with these angles. In case of *Ficus Cariaca*, folds are not always straight lines, veins are curved, antifolds (valleys) too. Only the central vein is a straight line. To fold with curved folds, we have used the symmetric of lateral lobes to the lateral antifold. We also refold the straight central vein using its secondary folds. For that we have taken the nearest solution, which can be unfolded on a plane and folded in a plane (Fig. 2).

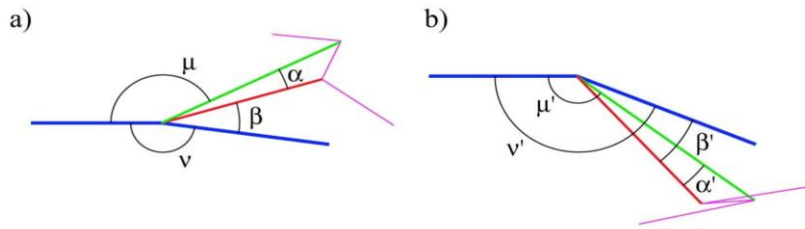


Figure 2. Numerical folding method. Secondary fold detail: unfolded (a) and folded in a plane (b). Blue and green segments are anticlinal folds while the synclinal fold is red. The “leaf” margin is depicted as a pink line. As seen on figure (a), the sum of all angles is $\alpha + \beta +$

$\mu + \nu = 2\pi$. Considering the angle ν' , the folded structure in figure (b) lays in a plane only if: $\nu' = \mu' + \beta' - \alpha'$. If the sum of angles is equal to 2π , this equation rewrites: $\nu' = \pi - \alpha'$. Folding figure (a) in figure (b) with keeping to the best the angle ν is minimizing the quantity $(\nu' - \nu)^2 + (\alpha' - \alpha)^2$ which rewrites $(\nu' - \nu)^2 + (\pi - \nu' - \alpha)^2$. One finds the best ν' value: $\nu' = (\pi + \nu - \alpha) / 2$. In the same way, one find: $\alpha' = (\pi + \alpha - \nu) / 2$, $\beta' = (\pi + \beta - \mu) / 2$ and $\mu' = (\pi + \mu - \beta) / 2$.

Fold and cut

If you fold a sheet of paper and cut it with scissors, you can obtain very different shapes. Each fold will be a local axe of symmetry of the unfolded contour. All the results of this article use this property. We show how different type of folding, and different type of cutting will determine shape of different leaves. What plays the role of scissors is still an open question but development acts exactly as if they existed actually.

Results and discussion

Successive folds

Tetrapanax papyriferus Leaves, as nearly all the palmate leaves, are folded when they are young. As for maple leaves, each fold correspond either to a sinus or to a lobe (Fig. 3a and b). Main lobes correspond to main folds, which originate from the centre of the leaf. There are also 1, 2 or 3 secondary folds along each lobe, which will correspond to secondary lobes once the leaf will unfold.

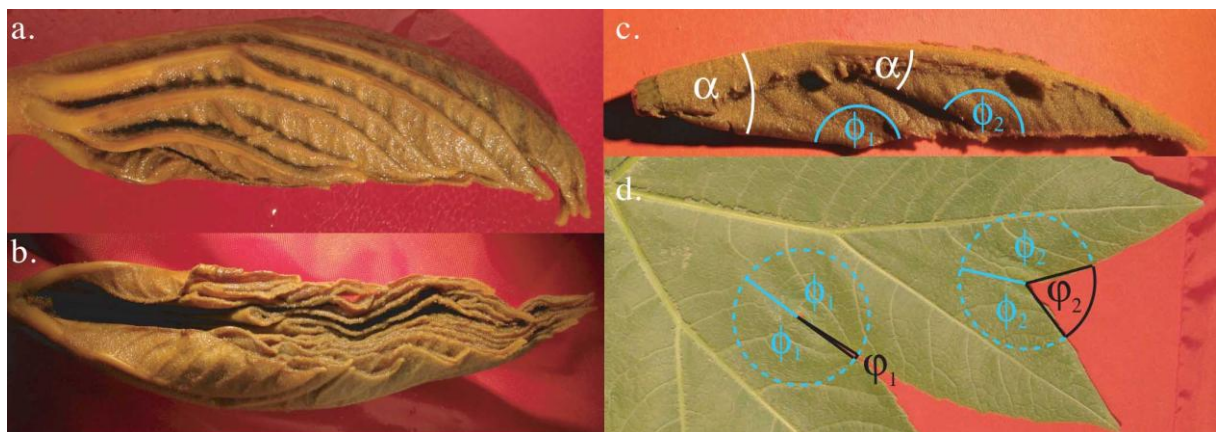


Figure 3. a. Lateral view of a folded leaf of *Tetrapanax papyriferus*. b. Frontal view of the same leaf. c. Longitudinal cut of a lobe of a lobe of *Tetrapanax papyriferus*. d. Partial view of a lobe of a mature *Tetrapanax papyriferus* leaf.

We can obtain the shape of kirigami leaves by folding a sheet of paper and then cut it along a line. This remark explain some feature of the leaf of *Tetrapanax papyriferus*, for instance, opening angle ϕ of the sinus increase along each lobe (Fig. 3d). If we take into account the folded phase of development the reason is simple. The key remark is that secondary folds bend the central vein (166° in average on 5 leaves, Fig. 3c). Measurements show that angle α between the vein and the fold does not depend on its place along the fold, indicating an identical lobe development (27.7° as mean for the

first angle along the lobe, 27.4° for the second one and 29° for the third on 5 leaves). Then, due to the curvature of the main vein due to these secondary folds, the angle ϕ , which the fold have with the cut plane, decreases along the lobe (Fig. 3c). As the angle ϕ gets smaller along the lobe, the angle φ of opening of sinus, which is equal to $2\pi-2\phi$, becomes larger along the successive lobes (Fig. 3d). This observation clarify the secondary lobe development: Reiteration acts not on secondary lobes and sinus shape, which depends on their place along the main fold, but at the level of secondary fold, which is independent on its place.

In a more general way, the angle of opening of a sinus can be predicted by using the angle of the precedent sinus and the angle between the folds. We have used five leaves of *Tetrapanax papyriferus* and measured the angles shown on Figure 4 a. We have calculated the angle of refolding by taking the nearest angle, which follows the theorem of Kobayashi (see methods, Fig. 2). We find the prediction is near the measurement but always under (Fig. 4 c). It is probably because we took account only of the curvature due to the fold. As we see on Fig 3c, the vein is curved between the folds too. So we underestimate the curvature of the central vein, overestimate φ and then underestimate ϕ . In this paragraph, we have shown with this example how secondary folds link the angles along a lobe.

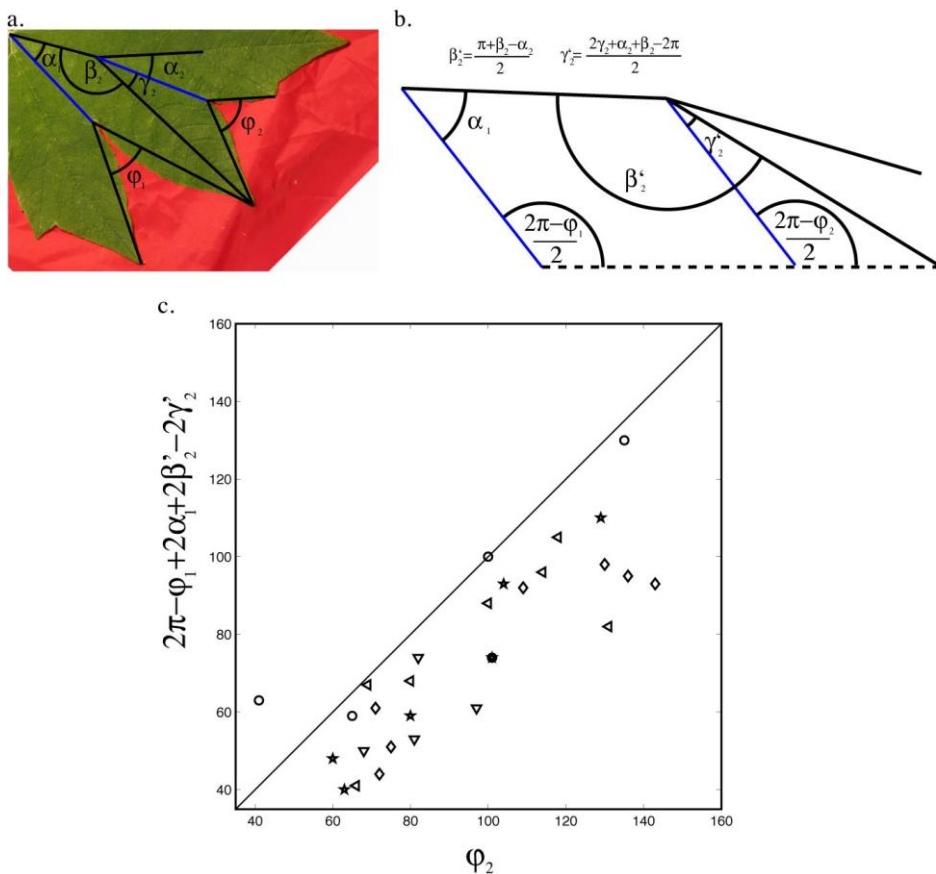


Figure 4. a. A lobe of a *Tetrapanax papyriferus* leaf. Notation for the measured angle. α_1 , ϕ_1 , α_2 , β_2 , γ_2 and ϕ_2 . b. The same lobe once folded. β_2' and γ_2' are the nearest angle from β_2 , γ_2 that you can fold in a plane. It is why we use them to make the prediction. c. Data obtain by measurement on five leaves of *Tetrapanax papyriferus*. We draw in abscissa ψ_2 and in ordinate the prediction made by assuming that all the lobe refold along the same line.

Tangential cuts

In the example of normal Kirigami leaves, such as *Acer pseudoplatanus* and *Tetrapanax papyriferus* (Fig. 1, 3), the cut direction is transverse to the fold (Fig. 5a). In this case, folds are axes of symmetry of the edge (Fig. 5a'). If the cut direction is tangent to the fold, the fold is no more an axe of symmetry of the margin (Fig. 5b-b'). What is amazing is that some plants follow the kirigami model even in these extreme phenomena. It is the case of beach leaves (and some palm leaves). The cutting edge of each leaf is on its abaxial side contrary to all the other species of kirigami leaves

(where it is on the adaxial one). The cut direction corresponds to the envelope of the bud, which is tangent to the folds on the sides (Fig. 6 a-b).

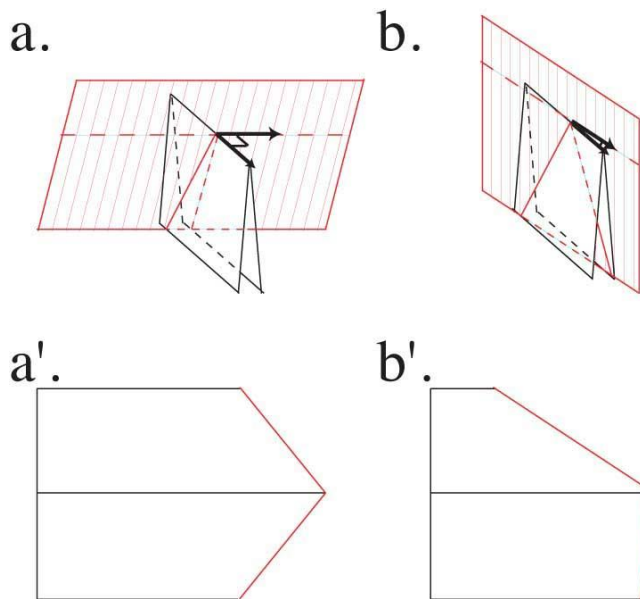


Figure 5. a. Transverse cut of a fold (i.e contain a vector normal to the fold). a'. Same fold than a once unfolded. The fold is axe of symmetry of the edge. b. Tangent cut of a fold. b'. Same fold than b once unfolded. The fold is no more axe of symmetry of the edge



Figure 6. a. A bud of *Fagus sylvatica* b. The same bud without its upper outer-shell. The fold of the leaves are not axes of symmetry anymore. c. A mature leaf. First folds along the central vein are not axis of symmetry of the margin (blue array) because they correspond to folds tangent to the outer-shell. Because the folding vein are also one above each other, the antifold is also not at the middle between the two nearby folds. Last folds along the central vein are axis of symmetry of the margin because they correspond to fold which are transverse to the outer-shell (red array), with also veins at the same height and in the middle of the folds.

We can still derive a numerical relation linking the angle of asymmetry of each folds, α , and the angle between fold and limiting surface, β , as detailed in Figure 7 c-d: $\cotan(\alpha/2) = h \tan(\beta)/e$. To verify that shape of beach leaves follow this relation we have taken folded beach leaf and measure the angle β between the fold and the contour of the folded leaf (which correspond to the outer-shell) and the angle α of asymmetry of the fold (Fig.7 a-b). These angles follow the numerical law (Fig.7 e). When β is small, the fold is tangent to the limiting surface and the asymmetry α is large. When β is

bigger, asymmetry is much smaller. We observe that on real leaves. The first folds along the central vein are tangent to the outer-shell. They are very asymmetric. On the contrary the last one are nearly perpendicular to the outer-shell so the folds are much more symmetric.

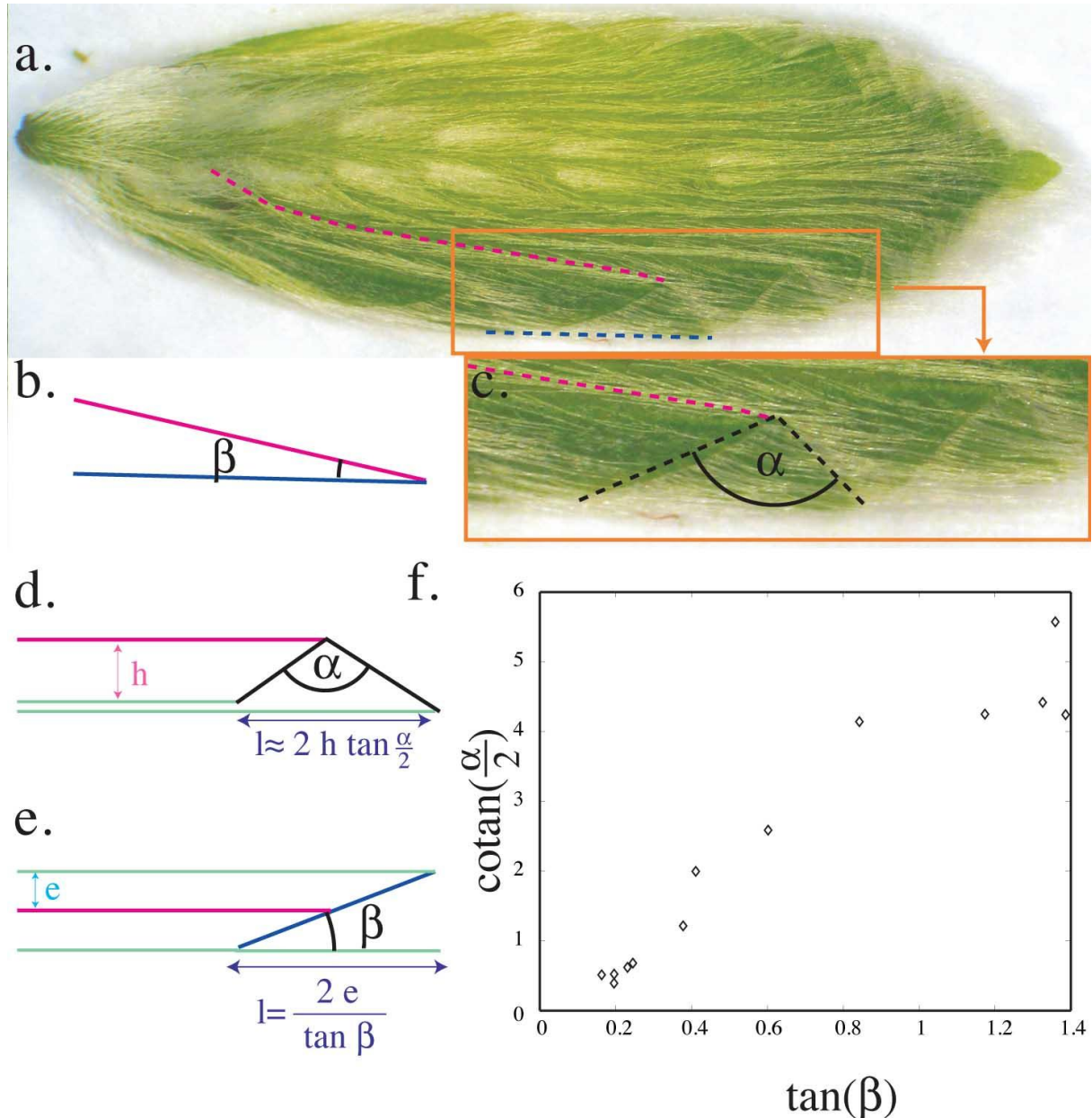


Fig 7. a. Schema of our measurements on the abaxial view of a beach leaf. Magenta dashed line corresponds to mountain fold. Blue dashed line links three consecutive sinus centered around the sinus at the valley fold tip just after the mountain fold. Blue dashed line corresponds to the limiting surface. b. β is the angle between the fit of the blue dashed line (represented by a blue continue line) and the fit of the magenta dashed line (represented by a magenta continue line). c. The angle α (black) correspond to the asymmetry. d. Schema of a lateral view of a fold. First way to calculate the length l with the angle of asymmetry α . e. Schema of an upper view of a fold. As the tissue has a positive thickness e the two valley folds (red line) do not superimpose with the mountain fold (black line). Second way to calculate the length l with the angle β between the fold and the edge. f. Measure for all the folds of the upper leaf.

Tangential cut result in leaves whose antifolds do not correspond always to sinus (Fig. 8 b'). It depends precisely on where the cut is between two consecutive veins. If the antifold cut is closer to the tip of the first vein then the antifold will give a sinus as normal (fig 8a a'). But if the cut is closer to the tip the second vein, the antifold will give an unusual small bump between the veins (Fig. 8 b b'). Both types of leaves exist.

It is particularly interesting to notice that another variety of beech, such as *Rohan obelix* (var.), is folded differently so that the limitation is not tangent but perpendicular, as usual. Folds are now axes of symmetry again (Fig. 9). Variation of leaf shape is a geometrical consequence of folding, which can change even for very close cultivar.

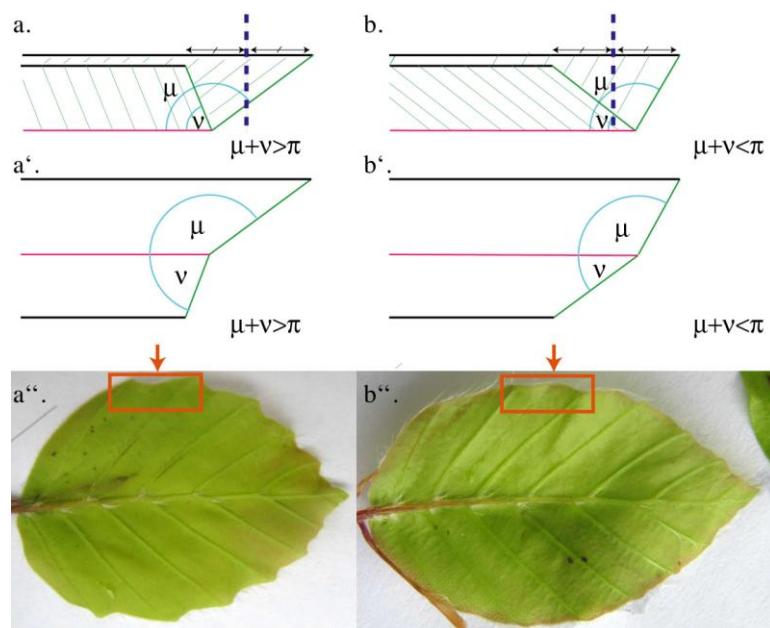


Figure 8. a. Black lines correspond to veins. The red line corresponds to an antifold or “valley” fold. Thick Green lines correspond to the leaf margin. If the antifold's end is nearer from the tip of the first vein than from the tip of the second one then $\mu + \nu > \pi$. a'. It will give a sinus when it will unfold. . a'' Beach leaf whose antifolds become sinus - red arrow. b.b' b''. If the antifold's end is nearer from the tip of the second vein than from the tip of the first one then $\mu + \nu < \pi$. It will give a beach leaf whose antifolds become lobe - red arrow.



Figure 9. a. A *Fagus sylvatica* (*Rohan obelix* var.) bud. The leaf margin is folded on the back of the previous leaf, transversally to the fold. a'. A transverse cut of a *Fagus sylvatica* (*Rohan obelix* var.) leaf in the bud. The two leaf margin meets in front of the central fold, which is enclosed by the leaf. a''. Front (adaxial view) of a *Fagus sylvatica* (*Rohan obelix* var.) leaf. Folds and antifolds are axis of symmetry of the margin. a'''. A mature *Fagus sylvatica* (*Rohan obelix* var.) leaf. b. A *Fagus sylvatica* bud. The leaf margin is folded on the back of the leaf. b'. A cut of a *Fagus sylvatica* leaf. The central fold is open on the previous leaf. b''. Front (adaxial view) of a *Fagus sylvatica* leaf. The margin does not appear because it is folded on the back (abaxial side) of the leaf. b'''. A *Fagus sylvatica* leaf.

Round Edge

What happens now for the shape if what limits the growth of the edge is no more a plane? This phenomenon occurs in *Ficus Cariaca* bud. *Ficus Cariaca*'s buds are like the Russian dolls. Each bud is constituted by a small leaf in front of a smaller bud, which itself contains a smaller leaf and a smaller bud (Fig. 10a). At first glance, the edge of the folded leaf seems to stay on a plane, which corresponds to the envelope of the smaller bud (Fig. 10 a b). But if we move slightly the central lobe

of the leaf in order to open slightly its separation with lateral lobes, we see that the edge of the beginning of the lobe did stay along the vein of the lateral lobe and not on the limit corresponding to the envelope of the smaller bud (Fig. 10 c d). This way to be folded is coherent with the spoon like shape of lobes. The beginning of a lobe is thin because it is limited by the lateral vein. The end of the lobe is larger because it is limited by the bud in front and no more by the lateral vein.

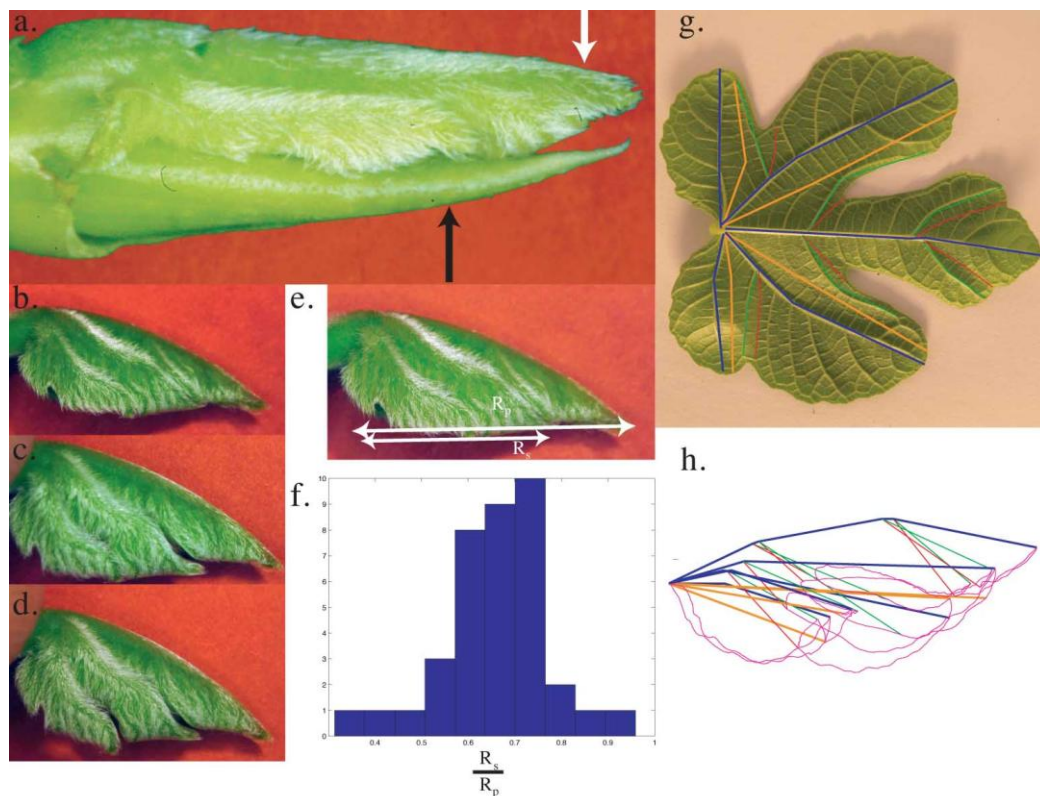


Figure 10. a. A *Ficus Cariaca* bud. The leaf (white arrow) is limited by another smaller bud in front of it (black arrow). b. A leaf of *Ficus carriaca* alone. c. We slightly separate the central lobe. We see that its lower border lies on the lateral lobe. d. We slightly move the first lateral lobe. Its lower border also lies on the next lateral one. e. R_p is the length of the entire edge of the leaf. R_s is the length of the edge until the beginning of the central lobe. f. Histogram of the ratio R_p / R_s , showing large variations. g. A mature leaf of *Ficus Cariaca*. Color corresponds to the different lobe. Blue for principal fold. Orange for main antifolds or valley folds. Green for secondary folds. Red for secondary sinus. h. The same leaf once folded numerically (see M&M).

There seems to be clear adaptation of the lower edge of the central lobe to the vein of the most lateral one. If we take different folded leaf we see that different young folded leaves can have very different shape (Fig. 10 e f). The ratio between the length of the edge of the lobe tip, which stay on the smaller bud, and the rest of the margin which stay on the smaller bud, can vary from 0.4 to 0.9. Leaves shapes are very different but the central edge lobe fits nevertheless the shape of lateral vein. Is it the vein which fit to the edge or the contrary? The question remains open.

The geometry of the bud leaves its imprints on leaf shape. If we refold the leaf we see the end of all lobes almost align, whereas the edge of lobe 's base stay along the next folded vein (in blue, Fig. 10 g h). The numerical folding of the mature leaf (Fig 10 g, h) brought the lobe edges close to a plane, despite latter expansive growth somewhat reducing the fit to a plane compared to the young folded leaf in Fig 10 e. Shape of *Ficus Cariaca* leaves is thus also determined by its way of folding and filling of the bud.

Conclusion

It is astonishing to see how varied are the geometry of leaves, and of their folding in buds. However one rule stay always true: buds are completely filled by the leaves. Leaf shape seems to be the consequence of folding and filling of the bud, and not the contrary. Lobes grow independently but at the end they all together fit the shape of the bud. To give a so precise result, regulation of each lobe growing independently should be very complicated. How would it work to allow so different leaf shapes in the same plant, all with filled buds? It is more probable that lobes grow independently but their growth is regulated by the space left, through contact regulation, either chemical or mechanic.

Where does take place contact regulation? Is it only at vein tips or everywhere along the margin? The second alternative fits more our results. Indeed. Even in the unusual cases of *Fagus sylvatica* and *Ficus Cariaca*, the whole leaf margin seems to adapt to the available volume in order to fill it.

If contact regulation is very common at higher scale of vegetal development like at the scale of the tree (an example is the shyness of crown) [9], or at the scale of the control of organ expansion [10], it has never been studied at the scale of leaf development. Recently researcher have shown that mechanic plays a role in primordia development [11], contact regulation could be a next step of this kind of research. Contact development did not appear earlier in developmental biology studies possibly because researcher have studied free flat leaves as the *Arabidopsis thaliana* ones. Leaves are stacked. It is easy to constrain surfaces by each other in the tree dimensional bud. In this article we focused on folded leaves, which are no more surfaces but three dimensional objects. Conflict for space in the bud and its consequences can't be discarded anymore, and the need for contact regulation of growth is clear in this case.

Acknowledgements

We thank Naomi Nakayama for her reading of the text and her advices.

References

1. Kobayashi, H. , Kresling, B. & Vincent, J.F.V. The geometry of unfolding tree leaves. *Proc. R. Soc. Lond. B* **265**, 147-154 (1998)
2. Bailey, I.W, Sinott, E.W. The climatic distribution of certain type of angiosperm leaves. *Am. J. Bot.* **3**, 24-39 (1916)
3. Hallé, F. Plaidoyer pour l'arbre. Actes sud. (2006)
4. Blein, T. Et al A Conserved Molecular Framework for Compound Leaf Development. *Science* **322**, 1835 – 1839 (2008)

5. Bharathan, G. Et al. Homologies in Leaf Form Inferred from KNOXI Gene Expression During Development. *Science*. **296**, 1858 – 1860 (2002)
6. Couturier, E., Courrech-Dupont, S., Douady, S. Steric constrain on leaf shape. arXiv:0903.1557 (2009)
7. Clos, D. Monographie de la préfoliation, dans ses rapports avec les divers degrés de classification. (Rouget frères et Delahaut, Toulouse, 1870)
8. Adanson, M. Familles des plantes : contenant une préface historique sur l'état ancien et actuel de la botanique, et une théorie de cette science. (Chez Vincent imprimeur du Comte de Provence, Paris, 1763)
9. Putz, F. E., Parker, G. G. and Archibald, R. M. Mechanical Abrasion and Intercrown Spacing. *American Midland Naturalist* 112:24-28. (1984)
10. Coutand, C., Moulia, B. Biomechanical study of the effect of a controlled bending on tomato stem elongation : local strain sensing and spatial integration of the signal. *Journal of Experimental Botany* 51 : 352 1825-1842 (2000)
11. Hamant, O. Developmental Patterning by Mechanical Signals in Arabidopsis *Science* **322**: 1650-1655 (2008).

Modelling secondary growth stresses in recent and fossil plants

Tom Masselter and Thomas Speck

Plant Biomechanics Group, Botanic Garden, University of Freiburg, Germany

Abstract

Analysis and modelling of secondary growth stresses in plant stems have been conducted for many years by using data either of indirect measurement methods, as e.g. strain sensors, or of direct methods, as e.g. pressure probe measurements, for determining the stress. These methods and models have several drawbacks and in particular they cannot be used for assessing growth stresses in fossil plants. Therefore we present a new approach and show that a mathematical/physical model can be used to make accurate assumptions on the magnitude of stresses in rather small bodied centri-symmetric woody plant stems, both recent and fossil. The model is based on Lamé's theories on the deformation of thick walled cylinders as well as on physical experiments with technical cellular solids. Tissues with different radial widths, Young's moduli and Poisson ratios can be defined in the model.

The model allows describing in good approximation the growth stresses measured at the inner surface of the sclerenchymatous cortex cylinder of *Aristolochia macrophylla*, an extant lianescent plant. We also applied the theoretical model to two fossil woody plants, the 'seed fern' species *Lyginopteris oldhamia* (c. 300 Myr old) and *Calamopitys* sp. (c. 340 Myr old). In these fossil 'seed ferns', the model is used for recalculating the values of stresses in the inner primary cortex tissues and to analyse whether the deformation observed in thin-ground sections of the very well preserved petrified stem material is entirely within the elastic or also within the plastic range. Thus it allows proving or disproving the assumption that the (sometimes large) deformations observed in the cortex tissues of the two fossil plant species occurred in vivo or are an artefact due to the fossilization process and later deformation.

Introduction

Secondary growth is an innate feature of most woody plants, both recent and fossil. The evolution of secondary growth has led to a number of adaptations, amongst others the evolution of a cortex cambium that can follow the circumferential extension due to the increasing volume of secondary vascular tissues [1]. While this key innovation is in place in recent plants, some fossil species did not yet have this feature evolved and had to cope with the increase in volume of secondary vascular tissues by other means. Two of these fossil plants, *Lyginopteris oldhamia* and *Calamopitys* sp., had evolved cortex tissues that were able to deal with these stresses in two different ways: *Calamopitys* sp. had a large outer cortex that was able to 'absorb' the strains imposed by the increase in size of the secondary vascular tissues (*Fig. 1A,B*) [2], while in *Lyginopteris oldhamia*, the rather thin outer cortex was stretched and ultimately sloughed off (*Fig. 1C,D*) [3,4].

The data provided by tissue measurements in different ontogenetic stages in these fossil plants all point towards the conclusion that the stresses exerted by secondary growth of secondary vascular tissues led to stresses and strains in the surrounding cortex tissues. An intriguing question is what the stress-strain relationships in fossil plants were really like? As fossil plants cannot be tested mechanically, other methods for answering this question had to be adopted. Due to the excellent preservation in coal balls, strains in tissues and even in individual cells can be measured in these plants

with high accuracy [3-5]. These strains can be used to calculate tissue stresses in *Calamopitys* and *L. oldhamia*. To this goal, a theoretical model was developed using technical foam rubbers, and measurements of the extant plant *Aristolochia macrophylla* for calibrating and verifying the model (as described below) were carried out.

A. macrophylla was chosen as extant model plant as a primary sclerenchymatous outer cylinder is ruptured due to the increase in volume of the inner secondary vascular tissues (Fig. 1E,F) [6,7]. Stresses that are needed to rupture this sclerenchymatous outer sheath can be calculated and these can be used to verify if the theoretical model is able to describe correctly the stress-strain relationships in this extant plant.

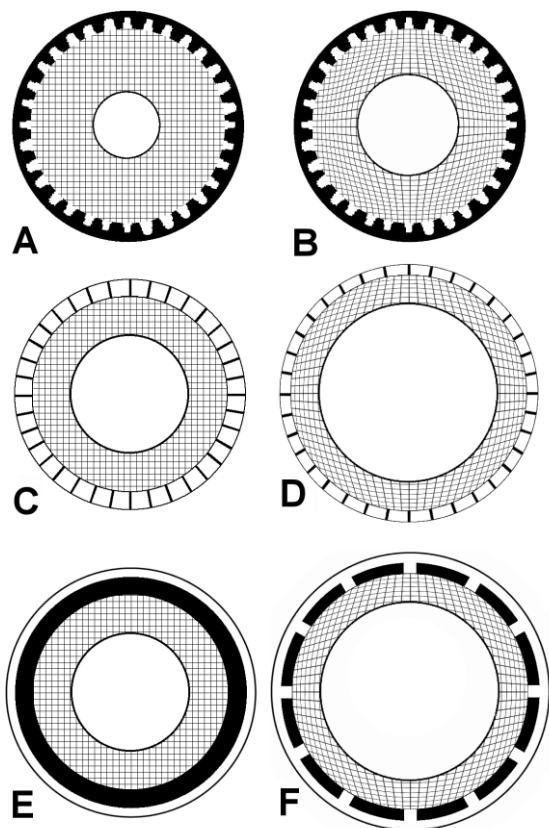


Fig. 1 Simplified models for tissue arrangement in various extant and fossil plants. (A,B) *Calamopitys* sp., A: unstrained 'young' axis, B: internally strained 'old' axis. (C,D) *Lyginopteris oldhamia*, C: unstrained 'young' axis, D: internally strained 'old' axis. (E,F) *Aristolochia macrophylla*, E: unstrained 'young' axis, F: internally strained 'old' axis. Types of tissues: secondary vascular tissues including central pith (inner white circle); inner primary cortex (chequered area); outer primary cortex (outermost rings; sclerenchymatous black: parenchymatous white).

Material and methods

Measurements of *Lyginopteris oldhamia* were made on slides from collections housed at the Natural History Museum, London, and the palaeobotanical collection at the Museum of the University of Tübingen as well as from well reproduced plates found in literature. *Calamopitys* material was obtained from fossil plant collections of the AMAP laboratory (Montpellier, France). Axes of *Aristolochia macrophylla* were cut from a specimen in the Botanic Garden, Freiburg.

For answering the central questions of the study

-how can the mechanical behaviour of cellular material be calculated and is it possible to model the stress-strain relationships analytically without using FEM?

-are the deformations in parenchymatous (cellular) tissues within the (visco-)elastic or within the plastic range?

several steps were taken (Fig. 2).

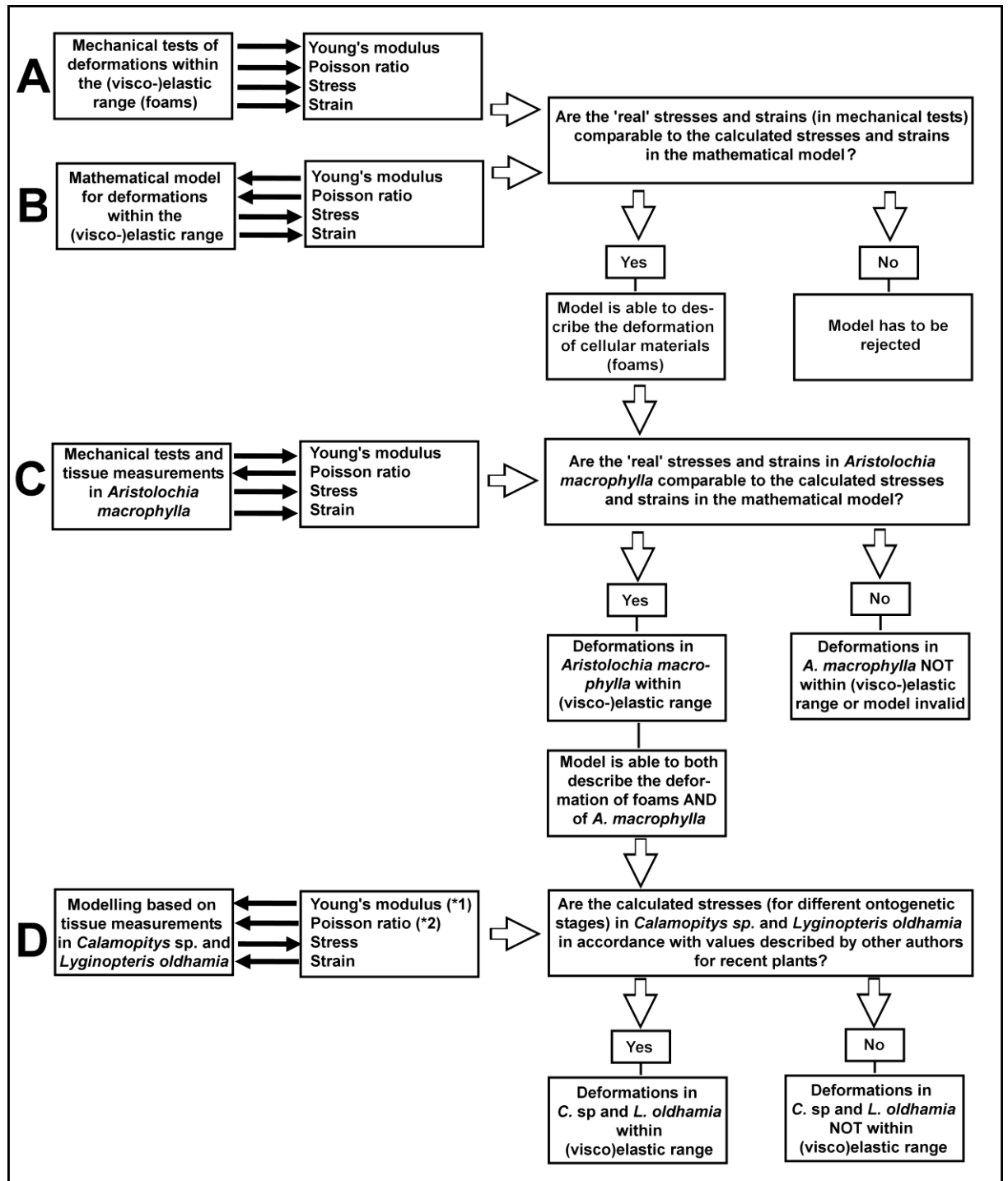


Fig. 2 Flow chart showing an overview of the succession of the measurements, tests and models necessary for the present study. Black arrows indicate the mechanical parameters that are either known and serve as input into the model/tests (arrows pointing towards the left hand side) or are a result of the model/tests/measurements (arrows pointing towards the right hand side). (*1) and (*2): Young's moduli and Poisson ratios were based on measurements of extant plants.

In a first step, a mathematical-physical model for the deformation of technical cellular material was established (Fig. 2A,B). To this purpose, the deformation of closed-cell technical foam rubbers (with Young's moduli and Poisson ratios known from mechanical measurements) was analysed (Fig. 2A)

and the measured stress-strain relationships were described with an analytical mathematical model (Fig. 2B).

For determining the stress-strain relationships of technical cellular material, cylindrical closed-cell foam rubbers were mounted in a special pressure vessel (Fig. 3A,B). Pressure was applied on the inside of the foams by means of water input into a thin elastic rubber cylinder (Fig. 3B). The pressure and the volume of the water column as well as the strain of the foam could be measured in different inner and outer zones (Fig. 3C,D). The centri-symmetric setup was chosen as it represents a simplified arrangement of tissues similar to the one in the selected plant genera. The incompressible water mimicks the secondary vascular tissues (comparatively high Young's modulus) and the foam rubbers represent the parenchymatous cellular cortex tissues (comparatively low Young's modulus). Additionally, a stiff outer cylinder can be placed around the foam rubbers. This is a functional representation of the stiff outer cortex tissues. This cortex tissue is disrupted during growth in *Lyginopteris oldhamia* and *Aristolochia macrophylla*. In a simplistic way, one could say that the model then changes from 'closed' (i.e. enclosed by a stiff outer cortex) to 'open' (i.e. not enclosed by a stiff outer cortex). This change in state of the foam rubber device has a great impact on the deformation of the foams (compare Figs. 3C and 3D).

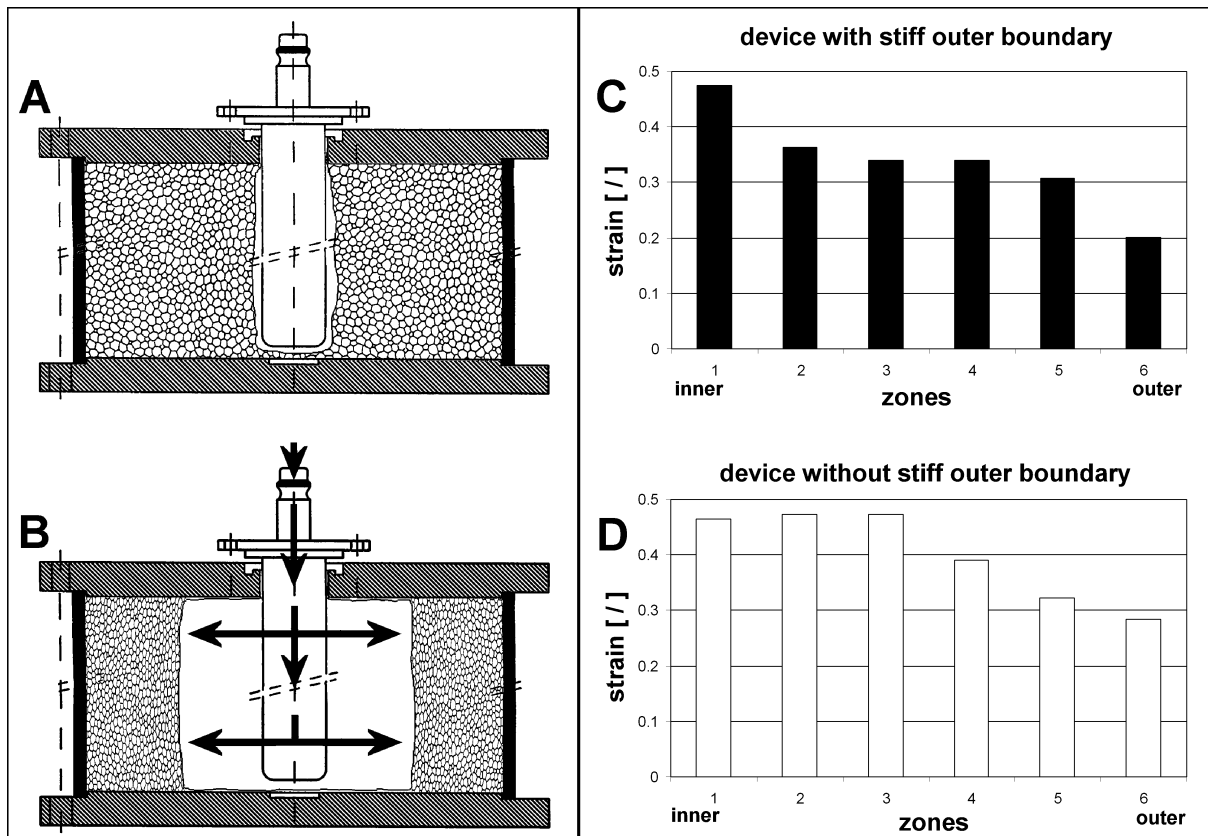


Fig. 3 (A,B) Lateral view of pressure vessel with mounted cylindrical foam rubber, A: unstrained foam rubber, B: strained foam rubber. (C,D) Measured strain in inner and outer zones of the cylindrical foam rubber, C: for a device with a stiff outer boundary, as shown in A, D: for a device without a stiff outer boundary.

A mathematical model (Figs. 2B, 4) that is based on Lamé's equations for the deformation of thick-walled cylinders [8] (see also appendix) is used for describing the deformation of technical cellular material.

The model can be used to describe any number of concentric cylinders with different radial widths, Young' moduli and Poisson ratios and can therefore also well describe arrangements of

centri-symmetric (plant) tissues. *Figure 4* shows stresses and strains for a model with two (A-C), respectively one (D-F) cylinder.

The model is based on several assumptions:

-The mechanical behaviour (in terms of stress-strain relationships) of both cellular plant material, i.e. parenchyma and technical cellular material is comparable [7]. This assumption could be verified in the study.

-The mechanical behaviour of parenchymatous tissue is similar in fossil and recent plants.

-Based on experimental data of tissues of recent plants, Young's moduli can be attributed to tissues of the fossil plants, cf. [4, 9-14].

In the next steps we analysed the ability of the model to describe the stress-strain relationships in *A. macrophylla* (*Fig. 2C*, for a detailed account of the studies in *A. macrophylla*, see [6,7] and also the strain seen in the parenchymatous cortex tissues of *L. oldhamia* [3,4] and *Calamopitys* sp. (*Fig. 2D*) [2].

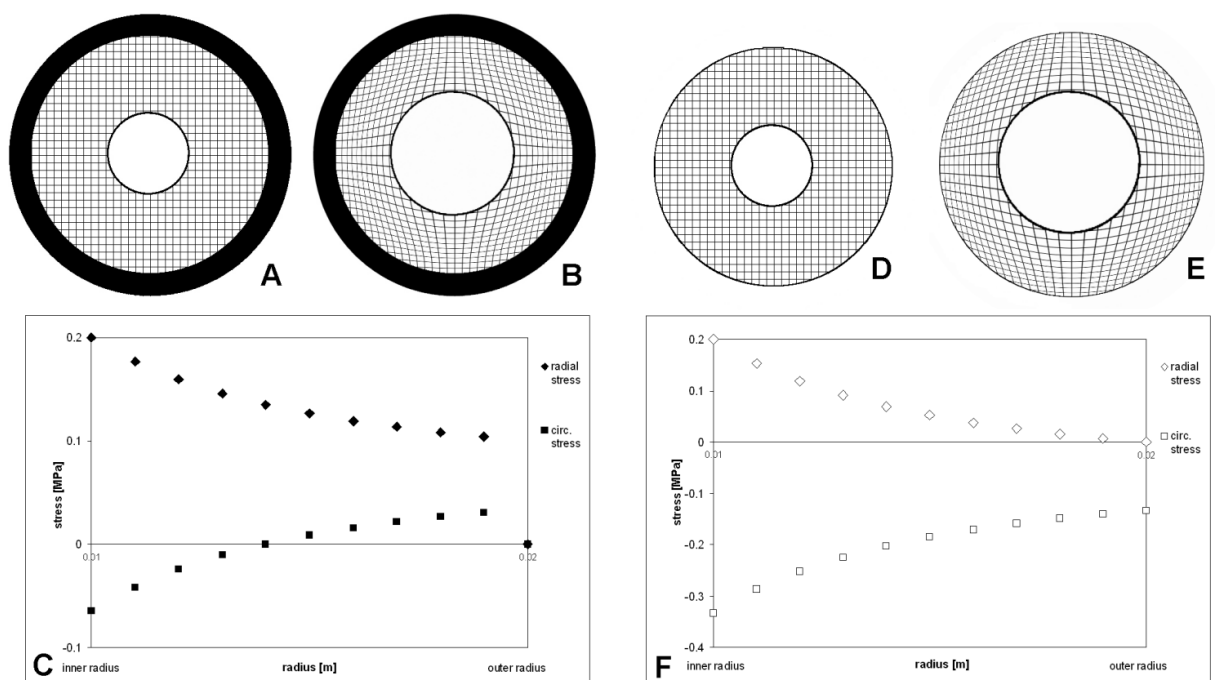


Fig. 4 Stresses and strains for theoretical cylinder models based on Lamé's equations. (A-C) Model with stiff outer boundary. (D-F) Model without stiff outer boundary. A,D: Unstrained state, B,E: strained state, C,F: calculated radial and circumferential stresses in different inner and outer zones of the cylinders.

Results and discussion

One of our main results was that the model based on Lamé's equations was able to describe the stress-strain relationships both in the technical foam rubbers and in *A. macrophylla*. This implies that the mathematical model is able to describe the deformation of technical and natural cellular materials and that the deformation observed in the parenchymatous cortex tissues of *A. macrophylla* is mainly within the (visco-)elastic range (as the mathematical model is only valid for deformation within the elastic range, cf. [8]). This is also supported by (1) the finding that the radial width of the parenchymatous tissue increases after rupture of the surrounding stiff sclerenchymatous cylinder, which is interpreted as a (visco-)elastic relaxation of the parenchymatous cortex tissue [7], and (2) by the qualitative observation that the mechanical deformations of foam rubber cells and parenchyma

cells of *A. macrophylla* closely resemble each other in different states of deformation (i.e. linear deformation, elastic buckling and crushing [7], see also [15]).

If the model is applied to the fossil plants, calculated radial stresses at the inner border of the parenchymatous cortex (i.e. the outer border of the secondary vascular tissues) necessary to cause the deformation in the parenchymatous cortex are very high ranging from 16 to 32 MPa in *Lyginopteris* and from 37 to 59 MPa in *Calamopitys*. These values are well above the 1.6-1.7 MPa that the model yielded in *A. macrophylla* as a result for the inner pressure that was necessary to cause the deformation in *A. macrophylla*. The values calculated for *A. macrophylla* are in good accordance with radial growth stresses found in other plants: approx. 1 MPa in *Eucalyptus regnans* [16] and in various other timbers measured by several authors, varying from 0.7 to 2.8 MPa [17-20].

So it can be stated that the model, which is only valid in the (visco-) elastic range, cannot adequately describe the deformations in *L. oldhamia* and *Calamopitys* sp. As a result, it has to be assumed that deformations in these two fossil plants are mainly within the plastic range. This is also supported by the observation of large compaction zones at the border of the secondary vascular tissues (where stresses are likely to be the highest) in *Calamopitys* sp. and to a lesser extent in some older axes of *L. oldhamia*.

Conclusions

(1) (Visco-)elastic deformations in both technical and natural cellular materials can be described in good approximation by a mathematical model.

(2) The deformations in the parenchymatous cortex tissues of the recent lianescent plant *Aristolochia macrophylla* are mainly within the (visco-)elastic range.

(3) Deformations in the parenchymatous cortex tissues of the fossil plants *Lyginopteris oldhamia* and *Calamopitys* sp. are mainly within the plastic range.

(4) A combination of physical and mathematical models can contribute to a better understanding of strains observed in the cortex tissues in extant and fossil plants. Secondary growth of the vascular tissues can 'explain' the deformation in these cortex tissues.

Acknowledgements

We gratefully acknowledge Professor H-C. Spatz from the Institute of Biology III, University of Freiburg, for valuable discussions about the experimental and modelling part.

References

1. Rowe, N.P. (2000): *The insides and outsides of plants: the long and chequered evolution of secondary growth*, in Plant Biomechanics 2000, Proceedings of the 3rd Plant Biomechanics Conference, eds.: Speck, T. and H.-C. Spatz, Thieme-Verlag: Stuttgart-New York. p. 129-140.
2. Masselter, T., Rowe, N.P., Galtier, J. and T. Speck (2009): *Secondary growth and deformation of stem tissues in the Lower Carboniferous seed fern Calamopitys*. International Journal of Plant Sciences (accepted).
3. Masselter, T., Speck, T. and N.P. Rowe (2006): *Ontogenetic reconstruction of the Carboniferous seed plant Lyginopteris oldhamia*. International Journal of Plant Sciences 167: 147-166.
4. Masselter, T., Rowe, N.P. and T. Speck (2007): *Biomechanical reconstruction of the Carboniferous seed fern Lyginopteris oldhamia: implications for growth form reconstruction and habit*. International Journal of Plant Sciences 168: 1177-1189.
5. Masselter, T., Rowe, N.P. and T. Speck (2004): *Adaptive Gewebebildung im Verlauf der Ontogenie in Achsen der karbonischen Samenpflanze Lyginopteris oldhamia*. Mitteilungen des badischen Landesvereins für Naturkunde und Naturschutz 18: 71-89.

6. Masselter, T. and T. Speck (2006): *Evaluating secondary growth processes in Aristolochia macrophylla by experiments and modelling*, in Proceedings of the 5th Plant Biomechanics Conference, ed.: Salmen, L., STFI-Packforsk AB: Stockholm, Sweden. p. 49-54.
7. Masselter, T. and T. Speck (2008): *Quantitative and qualitative changes in primary and secondary stem organization of Aristolochia macrophylla during ontogeny: functional growth analysis and experiments*. Journal of Experimental Botany 59: 2955-2967.
8. Stephens, R.C. (1970): *Strength of materials. Theory and examples*. London, New York, Melbourne, Auckland; Edward Arnold, Hodder.
9. Speck, T. and D. Vogellehner (1988): *Biophysical examinations of the bending stability of various stele types and the upright axes of early 'vascular' land plants*. Botanica Acta 101: 262-268.
10. Speck, T. and D. Vogellehner (1992): *Fossile Bäume, Spreizklimmer und Lianen. Versuch einer biomechanischen Analyse der Stammstruktur*. Courier Forschungsinstitut Senckenberg 147: 31-53.
11. Speck, T. (1994): *A biomechanical method to distinguish between self-supporting and non self-supporting fossil plants*. Review Palaeobotany and Palynology 81: 65-82.
12. Speck, T. and N.P. Rowe (1994): *Biomechanical analysis of Pitus dayi: early seed plant vegetative morphology and its implications on growth habit*. Journal of Plant Research 107: 443-460.
13. Speck, T. and N.P. Rowe (1999): *Biomechanical analysis*, in Fossil plants and spores: modern techniques, eds.: Jones, T.P. and N.P. Rowe, Geological Society London. p. 105-109.
14. Speck, T. and N.P. Rowe (2003): *Modelling primary and secondary growth processes in plants: a summary of the methodology and new data from an early lignophyte*. Philosophical Transactions of the Royal Society London, B Biological Sciences 358: 1473-1485.
15. Niklas, K. (1989): *Plant Biomechanics*. The University of Chicago Press, Chicago & London.
16. Boyd, J.D. (1950): *Tree growth stresses. I. Growth stress evaluation*. Australian Journal of Scientific Research 3: 270-293.
17. Jacobs, M.R. (1945): *The growth stresses of woody stems*. Commonwealth Forestry Bureau Australia Bulletin 28.
18. Kübler, H. (1959): *Studies on growth stresses in trees, Part I: The origin of growth stresses and the stresses in transverse direction*. Holz als Roh- und Werkstoff 17: 1-9.
19. Archer, R.R. (1986): *Growth stresses and strains in trees*. Berlin: Springer-Verlag.
20. Fournier, M., Bordonne, P.A. and D. Guitard. (1990): *Growth stress patterns in tree stems*. Wood Science and Technology 24: 131-142.

Appendix

Calculations for the mathematical model are based on the equations from *Lamé's* theory for the variation in radial and circumferential stresses in thick cylinders [8], where the radial thickness of the cylinder is appreciable in relation to the diameter. As in [8], it is assumed that the longitudinal strain ε_l is constant across the radial thickness, i.e. that a plane cross-section of the cylinder remains plane after the application of pressure, and that the longitudinal stress σ_l is also uniform across the thickness. Further assumptions that are detailed in [8, p. 278] lead to *Lamé's Equations*:

$$\sigma_r = a + \frac{b}{r^2} \quad (\sigma_r = \text{radial stress}) \quad (1)$$

$$\sigma_c = a - \frac{b}{r^2} \quad (\sigma_c = \text{circumferential or tangential stress}) \quad (2)$$

r_2 being the inner radius of the cylinder.

In any given application there will always be two boundary conditions sufficient to solve for the constants a and b and radial and circumferential stresses at any radius r can then be calculated [8].

There are three conceivable cases of such cylindrical setups:

- (a) There is just one cylinder (with internal pressure p only (*Fig. 4D-F*), then boundary conditions are the following (σ_r is the radial stress, σ_c is the circumferential stress, r_1 and r_2 being respectively the outer and inner radius of the cylinder):

$$\sigma_r = p \quad \text{when } r = r_2 \quad \text{and}$$

$$\sigma_r = 0 \quad \text{when } r = r_1$$

then it follows from (1) that:

$$p = a + \frac{b}{r_2^2}$$

and

$$0 = a + \frac{b}{r_1^2}$$

from which

$$a = -p \frac{r_2^2}{r_1^2 - r_2^2}$$

and

$$b = p \frac{r_1^2 r_2^2}{r_1^2 - r_2^2} \quad (3)$$

and using (1) and (2):

$$\sigma_r = -p \frac{r_2^2}{r_1^2 - r_2^2} \left(1 - \frac{r_1^2}{r^2} \right) \quad (4)$$

and

$$\sigma_c = -p \frac{r_2^2}{r_1^2 - r_2^2} \left(1 + \frac{r_1^2}{r^2} \right) \quad (5)$$

The maximum radial and circumferential stresses occur at $r = r_2$, when $\sigma_r = p$

and $\sigma_c = -p \frac{r_1^2 + r_2^2}{r_1^2 - r_2^2}$, the negative sign indicating tension.

The radial and circumferential strains ε_r and ε_c can be calculated as following [8], ν being the Poisson ratio:

$$\varepsilon_c = \frac{\sigma_c}{E_c} - \nu \frac{\sigma_r}{E_r} \quad (6)$$

$$\varepsilon_r = \frac{\sigma_r}{E_r} - \nu \frac{\sigma_c}{E_c} \quad (7)$$

Likewise, it is possible to recalculate the radial width of the inner “soft” tissue at initial state, i.e. before application of pressure, knowing the tissue’s Young’s Modulus, the Poisson ratio as well as stresses and strains at equilibrium state after induced stress. This also holds true for the following two other set-ups:

(b) The cylinder’s outward boundary is a solid with an infinitely high elastic modulus (*Fig. 4A-C*). Boundary conditions are (r_1 and r_2 being respectively the outer and inner radius of the cylinder, ε_c being the circumferential strain):

$$\sigma_r = p \quad \text{when } r = r_2 \quad \text{and}$$

$$\varepsilon_c = 0 \quad \text{when } r = r_1$$

(c) Compound cylinders with different Poisson ratios and Young’s moduli, consisting of several concentric cylinders. The simplest case is a two cylinder system with r_1 being the outer radius of the outer cylinder, r_2 being the inner radius of the inner cylinder and r_0 being the common surface of the two cylinders.

then

$$\sigma_r = p \quad \text{when } r = r_2 \quad \text{and}$$

$$\sigma_r = 0 \quad \text{when } r = r_1$$

and ε_c at the common surface r_0 must be equal for the inner and the outer cylinder.

Chiral structure in petiole vascular bundles.

Derek G. Gray and Joshua G. Lucate

McGill University, Canada

Abstract

In previous work, we observed that the helical cellulose coils reinforcing the vascular elements in *Apium graveolens* L. could be isolated by a gentle treatment with alkali and then with acid chlorite [1]. The long coils were chiral; only left handed helices were observed. This raises the question as to whether this chirality is species dependent, or whether, as in the helical winding of the S2 layer in woody plants, a single handedness is almost always observed. The leaf petioles of a selection of tree and plant species were examined, with the primary aim of checking the handedness of the helical coils by observation with a polarized light microscope. Preliminary examination of petioles of diverse tree species, including sugar maple, London plane, horse chestnut, tulip tree, ginko and paulownia, showed that they all contained long coiled structures surrounding the vessels, but it was sometimes difficult to determine the handedness of the coils due to their small diameter. In many cases, the coils were made up of multiple parallel strands, and left-handed helices predominated. The role of the coils is presumably to resist vessel collapse due to negative pressure in the vascular system, but the origin and significance of the handedness of the coils remains an open question.

Introduction

In a previous report, the isolation of long tightly-coiled cellulosic elements from the vessel walls of the vascular elements of celery (*apium graveolens* L.) was described. Spiralled thickening of the xylem secondary wall is of course well-known, but we were interested to note that the helical coils all appeared to be left-handed [1]. Here, we describe our polarized light microscope method for finding the coiled elements and determining their handedness, with the aim of checking if other plants show the left-handed coils observed in celery petioles. We have observed a purely physical chirality in the spontaneous self-assembly of cellulose nanocrystals in aqueous suspension [2, 3], but much remains to be learned about the mechanisms that generate chiral structures at larger length scales [4]. Here we report observations of the handedness of coils isolated from the petioles a number of angiosperm tree leaves.

Material and methods

Leaves were collected in summer from trees on the campus of McGill University, Montreal, or in the vicinity thereof. The leaf petioles were cut into ~1 cm lengths, and as much as possible of the petiole epidermis was removed with a razor blade, and discarded. The remains were sliced lengthwise. Cellulose was isolated from the petiole slices by a sequence of chemical treatments, with rinsing in water between each step. First, the samples were boiled for 1 h in distilled water, then in aqueous sodium dodecyl sulfate (1.5 – 2 %) for 1 h. This was followed by a basic treatment in 5% NaOH for 1h. at room temperature, or in 3.5% aq. NaOH at 85 – 100°C for 45 – 55 min., depending on the sample. Finally, after thorough rinsing in water until neutrality, the fibrous mass was bleached in a 8 – 10% soln. of sodium chlorite (NaClO₂) in 0.4M acetic acid for 3 h at ambient temperature. For

some samples, it was necessary to repeat the bleaching step. After rinsing, the petiole structure was then partially disrupted by a brief ultrasonic treatment in water.

The wet vascular bundles from the petioles were spread on microscope slides and examined by polarized-light microscopy (Nikon Eclipse LV100, with DS-Fi1 camera). The cellulose coils were readily distinguished from other vascular components by the transverse orientation of the cellulose major refractive index, as indicated by viewing between crossed polarizers with a 530nm. retardation plate. With this retardation plate in place, isotropic regions of the microscope image appear red, and birefringent elements appear blue or red when oriented at as shown in *Fig 1*.

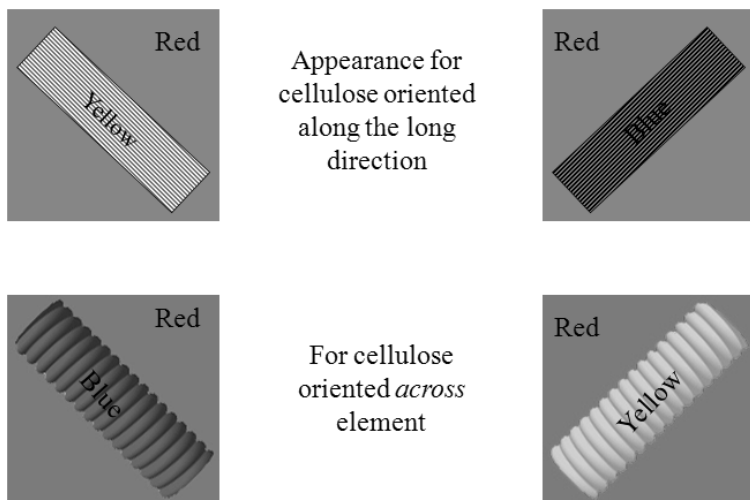


Fig. 1 Colours observed when viewing vascular elements with optical microscope between crossed polars with 530 nm red retardation plate.

The coiled regions of the vascular elements of the sample on the microscope slide were thus readily detected. The best results were obtained using the chemical treatment described above to isolate the cellulosic components, but for some tender petioles, a simple boiling water treatment prior to crushing was adequate to allow examination of the vascular elements.

To deduce the handedness of the coils requires some care. Viewed from above, a left-handed coil appears to be a tight S-helix. This is the usual situation. However some light may be transmitted through the cellulose coils, and if the the microscope is focused on the bottom of the coils rather than the top, a tight Z-helix is observed (*fig. 2*). The change from S- to Z-helix is observed as the plane of focus is moved from top to bottom of the sample. Often the handedness is more readily determined on stretched parts of the coils.

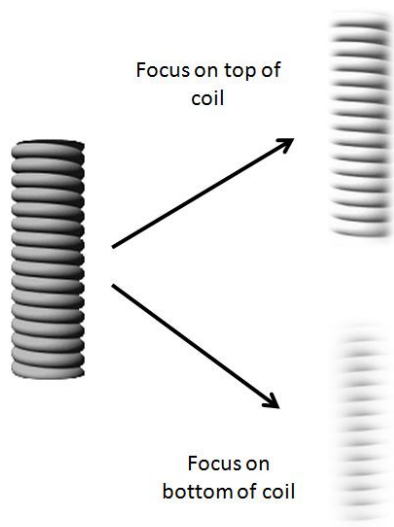


Fig. 2 Sketch showing that focusing on the top of a left-handed coil gives an apparent S-helix, while focusing on the bottom of the coil gives an apparent Z-helix.

Results and discussion

The change from S-helix to Z-helix on changing focus from top to bottom of the coil is illustrated in Figure 3 for a coil from the petiole of London Plane. The coil is thus left-handed. A left handed helical coil was observed for all the species that we examined (see *Table 1*).

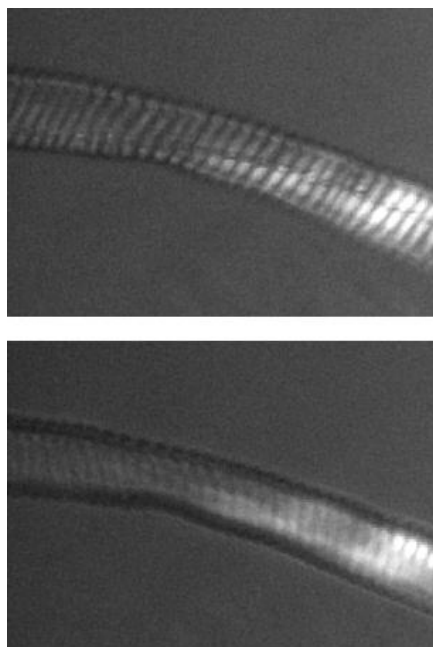


Fig. 3 Left-handed coil from petiole of London Plane (Platanus × hispanica). Upper and lower images focused on top and bottom of coil, respectively. Coil diameter, 24μm.

Table 1 Tree species displaying a left-handed helical arrangement of helical coils in petiole vascular elements. No right-handed coils were observed in these or other species.

Norway maple	<i>Acer platanoides</i>
Sugar maple	<i>Acer saccharum</i>
Horse chestnut	<i>Aesculus hippocastanum</i>
Ohio Buckeye	<i>Aesculus glabra</i>
Choke-cherry	<i>Amelanchier</i>
Ginko	<i>Ginkgo biloba</i>
Honey locust	<i>Gleditsia triacanthos</i>
Tulip tree	<i>Liriodendron tulipifera</i>
Magnolia	<i>Magnolia virginiana</i>
Paulownia	<i>Paulownia tomentosa</i>
London Plane	<i>Platanus × hispanica</i>
White Oak	<i>Quercus alba</i>
Willow	<i>Salix sp.</i>
Viburnum	<i>Viburnum sp.</i>

A unique handedness is also observed in the S2 layer of the wood cell wall (Meylan and Butterfield 1978), which forms a steep right-handed helix, rather than the shallow left-handed helix observed here for leaf petiole elements.

Stretching out the coils indicates that these leaf petioles are often composed of multiple fibrils. This is illustrated in Fig 4, which shows a coil isolated from a tulip tree petiole. (In this case, the petiole was simply treated repeatedly with boiling water, and the vascular elements were then mechanically separated.) The undeformed coil is seen on the right. The stretched region to the left shows multiple coils of three or four individual fibrils. Breaks in the fibrils result in some single and double coils in the image. Similar multiple coils were usually observed in samples isolated from the maple and

chestnut petioles, but were very rare in the celery petioles observed previously. Single and multiple (achiral) rings were also observed, presumably in developing vascular elements.

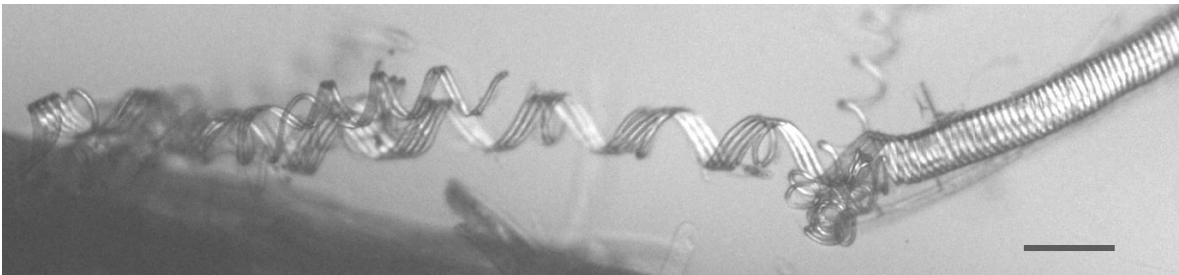


Fig.4 Multiple-coiled petiole elements from tulip tree (*Liriodendron tulipifera*) petiole. Scale bar, 100 μm .

We are not competent to comment on the possible biosynthetic and biophysical processes that result in these very long chiral helical cellulosic elements, but their biosynthesis certainly poses a topological challenge. In view of the length of the coils, coil ends were rare. It was thus of interest to observe the ends of some vascular elements in a sample from magnolia petioles Fig 5. In this sample at least, the coils extend to the tapered ends of the cells.

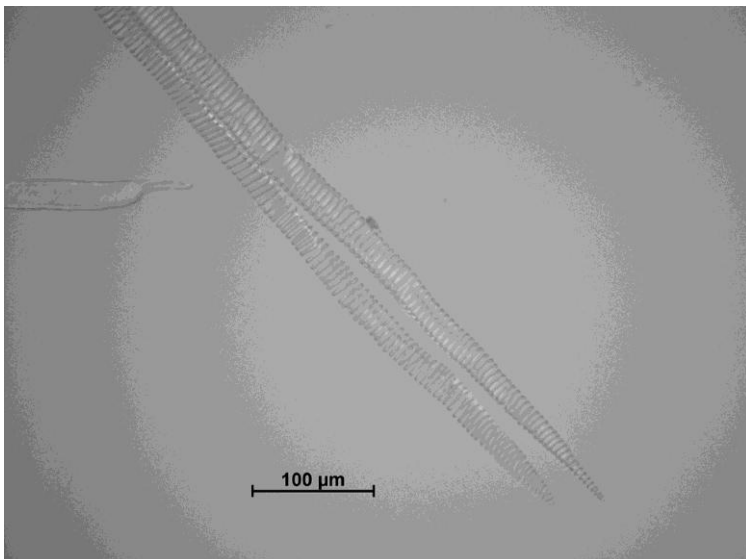


Fig.5 Tapered ends of vascular coils isolated from *Magnolia virginiana*.

Conclusion

The observation of the coiled components of leaf petioles was facilitated by polarized light microscopy. The handedness of the coils could be verified by comparing images of the coils obtained by focusing on the top and bottom of individual coils.

- Uniquely left-handed helical cellulose coils were observed in samples isolated from the leaf stalks of all tree species examined
- The diameter of the coils usually ranged between 15 and 35 μm , but the sizes and range of diameters vary with maturity and species.
- Stretching the coils showed that they could be single, double or multiple helices. Individual single rings were also observed.

Acknowledgements

We thank the Natural Sciences and Engineering Research Council of Canada for support.

References

1. Ulkem, N. and Gray, D.G. (2006): *Isolation of cellulose structures in the petiole of Apium graveolens L.* In: Salmen L (ed) 5th. Plant Biomechanics Conference. STFI-Packforsk AB, Stockholm, Stockholm, pp 211-214.
2. Revol J.-F., Bradford H., Giasson J., Marchessault R.H., Gray D.G. (1992): *Helicoidal self-ordering of cellulose microfibrils in aqueous suspension.* International Journal of Biological Macromolecules 14: 170-172.
3. Dong, X.-M. and Gray, D.G. (1997): *Induced circular dichroism of isotropic and magnetically-oriented chiral nematic suspensions of cellulose crystallites.* Langmuir 13: 3029-3034.
4. Schulgasser, K. and Witzum, A. (2004): *The hierarchy of chirality.* Journal of Theoretical Biology 230: 281-288.
5. Meylan, B.A. and Butterfield, B.G. (1978) *Helical Orientation of the Microfibrils in Tracheids, Fibres and Vessels.* Wood Sci. Technol. 12: 219-222.

Ontogenetic variations in morphology and attachment strength of permanent attachment pads of species of *Parthenocissus*

*Tina Steinbrecher*¹, *Oliver Kraft*^{1,2}, *Thomas Speck*³, *Björn Melzer*³ and *Ruth Schwaiger*^{1,2}

¹*Institute for Materials Research II, Forschungszentrum Karlsruhe, Germany;*

²*Institute for Reliability of Systems and Components, University of Karlsruhe, Germany;*

³*Plant Biomechanics Group Freiburg, Botanic Garden, University of Freiburg, Germany*

Abstract

Permanent attachment pads of Boston ivy (*Parthenocissus tricuspidata*) and Virginia creeper (*Parthenocissus quinquefolia*) have been investigated with respect to the development and the biomechanics of the attachment structures. Both species were observed to accept a wide range of inorganic and organic substrates whereas not every substrate led to the formation of mature attachment pads even when first attachment occurred. Tensile tests on young unligified and older lignified attachment pads were carried out. Attachment strength of young pads was on average only 28 % of the value found for older lignified pads. The attachment process can be described as a process of at least two steps that can be discerned as pre-attachment and final attachment.

Introduction

Climbing plants evolved different efficient mechanisms to survive in their habitat without investing energy in a massive trunk [1, 2]. A climbing habit evolved independently in at least 133 seed plant families [3] with about 30 different ways to grow [4] and it can therefore be considered a common strategy. The variety of climbing mechanisms is manifold and can be categorized as follows [1, 5]: twiners, hook climbers, root climbers, and tendril climbers as well as other contact sensitive attachment organs. This paper will focus on the climbing strategy of tendril climbers with permanent attachment pads at the tendril tips.

The nature of tendrils has been debated for more than a century [1, 6-9]. Among the various types of tendrils, mostly twiners coiling around stationary objects were investigated [2, 10-14]. The nature of the tactile response which signals the tendril to coil was studied on model systems of pea tendrils [2, 15] and tendrils of *Bryonia dioica* [12, 16, 17]. Mechanical questions about the growth process and the coiling mechanisms have been investigated during the last years [13, 18-21]. It has been shown that coiling and twining is caused by the presence of gelatinous fibers [22, 23]. Coiling tendrils and twining stems are limited in the diameter of objects they can ascend [13, 14]. In contrast, vines with adhesive elements are not limited by the diameter of their support.

Species of *Parthenocissus* possess tendrils that develop attachment pads at their tip to provide a save anchorage to the substrate. Each tendril is made up of a main axis with five to nine branchlets [24] that develop swollen tips which form into attachment pads. It is often proposed that self-clinging species of *Parthenocissus* are able to climb all kinds of surfaces but it has not been substantiated by detailed studies.

Several optical microscopy studies provide qualitative information on the *Parthenocissus* tendril [1, 6, 25-29] with a first detailed description by Malpighi [6]. The surface structure of the tendril

stalks, the developing pads and an assumed adhesive fluid were investigated by electron microscopy. These studies confirmed earlier findings on the morphology as well as the presence of an adhesive fluid which is most likely composed of an acidic mucopolysaccharide [24, 30, 31]. A first approach to identify the individual components of the adhesive fluid was an immunocytochemical characterization of attachment pads of *P. quinquefolia* [32].

Although the efficiency of holdfasts in climbing plants is well accepted, there is a clear lack of information regarding the attachment process itself, the preference for certain substrates, the biomechanical properties or the underlying (micro-)structures of these organs. In this paper, the attachment process of Boston ivy (*Parthenocissus tricuspidata*) and Virginia creeper (*Parthenocissus quinquefolia*) in correlation with the biomechanical properties of the attachment pads will be discussed, together with first insights into the acceptance of different substrates. Biomechanics of old mature attachment pads and fresh unclimbed ones will be compared and discussed.

Material and methods

Plant Material

Two self-clinging species of *Parthenocissus* with permanent attachment pads were selected as model systems: Boston ivy (*Parthenocissus tricuspidata*) with circular attachment pads and Virginia creeper (*Parthenocissus quinquefolia*) with kidney-shaped attachment pads (Figure 1).

P. tricuspidata and *P. quinquefolia* are tendrils-bearers within the grape family Vitaceae. Its tendrils develop swollen tips that form into attachment pads which then adhere to the substrate and enable the plants to climb. The investigated individuals belong to the cultivar *Parthenocissus tricuspidata* “Veitchii” and *Parthenocissus quinquefolia* “Engelmannii”. Samples were taken from well-established plants grown outdoors in the Botanical Garden at the University of Freiburg. Biomechanical investigations were conducted on fully lignified attachment pads as well as on fresh unclimbed attachment pads of *P. tricuspidata* grown on finery.

Different inorganic and organic substrates were presented as climbing substrates:

- | | |
|-------------------------------|--------------------------------|
| - beech wood | - aluminum |
| - spruce wood | - ceramic tiles |
| - carton (black/white) | - glass |
| - cork | - copper (roughened/untreated) |
| - sponge rubber (black/white) | - steel (roughened/untreated) |
| - mylar foil | |
| - PVC | |

The substrates were presented as plates of 5 cm x 10 cm attached with double-side tape to the finery. The different plates were randomly distributed over the experimental area.

Experimental Setup

Biomechanical tests were conducted with a mobile and adaptable custom-designed tensile testing device. The main components are a load sensor and a displacement sensor placed on a ball-ended very stable tripod. The freely rotating ball allows adjusting the direction of the force application as required by the samples. In all cases the tensile tester was set up in order to ensure force application in the direction normal to the substrate. The plant may typically be subjected to shear forces to a larger extent, however, such a well-defined load case allows for a reproducible comparison of different substrates, which was the focus of this study.

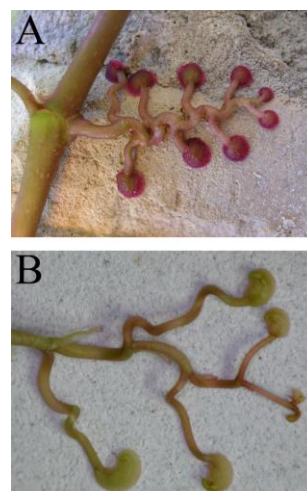


Fig. 1 a) *P. tricuspidata* tendril with circular attachment pads. b) *P. quinquefolia* tendril with kidney-shaped attachment pads.

The connection between load cell and sample was accomplished by the use of specialized tweezers. The surgical tweezers were equipped with fine teeth to grab and pull on the attachment structures without damaging the plant organs. The small and flat attachment pads cannot be held with tweezers, therefore glue droplets were put on the attachment structures in order to ensure a firm sample-tweezers connection (Figure 2). The solvent-free glue “UHU Sekundenalleskleber Gel” was used.

Force and displacement data were determined for both species of *Parthenocissus*. Since attachment pads of *P. quinquefolia* are curved in a kidney-shaped way, the preparation and the realization of tensile tests is rather difficult. A few measurements were carried out on *P. quinquefolia* for comparison, while systematic test series were carried out on circular mature and juvenile attachment pads of *P. tricuspidata*.

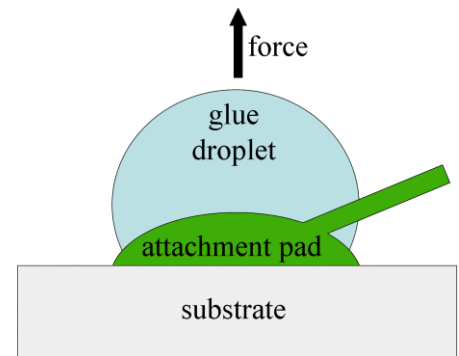


Fig.2 Schematic of the sample preparation. To grab the flat attachment pads a glue droplet is put on the samples and pulled in direction normal to the substrate.

Results and discussion

Climbing substrates

As shown in Table 1 *Parthenocissus* attaches to various types of substrates. In general, attachment was observed on both inorganic and organic substrates. However, the plants did not attach to Cu substrates (neither roughened nor untreated), which is likely due to the toxic effect of Cu in plants [33]. Fully grown mature attachment pads were found for *P. quinquefolia* and *P. tricuspidata* for rough organic substrates like wood and for smooth inorganic substrates like ceramic tiles. Except for ceramic tiles all inorganic substrates showed a tendency for small, stunted or secondary detached attachment structures, which were denoted as rudimentary. Figure 3 describes the different development paths of a tendril. The juvenile non-attached tendril is branched and develops swollen tips at the end of each branchlet. After contact with the substrate the attachment structures differentiate into attachment pads. If no appropriate substrate is found the tendril gets spiralized and/or dies. A pre-attached fresh, unligified tendril may also detach from the substrate again. After lignification, the attachment pads are tightly connected to the substrate which leads to the assumption that the attachment process is at least a two-step procedure.

Table 1 Attachment of *P. tricuspidata* and *P. quinquefolia* on various inorganic and organic climbing substrates. The attachment is defined as successful if a development of attachment pads on a given substrate is possible. A tendency for the development of rudimentary pads (cf. figure 3) is defined if more than 50 % of the developed attachment pads were small and stunted or detached after the pre-attachment phase.

Material		Attachment		Tendency for rudimentary attachment pads
		Yes	No	
Organic:	Beech wood	X		
	Spruce wood	X		
	Carton (black/white)	X		
	Cork	X		
	Sponge rubber (black/white)	X		
	Mylar foil	X		X
Inorganic:	PVC	X		X
	Al	X		X
	Ceramic tiles	X		
	Cu (roughened/untreated)		X	
	Glass	X		X
	Steel (roughened/untreated)	X		X

Black and white carton as well as black and white sponge rubber substrates were presented in order to investigate a possible influence of a phototropic reaction. Additionally, some glass substrates were presented with a black backside. No difference between the acceptance of light and dark substrates was observed in *P. quinquefolia* and *P. tricuspidata*. It can be concluded that the tendrils do not show a negatively phototropic reaction as it has been noticed for tendrils of many climbing plants [1].

As shown in Table 1, properties like light-dark, rough-smooth, hard-soft do not appear to be the crucial factors determining attachment. Fully grown attachment pads were found on all substrates but Cu. However, substrates leading to the formation of rudimentary tendrils only are tolerated but the climbing ability would definitely be restricted if such a substrate were the only substrate to climb on.

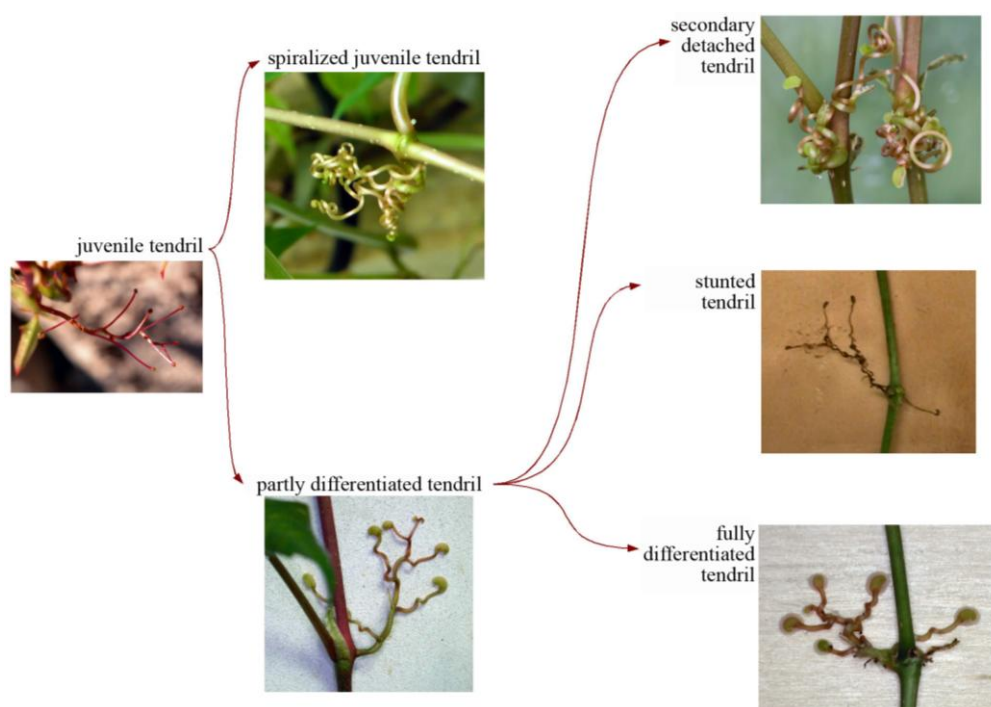


Fig. 3 Development of a tendril in *P. quinquefolia*. A juvenile tendril can differentiate either into an attached tendril with attachment pads or spiralize and not function as a holdfast. A partially differentiated tendril can detach after initial attachment. The differentiated attachment pads are no longer connected to the substrate. On some substrates (cf. Table 1) there is a tendency for stunted tendrils. These tendrils are of brown color and the connection between the main axis of the plant stem and the tendrils becomes brittle. An appropriate substrate leads to the formation of fully grown attachment pads which are tightly connected to the substrate.

Different organic and inorganic substrates result in different mean sizes of the attachment pads (Table 2). The attachment pads of *P. tricuspidata* are in general bigger than attachment pads of *P. quinquefolia*. In case of *P. quinquefolia* the mean size of the pads is $3.6 \pm 0.3 \text{ mm}^2$ on beech wood and $1.3 \pm 0.9 \text{ mm}^2$ on Al. There is a significant difference between the mean sizes on the different substrates (Rank-Sum test, $P < 0.001$). For *P. tricuspidata*, the mean size of the pads is $4.6 \pm 1.5 \text{ mm}^2$ on beech wood and $3.4 \pm 0.5 \text{ mm}^2$ on Al. In this case, there is no statistically significant difference between the mean sizes on the different substrates (Rank-Sum test, $P = 0.149$). The tendency for smaller attachment pads on “not-appropriate” substrates was thus only observed for Virginia creeper. However, due to the large variations as typical of biological samples a more comprehensive study should be carried out in further investigations.

Table 2 Area of attachment pads of Boston ivy (*P. tricuspidata*) and Virginia creeper (*P. quinquefolia*) on wooden and metallic substrate; Sample number: $n=20$.

	Mean attachment area [mm^2]	Maximum attachment area [mm^2]	Mean attachment area [mm^2]	Maximum attachment area [mm^2]
	<i>Parthenocissus quinquefolia</i>		<i>Parthenocissus tricuspidata</i>	
Beech wood	3.6 ± 0.3	5.1	4.6 ± 1.5	7.6
Al	1.3 ± 0.9	2.7	3.4 ± 0.5	3.9

Biomechanical investigation

A typical force-displacement curve for an individual attachment pad of *P. tricuspidata* is shown in Figure 4. The specimens were subjected to a continually increasing uniaxial tensile force. The load increases linearly with increasing displacement until failure occurs at 6.3 N. In general, the attachment pads showed force-displacement curves with almost linear portions up to final failure. A single lignified pad on finery withstands normal stresses at the interface of up to 4 MPa (at a maximum force of 14.1 N) while failure never occurred directly at the interface. Three different failure modes were observed: failure of the substrate, internal failure of the attachment pad, or a combination of the two modes. The attachment strength of young pads has been found to be significantly smaller than the attachment strength of older lignified ones (Figure 5). The mean attachment strength of young, fresh pads and of older, lignified pads is 1.6 ± 0.8 N and 5.6 ± 0.3 N, respectively. Therefore, the attachment strength of younger pads was on average only 28 % of the value found for the older pads. After initial contact an attachment pad is developed and the comparatively weak pre-attachment is formed, i.e. stage 1. The fully differentiated attachment pads get subsequently lignified and form a strong connection to the substrate, i.e. step 2. Lignified attachment pads stay attached to the substrate even if the plant dies.

The characterization of the attachment process as a multi step process correlates also with the findings in the tendril and attachment pad development. After a first attachment a secondary detachment is possible which is impossible after the complete attachment.

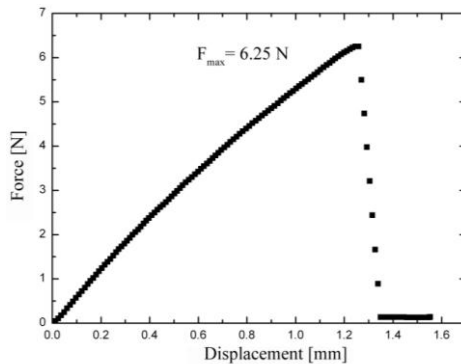


Fig. 4 Force-displacement curve for an individual lignified attachment pad of *P. tricuspidata*.

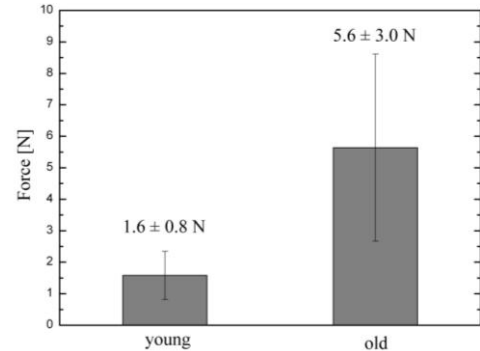


Fig. 5 Mean attachment strength of young, fresh attachment pads of *P. tricuspidata* compared to older lignified ones.

Conclusion

Boston ivy (*P. tricuspidata*) and Virginia creeper (*P. quinquefolia*) are both able to climb on a variety of substrates. The attachment strength of young attachment pads was found to be significantly lower compared to older pads. Therefore, the attachment process can be described at least as a two step process. Furthermore, the development of the attachment structures shows a correlation with the different substrate materials. In the case of *P. quinquefolia*, in addition the mean pad size is clearly correlated with the substrate materials.

Acknowledgements

Financial support from the “Landesstiftung Baden-Württemberg” within the scope of the program “Neue Materialien aus der Bionik” is greatly appreciated. We would also like to thank Dipl.-Biol. Elisabeth Danninger for her support.

References

1. Darwin, C. (1876): *The Movements and Habits of Climbing Plants*. D. Appleton and Company, New York
2. Jaffe, M.J. and A.W. Galston (1968): *The physiology of tendrils growth*. Ann. Rev. Plant Phys. 19: 417-434.
3. Gentry, A.H. (1991): *The distribution and evolution of climbing plants*, in *The biology of vines*, Putz FE M.H., Cambridge University Press, Cambridge. p. 181-204.
4. Menninger, E.A. (1970): *Flowering Vines of the World: An Encyclopedia of Climbing Plants*. Heartside, NY
5. Rowe, N., S. Isnard, F. Gallenmueller and T. Speck (2006): *Diversity of mechanical architectures in climbing plants: an ecological perspective*, in *Ecology and biomechanics: a mechanical approach to the ecology of animals and plants*, Herrel A., T. Speck and N. Rowe, Taylor & Francis, Boca Raton, Florida, USA. p. 35-59.
6. Malpighi, M. (1686): *Anatomes Planatarum*, in *Opera Omnia*, Malpighi M., Sawbridge and Wells, London.
7. Bugnon (1953): *Recherches sur la Ramnification des Ampelidacees*. Presses Universitaires de France, Paris.
8. Millington, W.F. (1966): *The tendril of Parthenocissus inserta: determination and development*. American Journal of Botany 53: 74-81.
9. Shah, J.J. and Y.S. Dave (1966): *Are tendrils of Vitaceae Axillary?* Current Science 22: 559-561.
10. Gofbel, K. (1900): *Organography of plants*. Clarendon Press, Oxford.
11. Putz, F.E. and N.M. Holbrook (1991): *Biomechanical studies of vines*, in *The Biology of Climbing Plants*, Putz F.E. and H.A. Mooney, Cambridge University Press, Cambridge. p. 53-78.
12. Weiler, E.W. (1993): *Octadecanoid-derived signaling molecules involved in touch perception in a higher plant*. Botanica Acta. 106: 2-4.
13. Sher, J.L., N.M. Holbrook and W.K. Silk (2001): *Temporal and spatial patterns of twining force and lignification in stems of Ipomea purpurea*. Planta. 213: 192-198.
14. Goriely, A. (2006): *Mechanics of Climbing and Attachment in Twining Plants*. PRL. 97: 184302.
15. Jaffe, M.J. (1970): *Physiological Studies on Pea Tendrils VI. The Characteristics of Sensory Perception and Transduction*. Plant Physiology. 45: 756-760.
16. Kaiser, I., J. Engelberth, B. Groth and E.W. Weiler (1994): *Touch- and methyl jasmonate-induced lignification in tendrils of Bryonia dioica Jacq.* Botanica Acta. 107: 24-29.
17. Engelberth, J. (2003): *Mechanosensing and Signaltransduction in Tendrils*. Advances in Space Research. 32: 1611-1619.
18. Silk, W.K. (1989): *Growth rate patterns which maintain a helical tissue tube*. Journal of Theoretical Biology. 138: 311-327.
19. Silk, W.K. and M. Hubbard (1991): *Axial forces and normal distributed loads in twining stems of morning glory*. Journal of Biomechanics. 24: 599-606.
20. Matista, A.A. and W.K. Silk (1997): *An electronic device for continuous, in vivo measurement of forces exerted by twining vines*. American Journal of Botany. 84: 1164-1168.
21. Silk, W.K. and N.M. Holbrook (2005): *The importance of frictional interactions in maintaining the stability of the twining habit*. American Journal of Botany. 92: 1820-1826.
22. Bowling, A.J. and K.C. Vaughn (2009): *Gelatinous Fibers are Widespread in Coiling Tendrils and Twining Vines*. American Journal of Botany. 96: 719-727.
23. Meloche, C.G., J.P. Knox and K.C. Vaughn (2007): *A cortical band of gelatinous fibers causes the coiling of redvine tendrils: a model based upon structural and immunocytochemical studies*. Planta. 225: 485-498.
24. Junker, S. (1976): *A Scanning Electron Microscopic Study on the Development of Tendrils of Parthenocissus Tricuspidata SIEB. & ZUCC*. New Phytologist. 77: 741-746.
25. Ewart, A.J. (1898): *On contact irritability*. Annales du Jardin Botanique de Buitenzorg. 15: 187-242.
26. Mohl, H. (1827): *Über den Bau und das Winden der Ranken- und Schlingpflanzen*. Laupp, Tübingen.
27. Lengerken, A.V. (1885): *Die Bildung der Haftballen an den Ranken einiger Arten der Gattung Ampelopsis*. Botanische Zeitung. 43: 337-346.
28. Moens, P. (1956): *Ontogenèse des vrilles et différenciation des ampoules adhésives chez quelques végétaux. (Ampélopsis, Bignonia, Glaziovia)*. La Cellule. 57: 317.
29. Chiang, S.-h.T. and M. Tu (1971): *Histological Study on the Tendril of Parthenocissus tricuspidata*. Taiwania. 16: 49-66.
30. Endress, A.G. and W.W. Thomson (1976): *Ultrastructural and cytochemical studies on the developing adhesive disc of boston ivy tendrils*. Protoplasma. 88: 315-331.
31. Endress, A.G. and W.W. Thomson (1977): *Adhesion of the boston ivy tendril*. Can J Bot. 55: 918-924.
32. Bowling, A.J. and K.C. Vaughn (2008): *Structural and Immunocytochemical Characterization of the Adhesive Tendril of Virginia Creeper (Parthenocissus quinquefolia [L.] Planch.)*. Protoplasma. 232: 153-163.
33. Fernandes, J.C. and F.S. Henriques (1991): *Biochemical physiological and structural effects of excess copper in plants*. Botanical Review. 57: 246-273.

Using vegetation to stabilize steep slopes in Southern China: root biomechanics as a factor in the choice of species

Murielle Ghestem¹, Alexia Stokes²,

Kunfang Cao³, Wenzhang Ma³, Jianlei Xie⁴

¹AgroParisTech, UMR AMAP, 34398 Montpellier, France; ²INRA, UMR AMAP, Montpellier cedex 5, 34938 Montpellier, France; ³Xishuangbanna Tropical Botanical Garden, Chinese Academy of Sciences, Menglun, Mengla, Yunnan 666303, China; ⁴Yunnan University of Agriculture, Heilongtan, Kunming, Yunnan 650204, China.

Abstract

In order to identify appropriate species to rehabilitate degraded slopes after landslides in Southern China, we measured two parameters important for fixing soil: root architecture and root tensile strength (T_r). We studied three pioneer species with different growth forms: two native species: *Artemisia lavandulaefolia* (Asteraceae, flowering herb) and *Chloris anomala* (Poaceae, herb), and one planted species: *Pueraria stricta* Kurz. (Fabaceae, shrub). We compared root systems on slopes where a shallow landslide had just occurred and on slopes where the landslide had been stabilized by vegetation. T_r was significantly different between species and with regard to slope type (stable/unstable). *A. lavandulaefolia* had the lowest T_r on stable slopes, but strength was significantly increased on unstable slopes, whereas *P. stricta* and *C. anomala* had lowest T_r on unstable compared to stable slopes. Therefore, with regard to T_r , *A. lavandulaefolia* appeared to be the most appropriate species to stabilize slopes. Results from the root architectural analysis suggested that a combination of the three species would be an optimal ecological combination to increase soil cohesion at all soil depths.

Introduction

In China, a country where two-thirds of the land is made up of hills and mountains, erosion and landslides are the result of deforestation, bad farming practice and over-exploitation of resources in the last 50 years [1][2][3]. China currently feeds 20% of the world population and possesses 7% of the world's croplands [4]. China is also an area with high seismic activity, causing many secondary landslides. The 2008 Wenchuan earthquake, resulted in 80,000 casualties with 20 000 caused by associated geohazards, and by the end of 2008 slopes in the area were not stabilized [5][6]. A major new problem to be faced is the building of roads linking villages to towns [7]. A survey along Nujiang Valley, Yunnan, showed that soil loss rates due to road building represent at least 80% of the total soil loss, and were over 600 times greater than the highest currently recorded in the USA [8]. China has therefore to combine sustainable land management with crop production and rural infrastructure development on sloping land.

Within such a context, mitigation strategies need to focus on target areas of a slope, concentrating on the most fragile zones (degradation hotspots). Recently proposed as a useful technique for restoring eroded land, the management of degradation hotspots [9][10] appears to be one of the most economically viable methods for rehabilitating steep slopes on a large scale. To improve hotspot management, the local ecology needs to be taken into account before a choice of species is made e.g. ethnobotanical knowledge should be used to identify the needs of local farmers and villagers, so that species can provide an income to the local community [11].

Vegetation has long been recognized as a factor useful for increasing the shear resistance of soil on an unstable slope [12]. To better understand how root systems occupy soil over time and space, and especially how root systems cross the potential shear surface of a slope, a landslide engineer needs to

take into account the three-dimensional (3D) root architecture and mechanical properties of any given species. Information on how species grow should be considered, especially during the early stages of growth, as soil conditions strongly affect root growth in the first weeks after germination [13].

The presence of plant roots crossing the potential shear surface results in an increase in soil cohesion through a reinforcing effect which usually augments superficial slope stability. The root – soil reinforcement model developed by Wu [14], and elaborated upon by Waldron [15], is widely used to estimate the additional cohesion taking into account the presence of roots in the soil [16] [17] [18]. This model states that the additional cohesion due to the presence of roots can be estimated as follows

$$C_r = 1.2 * T_r * RAR \quad (1)$$

where T_r is the average tensile strength of roots and RAR is the Root Area Ratio. In the literature, it is often reported that T_r decreases when root diameter d increases: fine roots are more resistant in tension than thicker roots [19][20].

In order to better estimate the efficiency of native species in stabilizing slopes, we studied root architecture and measured root tensile strength of three pioneer species on steep slopes in Southern China. So as to estimate their capacity of adaptive growth on slopes where erosive soil slippage was still underway, we selected two adjacent degradation hotspots: one stabilised by vegetation and one unstable. These hotspots were located near a high-biodiversity zone, including more than 25 identified species, which plays the role of a reservoir for colonisation of degradation hotspots. We chose species growing on degradation hotspots at the beginning of the rainy season, when slopes are more prone to landslides. Among the studied species, were two naturally-grown species, *Artemisia lavandulaefolia* (Asteraceae, flowering herb) and *Chloris anomala* (Poaceae, herb), and one planted species, *Pueraria stricta* Kurz. (Fabaceae, shrub).

Material and methods

Our study site is located in Southern China, in Yunnan province, 20 km east of the border with Myanmar (N26°01'60", E098°50'60"). In this area, the river Salween flows from North to South, strictly parallel to the Mekong and the Yangtze. Due to its topographic, climatic and geologic diversity (the Salween river bed follows a major seismic fault resulting from the Indo-Eurasian collision), as well as its location, (this valley was a north-south corridor for species migration especially during glaciation periods). This area is classified as a UNESCO World Heritage site since 2003. Over 6,000 plant species exist, among which more than 300 medicinal plants can be found (<http://whc.unesco.org/fr/list/1083>).

Altitudes range from 800 m to more than 3,000 m and slope angles can be >50°. This part of China is under the influence of the Indian monsoon, and described as a “warm-dry climate”, which is a combination between subtropical and alpine climates. Annual mean temperature (from 1961 to 2002) is 15.2°C, and mean annual precipitation is 1200 mm, the majority of which falls between May and October. The major soil type is a ferrallitic red clay soil, with many mineral coloured spots, e.g. iron and manganese. Except on degradation hotspots, soil and humus thickness are not limiting factors: being 0.2–2.0 m and 0–0.02 cm, respectively. Severe and numerous landslides occur during the monsoon season (May–October), and the slip surface of these landslides has been estimated at a mean depth of 0.5 m. We defined two hotspots of land type: L1 and L2, L1 being an active landslide, and L2 as stable, as natural regeneration and planted shrubs have been allowed to grow undisturbed for 8 years (Table 1). Only *C. anomala* was grazed slightly by cows at L2.

Hotspot	Area	A.S.L.	Slope	Orien- tation	Sliding cause	Sliding date	Bedrock depth	Shear resistance Mean ± CI _{95%} ¹
L1 unstable	20mx30m	1099m	50-60°		rain and gravity	Still sliding	30 cm	0.17±0.03 kg/m ²
L2 stable	100mx200m	949m	35-45°	300°	-	± 10 yrs ago	20 cm	0.27±0.03 kg/m ²

Table 1: Description of the two hotspots L1 and L2. ¹Shear resistance was measured on 20 points on each landslide, with a Shear Vane (Sols-mesures 14.10). A Mann-Withney Test showed that the shear resistance is significantly different on L1 and L2 ($p < 0.05$). A.S.L. is altitude above sea level.

Ten root systems of young individuals of each species were hand-excavated: six growing on L1 and four growing on L2 (Table 2). Excavations were carried out with extreme caution and without damaging the roots. Heights and widths of the plants are given, but cannot be used to determine an individual's age. As is often the case in tropical and sub-tropical climates, winter is not severe enough to arrest secondary growth and there is no clear annual ring formation in the stems.

Root system width and depth was measured for each plant and a general architectural description given. Tensile testing was successfully carried out on 1287 root samples, using a portable machine (In-Spec 2200 BT, Instron Corporation, www.instron.com) equipped with a force transducer (max. capacity 250 N, accuracy 0.25%). The length of each sample was at least 30 times its central diameter [21]. Crosshead speed was kept constant at 1.0 mm.min⁻¹ and both force and speed were measured constantly via Instron Series IX software during each test. We measured the force required to cause failure in tension of each root. In order to avoid slippage of roots out of the clamps, the clamps were chosen according to the diameter of the root. Tests were considered successful only when specimens failed approximately in the middle third of the root. Tensile stress was calculated as the maximal force required to cause failure in the root, divided by the root cross-sectional area (CSA) at the point of breakage.

	n	Min.-Max. height of plant crown (cm)	Min.-Max. width of plant crown (cm)	Min.-Max. root depth (cm)	Min.-Max. distance of the longest root to the stem (cm)	Min.-Max. root diameter (mm) (no. tests)	Ethnobotanical uses
<i>Artemisia lavandulaefolia</i>							
L1	6	7.3-20.3	18.4-36.4	18.5-45.0	38.0-51.8	0.01-3.31 (300)	Human and cattle medicine.
L2	4	4.6-17.0	13.4-24.0	24.0-34.0	34.7-61.0	0.02-1.5 (149)	
<i>Pueraria stricta</i>							
L1	6	15.0-117.0	5.3-31.0	30.0-54.0	25.4-97.0	0.02-4.56 (296)	Planted by government for slope stabilisation. Fixes nitrogen. Cattle forage and shade.
L2	4	15.5-34.0	14.3-32.5	34.0-49.0	11.0-123.0	0.05-4.88 (176)	
<i>Chloris anomala</i>							
L1	6	6.5-16.5	13.3-20.1	13.8-28.2	23.5-31.7	0.04-0.56 (205)	Cattle forage.
L2	4	3.9-12.7	5.5-27.6	11.0-37.0	19.5-63.5	0.01-0.51 (161)	

Table 2: Size of aerial and underground parts of plants (depth: perpendicular to the soil surface).

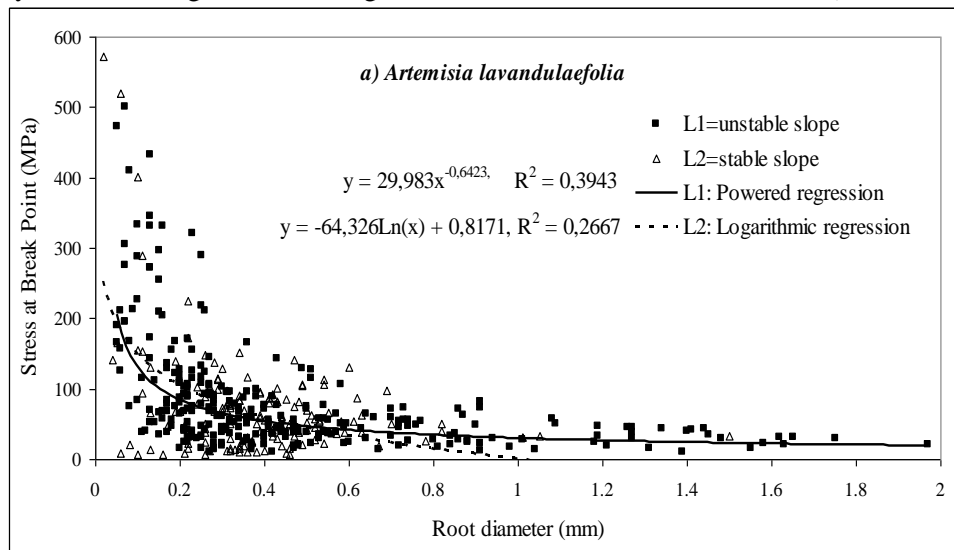
For each species and on each hotspot, we drew the best regression curve between tensile stresses and root diameters. To determine whether or not differences exist in root tensile stress between species and between hotspots, analysis of covariance (ANCOVA) was carried out with tensile stress as the dependent variable, species and hotspot type as the factors, and root diameter as the covariate. When data were not normally distributed ($p < 0.05$) and did not show the same deviation standard, a logarithmic transformation was performed. Noticeably, in this study, parametric tests were also performed on raw data considering the large amount of data in each dataset (Central Limit Theorem).

Results

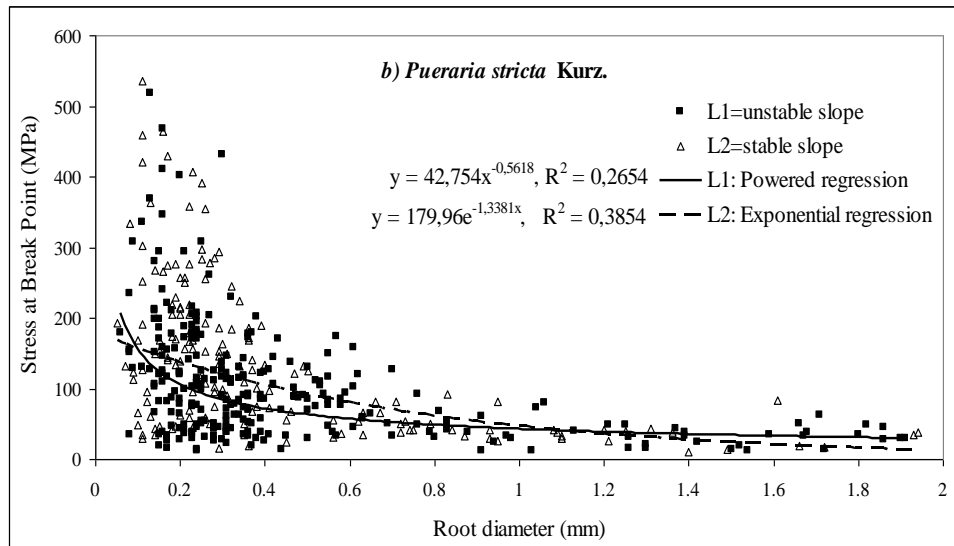
Root architecture

During the first stages of growth, *A. lavandulaefolia* had long lateral subhorizontal roots (macrorrhizae). In general, one taproot grew deeply and long lateral roots grew obliquely at an angle of approximately 45°. Macrorrhizae extremities branched into very fine roots. Small fibrous roots (brachyrrhizae) were dispersed in clusters along the long branches (Table 2, Fig 1a). *P. stricta* possessed one differentiated taproot with long subhorizontal branches. The taproot was often long and tortuous. Few root hairs were observed and fibrous brachyrrhizae were confined in a zone around the

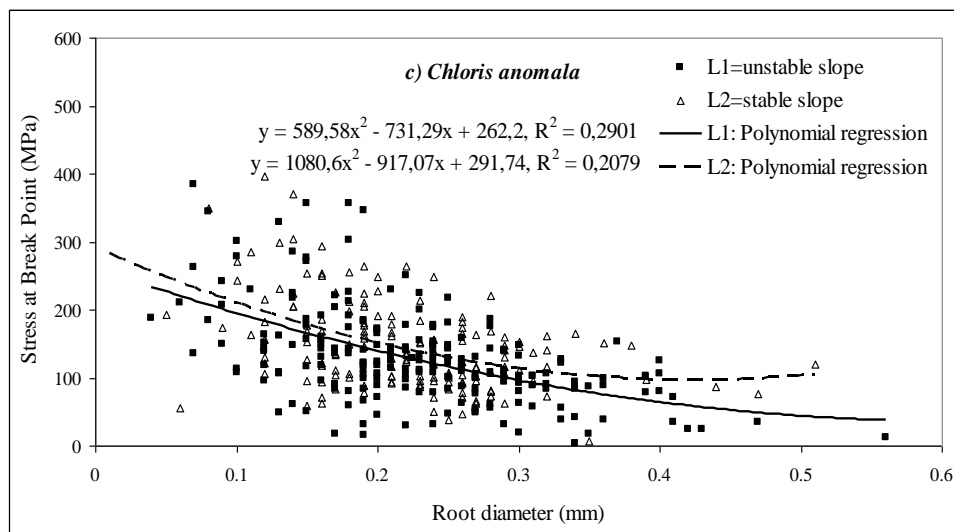
collar and at the extremities of long branches (Table 2, Fig. 1b). *C. anomala* possessed root systems with fine and short roots. Each plant had a small number of roots, but as individuals were clustered into tufts, a mat of roots existed under the soil surface. Individuals were able to develop a layered root system, allowing roots to emerge from the stem above the soil surface (Table 2, Fig. 1c).



a) *Artemisia lavandulaefolia*: long lateral roots



b) *Pueraria stricta*: taproot system



c) *Chloris anomala*: fine fibrous roots

Fig.1: Relationships between stress at rupture (MPa) and root diameter (mm), and the best-fit regression curve ($p < 0.005$) .a) *Artemisia*, b) *Pueraria*, c) *Chloris*, and their respective root systems.

Root tensile strength (Fig 1 and 2)

A. lavandulaefolia, *P. stricta* Kurz. and *C. anomala* had similar mean values for tensile strength, especially on the unstable hotspot, but variability in data dispersion was high (Fig 2). Tensile strengths were comparable or even higher than those observed on trees in other studies [18] [20]. *A. lavandulaefolia* had the highest minimal mean and *C. anomala* the maximal mean at the stable hotspot. *A. lavandulaefolia* possessed the lowest standard deviation (SD) at the stable hotspot, and the highest SD at the unstable hotspot. For all species, tensile strength decreased with increasing root diameter (Fig 1), following different regression models.

Tensile strength was significantly different on the two types of hotspots for each species ($F_{2, 1276} = 8.09$, $p < 0.001$, ANCOVA, Fig.2). *A. lavandulaefolia* had a much higher tensile strength on the unstable hotspot, whereas *P. stricta* and *C. anomala* possessed higher tensile strengths on the stable slope.

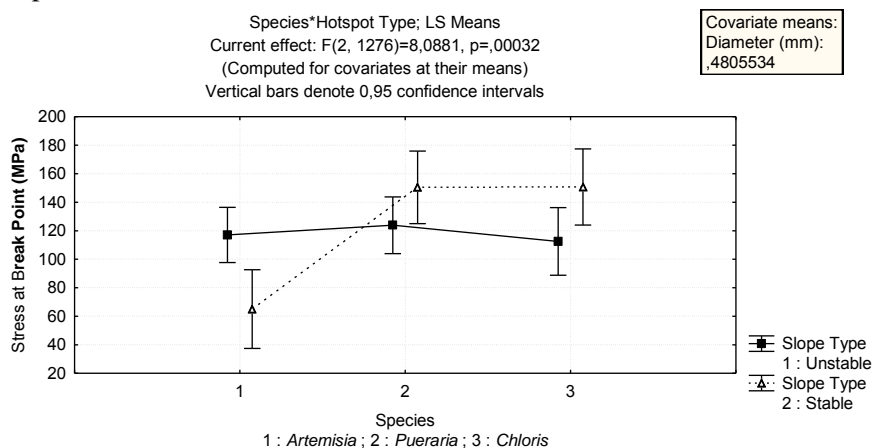


Fig.2: Analysis of covariance with tensile strength as dependent variable, species and hotspot types as factors and diameter as covariate. The effect of Species*Hotspot type is significant.

Discussion

With regard to root architecture, the ability of *C. anomala* to produce roots up the stem and above the soil surface is useful on slopes, when soil slippage can leave downhill roots exposed. By growing layers of roots uphill, the plant can stay anchored, although at an expense of producing deeper roots. This fast-growing herb is complementary to slower growing shrubs and trees, especially on unstable erosion hotspots where a shallow reinforcement of soil is required. *P. stricta* possessed a deeply growing taproot, fixing the soil through a thicker zone and thus crossing deeper potential shear surfaces. These three species, observed together on the slopes, seem to be an optimized ecological combination for soil stabilisation.

Considering mechanical properties of the roots, we suggest that *A. lavandulaefolia* is the species best adapted to soil slippage, as tensile strength increased when plants grew on unstable soil, contrary to *P. stricta* and *C. anomala*. Interestingly, *P. stricta* has been chosen by government authorities to plant on unstable slopes, even though root tensile strength decreases. The values we obtained for tensile strength in fine roots were extremely high, but similar values have been observed for fine roots of woody species [22]. It would be of great interest to carry out more testing of such small diameter roots, and to determine why tensile strength values may be so high in certain roots. We will also carry out a similar study on secondary succession species, and determine which mechanical and architectural traits are most useful at maintaining soil and preventing landslides on steep slopes.

Acknowledgements

Funding was received from INRA (Jeune Equipe), France and the Eco-pente project (CNRS). Thanks are due to Pr Pen Hua, Pr Shui Yumin and Dr Frédéric Jacques, Kunming Institute of Botany, CAS, for plant identification and Dr Claire Atger for help with root architectural descriptions. We are grateful to Dr Nick Rowe for his advice on mechanical measurements. AMAP (Botany and Computational Plant Architecture) is a joint research unit which associates CIRAD (UMR51), CNRS (UMR5120), INRA (UMR931), IRD (2M123), and Montpellier 2 University (UM27).

References

1. J. Liu and J. Diamond (2005): *China's environment in a globalizing world*, Nature, 435, 1179-1186.
2. A. Stokes, J.E. Norris, and J. Greenwood (2008): *Introduction to ecotechnological solutions*. Slope Stability and Erosion Control: Ecotechnological Solutions. Springer. p. 1-8.
3. S. Cao, L. Chen, and X. Yu (2009): *Impact of China's Grain for Green Project on the landscape of vulnerable arid and semi-arid agricultural regions: a case study in northern Shaanxi Province*. Journal of Applied Ecology. 46: 536-543.
4. FAO (2007): *La situation mondiale de l'alimentation et de l'agriculture (SOFA)*. Rome: Sous-division des politiques et de l'appui en matière de publications électroniques. Division de la communication.
5. G. Wang, T. Kamai, M. Chigira, and X. Wu (2008): *Some catastrophic landslides triggered by the May 12, 2008 Sichuan earthquake*. The First World Landslide Forum. United Nations University, Tokyo, Japan. Parallel Session Volume. ISDR, ICL. p. 647-651.
6. Y. Yin, F. Wang, and P. Sun (2008): *Landslide hazards triggered by the 12 May 2008 Wenchuan earthquake, Sichuan, China*. The First World Landslide Forum. United Nations University, Tokyo, Japan. Parallel Session Volume. ISDR, ICL p. 1-17.
7. A. Stokes, R.B. Sotir, W. Chen, and M. Ghestem (2009): *Soil Bio- and Eco-engineering in China: Past Experience and Future Priorities*. Ecological Engineering, in press. doi:10.1016/j.ecoleng.2009.07.008.
8. R.C. Sidle (2007): *Dark clouds over Shangri-La*. Japan Times. March 2007.
9. J. Poesen, T. Smets, and S. De Baets (2008): *The effectiveness of organic mulches and plant roots in controlling soil loss at water erosion hot spots in the landscape*. 2nd International Conference on Ground Bio- and Eco-engineering: The Use of Vegetation to Improve Slope Stability. LIAMA, Beijing, China.
10. G.A. Baigorria and C.C. Romero (2007): *Assessment of erosion hotspots in a watershed: Integrating the WEPP model and GIS in a case study in the Peruvian Andes*. Environmental Modelling & Software. 22: 1175-1183.
11. P. Grosjean and A. Kontoleon (2009). *How Sustainable are Sustainable Development Programs? The Case of the Sloping Land Conversion Program in China*. World Development. 37: 268-285.
12. M. Genet, A. Stokes, F. Salin, S. Mickovski, T. Fourcaud, J. Dumail, and R. van Beek (2005). *The Influence of Cellulose Content on Tensile Strength in Tree Roots*. Plant and Soil. 278: 1-9.
13. H. Khuder (2006): *Effet d'une pente sur l'architecture et les propriétés mécaniques des systèmes racinaires de semis d'arbres*. PhD thesis University of Bordeaux I, France.
14. T. Wu (1976): *Investigation of landslides on Prince of Wales Island, Alaska*. Ohio State University, Department. of Civil Engineering. Geotechnical Engineering Report. p. 93.
15. L.J. Waldron (1977): *The Shear Resistance of Root-Permeated Homogeneous and Stratified Soil*. Soil Science Society American Journal. 41: 843-849.
16. D.H. Gray and R.B. Sotir (1996): *Biotechnical and Soil Bioengineering Slope Stabilization: A Practical Guide for Erosion Control*. John Wiley & Sons Inc.
17. J.J. Roering, K.M. Schmidt, J.D. Stock, W.E. Dietrich, and D.R. Montgomery (2003): *Shallow landsliding, root reinforcement, and the spatial distribution of trees in the Oregon Coast Range*. Canadian Geotechnical Engineering. p. 237-253.
18. M. Genet, N. Kokutse, A. Stokes, T. Fourcaud, X. Cai, and J. Ji (2008): *Root reinforcement in plantations of Cryptomeria japonica D. Don: effect of tree age and stand structure on slope stability*. Forest Ecology and Management.
19. M. Genet (2007): *Variations spatio-temporelles des propriétés de renforcement racinaire de forêts naturelles et plantées dans le sud ouest de la Chine et leurs impacts sur la stabilité des pentes*. PhD Thesis, Université Bordeaux I, France.
20. G. Bischetti, E. Chiaradia, T. Epis, and E. Morlotti (2009): *Root cohesion of forest species in the Italian Alps*. Plant and Soil. In press.
21. P. Cofie (2001): *Mechanical properties of tree roots for soil reinforcement models*. PhD Thesis, University of Wageningen, Netherlands.
22. G. Bischetti, E. Chiaradia, T. Simonato, B. Speziali, B. Vitali, P. Vullo, and A. Zocco (2005): *Root Strength and Root Area Ratio of Forest Species in Lombardy (Northern Italy)*. Plant and Soil. 278: 11-22.

Multi-stemming and mechanics of trees and shrubs growing along avalanche paths

*François-Xavier Mine*¹, *Alexia Stokes*² *Loic Brancheriau*³

¹ ISARA-Lyon, 69634 Lyon cedex 07, France; ²INRA, UMR AMAP, Montpellier cedex 5,

³CIRAD - Département PERSYST, UPR 40, 73 Rue Jean François Breton, 34398
Montpellier Cedex 5, France

Abstract

We measured dynamic modulus of elasticity (E_d) and bending strength (σ) for several tree species growing in or around an avalanche path in the French Alps. Species were single- or multi-stemmed, the latter being more abundant at the centre or edges of the path. *Alnus viridis*, generally found at the centre of avalanche paths, had the lowest E_d and σ , and was strongly multi-stemmed, thus allowing this species to bend during an avalanche or to resprout if damaged. In several species where stem bases were procumbent after snow damage, E_d increased with height up the stem, conferring a mechanical advantage on these young stems which need to grow quickly upwards and dominate the canopy. E_d did not change along stems in *Corylus avellana*, a multi-stemmed shrub with stems often leaning on each other, thus providing mutual support, as also found in semi self-supporting plants.

Introduction

Whereas competition between species has traditionally been considered the driving process for selection and diversity, it is now postulated that in a world experiencing climate change and frequent human impacts in ecosystems, disturbance may become the driving process. Disturbance of a habitat may be abiotic (flooding, storms, fire) or biotic (grazing, insect outbreak). Plant resistance and resilience to disturbance can be reflected in a certain number of traits, including responses to nutrient and water availability, temperature and light. In the case of mechanical, abiotic disturbance often occurring on mountain slopes e.g. storms, landslides and avalanches, plant mechanical properties may determine whether or not a species will be adapted to the disturbance, depending on its frequency and intensity [1].

Avalanche paths provide specific habitats for a number of species, and are now recognised as rich in plant diversity [2]. If avalanches are to be avoided e.g. in populated areas, barriers are usually placed in the departure zones. However, the use of protection forests to stabilize the snow mantle at departure zones is now being explored in detail [3], although once an avalanche is underway, the energy needed to fracture and transport a dense forest of spruce trees is very small compared with the kinetic energy of a large avalanche [4]. The ability of a given species to fix the snow mantle is thus of interest, but opinions are conflicting as to which species confer the best protection against snow movement. Single-stemmed conifers which are $>2.0x$ taller than the depth of the snow are considered as best at stabilizing the snow mantle [3]. With regard to multi-stemmed species which do not reach this target height, it has been conjectured that they offer either no protection or even exacerbate avalanches as the snow held on branches can be released suddenly if the stems straighten up quickly, although under what conditions this may occur is not specified [5]. Avalanches in turn can cause uprooting and overturning of trees. Therefore, for a tree species to grow in an avalanche path, a certain number of strategies would increase its survival and persistence.

To resist mechanical failure due to an avalanche, stems should be small and flexible enough to bend under the weight of snow. Large stems typically break [6]. Even if stem breakage does occur, the

ability to resprout from the stem or stem base would improve survival of an individual, especially if the plant was well-anchored. The resprouting ability of a species depends on the type and time of disturbance throughout the year, as well as tree size [7,8].

We measured dynamic modulus of elasticity (E_d) and bending strength (σ) for several tree species (Table 1) growing in or around an avalanche path in the French Alps. Each species possesses a different ability to resprout, therefore influencing growth form of the individuals from which the samples were taken. *A. viridis* is typically found at the centre of the path, *F. sylvatica* and *C. avellana* at the periphery of the path and *A. incana* and *B. pendula* at a distance from the path or downslope of the path. An inventory of stem form for all species present was made in several transects along the avalanche path and the consequences of multi-stemming on mechanical properties discussed.

Material and methods

Tree species, number, vertical height, diameter at 1.3m (DBH) and the number of stems present per individual (Table 1) were determined in six 100m x 4 m transects, traversing an avalanche path (Combe Gilbert) at Allemont, Isère, French Alps. When more than one stem was present per individual, the mean DBH was calculated for the stems with a maximum of five stems measured. The avalanche path was approximately 600 m long and 21 avalanches have occurred over the last 45 years (<http://www.avalanches.fr/>). A major mudslide occurred in 1952, and natural regeneration has since occurred in a cone shape (Fig. 1). In March and April 2009, dormant stems were cut from individuals at the centre or the edges of the avalanche path at four different altitudes. These samples were immediately transported to the laboratory for mechanical analysis, kept moist at a temperature of 4°C and tested within 4 weeks.

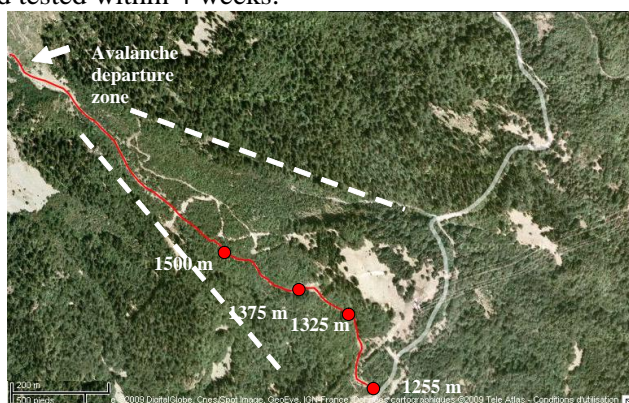


Fig. 1 Wood samples were taken at four altitudes along an avalanche path (solid line) at Allemont, Isère, French Alps. The path lies in an area where a rock- and mudslide occurred in 1952. Natural regeneration has since taken place, consisting mainly of broadleaf species (within the cone-shaped area bordered by dashed lines). Image courtesy of GoogleEarth.

Bending strength (σ) for stem segments for five species (Table 1) was determined using standard 4-point bending tests (European norm NF EN 408).

Dynamic modulus of elasticity (E_d) was measured in samples taken from *C. avellana*, *A. viridis*, *F. sylvatica* and *B. pendula*. Stems from individuals were cut into sections and the distance between the mid-point of the section and the tree base measured. Only samples from the main stem were measured, not side branches. We used the acoustic method, WISIS [9] to measure E_d . The WISIS system was designed by CIRAD as a nondestructive device to evaluate the mechanical state of in-service solid wood members in structure (<http://www.xylo-metry.org/en/wisis.html>). WISIS measures, among other parameters, E_d using a time of flight technique. Dynamic tests and standardized static tests (3 or 4-point bending) allow the estimation of the modulus of elasticity (E) considering wood matter as homogeneous. Equations of motion do not take into account the presence of annual rings, the cellular pattern and local differences of density. A plant stem sample is a wave guide and the wave length associated to a longitudinal acoustic wave is about 1 m or more. At this scale the interaction wave – one stem is equivalent to an interaction wave – is equivalent to a homogeneous ‘stem,’ therefore reflections from tissues are negligible. The assessment of E_d for a plant stem sample is however difficult and can be a source of high measurement error: the stem is not perfectly straight and its diameter varies. The length and density of the sample can thus be biased. Nevertheless, acoustic testing allows a mean E to be obtained for a short, thick stem sample which cannot be tested through static testing where a long span distance between supports is required.

For our study, the signal analysis was based on time analysis with a sampling frequency set to 2.5MHz and an acquisition duration of 13.11ms (length of samples ranged from 40 cm to 80 cm). WISIS gives an estimation of the time of flight τ , which can be considered as the phase delay of the fastest wave travelling into the medium. E_d can be computed using the wave velocity (L/τ) and the mean density ρ of the material (Equation 1):

$$E_d = \rho \left(\frac{L}{\tau} \right)^2 \quad (1)$$

where L is the length of the sample. The second moment of area (I) was calculated for each sample tested and flexural stiffness (EI) obtained.

To determine if differences existed in species stem height, DBH and number of stems, analysis of variance was carried out along with post-hoc Fisher's Least Significant Difference (LSD) tests. For mechanically tested samples, E_d was examined as a function of stem length. To homogenise data, the position of the sample along the stem was calculated as a percentage of total stem length. These proportional data were then arcsine square root transformed prior to analysis. For I and E_d , the normality of distribution was tested using an Anderson-Darling test. If data were not normally distributed ($P < 0.05$), a logarithmic transformation was performed. Analysis of covariance was used to investigate the relationships in I , EI and E_d between species using stem length as a covariate.

Table 1 Mean height, DBH, number of stems per individual and bending strength for species present within six 100m x 4m transects traversing the avalanche path. Bending strength was not measured for all species. Letters in superscript indicate significant differences between species ($P < 0.05$). Species with fewer than nine individuals present were not included in the statistical analysis. Data are means \pm standard deviation.

Species	Number of individuals	Height (m)	Mean DBH of stems (mm)	Number of stems	Bending strength (MPa)	n (bending strength tests)
<i>Fagus sylvatica</i> L.	162	7.6 \pm 4.3 ^{acd}	82.0 \pm 54.2 ^a	3.2 \pm 4.0 ^a	55.1 \pm 18.1 ^{abc}	17
<i>Corylus avellana</i> L.	15	5.9 \pm 1.8 ^{abcd}	42.6 \pm 12.6 ^b	13.4 \pm 14.6 ^b	62.3 \pm 22.0 ^{abc}	17
<i>Alnus incana</i> (L.) Moench	9	5.4 \pm 2.0 ^{abcd}	52.0 \pm 11.6 ^{ab}	3.9 \pm 2.6 ^{ac}	35.1 \pm 9.1 ^{bd}	14
<i>Alnus viridis</i> (Chaix) DC.	4	2.9 \pm 0.9	33.2 \pm 9.8	12.5 \pm 11.2	27.8 \pm 5.9 ^d	11
<i>Betula pendula</i> L.	27	6.9 \pm 2.4 ^{abc}	80.7 \pm 49.4 ^{ab}	1.5 \pm 1.4 ^{ac}	47.2 \pm 15.9 ^{bcd}	8
<i>Salix appendiculata</i> Vill.	23	5.6 \pm 2.4 ^{bcd}	75.4 \pm 31.9 ^{ab}	2.5 \pm 3.5 ^{ac}	-	-
<i>Quercus petraea</i> Liebl.	20	5.9 \pm 3.6 ^{abcd}	78.6 \pm 46.5 ^{ab}	1.0 \pm 0.2 ^c	-	-
<i>Pinus sylvestris</i> L.	6	2.9 \pm 2.4	63.5 \pm 46.7	1.0 \pm 0.0	-	-
<i>Picea abies</i> (L.) H. Karst.	36	4.8 \pm 3.3 ^{bd}	73.6 \pm 48.2 ^a	1.1 \pm 0.4 ^c	-	-
<i>Populus tremula</i> L.	2	3.1 \pm 0.5	39.0 \pm 11.3	1.0 \pm 0.0	-	-
<i>Acer pseudoplatanus</i> L.	2	7.3 \pm 1.9	72.0 \pm 25.5	2.0 \pm 0.0	-	-
<i>Prunus avium</i> (L.) L.	6	9.9 \pm 2.1	111.7 \pm 60.9	1.3 \pm 0.8	-	-
<i>Fraxinus excelsior</i> L.	3	7.0 \pm 1.1	81.3 \pm 23.8	1.0 \pm 0.0	-	-

Results

F. sylvatica was the most abundant species growing at the edge and near the avalanche path (Table 1). Several species, including *A. viridis* were present in very low numbers. *A. viridis* was only observed at the centre and edges of the path. *A. incana* was located on the avalanche debris downslope, along with *B. pendula* which was occasionally observed further upslope but not within the immediate vicinity of the avalanche path. *C. avellana* was present at the edges of the avalanche path and possessed the greatest number of stems compared to all other species. Apart from *P. abies* and *B. pendula*, single-stemmed trees (*Q. petraea*, *P. sylvestris*, *P. avium*, *F. excelsior*, *P. tremula*), were present in low numbers within transects (Table 1).

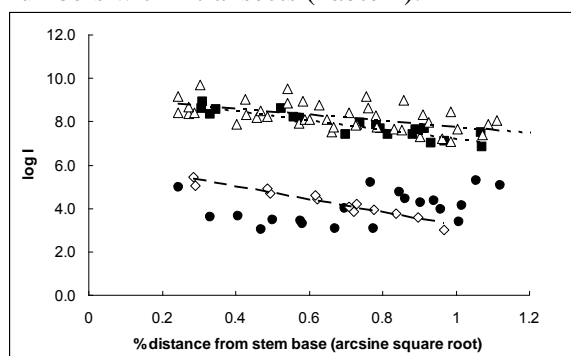
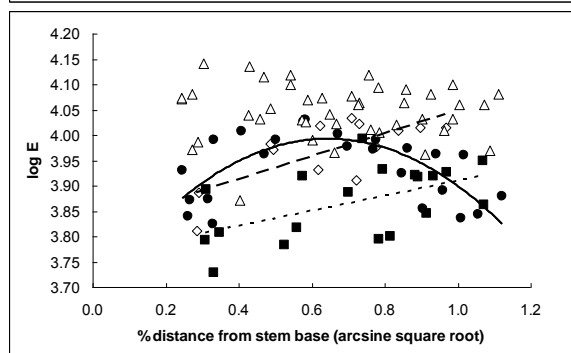
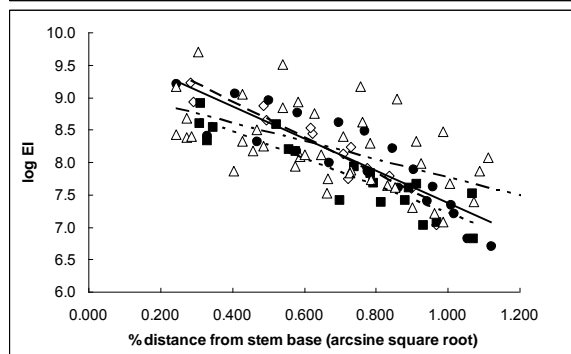


Fig. 2a) Logarithmic second moment of area ($\log I$) decreased significantly with relative distance from the stem base in all species examined except for European beech. $\log I$ was significantly greater in hazelnut (white triangles and dashed and dotted line) and Green alder (black squares and dotted line) compared to European beech (black circles) and silver birch (white diamonds and dashed line) ($P < 0.05$).



b) Logarithmic dynamic modulus of elasticity ($\log E$) was lowest at the stem base for all species except hazelnut, where it remained constant along the stem. In Silver birch and Green alder, E_d increased significantly from the stem base towards the apex. In European beech (solid line), E_d increased significantly along the stem length up to approximately 50% of the length before then decreasing.



c) Logarithmic flexural stiffness ($\log EI$) decreased significantly with distance from the stem base in all species ($P < 0.05$).

$\log I$ decreased significantly with relative distance from the stem base in all species examined except for *F. sylvatica* (Figure 2a, Table 2). $\log I$ was significantly greater in *C. avellana* and *A. viridis* compared to *F. sylvatica* (Figure 2a, Table 2). Bending strength was highest in *C. avellana* and *F. sylvatica* and lowest in *A. viridis*, with *A. incana* and *B. pendula* having intermediate values (Table 1). E_d was highest in *C. avellana* and lowest in *A. viridis* (Figure 2b, Table 2). In *B. pendula* and *A. viridis*, E_d increased linearly from the stem base to the apex and in *F. sylvatica*, E_d increased significantly along the stem length up to approximately 50% of the length before then decreasing (Figure 2b, Table 2). In *C. avellana*, E_d remained constant along the stem (Figure 2b, Table 2). In all species, $\log EI$ decreased significantly from the stem base to the apex (Figure 2c, Table 2).

Table 2 Regression equations, R^2 and probability (P) for the regressions shown in Figure 2a,b, and c.

Species	logI			logE			logEI		
	Regression	R^2	P	Regression	R^2	P	Regression	R^2	P
<i>F. sylvatica</i>	-1.89x+5.40	66	<0.001	-0.71x ² + 0.92x+3.69	47	0.001	-1.91x+9.34	64	<0.001
<i>C. avellana</i>	-1.39x+5.11	39	<0.001	-0.02x+4.05	1	0.551	-1.41x+9.17	37	<0.001
<i>A. viridis</i>	-2.11x+9.32	83	<0.001	0.15x+3.76	29	0.017	-2.11x+9.32	83	<0.001
<i>B. pendula</i>	-2.99x+5.21	86	<0.001	0.23x+3.82	54	0.004	-2.77x+10.0	90	<0.001

Discussion

The most common species found within and around the avalanche path possessed the ability to produce numerous stems, with the shrubs *C. avellana* and *A. viridis* having a highly multi-stemmed form. *F. sylvatica* demonstrated a strong morphological plasticity as both arborescent and shrubby forms co-existed, the latter being found at the edges of the avalanche path. *B. pendula* was rarely found near the centre of the path and was more abundant downslope of the path. Species with single stems generally grew at a distance or downslope of the avalanche path. Therefore, the ability to multi-stem in response to snow disturbance is likely an important survival strategy for trees growing in subalpine zones. Larger, single-stemmed trees will be more likely to fail if they cannot bend during an avalanche [6], resulting in death of the individual. By possessing the ability to regenerate new stems from the existing main stem or stem-root base, individuals will persist in the landscape, and not rely on seeding to remain dominant.

A. viridis had the lowest mean σ and E_d , and particularly low values of E_d at the stem base, thus enabling this species, generally found at the centre of avalanche paths, to bend easily during an avalanche disturbance, reducing the likelihood of stem breakage or uprooting. *C. avellana* and *F. sylvatica*, found at the edges of avalanche paths, possessed the highest mean E_d and σ . These two species may better resist the weight of the snow, compared to *A. viridis*, but were less flexible at the stem base. In all species except *C. avellana*, where E_d remained constant in stems, E_d increased from the stem base to the apex and in all individuals, EI decreased from the base to the apex, with little difference between species.

Usually, E decreases from old to younger stems in self-supporting plants such as trees and shrubs, therefore the stem bases of trees are mostly stiffer than the apical branches [10,11]. However, the stem bases might contain a transition zone between the stem and roots, and roots have lower E than stem wood [12]. In two populations of *A. viridis* from the Alps in Switzerland and the Black Forest Forest, Germany, Brüchert et al [13] found that E decreased with decreasing stem age, therefore E was higher at the stem base. It was not stated whether these populations were perturbed by frequent disturbance. In our study, stem bases of trees may be damaged by avalanches and debris entrained by the avalanche, resulting in scars and decayed wood which reduces E . Tension wood was probably present in large amounts along stems, but E in tension wood is usually higher than that of normal wood [14]. A further explanation for the increase in E up the stem in *B. pendula*, *A. viridis* and to a certain extent, *F. sylvatica*, is that when the snow melts in the spring, apical stem parts need to grow towards the dominant source (outwards and upwards, depending on slope angle and orientation). Being materially stiffer would allow these young stems to quickly form a canopy and benefit from most available light during the short subalpine growing season. Stem bases of the same species are larger and usually procumbent and therefore would need more time and energy to straighten up. If avalanches are frequent, plastic deformation of the stem base will occur and plant response to the frequent disturbance may be to invest little in wood structure or straightening up mechanisms from the stem base. In *A. viridis*, vegetative reproduction is common, and roots can grow from the prostrate stems [15]. An increase in E along the stem can also be found in climbing species such as lianas, where the ‘searcher

shoots' are relatively stiff compared to the basal parts of the stem, allowing individuals to find suitable supports for growth towards the canopy [10].

The differences in E along the stem observed between species may indicate differences in strategies for forming tension wood, which are known to occur at least between *F. sylvatica* and *A. incana* in experiments simulating substrate mass movement [16]. Tension wood efficiency also differs between species [17]. Although E increased along the stem in three species, it remained constant along the stem in *C. avellana*. *C. avellana* possessed significantly more stems than any other species at the site, and the stems were often leaning on each other, thus providing mutual support. A similar situation can be found in semi-self-supporting plants (species which often lean on the surrounding vegetation, rather than climbing via twining or tendrils), where E often remains unchanging and values can be relatively high in both young and old growth stages [10,11].

E augments significantly with a decrease in temperature [6, 18], therefore future experiments should focus on how E changes with temperature, and if this mechanical behaviour differs between species. We will also examine how mechanical properties and stem allometry change along the altitudinal gradient of the avalanche path and test the behaviour of conifer species present near path. The age of individuals will be determined using dendrochronological techniques and xylem structure along the stem examined.

Acknowledgements

Funding was received from INRA (Jeune Equipe), France. Thanks are due to D. Guibal and G. Chaix CIRAD, France, C. Atger (Pousse Conseil), M. Ghestem (Ministère d'Agriculture) and Z. Mao, Montpellier 2 University, France, for experimental help and to F. Munoz Montpellier 2 University, France, for species identification. AMAP (Botany and Computational Plant Architecture) is a joint research unit which associates CIRAD (UMR51), CNRS (UMR5120), INRA (UMR931), IRD (2M123), and Montpellier 2 University (UM27).

References

1. Read, J. and A. Stokes, (2006): *Plant biomechanics in an ecological context*. American Journal of Botany. 93: 1546 - 1565.
2. Rixen, C. and S. Haag, D. Kulalowski, P. Bebi, (2007): *Natural avalanche disturbance shapes plant diversity and species composition in subalpine forest belt*. Journal of Vegetation Science. 18: 735-742.
3. Bebi, P. and D. Kulakowski, C. Rixen, (2009): *Snow avalanche disturbances in forest ecosystems – State of research and implications for management*. Forest ecology and management. 257: 1883-1892.
4. Bartelt, P. and V. Stöckli, (2001): *The influence of tree and branch fracture, overturning and debris entrainment on snow avalanche flow*. Journal of Glaciology. 32: 209-216.
5. Gauquelin, X. and B. Courbaud, (2006): (Eds.) *Guide des Sylvicultures de Montagne. Alpes du Nord Françaises*. Cemagref, CRPF Rhône-Alpes, ONF, France.
6. Johnson, E.A. (1987): *The relative importance of snow avalanche disturbance and thinning on canopy plant populations*. Ecology. 68: 43-53.
7. Bond, W.J. and J.J. Midgeley, (2001): *Ecology of sprouting in woody plants: the persistence niche*. Trends in Ecology and Evolution. 16: 45-51.
8. Johansson, T. (2008): *Sprouting ability and biomass production of downy and silver birch stumps of different diameters*. Biomass and Bioenergy. 32: 944-951.
9. Brancheriau, L. and S. Paradis, (2007): *WISIS – Wood In Situ Inspection*. Version 1. CIRAD, France.
10. Speck, T. and N. Rowe, (1999): *Biomechanics of fossil and living plants: A quantitative approach to analytically defining size, form and habit*. In Hemsley, A. R. and M.H. Kurmann, (Eds) *The evolution of plant architecture*. Royal Botanic Gardens, Kew: 447-479.

11. Lahaye, R. and L. Civeyrel, T. Speck, N. Rowe, (2005): *Evolution of shrub-like growth forms in the lianoid subfamily Secamonoideae (Apocynaceae s.l.) of Madagascar: Phylogeny, biomechanics, and development*. *American Journal of Botany*. 92: 1381-1396.
12. Khuder, H. and A. Stokes, F. Danjon, K. Gouskou, F. Lagane, (2007): *Is it possible to manipulate root anchorage in young trees?* *Plant and Soil*. 294: 87-102.
13. Brüchert, F. and F. Gallenmüller, A. Bogenrieder, T. Speck, (2003): *Stem mechanics, functional anatomy and ecology of *Alnus viridis* and *Alnus glutinosa**. *Feddes Repertorium*. 114 : 181-197.
14. Fang, C.H. and D. Guibal, B. Clair, J. Gril, Y.M. Liu, S.Q. Liu, (2008): *Relationships between growth stress and wood properties I in Poplar I-69 (*Populus deltoides* Bartr. cv. "Lux" ex I-69/55)*. *Annals of Forest Science*. 65: 307.1-307.9.
15. Anthelme, F. and L. Cornillon, J.J. Brun, (2002): *Secondary succession of *Alnus viridis* (Chaix) DC. In Vanoise National Park, France: coexistence of sexual and vegetative strategies*. *Annals of Forest Science*. 59: 419-428.
16. Heinrich, I. and H. Gärtner, L. Monbaron, (2007): *Tension wood formed in *Fagus sylvatica* and *Alnus glutinosa* after simulated mass movement events*. *IAWA Journal*. 28: 39-48.
17. Almeras, T. and M. Fournier, (2009): *Biomechanical design and long-term stability of trees: Morphological and wood traits involved in the balance between weight increase and the gravitropic reaction*. *Journal of Theoretical Biology*. 256: 370–381.
18. Umbanhowar, C.E. and A.M. Lambert, L. VanDelinder, (2008): *Effects of freezing on Young's modulus for twigs of coniferous and deciduous trees and shrubs*. *Canadian Journal of Forest Research*. 38: 394-399.

Drag of red mangrove (Rhizophora mangle L.) seedlings in water.

Sophie D. Boizard, and Stephen J. Mitchell

University of British Columbia, Canada

Abstract

Red mangrove forms mono-specific communities along the shorelines of tropical oceans and is exposed to wave, current and wind energy. Mangroves are well adapted for life in the intertidal zone and likely have specific biomechanical adaptations to deal with this distinctive environment. During establishment, seedlings are particularly susceptible, limiting the habitats that they can successfully colonize. We tested mangrove seedlings ranging in height from 24 to 43 cm with three to five pairs of leaves in a flume at current velocities of 0 to 0.75 m/s. Frontal views were videotaped and used to calculate velocity-specific frontal area. As velocity increased, the upper leaves reoriented themselves with the flow, forming a cluster around the stem, reducing drag. This behaviour was not always observed in lower pair(s) of leaves. Leaf pairs oriented perpendicular to the flow often flapped up and down in the water column, while leaves on the upstream side sometimes bent downward, increasing frontal area. Stem bending at higher velocities also reduced frontal area and drag. Drag increased near-linearly with flow velocity. At these speeds, loads would be insufficient to cause uprooting or stem failure.

Introduction

Mangroves are a specialized group of woody plants that form extensive intertidal fringing communities along the shorelines of continents, islands and offshore atolls throughout the tropics and subtropics. Mangrove ecosystems are economically and ecologically important, providing a number of critical services, including shoreline protection from wind-generated waves, tropical storms and tsunamis, breeding and nursery ground for coastal fisheries and carbon sequestration [1]. While mangroves are well adapted to cope with the harshness of coastal environments, pressure from human activities coupled with increases in sea level rise and increase storm severity due to climate change are putting these ecosystems under considerable threat [1].

Mangroves are unique in that they have highly developed morphological and physiological adaptations to cope with exposure to both terrestrial and marine conditions, making them the only group of woody plants to have successfully colonized the sea [2]. *Rhizophora mangle* L. (red mangrove) communities are one of the most prominent features along the coastlines and islands of the Caribbean. It is often characterized as the seaward pioneer species [3, 4] due to its greater tolerance to frequent flooding and high salinity, and its ability to colonize across a gradient substrate and wave energy [5]. Like other mangrove species, *R. mangle* is viviparous; the propagule is positively buoyant and is dispersed by tidal action and currents [6]. The characteristic elongated-shape and size of its propagule allows it to colonize areas subjected to constant flooding and current and wave energy, giving *R. mangle* an advantage over other mangroves species with small, roundish propagules (e.g. *Avicennia*). Most information on the effect of waves and tidal current on propagule establishment success and early survival of seedlings comes from observational data or field transplant experiments: no work as yet investigated mangrove seedling response to flow and associated hydrodynamic forces.

In aquatic environments, exposure to flow and waves is considered one of the strongest factors influencing the distribution of plants [7-9]. The dominant hydrodynamic force imposed on aquatic plants is likely drag [8], which is defined as:

$$F_d = \frac{1}{2} \rho A C_d U^2 \quad (1)$$

where ρ is the density of water (seawater=1025 kg/m³, freshwater=1000 kg/m³), U is the water velocity (m/s) relative to the plant and A is the maximum projected area of the plant (m²). C_d is the drag coefficient (dimensionless) whose magnitude depends on the size and shape of the organism and the characteristics of flow around it [10, 11]. Values of C_d are high for bluff objects and low for streamlined objects [12].

Water density being 1000x greater than that of air, aquatic plants in moving water are exposed to drag forces greatly exceeding that experienced by terrestrial plants in a wind of same velocity [8]. To survive these drag, aquatic plants have evolved a variety of strategies [e.g. 9, 13]. Aquatic plants are flexible [14] and when exposed to flow they reorient themselves to become aligned with the direction of flow and then reconfigure to an even more streamlined posture through the folding of their blades [15]. This reduces the plant area presented perpendicular to the oncoming flow, effectively lowering the drag imposed on a plant body.

This study is part of a larger program of research on mangrove disturbance and regeneration dynamics. The main objective of this study was to characterize the response of *R. mangle* seedlings to flow. More specifically, we measured the change in frontal area and drag of seedlings exposed to increasing water flow under controlled condition in a re-circulating flume.

Material and methods

Eleven greenhouse-grown *Rhizophora mangle* L. were selected to span a range of sizes (stem height between 24-43 cm). Only healthy mangroves with unbranched, straight stem were selected. Prior to testing, stem height, stem diameter and seedling mass were measured. Stem height above ground was defined as the length of the stem 5 cm above the uppermost root to the base of the plumule. Stem diameter was measured at ground level (5 cm above uppermost root along hypocotyl), at the apex of the hypocotyl, at the base of the first leaf pair and midway along each shoot internode. Seedlings (potted individually in aquarium grade sandy-gravel) were kept in aerated freshwater under growing lights in a heated wet lab prior to testing; these conditions were similar to those under which the seedlings were grown at the University of British Columbia horticultural greenhouse.

The hydrodynamic performance of each individual was measured in freshwater in a re-circulating flume at the Bamfield Marine Science Centre, Bamfield BC. The dimensions of the flume working section were 10 m x 2 m x 1.2 m (L x W x D; *Fig. 1*). The flow was generated by one variable and three set velocity pumps, which were progressively switched on to obtain 5 different flow velocities. Water velocities were accurately measured using a flow meter (HFA, Höntzsch, Waiblingen, Germany; 0.01-3 m/s) located at 20 cm depth, 32 cm upstream and 16.5 cm to one side of the plants. Flow meter position was selected based on the average centre of pressure of the sample plants. Hydrodynamic performance variables, drag and frontal area were recorded at five velocities ranging from 0 to 0.75·m/s.

Drag was measured using a custom built double beam strain gauge transducer with a force sensitivity of 1g per 1 mV. Stems were wrapped in a piece of cushioned sand paper before being clamped to avoid slippage. The root system of seedlings was wrapped in saturated paper towel to minimize water losses during testing. Seedlings did not show any signs of wilting at the time of the experiment. The transducer beam was clamped to an aluminium mount that spanned across the width of the flume, positioning the test seedling upside down in the flume (*Fig. 1*). This was necessary to keep the force transducer dry. A false-bottom positioned at the water/air interface was built to reproduce the sediment water interface. The seedling stem extended through a slot (3 cm x 18 cm) in this false-bottom. We believe that this posture has little influence on the frontal area and stem curvature of the plant, as the buoyant forces are negligible compared to the stiffness of the leaves and stem. Further references to the position and orientation of a seedling reflect the natural, upright perspective, despite the experimental conditions. Data were recorded at a sampling rate of 1Hz for 120 sec at each velocity. Flow velocity took on average 40 sec to stabilize after each velocity increase. Drag at each velocity step was calculated as the averaged measures of drag taken over the last 60 sec

of data. The force transducer was calibrated by hanging weights of known masses and recording associated voltage output. Drag coefficients were calculated by rearranging eq. 1:

$$C_d = \frac{2F_d}{\rho AU^2} \quad (2)$$

Classically, the drag coefficient is calculated using the maximum projected area (frontal area) measured in still water, which is referred to here as the ‘Static C_d ’. In addition, we calculated the drag coefficient using water-velocity-specific frontal area, which is referred to as the ‘Dynamic C_d ’.

A high-resolution underwater camera (SV-DSP ZOOM, SHARK Marine technologies Inc, On, Canada) was deployed 1.6 m downstream of the sample to capture changes in frontal area (projected into the flow). Image scale was established in still water at the beginning of each run using a graduated rod held on the plane of the seedling. This was held horizontally and then vertically to enable detection of any vertical or horizontal image distortion. Still images were captured from the video in still-water, at 0 m/s, and at 90, 100 and 110 sec after the beginning of each velocity level. Frontal area was digitized from these still-images using ArcGIS (V.9.3, Redlands, CA). Frontal area at each velocity level was calculated as the average frontal area of the three still images captured.

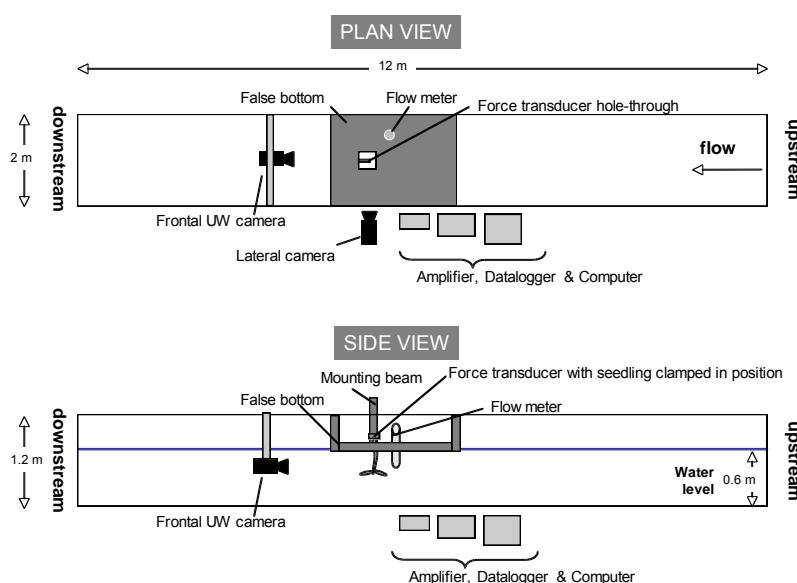


Fig. 1 Re-circulating flume for direct measurement of drag and reconfiguration of *Rhizophora* mangrove seedlings.

Results and discussion

Seedlings used in the study varied in size, ranging in height from 24 to 43 cm with 3 to 5 pairs of leaves and frontal area in still-water ranging from 20.0 to 49.2 cm² (Table 1).

As water velocity increased, seedlings reconfigured with the flow (Fig. 2). This reconfiguration was due to two separate mechanisms: the realignment of the seedling through stem deflection (low velocities) and the streamlining of the foliage (reduction in frontal area) at higher velocities (Fig. 3). At low velocities, stem deflection resulted in an increase in frontal area, as leaves that were oriented with their planar area parallel to the direction of flow became oriented at angle to the flow. Similar increase in frontal area at low velocities has also been observed in macroalgae [15] and in some species of hardwood tree [16]. As velocity increased further, the upper leaves streamlined with the flow forming a cluster around the stem, reducing frontal area. In contrast, lower leaves oriented perpendicular to the flow often flapped up and down in the water column as flow increased, while leaves on the upstream side of the stem often bent downward, increasing frontal area. Similarly, Vogel [17] noted that drag was lower for leaf clusters, as opposed to single leaf. Leaf cluster reconfigured into increasingly acute cones, while single leaves had a tendency to flutter, erratically in species with acute leaf bases and short petioles.



Fig. 2 Lateral photographs of a *Rhizophora mangle* seedling at a) 0 m/s and b) 0.75 m/s.

Table 1. Mean dimensions and weight of sample *Rhizophora mangle* seedlings.

Parameter	Mean \pm 1 SE	Min-max
Stem height (cm)	34.3 \pm 1.9	24.0-43.4
Stem diameter (mm)		
ground level	14.0 \pm 0.6	10.0-17.4
hypocotyl apex	8.8 \pm 0.4	7.4-11.2
base of 1 st leaf pair	5.2 \pm 0.2	4.2-5.9
internode	4.4 \pm 0.1	3.7-5.1
Seedling mass (g)	46 \pm 5	21-69
No. leaves	6.9 \pm 0.4	5-10
No. internodes	3.8 \pm 0.2	3-5
Still-water frontal area (cm ²)	31.7 \pm 3.2	20.0-49.2

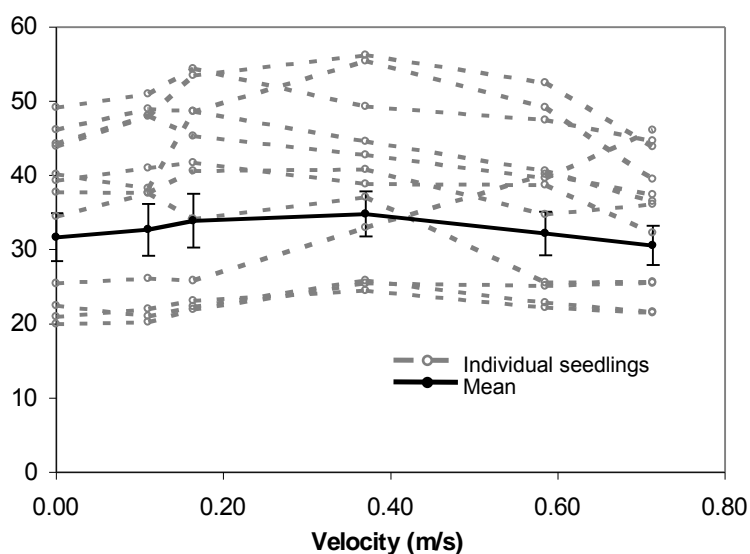


Fig. 3 Change in *Rhizophora mangle* frontal area with flow velocity. Error bars represent \pm 1 SE.

Drag was variable among individuals, ranging from 0.007 to 0.03 N at 0.12 m/s and from 0.14 to 0.51 N at 0.75 m/s (Fig. 4). At low flow velocities (<0.2 m/s), drag increased proportionally to the

square of the flow velocity, whereas at higher velocities (between 0.2-0.75 m/s), drag increased linearly with flow (Fig. 4). A similar pattern has been observed in *Arundo donax*, the giant reed [18]. Both static (calculated using still-water frontal area) and dynamic (calculated using water-velocity-specific frontal area) drag coefficients decreased with increasing flow velocity, but did not reach minima, suggesting that further reconfiguration and streamlining would occur at higher flow velocity (Fig. 5). Over the range of velocities sampled, the dynamic drag coefficient decreased more rapidly than the static drag coefficient. Given that frontal area increased at low velocities as the stem reconfigured with the flow, this was expected.

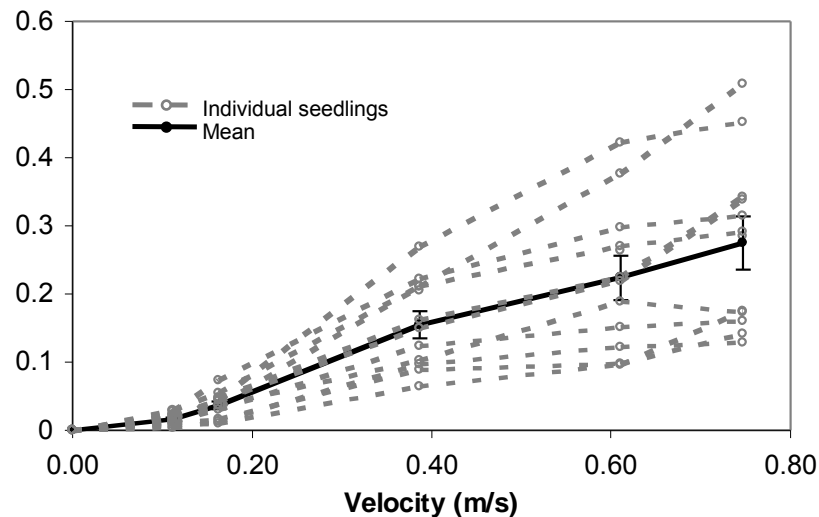


Fig. 4 Drag (F_d) on *Rhizophora mangle* seedlings over flow velocities from 0 to 0.75 m/s. Error bars represent ± 1 SE.

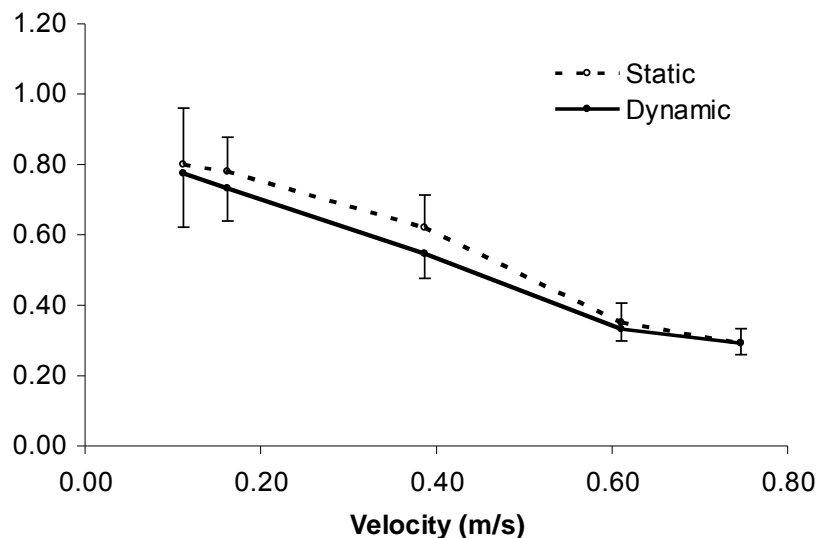


Fig. 5 Drag coefficients calculated using still-water frontal area (C_d static) and water-velocity-specific frontal area (C_d dynamic) for water velocities from 0.12 to 0.75 m/s for *Rhizophora mangle* seedlings. Error bars represent ± 1 SE.

Conclusion

Mangrove seedling stems and foliage are sufficiently flexible to limit the increase in drag as flow velocities increase. However the re-positioning of lower leaves is not always optimal to reduce drag. The recurring strains and flutter experienced by these lower leaves may also lead to weakening of petioles and more rapid abscission. Field observations of mangrove seedlings indicate that seedlings retain few leaf pairs below the water level and this may be one reason. Compared to the loads required for seedling uprooting or stem failure in our companion field experiment, much higher flow velocities would be needed to cause seedling failure.

Acknowledgements

This research was funded in part by the Natural Sciences and Engineering Research Council of Canada. Thanks to J. M. Gosline for assistance with force transducer design, L. Theriault for assistance with electronics and to U. Meissner-Chi for tending the seedlings at the University of British Columbia greenhouse. We are also thankful for the assistance of the staff at the Bamfield Marine Sciences Centre.

References

1. UNEP-WCMC (2006): In the front line: shoreline protection and other ecosystem services from mangroves and coral reefs. Publisher, UNEP-WCMC, Cambridge, UK. .
2. Hogarth, P. J. (2007): The biology of mangroves and seagrasses. Oxford University Press, Oxford, UK.
3. Davis, J. H. (1940): The ecology and geologic role of mangroves in Florida. Pap. Tortugas Lab. Carnegie Inst. Washington. 32, 303-412.
4. Chapman, V. J. (1944): The 1939 Cambridge University expedition to Jamaica. Journal of the Linnean Society of London 52, 407-533
5. Lugo, A. (1980): Mangrove ecosystems: Successional or steady-state. *Biotropica* 12, 65-72.
6. Tomlinson, P. B. (1986): The botany of mangroves. Cambridge University Press, Cambridge, England.
7. Spence, D. H. N. (1982): The zonation of plants in freshwater lakes. *Advances in Ecological Research* 12, 37-125.
8. Denny, M. and B. Gaylord (2002): The mechanics of wave-swept algae. *Journal of Experimental Biology* 205, 1355-1362.
9. Gaylord, B., C. A. Blanchette and M. W. Denny (1994): Mechanical consequences of size in wave-swept algae. *Ecological Monographs* 64, 287-313.
10. Denny, M. (1995): Predicting Physical Disturbance: Mechanistic Approaches to the Study of Survivorship on Wave-Swept Shores. *Ecological Monographs* 65, 371-418
11. Gaylord, B. (2000): Biological implications of surf-zone flow complexity. *Limnology and Oceanography* 45, 174-188.
12. Vogel, S. (1984): Drag and flexibility in sessile organisms. *American Zoologist* 24 28-34.
13. Koehl, M. A. R. (1986): Seaweeds in moving water: form and mechanical function. In: T. J. Givnish (Ed.), *On the economy of plant form and function*. Cambridge University Press, Oxford, pp. 603-634.
14. Koehl, M. A. R. (1984): How do benthic organisms withstand moving water. *American Zoologist* 24, 57-70.
15. Boller, M. L. and E. Carrington (2006): The hydrodynamic effects of shape and size change during reconfiguration of a flexible macroalga. *Journal Experimental Biology* 209, 1894-1903.
16. Vollsinger, S., S. J. Mitchell, K. E. Byrne, M. D. Novak and M. Rudnicki (2005): Wind tunnel measurements of crown streamlining and drag relationships for several hardwood species. *Canadian Journal of Forest Research-Revue Canadienne De Recherche Forestiere* 35, 1238-1249.
17. Vogel, S. (1989): Drag and reconfiguration of broad leaves in high winds. *Journal of Experimental Botany* 40, 941-948.
18. Speck, O. (2003): Field measurements of wind speed and reconfiguration in *Arundo donax* (Poaceae) with estimates of drag forces. *Am. J. Bot.* 90, 1253-1256.

Evolution of the mechanical architecture during domestication in manioc (cassava)

Nick Rowe¹, Léa Ménard¹, Bruno Clair², Gilda Mühlen³ & Doyle McKey⁴

¹UMR CNRS 5120, AMAP, Univ. Montpellier 2, France; ²UMR CNRS 5508 LMGC, Univ. Montpellier 2, France; ³Federal University of Rondônia, Brazil; ⁴UMR CNRS 5175, CEFE, Univ. Montpellier 2

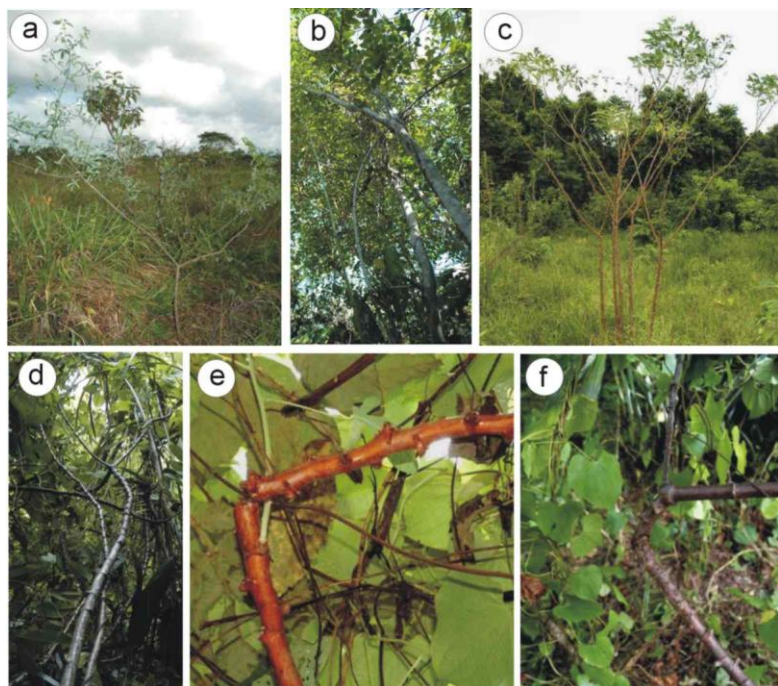
Abstract

The domesticated plant known as manioc, or cassava (*Manihot esculenta* ssp. *esculenta* Crantz, Euphorbiaceae), is grown commonly as a shrub in many parts of the tropics, including French Guiana and is an important staple for about 700 million people throughout the tropics. Cultivation involves selection and planting in soil of stem cuttings, which subsequently grow as self-supporting shrubs or treelets up to 3 m in height. Shrubs and treelets of manioc are a common sight in many parts of the tropics. Shrubs are subsequently uprooted, and their starch-bearing tuberous roots harvested and processed to make a range of food products. Recent and ongoing phylogenetic research suggests that cassava was derived from a wild species currently referred to as *Manihot esculenta* subsp. *flabellifolia* in Brazil and as *Manihot tristis* (considered synonymous) in French Guiana. Our ecological and biomechanical analyses of these wild taxa indicate a broad plasticity in growth form, with development of mature phenotypes as either self-supporting shrubs in open conditions or as climbing plants in forest understory. We compared growth variation, mechanical architecture and wood microfibril angle of domesticated cassava and its closest wild relatives (considered similar to their common ancestor). Our observations included material from a range of habitats and two regions of South America – southwestern Brazil and French Guiana. Domesticated cassava, at least in the studied areas of South America, has a tendency to grow as climbing lianoid growth forms if plantations of cultivated shrubs are abandoned. Field observations and bending tests up to stem failure indicate that stems of domesticated manioc are much more brittle than stems of the putative ancestor. The results suggest that selection during domestication did not noticeably modify the overall ontogenetic trajectory or developmental plasticity of the species, which enable them to grow as either shrub or climber depending on the ecological context, but did change the material properties of the wood of the stem, particularly in terms of failure characteristics and microfibril angle. Studies based on domestication of organisms offer a window of opportunity for studying evolutionary processes – an opportunity that Charles Darwin used to great effect. From a biomechanical point of view, the study has demonstrated a profound influence of domestication on material properties but *not* on ontogeny. The results have also provided evidence on a phenomenon that we have taken for granted for a number of years but have never been able to test adequately – that certain types of climbing habit *must* develop stem properties that are flexible and resistant to brittle fracture.

Introduction

Plant growth forms such as trees, shrubs, lianas, epiphytes and herbs represent complex associations of functional traits and biomechanics. Different growth forms such as woody trees or lianas have evolved quite different mechanical traits associated with their functioning and survival in different ecological niches [1]. Mature trees and shrubs require a certain degree of stiffness and rigidity in order to remain upright and mechanically support their branched crowns, whereas many mature climbers develop flexibility in order to protect their relatively narrow stems from mechanical damage [2]. This overall difference between trees and shrubs, on the one hand, and climbers on the other, is complex because (1) growth forms can show variable phases of mechanical adaptation during growth - early growth of trees or shrubs can actually produce relatively flexible properties, whereas early growth of many climbers actually produce relatively stiff properties, and (2) the mechanical architecture of a given species might vary significantly between different ecological conditions and constraints: a species might grow as an upright, rigid shrub or treelet in open conditions but as a flexible climber in more closed dense vegetation. Mechanical properties of the plant stem can therefore show significant differences resulting from ontogenetic, developmental and ecological variation. These sources of biomechanical variation might have a profound influence on evolutionary processes implicated in the diversity of plant growth forms and their evolution. Recent studies on biomechanical traits of plant growth forms in an evolutionary perspective suggest that the differential expression of juvenile or adult traits from putative ancestor to descendant (heterochrony) might be a key process in mediating profound architectural changes in plants and their growth forms [3,4]. Differential expression of juvenile and adult traits is possibly also an important underlying process permitting broad phenotypic plasticity. For example, certain ecological conditions, such as growth in open conditions, might maintain expression of juvenile traits and juvenile growth behaviour of some climbing species, whereas growth in closed conditions might trigger mature traits linked to adult flexible growth of the stem.

Fig 1. (a) *Manihot tristis*, self-supporting shrub in savannah. (b) *M. tristis*, climbing growth form in secondary forest. (c) *Manihot esculenta* ssp. *esculenta*, domesticated cassava, self-supporting growth form. (d) *M. esculenta*, climbing phenotype in abandoned plantation. (e)-(f) *M. esculenta*, climbing individuals showing evidence of brittle failure of the stem under natural conditions.



In the following study we investigate how growth form and stem biomechanics within the genus *Manihot* (Euphorbiaceae) varies between (1) wild type ancestor and domesticated descendant, (2) between phenotypes growing in open and closed conditions and (3) between different growth stages.

Material and methods

Manihot is a genus of approximately 98 species and includes domesticated cassava, *Manihot esculenta* ssp. *esculenta* Crantz (hereafter referred to as *M. esculenta*), which is an important

staple and source of carbohydrate in many tropical countries. Recent phylogenies indicate that the probable ancestor of domesticated cassava is the taxon *M. esculenta* ssp. *flabellifolia*, known in French Guiana as *Manihot tristis* [5]. We observed both wild type *M. tristis* and domesticated *M. esculenta*

phenotypes in the field and carried out a range of biomechanical analyses on their stems at various stages of growth and development. Field observations were carried out on both species in open and closed conditions at various sites in French Guiana. Phenotypes of *M. tristis* were chiefly studied in disturbed secondary forest areas and adjacent savannah in the vicinity of Macouria (“Savane Maillard”). Phenotypes of *M. esculenta* were observed in cultivated stands and abandoned cultivations belonging to the Palikur Amerindian village of Kamuyene, also in the vicinity of Macouria.

Ecological situation and growth form characterisation were carried out for each individual; growth sites were assessed as either "open" or "closed" and the growth form assessed as self-supporting and shrub-like or non-self-supporting and lianescent. Individuals were selected for biomechanical analysis, which included three main approaches: (1) tests on the elastic properties (Young's modulus) of the stem and changes in stiffness for different stages of growth and development; (2) tests on the approximate maximum stress sustained by stems under 3-point bending loads and their failure characteristics; (3) microfibril angle analysis of the wood component of stem segments. Overall the analysis included 39 specimens (22 self supporting, 17 climbing) of *M. tristis* and 34 specimens (19 self supporting, 15 climbing) of *M. esculenta*.

Both elastic and failure characteristics were measured using an "Instron Inspec 2200" portable mechanical measuring device. The apparatus was specially adapted for field use and 3-point bending experiments. Load rate and data acquisition were controlled by the system software: load was measured by a range of load cells (125, 250, 500 N capacities) and the deflection by the movement of the crosshead. The maximum load for the apparatus (500 N) dictated the type of failure tests that could be conveniently carried out under field conditions. While we would have preferred to have employed 4-point bending tests routinely for both elastic and failure properties, this was not possible because (a) the apparatus can not measure deflection of a specimen under bending in 4 point tests and (b) the maximum loads required for determining failure of specimens over 10 mm in diameter required loads in 4-point bending that exceeded the capacity of the apparatus. Also, (c) trials using 4-point bending tests produced problematic results resulting from unequally applied loads, owing to slight differences in thickness of the test specimen.

On this basis we decided to apply 3-point bending tests consistently to all specimens. Although the results are clearly influenced by both shear and localised, indenting effect of the crosshead probe, they do provide comparable approximations of the failure type across all sizes of plant stem. Finally, under natural conditions, stems are observed to have failed after loading via single point force applications such as falling debris and vertical stems displaced against other branches.

Elastic properties (Young's modulus) were calculated using the following formula:

$$E = L^3 \times b / 48 \times I \quad \text{eqn (1)}$$

where:

E = Young's modulus (MN/m²) measured in 3-point bending

L = bending span (mm)

b = the slope of the force/deflection curve in units of Force (N) / deflection (mm)

I = second moment of area of the stem (calculated using the stem cross-section approximated as an ellipse). The minimum span required to generate bending values with negligible influence of shear was found to be a span-to-depth ratio of 40 for both species of *Manihot* and for all growth stages.

Maximum stress in 3-point bending was calculated using the following formula:

$$\sigma_{\max} = (L \times F / 4) \times d / I \quad \text{eqn (2)}$$

where:

σ_{\max} = maximum stress (MN/m²)

L = bending span (mm)

F = maximum load (N)

d = diameter of test specimen/2

I = second moment of area (as above)

Span distances were applied using a distance of 15 times the diameter of the stem to ensure that the stem did not simply slide from the supports towards the end of the test. Different sizes of metal cylinder were available to attach to the crosshead and varied according to the thickness of the tested segment. In each test, a cylinder was used that approximated the thickness of each stem tested and thus standardized the "knife edge" effect of the failure test. Failure of the material was interpreted and approximated by reference to (a) the maximum stress calculated at the peak of the stress - strain curve and (b) qualitative observation of the stress-strain curve after the peak particularly presence/absence of sharp/gradual decreases in stress after maximum stress.

Microfibril angle (MFA) was measured by X-ray diffraction (XRD) on specimens measuring 0.5×2×20 mm respectively in radial, tangential and longitudinal directions. analyses were performed on a 4-circle diffractometer (Oxford Diffraction Gemini S) equipped with a 1024x1024 CCD camera. CuK α radiation was generated by an X-ray generator operating at 50 kV, 25 mA. Images were integrated between $2\theta = 21.5$ and 23.5 along the entire 360° azimuthal interval in order to plot the intensity diagram of the (200) plane. An automatic procedure allowed the detection of (200) peaks and their inflexion points. The T parameter, as defined by Cave [6], was measured as the half distance between intersections of tangents at inflexion points with the baseline. The average MFA of each sample was estimated using the "improved Cave's method" [7]. The results are given as the means of values obtained for the two 200 peaks. MFA was sampled from inner, inner middle, outer middle and outer parts of the wood cylinder. Special care was taken to avoid tension wood areas, visible as dark crescent-shaped areas in transverse section.

Results and discussion

Both wild type and domesticated species of *Manihot* show the ability to exist as shrubs in open conditions and as climbing individuals in denser, wooded vegetation (Fig. 1). Self-supporting phases of both species are substantial in size and may reach up to three metres in height with an appearance of upright treelets. In terms of growth form, this is indicative of a high degree of phenotypic plasticity. The observation is consistent with those from another tested wild species of the same genus, *Manihot* aff. *quinquepartita* from central French Guiana [8], which also grows both as substantial shrubs and climbers. All of these species of *Manihot* lack specialized attachment organs and climb into the surrounding vegetation by using widely angled branches.

Both species show relatively high values of Young's modulus in both self-supporting and climbing growth forms of between 2000 and 8000 MN/m².

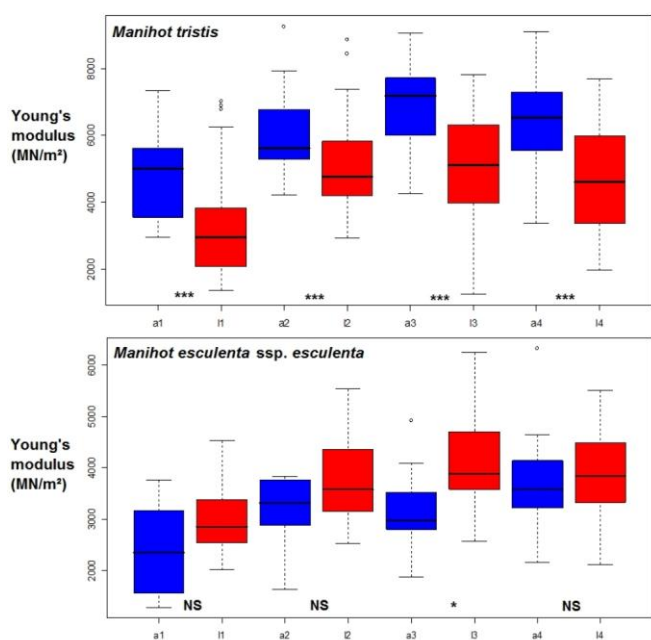


Fig. 2. Young's modulus, measured in 3-point bending of self-supporting (blue) "a1-a4" and climbing (red) "i1-i4" growth forms of *Manihot tristis* and *Manihot esculenta* ssp. *esculenta*. Stems tested are grouped in the following stem diameter classes (mm): **M. tristis**: 1 = $x < 5$, 2 = $5 < x < 7.5$, 3 = $7.5 < x < 11.5$, 4 = $x > 11.5$. **M. esculenta**: 1 = $x < 10.5$, 2 = $10.5 < x < 15.5$, 3 = $15.5 < x < 17.7$, 4 = $x > 17.7$. Box plots include median, interquartile range, full range and outliers. Degrees of significance are indicated following pair wise Wilcoxon rank sum tests (NS = non significant, *** = $p < 0.002$, * = $p < 0.003$).

Both species show a general increase in stiffness during development from young to older stages. In *M. tristis*, self-supporting stems are generally stiffer than equivalent sized climbing axes, whereas in the domesticated *M. esculenta*, there is little difference in Young's modulus between self-supporting and climbing axes. Largest and

oldest stems of *M. tristis*, in both self-supporting and climbing phenotypes, show slight reductions in *E*, indicating reductions in stiffness with ontogeny, but this was not clearly identified in either growth forms of *M. esculenta*.

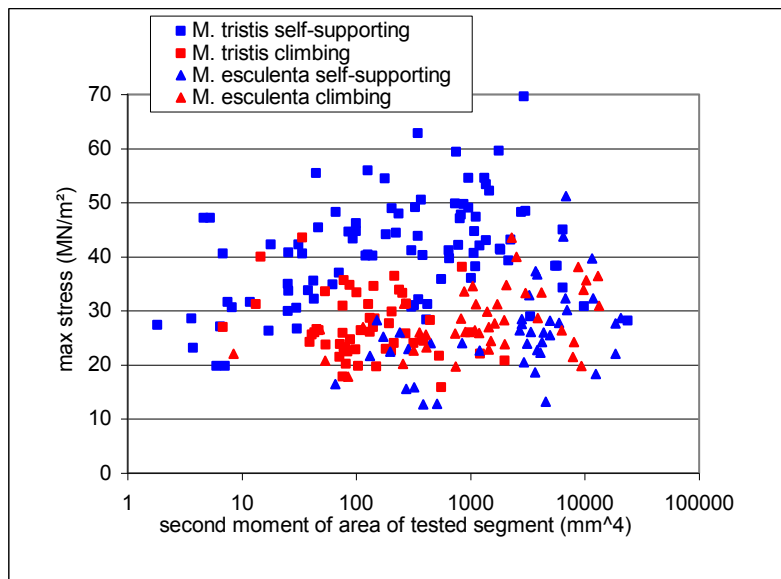


Fig. 3. Bivariate plot of maximum stress prior to failure in 3-point bending tests against second moment of area of the stem for self-supporting and climbing individuals of *M. tristis* and *M. esculenta*.

For a given size of stem, self-supporting individuals of *M. tristis* showed the highest values of maximum stress prior to failure (Fig. 3) and their stems were generally capable of withstanding 25 to 60 MN/m² before failure in 3 point bending tests.

All other phenotypes showed maximum values between

approximately 15 and 40 MN/m². There was a particularly clear difference between self-supporting stems of *M. tristis* and of *M. esculenta* (Fig. 3). Typical stress strain curves of each phenotype (Fig. 4) showed a consistent difference between stems of *M. tristis* and *M. esculenta*. Those of the latter often showed abrupt and brittle failure characteristics represented by sharp and catastrophic failure of the plant stem segment for both self-supporting and climbing phenotypes in 3-point bending (Fig. 4), often accompanied by complete fracture surface traversing the entire cross-section. Stems of *M. tristis*, however, consistently showed rounded peaks and gradual failure under 3-point bending loads, and especially climbing stems were capable of surviving extended strains without the formation of extensive fracture surfaces and total failure of the stem segment.

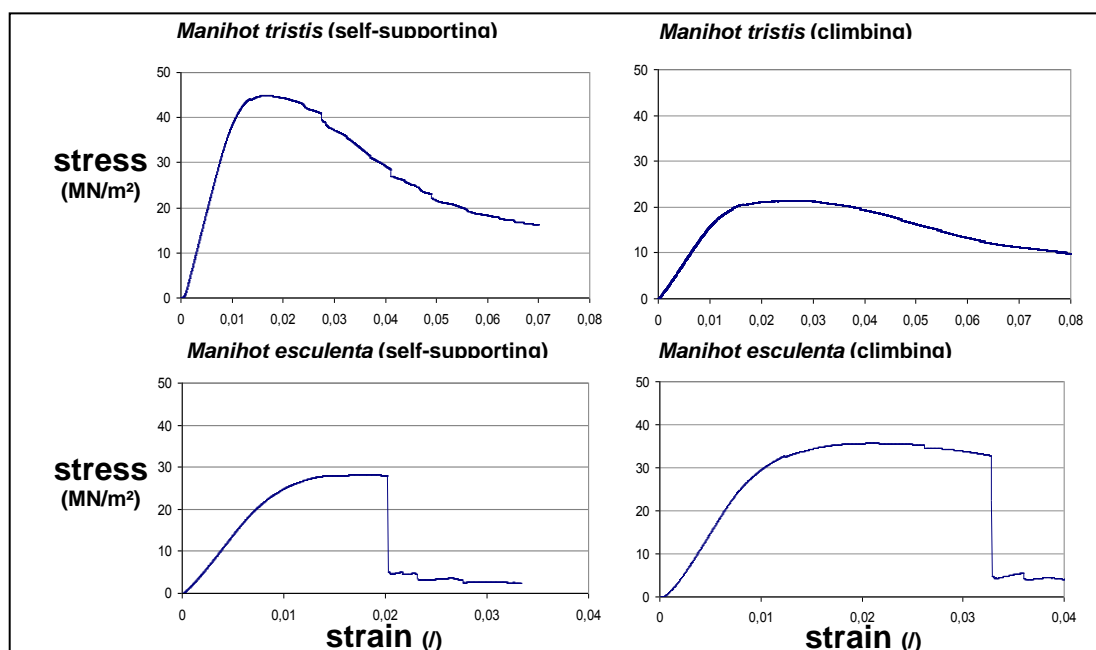


Fig. 4. Stress-strain curves of representative 3-point bending failure tests on self-supporting and climbing *Manihot tristis* and *Manihot esculenta*.

Micrifibril angle (MFA) consistently increased from the inner to outer part of the wood cylinder during development, varying between approximately 12° and 30° (Fig. 5). This characteristic was found in both self-supporting and climbing growth forms of both species. Micrifibril angle did not appear to differ between self-supporting and climbing individuals of *M. tristis*, but climbing individuals of *M. esculenta* showed markedly lower MFA values compared with self-supporting stems of the same species.

This brief survey of our results suggests that a number of specific changes have occurred during domestication, in terms of biomechanical architecture, between the wild ancestor and domesticated cassava.

First, it appears that domestication has not modified the overall ontogenetic trajectory and growth form plasticity in *Manihot*. The domesticated species *M. esculenta* shows both self-supporting growth in open conditions as well as climbing growth forms in secondary forest.

Second, the elastic properties (Young's modulus) of both wild type and domesticated species differ only marginally. Both species show a tendency for relatively stiff stem properties in both self-supporting and climbing phases of growth. Mature climbing stages of both species do show values that are lower than in younger stages, but these values do not approach the highly flexible values found in many woody twining lianas [9].

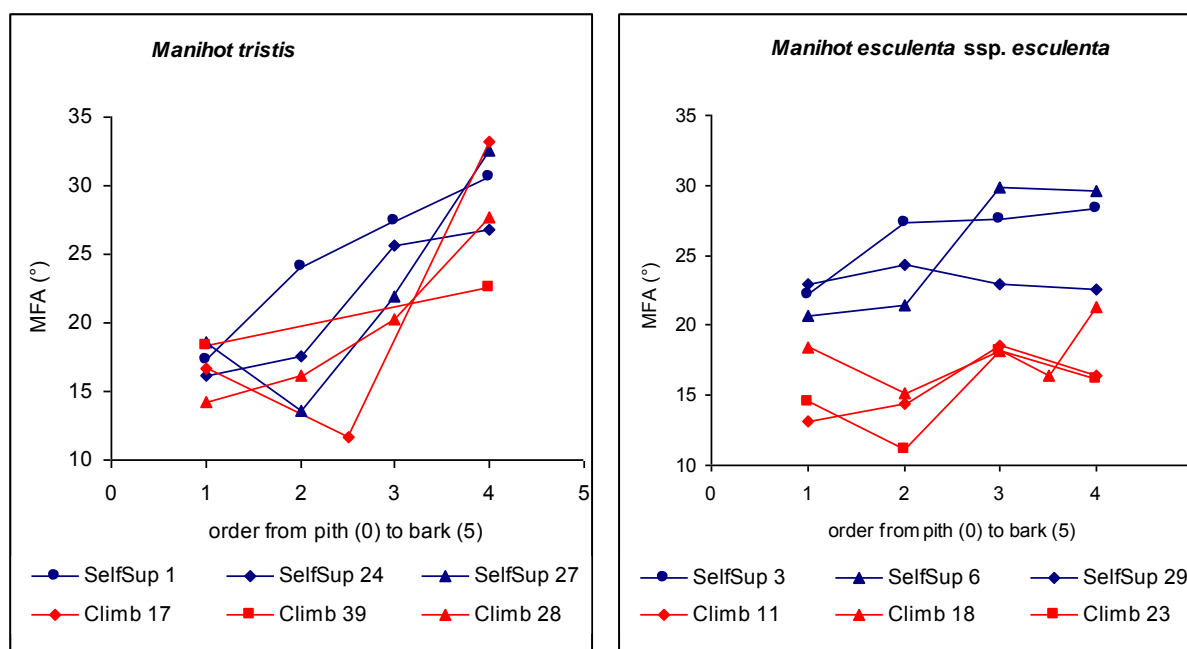


Fig. 5. Bivariate plots of microfibril angle in samples of wood from inner to outer part of the wood cylinder for self-supporting and climbing individuals of *M. tristis* and *M. esculenta*.

This is consistent with other tested species of *Manihot* [8] and indeed other climbing plant species from diverse groups that anchor themselves via rather unspecialised attachment organs, i.e., branches [9]. We have suggested elsewhere that such growth forms need to develop relatively stiff stems and branches in order to maintain stability and position until sufficient branches have been deployed as anchoring devices [8,9]. Interestingly, lianoid individuals of the domesticated species do not appear to reduce their stiffness.

Third, domestication appears to have unequivocally modified the failure properties of the stem in cassava. Generally, stem segments of all size classes show lower maximum stress and abrupt brittle failure, often accompanied by complete fracture. This phenomenon appears to have functional and ecological significance and possibly influences fitness and survival of climbing domesticated plants growing outside cultivation. Our observations of abandoned cassava stands in French Guiana indicated that mature climbing stems are vulnerable to brittle failure in the wild (Fig. 1, d, e). These observations of increased brittleness are also consistent with recent tests carried out on wild type and

domesticated cassava stems from southwestern Brazil (LM, DM, GM, NR pers. obs. 2008). Thus preservation of growth form plasticity and increased brittleness of the domesticated plant appears to be a phenomenon that has a possibly wider significance across the Amazon basin in the domestication of cassava.

Fourth, domestication appears to have also modified ultrastructural organisation of the wood tissue. A clear demarcation exists between microfibril angle of self-supporting and climbing growth forms that does not exist in the wild type. The difference is difficult to reconcile with the data on elastic properties. In *M. tristis*, there is a consistent difference in values of Young's modulus between relatively stiffer self-supporting stems and less stiff climbing stems but the MFA values for this species can not be distinguished between the two growth forms. In *M. esculenta* however, there is a less noticeable difference in measured Young's modulus between self-supporting and climbing growth forms, despite the fact that the MFA can be clearly distinguished between the two growth forms. While it is probable that microfibril angle contributes to stiffness and failure properties of *Manihot*, it is also probable that other developmental features, such as overall dimensions of tissues such as pith, wood and cortex, and traits such as wood density and fibre wall thickness to lumen ratios, contribute to whole stem stiffness and failure properties.

Conclusion

Human selection of vegetative traits during the domestication of manioc has maintained a capacity for wide phenotypic plasticity in terms of growth form and growth as either shrub-like treelets or climbing plants. However, domestication does appear to have influenced several biomechanical traits. These appear to have influenced both stem stiffness (Young's modulus) and brittleness. It appears that the quest for improving and increasing carbohydrate yield of this woody subsistence crop has successfully retained a natural diversity of growth forms, which is possibly an advantage for growing the crop in a wide range of open to closed habitats. Humans have selected not only starch-rich roots, but also starch-rich stems, because cuttings prepared from them grow more rapidly. It appears that partitioning carbon allocation for starch production and not mechanical support does however come with a cost - that of increasing stem brittleness. However, stem brittleness is possibly only a negative factor for the survival of mature climbing phenotypes. Under usual cultivation practices, at least those that we have observed in French Guiana and Brazil, plants are uprooted before vegetation in fields becomes so dense that climbing phenotypes would have an advantage. Stem brittleness, which compromises the survival of climbing phenotypes, might thus not be strongly counter-selected in the domesticate.

Acknowledgements

NR and BC gratefully acknowledges funding during the course of this work from a French National ANR Biodiversity programme project entitled "WOODIVERSITY". We also acknowledge the village community of the Palikur Amerindian settlement at Kamuyene, who kindly allowed us to sample from their cassava plantations. XRD experiments were performed in collaboration with A. Van der Lee (IEM, Montpellier).

References

1. Rowe N.P. and Speck T. (2005): *Plant growth forms: an ecological and evolutionary perspective*. The New Phytologist. 166: 61-72.
2. Speck T. and Rowe N.P. (1999): *A quantitative approach for analytically defining, growth form and habit in living and fossil plants*, in Kurmann M.H, Hemsley AR eds. *The evolution of plant architecture*. Kew: Royal Botanic Gardens. p. 447-479.

3. Bateman R.M., DiMichele W.A. (1994): *Saltational evolution of form in vascular plants: a neoGoldschmidtian synthesis*. In: Ingram D.S. and Hudson A. eds. *Shape and form in plants and fungi*. London: Academic Press. p. 63-102.
4. Lahaye R, Civeyrel L, Speck T, Rowe NP. 2005. *Evolution of shrub-like growth forms in the lianoid sub family Secamonoideae (Apocynaceae s.l.) of Madagascar: Phylogeny, biomechanics and development*. American Journal of Botany. 92: 1381-1396.
5. Duputié A., David P., Debain C. and McKey D. (2007): *Natural hybridization between a clonally propagated crop, cassava (Manihot esculenta ssp. flabellifolia) and a wild relative in French Guiana*. Molecular Ecology, 16: 3025–3038
6. Cave, I.D. (1966): *Theory of X-ray measurement of microfibril angle in wood*. Forest Products Journal. 16: 37-42.
7. Yamamoto, H., Okuyama, T., and Yoshida M. (1993): *Method of determining the mean microfibril angle of wood over a wide range by the improved Cave's method*. Mokuzai Gakkaishi. 39:375-381.
8. Ménard, L., McKey, D. and Rowe, N.P. 2009. *Developmental plasticity and biomechanics of treelets and lianas in Manihot aff. quinquepartita (Euphorbiaceae): a branch-angle climber of French Guiana*. Annals of Botany. 103: 1249-1259.
9. Rowe N.P., Isnard S., Gallenmüller F. and Speck T. (2006): *Diversity of mechanical architectures in climbing plants: an ecological perspective*. In: Herrel A, Speck T, Rowe NP eds. *Ecology and biomechanics: a mechanical approach to the ecology of animals and plants*. Boca Raton, Florida, USA: Taylor & Francis. p. 35-59.

Wood chemical and mechanical responses to modified lignin composition in upright and inclined hybrid poplar

Jameel Al-Haddad¹, Shawn Mansfield² and Frank W. Telewski^{1,3}

¹Department of Plant Biology, Michigan State University, U.S.A. ²Department of Wood Science, University of British Columbia, Canada ³W.J. Beal Botanical Garden, Office of Campus Planning and Administration, Michigan State University, U.S.A.

Abstract

Lignin is an important phenolic polymer in the secondary cell walls. These walls are responsible for the mechanical and some physiological features of the woody tissue in plants. In angiosperms, the predominant monomers of lignin are syringyl and guaiacyl. The ratio of these monomers was found to change in response to external stimuli such as wind or gravity. The latter induces the formation of special type of wood called tension wood. The impact that results from artificially modifying the lignin monomeric ratio was investigated in three types of wood tissues in one-year old hybrid poplar clone 717 (*Populus tremula* x *P. alba*). The clone was transformed to overexpress the F5H/Cald5H gene to different levels resulting in increased syringyl to guaiacyl ratio (S:G). Wild type poplars and the transgenic lines were left upright or inclined 45° from vertical for three months to induce the gravitropic responses including tension wood formation. Wild type poplar stems had 6.4% and 7.6% increase in percent syringyl in tension wood side than normal or opposite wood, respectively. Increasing syringyl formation increased percent acid soluble lignin 2.3 folds. Cell wall crystallinity was also higher in tension wood than the other types of wood tissues. Both tension and opposite woods had higher percent total sugars. Interestingly, in tension wood a 19.1% increase in percent syringyl led to 3.6% decrease in percent total sugars and 4.1% decrease in percent glucose. Percent galactose in tension wood was also higher but dropped 0.1% in response to the lignin monomer modification in the same tissue. Xylose and rhamnose were lower in tension wood than normal wood in wild type stems. Mechanically, the stems modulus of elasticity (MOE) did not change with increased syringyl when tested with 4-point bending or under compression. A decrease in the stems modulus of rupture (MOR) in response to increased S:G ratio was detected. Trees with increased S:G ratio seemed to adjust their stems to gravity faster after inclination. Evaluating the response of these lines to inclination will improve our understanding of the role lignin monomeric composition plays in altering xylem chemical composition and mechanical properties of normal and tension wood.

Introduction

Research is intensifying towards modifying woody plants to meet the increasing demand for an alternative source of biological ethanol. Poplar is considered a relatively faster renewable resource for bulk cellulose. To increase the efficiency to utilize the cellulose in the woody tissues millions of dollars are being put into research to modify genes that control cell wall structure and components.

Lignin is an important phenolic polymer in the secondary cell walls ranking second in abundance on earth behind cellulose. It acts as a cementing material in xylem tissues of trees providing support and insulation (Hacke *et al.*, 2001), thus is a major mechanical and physiological feature of the woody tissues in plants. Lignin is made up of three monomers; syringyl, guaiacyl and *p*-hydroxyphenyl. The latter occurs at higher concentrations in softwoods (Harris, 2005). In hardwoods the predominant monomers of lignin are syringyl and guaiacyl (Mosha and Goring, 1975). To understand the function of each monolignol in tree mechanics and physiology, several studies have looked at the differing ratios of monomers in different tissues or in different species (Yoshinaga *et al.*, 1992). The ratio of these monomers was also found to change in response to external stimuli such as wind (Koehler and

Telewski, 2006) or gravity as presented in this study. The latter induces the formation of special type of wood called tension wood. In the case of inclined trunks, it is formed only on the upper side of the stem while the other side is termed opposite wood. The major anatomical characteristic of tension wood is a unique fiber with an additional inner layer of gelatinous appearance (gelatinous layer), which is mostly composed of cellulose. In this layer the highly crystalline microfibrils are oriented almost parallel to the longitudinal axis of growth or what is referred to as approaching zero degrees (Pilate *et al.*, 2004). The combined mechanical strength of lignin in the opposite wood and potentially the cellulose in the gelatinous fibers of tension wood is necessary for trees to perform gravitropic responses.

Investigating the impact of lignin composition in transgenic lines of the same species will minimize possible bias by other anatomical parameters introduced when different plant species or different growth forms of the same species are compared. Successful attempts have been made to genetically alter the ratio of the monomers keeping lignin levels almost the same in poplar xylem tissues. Ferulate 5-hydroxylase (F5H) is the enzyme that acts downstream in the lignin biosynthetic pathway. It converts the intermediates for the synthesis of the monolignol guaiacyl into others that make the monolignol syringyl (Chen *et al.*, 2000). Up-regulation of the enzyme drives the lignin biosynthetic pathway towards producing more syringyl over guaiacyl without changing the overall lignin content. The purpose was to investigate the impact of modified lignin composition in transgenic hybrid poplar, as a model for woody perennial angiosperm, expressing different levels of syringyl and guaiacyl on cell wall biochemical components in tension, opposite and normal wood.

Materials and methods

This study was conducted on wild type hybrid poplar (*Populus tremula* x *P. alba*) clone 717 as well as on transgenic lines that were altered to express F5H gene at different levels resulting in higher syringyl to guaiacyl ratio from 68.5% in the wild type to 93.4% in the over-expression lines.

The plant material used in this study was propagated using root sprouts over multiple generations. The level of expression of the F5H gene in the different lines was proven to remain stable over time. Trees with 50-60 cm long stems were inclined 45° from vertical to induce the gravitropic responses including tension wood formation and were grown for 3 months along with uninclined controls. The stem samples were taken 15 cm from soil level to the center of the segments. They were debarked and air-dried at 60°C until constant weight. Stem segments from the inclined trees were longitudinally cut to separate tension wood from opposite wood for independent chemical analyses.

Using an Instron, with 500 N load cell and 20 mm/min crosshead speed, 14 cm stem segments were four-point bended to an extent enough to enable the calculation of flexural stiffness (EI) and the modulus of elasticity (MOE) within the elastic range. Same stems were dried and loaded again to rupture in order to calculate modulus of rupture (MOR). For calculation of the second moment of area (*I*), an idealized oval shape was assumed for the cross sections. Modulus of elasticity was also measured through testing the stems under compressive forces. Cylindrical debarked stem segments, twice as long as their diameter, were exposed to compressive force parallel to the grain using an Instron with 500N load cell at 3 mm/min crosshead speed. The same wood samples tested above were air dried and sent to University of Vancouver at British Columbia, Canada for testing using thioacidolysis technique to determine the syringyl to guaiacyl ratio (S:G) and total lignin content in the various poplar lines. Carbohydrates, cell wall crystallinity and microfibril angle were also quantified in the same samples.

Results and Discussion

Impact on lignin. In this study an increase in syringyl to guaiacyl ratio was found to result from inclining the trees to force the formation of tension wood. The wild type poplar had an average of 6.4% increase in syringyl content in tension wood than normal wood and an average of 7.6% increase than opposite wood. Similar increase in the ratio was also reported on the same type of hybrid poplar trees as a result of mechanically perturbing them to simulate wind sway (Koehler and Telewski, 2006).

The effect of inclination on S:G ratio diminished with increasing level of expression of the F5H gene in the modified trees. Tension wood of the trees with highest expression level had an insignificant 0.6% increase in syringyl compared to tension wood of wild type trees.

When the F5H gene was over-expressed to increase percent syringyl, trees with normal wood had slight, yet significant, decrease in their percent total lignin when compared to the unmodified control group. In another study using 13 different poplars, an evidence was presented showing a strong negative correlation between S:G ratio and the lignin content in those trees (Bose *et al.*, 2009). Percent total lignin (soluble and insoluble) in tension wood was significantly lower than normal or opposite wood. On the other hand and due to enhanced syringyl in the upright trees, percent acid insoluble lignin decreased 5.5%. Percent acid soluble lignin went up 2.3 folds in the same tissue. The increase in the percent soluble lignin was an expected outcome in this investigation since syringyl is considered more reactive than guaiacyl and a positive correlation existed between lignin solubility and syringyl monomer content which resulted in more than 60% reduction in pulping time and less use of hazardous chemicals in the process (Huntley *et al.*, 2003).

Impact on cellulose microfibril angle (MFA) and crystallinity. The wild type as well as the genetically modified trees that were displaced with regard to gravity expressed a typical gravitropic response by producing tension wood and returned to the vertical orientation. In those trees, MFA decreased (more parallel with the stem axis) in tension wood whereas cellulose crystallinity increased which goes along with previous reports (Boyd, 1977; Pilate *et al.*, 2004). However, altering S:G ratio did not impact MFA or crystallinity in the different wood tissues. During this experiment, preliminary data indicated a higher speed of recovery to the vertical position in poplar trees with increasing S:G ratio.

Impact on wood carbohydrate content. Tension and opposite woods had higher percent total sugars. Interestingly, there was a slight, yet significant, interaction between percent syringyl and percent total sugars in tension wood; a 19.1% increase in percent syringyl led to 3.6% decrease in percent total sugars and 4.1% decrease in percent glucose. A syringyl molecule is 16.7% heavier than a guaiacyl molecule. And since glucose is an essential carbon source for lignin biosynthesis, building of syringyl is a higher glucose requiring process than building guaiacyl (Amthor, 2003). Percent galactose in tension wood was also higher than normal wood but then dropped 0.1% in response to the lignin modification. Rhamnose significantly decreased on both sides of the stem (i.e. tension and opposite wood) due to the inclination, but it did not change with elevated syringyl. Both types of treatments, inclination and elevated syringyl, did not seem to have an effect on mannose or arabinose percentages.

Tension wood had significantly lower xylose (16.6%) when compared to opposite or normal wood to the contrary of a previous study by Andresson-Gunnerås *et al.* (2006) who reported that xylose was more abundant in poplar tension wood. They also reported a reduction in hemicellulose in the same tissue as was reported by Timell (1969), hence reduction in xylans and mannans (for review refer to Lerouxel *et al.*, 2006). The syringyl modification did not seem to have an impact on percent xylose in this study.

Compensatory regulation was mentioned to exist between lignin and cellulose deposition representing tree adaptation to sustain mechanical strength when lignin was reduced (Hu *et al.*, 1999) and in tension wood in response to gravitational and mechanical stimuli (Timell, 1986). Hu *et al.* (1999) observations suggested that cellulose synthesis is substrate limited and that the carbon, originally used to build lignin, is instead directed towards cellulose and hemicellulose synthesis when lignin synthesis was suppressed in woody plants, or towards building the gelatinous layer of tension wood (Schubert, 1965). This competition for carbon may explain the reduction in total sugars and glucose percentages in this study when the heavier syringyl was enhanced.

Impact on biomechanics. The stems modulus of elasticity (MOE) did not change with increased syringyl when tested with 4-point bending or under compression. A decrease in the stems modulus of rupture (MOR) in response to increased S:G ratio was detected. Lignin rich in syringyl is considered less condensed due to less branching of the lignin polymer (Abreu *et al.*, 2009), this may explain the lower MOR of the stems in all three poplar lines over-expressing F5H gene.

Conclusion

In addition to the currently used over-expression lines, RNAi-suppressed F5H poplars (*Populus tremula* x *P. alba*) clone 717 were generated in our lab to reduce S:G ratio. After propagating these new lines we will select a range of S:G ratio in those trees to extend our study on the influence of altered S:G on the trees mechanical, physiological and chemical properties. In addition, evaluating the response of these lines to inclination will improve our understanding of the role lignin monomeric composition plays in normal as well as in tension wood.

Acknowledgments

We thank Bradley Marks and Steve Marquie for Instron Universal Machine use. This research was supported by the National Research Initiative of the USDA CSREES grant number 2005-35103-15269

References

1. Abreu, H.S., J.V.F. Latorraca, R.P.W. Pereira, M.B.O. Monteiro, F.A. Abreu and K.F. Amparado, (2009): *Annals of the Brazilian Academy of Sciences* 81(1):137-142.
2. Amthor, J.S. (2003): *Efficiency of lignin biosynthesis: a quantitative analysis*. *Annals of Botany* 91:673-695.
3. Andersson-Gunnerås, S., E.J. Mellerowicz, J. Love, B. Segerman, Y. Ohmiya, P.M. Coutinho, P. Nilsson, B. Henrissat, T. Moritz and B. Sundberg, (2006): *Biosynthesis of cellulose-enriched tension wood in Populus: global analysis of transcripts and metabolites identifies biochemical and developmental regulators in secondary wall biosynthesis*. *The Plant Journal* 45:144-165.
4. Bose, S.K., R.C. Francis, M. Govender, T. Bush and A. Spark, (2009): *Lignin content versus syringyl to guaiacyl ratio amongst poplars*. *Bioresource Technology* 100:1628-1633.
5. Boyd, J.D. (1977): *Relationship between fibre morphology and shrinkage of wood*. *Wood Science and Technology* 11:3-22
6. Chen, C., H. Meyermans, B. Burggraeve, R.M. De Rycke, K. Inoue, V. De Vleeschauwer, M. Steenackers, M.C. Van Montagu, G.J. Engler and W.A. Boerjan, (2000): *Cell-Specific and Conditional Expression of Caffeoyl-Coenzyme A-3-O-Methyltransferase in Poplar*. *Plant Physiology* 123:853-867.
7. Hacke, U.G., J.S. Sperry, W.T. Pockman, S.D. Davis and K.A. McCulloh, (2001): *Trends in wood density and structure are linked to prevention of xylem implosion by negative pressure*. *Oecologia*. 126:457-461.
8. Harris, P.J. (2005): in *Plant Diversity and Evolution: Genotypic and phenotypic variation in higher plants*, ed Henry RJ (CAB, Wallingford, UK), pp 201–227.
9. Hu, W.-J., S.A. Harding, J. Lung, J.L. Popko, J. Ralph, D.D. Stokke, C.-J. Tsai and V.L. Chiang, (1999): *Repression of lignin biosynthesis promotes cellulose accumulation and growth in transgenic trees*. *Nature Biotechnology* 17:808-812.
10. Huntley, S., D. Ellis, M. Gilbert, C. Chapple and S.D. Mansfield, (2003): *Significant increases in pulping efficiency in C4H-F5H transformed poplars: Improved chemical savings and reduced environmental toxins*. *Journal of Agricultural and Food Chemistry* 51:6178-6183.
11. Koehler, L. and F.W. Telewski, (2006): *Biomechanics and transgenic wood*. *American Journal of Botany* 93(10):1433-1438.
12. Lerouxel, O., D.M. Cavalier, A.H. Liepman and K. Keegstra, (2006): *Biosynthesis of plant cell wall polysaccharides - a complex process*. *Current Opinion in Plant Biology* 9:621-630.
13. Mosha, Y. and D.A.I. Goring, (1975): *Distribution of syringyl and guaiacyl moieties in hardwood as indicated by ultraviolet microscopy*. *Wood Science and Technology* 9:45-58.
14. Pilate, G., B. Chabbert, B. Cathala, A. Yoshinaga, J-C Leplé, F. Laurans, C. Lapierre and K. Ruel, (2004): *Lignification and tension wood*. *C. R. Biologies* 327:889-901.
15. Schubert, W.J. (1965): *Lignin biochemistry*. Academic Press Inc., New York, pp.53-75.

16. Timell, T.E. (1969): *The chemical composition of tension wood*. Svensk papperstidning 72:173-181.
17. Timell, T.E. (1986): *Compression wood in Gymnosperms*, Vol 2. Heidelberg: Springer-Verlag, pp. 983-1262.
18. Yoshinaga, A., M. Fujita and H. Saiki, (1992): *Relationships between cell evolution and lignin structural varieties in oak xylem evaluated by microscopic spectrophotometry with separated cell-wall*. Mokuzai Gakkaishi 38:629-637.

Fire resistance of trees and bark heat insulation as concept generators for biomimetic insulation and fire-stopping materials

Georg Bauer¹, Thomas Speck^{1,2}, Andreas W. Liehr³ and Olga Speck^{1,2}

¹ Plant Biomechanics Group Freiburg, Botanic Garden, University of Freiburg, Germany, ² Competence Networks BIONIKON and Biomimetics, ³ Freiburger Materialforschungszentrum (FMF), University of Freiburg, Germany

Abstract

When exposed to a surface fire, the most frequent forest fire type not caused by man, a tree's probability to survive mainly depends on its capability to protect the cambium from lethal temperatures above 60°C. Thereby the bark, defined here as the entirety of all tissues outside the cambium, serves as an insulation layer. Laboratory experiments simulating the heat production of a surface fire were carried out on both dry and wet bark. A linear correlation between bark thickness and τ_{60} , a measure of the fire resistance, was found for all seven tree species tested. Further results show that the fire resistance increases with decreasing bark density. Concerning the bark structure the examined tree species can be classified into two groups: (1) tree species with low resistance show a faint bark structure, whereas (2) tree species with a high fire resistance show a pronounced bark structure.

Thorough analyses of the correlation between bark surface structure, internal structure, biochemistry and bark heat insulation capacity might be a source of ideas for the improvement of existing technical thermal insulation and fire-stopping materials or may even bring forth new biomimetic insulation materials. On the other hand also highly fire resistant and insulating barks, as found e.g. in *Sequoiadendron giganteum* and *Quercus suber*, can be used as a raw material for the production of bio-based technical insulation and fire-stopping materials. The already existing bio-based materials could be significantly improved by including additional information obtained by structural and functional analyses of the bark of highly fire resistant tree species.

Introduction

Despite their natural importance in many ecosystems forest fires are often looked upon as disasters. Whereas, due to high temperatures, ground fires and crown fires are mainly destructive in an ecological sense, fast moving low intensity surface fires typically reach lower temperatures between 200 °C and 220 °C. Thus this forest fire type, mainly not caused by man, may facilitate the breaking of cones, reduce parasites and fungal infections, kill competing sprouts and contribute to higher substrate turnover rates [1]. For trees, most of the lethal situations during surface fires occur when the temperature of the cambium increases above 60 °C [2]. The time span until this temperature is exceeded is called τ_{60} and characterizes the fire resistance of a tree [3]. Thereby the bark, a term which is used for reasons of simplicity in the following for the entirety of all tissues outside the cambium, serves as an insulation layer.

Material and methods

Seven tree species were examined differing in the fire regime of their natural distribution area: *Fagus sylvatica* L. (Common Beech), *Abies alba* MILL. (European Silver Fir) and *Tilia cordata* MILL. (Little Leaf Linden) are native in areas where forest fires do not play a decisive role, whereas forest fires are common with a fire period of a few years in the distribution areas of *Quercus suber* L. (Cork Oak) and *Sequoiadendron giganteum* LINDL. (Giant Sequoia). *Pinus sylvestris* L. (Scots Pine) and *Larix decidua* MILL. (European Larch) are native in areas where forest fires may occur, but not to the extent as in the distribution areas of the last-mentioned species.

To quantify the fire resistance of the seven tree species, a surface fire was simulated in the laboratory. Thereto bark samples were placed over a Bunsen burner with their outer surface facing downwards (Fig. 1). To examine the influence of the bark moisture content on the fire resistance of a tree both oven-dried bark samples and wet bark samples were used in the experiments. The wet bark samples had a moisture content similar to that of fresh bark. This was achieved by storing bark samples in a box with a relative humidity of 100 %. Bark thickness at the position heated was measured and the time span τ_{60} as a measure of fire resistance was recorded. If the inner bark surface did not exceed 60 °C within 21 minutes the experiment was ended without noting τ_{60} .

The bark gross density ρ was measured from air-dried bark samples using the equation $\rho = \frac{m}{V}$ (1) where m is the weight and V the volume of each sample, measured by xylometric methods [4].

For each bark sample the minimum and maximum bark thicknesses (d_{\min} and d_{\max}) as well as two values of bark thickness at randomly chosen points were measured. The mean value d_0 of these four values was calculated. The bark structure s was calculated for each tree species from $s = \frac{\bar{d}_{\max} - \bar{d}_{\min}}{\bar{d}_0}$

(2) where \bar{d}_{\max} is the mean value of all d_{\max} , \bar{d}_{\min} is the mean value of all d_{\min} and \bar{d}_0 is the mean value of all d_0 per tree species. The higher s is, the more pronounced is the surface structuring of a given bark sample.

Results and discussion

F. sylvatica, *A. alba* and *T. cordata* have the thinnest bark and the lowest fire resistance of all tree species examined. *Q. suber* and *S. giganteum* are characterized by both a thick bark and a high fire resistance. More than half of the bark samples of *S. giganteum* did not even reach 60 °C on the inner bark surface within 21 minutes. *P. sylvestris* and *L. decidua* have an intermediate bark thickness and fire resistance. Table 1 shows how bark thickness and fire tolerance of a tree go along with the fire regimes of its distribution area.

The maximum duration of the fire resistance analyses (21 minutes) considerably exceeds the typical duration of surface fires, which is about 2-9 min [5,6]. With 215 ± 20 °C the flame temperatures are in good accordance with temperatures measured for low intensity surface fires.

For all tree species τ_{60} of the wet bark samples was higher than τ_{60} of the oven-dried bark samples. When heated, the cooling effect of vaporising water in wet bark leads to a better heat insulation than that of dry bark which more than compensates for the increased thermal conductivity derived from a higher moisture content [5,7]. For a given bark thickness the fire resistance of wet bark is 2.4 times as large as that of dry bark. In both cases of dry and wet bark a linear correlation between bark thickness and τ_{60} was found. As this result was independent of the tree species examined, a tree's fire resistance is mainly determined by its bark thickness. Thus, a tree's ability to build up a bark within one fire period which is thick enough to survive a surface fire determines its fire resistance [8].

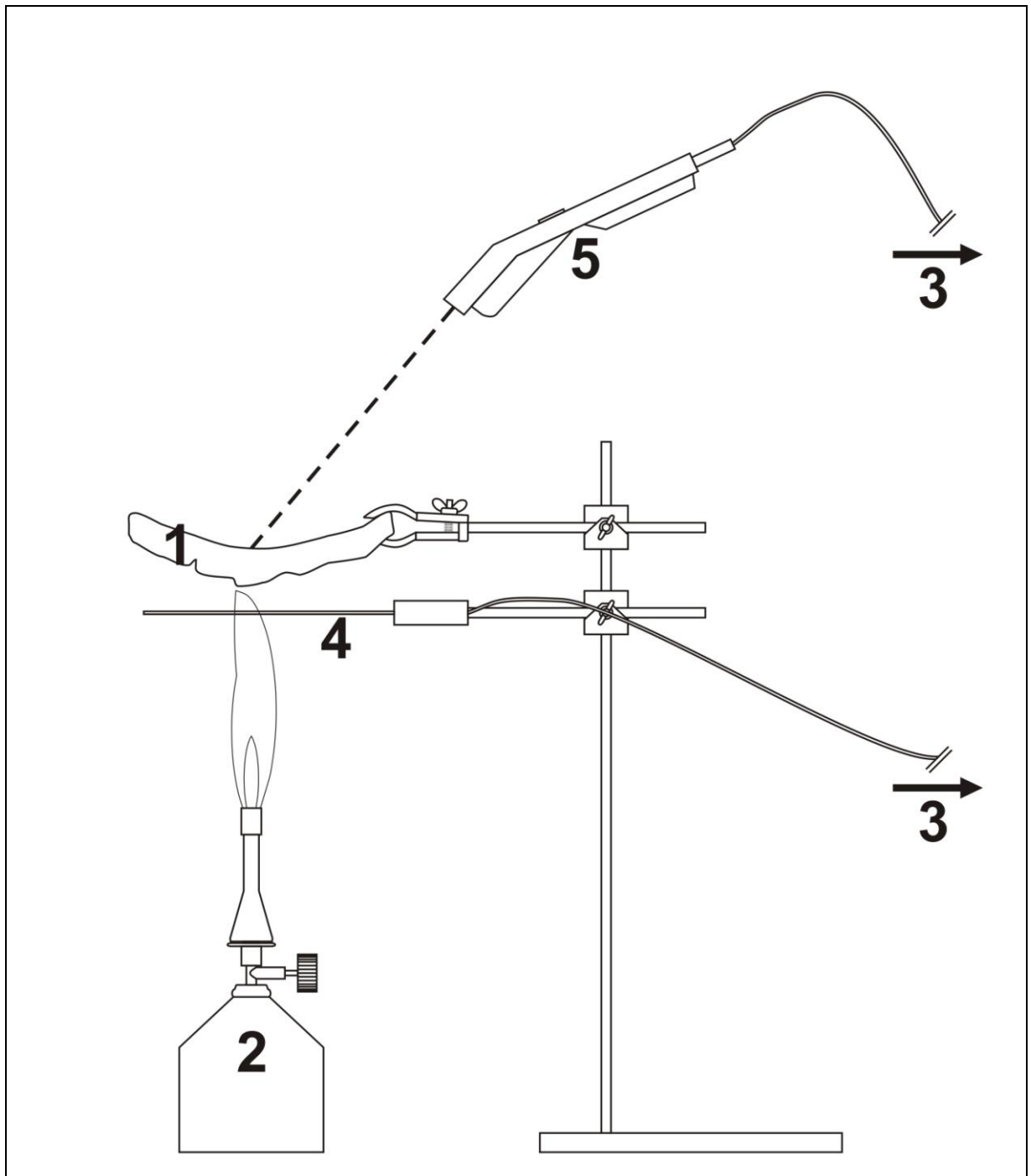


























Fig. 1 Experimental setup for fire resistance analyses: A bark sample (1) was placed over a Bunsen burner (2). A computer (3) recorded both the flame temperature, measured by a thermocouple (4), and the temperature of the inner bark surface, i.e. the position of the cambium in the living tree, measured contactless by an infrared thermometer (5).

Whereas bark density decreases with increasing fire resistance, the tree species can be divided into two groups differing significantly in their bark structure. *F. sylvatica*, *A. alba* and *T. cordata* can be clustered to a group of trees with a low surface structuring of their bark, while *L. decidua*, *P. sylvestris*, *Q. suber* and *S. giganteum* compose a second group of trees with a pronounced surface structuring of their bark (Table 1). Although bark density and bark structure may influence the fire resistance of a tree, their influence seems to matter less compared to the influence of bark thickness and bark moisture content for a tree's fire resistance.

Table 1 Forest fire frequency of the distribution areas, bark density and bark structure of the tree species

examined. Error bars represent standard deviations. Forest fire frequency: low , intermediate , high 

tree species	forest fire frequency	bark density [g/cm ³]	bark structure [-]
<i>F. sylvatica</i>		0,71 	0,14 
<i>A. alba</i>		0,70 	0,17 
<i>T. cordata</i>		0,57 	0,17 
<i>L. decidua</i>		0,46 	0,67 
<i>P. sylvestris</i>		0,45 	0,70 
<i>Q. suber</i>		0,33 	0,76 
<i>S. giganteum</i>		0,23 	0,70 

For several centuries bark is used as heat insulation on buildings. But also in many other technical products bark is used, especially due to its good heat and sound insulation. At temperatures below 90 °C bark doesn't exhibit better heat insulation than technical insulation materials, e.g. mineral wool or polyurethane hard foam, but is much more durable than the last-mentioned material. Most technical heat insulation materials used at higher temperatures, such as insulation wool made of magnesium oxide, silicon oxide or coated fiberglass composites may be harmful and thus bark may be favored over these technical materials. The application of bark as a heat insulation material reaches from flame-retardant particleboards [9] to heat insulation of intercontinental ballistic missiles [10]. Primarily the bark of the Cork Oak is used for these purposes. It is used untreated or mixed with additives to ensure an even better fire protection. The renewable raw material is gathered in the woodworking industry as a waste product and thus allows a sustainable usage of the whole tree. The bactericidal and fungicidal properties of the bark achieved by a high natural content of phenolic substances militate for a wide-ranging usage of this natural raw material. Bark and materials produced from bark may contribute to an enhanced indoor climate by their natural moisture content and their ability to accumulate humidity. But bark may also serve as a concept generator for biomimetic technical materials. Already in 1965 Hare [11] recognized bark as a natural design for an insulating board due to its numerous air cells and abundance of cork. The largely known chemistry of bark and findings from further investigations of bark cross sections may encourage the development of new biomimetic materials when combined with the established operating principles of current heat insulation materials. Analyses and comparisons of bark properties of tree species from distribution areas with different forest fire frequencies may provide manifold suggestions not only for heat insulating and fire-retardant biomimetic materials but also for other, for example moisture regulative or temperature regulative materials. For example a decrease of the moisture content of a technical material, achieved by water released at higher temperatures, might enhance its heat insulating quality in case of need.

Conclusion

The fire resistance of a tree is mainly affected by its bark thickness if bark moisture content is given. The influences of bark density and bark structure on the fire resistance seem to count less. New

biomimetic insulation materials may be developed or existing technical thermal insulation and fire-stopping materials may be improved by further examinations of the correlation between bark surface structure, internal structure, biochemistry and bark heat insulation capacity.

Acknowledgements

We thank Rudolf Hog from the Garten- und Tiefbauamt Freiburg, Wolfgang Lay, Dieter Rahm and Hans Bauer for providing plant material and Julia Mergner for her assistance in examining bark density.

References

1. Richter M. (1997): *Allgemeine Pflanzengeographie*. Teubner Stuttgart.
2. Wade D.D. (1993): *Thinning Young Loblolly Pine Stands with Fire*. Int. J. Wildland Fire. 3 (3): 169-178.
3. Van Mantgem P. and Schwartz M. (2003): *Bark heat resistance of small trees in Californian mixed conifer forests: testing some model assumptions*. Forest Ecology and Management. 178: 341-352.
4. Grammel R. (1989): *Forstbenutzung*, Verlag Paul Parey, Hamburg und Berlin.
5. Vines R.G. (1968): *Heat transfer through bark, and the resistance of trees to fire*. Aust. J. Bot. 16 (3): 499-514.
6. Hengst G.E. and Dawson J.O. (1994): *Bark properties and fire resistance of selected tree species from the central hardwood region of North America*. Canadian Journal of Forest Research. 24 (4): 688-696.
7. Johnson E.A. (2001): *Forest fires: behavior and ecological effects*. Academic Press, San Diego.
8. Bauer G., Speck T., Liehr A. and Speck O. (submitted): *Insulation capability of the bark of trees with different fire adaptation*
9. Megraw R.A. (1976): United States Patent 3,996,325: *Preparation of a three layer, fire retardant particleboard*.
10. Hovey R.W. (1965): *Cork Thermal Protection Design Data for Aerospace Vehicle Ascent Flight*. J. Spacecraft. 2 (3): 300-304.
11. Hare R.C. (1965): *Contribution of Bark to Fire Resistance of Southern Trees*. Journal of Forestry. 63 (4): 248-251.

On the characterization of mechanical properties of porous and heterogeneous bio- and bioinspired materials

Klaus G Nickel

*University Tuebingen Faculty of Geosciences
Dpt. Mineralogy & Geodynamics
Applied Mineralogy Germany*

Abstract

The mechanical characterization of partially or completely mineralized biological or bioinspired materials, for example, in terms of strength or physical parameters like elastic moduli, is often an important piece in the evaluation of the applicability of a construction inspired by natural principles. However, the interpretation of data obtained from conventional engineering practice can be misleading, because machine, measuring devices and material properties need to be understood to obtain significant and relevant numbers.

We will firstly discuss the pitfalls of such investigations, concentrating on the example of Young's modulus (E-modulus) from technical, biological and bioinspired materials. Examples of well defined dense inorganic materials and porous materials will be used to illustrate measurement problems, methods and theoretical aspects.

Biological materials from plants and marine animals often contain or consist of mineral phases, which provide further complications. Both silica and calcium carbonates are auxetic, that is, their crystals can expand perpendicular to a tensile loading, when properly oriented. And orientated growth of such crystals is common in nature.

Further complications arise from the extreme heterogeneity of biomaterials, which often combine pores and soft organic matter with stiff mineral materials ("hetero-modulus-composites"). Thus, anisotropy, periodicities, gradients and structural hierarchy all contribute to the mechanical properties and it requires appropriate characterization techniques and suitable data interpretation to elucidate the natural material at hand and the artificial bioinspired material developed from it. This will be shown using examples from sea urchin spines and biomimetic ceramics made inspired by those. Conclusions for the measuring of plants and plant-inspired materials will be presented.

Posture control of *Fagus sylvatica* L and *Acer pseudoplatanus* L. in natural stands after thinning

Paul Igor A. Hounzandji¹, Meriem Fournier², Thiéry Constant³, Catherine Collet⁴

¹*AgroParisTech-ENGREF, Laboratoire d'Etude de la Ressource Forêt Bois « LERFOB », UMR INRA AgroParisTech-ENGREF 1092, 14 rue Girardet F-54000 Nancy*

²*AgroParisTech-ENGREF, Laboratoire d'Etude de la Ressource Forêt Bois « LERFOB », UMR INRA AgroParisTech-ENGREF 1092, 14 rue Girardet F-54000 Nancy*

³*INRA, Ecologie des Forêts de Guyane « ECOFOG », UMR CIRAD 93 CNRS 8172 AgroParisTech-ENGREF INRA 745 UAG 43, BP 316, 97300 Kourou*

⁴*INRA, Laboratoire d'Etude de la Ressource Forêt Bois « LERFOB », UMR INRA AgroParisTech-ENGREF 1092, Centre de Nancy. F-54280 Champenoux*

Abstract

Forest management practices in French mixed broadleaved forests aim at promoting species diversity during regeneration. In this context, conceiving silvicultural pathways requires to understand the factors affecting the various stages of the recruitment process. The response to canopy opening of seedlings is an important stage. In the beech dominated, broadleaved former coppice with standards, Graouilly forest (40°00'48"N, 6°00'02"E, close to Metz in Lorraine, North-Eastern France), regeneration after openings is dominated by beech (*Fagus sylvatica* L) and sycamore maple (*Acer pseudoplatanus* L.). In the understorey, these two shade-tolerant species are quite plagiotropic to maximize light interception and just after opening, height growth is stimulated so that trees become more orthotropic. Moreover, openings may be associated to mechanical disturbance by wind, or gravity (growth is stimulated so weight increase is accelerated). Therefore, the posture control by both secondary and primary growths are supposed to play a key role in this developmental stage. Trees that will be able to right their trunks, and grow fast in height with lower expense in wood material, should be ecologically more competitive, and moreover, they will have vertical and cylindrical trunks that are interesting for wood production. In this study, 15 trees of each species are selected among a sample of seedlings which growth and 3D or 2D geometry have been observed during 4 years after opening in 2005. These observations have shown a significant upward movement (based on the general lean of the main stem) in both species. Sycamore maple reiterated more often than beech. Then, different parameters - mass distribution, bending moment applied at the trunk base, young's modulus, maturation strains, radial growth asymmetry - have been measured in order to explain the variability of upward movement kinetics between trees or species. Biomechanical models have oriented the choice of parameter combinations used for statistical analysis. Moreover, they were used to discuss whether the differences between maple and beech - reiteration or righting by secondary growth from the trunk base - can be explained by a physical determinism as one hypothesis could be that because of a lower stiffness and a higher centre of mass, maple could not insure its posture control only by the secondary growth and the maturation process, so that reiteration would be a physical necessity to maintain the tree habit.

9. Mechanics of biomaterials

Nonlinear elastic and moisture dependent behavior of wood: a first attempt to an adequate thermomechanical modeling

Jan Carmeliet¹, Robert Guyer² and Dominique Derome³

¹ ETH Zürich, EMPA, Switzerland; ²University of Massachusetts, Los Alamos National Laboratory, USA; ³Wood Laboratory EMPA, Switzerland

Abstract

A nonlinear elastic and moisture dependent constitutive model for wood is formulated based on a higher order formulation of the free energy including mechanical and moisture contributions and the coupling between moisture and mechanics. The nonlinear material properties can be directly obtained from mechanical testing at different relative humidity and free swelling / sorption tests. The model incorporates the sorption dependence on mechanical stress and is applied to predict free and restrained swelling of wood.

Introduction

Wood is a natural resource of many countries, such as Switzerland, with significant applications in material production, building construction and civil engineering. In use, wood is often subjected jointly to mechanical and moisture loads and inappropriate loading of wood can result in mechanical damage and biodegradation [1]. Thus, better knowledge of the hygromechanical behavior of wood is the fundament of the better design of new, durable structures and longer lives of the existing ones. In addition, the understanding of cellular materials opens the door to the development of new materials [2].

Experimental observations

From experimental observations, it becomes clear that wood has a strongly coupled mechanical and hygric behavior. Wood shows a moisture dependent elastic behavior. The elastic compliance (reverse of the elastic modulus) depends almost linearly on moisture content up to the fibre saturation point (FSP) [3, 4] (Figure 1b). An orthotropic behavior is observed in swelling [3, 4]. Swelling / shrinkage is found to depend linearly on moisture content up to the FSP (Figure 1a). Differences between the different orthotropic directions are attributed to the specific cellular architecture of wood and the microfibril angle, while differences between the species can be attributed, to a certain level, to density differences [5].

Other experiments show that the dynamic stiffness, when wood is loaded in compression, increases nonlinearly with the stress level (stiffening effect) showing hysteresis when unloading [6] (Figure 1c). When wood is restrained from swelling, swelling pressures arise, which almost linearly increase with the moisture content [7] (Figure 1d). At high swelling pressures, creep, mechano-sorptive processes [8] and plastic deformations start to play a role. It was also shown that sorption processes can be highly dependent on mechanical stress [9].

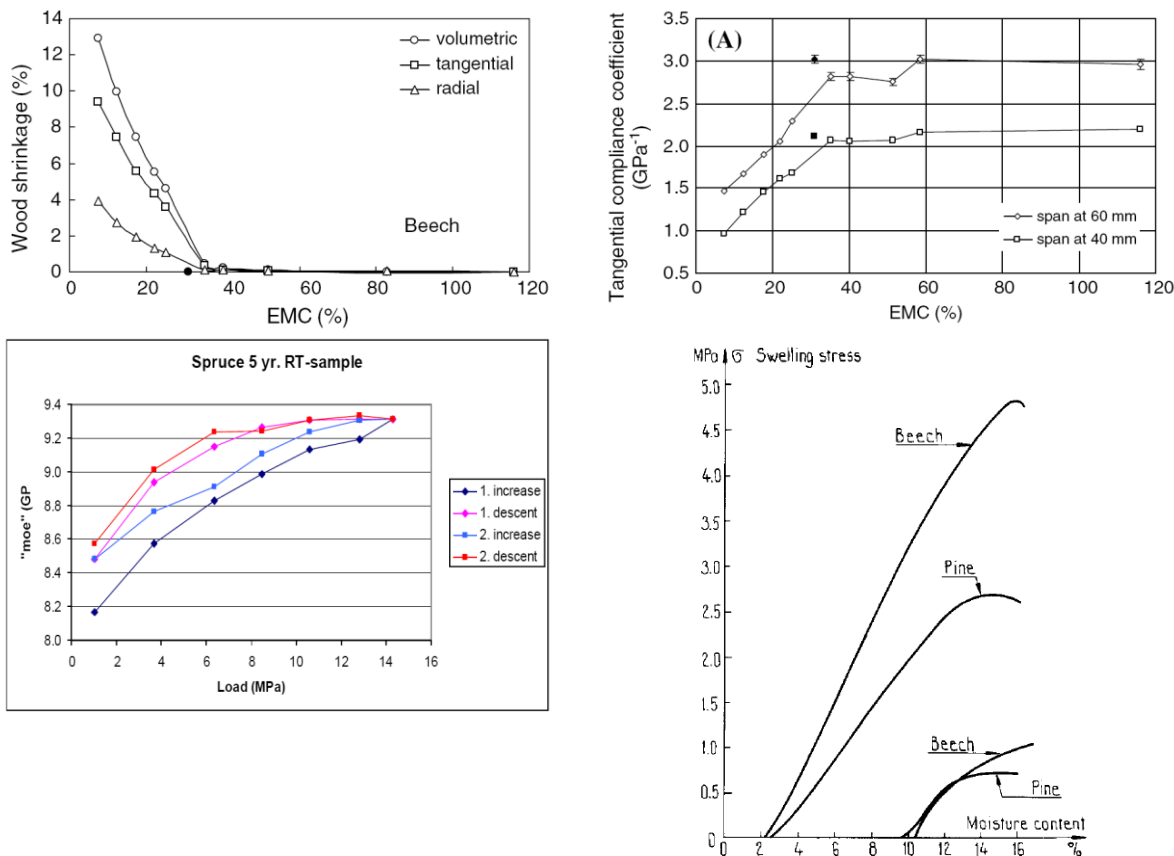


Fig. 1 (a) Shrinkage of beech. [3]. (b) Compliance versus moisture for beech. [3]. (c) Nonlinear behavior and hysteresis under dynamic loading [6]. (d) Stress required to restrain the swelling of a wood specimen from initial moisture content of 2 and 10% (from Keylwerth 1964, redrawn in [7]).

Classical theoretical approaches

In the classical continuum approach, wood is mostly considered as a linear elastic orthotropic material showing swelling. The constitutive law reads $\sigma_{ij} = D_{ijkl}(\varepsilon_{kl} - \varepsilon_{kl}^s)$, where the shrinkage strain is given by $\varepsilon_{ij}^s = \alpha_{ij} \Delta w$, which depends linearly on the moisture content variation Δw . The elastic stiffness is defined in the three orthotropic directions (longitudinal, radial and tangential) and is generally moisture dependent. Swelling is modeled by three different shrinkage coefficients α_{ii} in the three directions.

A more sophisticated way to take into account nonlinear elastic behavior is using enriched constitutive laws. An equation of state taking into account second and third-order elastic constants was derived by Murnaghan in 1944 [10] and Birch in 1947 [11], called the Birch-Murnaghan isothermal equation of state.

A more rigorous way of taking into account the interaction of fluids with the solid matrix in porous materials is based on the theory of poromechanics, introduced by [12]. Within the context of thermodynamics of open porous continua, Coussy [13] presented a general framework to formulate adequate constitutive equations for poroelastic, poroviscoelastic and poroplastic behavior. The energy formulation includes the mechanical energy of the solid, the energy due to adsorption of the fluid and the energy due to fluid-solid interactions in the porous material. Traditionally, these energies include second order terms in the basic variables, strain and fluid pressure. Using the Clausius Duhem equation, incremental constitutive equations and material properties can be obtained by second order differentiation of the energy equation. The poroelastic properties generally depend on strain and fluid pressure, which have to be determined from experiments. Therefore, the effective stress concept is mostly used to overcome the identification problem, limiting the mechanical dependencies to strain, and the moisture dependencies to fluid (capillary) pressure. This effective stress concept is generally applied for many engineering materials, such as rocks, soils and concrete [14, 15, 16]. The poroelastic

concept for unsaturated media allows predicting swelling and shrinkage of materials [13, 15]. Therefore, moisture interaction forces, such as capillary pressure and surface tension, are scaled up from pore level using a pore volume distribution [17]. For wood, this simplification is debatable, since experiments show a strong dependency of the elastic moduli on moisture content.

In this paper, a higher order model for wood is formulated based on a new formulation of the free energy including mechanical and moisture contributions and the coupling between moisture and mechanics. Attention is paid to the definition of adequate tests to directly determine the introduced parameters.

New formulation: higher order approach

We assume wood to consist of a solid material and a pore space partly filled by liquid water and a gas phase consisting of water vapor and dry air. All interactions between solid, liquid and gas phase are modeled by the liquid pressure p_l and gas pressure p_g . We assume that the gas phase remains constant and that interaction between gas phase and solid material are negligible. The material remains elastic and the temperature is assumed constant. For simplicity, we consider a one-dimensional formulation.

The energy state of wood in the isothermal case is described by the free energy $\Psi(\varepsilon, u)$, which depends on strain ε and moisture content u . Taking the Legendre transform $\Phi(\sigma, p_l)$ of the free energy $\Psi(\varepsilon, u)$, we get

$$\Phi(\sigma, p_l) = \Psi(\varepsilon, u) - \sigma \varepsilon - p_l u \quad (1)$$

with σ the stress. The incremental state equations for strain and moisture content are defined as

$$d\varepsilon = \frac{\partial^2 \Phi}{\partial \sigma^2} d\sigma + \frac{\partial^2 \Phi}{\partial \sigma \partial p_l} dp_l \quad \text{and} \quad du = \frac{\partial^2 \Phi}{\partial \sigma \partial p_l} d\sigma + \frac{\partial^2 \Phi}{\partial p_l^2} dp_l \quad (2)$$

Defining the material properties

$$C = \frac{\partial^2 \Phi}{\partial \sigma^2} \quad M = \frac{\partial^2 \Phi}{\partial p_l^2} \quad B = \frac{\partial^2 \Phi}{\partial \sigma \partial p_l} \quad (3)$$

we can write

$$d\varepsilon = C d\sigma + B dp_l \quad \text{and} \quad du = B d\sigma + M dp_l \quad (4)$$

The material properties depend on the stress and liquid water pressure or $C(\sigma, p_l)$, $M(\sigma, p_l)$ and $B(\sigma, p_l)$.

Considering the liquid pressure p_l in equation (4a) constant or $dp_l = 0$, we observe that $C = \partial \varepsilon / \partial \sigma$, which equals by definition the compliance. The compliance is measured in drained conditions, which refers to the condition where water is drained from the material in order to keep the liquid pressure in the material constant.

Considering the stress constant in equation (4b) or $d\sigma = 0$, we observe that $M = \partial u / \partial p_l$, which equals by definition the moisture capacity. In a standard sorption test, the wood specimen is conditioned at a given relative humidity ϕ until equilibrium and the moisture content u is measured. The relative humidity ϕ is related to the liquid pressure by Kelvin's law or $\phi = \exp(-p_l / \rho_l R_v T)$, where ρ_l is the density of water, R_v the ideal gas constant for vapor and T the absolute temperature. The specimen in a standard sorption test is not externally loaded or $\sigma = 0$. The moisture content measured in the unloaded condition is referred to as u_0 , where the subscript 0 refers to the zero stress condition. The relation between moisture content u_0 and liquid pressure p_l is described by the relation $u_0(p_l) = u_{0FSP} (1 - \ln \phi / A)^{-1/n}$, where u_{0FSP} is the moisture content at fibre saturation point and A and n are parameters. The moisture capacity at unloaded condition and which can be determined from this relation is referred to as $M_0 = \partial u_0 / \partial p_l$. According to equation (4a, $d\sigma = 0$), the coupling coefficient B describes the change in strain due to a change in liquid pressure, or the coupling coefficient B

describes swelling / shrinkage of the material. According to equation (4b, $dp_l = 0$), the coupling coefficient B also describes the change in moisture content due to a change in external stress, or the influence of mechanical stress on the sorption process.

We define the function $\Phi(\sigma, p_l)$ as

$$\Phi(\sigma, p) = \left[\frac{1}{2} C_0 \sigma^2 + \frac{1}{6} C_0 \alpha \sigma^3 + \frac{1}{12} C_0 \beta \sigma^4 \right] + [f(p_l)] + \left[g(p_l) \left(B_0 \sigma + \frac{B_1 \sigma^2}{2} \right) \right] \quad (5)$$

where C_0 , α , β , B_0 and B_1 are constants and f and g functions dependent on the fluid pressure p_l . The first term at the right hand side of equation (5) describes the energy contribution of the solid matrix (mechanical term). The second term describes the energy contribution of the liquid water (liquid term), while the third term describes the energy contribution due to the interaction between the solid matrix and liquid water. In classical poromechanics, the mechanical and liquid terms are of quadratic form in respectively σ and p_l , while the coupling term only contains the product σp_l . In the present model, the mechanical term is of the fourth order. The fluid term is described by the function $f(p_l)$, which has to be defined from experiments. The coupling term is described by the product of a function $g(p_l)$ and a second order term in σ . The function $g(p_l)$ has to be identified from experiments.

According to equation (3), we can derive, from equation (5), the following relations for the material properties:

$$C = C_0 (1 + \alpha \sigma + \beta \sigma^2) + g(p_l) B_1 \quad , \quad M = \frac{\partial^2 f}{\partial p_l^2} + \frac{\partial^2 g}{\partial p_l^2} \left(B_0 \sigma + \frac{B_1 \sigma^2}{2} \right)$$

$$B = \frac{\partial g}{\partial p_l} (B_0 + B_1 \sigma) \quad (6)$$

Equation (6a) gives the compliance as a function of the stress and liquid pressure. The compliance at zero stress level is the initial compliance and equals $C = C_0 + g(p_l) B_1$. In the experiments (fig. 1b), we observed that the initial compliance is a linear function of the moisture content up to fibre saturation point. This means that the function $g(p_l)$ equals the moisture content measured at zero external stress, or $g(p) = u_0(p)$. The dependence of the compliance on stress and moisture content then reads:

$$C = C_0 (1 + \alpha \sigma + \beta \sigma^2) + B_1 u_0 \quad (7a)$$

The constant B_1 can be determined directly from figure 1b as the slope of the compliance versus moisture content. The compliance C_0 in equation (7) is the compliance of the dry material ($u_0 = 0$) measured at zero stress ($\sigma = 0$). The quadratic dependence of compliance on stress is determined by the parameters α and β , which can be determined from experiments as given in figure 1c.

Equation (6b) gives the moisture capacity as a function of stress and liquid pressure. The moisture capacity at zero stress ($\sigma = 0$) is defined as $M_0 = \partial u_0 / \partial p_l$. Evaluating equation (6b) at zero stress shows that $M_0 = \partial^2 f / \partial p^2$. Since we found that $g(p_l) = u_0(p_l)$, equations (6b) and (6c) can be written as

$$M = M_0 + M_0' \left(B_0 \sigma + \frac{B_1 \sigma^2}{2} \right) \quad (7b) \quad , \quad B = M_0 (B_0 + B_1 \sigma) \quad (7c)$$

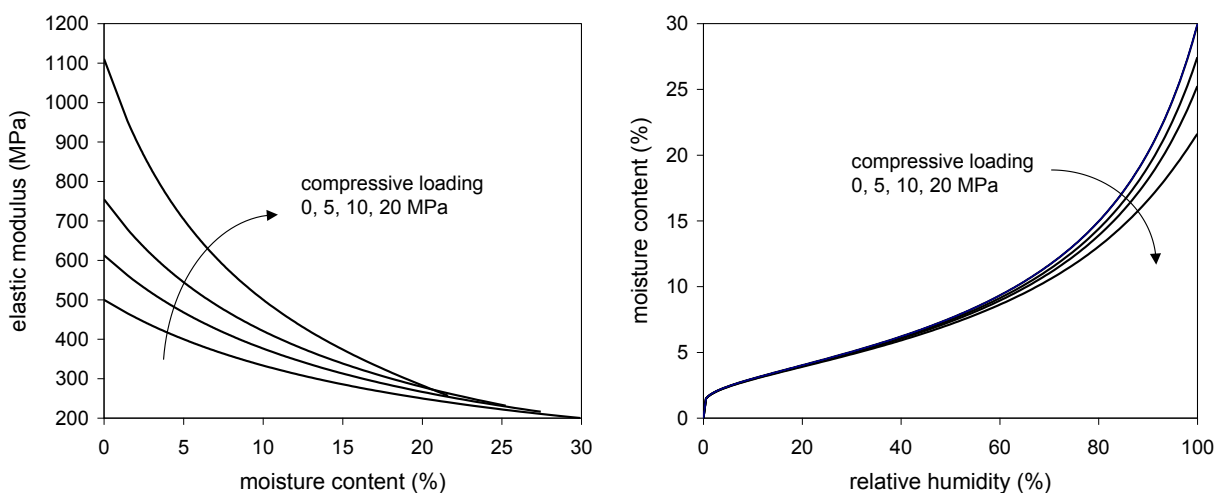
where $M_0' = \partial M_0 / \partial p_l$. The moisture capacity and the derivative of the moisture capacity can be determined from the function $u_0(p_l) = u_{0FSP} (1 - \ln \phi / A)^{1/n}$. Since the moisture content u_0 and the moisture capacity M_0 are a function of the liquid pressure p_l , equations 7a-c describe the dependencies of the material properties on the stress and on the liquid pressure. The parameters C_0 , α , β , B_1 and the function $u_0(p_l)$ are known. The parameter B_0 can be directly determined from a free swelling test where a wood specimen is exposed to environments of different relative humidity at unloaded condition ($\sigma =$

0, $d\sigma = 0$). According to equations (4a) and (7c) the swelling strain increment equals $d\varepsilon = M_0 B_0 dp_l$. According to equation (4b), the moisture content increment is related to the liquid pressure increment by $du_0 = M_0 dp_l$. Combining the last two equations, we find that $d\varepsilon = B_0 du_0$. This means that the parameter B_0 can be directly measured in a free swelling test as the slope of the swelling strain versus the moisture content (see figure 1a).

Results and discussion

The proposed model (equations 4 and 7) allows the study of the behavior of wood in different loading conditions. Especially, we focus on the mechano-sorptive behavior and study the influence of mechanical stress on moisture content. In the different tests, the following typical values for wood in tangential direction are used: $C_0 = 1/(500 \text{ MPa})$, $u_{0FSP} = 0.3 \text{ kg/kg}$, $A = 0.19$, $n = 1.12$, $\alpha = 1/(40 \text{ MPa})$, $\beta^{1/2} = 1/(40 \text{ MPa})$, $B_0 = 0.5$, $B_l = 1/(100 \text{ MPa})$.

In a first test, we analyse the swelling of wood when exposed to an increase in relative humidity. Using Kelvin's law, the fluid pressure is evaluated. A constant compressive stress (weight) is applied to the wood specimen during the whole experiment. The compressive stresses are respectively: 0, -5, -10 and -20 MPa. Note that the maximal compressive stress may introduce some plastic deformation of wood, which is neglected in this paper. The material properties C , M and B are evaluated by equations 7 and the swelling strain and sorption isotherm are respectively obtained by equations 4a and 4b. Figure 2a gives the elastic modulus (or reverse of compliance) as a function of the moisture content for different stress levels. We observe a softening effect when to moisture content increases and a stiffening effect, as seen on Figure 1c, when wood is loaded in compression. Figures 2b and 2c give the obtained sorption curves. We see that the amount of moisture adsorbed by the specimen reduces at high compressive stress, and that this stress effect on the sorption behavior is more pronounced at high relative humidities. Figure 2d gives the swelling strain as a function of the moisture content for the different compressive stress levels. The results follow the trends seen in experiments [9]. The strain at zero moisture content is the elastic strain due to the compressive loading at the beginning of the test. At zero compressive stress, the swelling strain increases linearly with the moisture content as found in the experiments. At higher compressive stress, the swelling curve becomes nonlinear, which can be explained by two effects: first according to equation 7c the coupling coefficient B decreases with compressive (negative) stress, second effect of stress on the sorption isotherm as shown in figures 2b and 2c.



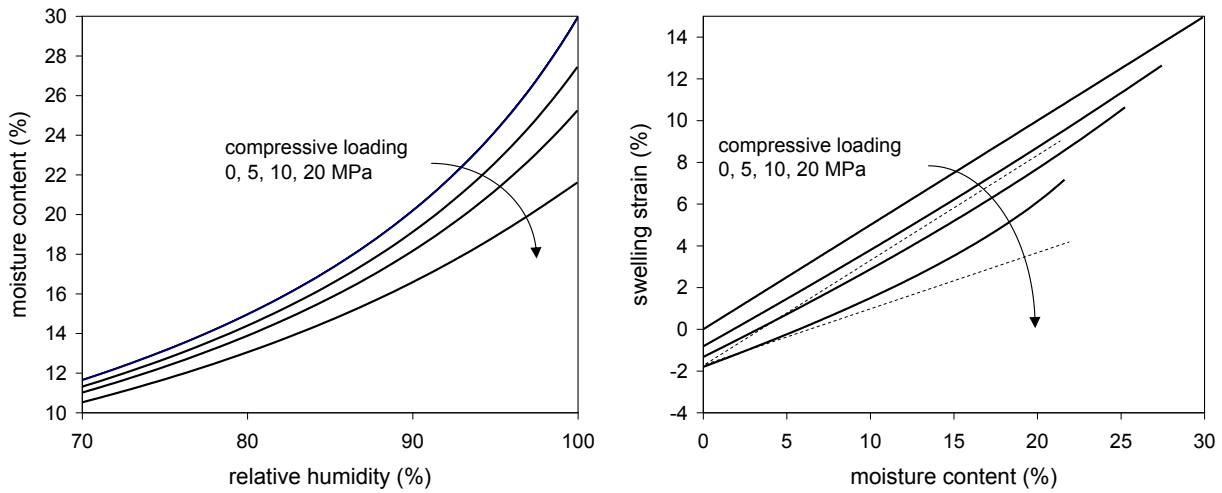


Fig. 2 Swelling test results at different compressive stresses: (a) stiffness as a function of relative humidity; (b) influence of mechanical stress on the sorption curves; (c) close-up of sorption curves at high RH; (d) swelling strain as a function of relative humidity.

In the second test, we analyse the behavior of wood in compression at different moisture contents. First, we wet the dry wood specimen to a certain moisture content u_0 in stress free conditions. Then a compression test is conducted by increasing the stress from 0 to -20 MPa. During mechanical loading, the liquid pressure remains constant and water will be expelled from the specimen (drained conditions). Figure 3a shows that the wood softens (lower elastic stiffness) when the moisture content is increased. The stress-strain curve is nonlinear showing a stiffening effect with increasing strain or compressive stress. Figure 3b shows the moisture that is expelled during the compressive test as a percentage of the initial moisture content. We observe that 8% of the initially moisture is expelled at -20 MPa for the specimen at fiber saturation point. For lower moisture contents, the percentages of expelled moisture are lower.

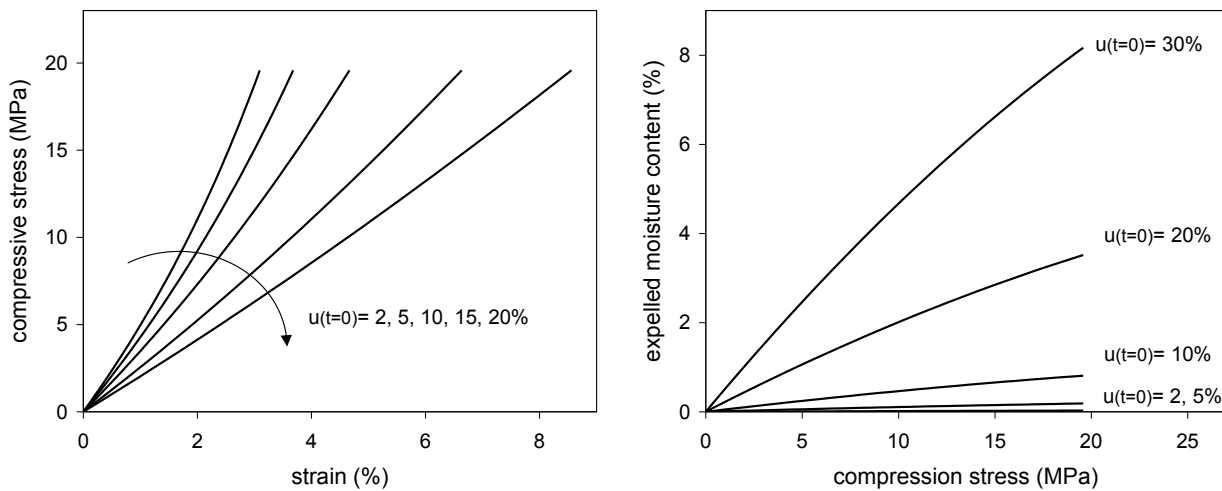


Fig. 3 Compression test results: (a) stress strain curves at different initial moisture contents; (b) influence of mechanical stress on expelled moisture.

In the third test, we expose the material to an increasing relative humidity from different initial moisture contents $u(t=0)=0, 7.5$ and 15% , while the swelling of the material is mechanically prohibited ($d\varepsilon=0$). We determine the resulting mechanical stress and the moisture content in the material. Figure 4a gives the swelling stress, increasing almost linearly with some deviations at maximal moisture content. These nonlinearities are due to the nonlinear mechanical behavior (nonlinear elastic modulus) and due to the effect of mechanical stress on moisture content. Due to the high mechanical stresses, less moisture will be taken up with increasing relative humidity (figure 4b).

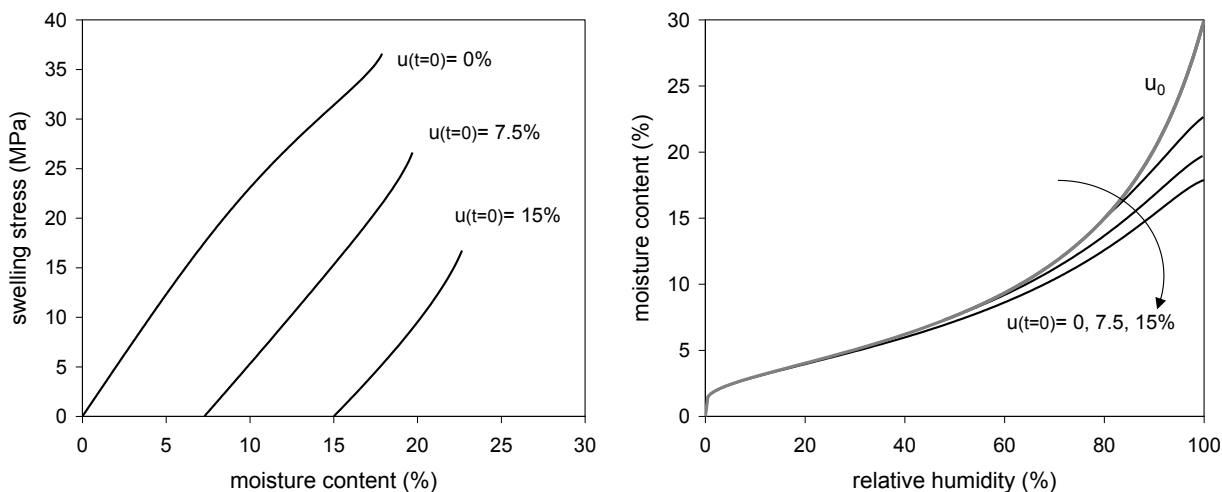


Fig. 4 Restrainted swelling results. (a) swelling stress as a function of moisture content; (b) mechanical influence on the sorption curves

Conclusion

A poroelastic constitutive model is formulated based on a higher order formulation of the free energy including mechanical and moisture contributions and the coupling between moisture and mechanics. The advantage of this higher order energy formulation is that the nonlinear dependence of the material properties, elastic modulus, moisture capacity and swelling coefficient is inherently taking into account leading to a consistent formulation of the dependence of the material properties on stress and capillary pressure. The parameters describing these dependencies can be directly determined from experiments. With the proposed constitutive model, free / restrained swelling tests and compression tests on wood are analyzed. The elastic modulus is found to depend nonlinearly on stress and moisture content. Mechanical compressive stresses are found to lead to lower moisture content on wood.

The main focus of this paper is on the formulation of the model. The next step will consist on the validation of the model using a consistent dataset under development especially for this purpose.

References

1. Sèbe, G. and M.A. Brook, (2001): *Hydrophobization of wood surfaces: covalent grafting of silicone polymers*, Wood Science and Technology 35: 269-282.
2. Woesz, A., J. Stampfl and P. Fratzl, (2004): *Cellular solids beyond the apparent density – an experimental assessment of mechanical properties*, Adv. Eng. Mat., 6:134-138.
3. Almeida, G. and R.E. Hernandez, (2006): *Changes in physical properties of tropical and temperate hardwoods below and above the fiber saturation point*, Wood Science and Technology, 40:599-613.
4. Neuhaus, F.H. (1981): *Elastizitätszahlen von Fichtenholz in Abhängigkeit von der Holzfeuchtigkeit*, PhD Thesis, Bochum.
5. Fratzl, P. and R. Weinkamer, (2007): *Nature's hierarchical materials*, Prog. Mat. Sci., 52:1263-1334.
6. Haeggstrom, E., T. Koponen, T. Karppinen, P. Saranpaa and R. Serimaa, (2006): *Ultrasonic study on hysteresis in modulus of elasticity in Norway spruce as a function of year ring*, Review of Quantitative Nondestructive Evaluation, 25:1366-1369.
7. Martensson, A. (1994): *Mechano-sorptive effects in wooden material*, Wood Science and Technology, 28:437-449.
8. Kojima, Y. and H. Yamamoto, (2005): *Effect of moisture content on the longitudinal tensile creep behavior of wood*, J. Wood Sci., 51:462-467.

9. Niemz, P. (1993): *Holzphysik*. DRW Verlag 1993 (in German).
10. Murnaghan, F.D. (1944): *The Compressibility of Media under Extreme Pressures*, Proceedings of the National Academy of Sciences, 30:244-247.
11. Birch, F. (1947): *Finite Elastic Strain of Cubic Crystals*, Physical Review, 71:809-824.
12. Biot, M.A. (1941): *General theory of three dimensional consolidation*, Journal of Applied Physics, 12:155-164.
13. Coussy, O. (2004): *Poromechanics*, John Wiley & Sons, Chichester.
14. Berryman, J.G. (2002): *Extension of poroelastic analysis to doubleporosity materials: new technique in microgeomechanics*, Journal of Engineering Mechanics, ASCE, 128:840-847.
15. Coussy, O., R. Eymard and T. Lassabatère, (1998): *Constitutive modelling of unsaturated drying deformable materials*, Journal of Engineering Mechanics, ASCE, 124:658-667.
16. Meschke, G. and S. Grasberger, (2003): *Numerical modeling of coupled hygromechanical degradation of cementitious materials*, Journal of Engineering Mechanics, ASCE, 129:383-392.
17. Coussy, O. (2007): *Revisiting the constitutive equations of unsaturated porous solids using a Lagrangian saturation concept*, Int. J. Numer. Anal. Meth. Geomech, 31:1631-1713.

The viscoelastic properties of some Guianese woods

J. Paul McLean¹, Olivier Arnould¹, Jacques Beauchêne², Bruno Clair¹

¹ *Laboratoire de Mécanique et Génie Civil Université Montpellier 2/CNRS UMR5508,
CC 048 Place Eugène Bataillon, 34095 Montpellier, France*

² *CIRAD, Ecologie des Forêt de Guyane (EcoFog),
BP 701, 97387 Kourou Cedex, Guyane, France*

Abstract

Samples of tension wood and opposite wood were obtained from four species (*Iryanthera sagotiana*, *Ocotea guyanensis*, *Virola michelii*, *Sextonia rubra*) growing in the tropical rainforest of French Guiana. Dynamic mechanical analysis was performed in the longitudinal dimension with samples in the green “never dried” condition. Temperature and frequency of the tests were regulated to be similar to conditions experienced by the living tree. Tension wood from the species containing a G-layer was found to have higher damping characteristics than opposite wood from the same species whilst no difference was found between the wood types of the non G-layer species. The research thus far does not permit a solid conclusion but speculation into the possible origin of these differences is drawn from the nature of the G-layer matrix.

Introduction

Reaction wood is formed in the cambium of living trees to readdress vertical orientation of the stem following mechanical stressing, often by weight overhang (e.g. irregular crown formation) or external environmental factors such as wind loading. Reaction wood changes with plant group and as such falls into two categories: compression wood or tension wood. Compression wood is formed by gymnosperms in the lower side of the leaning stem [1]. Tension wood is formed by Angiosperms and is, as the name suggests, found on the upper or tensile side. In biomechanical terms, tension wood corrects the stem verticality by creating a tensile force somewhat higher than that of the opposing (opposite) wood [2, 3]. The anatomical [4, 5] and mechanical properties [6, 7, 8] of tension wood can therefore be very different to those of the opposite wood in the same tree. Additionally the severity to which the tension wood is formed may affect the degree to which these properties vary [8]. Tension wood is further classified by the presence or absence of a gelatinous G-layer [9]. The G-layer is composed of highly crystalline cellulose aggregates, in which hemicelluloses and lignin occur in trace amounts [10]. As there is seemingly no difference in wood tensile stiffness between G-layer and non G-layer producing species, [11], the benefit of the G-layer to the living tree is currently not certain.

Wood is a polymeric composite material displaying viscoelastic behaviour [12], which by simple definition means that there is an elastic and viscous component to its mechanical behaviour. After unloading, purely elastic materials will return all of the energy imposed upon them whilst purely viscous materials will exhibit a delay in mechanical response and dissipate that energy. Viscoelastic materials will therefore return some of the imposed energy with a delay and dissipate the rest. Wood elasticity is mainly given by the stiffness and orientation of the crystalline cellulose microfibrils in the S₂ layer of the cell wall [13, 14], whilst wood viscosity originates from the lignin and hemi-cellulose matrix [12, 15]. Wood viscoelasticity is anisotropic and highly dependant on temperature and moisture content [12].

Viscoelastic properties of materials are commonly measured by dynamic mechanical analysis or DMA [16]. This technique can provide the conservative elastic modulus (E') and the damping

coefficient or “tangent delta” ($\tan \delta$). From an experimental view, $\tan \delta$ is the tangent of the phase angle between the oscillating applied stress and the resulting strain. Whilst an elastic only material will deform immediately and have no phase lag, a material with a viscous component will have a phase lag relative to the degree of viscosity. Consequently, a higher $\tan \delta$ indicates a more viscous material. This study presents an investigation into the viscoelastic properties of tension wood compared to opposite wood in tropical rainforest species

Material and methods

Material

Sample trees were collected in the vicinity of the Paracou experimental field station in French Guiana. Four common species were chosen (*Table 1*) representing 2 groups of taxonomically similar species where one was thought to contain a G-layer whilst the other was not. To maximise the possibility of tension wood content, individuals with a crooked or sweeping stem form were sought. To verify the asymmetrical trunk stresses associated with reaction wood formation [17] growth stress measurements were performed at 8 points around the circumference at breast height [8] using the strain gauge method [18, 19]. Trees were then felled and 8 radial sections corresponding to the growth stress measurement locations were cut from each. To obtain tension wood, the section with the highest growth stress was taken and the section directly opposite in relation to the standing tree was used for opposite wood. 3 samples of dimensions $150 \times 2 \times 12$ mm (LRT) were cut from the outer (bark) part of the tension wood and opposite wood sections of each tree. Sample material was maintained in the green state throughout the process by not being allowed to dry out. Anatomical measurements to confirm tension wood and identify fibre pattern (presence or absence of a G-layer) were carried out on adjacent sample material from one of the two sample trees per species [20]. Growth stress measurements and fibre characteristics are shown in *Table 1*.

Table 1 Sample material used in the study. GS = Growth Strain, TW = Tension Wood, OW = Opposite Wood

Family	Species	Tree	Tree diameter at breast height (cm)	GS TW (μ strain)	GS OW (μ strain)	Fibre Pattern
Lauraceae	<i>Sextonia</i>	1	25	-2362	-328	G Thick
	<i>rubra</i>	2	21	-1657	-59	
	<i>Ocotea</i>	1	19	-2097	-399	G Thin
	<i>guyanensis</i>	2	18	-2063	-718	
Myrsiticaceae	<i>Iyranthera</i>	1	26	-1485	12	No G
	<i>sagotiana</i>	2	22	-822	-7	
	<i>Virola</i>	1	36	-1708	45	No G
	<i>michelii</i>	2	29	-1699	-7	

Dynamic Mechanical Analysis

A BOSE-Electroforce 3230 Dynamic Mechanical Analyser equipped with a submersible 450N load cell and a custom built water bath temperature controlled by a Huber Ministat cc3 was used for the DMA tests. Submerged samples were tested in tension at constant 30°C temperature, chosen to resemble that of the natural environment of the trees in the tropical rainforest. To commence a charge of quasi-static loading was imposed to verify that there will be no slippage of the sample in the clamps during subsequent loading used for the determination of mechanical properties. A static ramp test was performed on each sample prior to DMA analysis to determine the tensile Young’s modulus and the quantity of stress to produce 0.02% strain with amplitude of 0.03%. The DMA test was a sinusoidal loading applied at a frequency of 1Hz to represent the oscillation of the correct order for a standing tree whilst remaining in a frequency range where the DMA has a more accurate response. $\tan \delta$ was calculated by Fourier Transformation analysis within the integral BOSE WinTest™ DMA Analysis software.

Statistical Analysis

In order to determine if there was a significant effect of wood type on the tensile modulus or tangent delta, analysis of variance was performed on the data grouped by species and wood type. An F-test was used to determine the significance ($\alpha = 0.05$) of wood type on each variable and where appropriate a Tukey HSD test was used to examine the differences in means between wood types and within species.

Results and discussion

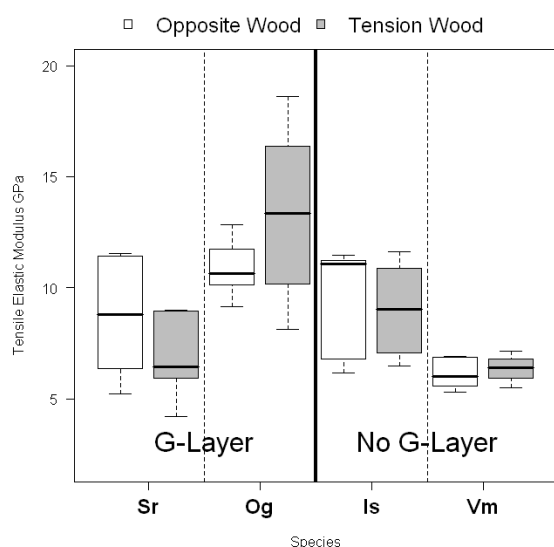


Fig. 1 Boxplot of tensile Young's modulus by species and wood type. Is = *Iryanthera sagotiana*, Og = *Ocotea guyanensis*, Vm = *Virola michelii*, Sr = *Sextonia rubra*. Significant differences ($\alpha=0.05$) were found in green Young's modulus between tension wood and opposite wood of the G-layer species, Sr tension wood was less rigid than Sr opposite wood and Og tension wood was more rigid than Og opposite wood. No significant difference was found for the non G-Layer species.

With the exception of the *Virola* samples, there was a lot of variation in the tensile modulus (Fig. 1). Analysis of variance followed by the Tukeys HSD test (Table 2) showed that the MOE of *Sextonia* tension wood was lower than *Sextonia* opposite wood by 1.8GPa, whereas the inverse was true of *Ocotea* tension wood which was greater than *Ocotea* opposite wood by 2.4GPa. No significant difference ($\alpha = 0.05$) was found between the tension wood and opposite wood of *Virola* or *Inga*. These results echo Ruelle et al. [7] who did not always find a significant difference between the air dry modulus of elasticity (MOE) of opposite wood and tension wood in Guianese species. Of the ten species studied by Ruelle et al. [7] only *Ocotea* was present in this study and the difference was in the same sense. Ruelle et al [7] presented a ratio of tension wood MOE over opposite wood MOE for this species equal to 1.28, the same ratio here was 1.22 and thus comparable though the effect of drying may change the ratio slightly. Ruelle et al. [7] also presented ratios less than one which showed the same trend for different species (*Virola surinamensis* and *Cecropia sciadophylla*) as the *Sextonia* here, i.e. the opposite wood was more rigid than tension wood. Neither the study by [7] nor these results can offer a definitive logic to the trends in longitudinal modulus within tropical species with reaction wood but do show the diversity of growth strategies and their underlying biomechanics in the tropical rainforest. It is important to note that the best comparison will be on the specific modulus to take account of density variations. The samples in this study are undergoing drying and further testing so that this comparison can be made.

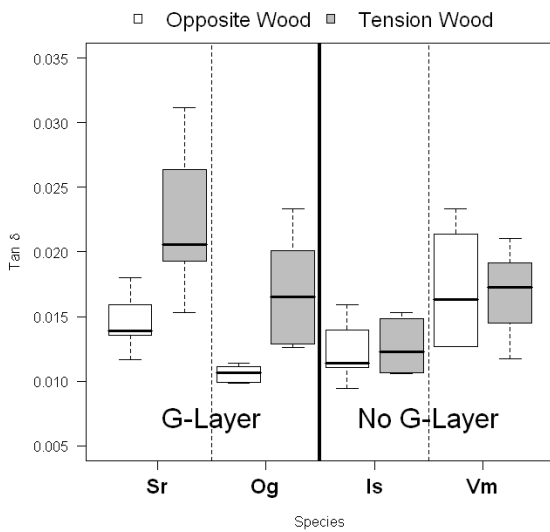


Fig. 2 Boxplot of tensile tangent delta at 1Hz by species and wood type. Is = *Iryanthera sagotiana*, Og = *Ocotea guyanensis*, Vm = *Virola michelii*, Sr = *Sextonia rubra*. Tension wood containing a G-layer was shown to have significantly ($\alpha=0.05$) higher damping than opposite wood from the same species at a frequency of 1Hz. There was no difference between tension wood and opposite wood from the non G-layer species.

Concerning the viscous part of this study, the measured $\tan \delta$ are presented in Fig. 2. Both species which exhibited G-layer formation had a visibly and significantly higher $\tan \delta$ in the tension wood as compared to the opposite wood (Table 2). The difference between the mean $\tan \delta$ of the tension wood and opposite wood of both *Sextonia* and *Ocotea* was 0.0082 though the *Sextonia* samples did tend to have a higher $\tan \delta$ in general. Differences between species were not assessed statistically due to the low number of sample trees. In contrast there was no visible or statistical difference between the tension wood and opposite wood of the species without a G-layer.

Table 2 Results from a Tukey HSD test examining the difference in Tensile Young's Modulus and Tangent Delta between the wood types of each species. OW = Opposite Wood, TW = Tension Wood, Is = *Iryanthera sagotiana*, Og = *Ocotea guyanensis*, Vm = *Virola michelii*, Sr = *Sextonia rubra*.

Parameter	Difference in wood type within species	Difference in Means	p-value
Tan δ	Is_TW - Is_OW	0,0002	1,0000
	Og_TW - Og_OW	0,0082	<0,0001
	Sr_TW - Sr_OW	0,0082	<0,0001
	Vm_TW - Vm_OW	-0,0008	0,9967
Tensile Young's Modulus (GPa)	Is_TW - Is_OW	-0,2563	0,9981
	Og_TW - Og_OW	2,4052	<0,0001
	Sr_TW - Sr_OW	-1,7837	0,0002
	Vm_TW - Vm_OW	0,2312	0,9996

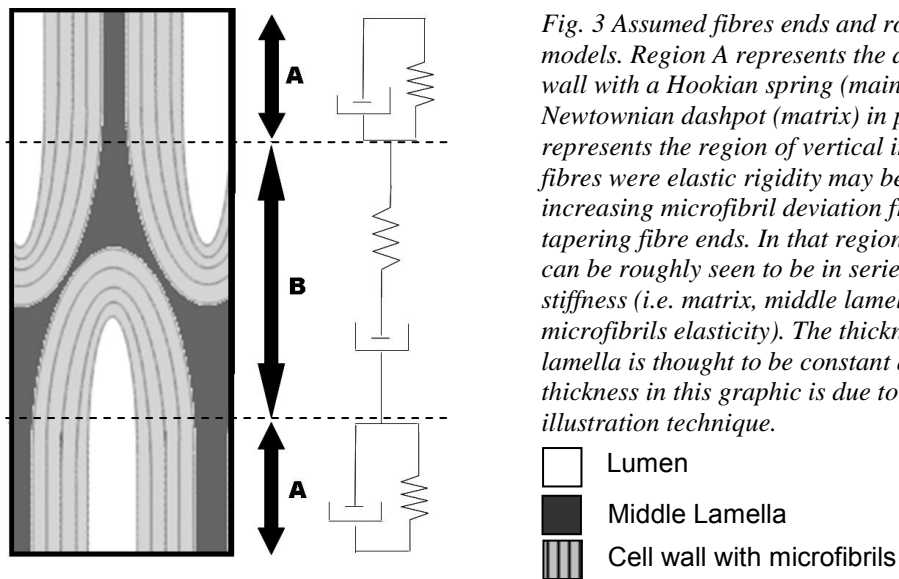


Fig. 3 Assumed fibres ends and rough viscoelastic models. Region A represents the axially aligned cell wall with a Hookian spring (mainly microfibrils) and a Newtonian dashpot (matrix) in parallel. Region B represents the region of vertical interaction between fibres where elastic rigidity may be lower due to increasing microfibril deviation from the vertical at the tapering fibre ends. In that region, constituent loading can be roughly seen to be in series with a lower spring stiffness (i.e. matrix, middle lamella and transverse microfibrils elasticity). The thickness of the middle lamella is thought to be constant and the varying thickness in this graphic is due to a limit of the current illustration technique.

The presence of a G-layer seems to indicate an increase in the viscosity of the material relative to the wood from the opposing side of the same tree. These experiments alone cannot offer a definitive origin of this phenomenon but there is room to speculate. Firstly it can be considered that the un-lignified gel-like matrix of the G-layer has properties different to those of the lignified wood cell wall (reviewed in [21]) and that consequently the gel matrix is more viscous. However, this corresponds only to region A of Fig. 3 and it is difficult to imagine that this difference in viscosity would be detectable in the case where stress is longitudinally applied to the tension wood cell wall as the load should be mostly carried by the microfibrils, which are well aligned to the fibre axis, and not by the matrix. Logically, the mechanical properties of the matrix should be more apparent for longitudinal stress applied to a cell wall with high microfibril angle (MFA) and a resulting lower specific modulus. Again it will be important to observe the specific elastic modulus of these samples, as proposed earlier, in order to see clearly the difference in the cell wall longitudinal elasticity and its possible effect or correlation with the viscous response variations.

Independently of the how the mean MFA effects the viscoelasticity of the main body of the cell wall (region A of Fig. 3), it is not certain of how microfibrils are aligned at the tapered ends of wood fibres. It is plausible that the microfibrils follow the course of this taper and are thus, even in tension wood, less aligned relative to the vertical at these points (region B of Fig. 3). If this were to be the case, then at this interconnecting region, an applied axial stress would act across rather than along the microfibrils and therefore the mechanical properties of the matrix and/or the compound middle lamella (the interfusion of primary cell walls and the middle lamella after lignification) would become more important. This is illustrated with a viscous and elastic component in series in Fig. 3. With respect to the G-layer fibre, the properties of the chemically different matrix could become more pronounced at these points. Alternatively, in the G-layer there may be lower cohesion between fibres, caused by the lack of lignification for example, and consequently at the end the fibre would have lower axial rigidity than in normal wood, increasing the contribution of the viscous middle lamella. Some supportive evidence may be seen in Wimmer and Lucas [22] who showed quantitatively that the cell corner middle lamella was 50% less rigid than the S_2 layer in *Picea rubens* wood and that, visually, there seemed to be a larger remaining plastic (permanent) deformation in the cell corner middle lamella for the same imposed force. Further research is required in this area in order to further understand this phenomenon and should consist of anatomical studies of fibre ends coupled with micromechanics.

From the biomechanical point of view it can be proposed that the increased damping capability of the tension side of the stem could decrease the risk of fracture associated with a sudden jolt induced by a gust of wind for example. In this case it is not clear why some species have adopted the G-layer strategy in tension wood whilst others have not. On an evolutionary timescale it appears that both sets of species appeared at similar times [23]. On the other hand this increased damping could simply be

the side effect or trade off of genetic mutation, the quantity of which is less important to the standing tree than architecturally related damping (e.g. [24, 25]).

Conclusion

The presence of a G-layer in the tension wood of the studied species was accompanied by an increased damping coefficient relative to the respective opposite wood. Hypotheses were put forward on the origin of this difference coming from the different chemical composition of the G-layer matrix or increased contribution of the middle lamella at fibre ends. A biomechanical implication was proposed in the damping of tension wood to an induced vibration and recommendations were made for future research.

Acknowledgements

We would like to thank the ANR project “Woodiversity”, CNRS, CIRAD and University of Montpellier 2 for funding. Professor Yamamoto (Nagoya University, Japan) for help in field measurements and sample collection. Soepe Koese for sample preparation at the CIRAD facility in Kourou, French Guiana. Finally, thanks to Gille Camp of LMGC, University of Montpellier 2, for building the water bath and other necessary additions to the DMA.

References

1. Timmel T.E., 1986. Compression wood in gymnosperms, Springer-Verlag., New York, New York, USA.
2. Wardop A.B., 1964. The reaction anatomy of arborescent angiosperms. In: Zimmermann M. H. (Ed.) Formation of wood in forest trees, Academic Press, New York, pp. 405-456.
3. Fisher J.B. and J.W. Stevenson, 1981. Occurrence of reaction wood in branches of dicotyledons and its role in tree architecture. *Botanical Gazette* 142(1): 82-95.
4. Jourez B., A. Riboux, et al., 2001. Anatomical characteristics of tension wood and opposite wood in young inclined stems of poplar (*Populus euramericana* cv 'Ghoy'). *Iawa Journal* 22(2): 133-157.
5. Ruelle J., B. Clair, et al., 2006. Tension wood and opposite wood in 21 tropical rain forest species 2. Comparison of some anatomical and ultrastructural criteria. *Iawa Journal* 27(4): 341-376.
6. Coutand C., G. Jeronimidis, et al., 2004. Comparison of mechanical properties of tension and opposite wood in *Populus*. *Wood Science and Technology* 38(1): 11-24.
7. Ruelle J., J. Beauchene, et al., 2007. Comparison of physical and mechanical properties of tension and opposite wood from ten tropical rainforest trees from different species. *Annals of Forest Science* 64(5): 503-510.
8. Fang C.H., B. Clair, et al., 2008. Growth stresses are highly controlled by the amount of G-layer in poplar tension wood. *Iawa Journal* 29(3): 237-246.
9. Onaka F., 1949. Studies on compression and tension wood. *Wood research bulletin*, Kyoto University, Japan.
10. Daniel G., L. Filonova, et al., 2006. Morphological and chemical characterisation of the G-layer in tension wood fibres of *Populus tremula* and *Betula verrucosa*: Labelling with cellulose-binding module CBM1(HjCel7A) and fluorescence and FE-SEM microscopy. *Holzforschung* 60(6): 618-624.
11. Clair B., J. Ruelle, et al., 2006. Tension wood and opposite wood in 21 tropical rain forest species 1. Occurrence and efficiency of the G-layer. *Iawa Journal* 27(3): 329-338.
12. Navi P. and S. Stanzl-Tschegg, 2009. Micromechanics of creep and relaxation of wood. A review COST Action E35 2004-2008: Wood machining - micromechanics and fracture. *Holzforschung* 63(2): 186-195.
13. Cave I.D., 1968. Anisotropic elasticity of plant cell wall. *Wood Science and Technology* 2(4): 268-&.
14. Salmen L. and I. Burgert, 2009. Cell wall features with regard to mechanical performance. A review COST Action E35 2004-2008: Wood machining - micromechanics and fracture. *Holzforschung* 63(2): 121-129.
15. Salmen L., 1984. Viscoelastic properties of insitu lignin under water-saturated conditions. *Journal of Materials Science* 19(9): 3090-3096.
16. Menard K.P., 2008. *Dynamic Mechanical Analysis: A Practical Introduction*, CRC Press, 240 p.
17. Trenard Y. and P. Gueneau, 1975. Relations between growth stresses and tension wood in beech. *Holzforschung* 29(6): 217-223.

18. Yoshida M. and T. Okuyama, 2002. Techniques for measuring growth stress on the xylem surface using strain and dial gauges. *Holzforschung* 56(5): 461-467.
19. Jullien D. and J. Gril, 2008. Growth strain assessment at the periphery of small-diameter trees using the two-grooves method: influence of operating parameters estimated by numerical simulations. *Wood Science and Technology* 42(7): 551-565.
20. Chang S.-S., B. Clair, et al., In print. Mesoporosity as a new parameter for understanding tension stress generation in trees. *Journal of Experimental Botany*.
21. Pilate G., B. Chabbert, et al., 2004. Lignification and tension wood. *Comptes Rendus Biologies* 327(9-10): 889-901.
22. Wimmer R., B.N. Lucas, et al., 1997. Longitudinal hardness and Young's modulus of spruce tracheid secondary walls using nanoindentation technique. *Wood Science and Technology* 31(2): 131-141.
23. Ruelle J., 2009. Personal Communication
24. Spatz H.C., F. Brochert, et al., 2007. Multiple resonance damping or how do trees escape dangerously large oscillations? *American Journal of Botany* 94(10): 1603-1611.
25. Moore J.R. and D.A. Maguire, 2008. Simulating the dynamic behavior of Douglas-fir trees under applied loads by the finite element method. *Tree Physiology* 28(1): 75-83..

Influence of the extractives of selected extraneous woods on the equilibrium moisture content - chemical and physical properties

*Peter Niemz¹, Tamás Hofmann², Levente Albert², Tamás Rétfalvi²;
and Rudolf Popper¹*

*¹ Swiss Federal Institute of Technology, Institute for Building Materials, Wood Physics,
Switzerland*

*² University of West Hungary, Faculty of Forestry, Institute of Chemistry and Soil Science
Hungary*

Abstract

The water vapour sorption behaviour of 13 different tropical wood species was examined. The experimentally determined values were analysed with the Hailwood-Horrobin sorption model. According to the Hailwood-Horrobin model following characteristic values were computed: the monomolecular U_m and polymolecular U_p sorption, the fiber saturation point U_{fs} , the inaccessibility Z of the sorbent to the sorbate as well as the specific surface of the sorbent Σ . Very large differences exist in the sorption behaviour between the individual wood species. In particular for Canalete (22,8%), Wengé (20,3%) and Doussié (17,8%) a very low fiber saturation point was determined, which is clearly below the values of European wood species (28-32%) and other examined tropical woods. The ethanol toluol extract of the wood correlates with the moisture content of the polymolecular U_p and total U_{tot} sorption. The higher the extractives content, the lower the equilibrium moisture content U_{tot} and U_p . The chemisorption remains therefore uninfluenced by EtOH-toluol extractives. The reduction of the sorption capacity by rising EtOH-toluol extractive content is due to the bulking effect.

Introduction

The wood is, due to the microscopical, the submicroscopical and the chemical structure, very complex. Many scientists in the past and also nowadays have tried to describe the phenomenon of sorption hysteresis and its physical causes to explain it (Everett, D.H. 1954, 1955; Peralta, P.N., Bangi, A.P. 1998; Time, B. 2002; Frandsen, H.L. et al., 2007; Frandsen, H.L., Svensson, S. 2007). A overview about the influence from extractive content was given by Hernandez (2007) and Labbè et al (2002). At Institute for Building Materials (ETH Zurich) accomplished water vapour adsorption and desorption measurements on selected exotic wood species were analysed by the Hailwood-Horrobin and tested the chemical composition.

Material and methods

Wood samples:

Wood species used in this study are summarized in *Table 1*.

Physical properties:

Test conditions The attempt samples were conditioned in a climate chamber (KPK 200, Feutron) at constant temperature of $20 \pm 0.2^\circ\text{C}$ and with relative humidity RH from 35%, 50%, 85% to 93% ($RH \leq \pm 3\%$). The equilibrium moisture content EMC of the attempt samples was determined according to DIN 52 183 (1977).

Table 1: The material tested

Wood species	Latin name	Plant family
Bilinga	<i>Nauclea diderrichii</i> Merrill	Rubiaceae
Bongossi	<i>Lophira alata</i> Banks ex Gaertn. f.	Ochnaceae
Canalete (Cordia)	<i>Cordia sp.</i>	Boraginaceae
Danta	<i>Nesogordonia papaverifera</i> (A. Chev.) R. Capuron	Sterculiaceae
Doussié	<i>Azelia sp.</i>	Caesalpiaceae
Makassar	<i>Diospyros celebica</i> Bakh.	Ebenaceae
Mansonia	<i>Mansonia altissima</i> A. Chev.	Sterculiaceae
Merbau; Hintsy	<i>Intsia sp.</i>	Caesalpiaceae
Okoumé	<i>Aucoumea klaineana</i> Pierre	Burseraceae
Ramin	<i>Gonystylus bancanus</i> (Miq.) Kurz	Gonystylaceae
White Lauan	<i>Shorea sp.</i>	Dipterocarpaceae
Wengé	<i>Milettia laurentii</i> De Wild.	Papilionaceae
Zebrano	<i>Microberlinia sp.</i>	Caesalpiaceae

Sorption analysis:

Hailwood-Horrobin model

For the characterisation of the interaction between the attempt material (wood) and the water vapour the Hailwood-Horrobin sorption model (1946) was used. The Hailwood-Horrobin sorption model (further called HH-model) is based on the assumption that the sorbed water exists as a simple solution and as hydrate of the wood. The HH-model assumes further that the sorbed layer which consists of no hydrated, hydrated wood and of free liquid water forms an ideal solid solution. This sorption model makes it possible to separate the monomolecular U_m from the polymolecular sorption U_p and the estimation of the fiber saturation point U_{FS} . The sorption equation for the HH-model is as follows:

$$U_{tot} = U_m + U_p \quad (1)$$

$$U_{tot} = \frac{1800}{M_p} \cdot \left(\frac{\alpha \cdot \beta \cdot h}{1 + \alpha \cdot \beta \cdot h} \right) + \frac{1800}{M_p} \left(\frac{\alpha \cdot h}{1 - \alpha \cdot h} \right), \quad (2)$$

Where U_{tot} total water sorbed (%),
 U_m monomolecular water sorbed (%),
 U_p polymolecular water sorbed (%),
 h relative vapour pressure,
 M_p hypothetical molecular weight of the dry wood polymer,
 α equilibrium constant of the hydrated wood,
 β equilibrium constant of the no hydrated wood.

Further allows the HH-model to calculate following values:

- The specific surface of the sorbent Σ
- and the inaccessibility of the sorbent to the sorbate Z .

Sorption hysteresis

At the sorption hysteresis are the pathways for the water uptake and release which tend to be different. The relative vapour pressure on adsorption of a porous material (wood) is greater than on desorption. This phenomenon is called sorption hysteresis. Possible explanation for the true hysteresis (the irreversible sorption) is the formation of metastable states of adsorbate in fixed pores (capillary condensation hysteresis) (Sing et al., 1985; Burgess et al., 1989 ; Liu et al., 1993; Neimark et al., 2000; Aharoni, 2002; Sander et al., 2005). It is assumed that the reason for hysteresis is the difference in the sorbate filling and sorbate emptying of the pores. This can be described with the fundamental Kelvin equation.

The equation for adsorption on a cylindrically concave surface is as follows:

$$\frac{P_{AD}}{P_o} = \exp\left[-\left(\frac{\gamma \cdot V_M}{r \cdot RT}\right) \cdot \cos\Theta\right] \quad (3)$$

The equation for desorption on a spherically concave surface can be written in the following manner:

$$\frac{P_{DES}}{P_o} = \exp\left[-\left(\frac{2 \cdot \gamma \cdot V_M}{r \cdot RT}\right) \cdot \cos\Theta\right] \quad (4)$$

From equation 3 and 4 follows:

$$P_{AD} > P_{DES} \quad (5)$$

Where:

P_{AD}	vapour pressure on adsorption in Pa,
P_{DES}	vapour pressure on desorption in Pa,
P_o	saturation vapour pressure in Pa,
γ	surface tension in $J.m^{-2}$,
r	pore radius in m,
V_M	molar Volume in $m^3.kmol^{-1}$,
R	gas constant in $J.K^{-1}.kmol^{-1}$,
T	Temperature in K,
Θ	contact angle in deg.

Chemical analyses:

Extraction: 20 g of wood samples were ground, homogenized and sieved. 0.25 g of the sieved wood samples (0.2-0.63 mm fraction) were extracted in 6 consecutive steps with 80% aqueous methanol using sonication. 8 ml of extraction solvent and 30 minutes of extraction time were applied in each step. The end volume of this original extract was adjusted to 50.0 ml.

Total phenols: Total phenol content was measured from the original extracts according to the method of Folin and Ciocăltău (Singleton and Rossi, 1965) using quercetin as a standard. Total phenol concentration was indicated in mmol quercetin/100g dry wood. Measurements were carried out in triplicate.

Total soluble carbohydrates: Measurements were also carried out from the original extracts according to the method of Dubois (Dubois et al. 1956) using glucose as standard. The concentration was indicated in mg glucose / g dry wood. Measurements were carried out in triplicate.

HPTLC analysis: 10 ml of the original extracts were evaporated to dryness at 40 °C (Rotavapor, Büchi, Switzerland) and the residue was dissolved in 1 ml methanol. These concentrated solutions have been applied for the HPTLC analysis. 5 µl of the concentrated extracts were applied bandwise onto HPTLC silicagel layers (Merck) with a sample application device (Linomat 5, Camag, Switzerland). Development and evaluation was performed according to the following methods:

Method I: development with 9:1 diisopropyl-ether : formic-acid (Fecka et al. 2001) to a distance of 6 cm. The developed plates were dried, then sprayed with vanillin- H_3PO_4 reagent (Stahl, 1962) finally heated 15 minutes at 120 °C. Flavan-3-ol type compounds emerge with characteristic red color.

Method II: development with 6:3:1 Toluol : Ethyl-acetate : formic-acid to a distance of 6 cm. The dried plates were sprayed with with Natural Products reagent (Stahl 1962) then with Polyethylene -

glycol 4000 (Stahl 1962) solutions. Flavonoids and phenolic-acids emerge with fluorescent bands under long wave UV light (366 nm).

Extractive content Ethanol-toluol-extraction

Wood extractives, also known as accessory components of the wood are chemical compounds, which do not take part in the anatomical structure and can be extracted from the wood with neutral solvents. The ethanol-toluol-extract (further called EtOH-toluol-extract) was determined according to TAPPI (1997a & 1997b). The extract portion was based on the oven dry weight of the wood.

Results and discussion

Table 2 and 3 describe the density, total phenol, soluble carbohydrate and ethanol-toluene soluble extract content values. It can clearly be seen that there is a great variability between different wood species. Doussié and Merbau can be characterized with the highest polar-type (MeOH-water soluble) extractive (total phenol and total soluble carbohydrate) contents. Regarding the ethanol-toluene soluble extract content (which gives information mostly about the non-polar extractive content) Doussié, Makassar and White Lauan had the highest values. The highest density could be measured in the case of Makassar and Merbau, while Okoumé could be characterised with the lowest density. Altogether Doussié and Merbau contain the highest levels of extractives, while Bongossi and Ramin the lowest. White Lauan contains non-polar extractives in high concentrations compared to its polar extractives.

Table 2. The total phenol und soluble carbohydrate content of the wood samples.

Sample	density (g/cm ³)	Total phenols (mmol/100g)	Total soluble carbohydrates (mg/g)	EtOH-toluene extract (%)
Bilinga	0.63	1.78 ± 0.15	21.25 ± 6.31	5.8
Bongossi	0.99	1.40 ± 0.01	8.18 ± 0.34	1.0
Canalete	0.82	5.05 ± 0.23	39.50 ± 0.50	9.7
Danta	0.72	2.48 ± 0.15	15.17 ± 1.97	2.2
Doussié	0.82	23.42 ± 0.51	100.29 ± 29.35	14.9
Makassar	1.13	13.47 ± 0.83	65.27 ± 13.97	10.4
Mansonia	0.65	4.73 ± 0.07	36.30 ± 3.52	3.9
Merbau	0.99	37.04 ± 1.22	139.17 ± 15.68	9.5
Okoumé	0.41	2.18 ± 0.05	15.13 ± 1.09	2.0
Ramin	0.63	1.46 ± 0.04	15.04 ± 1.64	1.2
White Lauan	0.66	1.55 ± 0.02	9.73 ± 1.71	10.0
Wengé	0.80	6.37 ± 0.08	30.24 ± 5.17	7.7
Zebrano	0.67	3.23 ± 0.04	24.36 ± 6.05	3.2

The quality and quantity of extractives influences the moisture sorption and wettability of wood (Nzokou and Kamdem, 2004). Polar (mostly hydrophylic) components such as polyphenols, phenolic-acids, sugars, etc. can increase, whereas non-polar (hydrophobic) constituents (e.g. terpenes, fatty-acids, esters, resins, etc). can decrease the water uptake significantly. Considering the extractives it's the phenols which show the greatest changes between the samples according to Table 2. For this reason the separation of phenolic extractives has been carried out using high performance thin layer chromatography (HPTLC).

Fig. 1. depicts the chromatogram obtained after separation and visualization according to Method I. This method is suitable for the detection of flavan-3-ol type compounds (catechins, proanthocyanidins) which emerge with characteristic red color after visualization. It should be mentioned although that the appearance of a red band in the chromatogram itself is not an unambiguous proof for a catechin-type compound. Neither (+)-catechin nor (-)-epicatechin could be detected in the wood samples. In the

track of Doussié four intense red bands can be observed, which – lacking the appropriate standard compounds – could not be identified with this method.

Since the stationary phase applied was silicagel (SiO₂), high retention of a given compound also means high polarity. Compounds with the highest polarity remain at the spotting position after the development. In the case of Merbau an intense, dark red-colored band can be observed at the spotting position after development and visualization (see Fig. 1. arrow). This could possibly be attributed to highly polar polymeric proanthocyanidins, which have already been described to be present in Merbau wood (Hillis and Yazaki 1973).



Fig. 1. Derivatization with vanillin-H₃PO₄. St (followed from the bottom up: (-)-epicatechin (red), (+)-catechin (red)). Samples and respective numbers: 1: Bilinga, 2: Bongossi 3: Canalete 4: Doussié 5: Makassar 6: Mansonia 7: Merbau 8: Okoumé 9: Ramin 10: White lauan 11: Wengé 12: Zebrano 13: Danta.

Fig. 2. depicts the chromatogram obtained with method II. Significant differences can be observed between the composition and concentration of the samples regarding the visualized phenolic compounds. Merbau does not seem to contain a large number of individual phenols, only a few but those in large concentrations. Compared to that Bilinga, Makassar, Mansonia and Wengé contain many phenolic extractives, yet their concentrations according to Table 2. is not very high. The main component of Merbau (indicated with the arrow) appearing with orange fluorescence has a very high concentration, causing the saturation of the stationary phase (ie.: tailing of the band). Doussié contains kaempferol in large amounts.

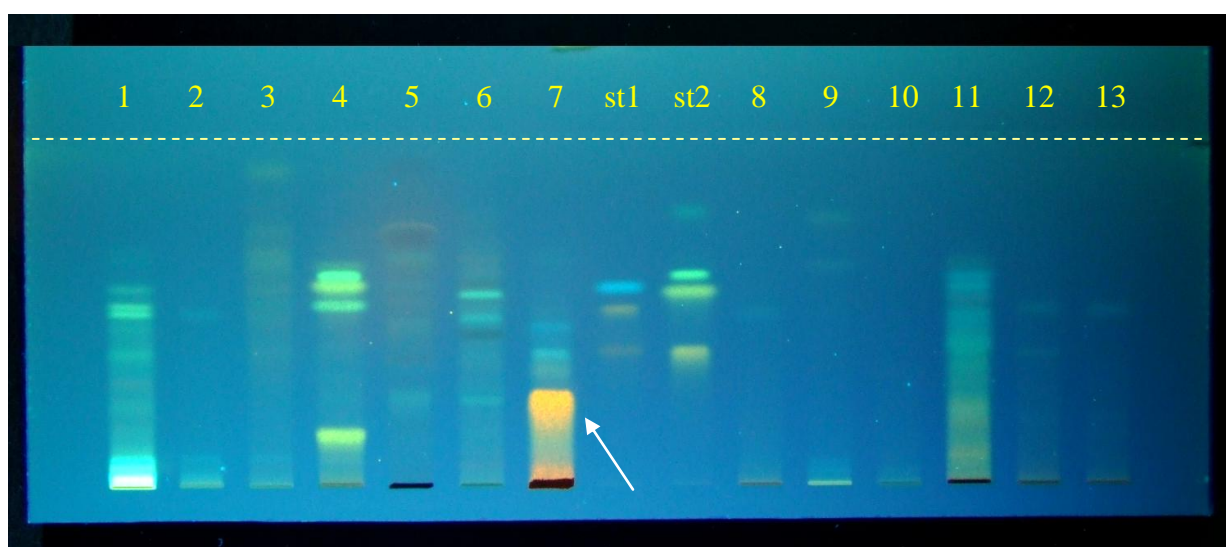


Fig. 2. Derivatization with natural products reagent and PEG 400 solution. Illumination: 366 nm. St1 track followed from the bottom up: taxifolin (orange), quercetin (orange), chlorogenic-acid (light-blue); St2 track followed from bottom up: fisetin (yellow), apigenin (yellow), kaempferol (green), 3-methoxyflavon (yellow).

Samples and respective numbers: 1: Bilinga, 2: Bongossi 3: Canaleta 4: Doussié 5: Makassar 6: Mansonia 7: Merbau 8: Okoumé 9: Ramin 10: White lauan 11: Wengé 12: Zebrano 13: Danta.

The identification of the main phenol of Merbau wood has also been accomplished with HPTLC by comparing the retention data of the unknown band with those of standard compounds and also by comparing their reflectance spectra (Fig. 3.) prior to the derivatization. The investigation resulted that the researched band was robinetin which has also been identified from Merbau wood already (Koch et al. 2006). The concentration of robinetin has also been determined with HPTLC by applying 5 point calibration (Fig. 4.). According to the quantitative evaluation the concentration of robinetin in Merbau wood is 14.65 ± 1.47 mg robinetin / g dry wood (1.465 %) which is a very high value. Although the concentration of robinetin is very high in Merbau wood, robinetin is poorly water soluble (ie: almost insoluble), which means that its contribution to the water adsorption of the wood can be lower than those of the proantocyanidin components.

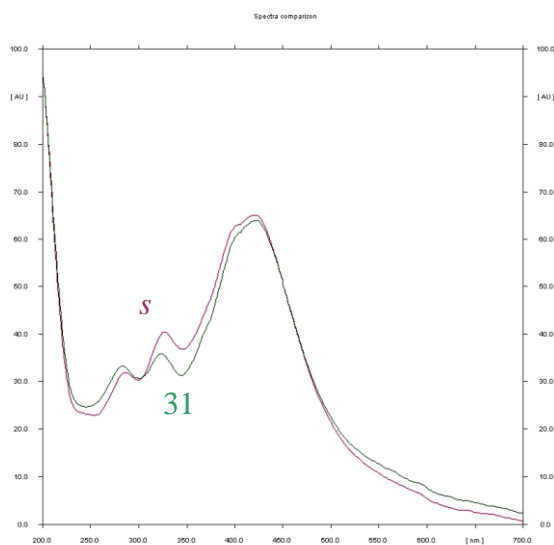


Fig. 3. The reflectance spectra of standard robinetin compound (s) and of the band from the Merbau extract (31) with the same retention as robinetin, prior to derivatization.

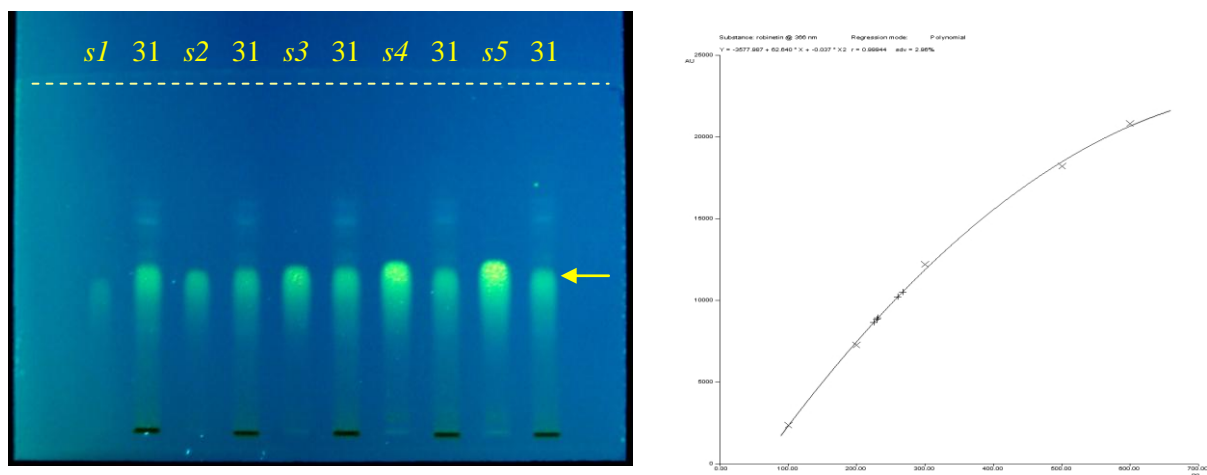


Fig. 4. Quantitative determination of robinetin with five point calibration (s1-s5) using scanning densitometry. 31: Merbau extract. The arrow indicates the band of robinetin.

Physical properties of the wood samples:

The adsorption and desorption of porous materials does not follow the same curve. The difference in such sorption behaviour is called sorption hysteresis.

Table 4 show the average values of the measured equilibrium moistures for the ad- and desorption at 20°C. For each wood species 3 samples were used.

The following figures 5 and 6 show the adsorption and desorption isotherms of the tested material computed according to the HH-model. From HH-model derived physical values are summarized in table 4. The agreement of the measured values with the computed isotherms is excellent. Fig. 7 shows the correlation between extractive content (influence from EtOH–toluene amount) and EMC.

Table 3. Computed values of the sorption analysis according to the Hailwood-Horrobin model for the attempt wood species at the fiber saturation point

Wood species	U_{am}/U_{dm} (%)	U_{ap}/U_{dp} (%)	U_{atot}/U_{dtot} (%)	$\Sigma a / \Sigma d$ (m ² /g)	Z_a/Z_d (%)
Bilinga	5.10/7.30	22.90/18.14	28.00/25.44	180/259	52/28
Bongossi	5.20/7.81	23.60/19.03	28.80/26.84	185/277	50/23
Canalete	4.60/6.87	18.20/13.85	22.80/20.72	163/244	56/33
Danta	5.40/7.54	23.00/19.33	28.40/26.87	192/268	48/26
Doussié	4.30/6.77	13.50/9.42	17.80/16.19	152/240	59/34
Makassar	4.90/7.34	21.90/17.17	26.70/24.51	172/260	54/28
Mansonia	4.70/6.68	24.30/20.22	29.00/26.90	167/237	55/35
Merbau	6.00/8.73	20.20/16.48	26.20/25.21	212/310	43/13
Okoumé	4.90/6.65	26.90/22.94	31.70/29.58	172/236	54/35
Ramin	4.70/6.37	28.30/23.84	33.00/30.21	168/226	55/38
White Lauan	5.00/6.69	23.90/21.14	28.90/27.83	176/237	53/35
Wengé	4.90/7.54	15.40/11.94	20.30/19.48	172/268	54/26
Zebrano	4.60/6.45	25.60/22.20	30.30/28.65	164/229	56/38
Spruce	5.04/6.80	27.94/20.90	32.97/27.70	179/241	52/34

Where

U_{am} Computed adsorbed water content in the monomolecular layer at relative vapour pressure of $h=1$,

U_{dm} Computed desorbed water content in the monomolecular layer at relative vapour pressure of $h=1$,

U_{ap} Computed adsorbed water content in the polymolecular layer at relative vapour pressure of $h=1$,

U_{dp} Computed desorbed water content in the polymolecular layer at relative vapour pressure of $h=1$,

U_{atot} Computed totally adsorbed water content at relative vapour pressure of $h=1$,

U_{dtot} Computed totally desorbed water content at relative vapour pressure of $h=1$,

Σa Computed specific surface on adsorption (m²/g),

Σd Computed specific surface on desorption (m²/g),

Z_a Computed inaccessibility of the sorptiv active sites of the sorbent to sorbate on adsorption (%),

Z_d Computed inaccessibility of the sorptiv active sites of the sorbent to sorbate on desorption (%).

Doussié has the lowest adsorbed water content in the monomolecular (U_m) and polymolecular layer (U_p) which could possibly be explained by the high EtOH-toluene extract content, meaning high amount of hydrophobic components on the cell walls/in the lumen of cells, whereas Merbau has the highest U_m value that could be explained with the extraordinarily high proportion of polar extractives (phenols, sugars) and relatively low amounts of hydrophobic compounds (see table 2 and 3). The water adsorption of the overhand layers is supposed to be primarily influenced by condensation.

Conclusion

The water vapour sorption behaviour of 13 different tropical wood species was examined. ed values were analysed with the Hailwood-Horrobin sorption model. According to the Hailwood-Horrobin model following characteristic values were computed: the monomolecular U_m and polymolecular U_p sorption, the fiber saturation point U_{fs} , the inaccessibility Z of the sorbent to the sorbate as well as the specific surface of the sorbent Σ . Very large differences exist in the sorption behaviour between the individual wood species. In particular for Canalete (22,8%), Wengé (20,3%) and Doussié (17,8%) a

very low fiber saturation point was determined (by using U_{atot}) which is clearly below the values of European wood species (28-32%) and other examined tropical woods. The ethanol toluol extract of the wood correlates with the moisture content of the polymolecular U_p and total U_{tot} sorption. The higher the extractives content, the lower the equilibrium moisture content U_{tot} and U_p . We have an influence from the chemical composition of the extractives. The results correlated which works from Hernández (2007)

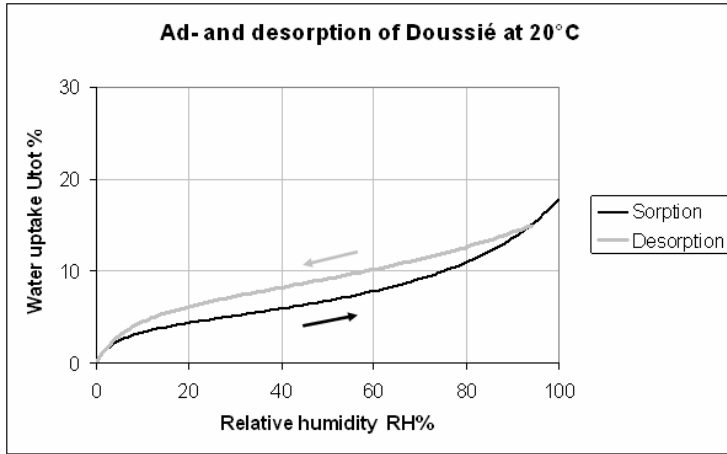


Figure 5: Ad- and desorption isotherm of Doussié (low FSP) at 20°C

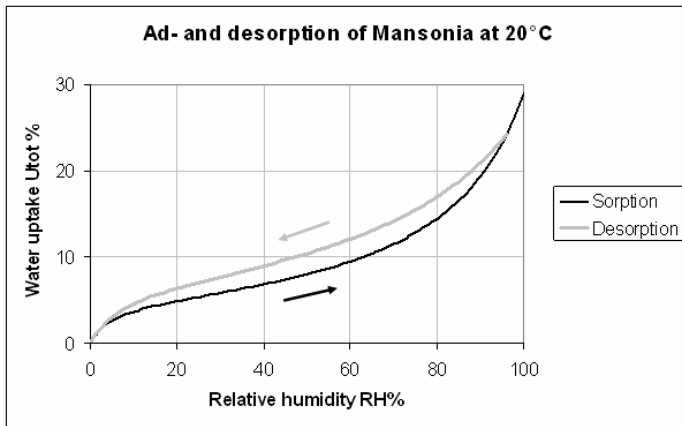


Figure 6: Ad- and desorption isotherm of Mansonia (High FSP) at 20°C

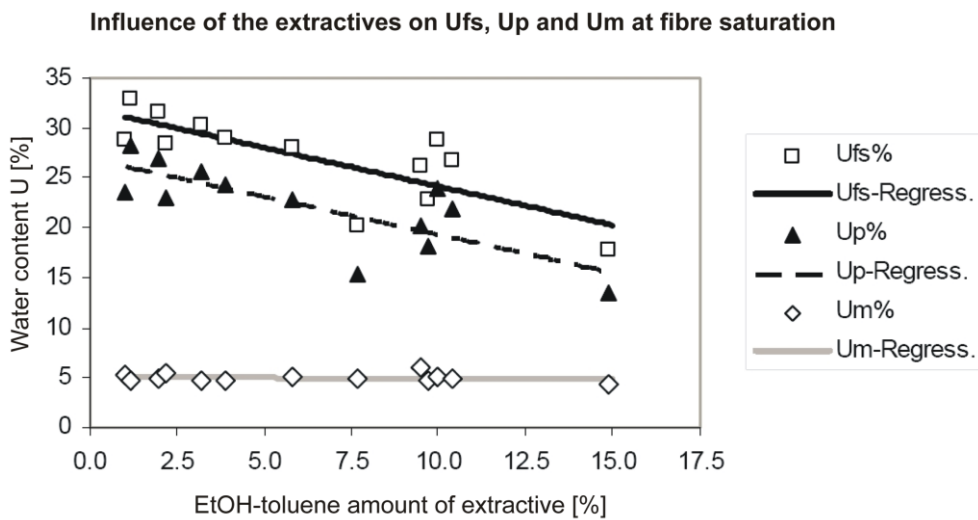


Fig. 7 : Influence from EtOH –toluene amount on water content from tested wood species

Acknowledgements

The authors would like to express gratitude to Mrs. Majsa Zoltánné and Mr. Marco Torres for her help in carrying out the chemical analyses and Stephané Croptier for experimental tests from physical properties.

References

1. Singleton, V. L., Rossi, J. A., Jr. (1965): *Colorimetry of Total Phenolics with Phosphomolybdic-Phosphotungstic Acid Reagents*. American Journal of Enology and Viticulture 16: 144-158.
2. Dubois, M., Gilles, K. A., Hamilton, J. K., Rebers, P. A., Smith, F. (1956): *Colorimetric method for determination of sugars and related substances*. Analytical Chemistry 28: 350-356.
3. Stahl, E. (1962): *Dünnsicht-Chromatographie – Ein Laboratoriumshandbuch*. Springer, Heidelberg, 1962.
4. Fecka, I., Cisowski, W., Luczkiewicz, M. (2001): *TLC determination of Catechin and Epicatechin in an extract from Uncaria tomentosa bark by chemically modified stationary Phases*. Planar Chromatography 2001, Lillafüred, Hungary, 2001, pp. 201-209.
5. Koch, G., Richter, H., G., Schmitt, U. (2006): *Topochemical investigation on phenolic deposits in the vessels of afzelia (Afzelia spp.) and merbau (Intsia spp.) heartwood*. Holzforschung 60: 583-588.
6. Hillis, W. E., Yazaki, Y. (1973): *Polyphenols of Intsia heartwoods*. Phytochemistry 12: 2491-2495.
7. Burgess, C.G.V., Everett, D.H., Nuttall, S. (1989): *Adsorption hysteresis in porous materials*. Pure App. Chem. 61: 1845-1852.
8. Ekman, R., Holmbom, B. (1989). *Analysis by gas chromatography of wood extractives in wood and pulp samples from mechanical pulping of spruce*. Nordic Pulp and Paper Research Journal 41: 16-24.
9. Frandsen, H.L., Svensson, S. (2007): *Implementation of sorption hysteresis in multi-Fickian moisture transport*. Holzforschung 61: 693-701.
10. Hailwood, A.J., Horrobin, S. 1946: *Absorption of water by polymers. Analysis in term of single model*. Trans. Faraday Soc. 42B: 84-102.
11. Nzokou, P., Kamdem, D. P. (2004): *Influence of Wood Extractives on Moisture Sorption and Wettability of Red Oak (Quercus Rubra), Black Cherry (Prunus Serotina), and Red Pine (Pinus Resinosa)*. Wood and Fiber Science 36: 482-492.
12. Kilic, A.; Niemz, P. 2009. *Extractive content of some tropical woods*. Submitted to Holz als Roh und Werkstoff
13. Popper, R.; Niemz, P.; Torres, M. (2006): *Einfluss des Extraktstoffanteils ausgewählter fremdländischer Holzarten auf deren Gleichgewichtsfeuchte*. Holz als Roh- und Werkstoff, Berlin 64: 491-496.
14. Labbé, N.; Jéso, B. D. J.; Lartigue, J.-C. ; Daudé, G. ; ratier, M. (2002): *Le Moisture Content and Extractive Materials in Maritime Pine Wood by Low Field 1H NMR*. Holzforschung 56: 25-31
15. Hernández, R. (2007): *Swelling properties of hardwoods as affected by their extraneous substances, wood density and interlocked grain*. Wood & fibre Science 39:146-158

Structural and Functional Differences Among Transgenic Hybrid Poplar Lines with Varying Lignin Contents

*Barbara Lachenbruch*¹, *Steven L. Voelker*¹, *Frederick C. Meinzer*² and *Steven H. Strauss*¹

¹*Oregon State University, USA; 2Pacific Northwest Research Station, Forest Service, USA*

Abstract

Lignin is an important component of wood, providing the matrix in which the microfibrils sit in the secondary cell wall, holding cells together at the middle lamella, providing strength especially in compression, and allowing creep to occur. Industrial uses of wood for pulp and bioenergy often necessitate lignin's partial removal, which is very expensive in terms of heat, chemicals, and wastewater remediation. These costs have motivated research into the development of trees with lowered lignin contents or lignin that is easier to extract. Little research has tested the growth and survival of these modified trees. We studied 14 transgenic lines of hybrid white poplar (*P. tremula* × *P. alba*, INRA-France 717-1B4) plus a control line to learn how modification of xylem lignin content affects water transport and biomechanics. The transgenic lines represented 14 independent gene insertions that down-regulated 4-coumarate:coenzyme A ligase (4CL), which is located early in the pathway of the synthesis of lignin, flavonoid-derived pigments and phenolic-based defensive compounds. Controls and the mutated lines were micro-propagated, grown in a greenhouse, transferred to a coldframe and then to the field where they were grown for two years with irrigation and weed control. Control poplar wood is white. Several of the transgenic lines showed distinct patches of brown wood, and pink to reddish wood when freshly cut. The five lines with more than 20 % brown wood had among the lowest lignin contents in the experiment, and all brown wood lines had ≤ 85 % the lignin content of the control line. Brown wood lines had lower specific conductivity, aboveground biomass, modulus of elasticity (MOE), and height/diameter than the other transgenic lines and controls, and higher tension wood proportion than the other transgenic lines and controls. Some of the vessels in the brown wood were occluded with dark extractives and tyloses and other vessels appeared crushed, both of which provide the structural basis for their lower specific conductivity, which in turn may have explained their lower biomass. All transgenic lines had lower average MOE, modulus of rupture (MOR), and height/diameter than the controls. The buckling safety factor, in contrast, was not correlated with lignin content suggesting that plants adjust their morphology with respect to their wood properties. This research supports the concept that even small modifications to the amount of lignin in the secondary xylem can have significant direct or indirect negative impacts on tree performance. These results show the importance of phenotyping transgenic trees under field conditions to help select lines that are both viable physiologically and meet the desired biotechnological aims.

Introduction

Wood is an abundant, renewable natural resource and its utilization for pulp or biofuels requires the costly and energy-intensive step of degrading and partial removal of lignin in woody cell walls. A reduction in the amount of lignin in wood, therefore, could reduce industrial costs significantly. Lignin is about 75-100 % more metabolically expensive for a plant to produce than is cellulose [17, 19] but nonetheless all modern arborescent plants (including palms and bamboos) have about 20 % lignin in their cell wall dry mass. This similar proportion of an expensive material across disparate taxa and environments suggests that lignin has important roles and calls into question the feasibility of

producing viable plants with reduced lignin. We assume that lignin plays important biomechanical roles especially in compression and creep, but it is also important as the primary material between xylem cells, as the matrix in which the microfibrils are embedded, as a contributor to decay resistance, and possibly as a sealant making cell walls relatively airtight. The few reports of wood mechanical properties from transgenic trees with altered lignin are inconclusive regarding whether trees with reduced lignin content may be viable for biomass production [15, 14].

The synthesis of lignin is influenced by many genes. Among the gene families that have been investigated is the 4CL (4-coumarate:CoA-Ligase) gene family, which codes for at least two isoenzymes in the phenylpropanoid pathway in angiosperms. One of the isoenzymes is thought to be associated mostly with production of lignins, and another isoenzyme is thought to be associated mostly with production of flavonoid-derived pigments and defensive compounds [9, 7, 18, 6, 4]. The transgenics studied in the current experiment derived from a variety of independent mutations to the 4CL gene family, and so their phenotypes as well as their lignin contents were expected to differ from one another. We expected that reductions in xylem lignin content would decrease the strength of the material, which could be manifested with greater stem taper, a higher proportion of tension wood, lower modulus of elasticity (MOE) and/or modulus of rupture (MOR), and microscopic evidence of imploded vessels. Indirect effects of decreased strength could include decreased plant size (caused, for example, by increased proportional allocation to stem, or poor water transport) and decreased specific conductivity (caused, for example, by increased proportion of fibre cells in the cross-section, or mechanical failure of the vessels).

Material and methods

Plant material--Studies were undertaken in a two-year field trial of 14 transgenic lines and a control line from a single clone of a hybrid white poplar (*P. tremula* × *P. alba*, INRA-France 717-1B4). The transgenics represented independent transformation events with antisense down-regulation of the Pt4CL1 gene family that encodes 4-coumarate:coenzyme A ligase (4CL). Stem segments and leaf disks from *in vitro* plantlets were incubated in an *Agrobacterium* suspension (strain C58) containing an antisense Pt4CL1 construct generated by fusing the Pt4CL1 cDNA coding sequence in an antisense orientation with respect to a duplicated-enhancer cauliflower mosaic virus 35S promoter. For controls, this step was not taken: tissue was not wounded and tissue was not incubated in the *Agrobacterium* suspension. Callus was induced from these explants, from which plants with roots and shoots were micro-propagated. For the mutants, to ensure transformation events were independent, a single clone per explant was selected for further propagation after confirmation of transgene presence by the polymerase chain reaction. The micro-propagated plants were transferred to small pots with soil and grown in a greenhouse for two months (April-May 2005), grown for another 2 months (June- July 2005) in tubular pots, and then moved to a coldframe for three months of acclimatization (August-October 2005). Plants were then moved to a field trial just outside of Corvallis, Oregon. They were planted with three meters between plants in one randomized complete block with 10 replicates of each line and numerous extra trees of each line in the buffer strip. Plants were hand-watered in 2006 and had a drip irrigation system in 2007. Weeds were controlled with nursery cloth on the soil surrounding each plant.

Lignin content--Three trees from each line were randomly chosen for lignin analysis. For each tree, basal stem sections were debarked, cut into small pieces, freeze-dried for 48 hours, ground in liquid nitrogen in a Waring blender, and then ball milled for 3 hours to obtain a homogenous powder. Aliquots of about 1 g of powder were submitted to sequential extraction to generate the cell wall residue used for lignin degradation analysis [10]. Note that in cases of brown or red wood, this coloration remained after the extraction procedure. Lignin contents and monomeric composition of cell wall residue were estimated using the alkaline nitrobenzene oxidation and thioacidolysis methods [27, 2], respectively.

Brown wood--Among transgenic lines, wood colour varied from being indistinguishable from that of controls, to light pink throughout, to a mottled appearance with red-brown patches next to control colour wood. The cross-sectional area in “brown wood” was estimated near the base of each tree by overlaying a grid of dots on a transparent plastic sheet over three cross-sections from each tree at three heights (stem base, 20 and 40 cm) and recording the relative frequency of brown wood as compared to the entire cross-sectional wood area.

Specific conductivity and biomass-- In late August 2007 we measured specific conductivity (k_s , $\text{kg m}^{-1}\text{s}^{-1}\text{MPa}^{-1}$) of wood from the main stem for three trees from each transgenic line and six control trees. Two xylem segments from the base of each tree were measured for wood specific conductivity, k_s . A measure of xylem transport efficiency, k_s can be from Darcy’s law (equation (1)):

$$k_s = Q/(A \Delta P/l) \quad (1)$$

where Q is the volume flow rate ($\text{m}^3 \text{s}^{-1}$), l is the length of the segment (m), A is the cross-sectional area of the segment (m^2), and ΔP is the pressure difference across the segment (MPa). In stems less than 1 cm in diameter, the entire segment was cut to a length of 12 cm and then used. In larger stems, two segments were chiselled to dimensions of approximately $1 \times 1 \times 12$ cm. Chiselled segments were submerged in pH 2 HCl solution and placed under vacuum overnight to remove embolisms. Segment ends were re-cut under water with a razor blade, and segment dimensions were then measured with digital calipers. Segments chiselled from stems were tightly wrapped in Parafilm to reduce variability in k_s due to radial leakage.

Tree height and basal diameter were measured in November 2007. At the end of 2007, six control trees and three or four trees that spanned the range in tree size for each transgenic event were harvested to determine allometric estimates of oven-dried aboveground biomass. These relationships were then used with diameter and height measurements to compare biomass estimates among lines. All other trees were eventually harvested during 2008 to compare other traits.

Tension wood--Tension wood was estimated with two methods. 1) We made hand-sections across the cross-section from the base of trees harvested for biomass measurements. Sections were stained with safranin and astra-blue to distinguish the G-layers of tension wood fibres from the rest of the wood [11]. We viewed the stained sections through a light microscope, recording the relative radial positions of tensionwood fibres in each of three radial scans, and estimated the percentage of the xylem cross-sectional area in tension wood fibres assuming that stems were circular in cross-section. 2). Cut-ends of trees not harvested for biomass were quantified for tension wood using the method described above for brown wood. Tension wood patches were identified by their lighter colour and smooth, shiny appearance compared to surrounding normal wood fibres.

Biomechanics--Initial mechanical testing was conducted in June 2006 on small branches (<1 cm diameter) from each line. Samples were dried and then conditioned to 12% moisture content for testing. Three-point dynamic bending tests were conducted using a portable mechanical tester fitted with a 45 kg load cell (In-Spec 2200, Instron, Norwood, MA). In 2008 a larger mechanical testing system (Sintech Model 1/G, MTS Systems Corp.) fitted with a Sensotec 230 kg load cell (Model 41/571-07, Honeywell International Inc.) was used to carry out further three-point bending tests on conditioned sections of main stems (mostly >1 cm diameter). Diameter inside the bark at each end and total length were recorded for each sample to calculate taper. The span tested for each sample was 16-20 times the estimated mid-point diameter (under bark). The MOE and MOR for each sample were calculated for a tapered beam [20]. Bark was not removed for bending tests because its influence should be negligible for comparisons among groups. For statistical comparisons of properties among lines in which stem diameter was not constant, we used the relative value of the transgenic sample compared with the value predicted (by regression equations) for a control specimen of the same diameter.

To compare an index of biomechanical function for trees that differed in both material properties and form we estimated *safety factor for buckling* as the critical buckling height (H_{crit}) [5] divided by the actual height of an individual tree. Equation (2) estimates a critical height (H_{crit}) for elastic buckling of a uniform column:

$$H_{crit} = 1.26 \times (E/W)^{1/3} \times (D)^{2/3} \quad (2)$$

where E is the apparent modulus of elasticity (MPa), W is the green wood density (density of wood plus its water, N/m³) and D is the basal diameter of the tree (m). For the data presented here, D was measured just above the basal flare associated with the root collar, 5-10 cm above the soil surface. Green densities were estimated for each line, not each tree. Although this model oversimplifies tree form, it has been shown to approximate well the height at which a tree of a given material and geometry becomes unstable and buckles under self loading [8].

Statistical analyses--Least-squares regression methods were used to assess relationships between tree form, size and wood mechanical properties. To compare trait values among lines (controls and transgenic events) we conducted analysis of variance tests. Traits were first compared with a global analysis of variance (PROC GLM, SAS version 9.2, SAS Institute Inc. Cary, NC, USA) to determine if significant variation among lines existed. Further analyses compared means among lines with Tukey HSD tests to control for Type 1 experiment-wise error.

Results and discussion

Lignin content--The transgenic lines ranged in average lignin contents from 54-95% of the control line (where 100% = 22.3 g lignin per gram cell wall residue). This range was similar to those of other studies of poplars containing a 4CL transgene [9].

Thioacidolysis lignin content in the stems was highly but non-linearly correlated with 4CL RNA expression [33]. Most traits showed a marked shift in lines with lignin contents below about 85% of the control values (*Fig. 1, 2*), which corresponded to having more than 20% brown wood. This result suggests that even small modifications in the amount of lignin in the secondary xylem can have significant and negative direct or indirect impacts on tree performance.

Brown wood--Five of the transgenic lines had more than 25 % brown wood in the trunk wood. These lines also tended to have the lowest lignin content (*Fig. 1*). Brown wood was found in all four of the lines that had less than 85% the lignin content of the control wood, in one of the two lines that had 85-87 % the lignin content of controls, and in none of the remaining seven transgenic lines that had >87 % the lignin concentration of the controls. This brown wood had dark extractives and tyloses in many of the vessels. The vessels in the outer part of the growth increment were often deformed, and looked as if they had been crushed [33].

Angiosperms have two or more isoenzymes that make up the 4CL gene family, with differing degrees of substrate affinities. Class 1 isoenzymes are most highly expressed in the xylem and thought to be associated with monolignol biosynthesis. Class 2 isoenzymes, although not missing from the xylem, are most highly expressed in green tissues and are thought to be associated with the synthesis of secondary metabolites important for various aspects of plant defence. It is possible that the lines having brown wood were derived from mutations in the class 2 isoenzymes. Patchy brown wood formation increased dramatically, nearing 60% of the stem cross-sectional area as lignin content was reduced by 15%. The brown wood lines thus appeared to experience “misregulation” or shunt pathway effects, as separate from the normal transgenics. Shunt pathways resulting in abnormally pink, red or brown xylem have been found in other 4CL mutants [12, 3] but are also found when enzymes either upstream or downstream of 4CL have been changed [15, 22, 1, 26, 31, 16, 21, 24, 10].

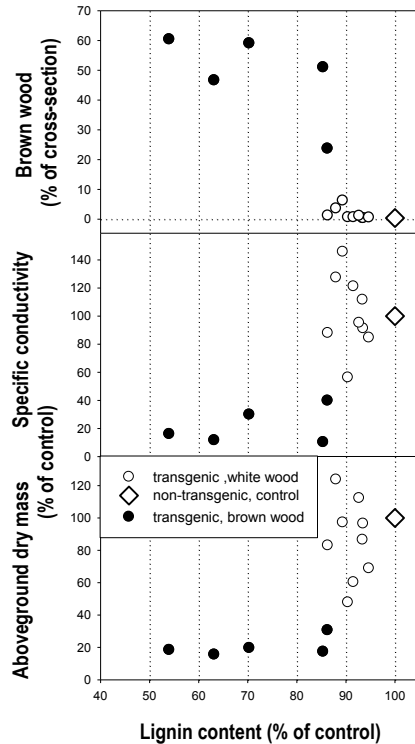


Fig. 1 Hydraulic and growth characteristics of hybrid poplar as a function of xylem lignin content: brown wood, specific hydraulic conductivity (k_s), and aboveground dry mass. All values except brown wood are expressed as the percentage value relative to non-transgenic controls.

Specific conductivity and biomass accumulation--The specific conductivity (k_s) of trunk wood and the total aboveground biomass were much lower in the lines that had brown wood than in the other lines (Fig. 1). The lower k_s in brown wood than normal wood could be explained potentially by the increased incidence of blockages. The brown-wood lines also had a much greater incidence of shoot die-back in late summer, presumably resulting from drought stress [33]. Biomass accumulation of the normal transgenics was similar to controls, suggesting that additive effects associated with brown wood occurrence rather than lower lignin *per se* caused the drastic growth reductions of transgenic lines with the lowest lignin content.

Poplar clones used for wood or biomass production tend to be sensitive to water supply [28]. If poplar clones are to be increasingly used industrially, they will have to be planted into less favourable sites, and would therefore benefit greatly from strategic assessment of traits that conferred both rapid growth and drought tolerance [32].

Tension wood--The brown-wood lines had much higher proportions of tension wood in their stems than the other lines (Fig. 2). The line with the highest lignin content averaged 20 % of its stem cross section in tension wood; the controls averaged 5 %. The increased production of tension wood may have been triggered mechanically to help provide support for the low-lignin stems.

Biomechanics--There was a positive correlation between both MOE and MOR and lignin proportion (Fig. 2). The mean MOE and MOR values of all transgenics were lower than values for controls. These data underscore the importance of the balance of chemical constituents in wood for strength (lignin, cellulose, and hemicelluloses), rather than the cellulose itself, which was negatively correlated with MOE and MOR [33].

Regardless of wood color, transgenic lines tended to be shorter for a given diameter than controls, and stem height/diameter was positively correlated with stem lignin proportion (Fig. 2). These trends are what would be expected if the weaker stems transmitted greater wind-induced stresses to the cambium [13, 29, 30]. There was no trend in the safety factor for stem buckling with the change in lignin concentration, implying that plants, which varied in MOE, adjusted their height relative to

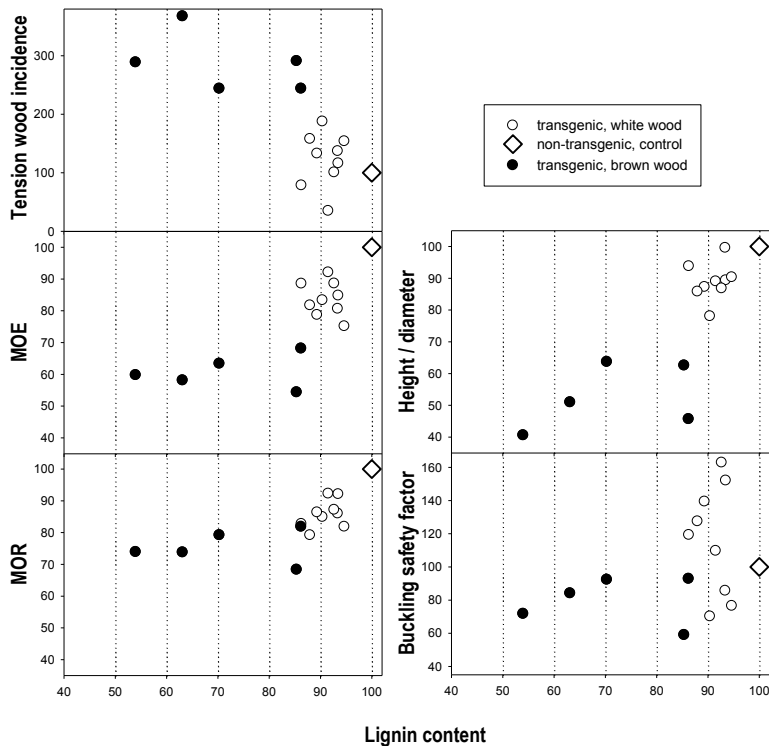


Fig. 2 Architectural and mechanical characteristics of hybrid poplar as a function of xylem lignin content: tension wood incidence, apparent stem modulus of elasticity (MOE), and apparent stem modulus of rupture (MOR, stem height / diameter, and safety factor for stem buckling. All values are expressed as the percentage value relative to non-transgenic controls.

diameter in a manner that maintained the safety factor for buckling at about the same level as control trees.

Conclusion

The largest decreases in lignin content relative to controls were associated with the production of brown wood. The brown-wood lines had much lower specific conductivity, aboveground biomass, MOE, MOR, and height/diameter than controls and the other transgenics. The other lines with reduced lignin that did not produce brown wood had lower MOE and MOR than the controls, although some lines had higher and some lines had lower values than the controls for specific conductivity, biomass, tension wood incidence, and buckling safety factor. Consistent with the notion that severe perturbations to the phenylpropanoid pathway will mediate a cascade of negative additive effects as in these brown-wood lines, only lines with modest reductions in lignin content sustained adequate growth and tree form. These findings begin to clarify the limitations to this first generation of transgenic systems for poplars. Hopefully such findings and new insights will stimulate more incisively designed research aimed not simply at further reductions in lignin, but toward more precise regulation of metabolic carbon fluxes with lesser effects on cell wall properties, tree growth and development. Assuming that the results obtained for one- and two-year-old wood in this study are applicable to older stems, then reduced wood stiffness and strength could affect industrial biomass production through reductions in survival due to critical loads from wind and ice. In the case of open grown trees, the observed reductions in stiffness may be compensated by stems that are more tapered, and thus sufficiently stable. This species, however, is light-demanding, and forest canopy closure increasingly limits light availability, decreases average wind loading, and results in trees with a less tapered form [23]. For woody biomass crops, spacing and its effects on trees with reduced lignin and wood stiffness could therefore be a key limitation to productivity that has not yet been investigated. To what extent woody crops grown for biomass in plantations with multi-year rotations can be expected to survive wind and ice storms with reduced lignin contents is an open question warranting further

investigation. Therefore more comprehensive considerations of “optimal” lignin concentrations for woody biomass production are still necessary.

Acknowledgements

The authors acknowledge the NSF Center for Advanced Forestry Systems, the USDA special grant to Oregon State University for wood utilization research, and the OSU-based Tree Biosafety and Genomics Research Cooperative for funding support of key personnel and activities that made this project possible. We also thank Dr. Vincent Chiang at North Carolina State University for providing *Agrobacterium* strain C58 and the gene construct used for transformation. BL thanks the Society for Wood Science and Technology for support of her participation in this conference.

References

1. Baucher, M., B. Chabbert, G. Pilate, J. Van Doorselaere, M. T. Tollier, M. Petit-Conil, D. Cornu, B. Monties, M. Van Montagu, D. Inze, L. Jouanin and W. Boerjan, (1996): *Red xylem and higher lignin extractability by down-regulating a cinnamyl alcohol dehydrogenase in poplar*. Plant Physiol. 112: 1479-1490.
2. Blee, K., J.W. Choi, A.P. O'Connell, S.C. Jupe, W. Schuch, N.G. Lewis and G.P. Bolwell. (2001): *Antisense and sense expression of cDNA coding for CYP73A15, a class II cinnamate-4-hydroxylase, leads to a delayed and reduced production of lignin in tobacco*. Phytochemistry. 57: 1159-1166.
3. Caihong, J., Z. Huayan, W. Hongzhi, X. Zhifeng, D. Kejiu, S. Yanru and W Jianhua, (2004): *Obtaining the transgenic poplars with the low lignin content through down-regulation of 4CL*. Chinese Science Bulletin. 46 (9): 905-909.
4. Costa, M.A., D.L. Bedgar, S.G.A. Moinuddin, K.-W. Kim, C.L. Cardenas, F.C. Cochrane, J.M. Shockey, G.L. Helms, Y. Amakura, H. Takahashi, J.K. Milhollan, L.B. Davin, J. Browse and N.G. Lewis, (2005): *Characterization in vitro and in vivo of the putative multigene 4-coumarate CoA ligase network in Arabidopsis: syringyl lignin and sinapate/sinapyl alcohol derivative formation*. Phytochemistry. 66: 2072-2091.
5. Greenhill, G., (1881): *Determination of the greatest height consistent with stability that a vertical pole or mast can be made, and the greatest height to which a tree of given proportions can grow*. Proc. Cambridge Philos. Soc. 4: 65-73.
6. Hamberger, B. and K. Hahlbrock, (2004): *The 4-coumarate:CoA ligase gene family in Arabidopsis thaliana comprises one rare, sinapate-activating and three commonly occurring isoenzymes*. Proc. Natl. Acad. Sci. 101 (7): 2209-2214.
7. Harding, S.A., J. Leshkevich, V.L. Chiang and C-J. Tsai, (2002): *Differential substrate inhibition couples kinetically distinct 4-coumarate:coenzyme A ligases with spatially distinct metabolic roles in quaking aspen*. Plant Phys. 128: 428-438.
8. Holbrook, N.M, and F.E. Putz, (1989) *Influence of neighbors on tree form: effects of lateral shade and prevention of sway on the allometry of Liquidambar styraciflua (sweet gum)*. Amer. J. Bot. 76 (12): 1740-1749.
9. Hu, W.-J., S.A. Harding, J. Lung, J.L. Popko, J. Ralph, D.D. Stokke, C.-J. Tsai and V.L. Chiang, (1999): *Nat. Biotechnol.* 17: 808-812.
10. Jourdes, M., C.L. Cardenas, D.D. Laskar, S.G.A. Moinuddin, L.B. Davin and N.G Lewis, (2007): *Plant cell walls are enfeebled when attempting to preserve native lignin configuration with poly-phydroxycinnamaldehydes: evolutionary implications*. Phytochemistry 68:1932-1956.
11. Jourez, B., A. Riboux and A. Leclercq, (2001): *Anatomical characteristics of tension wood and opposite wood in young inclined stems of poplar (Populus euramericana cv. 'Ghoy')*. IAWA J. 22: 133–157.
12. Kajita S., Y. Katayama and S. Omori, (1996): *Alteration in the biosynthesis of lignin in transgenic plants with chimeric genes for 4-coumarate:coenzyme A ligase*. Plant Cell Physiol. 37 (7): 957-965.
13. Kern, K.A, F.W. Ewers, F.W. Telewski and L. Köhler, (2005): *Mechanical perturbation affects conductivity, mechanical properties, and aboveground biomass of hybrid poplars*. Tree Physiol 25: 1243–1251.
14. Koehler, L. and F.W. Telewski. 2006. Biomechanics and transgenic wood. Am. J. Botany 93(10): 1433-1438.
15. Köhler, L. and H-C. Spatz., (2002): *Micromechanics of plant tissues beyond the linear-elastic range*. Planta. 215: 33-40.
16. LaPierre, C., B. Pollet, M. Petit-Conil, G. Toval, J. Romero, G. Pilate, J-C. Leplé, W. Boerjan, V. Ferret, V. De Nadai and L. Jouanin, (1999): *Structural alterations of lignins in transgenic poplars with depressed cinnamyl*

- alcohol dehydrogenase or caffeic acid O-methyltransferase activity have an opposite impact on the efficiency of industrial craft pulping. *Plant Phys.* 119: 153-163.
17. Lewis, N.G. and E. Yamamoto. (1989): *Tannins: their place in plant metabolism*, in Chemistry and significance of condensed tannins, Editors R.W. Hemingway and J.J. Karchesy, Plenum Press. p. 23-46.
18. Linder Mayer, C., B. Möllers, J. Fleigeman, A. Uhlmann, F. Lottspeich, H. Meimberg and J. Ebel, (2002): *Divergent members of a soybean (Glycine max L.) 4-coumarate:coenzyme A ligase gene family*. *Eur. J. Biochem.* 269: 1304-1315.
19. Loomis, R.S. and J.S. Amthor, (2000): *Yield potential, plant assimilatory capacity, and metabolic efficiencies*. *Ann. Bot-London.* 39: 1584-1596.
20. Maki, A.C. and E.W. Kuenzi, (1965): *Deflection and stresses of tapered wood beams*. Res. Paper FPL-RP-34. Madison, WI: U.S. Dept. of Agriculture, Forest Service, Forest Products Laboratory.
21. Meyermans, H., K. Morreel, C. Lapierre, B. Pollet, A. De Bruyn, R. Busson, P. Herdewijn, B. Devreese, J. Van Beeumen, J.M. Marita, J. Ralph, C. Chen, B. Burggraeve, M. Van Montagu, E. Messens and W. Boerjan, (2000): *Modifications in lignin and accumulation of phenolic glucosides in poplar xylem upon down-regulation of caffeoyl-coenzyme A o-methyltransferase, an enzyme involved in lignin biosynthesis*. *J. Biol. Chem.* 275: 36899-36909.
22. Miller, J.E., J.L. Geadleman and G.C. Marten, (1983): *Effect of the brown midrib-allele on maize silage quality and yield*. *Crop Sci.* 23:493-496.
23. Oliver, C.D. and B.C. Larson, (1996): *Forest Stand Dynamics*. John Wiley and Sons, New York.
24. Pilate G, E. Guiney, K. Holt, M. Petit-Conil, C. Lapierre, J.C. Leple, B. Pollet, I. Mila, E.A. Webster, H.G. Mastorp, D.W. Hopkins, L. Jouanin, W. Boerjan, W. Schuch, D. Cornu and C. Halpin, (2002): *Field and pulping performances of transgenic trees with altered lignification*. *Nat. Biotech.* 20: 607-612.
25. Porter, K.S., J.D. Axtell, V.L. Lechtenberg and V.F. Colenbrander, (1978): *Phenotype, fiber composition and in vitro dry matter disappearance of chemically induced brown midrib (bmr) mutants of sorghum*. *Crop Sci.* 18: 205-208.
26. Ralph, J., J.J. MacKay, R.D. Hatfield, D.M. O'Malley, R.W. Whetten and R.R. Sederoff, (1997): *Abnormal lignin in a loblolly pine mutant*. *Science.* 277: 235-239.
27. Rolando, C., B. Monties and C. Lapierre, (1992): *Thioacidolysis*, in *Methods in Lignin Chemistry*, Editors. S.Y. Lin and C.W. Dence, Springer-Verlag, Berlin, p. 334-349.
28. Shock, C.C., E.B.G. Feibert, M. Seddigh and L.D. Saunders, (2002): *Water requirements and growth of irrigated hybrid poplar in a semi-arid environment in eastern Oregon*. *West. J. Appl. For.* 17 (1): 46-53.
29. Telewski, F.W., (1995): *Wind-induced physiological and developmental responses in trees*, in *Wind and Trees*, Editors M.P. Coutts and J. Grace. Cambridge, Cambridge University Press. p. 237-263.
30. Telewski, F.W., (2006): *A unified hypothesis of mechanoperception in plants*. *Am. J. Bot.* 93 (10): 1466-1476.
31. Tsai, C.-J., J.L. Popko, M.R. Mielke, W.-J. Hu, G.K. Podila and V.L. Chiang, (1998): *Suppression of Omethyltransferase gene by homologous sense transgene in quaking aspen causes red-brown wood phenotypes*. *Plant Physiol.* 117: 101-112.
32. Tschaplinski, T.J., G.A. Tuskan, M.M. Sewell, G.M. Gebre, D.E. Todd and C.D. Pendley, (2006): *Phenotypic variation and quantitative trait locus identification for osmotic potential in an interspecific hybrid inbred F2 poplar pedigree grown in contrasting environments*. *Tree Phys.* 26: 595-604.
33. Voelker, S.L. (2009): *Functional decreases in hydraulic and mechanical properties of field-grown transgenic poplar trees caused by modification of the lignin synthesis pathway through downregulation of the 4-coumarate:coenzyme A ligase gene*. Dissertation of Oregon State University.

Yew wood: Axial elasticity, structure-function relationships and possible biomechanical background

Daniel Keunecke¹ and Peter Niemz¹

¹ *ETH Zurich, Switzerland*

Abstract

Common yew (*Taxus baccata* L.) is well known for its extraordinary high compliance and toughness. Among other things, its wood was used for certain historical weapons (longbows, lances, crossbows) requiring these material properties, particularly the low modulus of elasticity (MOE) and at the same time a high stretchability parallel to the grain.

Indisputably, there are further elastic conifer species, but none of them have a similarly high raw density as yew. Thus, yew holds an exceptional position, especially since there is usually a strong species-spanning positive interrelation between density and axial MOE.

Aim of this present study was to identify the reasons for this compliant mechanical response of yew despite its high density. For this purpose, the longitudinal MOE of yew and further properties were determined at different hierarchical levels, from the solid wood level to the tracheid level. Moreover, selected structural details were examined.

Deriving structure-property relations from the results yields a rather broad and at the same time detailed understanding of the elasto-mechanical behaviour of common yew. Based on these findings, we also speculate about the biomechanical background behind these unusual tissue characteristics.

Introduction

From the technological point of view, the softwood species Common yew (*Taxus baccata* L.) is well known for its extraordinary longitudinal elasticity and toughness [1]. In other words: yew is regarded as highly deformable in the longitudinal direction prior to and beyond the elastic limit, and yew is able to absorb a large amount of energy during deformation. Therefore, it is no coincidence that in earlier centuries, yew wood was frequently used e.g. for certain weapons (longbows, lances, crossbows; [2]) or cartwheels. These areas of application require one or several of these properties, i.e. flexibility, resistance to fracture and the ability to store energy that can be explosively released as in the case of a longbow shooting an arrow.

Being defined as the slope of a material's stress-strain curve in the linear-elastic range, the modulus of elasticity (MOE) describes a material's tendency to be elastically deformed under short-duration states of moderate stress. Although not providing any information about the length of the elastic range, which can considerably vary between (but also within) wood species, the longitudinal MOE (MOE_L) contributes to assessing their elasticity. Most of the few available literature references report MOE_L between 6.2 and 12 GPa for yew [3-6], which is not unusual for European softwoods. None of them, however, have such an extremely high raw density as yew (about 650 kg m^{-3} or even higher) although there is typically a reasonable species-spanning positive relationship between raw density and MOE_L (Fig 1).

Altogether yew clearly holds a distinctive position among softwoods regarding its longitudinal deformability. However, the background of the relatively compliant mechanical response in light of the high density was still unknown. This prompted us to delve deeper into the elasto-mechanical behaviour of yew wood as a case study for structure-function relationships.

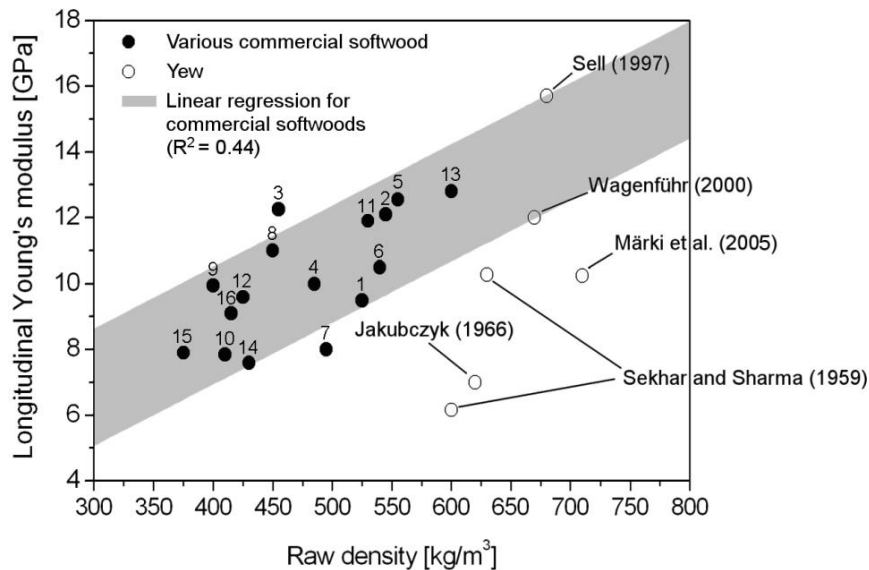


Fig. 1 Interrelation between air-dry density (= density at 20°C and 65% relative humidity) and longitudinal MOE for yew and various commercial softwoods, the latter as compiled by Sell [1]: Cedar (1), Douglas fir (2), Fir (3), Hemlock (4), Larch (5), Maritime pine (6), Mediterranean stone pine (7), Norway spruce (8), Radiata pine (9), Redwood (10), Scots pine (11), Sitka spruce (12), Southern Pine (13), Swiss stone pine (14), Western red cedar (15), Weymouth pine (16).

The behaviour of a material under load depends on its structure. In this respect yew wood is easily distinguishable from other softwoods. Its wood is characterised by narrow tree rings with often wavy tree ring boundaries. Compared to most other softwoods, a larger quantity of encased dead knots and irregular grain complicates the production of clear specimens as do large amounts of compression wood [see for example 5, 7, 8]. Only two cell types are formed in the xylem: tracheids and homocellular wood rays [5]. The tracheids are rather short (≈ 2 mm) with a high cell wall / lumen ratio causing a remarkably high density compared to other European conifers. The density gradient between earlywood and latewood tracheids is smaller than in other conifers [5]. In other words, even in the earlywood the tracheid walls of yew are relatively thick.

The conspicuous spiral thickenings are identifying features of the tracheids [9]; their mechanical effects, however, are largely unknown. In view of their small diameters compared to the remaining tracheid wall material, it can be assumed that their influence on the mechanical properties of yew is negligible.

The high percentage of wood rays indicates an increased radial reinforcement [cf. 10]. A further characteristic feature is the high extractives content [5, 11, 12] rather typical for tropical species. On the one hand, this makes yew heartwood extremely durable. On the other hand, a high extractives content influences the sorption behaviour by lowering the equilibrium moisture content of wood [13] which impacts swelling and shrinkage.

The overall objective of this study was a comprehensive evaluation of the longitudinal elasto-mechanical behaviour of yew at standard climatic conditions (20°C, 65% relative humidity). To determine this, we aimed to

- 1) evaluate the longitudinal stiffness of yew at three hierarchical levels (the solid wood level, the “tissue” level and the level of individual tracheids). The low longitudinal MOE of yew relative to its high density has been determined in mechanical tests on standardized solid wood specimens. However, it is still unknown if this compliant behaviour is also established at other levels of structural organisation. To answer this question, the MOE was analysed also at two lower hierarchical levels.
- 2) Moreover, we wanted to find structure-function interrelations explaining the mechanical response of yew.

To achieve these objectives, predominantly self-developed macro- and micromechanical approaches were followed. All mechanical tests were tension tests, and the load was applied within time periods short enough to neglect creep phenomena (less than 0.1 hours). Therefore, the initial deformations of wood caused by moderate external loads were assumed as linear-elastic (as is

common practice using the engineering notation of the generalised Hooke's law). In addition to the mechanical tests, anatomical features of yew were studied at different structural levels.

Although mechanical properties can cover a wide range within a species, a certain variation of test results may probably be put down to varying boundary conditions of the chosen testing procedures. Therefore, all of our tests were also performed on Norway spruce (*Picea abies* [L.] Karst.), a very suitable reference species due to its best known mechanical and structural properties.

Materials and methods

The specimens were cut from a total of five yew and five spruce stems (at breast height) grown at stands close to Zurich, Switzerland (at an altitude of about 500 m above sea level). The samples were taken from the outer heartwood region at a sufficient distance from the pith where the curvature of the growth rings can be neglected and the material can be treated as approximately orthotropic. Samples containing compression wood were omitted.

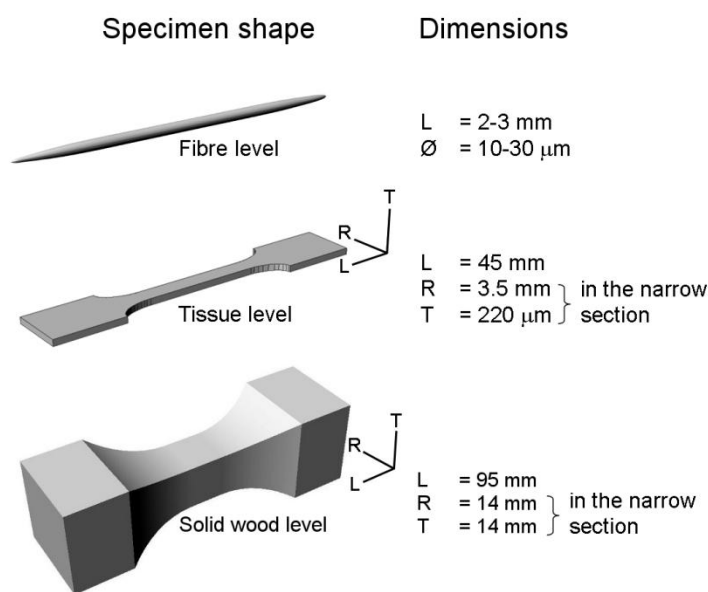


Fig. 2 Geometry of tension specimens tested at the fibre level [14] (the fibres were taken from the transition zone between earlywood and latewood), the „tissue“ level [15], and the solid wood level [16] to determine the longitudinal modulus of elasticity.

The number of tension specimens, their structural properties, their preparation, technical details of the testing setups (loading device, feed rate, loading time, strain measurement) and the calculation of MOE are described in great detail in [14] (or the literature cited herein; for tests at the fibre level), in [15] (for the „tissue“ level: specimens with a thickness of 220 μ m in the tangential direction and a width of 3.5 mm in the radial direction) and in [16] (for the solid wood level). An overview of the specimen dimensions and geometries is presented in Fig 2. All tests have been carried out at 20°C and 65% relative humidity, which corresponds to equilibrium moisture contents of 11% for yew and 12% for spruce samples.

Structural measurements on the specimens, but also on supplementary samples of both species, comprised various anatomical characteristics. However, they were particularly focussed on the microfibril angle (MFA) we measured with diverse techniques such as wide angle X-ray diffraction (WAXD), small angle X-ray scattering (SAXS), and the ray/tracheid cross-field pit aperture method.

Results and discussion

The comparative examination of yew and spruce wood led to an extensive insight into their mechanical response in the longitudinal direction within the linear-elastic range (under standard climatic conditions). In spite of a remarkably high raw density, yew showed a lower MOE_L under moderate loads compared to the 30% less dense spruce across all studied hierarchical levels (Table 1):

Table 1 Mean MOE_L of yew and spruce determined at three hierarchical levels at 20°C and 65% relative humidity.

Species	Hierarchical level	MOE_{CW} (GPa)	MOE_{CSA} (GPa)
Yew	Tracheids ¹	13.9 (36.6%)	-
	„Tissue“ ²	15.6 (26.9%)	7.0 (23.9%)
	Solid wood ³	17.0 (11.4%)	10.5 (13.6%)
Spruce	Tracheids ¹	26.2 (28.3%)	-
	„Tissue“ ²	29.4 (18.6%)	9.9 (21.5%)
	Solid wood ³	27.2 (8.2%)	12.8 (9.2%)

The data presented are mean values. Tracheid level: yew, number of specimens (n) = 18; spruce, n = 21. „Tissue“ level: yew, n = 41; spruce, n = 40. Solid wood level: yew, n = 12; spruce, n = 10. The data for the „tissue“ level are mean values for two specimen series per species. Figures in parentheses are coefficients of variation. MOE_{CW} = modulus of elasticity based on the cell wall area; MOE_{CSA} = modulus of elasticity based on the cross sectional area including lumens. The strain at the limit of linear elasticity was roughly twice as high for yew than for spruce; the lower the hierarchical level, the higher the strain for both wood species. ¹⁾ [14]; ²⁾ [15]; ³⁾ [16].

1) At the solid wood level, the longitudinal MOE of spruce was in good agreement with well known values quoted in literature references. The mean MOE_L was slightly lower for yew than for spruce (~10.5 vs. ~12.8 GPa). The specific MOE_L (= MOE_L related to raw density) actually revealed a remarkable difference between both species (~17.0 vs. ~27.2 GPa/kg m⁻³). This is in agreement with previous studies by our working group where we measured MOE_L of both species in three-point bending [17] and dynamically [18] at the macroscopic level.

2) The tests at the „tissue“ level revealed a similar relationship for yew as at the macro level: the MOE_{CSA} (= MOE based on the total cross sectional area) of yew is about one third lower than for spruce; the MOE_{CW} (= MOE calculated on basis of cell wall cross sectional areas; this corresponds to the specific MOE_L) of yew is only half as high as for spruce due to the higher density of yew. Including the density into the calculation of MOE_L clearly demonstrates that a fundamental difference must exist between yew and spruce regarding the structure-function relationships.

One problem inherent to investigations at this level is related to the representative specimen volume. In standard tests at the solid wood level, representative material characteristics of the specimens can, for example, be ensured by prescribing a minimum number of growth rings in the relevant cross section. This regulation is not simply transferable to the „tissue“ level. As a result, specimens with different numbers of annual ring boundaries (resulting in different latewood percentages), which are therefore not absolutely comparable, have been tested. As a compromise, we also calculated the MOE_L on the basis of the cell wall areas to consider density variations anyhow. This methodological weakness might influence the informative value of the results which thus cannot be regarded as representative for the effective material behaviour but as an approximation.

3) The tests on transition wood fibres revealed the same tendencies for both species as observed at the higher hierarchical levels: the MOE_{CSA} of yew fibres under tensile load was about half as high as that of spruce fibres.

It seems obvious that the low specific MOE of yew results, amongst other things, from its high extractives content (a value of 5-15% for yew and of 1-2% for spruce was measured after extraction in a Soxhlet apparatus with an acetone/water mixture at a ratio of 9:1) and its high ray percentage: a high extractives content increases the density but not the longitudinal stiffness, and a high ray percentage also implicates that a larger quantity of structural elements contributes to the density but not to the longitudinal stiffness. These relationships, however, are not necessarily true for the fibre level. But remarkably, the MOE_{CW} practically did not vary between the three levels in either species. Our findings indicate that one principle reason for the low MOE_L of yew must be present at all investigated hierarchical levels. In other words: The lower MOE_L was exhibited not only by specimens subjected to cell-cell interactions but also by individual tracheids for which pure cell wall mechanics applied.

Therefore, the axial stiffness of yew is obviously controlled by a feature that is present even at the cellular level.

Supplementary structural examination revealed differences in the cellular dimensions and intra-ring density distributions of both species. These differences, however, mainly influence the (elasto-) mechanical behaviour perpendicular to the grain. The crucial structural difference between both species is the MFA of the helically oriented cellulose fibrils in the S2 cell wall layer. As is well known, this angle in particular influences the MOE_L . The larger the MFA, the larger is the maximum strain and the lower is the MOE_L [e.g. 19].

Depending on the methodological approaches, varying MFAs were measured. Nonetheless, regardless of the measurement method (orientation of pit apertures in ray / tracheid crossing fields; X-ray diffraction; X-ray scattering) and the regional origin of the samples (central Europe: Switzerland, Germany, France), in either case our results indicate a large MFA of mature heart wood in yew compared to spruce. This applies particularly to latewood tracheids of yew (around and often slightly larger than 30°). Thus, there is evidence to suggest that the MFA of yew wood is generally large compared to much smaller MFAs ($\leq 10^\circ$) often reported for the mature wood of other northern conifers such as spruce [e.g. 20-23]. An example for measurements based on X-ray densitometry can be seen in Fig 3 where one yew and one spruce sample have been analysed with SilviScan III, a commercial automated wood microstructure analyzer.

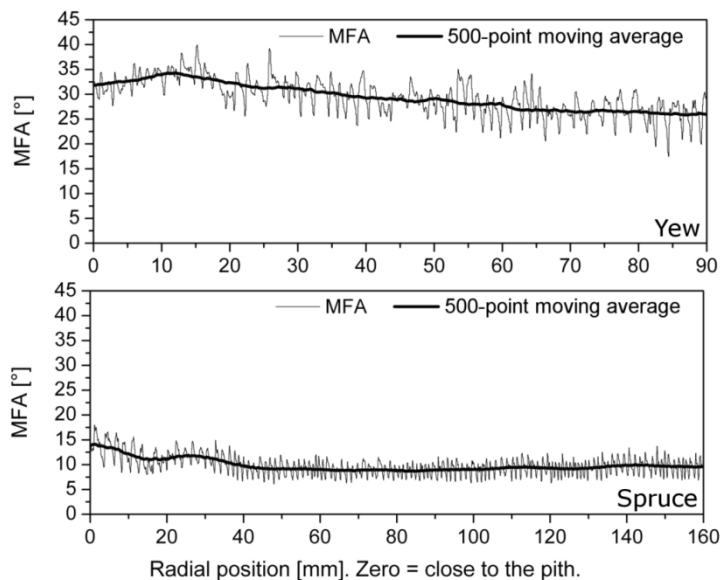


Fig. 3 Radial MFA profiles of one yew and one spruce sample (height in the longitudinal direction: 7 mm; width in the tangential direction: 2mm) measured by SilviScan using X-ray densitometry. Note that the curves are based on random samples only from two species – and hence are indicative only. The MFA of yew is obviously at a higher level compared to spruce. This applies for the mean MFA but also for a separate consideration of earlywood and latewood regions (within the growth rings, the MFA decreased with increasing density). For further details regarding the SilviScan measurements, see [24].

These anatomical principles are tremendously important for a better understanding of the elasto-mechanical response of yew under longitudinal load. The overall MOE_L is predominantly dictated by the latewood tracheids that are denser and have a smaller MFA compared to earlywood, and therefore limit the elasticity of the xylem being a compound of earlywood and latewood zones. Consequently, the structural properties of latewood can be regarded as a bottleneck for the elasticity and stretchability of the tissue. In other words, the large latewood MFA allows for the compliant behaviour of yew wood. This is particularly interesting as the high extractives content of yew results in a lower equilibrium moisture content (EMC) compared to spruce which usually increases the MOE_L .

Conclusions

Our findings reveal a typical characteristic of hierarchically organized materials: a feature of the material's ultra structure can have a strong impact on the mechanical behaviour of even clearly higher hierarchical levels. In other words: the compliant behaviour of yew wood was attributed to a feature present at the cell wall level, namely a relatively large MFA (particularly in the latewood tracheids)

measured by diverse techniques and on samples of different regional provenance. The large MFA also accounts for the high longitudinal strain observed at all hierarchical levels.

From its anatomical features and elastic behaviour it can be concluded that yew wood combines properties of normal and compression wood and thus rather takes an intermediate position between them, and a distinctive position among softwoods. It has to be noted that all yew characteristics ascertained within this study were derived from largely flawless specimens (i.e., without visible defects) as stipulated by testing standards. This so-called “clear wood”, however, only stands for a small proportion of the xylem produced in the stem, and therefore is not representative for yew wood in general.

However, the question still remains: What is the biomechanical background of the large yew MFAs? That is open to speculation. Taking into account that the genus *Taxus* exists since 140 million years (and the species *Baccata* since 15 million years), yew is the oldest tree species in Europe. Thus, many gymnosperm species are, from the evolutionary point of view, clearly younger and can be regarded as advancements of nature:

They are “specialists” optimized for their respective site conditions; they are often characterized by strong height increment and simultaneously low weight, i.e. a high slenderness ratio. This slenderness accompanied by bending and buckling risks (as in the case of side wind or snow load on branches) has to be compensated by higher stiffness. To achieve this, relatively small MFAs are generated. Due to these species, wood nowadays is considered as outstanding lightweight building material with good mechanical properties in spite of the low density.

Yew trees do not belong to this category of specialists. They are rather “generalists” and are able to adapt to different conditions: They are not particularly high (maximum under good conditions: 20 meters) and grow slowly, but they can reach remarkable diameters; therefore, their slenderness ratio is relatively small. With their large MFAs, they cannot generate a high stiffness. They compensate this disadvantage by their compact habitus and the high density, which protect them reasonably against buckling or breaking.

Altogether it is conceivable that the large yew MFA is only one of many pieces contributing to the yews’ character as generalists. The real progress has probably been achieved by the historically younger wood species with their smaller MFAs.

Acknowledgements

This work was supported by the European Cooperation in the field of Scientific and Technical Research (COST, Action E35). We would also like to express our gratitude to our colleagues Dr. I. Burgert, Dr. M. Eder and Dr. O. Paris (Max Planck Institute for Colloids and Interfaces, Potsdam/Germany), Dr. R. Evans (CSIRO Materials Science and Engineering, Clayton/Australia) and S. Hering (ETH Zurich – Institute for Building Materials, Zurich/Switzerland) for their contribution to our findings.

References

1. Sell, J. (1997): *Eigenschaften und Kenngrößen von Holzarten*. Dietikon: Baufachverlag.
2. Bariska, M. (1998): *Verwendung des Eibenholzes gestern und heute*. Schweizerische Zeitschrift für Forstwesen 149:340-348.
3. Sekhar, A. C., and R. S. Sharma (1959): *A note on mechanical properties of Taxus baccata*. Indian Forester 85:324-326.
4. Jakubczyk, B. (1966): *Technical properties of the yew wood from the preserve Wierzchlas*. Sylwan 10:79-86.
5. Wagenführ, R. (2000): *Holzatlas*. München: Fachbuchverlag Leipzig.
6. Märki, C., P. Niemz, and D. Mannes (2005): *Comparative studies on selected mechanical properties of yew and spruce*. Schweizerische Zeitschrift für Forstwesen 156:85-91.
7. Kucera, L.J. (1998): *Das Holz der Eibe*. Schweizerische Zeitschrift für Forstwesen 149:328-339.
8. Grosser, D. (1997): *Die Hölzer Mitteleuropas*. Berlin: Springer.
9. Wergin, W., and G. Casperson (1961): *Über Entstehung und Aufbau von Reaktionsholzzellen*. Holzforschung 15:44-49.

10. Burgert, I. (2000): *Die mechanische Bedeutung der Holzstrahlen im lebenden Baum*. Dissertation, Hamburg.
11. Uslu, Y. (1997): *Adi porsuk (Taxus baccata L.) odun ve kabugunun kimyasal bileşimi*. Master thesis, Karadeniz Technical University, Trabzon, 1997.
12. Mertoglu-Elmas, G. (2003): *Chemical components of heartwood and sapwood of common yew (Taxus baccata L.)*. Journal of Environmental Biology 24:489-492.
13. Nzokou, P., and D. P. Kamdem (2004): *Influence of wood extractives on moisture sorption and wettability of red oak (Quercus rubra), black cherry (Prunus serotina), and red pine (Pinus resinosa)*. Wood and Fiber Science 36:483-492.
14. Keunecke, D., M. Eder, I. Burgert, and P. Niemz (2008): *Micromechanical properties of common yew (Taxus baccata) and Norway spruce (Picea abies) transition wood fibers subjected to longitudinal tension*. Journal of Wood Science 54:420-422
15. Keunecke, D., and P. Niemz (2008): *Axial stiffness and selected structural properties of yew and spruce microtensile specimens*. Wood Research 53:1-14.
16. Keunecke, D., S. Hering, and P. Niemz (2008): *Three-dimensional elastic behaviour of common yew and Norway spruce*. Wood Science and Technology 42:633-647
17. Keunecke, D., C. Marki, and P. Niemz (2007): *Structural and mechanical properties of yew wood*. Wood Research 52:23-38.
18. Keunecke, D., W. Sonderegger, K. Pereteanu, T. Luthi, and P. Niemz (2007): *Determination of Young's and shear moduli of common yew and Norway spruce by means of ultrasonic waves*. Wood Science and Technology 41:309-327.
19. Reiterer, A., H. Lichtenegger, S. Tschegg, and P. Fratzl (1999): *Experimental evidence for a mechanical function of the cellulose microfibril angle in wood cell walls*. Philosophical Magazine a - Physics of Condensed Matter Structure Defects and Mechanical Properties 79:2173-2184.
20. Kantola, M., and S. Seitsonen (1969): *On the relation between Tracheid Length and Microfibrillar Orientation measured by X-Ray Diffraction in Conifer Wood*. Annales Academiae Scientiarum Fennicae Series A VI Phys.
21. Paakkari, T., and R. Serimaa (1984): *A Study of the Structure of Wood Cells by X-Ray-Diffraction*. Wood Science and Technology 18:79-85.
22. Fratzl, P., H. F. Jakob, S. Rinnerthaler, P. Roschger, and K. Klaushofer (1997): *Position-resolved small-angle X-ray scattering of complex biological materials*. Journal of Applied Crystallography 30 (2):765-769.
23. Saren, M. P., R. Serimaa, S. Andersson, T. Paakkari, P. Saranpaa, and E. Pesonen (2001): *Structural variation of tracheids in Norway spruce (Picea abies [L.] Karst.)*. Journal of Structural Biology 136 (2):101-109.
24. Keunecke, D., R. Evans, and P. Niemz (2009): *Microstructural properties of common yew and Norway spruce determined with SilviScan*. IAWA Journal 30 (2):165-178.

Soil property effects on the natural durability, extractive content and colour of teak (*Tectona grandis* L.f) wood in Togo

A.D. Kokutse¹, N. Amusant², N. Boutahar² G., Chaix³

¹Laboratoire de Botanique et Ecologie Végétale, Faculté des Sciences, Université de Lomé, BP1515, Lomé, Togo, Tel : (+228) 225-50-94, Fax: (+228) 221-85-95

mimidam@hotmail.com

²Cirad-Persyst, UR Valorisation des Bois Tropicaux, B.P. 5035, TA B40/16, 34398 Montpellier Cedex5, France, Tel. +33 (0) 467614497 – Fax +33 (0) 467615725

nadine.amusant@cirad.fr, nabila.bouthar@cirad.fr

³Cirad-Bios, UR Génétique Forestière, B.P. 5035, TA A39/16, 34398 Montpellier Cedex 5, France, Tel: +33 4 67 61 44 51 - Fax: +33 4 67 59 37 33 gilles.chaix@cirad.fr

Abstract

Togolese teak is highly resistant to pathogen attack, but natural durability and wood colour vary according to plantation sites and geographical zones. Therefore, further information concerning the influence of environmental parameters and their effects on teak wood quality is necessary and it could be possible to improve these characteristics through tree breeding and silviculture programs in Togo. In order to examine the influence of soil properties on teak wood characteristics, 321 wood samples issued from 20 trees were exposed to two fungi: *Antrodia sp.*, and *Coriolus versicolor*. Depending on type of soil in which they grew, trees had been randomly selected in two different sites in the same climatic area in Togo. The colour parameters of each sample were measured using the CIELAB system and total extractive content was determined using the Accelerated Solvent Extraction (ASE) procedure. Results showed a significantly lower total extractive content (11.1%) for trees that grew on hydromorphic tropical ferruginous (HTF) soil than trees from drained ferruginous soil (12.8%). Samples from HTF soil were lighter and the redness a* and yellow-blueness b* were significantly higher. Independently of soil quality, all the trees were highly durable regarding decay by *C. versicolor*. With *Antrodia sp.*, 90 % of the trees from both sites were highly durable and only 10% were durable. However, samples from HTF soil were less durable with regard to the two fungi.

Introduction

Teak (*Tectona grandis* L.f) is historically well known for highly durable wood, due largely to the presence of extracts in the heartwood, e.g. anthraquinones and tectoquinones (Pahup et al. 1989; Yamamoto et al. 1998; Simatupang and Yamamoto 1999 Haluk et al. 2001). Due to this natural durability, teak is often used for outdoor purposes, for example boat decking, bridge building and garden furniture as well as for traditional indoor uses such as flooring and furnishings. Such uses require a highly stable wood with regard to physical properties as well as an aesthetically pleasing colour and adequate resistance to pathogens. Because of the high demand, teak plantations are increasing and becoming an important timber source in tropical countries especially in West-Africa, Asia and South Africa. Over 14,000 ha of teak plantation exist in Togo (Tengué 1995). Although wood density and strength properties of Togolese teak wood are not significantly different compared to those from natural forests (Kokutse et al. 2004), natural durability and wood colour shows high variability within and between stands due to tree age (Kokutse et al. 2006), extractive content (Gierlinger, 2003) and to various ecological conditions (e.g. geomorphology, topographic, soil, rainfall) (Kokutse et al. 2006, Adjonou et al. 2009). Due to the variability in environmental conditions,

the reputation of teak wood for natural durability is often questioned when trees from plantations are supplied for outdoor uses (Bhat et al. 2004). Simatupang and Yamamoto (2000) have reported that teakwood from a wet plantation site is less resistant to fungi than teak from a dry site. Bhat et al. (2005) studied home garden teak and found that wood samples from a wet site with pale coloured wood and lower extractive content were more susceptible to fungi. The main objective of the present study was to examine the influence of soil properties on natural durability, wood colour and extractive content in teak wood from Togolese plantations.

Material and methods

Site description

The study sites, namely Tchorogo (established in 1972) and Oyou (established in 1966), were situated in the same area of the central part of Togo (1°00'E, 8°21'N), West Africa. This central area of Togo is covered by Guinean woody savannas and is situated at an altitude of 200-400 m. In this area, two major seasons exist annually, one long rainy season lasting 6–8 months followed by a long dry season. The mean annual precipitation is 1400-1600 mm and temperatures vary from 25°C to 40°C (Ern, 1979). The Oyou site is located on tropical ferruginous soils with a pseudogley layer and hydromorphic surface horizons. This kind of soil is periodically flooded in the rainy season. The substratum is made up of basic rocks, micashists and quartzites of Togo Mountains. The texture is muddy, sandy and clayey. Tchorogo site is located on a tropical ferruginous and well drained soil with a sandy-fine gravel texture. The description of the study sites is presented in Table 1.

Sample preparation

Twenty trees of 34 and 40 years of age, respectively were harvested in 2006 from Tchorogo and Oyou. A 550 cm long log was cut from each tree at breast height which was further sawn into boards in the radial direction (15 x 20 mm). Boards were sawn radially (550 mm in the longitudinal axis and 50 mm in the tangential axis) at breast height. Beams of heartwood (20 x 15 x 550 mm) were cut from each board and finally, 10 (20 x 15 x 50 mm in radial and tangential longitudinal directions) wood samples were cut per beam. The samples were conditioned at 20°C and 65 % RH. The location of each wood sample, according to its position in the stem, was recorded by measuring its cambial age and the distance from the pith. The samples were classed into three groups depending on cambial age of the samples: inner (5-10 years), intermediate (11-20 years) and outer heartwood (21-30 years). A total of 321 and 343 samples were used to evaluate durability and wood colour respectively. The remaining samples were then ground into wood meal for total extractive content measurement.

Extractive content

The extractive content was determined gravimetrically. The ground wood samples were extracted using a sequence of solvents: hexane, acetone and methanol 80% (technical grade). Extractions were performed with an ASE-200 apparatus (Dionex). 2.5 g of wood meal was weighed and the dry mass calculated after the determination of humidity on parallel samples. Extraction conditions were: temperature (80°C), pressure (100 bars), static time (5 min), static cycles (3), flush (100 %) and purge (90 s). Analyses were carried with three replicas. When the extraction was completed, the wood meal was removed from the cells and dried in an oven at 103°C until constant mass. The extractive content was determined using the equation: Extraction percentage = [dry mass before the extraction – dry mass after extraction] x100 / dry mass before the extraction.

Wood colour measurements

Colour measurements were performed along the tangential-radial side of the wood samples. The percentage of reflectance data was collected at 10 nm intervals over the visible spectrum (from 400 to 700 nm) using a portable spectrophotometer (Microflash Datacolor 200d). The reflectance readings were converted into L* a*b* values (CIELAB system), where L* describes the lightness (100 = white) or darkness (0 = black) of a colour, a* represents the X axis which is redness [red (+) to green (-)] and b* represents the Y axis, yellow-blueness [yellow (+) to blue (-)]. Illuminant A (representing

incandescent light), 10° standard observer with 6 mm apertures chosen and specular reflection setting was excluded.

Table 1. Site characteristics. A: altitude (m). D: density (tree.ha-1). MD: mean diameter (cm) at height 1.3 m. MH: Mean height (m).

Location	A	Year of plantation	Soil type	D	MD	MH
Tchorogo	419	1972	Ferruginous soil, sandy-silt structure	2600	21.8 ± 4.4	16.1 ± 1.7
Oyou	420	1966	Ferruginous soil clay, muddy sandy-structure	2600	23.4 ± 3.1	13.6 ± 0.6

Decay measurements

After colour measurements, the wood samples were used to determine natural durability. The test was performed according to the European standards NF-EN 350-1 (AFNOR 1994) and NF-EN113 (AFNOR 1996) guidelines. Two species of basidiomycetes fungi were used; namely *Coriolus versicolor* (strain CTBA 863 A), a white rot and *Antrodia sp.* (strain CTFT 57 A), a brown rot. One hundred sixty one samples were used to test the natural durability against *Antrodia sp.* And 160 samples for *Coriolus versicolor*. Reference samples of beech and pine were used as controls to test the virulence of the fungi. The sterilised wood samples from the outer, intermediate and inner heartwood were placed over 16 weeks in glass jars previously inoculated with a mycelia suspension of fungal mycelia (75 % RH and 27°C). At the end of the test, the mycelium was removed from the wood sample prior to drying at 103°C for 48 h. The mass loss was calculated and the durability rating against wood-destroying Basidiomycetes fungi based on the EN 350-1 standard (AFNOR 1994) was determined.

Results

The total extractive content ranged from 7.8 ± 0.1 to 14.5 % ± 1.1 for the tree samples from the Oyou site and from 11.0 ± 0.7 to 15.3 % ± 1.9 for the trees of the Tchorogo site. For both sites, the variability between trees was high within the stands and explained 17% of the total extractive content variability. When taking into account the position in the tree (inner, intermediate or outer heartwood), the radial position of the wood sample explained only 3 % of the variation of the total extractive content in the Oyou site, however it explained 10 % of the variation in Tchorogo site. The variance analysis showed significantly higher extractive content for trees from drained ferruginous soil (Tchorogo site) than from the hydromorphic tropical ferruginous (HTF) soil (Oyou site) (F1,19 = 5.88, P = 0.02).

The mean mass loss in the beech and pine control samples were 54.9 % for *Antrodia sp.* and 38.0 % for *C. versicolor*. These values were higher than the minimal values given in the standards indicating that the fungi were very virulent under tropical conditions and validates the durability of the test results. All the trees were highly durable with regard to *C. versicolor*. The mass losses varied from 0.4 to 3.7 % when considering the tree. For individual samples, the mean mass loss varied from 0.0 to 8.4 % in the Oyou site and from 0.0 to 5.0 % in the Tchorogo site and only four samples were durable. The radial position of the sample in the tree was found to have an influence on the degree of attack of *C. versicolor* in Tchorogo (F1,65 = 10.70, P = 0.002) and in Oyou sites (F1,58 = 10.15, P = 0.002). In

both cases the outer heartwood was less resistant to *C. versicolor* than the inner heartwood. However the intermediate heartwood was not significantly different from inner and outer heartwood. A significant difference was observed in the degree of decay of the teak wood, depending on the type of soil on which the trees grew, with regards to *C. versicolor*. Trees from hydromorphic tropical ferruginous (HTF) soil (i.e. the Oyou site) showed significantly higher mass losses ($F_{1,19} = 6.96$, $P = 0.02$). The mass losses obtained with *Antrodia sp.* were higher than those obtained with *C. versicolor* and ranged from 0.3 to 13.9 % in the Oyou samples and from 0.2 to 8.1 % in Tchorogo samples (Table 2). Out of 161 teak wood samples exposed to *Antrodia sp.*, 92 % were rated as very durable, 4 % were durable and 4 % were moderately durable for the Tchorogo site. However in the Oyou site, 89 % of samples were very durable, 4 % were durable and 7 % were moderately durable. The influence of the radial position on wood durability was not significant with the samples exposed to *Antrodia sp.*. Trees from HTF soil showed higher mass losses than trees from drained ferruginous soil even though the difference between the sites was not statistically significant.

The lightness L^* parameter of wood samples ranged from 54.0 ± 0.4 in Tchorogo site to 54.8 ± 0.2 in the Oyou site. No significant differences were observed in the samples from Tchorogo and Oyou regarding their light colour. When considering the redness a^* and the yellow-blueness b^* of the wood samples, Oyou samples differed from Tchorogo samples (Fig. 1). Samples from HTF soil (Oyou site) were significantly redder ($F_{1,342} = 8.54$, $P = 0.004$) and their yellow-blueness b^* value was significantly higher ($F_{1,342} = 20.08$, $P < 0.001$) than those from the drained ferruginous soil (Tchorogo site). The influence of the radial position on wood colour parameters was not significant in either site.

Fig. 1. Mean colour parameters - Redness a^* and Yellow-blueness b^* were significantly higher in teak trees from hydromorphic tropical ferruginous soil (white bars) than teak trees from drained ferruginous soil (black bars).

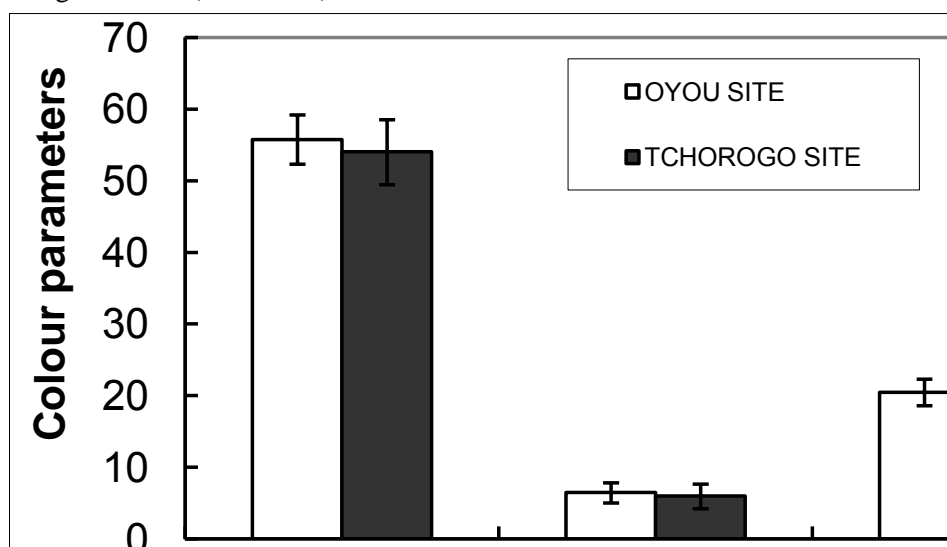


Table 2. Wood characteristics (Range, coefficient of variation CV%, and number of samples n)

	Oyou site				Tchorogo site			
	n	Min	Max	CV	n	Min	Max	CV
L^*	203	44.0	63.5	15.9	140	45.8	64.8	11.9
a^*	203	3.1	9.9	4.6	140	1.9	10.49	3.4
b^*	203	16.0	26.0	11.0	140	10.5	24.2	8.7
<i>Antrodia sp.</i>								

(mass loss %)	86	0.33	13.9	115	75	0.2	8.1	77
<i>Coriolus</i>								
<i>versicolor</i>	85	0.0	8.4	125	66	00	5.0	131
(mass loss%)								
Total extractive content (%)	57	7.18	15.1	5.7	60	9.4	15.3	6.4

DISCUSSION AND CONCLUSIONS

This study confirmed the high decay resistance of plantation teak wood. All the wood samples exposed to *C. versicolor* were highly durable (only four samples were durable) and out of the 161 exposed to *Antrodia sp.*, only 7 % were moderately durable. *Antrodia sp.*, a brown rot fungus isolated from tropical regions caused the most damage to wood samples, with up to 0-14 % dry mass loss. The influence of the radial position on wood durability was significant in samples exposed to *C. Versicolor*. A significant difference was observed in the degree of decay on teak wood, according to the type of soil on which the trees grew. With regard to *C. versicolor* and *Antrodia sp.*, the results showed that trees from hydromorphic tropical ferruginous soil were less durable compared to trees from drained soil. This loss of durability is reflected by the lower extractive content in trees grown on hydromorphic tropical soil. Many authors have found a direct relationship between wood durability and extractive content (e.g. Nelson and Heather 1972; Modesale et al. 1996; Haupt et al. 2003). Haupt et al. (2003) also showed that extractive content increased with tree age. In our study, trees from the Oyou site were older (40 years) than trees from the Tchorogo site (34 years old). Therefore, it can be expected that teak from Oyou site contained more extractives. However the results showed a significantly higher total extractive content in trees from the Tchorogo site. A genetic diversity analysis carried out on the teak plantations from Togo has shown that the genetic variability between the populations is very weak (Logossa, 2006). Our results therefore imply that the higher decay resistance and extractive contents of teak wood from well drained soil was mainly due to the environmental factors, especially the soil conditions rather than genetic diversity.

Concerning the colour of the wood which is one of the most appreciated criteria by end-users, results showed that samples from HTF soil (Oyou site) were significantly redder and their yellow-blueness b* value was significantly higher than those from drained ferruginous soil (Tchorogo site). The influence of site conditions on wood colour is still a controversial topic. According to Klumpers (1994), the wood is darker when the water content in the soil is high (wet site). Simatupang and Yamamoto (2000) have observed that teak trees from a wet site in Indonesia produced darker wood and were more susceptible to fungal decay. However, Bhat et al. (2005) studied home garden teak and found that a dry site produced darker coloured wood than a wet site. In the Ivory Coast, with similar ecological characteristics as Togo, Durand (1984) found that when the climate is humid and the soil is without hydromorphic traces, teak wood shows a greater brightness. In our study, teak from the hydromorphic Oyou and well drained Tchorogo sites, respectively, had similar lightness. However the redness and the yellow-blueness were different. Other studies on Togolese teak have showed that the plantations whose woods are redder are generally located on tropical ferruginous and ferrallitic soils which contain an important amount of clay (Adjonou et al. 2009). The existence of clay enables retention of water for a long time in the soil, leading to hydromorphy. This type of colouration is the most desirable for the end-users of teak wood, especially in Togo and in West-Africa. However, the plantations grown on hydromorphic soils are less durable, as shown by the present work. Further studies should be carried out on the mineral composition of the soils and their influence on wood colour. If the influence of the soil on wood colour and the extractive content as well as their interactions were better quantified, it may be possible to improve these characteristics through tree breeding and silviculture programs in Togolese teak plantations.

Acknowledgements

Funding was provided by the International Foundation for Science (IFS), Sweden

References

1. AFNOR, (1994): *Norme NF EN 350-1 Durability of wood based products—Natural durability of solid wood— part 1: Guide to principles testing and classification of the natural durability of wood*
2. AFNOR, (1996): *Norme NF EN 113 Wood Preservatives—Test method for determining the protective effectiveness against wood destroying Basidiomycetes—Determination of the toxic values*
3. Adjonou, K., Kokutse, A.D., Kokou, K., Ganglo, J. And B. de Foucault (2009): *Environmental and wood biophysical variabilities in teak plantations in Togo (West Africa)*. Acta Bot. Gallica (in press)
4. Bhat, K.M., Thulasidas, P.K., Florence, E.J.M.and K. Jayaraman, (2005): *Wood durability of home-garden teak against brown-rot and white-rot fungi*. Trees 19:654–660
5. Durand, P.Y., (1984): *A technological survey of plantation-grown Teak in Ivory Coast*. IUFRO Meeting–Project Group P5.01. Manaus, Brasil.
6. Ern, H., (1979): *Die Vegetation Togos. Gliederrung, Gefährdung*. Willdenowia, 9 : 295-312.
7. Gierlinger N., Jacques D., Schwanninger M., Wimmer R., and Paques L. E. (2003). *Rapid predictions of natural durability of larch heartwood using Fourier transform near-infrared spectroscopy*. Can. J. For. Res 33: 1727-1736.
8. Haluk, J.P., Roussel, C., and M. Thévenon, (2001): *Importance des quinones dans les propriétés antifongiques du Teck (Tectona grandis)*. Les cahiers Scientifiques du Bois. 2 : 77-83.
9. Haupt, M., Leithoff, D. Meier, D., Puls, J., Richter, H.G., and O. Faix, (2003): *Heartwood extractives and natural durability of plantation- grown teakwood (Tectona grandis L.) – a case study*. Holz als Roh- und Werkst 61:473–474
10. Klumpers, J., (1994) : *Le déterminisme de la couleur du bois de chêne. Etude sur les relations entre la couleur et les propriétés physiques, chimiques et anatomiques ainsi que des caractéristiques de croissance*. Thèse de Doctorat de l'ENGREF, Nancy, France. 195 pp.
11. Kokutse, A.D., Baillères, H., Stokes, A., and K. Kokou, (2004): *Proportion and quality of heartwood in Togolese teak (Tectona grandis L.f)*. Forest Ecology and Management. 189: 37-48
12. Kokutse, A.D., Stokes, A., Baillères, H., Kokou, K. and C. Baudassé, (2006): *Decay resistance of Togolese teak (Tectona grandis L.f) heartwood and relationship with colour*. Trees: Structure and Function 20: 219 – 223
13. Logossa, Z.T., (2006): *Caractérisation génétique des Tecks (Tectona grandis L.f) provenant des plantations du Togo*. Mémoire de Master II, Sciences du Bois et Fibres, Université de Bordeaux 1, 29 p.
14. Mosedale, J.R., Charrier, B. and G.Janin G (1996) *Genetic control of wood colour, density and heartwood ellagitannin concentration in European oaks (Quercus petraea and Q robur)*. Forestry 69:111–124
15. Nelson, N.D. and W.A. Heather.(1972): *Wood colour, basic density and decay resistance in heartwood of fast grown Eucalyptus grandis Hill ex Maiden*. Holzforschung 26:54–60
16. Pahup, S., Sunita, J. and B. Sangeeta. (1989): *A 1, 4-Anthraquinone derivate from Tectona grandis*. Phytochemistry. 28, 1258-1259.
17. Simatupang, H.M.and K.Yamamoto. (1999). *Properties of teakwood (Tectona grandis L.f) as influenced by wood extractives and its importance for tree breeding*. Regional seminar on site technology and productivity of teak plantations, Thailand.
18. Simatupang, H.M.and K.Yamamoto. (2000). *Properties of teakwood (Tectona grandis L.f) and Mahogany (Swietenia macrophylla King) from manmade forest and influence on utilization*. Proceedings of the seminar on high value timber species for plantation establishment, Thailand.
19. Tengué, K.M., (1995).- *Examen mi-parcours de 1995, rapport interne de l'Office de développement et d'exploitation des forêts du Togo «l'objectif an 2000 de l'OIBT », Lomé (Togo)*. 10pp.

20. Yamamoto, K., Simatupang, H., M., and R. Hashim. (1998). *Caoutchouc in teak wood (Tectona grandis L.f.) : formation, location, influence on sunlight irradiation, hydrophobicity and decay resistance*. Holz as Roh-und Werkstoff. 56: 201-209.

Mechanical damping of wood as related to species classification: a preliminary survey

Iris Brémaud^{1,2}, *Kazuya Minato*¹ and *Bernard Thibaut*³

¹ *Laboratory of Forest Resource Circulating Circles, Graduate School of Life and Environment Science, Kyoto Prefectural University, Japan.*; ² *Laboratoire de Mécanique et Génie Civil, Université Montpellier 2, CNRS, Montpellier, France*; ³ *Ecologie des Forêts de Guyane, CNRS, Kourou, French Guyana.*

Abstract

Some morphological and biochemical taxonomic markers are also affecting factors of dynamic mechanical properties of wood. Thus, could these properties reflect the classification/phylogeny of taxa? This work is a first insight into this question. It relied on the gathering (through experimental campaigns and exhaustive literature review) of a large database on the viscoelastic (i.e. including damping) vibrational properties of 445 woody species. The “standard” relationship between damping coefficient ($\tan\delta$) and specific modulus of elasticity (E'/ρ) was confirmed at a wide interspecific scale, but described no more than 40% of $\tan\delta$ variations. Damping and E'/ρ fluctuated between families, yet not in a way that could be easily related to the phylogenetic tree. Damping was a bit more discriminating than E'/ρ . Some families had nearly systematically lower (Fabaceae-Papilionoideae and, to a lesser extent, Lauraceae, Cupressaceae and Moraceae) damping than average, independently of E'/ρ . On the contrary, Fagaceae, Betulaceae and Sapindaceae had higher damping than average. While for some other families no clear characteristics could be observed – at least with the present number of represented species. In the future, increasing the amount of data and compiling anatomical and chemical markers / affecting factors will allow further analysis at sub-family levels, and a better understanding of this wide topic.

Introduction

Dynamic mechanical properties of wood in given conditions of time-frequencies, temperature and moisture content are related to superimposed effects of the organization and orientation of wood elements (cells and microfibrils) and of characteristics of chemical composition [1,2]. Such affecting factors may in turn be morphological and biochemical markers of the botanical classification or phylogeny of woody species. The usefulness of wood anatomy in systematic studies has been long recognized. Criteria such as the proportion of different types of cells / tissues and cell-wall thickness affect specific gravity. Yet little is currently known about any potential dependence on classification of parameters such as microfibril angle and grain deviation which are known to affect axial mechanical properties. On the other hand, different taxa can have different “enzymatic machineries” regulating their biosynthetic pathways. Especially, secondary metabolites are extremely diverse and their nature depends on families, genus or species (c.f. chemotaxonomic studies). They are also expected to play a significant, and probably compound-dependant, role in modulating mechanical damping [3,4,5,6].

Given these considerations, we expect that some of the wood morphological and biochemical diversity would be reflected in their mechanical behaviour. This work is a first insight into the potential categorization of taxa depending on their dynamic mechanical properties. Though, considering actual biodiversity, little information is currently available about inter-specific variability of mechanical damping. The prerequisite for our analyses thus relied on the gathering of a large

collection of information on the viscoelastic (i.e. including damping) vibrational properties of woody species [7]. In this paper, preliminary analyses are made at the botanical family level.

Methodology

Experimental characterizations

Characterizations of vibrational properties in axial direction were performed on 76 wood species. About 2 thirds of the material has been obtained from well-identified stocks from CIRAD, Montpellier. The remaining part was obtained from various sources and, when necessary, subsequently identified. The total sampling covered more than 1300 specimens.

Specimens (12×2×150mm, R×T×L) were first dried (in order to reach equilibrium in adsorption) for 48h at 60°C. After at least 3 weeks stabilization in controlled conditions of 20±1°C and 65±2%RH, vibrational measurements were performed by non-contact forced vibrations of free-free bars (see *Fig. 1*), e.g. [1,8]. Specimens were suspended by thin silk threads located at the nodes of vibration for the first mode. They were made to vibrate through an electro-magnet facing a thin iron plate glued on one end of specimens. Displacement was measured by a laser triangulation sensor. A frequency scanning allowed determining the resonance frequency and its bandwidth. Then excitation was set at the resonance frequency, then cut off and the decrement of amplitude was recorded. E'/ρ was deduced from the first resonant frequency according to the Euler-Bernoulli equation. Damping or loss coefficient –expressed as $\tan\delta$ – was measured both through the ‘quality factor’ Q (bandwidth at half-power; frequency domain) and through logarithmic decrement λ of amplitude after stopping the excitation (time domain). Measurement frequencies were in the range of 200-600 Hz. 3 repetitions were made for each probe and mean error on properties was $\leq 5\%$.

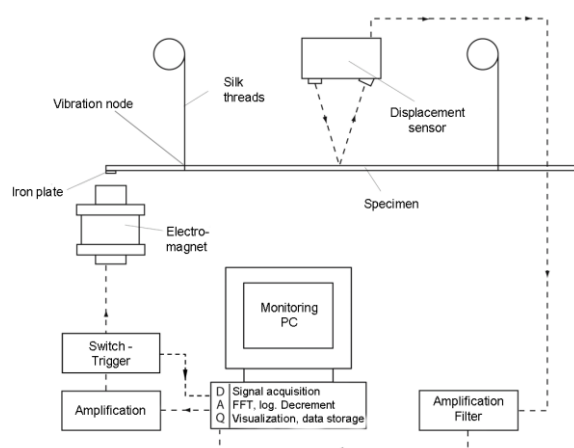


Fig. 1 Schematic drawing of the apparatus for non-contact forced vibrations of free-free slender beams.

Data compilation

Data obtained through our experimental characterizations were much extended by an extensive literature review on wood viscoelastic (i.e. data including damping coefficients) vibrational properties. Data were collected from 30 sources, including some hard-to-obtain ones. Great care has been taken about checking the compatibility of all collected values, especially considering the hygrothermic and frequency conditions of measurements. The data compiled were obtained on woods stabilized in controlled conditions of 20-25°C, at c.65% RH (55-70% RH were accepted but specified) and in the frequency range of 200-1500Hz (data at higher frequencies are listed separately). Basic set of properties includes specific gravity (ρ), Young's modulus (E), specific dynamic Young's modulus (E'/ρ) and damping coefficient ($\tan\delta$), along the grain (some information on anisotropy ratios were also collected). This “wood vibrational properties” collection contains data for 445 woody species (corresponding to the results of 6000 tests), including 65 gymnosperms (/softwoods), 8 monocotyledons and 377 dicotyledons angiosperms (with 268 tropical, and 104 temperate hardwoods). The nomenclature of species was checked in order to assign them up-to date valid

botanical name. Their classification was recorded both in the classical system and in the phylogenetic one according to the APG (Angiosperm Phylogeny Group, [9]) families and orders. The 445 compiled species belonged to 237 genera from 69 APG families.

Results and discussion

Properties distribution and relations

Across the 445 compiled species, damping coefficient ($\tan\delta$) ranged from 3.7 to 20 ‰. Its variations were roughly related (see Fig 2) to specific modulus of elasticity (E'/ρ) in a way very similar to the “standard” relationship established by Ono and Norimoto [10,11]. Though, this relation described less than 40% of actual variations in $\tan\delta$. However, in order to compare specifically the damping characteristics of taxa, it is necessary to de-correlate them from E'/ρ . This could be achieved by using two indicators: the specific loss modulus (E''/ρ) which is a mechanical property in itself (equation 1) or the deviation from standard damping ($\Delta\tan\delta$), a simple statistical indicator defined in equations (2) and (3), where $\tan\delta_s$ is the standard trend reported by [10].

$$E''/\rho = \tan\delta \times (E'/\rho) \quad (1)$$

$$\Delta\tan\delta = 100 \times \frac{\tan\delta_i - \tan\delta_s}{\tan\delta_s} \quad (2) \text{ with: } \tan\delta_s = 10^{-1.23} \times (E'/\rho)^{-0.68} \quad (3)$$

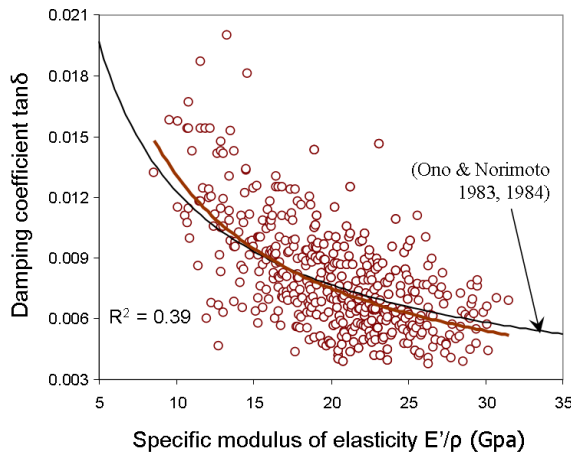


Fig. 2 Relationship between damping coefficient and dynamic specific modulus of elasticity. Each point is the mean of one species, N=445.

The collected set of species sounded quite representative, as the mean values (see Table 1) of specific gravity (ρ) and of E'/ρ across the 445 studied species are very close to those reported on bigger numbers of species: 0.73 for the mean specific gravity of 3805 species [12], 21.7 for the mean E'/ρ of 870 species [13]. Variations in specific modulus and damping coefficient were not related to those in specific gravity. Concerning characteristic damping indicators, “normalized damping” ($\Delta\tan\delta$) much better explained actual damping coefficient than E''/ρ did, thus, further analyses will make use of this indicator.

Table 1 Basic statistics of dynamic mechanical properties and specific gravity across the 445 studied species: Pearson’s correlation coefficients between properties (top rows), and mean values and range (bottom rows).

N=445	ρ	E'/ρ	$\tan\delta$	$\Delta\tan\delta$	E''/ρ
ρ	1				
E'/ρ	0.00	1			
$\tan\delta$	-0.19	-0.62	1		
$\Delta\tan\delta$	-0.26	-0.12	0.83	1	
E''/ρ	-0.26	0.20	0.60	0.95	1
		(GPa)	(‰)	(%)	(Mpa)
mean	0.72	20.1	8.1	+1	154
min	0.18	8.6	3.7	-55	59
max	1.33	31.5	20.0	+97	284

Properties variations between botanical families

Across 20 APG families represented by at least 5 species (from at least 3 genera), the mean values and the ranges of variations in normalized damping, and in specific Young's modulus, clearly fluctuated (see Fig. 3). Though, the ranges most often overlapped between families, and the fluctuations in mechanical properties did not appear to be easily linked to evolutionary patterns as roughly described by an arrangement according to the APG phylogeny tree – at least at the family level and with the present number of represented species. Yet, some families (or sub-families) had nearly systematically lower (e.g. Fabaceae-Papilionoideae, Lauraceae) or higher (e.g. Betulaceae, Sapindaceae) damping than average. Few families had ranges in E'/ρ clearly departing from the global mean value. However, discrepancies in sample size make it difficult to check out the significance of any apparent differences. In this scope, we further isolated 13 families represented by at least 10 species belonging to at least 3 genera (see Fig. 4).

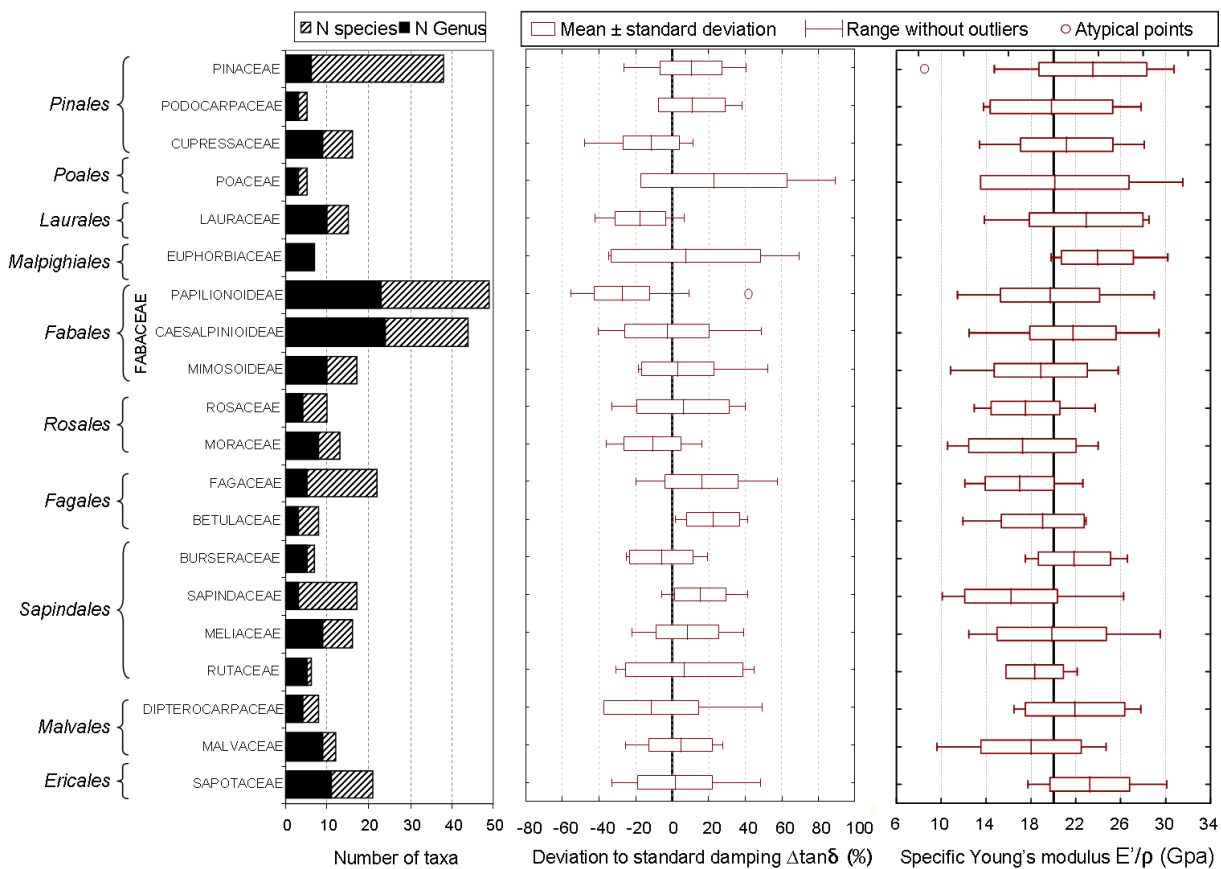


Fig. 3 Ranges of variations in normalized damping $\Delta \tan \delta$ and in specific modulus of elasticity E'/ρ for 20 APG families represented by at least 5 species from at least 3 genera. Families are roughly arranged vertically according to phylogenetic trees from [APG]. Bold lines represent the mean value of $\Delta \tan \delta$ and of E'/ρ on 445 species.

Some families had significantly different damping coefficient (Fig. 4a) from several others: Fabaceae-Papilionoideae had a lower $\tan \delta$ than $\frac{3}{4}$ of other studied families, Lauraceae followed a similar trend but with less numerous significant differences. In contrast, Sapindaceae and Fagaceae had significantly higher $\tan \delta$ than at least half of other families. These trends must be compared with specific modulus of elasticity (Fig. 4b): Fab-Papilionoideae were here not different from the mean, while Fagaceae and Sapindaceae had the lowest E'/ρ (statistically different from one third of other families). There were less numerous significant differences between families in E'/ρ than in $\tan \delta$. Pinaceae were the most clearly different in terms of higher E'/ρ (followed by, in a lesser extent, Sapotaceae and Lauraceae). As a result, although $\tan \delta$ of Pinaceae was within the global average, it was in fact significantly higher than standard (Fig. 4c), while the low $\tan \delta$ of Lauraceae resulted both from a high E'/ρ and from an intrinsically lower “viscosity”. On the other hand, the high damping

coefficient of Sapindaceae and Fagaceae resulted not only from their low E'/ρ but also from a significantly more viscous nature than usual. The sub-family Papilionoideae was an interesting case as its specific modulus of elasticity was strictly within average, while having the lowest and most atypical damping, independently of E'/ρ . It is also interesting to note the differences between the sub-families Papilionoideae and Caesalpinioideae, although the latter contains some species with notoriously low damping due to secondary metabolites [4], but its range extends from very low to quite high $\tan\delta$ and $\Delta\tan\delta$. Maybe the common presence [9] of secondary metabolites from the isoflavonoids group in the Papilionoideae would be of significance concerning their very low damping? Incidentally, the inclusion of the tribe Swartziae (which had been formerly described as basal between the two sub-families [14]) in the Papilionoideae rather than in the Caesalpinioideae plays a clear role in the observed differences between them. This also suggests that further analysis at sub-family levels (tribes, genera, when enough data are available) could bring more detailed understanding of the observed differences.

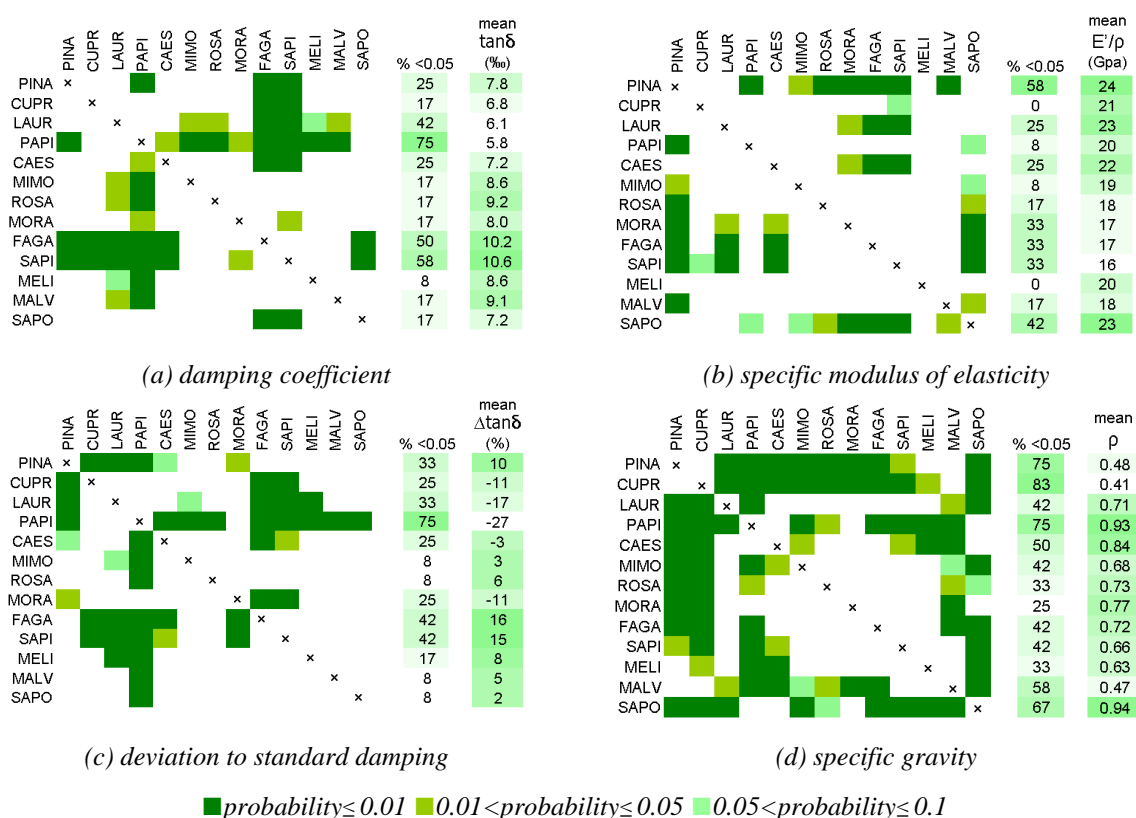


Fig. 4 One-to-one significance of differences in properties between 13 families represented by at least 10 species from at least 3 genera. ANOVA with Post-Hoc HSD Tukey test.

Finally, specific gravity (Fig. 4d) better discriminated families overall, but when considering only angiosperms, damping offered nearly as good distinctions. Yet, comparison of the scheme for dynamic mechanical properties and for specific gravity shows that differences between families follow different patterns depending on wood properties, presumably reflecting different levels of morphological and biochemical markers. Specific gravity basically reflects cellular organization (i.e. cell-walls to void ratios) with possible additional contribution of incrustated secondary metabolites (e.g. for several Papilionoideae, here). E'/ρ should result principally from cell-wall elastic properties (with strong influence of microfibril angles) but also to some aspects of cellular and tissue arrangement (ratios of fibres to other cellular types, fibres deviations/patterned grain). $\Delta\tan\delta$ should mostly reflect variations in chemical composition able to modify viscous behaviour. Thus, further steps for extending the present analysis should involve the compilation of such morphological and biochemical markers in order to interrelate them with dynamic mechanical properties.

Conclusion

This work was a first insight into the possible relations between species classification and wood dynamic mechanical properties, relying on an extensive data compilation on these properties. First analyses revealed that:

- The “standard” relation reported in the literature between damping coefficient ($\tan\delta$) and specific modulus of elasticity (E'/ρ) was corroborated at interspecific level on a large scale, but explained less than 40% of actual variations.
- Ranges in dynamic mechanical properties fluctuated between botanical families, but trends were not directly linked to phylogenetic trees at this level. Families were apparently better discriminated according to damping than to E'/ρ .
- Some families had nearly systematically lower intrinsic damping than average: Fabaceae-Papilionoideae, and in a lesser extent Lauraceae, Cupressaceae and Moraceae.
- On the contrary, Fagaceae, Betulaceae and Sapindaceae had higher damping than average. Despite their higher E'/ρ , Pinaceae also tended to have higher damping than standard.

Our results confirmed that dynamic mechanical properties are probably affected by some morphological and/or biochemical taxonomic markers. Further analyses should thus involve data compilation of such markers in order to interrelate them to properties. Analyses at sub-family levels should also prove useful in better describing the repercussion of biodiversity on wood properties.

Acknowledgements

This work has been supported by a Post-Doctoral fellowship from Japan Society for the Promotion of Science.

References

1. Obataya, E., T. Ono and M. Norimoto (2000). "Vibrational properties of wood along the grain." *Journal of Materials Science* 35:pp 2993-3001.
2. Brémaud, I., P. Cabrolier, J. Gril, B. Clair, J. Gérard, K. Minato and B. Thibaut (in press). "Identification of anisotropic vibrational properties of Padauk wood with varying grain angle." *To be published in Wood Science and Technology*.
3. Yano, H. (1994). "The changes in the acoustic properties of Western Red Cedar due to methanol extraction." *Holzforschung* 48(6):pp 491-495.
4. Minato, K., K. Sakai, M. Matsunaga and F. Nakatsubo (1997). "The vibrational properties of wood impregnated with extractives of some species of Leguminosae (Preliminary report)." *Mokuzai gakkaiishi* 43(12):pp 1035-1037.
5. Sakai, K., M. Masahiro, K. Minato and F. Nakatsubo (1999). "Effects of impregnation of simple phenolics and natural polycyclic compounds on physical properties of wood." *Journal of Wood Science* 45:pp 227-232.
6. Obataya, E., T. Umezawa, F. Nakatsubo and M. Norimoto (1999). "The effects of water-soluble extractives on the acoustic properties of reed (*Arundo donax* L.)." *Holzforschung* 53(1):pp 63-67.
7. Brémaud, I., B. Thibaut and K. Minato (2007). "A database linking woody species, vibrational properties, and uses in musical instruments of the world". ISMA (International Symposium on Musical Acoustics) 2007, 9-12 September 2007. Barcelona, Spain.
8. Brémaud, I. (2006). "Diversité des bois utilisés ou utilisables en facture d'instruments de musique. -Etude expérimentale des propriétés vibratoires en direction axiale de types de bois contrastés en majorité tropicaux. -Relations à des déterminants de microstructure et de composition chimique secondaire." Doctorat en Mécanique des Matériaux. Université Montpellier II. 302 p.

9. Stevens, P. F. (2001 onwards, 04 July 2009). "Angiosperm Phylogeny Website. Version 9, June 2008 [and more or less continuously updated since]." from <http://www.mobot.org/MOBOT/research/APweb/>.
10. Ono, T. and M. Norimoto (1983). "Study on Young's modulus and internal friction of wood in relation to the evaluation of wood for musical instruments." *Japanese journal of Applied physics* **22**(4):pp 611-614.
11. Ono, T. and M. Norimoto (1984). "On physical criteria for the selection of wood for soundboards of musical instruments." *Rheologica Acta* **23**:pp 652-656.
12. Détienne, P. and B. Chanson (1996). "L'éventail de la densité du bois des feuillus. Comparaison entre différentes régions du Monde." *Bois et Forêts des Tropiques* **250**(4):pp 19-30.
13. CIRAD « Base de données de propriétés technologiques de bois tropicaux" *Unpublished working resource*.
14. Angyalossy-Alfonso, V. and R. B. Miller (2002). "Wood anatomy of the Brazilian species of *Swartzia* and considerations within the tribe Swartzieae." *IAWA Journal* **23**(4):pp 359-390.

About structural determinants of the diversity of vibration properties of ten tropical hardwoods

Jana Dlouhá^{1,2}, Tancrède Alméras¹, Bruno Clair¹ and Joseph Gril¹

¹ Laboratoire de Mécanique et Génie Civil (LMGC), Université Montpellier 2, CNRS UMR-5508, cc 048 – Place Eugène Bataillon, 34095 Montpellier Cedex 5 France; ²Mendel University of Agriculture and Forestry in Brno (MZLU v Brně), Department of Wood Science, Zemědělská 3, Brno, 602 00 Czech Republic

Abstract

Diversity of vibration properties of ten tropical hardwoods covering wide range of densities and anatomical structures was investigated. Wood from tilted trees was included in the study to examine the intraspecific diversity along with the interspecific one. Moreover, the relation with structural parameters (basic density, microfibril angle) was studied. While the variability of the elastic modulus was in great part explained by the variations of basic density and microfibril angle, damping coefficient was not correlated to structural parameters. This was particularly true for reaction woods and therefore attributed to the intensive loading history likely leading to the formation of micro-cracks.

Introduction

Tropical rainforests represent highly competitive environments characterised by high density of stems, closed forest canopy and limited light availability. Numerous strategies have been developed by trees to survive in the forest until their reproductive maturity. Different growth dynamics result in different mechanical requirements during each stage of the tree life. Consequently, wood of tropical species represents a great variety of structural features and mechanical properties comparing to temperate ones. Studying tropical diversity is a good opportunity to bring some new highlights on the relation between wood properties and structures and investigate a possibility of trade-offs between different functions to be ensured during a tree life as well as the relation to ecological strategies.

In this study, we focused on the diversity and variability of structures and properties of wood from trees in juvenile stage (saplings) where the competition for height growth is a critical constraint. Diversity is present at several levels. The interspecific diversity comes from the choice of representative examples of different growth strategies and intraspecific diversity from differences in site conditions and growth history. Radial variability inside a single tree results from likely juvenile transition (it is difficult to know the age of trees in a tropical canopy and decide about the juvenility of such trees) and circumferential variability from occurrence of reaction tissues. Leaning trees included in the study represent very interesting material to investigate the limits of tree performances as well as limits of wood acclimation. Describe the variability of wood properties and structures and search for a connection with the growth strategy or site conditions is the first step of the study.

Usually, structure-properties relations are applied either to large sample of species with reduced intraspecific variability or to investigate intraspecific variability of some reduced number of commercial species. Studies including both types of variability, interspecific as well as intraspecific are scarce. Therefore, it can be interesting to investigate the general validity of these relations.

Material and methods

Ten tropical species were selected among common species of the tropical rainforest in French Guyana. Species were chosen in function of their growth strategy according to the Favrichon's ranking based on the species shade tolerance [1]. The study focused on properties of trees in juvenile transition. Diameter of trees at the breast height ranged between 4 and 7 cm. To maximise the interspecific variability, selection covered wide range of basic densities inside each growth strategy group. Concerning the intraspecific variability, the aim was to cover all wood types – normal wood as well as tension and opposite wood. For that reason, tilted trees with expected occurrence of reaction wood were also included in the study. Checking for occurrence of tension wood by anatomical observation was impossible considering the number of specimens (550) and also the fact that in some species as for example *V. michelii*, anatomical feature of tension wood does not exhibit any apparent difference relative to the normal wood [2]. Therefore, the mechanical definition considering tension wood as tissues characterised by high level of maturation stress was used. Some basic information about studied species along with the used abbreviations are summarised in *Table 1*.

Table 1 Summary table of some basic properties of studied species

Scientific name	Abreviation	Growth strategy	Specific gravity	Elastic modulus (MPa)
<i>Goupia glabra</i> Aubl.	Gg	Heliophilic	0.84	14 670
<i>Tachigali melinonii</i> (Harms) Barneby	Tm	Heliophilic		
<i>Virola michelii</i> Heckel	Vm	Heliophilic	0.57	10 072
<i>Dicorynia guyanensis</i> Amsh.	Dg	Hemi tolerant	0.79	14 799
<i>Eperua grandiflora</i> (Aubl.) Benth.	Eg	Hemi tolerant	0.92	16 824
<i>Licania alba</i> (Bernoulli) Cuatrec.	La	Tolerant	1.06	
<i>Lecythis persistens</i> Sagot	Lp	Tolerant	0.72	12 361
<i>Gustavia hexapetala</i> (Aubl.) J.E. Smith	Gh	Understorey	0.78	
<i>Oxandra asbeckii</i> (Pulle) R.E. Fries	Oa	Understorey	0.90	
<i>Pogonophora schomburgkiana</i> Miers ex Benth.	Ps	Understorey	1.05	

Specimens for vibration measurements were cut along the fibre direction (150 x 12 x 2mm, L x R x T) and stored in water at low temperatures ($T = 4 \pm 0.1^\circ\text{C}$). Before the measurement, samples were put out of the fridge to reach the room temperature and individual specimens were taken out from the water just before the measurement. Dynamic Young's modulus and damping coefficient in the longitudinal direction were determined by free-free flexural vibration method at the resonance frequency corresponding to the first vibration mode. Resonance frequency ranged from 200 to 650Hz. The damping coefficient was determined by half bandwidth method of the resonance frequency peak. Microfibril angle has been measured by X-Ray diffraction (XRD). As the specimens are not thick, we could directly use the damping specimens. The average MFA of each specimen was estimated by the "improved Cave's method" according to Yamamoto et al. [3].

Results and discussion

In the current study, we investigated the interspecific and intraspecific diversity of vibration properties of ten tropical hardwoods in the green state. According to Ono and Norimoto [4], results of vibration tests are represented in double logarithmic scale. Interspecific diversity is displayed in *Fig 1*. The same measurements are represented in *Fig 2* but this time in function of different wood types. We can see that both inter and intraspecific diversity affects significantly the vibration properties. Linear relationship is significant for all species excepting *Lp* however significant differences can be observed between species. Considering the effect of the wood type, we can note that both reaction woods *i.e.* the tension as well as opposite wood exhibit higher damping coefficient than normal wood for the same specific modulus. In the following, relationship between parameters usually considered to be

determinant for vibration properties (basic density, MFA) will be investigated in order to assess their capacity to explain the observed variability.

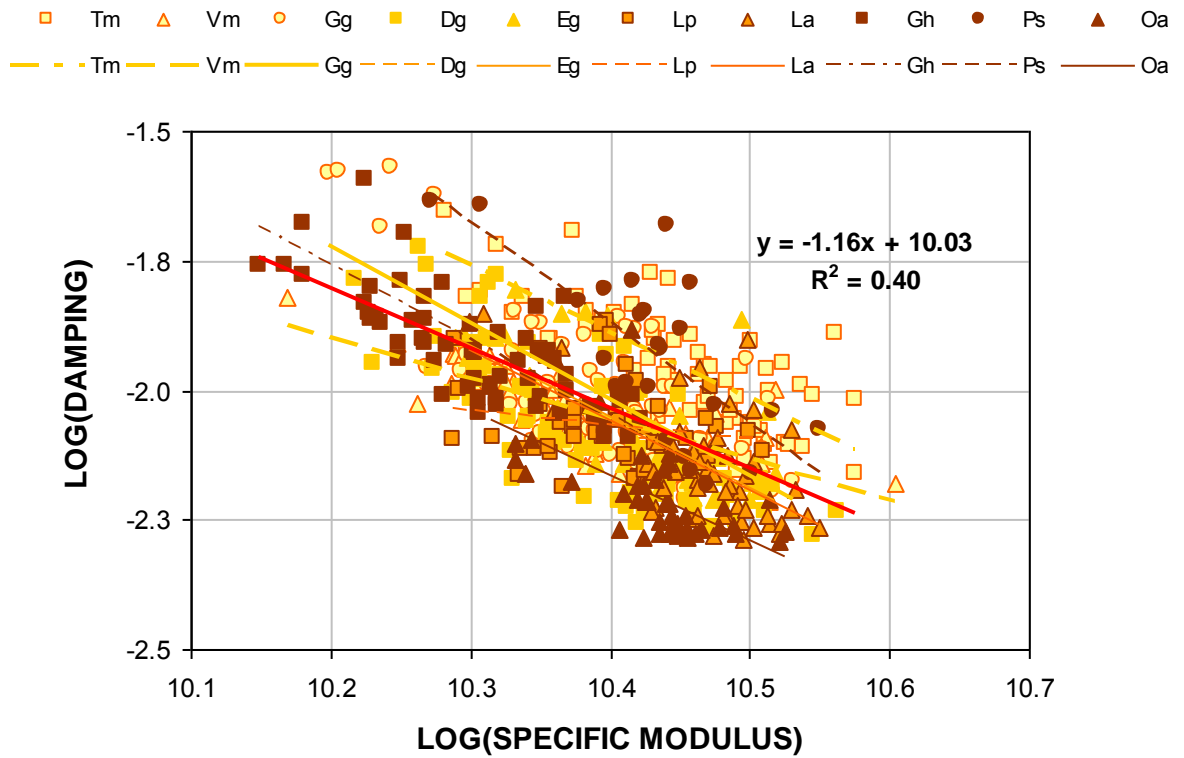


Fig. 1 Interspecific diversity of vibration properties in double logarithmic scale. See Table 1 for the species abbreviations.

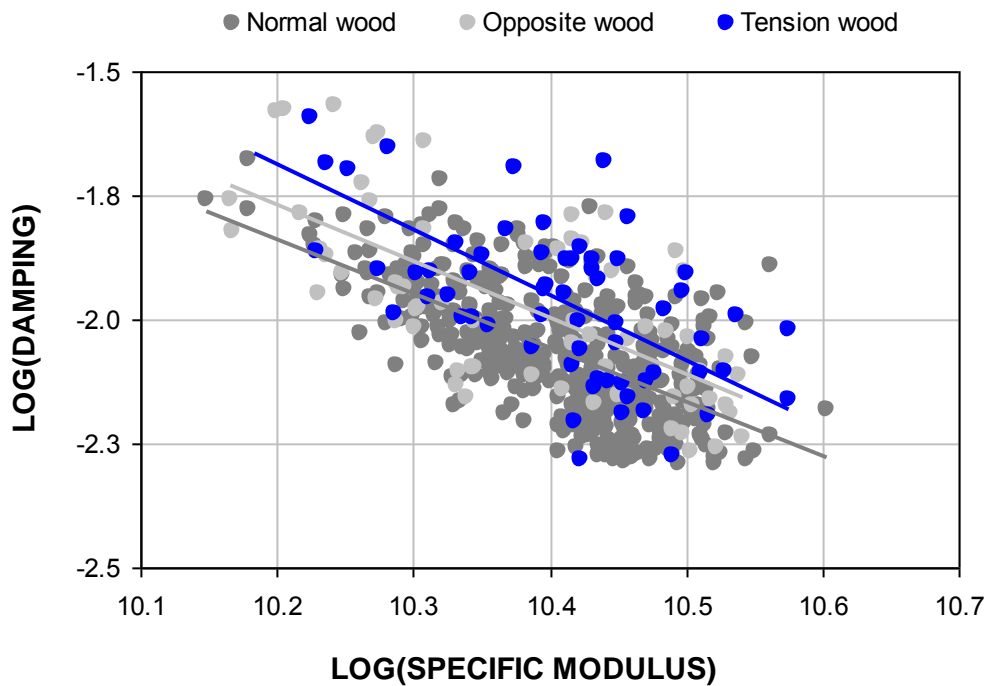


Fig. 2 Intraspecific diversity of vibration properties in double logarithmic scale. NW: normal wood, TW: tension wood; OW: opposite wood.

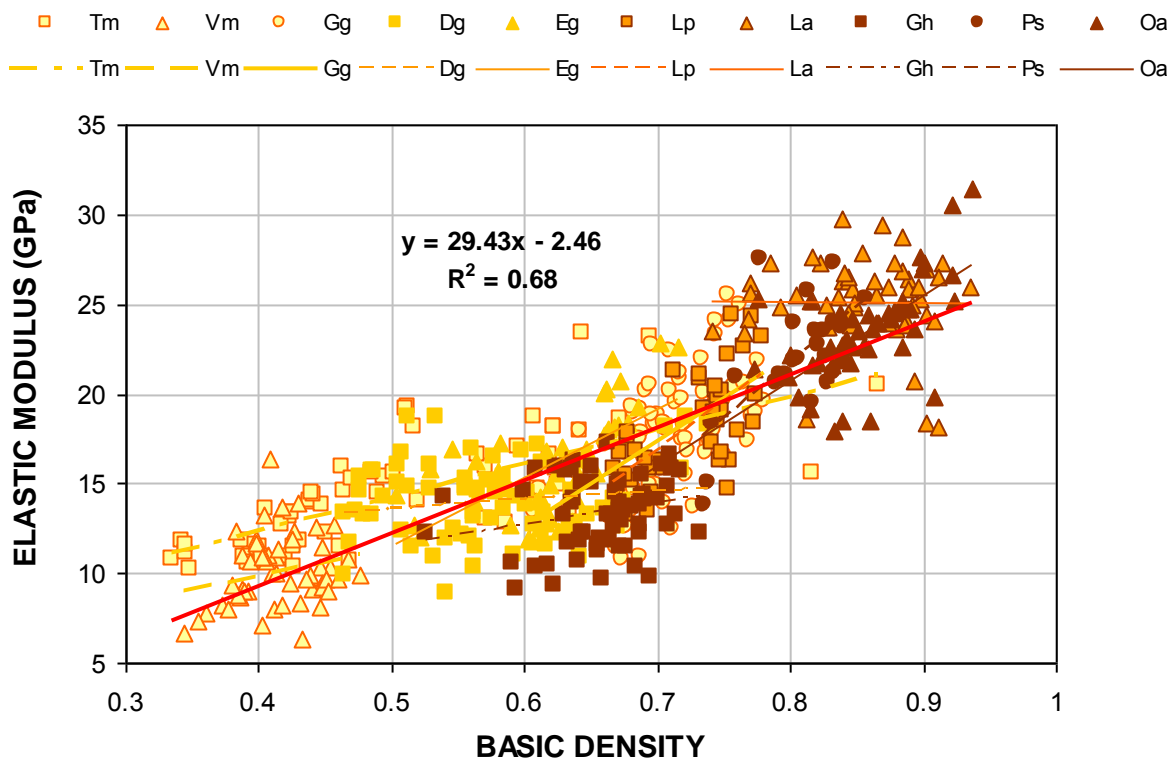


Fig. 3 Relationship between elastic modulus and basic density. See Table 1 for the species abbreviations.

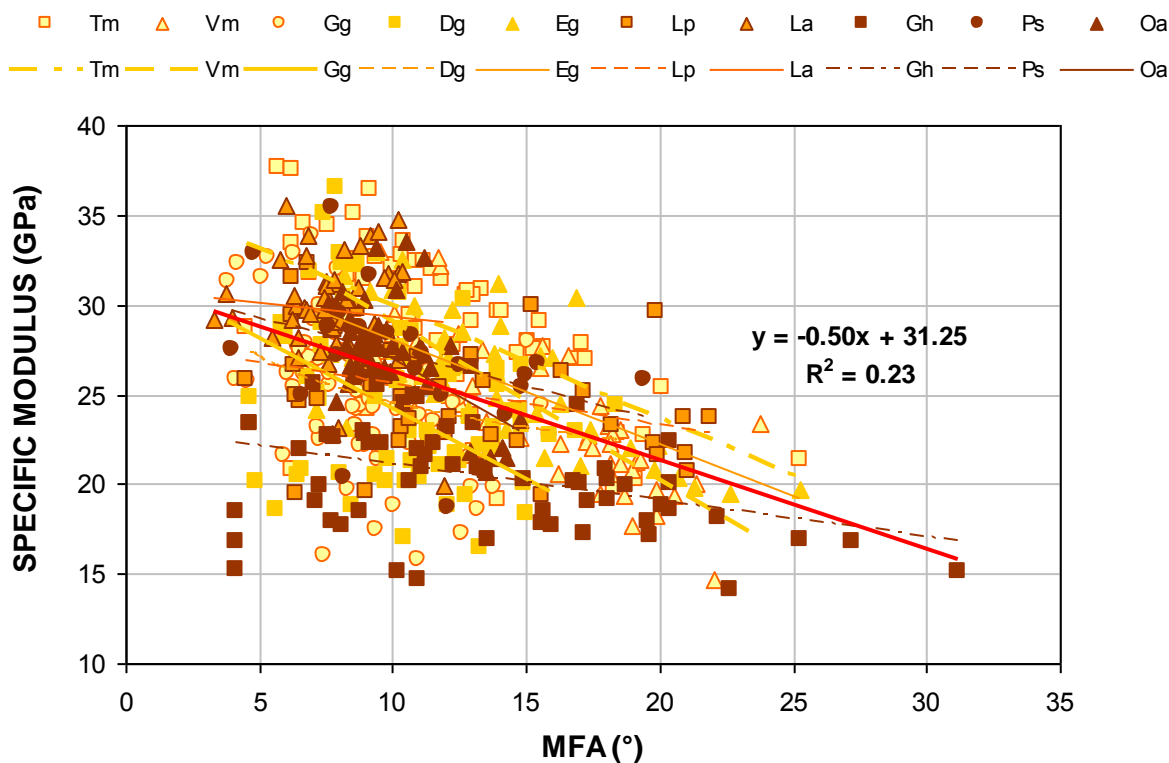


Fig. 4 Relationship between specific modulus and microfibril angle. See Table 1 for the species abbreviations.

Elastic modulus of a cellular solid such as wood is expected to be strongly related to its density. Indeed, strong relation between both parameters is observed, explaining 68% of the elastic modulus variability as we can see from Fig 3. The remaining variability is generally ascribed to the MFA variations. Thus, relationship between the specific modulus (ratio of elastic modulus and basic density) and MFA is represented in Fig 4. The correlation coefficient is considerably lower ($R^2 = 0.23$)

indicating that MFA is not the only parameter affecting the specific cell wall modulus. Large scatter of specific modulus values is observed in particular for low MFAs. This is probably due to the occurrence of tension wood exhibiting variable fibre ultra-structure along with different chemical composition compared to normal wood. Fig 5. shows the relationship between damping coefficient and microfibril angle. No significant relationship can be detected which was unexpected considering some previous reports [5, 6]. In addition, no intraspecific relations were significant (not shown). Thus, we face a paradox: while damping coefficient is significantly related to the specific modulus which one is generally thought to be determined by MFA, damping coefficient itself is not related to MFA on our sample.

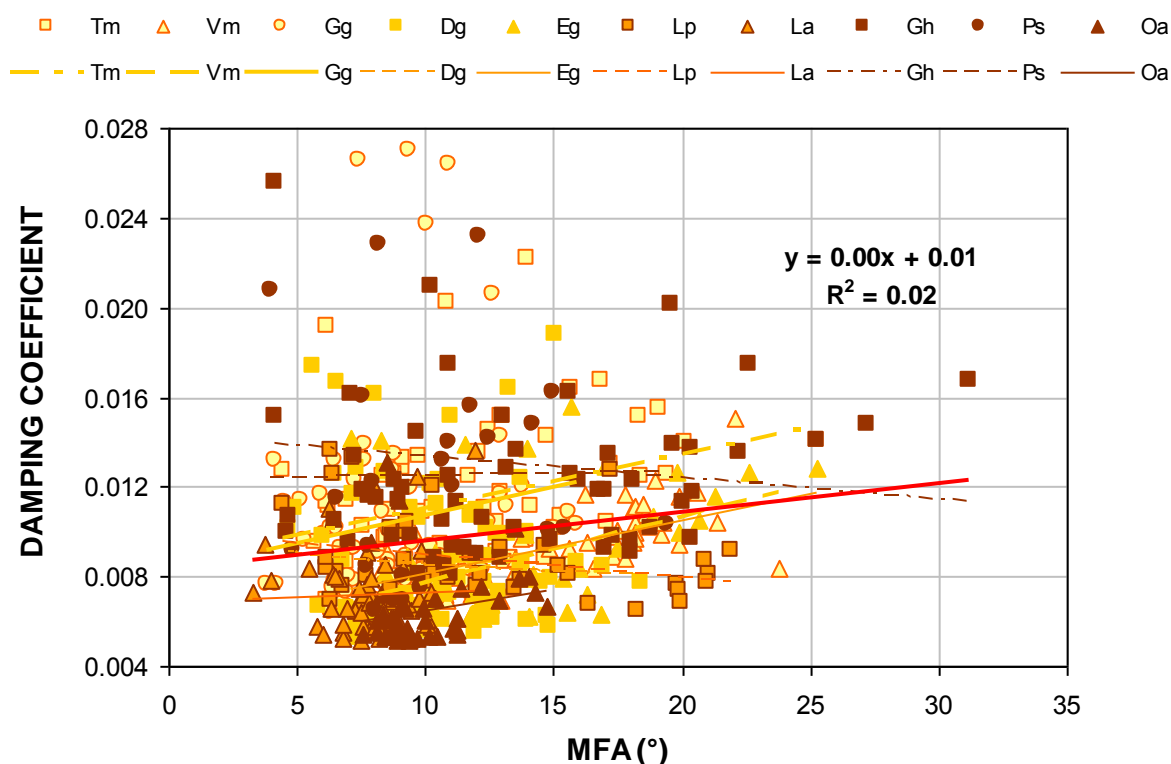


Fig. 5 Relationship between damping coefficient and microfibril angle. See Table 1 for the species abbreviations.

While investigating the wood type dependency of the damping coefficient-MFA relation, we can see that the variability of the damping coefficient is considerably higher for reaction (*i.e.* tension and opposite) woods than for normal wood as we can see from Fig 6. While damping coefficient of normal wood slightly increases with the increase of MFA following the theoretical relation, no tendency can be observed for reaction woods. This clearly shows that MFA is not a relevant parameter to describe the intraspecific variability of damping coefficient.

If mean values for each wood type are considered, opposite wood and tension wood shows nearly the same damping coefficient regardless different specific modulus. The damping coefficient of reaction woods is higher than that of normal wood (not shown). Considering the loading history of reaction woods produced by tilted trees that they try to pull up to the vertical position, it could be due to the mechanical fatigue of reaction tissues leading to the formation of micro-cracks. Such micro-cracks would dissipate more energy during a vibration test leading to higher damping coefficient. If this effect is large enough to dominate the difference of specific moduli, it may also explain the same damping coefficient observed for both reaction tissues regardless their different structure and chemical composition as well as higher damping coefficient in tension wood compared to normal wood unexpected at least in the case of tension wood exhibiting G-fibres (higher cellulose content and lower hemicelluloses and lignin contents).

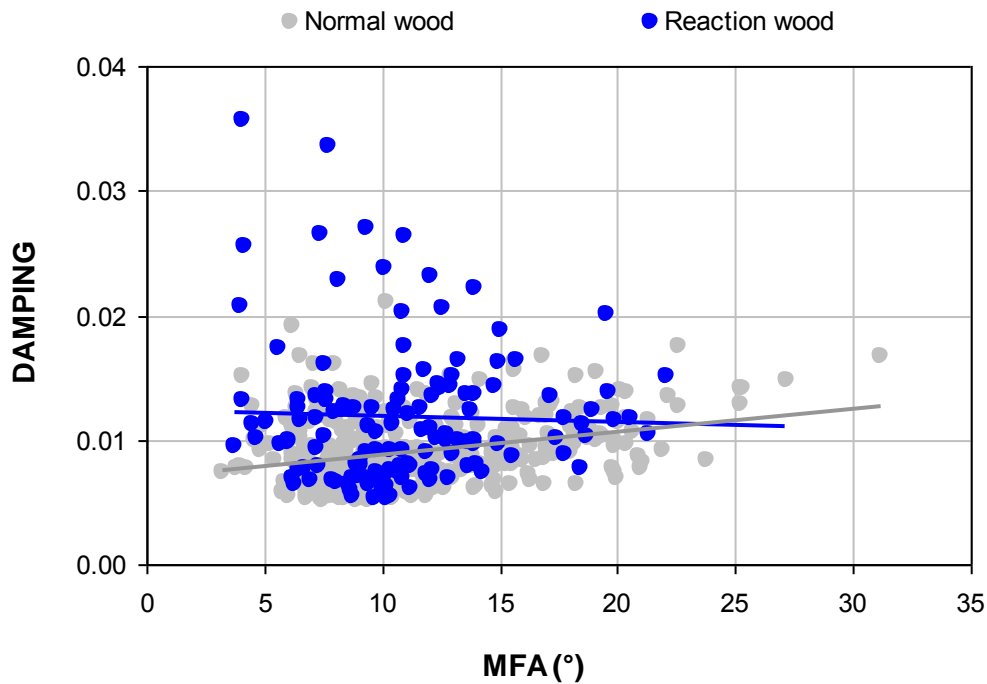


Fig. 6 Wood type dependency of the relationship between damping coefficient and microfibril angle. RW: reaction (tension + opposite) wood; NW: normal wood.

Conclusion

Diversity of the vibration properties of ten tropical hardwoods has been investigated. Excepting *L. persistens*, all species and wood types exhibited strong relationship between the damping coefficient and specific modulus. While 68% of the elastic modulus' variability has been explained by the basic density variations only 23% of the specific modulus variability has been explained by the MFA variations. Damping coefficient of normal wood was slightly correlated to the MFA while damping coefficient of reaction woods was found to be independent of MFA and higher than in normal wood. This finding was attributed to mechanical fatigue of reaction tissues likely leading to the formation of micro-cracks.

References

1. Favrichon, V. (1994): *Classification of Guiana forest tree species into functional groups for a dynamic community matrix of vegetation*. *Revue d'Ecologie*, 49 (4): p. 379-403.
2. Chang, S.-S., et al. (2009): *Mesoporosity as a new parameter for understanding tension stress generation in trees*. *J. Exp. Bot.*: p. erp133.
3. Yamamoto, H., T. Okuyama, and M. Yoshida (1993): *Method of determining the mean microfibril angle of wood over a wide range by the improved Cave's method*. *Mokuzai Gakkaishi*, 39(4): p. 375-381.
4. Ono, T. and M. Norimoto (1984): *On physical criteria for the selection of wood for soundboards of musical instruments*. *Rheologica acta*, 23: p. 652-656.
5. Brémaud, I. (2006): *Diversité des bois utilisés ou utilisables en facture d'instruments de musique. Etude expérimentale des propriétés vibratoires en direction axiale de types de bois contrastés en majorité tropicaux. Relations à des déterminants de microstructure et de composition chimique secondaire* Thesis of Université de Montpellier 2.
6. Norimoto, M., et al. (1986): *Specific dynamic Young's modulus and internal friction of wood in the longitudinal direction*. *Wood research and technical notes*, 22: p. 53-65.

Author index:

Aimene, Yamina	89	Courrech-Dupont, Sylvain	421
Albert, Levente	504	Coutand, Catherine	19, 47, 349
Al-Haddad, Jameel	164, 477	Couturier, Etienne P.	421
Alméras, Tancrede	75, 163, 228, 236, 314, 349, 542	Cuartero, Jesús	212
Amusant, Nadine	528	Darnige, T.	322
Angeles, Guillermo	156	de Bruyn, Gerd	398
Angyalossy, Veronica	156	de Langre, Emmanuel	59, 101
Arakawa, Y.	297	Decourteix, Mélanie	19
Argentina, Médéric	179	Derome, Dominique	53, 489
Arinero, Richard	228	Ditsch, Friedrich	202
Arnould, Olivier	228, 497	Dlouhá, Jana	542
Bag, Rahime	273	Dole, Patrice	273
Barbacci, Adelin	306	Domínguez, Eva	212
Báscones, Esther	335	Douady, Stéphane	11, 421
Bassman, Lori	67	Duchateau, Emmanuel	349
Bastien, Renaud	11	Dumais, Jacques	179
Bauer, Georg	194, 367, 482	Dupont, Sylvain	116
Beauchêne, Jacques	279, 497	Eberle, Annika	67
Beaugrand, Johnny	273	Elbaum, Rivka	244
Boiffin, Juliette	163	Endo, Yasuhiro	187
Boizard, Sophie D.	110, 463	España, Laura	212
Bonal, Damien	89	Ewers, Frank W.	164
Borodich, Feodor M.	176	Faraj Pour, Arash	350
Bou Daher, Firas	40	Fleck, Claudia	406
Boudaoud, Arezki	2	Fourcaud, Thierry	95
Boutahar, N.	528	Fournier, Meriem	163, 306, 314, 349, 487
Brancheriau, Loïc	285, 456	Fratzl, Peter	202, 343
Brémaud, Iris	535	Gallenmüller, Friederike	194
Brunel, Nicole	47	Gallet, Philippe	285
Brunet, Yves	116, 131	Gebeshuber, I.C.	374
Bührig-Polaczek, Andreas	406	Geitmann, Anja	40, 218
Burgert, Ingo	202, 259, 343	Genet, P.	322
Bytebier, Karl	228	Ghestem, Murielle	450
Cabrolier, Pierre	75, 279	Gorb, Elena V.	176
Cao, Kunfang	450	Gorb, Stanislav N.	27, 176, 194, 211
Carmeliet, Jan	53, 489	Gosselin, Frédéric	101
Chaix, G.	528	Gray, Derek G.	439
Clair, Bruno	228, 236, 289, 297, 349, 469, 497, 542	Gril, Joseph	297, 328, 542
Cochard, Hervé	47	Gruber, Petra	412
Collet, Catherine	487	Guillon, Thomas	95
Constant, Thiéry	306, 487	Guyer, Robert	489
Corson, Francis	2	Hamant, Olivier	2
Couder, Yves	2	Harrington, Matthew J.	202
		Hartmann, C.	322

Hémon, Pascal	131	Ménard, Léa	469
Heredia, Antonio	212	Minato, Kazuya	535
Hernández, Luis F.	3	Mine, François-Xavier	456
Hofmann, Tamás	504	Mitchell, Stephen J.	110, 463
Hounzandji, Paul Igor A.	487	Moullia, Bruno	11, 19, 59, 335
Isnard, Sandrine	163	Mühlen, Gilda	469
Jaouen, Gaëlle	349	Neinhuis, Christoph	202
Jeronimidis, George	47	Nellesen, Anke	367
Julien, Jean-Louis	19	Nepveu, Gérard	306
Jullien, Delphine	75, 236	Niemz, Peter	504, 521
Kappel, Roland	382	Noblin, Xavier	179
Keunecke, Daniel	521	Palin, Robert	265
Khademi Eslam, Habibollah	350	Pando, Valentín	335
Kinosita, Eichiro	187	Patino, Sandra	163
Kizilova, Natalya N.	148	Peñalvo, Alejandro	335
Knippers, J.	389	Pierce, Jeffrey A.	164
Kojima, Miho	75	Pilate, G.	236
Kokutse, Adzo Dzifa	528	Popper, Rudolf	504
Kolb, Evelyne	322	Poppinga, S.	389
Konrad, Wilfried	32	Pritchard, Jeremy	265
Kraft, Oliver	205, 444	Quartier, L.	322
Kubinski, Kirk-René	194	Quilliet, Catherine	170
Kurek, Bernard	273	Quinn, Kenny	67
Lachenbruch, Barbara	513	Rétfalvi, Tamás	504
Lasaygues, Philippe	285	Riekkel, C.	236
Leblanc-Fournier, Nathalie	19	Rodriguez, Mathieu	59
Lecoq, L.E.	322	Rojas, Nicolas	179
Lenne, Catherine	19	Roth-Nebelsick, Anita	32
Liehr, Andreas W.	482	Roux, Pascal	116
Lienhard, J.	389	Rowe, Nick	289, 469
Lintilhac, Philip M.	251	Ruelle, Julien	289, 297
Logvenkov, S.A.	140	Rüggeberg, Markus	259
Lucate, Joshua G.	439	Sakamoto, Jiro	187
Ludwig, Ferdinand	398	Schleicher, S.	389
Ma, Wenzhang	450	Schwaiger, Ruth	205, 444
Madero-Vega, Carolina	156	Seidel, Robin	205, 406
Magnenet, Vincent	306	Sellier, Damien	116
Majlis, B.Y.	374	Sengespeick, Andreas	367
Mansfield, Shawn	477	Shilina, Julia	121, 168
Marmottant, Philippe	170	Sierra-de-Grado, Rosario	335
Martin, Ludovic	19	Sober, Anu	121, 168
Martínez-Zurimendi, Pablo	335	Speck, Olga	482
Masselter, Tom	357, 389, 431	Speck, Thomas	194, 205, 259, 357, 367, 389, 398, 406, 431, 444, 482
Mattheck, Claus	83, 382	Stachelberger, H.	374
McKey, Doyle	469	Stahl, Clément	89
McLean, J. Paul	497	Stein, Alexander A.	140
Meinzer, Frederick C.	513		
Melzer, Björn	205, 444		

Steinbrecher, Tina	205, 444
Stokes, Alexia	450, 456
Strauss, Steven H.	513
Sugiyama, Junji	236, 328
Telewski, Frank W.	164,477
Tesari, Iwiza	83
Thaunay, Patrice	285
Thibaut, Bernard	89, 279, 535
Thielen, Marc	398
Thomas, Colin	265
Traas, Jan	2
Vincent, Olivier	170
Voelker, Steven L.	513
Voigt, Dagmar	194, 211
Wang, Yue	328
Wei, Chungfang	251
Westbrook, Jared	179
Xie, Jianlei	450
Yamamoto, Hiroyuki	75, 289, 297
Yoshida, M.	297
Yudina, E.N.	140
Zillig, Wolfgang	53